

## 中国石油大学（北京）

### 2025 年申报硕士研究生指导教师评审材料目录


申报人姓名	王瑶	申报学科专业	材料与化工
序号	送审材料名称		
1	第一作者发表论文— <i>Nature Communications</i>		
2	第一作者发表论文— <i>Advanced Materials</i>		
3	第一作者发表论文— <i>Advanced Energy Materials</i>		
4	第一作者发表论文— <i>Chemical Reviews</i>		
5	第一作者发表论文— <i>Advanced Functional Materials</i>		
6	第一作者发表论文— <i>eScience</i>		
7	第一作者发表论文— <i>Journal of Power Sources</i>		
8	共同通讯作者发表论文— <i>Energy Materials and Devices</i>		
9	共同第一作者发表论文— <i>Journal of Power Sources</i>		
10	第一作者发表论文— <i>ACS Applied Energy Materials</i>		
11	第一作者发表论文— <i>Corrosion Science</i>		
12	检索证明		
13	主持国家级项目—国家自然科学基金-青年科学基金项目（C类）		
14	主持省部级项目—博士后国（境）外交流项目—引进项目		
15	主持省部级项目—中国博士后科学基金面上项目		
16	主持校级项目—中国石油大学（北京）优秀青年学者项目		

# Di fluoro ester solvent toward fast-rate anion-intercalation lithium metal batteries under extreme conditions

Received: 12 January 2024

Accepted: 13 June 2024

Published online: 26 June 2024

 Check for updatesYao Wang<sup>1,3</sup>, Shuyu Dong<sup>2,3</sup>, Yifu Gao<sup>1</sup>, Pui-Kit Lee<sup>2</sup>, Yao Tian<sup>1</sup>, Yuefeng Meng<sup>1</sup>, Xia Hu<sup>1</sup>, Xin Zhao<sup>1</sup>, Baohua Li<sup>1</sup>✉, Dong Zhou<sup>1</sup>✉ & Feiyu Kang<sup>1</sup>✉

Anion-intercalation lithium metal batteries (AILMBs) are appealing due to their low cost and fast intercalation/de-intercalation kinetics of graphite cathodes. However, the safety and cyclability of existing AILMBs are constrained by the scarcity of compatible electrolytes. Herein, we showcase that a difluoroester can be applied as electrolyte solvent to realize high-performance AILMBs, which not only endows high oxidation resistance, but also efficiently tunes the solvation shell to enable highly reversible and kinetically fast cathode reaction beyond the trifluoro counterpart. The difluoroester-based electrolyte demonstrates nonflammability, high ionic conductivity, and electrochemical stability, along with excellent electrode compatibility. The Li|graphite AILMBs reach a high durability of 10000 cycles with only a 0.00128% capacity loss per cycle under fast-cycling of 1 A g<sup>-1</sup>, and retain ~63% of room-temperature capacity when discharging at -65 °C, meanwhile supply stable power output under deformation and overcharge conditions. The electrolyte design paves a promising path toward fast-rate, low-temperature, durable, and safe AILMBs.

Facing formidable environmental challenge, substantial progress in battery technology is paramount for enabling a transformative shift in energy paradigms, ultimately aiming for a society with reduced carbon footprints. As a promising candidate for next-generation battery system that offers higher energy density, lithium (Li) metal batteries (LMBs) are highly pursued owing to the unparalleled theoretical specific capacity (3860 mAh g<sup>-1</sup>) and the lowest redox potential (-3.04 V vs. standard hydrogen electrode) of Li metal anodes<sup>1–3</sup>. However, the practical implementation of LMBs has been plagued by the prevailing transition metal oxide-based cathodes, which not only suffer from high costs and raise concerns of an economically and geopolitically constrained supply, but also exhibit sluggish intercalation/de-intercalation kinetics and limited lifespan arising from cathode structure deterioration (e.g., transition metal dissolution, gas evolution)<sup>4</sup>. The later issues will be further exacerbated under fast-rate and low-temperature operating conditions<sup>2</sup>. Therefore, it is essential to eliminate transition

metal elements from cathode materials and thus, re-design battery chemistry for the developments of LMBs. In this regard, anion-intercalation LMBs (AILMB) have emerged by replacing the Li<sup>+</sup>-hosting transition-metal oxide cathodes with cost-efficient graphitic carbons as anion hosts<sup>5,6</sup>. In contrast to the “rocking-chair” mechanism in traditional LMBs based on transition-metal oxide cathodes, the simultaneous redox process on both the anion-intercalation cathode and cation-plating anode in AILMBs potentially weakens the de-solvation barrier, endowing this battery system with fast-rate and low-temperature characteristics<sup>7</sup>. However, the high operating voltage (5 V-class vs. Li/Li<sup>+</sup>) of the anion-intercalation chemistry at graphite cathodes causes irreversible side reactions with conventional electrolytes, leading to the formation of high-resistance cathode/electrolyte interphase (CEI) on the cathode surface which seriously inhibits anion insertion<sup>8–10</sup>. Moreover, the substantial and repeated cathode volume change (>130%) and the co-intercalation of solvent molecules trigger

<sup>1</sup>Tsinghua Shenzhen International Graduate School, Tsinghua University, Shenzhen 518055, China. <sup>2</sup>School of Energy and Environment, City University of Hong Kong, Hong Kong SAR 999077, China. <sup>3</sup>These authors contributed equally: Yao Wang, Shuyu Dong. ✉e-mail: [zhou.d@sz.tsinghua.edu.cn](mailto:zhou.d@sz.tsinghua.edu.cn); [fykang@tsinghua.edu.cn](mailto:fykang@tsinghua.edu.cn)

an exfoliation of graphite layers during cycling, significantly deteriorating the graphite cathode structure<sup>11</sup>. As for the Li metal anode, the fragile solid electrolyte interphase (SEI) and uncontrollable dendrite growth during cycling results in low Coulombic efficiency (CE) and even catastrophic safety issues (e.g., internal short circuit)<sup>3,12,13</sup>. These drawbacks lead to the degraded cycle life and serious self-discharge in existing AILMBs<sup>8,14</sup>.

Electrolyte engineering is promising for enhancing the electrode|electrolyte compatibility, thereby achieving durable AILMBs. Ether-based electrolytes have been widely employed in traditional LMBs due to their relatively low reactivity with Li metal<sup>15,16</sup>. Nevertheless, they are incompatible with anion-intercalation cathodes because of their intrinsic oxidative instability at high voltage (<4 V vs. Li<sup>+</sup>/Li)<sup>15,17</sup>. In contrast, linear carbonates represented by ethyl methyl carbonate (EMC) endow a reversible anion intercalation/deintercalation on graphite cathode in AILMBs. However, the safety concerns originating from their high flammability, the insufficient stability of linear carbonates toward Li metal anode together with solvent co-intercalation on the cathode, remain to be solved<sup>18,19</sup>. Although applying high-concentration salt can alleviate above issues via reducing the proportion of free solvent molecules, the high salt cost along with high viscosity and poor electrode wettability of such concentrated electrolytes significantly restrict the application feasibility<sup>20,21</sup>. Recently, ester solvents have been widely utilized to enhance the low-temperature and fast-charging performance of Li-ion batteries benefiting from their low freezing points and low viscosities<sup>22,23</sup>. However, their poor compatibility with Li metal anode and limited oxidation stability (<4.7 V vs. Li<sup>+</sup>/Li) greatly block their application in AILMBs<sup>24</sup>; to the best of our knowledge, the esters have not been reported as a solvent in AILMB system yet. Thereby, designing highly compatible electrolyte systems for safe, durable, fast-charging, and low-temperature AILMBs remains a significant challenge.

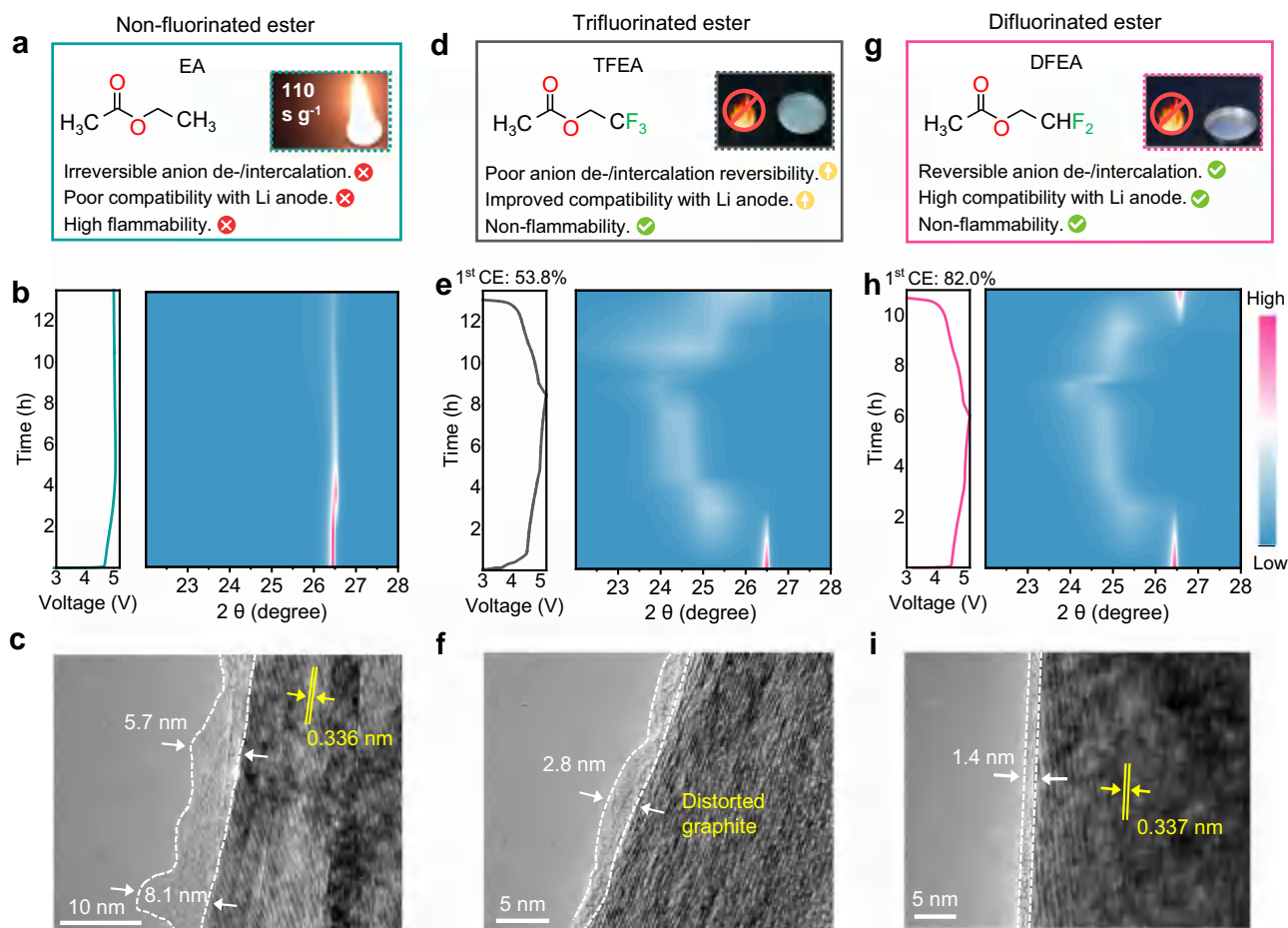
Herein, we systematically investigated a family of fluorinated esters as the solvent for the electrolytes of AILMBs. Our findings reveal that fluorination to ester molecules effectively enhances both the anti-oxidative property and stability with Li anode. Unexpectedly, as verified by computational modeling and experimental results, compared with the trifluoro (-CF<sub>3</sub>) counterpart, the difluoroester (-CHF<sub>2</sub>) effectively attenuates the anion-solvent interactions, thereby reducing corresponding anion de-solvation kinetic barrier and suppressing solvent co-intercalation into graphite cathodes. This balanced electrolyte design enables highly reversible and kinetically fast anion intercalation. The difluoro 2,2-difluoroethyl acetate (DFEA)-based electrolyte demonstrates high ionic conductivity (7.2 mS cm<sup>-1</sup>, 25 °C), remarkable electrochemical stability (up to 5.5 V vs. Li<sup>+</sup>/Li), excellent compatibility with the Li metal anode and high safety without combustion concerns. Under fast-cycling condition of 1 A g<sup>-1</sup>, the as-developed AILMB exhibits record-high durability of 10,000 cycles with a capacity retention of 88.0% (with negligible capacity fade of 0.00128% per cycle only), much beyond the reported LMBs based on LiFePO<sub>4</sub> (LFP) or LiNi<sub>0.8</sub>Co<sub>0.1</sub>Mn<sub>0.1</sub>O<sub>2</sub> (NCM811) cathodes. More importantly, this AILMB remains ~63% of room-temperature (RT, 25 °C) capacity when discharging at -65 °C, and offers steady power output of pouch cells under abusive conditions (e.g., deformation and overcharge). This work represents a significant advancement in LMB performance and is particularly advantageous for applications in extreme conditions (e.g., fast-charging electric vehicles, aerospace and polar region devices).

## Results

Screen of ester solvents and investigation on anion-intercalation. It is known that despite the merits including appropriate dielectric constant (6.02), low viscosity (0.45 mPa s), and low melting point (-84 °C)<sup>22</sup>, ethyl acetate (EA) exhibits large overpotential and poor Li stability in LMBs originating from the high de-solvation energy and the

inability to form a protective SEI, respectively<sup>22</sup>. Besides, as seen from inset of Fig. 1a, the 1.2 M LiPF<sub>6</sub> salt in EA electrolyte demonstrates high flammability with a self-extinguishing time (SET) of 110 s g<sup>-1</sup> due to the high volatility of EA solvent. More seriously, the EA-based electrolyte fails to support the anion-intercalation chemistry on the graphite cathode. During the initial charging process at 20 mA g<sup>-1</sup> (0.2 C) in an AIMB, this electrolyte exhibits an abnormal charging profile, characterized by a large irreversible charging capacity and an inability to reach the cutoff voltage of 5.2 V, which can be attributed to the continuous electrolyte decomposition (Fig. 1b, left panel). No distinct position change of the graphite (002) peak is observed in the X-ray diffraction (XRD) pattern (Fig. 1b), suggesting a constant graphite d(002) spacing (0.336 nm, Fig. 1c) caused by the blocked PF<sub>6</sub><sup>-</sup> anion intercalation by the thick, non-uniform CEI as oxidative product of electrolyte (5.7 to 8.1 nm, Fig. 1c). To tackle this issue, the terminal methyl group (-CH<sub>3</sub>) of the EA molecule was functionalized to an electron-withdrawing -CF<sub>3</sub> group, thereby enhancing both the Li metal compatibility and anti-oxidative stability (Fig. 1d). The as-obtained 1.2 M LiPF<sub>6</sub> salt in 2,2,2-trifluoroethyl acetate (TFEA) electrolyte delivers nonflammable properties with a SET of 0 s (inset of Fig. 1d). Furthermore, the TFEA-based electrolyte facilitates a reversible anion intercalation into/de-intercalation from the graphite host, as evidenced by the multiple voltage plateaus on the charge-discharge curve with a CE of 53.8% (the left panel of Fig. 1e) and redox peaks during the initial cyclic voltammetry (CV) curve (Supplementary Fig. 1a). Notably, the d(002) diffraction peak of graphite cathode progressively shifts to 23.9° (i.e., an interlayer spacing of 0.373 nm) upon charging to 5.2 V, whereas for the fully discharged state, the appearance of a distinct shoulder peak at lower angle implies incomplete PF<sub>6</sub><sup>-</sup> extraction or graphite expansion caused by solvent co-intercalation (the right panel of Fig. 1e and Supplementary Fig. 2). This phenomenon was verified by the irreversible lattice structure change of the distorted graphite cathode after 1st cycle, even though a thinner (~2.8 nm) and more uniform CEI is formed compared to the EA-based electrolyte (Fig. 1f). As revealed by the in-depth X-ray photoelectron spectroscopy (XPS) analysis, the graphite cathode after tested in EA electrolyte displays increasing amounts of organic species including C-O, C=O, ROCO<sub>2</sub>Li and Li<sub>2</sub>CO<sub>3</sub> (Supplementary Fig. 3a), as the accumulated decomposition products of EA solvent. Besides, large amounts of LiF and Li<sub>x</sub>PO<sub>y</sub>F<sub>z</sub> species are observed in the core F 1s spectrum due to the LiPF<sub>6</sub> decomposition (Supplementary Fig. 4a). In contrast, the TFEA electrolyte achieves reduced amount of these components for the cycled cathode (Supplementary Figs. 3b and 4b), confirming alleviated side reactions between the electrolyte and graphite electrode.

Subsequently, the degree of fluorination was tuned by transitioning from -CF<sub>3</sub> groups to -CHF<sub>2</sub>, resulting in a more stable solvent, DFEA (Fig. 1g). The asymmetric -CHF<sub>2</sub> group contains a local dipole, which enhances Li<sup>+</sup> solvation and reduces PF<sub>6</sub><sup>-</sup> coordination compared to the symmetric -CF<sub>3</sub> group, as discussed later. The commonly used fluoroethylene carbonate (FEC, 10 wt%) was added to the 1.2 M LiPF<sub>6</sub> salt in DFEA electrolyte (Supplementary Fig. 5), henceforth referred to as DFEA-based electrolyte. In addition to inheriting the high non-flammability from the TFEA (inset of Fig. 1g), the DFEA-based electrolyte enables a reversible anion de-/intercalation process on the graphite host (Supplementary Fig. 1b, c) with an improved CE of 82.0% (the left panel of Fig. 1f). The interlayer spacing of the graphite cathode expands to 0.370 nm at the fully charged state, and reversibly reverts to 0.337 nm upon discharging to 3.0 V (Fig. 1h and Supplementary Fig. 2). This illustrates that the application of DFEA solvent efficiently precludes solvent co-intercalation. The transmission electron microscope (TEM) image shows that the high resistance of DFEA to oxidation contributes to an in situ construction of a uniform and thin (~1.4 nm) CEI with reduced resistance for ion migration (Fig. 1i). The uniformity stability of the formed CEI was further verified by the XPS depth profiling, showing no obvious evolution in the LiF and Li<sub>x</sub>PO<sub>y</sub>F<sub>z</sub> contents as



**Fig. 1 | Investigation of esters on anion-intercalation.** Molecule structure and characteristics of (a) EA, (d) TFEA and (g) DFEA. Combustion tests for electrolyte samples are shown in the insets. Intensity contour maps obtained from the ex-situ XRD patterns of Li|graphite cells during initial charge-discharge processes at

20 mA g<sup>-1</sup> using (b) EA, (e) TFEA and (h) DFEA (with 10 wt% FEC) electrolytes. The corresponding voltage-testing time curves are shown on the left panels. TEM images of the graphite cathodes after the 1st cycle in (c) EA, (f) TFEA, and (i) DFEA (with 10 wt% FEC) electrolytes.

the etching time was increased (Supplementary Fig. 4c). In addition, amounts of products derived from solvent decomposition was significantly reduced (Supplementary Fig. 3c). All these verify the superiority of DFEA in developing durable AILMBs.

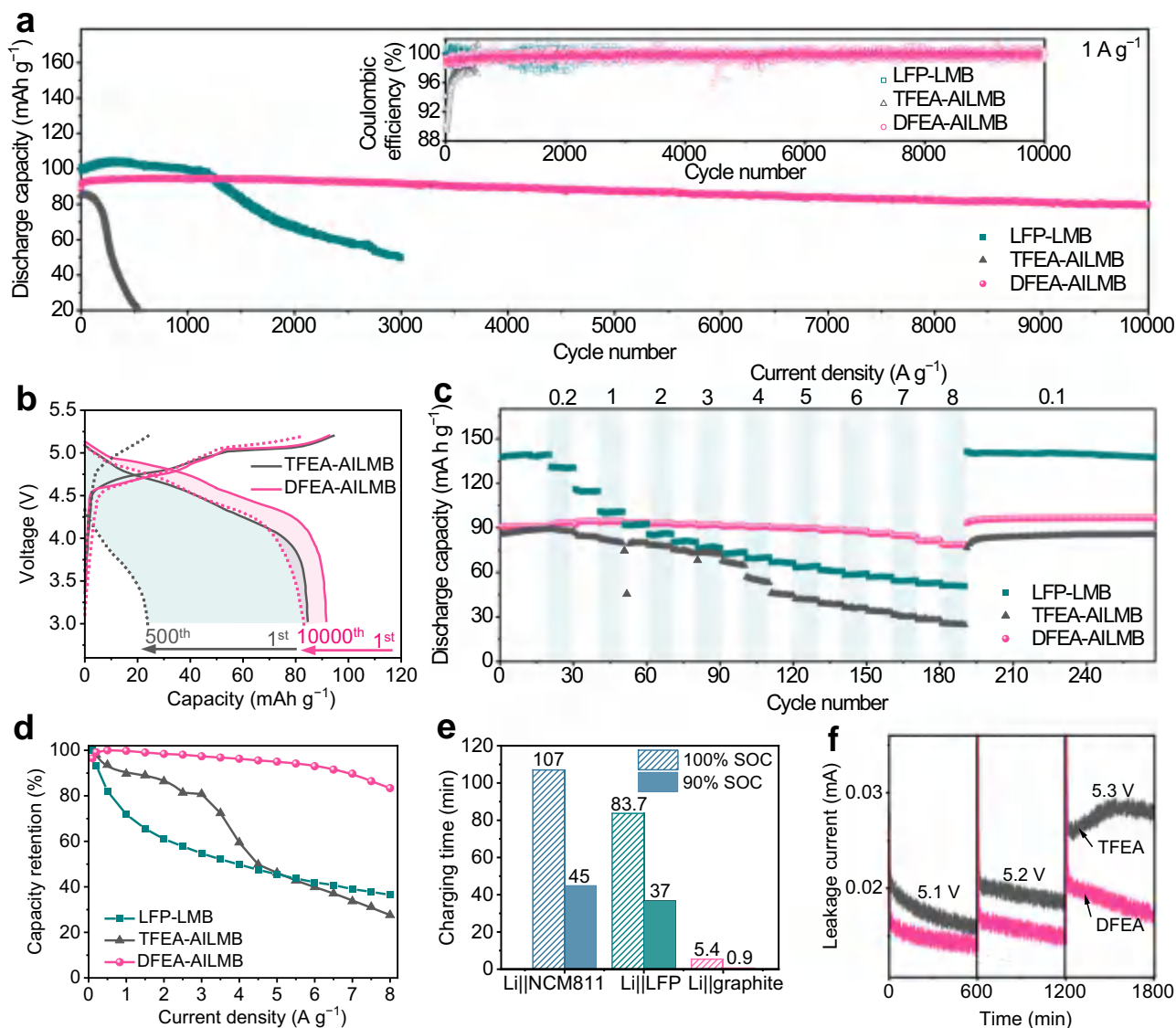
#### Electrochemical performance of the anion-intercalation Li metal batteries

Li|graphite AILMBs were assembled to assess their cycling performance under a high cycling current density of 1 A g<sup>-1</sup> (corresponding to 10 C, 1 C = 100 mAh g<sup>-1</sup> based on the mass of graphite active material) at 25 °C. Li|LFP LMBs using a commercial electrolyte of 1.2 M LiPF<sub>6</sub> salt in ethylene carbonate (EC)/diethyl carbonate (DEC) (denoted as EC/DEC electrolyte) were used for performance comparison (Fig. 2a). It is seen that the Li|LFP cell exhibits a 47.6% capacity retention after 3000 cycles (Supplementary Fig. 6), associating with a huge polarization increase upon cycling (Supplementary Fig. 7a). The AILMB with TFEA electrolyte delivers an initial discharge capacity of ~85.7 mAh g<sup>-1</sup>, which gradually declines to ~24.1 mAh g<sup>-1</sup> at the 500<sup>th</sup> cycle (Fig. 2a, b), accompanied by a noticeable growing polarization (Supplementary Fig. 7b) and low CE. This short lifetime is primarily caused by structural deterioration of graphite cathode (Supplementary Fig. 8a, seen from the wrinkled thin sheets) caused by solvent co-intercalation. In sharp contrast, the DFEA-based electrolyte effectively alleviates the rise in cell polarization (Supplementary Fig. 7c), ensuring the preservation of voltage platforms with minimal deviation upon cycling. Furthermore, the average CE is as high as ~99.7% over 10,000 cycles, benefiting from

the protective effect of interphases on both the graphite cathode and the Li metal anode. Notably, the cycled graphite electrode displays a well-maintained structural integrity with laminar microstructure (Supplementary Fig. 8b). Consequently, the AILMB operates stably for 10,000 cycles with a capacity retention of 88.0% and negligible capacity fade of 0.00128% per cycle. To the best of our knowledge, this work shows improved fast-cycling stability compared to LMBs based on LFP or NCM811 cathodes and other AILMBs (Supplementary Table 1).

Furthermore, cells employing the DFEA-based electrolyte demonstrate an exceptional rate performance (Fig. 2c and Supplementary Fig. 9a), with retentions as high as ~93.0%, ~89.7%, and ~83.4% of the maximum capacity at 0.5 A g<sup>-1</sup> when the cycling rate increases to 6 A g<sup>-1</sup>, 7 A g<sup>-1</sup>, and 8 A g<sup>-1</sup>, respectively (Fig. 2d). This remarkable ultra-fast rate capability suggests that the PF<sub>6</sub><sup>-</sup> anion de-/intercalation processes from/into the graphite cathode is facile and highly reversible in the DFEA-based electrolyte. In contrast, the TFEA electrolyte provides rapid capacity decay at current densities higher than 1 A g<sup>-1</sup>, associated with an increased cell polarization (Supplementary Fig. 9b). Although LFP-based LMB is capable of achieving higher capacities at low current rates (i.e., 0.1–1 A g<sup>-1</sup>), the reversible capacity is much inferior to that of AILMB when the current density exceeds 1.5 A g<sup>-1</sup>, with capacity retention of only 39% and 36.5% at 7 A g<sup>-1</sup> and 8 A g<sup>-1</sup>, respectively (Fig. 2c, d). The rapid capacity decay is ascribed to the growing cell polarization with increased current density (Supplementary Fig. 9c). The AILMB delivers a substantially shorter charging time of ~5.5 min to





**Fig. 2** | Electrochemical performance of the anion-intercalation Li metal batteries. **a** Long-term cycling performance of Li||graphite AILMBs (using TFEA and DFEA-based electrolytes) and Li||LFP LMB (using EC/DEC electrolyte) at 1 A g<sup>-1</sup> after three activation cycles at 20 mA g<sup>-1</sup>. Inset is the Coulombic efficiency. **b** Typical charge-discharge curves of AILMBs using TFEA and DFEA-based electrolytes. **c** Rate

performance and **(d)** corresponding capacity retention at various current densities from 100 mA g<sup>-1</sup> to 8 A g<sup>-1</sup> for AILMBs and LFP-based LMBs. **e** Comparisons of charging time for our AILMB and LMBs based on the LFP and NCM811 cathodes, at 90% SOC and 100% SOC, respectively. **f** Potentiostatic profiles of AILMBs with TFEA and DFEA-based electrolytes maintained at 5.1, 5.2, and 5.3 V for 10 h, subsequently.

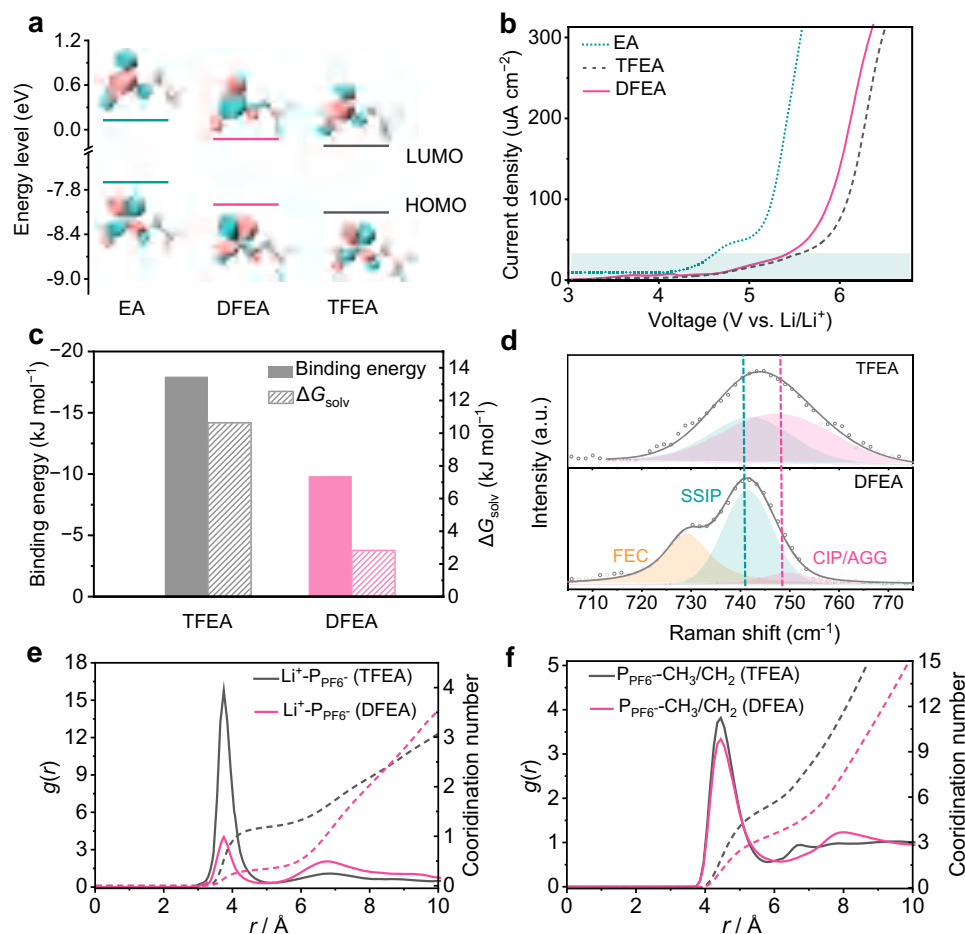
reach a 100% state-of-charge (SOC, i.e., the maximum reversible capacity), compared to ~1.4 h and ~1.8 h required for the LFP-based and NCM 811-based LMBs (Supplementary Fig. 10), respectively. The charging time of this AILMB can be further reduced to within 1 min when reaching a 90% SOC (Fig. 2e). These results suggest that the anion-intercalation cathode chemistry effectively enhances the high-rate capability of LMBs, which is among the best performance reported for fast-charging LMBs (Supplementary Table 2).

The parasitic reactions on the graphite surface of AILMBs at charged state were further examined by potentiostatic tests (Fig. 2f). The cells were pre-cycled at 20 mA g<sup>-1</sup> for three cycles, followed by charged to and maintained at a constant voltage of 5.1, 5.2, and 5.3 V for 10 h, subsequently. Notably, as the voltage is raised, the cell with TFEA electrolyte exhibits much higher leakage currents compared to that with the DFEA-based electrolyte. The AILMB with TFEA-based electrolyte displays a leakage current of ~0.03 mA at 5.3 V, mainly attributed to the serious side reactions between graphite cathode with co-intercalated solvent. In contrast, the DFEA-based electrolyte effectively

stabilizes the graphite cathode even at 5.3 V. Above excellent long-term durability and ultrafast-cycling capability infer that the DFEA-based electrolyte greatly facilitates the electrode reaction kinetics in AILMBs.

#### Physicochemical properties and coordination chemistry of electrolytes

Density functional theory (DFT) simulations were conducted to assess the highest occupied molecular orbital (HOMO) and the lowest unoccupied molecular orbital (LUMO) energies of EA, TFEA, and DFEA solvent molecules with various degree of fluorination. As depicted in Fig. 3a, TFEA (−8.1 eV) and DFEA (−8.0 eV) exhibit reduced HOMO energy levels compared to EA (−7.7 eV), suggesting superior anti-oxidative resistance due to the incorporation of electron-withdrawing fluorine atoms into the solvent structure<sup>25</sup>. This result was further confirmed by the anti-oxidative stability of electrolytes evaluated via linear sweeping voltammetry (LSV) on a Pt electrode. As expected, compared with the EA electrolyte with an oxidation potential of 4.6 V



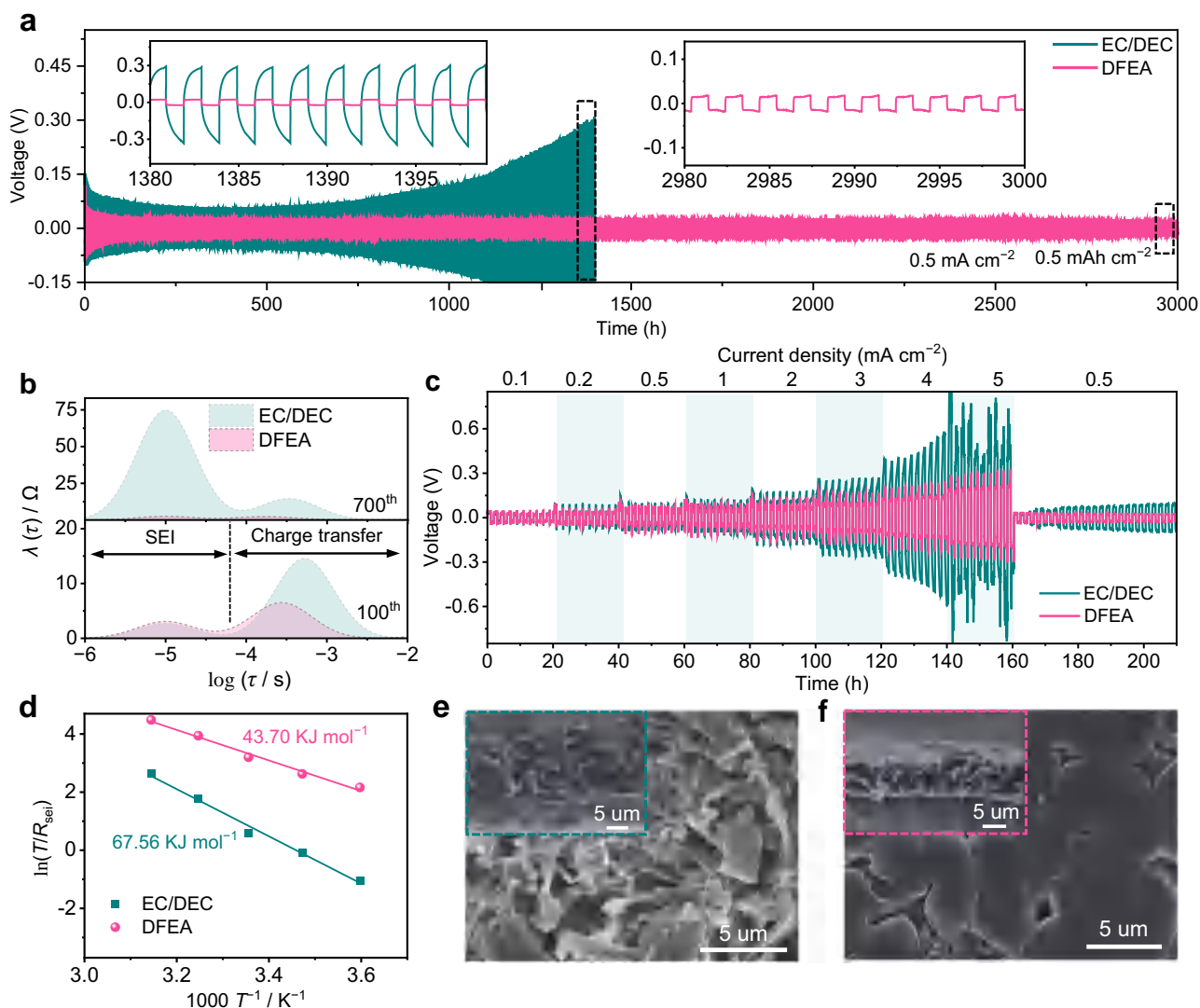
**Fig. 3 | Electrolyte properties and coordination chemistry.** **a** LUMO and HOMO energy values of the EA, DFEA, and TFEA solvent molecules. The molecular structures and corresponding visual LUMO and HOMO geometry structures are shown in the insets. Gray, white, red, and green balls represent carbon, hydrogen, oxygen, and fluorine atoms, respectively. **b** LSV curves of the electrolytes at a scan rate of  $5 \text{ mV s}^{-1}$ , employing a Pt foil as the working electrode and Li foil as the counter and

reference electrodes. **c** Solvation energy ( $\Delta G_{\text{solv}}$ ) values of electrolytes based on TFEA and DFEA solvents, and binding energies of  $\text{PF}_6^-$  anion with TFEA and DFEA molecules. **d** Raman spectra of TFEA and DFEA-based electrolytes. **e**  $\text{Li}^+$  and **f**  $\text{PF}_6^-$  RDF obtained from MD simulations of TFEA and DFEA-based electrolytes. Solid lines represent  $g(r)$  while dashed lines represent coordination number.

vs.  $\text{Li/Li}^+$ , both TFEA and DFEA-based electrolytes remain stable up to 5.5 V, satisfying the need of high-voltage anion-intercalation cathode (Fig. 3b). Meanwhile, TFEA and DFEA also display a decline of LUMO levels ( $-0.22 \text{ eV}$  and  $-0.13 \text{ eV}$ , respectively) compared with EA, benefiting their preferential reduction on Li metal anodes to form robust SEI layers. To verify the ion-solvent coordination environment in electrolytes, the electrostatic potential (ESP) distribution of solvent molecules (Supplementary Fig. 11) and binding energies of both  $\text{Li}^+$ -solvent complexes and  $\text{PF}_6^-$ -solvent complexes were calculated by DFT (Fig. 3c and Supplementary Fig. 12a–c). It is seen that the DFEA molecule exhibits stronger binding energy with  $\text{Li}^+$  ( $-101.27 \text{ kJ mol}^{-1}$  vs.  $-96.46 \text{ kJ mol}^{-1}$ ) but weaker binding energy ( $-9.84 \text{ kJ mol}^{-1}$  vs.  $-17.95 \text{ kJ mol}^{-1}$ ) with  $\text{PF}_6^-$  compared to the TFEA. This is consistent with the ESP results (Supplementary Fig. 11), suggesting a weakened DFEA- $\text{PF}_6^-$  interaction which reduces the corresponding anion de-solvation kinetic barriers and suppresses the co-intercalation of solvents during the charging process of AILMB. In addition, the DFEA- $\text{Li}^+$  interaction is enhanced due to the existence of local dipole on the  $-\text{CHF}_2$  (Supplementary Fig. 12d–h), which is similar to the recent report by Bao et al.<sup>3</sup>. Solvation energy ( $\Delta G_{\text{solv}}$ ) values of the electrolytes were further determined using a homemade H-type cell to investigate the solvation structures (Supplementary Fig. 13)<sup>26</sup>. The DFEA-based electrolyte exhibits a much lower  $\Delta G_{\text{solv}}$  ( $2.83 \text{ kJ mol}^{-1}$ ) compared to the TFEA electrolyte ( $10.64 \text{ kJ mol}^{-1}$ , Fig. 3c), further confirming the stronger

coordination between Li ions and DFEA, which promotes the Li salt dissociation and thus gives rise to a higher ionic conductivity of DFEA-based electrolyte ( $7.2 \text{ mS cm}^{-1}$  at  $25^\circ\text{C}$ ) than the TFEA-based electrolyte ( $2.5 \text{ mS cm}^{-1}$  at  $25^\circ\text{C}$ ). Moreover, the  $\text{Li}^+$  transference number of DFEA-based electrolyte (0.49, Supplementary Fig. 14 and Supplementary Table 3) is quite close to 0.5, which is beneficial to balance the active ions in the AILMBs.

Raman vibrational spectroscopy was applied to get an in-depth understanding of the electrolyte solvation structures (Fig. 3d). Two peaks at approximately  $741$  and  $749 \text{ cm}^{-1}$  are attributed to the solvent-separated ion pair (SSIP, i.e., uncoordinated  $\text{PF}_6^-$ ) and the contact ion pairs (CIPs, i.e.,  $\text{PF}_6^-$  ions interacting with one  $\text{Li}^+$  ion)/aggregates (AGGs, i.e.,  $\text{PF}_6^-$  ions interacting with two or more  $\text{Li}^+$  ions), respectively<sup>27</sup>. The peak at around  $729 \text{ cm}^{-1}$  is assigned to the FEC (Supplementary Fig. 15). Compared with the TFEA-based electrolyte, the weaker CIP/AGG peak for DFEA-based electrolyte indicates that  $\text{PF}_6^-$  anions predominately exist in the form of SSIP, enhancing the fast ion transport. This can be further validated by molecular dynamics (MD) simulations. The MD snapshot in Supplementary Fig. 16a reveals that TFEA electrolyte displays a CIP/AGG-rich structure, where 1.22  $\text{PF}_6^-$  coordinate to one  $\text{Li}^+$  based on the radial distribution functions result (Fig. 3e). In contrast, the difluoro DFEA facilitates a SSIP-rich electrolyte structure (Supplementary Fig. 16b), with 0.35  $\text{PF}_6^-$  coordinating to one  $\text{Li}^+$  (Fig. 3e). Moreover, it is seen that the solvated  $\text{PF}_6^-$  is



**Fig. 4** | Lithium plating/stripping behavior in different electrolytes. **a** Voltage profiles of Li|Li symmetric cells employing EC/DEC and DFEA-based electrolytes at  $0.5 \text{ mA cm}^{-2}$  with a cutoff capacity of  $0.5 \text{ mAh cm}^{-2}$ . **b** The corresponding DRT results at the 100<sup>th</sup> (the upper panel) and 700<sup>th</sup> (the lower panel) cycle. **c** Voltage profiles of Li|Li symmetric cells under different rates. **d** Activation energies of  $R_{\text{seI}}$

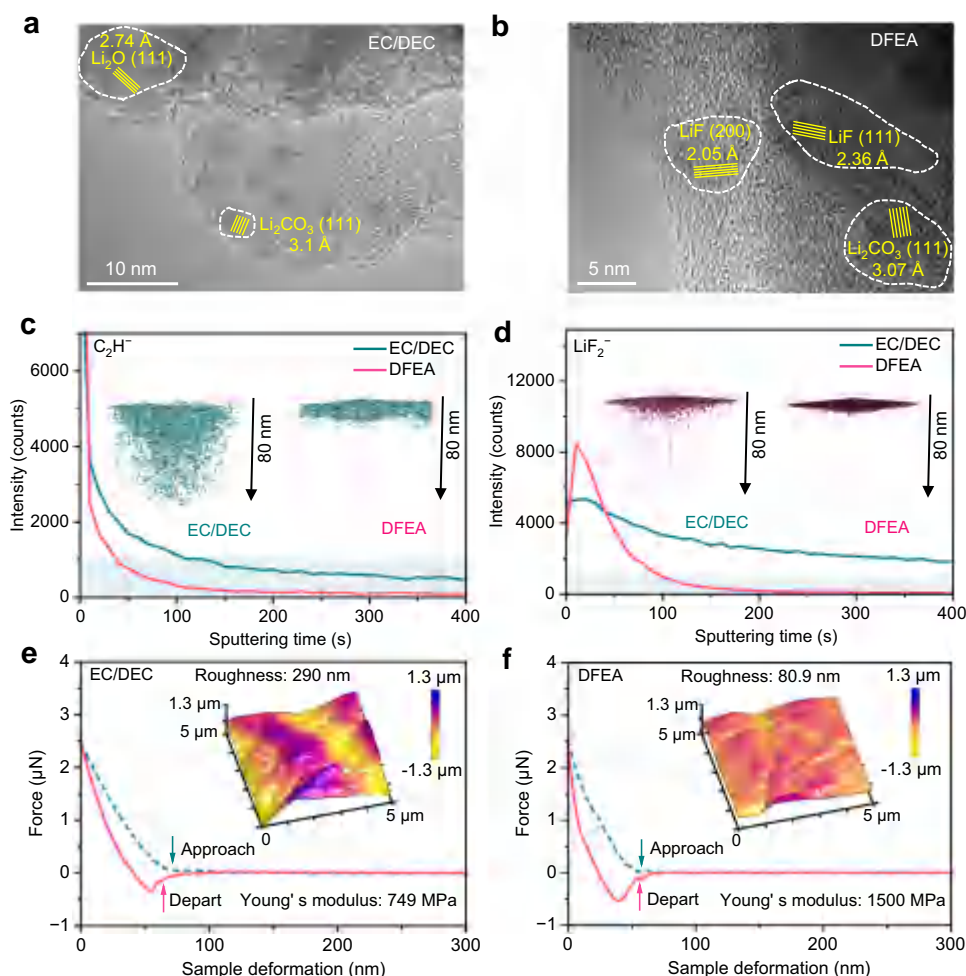
derived from Nyquist plots using EC/DEC and DFEA-based electrolytes. Top and cross-sectional (shown as insets) FE-SEM images of the Li deposition obtained by plating  $1 \text{ mAh cm}^{-2}$  Li on Cu substrate at  $0.2 \text{ mA cm}^{-2}$ , using the Li|Cu cells with (e) EC/DEC and (f) DFEA-based electrolytes.

distinctly coordinated with the  $-\text{CH}_3/\text{CH}_2$  groups on the fluorinated solvent molecules, confirming the synergetic solvation environment of  $\text{PF}_6^-$  (Fig. 3f). This result further verifies the balanced solvation affinity and salt dissociation of DFEA-based electrolyte, which is expected to achieve rapid de-solvation and fast ion migration of both  $\text{PF}_6^-$  and  $\text{Li}^+$  ions.

#### Interfacial compatibility between electrolyte and the Li metal anode

The Li plating/stripping cycling behavior was investigated using Li|Li symmetric cells at a constant current of  $0.5 \text{ mA cm}^{-2}$  (Fig. 4a). The cell employing EC/DEC electrolyte exhibits a substantial increase in overpotential upon cycling (302 mV at 1400 h), in stark contrast to the lower overpotential and extended lifespan (16.5 mV at 3000 h) achieved in the DFEA-based electrolyte (inset in Fig. 4a). Electrochemical impedance spectra (EIS) of symmetric Li|Li cells were conducted upon cycling to monitor the interfacial resistance, and thus, the distribution of relaxation times (DRT) analysis was derived. The peak located at  $\sim 10^{-6}$  to  $10^{-4}$  s represents the SEI, while the peak at  $\sim 10^{-4}$  to  $10^{-2}$  s is related to transfer process<sup>28,29</sup>. It is seen that the integrated area

of these two peaks for the cell using EC/DEC electrolyte increases remarkably with cycling (insets in the Fig. 4b and Supplementary Fig. 17), which is attributed to the thickening of highly resistive SEI on the Li metal and thus leading to rapid cell failure. On the contrary, the cell with DFEA-based electrolyte exhibits much smaller integral area values with slight variations as cycling, primarily due to the formation of a stable and highly conductive SEI against detrimental parasitic reactions (Fig. 4b and Supplementary Fig. 17). Moreover, the ability of the DFEA-based electrolyte to stabilize Li metal becomes more pronounced when increasing the plating/stripping current densities. At an improved current density of  $1 \text{ mA cm}^{-2}$  with a cycling capacity of  $1 \text{ mAh cm}^{-2}$ , a reduced lifespan is observed for the symmetric cell with EC/DEC electrolyte, with the overpotential rising to 777 mV after only 750 h (Supplementary Fig. 18). Impressively, DFEA-based electrolyte exhibits much smaller overpotential and negligible fluctuation upon repeated plating/stripping processes ( $\sim 80.0 \text{ mV}$  at 1660 h). Moreover, upon further increasing the plating/stripping areal capacities, the Li|Li cells employing DFEA-based electrolyte still demonstrate significant improvements in the cycling capability with areal capacities of  $3 \text{ mAh cm}^{-2}$  (930 h and 300 h at  $1 \text{ mA cm}^{-2}$  and  $3 \text{ mA cm}^{-2}$ , respectively)



**Fig. 5 |** Characterizations of the SEI on Li metal surface. TEM image of the SEI shell formed by plating/stripping Li on a Cu grid using (a) EC/DEC and (b) DFEA-based electrolytes. Depth profiles of (c)  $\text{C}_2\text{H}^+$  and (d)  $\text{LiF}_2^-$  in the SEI, obtained from the TOF-SIMS. Three dimensional (3D) spatial distributions of (e)  $\text{C}_2\text{H}^+$  and (f)  $\text{LiF}_2^-$

are displayed in the insets. Force-displacement curves of the SEI derived from (e) EC/DEC and (f) DFEA-based electrolytes. The corresponding 3D AFM scanning images of the SEI are shown in the insets.

and  $4 \text{ mAh cm}^{-2}$  (730 h and 500 h at  $1 \text{ mA cm}^{-2}$  and  $2 \text{ mA cm}^{-2}$ , respectively; Supplementary Fig. 19). These results represent a compelling advancement comparable with reported electrolytes (Supplementary Table 4). The  $\text{Li}||\text{Li}$  cell with DFEA-based electrolyte consistently exhibits low and stable overpotential within a wide range of current densities from  $0.5$  to  $5 \text{ mA cm}^{-2}$ , while substantial voltage fluctuation emerges in the cell using EC/DEC commercial electrolyte, especially when increasing the current density to  $5 \text{ mA cm}^{-2}$  (Fig. 4c). This further confirms that the DFEA-based electrolyte enables fast  $\text{Li}^+$  migration and robust SEI formation.

EIS measurements of the  $\text{Li}||\text{Li}$  cells after 20 cycles were conducted at various temperatures, and subsequently fitted by an equivalent circuit to calculate the activation energy ( $E_a$ ) values (Supplementary Fig. 20 and Supplementary Table 5). It is seen that  $E_a$  values of SEI ( $R_{\text{sei}}$ ) and charge transfer ( $R_{\text{ct}}$ ) resistances of the cell using DFEA-based electrolyte are much lower than that using EC/DEC electrolyte ( $43.70$  vs.  $67.56 \text{ kJ mol}^{-1}$ , Fig. 4d; and  $48.19$  vs.  $68.06 \text{ kJ mol}^{-1}$ , Supplementary Fig. 21, respectively). The former indicates that the SEI derived from DFEA-based electrolyte is advantageous for rapid  $\text{Li}^+$  transport, meanwhile the later verifies that the DFEA-based electrolyte facilitates  $\text{Li}^+$  de-solvation from the ion pairs. The stability of the electrolytes toward Li metal anodes was further estimated by the average Li plating/stripping Coulombic efficiency ( $\text{CE}_{\text{avg}}$ ) of  $\text{Li}||\text{Cu}$  asymmetric cells<sup>30</sup>. The  $\text{CE}_{\text{avg}}$  of DFEA-based electrolyte (99.0%) is dramatically higher

than the cell using EC/DEC electrolyte (81.4%, Supplementary Fig. 22). This phenomenon is associated with the Li deposition morphology on Cu foil presented by field emission scanning electron microscope (FE-SEM). As observed from Fig. 4e, the EC/DEC electrolyte shows a highly loose and dendritic Li deposition structure with a thickness of  $18.7 \mu\text{m}$ , far exceeding the theoretical value (about  $4.85 \mu\text{m}$ ) and leading to the low  $\text{CE}_{\text{avg}}$ . In comparison, the DFEA-based electrolyte contributes to a compact Li deposit as aggregated large bulks, with a thickness (approximately  $6.8 \mu\text{m}$ ) quite close to the theoretical value (Fig. 4f). This dendrite-free morphology is beneficial for achieving high  $\text{CE}_{\text{avg}}$  and long Li cycling stability.

The microstructures of SEI shells onto a Cu grid from  $\text{Li}||\text{Cu}$  cells (after 20 cycles and finishing with a charge process) were characterized via TEM. As displayed in Fig. 5a, for the SEI forming in the presence of EC/DEC-based electrolyte,  $\text{Li}_2\text{O}$  (111) plane,  $2.74 \text{ \AA}$  and  $\text{Li}_2\text{CO}_3$  (111) plane,  $3.1 \text{ \AA}$  nanoparticles dispersing within an amorphous SEI matrix mainly resulting from the decomposition of EC/DEC solvents. Upon cycling in the DFEA-based electrolyte (Fig. 5b), in contrast, the lattice spacing of  $2.05$  and  $2.36 \text{ \AA}$  are well matched with the (200) and (111) crystal planes of  $\text{LiF}$  nanoparticles. This  $\text{LiF}$ -rich SEI is believed to stabilize the  $\text{Li}||\text{electrolyte}$  interphase, and promote uniform Li plating during cycling. Time-of-flight secondary ion mass spectrometry (TOF-SIMS) characterizations were further performed to verify the composition/structural evolution of the SEI. It is seen that in the EC/DEC



electrolyte,  $\text{C}_2\text{H}^-$  (mass charge ratio ( $m/z$ ) = 25, as fragments of the organic products, Fig. 5c) and  $\text{LiF}_2^-$  ( $m/z$  = 45, fragment of LiF, Fig. 5d) signals were clearly observed throughout the 400 s-depth profiling, suggesting the formation of a thick SEI with the layer thickness exceeding 80 nm. However, the intensity of  $\text{C}_2\text{H}^-$  and  $\text{LiF}_2^-$  almost disappeared in DFEA-based electrolyte after sputtering for 35 s and 90 s, respectively. This indicates that the DFEA-based electrolyte contributes to a thinner SEI (around 18 nm) enriched in LiF, facilitating both rapid transport and uniform deposition of  $\text{Li}^+$ . The roughness and thickness of the SEI were examined by atomic force microscopy (AFM). As demonstrated in the inset of Fig. 5e, the plated Li in EC/DEC electrolyte exhibits a rough surface with an average roughness of ~290 nm, considerably higher than the value of ~80.9 nm in the DFEA-based electrolyte (inset of the Fig. 5f). In addition, the Young's modulus of the SEI derived from the DFEA-based electrolyte (1500 MPa, Fig. 5f) is much higher than that formed in the EC/DEC electrolyte (749 MPa, Fig. 5e), mainly attributes to the abundant LiF species with high shear modulus (~55.1 GPa, nearly 11 times higher than that of Li metal<sup>31</sup>) as the decomposition product of both  $\text{LiPF}_6$  salt and fluoride solvent in the SEI. This robust LiF-enriched SEI in the DFEA-based electrolyte is advantageous for improving the interfacial energy and durability against the dramatic volume change during cycling<sup>32</sup>, thus resulting in the superior Li plating/stripping performance in Fig. 4. Notably, it is the combined effect of FEC and DFEA that endows the Li||Li cell with long-term cycling stability (Supplementary Fig. 23a, b). Both FEC and DFEA solvent contribute to the LiF-rich SEI on the Li metal, while the FEC addition effectively suppress the excessive decomposition of DFEA solvent (Supplementary Figs. 24 and 25). Furthermore, it is the DFEA solvent, rather than the FEC addition, that supports the reversible cathode reaction (Supplementary Fig. 23c, d).

#### Low-temperature performance and battery safety evaluation

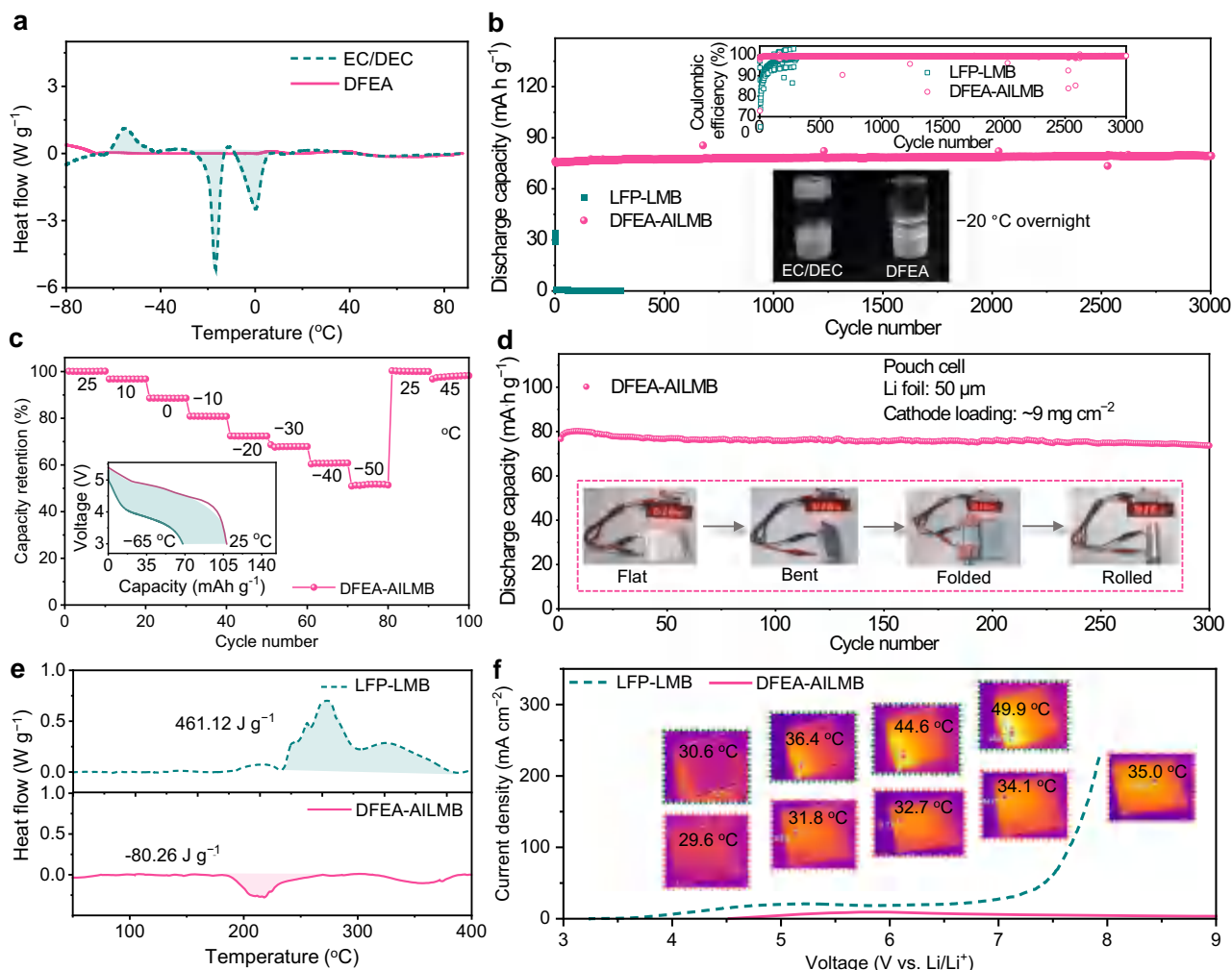
The ionic conductivities of the EC/DEC and DFEA-based electrolytes were compared to verify the feasibility of DFEA-based electrolyte in developing low-temperature AILMBs. As expected, the DFEA-based electrolyte exhibits high ionic conductivity (0.1–10.9  $\text{mS cm}^{-1}$ ) across a wide range of temperature (–60 to +60 °C, Supplementary Fig. 26), mainly due to its wide liquid range (as seen from the differential scanning calorimetry (DSC) measurement in Fig. 6a, where no phase change is observed within the temperature range from –80 °C to +90 °C) and balanced solvation affinity. In contrast, the EC/DEC electrolyte experiences a sudden decline in the ionic conductivity as the temperature drops below –20 °C, attributing to the electrolyte solidification which can be validated by the two distinct endothermic peaks at around –2.4 °C and –17.2 °C in the DSC curve (Fig. 6a). The low-temperature cycling performance of Li|DFEA-based electrolyte|graphite AILMB and Li|EC/DEC electrolyte|LFP LMB were assessed at –20 °C, employing the constant-current-constant-voltage (CCCV) model for charging process with a current density of 100  $\text{mA g}^{-1}$ , followed by discharging at 500  $\text{mA g}^{-1}$ . (Fig. 6b). The AILMB yields a remarkable cycle stability with a remaining capacity of ~80  $\text{mAh g}^{-1}$  over 3000 cycles without capacity degradation, the low-polarization voltage curves indicating a fast and reversible reaction kinetics of  $\text{PF}_6^-$  and  $\text{Li}^+$  at low temperature (Supplementary Fig. 27a). Even at an ultra-high discharge current density of 8  $\text{A g}^{-1}$  (i.e., 80 C) under –20 °C, the AILMB retains 87.7% of its maximum capacity at 0.1  $\text{A g}^{-1}$  (Supplementary Fig. 28). The conventional Li||LFP LMB, however, delivers a low reversible capacity of only ~34.0  $\text{mAh g}^{-1}$  in the initial cycle (Supplementary Fig. 27b), and subsequently suffers from battery failure within 4 cycles due to electrolyte freezing (Inset of Fig. 6b). It is noted that even changing the conventional carbonate-based electrolyte to ether-based electrolytes (Supplementary Fig. 29), the Li||LFP LMB still exhibits much lower reversible capacity in comparison with AILMB using DFEA-based electrolyte at –20 °C. Above findings indicate that the fast migration/reaction kinetics of both cations and anions in

AILMBs is pivotal in enhancing low-temperature applicability of LMBs. Moreover, the AILMB with DFEA-based electrolyte was cycled at various temperatures, as displayed in Fig. 6c. The AILMB retains 97%, 89%, 81%, 72%, 68%, 61%, and 51.5% of its RT capacity when cycled at 10, 0, –10, –20, –30, –40 and –50 °C, respectively. The clear discharge plateaus from charge/discharge curves at –50 °C illustrate the fast electrode reaction kinetics (Supplementary Fig. 30). Notably, when charging at RT followed by discharging at –65 °C, the cell still retains ~63% of its RT capacity (inset of Fig. 6c). Furthermore, the capacity of the AILMB with DFEA-based electrolyte successfully recovers to 100% and 98.3% of its RT capacity when the testing temperature is reverted to 25 and 45 °C, respectively, reflecting the applicability of this battery system under wide temperature range. Besides, critical parameters (e.g., the capacity ratio between the anode and cathode (N/P ratio)) in cell evaluation should be reduced for practical considerations<sup>33</sup>. It is seen that the AILMB exhibits a high capacity retention of ~93.0% with minimal cell polarization throughout 500 cycles under N/P ratio of ~5.7 (Supplementary Fig. 31a), and it can sustain 140 cycles with ~90.7% retainable capacity under N/P ratio of ~2.0 (Supplementary Fig. 31b).

Single-layer pouch cells comprising graphite (9  $\text{mg cm}^{-2}$ ) or LFP (8  $\text{mg cm}^{-2}$ ) cathodes, and Li foil anodes with a thickness of 50  $\mu\text{m}$ , were constructed to assess the cell safety and reliability under abusive conditions. The anion-intercalation Li||graphite pouch cell employing the DFEA-based electrolyte exhibits excellent cycling performance with 92.2% capacity retention after 300 cycles (charge at 1 C and discharge at 2 C, Fig. 6d), in stark contrast to the fast capacity degradation for the Li||LFP pouch cells (Supplementary Fig. 32). Beyond this, the AILMB pouch cell consistently powered a light-emitting diode under bending, folding and even rolling (insets in Fig. 6d), owing to the robust interphases on both cathode and anode against violent shape deformation. More importantly, the total exothermic heat generated from the delithiated LFP with EC/DEC electrolyte is as high as 461.12  $\text{J g}^{-1}$  (Fig. 6e), which is believed to be the origin of a succession of exothermic reactions that lead to uncontrollable battery thermal runaway<sup>34,35</sup>. Unexpectedly, the charged graphite cathode with DFEA-based electrolyte exhibits an endothermic peak during the DSC test (Fig. 6e). This finding is consistent with previous report<sup>36</sup>, clearly indicating the high thermal stability of the charged  $\text{C}_n(\text{PF}_6)$  cathode has been distinctively improved by the protective CEI layer derived from DFEA-based electrolyte. To further assess the safety of the DFEA electrolyte-based AILMB, an overcharge abuse test was carried out by charging the pouch cells from open circuit voltage (OCV) to 9 V at a rate of 20  $\text{mV s}^{-1}$  (Fig. 6f). Clearly, the current density of the LFP-based LMB increases abruptly from 6.5 V, accompanied by an elevated skin temperature of 49.9 °C at a voltage of around 7.8 V (upper-panel insets of Fig. 6f), typically triggered by the decomposition of the electrode interphases under thermal abuse. The AILMB utilizing the DFEA-based electrolyte, in contrast, exhibits superb overcharging resistance up to 9 V without obvious change in current density, as evidenced by the low skin temperature less than 35 °C (lower-panel insets of Fig. 6f). Such a high overcharge resistance is primarily attributed to the superior anti-oxidative stability of the DFEA-based electrolyte, the robustness of the protective CEI formed on the graphite cathode, as well as the intrinsic stability of the  $\text{C}_n(\text{PF}_6)$  structure. Above results well-support the dependability of our AILMB under extreme working conditions.

Furthermore, a 440  $\text{mAh Li||graphite}$  multi-layer pouch cell was packaged, with the specific energy being calculated as ~141.7  $\text{Wh kg}^{-1}$  (Supplementary Fig. 33 and Supplementary Table 6). Moving forward, it is imperative to conduct further research on modifying graphite cathodes (e.g., surface treatment, doping), optimizing electrolytes (e.g., anions with smaller sizes, multivalent anions with more charge numbers, and solvent with lower density), and refining engineering issues, to improve the specific energy of AILMBs without compromising their superior fast-cycling, low-temperature, and safety characteristics.





**Fig. 6 | Electrochemical performance of anion-intercalation Li metal batteries under low-temperature and abusive conditions.** **a** DSC cooling and heating curves of EC/DEC and DFEA-based electrolytes. **b** Long-term cycling performance of the AILMB (using DFEA-based electrolyte) and the LFP-LMB (using EC/DEC electrolyte) at  $-20\text{ }^{\circ}\text{C}$ , employing the CCCV model for charging process with a current density of  $100\text{ mA g}^{-1}$ , followed by discharging at  $500\text{ mA g}^{-1}$ . Insets show the Coulombic efficiency (upper panel) and the optical images of the electrolytes after storage at  $-20\text{ }^{\circ}\text{C}$  overnight (lower panel). **c** Capacity retentions of AILMB using DFEA-based electrolyte under various temperatures ( $45, 25, 10, 0, -10, -20, -30, -40$  and  $-50\text{ }^{\circ}\text{C}$ ). Inset shows the discharge profiles when the cell is charged at RT followed by discharged at RT or  $-65\text{ }^{\circ}\text{C}$ . **d** Cycling performance of the  $50\text{ }\mu\text{m}$ -thick Li foil | graphite pouch cell at a charge rate of  $1\text{ C}$  and a discharge rate of  $2\text{ C}$ . Optical images of the LED powered by the pouch cell under various deformations are shown in insets. **e** Heat generation of fully charged graphite and LFP cathodes together with their respective electrolytes measured by DSC. **f** LSV curves and corresponding infrared thermal imaging photographs (shown in insets) of the Li || graphite and Li || LFP pouch cells at a scan rate of  $20\text{ mV s}^{-1}$  from OCV to  $9\text{ V}$ .

## Discussion

We developed a difluoroester-based electrolyte to realize ultra-fast, long-term cycling stability of transition metal-free AILMBs under extreme working conditions. Compared with the trifluoro counterpart, the difluoroester as solvent effectively modulates the solvation structure by attenuating the anion-solvent interactions, thereby striking a balance between the solvation affinity and salt dissociation of DFEA-based electrolyte. This not only endows rapid de-solvation and fast migration for both  $\text{Li}^+$  cations and  $\text{PF}_6^-$  anions to accelerate electrode reaction kinetics, but also efficiently suppresses the co-intercalation of solvent molecules to promote the cathode reaction reversibility. Our DFEA-based electrolyte simultaneously possesses high ionic conductivity, remarkable thermodynamically oxidative stability, excellent Li metal cyclability, and high safety without the risk of combustion. Morphological analysis and interphase investigations confirm the formation of highly stable protecting interphases on both graphite cathode and Li metal anode, contributing to a durability of 10,000 cycles (with negligible capacity fade of  $0.00128\%$  per cycle) at  $1\text{ A g}^{-1}$ ,

an excellent rate capability at  $8\text{ A g}^{-1}$  (with a retention of  $\sim 83.4\%$  of the maximum capacity at  $0.5\text{ A g}^{-1}$ ), superior ultra-low temperature capability with  $\sim 63\%$  of their RT discharge capacity at  $-65\text{ }^{\circ}\text{C}$ , and abuse-tolerant capabilities (e.g., robustness against deformation and overcharge) for AILMBs. The electrolyte engineering proposed in this work is anticipated to expedite the re-design of Li metal batteries, enabling the adoption of cost-effective and environmental benign cathode materials, therefore advancing the development of high-rate cycling Li metal batteries under severe actual working conditions.

## Methods

**Electrolyte preparation**  
 $\text{LiPF}_6$  (purity  $\geq 99.95\%$ ) salt, FEC (purity  $\geq 99.99\%$ ) solvent, EC (purity  $\geq 99.99\%$ ) solvent, and DEC (purity  $\geq 99.99\%$ ) solvent were purchased from Dongguan Shanshan Battery Materials Co., Ltd. EA (purity  $> 99.5\%$ ) solvent was obtained from Aladdin Bio-Chem Technology Co. Ltd. DFEA (purity  $99\%$ ) solvent and TFEA solvent (purity  $99\%$ ) were purchased from Shangfluoro. Before use, all solvents were

further dehydrated using 4 Å molecular sieves (provided by Sigma-Aldrich) for 48 h. The electrolytes were prepared by dissolving 1.2 M LiPF<sub>6</sub> salt in EA, TFEA, DFEA, and commercial EC/DEC (1:1 by volume) solvents, respectively. 10 wt% FEC was added into the 1.2 M LiPF<sub>6</sub> in DFEA electrolyte. All electrolyte preparations were conducted in an argon-filled glove box with O<sub>2</sub> and H<sub>2</sub>O levels maintained below 0.1 ppm.

### Electrolyte characterizations

The Raman spectroscopy was conducted with a Micro-laser confocal Raman spectrometer (Horiba LabRAM HR800, France) with a 532 nm laser to investigate the solvation structure. In the combustion test, 1 g electrolyte samples were poured into a stainless-steel dish, then optical photographs and movies were recorded. The melting points of the electrolytes were evaluated using differential scanning calorimetry (DSC, MDTC-EQ-M06-01). The electrolytes were sealed in stainless-steel crucible, weighed (15 µL) and subjected to DSC measurement with a ramp rate of 5 °C min<sup>-1</sup>. The ionic conductivities of different electrolytes at various temperatures were determined from the EIS results, obtained using two symmetrically placed stainless-steel electrodes in the electrolyte. The test cells were equilibrated at each temperature for at least 1 h before EIS measurements. The electrochemical stabilities of the electrolytes were evaluated by LSV tests conducted on a three-electrode system, with a sweep rate of 5 mV s<sup>-1</sup>. Li foil served as counter and reference electrodes, while platinum foil was used as the working electrode<sup>37</sup>. The onset of the oxidation current density was defined as 30 µA cm<sup>-2</sup> and the potential values were recorded. The solvation energy of electrolytes was evaluated using an H-type cell, where symmetrical Li metal electrodes immersed in the reference electrolyte (1.2 M LiPF<sub>6</sub>-DEC) and the tested electrolyte were connected by a salt bridge (3 M LiPF<sub>6</sub>-EMC). The measured open circuit potential (E<sub>cell</sub>) determined the solvation free energy (ΔG<sub>sol</sub>), as illustrated below<sup>26</sup>:

$$E_{\text{cell}} = \frac{-\Delta G_{\text{sol}}}{F} \quad (1)$$

Where F is the Faraday constant.

To investigate the impact of the electrolyte on the long-term durability of the Li metal anode, galvanostatic cycling of Li||Li symmetric cells was conducted at current densities of 0.5 mA cm<sup>-2</sup> and 1 mA cm<sup>-2</sup>, respectively, with an areal capacity of 1 mAh cm<sup>-2</sup>. The rate capability of Li metal anode was assessed through repeated 1 h charge–1 h discharge cycles at various current densities ranging from 0.5 mA cm<sup>-2</sup> to 5 mA cm<sup>-2</sup>. For activation energy (E<sub>a</sub>) measurements, symmetric Li||Li cells with various electrolytes were cycled 20 times at a current density of 0.5 mA cm<sup>-1</sup> with an areal capacity of 0.5 mAh cm<sup>-1</sup>. Subsequently, these cycled cells were subjected to temperature-dependent EIS measurements at 278, 283, 288, 293, and 298 K. By fitting the EIS data via an equivalent circuit, the SEI resistance (R<sub>sei</sub>) and charge transfer resistance (R<sub>ct</sub>) values were derived. The E<sub>a</sub> was then calculated according to the Arrhenius equation as follows<sup>38,39</sup>:

$$k = \frac{T}{R_{\text{res}}} A \exp\left(-\frac{E_a}{RT}\right) \quad (2)$$

where k denotes the rate constant, T is the absolute temperature, R<sub>res</sub> corresponds to R<sub>ct</sub> or R<sub>sei</sub>, A signifies the preexponential constant, and R is the standard gas constant. The CEs of Li deposition/stripping were evaluated using Li||Cu cells, based on the Aurbach's CE test protocol<sup>30</sup>. Initially, the Cu electrode was pre-deposited with Li metal at a capacity of 5 mAh cm<sup>-2</sup> at a current density of 0.5 mA cm<sup>-2</sup> and subsequently stripped Li to 1 V. Next, the Cu was deposited with 5 mAh cm<sup>-2</sup> of Li to form a Li reservoir (Q<sub>T</sub>). Afterwards, the cell underwent repeated charge/discharge cycles with a capacity of 1 mAh cm<sup>-2</sup> (Q<sub>C</sub>) for n cycles,

followed by stripping all remaining Li reservoir to 1 V (Q<sub>S</sub>). The average CE (CE<sub>avg</sub>) over n cycles can be calculated as follows<sup>30</sup>:

$$CE_{\text{avg}} = \frac{nQ_C + Q_S}{nQ_C + Q_T} \quad (3)$$

### Battery assembly and characterizations

Metallic Li foils with thickness of 450 µm and 50 µm were purchased from China Energy Lithium Co. Ltd (Tianjin, China). Thinner Li foils with a thickness of 20 µm was purchased from Guangdong Canrd New Energy. Graphite (SAG-R) and LFP were purchased from Shenzhen Kejing Star Technology Co. Ltd. and Shenzhen Dynanonic Co., Ltd., respectively. Acetylene black and Super P were provided by Alfa Aesar. Polyacrylic acid (PAA, MW 450,000) binder and poly(vinylidene fluoride) (PVDF, MW 1,200,000) binder were purchased from Sigma Aldrich and Arkema, respectively. N-methylpyrrolidone (NMP, purity 99.9%) was provided by Aladdin Bio-Chem Technology Co. Ltd. NCM811 particles, 2032-type coin cells, and other battery materials were provided by Guangdong Canrd New Energy. The graphite cathode slurry was prepared by mixing graphite powder as the active material, acetylene black and carbon nanotubes (CNT, TUBALL BATT NMP) as conductive agents, and PAA as binder in a mass ratio of 85:4.5:0.5:10, using NMP as the solvent. The LFP and NCM 811 slurry were obtained by blending the active material, Super P and PVDF at a weight ratio of 80:10:10. These homogeneous slurries were coated onto Al foils with a doctor blade and dried at 80 °C. The dried electrodes were punched into circular sheets with a diameter of 12 mm, and the average mass loading of active material on each electrode was 2 ± 0.5 mg cm<sup>-2</sup>. The thickness was 33 ± 4 µm for graphite electrodes and was 30 ± 3 µm for LFP and NCM 811 electrodes. The graphite electrode was further dried at 150 °C, while the LFP and NCM811 electrodes were dried at 100 °C under vacuum overnight before cell assembly. The CR2032-type coin cells, comprising the obtained electrodes and Li metals (450 µm), were fabricated in an Ar-filled glove box with O<sub>2</sub> and H<sub>2</sub>O content below 0.1 ppm. A PVDF membrane (Merck Millipore Ltd., pore size: 0.2 µm) with a diameter of 19 mm was employed as the separator, and the electrolyte/graphite ratio in each cell was set at around 60 µL mg<sup>-1</sup>. Galvanostatic charge–discharge tests were carried out on a Neware battery testing system. The Li||graphite, Li||LFP, Li||NCM811 cells underwent three formation cycles at a current density of 20 mA g<sup>-1</sup>. Subsequently, the cells were cycled at a constant current of 1000 mA g<sup>-1</sup> within the voltage ranges of 3–5.2 V (for Li||graphite), 2.5–4.3 V (for Li||LFP), and 2.8–4.4 V (for Li||NCM811). The rate capability was assessed by varying the charge/discharge rate from 100 mA g<sup>-1</sup> to 8 A g<sup>-1</sup>. Potentiostatic tests were performed on Li||graphite cells, which were charged to and maintained at constant voltages of 5.1, 5.2, and 5.3 V for 10 h each. The CV, LSV, and impedance measurements were executed using the Bio-Logic potentiostat (VMP3). CV tests of Li||graphite cells were conducted at a scan rates of 0.1 mV s<sup>-1</sup>, while LSV tests were performed on a Ti working electrode at a sweep rate of 5 mV s<sup>-1</sup>. Impedance measurements were carried out by applying a 10 mV potential amplitude within the frequency range from 100 kHz to 10 mHz. The DRT analysis was carried out using the DRT tools developed by Francesco Ciucci et al.<sup>29</sup> For low-temperature electrochemical tests, the Li||graphite or Li||LFP cells were initially activated for 100 cycles at room temperature with a current density of 1000 mA g<sup>-1</sup>. The cells were then transferred to a temperature chamber allowed to equilibrate for 2 h to reach -20 °C, followed by cycling under a CCCV model. Specifically, the cells were charged to 5.4 V (Li||graphite) and 4.5 V (Li||LFP), respectively, at 100 mA g<sup>-1</sup> and the voltage was maintained until the charging current decreased to 10 mA g<sup>-1</sup>, followed by discharging at a constant current density of 500 mA g<sup>-1</sup>. To evaluate the capacity retention at various temperatures, after the activation process depicted above, the cells were charged at

200 mA g<sup>-1</sup> (45 °C), 100 mA g<sup>-1</sup> (45, 25, 10, 0, -10, -20 °C), 20 mA g<sup>-1</sup> (-30, -40 °C) and 10 mA g<sup>-1</sup> (-50 °C), respectively, using the CCCV mode, followed by discharging at a constant current density of 100 mA g<sup>-1</sup>. The test at -65 °C was conducted with RT-charge at 100 mA g<sup>-1</sup> using the CCCV mode, followed by discharging under -65 °C at 10 mA g<sup>-1</sup>.

Single-layer pouch cells were assembled utilizing the graphite electrode or the LFP electrode as the cathode (cathode dimension: 50 mm × 40 mm), paired with a 50 μm-thick Li foil as the anode (anode dimension: 52 mm × 42 mm). Al and Nickel strips were affixed to the sides of cathode and anode, respectively, to serve as electrode tabs. The mass loading of the cathode was 8–9 mg cm<sup>-2</sup>. The N/P ratios were ~15.5 and ~10.6 for the Li||graphite and the Li||LFP pouch cells, respectively. A PVDF separator impregnated with 20 μL cm<sup>-2</sup> electrolyte was laminated and assembled into Al plastic film packages, which were then sealed under vacuum. Subsequently, the cells were aged at 25 °C for 12 h and degassed following the initial cycle. The assembled pouch cells were pre-cycled between 3–5.2 V at 20 mA g<sup>-1</sup>. Subsequently, the pouch cells were charged at 100 mA g to 5.2 V and discharged at 200 mA g<sup>-1</sup>. A 440 mAh Li||graphite multi-layer pouch cell with a N/P ratio of ~2.4 was packaged. The pouch cell was charged at 20 mA g<sup>-1</sup> using the CCCV mode, followed by discharging at a constant current rate of 20 mA g<sup>-1</sup>. The specific energy of the AILMB was calculated as follows<sup>40,41</sup>:

$$E_{\text{full}} = C_{\text{full}} \times V_{\text{cell}} / (m_{\text{total}}) \quad (4)$$

where  $V_{\text{cell}}$  and  $C_{\text{full}}$  are the average working voltage and the reversible capacity of the full cell, respectively,  $m_{\text{total}}$  is the total weight based on the sum of current collector, cathode, anode, separator and electrolyte. The weight of the packing cell bag is excluded from the specific energy calculation due to our limited size of cell<sup>42,43</sup>. To assess the overcharge-safety, the pouch cells were charged from the open circuit voltage to 9 V at a scan rate of 20 mV s<sup>-1</sup>, and the infrared thermography images of the pouch cells were captured using a FLIR ONE PRO.

#### Postmortem analysis of cycled batteries

The cycled cells were disassembled in a glove box. The electrodes were rinsed with dimethyl carbonate (DMC) solvent several times to remove residual electrolyte, and then dried in the antechamber under vacuum of the glove box. Ex-situ XRD (Rigaku D/max-2500) with Cu Kα radiation ( $\lambda = 1.5418 \text{ \AA}$ ), was conducted to investigate the crystal structure changes during the initial charging and discharging processes. The evolutions in the interphases and morphologies for the cathode materials and Li metal anodes were studied using a field-emission scanning electron microscope (FE-SEM, SU8010) and a transmission electron microscope (TEM, FEI Tecnai G2 F30). X-ray photoelectron spectra (XPS) was obtained using a PHI 5000 Versa probe II spectrometer using monochromatic Al K(α) X-ray source. The depth values in the XPS depth profiles were estimated from the calibrated sputtering of SiO<sub>2</sub>. The collected spectra were calibrated based on the C 1s binding energy of 284.8 eV and analyzed using Multipak software. Time-of-flight secondary ion mass spectrometry (TOF-SIMS) was performed on a Nano TOF-2 instrument (ULVAC-PHI, Japan) with a 30 kV Bi<sub>3</sub><sup>++</sup> beam cluster primary-ion gun and Ar<sup>+</sup> beam (3 keV 100 nA) for depth profiling with a sputtering rate of 0.2 nm s<sup>-1</sup>. The surface roughness and 3D morphologies of the cycled Li metal anodes were characterized using atomic force microscopy (AFM, Bruker Dimension Icon). To investigate the thermal stability of the charged electrodes, the cells were pre-cycled twice and finally charged to 5.2 V (Li||graphite) and 4.3 V (Li||LFP), respectively. DSC samples were prepared by scraping the dried electrode materials off the Al current collector, and 1 mg of the material was sealed in a Mettler high-pressure stainless-steel pairing with 3 μL of electrolyte. The DSC measurement was

conducted from room temperature to 400 °C with a ramp rate of 5 °C min<sup>-1</sup>.

#### Computations

The ORCA software package was used to carry out DFT calculations, with molecular geometries for the ground states optimized at the B3LYP-D3/def2-TZVP level<sup>44</sup>. Molecular orbitals and ESPs were analyzed using Multiwfn and visualized through VMD<sup>45</sup>. MD simulations were conducted here to investigate the solvation structures of above electrolytes. Interactions between ions and molecules were described based on the Optimized Potentials for Liquid Simulation All-Atom (OPLS-AA) force field. All MD simulations were performed using the LAMMPS software<sup>46</sup>. The simulation boxes were constructed with PACKMOL software<sup>47</sup>. The molar ratios were taken from experiments in this study. Each system commenced with energy minimization employing the conjugate gradient algorithm, followed by a 1 ns Brownian dynamics at 500 K to relax the system temperature and randomize the initial shape of each component. Subsequently, a 10 ns NpT equilibration at 298 K was conducted to ensure the equilibrium of salt dissociations. A 20 ns NVT production run at 298 K and then performed, with the final 5 ns reserved for data analysis. The MD snapshots were visualized using Ovito software. A velocity-Verlet integrator was employed to update the positions and forces of atoms with a timestep of 1 fs. To account for long-range interactions, a particle-particle mesh method was utilized, with a global cutoff of 12 Å established for both Lennard-Jones and Coulombic interactions. Periodic boundary conditions were applied in all dimensions<sup>48</sup>.

#### Reporting summary

Further information on research design is available in the Nature Portfolio Reporting Summary linked to this article.

#### Data availability

The data that support the findings of this study are available from the corresponding author upon request.

#### References

- Cao, Y. et al. Bridging the academic and industrial metrics for next-generation practical batteries. *Nat. Nanotechnol.* 14, 200–207 (2019).
- Zhang, G. et al. A monofluoride ether-based electrolyte solution for fast-charging and low-temperature non-aqueous lithium metal batteries. *Nat. Commun.* 14, 1081 (2023).
- Yu, Z. et al. Rational solvent molecule tuning for high-performance lithium metal battery electrolytes. *Nat. Energy* 7, 94–106 (2022).
- Xue, W. et al. Ultra-high-voltage Ni-rich layered cathodes in practical Li metal batteries enabled by a sulfonamide-based electrolyte. *Nat. Energy* 6, 495–505 (2021).
- Sabaghi, D. et al. Ultrathin positively charged electrode skin for durable anion-intercalation battery chemistries. *Nat. Commun.* 14, 760 (2023).
- Wang, Y. et al. An all-fluorinated electrolyte toward high voltage and long cycle performance dual-ion batteries. *Adv. Energy Mater.* 12, 2103360 (2022).
- Holoubek, J. et al. Exploiting mechanistic solvation kinetics for dual-graphite batteries with high power output at extremely low temperature. *Angew. Chem. Int. Ed.* 131, 19068–19073 (2019).
- Han, X. et al. An in situ interface reinforcement strategy achieving long cycle performance of dual-ion batteries. *Adv. Energy Mater.* 9, 1804022 (2019).
- Yivlialin, R., Bussetti, G., Magagnin, L., Ciccacci, F. & Duo, L. Temporal analysis of blister evolution during anion intercalation in graphite. *Phys. Chem. Chem. Phys.* 19, 13855–13859 (2017).
- Qi, X. et al. Investigation of PF<sub>6</sub><sup>-</sup> and TFSI<sup>-</sup> anion intercalation into graphitized carbon blacks and its influence on high voltage lithium ion batteries. *Phys. Chem. Chem. Phys.* 16, 25306–25313 (2014).



11. Huesker, J., Froböse, L., Kwade, A., Winter, M. & Placke, T. In situ dilatometric study of the binder influence on the electrochemical intercalation of bis(trifluoromethanesulfonyl) imide anions into graphite. *Electrochim. Acta* 257, 423–435 (2017).
12. Cheng, X. B., Zhang, R., Zhao, C. Z. & Zhang, Q. Toward safe lithium metal anode in rechargeable batteries: a review. *Chem. Rev.* 117, 10403–10473 (2017).
13. Lin, D., Liu, Y. & Cui, Y. Reviving the lithium metal anode for high-energy batteries. *Nat. Nanotechnol.* 12, 194–206 (2017).
14. Ou, X., Gong, D., Han, C., Liu, Z. & Tang, Y. Advances and prospects of dual-ion batteries. *Adv. Energy Mater.* 11, 2102498 (2021).
15. Jiao, S. et al. Stable cycling of high-voltage lithium metal batteries in ether electrolytes. *Nat. Energy* 3, 739–746 (2018).
16. Ren, X. et al. High-concentration ether electrolytes for stable high-voltage lithium metal batteries. *ACS Energy Lett.* 4, 896–902 (2019).
17. Yu, D. et al. Advances in low-temperature dual-ion batteries. *ChemSusChem* 16, e202201595 (2023).
18. Zhou, X. et al. Strategies towards low-cost dual-ion batteries with high performance. *Angew. Chem. Int. Ed.* 59, 3802–3832 (2020).
19. Jiang, H. et al. A PF<sub>6</sub><sup>−</sup>-permeable polymer electrolyte with anion solvation regulation enabling long-cycle dual-ion battery. *Adv. Mater.* 34, 2108665 (2022).
20. Yamada, Y., Wang, J., Ko, S., Watanabe, E. & Yamada, A. Advances and issues in developing salt-concentrated battery electrolytes. *Nat. Energy* 4, 269–280 (2019).
21. Kravchyk, K. V. et al. High-energy-density dual-ion battery for stationary storage of electricity using concentrated potassium fluorosulfonylimide. *Nat. Commun.* 9, 4469 (2018).
22. Mo, Y. et al. Fluorinated solvent molecule tuning enables fast-charging and low-temperature lithium-ion batteries. *Adv. Energy Mater.* 13, 2301285 (2023).
23. Zou, Y. et al. Non-flammable electrolyte enables high-voltage and wide-temperature lithium-ion batteries with fast charging. *Angew. Chem. Int. Ed.* 135, e202216189 (2023).
24. Dong, X., Guo, Z., Guo, Z., Wang, Y. & Xia, Y. Organic batteries operated at −70 °C. *Joule* 2, 902–913 (2018).
25. Zhang, Z. et al. Fluorinated electrolytes for 5 V lithium-ion battery chemistry. *Energy Environ. Sci.* 6, 1806–1810 (2013).
26. Kim, S. C. et al. Potentiometric measurement to probe solvation energy and its correlation to lithium battery cyclability. *J. Am. Chem. Soc.* 143, 10301–10308 (2021).
27. Wu, J. et al. A synergistic exploitation to produce high-voltage quasi-solid-state lithium metal batteries. *Nat. Commun.* 12, 5746 (2021).
28. Lu, Y., Zhao, C.-Z., Huang, J.-Q. & Zhang, Q. The timescale identification decoupling complicated kinetic processes in lithium batteries. *Joule* 6, 1172–1198 (2022).
29. Wan, T. H., Saccoccio, M., Chen, C. & Ciucci, F. Influence of the discretization methods on the distribution of relaxation times deconvolution: implementing radial basis functions with DRT tools. *Electrochim. Acta* 184, 483–499 (2015).
30. Adams, B. D., Zheng, J., Ren, X., Xu, W. & Zhang, J. G. Accurate determination of coulombic efficiency for lithium metal anodes and lithium metal batteries. *Adv. Energy Mater.* 8, 1702097 (2017).
31. Zhao, J. et al. Surface fluorination of reactive battery anode materials for enhanced stability. *J. Am. Chem. Soc.* 139, 11550–11558 (2017).
32. Fan, X. et al. Fluorinated solid electrolyte interphase enables highly reversible solid-state Li metal battery. *Sci. Adv.* 4, eaau9245 (2018).
33. Chen, S. et al. Critical parameters for evaluating coin cells and pouch cells of rechargeable Li-metal batteries. *Joule* 3, 1094–1105 (2019).
34. Liu, X. et al. Thermal runaway of lithium-ion batteries without internal short circuit. *Joule* 2, 2047–2064 (2018).
35. Feng, X., Ren, D., He, X. & Ouyang, M. Mitigating thermal runaway of lithium-ion batteries. *Joule* 4, 743–770 (2020).
36. Zhao, Y., Xue, K., Tan, T. & Yu, D. Y. W. Thermal stability of graphite electrode as cathode for dual-ion batteries. *ChemSusChem* 16, e202201221 (2023).
37. Meng, Y. et al. Designing phosphazene-derivative electrolyte matrices to enable high-voltage lithium metal batteries for extreme working conditions. *Nat. Energy* 8, 1023–1033 (2023).
38. Xu, K. Charge-transfer process at graphite/electrolyte interface and the solvation sheath structure of Li<sup>+</sup> in nonaqueous electrolytes. *J. Electrochem. Soc.* 154, A162–A167 (2007).
39. Xu, K., Lam, Y., Zhang, S. S., Jow, T. R. & Curtis, T. B. Solvation sheath of Li<sup>+</sup> in nonaqueous electrolytes and its implication of graphite/electrolyte interface chemistry. *J. Phys. Chem. C* 111, 7411–7421 (2007).
40. Betz, J. et al. Theoretical versus practical energy: a plea for more transparency in the energy calculation of different rechargeable battery systems. *Adv. Energy Mater.* 9, 1803170 (2019).
41. Placke, T. et al. Perspective on performance, cost, and technical challenges for practical dual-ion batteries. *Joule* 2, 2528–2550 (2018).
42. Xia, Y. et al. Designing an asymmetric ether-like lithium salt to enable fast-cycling high-energy lithium metal batteries. *Nat. Energy* 8, 934–945 (2023).
43. Lu, Y. et al. Tuning the Li<sup>+</sup> solvation structure by a “Bulky Coordinating” strategy enables nonflammable electrolyte for ultra-high voltage lithium metal batteries. *ACS Nano* 17, 9586–9599 (2023).
44. Neese, F. The ORCA program system. *WIREs Comput. Mol. Sci.* 2, 73–78 (2011).
45. Lu, T. & Chen, F. Multiwfn: a multifunctional wavefunction analyzer. *J. Comput. Chem.* 33, 580–592 (2012).
46. Jorgensen, W. L. & Tirado-Rives, J. Potential energy functions for atomic-level simulations of water and organic and biomolecular systems. *Proc. Natl Acad. Sci. USA* 102, 6665–6670 (2005).
47. Martinez, L., Andrade, R., Birgin, E. G. & Martinez, J. M. PACKMOL: a package for building initial configurations for molecular dynamics simulations. *J. Comput. Chem.* 30, 2157–2164 (2009).
48. Hockney, R. W. & Eastwood, J. W. Computer simulation using particles. (CRC Press, 2021).

## Acknowledgements

F.K. would like to acknowledge the support from National Key Research and Development Program of China (2022YFB2404500) and Shenzhen Outstanding Talents Training Fund. D.Z. would like to acknowledge the support from the Fundamental Research Project of Shenzhen (NO. JCYJ20230807111702005). Y.W. would like to acknowledge the support from National Natural Science Foundation of China (NO. 22309102) and China Postdoctoral Science Foundation (Grant No. 2022M711788).

## Author contributions

D.Z. and F.K. conceived and designed this work. Y.W. performed the experiments and wrote the manuscript. Y.G. and Y.T. carried out the computations. S.D., P.L., Y.M., X.H., X.Z., and B. L. discussed the results and participated in the preparation of the paper.

## Competing interests

The authors declare no competing interests.

## Additional information

**Supplementary information** The online version contains supplementary material available at <https://doi.org/10.1038/s41467-024-49795-9>.

Correspondence and requests for materials should be addressed to Dong Zhou or Feiyu Kang.

**Peer review information** Nature Communications thanks Yuki Yamada and the other, anonymous, reviewer(s) for their contribution to the peer review of this work. A peer review file is available.

Reprints and permissions information is available at <http://www.nature.com/reprints>

**Publisher's note** Springer Nature remains neutral with regard to jurisdictional claims in published maps and institutional affiliations.

**Open Access** This article is licensed under a Creative Commons Attribution 4.0 International License, which permits use, sharing, adaptation, distribution and reproduction in any medium or format, as long as you give appropriate credit to the original author(s) and the source, provide a link to the Creative Commons licence, and indicate if changes were made. The images or other third party material in this article are included in the article's Creative Commons licence, unless indicated otherwise in a credit line to the material. If material is not included in the article's Creative Commons licence and your intended use is not permitted by statutory regulation or exceeds the permitted use, you will need to obtain permission directly from the copyright holder. To view a copy of this licence, visit <http://creativecommons.org/licenses/by/4.0/>.

© The Author(s) 2024



# Electric Field-Guided Ion Orchestration for Multi-Chemistry Zinc Metal Batteries

Yao Wang, Jinkai Zhang, Xin Zhao, Zetao Ren, Mingkun Tang, Ran Han, Guang Feng,\*  
Baohua Li, Dong Zhou,\* and Feiyu Kang\*

While nonaqueous cosolvents alleviate hydrogen evolution reaction and dendritic growth in aqueous zinc (Zn) metal batteries (ZMBs), persistent  $\text{H}_2\text{O}$  activity at Zn|electrolyte interfaces originating from unregulated ion distribution leads to premature failure. Here, an electric field-guided ion orchestration (EF-IO) strategy is proposed, leveraging cation interfacial modifiers to reconfigure electric double layers (EDLs) and solvation configurations. Interfacial simulations combined with experimental investigations verify that the ion-orchestrated-EDL synergistically diversifies  $\text{Zn}^{2+}/\text{Na}^+$  solvation configurations and homogenizes localized electric fields, thereby forming an organic–inorganic gradient solid electrolyte interphase (SEI) that suppresses parasitic reactions. This enables dendrite-free Zn plating with 3400 h cyclability in Zn||Zn symmetric cells, while Zn|| $\text{V}_{10}\text{O}_{24}\cdot 12\text{H}_2\text{O}$  full cells exhibit exceptional durability along with wide temperature adaptability ( $-45$  to  $55^\circ\text{C}$ ). Crucially, this EF-IO strategy unlocks  $\text{ClO}_4^-$ -based reversible anion storage in high-voltage organic cathodes. By bridging interfacial dynamics and multi-chemistry compatibility, this work establishes a promising paradigm for robust and versatile ZMBs.

## 1. Introduction

The global transition toward renewable energy systems necessitates advanced electrochemical storage technologies that reconcile operational safety with economic viability.<sup>[1]</sup> The aqueous zinc (Zn) metal battery (ZMB) have emerged as a

frontrunner in this energy revolution, leveraging unique advantages of the Zn metal anode including earth abundance, appropriate redox potential ( $-0.76$  V vs the standard hydrogen electrode (SHE)), and exceptional theoretical capacity ( $820\text{ mAh g}^{-1}$  gravimetric,  $5855\text{ mAh cm}^{-3}$  volumetric).<sup>[2]</sup> These attributes not only circumvent geopolitical constraints and flammability risks inherent to lithium-ion batteries (LIBs), but also establish ZMBs as technically and economically viable solutions for grid-scale storage.<sup>[3]</sup> Despite these merits, the practical realization of aqueous ZMBs faces formidable challenges rooted in the irreversibility of Zn metal anodes during repeated stripping/plating processes. The adoption of aqueous electrolyte fosters parasitic reactions and dendrite proliferation at the electrode|electrolyte interface,<sup>[4]</sup> where reactive  $\text{H}_2\text{O}$  molecules within electric double layers (EDLs) trigger persistent hydrogen evolution reaction ( $\text{HER}$ ,  $2\text{H}_2\text{O} + 2\text{e}^- \rightarrow \text{H}_2 + 2\text{OH}^-$ ) and Zn corrosion.<sup>[5]</sup> The resultant  $\text{OH}^-$  generation initiates self-accelerating degradation through irreversible byproduct formation,<sup>[6]</sup> while the low  $\text{H}_2\text{O}$  decomposition potential ( $1.23$  V vs SHE) severely limits high-voltage cathode operation due to oxygen evolution reaction (OER).<sup>[7]</sup> Therefore, the poor interfacial compatibility between highly active  $\text{H}_2\text{O}$  molecules and electrodes represents significant obstacles to the implementation of ZMBs.

The Introduction of nonaqueous cosolvent has emerged as a pivotal electrolyte engineering strategy to circumvent these issues and improve electrode compatibility.<sup>[8]</sup> Among them, deep eutectic electrolytes (DEEs), formed via intermolecular interactions (e.g., Lewis acid-base interactions, hydrogen bonding, and van der Waals interactions)<sup>[9]</sup> between multiple components, have gained prominence due to their facile synthesis and tunable solvation structures.<sup>[10]</sup> These DEEs not only suppress dendrites by stabilizing  $\text{Zn}^{2+}$  coordination environments<sup>[11]</sup> and confining  $\text{H}_2\text{O}$  within bulk solvation structures,<sup>[12]</sup> but also depressing freezing points of aqueous electrolytes. However, uncontrolled ion distribution and solvation structures at the Zn|electrolyte interface fail to fully eliminate residual  $\text{H}_2\text{O}$  activity, and the critical interplay between solvation configurations and electric field-driven interfacial behavior remains largely neglected. This oversight perpetuates thermodynamic instability at the Zn

Y. Wang, X. Zhao, Z. Ren, M. Tang, R. Han, B. Li, D. Zhou, F. Kang  
Tsinghua Shenzhen International Graduate School  
Tsinghua University  
Shenzhen 518055, China  
E-mail: [zhou.d@sz.tsinghua.edu.cn](mailto:zhou.d@sz.tsinghua.edu.cn); [fykang@tsinghua.edu.cn](mailto:fykang@tsinghua.edu.cn)

Y. Wang  
State Key Laboratory of Heavy Oil Processing  
College of Science  
China University of Petroleum (Beijing)  
Beijing 102249, China

J. Zhang, G. Feng  
State Key Laboratory of Coal Combustion  
School of Energy and Power Engineering  
Huazhong University of Science and Technology (HUST)  
Wuhan 430074, China  
E-mail: [gffeng@hust.edu.cn](mailto:gffeng@hust.edu.cn)

The ORCID identification number(s) for the author(s) of this article can be found under <https://doi.org/10.1002/adma.202511163>

DOI: 10.1002/adma.202511163

surface, accelerating parasitic reactions that degrade Coulombic efficiency (CE) and cycle life of ZMBs. Moreover, conventional DEEs exclusively cater to  $\text{Zn}^{2+}$  redox in typical vanadium- or manganese-based inorganic cathodes,<sup>[9]</sup> neglecting the untapped potential of anion storage in sustainable organic hosts. Such limitations stem from the disconnection between bulk solvation regulation and interfacial electrochemistry, ultimately restricting ZMBs to narrow chemical paradigms. These issues fundamentally hinder the rational design of durable and versatile ZMBs.

Herein, for the first time, we propose a paradigm shift through electric field-guided ion orchestration (EF-IO), a strategy that fundamentally enhances the diversity of interfacial solvation configurations to suppress parasitic reactions at the Zn|electrolyte interface. Rational cation screening based on hydration enthalpy identifies  $\text{Na}^+$  as an optimal interfacial modifier to reconfigure EDLs. Under operational electric fields,  $\text{Na}^+$  preferentially accumulates in the inner layer of EDLs, screening localized electric fields and inducing anion enrichment. This ion orchestrated-EDL diversifies  $\text{Zn}^{2+}/\text{Na}^+$  solvation configurations, driving the formation of an organic–inorganic gradient solid electrolyte interphase (SEI) that enables [002]-textured Zn deposition with dendrite suppression and dramatically reduces HER. This strategy yields an expanded electrochemical stability window (ESW) of 2.5 V, endows the Zn||Zn symmetric cell with remarkable cyclability exceeding 3400 h at 1 mA cm<sup>−2</sup> alongside a 44-fold reduction in corrosion current, and the Zn||Cu asymmetric cell with 99.5% average CE over 400 cycles. Practical validation using  $\text{V}_{10}\text{O}_{24}\cdot 12\text{H}_2\text{O}$  (VOH) cathode demonstrates exceptional full-cell durability (>10 000 cycles, 0.0076% capacity decay per cycle) with wide-temperature operation (−45 to 55 °C). Remarkably, this EF-IO design unlocks novel anion storage in high-voltage organic cathode of 1,4-bis(diphenylamino)benzene (BDB), delivering 103 mAh g<sup>−1</sup>; via reversible two-electron  $\text{ClO}_4^-$  redox. This work establishes new design principles for robust and multi-chemistry ZMBs, while advancing fundamental understanding of interfacial electrochemistry.

## 2. Results and Discussion

### 2.1. EF-IO Design and Investigation on Bulk Solvation Structures

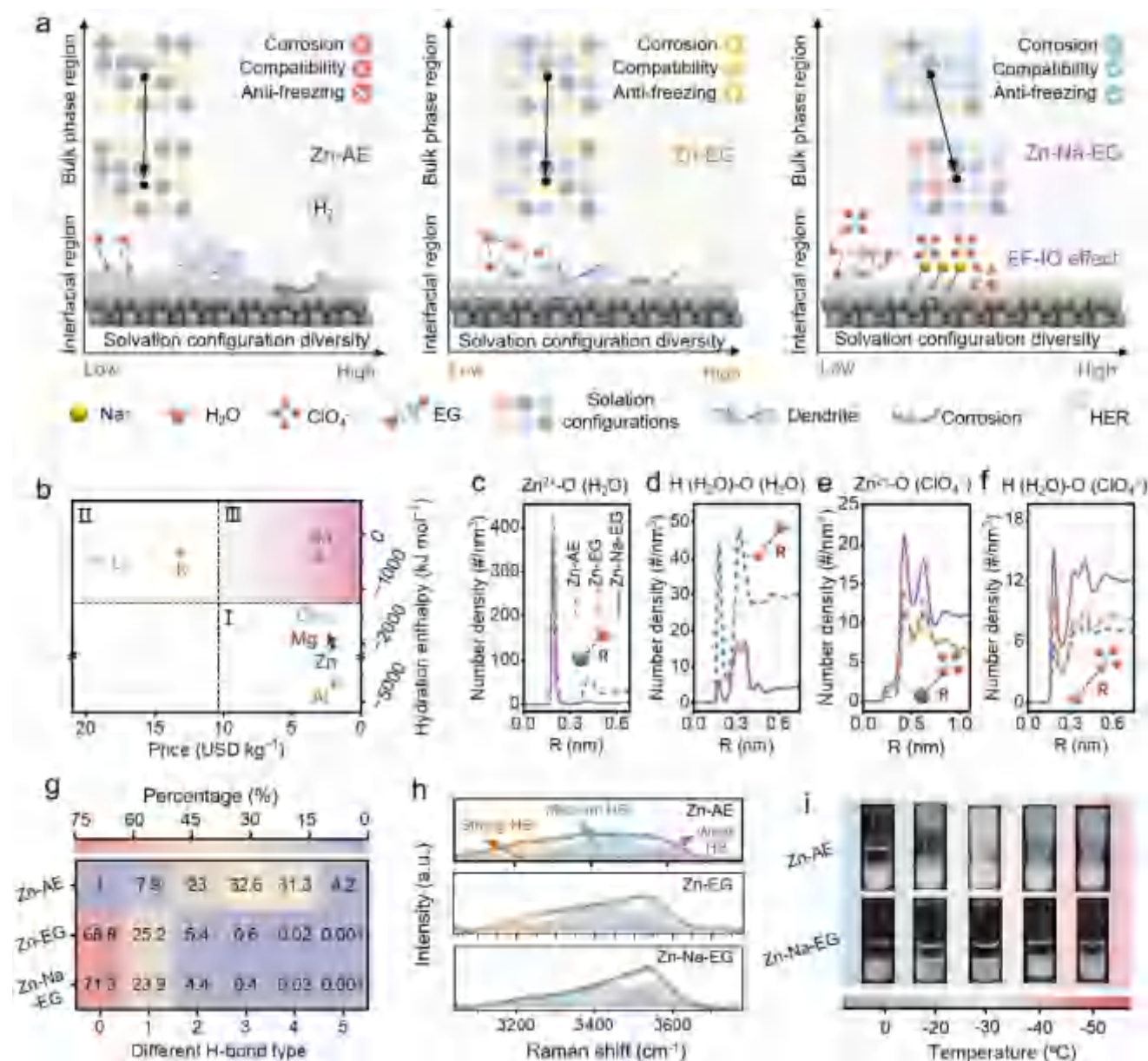
As depicted in the left panel of **Figure 1a**, the conventional aqueous  $\text{Zn}(\text{ClO}_4)_2\cdot 6\text{H}_2\text{O}\cdot \text{H}_2\text{O}$  system (denoted as Zn-AE), characterized by limited coordination diversity, induces exacerbated HER, Zn corrosion, electrolyte solidification at low temperatures, with its restricted ESW hindering multi-chemistry compatibility at high voltage. To mitigate these issues, a typical DEE system was constructed by mixing  $\text{Zn}(\text{ClO}_4)_2\cdot 6\text{H}_2\text{O}$  (acting as a Lewis acid and hydrogen bond (HB) acceptor) and ethylene glycol (EG, serving as a Lewis base and HB donor) with a rationalized formula of 2 m  $\text{Zn}(\text{ClO}_4)_2\cdot 6\text{H}_2\text{O}\cdot \text{EG}$  (denoted as Zn-EG, **Figure S1**, Supporting Information). Nevertheless, residual  $\text{H}_2\text{O}$  activity persists at the Zn|electrolyte interface due to unregulated ion distribution and suboptimal solvation structure (the middle panel of **Figure 1a**). To suppress interfacial  $\text{H}_2\text{O}$  activity in the Zn-EG system, a thermodynamic selection criterion is proposed for cationic modifiers based on their hydration characteristics. The designed strategy prioritizes cations with weak hydration tendencies to establish  $\text{H}_2\text{O}$ -depleted interfacial environments through

electric field-driven adsorption, thereby facilitating anion-enriched solvation structures and enhancing solvation configuration diversity (the right panel of **Figure 1a**), as will be validated later. The hydration propensity of cations ( $\text{M}^{z+}$ ) can be predicted through hydration enthalpy ( $\Delta H_{\text{hyd}}$ ) calculations using the established empirical relation:<sup>[13]</sup>

$$\Delta H_{\text{hyd}} = -\frac{930(z-0.2)^2}{r+1-(1/2z)} \text{ kJ mol}^{-1} \quad (1)$$

where  $z$  and  $r$  represent the charge number and Pauling univalent radius, respectively. Higher (more negative)  $\Delta H_{\text{hyd}}$  values correlate with stronger  $\text{M}^{z+}\cdot \text{H}_2\text{O}$  interactions that stabilize tightly bound hydration shells, thereby suppressing anion association (e.g.,  $\text{M}^{z+}\cdot \text{ClO}_4^-$  ion pairing). Although multivalent cations leverage economic advantages from abundant raw metal materials, their excessive hydration effects (e.g.,  $\Delta H_{\text{hyd}}$ ,  $\text{Al}^{3+} = -4665 \text{ kJ mol}^{-1}$ ) preclude effective interfacial engineering (Region I in **Figure 1b**). In contrast, monovalent cations in Region II (**Figure 1b**, e.g.,  $\text{Li}^+$ ,  $\text{K}^+$ ) demonstrate weaker hydration, but face scalability challenges due to cost limitations. This cost-performance paradox is resolved by  $\text{Na}^+$  in Region III (**Figure 1b**,  $\Delta H_{\text{hyd}}$ ,  $\text{Na}^+ = -405 \text{ kJ mol}^{-1}$ ), which balances sufficient hydration weakness for anion enrichment with favorable economic viability. Potential of mean force (PMF) calculations corroborate this selection criteria rationale, demonstrating significantly weaker  $\text{Na}^+\cdot \text{H}_2\text{O}$  binding compared to Region I cations (e.g.,  $\text{Zn}^{2+}$  and  $\text{Ca}^{2+}$ , **Figure S2** and **Table S1**, Supporting Information). Experimental results identify  $\text{NaClO}_4$  as the singularly effective modifier, constructing the 2 m  $\text{Zn}(\text{ClO}_4)_2\cdot 6\text{H}_2\text{O}\cdot 3 \text{ m NaClO}_4\cdot \text{EG}$  (henceforth referred to as Zn-Na-EG) system, which suppresses HER activity by attenuating  $\text{H}_2\text{O}$  penetration at the anode surface (**Figure S3**, Supporting Information). This superiority of the stems from the low hydration tendency of  $\text{Na}^+$  and its electric field-driven preferential accumulation in the inner EDLs, as demonstrated later.

To elucidate the solvation structure modulation mechanism, molecular dynamics (MD) simulations were systematically performed (**Figure S4**, Supporting Information). The radial number density analysis reveals that EG ligands effectively enter the first solvation shells of both  $\text{Zn}^{2+}$  and  $\text{H}_2\text{O}$ , as evidenced by pronounced O-atom distribution peaks at  $\approx 0.2 \text{ nm}$  from  $\text{Zn}^{2+}$  and H atoms of  $\text{H}_2\text{O}$ , respectively (**Figures S5** and **S6a,b**, Supporting Information). This competitive coordination displaces  $\text{H}_2\text{O}$  molecules from  $\text{Zn}^{2+}$  migration pathways, effectively decoupling  $\text{H}_2\text{O}$  activity from interfacial Zn deposition (**Figure 1c,d**). Concurrently, the induced EG ligand enhances  $\text{Zn}^{2+}\cdot \text{ClO}_4^-$  coordination, elevating contact ion pair (CIP) formation from 4% to 13% (**Figure S7a,b**, Supporting Information). This trend amplifies significantly upon  $\text{NaClO}_4$  addition (**Figures S6c** and **S7c**, Supporting Information), where  $\text{ClO}_4^-$  exhibits enhanced coordination with both  $\text{Zn}^{2+}$  and  $\text{H}_2\text{O}$  (**Figure 1e,f**). Notably, compared to  $\text{Zn}^{2+}$ , the induced  $\text{Na}^+$  exhibits stronger binding for  $\text{ClO}_4^-$  while weaker binding with  $\text{H}_2\text{O}$ , as revealed by PMF calculations (**Figure S8**, Supporting Information). This drives 87.3% of  $\text{Na}^+$  to form CIPs in the Zn-Na-EG system (**Figure S7c**, Supporting Information). This ion-specific selectivity is beneficial for adaptively establishing an anion-enriched and  $\text{H}_2\text{O}$ -depleted interfacial environment through electromigration accumulation during



**Figure 1.** EF-IO design and investigation on bulk solvation structures. a) Schematic illustration of the EF-IO strategy with diverse solvation configurations. b) Hydration enthalpy of cations and associated metallic costs. c–f) Radial number density distributions of O (H<sub>2</sub>O) around (c) Zn<sup>2+</sup> and (d) H (H<sub>2</sub>O), and O (ClO<sub>4</sub><sup>-</sup>) around (e) Zn<sup>2+</sup> and (f) H (H<sub>2</sub>O). g) Proportion of H<sub>2</sub>O molecules engaged in H-bonding interactions with neighboring H<sub>2</sub>O molecules. h) Raman spectra of various electrolytes. i) Optical photographs of the Zn-AE (the upper panel) and the Zn-Na-EG (the lower panel) systems at low temperatures.

cycling, which will be further validated later. Crucially, the solvation configuration diversity expands progressively across the electrolyte systems. In the baseline Zn-AE, Zn<sup>2+</sup> adopts only seven distinct coordination types dominated by [Zn(H<sub>2</sub>O)<sub>6</sub>]<sup>2+</sup> clusters (Figure S9a, Supporting Information), which results from the strong coordination between Zn<sup>2+</sup> and H<sub>2</sub>O (Figure 1c,e). The introduction of EG ligands dramatically expands this diversity to 17 unique configurations (Figure S9b, Supporting Information), primarily through the competitive displacement of H<sub>2</sub>O by hydroxyl groups of EG. In the Zn-Na-EG system, the O donors from H<sub>2</sub>O, ClO<sub>4</sub><sup>-</sup>, and EG effectively solvate Na<sup>+</sup>, all of which

exhibit a prominent peak at ≈0.25 nm (Figure S5c,e; Note S1, Supporting Information). Subsequent Na<sup>+</sup> incorporation in the Zn-Na-EG system further amplifies solvation configuration diversity, which is primarily driven by its strong affinity with anions that promote anion participation in solvation complexes, yielding over 46 resolvable solvation complexes (Figure S9c,d, Supporting Information). This enhancement of configuration multiplicity contributes to elevated system entropy, thermodynamically favoring interfacial stability as well as lowering the freezing point. In addition to the solvation structures, systematic investigations reveal fundamental restructuring of the HB network



of electrolyte systems. The Zn-AE system exhibits an extensively interconnected HB network, characterized by a high H<sub>2</sub>O-H<sub>2</sub>O HB concentration of 44.33 nm<sup>-3</sup> (Table S2, Supporting Information), where 91.1% of H<sub>2</sub>O molecules participate in forming multiple HBs (Figure 1g). Remarkably, the introduced EG ligands disrupt HB connectivity, reducing HB concentration by 97.7% to 1.04 (Table S2, Supporting Information) while dramatically increasing the population of non-bonded H<sub>2</sub>O molecules to 68.8% (Figure 1g). This disruption mechanism becomes more pronounced upon NaClO<sub>4</sub> introduction, where competitive H<sub>2</sub>O-ClO<sub>4</sub><sup>-</sup> interactions (Table S2, Supporting Information) further suppress multi-HB configurations, elevating isolated H<sub>2</sub>O content to 71.3% (Figure 1g).

Raman spectroscopy and Fourier-transform infrared (FTIR) spectroscopy provide critical insights into H<sub>2</sub>O speciation and ion coordination. As illustrated in Figure 1h, the broad Raman band corresponding to the O-H stretching vibrations of H<sub>2</sub>O molecules can be deconvoluted into three Gaussian components, representing strong (3230 cm<sup>-1</sup>), medium (3430 cm<sup>-1</sup>), and weak (3550 cm<sup>-1</sup>) HB configurations, respectively.<sup>[14]</sup> Quantitative analysis demonstrates that EG incorporation reduces the strong HB fraction from 31.3% (Zn-AE) to 18.3%, while enhancing the weak HB proportion from 16.5% (Zn-AE) to 28.1% (Figure S10, Supporting Information). NaClO<sub>4</sub> co-introduction amplifies this trend, diminishing strong HB content to 10.7%, indicative of synergistic anion-mediated HB suppression. FTIR analysis corroborates this structural evolution, showing a characteristic blueshift (1645 to 1650 cm<sup>-1</sup>, Figure S11a, Supporting Information) in the O-H bending vibration and decreased free H<sub>2</sub>O content in the Zn-Na-EG compared to the Zn-AE system.<sup>[15]</sup> This spectral shift confirms stronger H<sub>2</sub>O confinement via EG/ClO<sub>4</sub><sup>-</sup> coordination. Apparently, the anion coordination environment also changes, as evidenced by characteristic redshifts in both FTIR (1079 to 1069 cm<sup>-1</sup>, Figure S11b, Supporting Information) and Raman spectra of the ClO<sub>4</sub><sup>-</sup> vibration modes (934 to 932 cm<sup>-1</sup>, Figure S11c, Supporting Information), confirming a transition from free ClO<sub>4</sub><sup>-</sup> to coordinated ClO<sub>4</sub><sup>-</sup> species (i.e., Zn<sup>2+</sup>-ClO<sub>4</sub><sup>-</sup> ion pair and ClO<sub>4</sub><sup>-</sup>-H<sub>2</sub>O interactions).<sup>[16]</sup> These findings demonstrate that EG and NaClO<sub>4</sub> collaboratively restructure the electrolyte with suppressed free H<sub>2</sub>O activity.

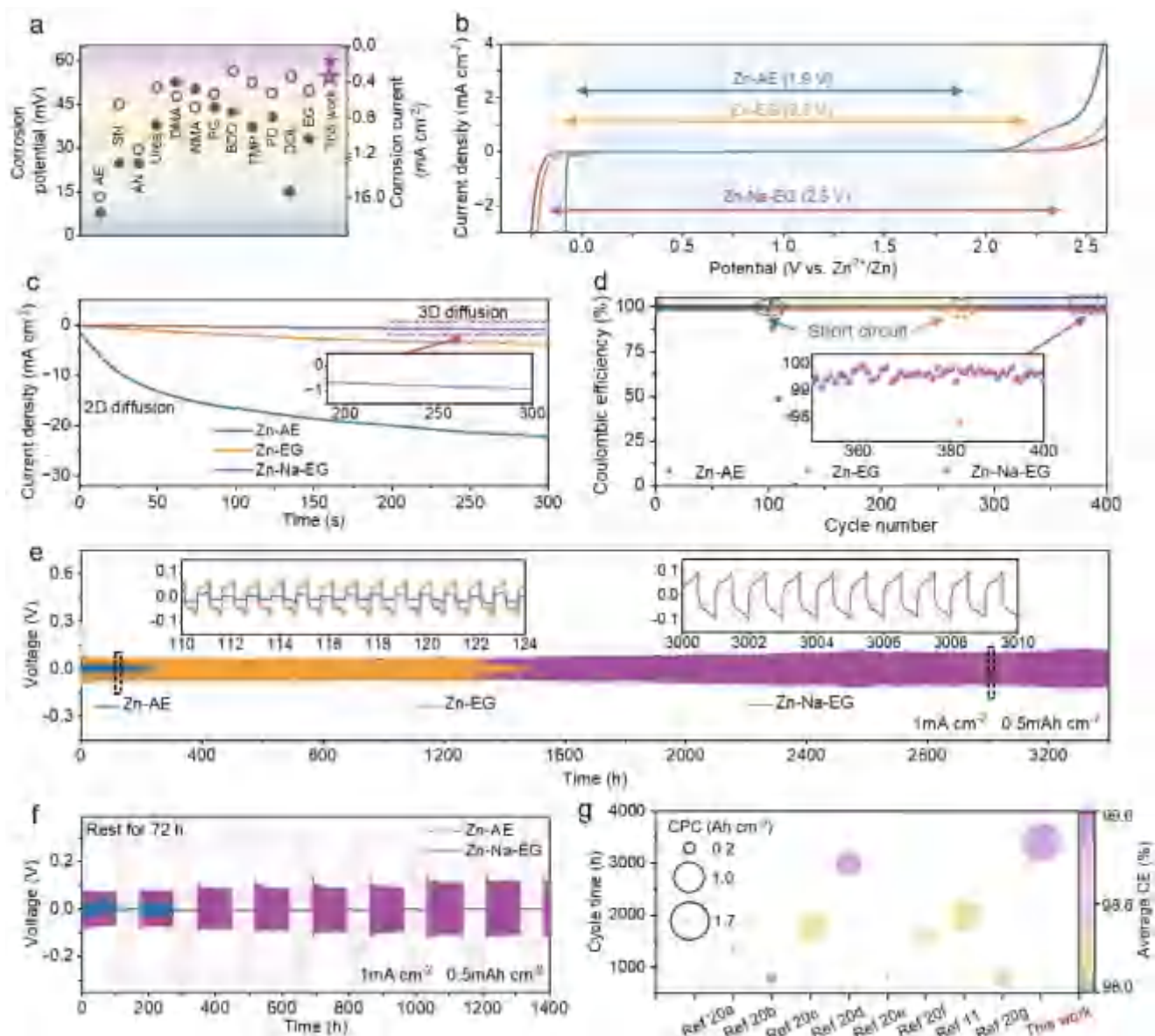
The deliberate disruption of long-range HB ordering within the Zn-Na-EG system also elevates the thermodynamic barrier for crystalline ice nucleation and formation, as demonstrated by differential scanning calorimetry (DSC) analysis (Figure S12, Supporting Information). Unlike conventional aqueous electrolytes exhibiting distinct freezing transitions at -20 °C, the Zn-Na-EG system maintains complete liquid characteristics down to -60 °C, indicating a significantly elevated energy barrier for ice nucleation and growth. This anomalous behavior is achieved through EG-mediated molecular confinement and anion-coordinated hydration shell distortion. Corresponding visual freezing tests corroborate these findings, demonstrating that the Zn-Na-EG electrolyte retains fluidity at -50 °C, contrasting sharply with the fully frozen aqueous counterpart (Figure 1i). These observations consistent with the above DSC results, establishing the Zn-Na-EG system as a robust strategy for wide-temperature ZMBs. Furthermore, volatility assessments reveal exceptional environmental stability, of the Zn-Na-EG system, with 100% electrolyte retention after 150 h versus 32% loss in

the AE aqueous electrolyte (Figure S13, Supporting Information). Such remarkable stability arises from strengthened anion-H<sub>2</sub>O coordination and EG-mediated H<sub>2</sub>O molecular confinement.

## 2.2. Electrochemical Behavior and Corrosion Resistance toward Zn Anode

The self-corrosion behaviors of Zn metal in various systems were systematically assessed through Tafel polarization analysis (Figure S14, Supporting Information). The corrosion potential ( $E_{\text{corr}}$ ) reflects thermodynamic susceptibility while the corrosion current ( $j_{\text{corr}}$ ) determines the corrosion kinetics of electrodes.<sup>[17]</sup> As summarized in Figure 2a, the Zn-Na-EG exhibits a higher  $E_{\text{corr}}$  (57.9 mV vs Zn<sup>2+</sup>/Zn) than that in the Zn-AE (7.42 mV), signifying suppressed thermodynamic corrosion propensity. More strikingly, it demonstrates a 44-fold reduction in  $j_{\text{corr}}$  (0.39 mA cm<sup>-2</sup>), endowing a diminished corrosion rate during the Zn plating/stripping process. This exceptional corrosion resistance outperforms most reported eutectic/organic electrolytes (Figure 2a), confirming exceptional interfacial protection through the EF-IO strategy. The ESW expansion mechanism was probed by linear sweep voltammetry (LSV) using an electrochemically inert titanium (Ti) working electrode. As demonstrated in Figure 2b, the Zn-AE displays a constrained ESW of 1.9 V (vs Zn/Zn<sup>2+</sup>) only, with premature HER initiation at -0.02 V and OER onset at 1.88 V, characteristic of unmitigated H<sub>2</sub>O reactivity. Strikingly, the Zn-Na-EG postpones the onset potential of HER to -0.15 V and OER to 2.35 V, achieving an expanded ESW of ≈2.5 V, which is critical for enabling high-voltage anion redox chemistry, as later experimentally validated. This significant improvement stems from the highly enhanced solvation disorder that reduces H<sub>2</sub>O molecule polarization susceptibility. Chronoamperometry (CA) analysis at an applied potential of -150 mV provides critical insights into the nucleation and deposition behavior of the Zn anode (Figure 2c). In the Zn-AE, the current density increases continuously due to the “tip effect” induced by non-uniform electric fields, implying an unrestricted 2D diffusion process during Zn plating. Consequently, Zn deposition occurs preferentially at the tips of pre-existing irregular crystal nuclei to minimize surface energy, ultimately leading to uncontrolled dendrite formation.<sup>[18]</sup> In contrast, the Zn-Na-EG maintains a near-constant current density through 3D diffusion control (Figure 2c), consistent with previous reports.<sup>[19]</sup> This behavior indicates homogeneous ion redistribution enabled by the EF-IO, which promotes the formation of a uniform and compact Zn deposition layer.

The electrochemical reversibility of Zn anodes was rigorously evaluated through Zn||Cu asymmetric and Zn||Zn symmetric cells. As illustrated in Figure 2d, under a current density of 1 mA cm<sup>-2</sup> with a fixed capacity of 1 mAh mA cm<sup>-2</sup>, the Zn||Cu cells utilizing the Zn-AE experiences rapid CE fluctuations and voltage profile instability after 110 cycles, ultimately failing due to dendrite-induced short circuits and cumulative interfacial side reactions. In stark contrast, the Zn-Na-EG enables an extended lifespan of over 400 cycles with a stabilized average CE of 99.5%, while maintaining remarkably consistent voltage profiles even post 400 cycles (Figure S15, Supporting Information). These results suggest the formation of a SEI with exceptional electrochemical stability. To further substantiate the benefit of the



**Figure 2.** Electrochemical behavior and corrosion resistance toward Zn anodes. a) Tafel polarization plots of Zn-AE, Zn-EG, Zn-Na-EG systems in comparison with state-of-the-art DEEs. b) LSV curves for various electrolyte systems. c) Chronoamperometric curves under constant potential polarization of  $-150$  mV in various electrolytes. Inset shows the enlarged view of the Zn-Na-EG system. d) CE measurements of Zn||Cu cells at  $1 \text{ mA cm}^{-2}$  with a capacity of  $1 \text{ mAh cm}^{-2}$ . The corresponding CE of the Zn-Na-EG system between 350 and 400 cycles is shown in the inset. e) Voltage profiles of Zn||Zn symmetric cells at  $1 \text{ mA cm}^{-2}$  with a capacity of  $0.5 \text{ mAh cm}^{-2}$ . f) Shelving-recovery performances for Zn||Zn symmetric cells with a 72h-aging after every 100 cycles. g) Comparative analysis of cycle time, average CE, and CPC of previously reported works on DEEs and this work.<sup>[11,20]</sup>

SEI, the long-term cycling stability of Zn||Zn symmetrical cells was investigated. As shown in Figure 2e, Zn||Zn cells with Zn-AE and Zn-EG electrolytes exhibit abrupt polarization fluctuations and short circuits after 220 and 1330 h of cycling, respectively, due to Zn dendrite growth and uncontrollable side reactions. In comparison, Zn||Zn cells formulated with the Zn-Na-EG showcase excellent long-term cycling durability exceeding 3400 h with stable polarization voltages. It is noted that Zn||Zn and Zn||Cu cells show satisfactory stability when replacing the EG by a more cost-effective ethanol solvent, and reducing the salt concentrations (Figures S44 and S45, Supporting Information),

suggesting the effectiveness of the EF-IO strategy in stabilizing Zn anodes. Rate capability assessments further demonstrate the interfacial robustness, where Zn-Na-EG maintains stable operation up to  $10 \text{ mA cm}^{-2}$  compared to Zn-AE failure at above  $5 \text{ mA cm}^{-2}$  (Figure S16, Supporting Information). This superior rate performance originates from enhanced interfacial charge transfer kinetics.

Practical reliability of the Zn-Na-EG system was assessed through shelving-recovery tests, where Zn||Zn cells were subjected to a 72h-rest period after every 100 cycles at  $1 \text{ mA cm}^{-2}$  with a capacity of  $0.5 \text{ mAh cm}^{-2}$  (Figure 2f). Remarkably, the cell with



the Zn-Na-EG exhibits stable operation for over 1400 h, dramatically outperforming the Zn-AE counterpart (< 200 h, Figure S17, Supporting Information). This finding underscores the superior interfacial passivation of the Zn-Na-EG system against parasitic reactions. To confirm that the enhanced electrochemical performance of the Zn anode was attributed to the Na salt, a Na<sup>+</sup>-free 5 m Zn-EG system was used as a control. Results reveal significantly reduced cycling stability (Figure S18, Supporting Information), compromised rate capability (Figure S19a, Supporting Information), and limited shelving endurance (≈700 h, Figure S19b, Supporting Information), unequivocally confirming the indispensable role of Na<sup>+</sup> in stabilizing dynamic interfaces through solvation configuration modulation. When benchmarked against state-of-the-art DEEs (Figure 2g; Table S3, Supporting Information), our Zn-Na-EG system excels in terms of cycle life, cumulative plated capacity (CPC), and average CE, representing a significant advancement in electrolyte design for durable ZMBs.

### 2.3. EF-IO Effect on Interfacial Architecture

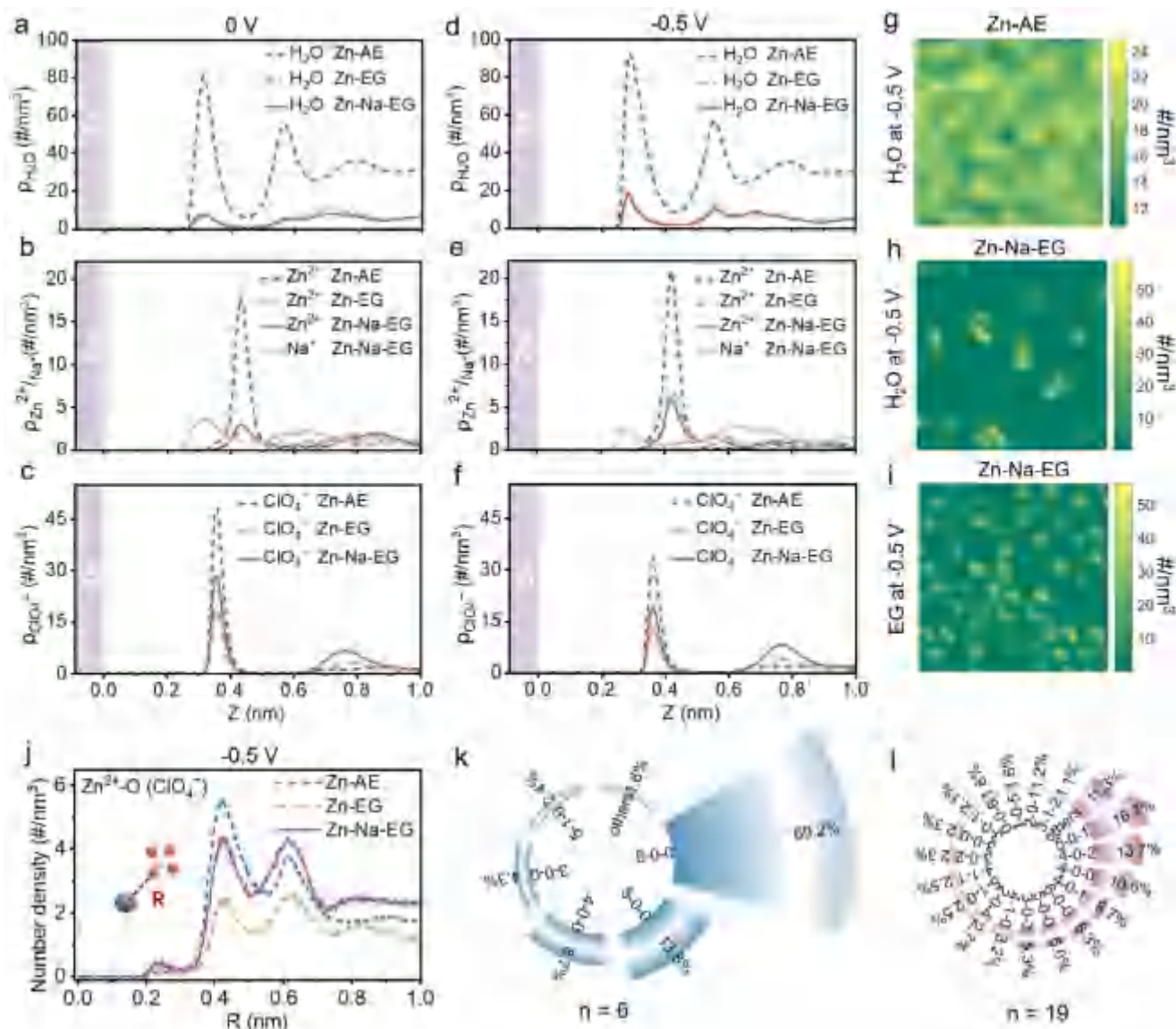
To elucidate the EF-IO effect and realistic solvation coordination under operational electric-fields, constant-potential molecular dynamics (MD) simulations were performed to probe the Zn|electrolyte interfacial dynamics. Simulations reveal critical reconfiguration of EDL, with H<sub>2</sub>O molecules exhibiting a characteristic adsorption peak at ≈0.3 nm from the Zn surface (Figure 3a), positioning closer than EG molecules which display a distinct adsorption peak at 0.4 nm (Figure S20a, Supporting Information). Notably, the Zn-Na-EG system exhibits distinct ion orchestration effects. While Zn<sup>2+</sup> occupies the second adsorption layer (peak at ≈0.4 nm), Na<sup>+</sup> preferentially accumulates in the inner layer of the EDLs (peak at ≈0.3 nm, Figure 3b) through potential-driven electrosorption. This stratified cation arrangement enables dual critical functions. First, the Na<sup>+</sup>-rich inner layer establishes electrostatic shielding to homogenize localized electric field distribution, effectively suppressing tip-enhanced dendrite growth.<sup>[21]</sup> Second, strong Na<sup>+</sup>-ClO<sub>4</sub><sup>-</sup> ion pairing induces substantial anion enrichment within the EDLs (Figure 3c). Under −0.5 V polarization, H<sub>2</sub>O and Zn<sup>2+</sup> maintain analogous number density distributions (Figure 3d,e). Despite electrostatic repulsion-driven anion depletion at the interface, Na<sup>+</sup> retains its preferential positioning in the Zn-Na-EG system. The robust Na<sup>+</sup>-ClO<sub>4</sub><sup>-</sup> association preserves interfacial anion enrichment (Figure 3f), which is critical for ion orchestration. Furthermore, EG exhibits potential-independent adsorption behavior (Figure S20, Supporting Information), governed primarily by van der Waals interactions rather than potential-dependent electrochemical adsorption. This unique property enables EG to suppress both H<sub>2</sub>O and ionic species adsorption at the anode surface (Figure S20a,b, Supporting Information), which largely reduces the absorption peak of water by ≈80% (Figure 3a,b). The competitive adsorption mechanism becomes particularly evident in spatial distribution analysis (Figures 3g–i; S21, Supporting Information), where EG molecules form a continuous interfacial matrix that sterically excludes H<sub>2</sub>O from reactive Zn sites, thereby mitigating HER. The reconstructed HB network provides further mechanistic insights into HER suppression. EG incorporation notably disrupts bulk-like H<sub>2</sub>O–H<sub>2</sub>O bonds, replacing them with H<sub>2</sub>O–EG and H<sub>2</sub>O–

ClO<sub>4</sub><sup>-</sup> interactions (Figure S22, Supporting Information). This HB redistribution kinetically hinders proton transport pathways along the original H<sub>2</sub>O network, creating an additional energy barrier for HER.

It is seen that the EF-IO fundamentally reconstructs cationic solvation configurations (Figures 3j; S24, Supporting Information). First, ClO<sub>4</sub><sup>-</sup> enrichment at the interfaces induces anion-mediated solvation configurations even under −0.5 V polarization, increasing anion coordination in the solvation shell of the interfacial Zn<sup>2+</sup>/Na<sup>+</sup> (Figures 3j; S23, Supporting Information). In addition, EG ligands preferentially coordinate via dual ether-oxygen chelation over H<sub>2</sub>O, which effectively solvate Zn<sup>2+</sup> with a peak of radial number density distribution exhibiting at 0.2 nm (Figure S24b, Supporting Information). For Na<sup>+</sup>, all of the species with O donor enter its first solvation shell, with peaks of radial number density distribution exhibiting at 0.25 nm (Figures S23 and Note S1, Supporting Information). These synergistic coordinated effects diversify interfacial solvation configurations, expanding from six distinct types in the Zn-AE to 18 in the Zn-EG, and ultimately achieving 51 Zn<sup>2+</sup>/Na<sup>+</sup> solvation variants in the Zn-Na-EG (Figures 3k,i; S25, Supporting Information). This highly diverse solvation configurations induced by EF-IO effect alters interfacial proton dynamics through disrupting HB concentration in the outer EDL regions (Figure S22, Supporting Information), significantly suppressing HER by impeding proton migration toward the electrode surface, as verified by highly improved electrochemical performance in Figure 2.

### 2.4. Surface Morphology and Component Analysis of Cycled Zn Anodes

Characteristics of cycled Zn anodes are explored by multiscale morphological and compositional analyses. The impact of the EF-IO on the regulation of Zn deposition behavior was investigated through real-time operando monitoring in a transparent Zn||Zn cell. As illustrated in Figure 4a, the cell with the Zn-AE system exhibits localized corrosive pits and progressive gas evolution during prolonged operation, resulting in chaotic Zn deposition with loosely packed dendrite architecture. This instability originates from restricted solvation configurations where active H<sub>2</sub>O molecules participate in both HER and non-uniform nucleation processes. In contrast, the induced diverse solvation configurations in the Zn-Na-EG system offers dual functionality. First, it effectively resists H<sub>2</sub>O-induced parasitic reactions through solvation sheath reconstruction, as evidenced by the absence of bubbles. Secondly, it guides Zn deposition to align parallel to the Zn surface in a planar configuration, contributing to a flattened and uniform deposition layer devoid of dendrites (Figure 4b). Confocal laser scanning microscopy (CLSM) and 3D topography reconstruction (500 μm × 500 μm, Figure 4c) demonstrate striking contrasts: the Zn-AE system develops dendritic architectures with severe surface corrugation (roughness: 2.91 μm), whereas the Zn-Na-EG system maintains exceptionally planarity (roughness: 0.69 μm) through 50 deposition cycles. This disparity highlights the critical role of ion orchestration in templating homogeneous Zn deposition through dynamic electric field modulation. The surface geometry and potential distribution of the cycled Zn anode were verified through atomic force

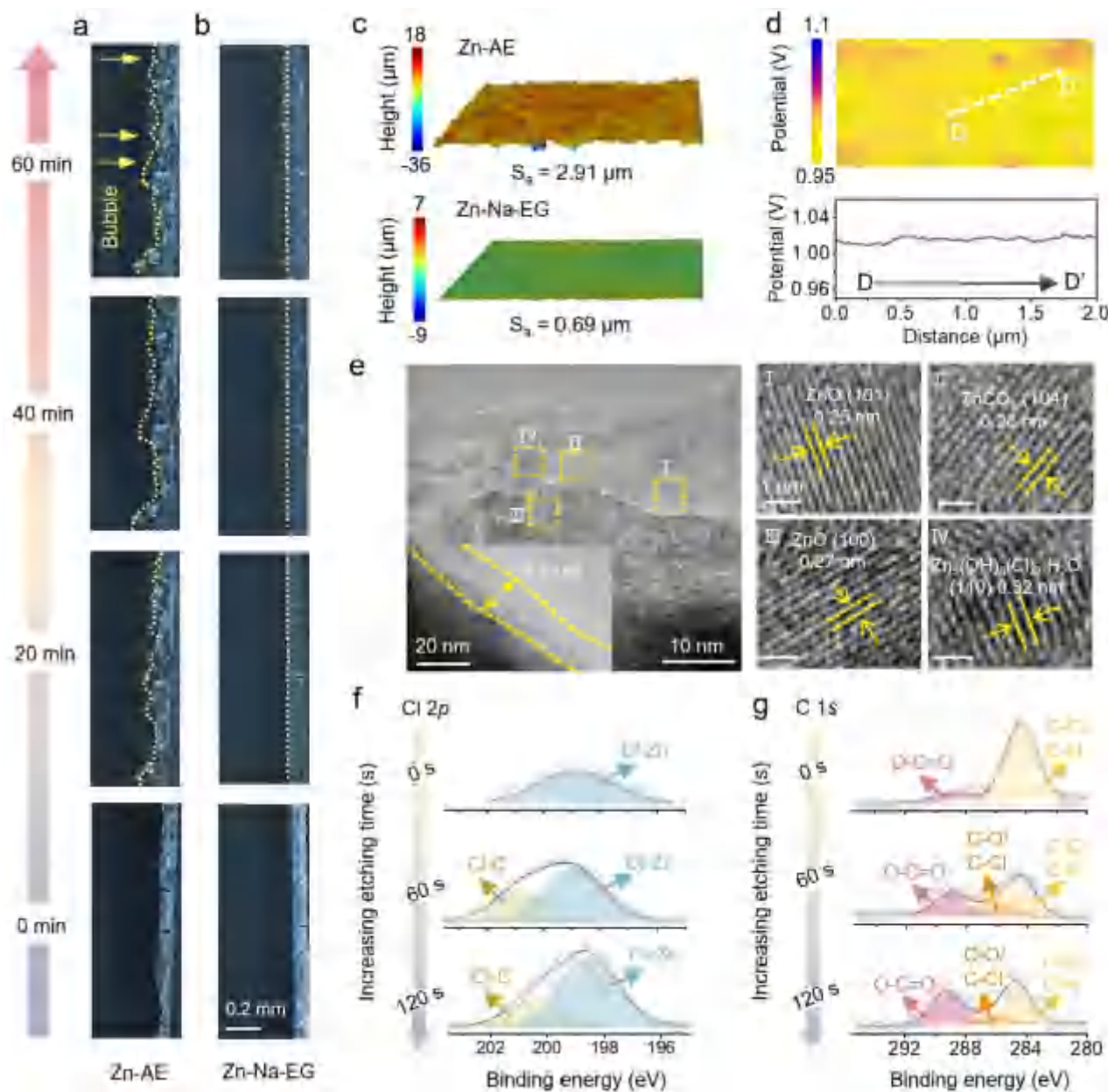


**Figure 3.** EF-IO effect and the consequent interfacial architecture restructuring. a–f) The number density distribution of (a)  $\text{H}_2\text{O}$ , (b)  $\text{Zn}^{2+}$ , and (c)  $\text{ClO}_4^-$  at 0 V, and (d)  $\text{H}_2\text{O}$ , (e)  $\text{Zn}^{2+}$ , and (f)  $\text{ClO}_4^-$  under the polarization of  $-0.5$  V. g–i) 2D number density distribution in the interfacial region of (g)  $\text{H}_2\text{O}$  in Zn-AE, (h)  $\text{H}_2\text{O}$  and (i) EG in Zn-Na-EG. j) Radial number density distribution of O ( $\text{ClO}_4^-$ ) around  $\text{Zn}^{2+}$  in the interfacial region. k, l) Proportion of  $\text{Zn}^{2+}$  with different number O-donors (from  $\text{H}_2\text{O}$ ,  $\text{ClO}_4^-$ , and EG) in the first solvation shell (0.3 nm) for (k) Zn-AE and (l) Zn-Na-EG systems. “n” refers to the number of  $\text{Zn}^{2+}$  solvation configurations from interfacial MD simulations. The configurations less than 1% are concluded in others.

microscopy (AFM) coupled with Kelvin probe force microscopy (KPFM, Figures 4d; S26 and S27, Supporting Information). The contact potential difference (CPD) variations with surface geometry were scrutinized by comparing the same position lines. In the Zn-AE, the cycled Zn anode exhibits localized charge accumulation at topographic peaks with a rough surface (average roughness  $R_a = 95.1$  nm), creating electric field hotspots that drive dendrite initiation through the “tip effect” (Figure S26a–d, Supporting Information). In contrast, the elimination of such tip effect is achieved in the Zn-Na-EG system via a uniform potential distribution as well as relatively flat and uniform surface morphologies ( $R_a = 25.3$  nm, Figure S26e,f, Supporting Information). Complementary scanning electron microscopy (SEM) characterization at

mesoscopic scales confirms these observations. It is noteworthy that flake-like deposits proceed along the interface with irregular Zn dendrites in the Zn-AE system (Figure S28a,b, Supporting Information). Oppositely, flat surfaces constituted with densely deposited Zn are observed using the Zn-Na-EG (Figure S28c,d, Supporting Information). The above results are attributed to the regulation of interfacial structure that effectively modulate the electric field distribution, which coincides with the CLSM and AFM observations.

X-ray diffraction (XRD) was carried out to evaluate the crystal structure and the composition of Zn deposits on anodes. The Zn-Na-EG system promotes the preferential growth of Zn deposits along the c axis, as evidenced by the dominant [002] plane,



**Figure 4.** Surface morphology and component analysis of cycled Zn anodes. a,b) In situ optical microscopy observations of the Zn deposition process at a current density of  $5 \text{ mA cm}^{-2}$  on Zn foil in (a) Zn-AE and (b) Zn-Na-EG. c) CLSM images of Zn foils after 50 cycles in Zn-AE (the upper panel) and Zn-Na-EG (the lower panel). d) CPD maps (the upper panel) and line profiles (the lower panel) taken from the KPFM images for the Zn deposition layer in the Zn-AE to 4.8, 1.1, and 7.1, respectively, in the Zn-Na-EG (Figure S29b, Supporting Information). e–g) Composition analysis of the SEI on the Zn electrodes after cycling in the Zn-Na-EG system using (e) HR-TEM images, (f) Cl 2p XPS spectra, and (g) C 1s XPS spectra.

in contrast to the [101] plane in the Zn-AE (Figure S29a, Supporting Information). Specially, the intensity ratios of the [002]/[102], [002]/[101], and [002]/[100] increase from 0.7, 0.7, and 0.1 in the Zn-AE to 4.8, 1.1, and 7.1, respectively, in the Zn-Na-EG (Figure S29b, Supporting Information). This crystallographic reorientation correlates with the ion orchestration-mediated  $\text{Zn}^{2+}$  flux homogenization, as the compact structure of [002] plane minimizes surface energy and dendrite propensity.<sup>[22]</sup> Critical compositional differences emerge in the  $10.5^\circ$ – $11^\circ$   $2\theta$  region (Figure S30, Supporting Information). While Zn-AE shows basic byprod-

ucts  $(\text{Zn}_x(\text{ClO}_4)_y(\text{OH})_{2x-y} \cdot n\text{H}_2\text{O})$ , e.g.,  $\text{Zn}_4\text{ClO}_4(\text{OH})_7$  from parasitic HER,<sup>[23]</sup> Zn-Na-EG reveals a distinct  $\text{Zn}_5(\text{OH})_8\text{Cl}_2 \cdot \text{H}_2\text{O}$  phase at  $10.9^\circ$ , confirming the formation of Cl-rich inorganic species. Immersion tests (Figure S30, Supporting Information) conclusively demonstrate that  $\text{Zn}_5(\text{OH})_8\text{Cl}_2 \cdot \text{H}_2\text{O}$  formation requires electrochemical cycling, rather than spontaneous chemical corrosion observed in the Zn-AE. The nanoscale architecture of the interface shells on Cu grids from Zn||Cu cells (after 10 cycles and finishing with a charge process) were examined via high-resolution transmission electron microscopy (HR-TEM).



In the Zn-AE system, a non-uniform SEI ( $\approx 38$  nm) dominated by amorphous basic byproducts (Figure S31, Supporting Information) forms through uncontrolled side reactions. In contrast, the Zn-Na-EG system generates a multi-component SEI, demonstrated by the presence of both crystallized and amorphous regions with a thickness of  $\approx 18.5$  nm (inset of Figure 4e). A mixture of crystalline lattice fringes of ZnO (101), ZnCO<sub>3</sub> (104), ZnO (100), and Zn<sub>5</sub>(OH)<sub>8</sub>Cl<sub>2</sub>·H<sub>2</sub>O (110) is identified within the interface (Figure 4e I–IV), which is believed to effectively resist detrimental side reactions due to its high interfacial energy.<sup>[24]</sup> This finding is consistent with the above XRD results and contributes significantly to the achievement of durable Zn anodes.

The chemical composition of the SEI in the Zn-Na-EG system was further delved by in-depth X-ray photoelectron spectroscopy (XPS). As shown in Figure 4f, the interface evolves into a chemically graded structure where Cl-Zn species (Zn<sub>5</sub>(OH)<sub>8</sub>Cl<sub>2</sub>·H<sub>2</sub>O) dominate the outer layer while organic (Cl–C)–inorganic hybrid components prevail in the inner region. Remarkably, the emergence of Cl–C bonding during sputtering implies a synergistic decomposition of the dual salts and EG molecules, consistent with previous finding.<sup>[10a,25]</sup> forming a stress-adaptive organic matrix that complements the inorganic framework. In contrast, obvious contrast is observed in Cl-related species for the Zn-AE, where only subtle phase transitions of Cl–Zn are found in the inner layer (Figure S32, Supporting Information). In the C 1s spectra for Zn anodes cycled in the Zn-Na-EG, as the sputtering time increases, the signals from the organic C–O/C–Cl and inorganic Cl–Zn components increase accompanied by the reduction in the C–C/C–H. Consistent with the Cl 2p spectra, the organic C–O/C–Cl species derived from the ligand decomposition is absent in the outer layer (Figure 4g). These findings validate the construction of a gradient-structured SEI in the Zn-Na-EG system, where the inorganic-dominated outer layer isolates the electrode from undesirable HER and corrosion reactions, while the inner inorganic-organic hybrid layer buffers interfacial stress to simultaneously achieve dendrite inhibition and strain relaxation during cycling.

## 2.5. Electrochemical Performance for VOH Cathode-Based ZMBs

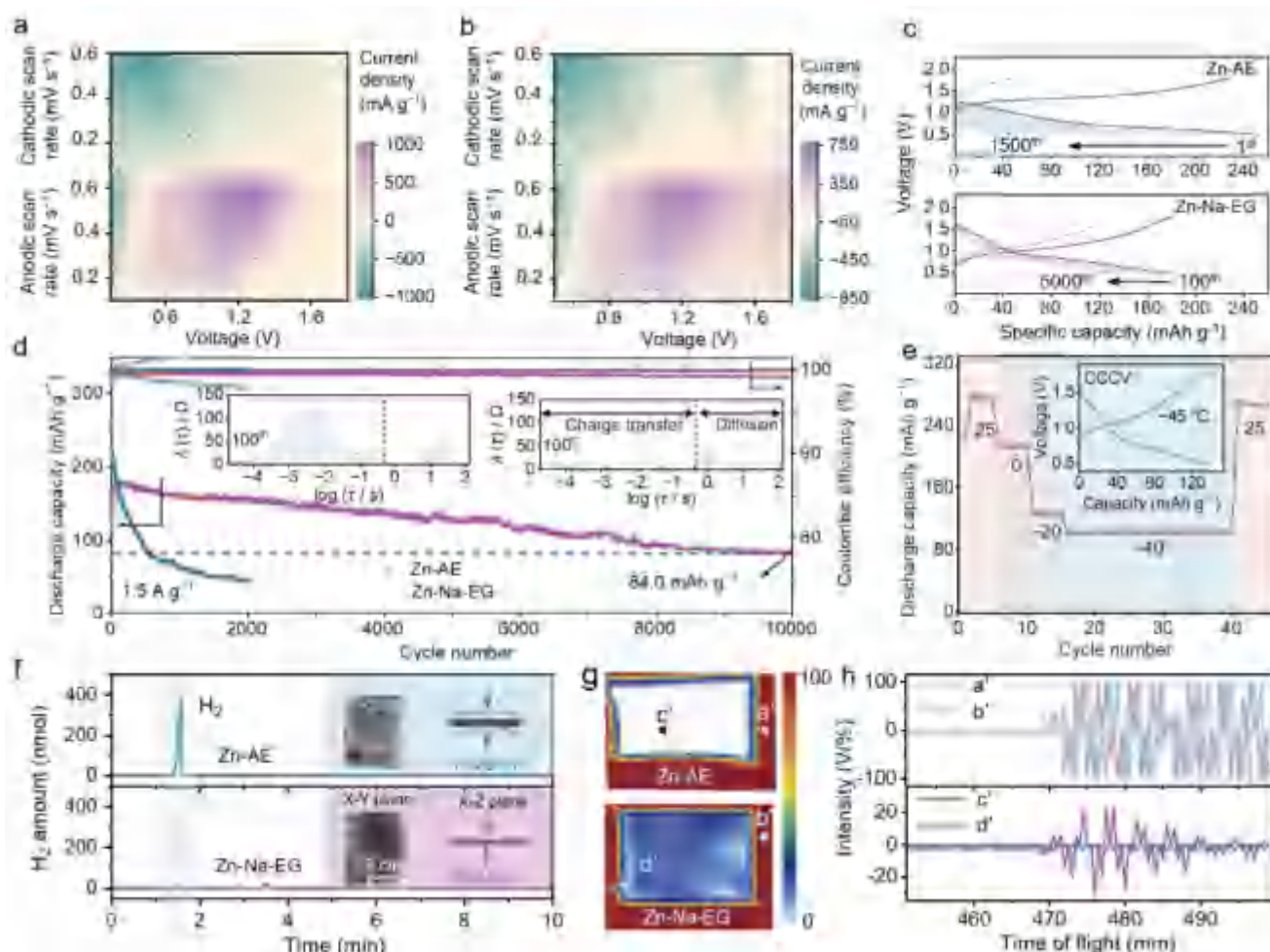
The effectiveness of the EF-IO design was further validated through full cells employing Zn metal anodes and layered VOH cathodes (Figure S33, Supporting Information). The cyclic voltammetry (CV) curves of Zn||VOH cell in the Zn-AE at various scan rates (from 0.1 to 0.6 mV s<sup>−1</sup>) exhibit two pairs of redox peaks, corresponding to the multistep insertion/extraction of Zn<sup>2+</sup>/H<sup>+</sup> (Figure 5a).<sup>[26]</sup> Apparently, a new pair of peaks emerge at  $\approx 1.66$  V (oxidation)/1.49 V (reduction) with the Zn-Na-EG system (Figure 5b), which can be ascribed to an additional storage process of the VOH cathode. These redox peaks persist as the scan rate increases, indicating reversible and rapid cathode reactions. This result is further corroborated by the significantly enhanced reversible capacity in the Zn-Na-EG compared to the Zn-AE system, particularly at high rates (Figure S34, Supporting Information). The long-term cycling stability of Zn||VOH cells was conducted at a current density of 1.5 A g<sup>−1</sup>. Although the initial capacity provided by the cell using the Zn-AE is relatively high, it rapidly decays to only 48.4 mAh g<sup>−1</sup> after 1500 cycles, as

evidenced by the huge voltage polarization (the upper panel of Figure 5c). In contrast, after 100 activation cycles, the cell based on the Zn-Na-EG maintains distinct voltage plateaus even after 5000 repeated cycles (the lower panel of Figure 5c). It is noted that the expanded voltage window (1.8 V cutoff) enhances capacity by 55.7% through full utilization of 1.66 V/1.49 V redox couples (Figure S35a, Supporting Information), which is mainly due to the inhibited OER at the cathode through reducing H<sub>2</sub>O activity. Notably, the Zn-Na-EG system achieves long-term stability for over 10 000 cycles with a low decay rate of 0.0076% per cycle (Figure S35b, Supporting Information), contrasting sharply with the faster capacity decline (< 20% capacity retention within 2000 cycles) in the Zn-AE system (Figure 5d). These results suggest that the Zn-Na-EG system effectively suppresses undesirable reactions on Zn anodes and mitigates the disintegration of V centers on cathodes,<sup>[3b]</sup> representing a significant advancement comparable to reported Zn||VOH performance (Table S4, Supporting Information). The distribution of relaxation times (DRT) analysis for cycled Zn||VOH cells was performed to evaluate the electrode|electrolyte interfacial behavior.<sup>[26]</sup> The peaks with different time constants were fitted based on the corresponding EIS results (Figure S36, Supporting Information). Clearly, the integrated areas of interfacial processes, particularly for charge transfer and Zn<sup>2+</sup> diffusion in the Zn-Na-EG, are significantly lower compared to those in the Zn-AE (Inset of Figure 5d), indicating less-resistive interfaces with decreased accumulation of by-products on both electrodes.

As verified earlier in Figures 1i and S12 (Supporting Information), the solvation entropy-enhanced system effectively depresses the freezing point via diversified cation coordination configurations. This strategy enables remarkable temperature adaptability, with Zn||VOH cells delivering specific capacities of  $\approx 103$  mAh g<sup>−1</sup> at  $-40$  °C and  $\approx 183$  mAh g<sup>−1</sup> at  $55$  °C (Figures 5e; S37, Supporting Information). Even under extreme conditions of  $-45$  °C, the system maintains a reversible capacity of 137.2 mAh g<sup>−1</sup> through implementing a constant current-constant voltage (CCCV) charging protocol. Extended cycling validation at  $-20$  °C confirms exceptional durability (Figure S38a, Supporting Information), with Zn||VOH battery maintaining a reversible capacity of 103.2 mAh g<sup>−1</sup> after 1200 cycles (92.3% capacity retention, Figure S38b, Supporting Information) and minimal voltage polarization during cycling (Figure S38c, Supporting Information). Thus, the Zn-Na-EG electrolyte enables stable electrochemical reversibility across an exceptional  $100$  °C temperature window ( $-45$  to  $55$  °C), stemming from the increased solvation configurations that promote rapid ion desolvation at cryogenic temperatures, a robust SEI that simultaneously regulate Zn<sup>2+</sup> flux and isolates active H<sub>2</sub>O from the Zn anode, and a reconfigured HB network that facilitate ion transport.

As one of the most critical metrics for practical energy storage deployment, the anti-self-discharge properties of Zn||VOH cells were explored. The Zn||VOH cells are charged to 1.8 V and rested for 30 days, followed by discharging to 0.5 V to record the available reversible capacity. The rate of self-discharge per day ( $r$ , the percentage of capacity loss per day) can be calculated based on the following equation:<sup>[27]</sup>

$$r = \frac{C_t - C_0}{C_0 t} \quad (2)$$



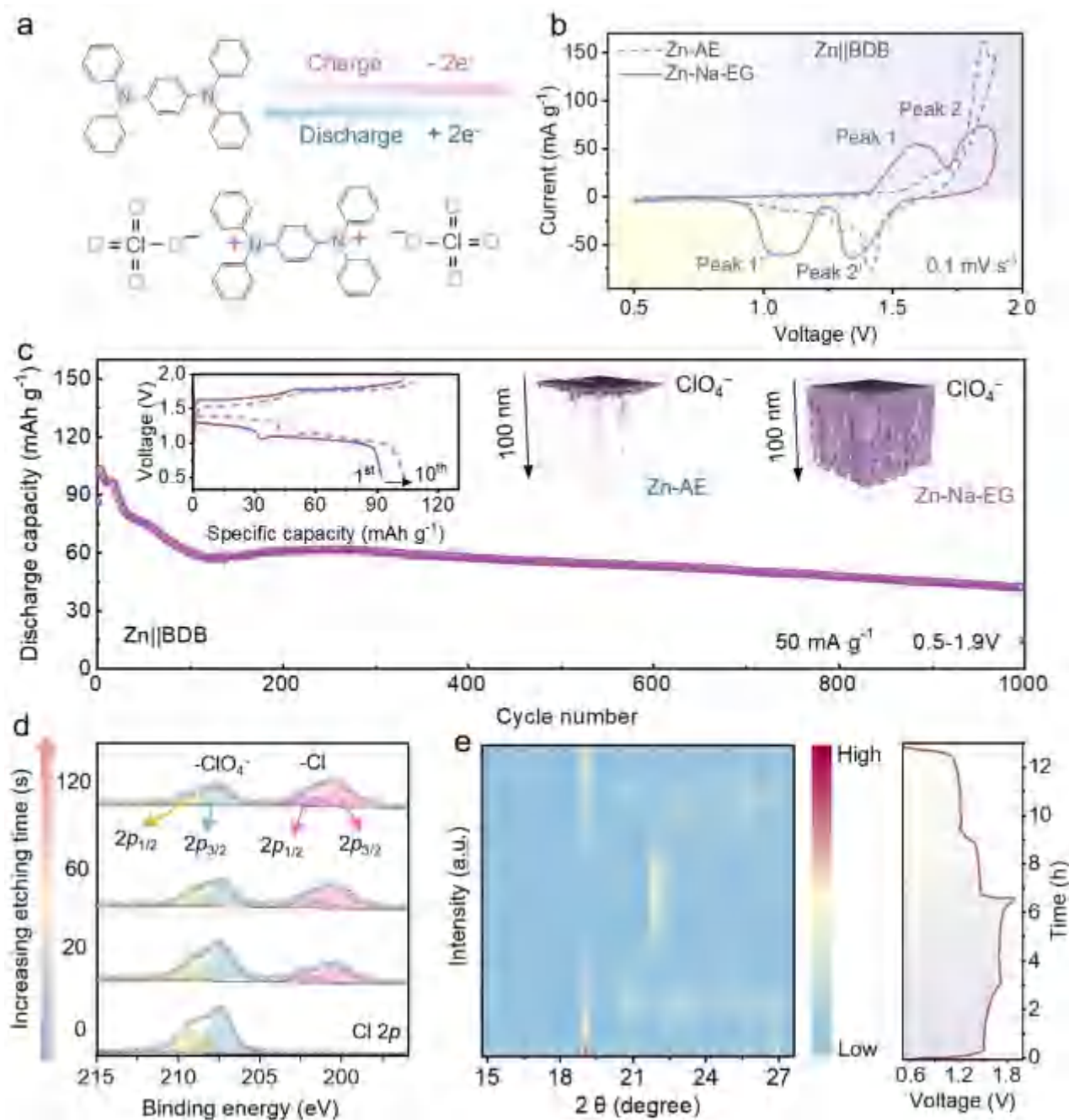
**Figure 5.** Electrochemical performance for VOH cathode-based ZMBs. a,b) CV curves at varying scan rates for Zn||VOH cells with (a) Zn-AE and (b) Zn-Na-EG. c) Voltage curves of the Zn||VOH cells after different cycles with Zn-AE (the upper panel) and Zn-Na-EG (the lower panel). d) Long-term cycle stability of the Zn||VOH cells under  $1.5 \text{ A g}^{-1}$ . The corresponding DRT profiles of the cells after 100 cycles are shown in the inset. e) Temperature-dependent reversible capacities (25 to  $-45^\circ\text{C}$ ) of Zn||VOH cells. f) Ex situ GCMS and relevant CT images (shown in insets) of Zn||VOH pouch cells with Zn-AE (the upper panel) and Zn-Na-EG (the lower panel). g,h) Ultrasonic transmission images and corresponding ultrasonic transmission waves at the positions marked by letters.

where  $C_t$  and  $C_0$  represent the discharge capacities before and after the rest, respectively. After aging for 30 days, the Zn-AE displays an ultralow CE of 5.0%, corresponding to a high  $r$  of 3.2%. The severe self-discharge with the Zn-AE primarily arises from the hydrolysis of the vanadium-based cathode material, corrosion of the Zn anode, as well as the reactivity of the electrolyte.<sup>[28]</sup> In comparison, the CE increases by ten times and the  $r$  decreases significantly in the Zn-Na-EG system (Figure S39, Supporting Information).

The single-layer pouch cell with a size of  $6 \text{ cm} \times 5 \text{ cm}$  was assembled to further validate the practicability of the EF-IO strategy. The pouch-type Zn|Zn-Na-EG|VOH cell provides a stable energy output, remaining 70.8% capacity retention after 1000 cycles without an obvious increase in the cell polarization (Figure S40a,b, Supporting Information). In contrast, the capacity of the Zn|Zn-AE|VOH pouch cell decreases to only  $\approx 19 \text{ mAh g}^{-1}$  within 300 cycles (Figure S40a, Supporting Information), due to a significant voltage polarization between the charging and

discharging process (Figure S40c, Supporting Information). Quantitative gas evolution analysis during Zn||VOH pouch cell cycling was conducted through gas chromatography-mass spectrometry (GCMS), as demonstrated in Figure 5f. The pouch cell in the Zn-AE system generates a significant amount of  $\text{H}_2$  gas after 100 cycles (the upper panel of Figure 5f), experiencing substantial volume expansion with a thickness of 1.429 cm, as quantified by non-destructive X-ray computed tomography (X-ray CT, the upper left panel in the inset of Figure 5f). This catastrophic gas accumulation correlates with extensive corrosion pit formation induced by heterogeneous Zn deposition and interfacial self-corrosion (the upper left panel in the inset of Figure 5f). In striking contrast, the Zn-Na-EG system demonstrates exceptional gas suppression capability, maintaining near-original thickness ( $0.333 \text{ cm}$ , the lower left panel in the inset of Figure 5f) with negligible  $\text{H}_2$  signal in GCMS (the lower panel in Figure 5f). The preserved anode morphology displays minimal surface roughness without noticeable corrosion features, confirming the





**Figure 6.** Anion-storage chemistry in BDB organic cathode-based ZMBs. a) Proposed anion-storage mechanism in BDB cathodes via reversible two-electron transfer. b) CV curves of Zn||BDB cells using the Zn-AE and Zn-Na-EG electrolytes. c) Cycling performance of the Zn||Zn-Na-EG||BDB cell. Inset shows charge-discharge curves for the 1st and 10th cycles (left) and spatial distributions of  $\text{ClO}_4^-$  on the cycled BDB cathodes over an etching time of 500 s ( $\approx 100 \text{ nm}$ ) by TOF-SIMS (right). d) In-depth profiling of Cl 2p XPS spectra for charged BDB cathodes in the Zn-Na-EG system. e) Ex situ XRD patterns of the BDB cathode with the Zn-Na-EG system during cycling.

effectiveness of the SEI in stabilizing the interfacial electrochemistry (the right panels in the inset of Figure 5f). Ultrasonic scanning was utilized to further detect gas generation during cycling. Figure 5g,h display ultrasonic transmission images and corresponding ultrasonic transmission waves at the positions marked by letters. The aluminum-laminate film and the flat gas bag exhibit high ultrasonic transmissivity (red areas a' and b'

in Figure 5g, and the upper panel of Figure 5h). The Zn-Na-EG system maintains homogeneous ultrasonic propagation through continuous electrolyte medium (blue area c' in Figure 5g, and the lower panel of Figure 5h), while the Zn-AE system reveals severe signal attenuation from gas bubble-induced acoustic impedance mismatch (white area d' in Figure 5g, and the lower panel of Figure 5h), further confirming significant  $\text{H}_2$  gas generation.

These findings highlight the effective suppression of HER and interfacial side reactions by the EF-IO effect in the Zn-Na-EG system, validating its potential for practical application in ZMBs.

## 2.6. Anion-Storage Chemistry in Organic Cathode-Based ZMBs

Beyond achieving long-term cyclability in conventional ZMB full cells, the EF-IO design also unlocks multi-chemical energy storage pathways through anion regulation. In the Zn-Na-EG system,  $\text{ClO}_4^-$  anion enrichment enables dual functionality-facilitating redox-active charge compensation while suppressing OER through reducing  $\text{H}_2\text{O}$  activity on cathodes. When employing the dual N-centered organic BDB as the cathode, two distinct cationic N sites emerge during charging, with charge neutrality maintained through reversible  $\text{ClO}_4^-$  anion (de-)intercalation, establishing a novel anion-storage mechanism (Figure 6a). As shown in Figure S41a (Supporting Information), the Zn||BDB cell exhibits poor reversibility in the Zn-AE, displaying an irreversible charge capacity of  $\approx 1000 \text{ mAh g}^{-1}$  with a low initial CE of  $\approx 12\%$ , due to the severe OER above 1.9 V. In contrast, the Zn-Na-EG system enables well-defined two-electron redox behavior, as evidenced by two pairs of oxidation/reduction peaks in the CV curve (Figure 6b, with a scan rate of  $0.1 \text{ mV s}^{-1}$ ). Corresponding galvanostatic profiles reveal distinct two-plateau characteristics, yielding stabilized anion storage reversibility (Figure 6c and inset of Figure 6c).

The anion storage mechanism is systematically validated through spatial distribution analysis. Time-of-flight secondary ion mass spectrometry (TOF-SIMS) reveals different distribution patterns. In conventional Zn-AE electrolytes, surface-localized  $\text{ClO}_4^-$  accumulation with severe bulk depletion occurs, while the Zn-Na-EG promotes homogeneous 3D anion distribution (inset of Figure 6c), validating reversible bulk-phase anion storage. Further mechanistic insights emerge from in-depth XPS, showing gradual attenuation of  $\text{ClO}_4^-$  signals with increasing sputtering depth (Figure 6d). The concurrent formation of a Cl-containing interfacial layer on the cathode during cycling suggests anion participation in both bulk redox and interfacial processes. Furthermore, structural reversibility of BDB cathodes during  $\text{ClO}_4^-$  (de-)intercalation is corroborated through XRD. Charging induces diminution of the  $\approx 19.5^\circ$  diffraction peak with concomitant emergence of new features at  $22^\circ$ , which completely revert upon discharging (Figure 6e). This reversible evolution confirms the structural integrity of BDB during anion (de-)intercalation processes, establishing BDB as a promising anion-host cathode for high-voltage ZMBs. Overall, this EF-IO strategy exhibits improvement in electrochemical performance compared to other related works (Table S5, Supporting Information). This work not only gain insight into Zn|electrolyte interfacial dynamics, but also exemplify the capability of EF-IO strategy to integrate multi-chemistry mechanisms within unified battery systems.

## 3. Conclusion

In summary, we present an electric field-guided ion orchestration (EF-IO) strategy that fundamentally reconfigures interfacial solvation configurations to resolve parasitic reactions and dendrite proliferation in ZMBs. Through rational  $\text{Na}^+$ -mediated EDL

reconfiguration under operational electric fields, the interfacial microenvironment is engineered to achieve diverse  $\text{Zn}^{2+}/\text{Na}^+$  solvation structures. This drives the construction of an organic-inorganic gradient SEI, endowing Zn||Zn symmetric cells with long cyclability exceeding 3400 h and a 44-fold reduction in corrosion current density. Practical Zn||VOH full cells demonstrate exceptional durability ( $>10\,000$  cycles, 0.0076% capacity decay per cycle) and wide-temperature adaptability ( $-45$  to  $55^\circ\text{C}$ ). Moreover, the EF-IO strategy unlocks  $\text{ClO}_4^-$ -based reversible anion storage in high-voltage organic cathodes via reversible two-electron redox. Our findings establish an interfacial design paradigm that bridges solvation thermodynamics, electric field-driven interfacial dynamics, and electrochemical performance, highlighting the transformative potential of EF-IO in enabling durable and multi-chemistry ZMBs.

## Supporting Information

Supporting Information is available from the Wiley Online Library or from the author.

## Acknowledgements

Y.W. and J.Z. contributed equally to this work. F.K. acknowledges support from the National Key Research and Development Program of China (2022YFB2404500) and Shenzhen Outstanding Talents Training Fund. D.Z. acknowledges support from Guangdong Innovative and Entrepreneurial Research Team Program (2023ZT10L039) and Guangdong Basic and Applied Basic Research Foundation (2024A1515012701). J.Z. and G.F. thank the support from the National Natural Science Foundation of China (92472109, T2325012) and the Program for HUST Academic Frontier Youth Team. Y.W. would like to acknowledge the support from National Natural Science Foundation of China (22309102) and the Scientific Research Foundation of China University of Petroleum (Beijing) (2462025YJRC015).

## Conflict of Interest

The authors declare no conflict of interest.

## Data Availability Statement

The data that support the findings of this study are available from the corresponding author upon reasonable request.

## Keywords

electric double layer, ion orchestration, multi-chemistry, solvation configuration, Zinc metal batteries

Received: June 12, 2025  
Revised: July 16, 2025  
Published online:

- [1] a) K. Xu, *Chem. Rev.* **2014**, *114*, 11503; b) Y. Deng, H. Wang, M. Fan, B. Zhan, L.-J. Zuo, C. Chen, L. Yan, *J. Am. Chem. Soc.* **2023**, *145*, 20109.

- [2] Q. Li, A. Chen, D. Wang, Z. Pei, C. Zhi, *Joule* **2022**, 6, 273.
- [3] a) C. Xu, B. Li, H. Du, F. Kang, *Angew. Chem., Int. Ed.* **2012**, 51, 933; b) X. Zhao, J. Fu, M. Chen, Y. Wang, C. Huang, K. Qian, G. Feng, B. Li, D. Zhou, F. Kang, *J. Am. Chem. Soc.* **2025**, 147, 2714; c) S. W. Gourley, R. Brown, B. D. Adams, D. Higgins, *Joule* **2023**, 7, 1415.
- [4] a) S. Wei, H. Shou, Z.-H. Qi, S. Chen, Y. Han, S. Shi, Y. Wang, P. Zhang, J. Shi, Z. Zhang, *J. Am. Chem. Soc.* **2025**, 147, 10943; b) C. Li, A. Shyamsunder, A. G. Hoane, D. M. Long, C. Y. Kwok, P. G. Kotula, K. R. Zavadil, A. A. Gewirth, L. F. Nazar, *Joule* **2022**, 6, 1103.
- [5] a) X. Bai, M. Sun, J. Yang, B. Deng, K. Yang, B. Huang, W. Hu, X. Pu, *Energy Environ. Sci.* **2024**, 17, 7330; b) Y. Shang, S. Chen, N. Chen, Y. Li, J. Lai, Y. Ma, J. Chen, F. Wu, R. Chen, *Energy Environ. Sci.* **2022**, 15, 2653; c) I. Aguilar, J. Brown, L. Godeffroy, F. Dorchies, V. Balland, F. Kanoufi, J.-M. Tarascon, *Joule* **2025**, 9, 101784; d) Y. Wang, B. Liang, D. Li, Y. Wang, C. Li, H. Cui, R. Zhang, S. Yang, Z. Chen, Q. Li, *Joule* **2025**, 6, 101944.
- [6] D. Kundu, B. D. Adams, V. Duffort, S. H. Vajargah, L. F. Nazar, *Nat. Energy* **2016**, 1, 16119.
- [7] K. Zhou, G. Liu, X. Yu, Z. Li, Y. Wang, *J. Am. Chem. Soc.* **2024**, 146, 9455.
- [8] a) F. Ming, Y. Zhu, G. Huang, A.-H. Emwas, H. Liang, Y. Cui, H. N. Alshareef, *J. Am. Chem. Soc.* **2022**, 144, 7160; b) J. Heo, D. Dong, Z. Wang, F. Chen, C. Wang, *Joule* **2025**, 9, 101844; c) N. C. Bhoumik, D. C. Madu, C. W. Moon, L. S. Arvisu, M. D. McGehee, C. J. Barile, *Joule* **2024**, 8, 1036.
- [9] H. Qiu, X. Du, J. Zhao, Y. Wang, J. Ju, Z. Chen, Z. Hu, D. Yan, X. Zhou, G. Cui, *Nat. Commun.* **2019**, 10, 5374.
- [10] a) W. Deng, Z. Deng, X. Zhang, Y. Chen, R. Feng, G. Li, X. Wang, *Angew. Chem., Int. Ed.* **2025**, 64, 202416482; b) M. Cheng, D. Li, J. Cao, T. Sun, Q. Sun, W. Zhang, Z. Zha, M. Shi, K. Zhang, Z. Tao, *Angew. Chem., Int. Ed.* **2024**, 63, 202410210.
- [11] S. Wang, G. Liu, W. Wan, X. Li, J. Li, C. Wang, *Adv. Mater.* **2024**, 36, 2306546.
- [12] M. Qiu, Y. Liang, J. Hong, J. Li, P. Sun, W. Mai, *Angew. Chem., Int. Ed.* **2024**, 63, 202407012.
- [13] D. W. Smith, *J. Chem. Educ.* **1977**, 54, 540.
- [14] X. Zhao, Y. Wang, C. Huang, Y. Gao, M. Huang, Y. Ding, X. Wang, Z. Si, D. Zhou, F. Kang, *Angew. Chem., Int. Ed.* **2023**, 62, 202312193.
- [15] a) N. Chang, T. Li, R. Li, S. Wang, Y. Yin, H. Zhang, X. Li, *Energy Environ. Sci.* **2020**, 13, 3527; b) M. Han, J. Huang, X. Xie, T. C. Li, J. Huang, S. Liang, J. Zhou, H. J. Fan, *Adv. Funct. Mater.* **2022**, 32, 2110957.
- [16] Y. Chen, K. Zhang, Z. Xu, F. Gong, R. Feng, Z. Jin, X. Wang, *Energy Environ. Sci.* **2025**, 18, 713.
- [17] a) L. Ma, S. Chen, N. Li, Z. Liu, Z. Tang, J. A. Zapien, S. Chen, J. Fan, C. Zhi, *Adv. Mater.* **2020**, 32, 1908121; b) R. Wang, M. Yao, M. Yang, J. Zhu, J. Chen, Z. Niu, *Proc. Natl. Acad. Sci. USA* **2023**, 120, 2221980120.
- [18] Y. Zhong, Z. Cheng, H. Zhang, J. Li, D. Liu, Y. Liao, J. Meng, Y. Shen, Y. Huang, *Nano Energy* **2022**, 98, 107220.
- [19] a) J. Wang, B. Zhang, S. Luo, X. Huang, A. Duan, H. Chen, W. Sun, *Angew. Chem., Int. Ed.* **2025**, <https://doi.org/10.1002/anie.202510354>; b) H. Wang, S. Deng, S. Wang, W. Li, S. Yuan, J. Han, H. Fu, B. Xu, L. Wei, *Angew. Chem., Int. Ed.* **2025**, 64, 202422395; c) S. Li, Y. Zhong, J. Huang, G. Lai, L. Li, L. Jiang, X. Xu, B. Lu, Y. Liu, J. Zhou, *Energy Environ. Sci.* **2025**, 18, 2599.
- [20] a) J. Shi, T. Sun, J. Bao, S. Zheng, H. Du, L. Li, X. Yuan, T. Ma, Z. Tao, *Adv. Funct. Mater.* **2021**, 31, 2102035; b) X. Lin, G. Zhou, M. J. Robson, J. Yu, S. C. Kwok, F. Ciucci, *Adv. Funct. Mater.* **2022**, 32, 2109322; c) Y. Zhong, X. Xie, Z. Zeng, B. Lu, G. Chen, J. Zhou, *Angew. Chem., Int. Ed.* **2023**, 135, 202310577; d) W. Deng, Z. Deng, Y. Chen, R. Feng, X. Wang, *Angew. Chem., Int. Ed.* **2024**, 136, 202316499; e) W. Yang, X. Du, J. Zhao, Z. Chen, J. Li, J. Xie, Y. Zhang, Z. Cui, Q. Kong, Z. Zhao, *Joule* **2020**, 4, 1557; f) H. Peng, K. Xiao, S. Tian, S. Han, J. Zhou, B. Lu, Z. Chen, J. Zhou, *Adv. Energy Mater.* **2024**, 14, 2303411; g) X. Lu, Z. Liu, A. Amardeep, Z. Wu, L. Tao, K. Qu, H. Sun, Y. Liu, J. Liu, *Angew. Chem., Int. Ed.* **2023**, 135, 202307475.
- [21] Z. Hu, F. Zhang, Y. Zhao, H. Wang, Y. Huang, F. Wu, R. Chen, L. Li, *Adv. Mater.* **2022**, 34, 2203104.
- [22] J. Zheng, L. A. Archer, *Chem. Rev.* **2022**, 122, 14440.
- [23] X. Shi, J. Xie, J. Wang, S. Xie, Z. Yang, X. Lu, *Nat. Commun.* **2024**, 15, 302.
- [24] B. Zhang, X. Wu, H. Luo, H. Yan, Y. Chen, S. Zhou, J. Yin, K. Zhang, H.-G. Liao, Q. Wang, *J. Am. Chem. Soc.* **2024**, 146, 4557.
- [25] L. Cao, D. Li, E. Hu, J. Xu, T. Deng, L. Ma, Y. Wang, X.-Q. Yang, C. Wang, *J. Am. Chem. Soc.* **2020**, 142, 21404.
- [26] Z. Zhang, X. Yang, P. Li, Y. Wang, X. Zhao, J. Safaei, H. Tian, D. Zhou, B. Li, F. Kang, *Adv. Mater.* **2022**, 34, 2206970.
- [27] Y. Wang, Y. Zhang, S. Dong, W. Zhou, P. K. Lee, Z. Peng, C. Dang, P. H. L. Sit, J. Guo, D. Y. Yu, *Adv. Energy Mater.* **2022**, 12, 2103360.
- [28] J. Sun, J. Zhang, S. Wang, P. Sun, J. Chen, Y. Du, S. Wang, I. Saadoun, Y. Wang, Y. Wei, *Energy Environ. Sci.* **2024**, 17, 4304.

# An All-Fluorinated Electrolyte Toward High Voltage and Long Cycle Performance Dual-Ion Batteries

Yao Wang, Yanjun Zhang, Shuyu Dong, Wenchong Zhou, Pui-Kit Lee, Zehua Peng, Chaoqun Dang, Patrick H.-L. Sit, Junpo Guo, and Denis Y. W. Yu\*

The dual-ion battery (DIB) is a promising energy storage system that demonstrates high-power characteristics and fast-charging capability. However, conventional electrolytes are not compatible with the high-voltage graphite cathode and the reactive Li metal anode, thus leading to the poor cycle stability and low Coulombic efficiency of the DIB. Here, an all-fluorinated electrolyte is reported that can enable a highly stable operation of the graphite||Li DIB up to 5.2 V by forming robust and less-resistive passivation films on both electrodes to reduce side reactions. The electrolyte allows reversible  $\text{PF}_6^-$  anion insertion/extraction and  $\text{Li}^+$  cation plating/stripping in the graphite||Li battery, achieving stable cycling with 94.5% capacity retention over 5000 cycles at 500 mA  $\text{g}^{-1}$ , high capacity utilization of 91.8% of the available charge capacity at 50 °C (5000 mA  $\text{g}^{-1}$ ), and also minimal self-discharge. At a low temperature of 0 °C, this all-fluorinated electrolyte exhibits 97.8% of the room temperature reversible capacity, along with  $\approx 100\%$  capacity retention after more than 3000 cycles, at 5 °C. This work sheds a new light on the development of fluorinated electrolytes for high voltage and long-lasting DIBs.

## 1. Introduction

Lithium-ion batteries (LIBs) have become the leading electrochemical energy storage technologies in various fields including portable electronics, battery electric vehicles, and energy storage

stations over the past few decades.<sup>[1]</sup> However, the rapid increase in the demand for LIB poses a great threat to the limited cobalt reserve and raises concerns related to eco-friendliness and cost of transition metals which will strongly limit its future grid-scale applications.<sup>[2]</sup> For the development of next-generation battery systems, in addition to enhancing their energy density, power capability, cycle life, and safety, it is also essential to explore sustainable electrode material such as Co-free and Ni-free cathode to improve material availability and to develop high energy-efficient battery technologies at reduced cost.<sup>[3]</sup> In this respect, dual-ion battery (DIB) with the use of a low-cost graphite material as the cathode is attractive and is gaining attention in the research community.<sup>[4]</sup> In addition, owing to the simultaneous redox reaction of anions with the cathode and cations with the anode upon charging,

DIBs have higher power density than traditional LIBs.<sup>[4g,h,5]</sup> As the reservoir to supply active ions for charge storage, the electrolyte plays a significant role in the cell performance (e.g., the cell voltage, reversible capacity, and energy/power density) for DIBs. However, the high working voltage for anion intercalation into graphite leads to severe and continuous side reactions between the electrolyte and the cathode material.<sup>[6]</sup> Hence, improving the stability of the electrolyte against oxidation is of vital importance that can promote stable and reversible anion insertion/extraction process.

Recently, highly concentrated electrolytes (HCEs) with larger electrochemical stability windows have been employed to improve the cycle performance of graphite cathode at a high working voltage of above 5.0 V.<sup>[4e,h,i,5a,7]</sup> For example, Heckmann et al. demonstrate significant increase in reversible capacity of DIB with HCEs from 50 mAh  $\text{g}^{-1}$  (1 M  $\text{LiPF}_6$ -EMC and 1 M  $\text{LiPF}_6$ -DMC) to  $\approx 90$  mAh  $\text{g}^{-1}$  for 4 M  $\text{LiPF}_6$ -DMC and 3.5 M  $\text{LiPF}_6$ -EMC electrolytes at a cathode cutoff voltage of 5 V versus Li/Li<sup>+</sup>.<sup>[7i]</sup> In another effort, Tang et al. show a stable graphite||Al DIB with a reversible capacity of 970 mAh  $\text{g}^{-1}$ , a capacity retention of 96.8% over 500 cycles and a high energy density of  $\approx 180$  Wh (kg electrodes)<sup>-1</sup> with 7.5 M lithium bis(fluorosulfonyl) imide ( $\text{LiFSI}$ ) HCE as the electrolyte.<sup>[4e]</sup> Though, the substantially increased viscosity with the higher salt concentration causes poor wettability of the separator and electrode by the electrolyte, leading to poor rate capability and under-utilization

Y. Wang, Y. Zhang, S. Dong, W. Zhou, P.-K. Lee, Z. Peng, P. H.-L. Sit, D. Y. W. Yu

School of Energy and Environment  
City University of Hong Kong  
Hong Kong SAR, China  
E-mail: denisyu@cityu.edu.hk

C. Dang  
Department of Mechanical Engineering  
City University of Hong Kong  
Hong Kong SAR, China

J. Guo  
Institute of Applied Physics and Materials Engineering  
University of Macau  
Macao SAR 999078, China

D. Y. W. Yu  
Center of Super-Diamond and Advanced Films (COSDAF)  
City University of Hong Kong  
Hong Kong SAR 999077, China

The ORCID identification number(s) for the author(s) of this article can be found under <https://doi.org/10.1002/aenm.202103360>.

DOI: 10.1002/aenm.202103360



of the full battery performance.<sup>[8]</sup> In addition, the increase in salt concentration raises the cost of the battery. These factors ultimately impede the practical applications of DIB. Therefore, the development of an electrolyte with lower salt concentration that has excellent compatibility with the graphite cathode and can facilitate stable anion de-/intercalation at high voltage is essential for the future commercialization of DIBs.

As the most common electrolyte solvents, carbonates such as ethylene carbonate (EC) and ethyl methyl carbonate (EMC) possess low oxidation potential, which limit their application in high voltage batteries. Several reports have shown that fluorinated carbonates such as 3, 3, 3-trifluoropropylene carbonate (TFPC), fluoroethylene carbonate (FEC), methyl 2, 2, 2-trifluoroethyl carbonate (FEMC), and 1, 3-dioxolan-2-one,4-[2, 3, 3, 3-tetrafluoro-2-(tri-fluoromethyl)propyl] (F-AEC) can increase the high voltage stability of the cathodes for LIBs.<sup>[9]</sup> However, few efforts have been made to investigate the effects of fluorinated carbonates on the stability of graphite cathode beyond 5 V and the corresponding anion de-/intercalation behaviors during discharge and charge.<sup>[10]</sup>

In this work, we study the electrochemical performances of a graphite||Li battery in electrolytes containing 1 M LiPF<sub>6</sub> salt and find that those with FEMC solvent has superior oxidation stability up to 5.2 V compared to electrolyte with EMC, resulting in significantly reduced amount of electrolyte decomposition and thinner CEI layer on the graphite cathode, as verified by X-ray photoemission spectroscopy (XPS) and transmission electron microscopy (TEM). Though, parasitic reaction between FEMC and Li metal anode leads to continuous growth in surface layer on Li, resulting in a rapid increase in overpotential and capacity fading over 250 cycles. The addition of FEC as co-solvent can protect the Li metal and suppress dendrite growth upon cycling by forming a dense SEI layer. As a result, graphite||Li battery in 1 M LiPF<sub>6</sub> FEC/FEMC electrolyte shows excellent cell lifetime of 5000 cycles with 94.5% capacity retention and a fast charging rate capability with capacity utilization of 91.8% even at 50 °C at room temperature. In addition, when charging/discharging at a low temperature of 0 °C at 5 C, 97.8% of the discharge capacity (with respect to that at room temperature) and a long-term cycle stability without capacity decay for 3000 cycles are achieved. FEC/FEMC electrolyte also reduces the amount self-discharge in the battery. The electrolyte engineering presented here offers guidelines for further designs of electrolyte formulations for DIB and other battery systems with large voltage ranges.

## 2. Results and Discussion

### 2.1. Effect of Electrolytes on the Graphite Cathode

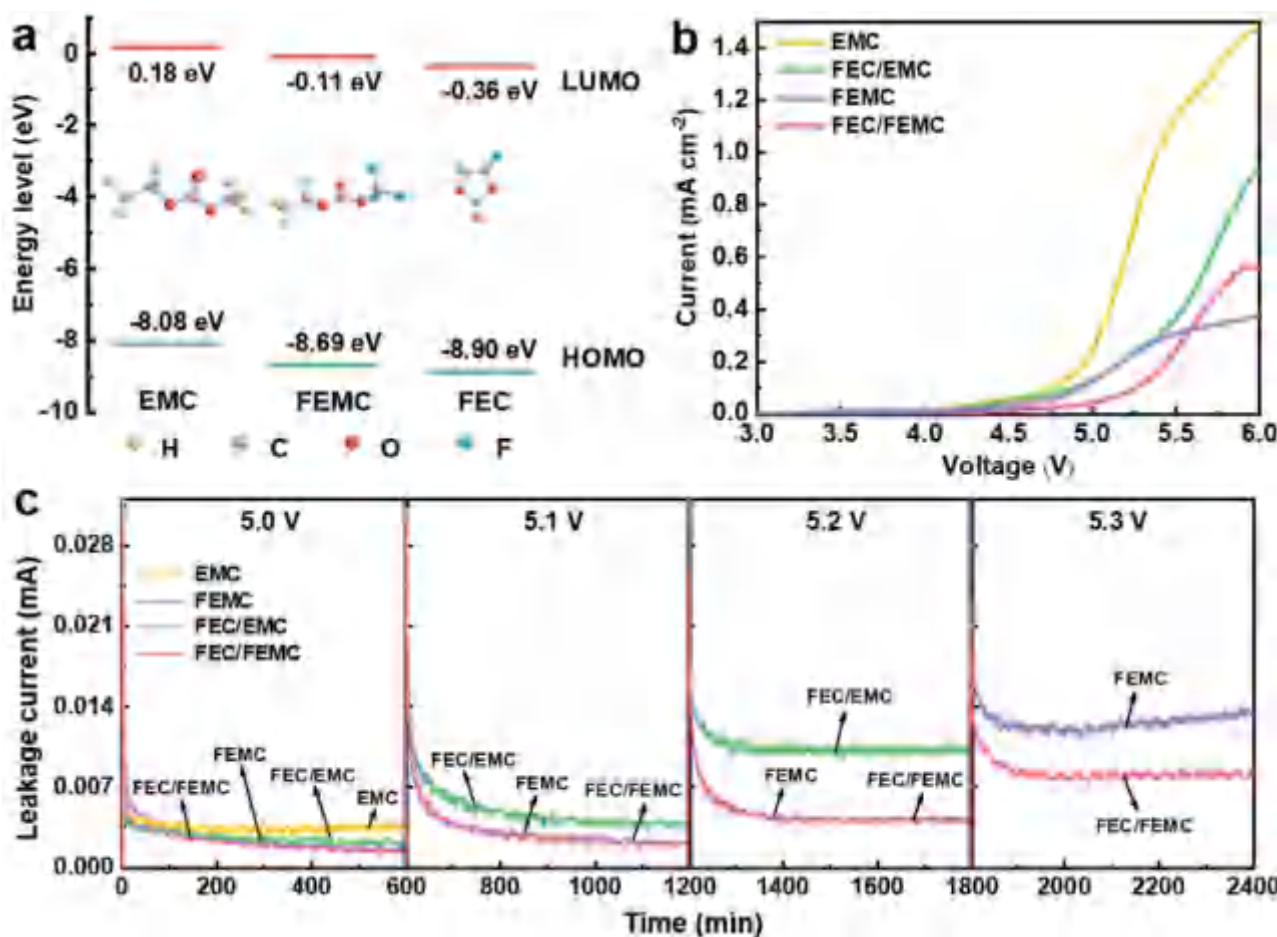
To gain insight into the oxidative and reductive stabilities of the solvents, the highest occupied molecular orbital (HOMO) and lowest unoccupied molecular orbital (LUMO) of EMC, FEC, and FEMC solvents used here were calculated using density functional theory (DFT) simulation.<sup>[9a,11]</sup> As **Figure 1a** indicates, the HOMO energies of these three solvents decrease in the following order: EMC (−0.88 eV) > FEMC (−0.69 eV) > FEC (−0.9 eV), suggesting FEC possesses the highest oxidative stability while EMC has the highest tendency to be oxidized under

high voltage within the three solvents. Meanwhile, the LUMO energies exhibit the same trend as HOMO energy levels, which are calculated to be 0.18, −0.11, and −0.36 eV for EMC, FEMC, and FEC, respectively, indicating FEC is more prone to be reduced. These results demonstrate that fluorination of the solvent can significantly lower the HOMO and LUMO energy levels due to the introduction of strong electron-withdrawing groups (such as −CF<sub>3</sub>) into the structure, thus increasing both the oxidation and reduction potential of the solvent, which are consistent with previous reports.<sup>[9a]</sup>

Various electrolytes were prepared by dissolving 1 M LiPF<sub>6</sub> salt in pure EMC, pure FEMC, mixed FEC/EMC (3:7 by volume), and mixed FEC/FEMC (3:7 by volume) solvents. To evaluate the anodic stability of electrolytes against oxidation under high voltage, linear sweep voltammetry (LSV) on an inert working electrode of titanium was performed, as presented in **Figure 1b**.<sup>[12]</sup> A decomposition potential of ≈5.0 V is observed for 1 M LiPF<sub>6</sub>-EMC electrolyte, whereas FEC and FEMC effectively expand the electrochemical stability window up to 5.5 V, which is well consistent with the DFT calculation.<sup>[13]</sup> Owing to the excellent anti-oxidation stability, FEC and FEMC solvents are therefore expected to have lower reactivity with the cathode under high voltage.

To investigate the parasitic reactions on the graphite surface, potentiostatic tests were conducted using graphite||Li cells with 1 M LiPF<sub>6</sub>-based electrolytes, as illustrated in **Figure 1c**. The cells were charged to and held at a constant voltage of 5.0, 5.1, 5.2, and 5.3 V, respectively. The cell with EMC electrolyte already shows a leakage current of ≈0.0035 mA when it was held at 5.0 V, indicating some degree of electrolyte decomposition. It is noted that leakage current is reduced with the introduction of fluorinated electrolytes. When the voltage is raised, the differences between the various electrolytes can be observed. Specifically, the cell with FEC/EMC shows higher current compared to those with FEMC or FEC/FEMC at 5.1 V or above, which is attributed to the oxidation decomposition of the EMC solvent. Both FEMC and FEC/FEMC shows similar stability up to 5.2 V, which indicates that FEMC is a promising electrolyte for high voltage batteries. When the voltage is further increased to 5.3 V, the electrolyte decomposition becomes more significant with a larger leakage current observed for FEMC electrolyte compared with FEC/FEMC electrolyte. Overall, FEC/FEMC electrolyte shows the best stability at high voltage.

The cycle performance of graphite||Li cells using the four 1 M LiPF<sub>6</sub>-based electrolytes were conducted within the voltage range of 3–5.2 V. **Figure 2a** shows the 1<sup>st</sup> charge-discharge curves at a current density of 10 mA g<sup>−1</sup> and **Figure 2b** compares the initial Coulombic efficiency (ICE) and average CE during cycling. The cell with 1 M LiPF<sub>6</sub>-EMC electrolyte shows abnormal charging profile, with the voltage not able to reach the cutoff voltage of 5.2 V (inset of **Figure 2a**), which is attributed to continuous electrolyte decomposition. The addition of FEC as a co-solvent into the electrolyte (i.e., FEC/EMC = 3:7) suppresses electrolyte decomposition (**Figure 2b**) due to the enhanced electrolyte anodic stability,<sup>[14]</sup> as suggested in **Figure 1c**. By replacing EMC by FEMC, the cell with FEC/FEMC exhibits an increased ICE of 76.5% (**Figure 2b**), revealing that the side reactions between electrolyte and cathode is reduced. Even though 1 M LiPF<sub>6</sub>-FEMC electrolyte without FEC also shows excellent compatibility with



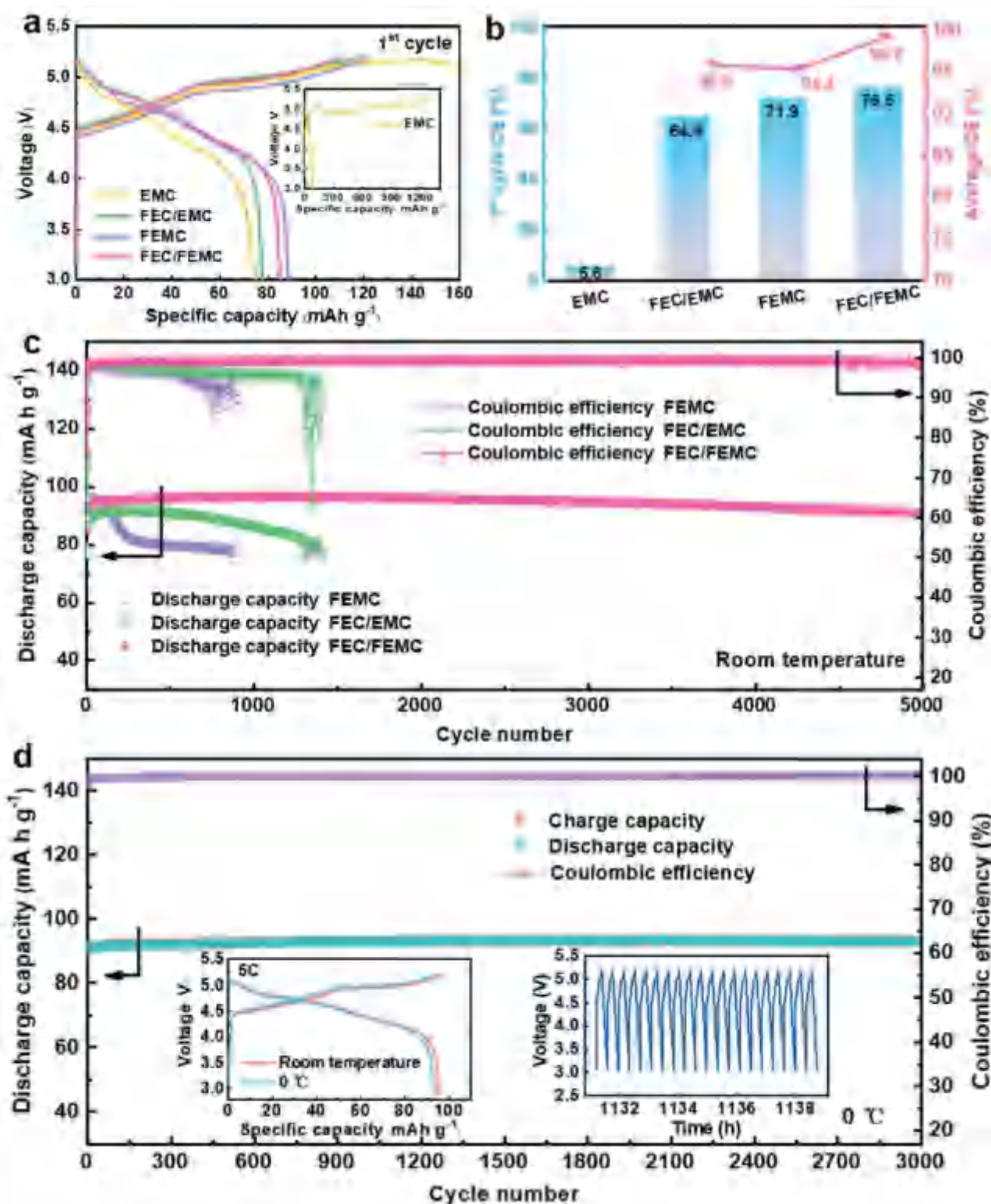
**Figure 1.** a) Structures and molecular orbital energies of EMC, FEC, and FEC solvents. b) LSV of a titanium electrode in 1 M LiPF<sub>6</sub>-based EMC, FEC/EMC, FEC, and FEC/FEMC electrolytes at a scan rate of 5 mV s<sup>-1</sup>. c) Potentiostatic profiles of graphite||Li cells with various electrolytes maintained at 5.0, 5.1, 5.2, and 5.3 V for 10 h.

graphite cathode up to 5.2 V (Figure 1c) with a high discharge capacity of 88.7 mAh g<sup>-1</sup> and CE of 71.9% for the first cycle, the graphite||Li cell experiences a fast capacity decay during the initial 250 cycles (Figure 2c), significantly worse than that with FEC/FEMC. This is mainly attributed to the incompatibility of FEC with the Li metal anode, and FEC co-solvent is needed to stabilize it, as discussed in a later section.

The comparison of long-term cycle performance of graphite||Li cells at a current of 500 mA g<sup>-1</sup> (5 C rate) with 1 M LiPF<sub>6</sub>-based electrolytes are displayed in Figure 2c. An obvious growing polarization (Figure S1b, Supporting Information) and declining CE is observed during cycling in FEC/EMC electrolyte, leading to battery failure within 1300 cycles. In contrast, FEC/FEMC electrolyte effectively reduce the cell polarization (Figure S1c, Supporting Information), maintaining a highly overlapping charge–discharge curves after 3000 cycles without capacity decay. More importantly, the cell CE is greatly enhanced to ≈99.2% during cycling, enabling a significantly improved capacity retention of 94.5% after 5000 cycles. To the best of our knowledge, this long-term cycling capability is one of the most outstanding results of DIBs for anion intercalation, as compared with other reports (summarized in Table S1, Supporting Information). It is noted that when cycling at a

low current density of 10 mA g<sup>-1</sup> (0.1 C), the CEs of the cells decrease for all electrolytes due to self-discharge (Figure S1d,e, Supporting Information), which will be discussed in Section 2.4. The superb cycle stability also suggests the parasite reactions between the graphite cathode and electrolyte is suppressed by replacing EMC with FEC, which can be attributed to a stabilized CEI layer.

Furthermore, at 0 °C, the graphite||Li battery employing 1 M LiPF<sub>6</sub>-FEC/FEMC retains 97.8% of the available capacity compared to that at room temperature with well-maintained voltage curves as well as superb cycle stability without capacity decay upon 3000 cycles under the high current rate of 5 C (Figure 2d). These results indicate that this all-fluorinated electrolyte can also enable a fast and reversible reaction kinetics of PF<sub>6</sub><sup>-</sup> and Li<sup>+</sup> at low temperature for graphite||Li DIBs. In rocking-chair batteries (e.g., LIBs), the ion-desolvation energy in electrolytes plays a significant role in the electrode reaction kinetics since the solvent molecules have to be stripped off from the Li<sup>+</sup> solvation structure near the anode and cathode during charge and discharge, respectively. Therefore, a sluggish Li<sup>+</sup> de-solvation process will affect both the cell charging and discharging performance especially at low temperature.<sup>[15]</sup> This is not the case for DIBs where ion-desolvation only occur during



**Figure 2.** a) The initial charge/discharge curves of graphite||Li cells with different electrolytes at 10 mA g<sup>-1</sup>. Inset is the charge/discharge profile with EMC electrolyte. b) The 1<sup>st</sup> cycle CE and average CE during the cell lifetime. c) Cycle performance and Coulombic efficiency of graphite||Li cells. d) Cycle stability of graphite||Li cells using 1 M LiPF<sub>6</sub>-FEC/FEMC electrolyte at 0 °C. Insets show the comparison of charge-discharge curves at room temperature and at 0 °C, and voltage curves of the last 20 cycles at 0 °C. Upper cutoff voltage: 5.2 V, current density: 500 mA g<sup>-1</sup> (1 C = 100 mA g<sup>-1</sup>).



charge process, thus can reduce the de-solvation barrier.<sup>[15c]</sup> In addition, according to previous studies,<sup>[16]</sup> the much weaker interaction between anions and solvent molecules would lead to a fast anion de-solvation process, thus facilitating rate and low-temperature performances.

## 2.2. Effect of Electrolyte on Li Anode

To evaluate the efficiency and reversibility of Li plating/stripping behavior, Li||Cu half cells with different electrolytes were cycled at 0.50 mA cm<sup>-2</sup> with a capacity of 1 mAh cm<sup>-2</sup>, as shown in Figure S2 (Supporting Information). The 1 M LiPF<sub>6</sub>-EMC and 1 M LiPF<sub>6</sub>-FEMC electrolyte present low CE of 11.0% and 35.0%, which quickly fails to less than 10% within five cycles due to side reactions. Introducing FEC as a co-solvent into these two electrolytes can stabilize the Li plating/stripping process and significantly improves the average CE to ≈95.8% and ≈97.2% (80 cycles) with 1 M LiPF<sub>6</sub>-FEC/EMC and 1 M LiPF<sub>6</sub>-FEC/FEMC electrolytes, respectively. These results suggest that FEMC reacts with Li anode, which is attributed to be the main factor leading to the fast capacity decay of the graphite||Li cell as shown in Figure 2c.

To further evaluate the stability of Li metal anodes against various electrolytes, galvanostatic cycling of Li||Li symmetric cells using the above-mentioned four electrolytes was also conducted at a current density of 1.0 mA cm<sup>-2</sup> with 12 min plating/stripping time. As shown in Figure 3a, the stability of the Li||Li cells in different electrolytes is in the order: EMC < FEMC < FEC/FEMC ≈ FEC/EMC. Specifically, the cell with 1 M LiPF<sub>6</sub>-EMC electrolyte lasts only 25 h with overpotential significantly increases to three times the initial level, which is attributed to the increase in surface resistance from continuous dendrite growth and electrolyte consumption.<sup>[17]</sup> When EMC is replaced by FEMC solvent, the increment in overpotential is reduced, though the symmetric cell can only survive ≈500 repeated Li plating/stripping cycles, implying the Li metal electrode is not stable in 1 M LiPF<sub>6</sub>-FEMC electrolyte. This explains the fast degradation of graphite||Li cell with FEMC electrolyte, as shown in Figure 2c. In contrast, with FEC/FEMC electrolyte, the voltage hysteresis declines to ≈±72 mV over 400 h and remains stable without obvious increment over the prolonged cycles, contributing to an outstanding cycle life of more than 2000 h. Similar stability of the Li||Li cell is also achieved with FEC/EMC electrolyte. The results suggest that FEC is a critical component in the electrolyte that leads to the ultra-long cycling life for DIBs with Li metal as anodes (Figure 2c), as FEC is able to form a stable and Li<sup>+</sup>-conducting interface on the Li metal surface.<sup>[18]</sup> These results are also consistent with our Li||Cu tests as discussed above.

Electrochemical impedance spectra (EIS) of symmetric Li||Li cells upon cycling were carried out to further track the interfacial resistance with various electrolytes and verify the benefit of FEC (Figure 3b–e). The Nyquist plot is composed of two typical semicircles representing interfacial resistance (high-to-middle frequency region) and charge transfer resistance (middle-to-low frequency region), respectively.<sup>[19]</sup> The Nyquist plots were fitted by employing the equivalent circuit in the inset of Figure 3b, where  $R_s$ ,  $R_i$ , and  $R_{ct}$  are attributed to resistances of the bulk

electrolyte, the interface, and the charge transfer, respectively. The evolution of  $R_s$  with cycling is displayed in Figure S3a (Supporting Information) and also summarized in Table 1. It is clear to note that the cell with EMC electrolyte exhibits a large increment of  $R_s$  upon electrochemical cycling to 2173 Ω after 100 cycles. Similarly,  $R_s$  of the FEMC electrolyte grows gradually to 106.8 Ω after 600 cycles, suggesting a large consumption of electrolyte accompanied with increase in surface resistance.<sup>[19]</sup> This phenomenon is attributed to the repeated breakdown and reparation of the interface (repeated SEI formation) on the Li electrode.<sup>[17b]</sup> In contrast, the  $R_s$  remains nearly unchanged for 800 cycles with the addition of FEC as a co-solvent (i.e., FEC/EMC and FEC/FEMC electrolytes), which indicates FEC is effective in reducing the harmful parasitic reactions between the electrolyte and Li metal, contributing to a more stable interface with smaller resistance change.

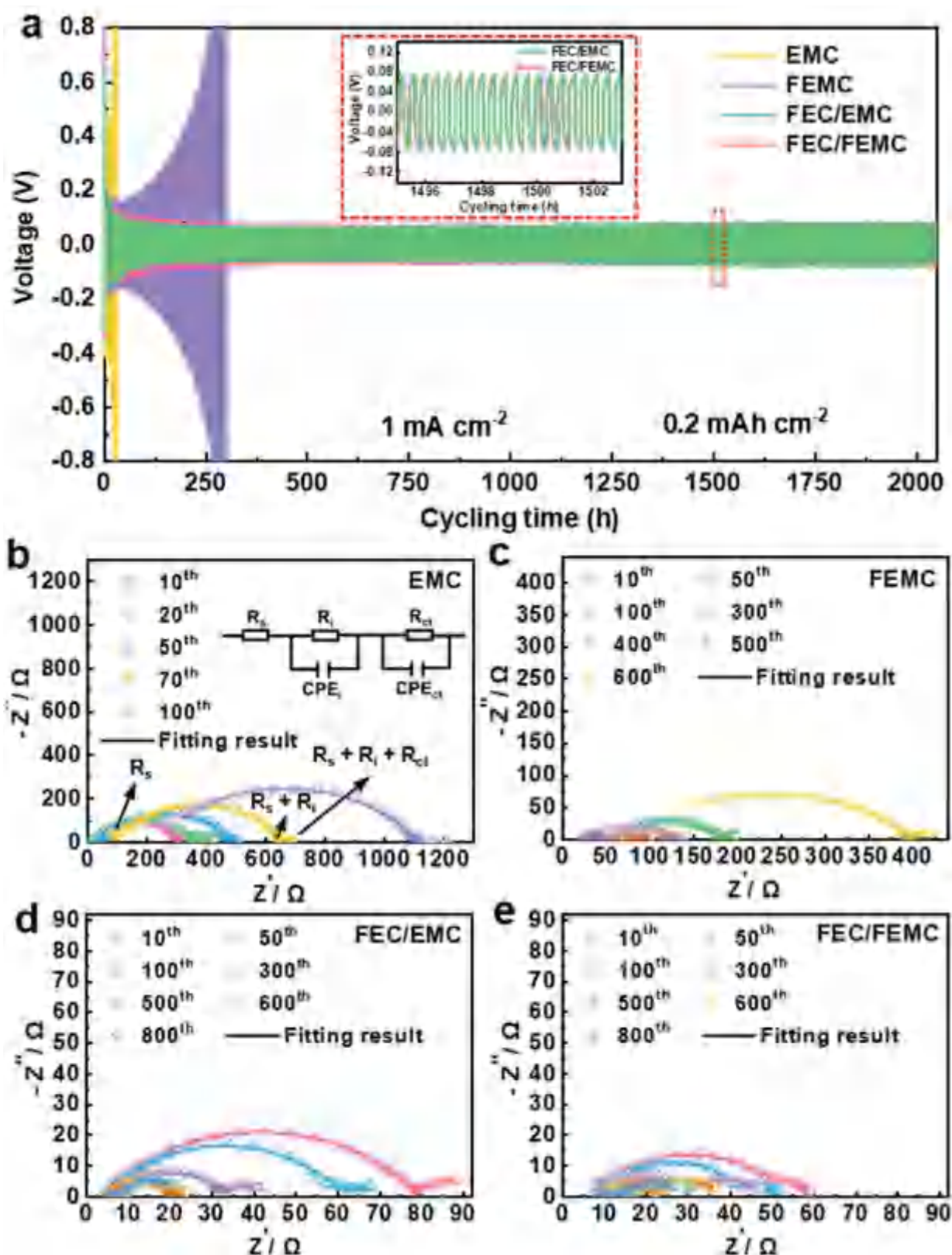
The evolution of  $R_i$  upon cycling exhibits a similar trend with  $R_s$  for each electrolyte, as shown in Figure S3b (Supporting Information, also summarized in Table 1). For the Li||Li cell with EMC electrolyte,  $R_i$  is ≈295 Ω at 10<sup>th</sup> cycle, which increases gradually with cycling. This phenomenon is attributed to the high-impedance interfacial layer formed on the Li metal, thus leading to the fast cell failure with EMC electrolyte (Figure 3a). Li||Li cell with FEMC also shows an increase in  $R_i$  with cycling, indicating that FEMC is not stable with Li. On the contrary, the introduction of FEC as a co-solvent (i.e., FEC/EMC and FEC/FEMC) reduces  $R_i$  upon cycling, which is attributed to the gradual stabilization of the interfacial layer through repeated charge–discharge.<sup>[17b,19b]</sup> The favorable effects of FEC-induced SEI on Li anode will be further elaborated in next section.

## 2.3. Characterizations of the Graphite Cathode and Lithium Anode after Cycling

To reveal the benefits of FEMC at high voltage, the composition and morphology of the CEI layer formed on graphite cathodes were investigated by X-ray photoelectron spectroscopy (XPS) and transmission electron microscopy (TEM), respectively, after 800 cycles. Compared to the major peak at ≈284.8 eV representing the C–C functionality for pristine graphite electrode (Figure S4a, Supporting Information), the electrode tested in FEC/EMC electrolyte shows increasing amounts of species attributed to C–O, C=O, ROCO<sub>2</sub>Li, and Li<sub>2</sub>CO<sub>3</sub> after cycling (Figure 4a), which is attributed to the accumulation of surface deposits from the decomposition of EMC. At the same time, the presence of LiF and Li<sub>x</sub>PO<sub>y</sub>F<sub>z</sub> species in the core F 1s spectrum (Figure 4d) suggests the decomposition of the LiPF<sub>6</sub> salt. In contrast, the electrodes cycled in the presence of FEMC (i.e., FEMC and FEC/FEMC electrolytes in Figure 4b,c,e,f) show reduced amount of C=O, ROCO<sub>2</sub>Li, LiF, and Li<sub>x</sub>PO<sub>y</sub>F<sub>z</sub> species, indicating less reaction between the electrolyte and graphite electrode. In addition, TEM images shows that the CEI layer on graphite is thinner when FEMC is used (Figure S5, Supporting Information).

The uniformity of the CEI layers on graphite with different electrolytes is further investigated by XPS depth profiling. In general, the contents of C–C and C–O increase, whereas the fraction of other species decreases from the outer to inner layer





**Figure 3.** a) Cycling stability of Li||Li symmetric cells in various electrolytes. Inset displays the enlarged figure of the red rectangle. Nyquist plots of Li||Li cells using b) EMC, c) FEMC, d) FEC/EMC, and e) FEC/FEMC electrolytes during cycling. Inset shows the equivalent circuit model for EIS analysis. Current density:  $1.0 \text{ mA cm}^{-2}$ , plating/stripping time: 12 min.

**Table 1.** Summary of fitting parameters ( $R_s$  and  $R_i$ ) for EIS results of Li||Li symmetrical cells.

Electrolyte		10 <sup>th</sup>	20 <sup>th</sup>	50 <sup>th</sup>	70 <sup>th</sup>	100 <sup>th</sup>	300 <sup>th</sup>	500 <sup>th</sup>	600 <sup>th</sup>	800 <sup>th</sup>
EMC	$R_s / \Omega$	14.1	20.3	46.9	89.4	217.3	—	—	—	—
	$R_i / \Omega$	295.2	332.7	439.3	570.5	900.1	—	—	—	—
FEMC	$R_s / \Omega$	23.6	—	30.3	—	33.0	36.8	42.6	56.3	106.8
	$R_i / \Omega$	41.6	—	28.8	—	21.5	52.8	80.8	125.2	288.8
FEC/ EMC	$R_s / \Omega$	4.3	—	5.8	—	5.0	5.5	5.1	5.2	5.1
	$R_i / \Omega$	74.4	—	55.5	—	28.0	14.2	3.2	2.9	2.9
FEC/ FEMC	$R_s / \Omega$	7.2	—	9.7	—	9.2	9.4	9.0	8.5	7.2
	$R_i / \Omega$	45.7	—	32.3	—	20.9	13.3	7.3	6.3	6.6

(Figure 4g). Though, the graphite cathode cycled in FEC/EMC electrolyte shows reduced amount of LiF and  $\text{Li}_x\text{PO}_y\text{F}_z$  species with increasing etching time (Figure 4h), suggesting that the surface CEI evolves with cycling, possibly due to additional  $\text{LiPF}_6$  decomposition upon cycling.<sup>[20]</sup> In contrast, both electrolytes containing FEMC reveal a small change in LiF content as the etching time is increased (Figure 4h). This suggests that the original CEI formed with FEMC and FEC/FEMC is stable after it is formed.<sup>[4b]</sup>

The morphologies of graphite cathodes in the three electrolytes were further studied by scanning electron microscope (SEM) (Figure 5a–c and Figure S6a, Supporting Information). It is clear that severe graphite exfoliation occurs with wrinkled or folded thin sheets after long-term charging/discharging with FEC/EMC electrolyte, as highlighted by the red rectangles in the image (Figure 5a). This is mainly due to the continuous side reactions between the electrolyte and the cathode under high charging voltage. In contrast, for the cathode cycled in FEMC electrolyte, the damage of the graphite structure is reduced, as evidenced by the smoother and more intact particle (Figure 5b). After adding FEC into this electrolyte, the electrolyte compatibility toward the graphite electrode is further enhanced, leading to a well-maintained structural integrity of the graphite particle with laminar microstructure (Figure 5c). These results further show that FEMC improves the stability of the graphite cathode.

The situation is different for the Li anode, which is shown from the cross-sectional images of cycled Li metal electrodes harvested from graphite||Li cells, as displayed in Figure 5d–f and Figure S6b (Supporting Information). With FEMC electrolyte, severe corrosion of the bulk Li metal with accumulation of a thick porous layer ( $\approx 190 \mu\text{m}$ ) is observed, which is due to the excessive reaction between FEMC and Li metal. FEC co-solvent is needed to suppress the continuous corrosion at the Li metal/electrolyte interface and formation of inactive Li, as evidenced from the reduced thickness of the reaction layer on the Li metal of about  $\approx 45 \mu\text{m}$  in the FEC/FEMC and FEC/EMC electrolytes. These results further confirm the important role of FEC solvent in generating a more stable and protective SEI on Li anode that can hinder subsequent corrosion reaction, promote uniform Li plating/stripping during cycling, and maintain excellent long-term cycle stability of graphite||Li cells.

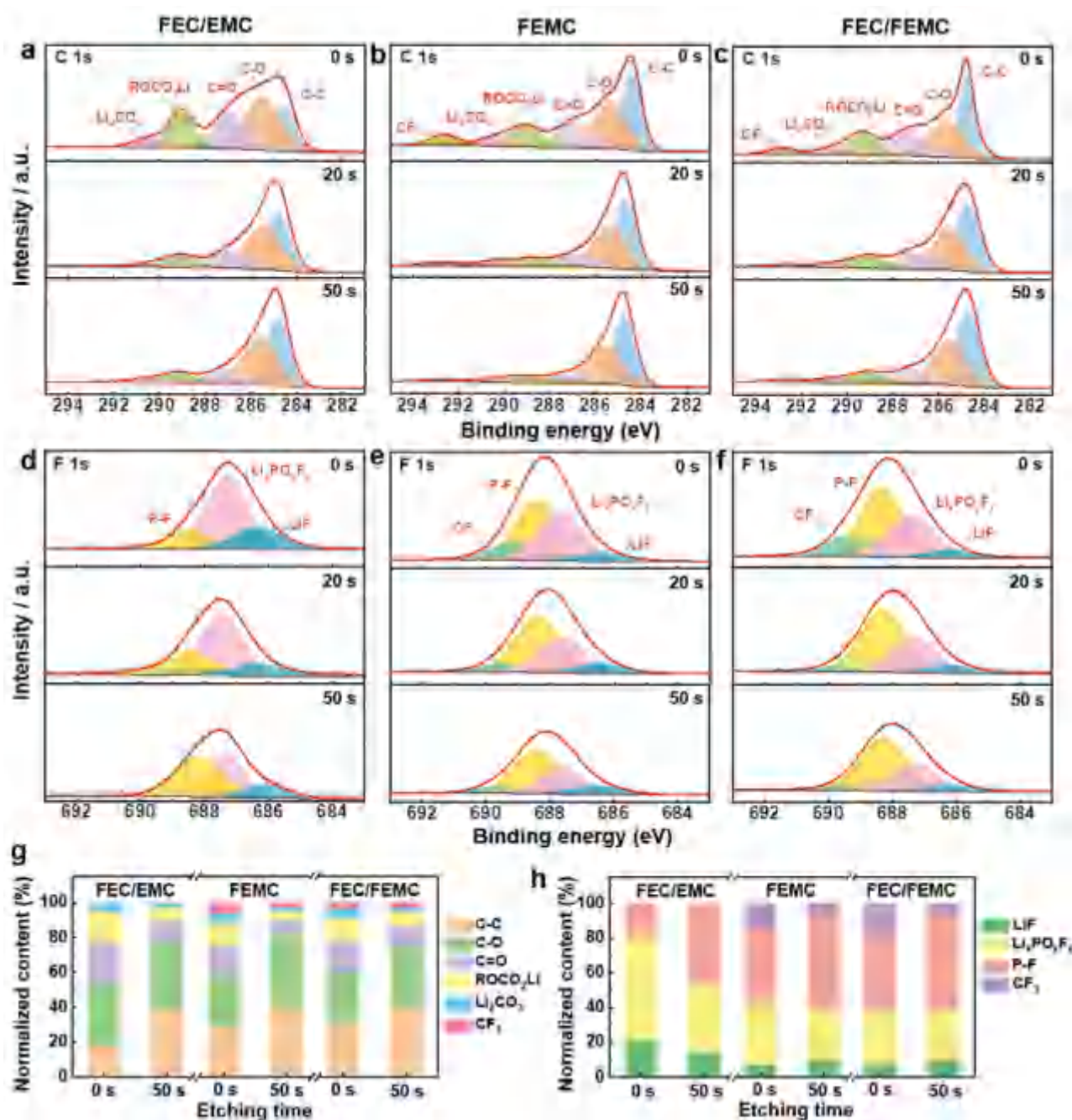
Based on the LUMO calculation from DFT in Figure 1a, FEC with lower LUMO is easier to be reduced than EMC and FEMC on the surface of Li anode, significantly reducing the consumption of solvent. According to previous reports, the reaction of

FEMC and EMC with Li lead to an organic component (e.g.,  $\text{ROCO}_2\text{Li}$ )-rich SEI, while FEC forms a LiF-rich SEI.<sup>[21]</sup> LiF is a robust electrical insulator ( $\approx 10^{-31} \text{ S cm}^{-1}$ ) that can prevent electrons from crossing the SEI layer, but also has a low surface diffusion barrier and high surface energy for  $\text{Li}^+$ , thus beneficial for the uniform Li deposition to suppress Li dendrite growth.<sup>[16a,19]</sup> These findings are consistent with our results, which are supported by the Li||Li symmetric cell (Figure 3), Li||Cu cell (Figure S2, Supporting Information), cross-sectional SEM images (Figure 5d–f), and DFT calculations (Figure 1a) results.

## 2.4. Rate and Self-Discharge Performances of Graphite||Li in Different Electrolytes

Apart from the long-term cycling stability of graphite||Li cells, we also investigated the effect of the various fluorinated electrolytes (FEMC, FEC/EMC, and FEC/FEMC) on the charge and discharge capability of the corresponding batteries at different current rates (Figure 6a–d, Figures S7 and S8, Supporting Information). To separate the effect of charging (intercalation of  $\text{PF}_6^-$  and deposition of  $\text{Li}^+$ ) and discharging (de-intercalation of  $\text{PF}_6^-$  and dissolution of  $\text{Li}$ ), the cells are either tested with constant charging current with varying discharging currents (Figure S7, Supporting Information) or constant discharging current with varying charging currents (Figure 6). Figure S6 (Supporting Information) shows the rate performance of the cells when charged at the same current rate of 1 C while discharged at different rates from 1 C to 50 C. For all cells, the capacity retention is nearly 100% even at a 50 C discharge rate for all three electrolytes, indicating the  $\text{PF}_6^-$  anion de-intercalation process from the graphite is facile and highly reversible and is not a rate limiting step in the battery. Though, the graphite||Li cell with FEMC shows larger polarization at a higher current rate with a lower average discharge voltage than the cells with FEC/EMC or FEC/FEMC (Figure S7b–g, Supporting Information). This is consistent with the higher impedance of the cell with FEMC (Table 1) and indicates that FEC co-solvent can improve kinetics of the Li anode.

When the discharge rate is kept at 1 C, but the charge rate is increased, the cells cycled with FEC/EMC and FEC/FEMC electrolytes can maintain superior charging capability (Figure 6a) with well-overlapping charge curves even when charging at 50 C rate, with a high capacity utilization of 91.3% and 91.8%,



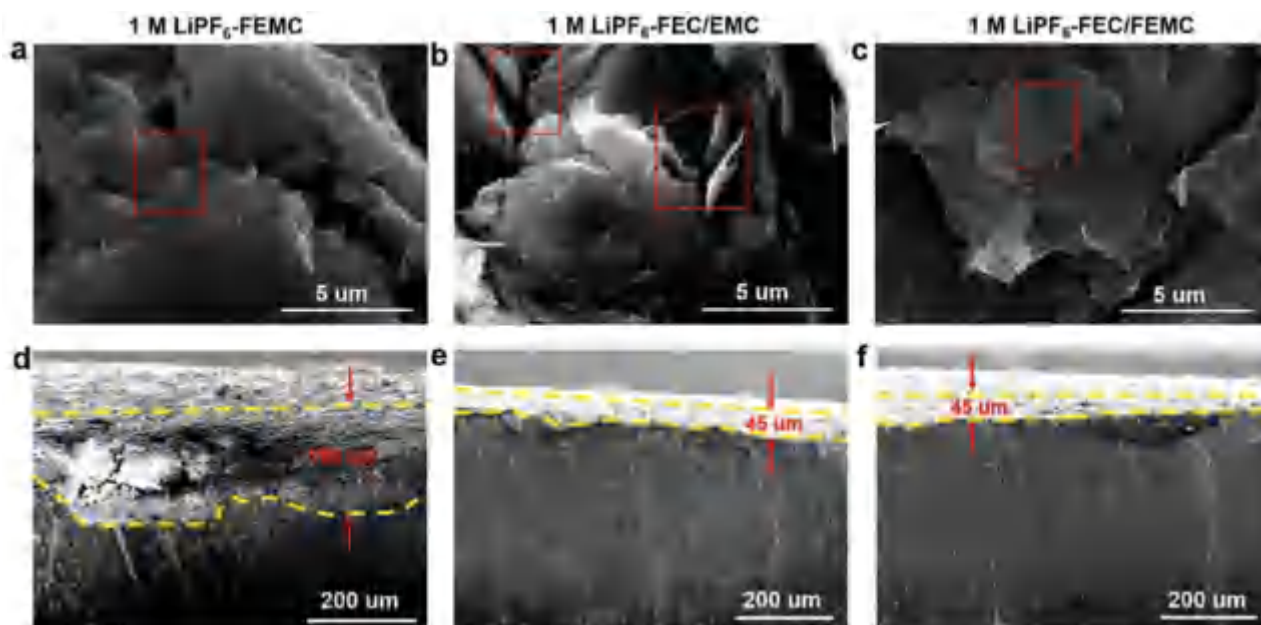
**Figure 4.** C 1s and F 1s XPS depth profiles of the graphite cathodes after 800 cycles in (a) and (d) FEC/EMC, (b,e) FEMC, (c,f) FEC/FEMC electrolytes, respectively. Normalized contents of different species of (g) C 1s and (h) F 1s in the CEI layer cycled in these three electrolytes, before and after etching for 50 s.

respectively, for the graphite||Li cell (Figure S8, Supporting Information). The voltage polarization of the cells in FEC/EMC and FEC/FEMC electrolytes are 0.35 and 0.37 V, respectively, at 50 °C. These results also indicate that graphite cathode is capable of allowing ultrafast PF<sub>6</sub><sup>-</sup> anion insertion at a high rate. It is noted that when the salt concentration is increased to 2 M, the DIB demonstrates similar fast-charging capability and cycle stability as compared to those with 1 M LiPF<sub>6</sub>/FEC/FEMC electrolyte (Figure S9, Supporting Information). For practical

applications, the salt concentration with respect to electrolyte amount, viscosity, power, and energy densities will have to be further optimized in future work.

Graphite||Li cell with FEMC electrolyte, on the other hand, shows poorer rate performance with a reduced capacity utilization of ≈45% and a huge polarization (≈0.93 V) at 50 °C (Figure 6b). The main reason for the difference is again the Li anode—FEMC is not compatible with Li, thus forming an SEI layer with large resistance, whereas FEC co-solvent can form an





**Figure 5.** SEM images of graphite cathodes and Li anodes after 800 cycles harvested from graphite||Li cells. Surface view of graphite electrodes cycled in a) FEMC, b) FEC/EMC, and c) FEC/FEMC electrolytes. Cross-sectional images of Li metal after cycling using d) FEMC, e) FEC/EMC, and f) FEC/FEMC electrolytes.

Li<sup>+</sup>-conductive and stable SEI and enhance interfacial dynamics of the anode. These results demonstrate that FEC/FEMC electrolyte is compatible with both the graphite cathode and Li anode and can ensure high rate performance of the DIB.

Since parasitic reactions can consume energy, here we also study the self-discharge behavior of graphite||Li cells in different fluorinated electrolytes. The cells are first charged to 5.2 V and rested for different time, and then discharged to 3 V to record the available discharge capacity (Figure 6e,f, Figure S10, Supporting Information). As shown in Figure 6e, the decrease in capacity is not linear with rest time, and the degree is highly dependent on the electrolyte. The rate of self-discharge ( $r$ ) (i.e., the percentage of capacity loss with time) can be calculated from the following equation:<sup>[22]</sup>

$$r = \frac{C_t - C_{t'}}{C_r(t - t')} \times 100\% \quad (1)$$

where  $C_r$  and  $C_t$  represent the discharge capacities after resting for  $t$  and  $t'$ , respectively. During the initial period (first 3 h after charging, as shown in the inset of Figure 6e),  $r$  is 2.26%/h, 1.99%/h, and 1.56%/h for graphite||Li cells using FEC/EMC, FEMC, and FEC/FEMC electrolytes, respectively, while the voltage of the battery decreases during rest in the same order: FEC/EMC > FEMC > FEC/FEMC (inset of Figure 6f). This trend coincides with the degree of electrolyte oxidation decomposition (Figure 1b,c), suggesting that the short-term self-discharge process is probably due to side reactions of the electrolyte under high voltage. In addition, the short-term self-discharge rate is found to depend linearly with the upper cut-off voltage (Figure S11, Supporting Information), further supporting that the initial loss in capacity is due to electrolyte decomposition. As the resting time increases, the self-discharge

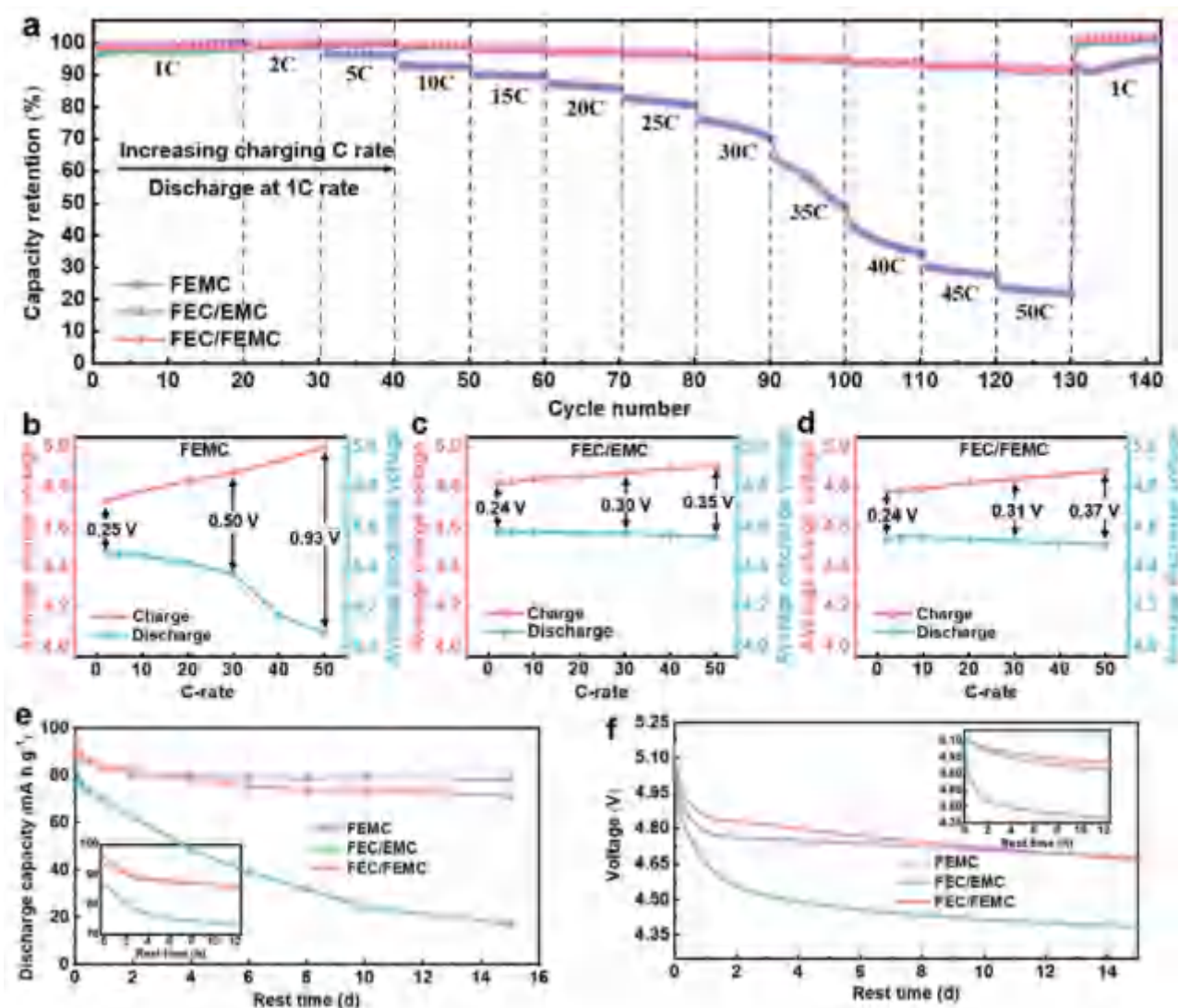
rate is also decreased (Figure 6e). This could be because the voltage of battery is now reduced to a level where electrolyte decomposition is not a dominant factor anymore (Figure 6f). The mechanism of long-term self-discharge remains unclear and should be investigated in future work.

In our work, the active mass loading of the graphite cathode is 2.0 mg cm<sup>-2</sup>, which is lower than electrode loading for traditional LIB cathode. This is because DIB is more suitable for high-rate applications. A simple calculation of the energy density of DIB is included in Note S1 and Table S2 (Supporting Information) based on a stacked layer of electrodes with electrolyte in between (Figure S12, Supporting Information). Since the electrolyte is the only source of cations and anions for the electrochemical storage processes, a larger amount of electrolyte is needed in DIB.<sup>[23]</sup> Practical energy density of DIB is between 20 and 70 Wh kg<sup>-1</sup>, and depends strongly on the use of the salt in the electrolyte (Figure S13, Supporting Information). Increasing active mass loading of graphite can slightly increase the energy density of DIB, but compromises the power capability as the rate performance is poorer (Figure S14, Supporting Information). In the future, electrode loading will have to be optimized with respect to energy and power densities for practical applications.

### 3. Conclusion

In this work, we have developed an all-fluorinated electrolyte, 1 M LiPF<sub>6</sub>-FEC/FEMC (3:7), that is suitable for DIB with graphite cathode up to 5.2 V. FEMC forms a stable CEI on the surface of the graphite cathode, protecting it from further reaction with the electrolyte. On the other hand, FEC co-solvent forms a protective SEI on the Li metal, stabilizing the anode. The





**Figure 6.** a) Rate capability of graphite||Li cells under increasing charge rate from 1 C to 50 C with a constant discharge rate of 1 C. Evolution of the average charge and discharge voltage of graphite cathodes under varying charge rates using b) FEMC, c) FEC/EMC, and d) FEC/FEMC electrolytes. The evolution of e) discharge capacity and f) voltage as a function of rest time after charging the cells to 5.2 V. 1 C = 100 mA g<sup>-1</sup>.

synergetic effect of the FEC/FEMC electrolyte enables reversible and highly efficient PF<sub>6</sub><sup>-</sup> insertion/extraction and Li<sup>+</sup> plating/stripping processes in a graphite||Li battery, achieving excellent cell lifetime of 5000 cycles with 94.5% capacity retention accompanied by an average Coulombic efficiency of ~99.2%, which is among the best cycle performance ever reported for a DIB. The electrolyte system also allows low-temperature applications of DIB, as evidence from the ~100% capacity retention for more than 3000 cycles at 0 °C (5 C). Meanwhile, the interface layers on the cathode and anode are highly conductive to ion transport with small voltage polarization, thus enabling ultrafast charging with 91.8% capacity utilization at 50 C. Moreover, the use of fluorinated electrolyte also suppresses electrolyte decomposition and self-discharge. Our work provides an alternative method to stabilize high-voltage anion intercalation reactions apart from increasing the salt concentration. DIB is a promising choice

for next-generation battery systems for room-temperature and low-temperature applications. Further work on clarifying the relationships among electrolyte properties (e.g., electrolyte ionic conductivity, melting point), electrolyte microstructure (e.g., solvation structure, de-solvation energy), interfacial behaviors (CEI layer, SEI layer), electrode material properties (e.g., particle size, morphology and structure), and electrochemical performances of DIBs from both scientific and practical viewpoints is underway and will be reported in the future.

## 4. Experimental Section

**Electrolyte Preparation and Cell Assembly:** LiPF<sub>6</sub> (purity ≥ 99.95%) salt, FEC (purity ≥ 99.99%) solvent, and EMC (purity ≥ 99.99%) solvent were purchased from Dongguan Shanshan Battery Materials Co., Ltd. FEMC (>99%) solvent was purchased from Halocarbon

Products Corp. The electrolytes were prepared by dissolving 1 M LiPF<sub>6</sub> salt in pure EMC, pure FEMC, mixed FEC/EMC (3:7 by volume) and mixed FEC/FEMC (3:7 by volume) solvents, respectively. All electrolytes were prepared in the Ar-filled glove box with O<sub>2</sub> < 0.1 ppm and H<sub>2</sub>O < 0.1 ppm.

The cathode slurry was prepared by blending graphite powder (MTI SAG-R) as the active material, acetylene black, and CNT (TUBALL BATT NMP) as conductive agents, and PAA (Sigma Aldrich, MW 450000) as binder at a weight ratio of 85: 4.5:0.5:10 by using NMP as the solvent. The homogeneous slurry was then coated onto an aluminum foil and dried at 80 °C. The dried electrode was punched into circular sheets with the diameter of 16 mm. The average mass loading of active material on each cathode and anode was  $2 \pm 0.2 \text{ mg cm}^{-2}$ . Electrodes were further dried at 150 °C overnight under vacuum prior to cell assembly. CR2032-type coin cells with the graphite cathode and lithium metal (China Energy Lithium Co., Ltd., diameter  $\times$  thickness:  $\phi 16 \times 0.6 \text{ mm}$ ) were fabricated in an Ar-filled glove box with both O<sub>2</sub> and H<sub>2</sub>O content being less than 0.1 ppm. A PVdF membrane (Merck Millipore Ltd., pore size: 0.2  $\mu\text{m}$ ) wetted with approximately 150  $\mu\text{L}$  electrolyte was used as the separator.

**Electrochemical Tests:** Galvanostatic charge–discharge tests were performed using a Neware battery tester. The graphite||Li cells were typically cycled with a constant current of 500 mA g<sup>-1</sup> (5 C) within the voltage range of 3–5.2 V (versus Li/Li<sup>+</sup>). The LSV tests were conducted on a working electrode of Ti foil at a sweep rate of 5 mV s<sup>-1</sup>. Potentiostatic tests were performed using graphite||Li cells which were charged to and held at a constant voltage of 5.0, 5.1, 5.2, and 5.3 V for 10 h, respectively. Two protocols were used to evaluate the electrolyte effects on the rate capability of graphite cathode: (1) the cells were charged with an increasing current rate from 1 C to 50 C with a constant discharge rate of 1 C; (2) the cells were charged at a constant rate of 1 C while discharging with an increasing current rate from 1 C to 50 C. For low temperature electrochemical tests, the cells using 1 M LiPF<sub>6</sub>-FEC/FEMC electrolyte were initially cycled for 50 times at room temperature with a current rate of 5 C to form the CEI and SEI. The cells were then transferred to a temperature chamber to rest for 7 h to reach 0 °C, followed by charging/discharging at 5 C.

To investigate the effect of the electrolyte on the Li metal, galvanostatic cycling of Li||Li symmetric cells were conducted at a current density of 1.0 mA cm<sup>-2</sup> with 12 min plating/stripping time. Impedance measurements were performed also using the Bio-Logic potentiostat (VMP3) by applying a 10 mV AC potential amplitude within the frequency range from 100 kHz to 10 mHz. The Coulombic efficiency measurements of Li||Cu cells were conducted at 0.5 mA cm<sup>-2</sup>. Li was first deposited on the Cu electrode with a capacity of 1 mAh cm<sup>-2</sup>, then stripped to a voltage of 1.0 V versus Li/Li<sup>+</sup>.

**Sample Characterizations:** To gain insights into the surface chemistry and morphological changes of the graphite cathodes and Li anodes, the cycled cells were disassembled in the glove box. The electrodes were rinsed with dimethyl carbonate (DMC) solvent for several times to remove the salt residuals, followed by drying in the antechamber of the glove box under vacuum. The morphological evolutions of the cathode material and Li metal were studied using a field-emission scanning electron microscope (FE-SEM, Zeiss SUPRA-55 microscope) and a transmission electron microscope (TEM, JEOL 2100F). X-ray photoelectron spectra (XPS) was carried out on Thermo Scientific ESCALAB Xi<sup>+</sup> XPS microprobe using Al K $\alpha$  radiation. The collected spectra were calibrated according to the C 1s binding energy of 284.8 eV and analyzed using Thermo Advantage software. Ar<sup>+</sup> etching was adopted to gain information about the CEI on the surface of graphite cathodes. The etching rate of the Ar<sup>+</sup> beam was set to be 0.35 nm s<sup>-1</sup> based on a Ta<sub>2</sub>O<sub>5</sub> standard sample and the etching time was set to 20 or 50 s.

**DFT Calculation:** The molecular orbital energy levels of the solvents (FEC, EMC, and FEMC) were calculated using the DFT module implemented in the NWChem package.<sup>[19]</sup> The structures of the solvent molecules were fully optimized using the 6–31+G\* basis sets and the Lee–Yang–Parr correlation functional (B3LYP) for the exchange correlation energy.<sup>[20]</sup>

## Supporting Information

Supporting Information is available from the Wiley Online Library or from the author.

## Acknowledgements

This work was supported by the Strategic Research Grant at City University of Hong Kong (P/J#7005285).

## Conflict of Interest

The authors declare no conflict of interest.

## Data Availability Statement

The data that support the findings of this study are available from the corresponding author upon reasonable request.

## Keywords

dual-ion batteries, fluorinated electrolytes, high voltage, PF<sub>6</sub><sup>-</sup> intercalation, surface protection

Received: October 27, 2021

Revised: December 30, 2021

Published online: February 9, 2022

- [1] a) G. E. Blomgren, *J. Electrochem. Soc.* **2016**, *164*, A5019; b) R. Schmich, R. Wagner, G. Hörpel, T. Placke, M. Winter, *Nat. Energy* **2018**, *3*, 267; c) D. Andre, S.-J. Kim, P. Lamp, S. F. Lux, F. Maglia, O. Paschos, B. Stiaszny, *J. Mater. Chem. A* **2015**, *3*, 6709.
- [2] P. K. Nayak, L. Yang, W. Brehm, P. Adelhelm, *Angew. Chem., Int. Ed.* **2018**, *57*, 102.
- [3] a) D. Larcher, J.-M. Tarascon, *Nat. Chem.* **2015**, *7*, 19; b) B. Lee, Y. Ko, G. Kwon, S. Lee, K. Ku, J. Kim, K. Kang, *Joule* **2018**, *2*, 61.
- [4] a) L. Zhang, H. Wang, X. Zhang, Y. Tang, *Adv. Funct. Mater.* **2021**, *31*, 2010958; b) D. Yu, Q. Zhu, L. Cheng, S. Dong, X. Zhang, H. Wang, N. Yang, *ACS Energy Lett.* **2021**, *6*, 949; c) Y. Wang, Y. Zhang, S. Wang, S. Dong, C. Dang, W. Hu, D. Y. W. Yu, *Adv. Funct. Mater.* **2021**, *31*, 2102360; d) Z. Huang, Y. Hou, T. Wang, Y. Zhao, G. Liang, X. Li, Y. Guo, Q. Yang, Z. Chen, Q. Li, L. Ma, J. Fan, C. Zhi, *Nat. Commun.* **2021**, *12*, 3106; e) L. Xiang, X. Ou, X. Wang, Z. Zhou, X. Li, Y. Tang, *Angew. Chem., Int. Ed.* **2020**, *59*, 17924; f) Y. Wang, Y. Zhang, Q. Duan, P.-K. Lee, S. Wang, D. Y. W. Yu, *J. Power Sources* **2020**, *471*, 228466; g) Y. Sui, C. Liu, R. C. Masse, Z. G. Neale, M. Atif, M. AlSalhi, G. Cao, *Energy Storage Mater.* **2020**, *25*, 1; h) C. Jiang, L. Xiang, S. Miao, L. Shi, D. Xie, J. Yan, Z. Zheng, X. Zhang, Y. Tang, *Adv. Mater.* **2020**, *32*, 1908470; i) X. Zhou, Q. Liu, C. Jiang, B. Ji, X. Ji, Y. Tang, H. M. Cheng, *Angew. Chem., Int. Ed.* **2020**, *59*, 3802; j) K. V. Kravchyk, M. V. Kovalenko, *Adv. Energy Mater.* **2019**, *9*, 1901749; k) Z. Hu, Q. Liu, K. Zhang, L. Zhou, L. Li, M. Chen, Z. Tao, Y.-M. Kang, L. Mai, S.-L. Chou, *ACS Appl. Mater. Interfaces* **2018**, *10*, 35978; l) W.-H. Li, H.-J. Liang, X.-K. Hou, Z.-Y. Gu, X.-X. Zhao, J.-Z. Guo, X. Yang, X.-L. Wu, *J. Energy Chem.* **2020**, *50*, 416; m) M. Zhang, X. Song, X. Ou, Y. Tang, *Energy Storage Mater.* **2019**, *16*, 65; n) I. A. Rodríguez-Pérez, L. Zhang, J. M. Wrogoemann, D. M. Driscoll, M. L. Sushko,

- K. S. Han, J. L. Fulton, M. H. Engelhard, M. Balasubramanian, V. V. Viswanathan, V. Murugesan, X. Li, D. Reed, V. Sprenkle, M. Winter, T. Placke, *Adv. Energy Mater.* **2020**, *10*, 2001256.
- [5] a) C. Song, Y. Li, H. Li, T. He, Q. Guan, J. Yang, X. Li, J. Cheng, B. Wang, *Nano Energy* **2019**, *60*, 285; b) I. A. Rodríguez-Pérez, X. Ji, *ACS Energy Lett.* **2017**, *2*, 1762; c) B. Heidrich, A. Heckmann, K. Beltrop, M. Winter, T. Placke, *Energy Storage Mater.* **2019**, *21*, 414.
- [6] a) J. A. Read, *J. Phys. Chem. C* **2015**, *119*, 8438; b) J. Gao, M. Yoshio, L. Qi, H. Wang, *J. Power Sources* **2015**, *278*, 452; c) X. Han, G. Xu, Z. Zhang, X. Du, P. Han, X. Zhou, G. Cui, L. Chen, *Adv. Energy Mater.* **2019**, *9*, 1804022.
- [7] a) S. He, S. Wang, H. Chen, X. Hou, Z. Shao, *J. Mater. Chem. A* **2020**, *8*, 2571; b) L. Zhang, Y. Huang, H. Fan, H. Wang, *ACS Appl. Energy Mater.* **2019**, *2*, 1363; c) K. V. Kravchyk, P. Bhauriyal, L. Piveteau, C. P. Guntlin, B. Pathak, M. V. Kovalenko, *Nat. Commun.* **2018**, *9*, 4469; d) X. Jiang, X. Liu, Z. Zeng, L. Xiao, X. Ai, H. Yang, Y. Cao, *Adv. Energy Mater.* **2018**, *8*, 1802176; e) S. Zhang, M. Wang, Z. Zhou, Y. Tang, *Adv. Funct. Mater.* **2017**, *27*, 1703035; f) L.-N. Wu, J. Peng, Y.-K. Sun, F.-M. Han, Y.-F. Wen, C.-G. Shi, J.-J. Fan, L. Huang, J.-T. Li, S.-G. Sun, *ACS Appl. Mater. Interfaces* **2019**, *11*, 18504; g) Z. Zhou, N. Li, Y. Yang, H. Chen, S. Jiao, W. L. Song, D. Fang, *Adv. Energy Mater.* **2018**, *8*, 1801439; h) X.-T. Xi, W.-H. Li, B.-H. Hou, Y. Yang, Z.-Y. Gu, X.-L. Wu, *ACS Appl. Energy Mater.* **2018**, *2*, 201; i) A. Heckmann, J. Thienenkamp, K. Beltrop, M. Winter, G. Brunklaus, T. Placke, *Electrochim. Acta* **2018**, *260*, 514; j) P. Qin, M. Wang, N. Li, H. Zhu, X. Ding, Y. Tang, *Adv. Mater.* **2017**, *29*, 1606805; k) T. Liu, X. Han, Z. Zhang, Z. Chen, P. Wang, P. Han, N. Ding, G. Cui, *J. Power Sources* **2019**, *437*, 226942.
- [8] a) X. Fan, L. Chen, O. Borodin, X. Ji, J. Chen, S. Hou, T. Deng, J. Zheng, C. Yang, S.-C. Liou, *Nat. Nanotechnol.* **2018**, *13*, 715; b) Y. Yamada, J. Wang, S. Ko, E. Watanabe, A. Yamada, *Nat. Energy* **2019**, *4*, 269.
- [9] a) Z. Zhang, L. Hu, H. Wu, W. Weng, M. Koh, P. C. Redfern, L. A. Curtiss, K. Amine, *Energy Environ. Sci.* **2013**, *6*, 1806; b) X. Wang, H. Lee, H. Li, X. Yang, X. Huang, *Electrochem. Commun.* **2010**, *12*, 386.
- [10] J. A. Read, A. V. Cresce, M. H. Ervin, K. Xu, *Energy Environ. Sci.* **2014**, *7*, 617;
- [11] a) Y. Wang, L. Xing, W. Li, D. Bedrov, *J. Phys. Chem. Lett.* **2013**, *4*, 3992; b) Q. Zheng, Y. Yamada, R. Shang, S. Ko, Y.-Y. Lee, K. Kim, E. Nakamura, A. Yamada, *Nat. Energy* **2020**, *5*, 291.
- [12] a) W. Giurlani, L. Sergi, E. Crestini, N. Calisi, F. Poli, F. Soavi, M. Innocenti, *J. Solid State Electrochem.* **2022**, *26*, 85; b) A. Karambakhsh, A. Afshar, S. Ghahramani, P. Malekinejad, *J. Mater. Eng. Perform.* **2011**, *20*, 1690.
- [13] L. Suo, W. Xue, M. Gobet, S. G. Greenbaum, C. Wang, Y. Chen, W. Yang, Y. Li, J. Li, *Proc. Natl. Acad. Sci. U. S. A.* **2018**, *115*, 1156.
- [14] a) L. Hu, Z. Zhang, K. Amine, *Electrochem. Commun.* **2013**, *35*, 76; b) D. Liu, K. Qian, Y.-B. He, D. Luo, H. Li, M. Wu, F. Kang, B. Li, *Electrochim. Acta* **2018**, *269*, 378; c) M. He, C. C. Su, Z. Feng, L. Zeng, T. Wu, M. J. Bedzyk, P. Fenter, Y. Wang, Z. Zhang, *Adv. Energy Mater.* **2017**, *7*, 1700109; d) E. Markevich, G. Salitra, K. Fridman, R. Sharabi, G. Gershtinsky, A. Garsuch, G. Semrau, M. A. Schmidt, D. Aurbach, *Langmuir* **2014**, *30*, 7414.
- [15] a) Q. Li, G. Liu, H. Cheng, Q. Sun, J. Zhang, J. Ming, *Chem. - Eur. J.* **2021**, *27*, 15842; b) X. Fan, X. Ji, L. Chen, J. Chen, T. Deng, F. Han, J. Yue, N. Piao, R. Wang, X. Zhou, *Nat. Energy* **2019**, *4*, 882; c) J. Holoubek, Y. Yin, M. Li, M. Yu, Y. S. Meng, P. Liu, Z. Chen, *Angew. Chem., Int. Ed.* **2019**, *131*, 19068; d) S. Zhang, K. Xu, T. Jow, *J. Power Sources* **2003**, *115*, 137; e) Q. Li, D. Lu, J. Zheng, S. Jiao, L. Luo, C.-M. Wang, K. Xu, J.-G. Zhang, W. Xu, *ACS Appl. Mater. Interfaces* **2017**, *9*, 42761; f) M. Petzl, M. Kasper, M. A. Danzer, *J. Power Sources* **2015**, *275*, 799.
- [16] a) A. von Wald Cresce, M. Gobet, O. Borodin, J. Peng, S. M. Russell, E. Wikner, A. Fu, L. Hu, H.-S. Lee, Z. Zhang, X.-Q. Yang, S. Greenbaum, K. Amine, K. Xu, *J. Phys. Chem. C* **2015**, *119*, 27255; b) Z. Chen, Y. Tang, X. Du, B. Chen, G. Lu, X. Han, Y. Zhang, W. Yang, P. Han, J. Zhao, G. Cui, *Angew. Chem., Int. Ed.* **2020**, *59*, 21769; c) D. M. Seo, O. Borodin, S.-D. Han, Q. Ly, P. D. Boyle, W. A. Henderson, *J. Electrochem. Soc.* **2012**, *159*, A553; d) V. V. Chaban, E. E. Fileti, *J. Mol. Model.* **2015**, *21*, 236.
- [17] a) J.-G. Zhang, W. Xu, J. Xiao, X. Cao, J. Liu, *Chem. Rev.* **2020**, *120*, 13312; b) W. Xu, J. Wang, F. Ding, X. Chen, E. Nasybulin, Y. Zhang, J.-G. Zhang, *Energy Environ. Sci.* **2014**, *7*, 513.
- [18] a) X. Q. Zhang, X. B. Cheng, X. Chen, C. Yan, Q. Zhang, *Adv. Funct. Mater.* **2017**, *27*, 1605989; b) R. Mogi, M. Inaba, S.-K. Jeong, Y. Iriyama, T. Abe, Z. Ogumi, *J. Electrochem. Soc.* **2002**, *149*, A1578; c) C. Fu, Y. Ma, S. Lou, C. Cui, L. Xiang, W. Zhao, P. Zuo, J. Wang, Y. Gao, G. Yin, *J. Mater. Chem. A* **2020**, *8*, 2066.
- [19] a) L. Yu, S. Chen, H. Lee, L. Zhang, M. H. Engelhard, Q. Li, S. Jiao, J. Liu, W. Xu, J.-G. Zhang, *ACS Energy Lett.* **2018**, *3*, 2059; b) P. Shi, L. Zhang, H. Xiang, X. Liang, Y. Sun, W. Xu, *ACS Appl. Mater. Interfaces* **2018**, *10*, 22201.
- [20] a) J. Cha, J.-G. Han, J. Hwang, J. Cho, N.-S. Choi, *J. Power Sources* **2017**, *357*, 97; b) Y.-M. Song, C.-K. Kim, K.-E. Kim, S. Y. Hong, N.-S. Choi, *J. Power Sources* **2016**, *302*, 22; c) J. Lee, Y.-J. Kim, H. S. Jin, H. Noh, H. Kwack, H. Chu, F. Ye, H. Lee, H.-T. Kim, *ACS Omega* **2019**, *4*, 3220; d) S. Leroy, F. Blanchard, R. Dedryvere, H. Martinez, B. Carré, D. Lemordant, D. Gonbeau, *Surf. Interface Anal.* **2005**, *37*, 773; e) L. Xia, B. Tang, L. Yao, K. Wang, A. Cheris, Y. Pan, S. Lee, Y. Xia, G. Z. Chen, Z. Liu, *ChemistrySelect* **2017**, *2*, 7353.
- [21] a) Q. C. Liu, J. J. Xu, S. Yuan, Z. W. Chang, D. Xu, Y. B. Yin, L. Li, H. X. Zhong, Y. S. Jiang, J. M. Yan, *Adv. Mater.* **2015**, *27*, 5241; b) Y. Lu, Z. Tu, L. A. Archer, *Nat. Mater.* **2014**, *13*, 961; c) J. Pan, Y.-T. Cheng, Y. Qi, *Phys. Rev. B* **2015**, *91*, 134116; d) W. Wang, J. Zhang, Q. Yang, S. Wang, W. Wang, B. Li, *ACS Appl. Mater. Interfaces* **2020**, *12*, 22901; e) C.-C. Su, M. He, R. Amine, T. Rojas, L. Cheng, A. T. Ngo, K. Amine, *Energy Environ. Sci.* **2019**, *12*, 1249; f) J. Wu, X. Wang, Q. Liu, S. Wang, D. Zhou, F. Kang, D. Shanmukaraj, M. Armand, T. Rojo, B. Li, G. Wang, *Nat. Commun.* **2021**, *12*, 5746; g) C.-C. Su, M. He, M. Cai, J. Shi, R. Amine, N. D. Rago, J. Guo, T. Rojas, A. T. Ngo, K. Amine, *Nano Energy* **2021**, *92*, 106720.
- [22] a) Z. Li, J. Liu, B. Niu, J. Li, F. Kang, *Small* **2018**, *14*, 1800745; b) S. Jiao, H. Lei, J. Tu, J. Zhu, J. Wang, X. Mao, *Carbon* **2016**, *109*, 276; c) Z. Lv, M. Han, J. Sun, L. Hou, H. Chen, Y. Li, M.-C. Lin, *J. Power Sources* **2019**, *418*, 233.
- [23] J. Betz, G. Bieker, P. Meister, T. Placke, M. Winter, R. Schmuck, *Adv. Energy Mater.* **2019**, *9*, 1803170.



## Fluorine Chemistry in Rechargeable Batteries: Challenges, Progress, and Perspectives

Yao Wang,<sup>†</sup> Xu Yang,<sup>†</sup> Yuefeng Meng,<sup>†</sup> Zuxin Wen, Ran Han, Xia Hu, Bing Sun, Feiyu Kang, Baohua Li,<sup>\*</sup> Dong Zhou,<sup>\*</sup> Chunsheng Wang,<sup>\*</sup> and Guoxiu Wang<sup>\*</sup>



Cite This: *Chem. Rev.* 2024, 124, 3494–3589



Read Online

ACCESS |

Metrics & More

Article Recommendations

**ABSTRACT:** The renewable energy industry demands rechargeable batteries that can be manufactured at low cost using abundant resources while offering high energy density, good safety, wide operating temperature windows, and long lifespans. Utilizing fluorine chemistry to redesign battery configurations/components is considered a critical strategy to fulfill these requirements due to the natural abundance, robust bond strength, and extraordinary electronegativity of fluorine and the high free energy of fluoride formation, which enables the fluorinated components with cost effectiveness, nonflammability, and intrinsic stability. In particular, fluorinated materials and electrode/electrolyte interphases have been demonstrated to significantly affect reaction reversibility/kinetics, safety, and temperature tolerance of rechargeable batteries. However, the underlining principles governing material design and the mechanistic insights of interphases at the atomic level have been largely overlooked. This review covers a wide range of topics from the exploration of fluorine-containing electrodes, fluorinated electrolyte constituents, and other fluorinated battery components for metal-ion shuttle batteries to constructing fluoride-ion batteries, dual-ion batteries, and other new chemistries. In doing so, this review aims to provide a comprehensive understanding of the structure–property interactions, the features of fluorinated interphases, and cutting-edge techniques for elucidating the role of fluorine chemistry in rechargeable batteries. Further, we present current challenges and promising strategies for employing fluorine chemistry, aiming to advance the electrochemical performance, wide temperature operation, and safety attributes of rechargeable batteries.



### CONTENTS

1. Introduction	3495	2.3.2. Fluorinated Binders and Current Collectors	3517
1.1. Brief Background on Rechargeable Li-Based Batteries and Beyond	3496	3. Understanding Fluorinated Interphases in Li-Based Batteries	3520
1.2. Role of Fluorine Chemistry in Rechargeable Batteries	3497	3.1. Fluorinated Solid Electrolyte Interphases on Anodes	3520
2. Fluorine Chemistry in Li-Based Batteries	3498	3.1.1. Components of the SEI	3521
2.1. Fluorine-Containing Electrode Materials	3498	3.1.2. Formation of a Fluorinated SEI	3521
2.1.1. Metal Fluorides	3498	3.1.3. Distribution and Impacts of Fluorides on the SEI	3523
2.1.2. Metal Hydroxyfluorides and Oxyfluorides	3501	3.2. Fluorinated Cathode–Electrolyte Interphases	3523
2.1.3. Fluorine-Substitution Electrode Materials	3502	3.2.1. Formation of a Fluorinated CEI	3524
2.1.4. Fluorinated Surface Modification	3503	3.2.2. Impact of the Fluorinated CEI on Battery Performance	3524
2.2. Fluorinated Electrolytes	3504		
2.2.1. Fluorinated Salts	3505		
2.2.2. Fluorinated Solvents and Cosolvents	3507		
2.2.3. Fluorinated Additives	3510		
2.2.4. Fluorinated Solid/Quasi-Solid-State Electrolytes	3512		
2.3. Other Fluorinated Battery Components	3514		
2.3.1. Fluorinated Separators	3514		

**Received:** November 11, 2023

**Revised:** February 19, 2024

**Accepted:** February 23, 2024

**Published:** March 13, 2024





3.3. Critical Role of Fluorinated Interphases for Extreme Li-Based Batteries	3526
3.4. Techniques To Probe Fluorinated Interphases	3529
3.4.1. Cryo-EM	3532
3.4.2. Quantifying Techniques	3534
3.4.3. Composition Analysis Techniques	3536
3.4.4. Functional Feature Analysis Techniques	3538
4. Fluorine Chemistry in Rechargeable Fluoride-Ion Batteries	3540
4.1. Fluoride Electrode Materials	3540
4.1.1. Conversion-Type Electrode Materials	3540
4.1.2. Intercalation-Type Electrode Materials	3542
4.2. Fluoride Electrolytes	3543
4.2.1. Solid-State Electrolytes	3543
4.2.2. Nonaqueous Liquid Electrolytes	3544
4.2.3. Aqueous Electrolytes	3550
5. Fluorine Chemistry in Other Rechargeable Batteries	3551
5.1. Na- and K-Based Batteries	3551
5.1.1. Fluorine-Containing Electrode Materials in Na-Based Batteries	3551
5.1.2. Fluorinated Electrolytes in Na-Based Batteries	3553
5.1.3. Fluorine-Containing Electrode Materials in K-Based Batteries	3554
5.1.4. Fluorinated Electrolytes in K-Based Batteries	3557
5.2. Multivalent Metal-Based Batteries	3559
5.2.1. Aqueous Multivalent Metal-Based Batteries	3559
5.2.2. Nonaqueous Multivalent Metal-Based Batteries	3561
5.3. Dual-Ion Batteries and Beyond	3562
6. Conclusions and Outlook	3565
6.1. Addressing the Instinctively Low Electrochemical Kinetics of Conversion-Type Metal Fluoride-Based Cathodes	3566
6.1.1. Striking a Balance between Electrochemical Performance, Stability, and Environmental Considerations for Optimizing F Substitution/Modification in Battery Components	3566
6.2. Tailoring Fluorinated Interphases for Li-Based Batteries at All Working Conditions	3566
6.2.1. Unlocking Fundamental Issues Regarding Chemical Compositions, Spatial Distributions, and Realistic Structures of the Interphases	3566
6.3. Revolution of the Electrode and Electrolyte Materials for High Energy Density and Cycling Stability FIBs	3567
6.4. Establishing Fluorinated Material–Function Relationships To Boost SIB/PIB Performance	3567
6.5. Exploring the Potential of F-Containing Materials for Other Battery Chemistries	3567
Author Information	3567
Corresponding Authors	3567
Authors	3567
Author Contributions	3568
Notes	3568
Biographies	3568
Acknowledgments	3569

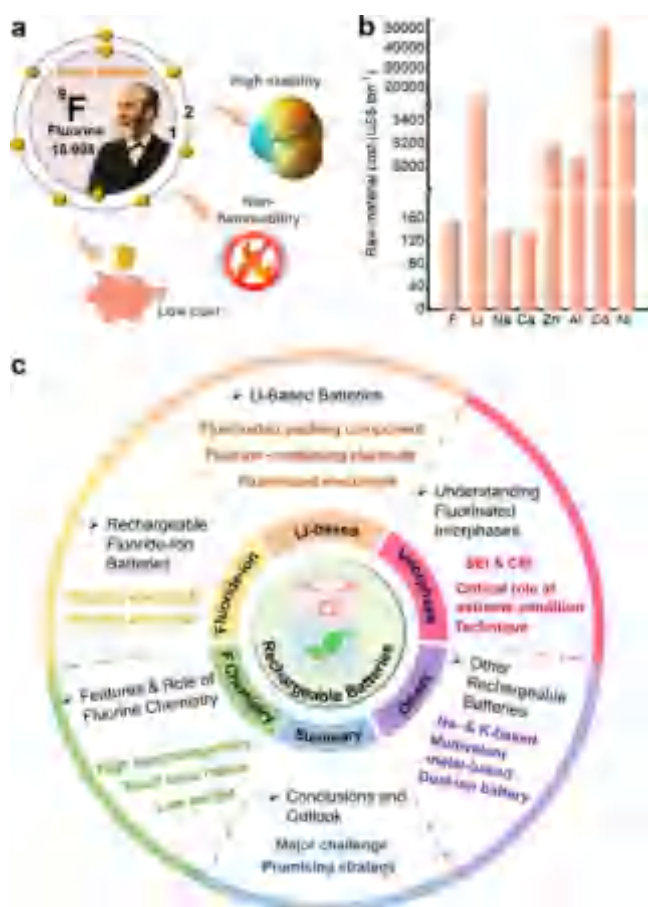
## References

3569

## 1. INTRODUCTION

To satisfy the ever-growing demand for energy storage, the development of next-generation rechargeable batteries hinges on advanced materials that possess low cost, abundant resources, long lifespan, and high safety, especially when considering high energy/power density, wide temperature range, and high-voltage operation applications.<sup>1–4</sup> Significant advancements in fulfilling these requirements have been successfully achieved by utilizing fluorine chemistry to redesign the battery configurations/components toward specific targeted applications. It is known that fluorine chemistry research can be traced to 1886 when Henri Moissan first isolated elemental fluorine.<sup>5,6</sup> Over the past century, fluorine chemistry has significantly contributed to technological innovations, which began with the creation of Freon for refrigeration applications in the 1930s.<sup>7,8</sup> Currently, fluorine chemistry has been successfully utilized in various fields, including pharmaceutical/agrochemical industries and fluoropolymer industry. The extraordinary electronegativity of fluorine and the high free energy of fluoride formation endow the fluorides with intrinsic high stability along with non/low flammability (Figure 1a). In addition, as the 13th most abundant element in the Earth's crust (~585 ppm),<sup>9,10</sup> fluorine (mined as CaF<sub>2</sub>) demonstrates an advantage in terms of raw material cost (Figure 1b).<sup>11</sup> However, the availability of resources remains a significant concern for essential elements employed in Li-based electrodes (e.g., Co and Ni are ~25 and ~84 ppm in the Earth's crust, respectively).<sup>10</sup> In this context, the integration of fluorine chemistry into battery components and novel configurations is thus a promising avenue for advancing battery technology, which has garnered growing interest among the research community. The rapid development of employing fluorine chemistry in various types of rechargeable batteries necessitates a comprehensive review. However, unlocking fluorine chemistry at the atomic scale presents a big challenge. More importantly, the design principles of fluorinated materials and the mechanistic understandings of fluorinated electrode/electrolyte interphases as well as their effects on the ionic conductivity and reaction kinetics/stability of charge carriers under extreme conditions (e.g., fast cycling rate, wide temperature range, and high working voltage) have been long overlooked.

In this review, we begin by providing a short overview of the operating mechanisms, characteristics, and current limitations of Li-based batteries along with beyond Li battery chemistry based on either low-cost metal ions or fluorine-containing charge carriers prior to moving into an in-depth and specific discussion of fluorine chemistry in rechargeable battery systems. From the physicochemical and electrochemical properties to the safety aspects related to battery operation, key research progress and technical achievements for the application of fluorine chemistry in battery materials are summarized, spanning from designing fluorine-containing electrodes, fluorinated electrolyte constituents (e.g., conducting salt, cosolvent/solvent, additive), and other fluorinated battery components for metal-ion shuttle batteries (e.g., Li-based batteries) to constructing rechargeable fluoride-ion batteries (FIBs), dual-ion batteries (DIBs), and beyond chemistries. We highlight the relationship between fluorinated materials and battery performance, the characteristics of



**Figure 1.** Features and interest of fluorine chemistry for use in rechargeable batteries. (a) Discovery and features of fluorine chemistry. (b) Comparisons of raw material costs of F (mined as  $\text{CaF}_2$ ), Li ( $\text{Li}_2\text{CO}_3$ ), Na ( $\text{Na}_2\text{CO}_3$ ), Ca ( $\text{CaO}$ ), Zn, Al, Co, and Ni in 2021. Data extracted from ref 11. (c) Schematic diagram of the main aspects covered in this review.

fluorinated interphases, along with the cutting-edge characterization techniques available for elucidating fluorine chemistry. We also identify the current major restrictions and design strategies for utilizing fluorine chemistry toward improving the performance of rechargeable batteries (Figure 1c).

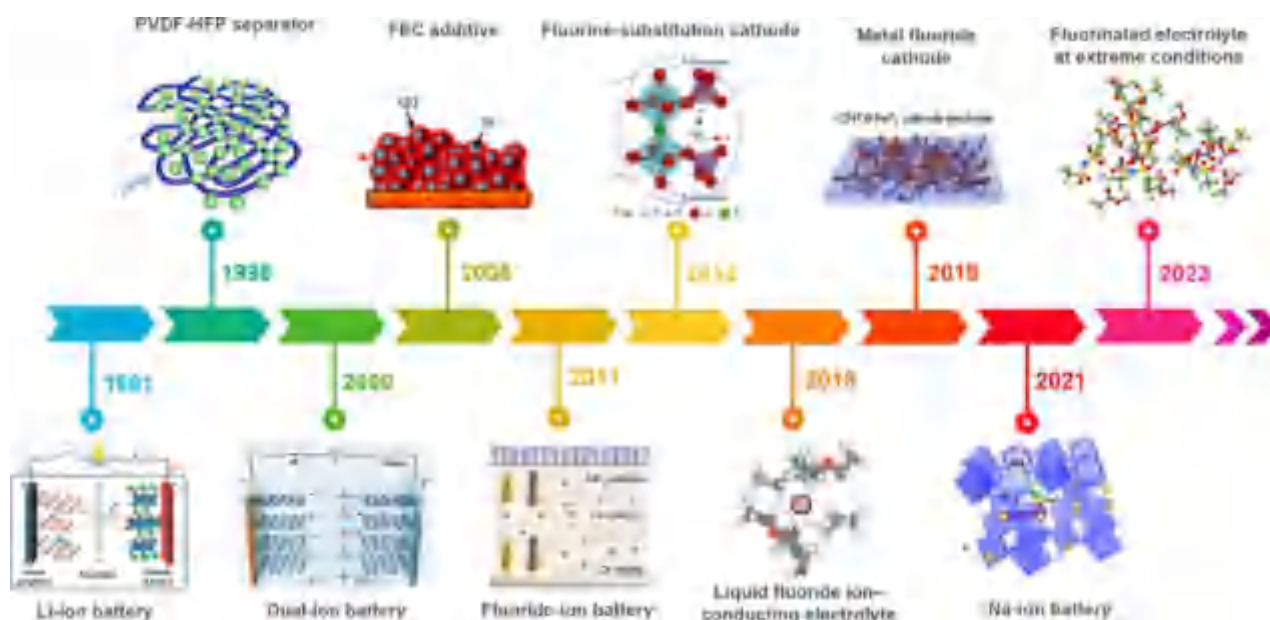
### 1.1. Brief Background on Rechargeable Li-Based Batteries and Beyond

Since the inception of lithium-ion batteries (LIBs) in the 1970s, extensive work has been conducted on the quest for a higher energy density and longer lifespan, solidifying LIBs as the most promising candidate for many applications. Typically, LIBs rely on the insertion of  $\text{Li}^+$  into host structures with a variety of layered oxides (e.g.,  $\text{LiCoO}_2$ ,  $\text{LiFePO}_4$ , and  $\text{LiMn}_2\text{O}_4$ ) and graphite as the cathode and anode materials, respectively. They were developed by John B. Goodenough and other researchers over the past four decades.<sup>12</sup> Nevertheless, the energy density of LIBs is expected to reach its intrinsic limits within a few years (around  $300 \text{ Wh kg}^{-1}$ ), which is incapable of satisfying the escalating demands for high energy density.<sup>13</sup> To further increase the energy density, the cathode and anode must offer high specific capacities and a substantial voltage gap between them. For instance, cathode materials with higher capacity and voltage platforms have been developed, such as Li-rich Mn-based materials ( $x\text{Li}_2\text{MnO}_3(1 -$

$x)\text{LiTMO}_2$  (TM = Ni, Mn, Co, etc.;  $0 < x < 1$ )) and Ni-rich  $\text{LiNi}_x\text{Mn}_y\text{Co}_{1-x-y}\text{O}_2$  (NMC,  $x \geq 0.5$ ,  $x + y < 1$ ),<sup>14–18</sup> in addition to advanced anodes (e.g., Li metal or Si/C anode) with low reaction potential and ultrahigh specific capacity.<sup>19–30</sup> Unfortunately, these electrode materials usually experience severe capacity fading especially in extreme conditions due to structure deterioration and side reactions. More significantly, safety issues and low Coulombic efficiency (CE) resulting from notorious Li dendrites (in the case of Li metal anode) or Li deposition on the non-Li metal anodes have not been fully addressed. Meanwhile, it is imperative to redesign electrolyte systems that exhibit sufficient antioxidative stability (typically  $>4.5 \text{ V vs Li/Li}^+$ ), high compatibility toward both electrodes (i.e., robust electrode/electrolyte interphases), excellent temperature tolerance (from  $-60$  to  $+60 \text{ }^\circ\text{C}$ ), and high safety characteristics (e.g., the risk of fire and explosion), which are critical for adapting to high energy density Li-based batteries.<sup>31</sup>

Alternative rechargeable batteries based on more abundant elements promise higher energy density and improved safety features. Among them, sodium-ion batteries (SIBs) and potassium-ion batteries (PIBs), utilizing the Earth's crust's sixth and seventh most abundant elements, are considered as outstanding complementary technologies to Li-based batteries.<sup>32</sup> Although they have with similar chemistry with Li-based batteries, SIBs and PIBs are facing several challenges due to their larger ionic radii (Shannon ionic radii:  $1.02$ ,  $1.38$ , and  $0.76 \text{ \AA}$  for  $\text{Na}^+$ ,  $\text{K}^+$ , and  $\text{Li}^+$ , respectively), higher redox potentials ( $-2.71 \text{ V}$  for Na,  $-2.936 \text{ V}$  for K, compared with  $-3.04 \text{ V}$  for Li vs standard hydrogen electrode (SHE)), greater atomic masses ( $23$ ,  $39$ , and  $7 \text{ g mol}^{-1}$  for Na, K, and Li, respectively), resulting in low specific capacity, poor rate capability, reduced lifespan, and low theoretical energy density.<sup>33–35</sup> In contrast, multivalent metal-based (e.g.,  $\text{Mg}^{2+}$ ,  $\text{Ca}^{2+}$ ,  $\text{Zn}^{2+}$ ,  $\text{Al}^{3+}$ ) batteries offer high energy density and low cost, benefiting from their multielectron redox capability and Earth's crust abundance. However, their larger ionic radii and greater charge density pose great challenges in ion transport, polarization, and reversibility.<sup>36,37</sup>

Anions, as charge carriers, typically offer faster mobilities due to their less effective nuclear charge and corresponding reduced solvation compared to cations with similar absolute charge. This feature has prompted the development of anion shuttle batteries, exemplified by FIBs employing the  $\text{F}^-$  anion as the charge carrier, which utilize abundant materials to achieve high theoretical energy density.<sup>9,38–42</sup> Specifically,  $\text{F}^-$  ions are released from the cathode material and transfer to the anode side during discharging, whereas the process occurs in reverse upon charging.<sup>9</sup> The high electronegativity of fluorine imparts the  $\text{F}^-$  anion with high oxidative stability, facilitating high-voltage redox reactions. The utilization of  $\text{F}^-$  also contributes to high theoretical energy densities from multiple-electron electrochemical processes,<sup>9,39,43–45</sup> along with dendrite-free anode reactions due to the absence of the metal plating process, highly enhancing safety over alkali metal batteries. Nevertheless, FIBs present several unique challenges, including significant volume changes in electrode materials during fluoridation and defluoridation, contact loss, and interphase degradation. In addition, the electrode dissolution in electrolytes exacerbates self-discharge and capacity decay. More importantly, development of chemically/electrochemically stable electrolytes possessing high room-temperature (RT) conductivity is crucial for FIB commercialization, which is still at an incipient stage.<sup>9</sup>



**Figure 2.** Timeline of the application of fluorine chemistry in rechargeable batteries. Reproduced with permission from ref 48. Copyright 2013 American Chemical Society. Reproduced with permission from ref 49. Copyright 1996 Elsevier. Reproduced with permission from ref 47. Copyright 2021 Wiley-VCH. Reproduced with permission from ref 38. Copyright 2021 Elsevier. Reproduced with permission from ref 50. Copyright 2012 Elsevier. Reproduced with permission from ref 51. Copyright 2006 Elsevier. Reproduced with permission from ref 52. Copyright 2018 American Association for the Advancement of Science. Reproduced with permission from ref 53. Copyright 2019 Springer Nature. Reproduced with permission from ref 54. Copyright 2021 Elsevier. Reproduced with permission from ref 55. Copyright 2023 Springer Nature.

Combining the cation and anion storage, DIBs provide advantages of low cost, material availability, safety, and high voltage. They operate by simultaneously incorporating anions into the cathode and cations into the anode upon charging with both ions being released back into the electrolyte during discharging.<sup>46,47</sup> Particularly, the deinsertion/insertion of anions occurring at high voltage is beneficial for enhancing the energy density. However, the insufficient oxidative stability and poor electrode compatibility of conventional organic electrolytes and the scarcity of electrode materials with high storage capacity and structural stability present substantial obstacles. Furthermore, emerging battery chemistries such as reverse dual-ion batteries (RDIBs) face significant challenges due to the lack of suitable electrolytes, impeding their practical advancement.

## 1.2. Role of Fluorine Chemistry in Rechargeable Batteries

Fluorine, as the most electronegative element with a comparably low atomic weight, small ionic size (1.33 Å), and natural abundance,<sup>56</sup> drives new levels of performance and safety in rechargeable batteries. To elucidate the role of fluorine chemistry in rechargeable batteries, the key progress and brief development history are presented, as outlined in Figure 2.

Owing to the electron-withdrawing properties of F atoms and the delocalized charge of anions, F-containing Li salts (e.g., lithium hexafluorophosphate,  $\text{LiPF}_6$ ) are generally highly soluble in dipolar aprotic solvents with good electrochemical stability at high voltage. The development of these salts for commercial LIBs dates back to the early 1990s,<sup>57–60</sup> but their chemical and thermal instability has prompted the search for alternative conducting salts, usually at the expense of other performance attributes. The utilization of fluorine has been extended to advanced battery components (e.g., separators, binders, current collectors) for Li-based batteries. Efforts can

be traced to 1996, when Tarascon et al. developed a fluorinated polymer (i.e., poly(vinylidene fluoride-hexafluoropropylene), PVDF-HFP) separator for the first time.<sup>49</sup> After that, fluorinated copolymers and grafted commercial separators by F-containing groups have been intensively utilized, enhancing the oxidation stability, thermal stability, ionic conductivity, and safety for battery operations. Moreover, due to the electron-withdrawing inductive effect, the substitution of fluorine to a hydrogen of electrolyte cosolvent/solvents and additives typically decreases the highest occupied molecular orbital (HOMO) and lowest unoccupied molecular orbital (LUMO) energy levels simultaneously, leading to higher resistance toward oxidation and poorer resistance to reduction.<sup>61–67</sup> Specifically, the prior reduction of fluorinated additives benefits the anode by generating an effective solid electrolyte interphase (SEI),<sup>68–70</sup> among which fluoroethylene carbonate (FEC) stands out as the most popular additive with excellent film-forming ability on various electrodes.<sup>51</sup> Besides the film-forming ability, the introduction of fluorine demonstrates unique physicochemical and electrochemical properties, including high oxidative stability, wide temperature range, and nonflammability. In particular, fluorinated interphases are pivotal for Li-based batteries under extreme conditions such as wide temperature range, extended cycling, fast cycling rate, and high-voltage operation. Significant progress was reported recently by Wang et al., designing a fluorinated electrolyte that yielded LiF-rich interphases on both the cathode and the anode, which enhanced the battery performance across the temperature range from  $-60\text{ }^{\circ}\text{C}$  to  $+60\text{ }^{\circ}\text{C}$  with high-voltage and fast-charging characteristics.<sup>55</sup> Despite advances, electrode materials remain a major bottleneck for energy density enhancement. The highly ionic character of the metal–fluorine bond and the light atom mass of the F element endow fluorinated cathodes with higher voltage and/or higher capacity.<sup>53</sup> Additionally, F-



Table 1. Comparisons of the Electrochemical Performance of F-Based Electrodes for LIBs

electrode materials	discharge voltage vs Li/Li <sup>+</sup> (V)	current density (mA g <sup>-1</sup> )	initial discharge capacity (mAh g <sup>-1</sup> )	retained discharge capacity (mAh g <sup>-1</sup> )	capacity retention	cycle number	ref
CuF	2.7	0.106	523	80	15.3%	5	95
FeF <sub>2</sub>	2.2	0.3	700	525	75%	50	96
Cu <sub>0.5</sub> Fe <sub>0.5</sub> F <sub>2</sub>	2.5	9.2	580	475	81.9%	5	102
FeF <sub>2</sub>	2	50	650	450	69.2%	100	53
FeF <sub>3</sub>	3	2000	92	90	97.8	100	97
Cu <sub>0.25</sub> Ni <sub>0.75</sub> F <sub>2</sub>	2	0.055	550	210	38.2%	6	98
CoF <sub>2</sub>	2	100	360	335	93%	200	99
CoF <sub>3</sub>	1.5	5	1000	400	40%	14	100
MnF <sub>2</sub>	0.5	6000	300	270	90%	4000	101
VO <sub>2</sub> F	3	13.1	200	150	75%	50	103
BiOF	2.5	30	343	148	43.1%	40	104
FeOF	2	10	500	355	71%	30	105
TiOF <sub>2</sub>	2	0.26	200	180	90%	30	106
NbO <sub>2</sub> F	1.3	30	650	180	27.7%	20	107

related chemistry involved in the modification strategy can improve the interphase stability and rate capability of the electrodes.

Apart from Li-based batteries, fluorine chemistry is integral to other univalent metal-based batteries such as SIBs and PIBs, where the increase of ionic M–X bonds in fluorides promotes redox reactions of transition metal cations instead of oxygen anions at high voltage. The lower molecular weight of the fluorine cation compared to polyanions enhances the specific capacity. Additionally, F-based compounds are considered to be more stable against oxidation, making metal fluorinated materials highly appealing. The diversity in compositions, structures, and properties of fluorinated electrode materials offers vast opportunities for cathode design. On the anode side, F doping improves the surface disorder of carbonaceous materials, creating large amounts of defects for facilitating K<sup>+</sup> adsorption.<sup>71</sup> In aqueous multivalent metal-based systems (i.e., Zn-ion batteries, ZIBs), fluorine chemistry enables the formation of fluoride-rich interphases for dendrite suppression and electrolyte stability. In nonaqueous systems, fluorinated materials accelerate plating kinetics in Mg-ion and Ca-ion batteries, thus expediting their practical applications.

Since the first proof-of-concept rechargeable FIB demonstrated by Fichtner et al. in 2011,<sup>43</sup> fluorine chemistry has been utilized in FIB developments, spanning from electrode materials to electrolyte formulations. The F<sup>−</sup> anion displays exceptional antioxidation stability, enabling the utilization of high-voltage redox couples. Besides, the F<sup>−</sup> storage is typically involved in multiple-electron reactions and metal fluoride formation reactions, which are characterized by substantial Gibbs free energy change, realizing high voltages. As the charge carrier, the F<sup>−</sup> anion possesses a smaller ionic radius and lower weight compared to Cl<sup>−</sup>, thus assisting in fast ionic transport and having a high theoretical energy density of 5000 Wh L<sup>−1</sup>.<sup>9,39,43,52,72–75</sup> FIBs are experiencing many challenges with electrodes and electrolytes, among which suitable electrolytes with sufficient F<sup>−</sup> conductivity is crucial. A significant advancement by Jones et al. in 2018 designed a novel fluoride salt possessing high RT ionic conductivity, a broad electrochemical stability window, and sufficient chemical stability in ether solvents, enabling a reversible/stable FIB at RT.<sup>52</sup> Ongoing efforts should be devoted to developing diverse conversion and intercalation-based electrode materials and fast

F<sup>−</sup> conducting electrolytes to make FIBs a promising option for commercial-grade batteries.<sup>76</sup>

As for DIBs, Dahn et al. studied the intercalation mechanism of the PF<sub>6</sub><sup>−</sup> anion into graphite cathodes in 2000 for the first time, proving staged phases of graphite via in situ X-ray diffraction (XRD).<sup>77</sup> Various anions with F-containing groups such as PF<sub>6</sub><sup>−</sup>,<sup>78–81</sup> bis(trifluoromethanesulfonyl)imide (TFSI<sup>−</sup>),<sup>82,83</sup> bis(fluorosulfonyl)imide (FSI<sup>−</sup>),<sup>83–86</sup> fluorosulfonyl-(trifluoromethanesulfonyl)imide (FTFSI<sup>−</sup>),<sup>87,88</sup> tetrafluoroborate (BF<sub>4</sub><sup>−</sup>),<sup>89,90</sup> difluoro(oxalato)borate (DFOB<sup>−</sup>),<sup>91</sup> trifluoromethanesulfonic (CF<sub>3</sub>SO<sub>3</sub><sup>−</sup>),<sup>92</sup> and tetrafluoroaluminate (AlF<sub>4</sub><sup>−</sup>)<sup>93</sup> have been extensively explored for their unique characteristics and electrochemical behavior. Besides, fluorination of other electrolyte components in DIBs imparts advantages such as a wide voltage window, a broad temperature range, nonflammability, and enhanced electrode/electrolyte compatibility, enhancing the reversibility/kinetics of anion insertion. Fluorine can also be introduced to cathode materials for boosting and stabilizing the properties of anion intercalation.

## 2. FLUORINE CHEMISTRY IN LI-BASED BATTERIES

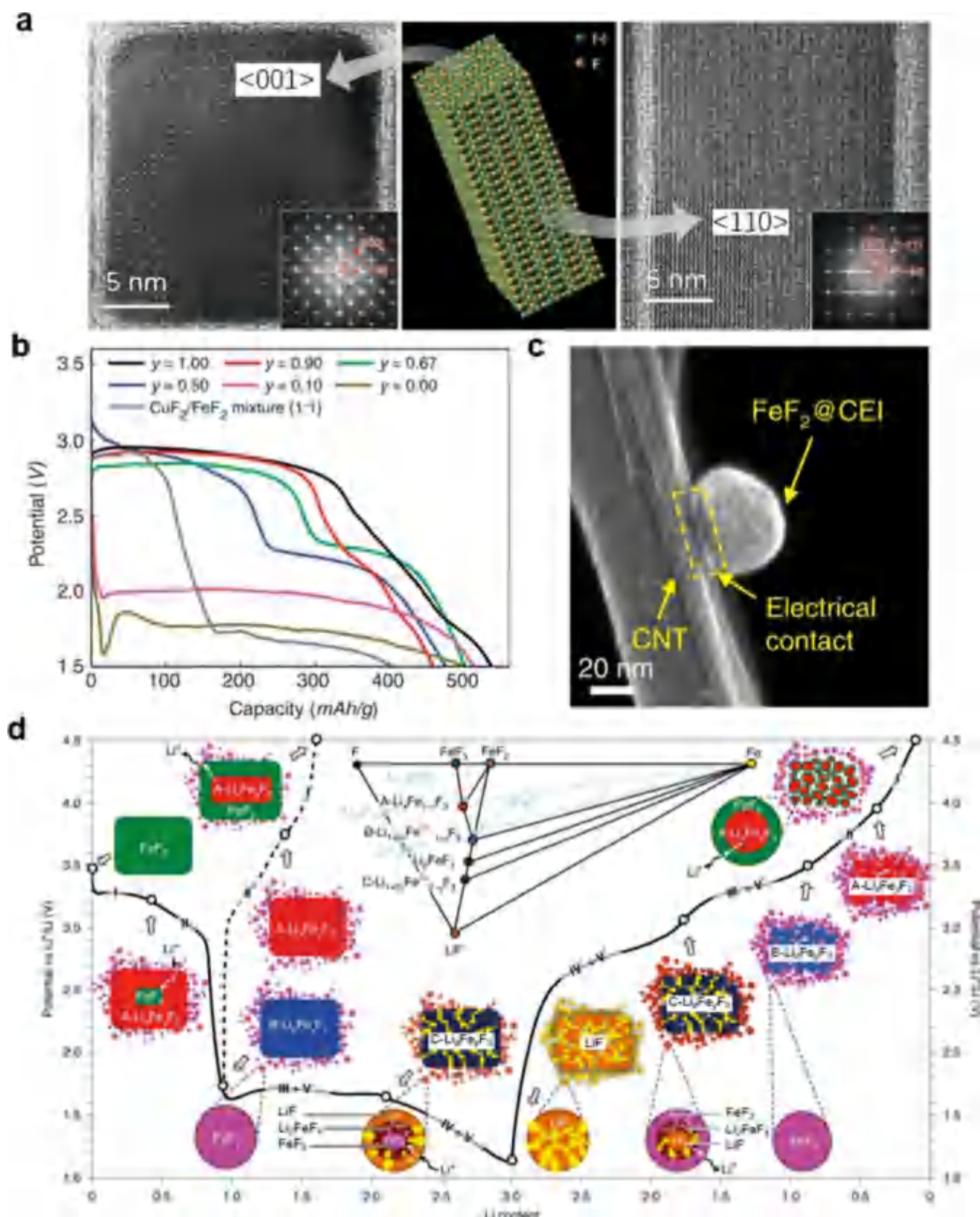
### 2.1. Fluorine-Containing Electrode Materials

The increasing demands for high energy density batteries with a long lifespan and low cost have prompted the research of advanced electrode materials, especially fluorine-containing materials. This is because fluorine elements are widely distributed on Earth and the strong electronegativity of fluorine endows the fluorine-containing materials with a high free energy of formation, generally leading to a high electrochemical energy density and stability. Here, we present a comprehensive review to reveal the roles of F chemistry in advanced fluoride electrodes and fluorine-doping materials.

**2.1.1. Metal Fluorides.** Metal fluoride cathodes for LIBs have been widely investigated as a promising next-generation rechargeable battery with high theoretical voltage and energy density owing to the highly ionic metal–fluorine bonding and low atom mass of the F element<sup>94</sup> as well as the multielectron transfer characteristics of the transition metal (M) in metal fluoride cathodes. The battery reaction of metal fluoride-based LIBs follows the following reaction



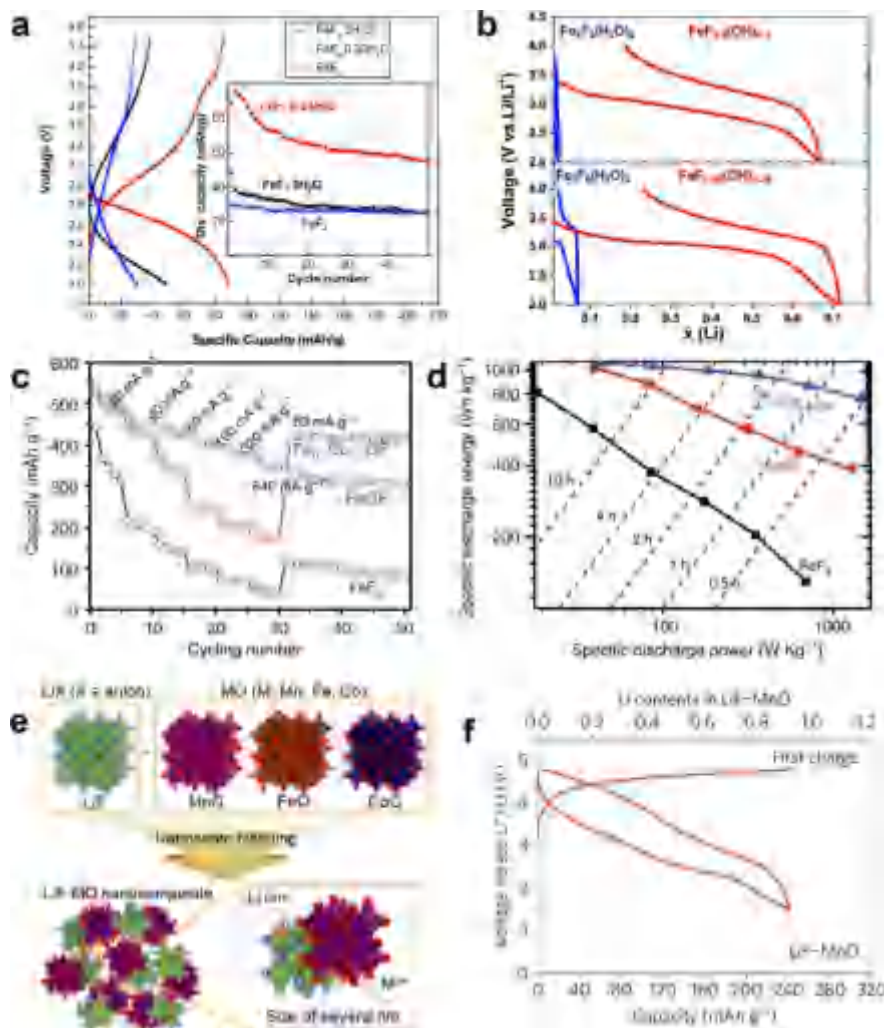




**Figure 3.** Metal fluorides as electrode materials for LIBs. (a) HRTEM images of a single  $\text{FeF}_2$  nanorod, and space-filling model of a single nanorod derived from the standard CIF file of  $\text{FeF}_2$ . Reproduced with permission from ref 96. Copyright 2020 Springer Nature. (b) Voltage profiles (first discharge at a current of  $5 \text{ mA g}^{-1}$ ) of the  $\text{Cu}_x\text{Fe}_{1-x}\text{F}_2$  series along with a simple mixture of  $\text{CuF}_2$  and  $\text{FeF}_2$ . Reproduced with permission from ref 102. Copyright 2015 Springer Nature. (c) Scanning transmission electron microscopy (STEM) image of an  $\text{FeF}_2$  particle on a single CNT. Reproduced with permission from ref 53. Copyright 2019 Springer Nature. (d) Simplified Li-Fe-F ternary phase diagram, and illustration of the reaction pathways of the  $\text{FeF}_3$ - $\text{FeF}_2$  system (with voltage curves for insertion charge and full reaction cycle, respectively, denoted using dashed and solid lines).

Figure 3. continued

solid lines). The reference phases in the phase diagram are labeled and indicated by light blue circles to show the positions of the A- and B- $\text{Li}_x\text{Fe}_y\text{F}_3$ , whose Fe concentration is off-stoichiometric. The color of each phase in the phase diagram is consistent with that in the pathway illustration. Impeded external and internal Li transport is indicated by black solid and white dashed arrows, respectively. Reproduced with permission from ref 108. Copyright 2021 Springer Nature.



**Figure 4.** Metal hydroxyfluorides and oxyfluorides for LIBs. (a) Discharge and charge profiles of  $\text{FeF}_3 \cdot 3\text{H}_2\text{O}$ ,  $\text{FeF}_3 \cdot 0.33\text{H}_2\text{O}$ , and anhydrous  $\text{FeF}_3$  at 0.5 C. (Inset) Cycling stability curves of  $\text{FeF}_3 \cdot 3\text{H}_2\text{O}$ ,  $\text{FeF}_3 \cdot 0.33\text{H}_2\text{O}$ , and  $\text{FeF}_3$  at 0.5 C in the voltage range of 2.0–4.5 V. Reproduced with permission from ref 109. Copyright 2013 Elsevier. (b) First cycle voltage–composition curves for Li/iron fluoride cells in the LP30 electrolyte at 0.05 C. (Upper panel) Comparison of  $\text{Fe}_2\text{F}_5(\text{H}_2\text{O})_2$  and  $\text{FeF}_{2.5}(\text{OH})_{0.5}$ . (Lower panel) Comparison of  $\text{Fe}_3\text{F}_8(\text{H}_2\text{O})_2$  and  $\text{FeF}_{2.66}(\text{OH})_{0.34}$ . Reproduced with permission from ref 110. Copyright 2019 American Chemical Society. (c) Rate capability for  $\text{Fe}_{0.9}\text{Co}_{0.1}\text{OF}$ ,  $\text{FeOF}$ , and  $\text{FeF}_3$  cathode materials. (d) Ragone plot of  $\text{FeF}_3$ ,  $\text{FeOF}$ , and  $\text{Fe}_{0.9}\text{Co}_{0.1}\text{OF}$  (based on active mass). Reproduced with permission from ref 111. Copyright 2018 Springer Nature. (e) Schematic of the positive electrode material design strategy using metal monoxide (MO). Metal monoxides that had electrochemical activity only as the negative electrode were designed as a positive electrode material by forming mixtures with LiF in nanoscale under high-energy ball milling. After mechanochemical mixing, LiF and MO exist without chemical reaction in the several nanometer scale. The crystal structure of all compounds is described by a polyhedral image: red, O; gray, F; green, Li; purple, Mn; brown, Fe; blue, Co. (f) First discharge and second charge profiles of LiF–MnO nanocomposites after the initial activating charge protocol as a positive electrode (1.5–4.8 V) in 1 M  $\text{LiPF}_6$  in ethyl carbonate/dimethyl carbonate (EC/DMC, 1:1 by volume) electrolyte at a 20  $\text{mA g}^{-1}$  (0.03  $\text{mA cm}^{-2}$ ) constant current rate. Reproduced with permission from ref 112. Copyright 2017 Springer Nature.

Abundant types of metal fluorides, including copper fluorides ( $\text{CuF}_2$ ),<sup>95</sup> iron fluorides ( $\text{FeF}_3/\text{FeF}_2$ ),<sup>53,96,97</sup> nickel fluorides ( $\text{NiF}_2$ ),<sup>98</sup> cobalt fluorides ( $\text{CoF}_3/\text{CoF}_2$ ),<sup>99,100</sup> and manganese fluorides ( $\text{MnF}_2$ ),<sup>101</sup> and multimetal fluoride solid-solutions have been investigated, and their attractive merits in terms of specific capacity, cycling stability, and rate performance have been verified (Table 1).

Iron(II) fluoride is a typical metal fluoride cathode for LIBs owing to its high theoretical specific capacity and abundant raw material resources.<sup>96</sup> However, the performance of the as-reported iron(II) fluoride cathode is not satisfactory for practical application, and the failure mechanism remains blurred. In 2020, Pasta and colleagues reported a single-crystalline, monodisperse  $\text{FeF}_2$  nanorod synthesized by a facile

colloidal method.<sup>96</sup> As shown in Figure 3a, the as-obtained 20 nm wide nanorods were single crystalline, monodisperse, and faceted. This FeF<sub>2</sub> cathode can deliver a high specific capacity (close to the theoretical value of 570 mA h g<sup>-1</sup>) and cycling stability (capacity retention > 90%) for more than 200 cycles at higher rates (0.5 C, 1 C = 570 mA g<sup>-1</sup>) and temperatures (50 °C) within an ionic liquid electrolyte. Based on the complex morphological features, lattice orientation relationships, and oxidation state changes from high-resolution transmission electron microscopy (HRTEM) analysis, the transformation mechanism of the FeF<sub>2</sub> nanorod was comprehensively estimated. This mechanism provided a new explanation that the phase evolution, diffusion kinetics, and cell failure were all critically affected by surface-specific reactions of the FeF<sub>2</sub> nanorod. Topotactic cation diffusion through an invariant lattice of F<sup>-</sup> ions and the nucleation of metallic particles on semicoherent interphases synergistically affected the reversibility of the FeF<sub>2</sub> cathode.

Feng and colleagues developed a ternary metal fluoride (Cu<sub>y</sub>Fe<sub>1-y</sub>F<sub>2</sub> solid solution) via a mechanochemical reaction method.<sup>102</sup> Synchrotron XRD and TEM characterization verified the distorted rutile structure of Cu<sub>y</sub>Fe<sub>1-y</sub>F<sub>2</sub> solid-solution in the form of complex agglomerates composed of small nanocrystallites under different Cu/Fe ratios ( $y = 0, 0.1, 0.33, 0.5, 0.67, 0.9, 1$ ). In the corresponding discharge voltage profiles in Figure 3b, no typical voltage dip of pure FeF<sub>2</sub> was found. This indicated that the electrochemical properties of Cu<sub>y</sub>Fe<sub>1-y</sub>F<sub>2</sub> solid-solution was significantly affected by the cooperative redox of Cu and Fe sitting on the same lattice. This ternary metal fluoride Cu<sub>y</sub>Fe<sub>1-y</sub>F<sub>2</sub> achieved the reversible Cu redox reaction (Cu<sup>2+/0</sup>) with a low-voltage hysteresis (<148 mV), which was uncommon in binary fluorides. The thermodynamics and kinetics of the lithium (re)conversion reactions following a two-stage (de)lithiation path of Cu<sub>y</sub>Fe<sub>1-y</sub>F<sub>2</sub> were supported by X-ray absorption spectroscopy (XAS) and TEM-electron energy loss spectrometer (EELS) characterization. Initially, Cu<sup>2+</sup> reduces into metallic Cu<sup>0</sup> with the concomitant formation of disordered FeF<sub>2</sub> followed by Fe<sup>2+/0</sup> reduction. In contrast, the delithiation path undergoes a different process, where Fe<sup>0</sup> is partially oxidized to Fe<sup>3+</sup> as a rutile framework followed by the reconversion of Cu<sup>2+</sup> to form a disordered rutile-like Cu–Fe–F final phase. This work promotes the development of Cu-based ternary metal fluorides as promising cathode candidates for LIBs. However, the reversible specific capacity of Cu conversion faded rapidly, which can be ascribed to the Cu<sup>+</sup> dissolution on the cathode–electrolyte interphase (CEI). Thus, construction of a stable CEI layer is one of the strategies to improve the cycling stability of metal fluoride cathodes in LIBs. Accordingly, Yushin and co-workers introduced solid polymer electrolytes (SPEs) to pair with a carbon nanotube (CNT)/FeF<sub>2</sub> composite cathode.<sup>53</sup> The obtained solid-state cells delivered a high specific capacity of more than 450 mA h g<sup>-1</sup> and a long cycle stability of over 300 cycles at 50 mA g<sup>-1</sup> and 50 °C. The introduction of SPE not only prompted the formation of an elastic, thin, and stable CEI on the FeF<sub>2</sub> surface (Figure 3c) but also reduced the electrolyte decomposition and maintained the cathode structural stability due to the enhanced mechanical properties. This work motivated research on the CEI, which will guarantee an improved lifespan of the metal fluoride cathode with merits of low cost and high energy density.

Although it has been widely accepted that metal fluorides are conversion-type cathodes for LIBs, Gray and colleagues

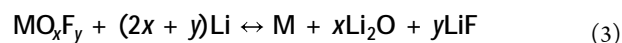
demonstrated a different viewpoint of reaction mechanisms in metal fluoride cathodes.<sup>108</sup> The material structure was well measured by X-ray total scattering and electron diffraction techniques over multiple length scales and analyzed by density functional theory (DFT) calculations. The results indicated that the mobility difference of displaced species affected the diffusion rate during the (de)lithiation of metal fluorides. The illustration of the reaction pathways of the FeF<sub>3</sub> system is demonstrated in Figure 3d. During a typical lithiation process, FeF<sub>3</sub> initially transforms into FeF<sub>2</sub> and a cation-ordered and stacking-disordered phase (A-Li<sub>x</sub>Fe<sub>y</sub>F<sub>3</sub>) on the surface of the cathode particles; then, the transition phase product successively converts into B-, C-Li<sub>x</sub>Fe<sub>y</sub>F<sub>3</sub> and ends in LiF and Fe as the final discharge products. The subsequent delithiation process follows a reversible pathway. This new mechanistic principle provides a reference model to develop more isomorphous metal fluorides as cathodes for high energy density LIBs.

### 2.1.2. Metal Hydroxyfluorides and Oxyfluorides.

Metal fluoride hydrates have also been investigated as cathode materials for LIBs. In 2013, Wang and co-workers synthesized a series of iron fluoride hydrates with different hydration water contents via the liquid-phase method.<sup>109</sup> Pure crystalline FeF<sub>3</sub>·3H<sub>2</sub>O, FeF<sub>3</sub>·0.33H<sub>2</sub>O, and FeF<sub>3</sub> were obtained during the dehydration process at increasing calcination temperature, which was verified by the XRD patterns and their Rietveld refinements. When applied in liquid LIBs, the orthorhombic FeF<sub>3</sub>·0.33H<sub>2</sub>O cathode delivered the highest discharge specific capacity of 88.0 mA h g<sup>-1</sup> and the lowest polarization among all three samples (Figure 4a). The authors attributed this better electrochemical performance of FeF<sub>3</sub>·0.33H<sub>2</sub>O to its huge hexagonal cavity for faster Li<sup>+</sup> transfer. These iron fluoride hydrates were simply ball milled with acetylene black to form high electronic conductive composite cathodes, and the initial discharge specific capacity of the FeF<sub>3</sub>·0.33H<sub>2</sub>O/C cathode was improved to 177.6 mA h g<sup>-1</sup> at 0.1 C (1 C = 237 mA g<sup>-1</sup>) with a high retention of 83.8% after 100 cycles. This reveals that optimization of the crystal structure is important in the development of high-performance metal fluoride hydrate cathodes for LIBs.

Later, in 2019, Lhoste and colleagues further investigated the structural effects of iron hydroxyfluorides as cathodes in LIBs.<sup>110</sup> First, two anion-deficient iron fluoride hydrates Fe<sub>2</sub>F<sub>5</sub>(H<sub>2</sub>O)<sub>2</sub> and Fe<sub>3</sub>F<sub>8</sub>(H<sub>2</sub>O)<sub>2</sub> were synthesized by a facile microwave synthesis method, which were unstable under the ambient atmosphere. After special heating treatments, two stable iron hydroxyfluorides FeF<sub>2.5</sub>(OH)<sub>0.5</sub> (pyrochlore structure) and FeF<sub>2.66</sub>(OH)<sub>0.34</sub> (hexagonal tungsten bronze structure) were obtained. When applied as cathodes in LIBs, the dehydrated iron hydroxyfluorides delivered a higher reversible specific capacity than their hydrated opponents (Figure 4b). The structure analysis by XRD and Mössbauer spectrometry proved that removal of structural water molecules within the hexagonal cavities opened the Li diffusion channels for the battery cycling process.

Metal oxyfluorides, such as VO<sub>2</sub>F,<sup>103</sup> BiOF,<sup>104</sup> FeOF,<sup>105,111</sup> TiOF<sub>2</sub>,<sup>106</sup> and NbO<sub>2</sub>F<sup>107</sup> (Table 1), have shown great potential as cathodes for LIBs owing to their high specific capacity, high voltage, good conductivity, and good cycling stability.<sup>113</sup> The battery reaction of metal oxyfluoride (MO<sub>x</sub>F<sub>y</sub>)-based LIBs follows the following reaction:





In 2018, Wang and coauthors reported a cobalt-doped iron oxyfluoride ( $\text{Fe}_{0.9}\text{Co}_{0.1}\text{OF}$ ) synthesized by a solvothermal method.<sup>111</sup> The specific capacity of  $\text{Fe}_{0.9}\text{Co}_{0.1}\text{OF}$  was much higher than that of the pristine  $\text{FeOF}$  and  $\text{FeF}_3$  (Figure 4c), achieving a high energy density of  $\sim 1000 \text{ Wh kg}^{-1}$  (Figure 4d). This  $\text{Fe}_{0.9}\text{Co}_{0.1}\text{OF}$  cathode delivered a high specific capacity of  $350 \text{ mAh g}^{-1}$  for 1000 cycles at  $500 \text{ mA g}^{-1}$ , and the voltage hysteresis was reduced to  $0.27 \text{ V}$ . Combined with TEM techniques, pair distribution function (PDF) analysis, and first-principles calculations, the author verified that the reaction kinetics of  $\text{Fe}_{0.9}\text{Co}_{0.1}\text{OF}$  was enhanced by the cosubstituted anion (O) and cation (Co) in  $\text{Fe}_{0.9}\text{Co}_{0.1}\text{OF}$ . In this case, the less reversible conversion reaction was replaced by a highly reversible intercalation–extrusion reaction due to the decrease in particle size and abundance of metallic  $\text{Fe}(\text{Co})$ . Hence, this cosubstitution strategy inspired the development of other conversion-type electrode materials with similar reversibility problems.

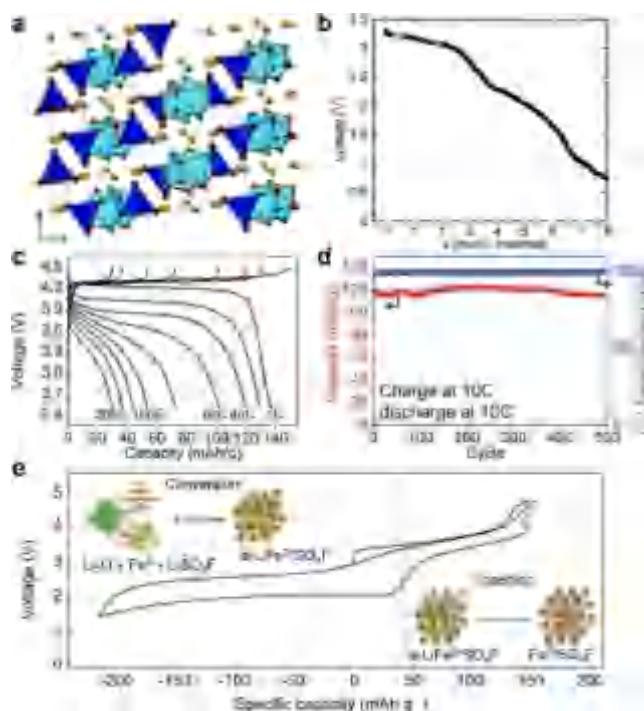
Unlike the crystalline oxyfluorides, Kang and colleagues reported a special  $\text{LiF}$ –metal monoxide ( $\text{MO}$ ,  $\text{M} = \text{Mn}$ ,  $\text{Fe}$ ,  $\text{Co}$ ) nanocomposite as a  $\text{Li}$ -free cathode for LIBs,<sup>112</sup> which was synthesized by blending the transition metal monoxides and nanosized lithium fluoride in a high-energy ball miller under an argon atmosphere (Figure 4e). This cathode material delivered a high specific capacity after the first charging step with a high voltage (e.g., average voltage of  $3.1 \text{ V}$  for  $\text{LiF}$ – $\text{MnO}$ , Figure 4f). In contrast with the conventional  $\text{Li}$  intercalation, the reaction mechanism of the  $\text{LiF}$ – $\text{MO}$  nanocomposite cathode can be ascribed to a surface conversion reaction as follows:



Moreover, the performance of the  $\text{LiF}$ – $\text{MO}$  nanocomposite cathode can be further improved by decreasing the particle size of the metal compounds. This novel mechanism is expected to be expanded to other transition metal compounds and  $\text{Li}$  salt couples for advanced cathode materials in LIBs.

**2.1.3. Fluorine-Substitution Electrode Materials.** To achieve higher electrochemical performance, fluorides are added to electrodes to improve the properties of the original cathode materials. Silver vanadium oxide ( $\text{Ag}_2\text{O} \cdot x\text{V}_2\text{O}_5$ ) has been commercialized as a cathode material in primary  $\text{Li}$  batteries for high-rate applications. The increase of the  $\text{Ag}:\text{V}$  ratio can extend the high-voltage plateau but is accompanied by poor kinetics and low conductivity. In 2005, Poeppelmeier and colleagues reported the synthesis of single crystals of  $\text{Ag}_4\text{V}_2\text{O}_6\text{F}_2$  ( $\text{Ag}_2\text{O} \cdot \text{V}_2\text{O}_5 \cdot 2\text{AgF}$ ) via a low-temperature hydrothermal technique.<sup>114</sup> Introduction of the  $\text{AgF}$  phase increased the  $\text{Ag}:\text{V}$  ratio and the reaction potential of the cathode. At the same time, the dimensionality of the vanadium oxide framework was partially reserved (Figure 5a), which served as the  $\text{Li}$ -ion conduction pathway between vanadium centers. Therefore, the  $\text{Ag}_4\text{V}_2\text{O}_6\text{F}_2$  cathode delivered an enhanced initial discharge plateau and higher specific capacity above  $3 \text{ V}$  ( $3.52 \text{ V}$  and  $148 \text{ mAh g}^{-1}$ ) compared to the undoped silver vanadium oxides ( $3.22 \text{ V}$  and  $100 \text{ mAh g}^{-1}$ , Figure 5b).

The strategy of fluoride doping can also multiply the rate energy density and performance of the cathode material. The low electronic conductivity and limited specific capacity are the main drawbacks of conventional polyanion compound cathodes,<sup>117</sup> including  $\text{LiFePO}_4$  phosphates,  $\text{LiMBO}_3$  borates,  $\text{Li}_2\text{MSiO}_4$  silicates, and  $\text{Li}_2\text{Fe}(\text{SO}_4)_2$ . In 2015, Kang and co-workers reported a fluorinated polyanion compound cathode ( $\text{LiVPO}_4\text{F}$ ) for LIBs,<sup>115</sup> which was synthesized by a scalable

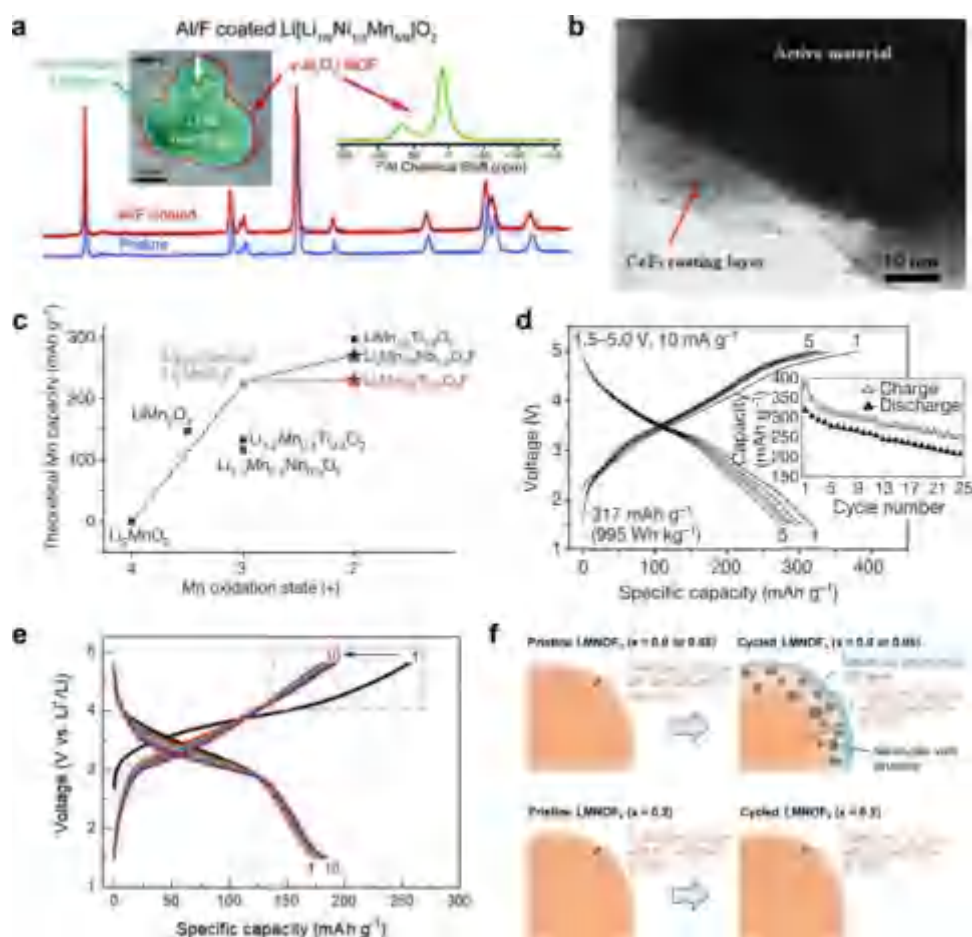


**Figure 5.** Fluoride-containing electrode materials. (a) Three-dimensional packing diagrams of  $\text{Ag}_4\text{V}_2\text{O}_6\text{F}_2$ . Yellow spheres represent silver atoms, vanadium oxide fluoride octahedra are in light blue, and vanadium oxide tetrahedra are in dark blue. (b) Constant current discharge curve of  $\text{Ag}_4\text{V}_2\text{O}_6\text{F}_2$ . Reproduced with permission from ref 114. Copyright 2005 American Chemical Society. (c) Charge/discharge voltage profiles of C-coated  $\text{LiVPO}_4\text{F}$  at various rates (right to left: discharging at 1, 20, 40, 60, 80, 100, 120, 150, and  $200 \text{ C}$  and charging at  $1 \text{ C}$  without a voltage hold). (d) Capacity retentions at  $10 \text{ C}$  charge/ $10 \text{ C}$  discharge for 500 cycles. The cutoff voltage was  $2.5$ – $5 \text{ V}$  (only for cycle retention). Reproduced with permission from ref 115. Copyright 2015 Wiley-VCH. (e) Charge/discharge profile with a schematic of the two-step reaction mechanism of  $\text{a-LiFeSO}_4\text{F}$  as insertion and conversion reactions. Reproduced with permission from ref 116. Copyright 2022 Springer Nature.

single-step solid-state reaction. As shown in Figure 5c, the  $\text{LiLiVPO}_4\text{F}$  cell achieved superior rate capability up to  $200 \text{ C}$  with low polarization and maintained a high specific capacity of  $\sim 120 \text{ mAh g}^{-1}$  at  $10 \text{ C}$  for 500 cycles with  $>95\%$  retention efficiency (Figure 5d). Owing to its higher operating voltage ( $>3.45 \text{ V}$ ),  $\text{LiVPO}_4\text{F}$  can achieve a higher energy density ( $\sim 521 \text{ Wh g}^{-1}$  at  $20 \text{ C}$ ,  $1 \text{ C} = 158 \text{ mA g}^{-1}$ ) than  $\text{LiFePO}_4$ . The smaller particle size, negligible number of antisite defects, and minimal surface oxidation endowed this  $\text{LiVPO}_4\text{F}$  cathode material with remarkable rate capability and energy density, overwhelming the commercial  $\text{LiFePO}_4$  cathode materials.

Moreover, fluorosulfates such as  $\text{LiFeSO}_4\text{F}$ <sup>118</sup> and  $\text{Li}(\text{Fe}_{1-\delta}\text{Mn}_\delta)\text{SO}_4\text{F}$ <sup>119</sup> have been investigated as cathode materials for LIBs for decades owing to the low cost and the abundant distribution of these transition metal elements on Earth. However, the low gravimetric specific capacity of the heavy polyanion group in the cathode materials restricts its commercial application. In 2022, Kang and colleagues reported an amorphous iron fluorosulfate ( $\text{a-LiFeSO}_4\text{F}$ ) synthesized by a simple ball-milling process of  $\text{LiF}$  and  $\text{FeSO}_4$ .<sup>116</sup> This fluoride-doping polyanion cathode demonstrated a high specific capacity of  $360 \text{ mAh g}^{-1}$  with  $\sim 98.6\%$  specific capacity retention after 200 cycles even at  $60^\circ\text{C}$ . With an average



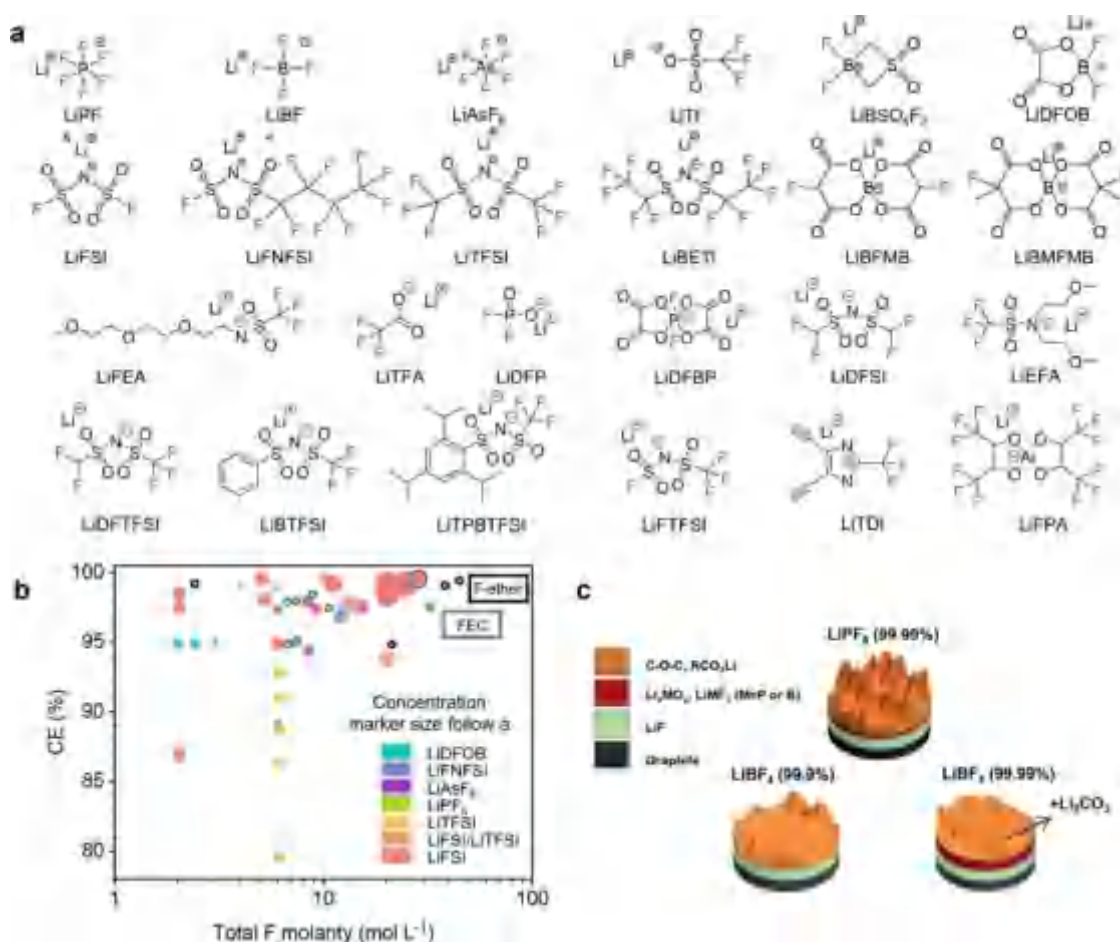


**Figure 6.** F-modified electrode materials. (a) Powder XRD pattern, TEM images, and  $^{27}\text{Al}$  NMR spectra of pristine and Al/F-coated  $\text{Li}[\text{Li}_{1/9}\text{Ni}_{1/3}\text{Mn}_{5/9}]\text{O}_2$ . Reproduced with permission from ref 121. Copyright 2012 Royal Society of Chemistry. (b) TEM image of 2 wt %  $\text{CeF}_3$ -coated  $\text{Li}[\text{Li}_{0.2}\text{Mn}_{0.54}\text{Ni}_{0.13}\text{Co}_{0.13}]\text{O}_2$ . Reproduced with permission from ref 122. Copyright 2014 Elsevier. (c) Theoretical Mn redox capacity of various Mn-based cathode materials. (d) Voltage profiles and capacity retention of  $\text{Li}_2\text{Mn}_{2/3}\text{Nb}_{1/3}\text{O}_2\text{F}$  under 1.5–5.0 V, 10  $\text{mA g}^{-1}$ . Reproduced with permission from ref 123. Copyright 2022 Springer Nature. (e) Voltage profiles at a higher voltage region during the first 10 cycles for  $\text{LMNOF}_x$ . (f) Schematics summarizing the observation of the structural and chemical evolutions in the  $\text{LMNOF}_x$  cathode particles. (Upper panel) For the  $\text{LMNOF}_x$  cathodes with zero or low F concentration ( $x = 0, 0.05$ ), the cycling process leads to the formation of nanoscale amorphous CEI layers on the surface and void-like nanoregions featuring severe loss of O, Mn, and Li at the subsurface, all of which can be detrimental to Li transport. (Lower panel) For the  $\text{LMNOF}_x$  cathodes with high F concentration ( $x = 0.2$ ), the crystalline structure at the cathode surface and the stoichiometric elemental distribution at the subsurface is mostly well preserved after cycling, which ensures facile Li transport at the surface. Reproduced with permission from ref 124. Copyright 2021 Wiley-VCH.

discharge voltage of  $\sim 2.52$  V, a high energy density of  $906$   $\text{Wh kg}^{-1}$  was achieved by a  $\text{LiFeSO}_4\text{F}$  cathode. Different from the conventional crystalline polymorphic  $\text{LiFeSO}_4\text{F}$ , the a- $\text{LiFeSO}_4\text{F}$  with a unique inherent amorphous structure underwent a three-electron redox reaction based on combined intercalation and conversion (Figure 5e), which maintained intact structural integrity for reversible cycle stability. This multimechanistic lithiation process of the amorphous intercalation material is promising for the development of high-capacity and low-cost cathodes for LIBs.

**2.1.4. Fluorinated Surface Modification.** F-modification technologies such as fluoride coating and fluorine substitution are widely used to improve the performance of conventional oxide-based cathodes for LIBs. The high electronic and ionic resistance caused by unstable CEI limits the rate capability and cycle life of Co-free layered oxide cathode materials.<sup>120</sup> In 2012, Grey and coauthors investigated the coating strategy of a layered  $\text{Li}[\text{Li}_{1/9}\text{Ni}_{1/3}\text{Mn}_{5/9}]\text{O}_2$  cathode processed by the commercial aluminum fluoride ( $\text{AlF}_3$ ) aqueous suspension

and followed by heat treatment.<sup>121</sup> As shown in Figure 6a, the XRD, TEM, energy-dispersive X-ray (EDX), and  $^{27}\text{Al}$  nuclear magnetic resonance (NMR) results proved that a uniform layer of fluorinated amorphous aluminum oxide ( $\text{Al}_2\text{O}_3$ ) was successfully coated on the surface of the cathode material. The  $\text{Li}[\text{Li}_{1/9}\text{Ni}_{1/3}\text{Mn}_{5/9}]\text{O}_2$  cathode with a low coating layer (1 mol % Al/F) delivered a specific capacity of  $215$   $\text{mA h g}^{-1}$  with a cutoff charging voltage of 4.6 V. Zhang and co-workers reported an amorphous  $\text{CeF}_3$ -coated layered lithium-rich oxide cathode via a facile chemical deposition method.<sup>122</sup> A 10 nm thick  $\text{CeF}_3$  layer (2 wt %) was evenly deposited on the surface of  $\text{Li}_{1.2}\text{Mn}_{0.54}\text{Ni}_{0.13}\text{Co}_{0.13}\text{O}_2$  cathode particles (Figure 6b). This  $\text{CeF}_3$ -coated cathode demonstrated a higher capacity retention (97.1%) than that of the pristine sample (82.1%) after 50 cycles. Additionally, the rate performance of the  $\text{CeF}_3$ -coated cathode also surpassed that of the pristine sample at  $1250$   $\text{mA g}^{-1}$  ( $103.1$  vs  $82.2$   $\text{mAh g}^{-1}$ ). The authors attributed the outstanding enhancement to this amorphous  $\text{CeF}_3$  coating layer, which effectively hindered the continuous decomposition



**Figure 7.** Fluorinated salts for Li-based batteries. (a) Structural formulas of the different Li salts. (b) CEs of Li/LiCu cells with Li salts of different F molarity. Reproduced with permission from ref 24. Copyright 2021 Springer Nature. (c) Schematic illustration of the SEI film obtained from electrolyte formulations based on LiPF<sub>6</sub> (99.99% battery grade purity), LiBF<sub>4</sub> (99.9% purity), and LiBF<sub>4</sub> (99.99% battery grade purity). Reproduced with permission from ref 131. Copyright 2013 Elsevier.

of the electrolyte on the cathode surface, thus controlling the growth of the insulated passivated interlayer and maintaining the structural stability of the cathode.

The fluorine substitution strategy was also utilized to improve the performance of electrode materials for LIBs. In 2018, Ceder and colleagues reported Co/Ni-free disordered-rocksalt Li-rich intercalation cathodes Li<sub>2</sub>Mn<sub>2/3</sub>Nb<sub>1/3</sub>O<sub>2</sub>F realized by the partial substitution of the fluoride anion and high-valent cation,<sup>123</sup> which have a Mn<sup>2+</sup>-involved theoretical specific capacity of 270 mAh g<sup>-1</sup>, much higher than that of a typical Mn-based Li-rich cathode (Figure 6c). As shown in Figure 6d, this cathode delivered a high discharge specific capacity of 317 mAh g<sup>-1</sup> and reached a state-of-the-art high-energy content of 995 Wh kg<sup>-1</sup> (3761 Wh l<sup>-1</sup>) due to the high amount of Mn<sup>2+</sup>/Mn<sup>4+</sup> redox couples combined with a small amount of O redox reactions. Giving rise to this strategy, the structural stability of the Mn-based Li-rich cathode was not affected by the extensive O redox, thus leading to high cathode performance.

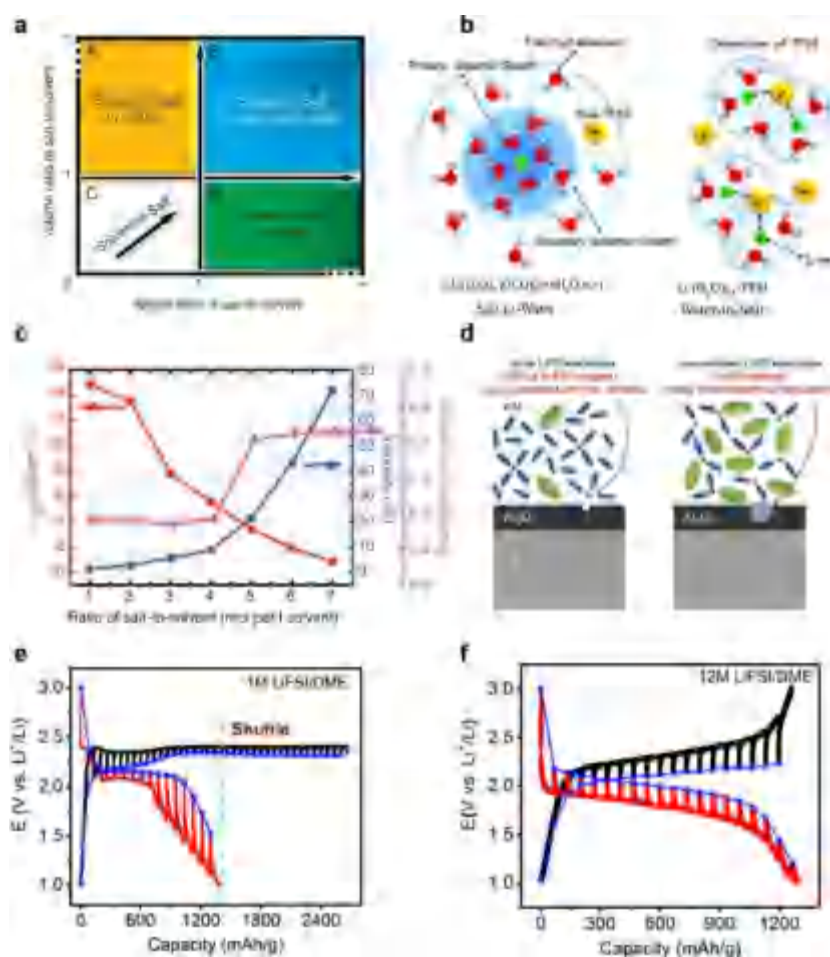
The surface stability of disordered rocksalt cathodes can also be enhanced by fluorine substitution. Wang and coauthors unveiled the relationship between high-level fluorine substitution and good surface stability.<sup>124</sup> The Mn-based disordered rocksalt cathodes with various fluorine substitutions (Li<sub>1.2</sub>Mn<sub>0.6+x/2</sub>Nb<sub>0.2-x/2</sub>O<sub>2.0-x</sub>F<sub>x</sub>) LMNOF<sub>x</sub>,  $x = 0-0.2$ ) were synthesized and compared in terms of electrochemistry and

characterization. The cycling stability of the LMNOF<sub>x</sub> cathode was significantly improved by increasing the F content from 0 to 0.2, while the O redox peaks nearly disappeared (Figure 6e). The results demonstrated that the increased fluorine substitution level in the disordered rocksalt cathode reduced the amorphous CEI layers at the top of the cathode surface, prevented damage to the internal crystal structure of the cathode, and maintained the uniform chemical distribution at the subsurface of the cathode particles (Figure 6f).

Fluorine chemistry is crucial in the development of Li-based batteries with high energy density and reversibility. High-voltage metal fluoride and oxyfluoride electrodes show great promise to improve the energy densities of Li-based batteries. In particular, metal fluorides based on multiple electron transfer reactions are expected to address the limitations of conventional cathode materials in LIBs.

## 2.2. Fluorinated Electrolytes

Electrolytes play a particularly essential and complex role in LIBs and Li metal batteries (LMBs). As the battery component is in contact with other active and passive parts of the battery, the electrolyte must fulfill the following requirements: a high degree of Li-ion conductivity, good thermal and chemical stability, electronic insulation to avoid self-discharge, relative nontoxicity to avoid environmental hazards, and low cost. Commonly used commercial electrolytes consist of a



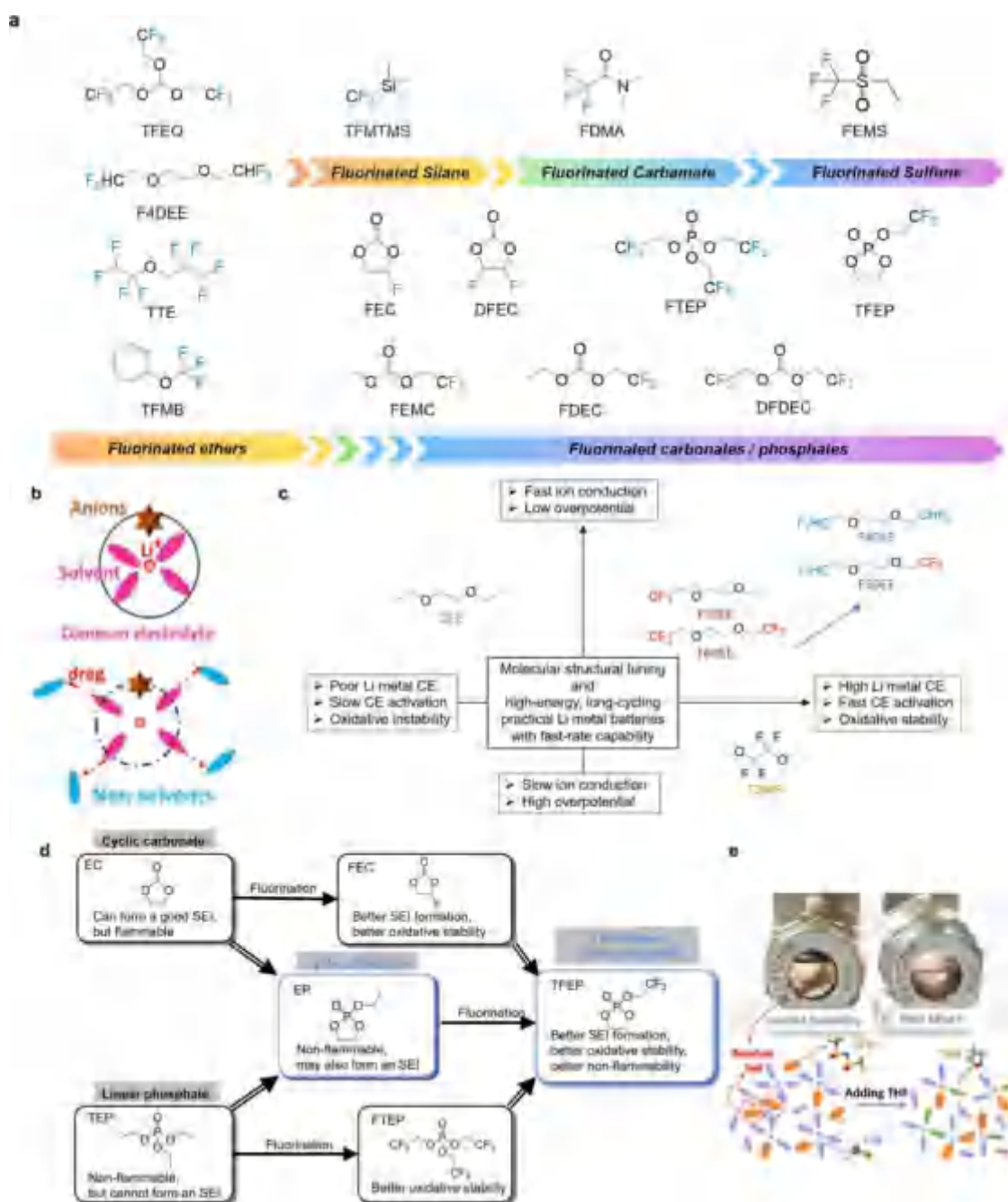
**Figure 8.** Electrolytes for Li-based batteries with highly concentrated fluorinated salts. (a) Classification of electrolytes according to the volume ratio and weight ratio. Reproduced with permission from ref 132. Copyright 2013 Springer Nature. (b) Schematic diagram of water-in-salt electrolyte. Reproduced with permission from ref 135. Copyright 2015 American Association for the Advancement of Science. (c) Viscosity, ionic conductivity, and Li-ion transference number at room temperature for the various electrolytes. Reproduced with permission from ref 132. Copyright 2013 Springer Nature. (d) Schematic illustrations of the behavior of Al current collectors in a dilute LiFSI/acetonitrile (AN) electrolyte (left) and a highly concentrated LiFSI/AN electrolyte (right) with little free solvent molecules and free FSI<sup>−</sup> anions. Reproduced with permission from ref 136. Copyright 2015 Wiley-VCH. GITT curves (e) in 1 M LiFSI/DME electrolyte and (f) in 12 M LiFSI/DME electrolyte. Reproduced with permission from ref 137. Copyright 2018 Elsevier.

conductive Li salt (usually LiPF<sub>6</sub>) and an organic solvent mixture of cyclic and linear organic carbonates. The salt–solvent–additive combination determines the overall performance of rechargeable Li batteries, such as conductivity, thermal stability, and electrochemical stability. However, demand for higher voltage Li batteries has forced researchers to look for new electrolyte formulations, including solid electrolytes, as current liquid electrolytes are unstable at potentials higher than 4.5 V and exhibit safety concerns. Power batteries typically contain high-energy active electrode materials, which tend to easily react with other elements, rendering the combination unusable. The fluorination of electrolyte components is a key strategy for advanced electrolyte engineering, which can enhance the electrode reaction reversibility, extend the battery life, and reduce the electrolyte flammability.

**2.2.1. Fluorinated Salts.** Li salts act as the conductor of Li ions in the electrolyte, and the nature of the Li salts is often determined by the structure of the anions. As shown in Figure 7a, F substitution is widely applied in Li salts for LIBs and LMBs. The presence of fluorine atoms and the delocalized charge of the anions make such F-containing Li salts highly

soluble in dipolar aprotic solvents.<sup>125</sup> For battery applications, Li salts need to possess characteristics such as a low molecular weight, low toxicity, stability over a wide electrochemical stability window (ESW), as well as electrolyte-electrode interphase formation ability. Among the F-substituted Li salts, LiPF<sub>6</sub> and Li sulfonate salts are the most widely used. LiPF<sub>6</sub> salt exhibits the advantages of high ionic conductivity, good passivation ability for Al collectors, and high oxidation stability, etc. However, the LiPF<sub>6</sub> salt has a serious disadvantage of high sensitivity to water, which is easily decomposed to produce HF and cause serious corrosion to the electrodes and the whole battery.<sup>126</sup> For comparison, benefiting from the presence of strong perfluoroalkyl electron-absorbing groups and conjugated structures leading to the delocalization of negative charges, the anion of Li sulfonate salts is relatively stable. Thus, Li sulfonate salts show the advantages of good thermal stability, high solubility, insensitivity to moisture, high dissociation constants, etc. However, severe Al foil dissolution occurs when charged to high voltage.<sup>127</sup> Furthermore, it is crucial to note that Li sulfonate salts, which contain  $-\text{CF}_2-$  and/or  $-\text{CF}_3$  functional





**Figure 9.** Fluorinated solvents and cosolvents. (a) Molecular structures of representative fluorinated solvents. (b) Established solvation structures of common diluent electrolyte, localized high-concentration electrolyte (LHCE), and nonsolvent-added electrolyte and their desolvation processes. Reproduced with permission from ref 149. Copyright 2023 Royal Society of Chemistry. (c) Optimization of ether electrolytes toward fast ion conduction, low overpotential, high Li metal efficiency, fast CE activation, and high oxidative stability. Reproduced with permission from ref 150. Copyright 2022 Springer Nature. (d) Design of the fluorinated cyclic phosphate solvent to achieve better SEI formation, better oxidation stability, and better nonflammability. Reproduced with permission from ref 151. Copyright 2020 Wiley-VCH. (e) Photographs of solubility tests in window cells of 0.1 M LiTFSI in FM (left) and 0.3 M LiTFSI and 0.3 M THF in FM (right). Reproduced with permission from ref 152. Copyright 2019 Elsevier.

groups, potentially pose environmental risks during production and utilization. Thus, strategies to mitigate these impacts should be developed before the evolution to more eco-friendly alternatives.<sup>128</sup> In addition to the commonly used F-substituted Li salts mentioned above, researchers synthesized new Li salts through asymmetric molecular structure design. For example, Liu et al. reported a new salt under the premise of retaining the strong electron-withdrawing group.<sup>129</sup> An ether

skeleton was introduced to enable F-substituted salt electron-donating ability to capture the migrated  $\text{Li}^+$ . The molecule had a large molecular dipole moment, which led to a high donor number (DN) and high  $\text{Li}^+$  transference number. Meanwhile, the quality of interphase film formation largely affects the compatibility with cathodes and anodes, thus determining the cycling stability of the entire battery. Gallant et al. discussed the interplays between CE and generic fluorine content across



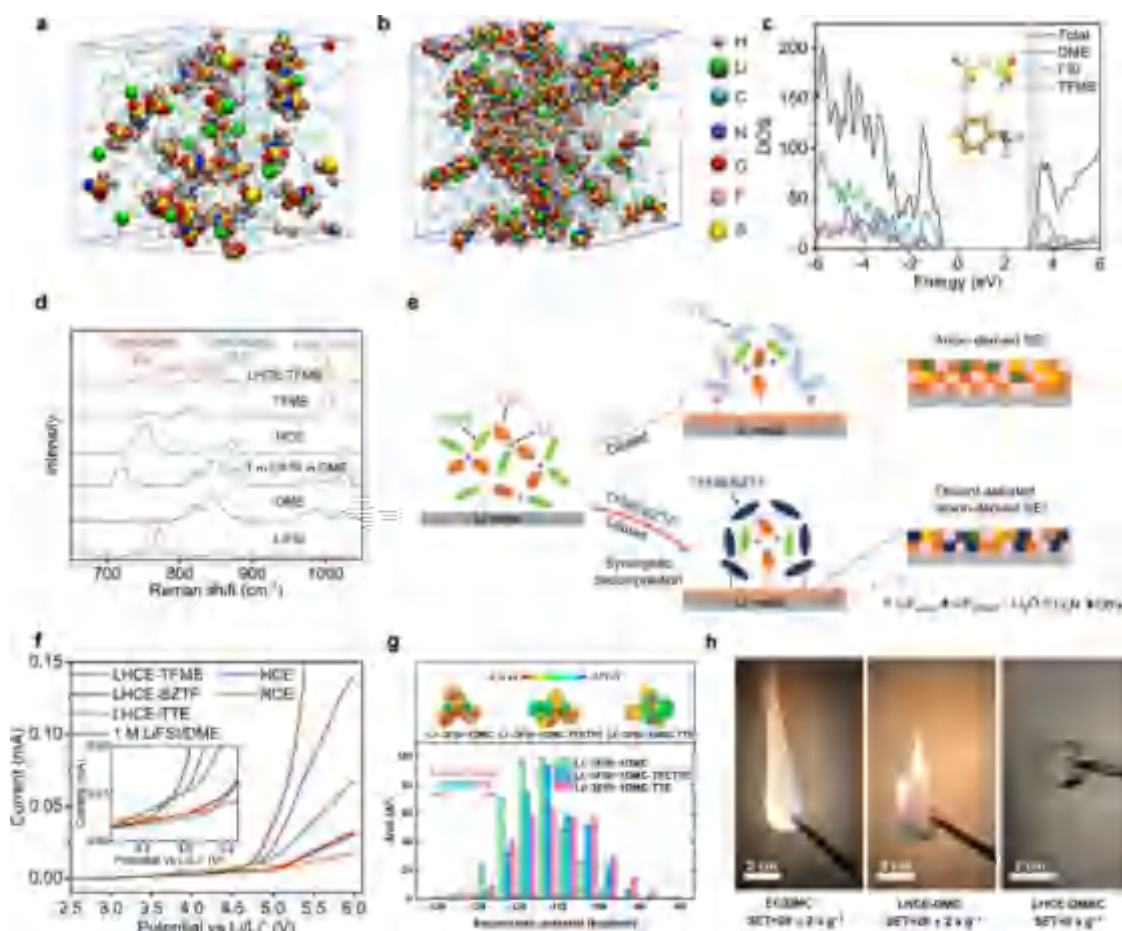
a wide range of electrolytes.<sup>24</sup> Figure 7b shows a positive correlation between CE and fluoride levels. Increasing the F concentration through “beneficial” fluorination appears to be a reliable strategy to achieve a high CE of Li plating/stripping, while further understanding of the chemistry and decomposition kinetics of the F source remains. Moreover, apart from the type of Li salts, their purity also has a significant impact on CE.<sup>130</sup> Enhancing the purity of LiBF<sub>4</sub> from 99.9% to 99.99% would result in a flatter morphology of the SEI, as depicted in Figure 7c. The purity of the conducting salt directly influences the morphology, composition, and possibly the quality of the formed protective layer. The formation of a more robust interphase that inhibits the growth of high surface area Li directly improves the cycling stability of cells containing fluorine-based conducting salts. To conclude, although LiPF<sub>6</sub> is not prominent in ionic conductivity, chemical stability, and thermal stability, it is still dominant in the commercial market of LIBs due to the ability to provide well-balanced properties. Selective fluorination of the anions of Li salts will decrease their interactions with Li<sup>+</sup> cations, thereby increasing the dissociation of the salts in the electrolyte solution and lifting the ionic conductivity. To achieve better performance, two or more F-containing salts are synergistically used to supplement their native deficiencies.

The properties of the electrolyte can be altered by adjusting the concentration of the Li salt. Conventional dilute electrolytes typically operate within a salt concentration range of 1–2 M, which strikes a balance between ionic conductivity, viscosity, and salt solubility. Thus, most of the studies use electrolytes in region C in Figure 8a. However, by carefully selecting appropriate salts and solvents, electrolytes can be relocated in regions A, B, and D, as depicted in Figure 8a, leading to some unexpected properties.<sup>132</sup> Aqueous electrolytes possess a narrow ESW of 1.23 V, which is insufficient to support most electrochemical couples in LIBs. Besides, hydrogen evolution at the anode side is another serious challenge as it occurs at a potential (2.21–3.04 V vs Li/Li<sup>+</sup>, depending on pH value) far higher than the operating voltage of most LIBs. Consequently, the maximum voltage achieved in aqueous LIBs was limited to 1.5 V.<sup>133,134</sup> Xu et al. developed a “water-in-salt” electrolyte by dissolving lithium bis(trifluoromethane sulfonyl) imide (LiTFSI) at extremely high concentrations (molality > 20 m) in water, leading to an anion-rich Li<sup>+</sup> solvation sheath and an expanded ESW (~3.0 V),<sup>135</sup> as exhibited in Figure 8b. This remarkable shift resulted from the formation of a dense interphase on the anode surface, primarily caused by the reduction of salt anions. The LiMn<sub>2</sub>O<sub>4</sub>||Mo<sub>6</sub>S<sub>8</sub> cells using “water-in-salt” electrolyte demonstrated an open-circuit voltage (OCV) of 2.3 V, and the CE was nearly 100% for up to 1000 cycles.

Research on nonaqueous electrolytes offers countless variations in aprotic solvents, Li salts, and their mixing ratios. For a given electrolyte with fixed salt and solvent, ionic conductivity depends on both the viscosity and the Li-ion mobility.<sup>132</sup> For 1 M LiTFSI-1,2-dimethoxyethane (DME)/1,3-dioxolane (DOL) (1:1 by volume), as is concluded in Figure 8c, when the salt concentration is increased, more and more Li–solvent pairs form due to the incomplete Li<sup>+</sup> solvation shell, and the viscosity at room temperature increases obviously. At the same time, the Li-ion transference number rises to a much higher value ( $t_{\text{Li}^+} = 0.73$ ) than that of dilute salt-in-solvent electrolytes (0.2–0.4).<sup>138</sup> For such electrolytes, Li ions are mostly coordinated with solvent in the first

solvation shell, leading to a large number of free anions and lower mobility of solvated Li cations. In the highly concentrated electrolyte system, more anions come into the first solvation shell and form more contact ion pairs (CIPs) and aggregates (AGGs), thus leading to a higher Li-ion transference number and lower ion conductivity.<sup>139</sup> Apart from these changes in physical properties, the concentrated electrolyte demonstrates unusual electrochemical properties that are remarkably distinct from a conventional dilute electrolyte. In 2003, Ogumi et al. reported that highly concentrated propylene carbonate (PC) electrolytes have shown dramatic changes in the behavior of graphite electrodes.<sup>140,141</sup> Further in 2008, the reversibility of Li metal deposition/stripping was notably improved in highly concentrated PC electrolytes.<sup>142</sup> From 2010 onward, Yamada et al. extended this method to a wide range of nonaqueous solvents of reversible graphite electrodes with EC-free solvent.<sup>143–145</sup> After this path-breaking work, the highly reversible Li metal electrodes with excellent cycling stability were reported by Xu et al.<sup>132</sup> in 2013 and Qian et al.<sup>146</sup> in 2015. These changes can be attributed to the reduction of free solvent in the solution, altering the solvation structure and shifting the energy level of the LUMO toward the salts, resulting in the reduction of the salts at a lower voltage.<sup>144</sup> For LiTFSI/lithium bis(fluoro sulfonyl) imide (LiFSI)-containing electrolyte, Al dissolution is suppressed at high voltage.<sup>147</sup> The presence of fewer free solvents and anions in the electrolyte leads to less dissolution of the Al current collectors, as shown in Figure 8d. For Li–S batteries, the high-concentration electrolytes can inhibit self-discharge caused by polysulfide shuttle (Figure 8e), which significantly improves the reversibility of the batteries (Figure 8f).<sup>137</sup> However, the application of such highly concentrated electrolytes is limited by the high cost and high viscosity due to the extensive use of Li salts.

**2.2.2. Fluorinated Solvents and Cosolvents.** Introducing fluorine into the molecular structures of electrolyte solvents and cosolvents imparts unique physicochemical properties, such as nonflammability, robust LiF-enriched SEI, high resistance against electrochemical oxidation, and an expanded operating temperature window, etc. These advantages make fluorinated electrolytes highly attractive for advanced battery applications. Representative fluorinated solvents and cosolvents are shown in Figure 9a, showing the dielectric constant increasing from left to right. These fluorinated solvents and cosolvents exhibit unique physicochemical properties because of the very high electronegativity and high ionic potential of the fluorine atom.<sup>148</sup> Partially fluorinated organic solvents possess relatively high polarity compared to perfluorinated organic solvents. This property allows partially fluorinated solvents to be used as functionalized solvents, while perfluorinated solvents are primarily employed as antisolvents due to their poor dissolving ability with Li salts. As shown in Figure 9b, Xie et al. proposed the dipole–dipole interactions model to enhance the compatibility of various electrolytes with graphite anode, thereby suppressing Li<sup>+</sup>–solvent cointercalation, preserving the graphite lattice and improving the electrochemical reversibility.<sup>149</sup> After introducing fluorobenzene (FB) into the LiFSI–3DME system (LiFSI–3DME/7FB), the cointercalation of the solvent was suppressed, leading to a high initial CE of 86% and stable cycling performance over 200 cycles with a capacity retention of up to 94%. The nonsolvents were kept out of the Li<sup>+</sup> solvation shell while exerting considerable dipole–dipole interactions toward



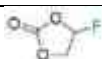













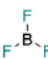
**Figure 10.** Functions of fluorinated cosolvents of LHCEs. MD simulation results of (a) dilute electrolyte and (b) LHCE. Reproduced with permission from ref 158. Copyright 2021 Wiley-VCH. (c) DOS obtained in quantum mechanical DFT-*ab initio* molecular dynamics (AIMD) simulations of LHCE with TFMB. Reproduced with permission from ref 160. Copyright 2022 American Chemical Society. (d) Raman spectra of various solvents, diluents, and electrolytes. (e) Schematic diagram of the electrolyte structure and the correspondingly formed SEI in different LHCEs. (f) Oxidation stability of various electrolytes in Li||Al half-cells characterized by LSV at a scan rate of 0.5 mV s<sup>-1</sup> from 2.5 to 6.0 V. Reproduced with permission from ref 158. Copyright 2022 American Chemical Society. (g) Electrostatic potential mapping of Li<sup>+</sup> solvation structures and the surface area in each ESP range on the van der Waals (vdW) surface of the FSI<sup>-</sup> anion part. Reproduced with permission from ref 161. Copyright 2022 American Chemical Society. (h) Flame-retarding testing of EC/DMC, LHCE-DMC, and LHCE-dimethylacetamide (DMAC). Reproduced with permission from ref 165. Copyright 2022 Wiley-VCH.

polar solvents, thus weakening the Coulombic attractions between Li<sup>+</sup> and solvents. Rational design by partial fluorination on ethers, e.g., locally polar -CHF<sub>2</sub>, is identified as the optimal group compared with fully fluorinated -CF<sub>3</sub> in popular designs. Such weak solvents could achieve a balance between fast ion conduction and electrode stability through fine tuning the solvation ability (Figure 9c).<sup>150</sup> These developed electrolytes simultaneously endowed high conductivity, a low and stable overpotential, high CE (>99.5%), and fast activation (CE > 99.3% within two cycles). Furthermore, some Li-unfriendly solvents can be optimized by fluorination. For instance, by introducing a fluorinated moiety into the nonflammable phosphate, the five-membered fluorinated cyclic phosphate solvent 2-(2,2,2-trifluoroethoxy)-1,3,2-dioxaphospholane 2-oxide (TFEP) was designed and synthesized, as shown in Figure 9d.<sup>151</sup> Such fluorinated phosphate solvent not only had effective nonflammability but also exhibited excellent electrode compatibility. Besides, fluorine substitution can broaden the range of liquid electrolytes. In 2019, Meng et al. proposed liquefied gas electrolytes, which showed high CE with a Li metal anode

(Figure 9e).<sup>152</sup> The 0.5 M LiTFSI and 0.5 M tetrahydrofuran (THF) in fluoromethane (FM) electrolyte exhibited a maximum conductivity of 3.9 mS·cm<sup>-1</sup> at 20 °C. And, the impressive low-temperature conductivity at -60 °C was 2.8 mS·cm<sup>-1</sup>, which was competitive among state-of-the-art low-temperature electrolytes.<sup>153,154</sup> Such enhanced liquefied gas electrolytes demonstrated average CEs of 99.6%, 99.4%, and 98.1% (±0.3%) at capacities of 0.5, 1, and 3 mAh cm<sup>-2</sup>, respectively, during long-term cycling performance.

As mentioned above, per-fluorinated solvents are usually applied as antisolvent or “dilute” in many works to make localized high-concentration electrolytes (LHCEs). Such LHCEs are widely investigated and always show enhanced interphasial stability.<sup>139,155</sup> Compared with HCEs, LHCEs exhibit lower viscosity and wider ESWs. Watanabe et al. used hydrofluoroether (HFE) and 1,1,2,2-tetrafluoroethyl 2,2,3,3-tetrafluoropropyl ether (TTE) to dilute highly concentrated ionic liquid electrolytes.<sup>156</sup> The work indicated that the addition of HFE maintained the solvation structure of the original salt-solvent complexes and effectively reduced the dissolution of Li<sub>2</sub>S<sub>n</sub>, which greatly enhanced the power density

**Table 2. Fluorinated Additives for Li-Based Batteries**<sup>168,170–183</sup>

additive	structural formula	original electrolyte component	main function	ref
5 wt.% FEC		1 M LiPF <sub>6</sub> -EC/ethyl methyl carbonate (EMC) (1:1 by vol.)	SEI formation	168
0.5 wt.% LiF		1 M LiPF <sub>6</sub> -EC/EMC	SEI formation	170
2 wt.% tris(2,2,2-trifluoroethyl) borate		1 M LiPF <sub>6</sub> -EC/DMC (1:2 by vol.)	SEI formation	171
5 wt.% methyl (2,2,2-trifluoroethyl) carbonate		1 M LiPF <sub>6</sub> -EC/EMC (1:1 by vol.)	CEI formation	172
0.5 wt.% 4-(trifluoromethyl) benzonitrile		1 M LiPF <sub>6</sub> -EC/EMC/DMC (1:1:1 by vol.)	CEI formation	173
5 wt.% tris(trifluoroethyl)phosphate		1 M LiPF <sub>6</sub> -EC/EMC (3:7 by vol.)	thermal stability; stabilize LiPF <sub>6</sub>	174
0.1–1.0 wt.% tris(2,2,2-trifluoroethyl) phosphite		1.2 M LiPF <sub>6</sub> -C/EC/EMC (3:3:4 by wt.)	thermal stability; stabilize LiPF <sub>6</sub>	175
5 wt.% (trifluoroethoxy)pentafluorocyclotriphosphazene		1 M LiPF <sub>6</sub> -EC/DMC (3:7 by vol.)	flame retardancy; CEI formation	176
5 wt.% (ethoxy)pentafluorocyclotriphosphazene		1 M LiPF <sub>6</sub> -EC/EMC/DMC (1:1:1 by vol.)	flame retardancy; CEI formation	177
2 vol.% phenoxy pentafluorocyclotriphosphazene		1 M LiPF <sub>6</sub> -EC/DMC (1:1 by vol.)	flame retardancy; CEI formation	178
3 mM <i>N</i> -ethyl-3,7-bis(trifluoromethyl)phenothiazine		1.2 M LiPF <sub>6</sub> -EC/EMC (3:7 by wt.)	overcharge protection	179
0.08 M <i>N</i> -ethyl-1,2,3,4,6,7,8,9-octafluorophenothiazine		1.2 M LiPF <sub>6</sub> -EC/EMC (3:7 by wt.)	overcharge protection	180
2 wt.% (4-(2,2,3,3,4,4,5,5,5-nonafluoropentyl)-1,3-dioxolan-2-one		1 M LiPF <sub>6</sub> -EC/EMC (3:7 by vol.)	overcharge protection	181
0.1 M Li <sub>3</sub> AlF <sub>6</sub>		1 M LiPF <sub>6</sub> -EC/DMC (1:1 by vol.)	suppress dendrite growth	182
0.01 M BF <sub>3</sub>		1 M LiPF <sub>6</sub> -EC/DMC (1:1 by vol.)	enhance the rate capability	183

of the Li–S batteries. By performing molecular dynamics (MD) simulation, the solvation structure can be shown pictorially. Zhang et al. introduced the concept of LHCEs, which consisted of 1.2 M LiFSI in a dimethyl carbonate (DMC)/bis(2,2,2-trifluoroethyl) ether (BTFE) (1:2 by mol)

mixture, exhibiting low concentration, low viscosity, and good wettability that facilitated practical applications of LMBs. The dilution with BTFE slightly weakened the association between Li<sup>+</sup> cations and FSI<sup>−</sup> anions, promoting FSI<sup>−</sup> anion decomposition as the dominant reduction reaction, which



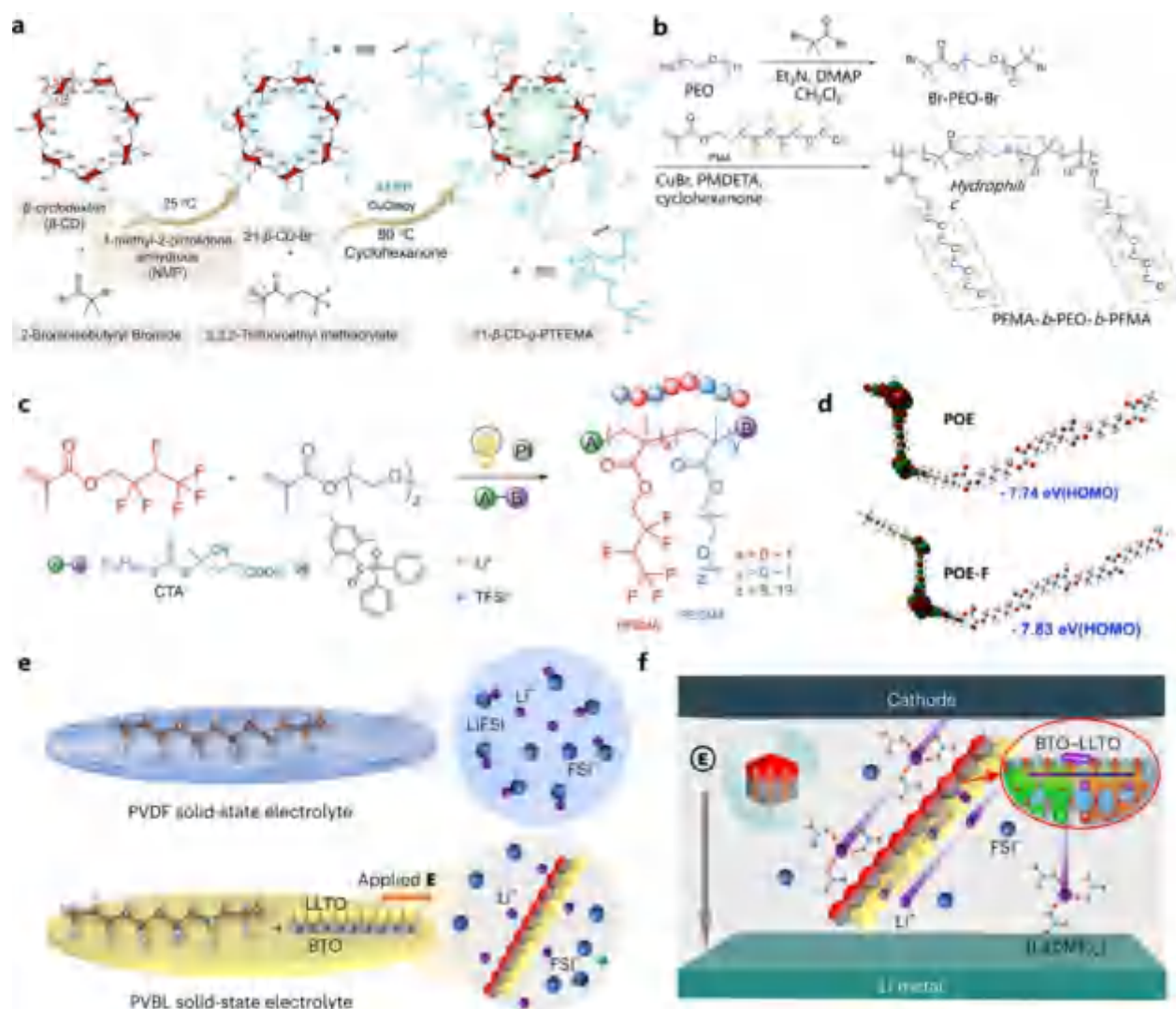
formed a robust FSI-derived SEI layer. The average CE of the electrolyte was greatly increased to  $\sim 99.7\%$ . After that, LHCEs have been extensively applied in LIBs, LMBs, and other electrochemical systems.<sup>157</sup> The dilution with BTFE slightly weakened the association between  $\text{Li}^+$  cations and  $\text{FSI}^-$  anions, which led to more  $\text{FSI}^-$  anion decomposition as the dominant reduction reaction, forming a robust FSI-derived SEI layer. The average CE of the electrolyte was largely increased to  $\sim 99.7\%$ . After that, LHCEs were widely applied in LIBs, LMBs, and other electrochemical systems. As shown in Figure 10a and 10b, Zhao et al.<sup>158</sup> introduced HFE into initial HCE and simulated the solvation structure. The bulk phase structure of local HCE electrolyte did not greatly change with the addition of HFE diluent. Thus, the salt usage was reduced, and the viscosity of the electrolyte became lower. As a result, the electrolyte has a better wettability with electrodes. Although the ionic conductivity usually increases with the decrease of the viscosity, the addition of diluent has a negative effect on the conductivity of LHCE.<sup>135</sup> The reason is probably the discontinuous Li conducting network separated by the diluent medium. To achieve a balance, the content of diluent should be restricted during the preparation of LHCE. Fluorinated ether diluents typically exhibit lower LUMO and HOMO energy levels. As a result, they may participate in the formation of electrolyte-electrolyte interphase. Wu et al. reported the HFE cosolvent decomposition and metal anode dissolution phenomenon in ether-based LHCE systems.<sup>159</sup> Such light decomposition behavior comes from diluents synergistically decomposed with anions on the Li metal anode. Figure 10c shows the density of states (DOS) of LHCE–trifluoromethoxybenzene (TFMB). In LHCE–TFMB, the LUMO is located at either TFMB or  $\text{FSI}^-$  with nearly equal probability, indicating that both the  $\text{FSI}^-$  anions and the TFMB molecules contribute to the SEI formation.<sup>160</sup> Besides, the existence of fluorinated ether antisolvent is also attributed to anion decomposition. The solvation structures in LHCE–TFMB were validated by Raman spectroscopy (Figure 10d). Upon coordination of DME with  $\text{Li}^+$ , the corresponding peaks of both DME and  $\text{FSI}^-$  shifted to longer wavenumbers. For the 5.0 M LiFSI/DME electrolyte, only the peak of  $\text{Li}^+$ -coordinated DME was observed, indicating that few free DME molecules were present in HCE. In LHCE–TFMB, the peak positions were nearly the same as those in HCE plus the vibration bands of free TFMB. Unlike TTE, which decomposed little at the anode side, the TFMB/benzotrifluoride (BZTF) diluents were partially decomposed along with the  $\text{FSI}^-$  anions and participated in forming the SEI on the Li metal anode (Figure 10e). This synergistic effect through anion–diluent pairing was expected to be of significant importance to the optimized electrochemical performance. Linear sweep voltammetry (LSV) was conducted on an Al electrode to unveil the electrochemical oxidation stability of these electrolytes (Figure 10f). The oxidation stability of LHCE–TFMB/BZTF was significantly improved, and no exponential increase in oxidation current was observed until 5.0 V. He et al. reported that the surface area in different electrostatic potential (ESP) ranges (Figure 10g) helped quantitatively analyze the characteristics of the molecular surface charge.<sup>161</sup> The reduced relative abundance of the ESP distribution on anions suggested that the reduction stability of  $\text{FSI}^-$  was reduced in the presence of antisolvents. In previous reports, the LHCE–TTE electrolytes demonstrated better cycling performance of Li||Cu cells (98.9% and 99.6%) than LHCE–TFETFE (98.2% and 99.4%).<sup>162</sup> However, the

intensified inductive effect caused by antisolvents reduced the binding energy of the Li–solvent interactions and changed with different antisolvents. The binding energies of the Li–solvent and Li–anion interactions were decreased with the addition of antisolvent compared with the HCEs, indicating the capability of antisolvents to help lower the desolvation energy and facilitate interphase kinetics in the electrochemical reaction.<sup>163,164</sup> The addition of fluorine also led to a decrease in the flammability of the electrolyte, as shown in Figure 10h.<sup>165</sup> Hereby,  $\text{F}^\bullet$  radicals were formed, which could scavenge the  $\text{H}^\bullet$  radicals. Owing to this approach, the free-radical reaction was quenched, and the flame propagation was suppressed. However, ether-based electrolytes are highly volatile and flammable, and flame retardancy cannot be achieved by adding fluorinated solvents/cosolvent alone. Aurbach et al. reported a synergy of fluorinated cosolvent and gelation treatment by a butenoxycyclotriphosphazene (BCPN) monomer, which facilitated the use of ether-based electrolyte for high-energy Li metal batteries.<sup>166</sup> The safety risks of fire and electrolyte leakage were eliminated by the fluorinated cosolvent and fireproof polymeric matrices.

**2.2.3. Fluorinated Additives.** Electrolyte additives are usually defined as the functional compounds added into the bulk electrolyte in a low amount (0.1–5%, either by weight or volume) by which electrolyte can be regulated economically and efficiently.<sup>130</sup> Compared to their nonfluorinated counterparts, fluorinated additives exhibit decreased cathodic stability, increased anodic stability, reduced flammability, etc., which endow fluorinated additives with tremendous application potential in (i) SEI/CEI formation, (ii) flame retardancy, (iii) overcharge protection, (iv) Li salt stability regulation, (v) electrolyte wettability adjustment, and (vi) electrolyte conductivity improvement.<sup>167</sup> Table 2 summarizes the components and functions of different fluorinated additives used in Li-based batteries. As the most widely reported organic additive, FEC is believed to be capable of improving the interphasial stability of the anode by the formation of LiF-rich SEI layers. Substitution of a hydrogen atom in EC by a fluorine atom sharply reduces the LUMO energy level from  $-0.38$  to  $-0.87$  eV, which makes it easier to be reduced on the anode side and form a SEI.<sup>168</sup> The C–F bond in FEC breaks first during the reduction process, eventually leading to the formation of a stable, compact SEI rich in LiF and poly(vinyl carbonate) (poly(VC)).<sup>168</sup> The combination of LiF and poly(VC) remarkably inhibits continuous electrolyte decomposition and facilitates uniform Li deposition, which exhibits an even better passivation effect than the VC-containing electrolyte.<sup>169</sup> Apart from the FEC, Archer and co-workers demonstrated that the direct use of 0.5 wt % LiF to a conventional electrolyte could enable high surface stability and fast surface diffusion of Li ions over the layer rich in LiF crystals,<sup>170</sup> further confirming the vital role of LiF in stabilizing the SEI. Yin and co-workers adopted a fluoride boron-based anion receptor, tris(2,2,2-trifluoroethyl) borate (TTFEB), as a bifunctional electrolyte additive to improve the performance of LMBs.<sup>171</sup> With 2 wt % TTFEB, uniform Li deposition without uncontrollable Li dendrites can be realized due to the LiF-rich SEI layer. Moreover, the electron-deficient boron-center atoms acted as anion receptors to tether the  $\text{PF}_6^-$  anions in the electrolyte, causing the increased Li-ion transference number.

In addition to the Li anode, the stability of the cathode is also crucial for the development of high energy density Li-based batteries. However, the CEI chemistry is even more





**Figure 11.** Fluorinated solid-state/quasi-solid-state polymer electrolytes. (a) Detailed synthetic scheme of 21-arm fluoropolymers. Reproduced with permission from ref 195. Copyright 2022 Springer Nature. (b) Synthesis paths of FB-PCPs. Reproduced with permission from ref 196. Copyright 2021 Elsevier. (c) Schematic of synthesizing FB-SPE by visible-light-driven photocontrolled radical polymerization (photo-CRP). Reproduced with permission from ref 197. Copyright 2021 Wiley-VCH. (d) Simulated HOMO energy level of POE (upper panel) and POE-F (lower panel). Reproduced with permission from ref 198. Copyright 2021 Wiley-VCH. Illustration of (e) the Li salt state in the PVDF and PVBL electrolytes and (f) the Li salt dissociation and Li<sup>+</sup> transport by the coupled BTO–LLTO in the PVBL electrolyte. Reproduced with permission from ref 199. Copyright 2023 Springer Nature.

complex, and the electrochemical performance of the cathode has been plagued by some challenges, including severe oxidative decomposition of the electrolyte, gas evolution, transition metal dissolution, cracking of primary/secondary particles, etc., especially for layered transition metal oxide cathodes under a high cutoff voltage.<sup>184</sup> The design of novel fluorinated additives such as fluorocarbonates, fluoronitriles, and fluoroborates can improve the oxidation stability after fluorination due to the ability to in situ form an F-containing CEI layer, which offers a promising solution for the aforementioned challenges.<sup>185</sup> Song and co-workers reported a fluorinated linear carbonate, methyl (2,2,2-trifluoroethyl) carbonate (FEMC), as a new electrolyte additive to achieve the performance improvement of commercial carbonate electrolyte at a 4.6 V cutoff voltage, far beyond the oxidation limit (4.3 V vs Li/Li<sup>+</sup>) of conventional carbonate electrolyte.<sup>172</sup> FEMC played a crucial role in generating a passivating layer rich in

metal fluorides and C–F-containing species, which effectively delayed the cathode degradation and capacity fade.

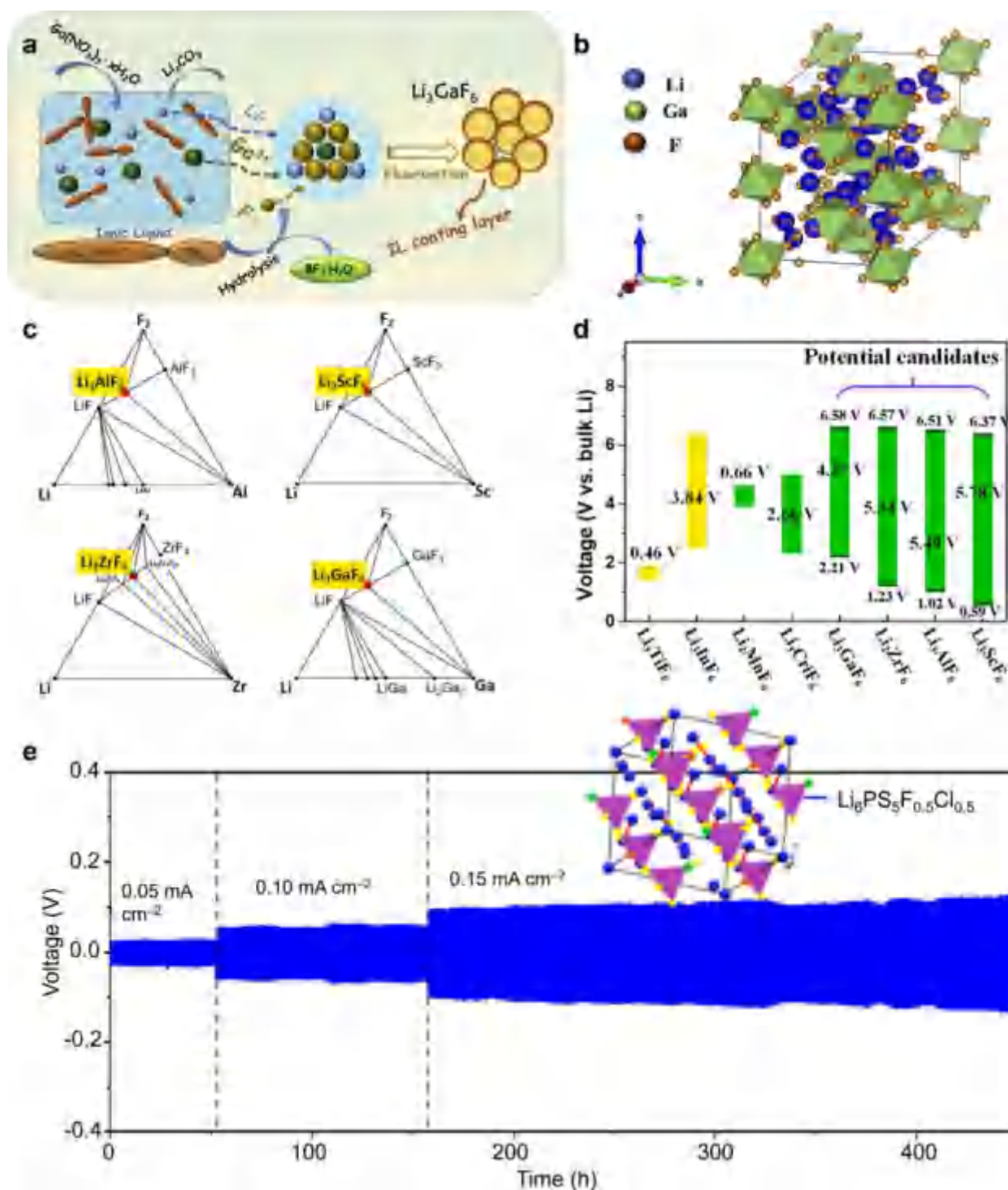
The practical application of batteries may encounter different abuse conditions such as thermal abuse, electronic abuse, and mechanical abuse, which trigger a series of exothermic reactions and thermal runaway of batteries.<sup>186</sup> Generally, fluorinated phosphates and fluorinated phosphites such as tris(trifluoroethyl)phosphate (TFP)<sup>174</sup> and tris(2,2,2-trifluoroethyl) phosphite (TTFP)<sup>175</sup> exhibit superior flame retardance over nonfluorinated counterparts. When heated, F• radicals can scavenge the hydrogen radicals and quench the free-radical reaction and flame propagation.<sup>187</sup> Addition of fluorinated phosphates or fluorinated phosphites in the organic electrolyte can remarkably promote the thermal stability and suppress the thermal decomposition of LiPF<sub>6</sub>.<sup>188</sup> However, to achieve nonflammable electrolyte formulation, the amount of fluorinated phosphates or fluorinated phosphites is usually required to be greater than 5%.<sup>130</sup> Phosphazene derivatives

rich in F, N, and P elements are considered as more outstanding flame-retardant additives than phosphates and phosphites. Feng and co-workers synthesized a novel (trifluoroethoxy)pentafluorocyclotriphosphazene (TFPN) and deployed a flame test, which revealed that only 5 wt % TFPN addition can enable electrolyte nonflammability.<sup>176</sup> Moreover, the preferential oxidative decomposition of fluorinated phosphazene derivatives also produced a multiphase CEI layer consisting of linear/multiring polymers, such as  $\text{Li}_3\text{N}$ ,  $\text{LiF}$ , etc., which suppressed decomposition of the electrolyte and achieved a high reversible capacity and better capacity retention.<sup>177,178</sup> As a typical electronic abuse, overcharge can cause premature electrode and electrolyte failure and catastrophic safety issues. Overcharge protection additives with an oxidation potential slightly higher than the delithiated potential (vs  $\text{Li}/\text{Li}^+$ ) can exert a preferential redox reaction, resulting in circuit break or a microshort circuit inside the batteries.<sup>189,190</sup> An electron-withdrawing substituent with F or  $\text{CF}_3$  groups provides a promising method to increase the oxidation potential of the overcharge protection additives for use as redox shuttles in high-voltage Li-based batteries. Odom and co-workers synthesized a series of F-substituted phenothiazine derivatives such as *N*-ethyl-3,7-bis-(trifluoromethyl)phenothiazine (BCF3EPT) for a  $\text{LiFePO}_4$  cathode<sup>179</sup> and *N*-ethyl-1,2,3,4,6,7,8,9-octafluorophenothiazine (OFEPT) for a high-voltage  $\text{LiNi}_{0.8}\text{Co}_{0.15}\text{Al}_{0.05}\text{O}_2$  cathode,<sup>180</sup> which acted as reversible redox shuttles to protect batteries from overcharge. All in all, although numerous fluorinated additives have been explored, the physicochemical properties of fluorinated additives do not show a simple monotonous correlation with the content of fluorine substitution.<sup>191</sup> Moreover, the decisive influence of the fluoride substitution position on the performance of additives still needs further investigation.

**2.2.4. Fluorinated Solid/Quasi-Solid-State Electrolytes.** Exploration of highly affordable batteries with enhanced safety is crucial for achieving electric devices with energy densities of  $400 \text{ Wh kg}^{-1}$ . To address this need, the development of all-solid-state batteries has emerged as a promising pathway. Traditionally, liquid electrolytes select organic solvents with strong polarity, creating a high dielectric constant environment conducive to Li-ion dissociation.<sup>192</sup> This strategy also applies to the selection of all-solid polymer electrolytes. The electrostatic force between ions in SPEs is significantly influenced by the polarity of the polymer. Since the report of ion conduction in poly(ethylene oxide) (PEO) in 1975, it has been considered as an intriguing polymeric matrix for electrolytes due to the excellent chemical and electrochemical stabilities.<sup>193,194</sup> However, the high crystallinity of PEO at room temperature results in low ionic conductivity ( $10^{-6}$ – $10^{-8} \text{ S cm}^{-1}$ ); meanwhile, the narrow ESW of PEO-based electrolytes also hinders their widespread application. Efforts to enhance PEO-based solid electrolytes are underway. As an example shown in Figure 11a, Hu et al. proposed a top-down design concept through atom transfer radical polymerization.<sup>195</sup> Through an orthogonal test method, the optimal composition of a F-rich macromolecule containing all-solid-state polymer electrolyte (FMC-ASPE) was determined. This new PEO electrolyte exhibited significantly improved high-voltage stability and transference number ( $t_{\text{Li}^+} = 0.88$ ) to suppress the side reaction at the cathode side and dendrite growth at the Li anode side. Additionally, the as-prepared FMC-ASPE showed improved physical and electrochemical

properties, including higher ionic conductivity, higher toughness (2.7 times higher than PEO-ASPE), and higher thermal stability. Sun et al. synthesized fluorine-containing ABA triblock copolymer electrolytes (FBCPEs) (perfluoroalkyl pendant in the A segment and PEO in the B segment) with a small number of  $-\text{CF}_2$  repeating units (Figure 11b).<sup>196</sup> Addition of  $-\text{CF}_2$  decreased the HOMO energy level of the whole electrolyte. Thus, the antioxidant capacity of FBCPEs was improved, resulting in a wider ESW of 4.9 V. Jia et al. proposed a fluorinated bifunctional solid polyelectrolyte, as shown in Figure 11c, in which fluorinated chains were covalently bonded to polyether-based fragments through the controlled radical polymerization.<sup>197</sup> Compared with conventional nonfluorinated polyether-derived solid polyelectrolytes, FB-SPEs were able to provide an electrochemical window of 5 V. In addition to PEO, fluorination plays an essential role in other all-solid-state polymer electrolytes as well. Sun et al. selected polyoxalic (POE) acid as the polymer matrix and found that the HOMO electrons of the POE were located at the terminal unit.<sup>198</sup> When trifluoroacetic acid was applied as the terminal unit (POE-F), the HOMO electrons were transferred to the middle oxalic acid unit, which improved the antioxidant capacity (Figure 11d). Furthermore, the interfacial compatibility between the Li metal and POE-F was also improved by generating a  $\text{LiF}$ -based SEI, and the stability of  $\text{Li||NMC811}$  full cells was significantly improved, which kept cycling stably over 200 cycles at 1 C.

Apart from all-solid-state polymer electrolytes, quasi-solid-state gel polymer electrolytes (GPEs) can also be optimized by fluorination. One of the extensively studied materials for quasi-solid-state polymer electrolytes is PVDF, first investigated in the 1980s.<sup>200</sup> In 1996, Warren et al. assembled the first LIB based on a PVDF-HFP-based GPE. The copolymer exhibited advantages of a low degree of crystallinity due to the addition of hexafluoropropylene (HFP), high mechanical flexibility, and good compatibility with electrodes.<sup>49,201</sup> Afterward, the number of studies on PVDF-based electrolytes gradually increased, with GPEs being the main focus. He et al. developed a highly conductive and dielectric GPE by compositing PVDF with coupled  $\text{BaTiO}_3$  (BTO) and  $\text{Li}_{0.33}\text{La}_{0.56}\text{TiO}_{3-x}$  (LLTO) (named as PVBL) nanowires, as shown in Figure 11e and 11f.<sup>199</sup> The PVBL effectively restrained the formation of the space charge layer with PVDF, and the coupling effects contributed to an exceptionally high ionic conductivity ( $8.2 \times 10^{-4} \text{ S cm}^{-1}$ ) and  $\text{Li}^+$  transference number (0.57) of the PVBL at 25 °C. The PVBL also homogenized the interfacial electric field with electrodes. The  $\text{Li||PVBL (LiNi}_{0.8}\text{Co}_{0.1}\text{Mn}_{0.1}\text{O}_2)$  NCM811 solid-state cells stably cycled 1500 times at a current density of  $180 \text{ mA g}^{-1}$ , and the pouch cells also exhibited excellent electrochemical performance and good safety. Nevertheless, various tough challenges need to be resolved before the practical application for PVDF-based electrolytes, including the following: (i) the in-depth understanding of interphase degradation mechanisms is still insufficient; (ii) achieving considerable ionic conductivity in solvent-less conditions is of significant importance; (iii) the rate performance should be promoted under high current density; (iv) the solid interface still has natural deficiency compared with liquid electrolytes; (v) to further improve the energy density, the thickness of the polymer electrolyte needs to be thinner up to 10–20  $\mu\text{m}$ ; (vi) the polymerized homogeneity of PVDF-based electrolytes in industrial conditions is insufficient, which will lead to uneven



**Figure 12.** Fluorinated inorganic solid electrolyte. (a) Schematic synthesis of  $\text{Li}_3\text{GaF}_6$ . (b) Crystal structures of  $\beta\text{-Li}_3\text{GaF}_6$  viewed along  $[111]$ . Reproduced with permission from ref 203. Copyright 2022 Springer Nature. (c) Li–M–F ternary phase diagram assessing the computed stability of Li–M–F compounds. Black solid circles indicate stable phases, while red solid circles show the targeted fluoride materials. (d) Electrochemical stability ranges of  $\text{Li}_x\text{MF}_6$  fluoride electrolytes. The yellow region reflects the possible extension of the voltage window over which decomposition occurs but without any metallic products. Reproduced with permission from ref 204. Copyright 2021 Elsevier. (e) The crystal structure of  $\text{Li}_6\text{PS}_5\text{F}_{0.5}\text{Cl}_{0.5}$  and the voltage profile of Li/Li symmetric cell cycling with  $\text{Li}_6\text{PS}_5\text{F}_{0.5}\text{Cl}_{0.5}$  under current densities of 0.05, 0.10, and 0.15  $\text{mA cm}^{-2}$ . Reproduced with permission from ref 205. Copyright 2022 American Chemical Society.

Li transportation. Understanding the above specific challenges faced by PVDF-based electrolytes will contribute to the development of next-generation all-solid-state batteries.

For inorganic solid-state electrolytes, although fluorination strategies have been successfully applied on oxide, sulfide, and

polyanion solid electrolyte systems, Li–fluoride solid electrolytes have yet to be reported.<sup>202</sup> To investigate the structure and corresponding synthesis strategy, Li et al. proposed a novel Li-rich fluoride electrolyte,  $\text{Li}_3\text{GaF}_6$ , with a high ionic conductivity close to  $10^{-4} \text{ S cm}^{-1}$  at room temperature



(Figure 12a).<sup>203</sup> The synergic effect of open bulk transport and compact interphase transport in  $\text{Li}_3\text{GaF}_6$  endowed  $\text{LiFePO}_4$ -based solid-state LMBs with an improved cycling performance for at least 150 cycles at 1 C. The crystal structure of the  $\text{Li}_3\text{GaF}_6$  derivative from the cryolite phase is shown in Figure 12b. The characteristic building units are  $\text{GaF}_6$  octahedra, and the Li atoms are octahedrally, pentahedrally, or tetrahedrally coordinated by F. To understand the phase stability relative to their corresponding separated phases, including elemental, binary, and ternary ones, Lin et al. used the grand canonical linear programming method (GCLP) to explore the phase diagram of  $\text{Li-M-F}$  compounds (Figure 12c).<sup>204</sup> The favorable combination was the decomposition of ternary  $\text{Li}_x\text{MF}_6$  into binary  $\text{LiF}$  and  $\text{MF}_3$  or  $\text{MF}_4$  with the order of decomposition energy ( $\Delta E = [E(\text{phase equilibrium}) - E(\text{Li}_x\text{MF}_6)] N_{\text{atoms}}^{-1}$ ) being as follows:  $\text{Li}_3\text{GaF}_6$  (52 meV  $\text{atom}^{-1}$ ) >  $\text{Li}_3\text{AlF}_6$  (38 meV  $\text{atom}^{-1}$ ) >  $\text{Li}_2\text{ZrF}_6$  (13 meV  $\text{atom}^{-1}$ ) >  $\text{Li}_3\text{ScF}_6$  (1 meV  $\text{atom}^{-1}$ ). Figure 12d shows the sequence of fluoride materials determined by their ESW:  $\text{Li}_3\text{ScF}_6$  (5.78 V) >  $\text{Li}_3\text{AlF}_6$  (5.49 V) >  $\text{Li}_2\text{ZrF}_6$  (5.34 V) >  $\text{Li}_3\text{GaF}_6$  (4.37 V). The fluoride materials exhibit a wider ESW compared to that of the sulfides.  $\text{Li}_3\text{AlF}_6$  exhibits a cathodic (anodic) limit of 0.56 V (6.0 V) versus bulk Li, while  $\text{Li}_3\text{PS}_4$  operates within a narrow window of 1.6–3.0 V. The electronically insulating and ionically conducting phase  $\text{LiF}$  is formed at low voltage, which may potentially serve as a passivating interphase that can act as a barrier against further solid electrolyte decomposition.

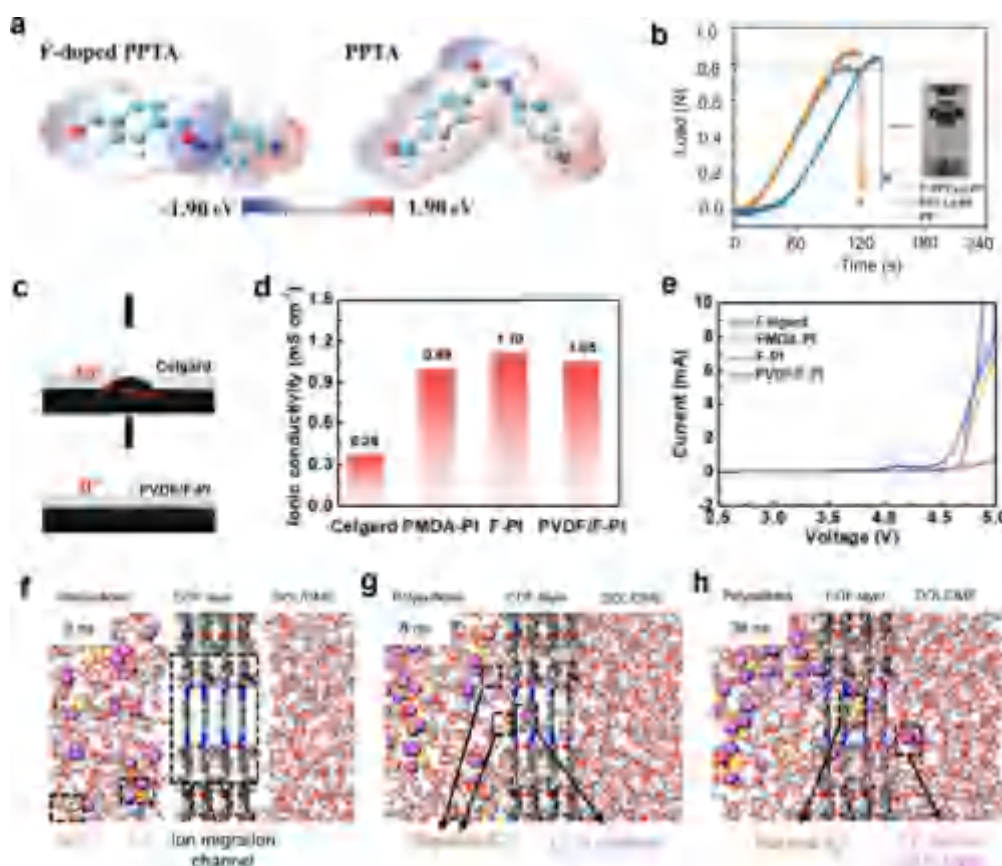
The LillNMC811 cells matched with  $\text{Li}_6\text{PS}_5\text{Cl}$  (LPSCl) electrolyte suffer from a fast capacity decay because the sulfide solid electrolyte is not stable to both the Li anode and the NMC811 cathode.<sup>206,207</sup> To solve this problem, Wang et al. added a small amount (0.32 wt %) of  $\text{CuF}_2\text{-LiNO}_3$  (CL) into LPSCl electrolyte to in situ form a mixed-conductive–lithiophobic and self-healing  $\text{LiF-Li}_3\text{N-Cu}$  SEI. The compatibility of LPSCl–CL electrolyte to single-crystalline NMC811 was further enhanced by adding a small amount (0.02 wt %) of  $\text{AlF}_3$ .<sup>208</sup> Doping F into LPSCl electrolyte largely improved the oxidation stability; thus, the LillNMC811 full cell achieved a high capacity retention of 69.4% after 100 cycles at 2.55 mA  $\text{cm}^{-2}$ /2.55 mAh  $\text{cm}^{-2}$ . In addition, Wang and co-workers reported F-doped  $\text{Li}_{5+y}\text{PS}_5\text{F}_y$  argyrodites with a tunable doping content and dual dopants ( $\text{F}^-/\text{Cl}^-$  and  $\text{F}^-/\text{Br}^-$ ) that were synthesized through a solvent-based approach, as shown in Figure 12e.<sup>205</sup> Among all compositions,  $\text{Li}_6\text{PS}_5\text{F}_{0.5}\text{Cl}_{0.5}$  exhibited the best cycling performance in Li symmetric cells owing to the enhanced interfacial stability against Li metal, which can be attributed to the formation of a stable SEI containing  $\text{Li}_3\text{P}$ ,  $\text{LiCl}$ , and  $\text{LiF}$ . Furthermore, Lill $\text{LiFePO}_4$  (LFP) cells using  $\text{Li}_6\text{PS}_5\text{F}_{0.5}\text{Cl}_{0.5}$  showed enhanced cycling performance with a specific discharge capacity above 105 mAh  $\text{g}^{-1}$  after 50 cycles. However, F doping also significantly reduced the ionic conductivity of LPSCl due to the high bonding between F and Li.<sup>209</sup> The excessive  $\text{LiF}$  precursor filled in the boundary/pore of the solid-state electrolytes after fluorine was incorporated into the LPSCl structure. This reduced the electronic conductivity while enhancing the rigidity to suppress the penetration of Li dendrites.

In conclusion, the electrolytes for high-performance Li-based batteries can be tailored by combining the benefits of different partially fluorinated/per-fluorinated electrolytes. Selective fluorination of the anions of Li salts will decrease their

interactions with  $\text{Li}^+$  cations, thereby increasing the dissociation of the salts in the electrolyte solution and lifting the ionic conductivity. Fluorinated solvents can also inhibit the progress of combustion, thus improving the safety of the electrolytes. It is important to achieve a balance between Li salt solubility and interfacial compatibility. Fluorinated additives containing well-tailored functional groups can transform into uniform and thickness controllable SEI/CEI films, which remains a hot field for future research. For the polymer all-solid-state electrolytes, the grafting of F-containing groups/chains on the polymer matrix can widen the electrochemical window and/or facilitate ion conduction; furthermore, F-containing polymers, such as PVDF and PVDF-HFP, have played a significant role in the quasi-solid-state gel polymer electrolytes. The exploration of fluorine chemistry in advanced solid-state battery systems aiming for enhanced performance is also in progress.

### 2.3. Other Fluorinated Battery Components

**2.3.1. Fluorinated Separators.** As an essential component in batteries, the separator not only offers transport paths for  $\text{Li}^+$  migration between two electrodes but also serves as a barrier isolating the cathode from the anode.<sup>210</sup> Despite their critical function, current commercial separators (e.g., polypropylene (PP), polyethylene (PE), and their multilayer composites) suffer from insufficient mechanical strength, inferior liquid electrolyte affinity, low thermal stability, and high flammability. The separator failure/collapse can lead to internal short circuits, potentially triggering thermal runaway, energy release, explosion, and other serious security risks in batteries.<sup>211</sup> Over the past few decades, intensive efforts have been dedicated to overcoming these limitations, among which polymeric separators,<sup>212–223</sup> blends and composites,<sup>224–226</sup> surface coating,<sup>227–229</sup> and surface grafting<sup>230–233</sup> have been mostly the focus. In particular, PVDF and its copolymers (e.g., PVDF–HFP, polyvinylidene-*co*-chlorotrifluoroethylene (PVDF–CTFE), poly(vinylidene fluoride)–trifluoroethylene (PVDF–TrFE)) have garnered great interest due to their high dielectric constant, strong polarity, and excellent anodic stability, which contribute to their good affinity toward polar electrolytes and their ability to assist in the dissociation of Li salts. For a detailed and specific summary of separators based on PVDF and copolymers, readers are encouraged to consult the excellent review articles.<sup>234,235</sup> It should be noted that the practical applications of PVDF separators are hindered by the low mechanical strength (<10 MPa) caused by their solubility in electrolytes combined with inferior thermal stability due to their low melting point (172 °C).<sup>225</sup> In addition, the formation of  $\text{LiF}$  and the  $\text{C}=\text{CF}$  bond in the crystallized PVDF, through interactions between F and Li or lithiated graphite, can resist  $\text{Li}^+$  transport and further deteriorate the rate capability of LIBs.<sup>236,237</sup> Blending two or more polymer solutions has been considered as an effective strategy to achieve complementary properties of each component. In 2014, Liu and co-workers blended PVDF–HFP with polyimide (PI) by cross-electrospinning, arranging the two polymer solutions alternately to construct a PVDF–HFP/PI composite membrane. This composite separator, combining the advantages of both polymers, demonstrated increased porosity, higher thermal dimensional stability, improved electrochemical stability, and higher ionic conductivity compared to the commercial Celgard 2400 separator.<sup>238</sup> Similarly, the poly(*m*-phenylene isophthalamide) (PMIA), known for its high mechanical strength and high temperature tolerance, was blended with PVDF to

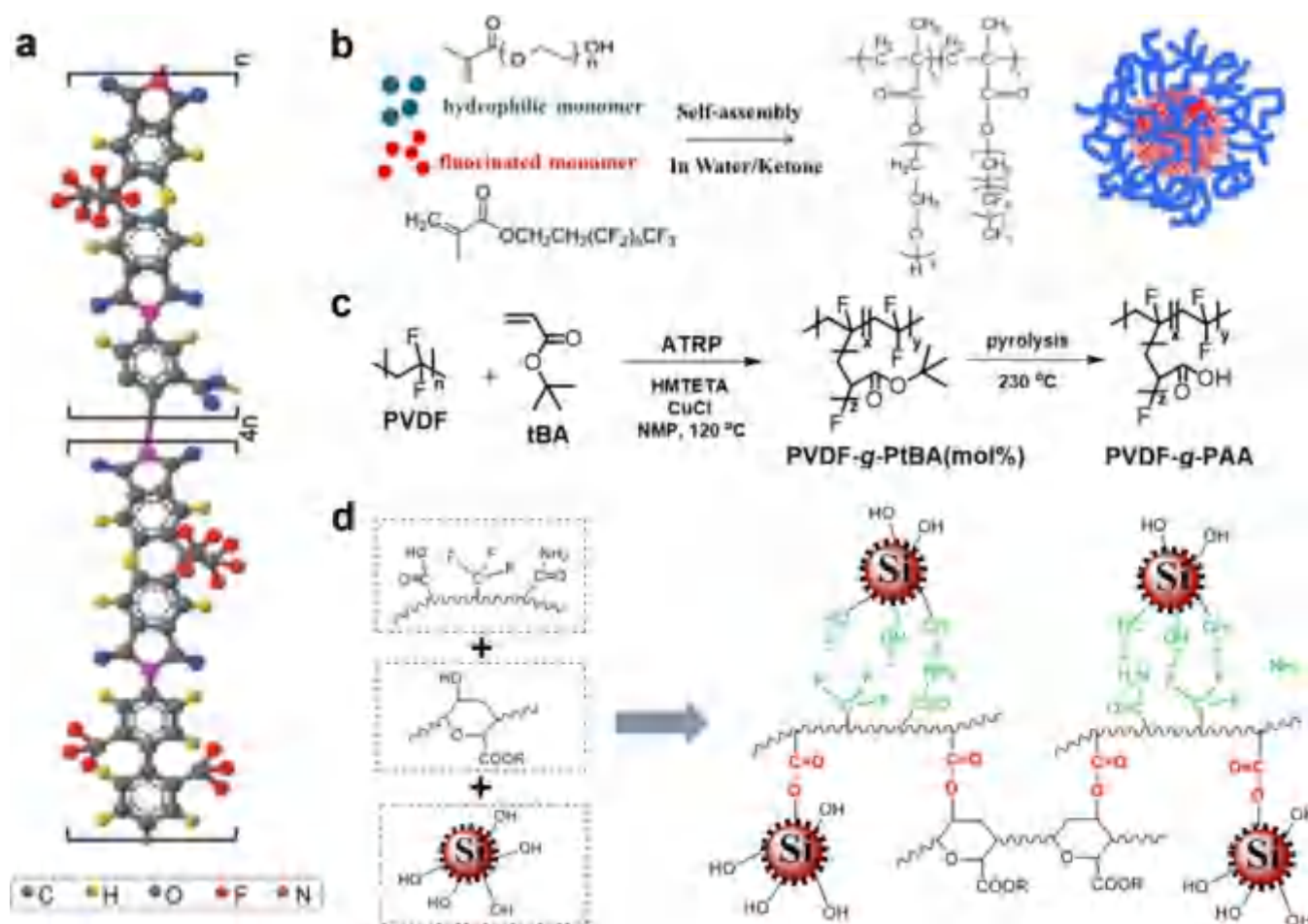


**Figure 13.** Functions of fluorinated separators in Li-based batteries. (a) Electrostatic potential surface for pristine PPTA and F-PPTA molecules. (b) Puncture strength curves of the PP, PPTA@PP, and F-PPTA@PP separators. Reproduced with permission from ref 243. Copyright 2022 Wiley-VCH. Evaluations of the (c) electrolyte contact angles, (d) ionic conductivity, and (e) LSV for the PVDF/F-PI separator and other separators. Reproduced with permission from ref 244. Copyright 2023 Wiley-VCH. Schematic illustration of the ion transport behavior through the fluorinated COF nanofluidic nanochannels at (f) 0, (g) 8, and (h) 38 ns. MD simulation results show that the fluorinated separator exhibits a higher Li<sup>+</sup> migration activity than the anion (TFSI<sup>-</sup> and S<sub>6</sub><sup>2-</sup>). Reproduced with permission from ref 245. Copyright 2023 American Chemical Society.

construct a sandwich-structured PVdF/PMIA/PVdF composite membrane. This membrane displayed high ionic conductivity, reinforced tensile strength (13.96 MPa), and excellent thermal stability as well as desirable electrochemical stability/rate performance for the assembled Li||LiCoO<sub>2</sub> battery.<sup>225</sup> The enhancement of the mechanical property and thermal stability of the PVDF-based separator was also achieved by blending with polyacrylonitrile (PAN).<sup>237</sup> Nevertheless, blending polymer solutions can increase the fiber diameter size and influence the fiber morphology, generally leading to a nonuniform fiber structure. Besides, the obtained ionic conductivity of the resulting blends needs to be further improved. To address these issues and enhance the separator properties such as electrolyte uptake, thermal stability, and ionic conductivity, nanoscale particles including Al<sub>2</sub>O<sub>3</sub>, SiO<sub>2</sub>, TiO<sub>2</sub>, and Sb<sub>2</sub>O<sub>3</sub> have been successfully incorporated into the polymer matrix.<sup>239,240</sup>

A variety of modification strategies have also been employed to enhance the physiochemical and electrochemical performance of the separators, among which the surface coating/grafting method has been considered as a promising candidate to address the above-mentioned drawbacks facing the common commercial separator.<sup>226,234</sup> By coating the composite material of graphite fluoride nanosheets (GFNs) and PVDF, the pristine PP separator was modified by Zhang et al. on a large

scale. Attributed to the reaction between GFNs and Li, a concrete-like protective layer with improved mechanical properties was constructed on the Li metal anode, enabling fast Li<sup>+</sup> transport, resisting Li dendrite growth and maintaining good integrity as well. In addition, owing to the lithiophilic feature of GFNs, sufficient physical contact between the Li anode and the protective layer was achieved, realizing low interphasial resistance and homogeneous Li deposition layer by layer.<sup>241</sup> As the most electronegative elements that have been known, F is capable of forming the strongest single covalent bond of C–F with a bond energy of 488 kJ mol<sup>-1</sup>.<sup>242</sup> A F-modified PPTA (poly-*p*-phenyleneterephthalamide) protective layer on the PP separator (F-PPTA@PP) was developed via coating PPTA nanofibers on a commercial PP membrane and subsequently grafting F-containing groups on the separator. As shown in Figure 13a, an F atom was grafted on the PPTA (F-doped PPTA) via a C–F bond, where the generated electronegativity around the C–F bond endowed a stronger organic affinity to promote the electrolyte wettability. This F-PPTA@PP separator exhibited high thermal stability to suppress thermal shrinkage, excellent physical strength to prevent potential mechanical abuse, and good capability to simultaneously in situ construct a LiF-rich SEI layer to promote the uniform electrodeposition of Li and eliminate Li dendrite risks (Figure 13b). With this separator, the assembled



**Figure 14.** Developments of fluorinated binders for enhancing electrode performance. (a) Molecular structures of synthesized FPI. Reproduced with permission from ref 262. Copyright 2018 Wiley-VCH. (b) Scheme of the preparation for self-assembled fluorinated copolymers. Reproduced with permission from ref 269. Copyright 2018 American Chemical Society. (c) Preparation routes for amphiphilic graft copolymer precursors (PVDF-g-PtBA) and pyrolytic transformation to PVDF-g-PAA. Reproduced with permission from ref 270. Copyright 2016 Wiley-VCH. (d) Illustration of the dual-cross-linked network combining covalent bonds and hydrogen bonds among the designed fluorinated copolymer, sodium alginate, and the Si surface. Reproduced with permission from ref 271. Copyright 2019 American Chemical Society.

LillNCM811 battery featured an initial capacity of 194.1 mAh g<sup>-1</sup> at 0.5 C and a stable cycling performance for over 1000 cycles. Under various extreme conditions, such as a wide temperature range from -10 to 100 °C, an ultrafast charging/discharging rate of 30 C, and lean electrolyte/high mass loading, the battery exhibited promising electrochemical performance.<sup>243</sup> Very recently, a novel fluorine-functionalized PVDF/fluorinated-PI (FPI) composite nanofibrous separator was developed for wide-temperature LMBs.<sup>244</sup> On one side, the abundant polar -CF<sub>3</sub> groups in the F-PI composite provided an electronegative environment for fast Li<sup>+</sup> transfer. Besides, the -CF<sub>3</sub> group contributed to enhanced thermal stability and fire retardancy for enabling the operation of LMBs in a wide temperature range. On the other side, the incorporation of PVDF enhanced the mechanical properties by increasing physical contacts among the F-PI nanofibers and facilitated the uniform Li deposition via homogenizing the pore size as well. This F-functionalization treatment endowed the separator not only with increased affinity toward organic electrolytes and high value of ionic conductivity but also a wider ESW (Figure 13c-e). Based on this separator, the LillLi cell sustained a steady cycling of 2400 h at 1 mA cm<sup>-2</sup> with an areal capacity of 1 mAh cm<sup>-2</sup>, which survived for 1000 h with a

low overpotential of 15 mV at 60 °C. Briefly, the fluorination method offers a promising and facial strategy for enhancing the overall properties of the separator, including the electrolyte wettability, ionic conductivity, thermal stability, and electrochemical stability, thus effectively resisting safety risks and improving the electrochemical performance of LMBs.

As one of the most promising high-energy Li-based rechargeable battery systems, the practical Li-S battery has been restricted by the irreversible cathode consumption due to the polysulfide shuttling as well as notorious Li dendrite growth, inducing severe capacity fading during cycling. Introducing modification layers or interlayers on separators has been adopted as a feasible strategy for entrapping negatively charged sulfur species.<sup>246,247</sup> Particularly, to utilize the polar active site of F atoms for immobilizing polysulfides, Dominko et al. synthesized fluorinated reduced graphene oxide (F-rGO) to act as a separator interlayer, which prevented the polysulfide shuttling and achieved improved cycling performance.<sup>248</sup> Unfortunately, the usage of fluorine gas or XeF<sub>2</sub> brings safety concerns for practical applications. Via a facile, cost-effective, safe, and scalable approach, fluorinated carbon was successfully constructed on a PP separator. Thanks to the strong chemical bonding ability of the F groups and physical



adsorption of the mesoporous structure, the polysulfide shuttling was suppressed significantly. In addition, the F doping induced a pseudocapacitive effect for fast  $\text{Li}^+$  diffusion, affording a dense and homogeneous Li deposition during repeated cycling.<sup>249</sup> However, most separator coating layers are unfavorable for the transfer/migration process of  $\text{Li}^+$ .<sup>250,251</sup> Very recently, a fluorinated covalent–organic framework (4F-COF)-based nanofluidic membrane was constructed for regulating the Li–S battery performance. The fluorine functionalities endowed the 4F-COF permselective nanofluidic channels to contain negatively charged sites, allowing  $\text{Li}^+$  cations to enter the 4F-COF layers while repelling the anion ( $\text{S}_6^{2-}$ ) transport (Figure 13f–h). With the fluorinated COF/PP separator, a highly stable Li metal was achieved with plating/stripping for 2000 h at  $1 \text{ mA cm}^{-2}$ . Besides, the assembled Li–S batteries demonstrated a stable cycling performance for over 1000 times with 82.3% capacity retention at 2 C, a high rate capability with  $568.0 \text{ mA h g}^{-1}$  at 10 C, as well as an areal capacity of  $7.60 \text{ mA h cm}^{-2}$  at a high sulfur cathode loading ( $\sim 9 \text{ mg cm}^{-2}$ ).<sup>245</sup>

**2.3.2. Fluorinated Binders and Current Collectors.** It is commonly known that during battery cycling, the electrodes are vulnerable to mechanical stress (i.e., severe volume changes for conversion- and alloy-type electrodes). Therefore, insufficient binding strength leads to severe pulverization and further capacity degradation. Thus, serving to provide the cathode and anode electrodes with both interconnected structures and mechanical strength for sufficient electron transport and ion migration upon charging/discharging, the polymeric binder is of vital significance to the battery performance.<sup>252</sup> Recently, owing to the high thermal stability, strong adhesive strength, and electrochemical/chemical inertness with a symmetrical linear F-bonded carbon skeleton, PVDF has been recognized as the earliest and most popular binder material for commercial LIBs. However, with the increasing versatile requirements of practical battery technologies, the current polymer binders should not only act as a binding reagent but also provide different functionalities, including high ionic/electric conductivity, stable electrode/electrolyte interphase, excellent polysulfide anchoring capability, and improved mechanical strength to buffer the volume change. These features cannot be achieved by the current PVDF binder. Especially at large volume expansion, conventional PVDF binder will lose the adhesion as a result of the slippage of the linear chain in the electrode.<sup>253</sup> More specific reviews focusing on different binders and their corresponding developments have been conducted earlier.<sup>254–256</sup> In this section, we will mainly introduce the mechanisms and properties of fluorinated binders on the electrodes and further on the battery performance. The design and application of fluorinated binders in Li-based batteries will provide opportunities to develop advanced binders.

When it comes to layered oxide cathode materials represented by  $\text{LiCoO}_2$ , PVDF has been the most widely used binder in industry. It was found that the crystallinity of PVDF was reduced via embedding maleic anhydride-grated-PVDF (MA-g-PVDF) into PVDF, which is favorable for improving electrolyte uptake. As a result, the rate capability and cycle performance of the  $\text{LiCoO}_2$  cathode were enhanced.<sup>257</sup> However, it was pointed out that the reduced crystallinity of PVDF with a lower molecular weight led to the decreased adhesion strength.<sup>258</sup> Therefore, the crystallinity degree should be carefully optimized and balanced to fulfill the

cathode performance. Unfortunately, it was demonstrated that the PVDF binder can be changed when charging the cathodes to a high voltage above 4.3 V. Due to the weak cohesive force, PVDF is unable to generate a robust layer on the cathode surface and easily causes detachment between cathodes and current collectors, which finally leads to continuous electrolyte decomposition and rapid capacity decay for high-voltage cathodes.<sup>259–261</sup> Therefore, it is necessary to explore electrochemically inactive binders beyond PVDF. With the obvious advantage of strong adhesion to the electrodes and good thermal stability, PI has been proved to improve the battery performance. By introducing six  $-\text{CF}_3$  functionalities per unit in the PI backbone (Figure 14a), the fluorinated PI (FPI) showed faster ion transfer, greater resistance to electrochemical oxidation, as well as higher thermal stability. The FPI had excellent binding ability to mitigate the degradation issue of the Li-rich cathode at 4.7 V while functioning as a surface protective layer on the cathode via constructing a robust thin film. The resulting cathode presented improved cycle stability in both half cells and full cells when paired with graphite anodes.<sup>262</sup> Moreover, employing ionic conductive polymers such as poly(ionic liquid)s (PILs) or single-ion conducting polymers (e.g., PEO) as binders has been considered as an effective strategy to improve the ionic conductivity and  $\text{Li}^+$  diffusion rate for high-performance LIBs.<sup>263–267</sup> Typically, cationic or anionic species are bonded to polymer backbones in the PILs, contributing to the high  $\text{Li}^+$  ionic conductivity as well as wide ESW.<sup>268</sup> By incorporating the ionic conducting lithiated poly(perfluoroalkylsulfonyl)imide (PFSILI) ionene with PVDF to serve as the binder, the  $\text{LiFePO}_4$  cathode exhibited increased working voltage, lower electrochemical polarization, and higher reversibility than that with PVDF binder, especially operated at elevated temperatures or high current rates. Besides, a higher reversible capacity and energy density (1.50 and 1.66 times) of the  $\text{LiFePO}_4$  cathode was enabled compared to the cathode with PVDF binder.<sup>266</sup> Lithiated perfluorosulfonate ionomer (Li–Nafion) was reported to demonstrate similar effects as the binder for  $\text{LiMn}_2\text{O}_4$  cathodes. The resultant Li–Nafion binder displayed an ionic conductivity of  $1.4 \times 10^{-4} \text{ S cm}^{-1}$ , generating an ion conducting layer on the  $\text{LiMn}_2\text{O}_4$  cathodes, which reduced the interphase resistance for high-rate cycling (5–20 C) and stabilized the cathode even at high temperature (60 °C).<sup>267</sup> Zhao et al. prepared an ionic conducting binder by pairing sulfonated polyether ether ketone with pendant lithiated fluorinated sulfonic groups (SPEEK-FSA–Li) in which sulfonated aromatic poly(ether ketone) had good thermal/mechanical stability; meanwhile, the charge delocalization over the lithiated fluorinated sulfonic side chains exhibited low lithium dissociation energy for improving  $\text{Li}^+$  conductivity. The SPEEK-FSA–Li binder contributed to a much smaller interphasial and charge transfer resistance, an enhanced discharge plateau voltage, and a higher reversible capacity for the  $\text{LiFePO}_4$  cathode, in contrast with that using PVDF binder.<sup>265</sup> Recently, the pyrrolidinium-type poly-(diallyldimethylammonium) (PDADMA) with fluorinated anions was used as a cathode binder, wherein the fluorine content (e.g., FSI, TFSI, bis(perfluoroethylsulfonyl) imide (BETI), and nonafluoro-1-butanedisulfonate (CFSO)) led to highly delocalized charge density for facilitating  $\text{Li}^+$  transport. The consequent high-voltage  $\text{LiNi}_{0.5}\text{Co}_{0.2}\text{Mn}_{0.3}\text{O}_2$  (NCM 523) electrode achieved improved rate capability and stable cycling performance.<sup>268</sup> Introducing ion conducting materials into

polymer binders is considered as another effective strategy to improve the overall electrochemical performance of LIBs. Copolymerizing the hydrophilic 2-(perfluorohexyl) ethyl methacrylate (PFHEMA) and hydrophobic poly(ethylene glycol) methacrylate (PEGMA), Kuo and co-workers designed a Li<sup>+</sup> conducting waterborne fluorinated binder (Figure 14b). The fluorinated moiety was expected to improve the electrochemical stability and adhesive properties, while the PEO segments in PEGMA achieved higher ionic conducting ability. The copolymer can self-assemble into a series of spherical nanoparticles (150–220 nm) dispersed in aqueous solution. The results showed that with an optimal ratio of 3:1 (PFHEMA:PEGMA), the LiFePO<sub>4</sub> cathode delivered great cyclability over 150 cycles without obvious capacity decay and nearly 100% CE.<sup>269</sup>

Relying on the weak van der Waals force to connect active materials and other components within the electrodes, a conventional PVDF binder is unsuitable for alloy-type anode materials (e.g., Si) with drastic volume changes during battery cycling. In general, the ideal binders for alloy-type anodes should be chemically stable at elevated temperatures, electrochemically inert to sustain a wide ESW, and mechanically tolerant to withstand extensive stresses while maintaining ionic or electronic conducting ability.<sup>272,273</sup> It has been elucidated that heating a Si electrode containing 8 wt % PVDF at 300 °C contributed to a more uniform distribution of PVDF on the surface of the active materials, which largely enhanced the adhesive strength and viscoelasticity for improved cycle performance with 600 mAh g<sup>-1</sup> available capacity after 50 cycles.<sup>274</sup> Nevertheless, less than 20% of the theoretical specific capacity of the Si anode was left, which is still far from the requirement of practical application. Thus, combining PVDF with other polymers can be developed to satisfy the needs of high-performance Si-based anode materials. Based on a tether model in which the binder was filled with carbon black, Dahn and co-workers designed an elastomeric binder of terpolymer PVDF fluoride-tetrafluoroethylene ethylene copolymer (PVDF-TFE-P) for the Si<sub>0.64</sub>Sn<sub>0.36</sub> alloy anode.<sup>275</sup> It was noted that 3-aminopropyltriethoxysilane was added as an adhesion promoter in the electrode, providing –NH<sub>2</sub> to bond with the carbon–carbon double bond in the backbone of PVDF-TFE-P. The resulting Si<sub>0.64</sub>Sn<sub>0.36</sub> anode exhibited a stable reversible capacity of ~800 mAh g<sup>-1</sup> with a volume change of 125%. To further improve the PVDF performance in Si-based anode materials, amphiphilic graft copolymer precursors PVDF-graft-poly(*tert*-butyl acrylate) (PVDF-g-PtBA) have been synthesized, wherein poly(acrylic acid) (PAA) with abundant carboxylic acid (–COOH) groups was generated through in situ pyrolytic transformation of PtBA (Figure 14c). Taking advantage of the synergistic effects from polymeric backbones (PVDF and PAA segments), excellent mechanical properties against volumetric expansion were achieved, enabling high charge and discharge capacities of 2672 and 2958 mAh g<sup>-1</sup>, respectively, along with a stable cycling performance over 50 cycles with 84% retention at 0.2 C. Moreover, this graft copolymer binder was proved to be effective in fulfilling the capability of both the LiN<sub>0.5</sub>M<sub>1.5</sub>O<sub>4</sub> cathode and the natural graphite (NG) anode, contributing to a high energy density of 546 Wh kg<sup>-1</sup> along with ~70% capacity retention after 50 cycles at both 0.5 and 1 C (1 C = 145 mA h g<sup>-1</sup>) for the Si/NG||LiN<sub>0.5</sub>M<sub>1.5</sub>O<sub>4</sub> full battery.<sup>270</sup> As an alternative choice, owing to the apolar structures and enriched hydrogen-bonding sites, polytetrafluoroethylene

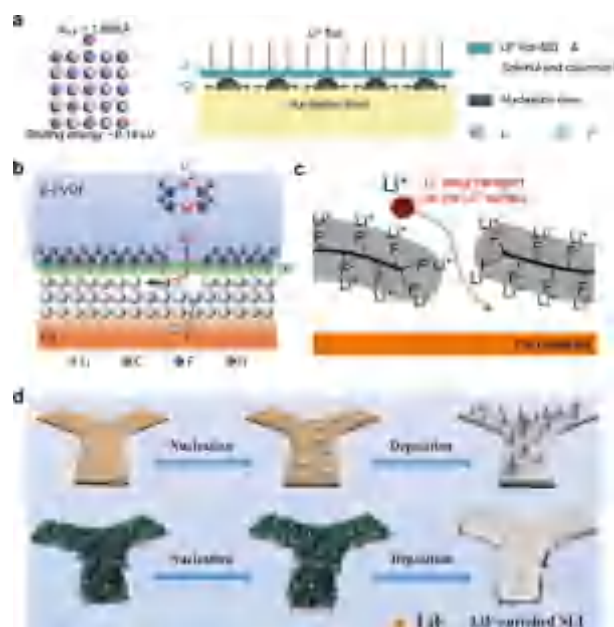
(PTFE) possessing high mechanical strain and tenacity was introduced, forming a PVDF-*b*-PTFE copolymer binder combining the high viscosity of PVDF with the high elasticity of PTFE. Besides, this binder achieved high ionic conductivity and thermal stability. As a consequence, the binder forms cobweb structures to coalesce Si particles, maintaining good electrical contact of the electrode materials during repeated cycles for superior cycle stability (~1000 mA h g<sup>-1</sup> capacity retained over 250 cycles).<sup>276</sup>

To strengthen the mechanical properties and further enhance the cycle stability of the Si-based electrodes, three-dimensional (3D) cross-linked binders with strengthened mechanical properties exhibited strong resistance to irreversible deformation of the Si-based electrodes, but they increased the stiffness of the electrode and finally deteriorated the electrochemical performance of the batteries.<sup>276–280</sup> From this point, Zhang et al. designed a fluorinated copolymer with massive polar groups (carboxylic acid, amide, and fluorinated groups) followed by thermal polymerized with sodium alginate (SA) to construct a dual-cross-linked network binder (FP2SA). It was found that esterification reactions among these functional groups formed a chemical cross-linked network; meanwhile, fluorine and nitrogen enhanced the reversible mechanical features during volume changes (Figure 14d). The uniqueness of this FP2SA, relying on both chemical and physical cross-linking, was able to maintain the structural integrity of the Si electrodes, contributing to a high specific capacity of 1557 mAh g<sup>-1</sup> after 200 cycles at 4 A g<sup>-1</sup>. More importantly, FP2SA binder also significantly improved the cycling performance of the Si–C electrode and the SiO–C electrodes with specific capacities of 600 mAh g<sup>-1</sup> after 200 cycles at 0.5 A g<sup>-1</sup> and 310 mAh g<sup>-1</sup> after 700 cycles at 1 A g<sup>-1</sup>, respectively.<sup>271</sup> However, it was revealed that an excessive cross-linked degree and fluorine content of the fluorinated binder could reduce the capacity and cycle stability of the Si-based electrodes, indicating a moderate cross-linking degree should be considered in designing such binders. In addition, lithiated fluorine-containing ionomers have been demonstrated as effective binders to improve the Li<sup>+</sup>-ion diffusion as well as ionic conductivity, especially cycling at high rates. Wen and co-workers developed a novel fluorine-containing ionic binder (lithiated sulfonated poly(ether–ether–ketone)) with sulfonimide groups and structural flexibility, i.e., SPEEK-PSA-Li. Compared with other binders, the ionic conducting SPEEK-PSI-Li binder exhibited high adhesion properties and significantly decreased overpotential during high-rate cycling. Owing to the combined features of high cohesion capability, low solubility in electrolytes, high adaptability to volume change, and high ionic conductivity, the Si anodes displayed superior electrochemical performance under high-rate cycling, i.e., maintained reversible capacities of 2000 and 500 mAh g<sup>-1</sup> at current densities of 400 and 2000 mA g<sup>-1</sup>, respectively, after 50 cycles.<sup>281</sup>

Serving as an indispensable component to support both electrodes and to transport electrons between electrodes and the external circuit, the current collector plays a critical role in guaranteeing the highly efficient operation of LIBs. Since the commercialization of LIBs, Al and Cu foils have been the most widely used current collectors in the cathodes and anodes, respectively.<sup>282</sup> Nevertheless, electrochemical dissolution of Al and Cu current collectors still occurs during cycling, which is induced by the electrolyte decomposition or side reactions between electrolyte components and these current collectors.

As mentioned above, although the LiTFSI salt possesses advantageous properties such as high ionic conductivity, good thermal stability, and chemical inertness toward the active material, water contaminant, as well as other battery components, it fails to repassivate the Al foil by forming a fluorinated interphase. More specifically, the TFSI<sup>−</sup> readily reacts with Al<sup>3+</sup>, which is released from the Al<sub>2</sub>O<sub>3</sub> passivation film, forming the soluble aluminum bis-(trifluoromethanesulfonyl)imide (Al(TFSI)<sub>3</sub>) product. The Al(TFSI)<sub>3</sub> then dissolves well in organic carbonate electrolytes and diffuses to the bulk electrolyte, causing severe capacity decay of Li-based batteries.<sup>283</sup> Despite huge attention having been paid to electrode materials engineering to enhance the battery performance, insufficient attention has been focused on this aspect, especially regarding the effects of fluorine chemistry on the current collectors. Since the review conducted by Lota et al. discussed the positive influence of fluorinated species on the Al current collector on the cathode performance, this section will mainly focus on the anode current collectors.<sup>283</sup>

Over the past few decades, intensive efforts have been devoted to achieving the dendrite-free plating/stripping of the Li anode, including SEI reconstruction,<sup>146,168,276,284–292</sup> uniformization of the Li-ion flux,<sup>293,294</sup> and 3D nanostructured scaffolds.<sup>295–300</sup> Among the existing approaches, interphase design and construction have been considered as an effective way to overcome problems toward the anode. Especially, the construction of halogenated interphases (e.g., LiF) is expected to effectively passivate the active Li surfaces, regulate the Li<sup>+</sup> migration, suppress Li dendrite nucleation/growth, and enhance the interphase mechanical stability.<sup>301–303</sup> A columnar and uniform Li anode was designed by Zhang and co-workers through a LiF-enriched Cu current collector. When directly immersing a Cu foil into an aqueous LiPF<sub>6</sub> solution, the in situ hydrolysis of LiPF<sub>6</sub> occurred and coated LiF particles on the Cu surface. The LiF (100) was calculated to give a weaker binding energy and higher diffusion energy barrier to Li than that of the Cu surface (Figure 15a), rendering a uniform spatial distribution of Li<sup>+</sup> and further contributing to the Li deposition with column structures. As a consequence, these ultrathin and columnar Li anodes exhibited highly improved cycle stability in both carbonate- and ether-based electrolytes.<sup>304</sup> As discussed earlier, PVDF has been extensively used as a binder, separator, or polymeric electrolyte in Li-based batteries. It is known that contrary to the nonpolar  $\alpha$  phase PVDF with a trans–gauche–trans–gauche conformation, the  $\beta$  phase PVDF presents an all-trans conformation with F and H atoms distributed on the opposite sides of the PVDF backbone, which contributes to a high dielectric constant within 8–13. A thin ( $\sim 4\ \mu\text{m}$ )  $\beta$ -PVDF was coated on the Cu current collector, achieving a uniform plating/stripping of Li at high current densities of 5 mA cm<sup>−2</sup>, a high plating capacity of up to 4 mAh cm<sup>−2</sup>, along with excellent cyclability. It was inferred that the strong interactions between Li<sup>+</sup> and the polar C–F groups of  $\beta$ -PVDF could redistribute the Li<sup>+</sup> flux, while the reaction of the PVDF surface and the fresh Li metal might form a stable and protective SEI layer. Besides, as illustrated in Figure 15b, the F alignment not only could promote the interaction between C–F and Li for layer-by-layer Li deposition but also offered preferential diffusion paths for Li<sup>+</sup> hopping across the coating layer. This work highlights that constructing an electronegative F-rich interphase is favorable for the layer-by-layer Li deposition.<sup>305</sup> Another effective approach to enriching LiF on Cu substrate is



**Figure 15.** Role of fluorine modification of current collectors on constructing the stable SEI and regulating the Li deposition. (a) Theoretical calculations of the binding energy for Li on the LiF (100) surface, and schematic illustration showing the Li deposition process regulated by LiF (Note: (1) LiF-rich SEI leads to a uniform spatial distribution of Li<sup>+</sup>, (2) uniform and dense nucleation sites are generated on the Cu foil and grow horizontally from these nucleation sites). Reproduced with permission from ref 304. Copyright 2017 Wiley-VCH. (b) Schematics of the layer-by-layer deposition and preferential diffusion pathways for Li<sup>+</sup>. Reproduced with permission from ref 305. Copyright 2018 Wiley-VCH. (c) Mechanism illustration of the SEI growth on the F-ECG surface after Li plating/stripping. Reproduced with permission from ref 309. Copyright 2022 Elsevier. (d) Schematic illustration of the Li nucleation and plating process on the pure Ni foam and the NiF<sub>x</sub>@NF current collectors. Reproduced with permission from ref 311. Copyright 2020 Elsevier.

employing fluorinated carbon materials such as fluorinated porous carbon materials and fluorinated carbon nanotubes.<sup>306,307</sup> For instance, Zhi et al. designed a 3D-fluorinated porous carbon as the multifunctional host, which mitigated dendrite growth and was retained for over 300 cycles with an average CE of 99% at 0.5 mA cm<sup>−2</sup> (cycling capacity of 1 mAh cm<sup>−2</sup>). Nevertheless, this host matrix sustained only 70 cycles with fluctuated CE when increasing the current density and cycling capacity to 2 mA cm<sup>−2</sup> and 2 mAh cm<sup>−2</sup>, respectively.<sup>308</sup> Based on this work, a novel LiF-rich dual-functional coating layer was designed on a Cu surface by Su and co-workers using fluorinated electrochemically exfoliated graphene (F-ECG) as a modifier. Thanks to the strong interlayer adhesion, the F-ECG layer could prevent volume expansion during plating/stripping cycles. In addition, LiF-enriched SEI film was successfully generated due to the reaction between Li and CF. This suppressed side reactions and facilitated Li<sup>+</sup> transport across the coating layer for a dendrite-free Li anode with long-term stability (Figure 15c).<sup>309</sup> In another report, a self-assembled monolayer (EAM) of 1,3-benzenedisulfonyl fluoride was introduced on the Cu substrate, where the benzenesulfinate created lithiophilic sites and fluoride generated a LiF nuclei in situ via self-assembly and thiol–Cu reaction. Notably, the EAM-modified Cu displayed a multilayer SEI composed of a LiF-enriched inner layer and an



amorphous outer layer, regulating the Li nucleation and uniform Li growth on the Cu substrate.<sup>310</sup>

Apart from introducing a F-rich coating/modification layer on the Cu current collector, the Li halides (e.g., LiF) can also be formed via the reaction between metal halides and highly active Li, achieving highly enhanced interphasial stability.<sup>312</sup> Through a one-step fluorination treatment, a hybrid  $\text{NiF}_x/\text{NF}$  current collector consisting of vertical lithiophilic  $\text{NiF}_x$  nanosheets and Ni foam was developed by Huang et al. The  $\text{NiF}_x$  decreased the Li nucleation barrier and served as even nucleation sites for Li deposition. Besides, a LiF-enriched SEI derived from the reaction between  $\text{NiF}_x$  and Li during the initial Li plating was constructed, ensuring smooth Li deposition (Figure 15d). Benefiting from this 3D  $\text{NiF}_x/\text{NF}$  current collector, outstanding Li stripping/plating with a CE of  $\sim 98\%$  over 450 cycles was obtained (at  $1 \text{ mA cm}^{-2}$  and  $1 \text{ mAh cm}^{-2}$ ). The  $\text{Li}@\text{NiF}_x/\text{NF}$  symmetric cell demonstrated a long cycle life over 1300 h with a low overpotential of  $\sim 20 \text{ mV}$  ( $1 \text{ mA cm}^{-2}$ ,  $1 \text{ mAh cm}^{-2}$ ). Remarkably, the as-prepared  $\text{Li}@\text{NiF}_x/\text{NF}||\text{LFP}$  full cell exhibited reasonable cycle performance and rate capability.<sup>311</sup> Recently, using a facile and safe  $\text{NF}_3$  plasma fluoridized strategy, the  $\text{NiF}_2$  layer was successfully coated on Ni foams (NFF). Following the same way, the  $\text{Li}^+$  flux preferentially deposited on the  $\text{NiF}_2$  sites, which was evenly distributed around the Ni surface. Also, the LiF-rich SEI layer from the  $\text{NiF}_2$  reaction toward Li greatly enhanced the interphasial stability. As a result, the  $\text{NFF}@\text{Li}$  anode sustained a long durability over 1600 cycles at  $1 \text{ mA cm}^{-2}$  and over 2000 cycles at  $2 \text{ mA cm}^{-2}$ . Moreover, the  $\text{NFF}@\text{Li}||\text{LFP}$  full battery delivered a high-capacity retention of 93% over 250 cycles at  $1 \text{ C}$ . These works demonstrated that constructing a lithiophilic metal fluoride coating is effective in regulating the Li deposition for a high-performance Li metal anode.<sup>313</sup>

Besides current collector modifications, interphase engineering has been recognized as a crucial strategy to stabilize the Li anodes since most of the knotty issues restricting the performance of Li metal anodes can be attributed to the instability of the Li anode/electrolyte interphase. Among them, constructing fluorinated interphases demonstrates prominent advantages in passivating active Li surfaces, regulating the diffusion and migration of  $\text{Li}^+$ , as well as enhancing the interphase mechanical stability. In particular, LiF has been determined to possess many extreme properties relative to other solids. The large band gap ( $14.6 \text{ eV}$ ) and the wide electrochemical stability window (from 0 to  $6.4 \text{ V}$  vs Li) of LiF contribute to the high electrochemical stability for inhibiting the continuous corrosion of active metallic Li;<sup>314</sup> the high Young's modulus ( $65 \text{ GPa}$ ) along with a high shear modulus ( $49 \text{ GPa}$ ) effectively enhance the mechanical stability of the SEI to enable long-term cycling;<sup>315</sup> the high interphase energy ( $\gamma$ ) can promote a uniform Li distribution and smooth Li deposition behaviors<sup>316</sup> with the negligible solubility of LiF in most electrolytes,<sup>303</sup> etc. A variety of strategies, including physical methods and chemical strategies, have been developed to construct a LiF-rich artificial SEI.<sup>289,317–329</sup> Compared with physical methods, chemical approaches (e.g., gas-, liquid-, and solid-phase reaction methods) via regulating chemical reactions between Li- and F-containing precursors were used to resolve the interphase issues between the artificial layer and the Li metal matrix. As a representative F-containing gas reaction strategy, a LiF coating was developed via treating Li metal in fluorine gas flow. The LiF layer was chemically stable and mechanically strong, significantly suppressing the

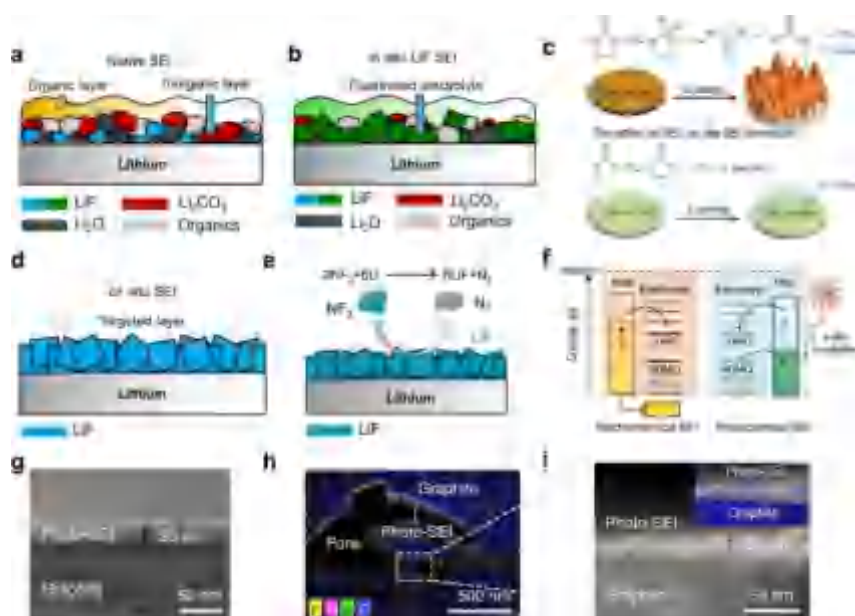
corrosion reaction between Li and carbonate electrolytes and thus realizing steady cycling for over 300 times with a high current density of  $5.0 \text{ mA cm}^{-2}$ .<sup>289</sup> The gas reaction method will not introduce other impurities; however, great attention should be paid to fluorine gas during operation to prevent leakage. In contrast, the LiF-rich interphases constructed via liquid-phase deposition/reaction strategies have been recognized as simpler and more effective strategies. By interposing an oil drop enriched in C–F (perfluoropolyether, PFPE) with low surface energy, a flowable fluorinated interphase was constructed for stabilizing the Li metal and regulating the Li plating. The electron-withdrawing feature of F endows the PFPE with high thermal and oxidative stability, along with good chemical inertness and nonflammability. In addition, the PFPE moieties close to the Li triggered C–F and Li–F species to reinforce the robustness of the SEI and the compactness of the Li plating.<sup>322</sup> Polymeric coating layers generally display superior mechanical deformability and low density, which are promising for constructing LiF-rich interphases. As reported by Goodenough et al., after incorporating graphite fluoride (GF) in molten Li at  $250^\circ\text{C}$ , a LiF layer was produced by the strong reaction between Li metal and the GF, eventually obtaining a GF–LiF protective layer. This as-prepared composite Li metal anode demonstrated high stability in an ambient environment as well as comparable electrochemical performance.<sup>330</sup>

To conclude, fluorine plays a critical role in modifying other components for enhancing the battery performance. Regarding separators, structural modifications and blending with other polymers or inorganic nanoparticles can address limitations such as low mechanical strength, thermal instability, and  $\text{Li}^+$  transport restrictions of PVDF. Besides, fluorine modification (e.g., surface coating and grafting method) can improve fire retardancy, mechanical abuse resistance, and LiF-rich SEI formation in Li metal batteries. Meanwhile, the abundant polar  $-\text{CF}_3$  groups would offer an electronegative environment to promote  $\text{Li}^+$  transfer. For binders, the fluorine group can be incorporated into polymer binders, enhancing ion transfer, oxidation resistance, and thermal stability, while fluorinated anions combined with ionic conductive polymers improve the binder performance for the cathode. However, excessive fluorine content in binders may compromise the specific capacity and cycle stability of these electrodes. When utilizing to modify current collectors with Li metal anodes, construction of LiF interfaces on Cu current collectors is expected to passivate the active Li surface and regulate the  $\text{Li}^+$  migration, further suppressing Li dendrite growth.

### 3. UNDERSTANDING FLUORINATED INTERPHASES IN LI-BASED BATTERIES

#### 3.1. Fluorinated Solid Electrolyte Interphases on Anodes

It is now broadly accepted that the SEI is significant for Li-based battery systems. In 1979, Peled et al. reported a SEI model that was applicable to all alkali metals in nonaqueous battery systems.<sup>331</sup> The SEI layer forms instantaneously upon contact between the anode and the electrolyte solution and consists of insoluble and partially soluble products generated by the reduction of electrolyte components. It exhibits properties similar to a layer of solid electrolyte with high electronic resistivity. As reported in recent years, the SEI played a significant role in determining the safety, power capability, reversibility, and cycle life of Li-based batteries.<sup>332</sup> The SEI must be both mechanically stable and flexible and



**Figure 16.** Different formation paths of the fluorinated SEI. (a) Native SEI from conventional carbonate electrolytes without fluoride enrichment. (b) In situ LiF-enriched SEI from fluorine-rich electrolytes. Reproduced with permission from ref 342. Copyright 2020 PNAS. (c) Decomposition mechanism of EC and FEC and the effect on SEI formation at the Li metal anode and Li diffusion near the anode surface. Reproduced with permission from ref 130. Copyright 2019 Wiley-VCH. (d) Ex situ LiF-enriched SEI from nonelectrolyte fluorine sources. (e) Schematic of the Li–NF<sub>3</sub> reaction to form LiF layers on Li. Reproduced with permission from ref 342. Copyright 2020 PNAS. (f) Distinct energy schemes in the formation of the SEI using electrochemical and photochemical approaches. (g) Cs-TEM image of the photographite with the photochemically driven SEI layer. (h) Low-magnification energy-dispersive X-ray spectroscopy (EDS) elemental map of the photo-SEI inside the pores of the photographite electrode. (i) High-magnification Cs-TEM image of the photo-SEI image and the corresponding EDS map (inset). Reproduced with permission from ref 343. Copyright 2021 Springer Nature.

should adhere well to the anode, while it is crucial to prevent the dissolution or corrosion of the anode. Therefore, the electrolyte must be designed to contain at least one SEI precursor that reacts rapidly with the anode to form an insoluble and stable SEI.

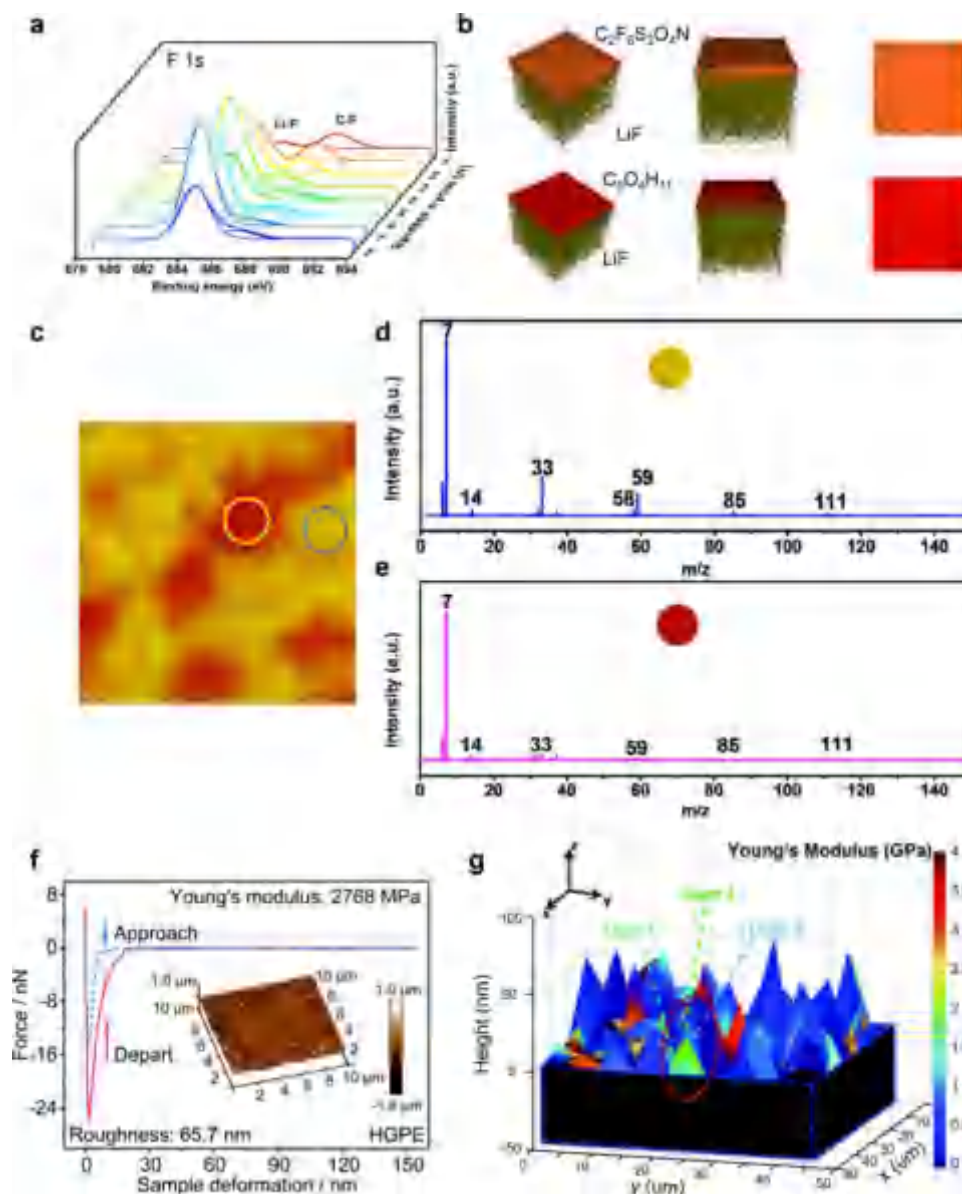
**3.1.1. Components of the SEI.** The chemical composition of the SEI on the anode side is highly dependent on the type of conducting salts, solvents, and additives. Although the role of these components in the formation of the SEI has not been fully understood, the presence of species such as LiF, fluoroborates, and fluorophosphates indicates the involvement of fluorinated components in the reduction mechanism of the electrolyte. LiF, in particular, has been identified as a major component of a fluorinated SEI, playing a critical role in regulating the diffusion of Li ions and the strength of the SEI.<sup>289,333,334</sup> Archer and co-workers showed that the presence of halide anions, especially fluorides, significantly increases the surface diffusivity of Li ions at the interphase between the electrolyte and the Li metal anode.<sup>333</sup> The role of LiF in a fluorinated SEI in regulating the nucleation and growth of Li deposition in LMBs was further investigated by a designed model system.<sup>304</sup> The fluorinated SEI facilitated uniform spatial diffusion of Li ions in carbonate- and ether-based electrolytes and guided the deposited Li into an ordered and aligned columnar structure.

Significant efforts have been made to develop artificial fluorinated coatings to enhance SEI performance, including inorganic LiF coatings and LiF-based composite coatings.<sup>320,335,336</sup> While computational simulations have provided insights into the diffusion mechanism of Li ions through fluorinated SEI, the practical SEI in practical battery systems is more complex and needs to be fully understood.<sup>89,337</sup>

Mashayek and co-workers elucidated that Li diffusion in the grain boundaries is generally faster than that in bulk, and the heterogeneous LiF/Li<sub>2</sub>O grain boundaries demonstrate the fastest Li-ion diffusion rate compared to the homogeneous LiF/LiF and Li<sub>2</sub>O/Li<sub>2</sub>O.<sup>89</sup> Further research is needed to comprehend the diffusion mechanism of Li ions through the SEI for practical applications.

**3.1.2. Formation of a Fluorinated SEI.** The formation of SEI can be generally classified into three modes: the “native” SEI is multicomponent including inorganic and organic phases formed by parasitic reactions between the anode and the electrolyte,<sup>331,338</sup> the “in situ” SEI formed over cycles of cells, and the “ex situ” SEI artificially applied on the anode surface.<sup>339</sup> LiF is a recurring motif found in nearly all functional SEIs (Figure 16a) given that fluorine is commonly present in prevailing electrolyte salts.<sup>340</sup> Among the SEI components, LiF is particularly spotlighted due to its high mechanical strength, low solubility, wide ESW (0–6.4 V vs Li/Li<sup>+</sup>), and low calculated barriers to Li diffusion. Besides, Wang et al. calculated the interfacial energy of different SEI components, among which LiF exhibited the highest interfacial energy of 73.28 meV Å<sup>−2</sup>, suggesting significant Li dendrite suppression ability.<sup>323</sup> These properties suggest that LiF may contribute to a homogeneous Li flux and robust SEI, making it a beneficial phase for the SEI on the anode side in recent years.<sup>341</sup>

Multiple studies have indicated that fluorine or fluoride enrichment in the electrolyte results in a LiF-enriched (in situ) SEI, as shown in Figure 16b. F-enriched electrolytes have included additives such as HF<sup>344</sup> and high loadings of LiF salt<sup>333</sup> as well as solvents such as FEC,<sup>168</sup> thus making significant improvements in the cycling stability and high CE



**Figure 17.** Characterization of fluorinated SEI in Li-based batteries. (a) F 1s XPS depth profile of the Li anode. (b) 3D distribution overlay between LiF and  $C_2F_6S_2O_2N$  (upper panel) and between LiF and  $C_6O_4H_{11}$  (lower panel). (c) Total mapping distribution and (d, e) related mass spectrum of the SEI on Li-metal anode (1 M LiTFSI–DME/DOL, 1:1 by volume with 2%  $LiNO_3$ ). Reproduced ref 351. Copyright 2022 American Chemical Society. (f) Heteroatom-based gel polymer electrolyte (HGPE)-derived SEI. (Inset) Corresponding 3D-AFM scanning images of SEI layers. Reproduced with permission from ref 353. Copyright 2021 Springer Nature. (g) Cross-section view of 3D plots. Black substrates indicate Li–Si alloys, and the z axis gives the thickness of the SEI films. The color bar of 0–4 GPa shows the Young's modulus for the SEI films. Reproduced with permission from ref 354. Copyright 2014 Royal Society of Chemistry.

(~89–99%). Postmortem analysis of cycled Li surfaces typically presents high levels of LiF. Figure 16c explains how the FEC molecule affects the mechanisms of SEI formation and the composition.<sup>345</sup> The breaking of C–F bond leads to the formation of LiF and vinyl carbonate (VC),<sup>168</sup> which results in a thinner SEI that prevents further electrolyte decomposition.<sup>346</sup> Such LiF-rich SEI prohibits high surface area lithium growth during Li stripping and plating.<sup>170</sup>

Ex situ fabrication of LiF layers on Li or Cu current collectors has also been widely studied, leading to the formation of an artificial (ex situ) LiF-enriched SEI (Figure 16d). Synthetic methods include hydrolysis of  $LiPF_6$  on Cu,<sup>304,347</sup> reactions between Li and fluorinated precursors,<sup>289,319</sup> physical vapor deposition,<sup>348</sup> and atomic layer

deposition (ALD).<sup>318,349</sup> To fabricate ex situ SEI layers, Gallant et al. used nitrogen trifluoride ( $NF_3$ ) gas to directly grow LiF on the Li foil (Figure 16e).<sup>342</sup> The reduction of  $NF_3$  as a fluorinated gas cathode in Li batteries led to copious amounts of LiF under electrochemical conditions.<sup>350</sup> Additionally,  $\gamma$ -rays can induce an artificial SEI layer with a favorable composition, and the composition of the SEI layer has a substantial effect on the charging rate. Choi et al. reported a  $\gamma$ -ray-driven SEI layer that allowed the battery to be charged to 80% capacity in 10.8 min of  $2.6 \text{ mAh cm}^{-2}$ . This exceptional charging performance was attributed to the LiF-rich SEI induced by salt-dominant decomposition via  $\gamma$ -ray irradiation.<sup>343</sup> Figure 16f illustrates the electron transfer in both electrochemical and photochemical processes. For the



electrochemical process, electrons were transferred unidirectionally from graphite to the LUMO level of the electrolyte to form the SEI layer, regulating compositions with relatively fewer components of the SEI layer. Besides,  $\gamma$ -ray irradiation could drive radical intermediates, and irradiation with  $\gamma$ -rays could preferentially decompose compounds, which improved the tunability of the SEI composition. The Cs-TEM image of photographtite indicates that the photo-SEI layer was uniformly deposited on the graphite surface with a thickness of  $\sim 20$  nm (Figure 16g). The photo-SEI layer was also observed to exist in the inner pores of the graphite particles (Figure 16h and 16i), implying that  $\gamma$ -ray irradiation was effective even in the interior of the graphite.

**3.1.3. Distribution and Impacts of Fluorides on the SEI.** The structure and chemical components of the SEI layer at different depths can be investigated by X-ray photoelectron spectroscopy (XPS) depth profiles. Taking the electrolyte of 1 M LiTFSI in DME/DOL (1:1 by volume) as an example,<sup>351</sup> the main elements of SEI are C, N, O, F, and S, which originated from the reduction reaction between the electrolyte and the Li anode. The depth analysis curves of the SEI are shown in Figure 17a. It can be observed that the signal of the element F increased with increasing sputtering time. The binding energies of 685.0 and 688.3 eV in the F 1s diagram represented Li–F and C–F. The intensity of the C–F signal on the surface was higher than that of Li–F, which indicated that residual LiTFSI salts existed on the surface. The time-of-flight secondary ion mass spectrometry (TOF-SIMS) technique can be applied to further investigate the SEI (Figure 17b). The inorganic phases of LiF-based compounds in 1 M LiTFSI in DME/DOL (1:1 by volume) with 2% LiNO<sub>3</sub>,<sup>351</sup> such as LiF ( $m/z = 26$ ), LiF<sub>2</sub> ( $m/z = 45$ ), LiF<sub>3</sub> ( $m/z = 64$ ), and Li<sub>2</sub>F<sub>3</sub> ( $m/z = 71$ ), were evenly distributed in the inner SEI layer. By overlaying the 3D distribution results of LiF ( $m/z = 26$ ), C<sub>2</sub>F<sub>6</sub>S<sub>2</sub>O<sub>4</sub>N ( $m/z = 280$ ), and C<sub>6</sub>O<sub>4</sub>H<sub>11</sub> ( $m/z = 147$ ), it was found that the Li salt was evenly distributed at the outermost SEI layer, which completely covered the LiF product. The results indicate that the SEI may not be a dense layer and the liquid electrolyte can be stored between the organic phase and the inorganic phase.<sup>352</sup> As shown in Figure 17c, two circles with equal area were extracted from the mapping image to obtain their mass spectrum. Compared to the light region (Figure 17d), the intensities of the ion fragments with mass charge ratios ( $m/z$ ) of 14, 33, 59, 85, and 111 decreased in the dark region (Figure 17e). Such fragments may come from the inorganic phase products formed by the strongly electro-negative atoms and the Li metal after the decomposition of LiTFSI, such as N, Li<sub>2</sub>F, Li<sub>3</sub>F<sub>2</sub>, Li<sub>4</sub>F<sub>3</sub>, and Li<sub>5</sub>N<sub>2</sub>O<sub>3</sub>.<sup>351</sup> Among them, Li<sub>2</sub>F ( $m/z = 33$ ) and Li<sub>3</sub>F<sub>2</sub> ( $m/z = 59$ ) exhibited the highest density, which suggested a strong electronegativity of fluorine in LiTFSI. These products were the main components of the inorganic phase of the SEI layer.

The Young's modulus of the SEI layer serves as a crucial metric for assessing the strength of the SEI, since a robust SEI can suppress the repeated rupture–reconstruction of the SEI due to the severe volume changes of the anodes during cycling. Such thin and stable SEI leads to low impedance of the interphase, thus enhancing cycling performance.<sup>166</sup> The Young's modulus of the SEI can be evaluated by 3D atomic force microscopy (3D-AFM) scanning. The proportion of LiF greatly increases the mechanical strength of the SEI (i.e., LiF possesses a shear modulus of 55.1 GPa, almost 11 times higher than that of Li metal (4.9 GPa)), which can significantly

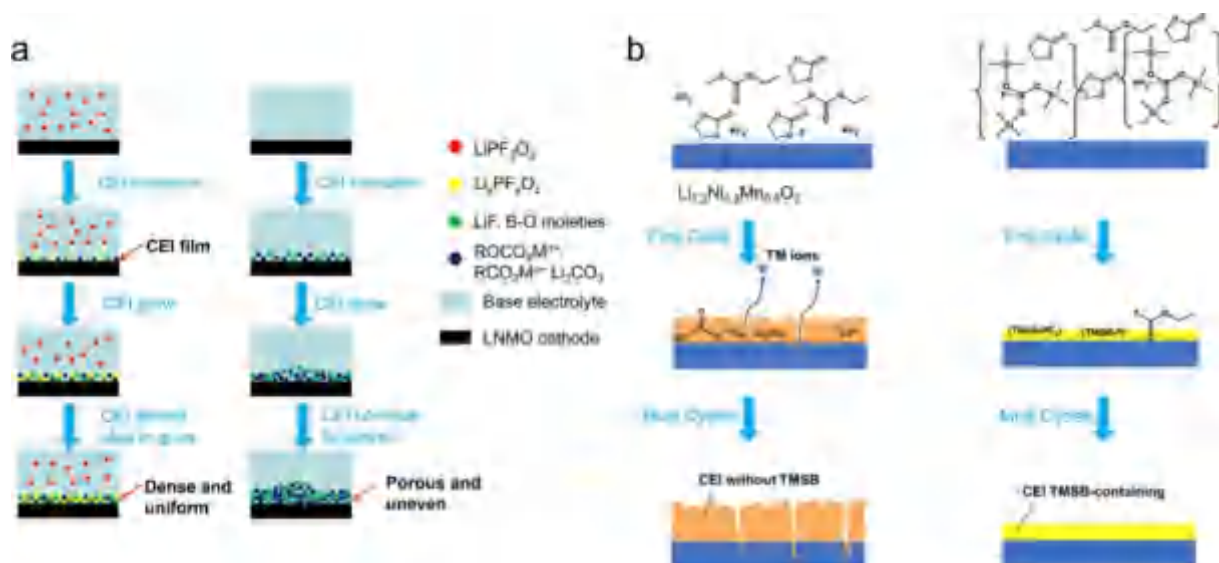
enhance the strength and interphasial energy of the SEI layers.<sup>355</sup> As a result, the SEI consisting of homogeneous LiF makes the anode more robust and uniform (Figure 17f). A 3D Young's modulus plot of discharged silicon electrodes with all force curves in a certain area can be drawn according to Young's moduli at each position at different indentation lengths on the surface of discharged anodes.<sup>354</sup> Some area was not covered by the SEI, and some area was covered by the thick SEI. The soft part of the SEI was always covering the outer layer. This can also be obtained from a cross-section view of the 3D plot, as shown in Figure 17g.<sup>354</sup> The uncovered area and the area with different layered structures with different Young's moduli can be observed clearly. This indicated that the organic species is usually situated on the outside with lower strength, and inorganic species like LiF support the internal SEI strength. It is, therefore, essential to explore the distribution and homogeneity of SEIs.

Despite the phenomenological improvements observed, it remains uncertain whether LiF has a directly beneficial function in the formation of the SEI. Variations among LiF-forming approaches (i.e., in situ vs ex situ) and the electrolytes used would lead to confusion in the understanding. For example, conflicting results about ex situ LiF were found in different works. A standalone layer was found to decrease CE due to inhomogeneous Li deposition,<sup>349</sup> whereas LiF layers on Li were elsewhere reported to improve cycle life in Li||Li symmetric cells.<sup>289,318</sup> Additionally, LiF is an ionic insulator ( $\sim 10^{-13}$ – $10^{-14}$  S cm<sup>-1</sup>), and it seems counterintuitive that LiF-enriched SEIs can impart benefits related to Li transport.<sup>356</sup> It remains unclear how such physical properties of LiF can support performance improvements.

## 3.2. Fluorinated Cathode–Electrolyte Interphases

The presence of a CEI layer was first suggested by Goodenough et al. on the LiCoO<sub>2</sub> cathode.<sup>357</sup> Considering that the interphasial reactivity increases at high-voltage cycling, the CEI layer behavior demonstrates an even more complicated response. When the cutoff voltage is increased to 4.5 V, the CEI layer becomes unstable and decomposes, as reported by Cherkashinin et al.<sup>358</sup> Until now, the detailed constituents and electrochemical behavior of the CEI layer have been under debate. However, it is generally accepted that the CEI is extremely sensitive to various factors, such as electrolyte composition, current densities, and cutoff voltage.

Previous studies usually treated the formation of the CEI layer independently. However, recent research results discovered a close relationship between the formation of the CEI on cathodes and the formation of the SEI on anodes.<sup>359–361</sup> A well-known example is the transition metal ion dissolution from cathode materials, which affects the SEI formation on anodes.<sup>362,363</sup> Recently, Xiong et al. verified the interaction between the ternary cathode (i.e., Li(Ni<sub>1/3</sub>Mn<sub>1/3</sub>Co<sub>1/3</sub>)O<sub>2</sub> and Li(Ni<sub>0.42</sub>Mn<sub>0.42</sub>Co<sub>0.16</sub>)O<sub>2</sub>) and the graphite anodes in batteries operating at high temperature and high voltage.<sup>364</sup> Jung et al. also demonstrated the enhanced cycling performance of the LiCoO<sub>2</sub>/graphite full cells by mitigating the coupled side reactions through Al<sub>2</sub>O<sub>3</sub> coating on the cathodes.<sup>365</sup> Noting that plenty of studies demonstrated that if the cathode was cycled in the high-voltage range, the effect of repeated formation–decomposition of SEI layers on Li anodes significantly influenced the formation of CEI layers on the cathodes. A deep investigation of the reactions on both the cathode and the Li anode is necessary to collect credible



**Figure 18.** Formation of fluorinated CEI of Li-based batteries. (a) Proposed mechanism of the LiDFP participating in the formation of CEI film. Reproduced with permission from ref 370. Copyright 2019 Elsevier. (b) Schematic of CEI formation during cycling in conventional and TMSB-containing electrolytes. Reproduced ref 371. Copyright 2019 American Chemical Society.

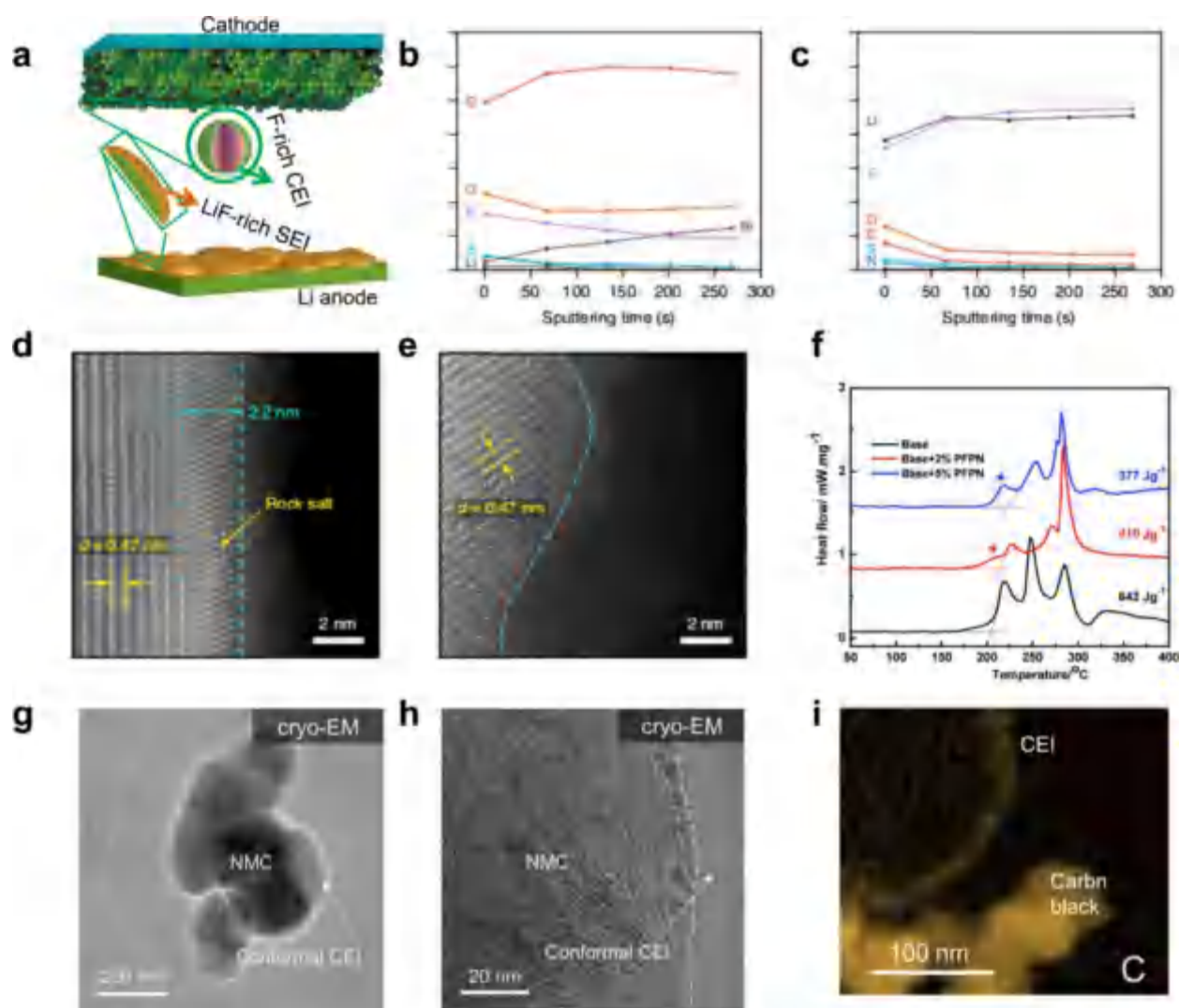
properties of the CEI layer on the cathode and achieve comprehensive understanding of the CEI formation mechanism.

**3.2.1. Formation of a Fluorinated CEI.** It is widely accepted that the CEI layer contains both inorganic components (e.g.,  $\text{LiF}$ ) and organic species (e.g., carbonates and oligomers/polymers).<sup>366–368</sup> In situ neutron scattering further proved that the CEI layer presented dynamic evolution during battery cycling within a low cutoff voltage (4.2 V vs  $\text{Li}/\text{Li}^+$ ). The thickness of the CEI layer gradually increases upon cycling.<sup>369</sup> Li and co-workers reported the progress of CEI formation with and without electrolyte additives.<sup>370</sup> As shown in Figure 18a, the CEI formed in the base electrolyte of 1 M LiDFOB–ethyl carbonate (EC)/DMC (1:1 by volume) was too loose to prevent direct contact between the electrolyte and the cathode; thereby, the carbonate solvents and salts underwent continuous decomposition reactions at high voltage, and the decomposition products were continuously deposited on the surface of the cathode, which caused continuous growth of the CEI layer. In contrast, for the CEI film formed in the electrolyte with the lithium difluorophosphate (LiDFP) additive, the preferred decomposition of LiDFP promoted the formation of a dense CEI film, effectively preventing the direct contact between the electrolyte and the cathode.

Figure 18b exhibits the mechanism of CEI formation with and without the fluorinated additive tris(trimethylsilyl)borate (TMSB).<sup>371</sup> Generally, the large polarity of EC molecules made them easily diffuse to the cathode surface with anions by a strong electrostatic force during the charge process. Hence, the cathode surface is EC/anion rich before CEI formation, which makes EC easily decompose. However, this effect gets impaired after the addition of TMSB because of the generation of the polyanion group  $(\text{TMSB}-\text{PF}_6)^-$  and  $(\text{TMSB}-\text{F})^-$  with weaker electrostatic force and less electronegativity. As a result, EC decomposition is suppressed effectively. Moreover, TMSB can participate in CEI formation by electrochemical reactions or by directly entering the CEI layer in the form of a polyanion group to optimize the quality of the CEI. The HOMO level

( $-6.749$  eV)<sup>372</sup> of TMSB is higher than that of the carbonate solvents ( $-11.905$  eV for EC and  $-11.541$  eV for EMC),<sup>373</sup> which offers an opportunity to participate in the formation of a high-quality CEI film before solvent decomposition to protect the active cathode material from erosion of the electrolyte and alleviate the capacity and voltage fading of  $\text{Li}_{1.2}\text{Ni}_{0.2}\text{Mn}_{0.6}\text{O}_2$ .<sup>374</sup>

**3.2.2. Impact of the Fluorinated CEI on Battery Performance.** Unlike the SEI, CEI formation involves not only the electrolytes but also active components in the cathodes, including transition metal dissolution, H abstraction from the solvents, and the formation of superoxides or peroxides. For unmodified NMC811 or  $\text{LiCoPO}_4$  (LCP) cathodes (Figures 19a), electrolyte components experience continuous oxidation until a dense and uniform CEI layer forms and blocks the electron transfer from the electrolyte to the cathodes. Compared with EC/DMC- and FEC/DMC-based electrolytes, the extremely high CEs achieved by the all-fluorinated electrolyte on aggressive cathodes should originate from the F-rich CEI that deactivated the catalytic activity of the NMC or LCP cathodes. Quantum chemistry calculations predict that direct oxidation of solvent molecules is energetically unfavorable around 5 V. Instead, solvent oxidation is accompanied by H transfer to another solvent and/or cathode surface. Intermolecular H transfer takes place around 5 V for EC and  $>5.5$  V for FEC, FEMC, and HFE. When the oxidation potential is calculated assuming open-loop  $\text{EC}^\bullet$  and  $\text{FEC}^\bullet$  radicals as the products, the oxidation stability decreases to  $\sim 4.2$  and 4.9 V, respectively. Thus, EC-containing electrolytes are expected to be oxidized from 4.2 V, even in the absence of the active materials. EC is a poor CEI former because the  $\text{EC}^\bullet(-\text{H})$  radical decomposes with a barrier of only 0.91 eV to evolve  $\text{CO}_2$ , leaving only a fraction of  $\text{EC}^\bullet(-\text{H})$  radicals to participate in the second H abstraction, eventually leading to polymerization. The resulting hydrogen-rich polymer is still susceptible to further degradation. Because of the higher barrier (1.28 eV) for the  $\text{FEC}^\bullet(-\text{H})$  ring-opening reaction compared to that of  $\text{EC}^\bullet(-\text{H})$ , the  $\text{FEC}^\bullet(-\text{H})$  is a longer lived radical compared to  $\text{EC}^\bullet(-\text{H})$  and will probably react with the formed  $\text{FEMC}^\bullet(-\text{H})$  and 1,1,2,2-tetrafluoroethyl-2',2',2'-



**Figure 19.** Characterization of fluorinated CEI in Li-based batteries. (a) SEI and CEI chemistries formed in all-fluorinated electrolyte. Reproduced with permission from ref 375. Copyright 2018 Springer Nature. Quantified atomic composition ratios of the CEI obtained by XPS spectra for the NMC811 electrodes collected from cells with (b) 1 M LiFSI–DME and (c) 1 M LiFSI–DME/TFEO electrolyte after 100 cycles. HAADF-STEM of NMC811 electrodes collected from cells with (d) 1 M LiFSI–DME and (e) 1 M LiFSI–DME/TFEO electrolytes after 100 cycles. Reproduced with permission from ref 376. Copyright 2019 Springer Nature. (f) Heat flow profiles of the  $\text{Li}_x\text{CoO}_2$  charged to 4.5 V after 2 cycles in the absence and presence of PFPN. Reproduced with permission from ref 178. Copyright 2017 Elsevier. (g, h) Cryo-EM images of conformal CEI formed on NMC cathodes. (i) Cryo-STEM EELS mapping of conformal CEI on NMC electrodes (yellow for carbon element). Reproduced with permission from ref 377. Copyright 2021 Elsevier.

trifluoroethyl ether (HFE) $^{\bullet}(-\text{H})$  radicals near the cathode surface, resulting in a fluorine-rich CEI as observed by Fourier-transform infrared spectroscopy. Alternatively, fluorinated radicals also bind to oxygen in  $\text{CoPO}_4$ , preventing the OH formation that facilitates transition metal dissolution. Thus, in all-fluorinated electrolytes, the composition of a protective CEI is inevitably highly fluorinated.<sup>375</sup>

Figure 19b and 19c shows the atomic ratios of the CEI layer formed on the surface of the NMC811 cathode in different electrolytes.<sup>376</sup> An LiF-rich CEI was formed on the cathode surface in the tris(2,2,2-trifluoroethyl)orthoformate (TFEO)-based electrolyte, while in the controlled carbonate and 1 M LiFSI in DME electrolytes, organic-rich CEIs were obtained. Figure 19d and Figure 19e shows the high-angle annular dark-field scanning transmission electron microscopy (HAADF-STEM) imaging results of the cycled NMC811 electrodes.<sup>376</sup> The structure reconstruction appeared in the NMC811

electrode cycled in 1 M LiFSI–DME with a rock salt layer ( $\sim 2.2$  nm) (Figure 19d). The surface lattice layers of the NMC811 electrode underwent some degree of mixing, with the Li sites partially occupied by antisite Ni ions.<sup>378</sup> In contrast, the electrode surface maintained a layered structure under the same cycling condition in 1 M LiFSI–DME/TFEO (Figure 19e). Such a result indicated the effective suppression of detrimental phase transformation. These beneficial effects can be attributed to the formation of a uniform LiF-rich CEI layer,<sup>379</sup> while the uneven and organic-rich CEI is less protective.

The thermal stability of both the electrolyte and the cathode material at the charged state is of vital importance to battery safety. Differential scanning calorimetry (DSC) was carried out to unravel the thermal stability of the electrolyte and electrode material. Figure 19f shows the DSC curves of the electrolyte with (phenoxy)pentafluorocyclotriphosphazene (PFPN) (red



and blue) and without PFPN (black).<sup>380</sup> It can be clearly seen that the main decomposition peak of the electrolyte shifted toward a higher temperature with the addition of more PFPN, indicating that the thermal stability of the electrolyte had been considerably improved. Several peaks can be identified in the DSC curves, corresponding to the step-by-step decomposition of the charged  $\text{Li}_x\text{CoO}_2$  material.<sup>380</sup> The electrolyte decomposition/oxidation at the surface of the  $\text{Li}_x\text{CoO}_2$  electrode usually occurs at around 200 °C.<sup>381</sup> In the presence of 2% PFPN, a new peak (indicated by the red asterisk) at 206 °C from the red DSC curve can be assigned to the thermal-polymerization reaction of PFPN. The calculation results (200–300 °C) demonstrate that the total exothermic heat generated from the  $\text{Li}_x\text{CoO}_2$  electrode in the presence of PFPN (2% PFPN, 36.1%; 5% PFPN, 41.3%) was less than that from the  $\text{Li}_x\text{CoO}_2$  electrode in the absence of PFPN (black), indicating that the thermal stability of the charged  $\text{Li}_x\text{CoO}_2$  electrode was distinctively improved after the addition of electrolyte additive.<sup>178</sup> The layer of the CEI after brief shorting on the positive electrode particle can be observed by cryogenic electron microscopy (cryo-EM) (Figure 19g and 19h). The electrode particle was uniformly coated with a thin layer of mostly amorphous materials, spanning from ~5 to 10 nm at the edge of the interphase. Furthermore, the conformal CEI and carbon black additives yielded an annular dark-field image along with a C K-edge map (Figures 19i), which indicated the organic polymeric composition of alkyl carbonates.<sup>377</sup>

Fluorinated electrolytes have shown significant potential in achieving improved performance and safety in high-voltage batteries. When hydrogen atoms in the electrolyte are replaced with fluorine atoms, the activation energy is reduced<sup>169</sup> and the HOMO and LUMO energy levels decrease, leading to increased reduction and oxidation potentials.<sup>345,382–384</sup> The decrease in HOMO energy level enhances the cycling performance by promoting the early formation of an effective CEI layer and reducing the overall impedance.<sup>130,384,385</sup> Numerous fluorinated CEI-forming additives have been reported in recent years.<sup>386–388</sup> Future research should focus on understanding the impact of the fluorine atom on the overall performance of Li-based cell chemistry, involving (i) correlating the molecular and (ii) electronic structures of fluorinated electrolyte components, (iii) identifying relevant physicochemical properties and (iv) reactivity, which includes investigating synergistic effects between fluorinated and nonfluorinated electrolyte components, studying the main operation and failure processes in Li-based cells, exploring different plausible reaction pathways, and analyzing the limiting and determining steps that rationalize the results. Systematic research on CEI electrochemistry/chemistry will enable the development of high-performance Li-based batteries with high energy density, energy efficiency, and superior capacity retention.

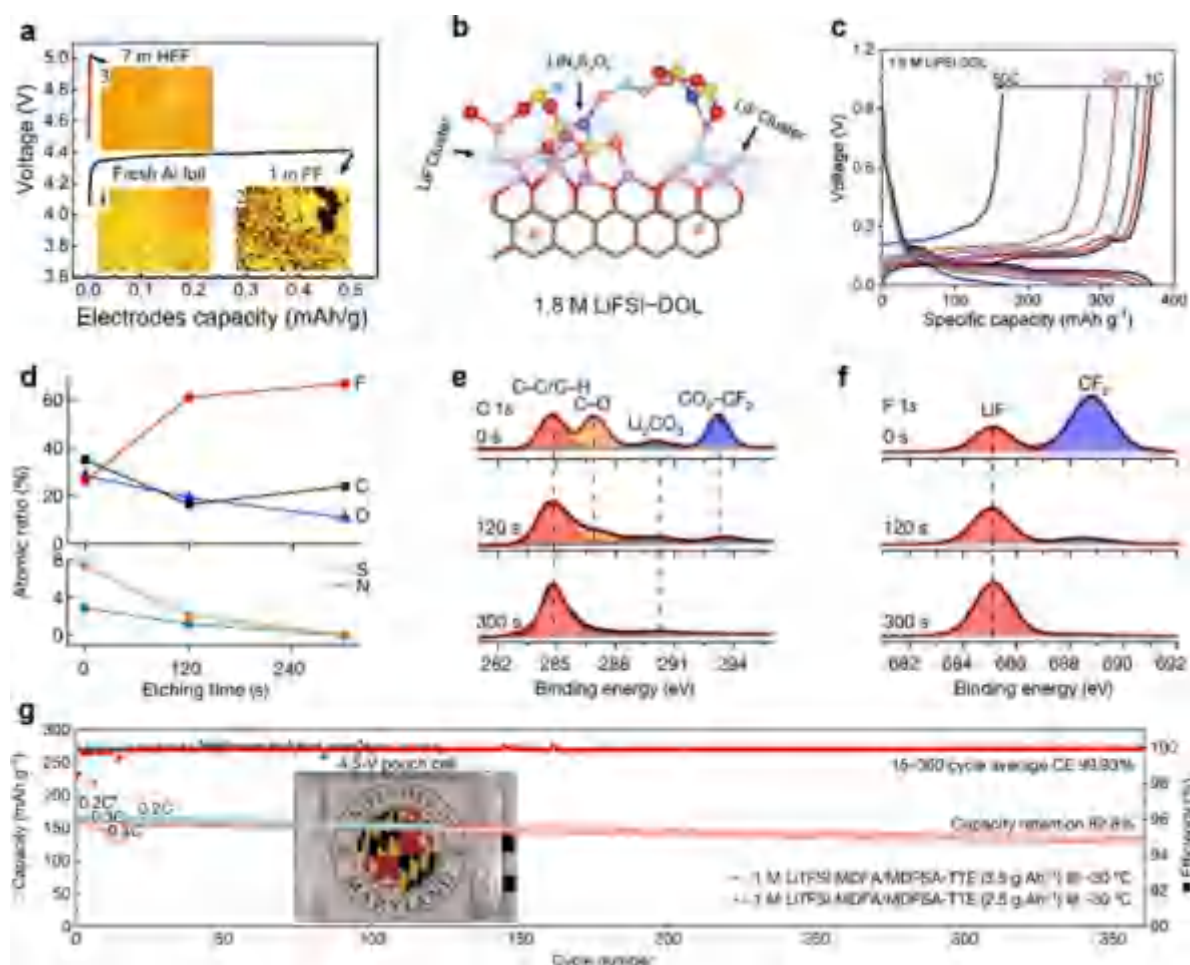
### 3.3. Critical Role of Fluorinated Interphases for Extreme Li-Based Batteries

With the continuous upsurge in demand for energy storage, Li-based batteries are increasingly required to survive/operate under extreme conditions, such as a wide temperature range (e.g.,  $\pm 60$  °C), extended charge/discharge cycling life, fast cycling rate (e.g.,  $\leq 15$  min), and high working voltage (e.g.,  $> 4.5$  V).<sup>55</sup> For instance, electric vehicles call for battery systems to sustain a stable operation in both hot conditions and cold environments. Some specific applications, including

subsurface exploration, defensive arsenals, space vehicles, etc., require the operation of rechargeable batteries under even more extreme conditions. Apart from these external influences, internal factors also trigger thermal fluctuations in Li-based batteries,<sup>303</sup> significantly raising safety concerns. As an essential region in which electrochemical reactions occur involving  $\text{Li}^+$  ions and electrons, the interphase on the electrode plays an essential role in maximizing the electrochemical performance of Li-based batteries. Regarding an ideal interphase, several features should be possessed, including high  $\text{Li}^+$ -ion conductivity, a compact structure with proper compositions, high chemical/electrochemical stability, and high elastic strength. However, the design of interphases under mild conditions makes it difficult to satisfy the requirements under extreme conditions. When a battery is operated under extreme conditions, the interphase formed on the electrode surface can grow much thicker and lose its protective ability, further causing battery performance decay through various aging mechanisms.<sup>389</sup> Currently, the features and roles of interphases at certain extreme conditions remain significant challenges in the operation of Li-based batteries. Fluorinated interphases have emerged as effective strategies for enhancing battery performance under various operation conditions. In particular, the fluorinated interphase is featured with its main component LiF.<sup>316,375,390</sup> However, the role of LiF for extreme Li-based batteries remains elusive. In the following section, recent in-depth understanding and key progress of the fluorinated interphase at extreme operation conditions of Li-based batteries are summarized, where the SEI formed on the anode will be the focus.

It is generally recognized that the bulk LiF is considered as a favorable SEI component formed via both in situ (derived from electrolyte components) or ex situ (artificial fabrication) approaches. It should be noted that despite the electric/ionic insulation nature of the bulk LiF,<sup>356,391</sup> the LiF-enriched SEI at the nanoscale level can yield a high ionic conductivity, low diffusion energy, and high surface energy, contributing to a uniform and highly stable Li deposition.<sup>333,392</sup> The difference between the macroscopic and the microscopic properties of LiF remains to be elucidated in the future. Moreover, understanding the role of LiF in the electrochemical performance of batteries is inevitably limited by several factors, including the distributions, particle sizes, and formation approaches, requiring great attention to identify the effects of the fluorinated interphase in extreme batteries.

Commercial carbonate electrolytes have largely restricted the battery operation temperature range (from  $-20$  to  $+50$  °C), leading to fast capacity degradation and even battery failure at low temperatures. The successful operation of typical Li-based batteries at low temperature depends on the melting points of the liquid electrolytes. For instance, the commercial electrolytes of Li-ion batteries contain a high proportion of EC solvent that freezes under  $-20$  °C, which results in extremely low ionic conductivity.<sup>393,394</sup> Besides, the thick SEI usually continuously consumes Li, significantly increasing the diffusion energy of  $\text{Li}^+$  ions.<sup>394</sup> In addition to the ionic mobility, the low-temperature performance of batteries is dominated by the sluggish kinetics of  $\text{Li}^+$  transport across the interphase, which is related to the high charge transfer resistance and poor structure stability of the SEIs.<sup>395</sup> To construct an effective interphase on the surface of both cathodes (e.g., LFP) and anodes (e.g., graphite or Li metal), various additives, such as FEC,  $\text{LiPO}_2\text{F}_2$ , and fluorosulfonyl isocyanate (FI), have been introduced to



**Figure 20.** Role of fluorinated interphases for Li-based batteries operated at extreme conditions. (a) Al dissolution in 1 M LiFSI–FEC (1 M FF) and 7 M LiFSI–FEC (7 M HFF) electrolytes when charging to 5 V at 0.5 mA. (Insets) Optical microscopy images of (1) fresh Al foil and Al foil in (2) 1 M FF electrolyte after charging 1 h and (3) 7 M HFF after charging to 5 V. Reproduced with permission from ref 316. Copyright 2018 PNAS. (b) AIMD-simulated atomic SEI structure between the electrolyte and the graphite anode: Li, pink; P, purple; F, cyan; C, brown; O, red; N, blue; S, yellow; graphite, brown wire frame. (c) Charge/discharge curves of graphite||Li cells with 1.8 M LiFSI DOL at various current rates. Reproduced with permission from ref 411. Copyright 2022 Wiley-VCH. (d–f) XPS results of the SEI on graphite anode in 1 M LiTFSI–MDFA/MDFA/TTE electrolyte: (d) quantified atomic ratios of the elements, (e) C 1s and (f) F 1s spectra displayed in columns of the corresponding depth profiling results. (g) Graphite||NCM811 pouch cell performance at  $-30\text{ }^{\circ}\text{C}$  and 0.2 C rate using 2.5 or 3.5 g  $\text{Ah}^{-1}$  electrolytes. Rate performance was conducted at various C rates (0.2 C for 5 cycles, 0.3 C for 5 cycles, 0.4 C for 5 cycles, and 0.2 C for 345 cycles) of 3.5 g  $\text{Ah}^{-1}$  (red color). (Inset) Photo of a 4.5 V pouch cell. Reproduced with permission from ref 55. Copyright 2023 Springer Nature.

optimize the electrolytes.<sup>394,396–398</sup> In addition, fluorinated antifreezing agents have been introduced as electrolyte cosolvent/solvent for low-temperature applications, such as 2,2,2-trifluoroethyl butyrate,<sup>399</sup> isobutyl formate,<sup>400</sup> and 2,2,2-trifluoroethyl *n*-caproate.<sup>401</sup> Recently, He et al. developed a fluorine–sulfur-based electrolyte by applying isobutyl formate (IF) as an antifreezing agent with an ultralow melting point of  $-132\text{ }^{\circ}\text{C}$ . This electrolyte demonstrated excellent physiochemical and electrochemical properties at ultralow temperature, e.g., forming stable LiF-rich SEI (10.48%) and CEI (17.91%) layers, achieving high  $\text{Li}^{+}$  conductivities ( $1.00 \times 10^{-5}\text{ mS cm}^{-1}$  for SEI and  $6.65 \times 10^{-5}\text{ mS cm}^{-1}$  for CEI) and high diffusion coefficients ( $1.10 \times 10^{-21}\text{ m}^2\text{ s}^{-1}$  for SEI and  $2.07 \times 10^{-20}\text{ m}^2\text{ s}^{-1}$  for CEI). It also enabled a stable cycling performance of the Lill  $\text{LiCoO}_2(\text{LCO})$  battery at  $-70\text{ }^{\circ}\text{C}$  with a high retainable capacity of 110 mAh  $\text{g}^{-1}$  over 170 cycles.<sup>400</sup> Typically, it has been accepted that the LiF-rich SEI formed on anode materials exhibited low interphase impedance and charge transfer resistance as well as high stability, thereby enhancing the  $\text{Li}^{+}$

diffusion at low temperatures. These results are consistent with the DFT calculations by Arias et al. They pointed out that the surface diffusivity of  $\text{Li}^{+}$  over a layer of LiF crystal was excellent, which also improved the stability of the SEI.<sup>402</sup> However, the role of LiF in the CEI on low-temperature performance is still under debate. Contrary to the desirable effect of a LiF-rich CEI on promoting the rapid  $\text{Li}^{+}$  diffusion as a result of the lower energy barrier,<sup>403</sup> Gao et al. observed less LiF content formed in the SEI with the FEC-containing electrolyte than that with the FEC-free electrolyte. They ascribed the smaller interfacial impedances to the less LiF, which would promote the low-temperature performance of the LFP electrode.<sup>404</sup>

Recently, by introducing low-polarity diluents, LHCEs have demonstrated great potential in achieving high  $\text{Li}^{+}$  mobility as well as low electrolyte viscosity for low-temperature batteries.<sup>405–407</sup> However, the SEI derived from  $\text{LiPF}_6$  in  $\text{LiPF}_6$ -based LHCEs generally exhibited high interphase resistance. After adding lithium difluorobis(oxalato) phosphate

(LiDFBOP) as a sacrificial additive, the SEI was regulated to be much thinner, which delivered low interphase impedance due to the decreased  $\text{Li}^+$  transport path. It was demonstrated that the addition of LiDFBOP changed the SEI composition, with inorganic LiF and porous organic  $\text{Li}_n(\text{FOP})_n$ -based layers facilitating  $\text{Li}^+$  diffusion and LiF along with  $\text{Li}_2\text{C}_2\text{O}_4$  increasing the stability of the SEI. Benefiting from this regulated interphase chemistry, the commercial graphite anodes exhibited outstanding low-temperature performance ( $\sim 240 \text{ mAh g}^{-1}$  at  $-20^\circ\text{C}$  with  $0.1 \text{ C}$ ) and high rate performance ( $\sim 225 \text{ mAh g}^{-1}$  at  $2 \text{ C}$ ).<sup>395</sup>

To satisfy the demand for high energy densities, Li-based batteries are developed to operate at extreme voltages, which are beyond the thermodynamic stability limits of traditional electrolytes. Meanwhile, these electrolytes, mainly consisting of carbonates or ethers, are extremely flammable, causing safety concerns for practical applications. LiF possesses the largest band gap ( $13.6 \text{ eV}$ ) and the widest ESW, which is believed to protect the high-voltage cathode.<sup>314</sup> To control the LiF formation, Li et al. designed an all-fluoride electrolyte with a large donatable fluorine concentration, i.e.,  $7 \text{ M LiFSI}$  in FEC, in which both the solvent and the salt donated F. It was revealed that LiF formation on the cathode with a large band gap resulted in a fast-tunneling decay rate, protecting Al from dissolution and suppressing electrolyte oxidation beyond  $5 \text{ V}$  (Figure 20a). When pairing the  $5 \text{ V LiNi}_{0.5}\text{Mn}_{1.5}\text{O}_4$  cathode with the Li metal anode, the full cell ( $1.4 \times$  excess Li) cycled stably for over 130 times at an industrial loading level of  $14.7 \text{ mg cm}^{-2}$ ,  $1.83 \text{ mAh cm}^{-2}$  at a current rate of  $0.36 \text{ C}$ . The promising performance was ascribed to the LiF nanolayer constructed on the surfaces of both the cathode and the anode; therefore, its features, such as a wide band gap, high surface energy, and small Burgers vector, favored the high-voltage stability and also resisted rupture during Li deposition.<sup>316</sup> Unlike using the sole solvent, Wang et al. proposed another all-fluorinated electrolyte consisting of  $1 \text{ M LiPF}_6$  in a mixture of FEC:FEMC:HFE with a weight ratio of  $2:6:2$ .<sup>375</sup> The high degree of fluorine substitution in each cosolvent rendered a F-rich CEI, where these F-containing species (e.g.,  $\text{CF}_x$  and  $\text{PO}_x\text{F}_y$ ) deactivated the catalytic activity of the cathode surface and further resisted unwanted oxidation reactions even charging to  $5 \text{ V}$ . Besides, the fluorinated cosolvents yielded a robust SEI with an extremely high LiF content ( $\sim 90\%$ ), promoting  $\text{Li}^+$  migration along the interphase and tuning the growth of the deposited Li in parallel to reduce the specific surface area. The resulting batteries exhibited outstanding cyclability with high CEs of  $99.2\%$  for Li plating/stripping and  $\sim 99.81\%$  for a  $5 \text{ V LiCoPO}_4$  cathode. Interestingly, the designed electrolyte displayed nonflammability, with F fluorination on the alkyl moiety of each cosolvent inhibiting the propagation of oxygen radicals during combustion.<sup>375</sup> Besides, using the fluorine-containing additives (e.g., FEC,  $\text{LiPO}_2\text{F}_2$ , LiDFOB) can also construct more robust SEIs/CEIs that consist of fluorinated species/polymers, which further blocks the continuous side reactions between the electrolyte solvents and the extremely oxidized cathode surface.<sup>408–410</sup> As reported by Ma et al., the perfluorophenylboronic acid (PFPPBA) additive was preferentially oxidized on the  $\text{LiNi}_{0.6}\text{Co}_{0.2}\text{Mn}_{0.2}\text{O}_2$  (NCM622) cathode surface due to the strong coordination with  $\text{PF}_6^-$ , forming an armor-like CEI with a LiF-rich inner layer and a  $\text{LiB}_x\text{O}_y$ -based outer part. The LiF inner layer in the CEI with high mechanical strength effectively resists the breakdown of the NCM622 cathode during

repeated cycling and enhances the  $\text{Li}^+$  conductivity. Besides, the outer layer with  $\text{LiB}_x\text{O}_y$  exhibited extremely low solubility in carbonate solvents, maintaining the stability of internal CEI species such as LiF. Consequently, the armor-like CEI prevented unwanted electrolyte decomposition as well as detrimental cathode structural change at high voltage, contributing to an excellent cycle stability with  $92.1\%$  capacity retention over 400 cycles at  $4.6 \text{ V}$ , and it sustained the battery to cycle for 150 times (with  $75.67\%$  retention) even at an ultrahigh voltage of  $4.8 \text{ V}$ .<sup>408</sup> As discussed above, the chemical sources of F were typically confined to negatively charged salt anions or fluorinated solvents/additives in electrolytes, which could not populate the inner Helmholtz layers of the electrode surface (e.g., Li anode) with a high Fermi energy level and thus hindering their participation in the interphasial chemistry. Zhang et al. synthesized a fluorinated cation, 1-methyl-1-propyl-3-fluoropyrrolidinium, and coupled it with an FSI<sup>−</sup> anion to form an ionic liquid (PMpyr<sup>+</sup>FSI<sup>−</sup>).<sup>410</sup> This electrolyte exhibited complete nonflammability and strong antianodic ability up to  $5.5 \text{ V}$ . More importantly, the fluorine sources on the cation and the anion offered unprecedented interphasial chemistries on both the NMC622 cathode and the Li anode, contributing to excellent battery electrochemical performance. The SEI enriched in  $\text{SO}_2\text{F}$ ,  $\text{C–F}$ , and LiF contributed from the decomposition/defluorination of FSI<sup>−</sup> and PMpyr<sup>+</sup> cations. Stable cycling performance without obvious capacity deterioration after 100 cycles was achieved with a high average CE of  $99.9\%$ . This work highlights the importance of exploring fluorinated cations in tailoring highly fluorinated interphases for batteries operated at extreme voltages.

Considerable efforts have been devoted to using FEC-based electrolytes for generating fluorinated SEIs in Li-based batteries, particularly with the graphite anodes or Li metal anodes.<sup>168,412–417</sup> The FEC-derived fluorinated SEI is characteristic of a high LiF amount, which exhibits low electronic conductivity ( $\sim 10^{-31} \text{ S cm}^{-1}$ ) and a high Young's modulus ( $\sim 64.9 \text{ GPa}$ ).<sup>418</sup> Unfortunately, the low  $\text{Li}^+$  conductivity of the LiF ( $\sim 10^{-12} \text{ S cm}^{-1}$ ) component largely restricts the fast charging capability especially for Li metal anodes as a result of the blocked transportation ability of  $\text{Li}^+$  and further aggravated Li dendrite growth at high current rates (e.g., above  $2.0 \text{ mAh cm}^{-2}$ ).<sup>419–423</sup> Very recently, a dual-anion-regulated electrolyte was designed by Xu's research group via using LiTFSI and LiDFBOP as anion regulators.<sup>424</sup> The TFSI<sup>−</sup> anion reduced the desolvation energy of  $\text{Li}^+$ , while the DFBOP<sup>−</sup> anion promoted the formation of highly ion conductive and robust inorganic-rich interphases on both cathodes (less LiF and stronger  $\text{Li}_x\text{PO}_y\text{F}_z$ ) and anodes (large amounts of  $\text{Li}_x\text{PO}_y\text{F}_z$  and  $\text{Li}_2\text{C}_2\text{O}_4$ ). These interphase features contributed to an outstanding cyclability ( $84.6\%$  capacity retention over 150 cycles) in  $6.0 \text{ Ah}$  pouch cells (Lill  $\text{LiNi}_{0.83}\text{Co}_{0.11}\text{Mn}_{0.06}\text{O}_2$ , NCM83) along with an ultrahigh rate capability ( $5 \text{ C}$ ) in  $2.0 \text{ Ah}$  pouch cells. More interestingly, a practical LillNCM83 pouch cell with an ultralarge capacity of  $39.0 \text{ Ah}$  realized an ultrahigh energy density of  $521.3 \text{ Wh kg}^{-1}$ , promoting the practical utilization of high energy density Li-based batteries via a facile electrolyte design. Apart from the beneficial effect of  $\text{Li}_x\text{PO}_y\text{F}_z$ , other interphase species have also been incorporated in enhancing the battery cycling stability, especially at fast charging rates. Interestingly, there exists another viewpoint believing the LiF-rich SEI is promising for fast kinetics since the wide band gap and high chemical/electrochemical stability of LiF could block the continuous side



reactions.<sup>323,425,354</sup> An extremely fast charging graphite anode as high as 50 °C without Li plating was achieved by designing two electrolytes, i.e., low-voltage 1.8 M LiFSI–DOL and high-voltage 1.0 M LiPF<sub>6</sub>–FEC/AN (7:3 by volume). It was revealed that the LiF formed on the graphite anode (Figure 20b) with high interphase energy and low ionic–electronic significantly suppressed side reactions of electrolytes, thus benefiting fast kinetics. The former electrolyte enabled the graphite anode to deliver a high reversible capacity of 180 mAh g<sup>−1</sup> even at 50 °C (1 C = 370 mAh g<sup>−1</sup>) (Figure 20c) and endowed the graphite||LFP full battery to retain a capacity of 60 mAh g<sup>−1</sup> at an extreme rate of 60 C (representing 1 min for full charge and discharge). The second electrolyte aided the graphite||NCM811 full battery (cathode loading = 2 mAh cm<sup>−2</sup>, N/P ratio = 1) in providing a capacity of 170 mAh g<sup>−1</sup> at 4 °C charge and 0.3 °C discharge rates.<sup>411,426</sup> Briefly, whether the LiF component in the SEI is sufficiently effective for high stability and fast Li<sup>+</sup> transport of Li-based batteries remains unclear, especially under fast charging conditions.

As mentioned above, the most widely used electrolytes based on carbonates fail to simultaneously meet all requirements for supporting extreme Li-based batteries such as higher voltages (≥4.5 V), fast charging (≤15 min), cycling over a wide temperature range (±60 °C), and nonflammability.<sup>12,58,427,428</sup> To tame the high affinity between the solvents and the ions and the high flammability of carbonate-based electrolytes, Wang and co-workers dissolved fluorinated electrolytes into highly fluorinated nonpolar solvents (e.g., tetrafluoro-1-(2,2,2-trifluoroethoxy)ethane (D2)) to obtain an electrolyte formulated with 1.28 M LiFSI–FEC/FEMC/D2. This designed electrolyte yielded both LiF-rich SEI and CEI. The high thermal stability and the excellent Arrhenius behavior of Li<sup>+</sup> conductivity for the LiF-rich interphases enhanced the high-temperature performance of both the cathode and the anode. The ionic conductivities of the SEI and CEI at ultralow temperatures were also significantly improved. The Li metal anode achieved high cycling CEs of 99.4%, and the graphite anode achieved high charge/discharge CEs of 99.9%. As for the high-voltage LiNi<sub>0.5</sub>Mn<sub>1.5</sub>O<sub>4</sub> (5.0 V) and LiCoMnO<sub>4</sub> (5.4 V) cathodes, high CEs of 99.9% and 99% were obtained, respectively. Especially, the Li||LiNi<sub>0.8</sub>Co<sub>0.15</sub>Al<sub>0.05</sub>O<sub>2</sub> battery maintained 56% of its capacity obtained at room temperature, even charging/discharging at −85 °C, along with high cycling stability at 60 °C. In addition to significantly improved wide-temperature performance, this electrolyte design displayed nonflammable characteristics.<sup>429</sup> Furthermore, Wang's group is dedicated to exploring the guiding principle to address the relationships between battery performance, electrolyte solvation structure, and interphase chemistry, especially focusing on extreme operating conditions. Their recent report validated an electrolyte design strategy based on a group of soft solvents with a relatively low DN (less than 10) and high dielectric constant (larger than 5) that stroke a balance between Li<sup>+</sup>–solvent interactions, sufficient dissociation of Li salts, and satisfactory electrochemistry. As a proof of concept, 1 M LiTFSI–methyl difluoroacetate (MDFA)/methyl 2,2-difluoro-2-(fluorosulfonyl)acetate MDFA (MDFSFA)/TTE electrolyte was developed successfully in which MDFSFA with a high reduction voltage of 2.2 V was introduced as a cosolvent for further strengthening the LiF-rich SEI and CEI. It was demonstrated that the similar LiF-enriched interphases on the NMC811 cathode and the graphite anode balanced the thermodynamic (capacity) and kinetic (interphase resistance)

matching between the two electrodes at extreme conditions, enabling the 4.5 V graphite||NMC811 full batteries to keep 75% of RT reversible capacity (0.1 °C) at −50 °C (−60 °C) with a practical areal capacity of 2.5 mAh cm<sup>−2</sup> and the pouch cells with lean electrolyte (2.5 g Ah<sup>−1</sup>) to stably cycle at −30 °C for over 300 times with an average CE of 99.9% (Figure 20d–g). This work opened a new electrolyte design direction for tuning fluorinated interphases toward practical batteries with high-voltage, fast-charging, and wide-temperature operating features.<sup>55</sup>

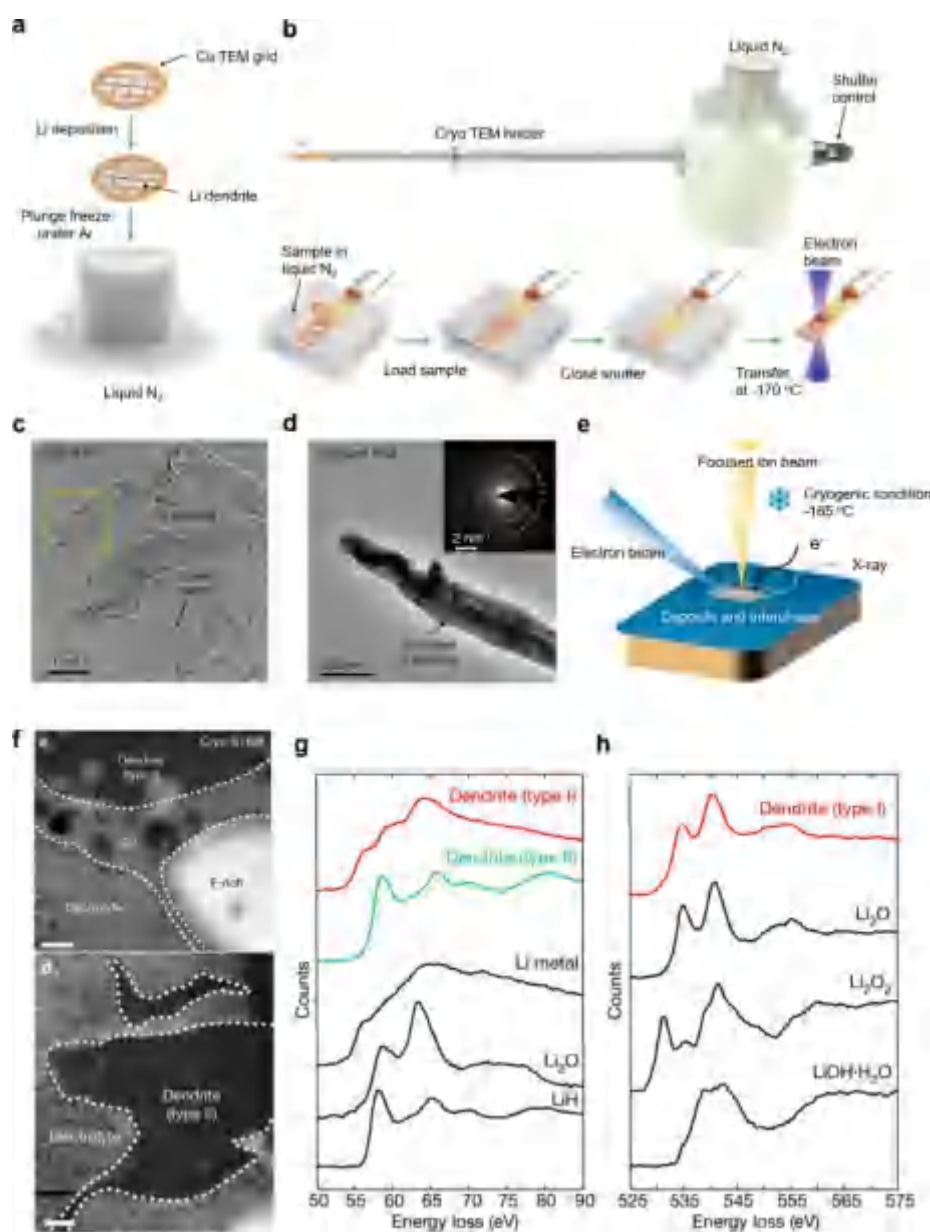
For practical Li-based batteries, there is a growing need for their stable operation under all conditions, including high voltage (e.g., ≥4.5 V), fast cycling rate (e.g., ≤15 min), wide temperature range (e.g., ±60 °C), and extended charge/discharge cycling, which are highly related to the interphases. In this case, fluorinated interphases featuring a LiF component demonstrate attractive prospects. LiF exhibits low solubility, high mechanical property, a wide band gap, excellent antioxidation ability, and high interphasial energy against Li metal, contributing to a robust SEI. Moreover, the high shear modulus of LiF suppresses anode pulverization. Unfortunately, the low Li<sup>+</sup> conductivity of LiF (~10<sup>−12</sup> S cm<sup>−1</sup>) in the interphase restricts the high-rate performance, particularly toward Li metal anodes. Incorporating fluorinated conducting components (e.g., Li<sub>x</sub>PO<sub>y</sub>F<sub>z</sub>) into the LiF-rich interphase can improve the cycling stability and fast-charging capability. Fluorinated components can also be combined with the organic SEI matrix to accommodate the large volume change of the Li anode. Although a LiF-enriched SEI displays low impedance and high stability to improve Li<sup>+</sup> diffusion at low temperatures, controversy remains over the impacts of LiF in the CEI components on the low-temperature performance. Further investigation is needed to unlock the roles and influencing factors of the macroscopic and microscopic properties for LiF, particularly under extreme conditions.

### 3.4. Techniques To Probe Fluorinated Interphases

As described above, the passivated interphase is electronically insulating but ionic conducting, arising from the decomposition of the electrolyte components on the surface of the electrode, which plays a vital role in determining the capacity, cyclability, rate performance, CE, and safety properties of Li-based batteries. Understanding the morphologies, chemical compositions, and mechanical properties of the CEI/SEI is significant for further designing fluorinated interphases on the active materials, especially on the anodes.<sup>430</sup> Since its first demonstration by Dey et al. in the 1970s, the SEI has attracted significant interest regarding the formation mechanisms, structures, phase, and chemical compositions; however, due to its spatially and temporally dynamic nature, an in-depth comprehensive understanding of the SEI, especially on the atomic scale, remains a huge challenge.<sup>284,389,431–437</sup> Generally, it is difficult to discern the SEI/CEI chemical components from the solvent species, and the SEI/CEI thickness is also hard to quantify with ambiguous boundaries. Besides, the SEI/CEI properties are highly affected by the testing conditions (e.g., electrolytes, operation temperature, current density, voltage range, and electrode materials) and the sample preparation environment (e.g., washing solvent, exposure to air<sup>389</sup> and moisture), which undergoes a dynamic evolution process during the charging and discharging. To provide valuable information on the interphase characteristics, various advanced techniques, including microscopy and spectroscopy,

**Table 3. Comparison of the Spatial Resolution, Useful Information (e.g., composition, structure, morphology), as Well as Corresponding Strengths and Limitations of Each Technique for Probing the Interphase**

characterization techniques	spatial resolution	composition	structure	morphology	other information	strengths	limitations	ref
cryo-(S)TEM	0.1 nm	yes	yes	yes		preserving the electrochemical state, corresponding structure, and chemical information on the interphase without destruction at cryogenic temperatures	hard to probe organic-enriched SEI derived from solvent decomposition; explaining chemical details in the disordered and amorphous phases remains challenging	444, 445, 447, 492, 493
cryo-FIB/SEM	nm	yes	yes	yes	obtain cross-sectional view of the interphase	obtain spectroscopy imaging from the cross-sectional view at the nanoscale	transfer time even within seconds may not be sufficient for some sensitive samples; requiring optimizing the procedures to eliminate sample exposure	494, 495
EQCM	$5 \times 10^{-11}$ g	yes	yes	yes	gravimetric information	quantify and monitor the real-time interphase evolution and component dissolution during the electrochemical process	lack of exact structural information	450, 496–503
TGC	$10^{-7}$ g	yes				quantify the contribution of the interphase $\text{Li}^+$ and unreacted metallic $\text{Li}^0$ to the capacity decay	requires a nondestructive approach to quantify residual Li during electrochemical cycling	504
XPS	nm	yes				precise in monitoring the electronic structures of interphase compositions	in situ XPS has yet to be fully designed due to ultrahigh vacuum, big challenges with sample preparation, data collection protocols, and data processing that can lead to misleading conclusions	458, 459, 461, 505–507
SIMS	nm	yes	yes			visualize the growth of the interphase microstructure	creation of secondary products due to the high-energy beam	457, 508–510
NMR		yes	yes		amount and time scale of $\text{Li}^+$ transport through the interphase	noninvasively identify chemical compositions and structures of the interphases	fails to probe the dynamic nature of the interphase	479, 480, 487
AFM	nm			yes	mechanical and electrical features	offers high-resolution topographical images; evaluates mechanical evolution of the interphase	fails to unveil chemical information, restricted magnification, and vertical range	462, 511, 512
TERS	nm	yes	yes	yes		provides both topographical and chemical mapping of the interphase with high sensitivity and selectivity	needs to increase the efficiency of motivation and collection to probe the interphase	466, 467, 513–515
NR	nm	yes	yes	yes	interphase evolution	quantitatively determine the interphase properties; detect evolutions of the interphase structure	requires a flat specimen to generate a strong signal; very limited facilities to handle the produced neutrons outside the particle accelerator	437, 473–475, 516
XAS	0.001 nm	yes	yes	yes	local atomic arrangement and electronic structure	high sensitivity to local chemical bonds and solvent environments for interphase investigation	requires a separate kind of electrochemical cell designed for in situ operation	471, 472, 517–520
SECM	from 10 nm to 1 $\mu\text{m}$	yes		yes		monitors the formation and evolution of the interphase; determines electrically insulating feature	probe positioning is complicated by the different faradaic current behavior for conductive and insulating surfaces	483, 484, 521



**Figure 21.** Probing the critical characteristics of sensitive interphases by cryo-EM. (a) Electrochemically depositing Li metal dendrites onto a copper TEM grid followed by plunging into liquid nitrogen after battery disassembly. (b) The specimen is then placed onto the cryo-TEM holder while still maintained in liquid nitrogen and isolated from the environment by a closed shutter. (c) Cryo-TEM image of Li metal dendrites with an electron dose rate  $< 1 \text{ e}^- \text{Å}^{-2} \text{s}^{-1}$ . (d) Typical TEM image of a Li metal dendrite after exposing it to air for  $\sim 1 \text{ s}$  at room temperature. (Inset) Corresponding SAED pattern. Reproduced with permission from ref 492. Copyright 2017 American Association for the Advancement of Science. (e) Illustration of the cryo-FIB/SEM setup at liquid nitrogen temperature. Reproduced with permission from ref 525. Copyright 2020 American Chemical Society. (f) HAADF cryo-STEM images displaying an extended SEI layer on (upper) type I dendrites but not on (lower) type II dendrites. EELS elemental mapping of SEIs on (g) type I dendrite enriched in O and Li and (h) type II dendrite without carbon. Reproduced with permission from ref 526. Copyright 2018 Springer Nature.

have been applied extensively. Scanning electron microscopy (SEM) and TEM are two powerful and most widely used tools for visualizing and monitoring the interphase directly,<sup>340,438–442</sup> particularly when conducting at cryogenic temperatures for preserving the pristine states of the interphases.<sup>24,352,376,420,443–449</sup> In addition, some properties of the growing interphase can be quantified to establish their correlation with the electrochemical performance of batteries, e.g., developing an electrochemical quartz crystal microbalance (EQCM) for quantifying the interphase dissolution phenomenon.<sup>450</sup> Various interphase analysis techniques, such as

SIMS,<sup>451–457</sup> XPS,<sup>458–461</sup> AFM,<sup>462–467</sup> XAS,<sup>468–472</sup> neutron reflectometry (NR),<sup>473–475</sup> XRD,<sup>476–478</sup> NMR,<sup>479–482</sup> and scanning electrochemical microscopy (SECM),<sup>483–486</sup> have also been widely employed to probe the elemental composition, interphase morphology, and mechanical/electrical properties of the interphase. Notably, due to the elusive and highly dynamic properties, different techniques need to be combined to comprehensively recognize the fluorinated interphases at the atomic level. However, most of these advanced techniques for investigating fluorinated interphases are under ex situ conditions, requiring the disassembling of the



batteries after charging/discharging to various states, which may cause the exposure of the samples to ambient conditions during the transport process for characterization. These processes may change the interphases by affecting the morphology, microstructure, chemical compositions, mechanical properties, etc., which may cause misleading results.<sup>437,473</sup> Therefore, in situ/operando measurements conducted at the operating conditions without disassembling the batteries are more reliable and valuable technologies to provide real-time information about the characteristics and evolution process of fluorinated interphases during battery cycling.

Since several review articles have comprehensively summarized the technical details, research progress, and applications on understanding the SEI using traditional techniques,<sup>430,437,473,487,488</sup> in this section, the focus will be on state-of-the-art developments of updated characterization techniques for fluorinated interphases, elucidating the chemical compositions, morphologies, micro/nanostructures, and other properties. Important features of each technique, including the spatial resolution, useful information, as well as corresponding strengths and limitations for probing the interphase, are compared in Table 3. To capture the moment of the reactions at the interphase, which occurs at the picosecond time scale,<sup>310,489,490</sup> the DFT and MD simulations have been extensively utilized. Besides, theoretical calculations can also help to predict and quantify the correlation between the structure and the properties of the interphases. Therefore, theoretical calculations and simulations are associated with the micro/nanostructure and properties of the SEI, in turn offering guidance in rationally designing and regulating the SEI characteristics for high-performance Li-based batteries. Considerable technical details of the theoretical calculations and simulations for understanding the interphases can be found in previous specialized reviews, which will not be discussed in this section.<sup>437,491</sup>

**3.4.1. Cryo-EM.** As discussed earlier, SEI layers are sensitive to oxygen and moisture during the transfer process to electron microscopes (e.g., TEM and SEM), causing insufficient resolution for characterizing the micro/nanostructures of the SEI. In addition, under the ultrahigh vacuum of the TEM chamber, Li metal anodes are extremely vulnerable to radiation damage, such as sample ionization and bond breakage, caused by the high electron dose in the incident beam and side chemical reactions induced by free radicals and secondary electrons. Inspired by biological imaging techniques, cryo-EM with a low electron dose and a frozen sample at low temperature has been used to resolve the crystalline atomic lattices of the SEI/CEI while preserving the delicate chemical composition and spatial features, which has demonstrated its advantage in visualizing and elucidating nanostructures and compositions of the beam-sensitive SEI at the atomic level.<sup>24,443</sup>

To preserve the pristine state of chemically reactive and beam-sensitive materials, especially the Li metal anode, Cui and co-workers pioneered cryo-TEM investigation by designing a cryo-transfer method.<sup>492</sup> As illustrated in Figure 21a and e 21b, Li was electrochemically deposited onto a copper grid followed by washing with 1,3-dioxolane to remove Li salts and flash freezing the specimen in liquid nitrogen immediately. Therefore, the electrochemical state as well as the corresponding structure and chemical information on Li dendrites were retained at cryogenic temperatures. Through visualizing individual Li dendrites, they achieved a high atomic resolution

(0.7 Å) image on the spherical aberration-corrected TEM. In contrast to the air-exposed Li dendrites with rough surfaces and darker contrast due to the formation of polycrystalline artifacts, the cryo-transferred Li dendrites preserved their states, which constructed a much smoother and thinner SEI layer on Li metal (Figure 21c and e 21d). Notably, with a standard EC/DEC electrolyte, the formed SEI was composed of small crystalline domains (diameter  $\approx$  3 nm) embedded randomly in the amorphous matrix. On the contrary, with 10 vol % FEC as the additive, a more ordered multilayer SEI was generated, which was consistent with the structure proposed by Aurbach et al.<sup>522</sup> However, LiF was not observed in the SEI layer, which may be because TEM is sensitive to crystalline phases when probing a small selected surface area.<sup>444,492</sup> In another work, Meng et al. developed a new cell configuration to obtain electrochemically deposited Li (EDLi) for cryo-TEM imaging. A copper grid was placed on the Cu foil and used as a part of the counterpart substrate.<sup>420</sup> After deposition, the cell was disassembled and rinsed with DMC before transferring. Then, the grid was loaded in a covered cryogenic dewar with continuous Ar flow, and the holder was pumped down to  $10^{-5}$  bar and immediately loaded into a vacuum chamber (cooled to 100 K) for transfer. It was revealed that the EDLi is amorphous with uneven SEIs containing amorphous organic species and crystalline LiF. Nevertheless, the crystalline LiF in the SEI layer possessed a low conductivity of  $<10^{-12}$  S cm<sup>-1</sup>, and the amorphous Li<sub>x</sub>PO<sub>y</sub>F<sub>z</sub> species could display a higher ionic conductivity,<sup>523,524</sup> which questioned the favorable effect and the working mechanism of LiF for high CEs. Soon after, using cryo-TEM, Cui and co-workers discovered the fundamental effects of SEI nanostructures (i.e., mosaic and multilayer) on the performance of a Li metal anode, pointing out that fluctuations in the crystalline grain distribution within the SEI played a vital role in differentiating the mosaic structure from the multilayer structure, thus dictating the battery performance.<sup>445</sup> Specifically, a multilayer nanostructure favored uniform Li stripping behavior, while a mosaic nanostructure resulted in fast Li dissolution.

To identify the dominant components and nanostructure of the SEI layer, an effective strategy to minimize Li pulverization was demonstrated by Zhang et al. via a fluorinated orthoformate solvent-based electrolyte. The in situ-formed SEI on the Li anode displayed a monolithic feature with the same composition from the surface to the bottom along with horizontally homogeneous coverage of the SEI observed from cryo-TEM imaging. This unique SEI with enriched inorganics significantly suppressed electrolyte depletion and minimized pulverization for a stable Li anode.<sup>376</sup> Moreover, the evolution of the SEI layer during cycling can be tracked with the aid of cryo-TEM.<sup>446</sup> Cui et al. revealed that the initial SEI generated during the first cycle was thin and amorphous, which evolved into two morphologies upon further cycling, i.e., a compact SEI containing inorganic components that passivated the electrode surface and a large extended SEI without inorganics due to incomplete passivation.<sup>493</sup> The extended SEI growth inevitably consumed massive Li and led to a porosity reduction, which could be prevented by inorganic species in the compact SEI layer. These results via cryo-TEM indicated that the vastly heterogeneous process for SEI growth could be effectively regulated by sufficient passivation of the SEI. Very recently, the same research group further adapted a thin film vitrification approach to preserve the SEI film in its native liquid electrolyte environment, yielding uniform thin films inside the holes of the

Cu grid. Afterward, these samples were probed through cryo-(S)TEM to visualize the intact structure and chemistry of the SEI films. It was demonstrated that the anion-derived SEI enriched with more inorganics contributed to a smaller swelling ratio, preserving its mechanical property and chemical stability for enhancing electrochemical cycling.<sup>352</sup> Encouraged by the successful interphase characterization in liquid electrolytes, cryo-TEM was also utilized to visualize the interphase structure between the anode and the solid polymer electrolytes atomically.<sup>527–533</sup> In 2020, the cryo-TEM results revealed a mosaic interphase between the Li anode and the PEO electrolyte, where various inorganic nanocrystals ( $\text{Li}_2\text{O}$ ,  $\text{LiOH}$ , and  $\text{Li}_2\text{CO}_3$ ) were randomly distributed inside the amorphous phase. The  $\text{Li}_2\text{S}$  addition favored the decomposition of  $\text{N}(\text{CF}_3\text{SO}_2)_2^-$  and thus promoted the enrichment of  $\text{LiF}$  nanocrystals in the Li/PEO interphase, as verified by both cryo-TEM and simulations. The  $\text{LiF}$  nanocrystals not only enhanced the  $\text{Li}^+$  diffusion kinetics and prevented the chain breaks of C–O but also suppressed side reactions between the Li anode and the PEO electrolyte, thus enabling outstanding electrochemical performance for both half cells and full cells.<sup>447</sup>

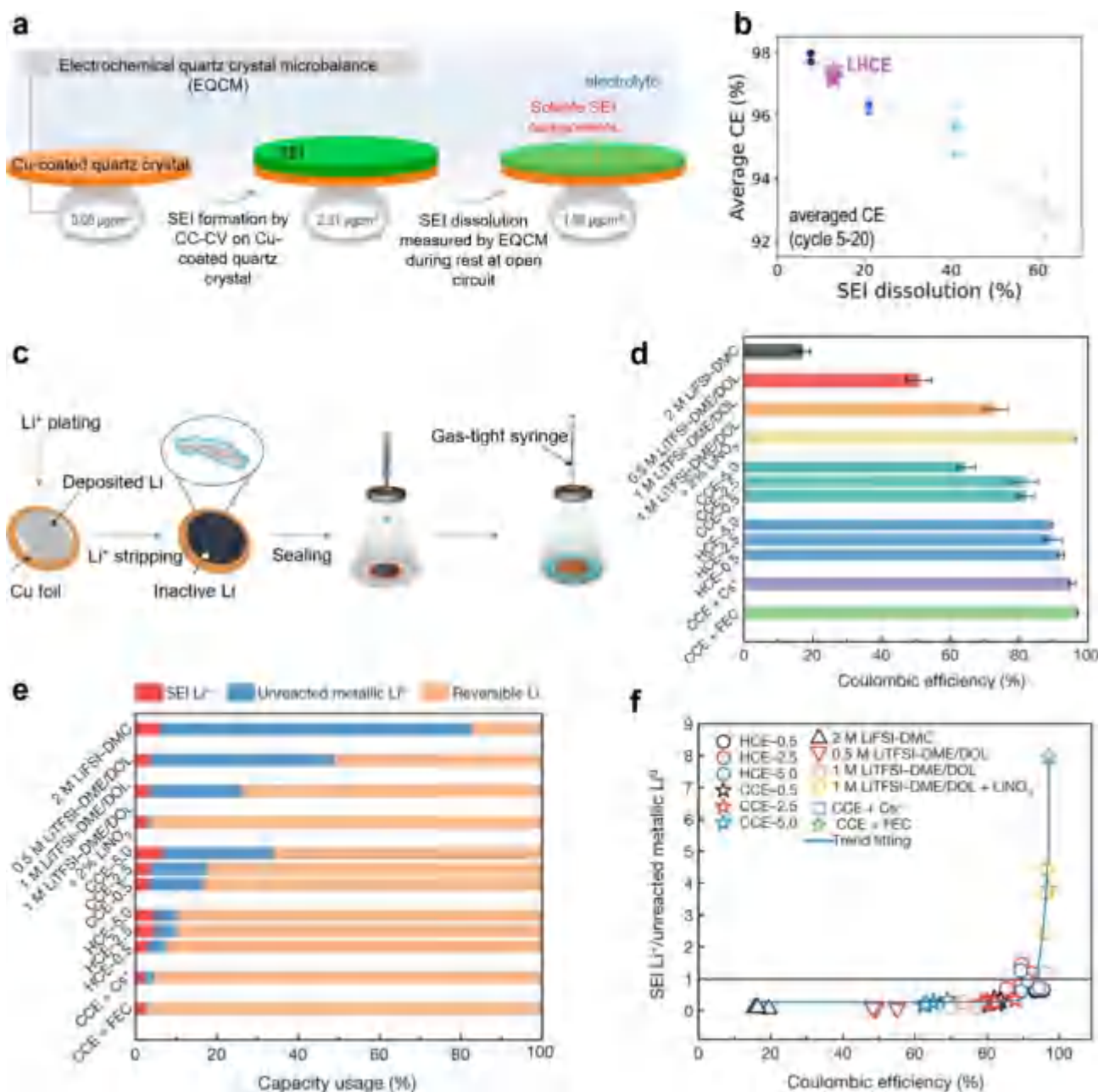
Cryo-TEM has been regarded as a powerful tool for confirming and refining SEI models, which have long been hypothesized. Nevertheless, compared to the extensively investigated inorganic components (e.g.,  $\text{LiF}$ ) by cryo-TEM, determining the properties of the organic-enriched SEI that are derived from solvent decomposition remains an enormous challenge. Besides, more efforts need to be put in regarding cryo-EM techniques for guiding the optimization of high-performance Li-based batteries, including exploring and explaining the chemical details in the disordered and amorphous phases, revealing more in-depth information from lattice imaging, etc.

Since cryo-TEM requires a thin specimen ( $<100$  nm) on the TEM grids, it is hard to probe the bulk electrode materials. In contrast to previous TEM investigations focusing on the surface structure, the focused ion beam (FIB) technique with milling capability has been applied for preparing TEM samples by lifting out the bulk structure of the electrode materials. Unfortunately, the FIB conducted at room temperature leads to various artifact issues, including surface damage, redeposition of beam-sensitive Li metals, and mechanical deformation related to “cutting” approaches. Therefore, cryo-FIB is necessary to process the electrode samples and interphases at cryogenic temperature ( $-170$  °C).<sup>437,534</sup>

Combining the milling characteristics of FIB at cryogenic temperatures to preserve solid–liquid interphases with the SEM technique to obtain spectroscopy imaging from the cross-sectional view at the nanoscale, the SEI film formed on anode materials can be precisely characterized (Figure 21e).<sup>525</sup> Using cryo-FIB/SEM characterization, Archer et al. reported that a pinhole-free  $\text{Al}_2\text{O}_3$  coating (with a thickness of 15 nm) served as an artificial solid–electrolyte interphase on the Cu foil, revealing that the deposited Li consisted of both a dense and a porous structure that highly improved the stability of Li deposition.<sup>494</sup> Via conducting imaging and spectroscopic mapping on the cross sections of Li deposits prepared by cryo-FIB milling, Kourkoutis et al. revealed that the intact surface layers and interphase compositions of the exposed reactive materials experienced negligible change, which could be characterized down to the nanoscale.<sup>495</sup> Obviously, a cryogenic sample temperature enabled energy-dispersive EDX

mapping of Li with increased signal over an extended period when coupling the new EDX detectors with the cryo-FIB/SEM technique. However, the rapid transfer time, even within seconds, may not be sufficient for some sensitive samples, requiring further improvements in these techniques to eliminate sample exposure.

It has been recognized that the element distribution and contents of the electrode materials can be determined by EDS and the EELS, offering valuable information about the chemical compositions, especially for some amorphous species.<sup>443</sup> Recent progress in cryo-TEM has been successfully used for beam-sensitive battery materials,<sup>420,448,492,526,535</sup> achieving atomic resolution imaging for SEI layers formed on the Si,<sup>449</sup> carbon,<sup>493</sup> and Li metal anodes.<sup>445,446,536</sup> To restrict the destructive change in structures and interphase chemistry during the cell disassembly and solvent-washing processes before cryo-TEM characterization, cryo-scanning transmission electron microscopy (STEM) combined with the cryo-FIB lift-out procedure was applied for visualizing the SEI layers. Significant work was conducted by Kourkoutis et al. using cryo-STEM, identifying two distinct types of dendrites on the Li anode.<sup>526</sup> According to the HAADF cryo-STEM imaging (Figure 21f), an extended SEI (300–500 nm thick) existed in the type I dendrite, suggesting a typical washing process had removed a large portion of the SEI layer. On the contrary, the type II dendrites with the thickness of hundreds of nanometers are more likely to disconnect with the electrodes due to much smaller contact areas, which could result in dead Li formation and capacity attenuation of batteries. In addition, abundant oxygen and Li in a type I SEI layer without F was observed from EELS elemental maps, while notably, an extended type II SEI was absent with a C-free, Li- and O-enriched type II dendrite ( $\sim 20$  nm). Based on the fine structures of the Li and O K-edge (Figure 21g and 21h), type I dendrite mainly contained Li metal and partial  $\text{Li}_2\text{O}$ , while type II dendrite was unexpectedly dominated by pure lithium hydride ( $\text{LiH}$ ). More significantly, the fluorinated electrolyte was confirmed to be able to mitigate the  $\text{LiH}$  dendrite formation and largely altered the Li deposition. The discovery of extended SEI layers as well as  $\text{LiH}$  dendrites on Li metal was informative to further efforts on overcoming their detrimental effects. Based on this recent progress, it was surprising that the recognized favorable  $\text{LiF}$  was not observed in the SEI, even using fluorinated electrolytes. Utilizing cryo-STEM and EELS techniques, Cui and his group elucidated that instead of participating in the compact SEI (15 nm) directly,  $\text{LiF}$  precipitated as large nanoparticles (100–400 nm) across the electrode surface, extending outside of the compact SEI for the indirect SEI regime. In other words,  $\text{LiF}$  cannot play a dominant role in passivating Li metal or promoting  $\text{Li}^+$  transport through the compact SEI. This report refined the traditional SEI structure across multiple length scales and nuanced the effects of the SEI species on the anode stability.<sup>537</sup> Besides the SEI formed on Li metal, the structural and chemical evolution of SEI layers on Si anodes were unveiled in three dimensions via combining sensitive elemental tomography with cryo-STEM. Owing to the continuous void growth and the condensation during the delithiation process, the unstable SEI on the Si anode grew toward the interior, which formed the core–shell structure in the initial cycle and further evolved to a “plum-pudding” structure comprising abundant voids and dead Si upon longer cycling. As a consequence, the engulfing of Si domains by the SEI was revealed, causing the disruption of electron transport



**Figure 22.** Quantifying the correlation between interfacial chemistry and electrochemical performance by EQCM and TGC methods. (a) The procedure for analyzing the SEI formation and dissolution with the EQCM technique. (b) Relationship between the average CE of the Li||Cu half-cell, and SEI dissolution results from EQCM. Reproduced with permission from ref 450. Copyright 2023 American Chemical Society. (c) Schematic illustration of the working principle of the TGC technique. (d) The average first CE of Li||Cu cells with various testing conditions. Eight electrolytes (HCE, CCE, 2 M LiFSI-DMC, 0.5 M LiTFSI-DME/DOL, 1 M LiTFSI-DME/DOL, 1 M LiTFSI-DME/DOL + 2%  $\text{LiNO}_3$ , CCE +  $\text{Cs}^+$ , and CCE + FEC) and three stripping rates (0.5, 2.5, and 5.0  $\text{mA cm}^{-2}$  to 1 V) are used. (e) The TGC method for analyzing the capacity usage (SEI  $\text{Li}^+$ , unreacted metallic  $\text{Li}^0$ , and reversible Li) with various testing conditions. (f) The ratio of SEI  $\text{Li}^+$  to unreacted metallic  $\text{Li}^0$  calculated by TGC (blue line refers to exponential fitting results). Reproduced with permission from ref 504. Copyright 2019 Springer Nature.

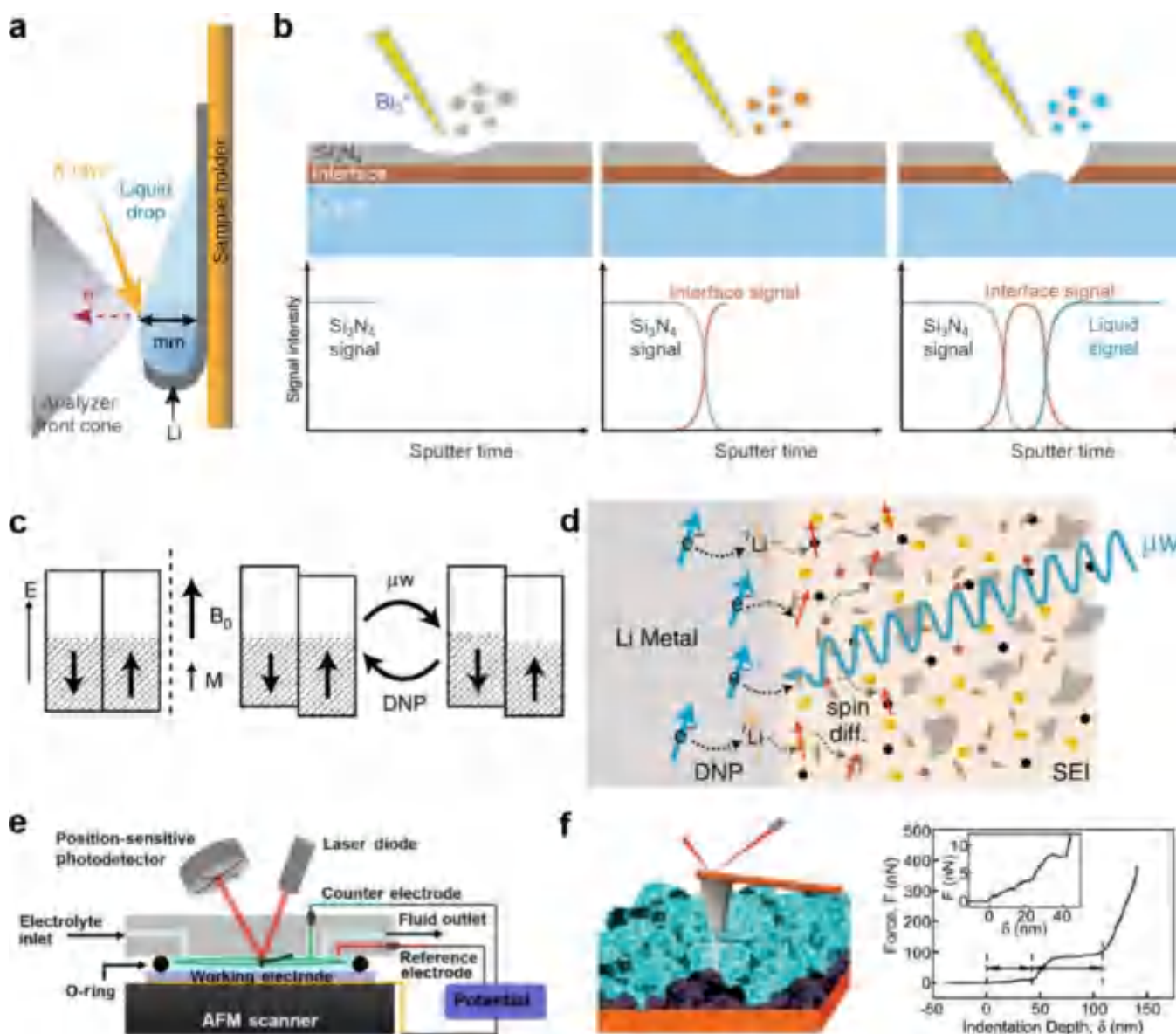
pathways and generation of dead Si, which further depleted the electrolyte and deteriorated the battery performance.<sup>437</sup>

**3.4.2. Quantifying Techniques.** Based on the piezoelectric effect, where the mechanical shear stress is induced in the crystal as a function of the applied voltage, EQCM has been regarded as an extremely sensitive mass monitoring approach to studying electrochemical reactions.<sup>499–503</sup> The electrode is generally deposited on an oscillating sensor (made of quartz crystal), which exhibits a linear relationship between the resonance frequency and its mass based on the Sauerbrey

equation in the ideal case of a homogeneous and rigid layer adhered to the sensor surface. Then, through probing the shift in resonance frequency, the mass change of the electrode can be obtained quantitatively. Therefore, the EQCM technique allows monitoring the real-time SEI evolution and component dissolution phenomenon as a function of applied voltage.<sup>450,498</sup>

Through in situ EQCM measurement, Pan et al. revealed that LiF and Li alkylcarbonates comprised the main SEI components on graphite anodes (1 M  $\text{LiPF}_6$ -EC/DMC electrolyte) at various voltages. LiF was formed at 1.5 V, and





**Figure 23.** Advanced characterization for analyzing chemical compositions, morphologies, structural information, mechanical properties, etc., for interphases. (a) Schematic illustration of liquid droplets on the Li substrate for APPES measurements. Reproduced with permission from ref 459. Copyright 2019 Springer Nature. (b) Schematic illustration of the developed in situ liquid-SIMS technique for SEI characterization. Reproduced with permission from ref 509. Copyright 2020 Springer Nature. (c, d) The mechanism of Li metal DNP. (c) The conduction electron spin bands of a metal plotted against energy ( $E$ ): in the absence of a magnetic field (left); (middle) in an applied magnetic field ( $B_0$ ), leading to a Pauli paramagnetic moment ( $M$ ); and after microwave ( $\mu\text{W}$ ) irradiation at the CESR frequency (right). Note: the arrows for each spin band denote the electron magnetic moment. (d) Schematic for hyperpolarization of Li metal on application of microwaves (DNP, black dashed arrows) and subsequent spin diffusion in the heterogeneous mixed organic/inorganic SEI (gray dashed arrows). Reproduced with permission from ref 556. Copyright 2020 Springer Nature. (e) Cross-sectional schematic diagram of an electrochemical AFM cell. Reproduced with permission from ref 511. Copyright 2015 Elsevier. (f) Schematic illustration of the AFM force spectroscopy measurements. (Inset) Indentation curve. Reproduced with permission from ref 462. Copyright 2012 American Chemical Society.

EC was initially reduced at 0.74 V. Moreover, it was very interesting to observe that the nascent interphase could be partially reoxidized during the very first delithiation cycle, which could be the reason for the reported metastability of the SEI ingredients in the nascent form.<sup>538</sup> In recent years, EQCM has been well developed, in which the energy dissipation of the resonating sensor is additionally considered. Introducing the SEI shear viscosity coefficient, SEI shear storage modulus, and electrolyte properties in a multilayered viscoelastic Voigt model, the dissipative properties of a nonrigid SEI and change in electrolyte viscosity are considered.<sup>539</sup> Combining the

EQCM with dissipation monitoring (EQCM-D), gravimetric and viscoelastic changes in  $\text{Li}_4\text{Ti}_5\text{O}_{12}$  anodes were assessed during the insertion/extraction of  $\text{Li}^+$  and formation/growth of the SEI. These results indicated that the intrinsic viscoelastic properties of the growing SEI layers could be quantified, and the SEI quality (recognized from the EQCM-D data) was improved by optimizing the electrolyte system (e.g., adding vinylene carbonate additive or using LiTFSI salt).<sup>497</sup> Typically, the EQCM-D technique can provide information on the structural change in more realistic nonrigid viscoelastic interphases.<sup>496</sup>

One should note that among all of the SEI properties, the dissolution in the electrolyte can directly influence the formation and growth of the SEI in the subsequent cycles. Generally, additional Li and electrolyte have to be consumed to repair the partially dissolved SEI, which will inevitably increase the SEI thickness,<sup>540,541</sup> resulting in severe capacity loss through the repeated SEI formation and growth process. The EQCM has been applied to quantify the mass loss of the SEI layer (after formation) upon standing at an open circuit. The SEI was found to lose more than one-half of its mass, demonstrating the potential of EQCM to quantify the SEI dissolution and further reveal the mechanisms of SEI formation and growth.<sup>450,542,543</sup> Very recently, utilizing operando EQCM, Cui et al. successfully quantified the SEI mass loss in ether-based electrolytes (Figure 22a and 22b).<sup>450</sup> By establishing the correlation among solubility, passivity, and cyclability, it was concluded that SEI dissolution was a major factor influencing the subsequent SEI formation and growth. In addition, it was elucidated that the calendar life of Li-based batteries can be extended by reducing the SEI dissolution, highlighting the significance of regulating the dissolution phenomenon for mitigating the SEI degradation.

Utilizing advanced characterization techniques, it has been recognized that establishing the correlation between interfacial chemistry and electrochemical performances is significant for resolving issues related to Li metal anode. Recently, using an analytical technique of titration gas chromatography (TGC), Meng et al. quantified the contribution of Li<sup>+</sup> in the SEI components (e.g., LiF, Li<sub>2</sub>CO<sub>3</sub>, Li<sub>2</sub>O) and unreacted metallic Li<sup>0</sup> to the total amount of inactive Li, respectively, which was critical for understanding the real mechanisms causing rapid capacity deterioration.<sup>504</sup> The critical difference exploited between the SEI Li<sup>+</sup> species and metallic Li<sup>0</sup> is their chemical reactivity, where only the metallic Li<sup>0</sup> reacted with protic solvents. For instance, Li<sup>0</sup> reacts with H<sub>2</sub>O to create H<sub>2</sub> gas (2Li + 2H<sub>2</sub>O → 2LiOH + H<sub>2</sub>↑). The H<sub>2</sub>O titration (all metallic Li<sup>0</sup> is reacted) was paired with a gas chromatography facility (quantify generated H<sub>2</sub> in the reaction) to a single analytical tool (TGC), exactly quantifying the amount of unreacted metallic Li<sup>0</sup> (Figure 22c). Then, a high resolution of 10<sup>-7</sup> g was obtained for analyzing metallic Li<sup>0</sup>, after combining with an advanced barrier ionization H<sub>2</sub> detector. Using this TGC methodology, the relationship between the amount of inactive Li with the CEs of LillCu cells in different electrolytes was correlated (Figure 22d). By quantifying the amount of metallic Li<sup>0</sup> directly by the TGC, the content of SEI Li<sup>+</sup> was calculated accordingly. Interestingly, as shown in Figure 22e, the content of Li<sup>+</sup> components in SEI remained constant at a low level, whereas the amount of unreacted metallic Li<sup>0</sup> increased significantly as the CE decreased. In addition, the ratio of Li<sup>+</sup> components in SEI and unreacted metallic Li<sup>0</sup> elucidated the CE below 95%. It was the unreacted metallic Li<sup>0</sup> rather than SEI formation that dictated the amount of inactive Li, further causing the capacity loss (Figure 22f). The SEI formation only dominated at very high CEs. This work provided interesting insights for advancing LMBs. Nevertheless, a nondestructive approach to quantify residual Li upon cycling without disassembling the cell is still urgently required.

**3.4.3. Composition Analysis Techniques.** To examine the surface chemistry of the interphases, various analysis approaches such as XPS, SIMS, and NMR have been extensively employed in recent research.<sup>517,544–550</sup> By utilizing the photons in the X-ray range that lead to the emission of the

core electrons from the specimen, XPS has been widely used for detecting all elements in the periodic table except H and He. Therefore, XPS is an ideal technology for monitoring the electronic structures of SEI compositions, such as LiF, Li<sub>2</sub>CO<sub>3</sub>, organics, and other species.<sup>505–507</sup> In 1985, based on a LiBF<sub>4</sub>-containing electrolyte, the existence of LiF in SEI components was proved for the first time by Takehara et al. using XPS.<sup>434</sup> Nevertheless, the ex situ XPS fails to disclose the natural state and properties of the interphases, making it necessary to develop in situ XPS to capture the real-time state of interphases during the battery cycling. Unfortunately, as a surface-sensitive technique with microscale in-plane spatial resolution, in situ XPS has yet to be fully designed due to the ultrahigh vacuum condition.<sup>458</sup>

To solve this challenge, in situ spectroscopies, such as ambient pressure photoelectron spectroscopy (APPEs), were employed by Hahlin et al. (Figure 23a), providing insights for future operando measurements on the dynamic chemical evolution of SEI.<sup>459</sup> Although liquid electrolytes could be used in this investigation, the electrochemical cycling tests were not applied, making this technique fail to reflect the real-time state of SEI in batteries. Despite the extensive application in analyzing the SEI chemical compositions,<sup>460,488,551–555</sup> XPS still exhibited some big challenges related to the sample preparation and data collection protocols, which can lead to misleading conclusions. Recently, an informative and significant work was conducted by Bent et al., identifying some key factors to be carefully considered to avoid erroneous interpretations of XPS for SEI investigation, including the spatial location of the sample, periods of sample inactivity under the ultrahigh vacuum in XPS chamber, and Ar<sup>+</sup> sputtering conditions.<sup>461</sup> Especially, the poorly rinsed sample introduced artifacts to the SEI components, with a 40% variation across the *x*–*y* plane for atomic percentage. It was also pointed out that SEI experienced obvious changes in chemical components with the ultrahigh vacuum condition or Ar<sup>+</sup> sputtering. This report offered rigorous guidelines to circumvent issues existing in XPS analysis, which will provide valuable guidelines in SEI understanding with accurate chemical characterization.

Through analyzing the ratio of gravimetric mass to surface charge (*m/z*) for specific elements, TOF-SIMS has been applied to obtain the chemical compositions of SEIs quantitatively. Generally, when interacting with a surface, the energetic primary ion beam emits secondary ions. These secondary ions pass through a flight tube, and then they are continuously analyzed, with the corresponding intensities being recorded over time. The ion intensities are proportional to element contents, thus forming a semiquantitative concentration-depth image for probing the chemical composition of the SEI layers.<sup>451,557–559</sup> Peled et al. were pioneers in applying SIMS for investigating the mechanism of SEI formation on the basal plane and cross-sectional edge of graphite. Since then, depth profiling by SIMS has been utilized widely to probe the SEIs generated on Cu,<sup>452,560</sup> graphite,<sup>426,453,454,518,561–563</sup> Si,<sup>452,455,564–567</sup> Li metal,<sup>351,452,456,568–571</sup> etc., demonstrating its ability to analyze the dynamic properties of SEI layers with high sensitivity. Especially, the speculated SEI chemical composition can be confirmed via SIMS by profiling their distribution in depths in the SEI layer. For instance, Wang et al. developed a Li-11 wt % Sr alloy anode to form a SrF<sub>2</sub>-rich interphase in fluorine-containing electrolyte.<sup>325</sup> With the aid of TOF-SIMS, the

thickness of the  $\text{SrF}_2$ -enriched SEI on the alloy anode was determined. After immersing in 2 M LiFSI for 12 h, the anode surface was investigated by beam over a  $5\ \mu\text{m} \times \mu\text{m}$  area. Strong signals of both F and Sr were observed with the thickness of the interphase determined to be 250 nm, which is consistent with the XPS results. In another report, a crowding dilutant (1,2-difluorobenzene) modified ionic liquid electrolyte (M-ILE) with energetic kinetics and a superhigh AGG portion was designed for a stable Li metal anode. TOF-SIMS was performed to reveal the distribution of the chemical components in the SEI layer with different sputter times. The  $\text{LiF}_2^-$  intensity was much higher than that for the ILE-induced SEI, confirming that the M-ILE electrolyte contributed to a LiF-enriched SEI. Besides, the 3D reconstruction of the  $\text{LiF}_2^-$  distribution map demonstrated that LiF was uniformly dispersed in the M-ILE-induced SEI. However, LiF only existed in the superficial layer of the ILE-derived SEI.<sup>572</sup> The SEI formation mechanism and the in-depth understanding of the interphasial chemistry and structure are still restricted by the ex situ measurements. Inspired by increasing requirements, real-time SEI formation was monitored by Zhu and co-workers by developing an in situ liquid secondary ion mass spectrometry (liquid-SIMS),<sup>457,508,510</sup> as illustrated in Figure 23b. To be specific, first, a thin  $\text{Si}_3\text{N}_4$  membrane was used to separate the liquid from the high vacuum, ensuring only  $\text{Si}_3\text{N}_4$ -related signals were detected at the initial stage. Then, the interfacial signals could be detected until a  $\text{Bi}^{3+}$  primary ion beam drilled through the  $\text{Si}_3\text{N}_4$  membrane. As soon as the interfacial layer was drilled through by the primary ion beam, the liquid signals were obtained. By bombarding the back of the Cu electrode and creating fragments, liquid-SIMS induced the dynamic chemical mapping of the interfacial components. Liquid-SIMS supported the establishment of an electric double layer before SEI formation. Furthermore, this technique displayed a structured SEI consisting of a dense and inorganic but LiF-depleted inner layer (electronic insulator but  $\text{Li}^+$  conductor) along with an organic-rich outer layer.<sup>509</sup>

As a nondestructive technique, NMR spectroscopy has been applied to investigate various SEI components (such as inorganics like LiF ( $^{19}\text{F}$ ),  $\text{Li}_2\text{CO}_3$  ( $^{13}\text{C}$ ), and organic compounds) via collecting  $^1\text{H}$ ,  $^7\text{Li}$ ,  $^{13}\text{C}$ ,  $^{19}\text{F}$ , as well as  $^{31}\text{P}$  signals in a time scale. Combining solution with solid-state NMR (ssNMR), Gray et al. characterized the soluble and insoluble SEI components derived from FEC decomposition.<sup>573</sup> To promote the characterization of organic SEI,  $^{13}\text{C}$ -FEC was prepared to conduct ssNMR with enhanced dynamic nuclear polarization (DNP) measurements. Notably, the defluorination reaction of the FEC molecule to soluble vinoxyl species ( $\text{HCOCH}_2\text{OR}$ ) was detected from the  $^1\text{H}$  and  $^{13}\text{C}$  NMR results. In the following step, they reacted to form both soluble and insoluble branched ethylene-oxide-based polymers, while neither vinoxyl species nor cross-linking units were investigated for the FEC-free electrolyte, suggesting that the generation of cross-linked polymers could be significant for improving the SEI stability on the Si anodes. Besides, Wagemaker et al. accessed the spontaneous  $\text{Li}^+$  transport via 2D Li ion exchange NMR, disclosing that  $\text{Li}^+$  interfacial transport through the interphase was the major limitation for the  $\text{Li}^+$  transport through the  $\text{Li}_2\text{S}$ – $\text{Li}_4\text{PS}_5\text{Br}$  solid-state batteries, which were largely affected by the electrode preparation and battery cycling conditions. For instance, ball-milling treatment was required to enable faster Li-ion exchange through the interphase and enhance the kinetics with regard to

the high utilization of the  $\text{Li}_2\text{S}$  cathode. This report exhibited the ability of exchange NMR as a noninvasive measurement to investigate  $\text{Li}^+$  interfacial transport behaviors, quantifying the amount and time scale of  $\text{Li}^+$  transport through the interphase in the bulk solid-state batteries.<sup>479</sup> The NMR technique was also applied to determine the cathode-to-anode crossover species that caused the SEI disruption on the Li metal anode and further catalyzed side reactions. It was disclosed that the crossed-over transition metal ions from the  $\text{Li-Ni}_{0.9}\text{Mn}_{0.05}\text{Co}_{0.05}\text{O}_2$  cathode exerted a minimal impact on the Li metal anode. In contrast, decomposition products such as  $\text{POF}_2\text{OH}$  (the doublet of the  $^{19}\text{F}$  spectra and the triplet in the  $^{31}\text{P}$  spectra) and polycarbonates form reactive Li metals that crossed over to the cathode side, significantly altering the CEI. As a result, this crossover phenomenon accelerated the impedance increase and capacity fading of the cathodes and caused instability of the anodes by dissolving these species into the electrolyte.<sup>480</sup>

Moreover, DNP-enhanced NMR has been recognized as a powerful tool for obtaining useful structural information under magic-angle spinning (MAS), which exploits an  $\sim 10^3$  times greater gyromagnetic ratio of paramagnetic electrons to hyperpolarize nuclear spins to increase the signal in NMR measurements.<sup>481</sup> The mechanism of Li metal DNP is illustrated in Figure 23c. Without applying a magnetic field, the partially filled up and down electron spin bands of a metal were degenerated, whereas the energies of these bands were shifted in opposite directions while maintaining a common Fermi level with an applied magnetic field. After irradiating the conduction electron spin resonance (CESR) transition, the populations of the spin bands were (partially) equalized. Based on this theory, Gray et al. reported the hyperpolarization by investigating the interphase between the Li metal and the SEI (Figure 23d).<sup>556</sup> They selectively enhanced the  $^7\text{Li}$ ,  $^1\text{H}$ , and  $^{19}\text{F}$  NMR spectra of the SEI species, which provided the chemical nature and spatial distribution of these species. To exploit the significant enhancement of the  $^7\text{Li}$ ,  $^7\text{Li} \rightarrow ^1\text{H}$  cross-polarization (CP) and  $^7\text{Li} \rightarrow ^{19}\text{F}$  CP,  $^7\text{Li}$  rotational echo double-resonance (REDOR) experiments were conducted, successfully identifying some SEI species, such as polymeric compounds, organic carbonates, and LiF. In situ measurements based on this technique will be more informative in identifying the chemical compositions and structures of the interphases in rechargeable batteries. The reduced collection time and enhanced signal-to-noise ratio of  $^{13}\text{C}$  to confirm organic species in SEI are among the most prominent advantages of the DNP technique. Unfortunately, it fails to probe the dynamic nature of the interphase, which requires the combination of NMR and cryogenic techniques. Moreover, in situ NMR has been realized for probing the real-time SEI evolution in batteries. The differences in the plating processes and transport properties of the interphase in commercial electrolytes (1 M  $\text{LiPF}_6$ –EC/DMC) without and with FEC additive were investigated via in situ NMR.  $^6\text{Li}$  isotopic labeling was employed to monitor the exchange between the bulk Li metal and the electrolyte via NMR, and a numerical model was developed to describe the process. It was revealed that compared to those of the FEC-free electrolytes, the  $^6\text{Li}/^7\text{Li}$  exchange was twice as fast in FEC-containing electrolyte with a much faster SEI formation rate, which could account for a more uniform Li deposition behavior. The authors also used this in situ NMR technology to quantify



some critical SEI parameters for regulating the nature of Li deposition, such as  $\text{Li}^+$  transport and the healing rate of the SEI. Other electrolyte additives or components should be explored via this methodology to optimize SEIs for uniform Li plating/stripping under practical conditions in the future.<sup>482</sup> It should be noted that a strict observation condition should be satisfied to avoid interfering signals when conducting in situ NMR for real-time monitoring of the SEI during cycling.<sup>487</sup>

**3.4.4. Functional Feature Analysis Techniques.** Based on the scattering of X-rays, the interference of which produces diffraction patterns from crystalline or partial crystalline structured materials, XRD has been widely employed to investigate the changes in crystal structures as well as phase transformations of electrode materials or the ordering and structures of interphases. For instance, according to the analysis of XRD, Huang and co-workers showed that the byproducts LiOH derived from side reactions between Li and oxygen-containing electrolyte were significantly suppressed via boric acid (BA) additive, suggesting the beneficial role of BA in inhibiting unwanted side reactions for high-performance Li-based batteries.<sup>476</sup> In addition, different SEI formation processes with 0.8 M KPF<sub>6</sub>–EC/EMC and potassium bis(fluorosulfonyl)imide (KFSI)–EMC (molar ratio of 1:2.5) electrolytes were investigated via operando XRD, revealing that the SEI mainly formed at high voltage in KFSI-based concentrated electrolyte, while the SEI was mainly generated at low voltage in KPF<sub>6</sub>-based dilute electrolyte.<sup>477</sup> However, as a technique to monitor the bulk information on the electrode, it is difficult for XRD to distinguish specific interactions on the interphases. Recently, synchrotron-based X-ray sources with much higher intensities and larger photon energies than laboratory equipment have been recognized as a powerful technique for in situ/operando investigations of battery systems due to the benefits of a fast period of measurement times, large penetration power, along with improved signal-to-noise ratios.<sup>477</sup> Therefore, the synchrotron-based XRD is able to collect high-quality data for a trace amount of sample without significant radiation damage.<sup>478</sup> In 2021, using synchrotron-based XRD and PDF analysis, Hu et al. identified and differentiated two elusive components, LiH and LiF, in the SEI components of Li metal anodes.<sup>574</sup> As revealed from synchrotron-based XRD, LiH existed as a face-centered-cubic (FCC) phase with a lattice parameter of 4.084 Å, which was further confirmed by the changes in the XRD patterns due to its moisture sensitivity. The origins of LiH not being identified could be attributed to two main factors. First, the typical XRD patterns of LiH and LiF were similar FCC structures with close lattice parameters (4.084 Å for LiH and 4.026 Å for LiF). Besides, owing to the high moisture sensitivity, LiH easily decomposed to make it undetectable. It was also found that the nanocrystalline LiF in the SEI components is clearly different from that in the bulk phase, especially featuring a larger lattice parameter ( $\sim 4.05$  Å) along with a smaller particle size ( $< 3$  nm), which enables fast  $\text{Li}^+$  transport for higher CE and improved electrochemical performance. It should be noted that the beam may easily lead to the damage of battery materials during testing.

As a nondestructive imaging approach, in situ AFM can monitor the formation and properties of interphases through high-resolution topographical images, providing intertopography information and mechanical properties. For instance, the elastic and plastic properties of the interphases can be evaluated in a quantitative way by analysis of the force–

distance curves.<sup>511</sup> In addition, to investigate the nano-mechanics of interphases, AFM-nanoindentation was designed as illustrated in Figure 23f. Through converting the tip deflection into normal force  $F$  and analyzing indentation depth  $\delta$  and the cantilever deflection  $\Delta d$ , the Young's modulus can be obtained as shown in the inset of Figure 23f, successfully quantifying the inhomogeneity of the SEI in both morphological and mechanical properties.<sup>462</sup> Following this work, more systematic investigations of SEI information have been conducted, including the two-layered structure and the thickness of the SEI on graphite anodes,<sup>575</sup> the mechanical properties of the organic–inorganic mixed SEI on the Si anode,<sup>575</sup> the effects of electrolyte components, configurations, and electrode face orientation on the SEI morphology and thickness,<sup>463–465,576</sup> the deformation and mechanical failure mechanism of the SEI,<sup>512</sup> etc. Among these progresses, it is interesting to mention that in situ AFM is powerful enough to distinguish the distributions of inorganic and organic species in the SEI at the nanometer level by probing the SEI in liquid electrolytes.

Unfortunately, the failure to unveil chemical information is a large limitation facing the AFM technique. To satisfy the nanometer spatial resolution required to disclose the correlation between the structure and the function in the interphases, tip-enhanced Raman spectroscopy (TERS) was developed.<sup>466,514,515</sup> Through raster scanning the interphase, the chemical fingerprint of the interphases can be obtained. Besides, TERS offers a spatial resolution at several nanometers or even on a subnanometer scale, which is attributed to the highly confined local electric field.<sup>467</sup> Therefore, TERS has been regarded as an effective technique for understanding the interphase as well as interfacial processes at the nanometer spatial resolution, eventually establishing the relationship between the structure and the performance. Although with a high spatial resolution, the one-point foundation makes inherently weaker signals for the TERS technique compared with surface-enhanced Raman scattering (SERS), making it necessary to increase the efficiency of TERS on motivation and collection when used to probe the interphases. Besides, to monitor the dynamic evolutions of the interphase structures and further quantify the interphase compositions at the nanometer spatial resolution and the molecular level, TERS should be developed into an operando technique.<sup>577</sup>

As a scattering technique, NR measures the specular reflection of neutrons from the surface, which changes with the wave vector transfer perpendicular to the sample surface, following the equation  $Q = [4\pi \sin(\theta)]/\lambda$  (where  $\theta$  represents the angle of incidence of the neutron beam with the sample surface and  $\lambda$  denotes the wavelength of the neutrons).<sup>578,579</sup> The thickness, roughness, as well as the layers' scattering length density (SLD) can be obtained by fitting the reflectivity via layered models, which is informative for determining the layer compositions. Therefore, NR has been increasingly employed for probing the interphasial properties of batteries.<sup>474,516</sup>

Particularly, the SLD depth profile yielded from fitting NR data in the surface normal direction can be used to detect the evolutions of the interphase structure during the charging/discharging process.<sup>473</sup> By using in situ NR and a novel designed electrochemical cell, Schmidt et al. detected the growth of a  $\sim 7$  nm thick SEI layer during delithiation of the Si electrode.<sup>550</sup> Later, the thickness and chemistry of the SEI on a Si anode were determined as a function of the state of charge

during cycling. Based on the SLD results, the SEI thickness decreased from 25 to 18 nm ( $\text{Li}_{3.7}\text{Si}$ ) after the delithiation process. Besides, the SEI evolved with more LiF component during lithiation, while more Li–C–O–F-like species was discovered during delithiation. More importantly, the SEI started to grow once the electrolyte was in contact with the Si electrode, even though no electrical bias was applied.<sup>580</sup> An opposite trend in SEI thickness was presented by Veith et al., who investigated the SEI on Si anodes using the electrolyte of 0.1 M LiTFSI in deuterated dimethyl perfluoroglutarate.<sup>581</sup> Based on the corresponding SLD profiles, they observed a decrease in the thickness of the SEI layer from 34 to 14 nm after the lithiation process. Moreover, in situ NR revealed that the SEI formed on tungsten thin film electrodes was composed of a porous outer layer enriched in solvent-derived components and a compact inner layer with abundant inorganic species.<sup>474</sup> Following this work, tungsten oxide (e.g.,  $\text{WO}_3$ ) was demonstrated to form a SEI with three layers during the reduction process. An innermost layer (the evolving conversion electrode) was assigned to a mixture of W,  $\text{Li}_2\text{O}$ , and incompletely reacted  $\text{WO}_3$  or  $\text{Li}_x\text{WO}_3$ , a layer enriched in protons and/or Li, which tentatively consisted of LiOH or LiH (the inner SEI), and an outermost layer adjacent to the electrolyte consisting of lower SLD species with solution-filled porosity or deuterium-rich species derived from the solvents (the outer and fragile SEI). A reverse of SEI evolution was observed during the oxidation process. These results were generally consistent with previous reports of the SEI using other characterization methods, indicating a bilayer structure of the SEI with more inorganic species in the inner layer and more organic components in the outer layer.<sup>475</sup>

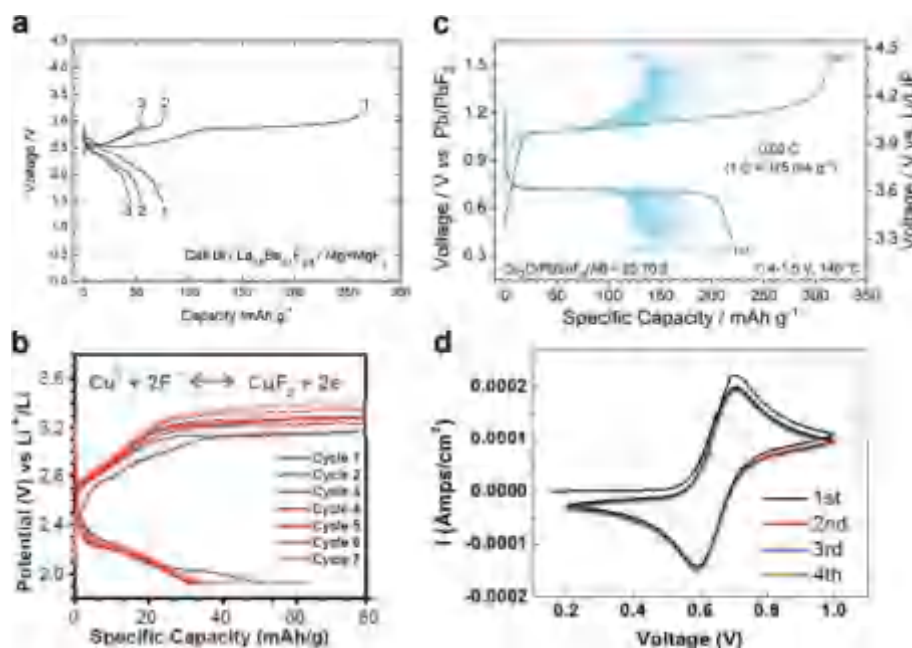
Overall, in situ NR sheds light on the study of the SEI generation mechanism by probing the evolution of the interphase structure during battery operation. Unfortunately, its widespread application is significantly restricted by several factors, such as a long analysis time, an excessive choice of electrolyte solvents to enhance contrast, a flat specimen required to generate a strong signal, and very limited facilities to handle the produced neutrons outside the particle accelerator.<sup>437</sup>

To investigate the various functional and morphological features of the interphases, other characterization methods that can offer complementary information have also been developed. For instance, in contrast to XRD providing information about the overall structure of a material, XAS has been considered as an effective technique to probe the local atomic arrangement and electronic structure of a material. XAS technology is based on X-ray photon-induced electronic excitations from the core level to an empty electronic state for the detected element. Thanks to its element-resolved feature and high sensitivity to the local chemical bonds and solvent environments, the XAS measurement shows great potential for interphase characterization.<sup>468–470,582</sup> Additionally, this technique can be used for determining amorphous phases as well as for small nanoparticles. Owing to the utilization of high-energy synchrotron radiation, the data acquisition process is quite fast, which promotes in situ analysis as well.<sup>583,584</sup> Although XAS has been successfully used for analyzing the SEI composition, in situ XAS probing in a full-cell mode remains a big challenge, which requires a special electrochemical cell design.<sup>471,472,517–520</sup>

SECM is considered a powerful tool that can probe the surface characteristics of the interphases with nanoscale

resolution. SECM relies on the stark difference in activities between the electronically conductive electrode surface and the electronically insulating feature of the SEI products.<sup>483,484</sup> The basic setup of SECM consists of four parts: a low-current bipotentiostat, a 3D positioning system, an ultramicroelectrode tip, and a data acquisition system.<sup>485</sup> The cell generally contains four electrodes, including the tip, the reference electrode, the counter electrode, and the working electrode. The SECM tip probes the chemical changes occurring at the interphase and detects spatial information on electrochemical reactions taking place at selected areas.<sup>484</sup> SECM has attracted increasing attention in investigating the formation and evolution of SEI layers by employing the feedback mode.<sup>484</sup> For instance, using the feedback mode of SECM with 2,5-di-*tert*-butyl-1,4-dimethoxybenzene (DBDMB) as the mediator, Wittstock et al. conducted in situ imaging of the spontaneous spatiotemporal changes for SEI layers formed on the graphite surface. The reduction in the mediator regeneration rate was accompanied by SEI formation. Besides, the currents remained stable in some regions of the SEI-covered electrodes, while the currents in other regions changed drastically with time. These changes could be attributed to the volume evolutions during charging/discharging, dissolution of SEI, or gas formation. In addition, the results show that deposition of metallic Li could take place upon charging and compromise battery safety, requiring the self-healing ability of the SEI with incidental defects. Moreover, the repassivation of damaged regions was detected in situ, which showed that it took several hours before these regions were susceptible to further short-term current fluctuation.<sup>486</sup> Later, operando SECM was adopted by Schuhmann et al., probing the electrically insulating feature of the Si surface during the delithiation/lithiation process. Combined with AFM, the SECM results suggested that there were two types of cracks (i.e., cracks partially covered by the SEI and SEI-free cracks) during the initial cycle. The SEI-free cracks contributed to a discontinuity in the electrically insulating feature of the Si surface, further accelerating electrolyte decomposition in the second cycle. More importantly, operando SECM confirmed the electrically insulating feature of the SEI layer on the Si electrode, and the volume changes during the delithiation/lithiation process were what caused the loss of “protecting” character of the SEI at the Si surface.<sup>585</sup>

In brief, to address fundamental questions regarding the chemical composition, spatial distribution, and structure of fluorinated interphases, nondestructive and in situ/operando techniques are essential for real-time, dynamic, and intuitive analysis of the interphase properties and their correlation with the battery performance. Taking cryo-TEM as an example, the combination of a low electron dose and ultralow temperature for the frozen sample reveals atomic-level crystal details, which preserves the delicate chemical and spatial features of interphases. For high-resolution imaging of interphasial evolution, dynamic in situ cell devices and sophisticated sample preparation techniques (e.g., cryo-FIB) should be equipped. It should be kept in mind that each technique has its unique advantages and significant limitations, requiring the synergistic combination of various techniques, which yields multidimensional or multimodal information for elucidating the structure–property relationships and guiding interphase design.



**Figure 24.** Conversion-type electrode materials for FIBs. (a) Voltage–composition profiles for a FIB with the Bi cathode vs the Mg + MgF<sub>2</sub> anode in the three first cycles. The charge/discharge curves were obtained at 150 °C for a current density of ca.  $\pm 4$  mA g<sup>-1</sup>. Reproduced with permission from ref 587. Copyright 2014 Royal Society of Chemistry. (b) Electrochemical charge and discharge curves for a three-electrode cell with a Cu@LaF<sub>3</sub> cathode in 1 M *N,N,N*-trimethyl-*N*-neopentylammonium fluoride (Np<sub>1</sub>F)–BTFE, cycled at 10 mA. Reproduced with permission from ref 52. Copyright 2018 The American Association for the Advancement of Science. (c) Charge/discharge profiles of Cu<sub>2</sub>O cathode material for cycles 1–35 at 0.02 C and 140 °C. Reproduced with permission from ref 590. Copyright 2021 Wiley-VCH. (d) CV curves of 4-hydroxy-TEMPO in aqueous 0.8 M NaF electrolyte with glassy carbon as the working electrode, platinum as the counter electrode, and the standard Ag/AgCl electrode as the reference electrode. Reproduced with permission from ref 591. Copyright 2019 IOP Science.

## 4. FLUORINE CHEMISTRY IN RECHARGEABLE FLUORIDE-ION BATTERIES

### 4.1. Fluoride Electrode Materials

The electrode material for FIBs can release or absorb F<sup>-</sup> ions while obtaining or losing electrons. Depending on the redox potential, the electrode materials for FIBs are utilized as cathodes with relatively high potential or anodes with relatively low potential. Due to the relatively light weight of the electrode materials in FIBs, the theoretical volumetric energy densities of FIBs can reach up to 5000 Wh L<sup>-1</sup> based on the total volume of the electrode materials,<sup>38</sup> which makes FIBs a promising candidate for next-generation high-energy rechargeable batteries. So far, the mechanism of F<sup>-</sup>-ion storage of electrodes in FIBs can be mainly classified into conversion type and intercalation type, which are further introduced below.

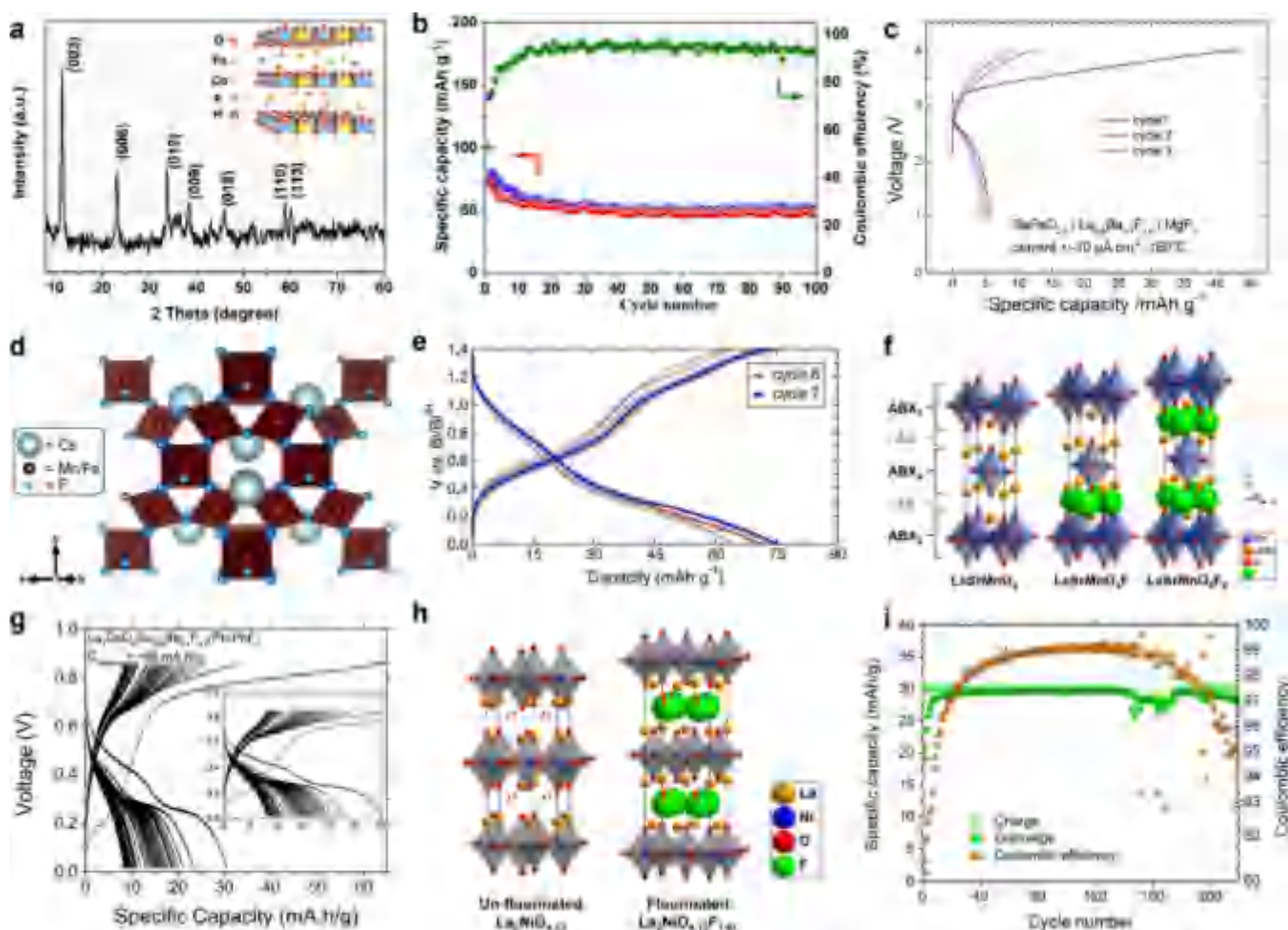
**4.1.1. Conversion-Type Electrode Materials.** The fluorination/defluorination process of conversion-type electrode materials (e.g., metal/metal fluorides) is accompanied by continuous breaking or reforming of the metal–fluorine bond. Conversion-type electrode materials for FIBs possess high energy density because they are able to transport more than one F<sup>-</sup> ion per redox-active metal species, and the active electrode materials typically possess lower molar masses.

Metal/metal fluorides (M/MF<sub>x</sub>) are the most extensively studied conversion-type electrode materials for FIBs. The electrons and F<sup>-</sup> ions transfer during the fluorination/defluorination between metal and metal fluorides. In 2011, Fichtner and Anji reported the feasibility of a series of metal fluorides (including SnF<sub>2</sub>, CuF<sub>2</sub>, KBiF<sub>2</sub>, and BiF<sub>3</sub>) as cathode materials in an all-solid-state FIBs system with a F<sup>-</sup>-ion solid-state electrolyte La<sub>1-x</sub>Ba<sub>x</sub>F<sub>3-x</sub> (0 ≤ x ≤ 0.15) at 150 °C.<sup>43</sup>

Cerium (Ce) metal was used as the anode due to the high F<sup>-</sup>-ion conductivity of its discharge product (cerium fluoride, CeF<sub>3</sub>).<sup>586</sup> The F<sup>-</sup>-ion full cell using BiF<sub>3</sub> as a cathode successfully realized reversible discharge and charge at 10 μA cm<sup>-2</sup> with a discharge capacity of 190 mAh g<sup>-1</sup> and an average voltage of 2.15 V. However, the irreversible volume changes, as a common problem of conversion-type electrode materials, limit the cycling performance of FIBs. Apart from the Ce metal anode, Fichtner and co-workers investigated the application of other potential anode materials such as CaF<sub>2</sub>, MgF<sub>2</sub>, and Mg + MgF<sub>2</sub> (i.e., the premixed composite of metal and metal fluoride, M + MF<sub>x</sub>) for all-solid-state FIBs in 2014.<sup>587</sup> When paired with a bismuth (Bi) cathode, the Mg + MgF<sub>2</sub> composite anode delivered an initial discharged specific capacity of about 80 mAh g<sup>-1</sup> at 4 mA g<sup>-1</sup> and 150 °C (Figure 24a). It revealed that the M + MF<sub>x</sub> composite anode can effectively enhance the cycling performance by improving interphase contacts between the reactive phases. In general, the low conductivity of the metal fluorides and the extreme volume change during the fluorination/defluorination process of M + MF<sub>x</sub> electrodes cause the massive side reactions<sup>588</sup> together with poor physical contact between active materials,<sup>589</sup> electrolytes, and conductive carbon particles, both of which lead to rapid capacity decay of FIBs.

M/MF<sub>x</sub> has also been applied in liquid FIBs. Simon and co-workers reported room-temperature operable FIBs based on organic solvent-based electrolyte in 2018.<sup>52</sup> In this system, a copper–lanthanum trifluoride core–shell cathode was developed, where the F<sup>-</sup>-ion conductive LaF<sub>3</sub> shell not only permitted F<sup>-</sup> diffusion but also inhibited the dissolution of the discharge product (CuF<sub>2</sub>). The Cu@LaF<sub>3</sub> cathode achieved



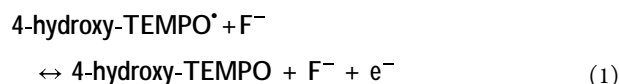


**Figure 25.** Intercalation-type electrode materials for FIBs. (a) XRD pattern of CoFe-F LDH. (Inset) structural model. (b) Cycling performance and CE for the cell Li||CoFe-F LDH. Reproduced with permission from ref 592. Copyright 2022 Wiley-VCH. (c) Voltage profiles measured during three charge/discharge cycles for the cell BaFeO<sub>2.5</sub>|La<sub>0.9</sub>Ba<sub>0.1</sub>F<sub>2.9</sub>|MgF<sub>2</sub> (current  $\pm 10 \mu\text{A cm}^{-2}$  at 150 °C). Reproduced with permission from ref 593. Copyright 2014 Royal Society of Chemistry. (d) Crystal structure of the defect fluoride pyrochlore CsMnFeF<sub>6</sub> viewed down the [110] direction. (e) Cycles 4–9 from galvanostatic cycling of a F-ion cell with a working electrode of mechanochemically synthesized CsMnFeF<sub>6</sub> and a Bi/BiF<sub>3</sub> composite counter electrode, cycled at room temperature at a rate of C/20 between 0.0 and 1.4 V vs Bi/BiF<sub>3</sub>. Cycles six and seven are shown in orange and blue, respectively. Reproduced with permission from ref 594. Copyright 2022 American Chemical Society. (f) K<sub>2</sub>NiF<sub>4</sub>-type structure of LaSrMnO<sub>4</sub> (left) in comparison to partly fluorinated LaSrMnO<sub>4</sub>F (middle) and fully fluorinated LaSrMnO<sub>4</sub>F<sub>2</sub> (right). Reproduced with permission from ref 72. Copyright 2017 American Chemical Society. (g) Electrochemical charging and discharging of La<sub>2</sub>CoO<sub>4</sub>/La<sub>2</sub>CoO<sub>4</sub>F at 170 °C;  $I_{\text{charging}} = +10.0 \mu\text{A}$ ,  $I_{\text{discharging}} = -1.0 \mu\text{A}$ . Reproduced with permission from ref 595. Copyright 2019 Wiley-VCH. (h) Schematic illustrations of the unfluorinated La<sub>2</sub>NiO<sub>4.13</sub> (left) and hypothetical fully fluorinated state La<sub>2</sub>NiO<sub>4.13</sub>F<sub>1.87</sub> (right). Fractional occupancies are depicted for the interstitial anion site. (i) Charge/discharge capacities and CE against cycle number for the cells with the cutoff capacities of 30 mAh g<sup>-1</sup> at  $T = 170 \text{ °C}$ ,  $I_{\text{charge}} = +24 \mu\text{A cm}^{-2}$ ,  $I_{\text{discharge}} = -12 \mu\text{A cm}^{-2}$ , and cutoff charge voltage = 2.3 V. Reproduced with permission from ref 596. Copyright 2020 Springer Nature.

seven reversible cycles in liquid FIBs at room temperature in a three-electrode cell (Figure 24b).

Metal oxide-based electrodes have been developed as a new conversion-type electrode material. In 2021, Uchimoto and co-workers reported a cuprous oxide (Cu<sub>2</sub>O) cathode with Cu<sup>+</sup>/Cu<sup>2+</sup> redox as a fast fluorination cathode material for all-solid-state FIBs.<sup>590</sup> As shown in Figure 24c, the Pb/PbF<sub>2</sub>|PbSnF<sub>4</sub>|Cu<sub>2</sub>O cell delivered an initial discharge specific capacity of 220 mAh g<sup>-1</sup> at 0.02 C (1 C = 375 mA g<sup>-1</sup>) that remained stable after stabilization of the partially irreversible amorphization phase. The superior rate capability of the Cu<sub>2</sub>O cathode (110 mAh g<sup>-1</sup> at 1 C) surpassed the simple M/MF<sub>x</sub> systems, which can be attributed to the fast F<sup>-</sup>-ion movement on the phase boundary.

An organic compound with radical groups has also been investigated as an electrode material for FIBs. In 2019, Chen and co-workers reported the utilization of 4-hydroxy-2,2,6,6-tetramethylpiperidin-1-oxyl (4-hydroxy-TEMPO) cathode in an aqueous rechargeable FIB.<sup>591</sup> The reaction mechanism of 4-hydroxy-TEMPO is as follows



where the electrostatic balance of 4-hydroxy-TEMPO was maintained by the transfer of the fluoride ions and electrons. The redox peak pairs at 0.706 and 0.594 V in the cyclic voltammetry (CV) curves (Figure 24d) can be distributed to the conversion between 4-hydroxy-TEMPO and 4-hydroxy-

TEMPO<sup>+</sup>F<sup>−</sup>. When paired with a BiF<sub>3</sub> anode in a NaF water solution electrolyte and cycled between 0.0 and 1.4 V, this aqueous FIB delivered an initial discharge specific capacity of 145.3 mAh g<sup>−1</sup> at 1000 mA g<sup>−1</sup>.

**4.1.2. Intercalation-Type Electrode Materials.** Different from the conversion-type electrodes, the F<sup>−</sup> ion can be reversibly stored in or released from the unoccupied interstitial sites or anion vacancies in the crystal structure of the intercalation-type electrodes for FIBs. Thus, the structural integrity of the intercalation-type electrode can be maintained due to the slight volume change during the intercalation/deintercalation of the F<sup>−</sup> ion, which ensures the highly reversible cycling stability and good rate performance of FIBs.

Recently, a F<sup>−</sup>-ion-intercalated CoFe-layered double hydroxide (CoFe-F LDH) was reported as a cathode material for FIBs. Zhang and co-workers prepared the CoFe-F LDH through a facile coprecipitation approach combined with an ion-exchange method (Figure 25a) and successfully paired this material as a cathode with a Li metal anode in a CsF-based organic liquid electrolyte.<sup>592</sup> The LiCoFe-F LDH cell delivered a stable specific capacity of 48.9 mAh g<sup>−1</sup> during 100 cycles at 10 mA g<sup>−1</sup> under room temperature (Figure 25b) owing to the unique topochemical transformation property and small volume change (~0.82%) of CoFe-F LDH materials accompanied by electrochemical intercalation/intercalation of F<sup>−</sup> ions. Moreover, the good rate performance of CoFe-F LDH indicated that the mitigation of the F<sup>−</sup> ion in the layer spacing was facilitated by the weak electrostatic interaction between the anions and the host layers with a low diffusion barrier.

The perovskite-type BaFeO<sub>2</sub> was reported as an intercalation-type electrode material for FIBs by Oliver and co-workers in 2014.<sup>593</sup> First, they demonstrated that BaFeO<sub>2.5</sub> can be directly fluoridated by heating BaFeO<sub>2.5</sub>F<sub>0.5</sub> in F<sub>2</sub>. The transformation of the monoclinic distorted phase to the cubic perovskite phase in the XRD pattern indicated the successful intercalation of the F<sup>−</sup> ion into the subcrystalline vacancies in BaFeO<sub>2.5</sub>. Then, the MgF<sub>2</sub>|La<sub>0.9</sub>Ba<sub>0.1</sub>F<sub>2.9</sub>|BaFeO<sub>2.5</sub> solid-state FIB was assembled and cycled between 3 and 4 V at 150 °C. As shown in Figure 4c, the long charge plateau at the initial cycle was attributed to the formation of a Fe<sup>4+</sup>-containing phase fraction of a BaFeO<sub>2.5</sub>F<sub>y</sub> compound, where the XRD pattern of electrochemical fluorination was consistent with that of the chemical fluorination result. However, the low reversible capacity in the following cycling suggested that the F<sup>−</sup> ions were not fully deintercalated from the BaFeO<sub>2.5</sub>F<sub>y</sub> cathode, which may be caused by the contact problems in the electrodes and side reactions of conductive carbon.

Likewise, CsMnFeF<sub>6</sub> was investigated as a cathode material for room-temperature FIBs by Jessica and co-workers in 2022.<sup>594</sup> CsMnFeF<sub>6</sub> in a defect pyrochlore structure with suitable particle size and phase purity was obtained through a mechanochemical method. The presence of Frenkel defects was required to endow the F<sup>−</sup> ion's diffusion through the network, so the defect pyrochlore CsMn<sup>2+</sup>Fe<sup>3+</sup>F<sub>6</sub> (Figure 25d) with the disorder in the MnFeF<sub>6</sub> substructure and ordered anionic vacancies became a suitable fluoride intercalation host, allowing fast F<sup>−</sup>-ion transport at room temperature. After combination with an organic liquid electrolyte (1.0 M tetra-*n*-butylammonium fluoride (TBAF)–THF) and cell activation cycles, the half-cell delivered a reversible capacity of 70 mAh g<sup>−1</sup> at room temperature with a high CE of 98% (Figure 25e), which almost approached the theoretical capacity for one fluoride-ion transportation. Ex situ XRD and ex situ XAS

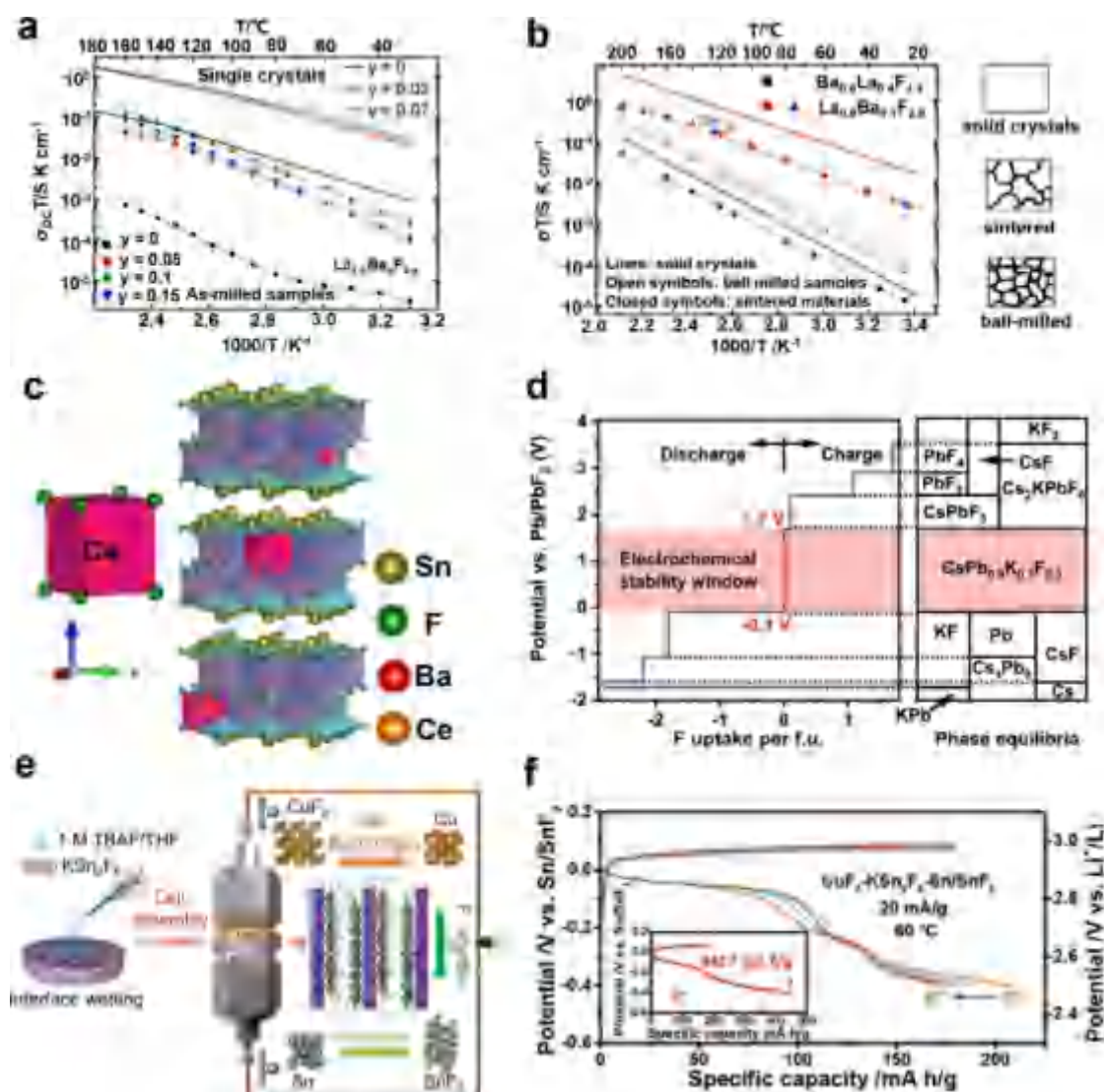
revealed that the CsMnFeF<sub>6</sub> underwent a topotactic transformation from the original defect pyrochlore structure into a related polytype; meanwhile, the Fe<sup>3+/2+</sup> and Mn<sup>3+/2+</sup> redox couples both functioned during the cycling.

Oliver and co-workers reported the investigation of LaSrMnO<sub>4</sub> with a K<sub>2</sub>NiF<sub>4</sub>-type structure as an intercalation-based high-voltage cathode material with high capacity for FIBs in 2017.<sup>72</sup> As shown in Figure 25f, the structure of K<sub>2</sub>NiF<sub>4</sub>-type compounds (A<sub>2</sub>BX<sub>4</sub>) can be described as built up by alternating layers of ABX<sub>3</sub> perovskite-type subunits and AX rock salt subunits along the *c* axis. The large interstitial sites that can store anions existed between the boundary of the rock salt and the perovskite phase layers. The highest F<sup>−</sup>-ion occupied interstitial sites (Y) per formula unit was 2, which resulted in the composition of A<sub>2</sub>BX<sub>4</sub>Y<sub>2</sub>. The Pb–PbF<sub>2</sub> anode was paired with the LaSrMnO<sub>4</sub>F cathode with the La<sub>0.9</sub>Ba<sub>0.1</sub>F<sub>2.9</sub> solid-state electrolyte, and the full cell was tested at 10 μA under 200 °C. Combined with the results of the electrochemical data, XRD spectra, and DFT calculations, two charge voltage plateaus at 1 and 2 V were confirmed as the first and the second steps of F<sup>−</sup>-ion intercalation (LaSrMnO<sub>4</sub> → LaSrMnO<sub>4</sub>F and LaSrMnO<sub>4</sub>F → LaSrMnO<sub>4</sub>F<sub>2−x</sub>, *x* ≈ 0.2). It is worth noting that the side reaction, fluorination of conductive carbon in the cathode, along with the charging process resulted in an overcharge capacity of 800 mAh g<sup>−1</sup>, which was much higher than the theoretical capacity (155 mAh g<sup>−1</sup>) of two F<sup>−</sup>-ion transfers from LaSrMnO<sub>4</sub> → LaSrMnO<sub>4</sub>F<sub>2</sub>. Moreover, the fluorination of conductive carbon also deteriorated electron transfer in the cathode, which then led to the low reversible discharge capacity of 20 mAh g<sup>−1</sup>.

To overcome this side reaction issue, Oliver and co-workers replaced the redox pairs of Mn<sup>3+</sup>/Mn<sup>4+</sup> with Co<sup>2+</sup>/Co<sup>3+</sup> to reduce the oxidation potentials in the K<sub>2</sub>NiF<sub>4</sub>-type compounds.<sup>595</sup> The obtained intercalation-type cathode La<sub>2</sub>CoO<sub>4</sub> showed a lower F<sup>−</sup>-ion interaction number of 1.2 per formula in the same battery system with LaSrMnO<sub>4</sub>. The unwanted side reactions in the cathode were effectively avoided by adjusting the charge cutoff capacity of 65 mAh g<sup>−1</sup>, which delivered a better discharge capacity of 32 mAh g<sup>−1</sup> with a capacity retention of ~25% for the initial discharge capacity after 50 cycles (Figure 25g). However, although the side reaction has been suppressed by a cutoff charge voltage of 1 V, the low discharge capacity of La<sub>2</sub>CoO<sub>4</sub>F<sub>1.2</sub> indicated that part of the F<sup>−</sup> ions was irreversibly fixed in the layered cathode, which was supported by the XRD structural analysis.

Then, Oliver and co-workers developed a high-voltage intercalation-type cathode (La<sub>2</sub>NiO<sub>4+d</sub>) and achieved an all-solid-state FIB with high cycling stability and a CE close to 100%.<sup>596</sup> As shown in Figure 25h, La<sub>2</sub>NiO<sub>4.13</sub> was successfully synthesized by a solid-state method, which delivered a maximum theoretical capacity of 125 mAh g<sup>−1</sup> after charging into La<sub>2</sub>NiO<sub>4.13</sub>F<sub>1.87</sub>, where all empty interstitial anion sites were filled by F<sup>−</sup> ions. When a charge cutoff capacity of 30 mAh g<sup>−1</sup> was applied, the Zn/ZnF<sub>2</sub>|La<sub>0.9</sub>Ba<sub>0.1</sub>F<sub>2.9</sub>|La<sub>2</sub>NiO<sub>4+d</sub> cell reached an average CE of 97.68% over 220 cycles (Figure 25i). As evidenced from the TEM images, automated diffraction tomography (ADT), EDX spectroscopy, and XAS indicated that the interstitial sites in the La<sub>2</sub>NiO<sub>4.13</sub> cathode were nearly fully occupied by F<sup>−</sup> ions, leading to the formation of a high fluorine content phase of La<sub>2</sub>NiO<sub>4.13</sub>F<sub>1.59</sub>. However, although the less reactive CNTs were used as conductors in the cathode, the side reaction did not stop in the charge process, as verified by electrochemical impedance spectroscopy





**Figure 26.** Developments of solid-state electrolytes for FIBs. (a) Arrhenius plot of the ionic conductivity for ball-milled  $\text{La}_{1-y}\text{Ba}_y\text{F}_{3-y}$  electrolyte. (b) Arrhenius plots of the ionic conductivities for tysonite-type  $\text{La}_{0.9}\text{Ba}_{0.1}\text{F}_{2.9}$  and fluorite-type  $\text{Ba}_{0.6}\text{La}_{0.4}\text{F}_{2.4}$  prepared by ball milling and sintering. Reproduced with permission from ref 276. Copyright 2014 American Chemical Society. (c) Crystal structures of the  $\text{Ba}_{0.95}\text{Ce}_{0.05}\text{SnF}_{4.05}$  phase. Reproduced with permission from ref 601. Copyright 2022 American Chemical Society. (d) ESW based on the calculated thermodynamic equilibrium voltage profiles and the phase equilibria for the  $\text{CsPb}_{0.9}\text{K}_{0.1}\text{F}_{2.9}$  electrolyte. Reproduced with permission from ref 602. Copyright 2022 Wiley-VCH. (e) Illustration of interphase wetting, cell assembly, and predicted reaction processes for Swagelok-cell-type CKClKSn<sub>2</sub>F<sub>5</sub>/SSKC FIB. (f) Voltage curves of the initial five cycles for a SSKClKSn<sub>2</sub>F<sub>5</sub>/CKC battery. Reproduced with permission from ref 603. Copyright 2023 Wiley-VCH.

(EIS) and XPS testing. Therefore, strategies aiming at improving the stability of the interphase between the active materials and the carbon-based additives in electrode composites (e.g., coating techniques or advanced engineering) should be further developed for development of FIBs.

In general, the conversion-type materials degrade fast due to poor interphase contacts originating from the significant volume change, incomplete conversion reaction, electrode material dissolution, and irreversible generation of oxyfluoride byproducts, while intercalation-type materials are limited by the relatively low capacity and low energy density. Moreover, side reactions between conductive carbons and fluorides in the electrode continuously degrade the performance of FIBs.

## 4.2. Fluoride Electrolytes

**4.2.1. Solid-State Electrolytes.** Since the pioneering work by Fichtner et al., which demonstrated the first rechargeable FIBs employing  $\text{La}_{0.9}\text{Ba}_{0.1}\text{F}_{2.9}$  solid electrolyte, there has been

extensive interest in the  $\text{F}^-$  conducting solid-state electrolytes. Generally, the  $\text{F}^-$ -ion conducting solid electrolytes can be categorized into a tysonite-type structure (rare-earth fluorides  $\text{MF}_3$ ,  $\text{M} = \text{La}$ ,  $\text{Ce}$ ,  $\text{Pr}$ ,  $\text{Nd}$ ), fluorite-type structure (alkaline-earth fluorides  $\text{MF}_2$ ,  $\text{M} = \text{Ba}$ ,  $\text{Ca}$ ,  $\text{Sr}$ ), and their doped phases, displaying an ionic conductivity of  $10^{-4} \text{ S cm}^{-1}$  at high temperature (e.g.,  $150^\circ\text{C}$ ).<sup>43</sup> Thus, insufficient  $\text{F}^-$  conductivity has been the restricting factor for the operation of solid-state FIBs at low or room temperature.

The  $\text{F}^-$ -ion transport through solid electrolytes is typically facilitated by the Schottky and anti-Frenkel point defects via the vacancy mechanism, interstitial mechanism, and interstitial–substitutional exchange mechanism. Thus, the fast ionic conductivity can be achieved by creating new defects within the solid structure. However, the defect mechanism highly depends on the structure of the solid electrolyte. Given that the  $\text{F}^-$  interstitial site is relatively smaller ( $0.84 \text{ \AA}$ ) compared to the

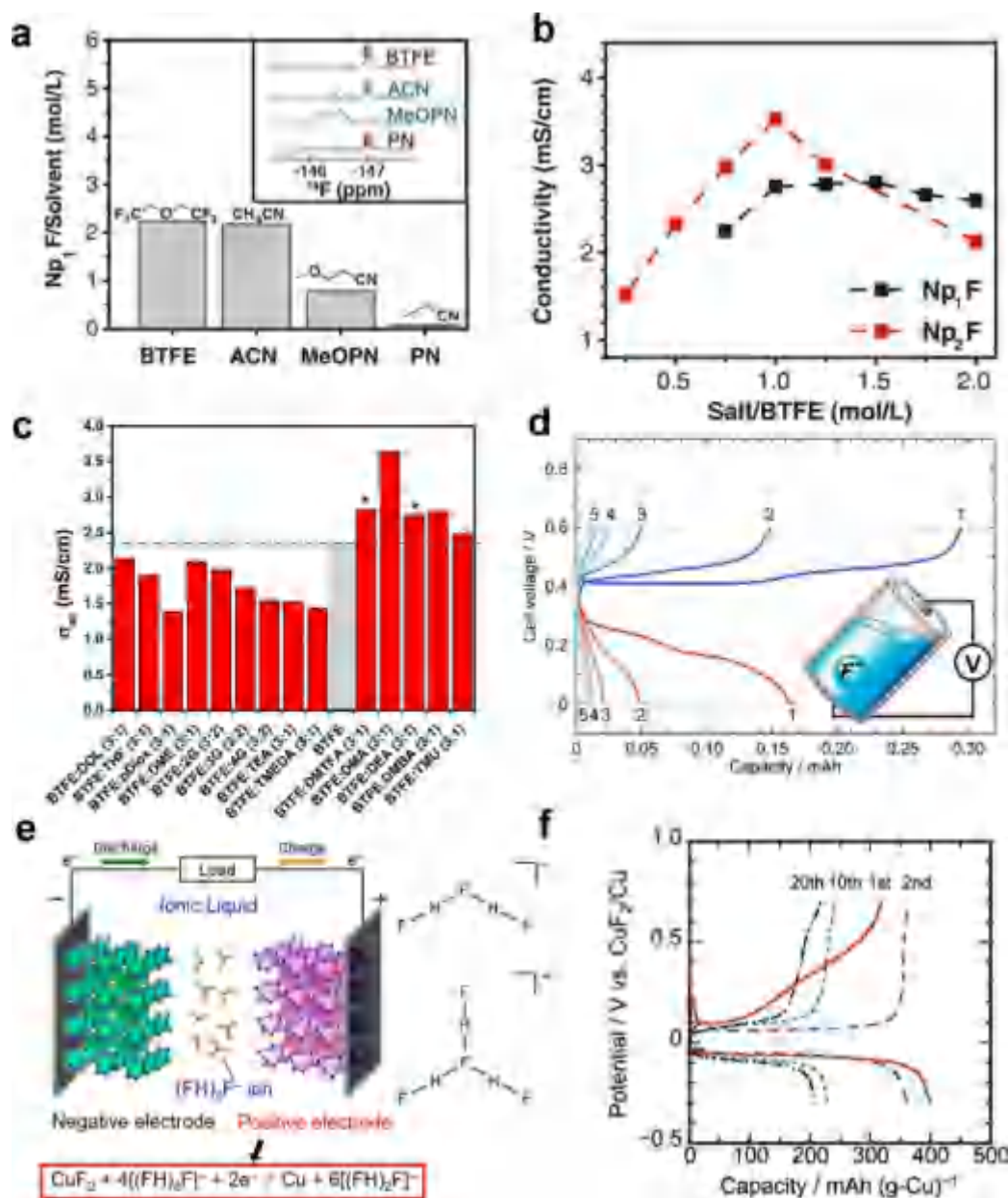


$F^-$  radius (1.19 Å), it is unlikely to be created in tysonite-type  $R_{1-x}M_xF_{3-x}$  fluorides (where R denotes the rare-earth element, while M represents the divalent element). In such instances, the formation of  $F^-$  vacancies has been demonstrated to be effective in improving the ionic conductivity of  $RF_3$  fluorides.<sup>72,586,597–600</sup> Doping the polycrystalline sintered  $CeF_3$  with various difluorides including  $CaF_2$ ,  $SrF_2$ , and  $BaF_2$  (5 mol %), Takahashi and co-workers revealed that the conductivity of  $CeF_3$  was significantly enhanced up to  $1.0 \times 10^{-2} \text{ S cm}^{-1}$  at 200 °C (for  $Ce_{0.95}Ca_{0.05}F_{2.95}$ ), which was attributed to the facile movement of vacancies.<sup>276</sup> In addition, the structural features of solid electrolytes have critical impacts on the  $F^-$  mobility. In the case of the tysonite  $Sm_{1-x}Ca_xF_{3-x}$  solid, as the Ca content increases, the distortion of the  $F1(Sm, Ca)_4$  tetrahedral site diminished, leading to an exponentially reduced ionic conductivity and an increase in the activation energy. Consequently, at room temperature, the highest conductivity of  $10^{-4} \text{ S cm}^{-1}$  was achieved for the lowest Ca content or the smallest fluorine vacancy content in the  $Sm_{0.95}Ca_{0.05}F_{2.95}$  tysonite.<sup>599</sup> The  $F^-$  conduction mechanism for the tysonite-type structure, however, was drastically different from that for fluorite-type solids. To reveal the conduction mechanism, Fichtner and co-workers prepared a series of  $La_{1-y}Ba_yF_{3-y}$  ( $0 \leq y \leq 0.15$ ) solid compounds using the ball-mill method, revealing that grain boundaries exert a detrimental effect on the  $F^-$  conduction of tysonite-type solids (Figure 26a and 26b). Sintering the compounds to reduce grain boundaries and improve grain growth contributed to higher ionic conductivities. Unfortunately, extending the sintering time beyond a certain threshold (20 h) did not further increase the ionic conductivity (compared to samples sintered for 2 h) due to the blocking effect of additional grain boundaries induced by oxides, silicates, or fluorite-type phase.<sup>276</sup>

The above-mentioned two mainstream fluorides have achieved substantial progress, yet they generally realize an ionic conductivity of  $10^{-4} \text{ S cm}^{-1}$  at high temperatures around 150 °C.<sup>604</sup> Their practical applications are still plagued by insufficient RT conductivity, prompting researchers to explore novel fluoride structures with faster transport of F ions at low temperature.<sup>43,605–607</sup> Sn(II)-based fluorides such as  $BaSnF_4$  compound are anticipated to deliver high  $F^-$  conductivity since the polarizable lone pair of electrons on  $Sn^{2+}$  can reorient during moving, enabling the mobile  $F^-$  between the Sn–Sn and the Sn–Ba layers to take part in the ionic conduction process.<sup>608–610</sup> Unfortunately, the strong electrostatic interaction between Ba and F in the Ba–Ba layer considerably impedes the F-ion migration. To eliminate this shielding effect, the introduction of point defects within  $BaSnF_4$  solids has been adopted for realizing efficient  $F^-$  shuttling. By partially substituting  $Ba^{2+}$  by  $Ce^{3+}$ , which has a similar atomic radius, point defects can be built in the tetragonal  $BaSnF_4$  crystal (Figure 26c). Accordingly, the Ba–Ba 3D barrier was disrupted, broadening the pathways for  $F^-$  transport.  $Ba_{0.95}Ce_{0.05}SnF_{4.05}$  displayed an enhanced RT conductivity of  $5.2 \times 10^{-4} \text{ S cm}^{-1}$  and a reduced activation energy of 0.15 eV compared to  $1.49 \times 10^{-4} \text{ S cm}^{-1}$  and 0.15 eV for  $BaSnF_4$  solid electrolyte, respectively. The assembled all-solid-state  $BiF_3|Ba_{0.95}Ce_{0.05}SnF_{4.05}|Sn$  FIB realized a high reversible specific capacity of 170.9 mA h  $g^{-1}$  and a stable cyclability over 30 cycles at RT.<sup>601</sup> Clearly, constructing point defects in  $F^-$  conducting solid electrolytes is promising for efficient shuttling of F ions. Although  $BaSnF_4$  delivered high RT ionic

conductivities comparable to those for solid electrolytes in LIBs,<sup>611</sup> its narrow ESW restricted the selection of cathode and anode materials, which led to a low average discharge voltage (usually less than 0.5 V).<sup>609,612,613</sup> To fulfill the requirements of high conductivity (e.g.,  $10^{-4} \text{ S cm}^{-1}$ ) at RT and an adequately broad ESW simultaneously, a solid electrolyte with the chemical formula of  $CsPb_{0.9}K_{0.1}F_{2.9}$  was designed. It was revealed that introducing F vacancies greatly facilitated the ionic transport of  $CsPb_{1-x}K_xF_{3-x}$  with the  $F^-$  conductivity reaching the maximum of  $1.23 \times 10^{-3} \text{ S cm}^{-1}$  when  $x$  was increased to 0.1. Moreover, the redox reaction was found to proceed through the valence change of Pb rather than Sn, as indicated by the calculation result. The reduction of Pb occurred at  $-0.1 \text{ V}$  (vs Pb/PbF<sub>2</sub>), while the oxidation to obtain high-valent Pb took place at 1.7 V, contributing to a wide ESW of 1.8 V for the  $CsPb_{0.9}K_{0.1}F_{2.9}$  electrolyte (Figure 26d). This result agreed well with LSV measurements, which showed a distinct oxidation started at 1.92 V and a reduction started at 0.11 V. Owing to these desirable features, a Pb/PbF<sub>2</sub>| $CsPb_{0.9}K_{0.1}F_{2.9}$ |Ag battery with high discharge voltage was constructed, maintaining high and stable specific capacity ( $\sim 140 \text{ mAh g}^{-1}$ ) after 72 cycles (4581 h) at a current density of 5.2 mA  $g^{-1}$ .<sup>602</sup> Most recently, Li et al. introduced a new class of layered Sn(II)-based fluoride conductor (i.e.,  $KSn_2F_5$ ) where  $F^-$  acted as charge carrier. The  $KSn_2F_5$  solid electrolyte exhibited a higher ionic conductivity ( $10^{-4} \text{ S cm}^{-1}$  at 60 °C) compared to typical tysonite-type and fluorite-type fluorides, mainly due to the increased charge carrier concentration and more frequent jumping process. Integrating this solid conductor with a high potential  $CuF_2$  cathode and a low potential Sn anode (Figure 26e), a high initial specific discharge capacity of 442 mA h  $g^{-1}$  was achieved (Figure 26f), retaining a reversible specific capacity of  $\sim 150 \text{ mAh g}^{-1}$  for more than 70 cycles at 60 °C. It should be noted that the interphase wetting of the solid electrolyte by the TBAF favors the  $F^-$  transfer between the electrode and the electrolyte.<sup>603</sup>

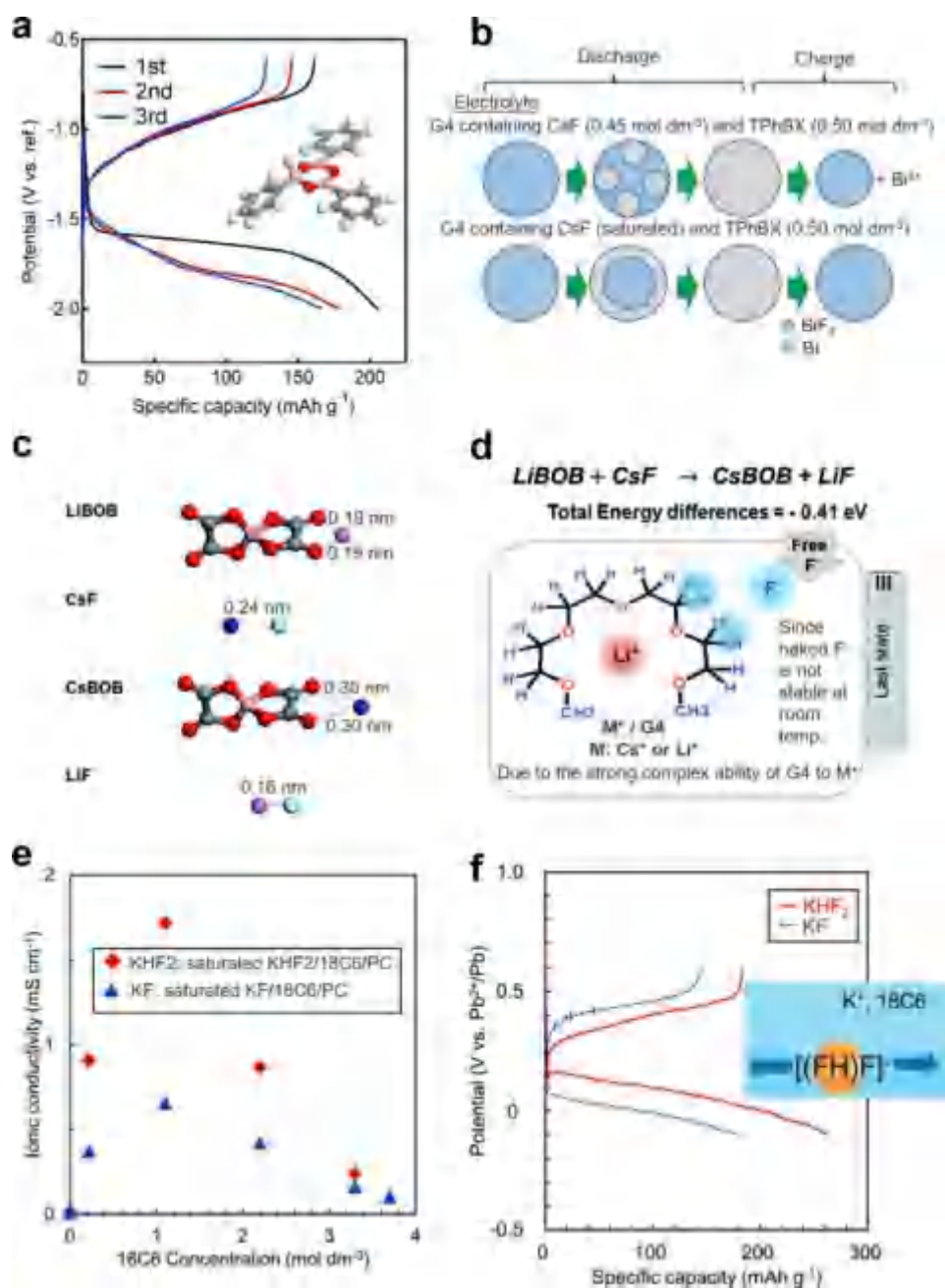
**4.2.2. Nonaqueous Liquid Electrolytes.** As discussed above, the physicochemical characteristics of  $F^-$  conducting solid-state electrolytes have been studied for several decades. Nevertheless, the majority of solid electrolytes necessitate an operation temperature above 150 °C for FIBs due to their low ionic conductivities at lower temperature. In contrast, liquid electrolytes are expected to exhibit superior  $F^-$  conductivities to enable RT FIBs. Besides, they demonstrate enhanced interphasial compatibility toward electrode materials, which is crucial for the commercialization of FIBs. Unfortunately, the developments of liquid electrolytes for RT FIBs has been largely constrained by two primary factors, i.e., the low solubility of fluoride salts in the electrochemically stable aprotic organic solvents and the strong chemical reactivity of  $F^-$  which is prone to create hydrofluoric acid (HF) in the presence of acidic hydrogen.<sup>9,42</sup> To establish liquid electrolytes for RT FIBs, several requirements should be satisfied, e.g., abundant free fluoride species ( $F^-$  or  $F_2H^-$ ) should exist in the electrolytes to support high ionic conductivity, sufficient electrochemical stability of the electrolytes to prevent decompositions during cycling, and high chemical stability of the electrolyte to prevent the dissolution of electrode active materials.<sup>40</sup> Thus, extensive attempts have been made to explore novel electrolytes for potential RT FIBs. However, initial efforts were disappointing due to the insolubility of most fluoride salts in organic solvents. Among these endeavors, a significant breakthrough was realized in 2018 by Jones et al.,



**Figure 27.** Room-temperature  $F^-$  conducting nonaqueous liquid electrolytes for FIBs. (a) Solubility of  $Np_1F$  salt in BTFE, AN, 3-methoxypropionitrile (MeOPN), and propionitrile (PN) solvents. (Inset)  $^{19}F$  NMR spectra in the bifluoride region for  $Np_1F$  salt dissolved in each solvent. (b) Ionic conductivity of  $Np_1F$  and  $Np_2F$  in BTFE solvent as a function of salt concentration. Reproduced with permission from ref 52. Copyright 2018 American Association for the Advancement of Science. (c) Ionic conductivity of  $Np_1F$  salt (0.75 M) in a mixture of BTFE and cosolvent. Reproduced with permission from ref 614. Copyright 2019 Royal Society of Chemistry. (d) Charge/discharge curves of the RT FIB based on a Bi cathode and a  $PbF_2/Pb$  anode in  $\sim 0.35$  M MPPF/TMPA–TFSA at  $20 \mu A cm^{-2}$ . Reproduced with permission from ref 618. Copyright 2017 American Chemical Society. (e) Schematic illustration of a FIB based on a fluorohydrogenate ionic liquid electrolyte, and structures of fluorohydrogenate anions ( $[(FH)_nF]^-$  when  $n = 2$  and  $3$ ). Reproduced with permission from ref 619. Copyright 2019 American Chemical Society. (f) Voltage curves of the Cu electrode in the  $[C_2C_1pyrr][F(H)_{2.3}F]$  electrolyte at RT with a current rate of  $0.05 C$  ( $= 42.2$  mA (g-Cu) $^{-1}$ ). Reproduced with permission from ref 620. Copyright 2021 Elsevier.

who designed RT  $F^-$  conducting electrolytes with high ionic conductivity, wide electrochemical stability window, as well as sufficient chemical stability via dissolving tetraalkylammonium fluoride salts (i.e., neopentyl (Np)-substituted alkylammonium fluorides) into ether solvents. The Np salt was chosen because the branched Np chain enhanced salt solubility while the absence of  $\beta$ -hydrogens inhibited  $HF_2^-$  generation. Results show that a high NpF salt concentration ( $>2.2$  M) could only be obtained when employing BTFE as the solvent without reacting with  $F^-$  (Figure 27a), exhibiting high ionic

conductivity comparable to that of LIB electrolytes (within the range from  $10^{-3}$  to  $10^{-2}$  S  $cm^{-1}$ , Figure 27b). It is important to note that the electron-withdrawing groups on the BTFE molecule could strengthen the partial positive charges on  $\alpha$ - $CH_2$ , guaranteeing adequate  $F^-$  solvation. When paired with a  $Cu@LaF_3$  core-shell nanostructure cathode, reversible electrochemical cycling with  $F^-$  shuttling was achieved at RT.<sup>52</sup> Though the cycle stability was far from satisfactory for practical battery systems, this report represents the pioneering work in exploring high-energy devices beyond that of LIBs. To



**Figure 28.** Employing anion acceptors and cation acceptors to improve the  $\text{F}^-$  conductivity for FIB electrolytes. (a) Discharge/charge curves of the  $\text{PbF}_2$  (C) electrodes (vs  $\text{Ag}/\text{Ag}^+$ ) at  $0.025 \text{ C}$  ( $1 \text{ C} = 219 \text{ mA g}^{-1}$ ). (Inset) Optimized molecular structure of  $\text{TPhBX-F}^-$ . Reproduced with permission from ref 627. Copyright 2019 Elsevier. (b) Scheme illustrating the effects of electrolyte concentrations ( $\text{CsF}$ :  $0.45 \text{ mol dm}^{-3}$  or saturated) on the  $\text{BiF}_3$  dissolution during cycling. Reproduced with permission from ref 636. Copyright 2019 American Chemical Society. (c) The most stable structures of lithium bis(oxalato)borate (LiBOB), CsF, CsBOB, and LiF. (d) Possible interactions in the  $\text{LiBOB}_{0.25}/\text{CsF}/\text{G4}$  electrolyte system. Reproduced with permission from ref 637. Copyright 2019 Royal Society of Chemistry. (e) Relationship between the 18C6 concentration and the ionic conductivity. (f) Charge/discharge curve of  $\text{BiF}_3$  electrodes at  $0.02 \text{ C}$  ( $1 \text{ C} = 302 \text{ mA g}^{-1}$ ;  $\text{KHF}_2$  represents the saturated  $\text{KHF}_2/18\text{C6}/\text{PC}$  electrolyte, KF denotes the saturated  $\text{KF}/18\text{C6}/\text{PC}$  electrolyte, while 18C6 concentration is  $1.10 \text{ M}$ ). (Inset)  $[(\text{FH})\text{F}]^-$  shuttling between two electrodes during charge/discharge. Reproduced with permission from ref 638. Copyright 2022 American Chemical Society.

gain a deep understanding of the factors affecting  $\text{F}^-$  ion-solvent properties in liquid FIBs, these authors further investigated various organic solvents in combination with the  $\text{Np}_1\text{F}$  salt. They revealed that partially fluorinated solvents possessing partial charge distribution and conformational flexibility achieved the highest level of salt dissolution, with BTFE being particularly prominent for its large  $\text{Np}_1\text{F}$  salt dissolution. Besides, introducing amide as a cosolvent promoted the ion dissociation between  $\text{Np}_1^+$  cations and  $\text{F}^-$

anions, thus enhancing the electrolyte ionic conductivity (Figure 27c).<sup>614</sup> Apart from organic fluoride salts, inorganic fluoride salts (i.e.,  $\text{CsF}$ ,  $\text{KF}$ , or  $\text{NaF}$ ) have been successfully employed as fluoride sources in the development of RT  $\text{F}^-$ -transporting liquid electrolytes, as demonstrated by the RISING project in Japan.<sup>615–617</sup> They introduced novel lactone ( $\gamma$ -butyrolactone, GBL)-based liquid electrolytes, which consist either of  $\text{CsF}$  or  $\text{KF}$ , through a solvent substitution method. Despite of the low  $\text{F}^-$  concentration of



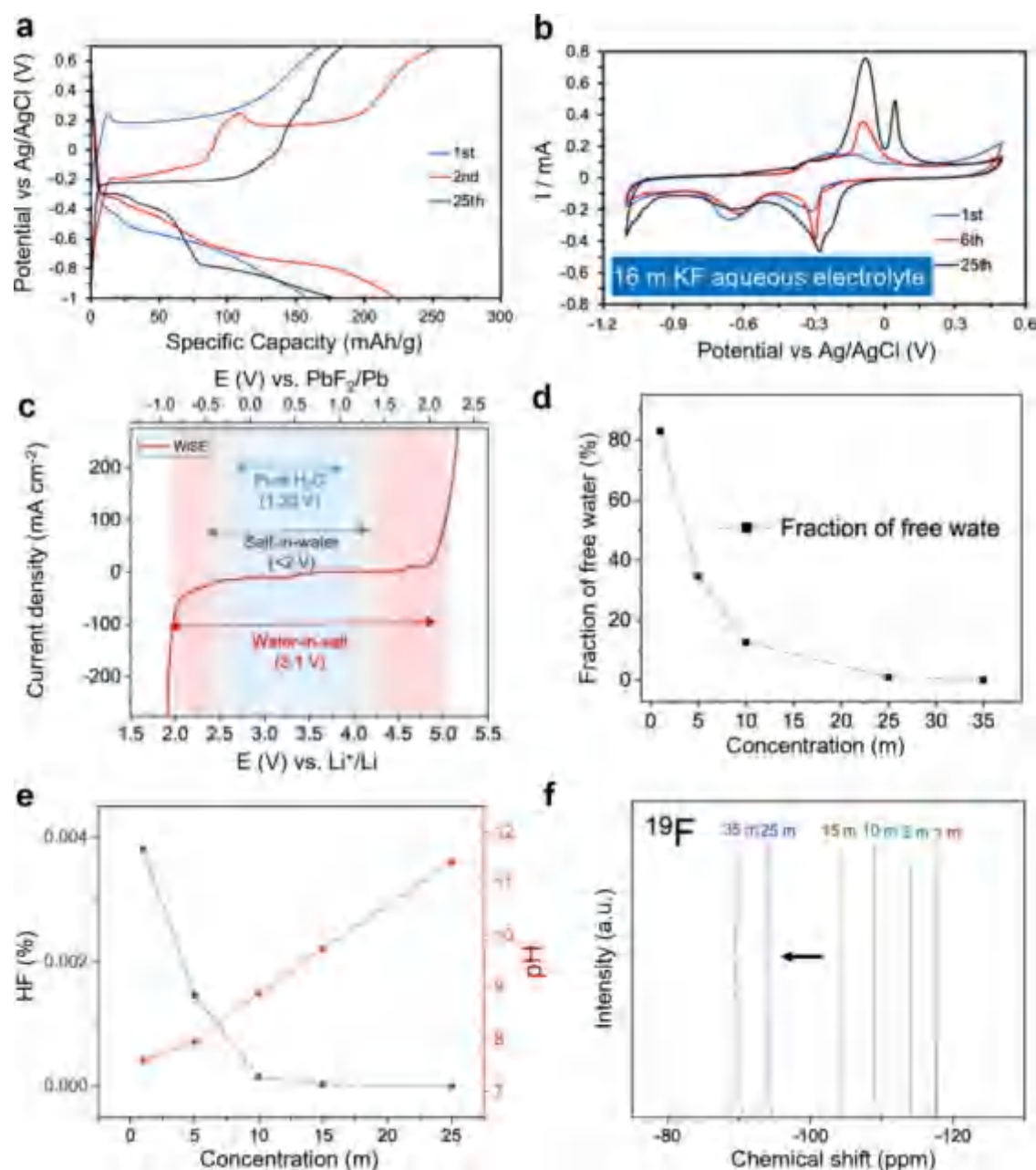
around 0.05 M, these electrolytes delivered high ionic conductivity of 0.8 mS cm<sup>-1</sup>, enabling reversible metal/metal–fluoride transformations for a wide range of metal electrodes. Nevertheless, the electrolyte solvent showed poor antireductive stability with the anode, which was promoted by the presence of fluoride ions.<sup>617</sup> In another effort, when 4.5 M LiFSI and 0.45 M CsF salts were dissolved in tetraglyme (G4) solvent as the electrolyte, this project revealed the formation of a SEI on a MgF<sub>2</sub> anode, which resulted from the irreversible decomposition of the liquid electrolyte during the reduction process. However, the detected LiF within the SEI could exert a detrimental impact on the FIB performance, given the poor electronic and F<sup>-</sup> conductivity of LiF.<sup>615</sup> Consequently, a thorough investigation of the SEI compositions and properties is warranted to optimize the FIB performance in the future.

Owing to their characteristic physicochemical properties, including high ionic conductivities, sufficient thermal and chemical stabilities, low volatilities, high nonflammability, and favorable solubility, RT (ionic liquids) ILs have been utilized for operating liquid FIBs. The first proof-of-principle RT FIB was presented by Darolles et al. in US patent 9166249, reporting an IL electrolyte consisting of tetramethylammonium fluoride (TMAF) in 1-methyl-1-propylpiperidinium bis-(trifluoromethanesulfonyl) imide (MPPTFSI). An ionic conductivity of  $\sim 10^{-3}$  S cm<sup>-1</sup> at RT and a stable voltage window > 4 V were realized, delivering an initial discharge specific capacity of 103 mAh g<sup>-1</sup> in a polyaniline (PANI)||PbF<sub>2</sub> battery.<sup>621</sup> Nevertheless, the extent of F<sup>-</sup> shuttling contributed to the cyclability was not adequately verified, the possible influence of IL cations on the cycling process remained unsolved, and the redox reactions associated with the PANI cathode were not thoroughly investigated, as noted by Hörmann et al. Despite these shortcomings and the very limited electrochemical performance, this patent remains seminal in the development of RTFIBs.<sup>40</sup> Subsequently, the RISING project in Japan has achieved notable progress in enhancing the ionic conductivity of ILs for the operation of RT FIBs. By dissolving the 1-methyl-1-propylpiperidinium fluoride (MPPF) in an IL, specifically *N,N,N*-trimethyl-*N*-propylammonium bis(trifluoromethanesulfonyl)amide (TMPA–TFSA), with a fluoride concentration of  $\sim 0.35$  M, a high conductivity of 2.5 mS cm<sup>-1</sup> was realized. When paired with a Bi cathode and a PbF<sub>2</sub>|Pb anode, the resulting liquid FIB exhibited distinct two-step plateaus in the initial charge/discharge profiles. However, some of the charged products (e.g., BiF<sub>3</sub>) was electrically detached from the Bi cathode through exfoliation, causing diminished charge–discharge efficiency and poor cycle stability (Figure 27d).<sup>618</sup> Notably, the possible generation of bifluoride ions from organic cations with  $\beta$ -hydrogens due to Hofmann elimination was not discussed in these IL-based electrolytes, presenting a significant challenge for the development of RT FIBs. To eliminate this issue, a novel liquid electrolyte based on fluorohydrogenate ionic liquids (FHILs) was designed by this project (Figure 27e), featuring the fluorohydrogenate anion ((FH)<sub>*n*</sub>F<sup>-</sup>), which possesses high ionic conductivities (e.g., 100 mS cm<sup>-1</sup> at RT for [C<sub>2</sub>C<sub>1</sub>im]<sup>+</sup>[(FH)<sub>2,3</sub>F]<sup>-</sup> (C<sub>2</sub>C<sub>1</sub>im = 1-ethyl-3-methylimidazolium)). When paired with this electrolyte, the CuF<sub>2</sub> cathode underwent reversible defluorination/fluorination, achieving 94.7% of the theoretical specific capacity (528 mAh (g-CuF<sub>2</sub>)<sup>-1</sup>) for the first cycle. However, a drastic capacity decay was observed upon subsequent cycling.<sup>619</sup> Afterward, these authors developed an alternative FHIL, [C<sub>2</sub>C<sub>1</sub>pyrr]<sup>+</sup>[(FH)<sub>2,3</sub>F]<sup>-</sup> (C<sub>2</sub>C<sub>1</sub>pyrr = *N*-ethyl-

*N*-methylpyrrolidinium), which, despite delivering reduced initial specific capacities (400 mAh (g-Cu)<sup>-1</sup>), extended the cycle life to 20 cycles while maintaining the specific capacity (Figure 27f). The improved cyclability was attributed to the low CuF<sub>2</sub> solubility in [C<sub>2</sub>C<sub>1</sub>pyrr]<sup>+</sup>[(FH)<sub>2,3</sub>F]<sup>-</sup>, which largely inhibits the aggregation of the Cu particles.<sup>620</sup>

Under acidic conditions,  $\beta$ -hydrogen elimination and/or other nucleophilic fluoride attacks toward atoms such as  $\alpha$ -H, C=O, ChN, P, Si, etc., take place relatively easily. These reactions can be mitigated by enhancing the solvation of F<sup>-</sup> through Lewis acidic solvating agents (i.e., anion acceptors (AAs)) such as organic compounds containing electropositive elements (e.g., B, Si, P, etc.). Among them, boron-based AAs have been proven to be effective in promoting the dissolution of Li salt (e.g., LiF, LiCl, Li<sub>2</sub>O, Li<sub>2</sub>O<sub>2</sub>) by reducing the cation–anion interactions.<sup>622–626</sup> Motivated by these findings, the RISING project in Japan undertook a series of research works to identify boron-containing compounds, including triphenylboroxine (TPhBX), triphenylborane (TPhB), fluorobis(2,4,6-trimethylphenyl) borane (FBTPhB), 4-(4,4,5,5-tetramethyl-1,3,2-dioxaborolan-2-yl)pyridine (DiOB-Py), etc., as AAs to form complexes with anions, thereby providing sufficient F<sup>-</sup> conductivity for operating RT FIBs.<sup>627–635</sup> Typically, fluoride salts such as CsF are challenging to dissolve in organic solvent such as G4. Through DFT calculations, the optimized molecular structure of TPhBX-F<sup>-</sup> was elucidated, revealing that the boron atom served as the most stable binding site for F<sup>-</sup>. Besides, the introduction of 0.5 M TPhBX greatly increased the solubility of CsF in G4 solvent from 0.00017 to 0.51 M, experimentally validating the effectiveness of TPhBX as an AA. The resulting PbF<sub>2</sub> (mixed with carbon) electrode delivered a high discharge specific capacity approaching the theoretical value (219 mAh g<sup>-1</sup>), which was sustained after the subsequent three cycles (Figure 28a).<sup>627</sup> While the solubility of CsF in G4 could be enhanced by AAs, it was found that the AA also led to the severe dissolution of the electrode active material, causing fast capacity degradation during cycling.<sup>633</sup> Subsequently, these researchers demonstrated that both the type of AA and the concentration of CsF can be optimized to balance the AA-F<sup>-</sup> interaction and the electrode dissolution. It was revealed that though the BiF<sub>3</sub> electrode could be discharged/charged normally in both electrolytes, the cycling performance with CsF (saturated)-TPhBX (0.50 M)-G4 electrolyte was higher than that with CsF (0.45 M)-TPhBX (0.50 M)-G4, attributed to the reduced dissolution of BiF<sub>3</sub> active material (Figure 28b). Additionally, it was proposed that the CsF/TPhBX ratio would significantly affect the formation state of Bi as well as the electrolyte decomposition products during the discharge process.<sup>636</sup>

Besides the AAs, another type of additive called cation acceptors (CAs) can also improve the conductivity of F<sup>-</sup> by promoting the dissolution of F salt in electrolytes. Unlike the AAs discussed above, CAs interact with cations instead of anions from the salts. As an extensively investigated salt additive to mitigate the cathode material dissolution/diffusion in LIBs, lithium bis(oxalato)borate (LiBOB) has exhibited great potential as a CA in liquid FIBs.<sup>637,639–643</sup> This is attributed to the strong interactions between BOB ions and alkali metal ions (such as Na<sup>+</sup> and Li<sup>+</sup>).<sup>644–646</sup> Kucuk et al. found that the optimum BOB<sup>-</sup> content to promote CsF dissolution in G4 was 0.25 M. Results revealed that BOB<sup>-</sup> addition not only reduced active material loss but also improved the electrolyte electrochemical stability during



**Figure 29.** Developments of “water-in-salt” aqueous electrolytes in FIBs. (a) Charge–discharge curves of the Cu electrode in 16 m KF aqueous electrolyte at 500 mA h g<sup>-1</sup>. (b) CV results for different cycles at a scan rate of 1 mV s<sup>-1</sup>. Reproduced with permission from ref 647. Copyright 2022 Royal Society of Chemistry. (c) ESW expansion using 25 m CsF aqueous electrolyte compared to pure water and other aqueous electrolytes. (d) The fraction of free water molecules calculated from the MD simulation. Fluoride-ion chemical species and electronic environment: (e) pH as a function of concentration, suggesting a decrease in the HF content, and (f) <sup>19</sup>F NMR spectroscopy. Reproduced with permission from ref 649. Copyright 2023 American Chemical Society.

redox reactions via the interactions between BOB<sup>-</sup> and Cs<sup>+</sup> as well as between fluoride and the CH<sub>2</sub> group of G4 solvent (Figure 28c and 28d).<sup>637</sup> More recently, instead of using CsF salt, a widely available potassium salt, potassium bifluoride (KHF<sub>2</sub>), was employed as the F<sup>-</sup> source. To increase the salt disassociation, the 18-crown-6 ether (18C6) was introduced as a CA to interact with potassium ions, significantly boosting the mobility of fluoride ions with an ionic conductivity of 1.72 mS cm<sup>-1</sup> (Figure 28e). As depicted in Figure 28f, the consequent BiF<sub>3</sub> electrode achieved a discharge specific and a charge specific capacity of 263 and 184 mAh g<sup>-1</sup>, respectively. In contrast, a higher voltage–polarization was observed for the

KF salt-based electrolyte with a reversible specific capacity below 140 mAh g<sup>-1</sup>. It is interesting to note that the fluoride ions existed in the form of [(FH)F]<sup>-</sup>, shuttling between the two electrodes during cycling. In addition, the HF generated from the equilibration reactions of [(FH)F]<sup>-</sup> was considered to dissolve metal fluorides, further enhancing the fluorination/defluorination reactivity of metal fluorides.<sup>638</sup> Based on these results, the AA (or CA) type as well as fluoride salt/AA (or CA) ratio should be carefully regulated to achieve high mobility of fluoride ions and to suppress the loss of active material. Furthermore, other types of supporting fluoride salts with higher dissociation levels (compared to the common

Table 4. Comparisons of the Electrochemical Performance and Remaining Issues of Liquid Electrolytes for RT FIBs Discussed in This Section<sup>a</sup>

electrolyte	anode/cathode	ionic conductivity (mS cm <sup>-1</sup> )	electrolyte stability window (V)	retained capacity (mAh g <sup>-1</sup> )/cycles	remaining issues	ref
1 M NpF-BTTE	Cu@LaF <sub>3</sub> (vs Li <sup>+</sup> /Li)	2–3	4.1	65/7th	poor cycle stability and large electrochemical polarization	52
0.05 M CsF-γ-butyrolactone	Zn  Ag	0.8		~0.068 mAh cm <sup>-2</sup> /24th	irreversible reductive reactions of the solvent restricted the negative potential to ca. -1.5 V vs SHE	617
6.3 mM KF + 0.5 M DiOB-Py-G4	BiF <sub>3</sub> /C (vs REF (0.587 V vs SHE))	1.02 × 10 <sup>-2</sup>	~3.2	316/1st	although dissolution of the active material was very low, fast capacity fading still existed	616
TMAF-MPPTFSI	PANI  PbF <sub>2</sub>	~1	>4	103/1st	contribution of F <sup>-</sup> shuttling to the cyclability was not verified; the possible influence of IL cations on the cycling process remained unclear	621
~0.35 M MPPF-TMPA/TFSA	PbF <sub>2</sub>   Pb  Bi	2.5		<0.01 mAh/5th	some charged products were electrically detached from the cathode by exfoliation, causing poor cycle stability, probably generated bifluoride ions	618
[C <sub>2</sub> C <sub>1</sub> im][[(FH) <sub>2</sub> 3F	CuF <sub>2</sub> (vs CuF <sub>2</sub> /Cu)	100		264 mAh (g-CuF <sub>2</sub> ) <sup>-1</sup> /10th	possible chemical dissolution of the CuF <sub>2</sub> produced during charging and its reprecipitation on the electrode surface	619
C <sub>2</sub> C <sub>1</sub> pyrr][[(FH) <sub>2</sub> 3F	Cu (vs CuF <sub>2</sub> /Cu)			210 mAh (g-Cu) <sup>-1</sup> /20th	electrochemical dissolution of Cu metal and chemical dissolution of CuF <sub>2</sub> still existed	620
0.51 dm <sup>-3</sup> CsF-tetraglyme + 0.5 dm <sup>-3</sup> TPhBX	PbF <sub>2</sub> @C (vs Ag/Ag <sup>+</sup> )		4.2	~170/3rd	TPHBX caused severe dissolution of the electrode active material	627
saturated CsF-tetraglyme + 0.5 dm <sup>-3</sup> TPhBX	BiF <sub>3</sub> (vs REF (0.587 V vs SHE))			~100/3rd	electrochemical reaction mechanism and performance were dependent on the CsF/TPHBX ratio	636
0.5 M CsF-tetraglyme + 0.25 M LiBOB	BiF <sub>3</sub> @C (vs REF (0.587 V vs SHE))	~1.6	~2.7	~125/1st	electrochemical polarization was large for redox reactions	637
saturated KHF <sub>2</sub> -PC + 18C6	BiF <sub>3</sub> (vs Pb <sup>2+</sup> /Pb)	1.72	3.7	184/1st	fluoride ions of the reactive species bond with protons, probably creating hydrogen during reduction at low potentials	638
0.8 M NaF-H <sub>2</sub> O	BiF <sub>3</sub>   TEMPO			89.5/85th	possibility of creating HF or bifluoride in the aqueous electrolyte; the electrolyte compatibility toward electrode materials were unclear	591
16 m KF-H <sub>2</sub> O	Cu (vs Ag/Ag <sup>+</sup> )			50/300th	uncontrolled KF precipitation on the electrode surface and the unregulated volumetric changes	647
7.5 M KF + 1.5 M KOH-H <sub>2</sub> O	Zn  Cu		~2.1 V	0.11 mAh cm <sup>-1</sup> /1600th	low reversible capacity for F <sup>-</sup> storage reaction	648
25 m CsF-H <sub>2</sub> O	symmetric Pb  PbF <sub>2</sub>	152	3.1 V	~65/50th	dissolution of active material still existed	649

<sup>a</sup>REF: a silver rod immersed in acetonitrile with 0.1 M silver nitrate and 0.1 M tetraethylammonium perchlorate as reference electrode.





associated with the active material for the reversible conversion between Cu and CuF<sub>2</sub> (the charged product of Cu). Furthermore, the KF solid embedded into the Cu electrode acted as part of the active material, contributing to a higher specific capacity of 222 mA h g<sup>-1</sup> (based on the Cu mass) in the initial cycle. It was observed that the cathodic peaks shifted to a higher potential to reduce the electrochemical polarization, which aligned with the voltage curves. (Figure 29a and 29b).<sup>647</sup> Soon after, a “water-in-salt” aqueous electrolyte composed of 7.5 M KF and 1.5 M KOH was designed, expanding the electrolyte stability window to ~2.1 V. Taking advantage of this electrolyte, a Zn||Cu battery based on the F<sup>-</sup> shuttling was constructed, realizing an improved discharge platform of 1.9 V and a steady operation over 1600 cycles.<sup>648</sup> This finding combined the advantages of the high conversion voltage of metal fluoride and the low-cost, environmental friendliness of Zn||Cu batteries. Most recently, the ESW of aqueous electrolytes was significantly increased to 3.1 V by dissolving 25 m CsF in water. As reflected in the <sup>17</sup>O NMR spectroscopy and MD simulation, the 25 m CsF electrolyte displayed an increased fraction of ion pairs and aggregates in addition to the elimination of free water molecules (compared with 1 m CsF), which confirmed the mechanism behind the expanded ESW (Figure 29c and 29d). More significantly, the chemical stability of fluorides was investigated through <sup>19</sup>F NMR coupled with pH measurements, demonstrating that HF formation was almost completely suppressed (Figure 29e and 29f). Therefore, the dissolution of active materials from electrodes such as Pb|PbF<sub>2</sub> and CuF<sub>2</sub> was inhibited, offering improved cycle stabilities.<sup>649</sup>

To conclude, in terms of solid-state electrolytes, the high operating temperature (e.g., >150 °C), low ionic transport capability, and poor interfacial contact remain challenging for most of the fluorite-type and tysonite-type solid-state electrolytes. Novel fluoride structures and modification strategies are urgently needed to promote the development of F<sup>-</sup> conducting solid-state electrolytes. Liquid electrolytes permit FIBs to operate at ambient temperature with minimal internal resistance. Nevertheless, several issues persisted, as outlined in Table 4. The majority of fluoride salts exhibit limited solubility in organic solvents, leading to low ionic conductivity. Besides, the narrow ESW strongly constrains the selection of active materials, thus lowering the energy density of FIBs. Dissolution issues related with active material are another main concern that cause unsatisfactory cycle stability. Notably, due to the high chemical reactivity of F<sup>-</sup> ions, most liquid electrolytes are corrosive and toxic toward cell components. To achieve high ionic conductivities and simultaneously inhibit nucleophilic  $\beta$ -hydrogen elimination and/or other nucleophilic fluoride attacks, novel fluoride salts (other than the common CsF) and/or suitable solvents should be explored. Besides, suitable anion acceptors acting via forming a complex with the F anion or cation acceptors interacting with cations can be employed for promoting the dissociation of fluoride salts. It should be noted that the anion acceptors may also facilitate the loss of active materials. For a more comprehensive overview of electrolyte advancements in rechargeable FIBs, readers are encouraged to refer to several excellent reviews.<sup>41,276</sup>

## 5. FLUORINE CHEMISTRY IN OTHER RECHARGEABLE BATTERIES

### 5.1. Na- and K-Based Batteries

**5.1.1. Fluorine-Containing Electrode Materials in Na-Based Batteries.** As mentioned above, fluorine is the most electronegative element with  $\chi = 3.98$  compared to 3.44 for oxygen on the Pauling scale, contributing to more ionic M–X bonds in fluorides and thus higher redox potentials of transition metal ions than oxygen ions (Figure 30a and 30b).<sup>54,650</sup> In addition, in contrast to polyanions such as PO<sub>4</sub><sup>3-</sup> and SO<sub>4</sub><sup>2-</sup>, the lower molecular weight of F<sup>-</sup> is favorable for enhanced specific capacity. Generally, F-based inorganic or organic compounds are more stable against oxidation. Therefore, F-containing compounds (Na<sub>x</sub>M<sub>y</sub>F<sub>z</sub>) can combine the benefits of the large gravimetric energy density of layered Na<sub>x</sub>MO<sub>2</sub> with the high structural stability of polyanions, which has been proposed as promising cathode materials for SIBs.<sup>54</sup> A summary of the main characteristics of fluorinated materials as the cathode materials of SIBs has been thoroughly reviewed by Maisonneuve et al.;<sup>651</sup> readers are encouraged to refer to this review dedicated solely to fluorinated cathodes based on the material structures and other related reviews focused on transition metal oxyfluorides, transition metal fluorides, etc.<sup>113,652</sup> Here, we mainly discuss some representative cathode materials of SIBs with the best overall performance, especially for 3D materials, analyzing the structure characteristics for further improving highly reversible/stable Na<sup>+</sup> uptake/release.

The metal difluorides (MF<sub>2</sub>) synthesized from the decomposition of metal trifluoroacetates were first employed in SIBs in 2014. Different from the direct conversion reaction with Li, FeF<sub>2</sub> reacted with Na by direct conversion at the surface region; then, it reacted heterogeneously with Na to convert to Fe<sup>3+</sup> and Fe<sup>0</sup>.<sup>653</sup> This work proved the disproportionation reaction mechanism in the conversion system, which helped to understand the nanoscale sodiation in metal difluorides. Sun et al. prepared a FeF<sub>2</sub>-reduced graphene oxide nanocomposite. When associated with a PAA (poly(acrylic acid)) binder, the reversible capacity of the nanocomposite was greatly improved from 100 to 175 mAh g<sup>-1</sup> and the high-rate capability was also achieved with a capacity of 78 mAh g<sup>-1</sup> at 10 A g<sup>-1</sup>.<sup>654</sup>

To increase the capacity based on conversion reactions, the oxyfluoride FeOF has also been employed in SIBs. FeOF was studied by Deng et al. for insertion–conversion reactions in SIBs, which was prepared through a facial alcohol-assisted solvothermal method. The obtained FeOF nanorods delivered a high reversible capacity of ~250 mAh g<sup>-1</sup> after 20 cycles at 10 mA g<sup>-1</sup>.<sup>657</sup> Afterward, FeO<sub>0.7</sub>F<sub>1.3</sub>/C nanocomposite was synthesized via a solution process for Na storage. This cathode material displayed a high initial discharge capacity of 496 mAh g<sup>-1</sup>, a reversible capacity of 388 mAh g<sup>-1</sup> at 50 °C, as well as satisfactory capacity retention of 92.8% after 50 cycles. Furthermore, it was elucidated that the reaction mechanism of FeO<sub>0.7</sub>F<sub>1.3</sub>/C included a hybridized mechanism of both intercalation and conversion reactions. The initial discharged products were NaF, Fe nanoparticles, and a newly formed rock salt phase (Na<sub>1.4</sub>FeO<sub>1.4</sub>F<sub>0.6</sub>). Then, the phase separation was observed during recharging, inducing huge irreversible capacity loss in the first cycle. As the competitive reactions involved the rock salt phase and rutile components could improve the cycling stability of nanosized electrode materials,<sup>658</sup> the

authors then proposed that the phase separation could stabilize the desodiation reactions during subsequent cycles.

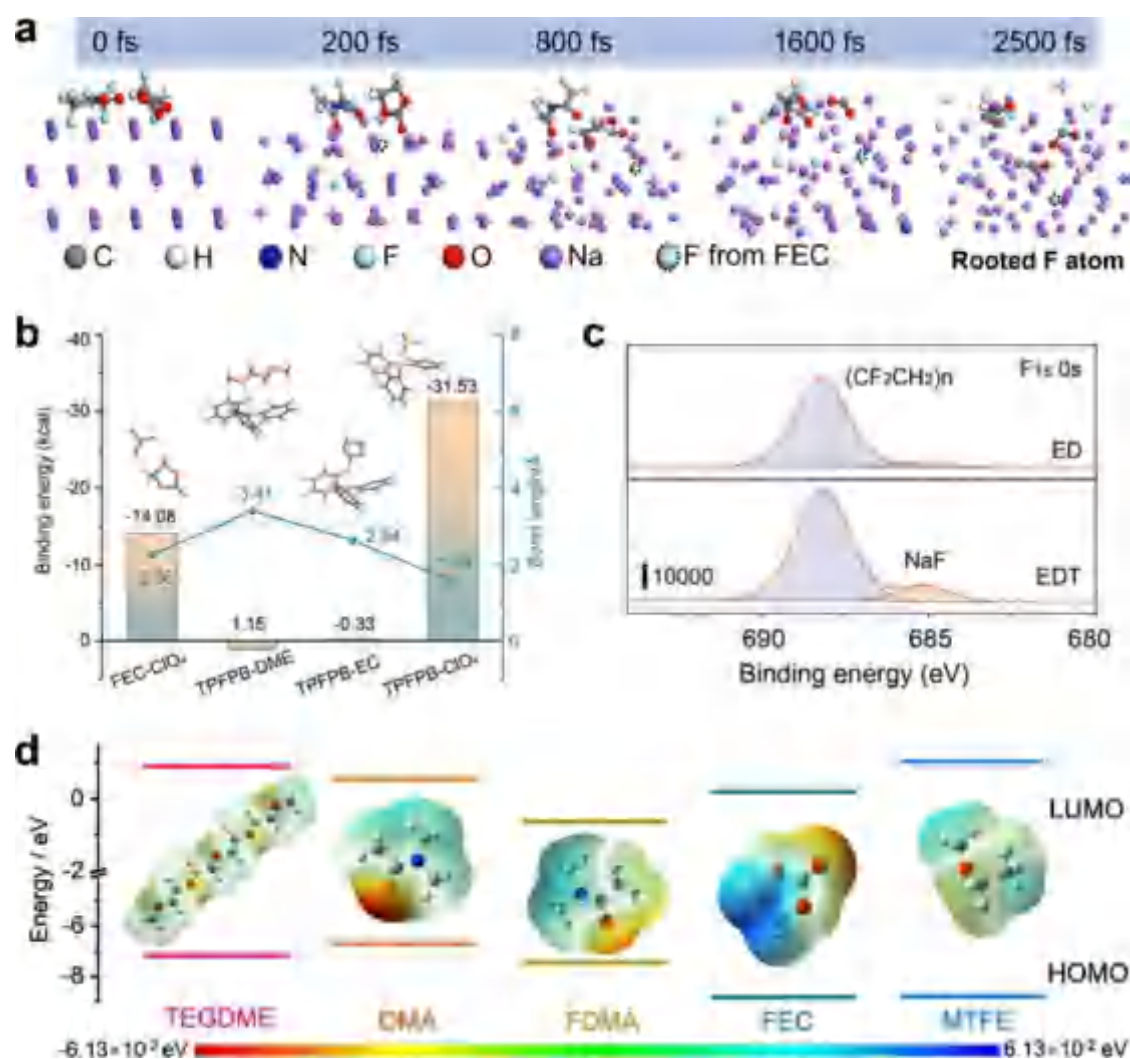
Apart from the above-mentioned potential high gravimetric energy densities, most  $\text{Na}_x\text{M}_y\text{F}_z$  materials exhibit excellent structural stability in the Na-deficient phase compared with layered  $\text{Na}_x\text{MO}_2$ , attributed to their three-dimensional framework. Using a similar solvothermal method for the preparation of  $\text{NaFeF}_4$  except at elevated temperature (230 °C), NaF was introduced into the one-dimensional (1D)  $\text{FeF}_3 \cdot 3\text{H}_2\text{O}$  host to stabilize the lattice structure, obtaining the novel weberite  $\text{Na}_2\text{Fe}_2\text{F}_7$  (via the  $\text{Fe}^{2+}/\text{Fe}^{3+}$  redox reaction). A high insertion voltage of 3.25 V vs  $\text{Na}^+/\text{Na}$  was achieved, but the  $\text{Na}_2\text{Fe}_2\text{F}_7$  cathode delivered a rather low discharge capacity of 58 mAh  $\text{g}^{-1}$  and poor cyclability.<sup>659</sup> A more recent report by Kim et al. demonstrated the  $\text{Na}_x\text{Fe}_2\text{F}_7$  cathode material with the crystal structure composed of point-shared  $\text{FeF}_6$  octahedra could deliver a high capacity of 184 mA h  $\text{g}^{-1}$  at C/20 (1 C = 184 mA  $\text{g}^{-1}$ ), attributed to a single-phase reaction without phase transition and negligible volume change during  $\text{Na}^+$  extraction/insertion. The activation barrier energies for  $\text{Na}^+$ -ion migration in  $\text{Na}_x\text{Fe}_2\text{F}_7$  were theoretically predicted by the nudged elastic band (NEB) according to first-principles calculations (Figure 30c), revealing the low activation barrier energies for efficient  $\text{Na}^+$  diffusion along 3D pathways. This structure characteristics favor a long-term cycle span of over 1000 cycles at 2 C with ~88% capacity retention and an outstanding rate capability, as shown in Figure 30d.<sup>54</sup> Although  $\text{Na}_2\text{Fe}_2\text{F}_7$  had the best reported performance for weberite cathode, the relationships between the structures and the properties remained unclear. To investigate the structure features and electrochemical behavior of the  $\text{Na}_2\text{Fe}_2\text{F}_7$  weberite cathode in detail, an experimental–computational approach was adopted by Foley et al.<sup>660</sup> The results showed that  $\text{Na}_2\text{Fe}_2\text{F}_7$  was metastable with a mixture of polymorphs (e.g., the orthorhombic (2O), trigonal (3T), and monoclinic (4M) weberite polymorphs). As the  $\text{Na}_2\text{Fe}_2\text{F}_7$  phases preferred to transform to the more stable  $\text{NaFeF}_3$  perovskite, the cathode experienced capacity fading upon cycling. Interestingly, these various polymorphs would not exert a large impact on the Na storage behavior, as indicated from the first-principle investigations. Further comprehensive investigations on regulating the weberite polymorphism and phase stability for advanced SIB cathodes are needed.

Except for  $\text{Na}_2\text{Fe}_2\text{F}_7$ , the weberite structure contains a large family of materials featuring the chemical formula of  $\text{Na}_2\text{M}^{\text{II}}\text{M}^{\text{III}}\text{F}_7$  (e.g.,  $\text{M}^{\text{II}} = \text{Mg, Fe, Mn, Co, Ni, etc.}$ ,  $\text{M}^{\text{III}} = \text{Al, Fe, Mn, V, Cr}$ ),<sup>661,662</sup> which have not been employed as cathode materials for SIBs. Zhou et al. synthesized three vanadium-based weberite-type fluorides,  $\text{Na}_2\text{MVF}_7$  (M denotes Mn, Fe, and Co), through a polytetrafluoroethylene-assisted fluorination process. Based on the redox reactions of  $\text{Fe}^{2+}/\text{Fe}^{3+}$  and  $\text{V}^{3+}/\text{V}^{4+}$ , a reversible capacity of 146.5 mA h  $\text{g}^{-1}$  was obtained for the optimal  $\text{Na}_2\text{FeVF}_7$  cathode. Furthermore, 95% capacity was retained after 200 cycles owing to the robust crystal structure during repeated  $\text{Na}^+$  deintercalation/intercalation.<sup>663</sup> More recently, a novel  $\text{Fe}^{2+}/\text{Ti}^{3+}$ -based fluoride,  $\text{Na}_2\text{TiFeF}_7$ , was prepared as a SIB cathode materials. The  $\text{Fe}^{2+}$  and  $\text{Ti}^{3+}$  ions in the  $\text{Na}_2\text{TiFeF}_7$  structure enabled the full utilization of  $\text{Ti}^{3+}/\text{Ti}^{4+}$  and  $\text{Fe}^{2+}/\text{Fe}^{3+}$  redox couples for a high specific capacity of ~185 mAh  $\text{g}^{-1}$  at C/20 (1 C = 189 mA  $\text{g}^{-1}$ ). Moreover, the high  $\text{Fe}^{2+}/\text{Fe}^{3+}$  redox potential (~3.75 V vs  $\text{Na}^+/\text{Na}$ ) increased the average operating voltage of the cathode to 3.37 V (Figure 30e). Notably, the  $\text{Na}_2\text{TiFeF}_7$

cathode still delivered a specific capacity of ~136 mAh  $\text{g}^{-1}$  even at 5 C, which was associated with the low activation energy barriers (~477.68 meV, Figure 30f) and low band-gap energy (~1.83 eV) for high-power SIB applications.<sup>656</sup>

$\text{MX}_3$ -type fluorides, in particular  $\text{FeF}_3$ , have been widely studied for SIBs. Among its three allotropic varieties ( $\text{ReO}_3$ , hexagonal tungsten bronze (HTB), and pyrochlore), the hydrated  $\text{FeF}_3 \cdot 0.33\text{H}_2\text{O}$  HTB has gained visibly increasing interest in recent years due to its high average voltage (~2.74 V vs  $\text{Na}/\text{Na}^+$ ), high theoretical specific capacity, nontoxicity, and low cost.<sup>664,665</sup> The presence of cavities could remove water molecules from the [001] hexagonal channels and insert  $\text{Na}^+$  ions. In 2013, an HTB-type  $\text{FeF}_3 \cdot 0.33\text{H}_2\text{O}$  was synthesized through a solid–solid transformation, where thermally vulnerable channels in  $\text{FeF}_3 \cdot 3\text{H}_2\text{O}$  were expanded into more robust ones. At the same time, the micro-sized precursor underwent particle nanosizing. During this process, the characteristic Fe-based octahedral chains isolated in  $\text{FeF}_3 \cdot 3\text{H}_2\text{O}$  precursor were preserved, mainly due to the infiltration and capping of IL (1-butyl-3-methylimidazolium tetrafluoroborate ( $\text{BmimBF}_4$ )), followed by the alleviated release of hydration  $\text{H}_2\text{O}$  from  $\text{FeF}_3 \cdot 3\text{H}_2\text{O}$ . Beneficial from the well-suited Na-insertable cavities, this HTB-type  $\text{FeF}_3 \cdot 0.33\text{H}_2\text{O}$  electrode (wired by 10 wt % single-wall CNT (SWCNTs)) delivered a high discharge capacity of 130 mAh  $\text{g}^{-1}$  in the first cycle and good capacity retention (74 mAh  $\text{g}^{-1}$ ) after 50 cycles.<sup>666</sup> Despite these advantages, the low electronic and ionic conductivities of  $\text{FeF}_3 \cdot 0.33\text{H}_2\text{O}$ , induced by the highly ionic character of the Fe–F bond, strongly hinder the practical application of SIBs. To improve the electrochemical performance, the  $\text{FeF}_3 \cdot 0.33\text{H}_2\text{O}$  nanoparticles were packaged into 3D ordered mesoporous carbons (3D-OMCs) to serve as a SIB cathode material, where the 3D-OMCs as the carbon source facilitated the electron transfer and shortened the  $\text{Na}^+$  diffusion path while improving the structural stability and suppressing nanoparticle aggregation upon the  $\text{Na}^+$  deintercalation/intercalation. Besides, 3D-OMCs provided a large surface area for high mass loading as well as increased contact area of the electrode/electrolyte interphase. Consequently, the  $\text{FeF}_3 \cdot 0.33\text{H}_2\text{O}@3\text{D-OMCs}$  nanocomposite exhibited a high first discharge capacity of 386 mAh  $\text{g}^{-1}$  with a steady capacity of 238.0 mAh  $\text{g}^{-1}$  over 100 cycles at 20 mA  $\text{g}^{-1}$ . This nanocomposite cathode also demonstrated remarkable rate performance with a reversible capacity of 201 mAh  $\text{g}^{-1}$  even at 100 mA  $\text{g}^{-1}$ .<sup>665</sup> Although the electrochemical properties were enhanced, the intrinsic conductivity of  $\text{FeF}_3 \cdot 0.33\text{H}_2\text{O}$  was still the same. Previous studies revealed that the band gap of this material could be decreased through ion doping, thus improving the intrinsic conductivities of  $\text{FeF}_3 \cdot 0.33\text{H}_2\text{O}$ .<sup>667–670</sup> For instance, with a smaller ionic radius (0.0615 nm) than that of  $\text{Fe}^{3+}$  (0.0645 nm),  $\text{Cr}^{3+}$  is easier to enter into the lattice of  $\text{FeF}_3 \cdot 0.33\text{H}_2\text{O}$ . According to the DFT calculation results,  $\text{Cr}^{3+}$  doping could redistribute the charge of  $\text{FeF}_3 \cdot 0.33\text{H}_2\text{O}$ , which reduced the band gap from 0.88 to 0.49 eV to improve its intrinsic conductivity. The optimized  $\text{Fe}_{0.95}\text{Cr}_{0.05}\text{F}_3 \cdot 0.33\text{H}_2\text{O}$  cathode delivered a reversible capacity of 194.02 mAh  $\text{g}^{-1}$  at 0.1 C, which is much larger than that obtained with the  $\text{FeF}_3 \cdot 0.33\text{H}_2\text{O}$  cathode (136.47 mAh  $\text{g}^{-1}$ ). In addition, this doping cathode displayed much lower impedance than that of the  $\text{FeF}_3 \cdot 0.33\text{H}_2\text{O}$  cathode, further proving the increased electronic conductivity of the cathode material after  $\text{Cr}^{3+}$  doping.<sup>671</sup> In brief, these findings suggest that the thermodynamically stable phases of the fluoride-based





**Figure 31.** F-containing additives and (co)solvents for stable operation of Na-based batteries. (a) AIMD simulations with ECDA and FEC. Reproduced with permission from ref 680. Copyright 2023 Elsevier. (b) Binding energies and bond lengths of  $\text{FEC-ClO}_4^-$ , TFPFB-DME, TFPFB-EC, and TFPFB- $\text{ClO}_4^-$  through H–O, B–O, B–O, and B–O interactions, respectively. (c) XPS spectra of F 1s using electrolytes without and with TFPFB additive. Reproduced with permission from ref 685. Copyright 2023 Wiley-VCH. (d) LUMO and HOMO energy values of electrolyte components. (Inset) Electrostatic potential mapping of these components. Reproduced with permission from ref 686. Copyright 2022 Wiley-VCH.

cathodes are promising to achieve excellent electrochemical performance in SIBs, especially in terms of power capability and cycle durability.

Although great progress has been achieved, fluoride-based cathode materials have been limited to a small number of candidates. In addition, presodiation is required for some of these developed fluoride-based cathodes to utilize their high theoretical capacities. More notably, owing to the large band-gap energies and low electronic conductivities, fluoride-based cathode materials typically suffer from poor electrochemical kinetics, which further causes rapid capacity deterioration, especially at high charging rates, significantly restricting their applications in SIBs.

### 5.1.2. Fluorinated Electrolytes in Na-Based Batteries.

Similar to Li-based batteries, the battery performance of SIBs is largely determined by the selection of electrolytes,<sup>672–674</sup> especially the stability of the electrolytes toward the high electrochemical polarization of both the cathode and the anode. The ability to form passivation layers on the electrode surfaces must be considered for the stable operation of SIBs.

Encouraged by the positive results obtained from Li-based battery systems, the effect of FEC on the performance of SIBs was first examined in 2011, revealing an improved reversibility insertion/extraction of  $\text{Na}^+$  ions for the hard carbon (HC) anode and the  $\text{NaNi}_{1/2}\text{Mn}_{1/2}\text{O}_2$  cathode. Besides, FEC benefited the passivation of Na metal anode for suppressing undesirable reactions, thus enhancing the deposition/dissolution of metallic Na with higher reversibility.<sup>675</sup> The favorable role of FEC toward both the anode (e.g., hard carbon, Na metal) and the cathode (e.g.,  $\text{Na}_{0.44}\text{MnO}_2$ ) material was further verified by researchers, demonstrating the formation of a desirable passivation layer with FEC for improving the cycle stability and of SIBs.<sup>676–679</sup>

Very recently, a unique SEI was designed via in situ preimplantation of F atoms rooted in Na metal.<sup>680</sup> As a fluorine booster, the soluble functional molecule, amide molecule bis(trifluoroacetamide) (ECDA), can be anchored onto the Na metal. Owing to the strong induction effect and electrostatic repulsion of Na toward ECDA, abundant FEC-decomposed F atoms were driven to penetrate deeply into the

Na metal from the outside inward, which resulted in a desired functional rooted interphase (Figure 31a). Afterward, this interphase promoted the generation of a multilayer, inorganic-rich (e.g., NaF, Na<sub>x</sub>N, and Na<sub>2</sub>O) SEI with a concentration gradient, ultimately enabling a high CE of 97.3% with an extended Na plating/stripping lifetime (1700 h) at 1 mA cm<sup>-2</sup>. In addition, the 4.5 V Prussian Blue||Na@Cu battery delivered a high capacity retention of 86% over 200 cycles with a limited amount of Na.<sup>680</sup> Unfortunately, these strategies failed to satisfy the wide temperature applications of SIBs. Generally, unwanted electrolyte decomposition on the cathode surface aggravates rapidly with increasing temperature, where the unstable CEI layer is commonly accompanied by continuous electrolyte decomposition, surface reconstruction, and capacity fading.<sup>681–683</sup> In addition, the defects of the uncontrollable CEI would be further aggravated with high-voltage and high-temperature conditions.<sup>684</sup> Recently, Chou and co-workers introduced an anion receptor tris(pentafluorophenyl)borane (TPFPB) containing an electron-deficient B center, which preferentially oxidized for constructing the NaF-rich CEI layer. The strong interactions between the ClO<sub>4</sub><sup>-</sup> anion and the TFPBP additive effectively reduced the involvement of ClO<sub>4</sub><sup>-</sup> in the first solvation sheath and contributed to facilitated coordination capability between organic solvents and Na<sup>+</sup> cations, which greatly enhanced the antioxidative stability (Figure 31b and 31c). With the TFPBP-containing electrolyte, the resulting Na<sub>3</sub>V<sub>2</sub>(PO<sub>4</sub>)<sub>3</sub> cathode delivered a capacity retention of 86.9% over 100 cycles, when operated with a high cutoff voltage of 4.2 V (vs Na<sup>+</sup>/Na) and at a high operating temperature of 60 °C. This electrolyte also exhibited promising performance over a wide temperature range from -30 to 60 °C, highlighting the significance of tailoring the solvation chemistry for high-voltage and high-temperature SIBs.<sup>685</sup>

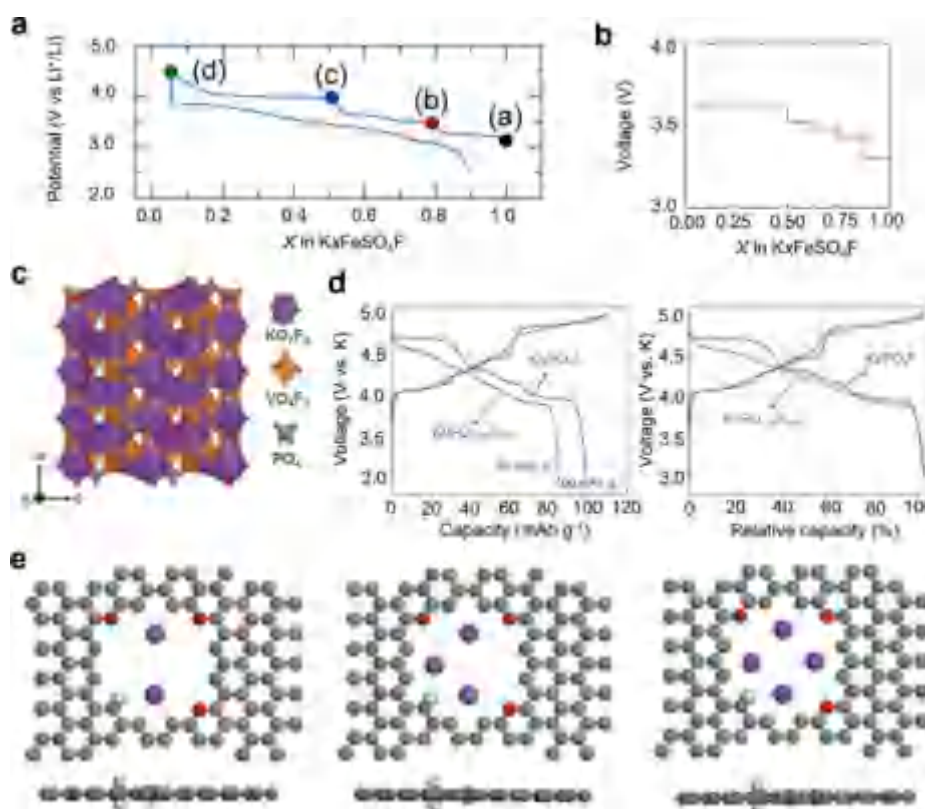
Learning from the Li-based battery electrolyte systems, fluorinated “inert” diluents have been successfully employed in SIBs for tuning the solvation structure and the related electrochemical behavior. In 2018, Zhang et al. designed a LHCE in SIBs by introducing a hydrofluoroether diluent (i.e., BTFE) to decrease the concentration of NaFSI–DME electrolyte to less than 1.5 M.<sup>687</sup> Taking advantage of the “inert” nature of the fluorinated diluent, the interphasial reaction kinetics and interphasial stability of the Na metal anode were largely improved, which was attributed to the formation of a F-enriched protective SEI layer. Consequently, a dendrite-free Na deposition process along with stable cycling (90.8% capacity retention over 40000 cycles) and fast charging (20 C) were achieved in the Na||Na<sub>3</sub>V<sub>2</sub>(PO<sub>4</sub>)<sub>3</sub> battery. Afterward, the authors reported a nonflammable LHCE composed of NaFSI-triethyl phosphate (TEP)/TTE (1:1.5:2 in molar ratio) for highly reversible SIBs. This electrolyte stabilized the interphases on both the layered Na-Cu<sub>1/9</sub>Ni<sub>2/9</sub>Fe<sub>1/3</sub>Mn<sub>1/3</sub>O<sub>2</sub> (Na–NCFM) cathodes and the HC anodes, enabling high CE and long-term cyclability for the HCl||Na–NCFM full cells.<sup>688</sup>

More interestingly, fluorine chemistry has also been utilized in designing novel salts for SIBs. Despite high ionic conductivity, NaPF<sub>6</sub> is susceptible to undergoing hydrolysis, leading to toxic species such as HF and PO<sub>2</sub>F<sub>3</sub> and posing severe safety concerns.<sup>689,690</sup> Meanwhile, alternative Na salts suffer from poor electrochemical performance, severe safety concerns, or high cost. Borate anions with various attractive features have gained interest as electrolyte salts recently,

especially when possessing varying degrees of fluorination for greater ESW. Wright et al. prepared a series of Na borate salts with varying steric and electronic properties, where Na[B(hfp)<sub>4</sub>]·DME (hfp = hexafluoroisopropoxy, O<sup>-</sup>Pr<sup>F</sup>) and Na[B(pp)<sub>2</sub>] (pp = perfluorinated pinacolato, O<sub>2</sub>C<sub>2</sub>(CF<sub>3</sub>)<sub>4</sub>) stood out with increased oxidative stability as well as excellent electrochemical performance.<sup>691</sup>

Combining the Na anode with an abundant, nontoxic, and high-capacity (1675 mAh g<sup>-1</sup>) sulfur cathode, sodium–sulfur (Na–S) batteries have been technologically attractive for grid-scale energy storage. High-temperature Na–S batteries have been commercialized since 2002 with a high efficiency of ~100% as well as a theoretical energy density of 760 Wh kg<sup>-1</sup> (based on both the Na anode and the sulfur cathode), the safety concerns and additional maintenance costs brought by the high operating temperature (300–350 °C) still remain unsolved. Besides, the capacity utilization of the sulfur cathode is only ~1/3 of the theoretical value, which is ascribed to the incomplete sulfur conversion reactions. Motivated by these issues, increasing efforts have been focused on RT Na–S batteries, which operate through a complete sulfur conversion with sodium sulfide (Na<sub>2</sub>S) as the final discharge product instead of Na polysulfides, improving the theoretical energy density to 1274 Wh kg<sup>-1</sup>. Nevertheless, RT Na–S batteries are strongly restricted by low reversible capacity, serious self-discharge, and insufficient cycle stability, which are mainly attributed to the incompatible electrolyte systems toward the electrodes. By introducing FEC as the electrolyte cosolvent, Wang et al. discovered that the solubility of Na polysulfides in the electrolyte was successfully inhibited due to the low binding energy between FEC and Na polysulfides. Meanwhile, a stable and robust F-rich SEI was generated on the anode, protecting the Na metal from dendrite growth.<sup>692</sup> Recently, their continuous work demonstrated highly reversible long-term Na–S batteries through developing an all-fluorinated electrolyte, consisting of 2,2,2-trifluoro-*N,N*-dimethylacetamide (FDMA) as solvent, 1,1,2,2-tetrafluoroethyl methyl ether (MTFE) as antisolvent, and FEC as additive. The MTFE with a reduced HOMO value would strengthen the electrolyte antioxidative stability. Besides, the decreased negative charge density of the FDMA–MTFE system could suppress the dissolution of polar polysulfide and also lead to weak solvation of Na salts, which contributed to anion-dominated SEI construction (Figure 31d). It was also demonstrated that the FDMA solvent and FEC additive controllably reacted with Na polysulfides to form a NaF- and Na<sub>3</sub>N-rich CEI, enabling a “quasi-solid-phase” Na–S conversion. As a consequence, the RT Na–S batteries delivered a high reversible capacity of 1114 mAh g<sup>-1</sup> (based on the mass of sulfur) along with an extended lifespan.<sup>686</sup>

**5.1.3. Fluorine-Containing Electrode Materials in K-Based Batteries.** Typically, the larger radius of K<sup>+</sup> (1.38 Å) than Li<sup>+</sup> (0.76 Å) and Na<sup>+</sup> (1.02 Å) causes sluggish intercalation kinetics, which further leads to low storage capacity, unsatisfactory rate capability, and poor cycle stability of PIBs. Thus, exploring appropriate host materials for high-performance PIBs is urgently needed.<sup>693</sup> In PIBs, polyanion compounds possessing 3D open-framework structures have been extensively explored as cathode materials due to the fast K<sup>+</sup> diffusion kinetics and high redox voltages, among which fluorophosphates and fluorosulfates have attracted great interest.<sup>694–700</sup> As early as 2012, a family of potassium fluorosulfates, KMSO<sub>4</sub>F (M = Fe, Co, and Ni), has been



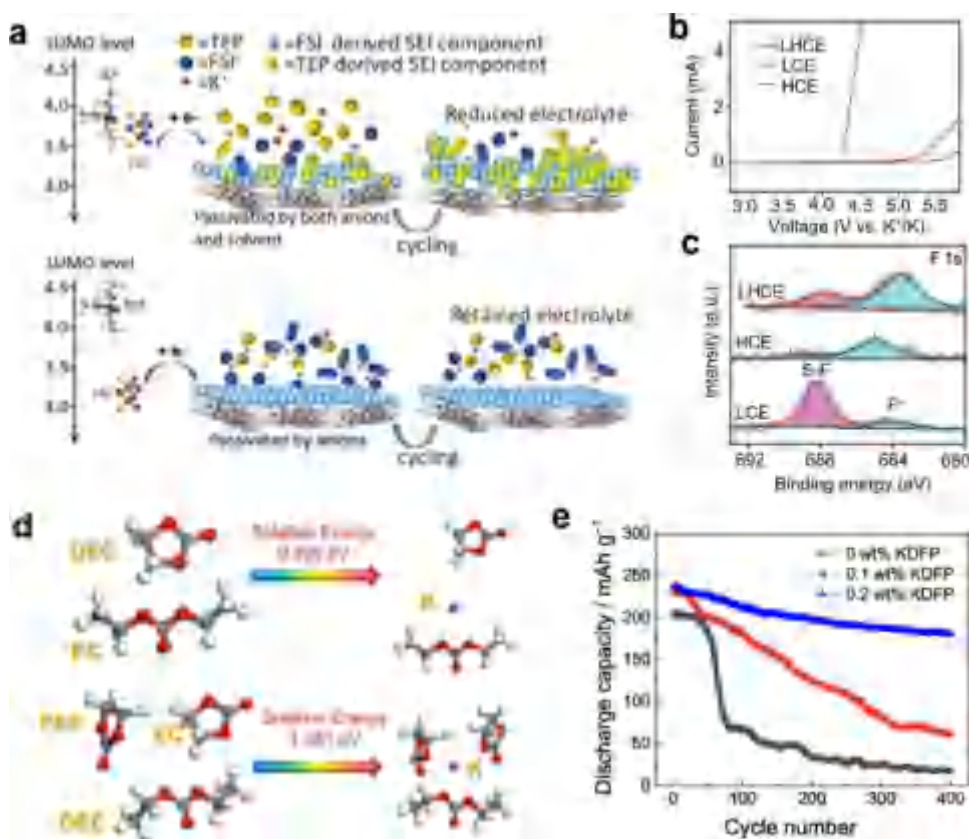
**Figure 32.** Effect of fluorine on improving the electrochemical performance of polyanion cathode or carbonaceous anode materials in PIBs. (a) Voltage curve of the Li||KFeSO<sub>4</sub>F cell starting with the charging process. Reproduced with permission from ref 701. Copyright 2012 American Chemical Society. (b) Voltage curve predicted for the extraction of K<sup>+</sup> from KFeSO<sub>4</sub>F cathode material. Reproduced with permission from ref 702. Copyright 2013 Royal Society of Chemistry. (c) Crystal structure of KVPO<sub>4</sub>F cathode material. (d) Charge/discharge curves of KVPO<sub>4</sub>F and KVPO<sub>4.36</sub>F<sub>0.64</sub> in the second cycle at a current rate of 5 mA g<sup>−1</sup>. Reproduced with permission from ref 699. Copyright 2018 Wiley-VCH. (e) The optimized mode after absorbing two, three, and four K atoms in the O/F dual-doped carbon (viewed from top and side). Reproduced with permission from ref 71. Copyright 2019 Wiley-VCH.

explored for the insertion/extraction of various alkali ions including Li<sup>+</sup>, Na<sup>+</sup>, or K<sup>+</sup>. KFeSO<sub>4</sub>F crystallizes in an orthorhombic unit cell (space group *Pna2*<sub>1</sub>), and its structure consists of chains of FeO<sub>4</sub>F<sub>2</sub> octahedra linked via F<sup>−</sup> ions. With the removal of K<sup>+</sup> from KFeSO<sub>4</sub>F (Figure 32a), no obvious structural change was observed for the K<sub>0.55</sub>MSO<sub>4</sub>F composition. Further removal of K<sup>+</sup> ( $x < 0.5$ ) leads to a new oxidized phase with a formula of “FeSO<sub>4</sub>F”. Notably, this new phase with large and empty channels displayed excellent versatility as reversible hosts for a variety of alkali guests.<sup>701</sup> Afterward, a mechanistic investigation for the K<sup>+</sup> removal from the KFeSO<sub>4</sub>F cathode was conducted. Based on the first-principles calculations, the mechanism that induced this phase transition upon K<sup>+</sup> extraction was studied at the atomic scale. It was unveiled that the crystal structure was stable for the phase transition from KFeSO<sub>4</sub>F to K<sub>0.5</sub>FeSO<sub>4</sub>F, where only neighboring Fe<sup>2+</sup>–Fe<sup>3+</sup> pairs were formed through selective oxidation. The continuous removal of K<sup>+</sup> ( $x < 0.5$ ) would cause Fe<sup>3+</sup>–Fe<sup>3+</sup> pairs with strong electrostatic repulsion, thus triggering a structure transition to a more ordered “FeSO<sub>4</sub>F” phase (enlarging the Fe<sup>3+</sup>–Fe<sup>3+</sup> distance). Apart from the structural stability, such strong electrostatic repulsion also played a critical role in the voltage curve of the cathode, with multiple voltage plateaus from  $x = 1$  to  $x = 0.5$  and just a single plateau when  $x < 0.5$  (Figure 32b).<sup>702</sup> Nevertheless, the electronic conductivities of these KMSO<sub>4</sub>F compounds were insufficient for achieving high electrochemical performance. To

tackle this issue, Chen et al. synthesized graphene-decorated KFeSO<sub>4</sub>F (KFSF@G) submicrometer particles.<sup>700</sup> The ball-milling treatment facilitated a tight wrap of graphene to the KFeSO<sub>4</sub>F particle for efficient electron and K<sup>+</sup> transport while largely reducing the particle size to increase reaction sites. The obtained KFSF@G not only displayed a reversible capacity of 111.5 mAh g<sup>−1</sup> with a high average operating voltage of 3.55 V but also exhibited excellent rate capability with a discharge capacity of 82.8 mAh g<sup>−1</sup> at 5 C (1 C = 128 mA h g<sup>−1</sup>). Unfortunately, all of these efforts have not achieved a satisfactory long-term lifespan of the KFeSO<sub>4</sub>F-based PIBs.

Compared with the above-mentioned fluorosulfates, V-based polyanion compounds with enhanced cycle stability have attracted great interest in recent years. In 2017, KVPO<sub>4</sub>F was investigated as a high-voltage cathode material for PIBs, displaying a reversible capacity of 92 mAh g<sup>−1</sup> and a high average working voltage above 4.0 V (vs K/K<sup>+</sup>) in 1 M KPF<sub>6</sub>–EC/PC electrolyte. Notably, the lattice volume of the cathode material shrank only 5.8% after charging to 5 V, which was promising for applying as high-voltage cathodes in PIBs.<sup>695</sup> In these fluorophosphates, F<sup>−</sup> could be substituted by some O<sup>2−</sup> (oxygenation), thus reducing the average working voltage and reversible capacity. To illustrate the effects of the fluorine, a stoichiometric KVPO<sub>4</sub>F synthesized via a two-step reaction was evaluated by Ceder et al.<sup>699</sup> Such KVPO<sub>4</sub>F cathode achieved a reversible capacity of ~105 mAh g<sup>−1</sup> along with a high average voltage of ~4.33 V (Figure 32c and 32d),





**Figure 33.** Fluorine-containing salts and electrolyte additives explored in PIBs. (a) Schematic illustration of the SEI constructed with 0.9 M KFSI/TEP and 2 M KFSI/TEP electrolytes. Reproduced with permission from ref 714. Copyright 2020 Wiley-VCH. (b) LSV measurements of low-concentration electrolyte (LCE), HCE, and LHCE. (c) XPS F 1s spectra of the NCP anode with different electrolytes. Reproduced with permission from ref 715. Copyright 2023 Wiley-VCH. (d) DFT calculations for the solvation energies estimated from the binding energy of the clusters. Reproduced with permission from ref 707. Copyright 2018 Elsevier. (e) Cycle stability of the graphite anode in 0.5 M KPF<sub>6</sub>-EC/DEC electrolyte containing 0, 0.1, and 0.2 wt % of KDFP at 1/3 C (1 C = 279 mA g<sup>-1</sup>). Reproduced with permission from ref 716. Copyright 2020 American Chemical Society.

corresponding to a promising energy density of  $\sim 454$  Wh kg<sup>-1</sup>. In addition, they revealed that intermediate phases at  $x = 0.75$ , 0.625, and 0.5 for the K<sub>x</sub>VPO<sub>4</sub>F cathode were formed upon cycling. The oxygenation of KVPO<sub>4</sub>F not only caused a disordered structure to suppress the K<sup>+</sup>/vacancy formation but also reduced the reversible K<sup>+</sup> storage capacity and the operating voltage. To improve the cycle stability of the KVPO<sub>4</sub>F cathode, Chen et al. prepared KVPO<sub>4</sub>F through flower-like carbon-coated VPO<sub>4</sub> and then developed these primary particles in carbon frameworks (KVPO<sub>4</sub>F/C). The carbon framework enhanced the electronic conductivity and acted as a reducing agent to control the F content in KVPO<sub>4</sub>F. It was elucidated that with a higher carbon content in the KVPO<sub>4</sub>F/C material, the oxidation of V and the desorption of F could be suppressed. The optimized KVPO<sub>4</sub>F/C manifested a reversible capacity of 103 mAh g<sup>-1</sup> at 20 mA g<sup>-1</sup> and a stable cycle life of 900 cycles at 1 A g<sup>-1</sup>. Such cathode also exhibited superior discharging capability with a reversible capacity of 87.6 mAh g<sup>-1</sup> at 5 A g<sup>-1</sup>. More promisingly, a full cell based on this KVPO<sub>4</sub>F/C cathode and a VPO<sub>4</sub> anode demonstrated a long lifespan of over 2000 cycles, an excellent capacity retention of 86.8%, and an average CE of 99.5% (at 1 A g<sup>-1</sup>).<sup>697</sup>

As regards the anode materials, since the first report on the successful electrochemical K<sup>+</sup> insertion into graphite by Ji et al. in 2015,<sup>703</sup> carbonaceous materials have become the focus for

PIB anodes because of their low cost, high electronic conductivity, and environmental friendliness. Unfortunately, these carbonaceous anodes such as graphite suffer from a low specific capacity with a theoretical capacity of only 279 mA h g<sup>-1</sup> with the formation of KC<sub>8</sub> after discharging along with poor cycle stability and a huge volume change (61%) upon potassiation. To enhance electrochemical properties of this anode material, heteroatom doping was adopted by Chen et al.<sup>71</sup> The F doping was reported to improve the surface disorder of the carbonaceous material, which could create large amounts of surface defects to facilitate K<sup>+</sup> adsorption. In addition, the O doping decreased the inert surface area and generated abundant active sites as well. The codoping of O/F into the porous carbon framework regulated the electronic structure of the carbon atoms and enhanced the adsorption of K<sup>+</sup>, as suggested by the structural integrity after absorbing a number of K atoms (Figure 32e). Consequently, the O/F-codoped anode material achieved a high reversible capacity of 481 mA h g<sup>-1</sup> at 0.05 A g<sup>-1</sup> and excellent cycle performance with 92% capacity retained over 2000 cycles at 1 A g<sup>-1</sup>. Even at a current density of 10 A g<sup>-1</sup>, an ultralong lifespan of 5000 cycles can be enabled with a retained capacity of 111 mAh g<sup>-1</sup>. In brief, structure modification, carbon coating, and heteroatom doping are effective strategies to enhance the overall electrochemical performance of polyanion (e.g., KVPO<sub>4</sub>F and KFeSO<sub>4</sub>F) cathode or carbonaceous anode materials.

### 5.1.4. Fluorinated Electrolytes in K-Based Batteries.

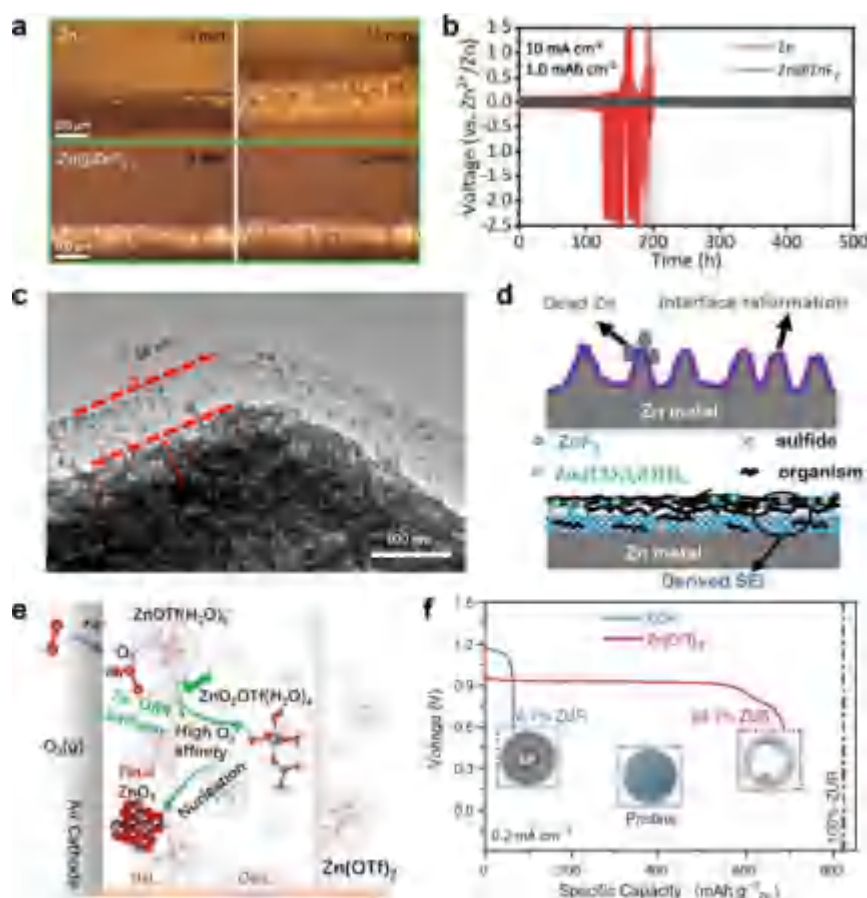
As within LIBs, electrolytes play a critical role in deciding the performance of K-based batteries.<sup>704</sup> With regard to the electrolyte salts, since the electron-withdrawing feature of F atoms favors high solubility in organic aprotic solvents, most K salts contain fluorinated anions.<sup>705</sup> Wu et al. investigated various electrolyte formulations based on KPF<sub>6</sub>, potassium bis(trifluoromethylsulfonyl)imide (KTFSI), and KFSI salts, demonstrating that only KFSI/DME electrolyte enabled a reversible/stable plating/stripping behavior for K metal.<sup>706</sup> This result was attributed to the cleavage of weak S–F bonds in FSI<sup>−</sup>, forming a stable KF-rich SEI layer. Besides chemical compositions, the choice of electrolyte salts also affects the structure, mechanical properties, and electrical properties of the SEI layer.<sup>707–711</sup> As revealed by Guo et al., a thinner SEI with higher viscoelasticity was formed with the KFSI-based electrolyte instead of the KPF<sub>6</sub>-based electrolyte, largely alleviating the stress induced by volume changes during plating/stripping of K metal.<sup>710</sup> Besides, compared with the KPF<sub>6</sub>-based electrolyte, the SEI constructed in KFSI-based electrolyte exhibited an improved thermal stability with more thermodynamic inorganic species, as evidenced by the decomposition reaction that occurred at ~117 °C.<sup>712</sup> Afterward, DFT and MD calculations were conducted to reveal the underlining mechanism for different salts. Both the KFSI and the KFSI–solvent complexes exhibited lower LUMO energy levels compared with the corresponding KPF<sub>6</sub> and KPF<sub>6</sub>–solvent complexes. The solvation energy of K<sup>+</sup> was higher in KFSI-based electrolyte than that in KPF<sub>6</sub>-based electrolyte. These findings suggested that the SEI layer constructed with KFSI electrolytes was salt anion dominated while the layer with KPF<sub>6</sub> was derived from solvent decomposition.<sup>713</sup>

Based on KFSI as the conducting salt and the flame-retardant TEP as the sole solvent, an intrinsically nonflammable electrolyte was demonstrated for K-based batteries.<sup>714</sup> Compared with the requirements of highly concentrated phosphate electrolytes in LIBs and SIBs, a rather dilute electrolyte with a concentration of 0.9 M was sufficient to run the K-based battery system. Further optimizing the concentration of the KFSI–TEP electrolyte to 2.0 M, a uniform and robust anion-derived SEI layer was constructed along with the synergistic merits of low cost, low viscosity, and high ionic conductivity of the optimized electrolyte (Figure 33a), significantly suppressing the solvent decomposition and allowing a high CE of 99.6% for K-metal plating/stripping without dendrites. This advanced electrolyte was superior to conventional carbonate electrolytes, offering a new avenue for designing nonflammable electrolytes with high safety.

Following the design of LHCEs in LIBs discussed in section 3.2, a low-polarity diluent that does not dissolve K salts was introduced to enhance the performance of LHCEs in K-based batteries. The first attempt adopted the highly fluorinated HFE as a diluent based on the concentrated KFSI–DME electrolyte, forming a LHCE with a molar ratio of 1:1.90:0.95 for the KFSI:DME:HFE components. Such a LHCE displayed higher antioxidation stability, lower flammability, and higher ionic conductivity than the concentrated KFSI–DME electrolyte. In addition, with a durable KF-rich SEI layer constructed on the surface of graphite, the graphite anode with a high mass loading of ~8 mg cm<sup>−2</sup> survived for more than 300 cycles with a reversible capacity of 200 mA h g<sup>−1</sup> along with a high CE of 99.5%.<sup>717</sup> This report employed LHCE to achieve highly reversible graphite anodes. However, the influence of “inert”

diluent molecules on the K<sup>+</sup> solvation structure and the local coordination environment is still ambiguous. Later, a fire-retardant electrolyte was developed by blending concentrated KFSI–TEP electrolyte with TTE as an “inert” diluent. Results revealed that such LHCE retained a relatively weakened anion-coordinated solvation environment and the TTE diluent was nonsolvated. Combining the synergistic effects of the KFI<sup>−</sup> anions and the highly fluorinated diluent, a SEI film containing well-balanced inorganic/organic species was tailored in situ on the graphite anode, protecting the graphite anode from continuous side reactions and meanwhile facilitating the K-ion transport. Consequently, the graphite anode retained 92.4% capacity retention after 1400 cycles at 0.1 A g<sup>−1</sup>.<sup>155</sup> Apart from the effects on graphite anodes, LHCEs were also designed to improve the compatibility between electrolytes and carbon-based anode materials in PIBs. Very recently, a LHCE was designed by introducing the nonsolvent TTE into the concentrated KFSI–DME electrolyte. This LHCE broke the interconnected 3D K<sup>+</sup>-solvated shell while maintaining the original individual K<sup>+</sup>-solvated structure, thus improving the ionic conductivity and ensuring sufficient oxidation resistance of the electrolyte (Figure 33b). More promisingly, a uniform and durable KF-rich SEI layer was formed on the carbonous (nitrogen-doped carbon spheres, NCP) anode (Figure 33c), delivering a high reversible capacity of 232.5 mA h g<sup>−1</sup> along with 78.7% capacity retention over 200 cycles.<sup>715</sup> These reports discovered the significance of “inert” diluents combined with salts and solvents for the design of LHCE systems for enhanced K-based batteries.

Besides the fluorine-containing salts, appropriate electrolyte additives can also stabilize the electrode/electrolyte interphase and further enhance the battery performance, which has been widely applied in LIBs and SIBs. Among them, as a widely applied film-forming additive, FEC has demonstrated excellent capability to solve the interfacial incompatibility of electrolytes toward reactive metal anodes. Owing to the antioxidative ability of the F-containing group, FEC additive was adopted to reduce side reactions of the Prussian blue analog (PBA) cathodes in PIBs, thus increasing the CE and cycle stability of the K||PBA half cell.<sup>718,719</sup> However, the FEC additive sometimes worsened the electrochemical performance of full cells, especially when intercalation-based or alloy-based anode materials were used. This may be related to the excessive reduction of FEC that induces undesirable SEI formation during repeated cycling.<sup>720</sup> Through DFT calculation, Guo et al. verified that the electrolyte with FEC increased the solvation energy from 0.305 to 1.281 eV (Figure 33d), pointing out a larger resistance for the K<sup>+</sup> diffusion and desolvation in the FEC-containing electrolyte, thus leading to poor performance.<sup>707</sup> Similarly, the addition of FEC exerted a negative influence on the electrochemical performance of the Sn<sub>4</sub>P<sub>3</sub> anode with fast capacity decay at high current rates. The FEC additive generated more components with carbonyl groups and K–F bonds in an unstable SEI layer that failed to suppress continuous side reactions, resulting in the quick resistance increase and rapid capacity degradation.<sup>708</sup> Later, such excessive SEI layer induced by FEC additive was further observed by Mai et al., displaying a lower initial CE of 58%. In addition, FEC stimulated a large amount of electrolyte decomposition, which inevitably led to an increase in cell resistance and a decrease in capacity.<sup>709</sup> Contrary to the unfavorable role of FEC additive on these anodes, by employing potassium difluorophosphate (KDFP) as additive



**Figure 34.** Fluorine chemistry in aqueous multivalent metal-based batteries. (a) Time–voltage curves for Zn||Zn and Zn@ZnF<sub>2</sub>||Zn@ZnF<sub>2</sub> symmetrical cells at 10 mA cm<sup>−1</sup> with a plating/stripping capacity of 1 mAh cm<sup>−2</sup>. (b) In situ optical observation results of the Zn deposition morphologies on the Zn foil and Zn@ZnF<sub>2</sub> electrode at a current density of 10 mA cm<sup>−2</sup> for 20 min. Reproduced with permission from ref 722. Copyright 2021 Wiley-VCH. (c) TEM images of the cycled Zn anode surface in 4 m Zn(OTf)<sub>2</sub> + 0.5 m Me<sub>3</sub>EtNOTF. Reproduced with permission from ref 723. Copyright 2021 Springer Nature. (d) Illustration of the surface evolution mechanism. (Upper panel) Zn dendrite growth in aqueous electrolytes. The water-passivation-induced porous ZnO layer (purple) constantly breaks and reforms, leading to nonuniform Zn electrodeposition, dendrite formation, and dead Zn during Zn plating/stripping. (Lower panel) Formation mechanism of ZnF<sub>2</sub>–Zn<sub>5</sub>(CO<sub>3</sub>)<sub>2</sub>(OH)<sub>6</sub>–organic SEI. The presence of NO<sub>3</sub><sup>−</sup> promotes the formation of an electrically and ionically insulating Zn<sub>5</sub>(OH)<sub>8</sub>(NO<sub>3</sub>)<sub>2</sub>·2H<sub>2</sub>O layer (red), which subsequently transforms into an electrically insulating but ionically conductive SEI in which the ZnF<sub>2</sub>–Zn<sub>5</sub>(CO<sub>3</sub>)<sub>2</sub>(OH)<sub>6</sub> inner part is coated by the organic outer part. Reproduced with permission from ref 724. Copyright 2021 Wiley-VCH. (e) Galvanostatic discharge profiles of Zn–air cells in KOH (blue) and Zn(OTf)<sub>2</sub> (red) electrolytes at 0.2 mA cm<sup>−2</sup> (cutoff voltage: 0.6 V). The corresponding ZURs are indexed for comparison. (Insets) Photographs of the pristine Zn anode (middle), the Zn anode after discharge in KOH (left), and Zn(OTf)<sub>2</sub> (right) electrolytes. (f) Schematic illustration of reaction processes in the inner Helmholtz layer (IHL) and outer Helmholtz layer (OHL) at the surface of the air cathode in Zn(OTf)<sub>2</sub> and ZnSO<sub>4</sub> electrolytes, respectively. Reproduced with permission from ref 725. Copyright 2021 The American Association for the Advancement of Science.

to the KPF<sub>6</sub>–EC/DEC electrolyte, Matsumoto et al. successfully constructed a stable K<sup>+</sup> conducting SEI (enriched in KF and PO<sub>x</sub> species) on the graphite anode, which promoted a highly reversible capacity of 274 mAh g<sup>−1</sup> with the formation of a suitable potassium–graphite intercalation compound (K–GIC, KC<sub>8</sub>).<sup>716</sup> The KDFP electrolyte enabled a fast depotassiation/potassiation kinetic process, an increased cyclability with 76.8% capacity retention, and a high average CE of ~99.9% over 400 cycles (Figure 33e). To briefly summarize, compared with the favorable effects of FEC additive on forming stable and robust SEI layers in LIBs and SIBs, the role of FEC in PIBs remains unclear and needs further investigation. Other effective functional F-containing additives should be explored to avoid undesired reactions between the anode materials and the electrolytes. It is noteworthy that the full cell performance, including both the

cathode and the anode, should be implemented to reveal the real functions of these additives.

Overall, fluorinated electrode materials are of great interest to SIBs, where F<sup>−</sup> anions (compared with large polyanions such as PO<sub>4</sub><sup>3−</sup>, SO<sub>4</sub><sup>2−</sup>) can improve the specific capacity and fluorinated compounds are relatively stable against oxidation. The research is currently focusing on 3D fluorinated phases such as cubic perovskite fluorides due to their high-power capability and 3D network stability, but further investigation is needed to regulate polymorphism and phase transition during Na<sup>+</sup> storage. Furthermore, establishing structure–performance relationships of these materials can reduce the activation energy barriers and lower the band-gap energy for efficient Na<sup>+</sup> diffusion. For PIBs, though 3D open-framework polyanion compounds (e.g., potassium fluorophosphates and fluorosulfates) can enable fast K<sup>+</sup> diffusion and high redox potential, the low electronic conductivity of these materials requires surface



modifications. Meanwhile, V-based fluorosulfates offer high working voltages when used as cathodes, but the fluorine to oxygen ratio should be controlled to prevent disordered fluorosulfate structures. Analogous to Li-based batteries, fluorine substitution in cosolvents/solvents and additives can address critical issues in SIBs and PIBs, including interphasial instability, flammability, and capacity decay under fast charging or wide temperature ranges. Notably, strategies from fluorinated electrolytes in Li-based electrolytes cannot be directly applied to SIBs and PIBs, for instance, FEC exhibits a negative influence on certain anodes by stimulating electrolyte decomposition and forming unstable interphases. The current understanding of fluorinated electrolytes and corresponding interphases in SIBs and PIBs is still in the primary stage, and efforts should concentrate on these aspects.

## 5.2. Multivalent Metal-Based Batteries

### 5.2.1. Aqueous Multivalent Metal-Based Batteries.

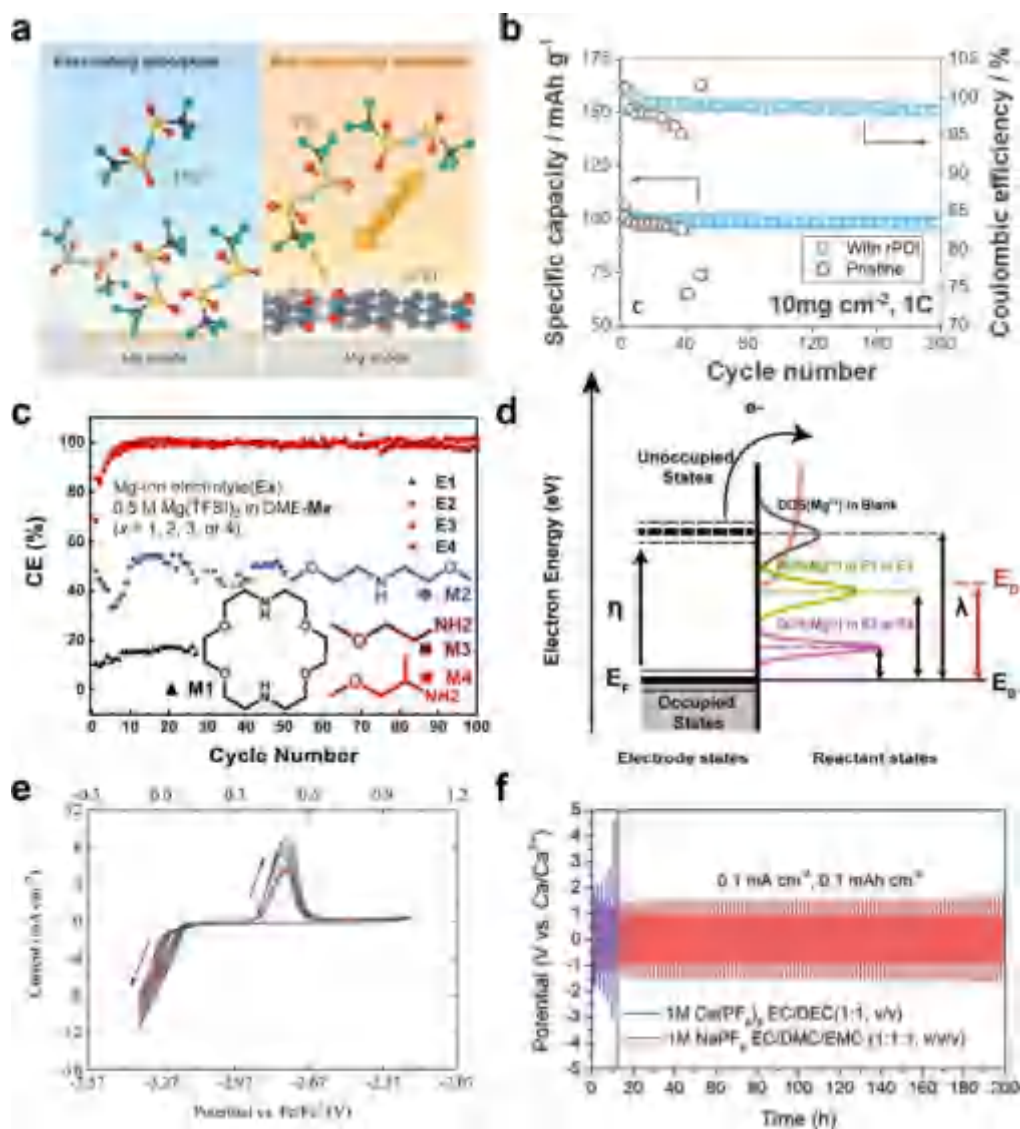
Aqueous multivalent metal-based batteries, such as the aqueous ZIBs, have become a research hotspot owing to the merits of high safety, high specific capacity, low cost, and abundant distribution in the Earth's crust. Zn metal is considered an ideal anode due to its high theoretical specific capacity ( $820 \text{ mAh g}^{-1}$ ), low electrode potential ( $-0.76 \text{ V}$  vs standard hydrogen electrode), abundant distribution, and low toxicity. However, when applied in aqueous electrolytes, Zn metal anodes still face serious issues such as corrosion reactions, hydrogen evolution, and uncontrolled dendrite formation.<sup>721</sup> These problems lead to low CE, poor cycle life, continuous electrolyte consumption, and even internal short circuits.

Fluoride plays an important role in constructing highly reversible Zn metal anodes. In 2021, Li et al. devised a novel approach to create durable Zn metal anodes protected by a 3D  $\text{ZnF}_2$  matrix, effectively preventing dendrite formation and extending the lifespan.<sup>722</sup> In their study, a 3D interconnected  $\text{ZnF}_2$  matrix was engineered onto the surface of the Zn foil, denoted as  $\text{Zn@ZnF}_2$ , using a rapid and straightforward anodic growth technique. This  $\text{Zn@ZnF}_2$  electrode served as a versatile protective layer, facilitating the redistribution of  $\text{Zn}^{2+}$  ions and significantly reducing the desolvation active energy, resulting in stable and efficient Zn deposition. The findings demonstrated that the  $\text{Zn@ZnF}_2$  electrode effectively suppressed dendrite growth, mitigated hydrogen evolution reactions, and exhibited outstanding plating/stripping of  $\text{Zn}^{2+}$ /Zn. In addition, the authors used in situ optical microscopy to capture the dynamic Zn plating process within 20 min, revealing the growth of Zn dendrites and large hydrogen bubbles on the pristine Zn electrode. In contrast, the smooth Zn deposition was observed on the surface of the  $\text{Zn@ZnF}_2$  electrode without dendrites or gas bubbles (Figure 34a). Consequently, the  $\text{Zn@ZnF}_2$  electrode displayed an impressive cycle life, exceeding 800 h at a current density of  $1 \text{ mA cm}^{-2}$  in a symmetrical cell test (Figure 34b). This excellent performance was also confirmed in  $\text{Zn@ZnF}_2\|\text{MnO}_2$  and  $\text{Zn@ZnF}_2\|\text{V}_2\text{O}_5$  full cells. Notably, a hybrid Zn-ion capacitor employing the  $\text{Zn@ZnF}_2\|\text{active carbon (AC)}$  configuration demonstrated exceptional durability, maintaining a high capacity retention of 92.8% over 5000 cycles at an ultrahigh current density of approximately  $60 \text{ mA cm}^{-2}$ .

Fluorine chemistry is widely used in aqueous electrolytes and interface control. Wang et al. reported the development of an aqueous Zn metal battery.<sup>723</sup> They utilized a dilute and

acidic aqueous electrolyte containing 4 m zinc trifluoromethanesulfonate ( $\text{Zn}(\text{OTf})_2$ ) and an alkylammonium salt (trimethylethylammonium trifluoromethanesulfonate,  $\text{Me}_3\text{EtNOTf}$ ) as the additive to facilitate the creation of a robust,  $\text{Zn}^{2+}$  conducting, and waterproof SEI. TEM analysis revealed the presence of a 64 nm thick  $\text{ZnF}_2$ -rich interphase on the deposited Zn surface when  $\text{Me}_3\text{EtNOTf}$  was introduced (Figure 34c). This SEI acted as an electron barrier, preventing the reduction of water while allowing the migration of  $\text{Zn}^{2+}$ . The presence of this SEI led to outstanding performance, including dendrite-free Zn plating and stripping, a remarkable 99.9% CE over 1000 cycles in a  $\text{TillZn}$  asymmetric cell, stable cycling behavior for 6000 cycles (equivalent to 6000 h) in a  $\text{Zn}\|\text{Zn}$  symmetric cell, and impressive energy densities in full cells with limited Zn source (e.g.,  $136 \text{ Wh kg}^{-1}$  in a  $\text{Zn}\|\text{VOPO}_4$  full cell with 88.7% capacity retention over 6000 cycles;  $218 \text{ Wh kg}^{-1}$  in a  $\text{Zn}\|\text{MnO}_2$  full cell with 88.5% capacity retention over 1000 cycles). Furthermore, the electrolyte is conducive to SEI formation, allowing the reversible operation of an anode-free pouch cell. The  $\text{Till Zn}_x\text{VOPO}_4$  full cell can be cycled at 100% depth of discharge for 100 cycles, enabling aqueous Zn-based batteries as practical and viable energy storage systems for various applications. Wang et al. also reported the development of a Zn-ion conductive, water-resistant, and  $\text{ZnF}_2$ -rich SEI on the Zn anode.<sup>724</sup> A designed low-concentration aqueous electrolyte composed of fluorine-containing  $\text{Zn}(\text{OTf})_2$  and  $\text{Zn}(\text{NO}_3)_2$  was developed. This electrolyte facilitated the in situ formation of a robust SEI with an inorganic inner layer made of  $\text{ZnF}_2$  and  $\text{Zn}_5(\text{CO}_3)_2(\text{OH})_6$  to enhance Zn-ion diffusion, and an organic outer layer acted as a barrier against water infiltration. Their research revealed that the initial layer formed on the Zn anode surface was an insulating  $\text{Zn}_5(\text{OH})_8(\text{NO}_3)_2 \cdot 2\text{H}_2\text{O}$ , resulting from a self-terminated chemical reaction involving  $\text{NO}_3^-$ ,  $\text{Zn}^{2+}$ , and  $\text{OH}^-$  generated through the hydrogen evolution reaction (HER). Subsequently, this inorganic layer transformed into Zn-ion conducting  $\text{Zn}_5(\text{CO}_3)_2(\text{OH})_6$ , promoting the formation of  $\text{ZnF}_2$  as the inner layer (Figure 34d). The organic-dominated outer layer was established through the reduction of OTf. This in situ-formed SEI exhibited remarkable performance, achieving a high CE of 99.8% over 200 h in  $\text{TillZn}$  half cells and maintaining a high energy density of  $168 \text{ Wh kg}^{-1}$  in  $\text{Zn}\|\text{MnO}_2$  full cells with 96.5% capacity retention after 700 cycles, even with a N/P ratio of 2:1.

Rechargeable Zn–air batteries hold the promise of delivering both high energy density and safety. However, they encounter huge challenges due to the sluggish 4-electron ( $\text{e}^-$ )/oxygen ( $\text{O}_2$ ) reaction that relies on water participation. The electrochemical reversibility stems from unwanted side reactions driven by the harsh electrolytes and atmospheric carbon dioxide. In 2021, Winter et al. reported a breakthrough result in the form of Zn– $\text{O}_2$ /zinc peroxide ( $\text{ZnO}_2$ ) chemistry, which was operated via a  $2\text{-e}^-/\text{O}_2$  reaction in nonalkaline aqueous electrolytes.<sup>725</sup> The new reaction mechanism facilitated highly reversible redox reactions for Zn–air batteries. The success of this  $\text{ZnO}_2$ -based chemistry can be attributed to the formation of a water-scarce and  $\text{Zn}^{2+}$ -rich inner Helmholtz layer (IHZ) on the air cathode, induced by the hydrophobic trifluoromethanesulfonate anions (Figure 34e). In a nonalkaline electrolyte containing  $1 \text{ mol kg}^{-1}$   $\text{Zn}(\text{OTf})_2$ , the Zn–air battery exhibited a well-defined discharge plateau at approximately 1.0 V, boasting an areal capacity of  $52 \text{ mAh cm}^{-2}$ , corresponding to a specific capacity



**Figure 35.** Fluorine chemistry in nonaqueous multivalent metal-based batteries. (a) Schematic illustration of passivating adsorption and nonpassivating adsorption. (Left panel) Passivating anions (TFSI<sup>-</sup>) adsorb on the Mg anode and form the passivation layer. (Right panel) Nonpassivating anions (rPDI) with higher adsorption energy repel TFSI<sup>-</sup> away to prevent Mg anode passivation. (b) Cycling stability of Mg–PDI full cells with pristine (gray) and rPDI (blue) electrolyte at 15 °C under 1 mg cm<sup>-2</sup> (1 C = 128 mA g<sup>-1</sup>). Reproduced with permission from ref 729. Copyright 2021 American Chemical Society. (c) CEs for Mg plating and stripping in Ex in Mg||SS cells cycled at 0.1 mA cm<sup>-2</sup>. Mg-ion electrolyte (Ex): 0.5 M Mg(TFSI)<sub>2</sub>–DME/Mx (x = 1, 2, 3, or 4). (d) Marcus–Gerischer diagram of electron transfer at the metal electrode/electrolyte interphase.  $E_F$  refers to the Fermi level of the metal electrode, and  $E_0$  refers to the energy level of the electrolyte and electrode at equilibrium. Red, green, and black Gaussians represent the DOS of Mg<sup>2+</sup> in the electrolyte. The orange curve represents the DOS of other electrolyte components, and  $E_D$  refers to the onset potential of the electrolyte decomposition. Reproduced with permission from ref 730. Copyright 2021 The American Association for the Advancement of Science. (e) CVs of Ca plating/stripping in the electrolyte containing Fc as the internal reference with a three-electrode configuration using Pt, Ag, and Ca as the working electrode, reference electrode, and counter electrode, respectively, at a scan rate of 80 mV s<sup>-1</sup>. Reproduced with permission from ref 731. Copyright 2019 Royal Society of Chemistry. (f) Cycling stability of voltage–time curves with a capacity of ~0.1 mAh cm<sup>-2</sup> at 0.1 mA cm<sup>-2</sup> of Ca||Ca symmetrical batteries. Reproduced with permission from ref 732. Copyright 2020 Wiley-VCH.

of 684 mAh g<sup>-1</sup> (based on the weight of the Zn anode). Additionally, as shown in Figure 34f, it achieved a remarkable Zn utilization ratio (ZUR) of 83.1%. In contrast, the Zn–air battery with an alkaline electrolyte composed of 6 mol kg<sup>-1</sup> KOH only achieved a ZUR of 8.1%. The photographic evidence of pristine and cycled Zn anodes immersed in different electrolytes confirmed the superior ZUR in the Zn(OTf)<sub>2</sub> electrolyte, where most of the Zn foil dissolves. As a result, the nonalkaline Zn–air battery not only maintained stable performance in ambient air but also demonstrated

significantly improved reversibility compared to its alkaline counterpart. Similar fluorine chemistry-involved electrolyte engineering strategies can be promisingly extended to other aqueous multivalent-ion systems (e.g., Mg-ion, Ca-ion, and Al-ion batteries).

Moreover, F-containing materials have also been applied as cathodes in aqueous multivalent-ion batteries. In 2021, Gregorio et al. developed a trigonal Na<sub>3</sub>V(PO<sub>4</sub>)<sub>2</sub>F<sub>2</sub> as the cathode for Mg-ion batteries.<sup>726</sup> Beneficial from the multi-electron transfer redox couples of V<sup>4+</sup>/V<sup>3+</sup> and V<sup>5+</sup>/V<sup>4+</sup>, the

Mg|0.5 M magnesium bis(trifluoromethanesulfonyl)imide ( $\text{Mg}(\text{TFSI})_2$ )–DME + 0.4 M  $\text{H}_2\text{O}|\text{Na}_5\text{V}(\text{PO}_4)_2\text{F}_2$  cell delivered a reversible specific capacity of 136 mA h  $\text{g}^{-1}$ , achieving a high energy density of 190 W h  $\text{kg}^{-1}$  with an average discharge voltage of 1.4 V. It should be noted that the regulation of the  $\text{F}^-/\text{O}^{2-}$  ratio in sodium–vanadium fluorophosphate directly affected the content of  $\text{V}^{3+}/\text{V}^{4+}$  and changed the specific capacity of the cathode materials.

**5.2.2. Nonaqueous Multivalent Metal-Based Batteries.** F-related chemistry also plays an important role in the development of nonaqueous multivalent metal-ion batteries (e.g., Mg-ion batteries, Ca-ion batteries, and Al-ion batteries) as promising energy storage systems owing to the high energy densities and low cost. The multielectron redox capability contributes to the high energy density, and the abundant distribution of these multivalent metal ions in the Earth's crust ensures the low manufacturing costs. However, the larger ionic radii and greater charge density of multivalent metal ions bring significant challenges associated with slow ion transport, large polarization, and low reversibility, making them less competitive than Li-based batteries in the race toward ever-rising energy density targets.<sup>727</sup>

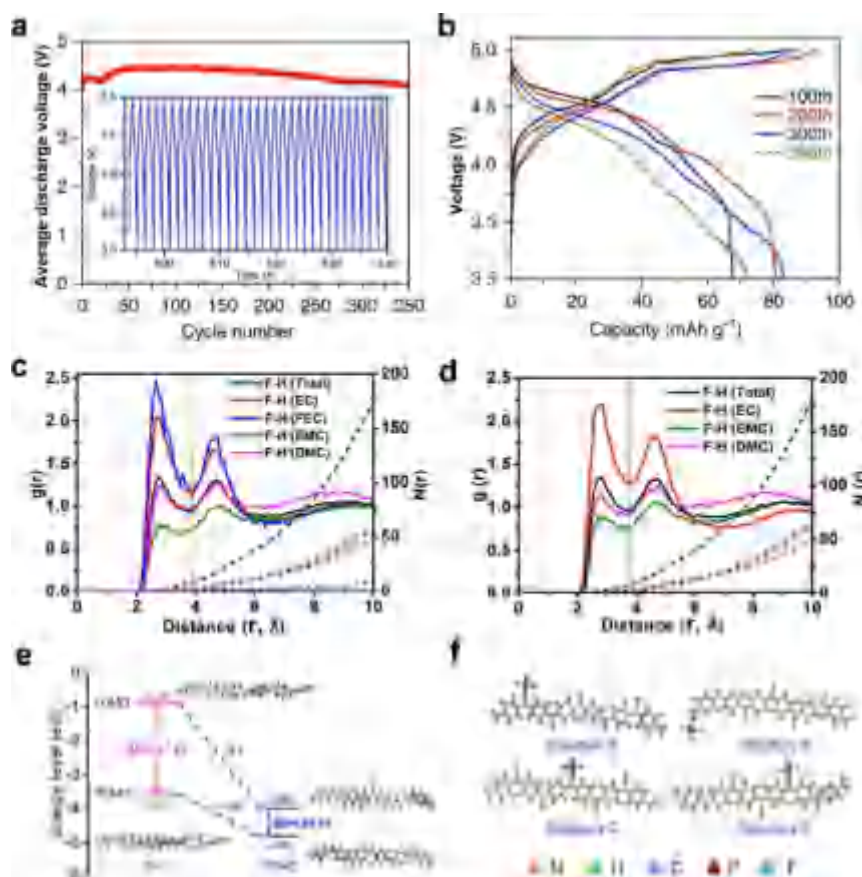
A strategy aiming at balancing the protection and passivation effect of the F-containing layer on the anode surface has been widely applied to realize high-performance multivalent metal-ion batteries. For instance, Mg-based batteries often face several challenges, such as low power density and limited cycle life, primarily due to the issue of severe passivation of the Mg anode. Although using nucleophilic electrolytes can effectively stabilize the Mg anode, their high chemical reactivity prevents the use of organic and conversion cathodes. To solve this issue, Lu et al. introduced a nonpassivating anion additive known as reduced perylene diimide-ethylenediamine (rPDI). This additive has been proven effective in facilitating rapid and reversible Mg deposition/dissolution in a straightforward  $\text{Mg}(\text{TFSI})_2$ – $\text{MgCl}_2$ -based electrolyte with only a minimal addition of 0.2 mM rPDI. The ability of rPDI to selectively adhere to a Mg anode is the key factor for the enhanced performance, thus repelling  $\text{TFSI}^-$  anions from the surface of the Mg anode. This prevented  $\text{TFSI}^-$  decomposition and subsequent Mg passivation (Figure 35a). Leveraging rPDI's millimolar-level solubility in the electrolyte, it was employed as an electrolyte additive in both symmetric cells and full cells. With the addition of only 0.2 mM rPDI as the electrolyte additive, Mg symmetric cells with an electrolyte of 0.25 M  $\text{Mg}(\text{TFSI})_2$ – $2\text{MgCl}_2$ /DME demonstrated impressive results, achieving highly reversible cycling performance for 300 h at 1.0 mA  $\text{cm}^{-2}$ . More importantly, the protective effect of rPDI persisted even when the electrolyte was exposed to air, which remarkably extended the cycling stability. Furthermore, the researchers showcased the performance of a Mg–organic full cell, demonstrating fast and reversible  $\text{Mg}^{2+}$  storage at 50 C (6.4 A  $\text{g}^{-1}$ ). This configuration achieved a superior specific power density of 8.78 kW  $\text{kg}^{-1}$  and a stable cycle life exceeding 1000 cycles at 15 C. Exceptional areal power density (2.0 mW  $\text{cm}^{-2}$ ) and energy density (1.6 mWh  $\text{cm}^{-2}$ ) were attained at 1 C, along with the highest reported areal capacity of 1.0 mAh  $\text{cm}^{-2}$  and a stable cycle life extending beyond 200 cycles (Figure 35b). In another case, Zhao et al. effectively synthesized magnesium tetrakis(hexafluoroisopropoxy)-borate, denoted as  $\text{Mg}[\text{B}(\text{hfp})_4]_2$ , showcasing its exceptional characteristics as a viable and efficient electrolyte for prospective high-energy Mg-based batteries.<sup>728</sup>

Similar to Mg-based batteries, rechargeable Ca-based batteries show great promise as alternatives to LIBs due to the abundant resource of Ca element in the Earth's crust and the high theoretical specific capacity. However, these batteries face significant challenges related to slow reaction kinetics and unwanted side reactions. Wang et al. developed a significant breakthrough by demonstrating that multidentate methoxyethyl-amine chelates  $[-(\text{CH}_2\text{OCH}_2\text{CH}_2\text{N})_n-]$ , located in the first solvation sheath of  $\text{Mg}^{2+}$  and  $\text{Ca}^{2+}$ , facilitate both highly reversible reactions on Mg and Ca anodes as well as high-voltage layered oxide cathodes.<sup>730</sup> Specifically, 0.5 M  $\text{Mg}(\text{TFSI})_2$ –DME was selected as the baseline electrolyte. Four types of multidentate chelates ( $\text{Mx}$ ,  $x = 1, 2, 3$ , or 4) were added to the baseline electrolyte to form the electrolytes  $\text{Ex}$  ( $x = 1, 2, 3$ , or 4). The overpotentials during the Mg plating and stripping processes were significantly reduced from 2.0 V (blank) to below 0.1 V ( $\text{E}_4$ ) with a high CE of 99.5% (Figure 35c). Solvation sheath analysis demonstrated that the solvation sheath became less compact and more polarizable, leading to a decrease in solvation sheath reorganization energy ( $\lambda$ ) for electron transfer (Figure 35d). This, in turn, lowered the overpotential by preventing electrolyte decomposition and facilitating stable Mg and Ca plating and stripping. Calcium tetrakis(hexafluoroisopropoxy)borate, known as  $\text{Ca}[\text{B}(\text{hfp})_4]_2$ , was developed as a prospective electrolyte for room-temperature rechargeable Ca batteries, which demonstrated room-temperature reversible Ca plating and stripping (Figure 35e), exceptional oxidative stability up to 4.5 V, and a high ionic conductivity exceeding 8 mS  $\text{cm}^{-1}$ .<sup>731</sup>

Wang et al. showcased that a hybrid Na/Ca-based SEI surpassed a purely Ca-based SEI in achieving stable Ca plating and stripping processes.<sup>732</sup> In the case of fluorine-based electrolytes like calcium hexafluorophosphate ( $\text{Ca}(\text{PF}_6)_2$ ) and calcium tetrafluoroborate ( $\text{Ca}(\text{BF}_4)_2$ ) ethers and esters solutions, Ca metal underwent passivation with a SEI primarily composed of  $\text{CaF}_2$  (pure Ca SEI). This  $\text{CaF}_2$  layer served as both an ionic and an electronic insulating barrier. Conversely, when using  $\text{NaPF}_6$  in an electrolyte composed of EC/DMC/EMC in a 1:1:1 ratio by volume, an in situ evolution of a hybrid Na/Ca-based SEI occurred. These hybrid SEIs exhibited excellent ion conductivity for both  $\text{Ca}^{2+}$  and  $\text{Na}^+$  ions, simultaneously preventing anions from deeply penetrating and averting uncontrolled decomposition of the electrolyte upon the freshly deposited Ca. Consequently, long-term Ca plating and stripping (lasting over 1000 h with minimal polarization shift) can be reliably achieved by utilizing Ca metal itself as the current collector (Figure 35f). Furthermore, Ca metal safeguarded by the hybrid Na/Ca-based SEIs also maintains impressive high-voltage stability, extending up to 4.5 V when used in full cells.

Aluminum, the third most abundant element in the Earth's crust with an oxidation state of 3+, endows the construction of cost-effective and high energy density batteries, boosting the high specific capacity in the form of Al metal anodes and enhanced safety due to its air-stable passive surface layer compared to Li metal. In 2017, Masashi et al. reported a fluoropolymer-supported  $\text{Al}^{3+}$  conducting solid-state electrolyte.<sup>733</sup> By tuning the ratio of PVDF and  $\text{AlCl}_3$  (F/Al ratio), the optimized  $\text{Al}^{3+}$  conductivity at room temperature reached  $4.4 \times 10^{-4}$  S  $\text{cm}^{-1}$  with a F/Al ratio of 8. This  $\text{Al}^{3+}$  conducting solid-state electrolyte also showed a stable electrochemical window of 0–2.4 V vs  $\text{Al}^{3+}/\text{Al}$ , fulfilling the redox potential of the reported cathode materials of Al-ion batteries. This





**Figure 36.** Fluorine-containing electrolytes or electrodes for high-performance DIBs. (a) Average discharge voltage and (b) corresponding charge-discharge profiles of the Callgraphite DIB at a current density of 100 mA g<sup>-1</sup>. (Inset of a) Enlarged curves for the final 30 cycles. Reproduced with permission from ref 739. Copyright 2018 Springer Nature. MD simulation for the RDFs  $g(r)$  (solid lines) and coordination number  $N(r)$  (dashed lines) of F-H interactions in 1.0 M NaPF<sub>6</sub>-EC/DMC/EMC (1:1:1 by volume) electrolytes (c) with 10 wt % FEC and (d) without FEC additive. Reproduced with permission from ref 740. Copyright 2021 American Chemical Society. (e) HOMO-LUMO energies and energy gaps of PHC and FPHC molecules. (f) Four optimized models of PF<sub>6</sub>-FPHC with PF<sub>6</sub><sup>-</sup> at the near end group, PF<sub>6</sub><sup>-</sup> at the end group, PF<sub>6</sub><sup>-</sup> at the middle group, and PF<sub>6</sub><sup>-</sup> at the near middle group. Reproduced with permission from ref 741. Copyright 2022 Wiley-VCH.

fluoropolymer-based solid-state electrolyte is promising to eliminate the safety issues such as the leakage of highly corrosive liquid electrolytes in conventional aluminum-ion batteries.

The cathode materials of nonaqueous multivalent metal-based batteries also benefit from fluorine chemistry. In 2021, Xu and colleagues applied a polyanion fluoride (Na<sub>1.5</sub>VPO<sub>4.8</sub>F<sub>0.7</sub>, NVPF) as the cathode material for a nonaqueous Ca-ion battery and achieved a high reversible performance of over 500 cycles with a low capacity fading of 0.02% per cycle.<sup>734</sup> A variety of characterization methods revealed that the volume change relating to the insertion/extraction of Ca<sup>2+</sup>, the diffusion resistances, and the activation of large Ca<sup>2+</sup>-ion barriers were successfully suppressed owing to the rigid open framework of VPO<sub>4.8</sub>F<sub>0.7</sub>.

In general, for aqueous multivalent metal-based systems (e.g., ZIBs), the strategy of constructing fluoride-rich anode electrolyte interphases can effectively suppress the anode dendrite growth and electrolyte decomposition. Moreover, the sluggish plating kinetics of the anode in nonaqueous multivalent metal-based systems (e.g., Mg-ion and Ca-ion batteries) can be improved by solvation structure modification via the introduction of fluorinated salts, solvents, and additives. All of these fluorine chemistry-involving strategies are

accelerating the real-world application of multivalent metal-based batteries.

### 5.3. Dual-Ion Batteries and Beyond

In DIBs, anion insertion is considered to be the most important reaction on the cathode side, whereas various inserted anions with F-containing groups were intensively investigated, such as PF<sub>6</sub><sup>-</sup>,<sup>78–81</sup> TFSI<sup>-</sup>,<sup>82,735</sup> FSI<sup>-</sup>,<sup>83–86</sup> FTFSI<sup>-</sup>,<sup>87,88</sup> BF<sub>4</sub><sup>-</sup>,<sup>736</sup> DFOB<sup>-</sup>,<sup>91</sup> CF<sub>3</sub>SO<sub>3</sub><sup>-</sup>,<sup>92</sup> AlF<sub>4</sub><sup>-</sup>,<sup>93</sup> tris-(pentafluoroethyl) trifluorophosphate [(C<sub>2</sub>F<sub>5</sub>)<sub>3</sub>PF<sub>3</sub>]<sup>-</sup>,<sup>737</sup> and BETI<sup>-</sup>.<sup>87</sup> To improve the performance of Al||graphite DIBs, Tang et al. developed an electrolyte of 7.5 m LiFSI-EC/DMC (1:1 v/v) which not only elongated the cycle stability of the graphite cathode during repeated deintercalation/intercalation of FSI<sup>-</sup> anions but also enhanced the structural stability of the Al anode via constructing a LiF-rich SEI layer.<sup>738</sup> Motivated by this Al-graphite electrochemistry, Chen et al. developed an EMC/DMC carbonate electrolyte with binary salts of LiPF<sub>6</sub> and AlF<sub>3</sub>. It was revealed that the Al anode was protected from dissolving after adding AlF<sub>3</sub> into the electrolyte. More notably, AlF<sub>4</sub><sup>-</sup> complex anions were formed via combination of the dissolved Al<sup>3+</sup> and F<sup>-</sup> in the electrolyte, which deintercalated/intercalated from/into the graphite during discharging/charging together with PF<sub>6</sub><sup>-</sup>. Based on this electrochemistry, the battery exhibited a high average working voltage of 4.0–4.5

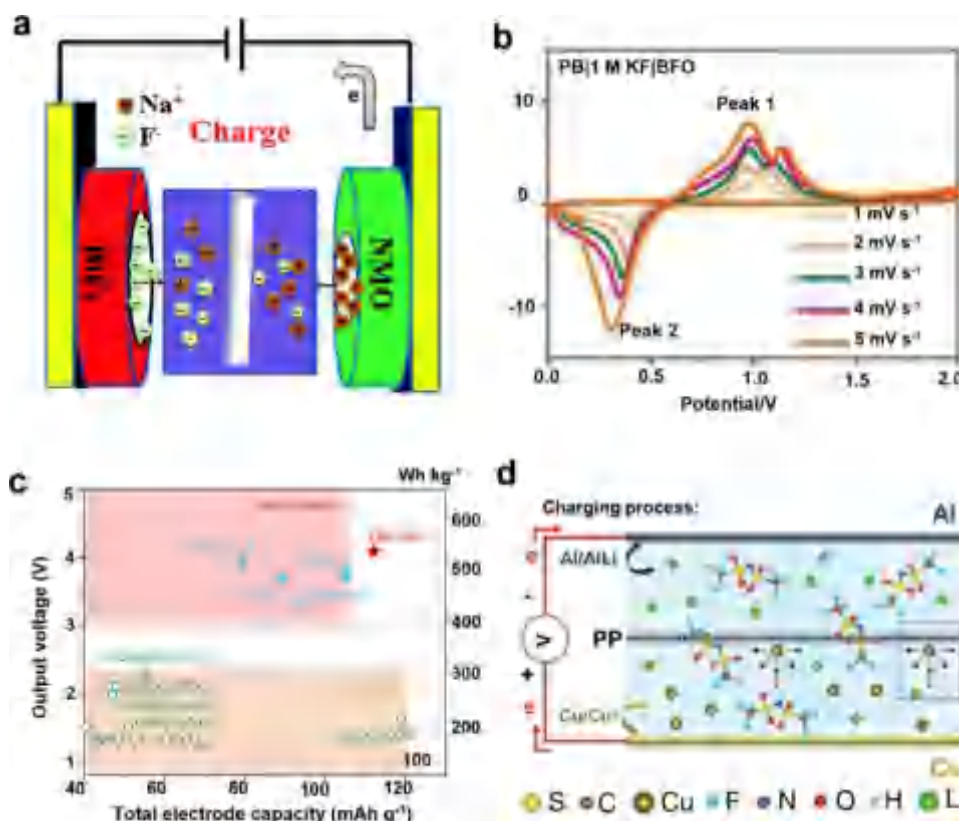
V and a high reversible capacity of  $\sim 100 \text{ mAh g}^{-1}$  along with a high CE of  $\sim 99\%$  over 600 cycles.<sup>93</sup> Besides the Al anode,  $\text{Ca}^{2+}/\text{Ca}$  redox chemistry shows promising prospects for rechargeable batteries due to its low polarization and low reduction potential ( $-2.87 \text{ V}$  vs SHE). Unfortunately, Ca-based batteries experience critical issues, including unsuitable electrode materials for reversible  $\text{Ca}^{2+}$  storage, low working voltages ( $< 2 \text{ V}$ ), and poor cycle stability, especially at RT. To tackle these issues, Tang et al. designed a new battery configuration by employing graphite as the cathode material and Sn foil as both the anode material and the current collector. With an electrolyte consisting of  $0.8 \text{ M Ca}(\text{PF}_6)_2$  in mixed solvents (EC:PC:DMC:EMC = 2:2:3:3 by volume), highly reversible redox reactions incorporating the deintercalation/intercalation of the  $\text{PF}_6^-$  anion at the cathode and the dealloying/alloying of  $\text{Ca}^{2+}$  ions at the metal anode were achieved. The resulting DIBs yielded a high discharge voltage of up to  $4.45 \text{ V}$  and high cycling stability (95% capacity retention over 350 cycles), as displayed in Figure 36a and 36b.<sup>739</sup>

Apart from the F-containing salts, fluorination treatment of other electrolyte components also endows DIBs with unique features such as wide working windows, a wide temperature range, nonflammability, and enhanced electrode/electrolyte compatibility. Read et al. employed a fluorinated solvent and additive in DIBs. The designed  $1.7 \text{ M LiPF}_6\text{--FEC/EMC}$  electrolyte with  $5 \text{ mM}$  tris(hexafluoroisopropyl) phosphate (HFIP) as the additive supported a graphite/graphite cell with a charge voltage up to  $5.2 \text{ V}$ , enabling the accommodation of  $\text{PF}_6^-$  and  $\text{Li}^+$  at the graphite cathode and the graphite anode simultaneously with a high CE of  $97\%$ .<sup>742</sup> Thereafter, the role of FEC on the anion solvation status and the anion insertion/extraction behaviors in DIBs was carefully evaluated by Yang et al.<sup>740</sup> It was revealed that FEC tuned the solvation structures of both  $\text{Na}^+$  and  $\text{PF}_6^-$  by replacing part of the original EMC solvent in the solvation shell (Figure 36c and 36d), inducing the formation of a fluorinated CEI film to resist the electrolyte side reactions at high voltages and suppress the expansion of graphitic layers in the cathodes during long-term cycling. The CEI layer on cathodes can also be modified by different salts as additives, as evidenced by the work conducted by Yu et al.<sup>743</sup> With the addition of  $\sim 0.5 \text{ wt } \%$  LiDFOB (with) in the electrolyte, a less resistive  $\text{Li}_x\text{BO}_y\text{F}_z$ -enriched CEI layer was constructed on the cathode surface. The LiDFOB salt has a higher HOMO energy level than that of the baseline solvent (EMC), inducing the preferential decomposition of LiDFOB. This robust and durable CEI enabled fast electrode reaction kinetics and achieved an ultrafast charging capability within 2 min. Later, the authors designed an all-fluorinated electrolyte ( $1 \text{ M LiPF}_6\text{--FEC/FEMC}$ ) that synergistically guaranteed a highly stable operation of the DIB up to  $5.2 \text{ V}$  by generating robust and ion-conductive passivation films on both electrodes to reduce undesired side reactions. More significantly, this fluorinated electrolyte facilitated the fast reaction kinetics of  $\text{PF}_6^-$  and  $\text{Li}^+$  at low temperatures, delivering  $97.8\%$  reversible capacity at RT, together with  $\sim 100\%$  capacity retention over 3000 cycles at  $500 \text{ mA g}^{-1}$ .<sup>744</sup> The all-fluorinated electrolyte system endows DIBs as a promising choice for wide-temperature applications. In addition to a wide operational temperature range, safety concerns (e.g., fire, explosion, and leakage of toxic electrolyte components) should be given sufficient consideration. Based on the all-fluorinated electrolyte ( $1 \text{ M LiPF}_6\text{--FEC/FEMC/THE}$ , 1:6:3 by volume), Wang et al.

prepared a GPE via in situ polymerization of diethyl allyl phosphate (DAP) monomer and pentaerythritol tetraacrylate (PETEA) cross-linker.<sup>353</sup> This GPE with a 3D polymer matrix showcased high safety features (e.g., nonflammability), sufficient ionic conductivity ( $1.99 \text{ mS cm}^{-1}$ ), superior stability up to  $5.5 \text{ V}$  (vs.  $\text{Li/Li}^+$ ), and high compatibility toward both electrodes.

To tackle concerns of cost, eco-friendliness, and safety caused by organic electrolytes, aqueous or hybrid aqueous/nonaqueous electrolytes have emerged as a highly interesting alternative for promoting practical applications of DIBs. Particularly, the pioneering work by Xu et al. proposed the concept of “water-in-salt” (WiS) electrolyte, which significantly enlarged the ESW of aqueous electrolytes from  $1.23$  to  $\sim 4.9 \text{ V}$ .<sup>135,745</sup> Encouraged by this widely adopted strategy in aqueous metal-ion batteries, especially in LIBs, a WiS electrolyte formulated with  $21 \text{ M LiTFSI}$  in aqueous electrolyte  $\text{H}_2\text{O}$  was combined with  $9.25 \text{ M LiTFSI--DMC}$  (mass ratio 1:1) nonaqueous electrolyte by Placke et al.<sup>746</sup> This hybrid electrolyte not only guaranteed adequate safety with the nonflammable feature from the WiS aqueous electrolyte but also protected the anode from side reactions by forming a stable SEI with the assistance of the nonaqueous component. Therefore, a stage-2 graphite intercalation compound (GIC) for  $\text{TFSI}^-$  intercalation was achieved in aqueous-based electrolytes. Afterward, an aqueous WiS consisting of  $20 \text{ m NaFSI}$  and  $0.5 \text{ m Zn}(\text{TFSI})_2$  was developed by Placke et al. in a Zn/graphite DIB.<sup>747</sup> The role of the high-concentration NaFSI salt was to reduce the free water molecules in the WiS electrolyte and to suppress the occurrence of the oxygen evolution reaction (OER). It was interesting to note that instead of the cointercalation of  $\text{FSI}^-$  and  $\text{TFSI}^-$ ,  $\text{TFSI}^-$  anions were proved to predominantly undergo the intercalation process into the graphite layers, which was associated with its lower intercalation barrier. Benefiting from this advanced electrolyte design, the consequent Zn/graphite DIB exhibited a high working voltage of  $\sim 2.3\text{--}2.5 \text{ V}$  and a high reversible capacity of  $\sim 110 \text{ mAh g}^{-1}$  with  $> 80\%$  capacity retention after 200 cycles.

Besides its beneficial effects on electrolyte optimization, the fluorine element can also be introduced to the cathode material to boost and stabilize anion intercalations. It is generally known that with strong electronegativity, a low van der Waals radius, and low polarizability properties, F is considered to have the ability to tune the photoelectric properties of conducting conjugated polymers such as PANI.<sup>741</sup> Based on these merits, a novel fluoridized-polyaniline- $\text{H}^+/\text{CNT}$  composite (FPHC) has been developed as the cathode material for DIBs. The introduction of F effectively reduced the energy gap between the HOMO and the LUMO (Figure 36e), thus enabling highly efficient storage of anions in the FPHC cathode. This result was further reflected by the higher electronic conductivity of  $0.162 \text{ S cm}^{-1}$  compared with the nonfluorinated PHC cathode ( $0.138 \text{ S cm}^{-1}$ ). In addition, the combinative formation of  $\text{PF}_6^-$  anion in the FPHC cathode was verified, suggesting that  $\text{F}^-$  of the  $\text{PF}_6^-$  anion tended to form a stable covalent bond with  $-\text{NH}$  in FPHC and thus exhibiting a symmetric structure of the whole  $\text{PF}_6^-$ -FPHC molecule, as shown in Figure 36f. This fluoridized treatment guaranteed a stable cycling of 2000 times at  $2 \text{ A g}^{-1}$  with a retained discharge capacity of  $73 \text{ mAh g}^{-1}$  along with a high power density of  $7720 \text{ W kg}^{-1}$  at an energy density of  $310 \text{ Wh kg}^{-1}$ .<sup>741</sup>



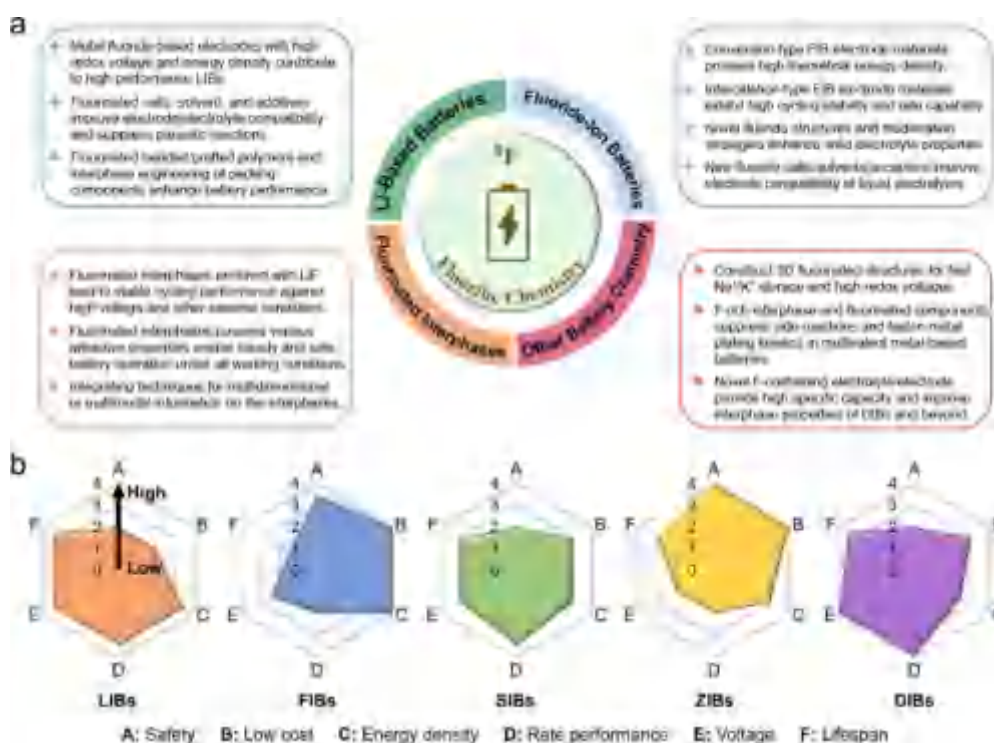
**Figure 37.** Beneficial effects of fluorine on the RDIB and beyond battery chemistries. (a) Schematics of the aqueous  $\text{BiF}_3/\text{Na}_{0.44}\text{MnO}_2$  RDIB based on the  $\text{F}^-$  anion and  $\text{Na}^+$  cation electrochemistry during the charging process. Reproduced with permission from ref 748. Copyright 2018 Royal Society of Chemistry. (b) Voltage curves of the RDIB with BF and modified BFO anode material at  $1 \text{ A g}^{-1}$ . Reproduced with permission from ref 589. Copyright 2021 Wiley-VCH. (c) Energy density of the highly fluorinated HFE/PEO-protected graphite|| $(\text{LiBr})_{0.5}(\text{LiCl})_{0.5}\text{C}_{\sim 3.7}$  full cell with an aqueous gel electrolyte compared with various state-of-the-art commercial and experimental Li-ion chemistries using nonaqueous (blue circles) and aqueous (green circles) electrolytes. Note: all energy densities were converted using the total weight of the cathode and the anode. Reproduced with permission from ref 749. Copyright 2019 Springer Nature. (d) Schematic diagram of the 3 V Al||Cu battery in 3 M LiTFSI-FEC electrolyte with a PP membrane. Reproduced with permission from ref 750. Copyright 2020 Wiley-VCH.

In addition to the above-mentioned DIBs, another emerging battery system also based on both cations and anions as charge carriers for electrochemical reactions is called RDIBs, except that the sequence of the anion- and cation-storage chemistries is flipped between the cathode and the anodes. To date, the RDIB chemistries have been only realized in aqueous electrolytes. In 2018, Hou et al. developed a novel RDIB relying on  $\text{F}^-$  anion and  $\text{Na}^+$  cation electrochemistry, which was comprised of a 0.8 M NaF aqueous solution as the electrolyte,  $\text{Na}_{0.44}\text{MnO}_2$  as the cathode material, and  $\text{BiF}_3$  as the anode material.<sup>748</sup> During the charge process, the  $\text{BiF}_3$  anode released  $\text{F}^-$  ions and the  $\text{Na}_{0.44}\text{MnO}_2$  cathode deintercalated  $\text{Na}^+$  ions to the aqueous electrolyte simultaneously. During the discharge process, the  $\text{F}^-$  ions in the electrolyte were captured by the anode to obtain  $\text{BiF}_3$  and the  $\text{Na}^+$  ions were intercalated into the cathode material as well (Figure 37a). This RDIB delivered a high discharge capacity of  $\sim 123 \text{ mAh g}^{-1}$  at a current density of  $100 \text{ mA g}^{-1}$  based on the mass of  $\text{BiF}_3$  anode materials. However, the capacity deteriorated very rapidly to  $47.28 \text{ mAh g}^{-1}$  over just 40 cycles, which was probably due to the instability of the anode material. An obvious volume change of the anode material was observed during cycling, i.e., 57.3% volume contraction for the phase transition from  $\text{BiF}_3$  into Bi and a large volume expansion of 134.0% for the reverse transition from Bi to  $\text{BiF}_3$ . Therefore, strategies such as structure modifications or surface

coatings should be explored to enhance the cycling stability of the Bi/ $\text{BiF}_3$  electrode. Afterward, another RDIB was designed by Li et al. (Figure 37b) utilizing KF aqueous electrolyte, Prussian blue (PB) cathode material, and  $\text{BiF}_3/\text{Bi}_{11}\text{O}_5/\text{BFO}$  reduced graphene oxide (BFO) anode material.<sup>589</sup> It was elucidated that the low electrolyte concentration improved the cycle stability of the BFO||PB RDIB despite the reduced discharge capacity. The reduction of  $\text{F}^-$  ions in the dilute electrolytes suppresses the dissolution of  $\text{Bi}^{3+}$  ions generated upon the discharge process, reducing the deposition of the side products on the electrode surface. In addition, this  $\text{Bi}^{3+}$  dissolution phenomenon can also be mitigated by the graphene coating on the surface of the BFO anode material. The resulting F/K-based RDIB achieved a high discharge capacity of  $218 \text{ mAh g}^{-1}$  at  $1 \text{ A g}^{-1}$  as well as fast rate capability with a capacity retention of 47% at a high current density of  $5 \text{ A g}^{-1}$ , which were calculated based on the weight of the BFO anode material.

Interestingly, Wang et al. demonstrated a novel conversion–intercalation chemistry based on the sequential intercalation of  $\text{Br}^-$  and  $\text{Cl}^-$  into a composite cathode consisting of  $(\text{LiBr})_{0.5}(\text{LiCl})_{0.5}\text{C}_{\sim 3.7}$  (LBC-G) using a highly concentrated “water-in-bisalt” aqueous gel electrolyte. Benefiting from the formed hydrated  $\text{LiBr}/\text{LiCl}$  layer ( $\text{LiBr} \cdot 0.34\text{H}_2\text{O} - \text{LiCl} \cdot 0.34\text{H}_2\text{O}$ ) by extracting water from the electrolyte, the LBC-G surface was separated from the electrolyte accordingly. Upon





**Figure 38.** Fluorine chemistry in rechargeable batteries. (a) Strategies and prospects of fluorine chemistry in rechargeable batteries. (b) Radar diagrams of various batteries based on six parameters: (A, safety; B, low cost; C, energy density; D, rate performance; E, voltage; F, lifespan).

charging, the  $\text{Br}^-$  within the hydration layer was first oxidized to  $\text{Br}_0$  and then intercalated into the graphite. As the charging process continued, the oxidation and intercalation of  $\text{Cl}^-$  occurred, leading to a mixed intercalation compound. This unique mechanism contributed to a stage-1 GIC, which accounted for a high reversible capacity of  $243 \text{ mAh g}^{-1}$  at a high average voltage of  $4.2 \text{ V vs Li}^+/\text{Li}$ . When coupled with a highly fluorinated ether (i.e., HFE)/PEO-protected graphite anode, the  $4 \text{ V}$  class full cell achieved a high energy density of  $460 \text{ Wh kg}^{-1}$  (calculated based on the total weight of the cathode and anode, Figure 37c) along with a CE of  $\sim 100\%$ .<sup>749</sup>

It can be reasonably concluded that anion-hosting cathode materials generally provide limited theoretical capacities, requiring the exploration of new cathode chemistry to enhance the energy density of the battery systems.<sup>751</sup> Along this line, Yu et al. proposed a novel metal–metal system that uses Cu and Al metal foils directly as the cathode and anode, respectively.<sup>750</sup> The electrochemical reactions proceed via the stripping/plating of Cu at the cathode and the alloying/dealloying of AlLi at the anode (Figure 37d). However, the  $\text{Cu}^+$  ions inevitably shuttled from the cathode to the anode, causing severe self-discharge and low CE during cycling. By utilizing  $3 \text{ M LiTFSI}$ –FEC electrolyte, they disclosed that  $\text{Cu}^+$  ions were bound by FEC and TFSI $^-$  to form the solvation complex, which prevented the  $\text{Cu}^+$  ions from transporting through the PP membrane due to high interfacial tension between the FEC molecules and the membrane. The blocking effect by FEC contributed to a stable operation of the  $3 \text{ V AlLi/Cu}$  battery for more than 1000 cycles. For comparison, a LiLi/Cu battery was designed by Ji et al. with a different operation mechanism.<sup>751</sup> Upon charging, Cu was oxidized to  $\text{Cu}^{2+}$  to precipitate as copper(II) bis(trifluoromethane sulfonyl)imide ( $\text{Cu}(\text{TFSI})_2$ ) on the cathode; meanwhile,  $\text{Li}^+$  was plated on the Li anode. During the discharge process,  $\text{Cu}^{2+}$  was first

reduced to  $\text{Cu}^+$  and continuously reduced to Cu, while the anode strips into Li. An anion exchange membrane was placed between the two electrodes to prohibit the crossover of cations during charging. Besides, the catholyte/anolyte concentration was regulated to  $2 \text{ m}/6 \text{ m}$  for mitigating the negative concentration gradient of TFSI $^-$ , therefore utilizing the Cu capacity and suppressing  $\text{Cu}^{2+}/\text{Cu}^+$  crossover. Although a high reversible capacity of  $762 \text{ mAh g}^{-1}$  was enabled at an average discharge voltage of  $3.2 \text{ V vs Li}^+/\text{Li}$ , the solubility of charged product  $\text{Cu}(\text{TFSI})_2$  leads to unsatisfactory reversibility, the heavy TFSI $^-$  as counterions limits the battery energy density, and the usage of AEM increases the cost of the battery system.

Overall, anion insertion with F-containing groups is crucial for DIB/RDIB performance, whereas no existing anion is ideal for satisfying the high energy density, fast charging rate, long lifespan, and low cost simultaneously. Further research should explore novel anions toward higher theoretical specific capacity and energy density of DIBs and RDIBs. Besides, fluorination of the electrolyte components can endow DIBs with broad ESW, wide temperature range, nonflammability, and improved electrode/electrolyte compatibility. Moreover, though RDIB chemistry can be realized in KF and NaF aqueous electrolytes, the rapid capacity deterioration associated with incompatible electrode materials remains a significant obstacle, requiring further exploration of F-containing salts and novel organic electrolytes to construct protective and robust interphases.

## 6. CONCLUSIONS AND OUTLOOK

Taking advantage of the extraordinary electronegativity, low atomic weight, small ionic size, natural abundance, and low cost of fluorine, fluorine chemistry has significantly advanced rechargeable battery technology. However, atomic-level insights into fluorine chemistry remain underexplored, especially under extreme conditions, and are not fully understood. This

review summarizes the state-of-the-art research and technical achievements in fluorine-containing materials/interphases for metal ion-batteries, FIBs, DIBs, and beyond (Figure 38a). Specifically, fluorine chemistry can address challenges in various battery materials, including poor intrinsic conductivity and severe structure deterioration during conversion reactions, large volume change and low redox potential during intercalation reactions, safety issues related with anode materials, insufficient chemical/electrochemical stability and/or low ionic conductivity for electrolytes, and performance restrictions of other battery components. This review highlights the pivotal role of fluorinated interphases, material structure–performance relationships, and cutting-edge techniques for probing fluorine chemistry. From a fundamental and practical perspective, the promising research directions to enhance the benefits of fluorine chemistry in rechargeable batteries can be identified as the following five aspects.

### 6.1. Addressing the Instinctively Low Electrochemical Kinetics of Conversion-Type Metal Fluoride-Based Cathodes

First, systematic studies on the redox mechanisms and structural evolution are essential for a deeper understanding of these cathodes. Theoretical studies on these materials are limited to simple metal fluorides such as  $\text{FeF}_2$  and  $\text{CuF}_2$ . The expanding research of metal fluoride-based cathodes via theoretical simulation and heterometal modification will achieve structurally stable metal fluoride-based cathodes with rapid ion diffusion, which is promising for practical applications. Moreover, the low mass loadings and areal capacities of reported metal fluoride-based cathodes hinder a comprehensive evaluation of their energy density and cycling performance compared to conventional LIB cathodes. Therefore, developing high-loading metal fluoride-based cathodes with increased areal capacities is a priority. In parallel, fluorine chemistry can enhance conventional LIB cathodes such as layered oxides, through F substitution, F doping, and surface fluoridation, improving the cycling stability and energy density of the cathodes and providing insights for the development of high-performance LIBs.

**6.1.1. Striking a Balance between Electrochemical Performance, Stability, and Environmental Considerations for Optimizing F Substitution/Modification in Battery Components.** The electrolytes for high-performance Li-based batteries can be tailored by combining the benefits of different partially fluorinated/per-fluorinated electrolytes. Future design for Li salts should focus on integrating functional groups with complementary roles for enhanced overall performance. Fluorinated solvents and cosolvents display unique physicochemical properties due to the high electronegativity, high ionic potential, and low polarizability of fluorine. Partial fluorination or optimization of the fluorination positions can be applied to develop single-solvent electrolytes. In parallel, introducing per-fluorinated cosolvent into non-fluorinated solvents for multisolvent electrolytes is also viable.

Fluorine can also be utilized to modify and functionalize battery separators, enhancing fire retardancy, preventing potential mechanical abuse, and also promoting the formation of a LiF-enriched SEI. Regarding battery binders, fluorine groups can be incorporated into polymer backbones, while fluorinated anions can be combined with ionic conductive polymers, enabling higher ion transfer, greater resistance to electrochemical oxidation, and enhanced thermal stability.

Especially, a fluorinated cross-linked network binder should be designed for alloy-type anodes, where massive fluorine groups improve the mechanical features while chemical/physical cross-linking maintains the electrode structures against volume changes. However, excessive fluorine content may lead to a decay in the electrode performance. Furthermore, current collectors can be modified by fluorinated carbon materials, lithiophilic metal fluoride coatings, F-containing interlayers, etc., which regulate Li deposition and enhance interphasial stability. However, the environmental issues brought by F substitution/modification must be taken seriously. Fluorinated compounds in prevalent battery components (e.g., LiTFSI, PVDF, and PTFE), which contain  $\text{CF}_3$  or  $-\text{CF}_2-$  groups, are under consideration for prohibition under European Union regulations. Therefore, optimization of F substitution/modification in battery components should be scrutinized to strike a balance between electrochemical performance, stability, and environmental considerations.<sup>128</sup>

### 6.2. Tailoring Fluorinated Interphases for Li-Based Batteries at All Working Conditions

The efficient operation of Li-based batteries especially under extreme conditions relies highly on the stability of interphases, including chemical stability, electrochemical stability, mechanical stability, and thermal stability. Interdisciplinary research should be encouraged to reveal the chemical nature of the SEI/CEI. Considering that the low  $\text{Li}^+$  conductivity of LiF ( $\sim 10^{-12} \text{ S cm}^{-1}$ ) restricts the high-rate performance, other fluorinated conducting components (e.g.,  $\text{Li}_x\text{PO}_y\text{F}_z$ ) should be incorporated into LiF-rich interphases. A polymer-based organic SEI matrix can also be combined with fluorinated components to accommodate the large volume change of the Li anodes. Besides, a LiF-rich CEI possessing excellent electrochemical stability can effectively protect high-voltage cathodes. Although the LiF-enriched SEI displays low interphase impedance/charge transfer resistance and high stability for facilitating low-temperature operation, the LiF effects on the CEI at low temperatures remain a subject of debate. Further investigation is needed to deeply understand the macroscopic and microscopic properties of LiF, especially the roles and factors (e.g., the distribution, particle size, and formation approach) affecting the performance of Li-based batteries under extreme conditions.

**6.2.1. Unlocking Fundamental Issues Regarding Chemical Compositions, Spatial Distributions, and Realistic Structures of the Interphases.** Nondestructive and/or in situ/operando techniques (e.g., cryo-TEM, operando EQCM, in situ XPS, liquid TOF-SIMS, in situ NMR, and synchrotron-based XRD) are imperative for real-time, dynamic, and intuitive investigations of the structural, morphological, and chemical characteristics of interphases and their correlations with the battery performance. Therefore, suitable electrochemical cells for in situ operations should be carefully designed as different cell configurations can cause inconsistent and even misleading results. An integrated approach with complementary techniques is highly desirable for obtaining multidimensional and/or multimodal insights into interphases, facilitating the elucidation of the structure–property relationships and guiding the design of stable interphases.

### 6.3. Revolution of the Electrode and Electrolyte Materials for High Energy Density and Cycling Stability FIBs

The volume change and polarization issues of conversion-type electrode materials should be solved by reducing the particle size and constructing the conductive network, seeking for high-capacity intercalation-type electrode materials via theoretical screening and experimental verification, and preventing the fluorination of conductive additive through the carbon stabilization process. In parallel, to advance the development of F<sup>−</sup> conducting solid-state electrolytes, novel fluoride structures and modification strategies, such as creating point defects, introducing F vacancies, and optimizing synthesis methods, are highly required. For liquid electrolytes, it is essential to explore novel fluoride salts, solvents, and suitable anion/cation acceptors to facilitate the dissociation of fluoride salts. Furthermore, the “water-in-salt” strategy exhibits great prospect in expanding the ESW, suppressing the active material dissolutions, and addressing HF formation in aqueous electrolytes.

### 6.4. Establishing Fluorinated Material–Function Relationships To Boost SIB/PIB Performance

In SIBs, the development of F-based electrodes is shifted toward 3D fluorinated phases. An in-depth investigation is necessary to regulate the structure and phase transitions to mitigate volume changes and to elucidate the structure–performance correlations, thereby reducing the activation energy barrier and band-gap energy for efficient Na<sup>+</sup> diffusion. As for PIBs, surface modifications of potassium fluorophosphate compounds are necessary to improve both the electron and the K<sup>+</sup> transport. Besides, the fluorine to oxygen ratio should be carefully controlled to prevent disordered structures of fluorosulfates that suppresses the K<sup>+</sup>/vacancy formation and decreases the reversible K<sup>+</sup> storage capacity. Moreover, F doping can improve the surface disorder of carbonaceous anode materials, creating large amounts of surface defects to facilitate Na<sup>+</sup>/K<sup>+</sup> adsorption. As for electrolyte developments in SIBs/PIBs, strategies from Li-based batteries are not directly applicable due to potential adverse effects (e.g., FEC). Notably, fluorine chemistry facilitates the discovery of novel conducting salts with wide ESW, film-forming ability, and fast ionic transport. However, the molecular structure–function relationships of the fluorinated components remain unclear, necessitating targeted molecular selection. Further efforts should be focused on the challenging aspects of fluorinated interphases to optimize their properties.

### 6.5. Exploring the Potential of F-Containing Materials for Other Battery Chemistries

Challenges including the insufficient energy density of existing electrodes, the sluggish plating/stripping dynamics kinetics of a metallic anode, and the poor stability of the electrolyte/electrode interphase hinder the utilization of multivalent metal-based batteries with attractive advantages (e.g., low cost and high energy density). Fluorine chemistry is important for seeking suitable F-containing electrode materials as well as providing a deep understanding of the construction of a F-involved SEI film, which could positively or negatively affect the battery performance. As for DIBs/RDIBs, novel anions with smaller sizes and higher antioxidative stability as well as multivalent anions with more charge numbers can potentially provide high theoretical specific capacity and energy density. Though fluorination treatment of the electrolyte components can endow DIBs with enhanced performance, the fundamental

role of these fluorinated components in the anion solvation, the relationship between fluorinated CEI features (e.g., chemical components, micro/nanostructures, mechanical properties), and battery performance remain unclear. Furthermore, other battery chemistries necessitate the exploration of F-containing salts and novel electrolytes to construct protective and robust interphases.

The high-temperature sintering of inorganic materials containing the fluorine element is potentially detrimental to the furnace, impeding its scalability for large-scale synthesis. Thus, alternative soft chemical synthesis methods such as low-temperature solid-phase synthesis, chemical transfer synthesis, and solvent thermal synthesis should be developed for preparing F-containing cathode and solid-state electrolyte materials in the future. Overall, significant breakthrough progress has been achieved by utilizing fluorine chemistry in rechargeable batteries. Although traditional lithium-ion batteries maintain a leading position in overall performance due to decades of research, other alternative battery systems also demonstrate significant advantages in specific aspects (Figure 38b). Thus, expanding fluorine chemistry research into these areas is expected to accelerate the application of these rising battery systems. Nonetheless, the ongoing development of fluorine chemistry is bringing many scientific and technical challenges, leaving substantial investigation room for its future applications. Thus, researchers are highly encouraged to unlock the fundamental role of fluorine chemistry in addressing the obstacles for various types of battery materials, thus promoting the widespread effectuation of fluorine chemistry in rechargeable batteries. More significantly, we hope this review can raise interest and provide key insights into the further development of fluorine chemistry for high-performance rechargeable batteries.

## AUTHOR INFORMATION

### Corresponding Authors

**Baohua Li** – Tsinghua Shenzhen International Graduate School, Tsinghua University, Shenzhen 518055, P. R. China; [orcid.org/0000-0001-5559-5767](https://orcid.org/0000-0001-5559-5767); Email: [libh@sz.tsinghua.edu.cn](mailto:libh@sz.tsinghua.edu.cn)

**Dong Zhou** – Tsinghua Shenzhen International Graduate School, Tsinghua University, Shenzhen 518055, P. R. China; [orcid.org/0000-0002-2578-7124](https://orcid.org/0000-0002-2578-7124); Email: [zhou.d@sz.tsinghua.edu.cn](mailto:zhou.d@sz.tsinghua.edu.cn)

**Chunsheng Wang** – Department of Chemical and Biomolecular Engineering, University of Maryland, College Park, Maryland 20742, United States; [orcid.org/0000-0002-8626-6381](https://orcid.org/0000-0002-8626-6381); Email: [cswang@umd.edu](mailto:cswang@umd.edu)

**Guoxiu Wang** – Centre for Clean Energy Technology, School of Mathematical and Physical Sciences, Faculty of Science, University of Technology Sydney, Sydney, New South Wales 2007, Australia; [orcid.org/0000-0003-4295-8578](https://orcid.org/0000-0003-4295-8578); Email: [Guoxiu.Wang@uts.edu.au](mailto:Guoxiu.Wang@uts.edu.au)

### Authors

**Yao Wang** – Tsinghua Shenzhen International Graduate School, Tsinghua University, Shenzhen 518055, P. R. China

**Xu Yang** – Centre for Clean Energy Technology, School of Mathematical and Physical Sciences, Faculty of Science, University of Technology Sydney, Sydney, New South Wales 2007, Australia

**Yuefeng Meng** – Tsinghua Shenzhen International Graduate School, Tsinghua University, Shenzhen 518055, P. R. China



**Zuxin Wen** – *Tsinghua Shenzhen International Graduate School, Tsinghua University, Shenzhen 518055, P. R. China*

**Ran Han** – *Tsinghua Shenzhen International Graduate School, Tsinghua University, Shenzhen 518055, P. R. China*

**Xia Hu** – *Tsinghua Shenzhen International Graduate School, Tsinghua University, Shenzhen 518055, P. R. China*

**Bing Sun** – *Centre for Clean Energy Technology, School of Mathematical and Physical Sciences, Faculty of Science, University of Technology Sydney, Sydney, New South Wales 2007, Australia; [orcid.org/0000-0002-4365-486X](https://orcid.org/0000-0002-4365-486X)*

**Feiyu Kang** – *Tsinghua Shenzhen International Graduate School, Tsinghua University, Shenzhen 518055, P. R. China*

Complete contact information is available at:

<https://pubs.acs.org/10.1021/acs.chemrev.3c00826>

### Author Contributions

<sup>†</sup>Y.W., X.Y., and Y.M.: These authors contributed equally. The manuscript was written through contributions of all authors. All authors have given approval to the final version of the manuscript. CRediT: Yao Wang, Xu Yang, and Yuefeng Meng: investigation, mechanisms, writing—original draft. Zuxin Wen, Ran Han, Xia Hu, and Bing Sun: methodology, validation, editing. Baohua Li, Dong Zhou, Chunsheng Wang, and Guoxiu Wang: conceptualization, project administration, supervision, writing—original draft, writing—review and editing.

### Notes

The authors declare no competing financial interest.

### Biographies

Yao Wang is currently a postdoctoral researcher at Tsinghua Shenzhen International Graduate School, Tsinghua University (China). She received her Ph.D. degree from City University of Hong Kong (CityU) in 2021. Her research mainly focuses on designing electrolyte systems and investigating electrode/electrolyte interphases for high-voltage and low-cost rechargeable batteries.

Xu Yang is currently a Ph.D. student in the Centre for Clean Energy Technology at the University of Technology Sydney (UTS). He received his B.Sc. (2017) and M.Sc. (2019) degrees at the Harbin Institute of Technology. His research interests focus on the development of low-cost rechargeable batteries and all-solid-state lithium-ion batteries.

Yuefeng Meng received her B.Sc. (2018) and M.Sc. (2023) degrees majoring in Materials Science and Engineering at Tsinghua University (China). Her current research interests include safe electrolyte design and interphase chemistry for high-voltage lithium metal batteries.

Zuxin Wen is currently a Ph.D. student at Tsinghua Shenzhen International Graduate School, Tsinghua University (China). He received his B.Sc. (2020) and M.Sc. (2023) degrees at Central South University. His research interests focus on the development of low-cost rechargeable batteries and all-solid-state lithium-ion batteries.

Ran Han received his B.Sc. (2020) degree at Hefei University of Technology and M.Sc. (2023) degree at Shanghai University. His research interests focus on the development of low-temperature rechargeable batteries and aqueous batteries.

Xia Hu is currently a Ph.D. student at Tsinghua Shenzhen International Graduate School, Tsinghua University (China). She obtained her B.Sc. (2015) and M.Sc. (2018) degrees from Central South University. Her research is currently centered on the development of solid-state lithium-based batteries and the associated critical materials.

Bing Sun received his Ph.D. degree in 2012 at the University of Technology Sydney (UTS), Australia. Currently, he is a senior lecturer in the Centre for Clean Energy Technology at the UTS. His research interests focus on the development of next-generation battery materials and technology for lithium-based batteries and sodium-based batteries. He is the recipient of the Australian Research Council (ARC) Discovery Early Career Researcher Award and the ARC Future Fellowship.

Feiyu Kang is a full professor in the Department of Materials Science and Engineering and also a dean in the Graduate School at Shenzhen, Tsinghua University (China). He received his Ph.D. degree from Hong Kong University of Science and Technology (HKUST). His research focuses on nanocarbon materials, graphite, thermal conductive materials, lithium-ion batteries, supercapacitors, electric vehicles, porous carbon and adsorption, indoor air clearing, and water purification. He has published more than 630 refereed journal papers. His publications have attracted over 77 000 citations with an h-index of 143 (Google Scholar). He was ranked as the Global Highly Cited Researchers (top 1% by citation) by Clarivate Analytics in 2018–2023.

Baohua Li is currently a full professor and director of the Division of Energy and Environment at Tsinghua Shenzhen International Graduate School, Tsinghua University (China). He received his Ph.D. degree from the Institute of Coal Chemistry (ICC), Chinese Academy of Sciences (CAS) in 2003. His research interests focus on carbon materials for energy storage, such as electrode materials for supercapacitors and lithium-ion batteries. He has published more than 290 refereed journal papers. His publications have attracted over 38 000 citations with an h-index of 104 (Google Scholar). He was ranked as the World's Top 2% Scientist by Stanford University in 2021. He is also the director of the Advanced Battery and Material Engineering Research Center of Guangdong and a member of the Academic Committee of Guangdong Key Laboratory of Thermal Management Engineering and Materials.

Dong Zhou is currently an assistant professor and Ph.D. supervisor at Tsinghua Shenzhen International Graduate School, Tsinghua University (China). He received his Ph.D. degree from Tsinghua University in 2017 and then worked as a postdoctoral research associate in the University of Technology Sydney, Australia and the University of Tokyo, Japan. His research mainly focuses on the design and synthesis of specialized solid polymer electrolytes and nano-electrode materials for various advanced energy storage devices and investigation of the interfacial mechanisms. As first-/corresponding author, his research has resulted in more than 30 refereed journal articles with a total citation of over 7200 (Google Scholar). He is the recipient of the First Prize of Guangdong Natural Science in 2020, the Discovery Early Career Researcher Award (DECRA), and the Japan Society for the Promotion of Science (JSPS) Fellowship.

Chunsheng Wang is a Robert Franklin and Frances Riggs Wright Distinguished Chair Professor in the Chemical & Biomolecular Engineering, Department of Chemistry and Biochemistry, at the University of Maryland. He is an associate editor of *ACS Applied Energy Materials* and UMD Director of the UMD-ARL Center for Research in Extreme Battery. His research focuses on rechargeable batteries and fuel cells. He has published more than 340 refereed journal papers. His publications have attracted over 70 000 citations with an h-index of 138 (Google Scholar). He was ranked as the Global Highly Cited Researchers (top 1% by citation) by Clarivate Analytics in 2018–2023.

Guoxiu Wang is the Director of the Centre for Clean Energy Technology and a Distinguished Professor at the University of

Technology Sydney (UTS), Australia. Currently, he serves as an associate editor for *Electrochemical Energy Reviews* (Springer-Nature) and *Energy Storage Materials* (Elsevier). His research interests include lithium-ion batteries, lithium–air batteries, sodium-ion batteries, lithium–sulfur batteries, supercapacitors, fuel cells, 2D materials such as graphene and MXenes, and electrocatalysis for hydrogen production. He has published more than 680 refereed journal papers. His publications have attracted over 75 000 citations with an h-index of 150 (Google Scholar). He has been recognized as a highly cited researcher in Chemistry and Materials Science by the Web of Science/Clarivate Analytics. He is an elected fellow of the European Academy of Sciences (EurASc), a fellow of the International Society of Electrochemistry (ISE), and a fellow of the Royal Society of Chemistry (RSC).

## ACKNOWLEDGMENTS

B.L. acknowledges the support by the National Natural Science Foundation of China (Nos. 52072208 and 52261160384), the Shenzhen Science and Technology Program (KCXFZ20211020163810015), the Fundamental Research Project of Shenzhen (No. JCYJ20220818101004009), and the Local Innovative and Research Teams Project of Guangdong Pearl River Talents Program (2017BT01N111). G.W. acknowledges the support from the Australian Research Council (ARC) through the Discovery Projects (DP210101389 and DP230101579), the ARC Linkage Project (LP200200926), and the ARC Research Hub for Integrated Energy Storage Solutions (IH180100020). Y.W. acknowledges the support by the National Natural Science Foundation of China (No. 22309102) and the China Postdoctoral Science Foundation (Grant No. 2022M711788). B.S. is thankful for the financial support from the ARC through the ARC Future Fellowship (FT220100561).

## REFERENCES

- (1) Whittingham, M. S. Lithium Batteries and Cathode Materials. *Chem. Rev.* **2004**, *104*, 4271–4301.
- (2) Dunn, B.; Kamath, H.; Tarascon, J. M. Electrical Energy Storage for the Grid: A Battery of Choices. *Science* **2011**, *334*, 928–935.
- (3) Schmuck, R.; Wagner, R.; Höppl, G.; Placke, T.; Winter, M. Performance and Cost of Materials for Lithium-Based Rechargeable Automotive Batteries. *Nat. Energy* **2018**, *3*, 267–278.
- (4) Blomgren, G. E. The Development and Future of Lithium Ion Batteries. *J. Electrochem. Soc.* **2017**, *164*, A5019–A5025.
- (5) Bigelow, L. A. The Action of Elementary Fluorine upon Organic Compounds. *Chem. Rev.* **1947**, *40*, 51–115.
- (6) Groult, H.; Lantelme, F.; Salanne, M.; Simon, C.; Belhomme, C.; Morel, B.; Nicolas, F. Role of Elemental Fluorine in Nuclear Field. *J. Fluor. Chem.* **2007**, *128*, 285–295.
- (7) Dolbier, W. R. Fluorine Chemistry at the Millennium. *J. Fluor. Chem.* **2005**, *126*, 157–163.
- (8) Gardiner, J. Fluoropolymers: Origin, Production, and Industrial and Commercial Applications. *Aust. J. Chem.* **2015**, *68*, 13.
- (9) Xiao, A. W.; Galatolo, G.; Pasta, M. The Case for Fluoride-Ion Batteries. *Joule* **2021**, *5*, 2823–2844.
- (10) CRC Handbook of Chemistry and Physics: A Ready-Reference of Chemical and Physical Data, 85th ed.; Lide, D. R., Ed. (National Institute of Standards and Technology); CRC Press LLC: Boca Raton, FL, 2004; pp 2712.
- (11) Mineral Commodity Summaries 2021; U.S. Geological Survey: Reston, VA, 2021, DOI: 10.3133/mcs2021.
- (12) Goodenough, J. B.; Kim, Y. Challenges for Rechargeable Li Batteries. *Chem. Mater.* **2010**, *22*, 587–603.
- (13) Najib, S.; Erdem, E. Current Progress Achieved in Novel Materials for Supercapacitor Electrodes: Mini Review. *Nanoscale Adv.* **2019**, *1*, 2817–2827.
- (14) Ben Yahia, M.; Vergnet, J.; Saubane, M.; Doublet, M. L. Unified Picture of Anionic Redox in Li/Na-Ion Batteries. *Nat. Mater.* **2019**, *18*, 496–502.
- (15) Hu, E.; Yu, X.; Lin, R.; Bi, X.; Lu, J.; Bak, S.; Nam, K.-W.; Xin, H. L.; Jaye, C.; Fischer, D. A.; et al. Evolution of Redox Couples in Li- and Mn-Rich Cathode Materials and Mitigation of Voltage Fade by Reducing Oxygen Release. *Nat. Energy* **2018**, *3*, 690–698.
- (16) Yan, P.; Zheng, J.; Liu, J.; Wang, B.; Cheng, X.; Zhang, Y.; Sun, X.; Wang, C.; Zhang, J.-G. Tailoring Grain Boundary Structures and Chemistry of Ni-Rich Layered Cathodes for Enhanced Cycle Stability of Lithium-Ion Batteries. *Nat. Energy* **2018**, *3*, 600–605.
- (17) Akhilash, M.; Salini, P. S.; John, B.; Mercy, T. D. A Journey through Layered Cathode Materials for Lithium Ion Cells - from Lithium Cobalt Oxide to Lithium-Rich Transition Metal Oxides. *J. Alloys Compd.* **2021**, *869*, 159239.
- (18) Akhilash, M.; Salini, P. S.; Jalaja, K.; John, B.; Mercy, T. D. Synthesis of  $\text{Li}_{1.5}\text{Ni}_{0.25}\text{Mn}_{0.75}\text{O}_{2.5}$  Cathode Material via Carbonate Coprecipitation Method and Its Electrochemical Properties. *Inorg. Chem. Commun.* **2021**, *126*, 108434.
- (19) Kim, T.; Song, W.; Son, D.-Y.; Ono, L. K.; Qi, Y. Lithium-Ion Batteries: Outlook on Present, Future, and Hybridized Technologies. *J. Mater. Chem. A* **2019**, *7*, 2942–2964.
- (20) Cheng, X.-B.; Zhao, C.-Z.; Yao, Y.-X.; Liu, H.; Zhang, Q. Recent Advances in Energy Chemistry between Solid-State Electrolyte and Safe Lithium-Metal Anodes. *Chem.* **2019**, *5*, 74–96.
- (21) Wang, H.; Yu, D.; Kuang, C.; Cheng, L.; Li, W.; Feng, X.; Zhang, Z.; Zhang, X.; Zhang, Y. Alkali Metal Anodes for Rechargeable Batteries. *Chem.* **2019**, *5*, 313–338.
- (22) Zhang, J. G.; Xu, W.; Xiao, J.; Cao, X.; Liu, J. Lithium Metal Anodes with Nonaqueous Electrolytes. *Chem. Rev.* **2020**, *120*, 13312–13348.
- (23) Wei, C.; Tan, L.; Tao, Y.; An, Y.; Tian, Y.; Jiang, H.; Feng, J.; Qian, Y. Interfacial Passivation by Room-Temperature Liquid Metal Enabling Stable 5 V-class Lithium-Metal Batteries in Commercial Carbonate-Based Electrolyte. *Energy Storage Mater.* **2021**, *34*, 12–21.
- (24) Hobold, G. M.; Lopez, J.; Guo, R.; Minafra, N.; Banerjee, A.; Shirley Meng, Y.; Shao-Horn, Y.; Gallant, B. M. Moving beyond 99.9% Coulombic Efficiency for Lithium Anodes in Liquid Electrolytes. *Nat. Energy* **2021**, *6*, 951–960.
- (25) Zou, P.; Sui, Y.; Zhan, H.; Wang, C.; Xin, H. L.; Cheng, H. M.; Kang, F.; Yang, C. Polymorph Evolution Mechanisms and Regulation Strategies of Lithium Metal Anode under Multiphysical Fields. *Chem. Rev.* **2021**, *121*, 5986–6056.
- (26) Tan, S. J.; Wang, W. P.; Tian, Y. F.; Xin, S.; Guo, Y. G. Advanced Electrolytes Enabling Safe and Stable Rechargeable Li-Metal Batteries: Progress and Prospects. *Adv. Funct. Mater.* **2021**, *31*, 2105253.
- (27) Li, X.; Zhao, R.; Fu, Y.; Manthiram, A. Nitrate Additives for Lithium Batteries: Mechanisms, Applications, and Prospects. *eScience* **2021**, *1*, 108–123.
- (28) Ma, H.; Cheng, F.; Chen, J. Y.; Zhao, J. Z.; Li, C. S.; Tao, Z. L.; Liang, J. Nest-like Silicon Nanospheres for High-Capacity Lithium Storage. *Adv. Mater.* **2007**, *19*, 4067–4070.
- (29) Peng, B.; Cheng, F.; Tao, Z.; Chen, J. Lithium Transport at Silicon Thin Film: Barrier for High-Rate Capability Anode. *J. Chem. Phys.* **2010**, *133*, 034701.
- (30) Huang, A.; Ma, Y.; Peng, J.; Li, L.; Chou, S.-L.; Ramakrishna, S.; Peng, S. Tailoring the Structure of Silicon-Based Materials for Lithium-Ion Batteries via Electrospinning Technology. *eScience* **2021**, *1*, 141–162.
- (31) Nayak, P. K.; Yang, L.; Brehm, W.; Adelhelm, P. From Lithium-Ion to Sodium-Ion Batteries: Advantages, Challenges, and Surprises. *Angew. Chem., Int. Ed.* **2018**, *57*, 102–120.
- (32) Xu, J.; Dou, Y.; Wei, Z.; Ma, J.; Deng, Y.; Li, Y.; Liu, H.; Dou, S. Recent Progress in Graphite Intercalation Compounds for Rechargeable Metal (Li, Na, K, Al)-Ion Batteries. *Adv. Sci.* **2017**, *4*, 1700146.

- (33) Min, X.; Xiao, J.; Fang, M.; Wang, W.; Zhao, Y.; Liu, Y.; Abdelkader, A. M.; Xi, K.; Kumar, R. V.; Huang, Z. Potassium-Ion Batteries: Outlook on Present and Future Technologies. *Energy Environ. Sci.* **2021**, *14*, 2186–2243.
- (34) Vaalma, C.; Buchholz, D.; Weil, M.; Passerini, S. A Cost and Resource Analysis of Sodium-Ion Batteries. *Nat. Rev. Mater.* **2018**, *3*, 18013.
- (35) Rajagopalan, R.; Tang, Y.; Ji, X.; Jia, C.; Wang, H. Advancements and Challenges in Potassium Ion Batteries: A Comprehensive Review. *Adv. Funct. Mater.* **2020**, *30*, 1909486.
- (36) Liang, Y.; Dong, H.; Aurbach, D.; Yao, Y. Current Status and Future Directions of Multivalent Metal-Ion Batteries. *Nat. Energy* **2020**, *5*, 646–656.
- (37) Xie, J.; Zhang, Q. Recent Progress in Multivalent Metal (Mg, Zn, Ca, and Al) and Metal-Ion Rechargeable Batteries with Organic Materials as Promising Electrodes. *Small* **2019**, *15*, No. e1805061.
- (38) Liu, Q.; Wang, Y.; Yang, X.; Zhou, D.; Wang, X.; Jaumaux, P.; Kang, F.; Li, B.; Ji, X.; Wang, G. Rechargeable Anion-Shuttle Batteries for Low-Cost Energy Storage. *Chem.* **2021**, *7*, 1993–2021.
- (39) Sandstrom, S. K.; Chen, X.; Ji, X. A Review of Halide Charge Carriers for Rocking-Chair and Dual-Ion Batteries. *Carbon Energy* **2021**, *3*, 627–653.
- (40) Gschwind, F.; Rodriguez-Garcia, G.; Sandbeck, D. J. S.; Gross, A.; Weil, M.; Fichtner, M.; Hörmann, N. Fluoride Ion Batteries: Theoretical Performance, Safety, Toxicity, and a Combinatorial Screening of New Electrodes. *J. Fluor. Chem.* **2016**, *182*, 76–90.
- (41) Nowroozi, M. A.; Mohammad, I.; Molaiyan, P.; Wissel, K.; Munnangi, A. R.; Clemens, O. Fluoride Ion Batteries - Past, Present, and Future. *J. Mater. Chem. A* **2021**, *9*, 5980–6012.
- (42) Gopinadh, S. V.; Phanendra, P. V. R. L.; John, B.; Mercy, T. D. Fluoride-Ion Batteries: State-of-the-Art and Future Perspectives. *SM&T* **2022**, *32*, No. e00436.
- (43) Anji Reddy, M.; Fichtner, M. Batteries Based on Fluoride Shuttle. *J. Mater. Chem.* **2011**, *21*, 17059.
- (44) Zhou, M.; Zhao, L.; Doi, T.; Okada, S.; Yamaki, J.-I. Thermal Stability of FeF<sub>3</sub> Cathode for Li-Ion Batteries. *J. Power Sources* **2010**, *195*, 4952–4956.
- (45) Zhou, M.; Zhao, L.; Okada, S.; Yamaki, J.-I. Thermal Characteristics of a FeF<sub>3</sub> Cathode via Conversion Reaction in Comparison with LiFePO<sub>4</sub>. *J. Power Sources* **2011**, *196*, 8110–8115.
- (46) Zhang, L.; Wang, H.; Zhang, X.; Tang, Y. A Review of Emerging Dual-Ion Batteries: Fundamentals and Recent Advances. *Adv. Funct. Mater.* **2021**, *31*, 2010958.
- (47) Ou, X.; Gong, D.; Han, C.; Liu, Z.; Tang, Y. Advances and Prospects of Dual-Ion Batteries. *Adv. Energy Mater.* **2021**, *11*, 2102498.
- (48) Goodenough, J. B.; Park, K. S. The Li-Ion Rechargeable Battery: A Perspective. *J. Am. Chem. Soc.* **2013**, *135*, 1167–1176.
- (49) Tarascon, J. M.; Gozdz, A. S.; Schmutz, C.; Shokoohi, F.; Warren, P. C. Performance of Bellcore's Plastic Rechargeable Li-Ion Batteries. *Solid State Ion.* **1996**, *86–88*, 49–54.
- (50) Park, Y. U.; Seo, D. H.; Kim, B.; Hong, K. P.; Kim, H.; Lee, S.; Shakoob, R. A.; Miyasaka, K.; Tarascon, J. M.; Kang, K. Tailoring a Fluorophosphate as a Novel 4 V Cathode for Lithium-Ion Batteries. *Sci. Rep.* **2012**, *2*, 704.
- (51) Choi, N.-S.; Yew, K. H.; Lee, K. Y.; Sung, M.; Kim, H.; Kim, S.-S. Effect of Fluoroethylene Carbonate Additive on Interfacial Properties of Silicon Thin-Film Electrode. *J. Power Sources* **2006**, *161*, 1254–1259.
- (52) Davis, V. K.; Bates, C. M.; Omichi, K.; Savoie, B. M.; Momcilovic, N.; Xu, Q.; Wolf, W. J.; Webb, M. A.; Billings, K. J.; Chou, N. H.; et al. Room-Temperature Cycling of Metal Fluoride Electrodes: Liquid Electrolytes for High-Energy Fluoride Ion Cells. *Science* **2018**, *362*, 1144–1148.
- (53) Huang, Q.; Turcheniuk, K.; Ren, X.; Magasinski, A.; Song, A. Y.; Xiao, Y.; Kim, D.; Yushin, G. Cycle Stability of Conversion-Type Iron Fluoride Lithium Battery Cathode at Elevated Temperatures in Polymer Electrolyte Composites. *Nat. Mater.* **2019**, *18*, 1343–1349.
- (54) Park, H.; Lee, Y.; Cho, M.-K.; Kang, J.; Ko, W.; Jung, Y. H.; Jeon, T.-Y.; Hong, J.; Kim, H.; Myung, S.-T.; et al. Na<sub>2</sub>Fe<sub>2</sub>F<sub>7</sub>: a fluoride-based cathode for high power and long life Na-ion batteries. *Energy Environ. Sci.* **2021**, *14*, 1469–1479.
- (55) Xu, J.; Zhang, J.; Pollard, T. P.; Li, Q.; Tan, S.; Hou, S.; Wan, H.; Chen, F.; He, H.; Hu, E.; et al. Electrolyte Design for Li-Ion Batteries under Extreme Operating Conditions. *Nature* **2023**, *614*, 694–700.
- (56) Shannon, R. D. Revised Effective Ionic Radii and Systematic Studies of Interatomic Distances in Halides and Chalcogenides. *Acta Crystallogr. A* **1976**, *32*, 751–767.
- (57) Xu, K. Li-Ion Battery Electrolytes. *Nat. Energy* **2021**, *6*, 763–763.
- (58) Winter, M.; Barnett, B.; Xu, K. Before Li Ion Batteries. *Chem. Rev.* **2018**, *118*, 11433–11456.
- (59) Reddy, M. V.; Mauger, A.; Julien, C. M.; Paoletta, A.; Zaghbi, K. Brief History of Early Lithium-Battery Development. *Materials* **2020**, *13*, 1884.
- (60) Aurbach, D.; Talyosef, Y.; Markovsky, B.; Markevich, E.; Zinigrad, E.; Asraf, L.; Gnanaraj, J. S.; Kim, H.-J. Design of Electrolyte Solutions for Li and Li-Ion Batteries: A Review. *Electrochim. Acta* **2004**, *50*, 247–254.
- (61) Kim, K.; Park, I.; Ha, S.-Y.; Kim, Y.; Woo, M.-H.; Jeong, M.-H.; Shin, W. C.; Ue, M.; Hong, S. Y.; Choi, N.-S. Understanding the Thermal Instability of Fluoroethylene Carbonate in LiPF<sub>6</sub>-Based Electrolytes for Lithium-Ion Batteries. *Electrochim. Acta* **2017**, *225*, 358–368.
- (62) Su, C.-C.; He, M.; Redfern, P. C.; Curtiss, L. A.; Shkrob, I. A.; Zhang, Z. Oxidatively Stable Fluorinated Sulfone Electrolytes for High Voltage High Energy Lithium-Ion Batteries. *Energy Environ. Sci.* **2017**, *10*, 900–904.
- (63) Nambu, N.; Sasaki, Y. Physical and Electrolytic Properties of Monofluorinated Ethyl Acetates and Their Application to Lithium Secondary Batteries. *Open J. Met.* **2015**, *05*, 1–9.
- (64) Bolloli, M.; Kalhoff, J.; Alloin, F.; Bresser, D.; Phung Le, M. L.; Langlois, B.; Passerini, S.; Sanchez, J.-Y. Fluorinated Carbamates as Suitable Solvents for LiTFSI-Based Lithium-Ion Electrolytes: Physicochemical Properties and Electrochemical Characterization. *J. Phys. Chem. C* **2015**, *119*, 22404–22414.
- (65) Meister, P.; Qi, X.; Kloepsch, R.; Kramer, E.; Streipert, B.; Winter, M.; Placke, T. Anodic Behavior of the Aluminum Current Collector in Imide-Based Electrolytes: Influence of Solvent, Operating Temperature, and Native Oxide-Layer Thickness. *ChemSusChem* **2017**, *10*, 804–814.
- (66) He, M.; Hu, L.; Xue, Z.; Su, C. C.; Redfern, P.; Curtiss, L. A.; Polzin, B.; Von Cresce, A.; Xu, K.; Zhang, Z. Fluorinated Electrolytes for 5-V Li-Ion Chemistry: Probing Voltage Stability of Electrolytes with Electrochemical Floating Test. *J. Electrochem. Soc.* **2015**, *162*, A1725–A1729.
- (67) Oldiges, K.; Von Aspern, N.; Cekic-Laskovic, I.; Winter, M.; Brunklaus, G. Impact of Trifluoromethylation of Adiponitrile on Aluminum Dissolution Behavior in Dinitrile-Based Electrolytes. *J. Electrochem. Soc.* **2018**, *165*, A3773–A3781.
- (68) Tornheim, A.; He, M.; Su, C.-C.; Zhang, Z. The Role of Additives in Improving Performance in High Voltage Lithium-Ion Batteries with Potentiostatic Holds. *J. Electrochem. Soc.* **2017**, *164*, A6366–A6372.
- (69) Luo, Y.; Lu, T.; Zhang, Y.; Yan, L.; Xie, J.; Mao, S. S. Enhanced Electrochemical Performance of LiNi<sub>0.5</sub>Mn<sub>1.5</sub>O<sub>4</sub> Cathode Using an Electrolyte with 3-(1,1, 2,2-Tetrafluoroethoxy)-1,1, 2,2-Tetrafluoropropane. *J. Power Sources* **2016**, *323*, 134–141.
- (70) Wang, C.; Tang, S.; Zuo, X.; Xiao, X.; Liu, J.; Nan, J. 3-(1,1,2,2-Tetrafluoroethoxy)-1,1,2,2-Tetrafluoropropane as a High Voltage Solvent for LiNi<sub>1/3</sub>Co<sub>1/3</sub>Mn<sub>1/3</sub>O<sub>2</sub>/Graphite Cells. *J. Electrochem. Soc.* **2015**, *162*, A1997–A2003.
- (71) Lu, J.; Wang, C.; Yu, H.; Gong, S.; Xia, G.; Jiang, P.; Xu, P.; Yang, K.; Chen, Q. Oxygen/Fluorine Dual-Doped Porous Carbon Nanopolyhedra Enabled Ultrafast and Highly Stable Potassium Storage. *Adv. Funct. Mater.* **2019**, *29*, 1906126.



- (72) Nowroozi, M. A.; Wissel, K.; Rohrer, J.; Munnangi, A. R.; Clemens, O. LaSrMnO<sub>4</sub>: Reversible Electrochemical Intercalation of Fluoride Ions in the Context of Fluoride Ion Batteries. *Chem. Mater.* **2017**, *29*, 3441–3453.
- (73) Bhatia, H.; Thieu, D. T.; Pohl, A. H.; Chakravadhanula, V. S. K.; Fawey, M. H.; Kubel, C.; Fichtner, M. Conductivity Optimization of Tysonite-type La<sub>1-x</sub>Ba<sub>x</sub>F<sub>3-x</sub> Solid Electrolytes for Advanced Fluoride Ion Battery. *ACS Appl. Mater. Interfaces* **2017**, *9*, 23707–23715.
- (74) Gschwind, F.; Bastien, J. Parametric Investigation of Room-Temperature Fluoride-Ion Batteries: Assessment of Electrolytes, Mg-Based Anodes, and BiF<sub>3</sub>-Cathodes. *J. Mater. Chem. A* **2015**, *3*, 5628–5634.
- (75) Zhang, L.; Reddy, M. A.; Gao, P.; Diemant, T.; Jürgen Behm, R.; Fichtner, M. Study of All Solid-State Rechargeable Fluoride Ion Batteries Based on Thin-Film Electrolyte. *J. Solid State Electrochem.* **2017**, *21*, 1243–1251.
- (76) Gong, C.; Pu, S. D.; Gao, X.; Yang, S.; Liu, J.; Ning, Z.; Rees, G. J.; Capone, I.; Pi, L.; Liu, B.; et al. Revealing the Role of Fluoride-Rich Battery Electrode Interphases by Operando Transmission Electron Microscopy. *Adv. Energy Mater.* **2021**, *11*, 2003118.
- (77) Seel, J. A.; Dahn, J. R. Electrochemical Intercalation of PF<sub>6</sub><sup>-</sup> into Graphite. *J. Electrochem. Soc.* **2000**, *147*, 892.
- (78) Shi, X.; Zhang, W.; Wang, J.; Zheng, W.; Huang, K.; Zhang, H.; Feng, S.; Chen, H. (EMIm)<sup>+</sup>(PF<sub>6</sub>)<sup>-</sup> Ionic Liquid Unlocks Optimum Energy/Power Density for Architecture of Nanocarbon-Based Dual-Ion Battery. *Adv. Energy Mater.* **2016**, *6*, 1601378.
- (79) Jiang, H.; Han, X.; Du, X.; Chen, Z.; Lu, C.; Li, X.; Zhang, H.; Zhao, J.; Han, P.; Cui, G. A PF<sub>6</sub><sup>-</sup>-Permeable Polymer Electrolyte with Anion Solvation Regulation Enabling Long-Cycle Dual-Ion Battery. *Adv. Mater.* **2022**, *34*, No. e2108665.
- (80) Yang, H.; Qin, T.; Zhou, X.; Feng, Y.; Wang, Z.; Ge, X.; Yue, N.; Li, D.; Zhang, W.; Zheng, W. Boosting the Kinetics of PF<sub>6</sub><sup>-</sup> into Graphitic Layers for the Optimal Cathode of Dual-Ion Batteries: The Rehearsal of Pre-intercalating Li<sup>+</sup>. *J. Energy Chem.* **2022**, *71*, 392–399.
- (81) Placke, T.; Heckmann, A.; Schmich, R.; Meister, P.; Beltrop, K.; Winter, M. Perspective on Performance, Cost, and Technical Challenges for Practical Dual-Ion Batteries. *Joule* **2018**, *2*, 2528–2550.
- (82) Qi, X.; Bliznac, B.; Dupasquier, A.; Meister, P.; Placke, T.; Oljaca, M.; Li, J.; Winter, M. Investigation of PF<sub>6</sub><sup>-</sup> and TFSI<sup>-</sup> Anion Intercalation into Graphitized Carbon Blacks and Its Influence on High Voltage Lithium-Ion Batteries. *Phys. Chem. Chem. Phys.* **2014**, *16*, 25306–25313.
- (83) Aladinli, S.; Bordet, F.; Ahlbrecht, K.; Tübke, J.; Holzapfel, M. Anion Intercalation into a Graphite Cathode from Various Sodium-Based Electrolyte Mixtures for Dual-Ion Battery Applications. *Electrochim. Acta* **2017**, *231*, 468–478.
- (84) Tan, H.; Zhai, D.; Kang, F.; Zhang, B. Synergistic PF<sub>6</sub><sup>-</sup> and FSI<sup>-</sup> Intercalation Enables Stable Graphite Cathode for Potassium-Based Dual Ion Battery. *Carbon* **2021**, *178*, 363–370.
- (85) Kravchik, K. V.; Bhauriyal, P.; Piveteau, L.; Guntlin, C. P.; Pathak, B.; Kovalenko, M. V. High-Energy-Density Dual-Ion Battery for Stationary Storage of Electricity Using Concentrated Potassium Fluorosulfonylimide. *Nat. Commun.* **2018**, *9*, 4469.
- (86) Tong, X.; Ou, X.; Wu, N.; Wang, H.; Li, J.; Tang, Y. High Oxidation Potential ≈6.0 V of Concentrated Electrolyte toward High-Performance Dual-Ion Battery. *Adv. Energy Mater.* **2021**, *11*, 2100151.
- (87) Beltrop, K.; Meister, P.; Klein, S.; Heckmann, A.; Grünebaum, M.; Wiemhöfer, H.-D.; Winter, M.; Placke, T. Does Size really Matter? New Insights into the Intercalation Behavior of Anions into a Graphite-Based Positive Electrode for Dual-Ion Batteries. *Electrochim. Acta* **2016**, *209*, 44–55.
- (88) Hao, J.; Li, X.; Song, X.; Guo, Z. Recent Progress and Perspectives on Dual-Ion Batteries. *EnergyChem.* **2019**, *1*, 100004.
- (89) Zhang, Q.; Pan, J.; Lu, P.; Liu, Z.; Verbrugge, M. W.; Sheldon, B. W.; Cheng, Y. T.; Qi, Y.; Xiao, X. Synergetic Effects of Inorganic Components in Solid Electrolyte Interphase on High Cycle Efficiency of Lithium Ion Batteries. *Nano Lett.* **2016**, *16*, 2011–2016.
- (90) Huang, Y.; Wang, H. How Ethylene Carbonate/γ-Butyrolactone Mixtures Affect BF<sub>4</sub><sup>-</sup> Intercalation into Graphite Electrode. *J. Electrochem. Soc.* **2019**, *166*, A3838–A3843.
- (91) Li, C.; Lao, B.; Li, Z.; Yin, H.; Yang, Z.; Wang, H.; Chen, D.; Zhang, X.; Xu, Y.; Sun, C. Dual-Ion Battery with MoS<sub>2</sub> Cathode. *Energy Storage Mater.* **2020**, *32*, 159–166.
- (92) Carlin, R. T.; De Long, H. C.; Fuller, J.; Trulove, P. C. Dual Intercalating Molten Electrolyte Batteries. *J. Electrochem. Soc.* **1994**, *141*, L73–L76.
- (93) Wang, S.; Jiao, S.; Tian, D.; Chen, H. S.; Jiao, H.; Tu, J.; Liu, Y.; Fang, D. N. A Novel Ultrafast Rechargeable Multi-Ions Battery. *Adv. Mater.* **2017**, *29*, 1606349.
- (94) Liu, C.; Neale, Z. G.; Cao, G. Understanding Electrochemical Potentials of Cathode Materials in Rechargeable Batteries. *Mater. Today* **2016**, *19*, 109–123.
- (95) Hu, Q.; Yu, Z.; Tian, L.; Zhao, Y.; Liu, H.; Lai, C.; Yuan, Z. Porous Anhydrous CuF<sub>2</sub> with a Micro-Nano-Hierarchical Structure as High-Performance Cathode Material for Li-Ion Battery. *J. Mater. Sci.* **2023**, *58*, 10120–10130.
- (96) Xiao, A. W.; Lee, H. J.; Capone, I.; Robertson, A.; Wi, T. U.; Fawdon, J.; Wheeler, S.; Lee, H. W.; Grobert, N.; Pasta, M. Understanding the conversion mechanism and performance of monodisperse FeF<sub>2</sub> nanocrystal cathodes. *Nat. Mater.* **2020**, *19*, 644–654.
- (97) Lee, J.; Kang, B. Superior Electrochemical Performance of N-Doped Nanocrystalline FeF<sub>3</sub>/C with a Single-Step Solid-State Process. *Chem. Commun.* **2016**, *52*, 12100–12103.
- (98) Villa, C.; Kim, S.; Lu, Y.; Dravid, V. P.; Wu, J. Cu-Substituted NiF<sub>2</sub> as a Cathode Material for Li-Ion Batteries. *ACS Appl. Mater. Interfaces* **2019**, *11*, 647–654.
- (99) Wang, X.; Gu, W.; Lee, J. T.; Nitta, N.; Benson, J.; Magasinski, A.; Schauer, M. W.; Yushin, G. Carbon Nanotube-CoF<sub>2</sub> Multifunctional Cathode for Lithium Ion Batteries: Effect of Electrolyte on Cycle Stability. *Small* **2015**, *11*, 5164–5173.
- (100) Groult, H.; Neveu, S.; Leclerc, S.; Porras-Gutierrez, A. G.; Julien, C. M.; Tressaud, A.; Durand, E.; Penin, N.; Labrugere, C. Nano-CoF<sub>3</sub> prepared by direct fluorination with F<sub>2</sub> gas: Application as electrode material in Li-ion battery. *J. Fluor. Chem.* **2017**, *196*, 117–127.
- (101) Rui, K.; Wen, Z.; Lu, Y.; Shen, C.; Jin, J. Anchoring Nanostructured Manganese Fluoride on Few-Layer Graphene Nano-sheets as Anode for Enhanced Lithium Storage. *ACS Appl. Mater. Interfaces* **2016**, *8*, 1819–1826.
- (102) Wang, F.; Kim, S. W.; Seo, D. H.; Kang, K.; Wang, L.; Su, D.; Vajo, J. J.; Wang, J.; Graetz, J. Ternary Metal Fluorides as High-Energy Cathodes with Low Cycling Hysteresis. *Nat. Commun.* **2015**, *6*, 6668.
- (103) Cambaz, M. A.; Vinayan, B. P.; Clemens, O.; Munnangi, A. R.; Chakravadhanula, V. S.; Kubel, C.; Fichtner, M. Vanadium Oxy-fluoride/Few-Layer Graphene Composite as a High-Performance Cathode Material for Lithium Batteries. *Inorg. Chem.* **2016**, *55*, 3789–3796.
- (104) Ni, D.; Sun, W.; Xie, L.; Fan, Q.; Wang, Z.; Sun, K. Bismuth Oxyfluoride @ CMK-3 Nanocomposite as Cathode for Lithium Ion Batteries. *J. Power Sources* **2018**, *374*, 166–174.
- (105) Kitajou, A.; Komatsu, H.; Nagano, R.; Okada, S. Synthesis of FeOF Using Roll-Quenching Method and the Cathode Properties for Lithium-Ion Battery. *J. Power Sources* **2013**, *243*, 494–498.
- (106) Louvain, N.; Karkar, Z.; El-Ghozzi, M.; Bonnet, P.; Guérin, K.; Willmann, P. Fluorination of Anatase TiO<sub>2</sub> Towards Titanium Oxyfluoride TiOF<sub>2</sub>: A Novel Synthesis Approach and Proof of the Li-Insertion Mechanism. *J. Mater. Chem. A* **2014**, *2*, 15308–15315.
- (107) Reddy, M. V.; Madhavi, S.; Subba Rao, G. V.; Chowdari, B. V. R. Metal Oxyfluorides TiOF<sub>2</sub> and NbO<sub>2</sub>F as Anodes for Li-Ion Batteries. *J. Power Sources* **2006**, *162*, 1312–1321.
- (108) Hua, X.; Eggeman, A. S.; Castillo-Martinez, E.; Robert, R.; Geddes, H. S.; Lu, Z.; Pickard, C. J.; Meng, W.; Wiaderek, K. M.; Pereira, N.; et al. Revisiting Metal Fluorides as Lithium-Ion Battery Cathodes. *Nat. Mater.* **2021**, *20*, 841–850.

- (109) Liu, L.; Guo, H.; Zhou, M.; Wei, Q.; Yang, Z.; Shu, H.; Yang, X.; Tan, J.; Yan, Z.; Wang, X. A Comparison among  $\text{FeF}_3 \cdot 3\text{H}_2\text{O}$ ,  $\text{FeF}_3 \cdot 0.33\text{H}_2\text{O}$  and  $\text{FeF}_3$  Cathode Materials for Lithium Ion Batteries: Structural, Electrochemical, and Mechanism Studies. *J. Power Sources* **2013**, *238*, 501–515.
- (110) Lemoine, K.; Zhang, L.; Dambournet, D.; Grenèche, J.-M.; Hémon-Ribaud, A.; Leblanc, M.; Borkiewicz, O. J.; Tarascon, J.-M.; Maisonneuve, V.; Lhoste, J. Synthesis by Thermal Decomposition of Two Iron Hydroxyfluorides: Structural Effects of Li Insertion. *Chem. Mater.* **2019**, *31*, 4246–4257.
- (111) Fan, X.; Hu, E.; Ji, X.; Zhu, Y.; Han, F.; Hwang, S.; Liu, J.; Bak, S.; Ma, Z.; Gao, T.; et al. High Energy-Density and Reversibility of Iron Fluoride Cathode Enabled via an Intercalation-Extrusion Reaction. *Nat. Commun.* **2018**, *9*, 2324.
- (112) Jung, S.-K.; Kim, H.; Cho, M. G.; Cho, S.-P.; Lee, B.; Kim, H.; Park, Y.-U.; Hong, J.; Park, K.-Y.; Yoon, G.; et al. Lithium-Free Transition Metal Monoxides for Positive Electrodes in Lithium-Ion Batteries. *Nat. Energy* **2017**, *2*, 16208.
- (113) Deng, D. Transition Metal Oxyfluorides for Next-Generation Rechargeable Batteries. *ChemNanoMat* **2017**, *3*, 146–159.
- (114) Sorensen, E. M.; Izumi, H. K.; Vaughey, J. T.; Stern, C. L.; Poeppelmeier, K. R.  $\text{Ag}_4\text{V}_2\text{O}_6\text{F}_2$ : An Electrochemically Active and High Silver Density Phase. *J. Am. Chem. Soc.* **2005**, *127*, 6347–6352.
- (115) Kim, M.; Lee, S.; Kang, B. Fast-Rate Capable Electrode Material with Higher Energy Density than  $\text{LiFePO}_4$ :  $4.2\text{V LiVPO}_4\text{F}$  Synthesized by Scalable Single-Step Solid-State Reaction. *Adv. Sci.* **2016**, *3*, 1500366.
- (116) Heo, J.; Jung, S.-K.; Hwang, I.; Cho, S.-P.; Eum, D.; Park, H.; Song, J.-H.; Yu, S.; Oh, K.; Kwon, G.; et al. Amorphous Iron Fluorosulfate as a High-Capacity Cathode Utilizing Combined Intercalation and Conversion Reactions with Unexpectedly High Reversibility. *Nat. Energy* **2023**, *8*, 30–39.
- (117) Jin, T.; Li, H.; Zhu, K.; Wang, P. F.; Liu, P.; Jiao, L. Polyanion-Type Cathode Materials for Sodium-Ion Batteries. *Chem. Soc. Rev.* **2020**, *49*, 2342–2377.
- (118) Recham, N.; Chotard, J. N.; Dupont, L.; Delacourt, C.; Walker, W.; Armand, M.; Tarascon, J. M. A 3.6 V Lithium-Based Fluorosulphate Insertion Positive Electrode for Lithium-Ion Batteries. *Nat. Mater.* **2010**, *9*, 68–74.
- (119) Barpanda, P.; Ati, M.; Melot, B. C.; Rousse, G.; Chotard, J. N.; Doublet, M. L.; Sougrati, M. T.; Corr, S. A.; Jumas, J. C.; Tarascon, J. M. A 3.90 V Iron-Based Fluorosulphate Material for Lithium-Ion Batteries Crystallizing in the Triplite Structure. *Nat. Mater.* **2011**, *10*, 772–779.
- (120) Andersson, A. M.; Abraham, D. P.; Haasch, R.; Maclaren, S.; Liu, J.; Amine, K. Surface Characterization of Electrodes from High Power Lithium-Ion Batteries. *J. Electrochem. Soc.* **2002**, *149*, A1358.
- (121) Rosina, K. J.; Jiang, M.; Zeng, D.; Salager, E.; Best, A. S.; Grey, C. P. Structure of Aluminum Fluoride Coated  $\text{Li}[\text{Li}_{1/9}\text{Ni}_{1/3}\text{Mn}_{5/9}]\text{O}_2$  Cathodes for Secondary Lithium-Ion Batteries. *J. Mater. Chem.* **2012**, *22*, 20602.
- (122) Lu, C.; Wu, H.; Zhang, Y.; Liu, H.; Chen, B.; Wu, N.; Wang, S. Cerium Fluoride Coated Layered Oxide  $\text{Li}_{1.2}\text{Mn}_{0.54}\text{Ni}_{0.13}\text{Co}_{0.13}\text{O}_2$  as Cathode Materials with Improved Electrochemical Performance for Lithium-Ion Batteries. *J. Power Sources* **2014**, *267*, 682–691.
- (123) Lee, J.; Kitchaev, D. A.; Kwon, D. H.; Lee, C. W.; Papp, J. K.; Liu, Y. S.; Lun, Z.; Clement, R. J.; Shi, T.; McCloskey, B. D.; et al. Reversible  $\text{Mn}^{2+}/\text{Mn}^{4+}$  Double Redox in Lithium-Excess Cathode Materials. *Nature* **2018**, *556*, 185–190.
- (124) Li, L.; Ahn, J.; Yue, Y.; Tong, W.; Chen, G.; Wang, C. Fluorination-Enhanced Surface Stability of Disordered Rocksalt Cathodes. *Adv. Mater.* **2022**, *34*, No. e2106256.
- (125) Bieker, P.; Winter, M. Lithium-Ionen-Technologie und Was Danach Kommen Könnte. *Chemie Unserer Zeit* **2016**, *50*, 172–186.
- (126) Barlow, C. G. Reaction of Water with Hexafluorophosphates and with Li Bis(perfluoroethylsulfonyl)imide Salt. *Electrochem. Solid-State Lett.* **1999**, *2*, 362.
- (127) Matsumoto, K.; Inoue, K.; Nakahara, K.; Yuge, R.; Noguchi, T.; Utsugi, K. Suppression of Aluminum Corrosion by Using High Concentration LiTFSI Electrolyte. *J. Power Sources* **2013**, *231*, 234–238.
- (128) Lohmann, R.; Cousins, I. T.; Dewitt, J. C.; Gluge, J.; Goldenman, G.; Herzke, D.; Lindstrom, A. B.; Miller, M. F.; Ng, C. A.; Patton, S.; et al. Are Fluoropolymers Really of Low Concern for Human and Environmental Health a Separate from Other PFAS? *Environ. Sci. Technol.* **2020**, *54*, 12820–12828.
- (129) Xia, Y.; Zhou, P.; Kong, X.; Tian, J.; Zhang, W.; Yan, S.; Hou, W.-H.; Zhou, H.-Y.; Dong, H.; Chen, X.; et al. Designing an Asymmetric Ether-Like Lithium Salt to Enable Fast-Cycling High-Energy Lithium Metal Batteries. *Nat. Energy* **2023**, *8*, 934–945.
- (130) Von Aspern, N.; Roschenthaler, G. V.; Winter, M.; Cekic-Laskovic, I. Fluorine and Lithium: Ideal Partners for High-Performance Rechargeable Battery Electrolytes. *Angew. Chem., Int. Ed.* **2019**, *58*, 15978–16000.
- (131) Nakajima, T. Fluorine Compounds as Energy Conversion Materials. *J. Fluor. Chem.* **2013**, *149*, 104–111.
- (132) Suo, L.; Hu, Y. S.; Li, H.; Armand, M.; Chen, L. A New Class of Solvent-in-Salt Electrolyte for High-Energy Rechargeable Metallic Lithium Batteries. *Nat. Commun.* **2013**, *4*, 1481.
- (133) Kim, H.; Hong, J.; Park, K. Y.; Kim, H.; Kim, S. W.; Kang, K. Aqueous Rechargeable Li and Na Ion Batteries. *Chem. Rev.* **2014**, *114*, 11788–11827.
- (134) Wang, Y.; Yi, J.; Xia, Y. Recent Progress in Aqueous Lithium-Ion Batteries. *Adv. Energy Mater.* **2012**, *2*, 830–840.
- (135) Suo, L.; Borodin, O.; Gao, T.; Olguin, M.; Ho, J.; Fan, X.; Luo, C.; Wang, C.; Xu, K. “Water-in-Salt” Electrolyte Enables High-Voltage Aqueous Lithium-Ion Chemistries. *Science* **2015**, *350*, 938–943.
- (136) Yamada, Y.; Chiang, C. H.; Sodeyama, K.; Wang, J.; Tateyama, Y.; Yamada, A. Corrosion Prevention Mechanism of Aluminum Metal in Superconcentrated Electrolytes. *ChemElectroChem.* **2015**, *2*, 1687–1694.
- (137) Zheng, J.; Fan, X.; Ji, G.; Wang, H.; Hou, S.; Demella, K. C.; Raghavan, S. R.; Wang, J.; Xu, K.; Wang, C. Manipulating Electrolyte and Solid Electrolyte Interphase to Enable Safe and Efficient Li-S Batteries. *Nano Energy* **2018**, *50*, 431–440.
- (138) Diederichsen, K. M.; Mcshane, E. J.; McCloskey, B. D. Promising Routes to a High  $\text{Li}^+$  Transference Number Electrolyte for Lithium Ion Batteries. *ACS Energy Lett.* **2017**, *2*, 2563–2575.
- (139) Yamada, Y.; Wang, J.; Ko, S.; Watanabe, E.; Yamada, A. Advances and Issues in Developing Salt-Concentrated Battery Electrolytes. *Nat. Energy* **2019**, *4*, 269–280.
- (140) Pei, Z.; Gu, J.; Wang, Y.; Tang, Z.; Liu, Z.; Huang, Y.; Huang, Y.; Zhao, J.; Chen, Z.; Zhi, C. Component Matters: Paving the Roadmap toward Enhanced Electrocatalytic Performance of Graphitic  $\text{C}_3\text{N}_4$ -Based Catalysts via Atomic Tuning. *ACS Nano* **2017**, *11*, 6004–6014.
- (141) Jeong, S.-K.; Inaba, M.; Iriyama, Y.; Abe, T.; Ogumi, Z. Interfacial Reactions between Graphite Electrodes and Propylene Carbonate-Based Solutions: Electrolyte-Concentration Dependence of Electrochemical Lithium Intercalation Reaction. *J. Power Sources* **2008**, *175*, 540–546.
- (142) Jeong, S.-K.; Seo, H.-Y.; Kim, D.-H.; Han, H.-K.; Kim, J.-G.; Lee, Y. B.; Iriyama, Y.; Abe, T.; Ogumi, Z. Suppression of Dendritic Lithium Formation by Using Concentrated Electrolyte Solutions. *Electrochem. Commun.* **2008**, *10*, 635–638.
- (143) Yamada, Y.; Takazawa, Y.; Miyazaki, K.; Abe, T. Electrochemical Lithium Intercalation into Graphite in Dimethyl Sulfoxide-Based Electrolytes: Effect of Solvation Structure of Lithium Ion. *J. Phys. Chem. C* **2010**, *114*, 11680–11685.
- (144) Yamada, Y.; Furukawa, K.; Sodeyama, K.; Kikuchi, K.; Yaegashi, M.; Tateyama, Y.; Yamada, A. Unusual Stability of Acetonitrile-Based Superconcentrated Electrolytes for Fast-Charging Lithium-Ion Batteries. *J. Am. Chem. Soc.* **2014**, *136*, 5039–5046.
- (145) Yamada, Y.; Usui, K.; Chiang, C. H.; Kikuchi, K.; Furukawa, K.; Yamada, A. General Observation of Lithium Intercalation into Graphite in Ethylene-Carbonate-Free Superconcentrated Electrolytes. *ACS Appl. Mater. Interfaces* **2014**, *6*, 10892–10899.

- (146) Qian, J.; Henderson, W. A.; Xu, W.; Bhattacharya, P.; Engelhard, M.; Borodin, O.; Zhang, J. G. High Rate and Stable Cycling of Lithium Metal Anode. *Nat. Commun.* **2015**, *6*, 6362.
- (147) Mcowen, D. W.; Seo, D. M.; Borodin, O.; Vatamanu, J.; Boyle, P. D.; Henderson, W. A. Concentrated Electrolytes: Decrypting Electrolyte Properties and Reassessing Al Corrosion Mechanisms. *Energy Environ. Sci.* **2014**, *7*, 416–426.
- (148) Möller, K. C.; Hodal, T.; Appel, W. K.; Winter, M.; Besenhard, J. O. Fluorinated Organic Solvents in Electrolytes for Lithium Ion Cells. *J. Power Sources* **2001**, *97–98*, S95–S97.
- (149) Qin, M.; Zeng, Z.; Wu, Q.; Yan, H.; Liu, M.; Wu, Y.; Zhang, H.; Lei, S.; Cheng, S.; Xie, J. Dipole-Dipole Interactions for Inhibiting Solvent Co-intercalation into a Graphite Anode to Extend the Horizon of Electrolyte Design. *Energy Environ. Sci.* **2023**, *16*, 546–556.
- (150) Yu, Z.; Rudnicki, P. E.; Zhang, Z.; Huang, Z.; Celik, H.; Oyakhire, S. T.; Chen, Y.; Kong, X.; Kim, S. C.; Xiao, X.; et al. Rational Solvent Molecule Tuning for High-Performance Lithium Metal Battery Electrolytes. *Nat. Energy* **2022**, *7*, 94–106.
- (151) Lee, S.; Park, K.; Koo, B.; Park, C.; Jang, M.; Lee, H.; Lee, H. Safe, Stable Cycling of Lithium Metal Batteries with Low-Viscosity, Fire-Retardant Locally Concentrated Ionic Liquid Electrolytes. *Adv. Funct. Mater.* **2020**, *30*, 2003132.
- (152) Yang, Y.; Davies, D. M.; Yin, Y.; Borodin, O.; Lee, J. Z.; Fang, C.; Olguin, M.; Zhang, Y.; Sablina, E. S.; Wang, X.; et al. High-Efficiency Lithium-Metal Anode Enabled by Liquefied Gas Electrolytes. *Joule* **2019**, *3*, 1986–2000.
- (153) Smart, M. C.; Ratnakumar, B. V.; Surampudi, S. Use of Organic Esters as Cosolvents in Electrolytes for Lithium-Ion Batteries with Improved Low Temperature Performance. *J. Electrochem. Soc.* **2002**, *149*, A361.
- (154) Dong, X.; Guo, Z.; Guo, Z.; Wang, Y.; Xia, Y. Organic Batteries Operated at  $-70^{\circ}\text{C}$ . *Joule* **2018**, *2*, 902–913.
- (155) Liang, H. J.; Gu, Z. Y.; Zhao, X. X.; Guo, J. Z.; Yang, J. L.; Li, W. H.; Li, B.; Liu, Z. M.; Sun, Z. H.; Zhang, J. P.; et al. Advanced Flame-Retardant Electrolyte for Highly Stabilized K-ion Storage in Graphite Anode. *Sci. Bull.* **2022**, *67*, 1581–1588.
- (156) Dokko, K.; Tachikawa, N.; Yamauchi, K.; Tsuchiya, M.; Yamazaki, A.; Takashima, E.; Park, J.-W.; Ueno, K.; Seki, S.; Serizawa, N.; et al. Solvate Ionic Liquid Electrolyte for Li-S Batteries. *J. Electrochem. Soc.* **2013**, *160*, A1304–A1310.
- (157) Chen, S.; Zheng, J.; Mei, D.; Han, K. S.; Engelhard, M. H.; Zhao, W.; Xu, W.; Liu, J.; Zhang, J. G. High-Voltage Lithium-Metal Batteries Enabled by Localized High-Concentration Electrolytes. *Adv. Mater.* **2018**, *30*, No. e1706102.
- (158) Lin, S.; Hua, H.; Lai, P.; Zhao, J. A Multifunctional Dual-Salt Localized High-Concentration Electrolyte for Fast Dynamic High-Voltage Lithium Battery in Wide Temperature Range. *Adv. Energy Mater.* **2021**, *11*, 2101775.
- (159) Chen, X.; Qin, L.; Sun, J.; Zhang, S.; Xiao, D.; Wu, Y. Phase Transfer-Mediated Degradation of Ether-Based Localized High-Concentration Electrolytes in Alkali Metal Batteries. *Angew. Chem., Int. Ed.* **2022**, *61*, No. e202207018.
- (160) Zhu, C.; Sun, C.; Li, R.; Weng, S.; Fan, L.; Wang, X.; Chen, L.; Noked, M.; Fan, X. Anion-Diluent Pairing for Stable High-Energy Li Metal Batteries. *ACS Energy Lett.* **2022**, *7*, 1338–1347.
- (161) Wu, Y.; Wang, A.; Hu, Q.; Liang, H.; Xu, H.; Wang, L.; He, X. Significance of Antisolvents on Solvation Structures Enhancing Interfacial Chemistry in Localized High-Concentration Electrolytes. *ACS Cent. Sci.* **2022**, *8*, 1290–1298.
- (162) Ding, J. F.; Xu, R.; Yao, N.; Chen, X.; Xiao, Y.; Yao, Y. X.; Yan, C.; Xie, J.; Huang, J. Q. Non-Solvating and Low-Dielectricity Cosolvent for Anion-Derived Solid Electrolyte Interphases in Lithium Metal Batteries. *Angew. Chem., Int. Ed.* **2021**, *60*, 11442–11447.
- (163) Kim, S. C.; Kong, X.; Vila, R. A.; Huang, W.; Chen, Y.; Boyle, D. T.; Yu, Z.; Wang, H.; Bao, Z.; Qin, J.; et al. Potentiometric Measurement to Probe Solvation Energy and Its Correlation to Lithium Battery Cyclability. *J. Am. Chem. Soc.* **2021**, *143*, 10301–10308.
- (164) Piao, N.; Ji, X.; Xu, H.; Fan, X.; Chen, L.; Liu, S.; Garaga, M. N.; Greenbaum, S. G.; Wang, L.; Wang, C.; et al. Countersolvent Electrolytes for Lithium-Metal Batteries. *Adv. Energy Mater.* **2020**, *10*, 1903568.
- (165) Zhang, Q. K.; Zhang, X. Q.; Hou, L. P.; Sun, S. Y.; Zhan, Y. X.; Liang, J. L.; Zhang, F. S.; Feng, X. N.; Li, B. Q.; Huang, J. Q. Regulating Solvation Structure in Nonflammable Amide-Based Electrolytes for Long-Cycling and Safe Lithium Metal Batteries. *Adv. Energy Mater.* **2022**, *12*, 2200139.
- (166) Meng, Y.; Zhou, D.; Liu, R.; Tian, Y.; Gao, Y.; Wang, Y.; Sun, B.; Kang, F.; Armand, M.; Li, B.; et al. Designing Phosphazene-Derivative Electrolyte Matrices to Enable High-Voltage Lithium Metal Batteries for Extreme Working Conditions. *Nat. Energy* **2023**, *8*, 1023–1033.
- (167) Xu, K. Nonaqueous Liquid Electrolytes for Lithium-Based Rechargeable Batteries. *Chem. Rev.* **2004**, *104*, 4303–4417.
- (168) Zhang, X.-Q.; Cheng, X.-B.; Chen, X.; Yan, C.; Zhang, Q. Fluoroethylene Carbonate Additives to Render Uniform Li Deposits in Lithium Metal Batteries. *Adv. Funct. Mater.* **2017**, *27*, 1605989.
- (169) Okuno, Y.; Ushirogata, K.; Sodeyama, K.; Tateyama, Y. Decomposition of the Fluoroethylene Carbonate Additive and the Glue Effect of Lithium Fluoride Products for the Solid Electrolyte Interphase: An Ab Initio Study. *Phys. Chem. Chem. Phys.* **2016**, *18*, 8643–8653.
- (170) Choudhury, S.; Archer, L. A. Lithium Fluoride Additives for Stable Cycling of Lithium Batteries at High Current Densities. *Adv. Electron. Mater.* **2016**, *2*, 1500246.
- (171) Ma, Y.; Zhou, Z.; Li, C.; Wang, L.; Wang, Y.; Cheng, X.; Zuo, P.; Du, C.; Huo, H.; Gao, Y.; et al. Enabling Reliable Lithium Metal Batteries by a Bifunctional Anionic Electrolyte Additive. *Energy Storage Mater.* **2018**, *11*, 197–204.
- (172) Lee, Y.-M.; Nam, K.-M.; Hwang, E.-H.; Kwon, Y.-G.; Kang, D.-H.; Kim, S.-S.; Song, S.-W. Interfacial Origin of Performance Improvement and Fade for 4.6 V  $\text{LiNi}_{0.5}\text{Co}_{0.2}\text{Mn}_{0.3}\text{O}_2$  Battery Cathodes. *J. Phys. Chem. C* **2014**, *118*, 10631–10639.
- (173) Wang, X.; Liao, X.; Huang, W.; Xing, L.; Liao, Y.; Huang, Q.; Xu, M.; Li, W. Improved Cyclic Stability of Layered Lithium Cobalt Oxide at High Potential via Cathode Electrolyte Interphase Formed by 4-(Trifluoromethyl) Benzonitrile. *Electrochim. Acta* **2015**, *184*, 94–101.
- (174) Doughty, D. H.; Roth, E. P.; Crafts, C. C.; Nagasubramanian, G.; Henriksen, G.; Amine, K. Effects of Additives on Thermal Stability of Li Ion Cells. *J. Power Sources* **2005**, *146*, 116–120.
- (175) Zhang, S. S.; Xu, K.; Jow, T. R. Tris(2,2, 2-Trifluoroethyl) Phosphite as a Co-solvent for Nonflammable Electrolytes in Li-Ion Batteries. *J. Power Sources* **2003**, *113*, 166–172.
- (176) Li, Y.; An, Y.; Tian, Y.; Fei, H.; Xiong, S.; Qian, Y.; Feng, J. Stable and Safe Lithium Metal Batteries with Ni-Rich Cathodes Enabled by a High Efficiency Flame Retardant Additive. *J. Electrochem. Soc.* **2019**, *166*, A2736–A2740.
- (177) Liu, J.; Song, X.; Zhou, L.; Wang, S.; Song, W.; Liu, W.; Long, H.; Zhou, L.; Wu, H.; Feng, C.; et al. Fluorinated Phosphazene Derivative - a Promising Electrolyte Additive for High Voltage Lithium Ion Batteries: From Electrochemical Performance to Corrosion Mechanism. *Nano Energy* **2018**, *46*, 404–414.
- (178) Ji, Y.; Zhang, P.; Lin, M.; Zhao, W.; Zhang, Z.; Zhao, Y.; Yang, Y. Toward a Stable Electrochemical Interphase with Enhanced Safety on High-Voltage  $\text{LiCoO}_2$  Cathode: A Case of Phosphazene Additives. *J. Power Sources* **2017**, *359*, 391–399.
- (179) Casselman, M. D.; Kaur, A. P.; Narayana, K. A.; Elliott, C. F.; Risko, C.; Odom, S. A. The Fate of Phenothiazine-Based Redox Shuttles in Lithium-Ion Batteries. *Phys. Chem. Chem. Phys.* **2015**, *17*, 6905–6912.
- (180) Kaur, A. P.; Casselman, M. D.; Elliott, C. F.; Parkin, S. R.; Risko, C.; Odom, S. A. Overcharge Protection of Lithium-Ion Batteries above 4 V with a Perfluorinated Phenothiazine Derivative. *J. Mater. Chem. A* **2016**, *4*, 5410–5414.
- (181) Beichel, W.; Klose, P.; Blattmann, H.; Hoecker, J.; Kratzert, D.; Krossing, I. Simple Green Synthesis and Electrochemical



Performance of a New Fluorinated Carbonate as Additive for Lithium-Ion Batteries. *ChemElectroChem*. **2018**, *5*, 1415–1420.

(182) Hu, J.; Chen, K.; Li, C. Nanostructured Li-Rich Fluoride Coated by Ionic Liquid as High Ion-Conductivity Solid Electrolyte Additive to Suppress Dendrite Growth at Li Metal Anode. *ACS Appl. Mater. Interfaces* **2018**, *10*, 34322–34331.

(183) Li, Q.; Xue, W.; Sun, X.; Yu, X.; Li, H.; Chen, L. Gaseous Electrolyte Additive BF<sub>3</sub> for High-Power Li/CF<sub>x</sub> Primary Batteries. *Energy Storage Mater.* **2021**, *38*, 482–488.

(184) Xue, W.; Huang, M.; Li, Y.; Zhu, Y. G.; Gao, R.; Xiao, X.; Zhang, W.; Li, S.; Xu, G.; Yu, Y.; et al. Ultra-High-Voltage Ni-Rich Layered Cathodes in Practical Li Metal Batteries Enabled by a Sulfonamide-Based Electrolyte. *Nat. Energy* **2021**, *6*, 495–505.

(185) Zhao, Q.; Stalin, S.; Archer, L. A. Stabilizing Metal Battery Anodes through the Design of Solid Electrolyte Interphases. *Joule* **2021**, *5*, 1119–1142.

(186) Jiang, F. N.; Cheng, X. B.; Yang, S. J.; Xie, J.; Yuan, H.; Liu, L.; Huang, J. Q.; Zhang, Q. Thermoresponsive Electrolytes for Safe Lithium-Metal Batteries. *Adv. Mater.* **2023**, *35*, No. e2209114.

(187) Xia, L.; Xia, Y.; Liu, Z. A Novel Fluorocyclophosphazene as Bifunctional Additive for Safer Lithium-Ion Batteries. *J. Power Sources* **2015**, *278*, 190–196.

(188) Zhang, S. S.; Xu, K.; Jow, T. R. A Thermal Stabilizer for LiPF<sub>6</sub>-Based Electrolytes of Li-Ion Cells. *Electrochem. Solid-State Lett.* **2002**, *5*, A206–A208.

(189) Buhrmester, C.; Chen, J.; Moshurchak, L.; Jiang, J.; Wang, R. L.; Dahn, J. R. Studies of Aromatic Redox Shuttle Additives for LiFePO<sub>4</sub>-Based Li-Ion Cells. *J. Electrochem. Soc.* **2005**, *152*, A2390.

(190) Chen, J.; Buhrmester, C.; Dahn, J. R. Chemical Overcharge and Overdischarge Protection for Lithium-Ion Batteries. *Electrochem. Solid-State Lett.* **2005**, *8*, A59–A62.

(191) Wang, Y.; Li, Z.; Hou, Y.; Hao, Z.; Zhang, Q.; Ni, Y.; Lu, Y.; Yan, Z.; Zhang, K.; Zhao, Q.; et al. Emerging Electrolytes with Fluorinated Solvents for Rechargeable Lithium-Based Batteries. *Chem. Soc. Rev.* **2023**, *52*, 2713–2763.

(192) Hall, D. S.; Self, J.; Dahn, J. R. Dielectric Constants for Quantum Chemistry and Li-Ion Batteries: Solvent Blends of Ethylene Carbonate and Ethyl Methyl Carbonate. *J. Phys. Chem. C* **2015**, *119*, 22322–22330.

(193) Meyer, W. H. Polymer Electrolytes for Lithium-Ion Batteries. *Adv. Mater.* **1998**, *10*, 439–448.

(194) Young, W.-S.; Albert, J. N. L.; Schantz, A. B.; Epps, T. H. Mixed-Salt Effects on the Ionic Conductivity of Lithium-Doped PEO-Containing Block Copolymers. *Macromolecules* **2011**, *44*, 8116–8123.

(195) Su, Y.; Rong, X.; Gao, A.; Liu, Y.; Li, J.; Mao, M.; Qi, X.; Chai, G.; Zhang, Q.; Suo, L.; et al. Rational Design of a Topological Polymeric Solid Electrolyte for High-Performance All-Solid-State Alkali Metal Batteries. *Nat. Commun.* **2022**, *13*, 4181.

(196) Sun, Y.; Zhang, X.; Ma, C.; Guo, N.; Liu, Y.; Liu, J.; Xie, H. Fluorine-Containing Triblock Copolymers as Solid-State Polymer Electrolytes for Lithium Metal Batteries. *J. Power Sources* **2021**, *516*, 230686.

(197) Jia, M.; Wen, P.; Wang, Z.; Zhao, Y.; Liu, Y.; Lin, J.; Chen, M.; Lin, X. Fluorinated Bifunctional Solid Polymer Electrolyte Synthesized under Visible Light for Stable Lithium Deposition and Dendrite-Free All-Solid-State Batteries. *Adv. Funct. Mater.* **2021**, *31*, 2101736.

(198) Sun, H.; Xie, X.; Huang, Q.; Wang, Z.; Chen, K.; Li, X.; Gao, J.; Li, Y.; Li, H.; Qiu, J.; et al. Fluorinated Poly-oxalate Electrolytes Stabilizing both Anode and Cathode Interfaces for All-Solid-State Li/NMC811 Batteries. *Angew. Chem., Int. Ed.* **2021**, *60*, 18335–18343.

(199) Shi, P.; Ma, J.; Liu, M.; Guo, S.; Huang, Y.; Wang, S.; Zhang, L.; Chen, L.; Yang, K.; Liu, X.; et al. A Dielectric Electrolyte Composite with High Lithium-Ion Conductivity for High-Voltage Solid-State Lithium Metal Batteries. *Nat. Nanotechnol.* **2023**, *18*, 602–610.

(200) Tsuchida, E.; Ohno, H.; Tsunemi, K. Conduction of Lithium Ions in Polyvinylidene Fluoride and Its Derivatives—I. *Electrochim. Acta* **1983**, *28*, 591–595.

(201) Jiang, Z.; Carroll, B.; Abraham, K. M. Studies of Some Poly(vinylidene fluoride) Electrolytes. *Electrochim. Acta* **1997**, *42*, 2667–2677.

(202) Feinauer, M.; Euchner, H.; Fichtner, M.; Reddy, M. A. Unlocking the Potential of Fluoride-Based Solid Electrolytes for Solid-State Lithium Batteries. *ACS Appl. Energy Mater.* **2019**, *2*, 7196–7203.

(203) Hu, J.; Yao, Z.; Chen, K.; Li, C. High-Conductivity Open Framework Fluorinated Electrolyte Bonded by Solidified Ionic Liquid Wires for Solid-State Li Metal Batteries. *Energy Storage Mater.* **2020**, *28*, 37–46.

(204) Zhang, B.; Zhong, J.; Zhang, Y.; Yang, L.; Yang, J.; Li, S.; Wang, L.-W.; Pan, F.; Lin, Z. Discovering a New Class of Fluoride Solid-Electrolyte Materials via Screening the Structural Property of Li-Ion Sublattice. *Nano Energy* **2021**, *79*, 105407.

(205) Arnold, W.; Shreyas, V.; Li, Y.; Koralalage, M. K.; Jasinski, J. B.; Thapa, A.; Sumanasekera, G.; Ngo, A. T.; Narayanan, B.; Wang, H. Synthesis of Fluorine-Doped Lithium Argyrodite Solid Electrolytes for Solid-State Lithium Metal Batteries. *ACS Appl. Mater. Interfaces* **2022**, *14*, 11483–11492.

(206) Li, X.; Ren, Z.; Norouzi Banis, M.; Deng, S.; Zhao, Y.; Sun, Q.; Wang, C.; Yang, X.; Li, W.; Liang, J.; et al. Unravelling the Chemistry and Microstructure Evolution of a Cathodic Interface in Sulfide-Based All-Solid-State Li-Ion Batteries. *ACS Energy Lett.* **2019**, *4*, 2480–2488.

(207) Ryu, H.-H.; Namkoong, B.; Kim, J.-H.; Belharouak, I.; Yoon, C. S.; Sun, Y.-K. Capacity Fading Mechanisms in Ni-Rich Single-Crystal NCM Cathodes. *ACS Energy Lett.* **2021**, *6*, 2726–2734.

(208) Wan, H.; Zhang, J.; Xia, J.; Ji, X.; He, X.; Liu, S.; Wang, C. F. and N Rich Solid Electrolyte for Stable All-Solid-State Battery. *Adv. Funct. Mater.* **2022**, *32*, 2110876.

(209) Zhao, F.; Sun, Q.; Yu, C.; Zhang, S.; Adair, K.; Wang, S.; Liu, Y.; Zhao, Y.; Liang, J.; Wang, C.; et al. Ultrastable Anode Interface Achieved by Fluorinating Electrolytes for All-Solid-State Li Metal Batteries. *ACS Energy Lett.* **2020**, *5*, 1035–1043.

(210) Liu, J.; Wang, J.; Zhu, L.; Chen, X.; Ma, Q.; Wang, L.; Wang, X.; Yan, W. A High-Safety and Multifunctional MOFs Modified Aramid Nanofiber Separator for Lithium-Sulfur Batteries. *Chem. Eng. J.* **2021**, *411*, 128540.

(211) Feng, X.; Ren, D.; He, X.; Ouyang, M. Mitigating Thermal Runaway of Lithium-Ion Batteries. *Joule* **2020**, *4*, 743–770.

(212) Choi, S.-S.; Lee, Y. S.; Joo, C. W.; Lee, S. G.; Park, J. K.; Han, K.-S. Electrospun PVDF Nanofiber Web as Polymer Electrolyte or Separator. *Electrochim. Acta* **2004**, *50*, 339–343.

(213) Liang, Y.; Lin, Z.; Qiu, Y.; Zhang, X. Fabrication and Characterization of LATP/PAN Composite Fiber-Based Lithium-Ion Battery Separators. *Electrochim. Acta* **2011**, *56*, 6474–6480.

(214) Lee, P.-C.; Han, T.-H.; Hwang, T.; Oh, J.-S.; Kim, S.-J.; Kim, B.-W.; Lee, Y.; Choi, H. R.; Jeoung, S. K.; Yoo, S. E.; et al. Electrochemical Double Layer Capacitor Performance of Electrospun Polymer Fiber-Electrolyte Membrane Fabricated by Solvent-Assisted and Thermally Induced Compression Molding Processes. *J. Membr. Sci.* **2012**, *409–410*, 365–370.

(215) Kim, Y.-J.; Kim, H.-S.; Doh, C.-H.; Kim, S. H.; Lee, S.-M. Technological Potential and Issues of Polyacrylonitrile Based Nanofiber Non-woven Separator for Li-Ion Rechargeable Batteries. *J. Power Sources* **2013**, *244*, 196–206.

(216) Cai, M.; Yuan, D.; Zhang, X.; Pu, Y.; Liu, X.; He, H.; Zhang, L.; Ning, X. Lithium Ion Battery Separator with Improved Performance via Side-by-Side Bicomponent Electrospinning of PVDF-HFP/PI Followed by 3D Thermal Crosslinking. *J. Power Sources* **2020**, *461*, 228123.

(217) Hwang, K.; Kwon, B.; Byun, H. Preparation of PVdF Nanofiber Membranes by Electrospinning and Their Use as Secondary Battery Separators. *J. Membr. Sci.* **2011**, *378*, 111–116.

(218) Orendorff, C. J.; Lambert, T. N.; Chavez, C. A.; Bencomo, M.; Fenton, K. R. Polyester Separators for Lithium-Ion Cells: Improving Thermal Stability and Abuse Tolerance. *Adv. Energy Mater.* **2013**, *3*, 314–320.

- (219) Croce, F.; Focarete, M. L.; Hassoun, J.; Meschini, I.; Scrosati, B. A Safe, High-Rate and High-Energy Polymer Lithium-Ion Battery Based on Gelled Membranes Prepared by Electrospinning. *Energy Environ. Sci.* **2011**, *4*, 921–927.
- (220) Raghavan, P.; Zhao, X.; Shin, C.; Baek, D.-H.; Choi, J.-W.; Manuel, J.; Heo, M.-Y.; Ahn, J.-H.; Nah, C. Preparation and Electrochemical Characterization of Polymer Electrolytes Based on Electrospun Poly(vinylidene Fluoride-Co-Hexafluoropropylene)/Polyacrylonitrile Blend/Composite Membranes for Lithium Batteries. *J. Power Sources* **2010**, *195*, 6088–6094.
- (221) Zhou, X.; Yue, L.; Zhang, J.; Kong, Q.; Liu, Z.; Yao, J.; Cui, G. A Core-Shell Structured Polysulfonamide-Based Composite Nonwoven towards High Power Lithium Ion Battery Separator. *J. Electrochem. Soc.* **2013**, *160*, A1341–A1347.
- (222) Zhang, F.; Ma, X.; Cao, C.; Li, J.; Zhu, Y. Poly(vinylidene fluoride)/SiO<sub>2</sub> Composite Membranes Prepared by Electrospinning and Their Excellent Properties for Nonwoven Separators for Lithium-Ion Batteries. *J. Power Sources* **2014**, *251*, 423–431.
- (223) Hao, J.; Lei, G.; Li, Z.; Wu, L.; Xiao, Q.; Wang, L. A Novel Polyethylene Terephthalate Nonwoven Separator Based on Electrospinning Technique for Lithium Ion Battery. *J. Membr. Sci.* **2013**, *428*, 11–16.
- (224) Zhang, C.; Bai, Y.; Sun, Y.; Gu, J.; Xu, Y. Preparation of Hydrophilic HDPE Porous Membranes via Thermally Induced Phase Separation by Blending of Amphiphilic PE-b-PEG Copolymer. *J. Membr. Sci.* **2010**, *365*, 216–224.
- (225) Zhai, Y.; Wang, N.; Mao, X.; Si, Y.; Yu, J.; Al-Deyab, S. S.; El-Newehy, M.; Ding, B. Sandwich-Structured PVdF/PMIA/PVdF Nanofibrous Separators with Robust Mechanical Strength and Thermal Stability for Lithium-Ion Batteries. *J. Mater. Chem. A* **2014**, *2*, 14511–14518.
- (226) Lee, Y. M.; Kim, J.-W.; Choi, N.-S.; Lee, J. A.; Seol, W.-H.; Park, J.-K. Novel Porous Separator Based on PVdF and PE Nonwoven Matrix for Rechargeable Lithium Batteries. *J. Power Sources* **2005**, *139*, 235–241.
- (227) Song, K. W.; Kim, C. K. Coating with Macroporous Polyarylate via a Nonsolvent Induced Phase Separation Process for Enhancement of Polyethylene Separator Thermal Stability. *J. Membr. Sci.* **2010**, *352*, 239–246.
- (228) Ryou, M. H.; Lee, Y. M.; Park, J. K.; Choi, J. W. Mussel-Inspired Polydopamine-Treated Polyethylene Separators for High-Power Li-Ion Batteries. *Adv. Mater.* **2011**, *23*, 3066–3070.
- (229) Dai, J.; Shi, C.; Li, C.; Shen, X.; Peng, L.; Wu, D.; Sun, D.; Zhang, P.; Zhao, J. A Rational Design of Separator with Substantially Enhanced Thermal Features for Lithium-Ion Batteries by the Polydopamine-Ceramic Composite Modification of Polyolefin Membranes. *Energy Environ. Sci.* **2016**, *9*, 3252–3261.
- (230) Yang, C. L.; Li, Z. H.; Li, W. J.; Liu, H. Y.; Xiao, Q. Z.; Lei, G. T.; Ding, Y. H. Batwing-Like Polymer Membrane Consisting of PMMA-Grafted Electrospun PVdF-SiO<sub>2</sub> Nanocomposite Fibers for Lithium-Ion Batteries. *J. Membr. Sci.* **2015**, *495*, 341–350.
- (231) Li, S.; Gao, K. The Study on Methyl Methacrylate Graft-Copolymerized Composite Separator Prepared by Pre-irradiation Method for Li-Ion Batteries. *Surf. Coat. Technol.* **2010**, *204*, 2822–2828.
- (232) Jin, S. Y.; Manuel, J.; Zhao, X.; Park, W. H.; Ahn, J.-H. Surface-Modified Polyethylene Separator via Oxygen Plasma Treatment for Lithium Ion Battery. *J. Ind. Eng. Chem.* **2017**, *45*, 15–21.
- (233) Li, X.; He, J.; Wu, D.; Zhang, M.; Meng, J.; Ni, P. Development of Plasma-Treated Polypropylene Nonwoven-Based Composites for High-Performance Lithium-Ion Battery Separators. *Electrochim. Acta* **2015**, *167*, 396–403.
- (234) Bicy, K.; Gueye, A. B.; Rouxel, D.; Kalarikkal, N.; Thomas, S. Lithium-Ion Battery Separators Based on Electrospun PVDF: A Review. *Surf. Interfaces* **2022**, *31*, 101977.
- (235) Costa, C. M.; Silva, M. M.; Lanceros-Méndez, S. Battery Separators Based on Vinylidene Fluoride (VDF) Polymers and Copolymers for Lithium Ion Battery Applications. *RSC Adv.* **2013**, *3*, 11404.
- (236) Abbrent, S.; Pleštil, J.; Hlavata, D.; Lindgren, J.; Tegenfeldt, J.; Wendsjö, Å. Crystallinity and Morphology of PVdF-HFP-Based Gel Electrolytes. *Polymer* **2001**, *42*, 1407–1416.
- (237) Wu, Q.-Y.; Liang, H.-Q.; Gu, L.; Yu, Y.; Huang, Y.-Q.; Xu, Z.-K. PVDF/PAN Blend Separators via Thermally Induced Phase Separation for Lithium Ion Batteries. *Polymer* **2016**, *107*, 54–60.
- (238) Chen, W.; Liu, Y.; Ma, Y.; Liu, J.; Liu, X. Improved Performance of PVdF-HFP/PI Nanofiber Membrane for Lithium-Ion Battery Separator Prepared by a Bicomponent Cross-Electrospinning Method. *Mater. Lett.* **2014**, *133*, 67–70.
- (239) Bicy, K.; Mathew, D. E.; Stephen, A. M.; Royaud, I.; Poncot, M.; Godard, O.; Aranda, L.; Rouxel, D.; Kalarikkal, N.; Thomas, S. Sustainable Lithium-Ion Battery Separators Derived from Polyethylene Oxide/Lignocellulose Coated Electrospun P(VDF-TrFE) Nanofibrous Membranes. *Surf. Interfaces* **2022**, *29*, 101716.
- (240) K, B.; Paul, P. A.; Kalarikkal, N.; Stephen, A. M.; G, G. V.; Rouxel, D.; Thomas, S. Effects of Nanofillers on Morphology and Surface Wetting of Microporous Polypropylene Composite Membranes. *Mater. Chem. Phys.* **2021**, *257*, 123742.
- (241) Xiao, J.; Zhai, P.; Wei, Y.; Zhang, X.; Yang, W.; Cui, S.; Jin, C.; Liu, W.; Wang, X.; Jiang, H.; et al. In-Situ Formed Protecting Layer from Organic/Inorganic Concrete for Dendrite-Free Lithium Metal Anodes. *Nano Lett.* **2020**, *20*, 3911–3917.
- (242) Jeon, I.-Y.; Ju, M. J.; Xu, J.; Choi, H.-J.; Seo, J.-M.; Kim, M.-J.; Choi, I. T.; Kim, H. M.; Kim, J. C.; Lee, J.-J.; et al. Edge-Fluorinated Graphene Nanoplatelets as High Performance Electrodes for Dye-Sensitized Solar Cells and Lithium Ion Batteries. *Adv. Funct. Mater.* **2015**, *25*, 1170–1179.
- (243) Sun, S.; Wang, J.; Chen, X.; Ma, Q.; Wang, Y.; Yang, K.; Yao, X.; Yang, Z.; Liu, J.; Xu, H.; et al. Thermally Stable and Dendrite-Resistant Separators toward Highly Robust Lithium Metal Batteries. *Adv. Energy Mater.* **2022**, *12*, 2202206.
- (244) Qian, Y.; Chen, K.; Feng, Z.; Ouyang, Y.; Lan, Q.; Zhang, C.; Feng, W.; Miao, Y.-E.; Liu, T. A Fluorinated-Polyimide-Based Composite Nanofibrous Separator with Homogenized Pore Size for Wide-Temperature Lithium Metal Batteries. *Small Struct.* **2023**, *4*, 2200383.
- (245) Zhang, K.; Li, X.; Ma, L.; Chen, F.; Chen, Z.; Yuan, Y.; Zhao, Y.; Yang, J.; Liu, J.; Xie, K.; et al. Fluorinated Covalent Organic Framework-Based Nanofluidic Interface for Robust Lithium-Sulfur Batteries. *ACS Nano* **2023**, *17*, 2901–2911.
- (246) Wang, Z.; Zhang, J.; Yang, Y.; Yue, X.; Hao, X.; Sun, W.; Rooney, D.; Sun, K. Flexible Carbon Nanofiber/Polyvinylidene Fluoride Composite Membranes as Interlayers in High-Performance Lithium Sulfur Batteries. *J. Power Sources* **2016**, *329*, 305–313.
- (247) Wei, H.; Ma, J.; Li, B.; Zuo, Y.; Xia, D. Enhanced Cycle Performance of Lithium-Sulfur Batteries Using a Separator Modified with a PVDF-C Layer. *ACS Appl. Mater. Interfaces* **2014**, *6*, 20276–20281.
- (248) Vizintin, A.; Lozinšek, M.; Chellappan, R. K.; Foix, D.; Krajnc, A.; Mali, G.; Drazic, G.; Genorio, B.; Dedryvère, R.; Dominko, R. Fluorinated Reduced Graphene Oxide as an Interlayer in Li-S Batteries. *Chem. Mater.* **2015**, *27*, 7070–7081.
- (249) Xia, S.; Zhang, X.; Yang, G.; Shi, L.; Cai, L.; Xia, Y.; Yang, J.; Zheng, S. Bifunctional Fluorinated Separator Enabling Polysulfide Trapping and Li Deposition for Lithium-Sulfur Batteries. *ACS Appl. Mater. Interfaces* **2021**, *13*, 11920–11929.
- (250) Xiong, P.; Zhang, F.; Zhang, X.; Liu, Y.; Wu, Y.; Wang, S.; Safaei, J.; Sun, B.; Ma, R.; Liu, Z.; et al. Atomic-Scale Regulation of Anionic and Cationic Migration in Alkali Metal Batteries. *Nat. Commun.* **2021**, *12*, 4184.
- (251) Liu, W.; Zhang, K.; Ma, L.; Ning, R.; Chen, Z.; Li, J.; Yan, Y.; Shang, T.; Lyu, Z.; Li, Z.; et al. An Ion Sieving Conjugated Microporous Thermoset Ultrathin Membrane for High-Performance Li-S Battery. *Energy Storage Mater.* **2022**, *49*, 1–10.
- (252) Zou, F.; Manthiram, A. A Review of the Design of Advanced Binders for High-Performance Batteries. *Adv. Energy Mater.* **2020**, *10*, 2002508.



- (253) Huang, S.; Ren, J.; Liu, R.; Yue, M.; Huang, Y.; Yuan, G. The Progress of Novel Binder as a Non-ignorable Part to Improve the Performance of Si-Based Anodes for Li-Ion Batteries. *Int. J. Energy Res.* **2018**, *42*, 919–935.
- (254) Ai, G.; Dai, Y.; Ye, Y.; Mao, W.; Wang, Z.; Zhao, H.; Chen, Y.; Zhu, J.; Fu, Y.; Battaglia, V.; et al. Investigation of Surface Effects Through the Application of Functional Binders in Lithium-Sulfur Batteries. *Nano Energy* **2015**, *16*, 28–37.
- (255) Kwon, T. W.; Choi, J. W.; Coskun, A. The Emerging Era of Supramolecular Polymeric Binders in Silicon Anodes. *Chem. Soc. Rev.* **2018**, *47*, 2145–2164.
- (256) Chen, H.; Ling, M.; Hencz, L.; Ling, H. Y.; Li, G.; Lin, Z.; Liu, G.; Zhang, S. Exploring Chemical, Mechanical, and Electrical Functionalities of Binders for Advanced Energy-Storage Devices. *Chem. Rev.* **2018**, *118*, 8936–8982.
- (257) Fu, Z.; Feng, H. L.; Xiang, X. D.; Rao, M. M.; Wu, W.; Luo, J. C.; Chen, T. T.; Hu, Q. P.; Feng, A. B.; Li, W. S. A Novel Polymer Composite as Cathode Binder of Lithium-Ion Batteries with Improved Rate Capability and Cyclic Stability. *J. Power Sources* **2014**, *261*, 170–174.
- (258) Byun, S.; Choi, J.; Roh, Y.; Song, D.; Ryou, M.-H.; Lee, Y. M. Mechanical Robustness of Composite Electrode for Lithium-Ion Battery: Insight into Entanglement & Crystallinity of Polymeric Binder. *Electrochim. Acta* **2020**, *332*, 135471.
- (259) Huang, H.; Li, Z.; Gu, S.; Bian, J.; Li, Y.; Chen, J.; Liao, K.; Gan, Q.; Wang, Y.; Wu, S.; et al. Dextran Sulfate Lithium as Versatile Binder to Stabilize High-Voltage  $\text{LiCoO}_2$  to 4.6 V. *Adv. Energy Mater.* **2021**, *11*, 2101864.
- (260) Pieczonka, N. P. W.; Borgel, V.; Ziv, B.; Leifer, N.; Dargel, V.; Aurbach, D.; Kim, J.-H.; Liu, Z.; Huang, X.; Krachkovskiy, S. A.; et al. Lithium Polyacrylate (LiPAA) as an Advanced Binder and a Passivating Agent for High-Voltage Li-Ion Batteries. *Adv. Energy Mater.* **2015**, *5*, 1501008.
- (261) Liang, J.; Chen, D.; Adair, K.; Sun, Q.; Holmes, N. G.; Zhao, Y.; Sun, Y.; Luo, J.; Li, R.; Zhang, L.; et al. Insight into Prolonged Cycling Life of 4 V All-Solid-State Polymer Batteries by a High-Voltage Stable Binder. *Adv. Energy Mater.* **2021**, *11*, 2002455.
- (262) Pham, H. Q.; Kim, G.; Jung, H. M.; Song, S.-W. Fluorinated Polyimide as a Novel High-Voltage Binder for High-Capacity Cathode of Lithium-Ion Batteries. *Adv. Funct. Mater.* **2018**, *28*, 1704690.
- (263) Li, J.; Le, D.-B.; Ferguson, P. P.; Dahn, J. R. Lithium Polyacrylate as a Binder for Tin-Cobalt-Carbon Negative Electrodes in Lithium-Ion Batteries. *Electrochim. Acta* **2010**, *55*, 2991–2995.
- (264) Tsao, C.-H.; Hsu, C.-H.; Kuo, P.-L. Ionic Conducting and Surface Active Binder of Poly(ethylene oxide)-Block-Poly(acrylonitrile) for High Power Lithium-Ion Battery. *Electrochim. Acta* **2016**, *196*, 41–47.
- (265) Wei, Z.; Xue, L.; Nie, F.; Sheng, J.; Shi, Q.; Zhao, X. Study of Sulfonated Polyether Ether Ketone with Pendant Lithiated Fluorinated Sulfonic Groups as Ion-Conductive Binder in Lithium-Ion Batteries. *J. Power Sources* **2014**, *256*, 28–31.
- (266) Shi, Q.; Xue, L.; Wei, Z.; Liu, F.; Du, X.; Desmarteau, D. D. Improvement in  $\text{LiFePO}_4$ -Li Battery Performance via Poly(perfluoroalkylsulfonfyl)imide (PFSI) Based Ionene Composite Binder. *J. Mater. Chem. A* **2013**, *1*, 15016.
- (267) Chiu, K.-F.; Su, S. H.; Leu, H.-J.; Chen, Y. S. Application of Lithiated Perfluorosulfonate Ionomer Binders to Enhance High Rate Capability in  $\text{LiMn}_2\text{O}_4$  Cathodes for Lithium-Ion Batteries. *Electrochim. Acta* **2014**, *117*, 134–138.
- (268) Vauthier, S.; Alvarez-Tirado, M.; Guzmán-González, G.; Tomé, L. C.; Cotte, S.; Castro, L.; Guéguen, A.; Mecerreyes, D.; Casado, N. High-Performance Pyrrolidinium-Based Poly(ionic Liquid) Binders for Li-Ion and Li-Air Batteries. *Mater. Today Chem.* **2023**, *27*, 101293.
- (269) Tsao, C.-H.; Wu, E. T.; Lee, W.-H.; Chiu, C.-C.; Kuo, P.-L. Fluorinated Copolymer Functionalized with Ethylene Oxide as Novel Water-Borne Binder for a High-Power Lithium Ion Battery: Synthesis, Mechanism, and Application. *ACS Appl. Energy Mater.* **2018**, *1*, 3999–4008.
- (270) Lee, J. I.; Kang, H.; Park, K. H.; Shin, M.; Hong, D.; Cho, H. J.; Kang, N. R.; Lee, J.; Lee, S. M.; Kim, J. Y.; et al. Amphiphilic Graft Copolymers as a Versatile Binder for Various Electrodes of High-Performance Lithium-Ion Batteries. *Small* **2016**, *12*, 3119–3127.
- (271) Cai, Y.; Li, Y.; Jin, B.; Ali, A.; Ling, M.; Cheng, D.; Lu, J.; Hou, Y.; He, Q.; Zhan, X.; et al. Dual Cross-Linked Fluorinated Binder Network for High-Performance Silicon and Silicon Oxide Based Anodes in Lithium-Ion Batteries. *ACS Appl. Mater. Interfaces* **2019**, *11*, 46800–46807.
- (272) Preman, A. N.; Lee, H.; Yoo, J.; Kim, I. T.; Saito, T.; Ahn, S.-K. Progress of 3D Network Binders in Silicon Anodes for Lithium Ion Batteries. *J. Mater. Chem. A* **2020**, *8*, 25548–25570.
- (273) Li, S.; Liu, Y.-M.; Zhang, Y.-C.; Song, Y.; Wang, G.-K.; Liu, Y.-X.; Wu, Z.-G.; Zhong, B.-H.; Zhong, Y.-J.; Guo, X.-D. A Review of Rational Design and Investigation of Binders Applied in Silicon-Based Anodes for Lithium-Ion Batteries. *J. Power Sources* **2021**, *485*, 229331.
- (274) Li, J.; Christensen, L.; Obrovac, M. N.; Hewitt, K. C.; Dahn, J. R. Effect of Heat Treatment on Si Electrodes Using Polyvinylidene Fluoride Binder. *J. Electrochem. Soc.* **2008**, *155*, A234.
- (275) Chen, Z.; Christensen, L.; Dahn, J. R. Large-Volume-Change Electrodes for Li-Ion Batteries of Amorphous Alloy Particles Held by Elastomeric Tethers. *Electrochem. commun.* **2003**, *5*, 919–923.
- (276) Rongeat, C.; Anji Reddy, M.; Witter, R.; Fichtner, M. Solid Electrolytes for Fluoride Ion Batteries: Ionic Conductivity in Polycrystalline Tysonite-Type Fluorides. *ACS Appl. Mater. Interfaces* **2014**, *6*, 2103–2110.
- (277) Choi, S.; Kwon, T. W.; Coskun, A.; Choi, J. W. Highly Elastic Binders Integrating Polyrotaxanes for Silicon Microparticle Anodes in Lithium Ion Batteries. *Science* **2017**, *357*, 279–283.
- (278) Koo, B.; Kim, H.; Cho, Y.; Lee, K. T.; Choi, N. S.; Cho, J. A Highly Cross-Linked Polymeric Binder for High-Performance Silicon Negative Electrodes in Lithium-Ion Batteries. *Angew. Chem., Int. Ed.* **2012**, *51*, 8762–8767.
- (279) Li, C.; Shi, T.; Yoshitake, H.; Wang, H. Improved Performance in Micron-Sized Silicon Anodes by In Situ Polymerization of Acrylic Acid-Based Slurry. *J. Mater. Chem. A* **2016**, *4*, 16982–16991.
- (280) Song, J.; Zhou, M.; Yi, R.; Xu, T.; Gordin, M. L.; Tang, D.; Yu, Z.; Regula, M.; Wang, D. Interpenetrated Gel Polymer Binder for High-Performance Silicon Anodes in Lithium-ion Batteries. *Adv. Funct. Mater.* **2014**, *24*, 5904–5910.
- (281) Qin, D.; Xue, L.; Du, B.; Wang, J.; Nie, F.; Wen, L. Flexible Fluorine-Containing Ionic Binders to Mitigate the Negative Impact Caused by the Drastic Volume Fluctuation from Silicon Nanoparticles in High-Capacity Anodes of Lithium-Ion Batteries. *J. Mater. Chem. A* **2015**, *3*, 10928–10934.
- (282) Wang, L.; He, X.; Li, J.; Gao, J.; Fang, M.; Tian, G.; Wang, J.; Fan, S. Graphene-Coated Plastic Film as Current Collector for Lithium/Sulfur Batteries. *J. Power Sources* **2013**, *239*, 623–627.
- (283) Gabryelczyk, A.; Ivanov, S.; Bund, A.; Lota, G. Corrosion of aluminium current collector in lithium-ion batteries: A review. *J. Energy Storage* **2021**, *43*, 103226.
- (284) Zheng, J.; Engelhard, M. H.; Mei, D.; Jiao, S.; Polzin, B. J.; Zhang, J.-G.; Xu, W. Electrolyte Additive Enabled Fast Charging and Stable Cycling Lithium Metal Batteries. *Nat. Energy* **2017**, *2*, 17012.
- (285) Ding, F.; Xu, W.; Graff, G. L.; Zhang, J.; Sushko, M. L.; Chen, X.; Shao, Y.; Engelhard, M. H.; Nie, Z.; Xiao, J.; et al. Dendrite-Free Lithium Deposition via Self-Healing Electrostatic Shield Mechanism. *J. Am. Chem. Soc.* **2013**, *135*, 4450–4456.
- (286) Yan, C.; Cheng, X.-B.; Zhao, C.-Z.; Huang, J.-Q.; Yang, S.-T.; Zhang, Q. Lithium Metal Protection Through In-Situ Formed Solid Electrolyte Interphase in Lithium-Sulfur Batteries: The Role of Polysulfides on Lithium Anode. *J. Power Sources* **2016**, *327*, 212–220.
- (287) Cheng, X. B.; Zhao, M. Q.; Chen, C.; Pentecost, A.; Maleski, K.; Mathis, T.; Zhang, X. Q.; Zhang, Q.; Jiang, J.; Gogotsi, Y. Nanodiamonds Suppress the Growth of Lithium Dendrites. *Nat. Commun.* **2017**, *8*, 336.



- (288) Li, N. W.; Yin, Y. X.; Yang, C. P.; Guo, Y. G. An Artificial Solid Electrolyte Interphase Layer for Stable Lithium Metal Anodes. *Adv. Mater.* **2016**, *28*, 1853–1858.
- (289) Zhao, J.; Liao, L.; Shi, F.; Lei, T.; Chen, G.; Pei, A.; Sun, J.; Yan, K.; Zhou, G.; Xie, J.; et al. Surface Fluorination of Reactive Battery Anode Materials for Enhanced Stability. *J. Am. Chem. Soc.* **2017**, *139*, 11550–11558.
- (290) Fu, K.; Gong, Y.; Hitz, G. T.; Mcowen, D. W.; Li, Y.; Xu, S.; Wen, Y.; Zhang, L.; Wang, C.; Pastel, G.; et al. Three-Dimensional Bilayer Garnet Solid Electrolyte Based High Energy Density Lithium Metal-Sulfur Batteries. *Energy Environ. Sci.* **2017**, *10*, 1568–1575.
- (291) Liu, Y.; Lin, D.; Yuen, P. Y.; Liu, K.; Xie, J.; Dauskardt, R. H.; Cui, Y. An Artificial Solid Electrolyte Interphase with High Li-Ion Conductivity, Mechanical Strength, and Flexibility for Stable Lithium Metal Anodes. *Adv. Mater.* **2017**, *29*, 1605531.
- (292) Pang, Q.; Liang, X.; Shyamsunder, A.; Nazar, L. F. An In Vivo Formed Solid Electrolyte Surface Layer Enables Stable Plating of Li Metal. *Joule* **2017**, *1*, 871–886.
- (293) Liu, W.; Lin, D.; Pei, A.; Cui, Y. Stabilizing Lithium Metal Anodes by Uniform Li-Ion Flux Distribution in Nanochannel Confinement. *J. Am. Chem. Soc.* **2016**, *138*, 15443–15450.
- (294) Cheng, X. B.; Hou, T. Z.; Zhang, R.; Peng, H. J.; Zhao, C. Z.; Huang, J. Q.; Zhang, Q. Dendrite-Free Lithium Deposition Induced by Uniformly Distributed Lithium Ions for Efficient Lithium Metal Batteries. *Adv. Mater.* **2016**, *28*, 2888–2895.
- (295) Li, N.; Ye, Q.; Zhang, K.; Yan, H.; Shen, C.; Wei, B.; Xie, K. Normalized Lithium Growth from the Nucleation Stage for Dendrite-Free Lithium Metal Anodes. *Angew. Chem., Int. Ed.* **2019**, *58*, 18246–18251.
- (296) Chen, X.; Hou, T.-Z.; Li, B.; Yan, C.; Zhu, L.; Guan, C.; Cheng, X.-B.; Peng, H.-J.; Huang, J.-Q.; Zhang, Q. Towards Stable Lithium-Sulfur Batteries: Mechanistic Insights into Electrolyte Decomposition on Lithium Metal Anode. *Energy Storage Mater.* **2017**, *8*, 194–201.
- (297) Zuo, T. T.; Wu, X. W.; Yang, C. P.; Yin, Y. X.; Ye, H.; Li, N. W.; Guo, Y. G. Graphitized Carbon Fibers as Multifunctional 3D Current Collectors for High Areal Capacity Li Anodes. *Adv. Mater.* **2017**, *29*, 1700389.
- (298) Zhang, R.; Chen, X. R.; Chen, X.; Cheng, X. B.; Zhang, X. Q.; Yan, C.; Zhang, Q. Lithiophilic Sites in Doped Graphene Guide Uniform Lithium Nucleation for Dendrite-Free Lithium Metal Anodes. *Angew. Chem., Int. Ed.* **2017**, *56*, 7764–7768.
- (299) Sun, Y.; Zheng, G.; Seh, Z. W.; Liu, N.; Wang, S.; Sun, J.; Lee, H. R.; Cui, Y. Graphite-Encapsulated Li-Metal Hybrid Anodes for High-Capacity Li Batteries. *Chem.* **2016**, *1*, 287–297.
- (300) Liu, L.; Yin, Y.-X.; Li, J.-Y.; Li, N.-W.; Zeng, X.-X.; Ye, H.; Guo, Y.-G.; Wan, L.-J. Free-Standing Hollow Carbon Fibers as High-Capacity Containers for Stable Lithium Metal Anodes. *Joule* **2017**, *1*, 563–575.
- (301) Yang, Q.; Li, C. Li Metal Batteries and Solid State Batteries Benefiting from Halogen-Based Strategies. *Energy Storage Mater.* **2018**, *14*, 100–117.
- (302) Li, T.; Zhang, X.-Q.; Shi, P.; Zhang, Q. Fluorinated Solid-Electrolyte Interphase in High-Voltage Lithium Metal Batteries. *Joule* **2019**, *3*, 2647–2661.
- (303) Wang, Y.; Liang, J.; Song, X.; Jin, Z. Recent Progress in Constructing Halogenated Interfaces for Highly Stable Lithium Metal Anodes. *Energy Storage Mater.* **2023**, *54*, 732–775.
- (304) Zhang, X. Q.; Chen, X.; Xu, R.; Cheng, X. B.; Peng, H. J.; Zhang, R.; Huang, J. Q.; Zhang, Q. Columnar Lithium Metal Anodes. *Angew. Chem., Int. Ed.* **2017**, *56*, 14207–14211.
- (305) Luo, J.; Fang, C.-C.; Wu, N.-L. High Polarity Poly(vinylidene difluoride) Thin Coating for Dendrite-Free and High-Performance Lithium Metal Anodes. *Adv. Energy Mater.* **2018**, *8*, 1701482.
- (306) Cheng, H.; Mao, Y.; Lu, Y.; Zhang, P.; Xie, J.; Zhao, X. Trace Fluorinated-Carbon-Nanotube-Induced Lithium Dendrite Elimination for High-Performance Lithium-Oxygen Cells. *Nanoscale* **2020**, *12*, 3424–3434.
- (307) Cui, C.; Yang, C.; Eidson, N.; Chen, J.; Han, F.; Chen, L.; Luo, C.; Wang, P. F.; Fan, X.; Wang, C. A Highly Reversible, Dendrite-Free Lithium Metal Anode Enabled by a Lithium-Fluoride-Enriched Interphase. *Adv. Mater.* **2020**, *32*, No. e1906427.
- (308) Li, Z.; Li, X.; Zhou, L.; Xiao, Z.; Zhou, S.; Zhang, X.; Li, L.; Zhi, L. A Synergistic Strategy for Stable Lithium Metal Anodes Using 3D Fluorine-Doped Graphene Shuttle-Implanted Porous Carbon Networks. *Nano Energy* **2018**, *49*, 179–185.
- (309) Jamaluddin, A.; Sin, Y.-Y.; Adhitama, E.; Prayogi, A.; Wu, Y.-T.; Chang, J.-K.; Su, C.-Y. Fluorinated Graphene as a Dual-Functional Anode to Achieve Dendrite-Free and High-Performance Lithium Metal Batteries. *Carbon* **2022**, *197*, 141–151.
- (310) Gao, Y.; Rojas, T.; Wang, K.; Liu, S.; Wang, D.; Chen, T.; Wang, H.; Ngo, A. T.; Wang, D. Low-Temperature and High-Rate-Charging Lithium Metal Batteries Enabled by an Electrochemically Active Monolayer-Regulated Interface. *Nat. Energy* **2020**, *5*, 534–542.
- (311) Huang, G.; Chen, S.; Guo, P.; Tao, R.; Jie, K.; Liu, B.; Zhang, X.; Liang, J.; Cao, Y.-C. In Situ Constructing Lithiophilic NiF<sub>x</sub> Nanosheets on Ni Foam Current Collector for Stable Lithium Metal Anode via a Succinct Fluorination Strategy. *Chem. Eng. J.* **2020**, *395*, 125122.
- (312) Cao, J.; Qian, G.; Lu, X.; Lu, X. Advanced Composite Lithium Metal Anodes with 3D Frameworks: Preloading Strategies, Interfacial Optimization, and Perspectives. *Small* **2023**, *19*, No. e2205653.
- (313) Hou, W.; Li, S.; Liang, J.; Yuan, B.; Hu, R. Lithiophilic NiF<sub>2</sub> Coating Inducing LiF-Rich Solid Electrolyte Interphase by a Novel NF<sub>3</sub> Plasma Treatment for Highly Stable Li Metal Anode. *Electrochim. Acta* **2022**, *402*, 139561.
- (314) Richards, W. D.; Miar, L. J.; Wang, Y.; Kim, J. C.; Ceder, G. Interface Stability in Solid-State Batteries. *Chem. Mater.* **2016**, *28*, 266–273.
- (315) Mason, W. P.; Mayer, W. G. Physical Acoustics, Principles and Methods. *Phys. Today* **1965**, *18*, 67–67.
- (316) Suo, L.; Xue, W.; Gobet, M.; Greenbaum, S. G.; Wang, C.; Chen, Y.; Yang, W.; Li, Y.; Li, J. Fluorine-Donating Electrolytes Enable Highly Reversible 5-V-Class Li Metal Batteries. *Proc. Natl. Acad. Sci. U.S.A.* **2018**, *115*, 1156–1161.
- (317) Xu, R.; Zhang, X.-Q.; Cheng, X.-B.; Peng, H.-J.; Zhao, C.-Z.; Yan, C.; Huang, J.-Q. Artificial Soft-Rigid Protective Layer for Dendrite-Free Lithium Metal Anode. *Adv. Funct. Mater.* **2018**, *28*, 1705838.
- (318) Chen, L.; Chen, K. S.; Chen, X.; Ramirez, G.; Huang, Z.; Geise, N. R.; Steinruck, H. G.; Fisher, B. L.; Shahbazian-Yassar, R.; Toney, M. F.; et al. Novel ALD Chemistry Enabled Low-Temperature Synthesis of Lithium Fluoride Coatings for Durable Lithium Anodes. *ACS Appl. Mater. Interfaces* **2018**, *10*, 26972–26981.
- (319) Lin, D.; Liu, Y.; Chen, W.; Zhou, G.; Liu, K.; Dunn, B.; Cui, Y. Conformal Lithium Fluoride Protection Layer on Three-Dimensional Lithium by Nonhazardous Gaseous Reagent Freon. *Nano Lett.* **2017**, *17*, 3731–3737.
- (320) Yan, C.; Cheng, X. B.; Yao, Y. X.; Shen, X.; Li, B. Q.; Li, W. J.; Zhang, R.; Huang, J. Q.; Li, H.; Zhang, Q. An Armored Mixed Conductor Interphase on a Dendrite-Free Lithium-Metal Anode. *Adv. Mater.* **2018**, *30*, No. e1804461.
- (321) Pathak, R.; Chen, K.; Gurung, A.; Reza, K. M.; Bahrami, B.; Pokharel, J.; Baniya, A.; He, W.; Wu, F.; Zhou, Y.; et al. Fluorinated Hybrid Solid-Electrolyte-Interphase for Dendrite-Free Lithium Deposition. *Nat. Commun.* **2020**, *11*, 93.
- (322) Yang, Q.; Hu, J.; Meng, J.; Li, C. C-F-rich Oil Drop as a Non-expendable Fluid Interface Modifier with Low Surface Energy to Stabilize a Li Metal Anode. *Energy Environ. Sci.* **2021**, *14*, 3621–3631.
- (323) Fan, X.; Ji, X.; Han, F.; Yue, J.; Chen, J.; Chen, L.; Deng, T.; Jiang, J.; Wang, C. Fluorinated Solid Electrolyte Interphase Enables Highly Reversible Solid-State Li Metal Battery. *Sci. Adv.* **2018**, *4*, No. eaau9245.
- (324) Hu, A.; Chen, W.; Du, X.; Hu, Y.; Lei, T.; Wang, H.; Xue, L.; Li, Y.; Sun, H.; Yan, Y.; et al. An Artificial Hybrid Interphase for an Ultrahigh-Rate and Practical Lithium Metal Anode. *Energy Environ. Sci.* **2021**, *14*, 4115–4124.

- (325) Liu, S.; Ji, X.; Yue, J.; Hou, S.; Wang, P.; Cui, C.; Chen, J.; Shao, B.; Li, J.; Han, F.; et al. High Interfacial-Energy Interphase Promoting Safe Lithium Metal Batteries. *J. Am. Chem. Soc.* **2020**, *142*, 2438–2447.
- (326) Wang, Y.; Liu, F.; Fan, G.; Qiu, X.; Liu, J.; Yan, Z.; Zhang, K.; Cheng, F.; Chen, J. Electroless Formation of a Fluorinated Li/Na Hybrid Interphase for Robust Lithium Anodes. *J. Am. Chem. Soc.* **2021**, *143*, 2829–2837.
- (327) Yan, C.; Cheng, X. B.; Tian, Y.; Chen, X.; Zhang, X. Q.; Li, W. J.; Huang, J. Q.; Zhang, Q. Dual-Layered Film Protected Lithium Metal Anode to Enable Dendrite-Free Lithium Deposition. *Adv. Mater.* **2018**, *30*, No. e1707629.
- (328) Liu, S.; Xia, X.; Deng, S.; Xie, D.; Yao, Z.; Zhang, L.; Zhang, S.; Wang, X.; Tu, J. In Situ Solid Electrolyte Interphase from Spray Quenching on Molten Li: A New Way to Construct High-Performance Lithium-Metal Anodes. *Adv. Mater.* **2019**, *31*, No. e1806470.
- (329) Gao, Y.; Yan, Z.; Gray, J. L.; He, X.; Wang, D.; Chen, T.; Huang, Q.; Li, Y. C.; Wang, H.; Kim, S. H.; et al. Polymer-Inorganic Solid-Electrolyte Interphase for Stable Lithium Metal Batteries under Lean Electrolyte Conditions. *Nat. Mater.* **2019**, *18*, 384–389.
- (330) Shen, X.; Li, Y.; Qian, T.; Liu, J.; Zhou, J.; Yan, C.; Goodenough, J. B. Lithium Anode Stable in Air for Low-Cost Fabrication of a Dendrite-Free Lithium Battery. *Nat. Commun.* **2019**, *10*, 900.
- (331) Peled, E. The Electrochemical Behavior of Alkali and Alkaline Earth Metals in Nonaqueous Battery Systems—The Solid Electrolyte Interphase Model. *J. Electrochem. Soc.* **1979**, *126*, 2047–2051.
- (332) Peled, E.; Menkin, S. Review—SEI: Past, Present and Future. *J. Electrochem. Soc.* **2017**, *164*, A1703–A1719.
- (333) Lu, Y.; Tu, Z.; Archer, L. A. Stable Lithium Electrodeposition in Liquid and Nanoporous Solid Electrolytes. *Nat. Mater.* **2014**, *13*, 961–969.
- (334) Ko, J.; Yoon, Y. S. Recent Progress in LiF Materials for Safe Lithium Metal Anode of Rechargeable Batteries: Is LiF the Key to Commercializing Li Metal Batteries? *Ceram. Int.* **2019**, *45*, 30–49.
- (335) Yuan, Y.; Wu, F.; Chen, G.; Bai, Y.; Wu, C. Porous LiF Layer Fabricated by a Facile Chemical Method toward Dendrite-Free Lithium Metal Anode. *J. Energy Chem.* **2019**, *37*, 197–203.
- (336) Cheng, X.-B.; Yan, C.; Chen, X.; Guan, C.; Huang, J.-Q.; Peng, H.-J.; Zhang, R.; Yang, S.-T.; Zhang, Q. Implantable Solid Electrolyte Interphase in Lithium-Metal Batteries. *Chem.* **2017**, *2*, 258–270.
- (337) Breuer, S.; Pregartner, V.; Lunghammer, S.; Wilkening, H. M. R. Dispersed Solid Conductors: Fast Interfacial Li-Ion Dynamics in Nanostructured LiF and LiF:γ-Al<sub>2</sub>O<sub>3</sub> Composites. *J. Phys. Chem. C* **2019**, *123*, 5222–5230.
- (338) Zaban, A.; Zinigrad, E.; Aurbach, D. Impedance Spectroscopy of Li Electrodes. 4. A General Simple Model of the Li-Solution Interphase in Polar Aprotic Systems. *J. Phys. Chem.* **1996**, *100*, 3089–3101.
- (339) Rehnlund, D.; Ihrfors, C.; Maibach, J.; Nyholm, L. Dendrite-Free Lithium Electrode Cycling via Controlled Nucleation in Low LiPF<sub>6</sub> Concentration Electrolytes. *Mater. Today* **2018**, *21*, 1010–1018.
- (340) Jurng, S.; Brown, Z. L.; Kim, J.; Lucht, B. L. Effect of Electrolyte on the Nanostructure of the Solid Electrolyte Interphase (SEI) and Performance of Lithium Metal Anodes. *Energy Environ. Sci.* **2018**, *11*, 2600–2608.
- (341) Monroe, C.; Newman, J. The Effect of Interfacial Deformation on Electrodeposition Kinetics. *J. Electrochem. Soc.* **2004**, *151*, A880.
- (342) He, M.; Guo, R.; Hobold, G. M.; Gao, H.; Gallant, B. M. The Intrinsic Behavior of Lithium Fluoride in Solid Electrolyte Interphases on Lithium. *Proc. Natl. Acad. Sci. U.S.A.* **2020**, *117*, 73–79.
- (343) Baek, M.; Kim, J.; Jin, J.; Choi, J. W. Photochemically Driven Solid Electrolyte Interphase for Extremely Fast-Charging Lithium-Ion Batteries. *Nat. Commun.* **2021**, *12*, 6807.
- (344) Shiraishi, S.; Kanamura, K.; Takehara, Z. I. Surface Condition Changes in Lithium Metal Deposited in Nonaqueous Electrolyte Containing HF by Dissolution-Deposition Cycles. *J. Electrochem. Soc.* **1999**, *146*, 1633–1639.
- (345) Xia, J.; Petibon, R.; Xiao, A.; Lamanna, W. M.; Dahn, J. R. Some Fluorinated Carbonates as Electrolyte Additives for Li-(Ni<sub>0.4</sub>Mn<sub>0.4</sub>Co<sub>0.2</sub>)O<sub>2</sub>/Graphite Pouch Cells. *J. Electrochem. Soc.* **2016**, *163*, A1637–A1645.
- (346) Wang, J.; Liu, W.; Luo, G.; Li, Z.; Zhao, C.; Zhang, H.; Zhu, M.; Xu, Q.; Wang, X.; Zhao, C.; et al. Synergistic Effect of Well-Defined Dual Sites Boosting the Oxygen Reduction Reaction. *Energy Environ. Sci.* **2018**, *11*, 3375–3379.
- (347) Chang, W.; Park, J. H.; Steingart, D. A. Poor Man's Atomic Layer Deposition of LiF for Additive-Free Growth of Lithium Columns. *Nano Lett.* **2018**, *18*, 7066–7074.
- (348) Fan, L.; Zhuang, H. L.; Gao, L.; Lu, Y.; Archer, L. A. Regulating Li Deposition at Artificial Solid Electrolyte Interphases. *J. Mater. Chem. A* **2017**, *5*, 3483–3492.
- (349) Xie, J.; Liao, L.; Gong, Y.; Li, Y.; Shi, F.; Pei, A.; Sun, J.; Zhang, R.; Kong, B.; Subbaraman, R.; et al. Stitching H-BN by Atomic Layer Deposition of LiF as a Stable Interface for Lithium Metal Anode. *Sci. Adv.* **2017**, *3*, No. eaao3170.
- (350) He, M.; Li, Y.; Guo, R.; Gallant, B. M. Electrochemical Conversion of Nitrogen Trifluoride as a Gas-to-Solid Cathode in Li Batteries. *J. Phys. Chem. Lett.* **2018**, *9*, 4700–4706.
- (351) Ma, C.; Xu, F.; Song, T. Dual-Layered Interfacial Evolution of Lithium Metal Anode: SEI Analysis via TOF-SIMS Technology. *ACS Appl. Mater. Interfaces* **2022**, *14*, 20197–20207.
- (352) Zhang, Z.; Li, Y.; Xu, R.; Zhou, W.; Li, Y.; Oyakhire, S. T.; Wu, Y.; Xu, J.; Wang, H.; Yu, Z.; et al. Capturing the Swelling of Solid-Electrolyte Interphase in Lithium Metal Batteries. *Science* **2022**, *375*, 66–70.
- (353) Wu, J.; Wang, X.; Liu, Q.; Wang, S.; Zhou, D.; Kang, F.; Shanmukaraj, D.; Armand, M.; Rojo, T.; Li, B.; et al. A Synergistic Exploitation to Produce High-Voltage Quasi-Solid-State Lithium Metal Batteries. *Nat. Commun.* **2021**, *12*, 5746.
- (354) Zheng, J.; Zheng, H.; Wang, R.; Ben, L.; Lu, W.; Chen, L.; Chen, L.; Li, H. 3D Visualization of Inhomogeneous Multi-Layered Structure and Young's Modulus of the Solid Electrolyte Interphase (SEI) on Silicon Anodes for Lithium-Ion Batteries. *Phys. Chem. Chem. Phys.* **2014**, *16*, 13229–13238.
- (355) Jaumaux, P.; Wu, J.; Shanmukaraj, D.; Wang, Y.; Zhou, D.; Sun, B.; Kang, F.; Li, B.; Armand, M.; Wang, G. Non-Flammable Liquid and Quasi-Solid Electrolytes toward Highly-Safe Alkali Metal-Based Batteries. *Adv. Funct. Mater.* **2021**, *31*, 2008644.
- (356) Yildirim, H.; Kinaci, A.; Chan, M. K.; Greeley, J. P. First-Principles Analysis of Defect Thermodynamics and Ion Transport in Inorganic SEI Compounds: LiF and NaF. *ACS Appl. Mater. Interfaces* **2015**, *7*, 18985–18996.
- (357) Thomas, M.; Bruce, P.; Goodenough, J. Lithium Mobility in the Layered Oxide Li<sub>1-x</sub>CoO<sub>2</sub>. *Solid State Ion.* **1985**, *17*, 13–19.
- (358) Cherkashinin, G.; Nikolowski, K.; Ehrenberg, H.; Jacke, S.; Dimesso, L.; Jaegermann, W. The Stability of the SEI Layer, Surface Composition and the Oxidation State of Transition Metals at the Electrolyte-Cathode Interface Impacted by the Electrochemical Cycling: X-ray Photoelectron Spectroscopy Investigation. *Phys. Chem. Chem. Phys.* **2012**, *14*, 12321–12331.
- (359) Krueger, S.; Kloepsch, R.; Li, J.; Nowak, S.; Passerini, S.; Winter, M. How Do Reactions at the Anode/Electrolyte Interface Determine the Cathode Performance in Lithium-Ion Batteries? *J. Electrochem. Soc.* **2013**, *160*, A542–A548.
- (360) Dedryvère, R.; Foix, D.; Franger, S.; Patoux, S.; Daniel, L.; Gonbeau, D. Electrode/Electrolyte Interface Reactivity in High-Voltage Spinel LiMn<sub>1.6</sub>Ni<sub>0.4</sub>O<sub>4</sub>/Li<sub>4</sub>Ti<sub>5</sub>O<sub>12</sub> Lithium-Ion Battery. *J. Phys. Chem. C* **2010**, *114*, 10999–11008.
- (361) Li, S. R.; Chen, C. H.; Xia, X.; Dahn, J. R. The Impact of Electrolyte Oxidation Products in LiNi<sub>0.5</sub>Mn<sub>1.5</sub>O<sub>4</sub>/Li<sub>4</sub>Ti<sub>5</sub>O<sub>12</sub> Cells. *J. Electrochem. Soc.* **2013**, *160*, A1524–A1528.
- (362) Aurbach, D.; Markovsky, B.; Salitra, G.; Markevich, E.; Talyossef, Y.; Koltypin, M.; Nazar, L.; Ellis, B.; Kovacheva, D. Review



on Electrode-Electrolyte Solution Interactions, Related to Cathode Materials for Li-Ion Batteries. *J. Power Sources* **2007**, *165*, 491–499.

(363) Komaba, S.; Kumagai, N.; Kataoka, Y. Influence of Manganese(II), Cobalt(II), and Nickel(II) Additives in Electrolyte on Performance of Graphite Anode for Lithium-Ion Batteries. *Electrochim. Acta* **2002**, *47*, 1229–1239.

(364) Xiong, D. J.; Petibon, R.; Nie, M.; Ma, L.; Xia, J.; Dahn, J. R. Interactions between Positive and Negative Electrodes in Li-Ion Cells Operated at High Temperature and High Voltage. *J. Electrochem. Soc.* **2016**, *163*, A546–A551.

(365) Jung, Y. S.; Lu, P.; Cavanagh, A. S.; Ban, C.; Kim, G.-H.; Lee, S.-H.; George, S. M.; Harris, S. J.; Dillon, A. C. Unexpected Improved Performance of ALD Coated  $\text{LiCoO}_2$ /Graphite Li-Ion Batteries. *Adv. Energy Mater.* **2013**, *3*, 213–219.

(366) Xu, K. Electrolytes and Interphases in Li-Ion Batteries and Beyond. *Chem. Rev.* **2014**, *114*, 11503–11618.

(367) Gauthier, M.; Carney, T. J.; Grimaud, A.; Giordano, L.; Pour, N.; Chang, H. H.; Fenning, D. P.; Lux, S. F.; Paschos, O.; Bauer, C.; et al. Electrode-Electrolyte Interface in Li-Ion Batteries: Current Understanding and New Insights. *J. Phys. Chem. Lett.* **2015**, *6*, 4653–4672.

(368) Aurbach, D.; Markovsky, B.; Rodkin, A.; Levi, E.; Cohen, Y. S.; Kim, H. J.; Schmidt, M. On the Capacity Fading of  $\text{LiCoO}_2$  Intercalation Electrodes. *Electrochim. Acta* **2002**, *47*, 4291–4306.

(369) Minato, T.; Kawaura, H.; Hirayama, M.; Taminato, S.; Suzuki, K.; Yamada, N. L.; Sugaya, H.; Yamamoto, K.; Nakanishi, K.; Orikasa, Y.; et al. Dynamic Behavior at the Interface between Lithium Cobalt Oxide and an Organic Electrolyte Monitored by Neutron Reflectivity Measurements. *J. Phys. Chem. C* **2016**, *120*, 20082–20088.

(370) Liu, B.; Zhou, H.; Yin, C.; Guan, H.; Li, J. Enhanced Electrochemical Performance of  $\text{LiNi}_{0.5}\text{Mn}_{1.5}\text{O}_4$  Cathode by Application of  $\text{LiPF}_2\text{O}_2$  for Lithium Difluoro(oxalate)borate Electrolyte. *Electrochim. Acta* **2019**, *321*, 134690.

(371) Meng, Y.; Chen, G.; Shi, L.; Liu, H.; Zhang, D. Operando Fourier Transform Infrared Investigation of Cathode Electrolyte Interphase Dynamic Reversible Evolution on  $\text{Li}_{1.2}\text{Ni}_{0.2}\text{Mn}_{0.6}\text{O}_2$ . *ACS Appl. Mater. Interfaces* **2019**, *11*, 45108–45117.

(372) Wang, F.; Lin, Y.; Suo, L.; Fan, X.; Gao, T.; Yang, C.; Han, F.; Qi, Y.; Xu, K.; Wang, C. Stabilizing High Voltage  $\text{LiCoO}_2$  Cathode in Aqueous Electrolyte with Interphase-Forming Additive. *Energy Environ. Sci.* **2016**, *9*, 3666–3673.

(373) Song, Y.-M.; Han, J.-G.; Park, S.; Lee, K. T.; Choi, N.-S. A Multifunctional Phosphite-Containing Electrolyte for 5 V-Class  $\text{LiNi}_{0.5}\text{Mn}_{1.5}\text{O}_4$  Cathodes with Superior Electrochemical Performance. *J. Mater. Chem. A* **2014**, *2*, 9506–9513.

(374) Zhang, H.; Eshetu, G. G.; Judez, X.; Li, C.; Rodriguez-Martinez, L. M.; Armand, M. Electrolyte Additives for Lithium Metal Anodes and Rechargeable Lithium Metal Batteries: Progress and Perspectives. *Angew. Chem., Int. Ed.* **2018**, *57*, 15002–15027.

(375) Fan, X.; Chen, L.; Borodin, O.; Ji, X.; Chen, J.; Hou, S.; Deng, T.; Zheng, J.; Yang, C.; Liou, S. C.; et al. Non-flammable Electrolyte Enables Li-Metal Batteries with Aggressive Cathode Chemistries. *Nat. Nanotechnol.* **2018**, *13*, 715–722.

(376) Cao, X.; Ren, X.; Zou, L.; Engelhard, M. H.; Huang, W.; Wang, H.; Matthews, B. E.; Lee, H.; Niu, C.; Arey, B. W.; et al. Monolithic Solid-Electrolyte Interphases Formed in Fluorinated Orthoformate-Based Electrolytes Minimize Li Depletion and Pulverization. *Nat. Energy* **2019**, *4*, 796–805.

(377) Zhang, Z.; Yang, J.; Huang, W.; Wang, H.; Zhou, W.; Li, Y.; Li, Y.; Xu, J.; Huang, W.; Chiu, W.; et al. Cathode-Electrolyte Interphase in Lithium Batteries Revealed by Cryogenic Electron Microscopy. *Matter* **2021**, *4*, 302–312.

(378) Zou, L.; Liu, Z.; Zhao, W.; Jia, H.; Zheng, J.; Yang, Y.; Wang, G.; Zhang, J.-G.; Wang, C. Solid-Liquid Interfacial Reaction Triggered Propagation of Phase Transition from Surface into Bulk Lattice of Ni-Rich Layered Cathode. *Chem. Mater.* **2018**, *30*, 7016–7026.

(379) Wang, C.; Meng, Y. S.; Xu, K. Perspective—Fluorinating Interphases. *J. Electrochem. Soc.* **2019**, *166*, A5184–A5186.

(380) Macneil, D. D.; Dahn, J. R. The Reactions of  $\text{Li}_{0.5}\text{CoO}_2$  with Nonaqueous Solvents at Elevated Temperatures. *J. Electrochem. Soc.* **2002**, *149*, A912.

(381) Baba, Y. Thermal Stability of  $\text{Li}_x\text{CoO}_2$  Cathode for Lithium Ion Battery. *Solid State Ion.* **2002**, *148*, 311–316.

(382) Gallus, D. R.; Wagner, R.; Wiemers-Meyer, S.; Winter, M.; Cekic-Laskovic, I. New Insights into the Structure-Property Relationship of High-Voltage Electrolyte Components for Lithium-Ion Batteries Using the pKa Value. *Electrochim. Acta* **2015**, *184*, 410–416.

(383) Wang, F.-M.; Pradanawati, S. A.; Yeh, N.-H.; Chang, S.-C.; Yang, Y.-T.; Huang, S.-H.; Lin, P.-L.; Lee, J.-F.; Sheu, H.-S.; Lu, M.-L.; et al. Robust Benzimidazole-Based Electrolyte Overcomes High-Voltage and High-Temperature Applications in 5 V Class Lithium Ion Batteries. *Chem. Mater.* **2017**, *29*, 5537–5549.

(384) He, M.; Su, C. C.; Peebles, C.; Feng, Z.; Connell, J. G.; Liao, C.; Wang, Y.; Shkrob, I. A.; Zhang, Z. Mechanistic Insight in the Function of Phosphite Additives for Protection of  $\text{Li-Ni}_{0.5}\text{Co}_{0.2}\text{Mn}_{0.3}\text{O}_2$  Cathode in High Voltage Li-Ion Cells. *ACS Appl. Mater. Interfaces* **2016**, *8*, 11450–11458.

(385) Mun, J.; Lee, J.; Hwang, T.; Lee, J.; Noh, H.; Choi, W. Lithium Difluoro(oxalate)borate for Robust Passivation of  $\text{Li-Ni}_{0.5}\text{Mn}_{1.5}\text{O}_4$  in Lithium-Ion Batteries. *J. Electroanal. Chem.* **2015**, *745*, 8–13.

(386) Wang, X. T.; Gu, Z. Y.; Li, W. H.; Zhao, X. X.; Guo, J. Z.; Du, K. D.; Luo, X. X.; Wu, X. L. Regulation of Cathode-Electrolyte Interphase via Electrolyte Additives in Lithium Ion Batteries. *Chem. Asian J.* **2020**, *15*, 2803–2814.

(387) Wölke, C.; Diddens, D.; Heidrich, B.; Winter, M.; Cekic-Laskovic, I. Understanding the Effectiveness of Phospholane Electrolyte Additives in Lithium-Ion Batteries under High-Voltage Conditions. *ChemElectroChem.* **2021**, *8*, 972–982.

(388) Xu, N.; Shi, J.; Liu, G.; Yang, X.; Zheng, J.; Zhang, Z.; Yang, Y. Research Progress of Fluorine-Containing Electrolyte Additives for Lithium Ion Batteries. *J. Power Sources Adv.* **2021**, *7*, 100043.

(389) Adenusi, H.; Chass, G. A.; Passerini, S.; Tian, K. V.; Chen, G. Lithium Batteries and the Solid Electrolyte Interphase (SEI)—Progress and Outlook. *Adv. Energy Mater.* **2023**, *13*, 2203307.

(390) Lang, J.; Long, Y.; Qu, J.; Luo, X.; Wei, H.; Huang, K.; Zhang, H.; Qi, L.; Zhang, Q.; Li, Z.; et al. One-Pot Solution Coating of High Quality LiF Layer to Stabilize Li Metal Anode. *Energy Storage Mater.* **2019**, *16*, 85–90.

(391) Stoebe, T. G. Influence of  $\text{OH}^-$  Ions on Infrared Absorption and Ionic Conductivity in Lithium Fluoride Crystals. *J. Phys. Chem. Solids* **1967**, *28*, 1375–1382.

(392) Yuan, Y.; Wu, F.; Bai, Y.; Li, Y.; Chen, G.; Wang, Z.; Wu, C. Regulating Li Deposition by Constructing LiF-Rich Host for Dendrite-Free Lithium Metal Anode. *Energy Storage Mater.* **2019**, *16*, 411–418.

(393) Hou, J.; Yang, M.; Wang, D.; Zhang, J. Fundamentals and Challenges of Lithium Ion Batteries at Temperatures between  $-40$  and  $60^\circ\text{C}$ . *Adv. Energy Mater.* **2020**, *10*, 1904152.

(394) Smart, M. C.; Lucht, B. L.; Dalavi, S.; Krause, F. C.; Ratnakumar, B. V. The Effect of Additives upon the Performance of MCMB/ $\text{LiNi}_{1-x}\text{Co}_x\text{O}_2$  Li-Ion Cells Containing Methyl Butyrate-Based Wide Operating Temperature Range Electrolytes. *J. Electrochem. Soc.* **2012**, *159*, A739–A751.

(395) Song, G.; Yi, Z.; Su, F.; Xie, L.; Wang, Z.; Wei, X.-X.; Xu, G.; Chen, C.-M. Boosting the Low-Temperature Performance for Li-Ion Batteries in  $\text{LiPF}_6$ -Based Local High-Concentration Electrolyte. *ACS Energy Lett.* **2023**, *8*, 1336–1343.

(396) Li, Q.; Liu, G.; Cheng, H.; Sun, Q.; Zhang, J.; Ming, J. Low-Temperature Electrolyte Design for Lithium-Ion Batteries: Prospect and Challenges. *Chemistry* **2021**, *27*, 15842–15865.

(397) Yang, B.; Zhang, H.; Yu, L.; Fan, W.; Huang, D. Lithium Difluorophosphate as an Additive to Improve the Low Temperature Performance of  $\text{LiNi}_{0.5}\text{Co}_{0.2}\text{Mn}_{0.3}\text{O}_2$ /graphite Cells. *Electrochim. Acta* **2016**, *221*, 107–114.

(398) Shi, J.; Ehteshami, N.; Ma, J.; Zhang, H.; Liu, H.; Zhang, X.; Li, J.; Paillard, E. Improving the Graphite/Electrolyte Interface in



Lithium-Ion Battery for Fast Charging and Low Temperature Operation: Fluorosulfonyl Isocyanate as Electrolyte Additive. *J. Power Sources* **2019**, *429*, 67–74.

(399) Smith, K. A.; Smart, M. C.; Prakash, G. K. S.; Ratnakumar, B. V. Electrolytes Containing Fluorinated Ester Co-Solvents for Low-Temperature Li-Ion Cells. *ECS Trans.* **2008**, *11*, 91–98.

(400) Liu, J.; Yuan, B.; He, N.; Dong, L.; Chen, D.; Zhong, S.; Ji, Y.; Han, J.; Yang, C.; Liu, Y.; et al. Reconstruction of LiF-Rich Interphases through an Anti-freezing Electrolyte for Ultralow-Temperature LiCoO<sub>2</sub> Batteries. *Energy Environ. Sci.* **2023**, *16*, 1024–1034.

(401) Lu, W.; Xie, K.; Chen, Z.; Xiong, S.; Pan, Y.; Zheng, C. A New Co-Solvent for Wide Temperature Lithium-Ion Battery Electrolytes: 2,2,2-Trifluoroethyl n-Caproate. *J. Power Sources* **2015**, *274*, 676–684.

(402) Ozhables, Y.; Gunceler, D.; Arias, T. Stability and Surface Diffusion at Lithium-Electrolyte Interphases with Connections to Dendrite Suppression. *arXiv* **2015**, 1504.05799.

(403) Yang, T.; Li, S.; Wang, W.; Lu, J.; Fan, W.; Zuo, X.; Nan, J. Nonflammable Functional Electrolytes with All-Fluorinated Solvents Matching Rechargeable High-Voltage Li-Metal Batteries with Ni-Rich Ternary Cathode. *J. Power Sources* **2021**, *505*, 230055.

(404) Liao, L.; Cheng, X.; Ma, Y.; Zuo, P.; Fang, W.; Yin, G.; Gao, Y. Fluoroethylene Carbonate as Electrolyte Additive to Improve Low Temperature Performance of LiFePO<sub>4</sub> Electrode. *Electrochim. Acta* **2013**, *87*, 466–472.

(405) Dong, X.; Lin, Y.; Li, P.; Ma, Y.; Huang, J.; Bin, D.; Wang, Y.; Qi, Y.; Xia, Y. High-Energy Rechargeable Metallic Lithium Battery at –70 Degrees C Enabled by a Cosolvent Electrolyte. *Angew. Chem., Int. Ed.* **2019**, *58*, 5623–5627.

(406) Peng, Z.; Cao, X.; Gao, P.; Jia, H.; Ren, X.; Roy, S.; Li, Z.; Zhu, Y.; Xie, W.; Liu, D.; et al. High-Power Lithium Metal Batteries Enabled by High-Concentration Acetonitrile-Based Electrolytes with Vinylene Carbonate Additive. *Adv. Funct. Mater.* **2020**, *30*, 2001285.

(407) Jiang, L. L.; Yan, C.; Yao, Y. X.; Cai, W.; Huang, J. Q.; Zhang, Q. Inhibiting Solvent Co-Intercalation in a Graphite Anode by a Localized High-Concentration Electrolyte in Fast-Charging Batteries. *Angew. Chem., Int. Ed.* **2021**, *60*, 3402–3406.

(408) Yang, Y.; Wang, H.; Zhu, C.; Ma, J. Armor-like Inorganic-rich Cathode Electrolyte Interphase Enabled by the Pentafluorophenylboronic Acid Additive for High-voltage Li|NCM622 Batteries. *Angew. Chem., Int. Ed.* **2023**, *62*, No. e202300057.

(409) Sun, Z.; Li, F.; Ding, J.; Lin, Z.; Xu, M.; Zhu, M.; Liu, J. High-Voltage and High-Temperature LiCoO<sub>2</sub> Operation via the Electrolyte Additive of Electron-Defect Boron Compounds. *ACS Energy Lett.* **2023**, *8*, 2478–2487.

(410) Liu, Q.; Jiang, W.; Xu, J.; Xu, Y.; Yang, Z.; Yoo, D. J.; Pupek, K. Z.; Wang, C.; Liu, C.; Xu, K.; et al. A Fluorinated Cation Introduces New Interphasial Chemistries to Enable High-Voltage Lithium Metal Batteries. *Nat. Commun.* **2023**, *14*, 3678.

(411) Sun, C.; Ji, X.; Weng, S.; Li, R.; Huang, X.; Zhu, C.; Xiao, X.; Deng, T.; Fan, L.; Chen, L.; et al. 50C Fast-Charge Li-Ion Batteries using a Graphite Anode. *Adv. Mater.* **2022**, *34*, No. e2206020.

(412) Shin, H.; Park, J.; Sastry, A. M.; Lu, W. Effects of Fluoroethylene Carbonate (FEC) on Anode and Cathode Interfaces at Elevated Temperatures. *J. Electrochem. Soc.* **2015**, *162*, A1683–A1692.

(413) Hu, L.; Zhang, Z.; Amine, K. Fluorinated Electrolytes for Li-Ion Battery: An FEC-Based Electrolyte for High Voltage LiNi<sub>0.5</sub>Mn<sub>1.5</sub>O<sub>4</sub>/Graphite Couple. *Electrochem. commun.* **2013**, *35*, 76–79.

(414) Ehteshami, N.; Ibing, L.; Stolz, L.; Winter, M.; Paillard, E. Ethylene Carbonate-Free Electrolytes for Li-Ion Battery: Study of the Solid Electrolyte Interphases Formed on Graphite Anodes. *J. Power Sources* **2020**, *451*, 227804.

(415) Shen, C.; Hu, G.; Cheong, L. Z.; Huang, S.; Zhang, J. G.; Wang, D. Direct Observation of the Growth of Lithium Dendrites on Graphite Anodes by Operando EC-AFM. *Small Methods* **2018**, *2*, 1700298.

(416) Hwang, J.-Y.; Park, S.-J.; Yoon, C. S.; Sun, Y.-K. Customizing a Li-Metal Battery That Survives Practical Operating Conditions for Electric Vehicle Applications. *Energy Environ. Sci.* **2019**, *12*, 2174–2184.

(417) Markevich, E.; Salitra, G.; Chesneau, F.; Schmidt, M.; Aurbach, D. Very Stable Lithium Metal Stripping-Plating at a High Rate and High Areal Capacity in Fluoroethylene Carbonate-Based Organic Electrolyte Solution. *ACS Energy Lett.* **2017**, *2*, 1321–1326.

(418) Guo, J. C.; Tan, S. J.; Zhang, C. H.; Wang, W. P.; Zhao, Y.; Wang, F.; Zhang, X. S.; Wen, R.; Zhang, Y.; Fan, M.; et al. A Self-Reconfigured, Dual-Layered Artificial Interphase Toward High-Current-Density Quasi-Solid-State Lithium Metal Batteries. *Adv. Mater.* **2023**, *35*, No. e2300350.

(419) Park, S.-J.; Hwang, J.-Y.; Sun, Y.-K. Trimethylsilyl Azide (C<sub>3</sub>H<sub>9</sub>N<sub>3</sub>Si): A Highly Efficient Additive for Tailoring Fluoroethylene Carbonate (FEC) Based Electrolytes for Li-Metal Batteries. *J. Mater. Chem. A* **2019**, *7*, 13441–13448.

(420) Wang, X.; Zhang, M.; Alvarado, J.; Wang, S.; Sina, M.; Lu, B.; Bouwer, J.; Xu, W.; Xiao, J.; Zhang, J. G.; et al. New Insights on the Structure of Electrochemically Deposited Lithium Metal and Its Solid Electrolyte Interphases via Cryogenic TEM. *Nano Lett.* **2017**, *17*, 7606–7612.

(421) Guo, L.; Huang, F.; Cai, M.; Zhang, J.; Ma, G.; Xu, S. Organic-Inorganic Hybrid SEI Induced by a New Lithium Salt for High-Performance Metallic Lithium Anodes. *ACS Appl. Mater. Interfaces* **2021**, *13*, 32886–32893.

(422) Guo, Z.; Yang, H.; Wei, Q.; Xu, S.; Hu, G.; Bai, S.; Li, F. Dual-Additives Enable Stable Electrode-Electrolyte Interfaces for Long-Life Li-SPAN Batteries. *Chin. Chem. Lett.* **2024**, *35*, 108622.

(423) Yang, H.-W.; Kang, W. S.; Kim, S.-J. A Significant Enhancement of Cycling Stability at Fast Charging Rate through Incorporation of Li<sub>3</sub>N into LiF-Based SEI in SiO Anode for Li-Ion Batteries. *Electrochim. Acta* **2022**, *412*, 140107.

(424) Su, H.; Chen, Z.; Li, M.; Bai, P.; Li, Y.; Ji, X.; Liu, Z.; Sun, J.; Ding, J.; Yang, M.; et al. Achieving Practical High-Energy-Density Lithium-Metal Batteries by a Dual-Anion Regulated Electrolyte. *Adv. Mater.* **2023**, *35*, No. e2301171.

(425) Dong, L.; Liu, Y.; Wen, K.; Chen, D.; Rao, D.; Liu, J.; Yuan, B.; Dong, Y.; Wu, Z.; Liang, Y.; et al. High-Polarity Fluoroalkyl Ether Electrolyte Enables Solvation-Free Li<sup>+</sup> Transfer for High-Rate Lithium Metal Batteries. *Adv. Sci.* **2022**, *9*, No. e2104699.

(426) Yue, X.; Zhang, J.; Dong, Y.; Chen, Y.; Shi, Z.; Xu, X.; Li, X.; Liang, Z. Reversible Li Plating on Graphite Anodes through Electrolyte Engineering for Fast-Charging Batteries. *Angew. Chem., Int. Ed.* **2023**, *62*, No. e202302285.

(427) Rodrigues, M.-T. F.; Babu, G.; Gullapalli, H.; Kalaga, K.; Sayed, F. N.; Kato, K.; Joyner, J.; Ajayan, P. M. A Materials Perspective on Li-Ion Batteries at Extreme Temperatures. *Nat. Energy* **2017**, *2*, 1–14.

(428) Liu, Y.; Zhu, Y.; Cui, Y. Challenges and Opportunities towards Fast-Charging Battery Materials. *Nat. Energy* **2019**, *4*, 540–550.

(429) Fan, X.; Ji, X.; Chen, L.; Chen, J.; Deng, T.; Han, F.; Yue, J.; Piao, N.; Wang, R.; Zhou, X.; et al. All-Temperature Batteries Enabled by Fluorinated Electrolytes with Non-polar Solvents. *Nat. Energy* **2019**, *4*, 882–890.

(430) Liu, W.; Liu, P.; Mitlin, D. Review of Emerging Concepts in SEI Analysis and Artificial SEI Membranes for Lithium, Sodium, and Potassium Metal Battery Anodes. *Adv. Energy Mater.* **2020**, *10*, 2002297.

(431) Dey, A. N. Lithium Anode Film and Organic and Inorganic Electrolyte Batteries. *Thin Solid Films* **1977**, *43*, 131–171.

(432) Nazri, G.; Muller, R. H. Composition of Surface Layers on Li Electrodes in PC, LiClO<sub>4</sub> of Very Low Water Content. *J. Electrochem. Soc.* **1985**, *132*, 2050–2054.

(433) Zaban, A.; Aurbach, D. Impedance Spectroscopy of Lithium and Nickel Electrodes in Propylene Carbonate Solutions of Different Lithium Salts a Comparative Study. *J. Power Sources* **1995**, *54*, 289–295.

- (434) Kanamura, K.; Tamura, H.; Shiraishi, S.; Takehara, Z. I. XPS Analysis of Lithium Surfaces Following Immersion in Various Solvents Containing  $\text{LiBF}_4$ . *J. Electrochem. Soc.* **1995**, *142*, 340–347.
- (435) Peled, E.; Golodnitsky, D.; Ardel, G. Advanced Model for Solid Electrolyte Interphase Electrodes in Liquid and Polymer Electrolytes. *J. Electrochem. Soc.* **1997**, *144*, L208–L210.
- (436) Ein-Eli, Y. A New Perspective on the Formation and Structure of the Solid Electrolyte Interface at the Graphite Anode of Li-Ion Cells. *Electrochem. Solid-State Lett.* **1999**, *2*, 212.
- (437) Wu, J.; Ihsan-Ul-Haq, M.; Chen, Y.; Kim, J.-K. Understanding Solid Electrolyte Interphases: Advanced Characterization Techniques and Theoretical Simulations. *Nano Energy* **2021**, *89*, 106489.
- (438) Kominato, A.; Yasukawa, E.; Sato, N.; Ijuuin, T.; Asahina, H.; Mori, S. Analysis of Surface Films on Lithium in Various Organic Electrolytes. *J. Power Sources* **1997**, *68*, 471–475.
- (439) Dollé, M. L.; Sannier, L.; Beaudoin, B.; Trentin, M.; Tarascon, J.-M. Live Scanning Electron Microscope Observations of Dendritic Growth in Lithium/Polymer Cells. *Electrochem. Solid-State Lett.* **2002**, *5*, A286–A289.
- (440) Sacci, R. L.; Dudney, N. J.; More, K. L.; Parent, L. R.; Arslan, I.; Browning, N. D.; Unocic, R. R. Direct Visualization of Initial SEI Morphology and Growth Kinetics During Lithium Deposition by In Situ Electrochemical Transmission Electron Microscopy. *Chem. Commun.* **2014**, *50*, 2104–2107.
- (441) Sacci, R. L.; Black, J. M.; Balke, N.; Dudney, N. J.; More, K. L.; Unocic, R. R. Nanoscale Imaging of Fundamental Li Battery Chemistry: Solid-Electrolyte Interphase Formation and Preferential Growth of Lithium Metal Nanoclusters. *Nano Lett.* **2015**, *15*, 2011–2018.
- (442) Lee, S.-B.; Pyun, S.-I. The Effect of Electrolyte Temperature on the Passivity of Solid Electrolyte Interphase Formed on a Graphite Electrode. *Carbon* **2002**, *40*, 2333–2339.
- (443) Li, Y.; Huang, W.; Li, Y.; Chiu, W.; Cui, Y. Opportunities for Cryogenic Electron Microscopy in Materials Science and Nanoscience. *ACS Nano* **2020**, *14*, 9263–9276.
- (444) Liu, Q. C.; Xu, J. J.; Yuan, S.; Chang, Z. W.; Xu, D.; Yin, Y. B.; Li, L.; Zhong, H. X.; Jiang, Y. S.; Yan, J. M.; et al. Artificial Protection Film on Lithium Metal Anode toward Long-Cycle-Life Lithium-Oxygen Batteries. *Adv. Mater.* **2015**, *27*, 5241–5247.
- (445) Li, Y.; Huang, W.; Li, Y.; Pei, A.; Boyle, D. T.; Cui, Y. Correlating Structure and Function of Battery Interphases at Atomic Resolution Using Cryoelectron Microscopy. *Joule* **2018**, *2*, 2167–2177.
- (446) Huang, W.; Boyle, D. T.; Li, Y.; Li, Y.; Pei, A.; Chen, H.; Cui, Y. Nanostructural and Electrochemical Evolution of the Solid-Electrolyte Interphase on CuO Nanowires Revealed by Cryogenic-Electron Microscopy and Impedance Spectroscopy. *ACS Nano* **2019**, *13*, 737–744.
- (447) Sheng, O.; Zheng, J.; Ju, Z.; Jin, C.; Wang, Y.; Chen, M.; Nai, J.; Liu, T.; Zhang, W.; Liu, Y.; et al. In Situ Construction of a LiF-Enriched Interface for Stable All-Solid-State Batteries and its Origin Revealed by Cryo-TEM. *Adv. Mater.* **2020**, *32*, No. e2000223.
- (448) Li, Y.; Zhou, W.; Li, Y.; Huang, W.; Zhang, Z.; Chen, G.; Wang, H.; Wu, G. H.; Rolston, N.; Vila, R.; et al. Unravelling Atomic Structure and Degradation Mechanisms of Organic-Inorganic Halide Perovskites by Cryo-EM. *Joule* **2019**, *3*, 2854–2866.
- (449) Huang, W.; Wang, J.; Braun, M. R.; Zhang, Z.; Li, Y.; Boyle, D. T.; McIntyre, P. C.; Cui, Y. Dynamic Structure and Chemistry of the Silicon Solid-Electrolyte Interphase Visualized by Cryogenic Electron Microscopy. *Matter* **2019**, *1*, 1232–1245.
- (450) Sayavong, P.; Zhang, W.; Oyakhire, S. T.; Boyle, D. T.; Chen, Y.; Kim, S. C.; Vila, R. A.; Holmes, S. E.; Kim, M. S.; Bent, S. F.; et al. Dissolution of the Solid Electrolyte Interphase and Its Effects on Lithium Metal Anode Cyclability. *J. Am. Chem. Soc.* **2023**, *145*, 12342–12350.
- (451) Benninghoven, A. Surface Investigation of Solids by the Static Method of Secondary Ion Mass Spectroscopy (SIMS). *Surf. Sci.* **1973**, *35*, 427–457.
- (452) Otto, S. K.; Riegger, L. M.; Fuchs, T.; Kayser, S.; Schweitzer, P.; Burkhardt, S.; Henss, A.; Janek, J. In Situ Investigation of Lithium Metal-Solid Electrolyte Anode Interfaces with ToF-SIMS. *Adv. Mater. Interfaces* **2022**, *9*, 2102387.
- (453) Peled, E.; Bar Tow, D.; Merson, A.; Gladkikh, A.; Burstein, L.; Golodnitsky, D. Composition, Depth Profiles and Lateral Distribution of Materials in the SEI Built on HOPG-TOF SIMS and XPS Studies. *J. Power Sources* **2001**, *97–98*, S2–S7.
- (454) Yamagishi, Y.; Morita, H.; Nomura, Y.; Igaki, E. Visualizing Lithiation of Graphite Composite Anodes in All-Solid-State Batteries Using Operando Time-of-Flight Secondary Ion Mass Spectrometry. *J. Phys. Chem. Lett.* **2021**, *12*, 4623–4627.
- (455) Pereira-Nabais, C.; Swiatowska, J.; Rosso, M.; Ozanam, F.; Seyeux, A.; Gohier, A.; Tran-Van, P.; Cassir, M.; Marcus, P. Effect of Lithiation Potential and Cycling on Chemical and Morphological Evolution of Si Thin Film Electrode Studied by ToF-SIMS. *ACS Appl. Mater. Interfaces* **2014**, *6*, 13023–13033.
- (456) Otto, S.-K.; Moryson, Y.; Krauskopf, T.; Peppler, K.; Sann, J.; Janek, J.; Henss, A. In-Depth Characterization of Lithium-Metal Surfaces with XPS and ToF-SIMS: Toward Better Understanding of the Passivation Layer. *Chem. Mater.* **2021**, *33*, 859–867.
- (457) Zhu, Z.; Zhou, Y.; Yan, P.; Vemuri, R. S.; Xu, W.; Zhao, R.; Wang, X.; Thevuthasan, S.; Baer, D. R.; Wang, C. M. In Situ Mass Spectrometric Determination of Molecular Structural Evolution at the Solid Electrolyte Interphase in Lithium-Ion Batteries. *Nano Lett.* **2015**, *15*, 6170–6176.
- (458) Papp, C.; Steinrück, H.-P. In Situ High-Resolution X-ray Photoelectron Spectroscopy - Fundamental Insights in Surface Reactions. *Surf. Sci. Rep.* **2013**, *68*, 446–487.
- (459) Maibach, J.; Kallquist, I.; Andersson, M.; Urpelainen, S.; Edstrom, K.; Rensmo, H.; Siegbahn, H.; Hahlin, M. Probing a Battery Electrolyte Drop with Ambient Pressure Photoelectron Spectroscopy. *Nat. Commun.* **2019**, *10*, 3080.
- (460) Xu, C.; Sun, B.; Gustafsson, T.; Edström, K.; Brandell, D.; Hahlin, M. Interface Layer Formation in Solid Polymer Electrolyte Lithium Batteries: An XPS Study. *J. Mater. Chem. A* **2014**, *2*, 7256–7264.
- (461) Oyakhire, S. T.; Gong, H.; Cui, Y.; Bao, Z.; Bent, S. F. An X-ray Photoelectron Spectroscopy Primer for Solid Electrolyte Interphase Characterization in Lithium Metal Anodes. *ACS Energy Lett.* **2022**, *7*, 2540–2546.
- (462) Zhang, J.; Wang, R.; Yang, X.; Lu, W.; Wu, X.; Wang, X.; Li, H.; Chen, L. Direct Observation of Inhomogeneous Solid Electrolyte Interphase on MnO Anode with Atomic Force Microscopy and Spectroscopy. *Nano Lett.* **2012**, *12*, 2153–2157.
- (463) Shen, C.; Wang, S.; Jin, Y.; Han, W. Q. In Situ AFM Imaging of Solid Electrolyte Interfaces on HOPG with Ethylene Carbonate and Fluoroethylene Carbonate-Based Electrolytes. *ACS Appl. Mater. Interfaces* **2015**, *7*, 25441–25447.
- (464) Shi, Y.; Yan, H. J.; Wen, R.; Wan, L. J. Direct Visualization of Nucleation and Growth Processes of Solid Electrolyte Interphase Film Using in Situ Atomic Force Microscopy. *ACS Appl. Mater. Interfaces* **2017**, *9*, 22063–22067.
- (465) Liu, R. R.; Deng, X.; Liu, X. R.; Yan, H. J.; Cao, A. M.; Wang, D. Facet-Dependent SEI Formation on the  $\text{LiNi}_{0.5}\text{Mn}_{1.5}\text{O}_4$  Cathode Identified by In Situ Single Particle Atomic Force Microscopy. *Chem. Commun.* **2014**, *50*, 15756–15759.
- (466) Anderson, M. S. Locally Enhanced Raman Spectroscopy with an Atomic Force Microscope. *Appl. Phys. Lett.* **2000**, *76*, 3130–3132.
- (467) Zhang, R.; Zhang, Y.; Dong, Z. C.; Jiang, S.; Zhang, C.; Chen, L. G.; Zhang, L.; Liao, Y.; Aizpurua, J.; Luo, Y.; et al. Chemical Mapping of a Single Molecule by Plasmon-Enhanced Raman Scattering. *Nature* **2013**, *498*, 82–86.
- (468) Hong, L.; Li, L.; Chen-Wiegar, Y. K.; Wang, J.; Xiang, K.; Gan, L.; Li, W.; Meng, F.; Wang, F.; Wang, J.; et al. Two-Dimensional Lithium Diffusion Behavior and Probable Hybrid Phase Transformation Kinetics in Olivine Lithium Iron Phosphate. *Nat. Commun.* **2017**, *8*, 1194.

- (469) Wang, J.; Karen Chen-Wiegar, Y. C.; Eng, C.; Shen, Q.; Wang, J. Visualization of Anisotropic-Isotropic Phase Transformation Dynamics in Battery Electrode Particles. *Nat. Commun.* **2016**, *7*, 12372.
- (470) Takamatsu, D.; Nakatsutsumi, T.; Mori, S.; Orikasa, Y.; Mogi, M.; Yamashige, H.; Sato, K.; Fujimoto, T.; Takanashi, Y.; Murayama, H.; et al. Nanoscale Observation of the Electronic and Local Structures of LiCoO<sub>2</sub> Thin Film Electrode by Depth-Resolved X-ray Absorption Spectroscopy. *J. Phys. Chem. Lett.* **2011**, *2*, 2511–2514.
- (471) Jarry, A.; Gottis, S.; Yu, Y. S.; Roque-Rosell, J.; Kim, C.; Cabana, J.; Kerr, J.; Kostecki, R. The Formation Mechanism of Fluorescent Metal Complexes at the Li<sub>x</sub>Ni<sub>0.5</sub>Mn<sub>1.5</sub>O<sub>4-δ</sub>/Carbonate Ester Electrolyte Interface. *J. Am. Chem. Soc.* **2015**, *137*, 3533–3539.
- (472) Bleith, P.; Van Beek, W.; Kaiser, H.; Novák, P.; Villeveille, C. Simultaneous In Situ X-ray Absorption Spectroscopy and X-ray Diffraction Studies on Battery Materials: The Case of Fe<sub>0.5</sub>TiOPO<sub>4</sub>. *J. Phys. Chem. C* **2015**, *119*, 3466–3471.
- (473) Liu, D.; Shadike, Z.; Lin, R.; Qian, K.; Li, H.; Li, K.; Wang, S.; Yu, Q.; Liu, M.; Ganapathy, S.; et al. Review of Recent Development of In Situ/Operando Characterization Techniques for Lithium Battery Research. *Adv. Mater.* **2019**, *31*, No. e1806620.
- (474) Rus, E. D.; Dura, J. A. In Situ Neutron Reflectometry Study of Solid Electrolyte Interface (SEI) Formation on Tungsten Thin-Film Electrodes. *ACS Appl. Mater. Interfaces* **2019**, *11*, 47553–47563.
- (475) Rus, E. D.; Dura, J. A. In Situ Neutron Reflectometry Study of a Tungsten Oxide/Li-Ion Battery Electrolyte Interface. *ACS Appl. Mater. Interfaces* **2023**, *15*, 2832–2842.
- (476) Huang, Z.; Ren, J.; Zhang, W.; Xie, M.; Li, Y.; Sun, D.; Shen, Y.; Huang, Y. Protecting the Li-Metal Anode in a Li-O<sub>2</sub> Battery by using Boric Acid as an SEI-Forming Additive. *Adv. Mater.* **2018**, *30*, No. e1803270.
- (477) Fan, L.; Ma, R.; Zhang, Q.; Jia, X.; Lu, B. Graphite Anode for a Potassium-Ion Battery with Unprecedented Performance. *Angew. Chem., Int. Ed.* **2019**, *58*, 10500–10505.
- (478) Sun, Y.; Ren, Y. In Situ Synchrotron X-Ray Techniques for Real-Time Probing of Colloidal Nanoparticle Synthesis. *Part. Part. Syst. Charact.* **2013**, *30*, 399–419.
- (479) Yu, C.; Ganapathy, S.; Eck, E.; Wang, H.; Basak, S.; Li, Z.; Wagemaker, M. Accessing the Bottleneck in All-Solid State Batteries, Lithium-Ion Transport over the Solid-Electrolyte-Electrode Interface. *Nat. Commun.* **2017**, *8*, 1086.
- (480) Langdon, J.; Manthiram, A. Crossover Effects in Batteries with High-Nickel Cathodes and Lithium-Metal Anodes. *Adv. Funct. Mater.* **2021**, *31*, 2010267.
- (481) Zhu, Y.; Hilty, C.; Savukov, I. Dynamic Nuclear Polarization Enhanced Nuclear Spin Optical Rotation. *Angew. Chem., Int. Ed.* **2021**, *60*, 8823–8826.
- (482) Gunnarsdóttir, A. B.; Vema, S.; Menkin, S.; Marbella, L. E.; Grey, C. P. Investigating the Effect of a Fluoroethylene Carbonate Additive on Lithium Deposition and the Solid Electrolyte Interphase in Lithium Metal Batteries Using In Situ NMR Spectroscopy. *J. Mater. Chem. A* **2020**, *8*, 14975–14992.
- (483) Kolesov, D. V.; Gorelkin, P. V.; Prelovskaya, A. O.; Erofeev, A. S. Scanning Electrochemical Microscopy for the Study of Energy Accumulators: Principles, Equipment, and Application. *Mosc. Univ. Phys. Bull.* **2022**, *77*, 801–810.
- (484) Ventosa, E.; Schuhmann, W. Scanning Electrochemical Microscopy of Li-Ion Batteries. *Phys. Chem. Chem. Phys.* **2015**, *17*, 28441–28450.
- (485) Zoski, C. G. Review—Advances in Scanning Electrochemical Microscopy (SECM). *J. Electrochem. Soc.* **2016**, *163*, H3088–H3100.
- (486) Bulter, H.; Peters, F.; Schwenzel, J.; Wittstock, G. Spatiotemporal Changes of the Solid Electrolyte Interphase in Lithium-Ion Batteries Detected by Scanning Electrochemical Microscopy. *Angew. Chem., Int. Ed.* **2014**, *53*, 10531–10535.
- (487) Shan, X.; Zhong, Y.; Zhang, L.; Zhang, Y.; Xia, X.; Wang, X.; Tu, J. A Brief Review on Solid Electrolyte Interphase Composition Characterization Technology for Lithium Metal Batteries: Challenges and Perspectives. *J. Phys. Chem. C* **2021**, *125*, 19060–19080.
- (488) Verma, P.; Maire, P.; Novák, P. A Review of the Features and Analyses of the Solid Electrolyte Interphase in Li-Ion Batteries. *Electrochim. Acta* **2010**, *55*, 6332–6341.
- (489) Wang, A.; Kadam, S.; Li, H.; Shi, S.; Qi, Y. Review on Modeling of the Anode Solid Electrolyte Interphase (SEI) for Lithium-Ion Batteries. *Npj Comput. Mater.* **2018**, *4*, 15.
- (490) Chen, J.; Li, Q.; Pollard, T. P.; Fan, X.; Borodin, O.; Wang, C. Electrolyte design for Li metal-free Li batteries. *Mater. Today* **2020**, *39*, 118–126.
- (491) Yao, N.; Chen, X.; Fu, Z. H.; Zhang, Q. Applying Classical, Ab Initio, and Machine-Learning Molecular Dynamics Simulations to the Liquid Electrolyte for Rechargeable Batteries. *Chem. Rev.* **2022**, *122*, 10970–11021.
- (492) Li, Y.; Li, Y.; Pei, A.; Yan, K.; Sun, Y.; Wu, C. L.; Joubert, L. M.; Chin, R.; Koh, A. L.; Yu, Y.; et al. Atomic Structure of Sensitive Battery Materials and Interfaces Revealed by Cryo-Electron Microscopy. *Science* **2017**, *358*, 506–510.
- (493) Huang, W.; Attia, P. M.; Wang, H.; Renfrew, S. E.; Jin, N.; Das, S.; Zhang, Z.; Boyle, D. T.; Li, Y.; Bazant, M. Z.; et al. Evolution of the Solid-Electrolyte Interphase on Carbonaceous Anodes Visualized by Atomic-Resolution Cryogenic Electron Microscopy. *Nano Lett.* **2019**, *19*, 5140–5148.
- (494) Tu, Z.; Zachman, M. J.; Choudhury, S.; Khan, K. A.; Zhao, Q.; Kourkoutis, L. F.; Archer, L. A. Stabilizing Protic and Aprotic Liquid Electrolytes at High-Bandgap Oxide Interphases. *Chem. Mater.* **2018**, *30*, 5655–5662.
- (495) Xiaobing, L.; Holland, J.; Burgess, S.; Bhadare, S.; Yamaguchi, S.; Birtwistle, D.; Statham, P.; Rowlands, N. Detection of Lithium X-rays by EDS. *Microsc. Microanal.* **2013**, *19*, 1136–1137.
- (496) Hubaud, A. A.; Yang, Z.; Schroeder, D. J.; Dogan, F.; Trahey, L.; Vaughey, J. T. Interfacial Study of the Role of SiO<sub>2</sub> on Si Anodes Using Electrochemical Quartz Crystal Microbalance. *J. Power Sources* **2015**, *282*, 639–644.
- (497) Dargel, V.; Shpigel, N.; Sigalov, S.; Nayak, P.; Levi, M. D.; Daikhin, L.; Aurbach, D. In Situ Real-Time Gravimetric and Viscoelastic Probing of Surface Films Formation on Lithium Batteries Electrodes. *Nat. Commun.* **2017**, *8*, 1389.
- (498) Levi, M. D.; Shpigel, N.; Sigalov, S.; Dargel, V.; Daikhin, L.; Aurbach, D. In Situ Porous Structure Characterization of Electrodes for Energy Storage and Conversion by EQCM-D: a Review. *Electrochim. Acta* **2017**, *232*, 271–284.
- (499) Munoz, R. a. A.; Toma, S. H.; Toma, H. E.; Araki, K.; Angnes, L. Investigation of Interfacial Processes at Tetraethylenated Zinc Porphyrin Films Using Electrochemical Surface Plasmon Resonance and Electrochemical Quartz Crystal Microbalance. *Electrochim. Acta* **2009**, *54*, 2971–2976.
- (500) Levi, M. D.; Levy, N.; Sigalov, S.; Salitra, G.; Aurbach, D.; Maier, J. Electrochemical Quartz Crystal Microbalance (EQCM) Studies of Ions and Solvents Insertion into Highly Porous Activated Carbons. *J. Am. Chem. Soc.* **2010**, *132*, 13220–13222.
- (501) Griffin, J. M.; Forse, A. C.; Tsai, W. Y.; Taberna, P. L.; Simon, P.; Grey, C. P. In Situ NMR and Electrochemical Quartz Crystal Microbalance Techniques Reveal the Structure of the Electrical Double Layer in Supercapacitors. *Nat. Mater.* **2015**, *14*, 812–819.
- (502) Song, X.; Liu, T.; Amine, J.; Duan, Y.; Zheng, J.; Lin, Y.; Pan, F. In-Situ Mass-Electrochemical Study of Surface Redox Potential and Interfacial Chemical Reactions of Li(Na)FePO<sub>4</sub> Nanocrystals for Li(Na)-Ion Batteries. *Nano Energy* **2017**, *37*, 90–97.
- (503) Shpigel, N.; Levi, M. D.; Sigalov, S.; Girshevitz, O.; Aurbach, D.; Daikhin, L.; Pikma, P.; Marandi, M.; Janes, A.; Lust, E.; et al. In Situ Hydrodynamic Spectroscopy for Structure Characterization of Porous Energy Storage Electrodes. *Nat. Mater.* **2016**, *15*, 570–575.
- (504) Fang, C.; Li, J.; Zhang, M.; Zhang, Y.; Yang, F.; Lee, J. Z.; Lee, M. H.; Alvarado, J.; Schroeder, M. A.; Yang, Y.; et al. Quantifying Inactive Lithium in Lithium Metal Batteries. *Nature* **2019**, *572*, 511–515.
- (505) Kasahara, S.; Ogoe, T.; Ikemiya, N.; Yamamoto, T.; Natsui, K.; Yokota, Y.; Wong, R. A.; Iizuka, S.; Hoshi, N.; Tateyama, Y.; et al.



In Situ Spectroscopic Study on the Surface Hydroxylation of Diamond Electrodes. *Anal. Chem.* **2019**, *91*, 4980–4986.

(506) Sherwood, P. M. A. Photoelectron Spectroscopic Studies of Electrode and Related Surfaces. *Chem. Soc. Rev.* **1985**, *14*, 1.

(507) Bagus, P. S.; Ilton, E. S.; Nelin, C. J. The Interpretation of XPS Spectra: Insights into Materials Properties. *Surf. Sci. Rep.* **2013**, *68*, 273–304.

(508) Wang, J. G.; Zhang, Y.; Yu, X.; Hua, X.; Wang, F.; Long, Y. T.; Zhu, Z. Direct Molecular Evidence of Proton Transfer and Mass Dynamics at the Electrode-Electrolyte Interface. *J. Phys. Chem. Lett.* **2019**, *10*, 251–258.

(509) Zhou, Y.; Su, M.; Yu, X.; Zhang, Y.; Wang, J. G.; Ren, X.; Cao, R.; Xu, W.; Baer, D. R.; Du, Y.; et al. Real-Time Mass Spectrometric Characterization of the Solid-Electrolyte Interphase of a Lithium-Ion Battery. *Nat. Nanotechnol.* **2020**, *15*, 224–230.

(510) Zhang, Y.; Wang, J.-G.; Yu, X.; Baer, D. R.; Zhao, Y.; Mao, L.; Wang, F.; Zhu, Z. Potential-Dynamic Surface Chemistry Controls the Electrocatalytic Processes of Ethanol Oxidation on Gold Surfaces. *ACS Energy Lett.* **2019**, *4*, 215–221.

(511) Liu, X.; Wang, D.; Wan, L. Progress of Electrode/Electrolyte Interfacial Investigation of Li-Ion Batteries via In Situ Scanning Probe Microscopy. *Sci. Bull.* **2015**, *60*, 839–849.

(512) Kumar, R.; Tokranov, A.; Sheldon, B. W.; Xiao, X.; Huang, Z.; Li, C.; Mueller, T. In Situ and Operando Investigations of Failure Mechanisms of the Solid Electrolyte Interphase on Silicon Electrodes. *ACS Energy Lett.* **2016**, *1*, 689–697.

(513) Nanda, J.; Yang, G.; Hou, T.; Voylov, D. N.; Li, X.; Ruther, R. E.; Naguib, M.; Persson, K.; Veith, G. M.; Sokolov, A. P. Unraveling the Nanoscale Heterogeneity of Solid Electrolyte Interphase Using Tip-Enhanced Raman Spectroscopy. *Joule* **2019**, *3*, 2001–2019.

(514) Stöckle, R. M.; Suh, Y. D.; Deckert, V.; Zenobi, R. Nanoscale Chemical Analysis by Tip-Enhanced Raman Spectroscopy. *Chem. Phys. Lett.* **2000**, *318*, 131–136.

(515) Hayazawa, N.; Inouye, Y.; Sekkat, Z.; Kawata, S. Metallized Tip Amplification of Near-Field Raman Scattering. *Opt. Commun.* **2000**, *183*, 333–336.

(516) Steinhauer, M.; Stich, M.; Kurniawan, M.; Seidlhofer, B. K.; Trapp, M.; Bund, A.; Wagner, N.; Friedrich, K. A. In Situ Studies of Solid Electrolyte Interphase (SEI) Formation on Crystalline Carbon Surfaces by Neutron Reflectometry and Atomic Force Microscopy. *ACS Appl. Mater. Interfaces* **2017**, *9*, 35794–35801.

(517) Akai, T.; Ota, H.; Namita, H.; Yamaguchi, S.; Nomura, M. XANES Study on Solid Electrolyte Interface of Li Ion Battery. *Phys. Scr.* **2005**, *2005*, 408.

(518) Ota, H.; Akai, T.; Namita, H.; Yamaguchi, S.; Nomura, M. XAFS and TOF-SIMS Analysis of SEI Layers on Electrodes. *J. Power Sources* **2003**, *119*–121, 567–571.

(519) Ruther, R. E.; Zhou, H.; Dhital, C.; Saravanan, K.; Kercher, A. K.; Chen, G.; Huq, A.; Delnick, F. M.; Nanda, J. Synthesis, Structure, and Electrochemical Performance of High Capacity  $\text{Li}_2\text{Cu}_{0.5}\text{Ni}_{0.5}\text{O}_2$  Cathodes. *Chem. Mater.* **2015**, *27*, 6746–6754.

(520) Schellenberger, M.; Golnak, R.; Quevedo Garzon, W. G.; Risse, S.; Seidel, R. Accessing the Solid Electrolyte Interphase on Silicon Anodes for Lithium-Ion Batteries In-Situ through Transmission Soft X-ray Absorption Spectroscopy. *Mater. Today Adv.* **2022**, *14*, 100215.

(521) Wei, C.; Bard, A. J. Scanning Electrochemical Microscopy: XXIX. In Situ Monitoring of Thickness Changes of Thin Films on Electrodes. *J. Electrochem. Soc.* **1995**, *142*, 2523–2527.

(522) Aurbach, D.; Ein-Ely, Y.; Zaban, A. The Surface Chemistry of Lithium Electrodes in Alkyl Carbonate Solutions. *J. Electrochem. Soc.* **1994**, *141*, L1–L3.

(523) Geschwind, G. Anion Reduced Ionic Conductivity in  $\text{LiF}$ . *J. Phys. Chem. Solids* **1969**, *30*, 1631–1635.

(524) Pan, J.; Cheng, Y.-T.; Qi, Y. General Method to Predict Voltage-Dependent Ionic Conduction in a Solid Electrolyte Coating on Electrodes. *Phys. Rev. B* **2015**, *91*, 134116.

(525) Zachman, M. J.; Tu, Z.; Archer, L. A.; Kourkoutis, L. F. Nanoscale Elemental Mapping of Intact Solid-Liquid Interfaces and

Reactive Materials in Energy Devices Enabled by Cryo-FIB/SEM. *ACS Energy Lett.* **2020**, *5*, 1224–1232.

(526) Zachman, M. J.; Tu, Z.; Choudhury, S.; Archer, L. A.; Kourkoutis, L. F. Cryo-STEM Mapping of Solid-Liquid Interfaces and Dendrites in Lithium-Metal Batteries. *Nature* **2018**, *560*, 345–349.

(527) Zhang, X.; Su, Q.; Du, G.; Xu, B.; Wang, S.; Chen, Z.; Wang, L.; Huang, W.; Pang, H. Stabilizing Solid-state Lithium Metal Batteries through In Situ Generated Janus-heterarchical  $\text{LiF}$ -rich SEI in Ionic Liquid Confined 3D MOF/Polymer Membranes. *Angew. Chem., Int. Ed.* **2023**, *62*, No. e202304947.

(528) Han, B.; Zou, Y.; Xu, G.; Hu, S.; Kang, Y.; Qian, Y.; Wu, J.; Ma, X.; Yao, J.; Li, T.; et al. Additive Stabilization of SEI on Graphite Observed Using Cryo-Electron Microscopy. *Energy Environ. Sci.* **2021**, *14*, 4882–4889.

(529) Lu, X.; Cheng, Y.; Li, M.; Zou, Y.; Zhen, C.; Wu, D.; Wei, X.; Li, X.; Yang, X.; Gu, M. A Stable Polymer-based Solid-State Lithium Metal Battery and its Interfacial Characteristics Revealed by Cryogenic Transmission Electron Microscopy. *Adv. Funct. Mater.* **2023**, *33*, 2212847.

(530) Jabbari, V.; Yurkiv, V.; Rasul, M. G.; Phakatkar, A. H.; Mashayek, F.; Shahbazian-Yassar, R. In Situ Formation of Stable Solid Electrolyte Interphase with High Ionic Conductivity for Long Lifespan All-Solid-State Lithium Metal Batteries. *Energy Storage Mater.* **2023**, *57*, 1–13.

(531) Han, B.; Zhang, Z.; Zou, Y.; Xu, K.; Xu, G.; Wang, H.; Meng, H.; Deng, Y.; Li, J.; Gu, M. Poor Stability of  $\text{Li}_2\text{CO}_3$  in the Solid Electrolyte Interphase of a Lithium-Metal Anode Revealed by Cryo-Electron Microscopy. *Adv. Mater.* **2021**, *33*, No. e2100404.

(532) Sheng, O.; Jin, C.; Chen, M.; Ju, Z.; Liu, Y.; Wang, Y.; Nai, J.; Liu, T.; Zhang, W.; Tao, X. Platinum Nano-Interlayer Enhanced Interface for Stable All-Solid-State Batteries Observed via Cryo-Transmission Electron Microscopy. *J. Mater. Chem. A* **2020**, *8*, 13541–13547.

(533) Liu, T.; Zheng, J.; Hu, H.; Sheng, O.; Ju, Z.; Lu, G.; Liu, Y.; Nai, J.; Wang, Y.; Zhang, W.; et al. In-Situ Construction of a Mg-Modified Interface to Guide Uniform Lithium Deposition for Stable All-Solid-State Batteries. *J. Energy Chem.* **2021**, *55*, 272–278.

(534) Alvarado, J.; Schroeder, M. A.; Pollard, T. P.; Wang, X.; Lee, J. Z.; Zhang, M.; Wynn, T.; Ding, M.; Borodin, O.; Meng, Y. S.; et al. Bisalt Ether Electrolytes: A Pathway towards Lithium Metal Batteries with Ni-Rich Cathodes. *Energy Environ. Sci.* **2019**, *12*, 780–794.

(535) Li, Y.; Wang, K.; Zhou, W.; Li, Y.; Vila, R.; Huang, W.; Wang, H.; Chen, G.; Wu, G. H.; Tsao, Y.; et al. Cryo-EM Structures of Atomic Surfaces and Host-Guest Chemistry in Metal-Organic Frameworks. *Matter* **2019**, *1*, 428–438.

(536) Wang, J.; Huang, W.; Pei, A.; Li, Y.; Shi, F.; Yu, X.; Cui, Y. Improving Cyclability of Li Metal Batteries at Elevated Temperatures and Its Origin Revealed by Cryo-Electron Microscopy. *Nat. Energy* **2019**, *4*, 664–670.

(537) Huang, W.; Wang, H.; Boyle, D. T.; Li, Y.; Cui, Y. Resolving Nanoscopic and Mesoscopic Heterogeneity of Fluorinated Species in Battery Solid-Electrolyte Interphases by Cryogenic Electron Microscopy. *ACS Energy Lett.* **2020**, *5*, 1128–1135.

(538) Liu, T.; Lin, L.; Bi, X.; Tian, L.; Yang, K.; Liu, J.; Li, M.; Chen, Z.; Lu, J.; Amine, K.; et al. In Situ Quantification of Interphasial Chemistry in Li-Ion Battery. *Nat. Nanotechnol.* **2019**, *14*, 50–56.

(539) Voinova, M. V.; Rodahl, M.; Jonson, M.; Kasemo, B. Viscoelastic Acoustic Response of Layered Polymer Films at Fluid-Solid Interfaces: Continuum Mechanics Approach. *Phys. Scr.* **1999**, *59*, 391–396.

(540) Broussely, M.; Biensan, P.; Bonhomme, F.; Blanchard, P.; Herreyre, S.; Nechev, K.; Staniewicz, R. J. Main Aging Mechanisms in Li Ion Batteries. *J. Power Sources* **2005**, *146*, 90–96.

(541) Heiskanen, S. K.; Kim, J.; Lucht, B. L. Generation and Evolution of the Solid Electrolyte Interphase of Lithium-Ion Batteries. *Joule* **2019**, *3*, 2322–2333.

(542) Tan, J.; Matz, J.; Dong, P.; Shen, J.; Ye, M. A Growing Appreciation for the Role of  $\text{LiF}$  in the Solid Electrolyte Interphase. *Adv. Energy Mater.* **2021**, *11*, 2100046.

- (543) Kitz, P. G.; Lacey, M. J.; Novak, P.; Berg, E. J. Operando EQCM-D with Simultaneous in Situ EIS: New Insights into Interphase Formation in Li Ion Batteries. *Anal. Chem.* **2019**, *91*, 2296–2303.
- (544) Edström, K.; Herstedt, M.; Abraham, D. P. A New Look at the Solid Electrolyte Interphase on Graphite Anodes in Li-Ion Batteries. *J. Power Sources* **2006**, *153*, 380–384.
- (545) Malmgren, S.; Ciosek, K.; Hahlin, M.; Gustafsson, T.; Gorgoi, M.; Rensmo, H.; Edström, K. Comparing Anode and Cathode Electrode/Electrolyte Interface Composition and Morphology Using Soft and Hard X-ray Photoelectron Spectroscopy. *Electrochim. Acta* **2013**, *97*, 23–32.
- (546) Aurbach, D.; Markovsky, B.; Levi, M. D.; Levi, E.; Schechter, A.; Moshkovich, M.; Cohen, Y. New Insights into the Interactions between Electrode Materials and Electrolyte Solutions for Advanced Nonaqueous Batteries. *J. Power Sources* **1999**, *81*–82, 95–111.
- (547) Laruelle, S.; Pilard, S.; Guenot, P.; Grugeon, S.; Tarascon, J. M. Identification of Li-Based Electrolyte Degradation Products Through DEI and ESI High-Resolution Mass Spectrometry. *J. Electrochem. Soc.* **2004**, *151*, A1202.
- (548) Zhang, Z.; Smith, K.; Jervis, R.; Shearing, P. R.; Miller, T. S.; Brett, D. J. L. Operando Electrochemical Atomic Force Microscopy of Solid-Electrolyte Interphase Formation on Graphite Anodes: The Evolution of SEI Morphology and Mechanical Properties. *ACS Appl. Mater. Interfaces* **2020**, *12*, 35132–35141.
- (549) Campana, F. P.; Buqa, H.; Novák, P.; Kötz, R.; Siegenthaler, H. In Situ Atomic Force Microscopy Study of Exfoliation Phenomena on Graphite Basal Planes. *Electrochem. commun.* **2008**, *10*, 1590–1593.
- (550) Jerliu, B.; Dorner, L.; Huger, E.; Borchardt, G.; Steitz, R.; Geckle, U.; Oberst, V.; Bruns, M.; Schneider, O.; Schmidt, H. Neutron Reflectometry Studies on the Lithiation of Amorphous Silicon Electrodes in Lithium-Ion Batteries. *Phys. Chem. Chem. Phys.* **2013**, *15*, 7777–7784.
- (551) Schulz, N.; Hausbrand, R.; Wittich, C.; Dimesso, L.; Jaegermann, W. XPS-Surface Analysis of SEI Layers on Li-Ion Cathodes: Part II. SEI-Composition and Formation inside Composite Electrodes. *J. Electrochem. Soc.* **2018**, *165*, A833–A846.
- (552) Zhang, H.; Wang, D.; Shen, C. In-Situ EC-AFM and Ex-Situ XPS Characterization to Investigate the Mechanism of SEI Formation in Highly Concentrated Aqueous Electrolyte for Li-Ion Batteries. *Appl. Surf. Sci.* **2020**, *507*, 145059.
- (553) Li, J.-T.; Światowska, J.; Maurice, V.; Seyeux, A.; Huang, L.; Sun, S.-G.; Marcus, P. XPS and ToF-SIMS Study of Electrode Processes on Sn-Ni Alloy Anodes for Li-Ion Batteries. *J. Phys. Chem. C* **2011**, *115*, 7012–7018.
- (554) Leroy, S.; Blanchard, F.; Dedryvère, R.; Martinez, H.; Carré, B.; Lemordant, D.; Gonbeau, D. Surface Film Formation on a Graphite Electrode in Li-Ion Batteries: AFM and XPS Study. *Surf. Interface Anal.* **2005**, *37*, 773–781.
- (555) Li, J.-T.; Światowska, J.; Seyeux, A.; Huang, L.; Maurice, V.; Sun, S.-G.; Marcus, P. XPS and ToF-SIMS Study of Sn-Co Alloy Thin Films as Anode for Lithium Ion Battery. *J. Power Sources* **2010**, *195*, 8251–8257.
- (556) Hope, M. A.; Rinkel, B. L. D.; Gunnarsdottir, A. B.; Marker, K.; Menkin, S.; Paul, S.; Sergeyev, I. V.; Grey, C. P. Selective NMR Observation of the SEI-Metal Interface by Dynamic Nuclear Polarisation from Lithium Metal. *Nat. Commun.* **2020**, *11*, 2224.
- (557) Benninghoven, A. Die Analyse Monomolekularer Festkörperschichten mit Hilfe der Sekundärionenemission. *Z. anorg. allg. Chem.* **1970**, *230*, 403–417.
- (558) Shotyk, W.; Metson, J. B. Secondary Ion Mass Spectrometry (SIMS) and Its Application to Chemical Weathering. *Rev. Geophys.* **1994**, *32*, 197.
- (559) Benninghoven, A.; Loebach, E. Analysis of Monomolecular Layers of Solids by the Static Method of Secondary Ion Mass Spectroscopy (SIMS). *J. Radioanal. Chem.* **1972**, *12*, 95–99.
- (560) Menkin, S.; O'keefe, C. A.; Gunnarsdottir, A. B.; Dey, S.; Pesci, F. M.; Shen, Z.; Aguadero, A.; Grey, C. P. Toward an Understanding of SEI Formation and Lithium Plating on Copper in Anode-Free Batteries. *J. Phys. Chem. C* **2021**, *125*, 16719–16732.
- (561) Xu, H.; Li, Z.; Liu, T.; Han, C.; Guo, C.; Zhao, H.; Li, Q.; Lu, J.; Amine, K.; Qiu, X. Impacts of Dissolved Ni<sup>2+</sup> on the Solid Electrolyte Interphase on a Graphite Anode. *Angew. Chem., Int. Ed.* **2022**, *61*, No. e202202894.
- (562) Ota, H.; Sakata, Y.; Inoue, A.; Yamaguchi, S. Analysis of Vinylene Carbonate Derived SEI Layers on Graphite Anode. *J. Electrochem. Soc.* **2004**, *151*, A1659.
- (563) Zhao, D.; Wang, J.; Wang, P.; Liu, H.; Li, S. Regulating the Composition Distribution of Layered SEI Film on Li-Ion Battery Anode by LiDFBOP. *Electrochim. Acta* **2020**, *337*, 135745.
- (564) Pereira-Nabais, C.; Światowska, J.; Chagnes, A.; Ozanam, F.; Gohier, A.; Tran-Van, P.; Cojocaru, C.-S.; Cassir, M.; Marcus, P. Interphase Chemistry of Si Electrodes Used as Anodes in Li-Ion Batteries. *Appl. Surf. Sci.* **2013**, *266*, 5–16.
- (565) Bordes, A.; De Vito, E.; Haon, C.; Boulineau, A.; Montani, A.; Marcus, P. Multiscale Investigation of Silicon Anode Li Insertion Mechanisms by Time-of-Flight Secondary Ion Mass Spectrometer Imaging Performed on an In Situ Focused Ion Beam Cross Section. *Chem. Mater.* **2016**, *28*, 1566–1573.
- (566) Zhou, L.; Zuo, T.; Li, C.; Zhang, Q.; Janek, J.; Nazar, L. F. Li<sub>3-x</sub>Zr<sub>x</sub>(Ho/Lu)<sub>1-x</sub>Cl<sub>6</sub> Solid Electrolytes Enable Ultrahigh-Loading Solid-State Batteries with a Prelithiated Si Anode. *ACS Energy Lett.* **2023**, *8*, 3102–3111.
- (567) Kim, M.; Harvey, S. P.; Huey, Z.; Han, S.-D.; Jiang, C.-S.; Son, S.-B.; Yang, Z.; Bloom, I. A New Mechanism of Stabilizing SEI of Si Anode Driven by Crosstalk Behavior and Its Potential for Developing High Performance Si-Based Batteries. *Energy Storage Mater.* **2023**, *55*, 436–444.
- (568) Huo, H.; Chen, Y.; Li, R.; Zhao, N.; Luo, J.; Pereira Da Silva, J. G.; Mücke, R.; Kaghazchi, P.; Guo, X.; Sun, X. Design of a Mixed Conductive Garnet/Li Interface for Dendrite-Free Solid Lithium Metal Batteries. *Energy Environ. Sci.* **2020**, *13*, 127–134.
- (569) Paul-Orecchio, A. G.; Weeks, J. A.; Dolocan, A.; Mullins, C. B. High-Stability Lithium Metal Batteries Enabled by a Tetrahydrofuran-Based Electrolyte Mixture. *ACS Appl. Energy Mater.* **2022**, *5*, 9437–9446.
- (570) Fang, R.; Xu, B.; Grundish, N. S.; Xia, Y.; Li, Y.; Lu, C.; Liu, Y.; Wu, N.; Goodenough, J. B. Li<sub>2</sub>S<sub>6</sub>-Integrated PEO-Based Polymer Electrolytes for All-Solid-State Lithium-Metal Batteries. *Angew. Chem., Int. Ed.* **2021**, *60*, 17701–17706.
- (571) Sun, H.-H.; Dolocan, A.; Weeks, J. A.; Rodriguez, R.; Heller, A.; Mullins, C. B. In Situ Formation of a Multicomponent Inorganic-Rich SEI Layer Provides a Fast Charging and High Specific Energy Li-Metal Battery. *J. Mater. Chem. A* **2019**, *7*, 17782–17789.
- (572) Tu, H.; Li, L.; Wang, Z.; Wang, J.; Lin, H.; Wang, M.; Yan, C.; Liu, M. Tailoring Electrolyte Solvation for LiF-Rich Solid Electrolyte Interphase toward a Stable Li Anode. *ACS Nano* **2022**, *16*, 16898–16908.
- (573) Jin, Y.; Kneusels, N. H.; Magusin, P.; Kim, G.; Castillo-Martinez, E.; Marbella, L. E.; Kerber, R. N.; Howe, D. J.; Paul, S.; Liu, T.; et al. Identifying the Structural Basis for the Increased Stability of the Solid Electrolyte Interphase Formed on Silicon with the Additive Fluoroethylene Carbonate. *J. Am. Chem. Soc.* **2017**, *139*, 14992–15004.
- (574) Shadik, Z.; Lee, H.; Borodin, O.; Cao, X.; Fan, X.; Wang, X.; Lin, R.; Bak, S. M.; Ghose, S.; Xu, K.; et al. Identification of LiH and Nanocrystalline LiF in the Solid-Electrolyte Interphase of Lithium Metal Anodes. *Nat. Nanotechnol.* **2021**, *16*, 549–554.
- (575) Cresce, A. v.; Russell, S. M.; Baker, D. R.; Gaskell, K. J.; Xu, K. In Situ and Quantitative Characterization of Solid Electrolyte Interphases. *Nano Lett.* **2014**, *14*, 1405–1412.
- (576) Liu, X. R.; Wang, L.; Wan, L. J.; Wang, D. In Situ Observation of Electrolyte-Concentration-Dependent Solid Electrolyte Interphase on Graphite in Dimethyl Sulfoxide. *ACS Appl. Mater. Interfaces* **2015**, *7*, 9573–9580.



- (577) Wang, X.; Huang, S. C.; Huang, T. X.; Su, H. S.; Zhong, J. H.; Zeng, Z. C.; Li, M. H.; Ren, B. Tip-Enhanced Raman Spectroscopy for Surfaces and Interfaces. *Chem. Soc. Rev.* **2017**, *46*, 4020–4041.
- (578) Veith, G. M.; Browning, K. L.; Doucet, M.; Browning, J. F. Solid Electrolyte Interphase Architecture Determined through In Situ Neutron Scattering. *J. Electrochem. Soc.* **2021**, *168*, 060523.
- (579) Veith, G. M.; Doucet, M.; Sacci, R. L.; Vacaliuc, B.; Baldwin, J. K.; Browning, J. F. Determination of the Solid Electrolyte Interphase Structure Grown on a Silicon Electrode Using a Fluoroethylene Carbonate Additive. *Sci. Rep.* **2017**, *7*, 6326.
- (580) Veith, G. M.; Doucet, M.; Baldwin, J. K.; Sacci, R. L.; Fears, T. M.; Wang, Y.; Browning, J. F. Direct Determination of Solid-Electrolyte Interphase Thickness and Composition as a Function of State of Charge on a Silicon Anode. *J. Phys. Chem. C* **2015**, *119*, 20339–20349.
- (581) Fears, T. M.; Doucet, M.; Browning, J. F.; Baldwin, J. K.; Winiarz, J. G.; Kaiser, H.; Taub, H.; Sacci, R. L.; Veith, G. M. Evaluating the Solid Electrolyte Interphase Formed on Silicon Electrodes: A Comparison of Ex Situ X-ray Photoelectron Spectroscopy and In Situ Neutron Reflectometry. *Phys. Chem. Chem. Phys.* **2016**, *18*, 13927–13940.
- (582) Takamatsu, D.; Orikasa, Y.; Mori, S.; Nakatsutsumi, T.; Yamamoto, K.; Koyama, Y.; Minato, T.; Hirano, T.; Tanida, H.; Arai, H.; et al. Effect of an Electrolyte Additive of Vinylene Carbonate on the Electronic Structure at the Surface of a Lithium Cobalt Oxide Electrode under Battery Operating Conditions. *J. Phys. Chem. C* **2015**, *119*, 9791–9797.
- (583) Khalid, S.; Caliebe, W.; Siddons, P.; So, I.; Clay, B.; Lenhard, T.; Hanson, J.; Wang, Q.; Frenkel, A. I.; Marinkovic, N.; et al. Quick Extended X-ray Absorption Fine Structure Instrument with Millisecond Time Scale, Optimized for In Situ Applications. *Rev. Sci. Instrum.* **2010**, *81*, 015105.
- (584) Stotzel, J.; Lutzenkirchen-Hecht, D.; Fonda, E.; De Oliveira, N.; Briois, V.; Frahm, R. Novel Angular Encoder for a Quick-Extended X-ray Absorption Fine Structure Monochromator. *Rev. Sci. Instrum.* **2008**, *79*, 083107.
- (585) Ventosa, E.; Wilde, P.; Zinn, A. H.; Trautmann, M.; Ludwig, A.; Schuhmann, W. Understanding Surface Reactivity of Si Electrodes in Li-ion Batteries by In Operando Scanning Electrochemical Microscopy. *Chem. Commun.* **2016**, *52*, 6825–6828.
- (586) Takahashi, T.; Iwahara, H.; Ishikawa, T. Ionic Conductivity of Doped Cerium Trifluoride. *J. Electrochem. Soc.* **1977**, *124*, 280–284.
- (587) Rongeat, C.; Anji Reddy, M.; Diemant, T.; Behm, R. J.; Fichtner, M. Development of New Anode Composite Materials for Fluoride Ion Batteries. *J. Mater. Chem. A* **2014**, *2*, 20861–20872.
- (588) Grenier, A.; Porras-Gutierrez, A. G.; Body, M.; Legein, C.; Chrétien, F.; Raymundo-Piñero, E.; Dollé, M.; Groult, H.; Dambournet, D. Solid Fluoride Electrolytes and Their Composite with Carbon: Issues and Challenges for Rechargeable Solid State Fluoride-Ion Batteries. *J. Phys. Chem. C* **2017**, *121*, 24962–24970.
- (589) Li, X.; Tang, Y.; Zhu, J.; Lv, H.; Xu, Y.; Wang, W.; Zhi, C.; Li, H. Initiating a Room-Temperature Rechargeable Aqueous Fluoride-Ion Battery with Long Lifespan through a Rational Buffering Phase Design. *Adv. Energy Mater.* **2021**, *11*, 2003714.
- (590) Zhang, D.; Yamamoto, K.; Wang, Y.; Gao, S.; Uchiyama, T.; Watanabe, T.; Takami, T.; Matsunaga, T.; Nakanishi, K.; Miki, H.; et al. Reversible and Fast (De)fluorination of High-Capacity Cu<sub>2</sub>O Cathode: One Step Toward Practically Applicable All-Solid-State Fluoride-Ion Battery. *Adv. Energy Mater.* **2021**, *11*, 2102285.
- (591) Hou, X.; Zhang, Z.; Shen, K.; Cheng, S.; He, Q.; Shi, Y.; Yu, D. Y. W.; Su, C.-Y.; Li, L.-J.; Chen, F. An Aqueous Rechargeable Fluoride Ion Battery with Dual Fluoride Electrodes. *J. Electrochem. Soc.* **2019**, *166*, A2419–A2424.
- (592) Zhang, S.; Wang, T.; Zhang, J.; Miao, Y.; Yin, Q.; Wu, Z.; Wu, Y.; Yuan, Q.; Han, J. A Zero-Strain Insertion Cathode Material for Room-Temperature Fluoride-Ion Batteries. *ACS Appl. Mater. Interfaces* **2022**, *14*, 24518–24525.
- (593) Clemens, O.; Rongeat, C.; Reddy, M. A.; Giehr, A.; Fichtner, M.; Hahn, H. Electrochemical Fluorination of Perovskite Type BaFeO<sub>2.5</sub>. *Dalton Trans.* **2014**, *43*, 15771–15778.
- (594) Andrews, J. L.; McClure, E. T.; Jew, K. K.; Preefer, M. B.; Irshad, A.; Lertola, M. J.; Robertson, D. D.; Salamat, C. Z.; Brady, M. J.; Piper, L. F. J.; et al. Room-Temperature Electrochemical Fluoride (De)insertion into CsMnFeF<sub>6</sub>. *ACS Energy Lett.* **2022**, *7*, 2340–2348.
- (595) Nowroozi, M. A.; Ivlev, S.; Rohrer, J.; Clemens, O. La<sub>2</sub>CoO<sub>4</sub>: A New Intercalation Based Cathode Material for Fluoride Ion Batteries with Improved Cycling Stability. *J. Mater. Chem. A* **2018**, *6*, 4658–4669.
- (596) Nowroozi, M. A.; Wissel, K.; Donzelli, M.; Hosseinpourkavaz, N.; Plana-Ruiz, S.; Kolb, U.; Schoch, R.; Bauer, M.; Malik, A. M.; Rohrer, J.; et al. High Cycle Life All-Solid-State Fluoride Ion Battery with La<sub>2</sub>NiO<sub>4+d</sub> High Voltage Cathode. *Commun. Mater.* **2020**, *1*, 27.
- (597) Roos, A.; Vandepol, F.; Keim, R.; Schoonman, J. Ionic Conductivity in Tysonite-Type Solid Solutions La<sub>1-x</sub>BaxF<sub>3-x</sub>. *Solid State Ion.* **1984**, *13*, 191–203.
- (598) Dieudonne, B.; Chable, J.; Body, M.; Legein, C.; Durand, E.; Mauvy, F.; Fourcade, S.; Leblanc, M.; Maisonneuve, V.; Demourgues, A. The Key Role of the Composition and Structural Features in Fluoride Ion Conductivity in Tysonite Ce<sub>1-x</sub>Sr<sub>x</sub>F<sub>3-x</sub> Solid Solutions. *Dalton Trans.* **2017**, *46*, 3761–3769.
- (599) Dieudonné, B.; Chable, J.; Mauvy, F.; Fourcade, S.; Durand, E.; Lebraud, E.; Leblanc, M.; Legein, C.; Body, M.; Maisonneuve, V.; et al. Exploring the Sm<sub>1-x</sub>Ca<sub>x</sub>F<sub>3-x</sub> Tysonite Solid Solution as a Solid-State Electrolyte: Relationships between Structural Features and F-Ionic Conductivity. *J. Phys. Chem. C* **2015**, *119*, 25170–25179.
- (600) Tran, Q. C.; Bui, V. T.; Dao, V. D.; Lee, J. K.; Choi, H. S. Ionic Liquid-Based Polymer Electrolytes via Surfactant-Assisted Polymerization at the Plasma-Liquid Interface. *ACS Appl. Mater. Interfaces* **2016**, *8*, 16125–16135.
- (601) Liu, J.; Yi, L.; Zeng, P.; Zou, C.; Chen, X.; Tao, X.; Liu, X.; Yang, L.; Zang, Z.; Chang, B.; et al. Point Defect Engineering Enabled the High Ionic Conductivity of BaSnF<sub>4</sub> for Solid-State Fluoride-Ion Batteries at Room Temperature. *Energy Fuels* **2022**, *36*, 15258–15267.
- (602) Wang, J.; Hao, J.; Duan, C.; Wang, X.; Wang, K.; Ma, C. A Fluoride-Ion-Conducting Solid Electrolyte with Both High Conductivity and Excellent Electrochemical Stability. *Small* **2022**, *18*, No. e2104508.
- (603) Yu, Y.; Lei, M.; Li, D.; Li, C. Near-Room-Temperature Quasi-Solid-State F-Ion Batteries with High Conversion Reversibility Based on Layered Structured Electrolyte. *Adv. Energy Mater.* **2023**, *13*, 2203168.
- (604) Rongeat, C.; Reddy, M. A.; Witter, R.; Fichtner, M. Nanostructured Fluorite-Type Fluorides as Electrolytes for Fluoride Ion Batteries. *J. Phys. Chem. C* **2013**, *117*, 4943–4950.
- (605) Mori, K.; Mineshige, A.; Emoto, T.; Sugiura, M.; Saito, T.; Namba, K.; Otomo, T.; Abe, T.; Fukunaga, T. Electrochemical, Thermal, and Structural Features of BaF<sub>2</sub>-SnF<sub>2</sub> Fluoride-Ion Electrolytes. *J. Phys. Chem. C* **2021**, *125*, 12568–12577.
- (606) Murakami, M.; Morita, Y.; Mizuno, M. <sup>19</sup>F/<sup>119</sup>Sn/<sup>207</sup>Pb NMR Studies on Ion Dynamics in Tetragonal PbSnF<sub>4</sub>: Spectroscopic Evidence for Defect-Driven Conductivity. *J. Phys. Chem. C* **2017**, *121*, 2627–2634.
- (607) Murakami, M.; Morita, Y.; Yonemura, M.; Shimoda, K.; Mori, M.; Koyama, Y.; Kawaguchi, T.; Fukuda, K.; Ishikawa, Y.; Kamiyama, T.; et al. High Anionic Conductive Form of Pb<sub>x</sub>Sn<sub>2-x</sub>F<sub>4</sub>. *Chem. Mater.* **2019**, *31*, 7704–7710.
- (608) Denes, G.; Birchall, T.; Sayer, M.; Bell, M. BaSnF<sub>4</sub> — a New Fluoride Ionic Conductor with the α-PbSnF<sub>4</sub> Structure. *Solid State Ion.* **1984**, *13*, 213–219.
- (609) Liu, L.; Yang, L.; Liu, M.; Li, X.; Shao, D.; Luo, K.; Wang, X.; Luo, Z. SnF<sub>2</sub>-Based Fluoride Ion Electrolytes MSnF<sub>4</sub> (M = Ba, Pb) for the Application of Room-Temperature Solid-State Fluoride Ion Batteries. *J. Alloys Compd.* **2020**, *819*, 152983.



- (610) Liu, L.; Yang, L.; Shao, D.; Luo, K.; Zou, C.; Luo, Z.; Wang, X.  $\text{Nd}^{3+}$  Doped  $\text{BaSnF}_4$  Solid Electrolyte for Advanced Room-Temperature Solid-State Fluoride Ion Batteries. *Ceram. Int.* **2020**, *46*, 20521–20528.
- (611) Bachman, J. C.; Muy, S.; Grimaud, A.; Chang, H. H.; Pour, N.; Lux, S. F.; Paschos, O.; Maglia, F.; Lupart, S.; Lamp, P.; et al. Inorganic Solid-State Electrolytes for Lithium Batteries: Mechanisms and Properties Governing Ion Conduction. *Chem. Rev.* **2016**, *116*, 140–162.
- (612) Mohammad, I.; Witter, R.; Fichtner, M.; Anji Reddy, M. Room-Temperature, Rechargeable Solid-State Fluoride-Ion Batteries. *ACS Appl. Energy Mater.* **2018**, *1*, 4766–4775.
- (613) Mohammad, I.; Witter, R.; Fichtner, M.; Reddy, M. A. Introducing Interlayer Electrolytes: Toward Room-Temperature High-Potential Solid-State Rechargeable Fluoride Ion Batteries. *ACS Appl. Energy Mater.* **2019**, *2*, 1553–1562.
- (614) Davis, V. K.; Munoz, S.; Kim, J.; Bates, C. M.; Momčilović, N.; Billings, K. J.; Miller, T. F.; Grubbs, R. H.; Jones, S. C. Fluoride-Ion Solvation in Non-aqueous Electrolyte Solutions. *Mater. Chem. Front.* **2019**, *3*, 2721–2727.
- (615) Kobayashi, S.; Nakamoto, H.; Yokoe, D.; Kuwabara, A.; Abe, T.; Ikuhara, Y. Nanoscale Defluorination Mechanism and Solid Electrolyte Interphase of a  $\text{MgF}_2$  Anode in Fluoride-Shuttle Batteries. *ACS Appl. Energy Mater.* **2021**, *4*, 996–1003.
- (616) Celik Kucuk, A.; Yamanaka, T.; Yokoyama, Y.; Abe, T. Low-Cost Fluoride Source for Organic Liquid Electrolyte-Based Fluoride Shuttle Battery. *J. Electrochem. Soc.* **2021**, *168*, 010501.
- (617) Kawasaki, M.; Morigaki, K.-I.; Kano, G.; Nakamoto, H.; Takekawa, R.; Kawamura, J.; Minato, T.; Abe, T.; Ogumi, Z. Lactone-Based Liquid Electrolytes for Fluoride Shuttle Batteries. *J. Electrochem. Soc.* **2021**, *168*, 010529.
- (618) Okazaki, K.-I.; Uchimoto, Y.; Abe, T.; Ogumi, Z. Charge-Discharge Behavior of Bismuth in a Liquid Electrolyte for Rechargeable Batteries Based on a Fluoride Shuttle. *ACS Energy Lett.* **2017**, *2*, 1460–1464.
- (619) Yamamoto, T.; Matsumoto, K.; Hagiwara, R.; Nohira, T. Room-Temperature Fluoride Shuttle Batteries Based on a Fluorohydrogenate Ionic Liquid Electrolyte. *ACS Appl. Energy Mater.* **2019**, *2*, 6153–6157.
- (620) Yamamoto, T.; Matsumoto, K.; Hagiwara, R.; Nohira, T. Charge-Discharge Performance of Copper Metal Positive Electrodes in Fluorohydrogenate Ionic Liquids for Fluoride-Shuttle Batteries. *J. Electrochem. Soc.* **2021**, *168*, 040530.
- (621) Darolles, I.; Weiss, C. M.; Alam, M. M.; Tiruvannamalai, A.; Jones, S. C. Fluoride Ion Battery Compositions. U.S. Patent US9166249B2, 2015.
- (622) Lee, H. S.; Yang, X. Q.; Xiang, C. L.; McBreen, J.; Choi, L. S. The Synthesis of a New Family of Boron-Based Anion Receptors and the Study of Their Effect on Ion Pair Dissociation and Conductivity of Lithium Salts in Nonaqueous Solutions. *J. Electrochem. Soc.* **1998**, *145*, 2813–2818.
- (623) Lee, H. S.; Sun, X.; Yang, X. Q.; McBreen, J. Synthesis and Study of New Cyclic Boronate Additives for Lithium Battery Electrolytes. *J. Electrochem. Soc.* **2002**, *149*, A1460.
- (624) Li, L. F.; Lee, H. S.; Li, H.; Yang, X. Q.; Nam, K. W.; Yoon, W. S.; McBreen, J.; Huang, X. J. New Electrolytes for Lithium Ion Batteries Using LiF Salt and Boron Based Anion Receptors. *J. Power Sources* **2008**, *184*, 517–521.
- (625) Xie, B.; Lee, H. S.; Li, H.; Yang, X. Q.; McBreen, J.; Chen, L. Q. New Electrolytes Using  $\text{Li}_2\text{O}$  or  $\text{Li}_2\text{O}_2$  Oxides and Tris-(pentafluorophenyl) Borane as Boron-Based Anion Receptor for Lithium Batteries. *Electrochem. commun.* **2008**, *10*, 1195–1197.
- (626) Chen, Z.; Amine, K. Computational Estimates of Fluoride Affinity of Boron-Based Anion Receptors. *J. Electrochem. Soc.* **2009**, *156*, A672.
- (627) Konishi, H.; Minato, T.; Abe, T.; Ogumi, Z. Electrochemical Performance of a Lead Fluoride Electrode Mixed with Carbon in an Electrolyte Containing Triphenylboroxine as an Anion Acceptor for Fluoride Shuttle Batteries. *Mater. Chem. Phys.* **2019**, *226*, 1–5.
- (628) Konishi, H.; Minato, T.; Abe, T.; Ogumi, Z. Reversible Electrochemical Reaction of a Fluoride Shuttle Battery with a Bismuth(III) Fluoride Electrode and Electrolyte Containing Triphenylboroxine as an Anion Acceptor. *ChemistrySelect* **2020**, *5*, 6237–6241.
- (629) Konishi, H.; Minato, T.; Abe, T.; Ogumi, Z. Triphenylboroxine and Triphenylborane as Anion Acceptors for Electrolyte in Fluoride Shuttle Batteries. *Chem. Lett.* **2018**, *47*, 1346–1349.
- (630) Konishi, H.; Takekawa, R.; Minato, T.; Ogumi, Z.; Abe, T. Effect of Anion Acceptor Added to the Electrolyte on the Electrochemical Performance of Bismuth(III) Fluoride in a Fluoride Shuttle Battery. *Chem. Phys. Lett.* **2020**, *755*, 137785.
- (631) Konishi, H.; Minato, T.; Abe, T.; Ogumi, Z. Reactivity of the Anion Acceptor in Electrolyte: An Important Factor in Achieving High Electrochemical Performance of a Lead (II) Fluoride Electrode in a Fluoride Shuttle Battery. *J. Electroanal. Chem.* **2020**, *871*, 114103.
- (632) Konishi, H.; Minato, T.; Abe, T.; Ogumi, Z. Electrochemical Performance of a Bismuth Fluoride Electrode in a Reserve-Type Fluoride Shuttle Battery. *J. Electrochem. Soc.* **2017**, *164*, A3702–A3708.
- (633) Konishi, H.; Minato, T.; Abe, T.; Ogumi, Z. Improvement of Cycling Performance in Bismuth Fluoride Electrodes by Controlling Electrolyte Composition in Fluoride Shuttle Batteries. *J. Appl. Electrochem.* **2018**, *48*, 1205–1211.
- (634) Celik Kucuk, A.; Abe, T. Borolan-2-yl Involving Anion Acceptors for Organic Liquid Electrolyte-Based Fluoride Shuttle Batteries. *J. Fluorine Chem.* **2020**, *240*, 109672.
- (635) Celik Kucuk, A.; Yamanaka, T.; Abe, T. Using Siloxane-Based Liquid Electrolytes with High Stability for Fluoride Shuttle Batteries. *J. Mater. Chem. A* **2020**, *8*, 22134–22142.
- (636) Konishi, H.; Minato, T.; Abe, T.; Ogumi, Z. Influence of Electrolyte Composition on the Electrochemical Reaction Mechanism of Bismuth Fluoride Electrode in Fluoride Shuttle Battery. *J. Phys. Chem. C* **2019**, *123*, 10246–10252.
- (637) Celik Kucuk, A.; Minato, T.; Yamanaka, T.; Abe, T. Effects of LiBOB on Salt Solubility and  $\text{BiF}_3$  Electrode Electrochemical Properties in Fluoride Shuttle Batteries. *J. Mater. Chem. A* **2019**, *7*, 8559–8567.
- (638) Kawachi, S.; Nakamoto, H.; Takekawa, R.; Kobayashi, T.; Abe, T. Electrolytes for Room-Temperature Rechargeable Fluoride Shuttle Batteries. *ACS Appl. Energy Mater.* **2022**, *5*, 2096–2103.
- (639) Celik Kucuk, A.; Yamanaka, T.; Minato, T.; Abe, T. Influence of LiBOB as an Electrolyte Additive on the Performance of  $\text{BiF}_3/\text{C}$  for Fluoride Shuttle Batteries. *J. Electrochem. Soc.* **2020**, *167*, 120508.
- (640) Yamanaka, T.; Kucuk, A. C.; Ogumi, Z.; Abe, T. Evolution of Fluoride Shuttle Battery Reactions of  $\text{BiF}_3$  Microparticles in a  $\text{CsF}/\text{LiBOB}/\text{Tetraglyme}$  Electrolyte: Dependence on Structure, Size, and Shape. *ACS Appl. Energy Mater.* **2020**, *3*, 9390–9400.
- (641) Celik Kucuk, A.; Yamanaka, T.; Abe, T. Fluoride Shuttle Batteries: On the Performance of the  $\text{BiF}_3$  Electrode in Organic Liquid Electrolytes Containing a Mixture of Lithium Bis(oxalato)borate and Triphenylboroxine. *Solid State Ion.* **2020**, *357*, 115499.
- (642) Celik-Kucuk, A.; Abe, T. Electrochemical Behavior of  $\text{CuF}_2$  as Reversible Cathode in an Organic Liquid Electrolyte for Room-Temperature Fluoride-Shuttle Batteries. *J. Power Sources* **2021**, *496*, 229828.
- (643) Celik Kucuk, A.; Abe, T. Influence of Conductive Additives on the Electrochemical Compatibility of Copper Fluoride Cathode for FSB. *J. Electroanal. Chem.* **2021**, *900*, 115744.
- (644) Chen, J.; Huang, Z.; Wang, C.; Porter, S.; Wang, B.; Lie, W.; Liu, H. K. Sodium-Difluoro(oxalato)borate ( $\text{NaDFOB}$ ): A New Electrolyte Salt for Na-Ion Batteries. *Chem. Commun.* **2015**, *51*, 9809–9812.
- (645) Zavalij, P. Y.; Yang, S.; Whittingham, M. S. Structures of Potassium, Sodium and Lithium Bis(oxalato)borate Salts from Powder Diffraction Data. *Acta Crystallogr. B* **2003**, *59*, 753–759.
- (646) Ge, C.; Wang, L.; Xue, L.; Wu, Z.-S.; Li, H.; Gong, Z.; Zhang, X.-D. Synthesis of Novel Organic-Ligand-Doped Sodium Bis(oxalato)-Borate Complexes with Tailored Thermal Stability and

Enhanced Ion Conductivity for Sodium Ion Batteries. *J. Power Sources* **2014**, *248*, 77–82.

(647) Gallagher, T. C.; Sandstrom, S. K.; Wu, C. Y.; Stickle, W.; Fulkerson, C. R.; Hagglund, L.; Ji, X. Copper Metal Electrode Reversibly Hosts Fluoride in a 16 m KF Aqueous Electrolyte. *Chem. Commun.* **2022**, *58*, 10218–10220.

(648) Fang, Z.; Li, M.; Wang, L.; Duan, X.; Zhao, H. A Long-Life Aqueous Fluoride-Ion Battery Based on Water-in-Salt Electrolyte. *Inorg. Chem. Commun.* **2023**, *148*, 110275.

(649) Alshangiti, O.; Galatolo, G.; Rees, G. J.; Guo, H.; Quirk, J. A.; Dawson, J. A.; Pasta, M. Solvent-in-Salt Electrolytes for Fluoride Ion Batteries. *ACS Energy Lett.* **2023**, *8*, 2668–2673.

(650) Ali, G.; Oh, S. H.; Kim, S. Y.; Kim, J. Y.; Cho, B. W.; Chung, K. Y. An Open-Framework Iron Fluoride and Reduced Graphene Oxide Nanocomposite as a High-Capacity Cathode Material for Na-Ion Batteries. *J. Mater. Chem. A* **2015**, *3*, 10258–10266.

(651) Lemoine, K.; Hemon-Ribaud, A.; Leblanc, M.; Lhoste, J.; Tarascon, J. M.; Maisonneuve, V. Fluorinated Materials as Positive Electrodes for Li- and Na-Ion Batteries. *Chem. Rev.* **2022**, *122*, 14405–14439.

(652) Zhang, N.; Xiao, X.; Pang, H. Transition Metal (Fe, CO, Ni) Fluoride-Based Materials for Electrochemical Energy Storage. *Nano-scale Horiz.* **2019**, *4*, 99–116.

(653) He, K.; Zhou, Y.; Gao, P.; Wang, L.; Pereira, N.; Amatucci, G. G.; Nam, K. W.; Yang, X. Q.; Zhu, Y.; Wang, F.; et al. Sodiation via Heterogeneous Disproportionation in FeF<sub>2</sub> Electrodes for Sodium-Ion Batteries. *ACS Nano* **2014**, *8*, 7251–7259.

(654) Ni, D.; Sun, W.; Lu, C.; Wang, Z.; Qiao, J.; Cai, H.; Liu, C.; Sun, K. Improved Rate and Cycling Performance of FeF<sub>2</sub>-rGO Hybrid Cathode with Poly (Acrylic Acid) Binder for Sodium Ion Batteries. *J. Power Sources* **2019**, *413*, 449–458.

(655) Zu, C.-X.; Li, H. Thermodynamic Analysis on Energy Densities of Batteries. *Energy Environ. Sci.* **2011**, *4*, 2614.

(656) Kang, J.; Ahn, J.; Park, H.; Ko, W.; Lee, Y.; Lee, S.; Lee, S.; Jung, S. K.; Kim, J. Highly Stable Fe<sup>2+</sup>/Ti<sup>3+</sup>-Based Fluoride Cathode Enabling Low-Cost and High-Performance Na-Ion Batteries. *Adv. Funct. Mater.* **2022**, *32*, 2201816.

(657) Zhu, J.; Deng, D. Wet-Chemical Synthesis of Phase-Pure FeOF Nanorods as High-Capacity Cathodes for Sodium-Ion Batteries. *Angew. Chem., Int. Ed.* **2015**, *54*, 3079–3083.

(658) Zhou, Y.-N.; Sina, M.; Pereira, N.; Yu, X.; Amatucci, G. G.; Yang, X.-Q.; Cosandey, F.; Nam, K.-W. FeO<sub>0.7</sub>F<sub>1.3</sub>/C Nanocomposite as a High-Capacity Cathode Material for Sodium-Ion Batteries. *Adv. Funct. Mater.* **2015**, *25*, 696–703.

(659) Dey, U. K.; Barman, N.; Ghosh, S.; Sarkar, S.; Peter, S. C.; Senguttuvan, P. Topochemical Bottom-Up Synthesis of 2D- and 3D-Sodium Iron Fluoride Frameworks. *Chem. Mater.* **2019**, *31*, 295–299.

(660) Foley, E. E.; Wu, V. C.; Jin, W.; Cui, W.; Yoshida, E.; Manche, A.; Clement, R. J. Polymorphism in Weberite Na<sub>2</sub>Fe<sub>2</sub>F<sub>7</sub> and its Effects on Electrochemical Properties as a Na-Ion Cathode. *Chem. Mater.* **2023**, *35*, 3614–3627.

(661) Peschel, B.; Molinier, M.; Babel, D. Kristallstrukturbestimmungen an Vier Monoklinen Weberiten Na<sub>2</sub>M<sup>II</sup>M<sup>III</sup>F<sub>7</sub> (M<sup>II</sup> = Fe, Co; M<sup>III</sup> = V, Cr). *Z. Physik* **1995**, *621*, 1573–1581.

(662) Peschel, B.; Babel, D. Die Kristallstrukturen der Vanadium-Weberite Na<sub>2</sub>M<sup>II</sup>V<sup>III</sup>F<sub>7</sub> (M<sup>II</sup> = Mn, Ni, Cu) und von NaVF<sub>4</sub>. *Z. Physik* **1997**, *623*, 1614–1620.

(663) Liao, J.; Han, J.; Xu, J.; Du, Y.; Sun, Y.; Duan, L.; Zhou, X. Scalable Synthesis of Na<sub>2</sub>MVF<sub>7</sub> (M = Mn, Fe, and Co) as High-Performance Cathode Materials for Sodium-Ion Batteries. *Chem. Commun.* **2021**, *57*, 11497–11500.

(664) Leblanc, M.; Ferey, G.; Chevallier, P.; Calage, Y.; De Pape, R. Hexagonal Tungsten Bronze-Type Fe<sup>III</sup> Fluoride: (H<sub>2</sub>O)<sub>0.33</sub>FeF<sub>3</sub>; Crystal Structure, Magnetic Properties, Dehydration to a New Form of Iron Trifluoride. *J. Solid State Chem.* **1983**, *47*, 53–58.

(665) Zhang, R.; Wang, X.; Wang, X.; Liu, M.; Wei, S.; Wang, Y.; Hu, H. Iron Fluoride Packaged into 3D Order Mesoporous Carbons as High-Performance Sodium-Ion Battery Cathode Material. *J. Electrochem. Soc.* **2018**, *165*, A89–A96.

(666) Li, C.; Yin, C.; Mu, X.; Maier, J. Top-Down Synthesis of Open Framework Fluoride for Lithium and Sodium Batteries. *Chem. Mater.* **2013**, *25*, 962–969.

(667) Liu, M.; Wang, Q.; Chen, B.; Lei, H.; Liu, L.; Wu, C.; Wang, X.; Yang, Z. Band-Gap Engineering of FeF<sub>3</sub>·0.33H<sub>2</sub>O Nanosphere via Ni Doping as a High-Performance Lithium-Ion Battery Cathode. *ACS Sustain. Chem. Eng.* **2020**, *8*, 15651–15660.

(668) Wei, S.; Wang, X.; Yu, R.; Zhang, R.; Liu, M.; Yang, Z.; Hu, H. Ti-Doped Fe<sub>1-x</sub>Ti<sub>x</sub>F<sub>3</sub>·0.33H<sub>2</sub>O/C Nanocomposite as an Ultrahigh Rate Capability Cathode Materials of Lithium Ion Batteries. *J. Alloys Compd.* **2017**, *702*, 372–380.

(669) Yang, Z.; Zhang, Z.; Yuan, Y.; Huang, Y.; Wang, X.; Chen, X.; Wei, S. First-Principles Study of Ti Doping in FeF<sub>3</sub>·0.33H<sub>2</sub>O. *Curr. Appl. Phys.* **2016**, *16*, 905–913.

(670) Ding, J.; Zhou, X.; Wang, H.; Yang, J.; Gao, Y.; Tang, J. Mn-Doped Fe<sub>1-x</sub>Mn<sub>x</sub>F<sub>3</sub>·0.33H<sub>2</sub>O/C Cathodes for Li-Ion Batteries: First-Principles Calculations and Experimental Study. *ACS Appl. Mater. Interfaces* **2019**, *11*, 3852–3860.

(671) Zhang, C.; Yan, M.; Li, W.; Han, C.; Li, J.; Zhao, H.; Jia, G.; An, S.; Qiu, X. Cr-Doped Fe<sub>1-x</sub>Cr<sub>x</sub>F<sub>3</sub>·0.33H<sub>2</sub>O Nanomaterials as Cathode Materials for Sodium-Ion Batteries. *ACS Appl. Mater. Interfaces* **2021**, *13*, 48653–48660.

(672) Eshetu, G. G.; Elia, G. A.; Armand, M.; Forsyth, M.; Komaba, S.; Rojo, T.; Passerini, S. Electrolytes and Interphases in Sodium-Based Rechargeable Batteries: Recent Advances and Perspectives. *Adv. Energy Mater.* **2020**, *10*, 2000093.

(673) Bommier, C.; Ji, X. Electrolytes, SEI Formation, and Binders: A Review of Nonelectrode Factors for Sodium-Ion Battery Anodes. *Small* **2018**, *14*, No. e1703576.

(674) Lin, Z.; Xia, Q.; Wang, W.; Li, W.; Chou, S. Recent Research Progresses in Ether- and Ester-Based Electrolytes for Sodium-Ion Batteries. *InfoMat* **2019**, *1*, 376–389.

(675) Komaba, S.; Ishikawa, T.; Yabuuchi, N.; Murata, W.; Ito, A.; Ohsawa, Y. Fluorinated Ethylene Carbonate as Electrolyte Additive for Rechargeable Na Batteries. *ACS Appl. Mater. Interfaces* **2011**, *3*, 4165–4168.

(676) Dahbi, M.; Nakano, T.; Yabuuchi, N.; Fujimura, S.; Chihara, K.; Kubota, K.; Son, J.-Y.; Cui, Y.-T.; Oji, H.; Komaba, S. Effect of Hexafluorophosphate and Fluoroethylene Carbonate on Electrochemical Performance and the Surface Layer of Hard Carbon for Sodium-Ion Batteries. *ChemElectroChem* **2016**, *3*, 1856–1867.

(677) Yi, Q.; Lu, Y.; Sun, X.; Zhang, H.; Yu, H.; Sun, C. Fluorinated Ether Based Electrolyte Enabling Sodium-Metal Batteries with Exceptional Cycling Stability. *ACS Appl. Mater. Interfaces* **2019**, *11*, 46965–46972.

(678) Zheng, X.; Gu, Z.; Liu, X.; Wang, Z.; Wen, J.; Wu, X.; Luo, W.; Huang, Y. Bridging the Immiscibility of an All-Fluoride Fire Extinguishant with Highly-Fluorinated Electrolytes toward Safe Sodium Metal Batteries. *Energy Environ. Sci.* **2020**, *13*, 1788–1798.

(679) Nimkar, A.; Shpigel, N.; Malchik, F.; Bubli, S.; Fan, T.; Penki, T. R.; Tsubery, M. N.; Aurbach, D. Unraveling the Role of Fluorinated Alkyl Carbonate Additives in Improving Cathode Performance in Sodium-Ion Batteries. *ACS Appl. Mater. Interfaces* **2021**, *13*, 46478–46487.

(680) Wang, C.; Sun, Z.; Liu, L.; Ni, H.; Hou, Q.; Fan, J.; Yuan, R.; Zheng, M.; Dong, Q. A Rooted Interphase on Sodium via In Situ Pre-implantation of Fluorine Atoms for High-Performance Sodium Metal Batteries. *Energy Environ. Sci.* **2023**, *16*, 3098–3109.

(681) Guo, X. F.; Yang, Z.; Zhu, Y. F.; Liu, X. H.; He, X. X.; Li, L.; Qiao, Y.; Chou, S. L. High-Voltage, Highly Reversible Sodium Batteries Enabled by Fluorine-Rich Electrode/Electrolyte Interphases. *Small Methods* **2022**, *6*, No. e2200209.

(682) Zou, Y.; Shen, Y.; Wu, Y.; Xue, H.; Guo, Y.; Liu, G.; Wang, L.; Ming, J. A Designed Durable Electrolyte for High-Voltage Lithium-Ion Batteries and Mechanism Analysis. *Chemistry* **2020**, *26*, 7930–7936.

(683) Zheng, X.; Cao, Z.; Gu, Z.; Huang, L.; Sun, Z.; Zhao, T.; Yu, S.; Wu, X.-L.; Luo, W.; Huang, Y. Toward High Temperature Sodium



Metal Batteries via Regulating the Electrolyte/Electrode Interfacial Chemistries. *ACS Energy Lett.* **2022**, *7*, 2032–2042.

(684) Feng, Y.; Zhou, L.; Ma, H.; Wu, Z.; Zhao, Q.; Li, H.; Zhang, K.; Chen, J. Challenges and Advances in Wide-Temperature Rechargeable Lithium Batteries. *Energy Environ. Sci.* **2022**, *15*, 1711–1759.

(685) Zhou, X.; Chen, X.; Yang, Z.; Liu, X.; Hao, Z.; Jin, S.; Zhang, L.; Wang, R.; Zhang, C.; Li, L.; et al. Anion Receptor Weakens  $\text{ClO}_4^-$  Solvation for High-Temperature Sodium-Ion Batteries. *Adv. Funct. Mater.* **2024**, *35*, 2302281.

(686) Wu, J.; Tian, Y.; Gao, Y.; Gao, Z.; Meng, Y.; Wang, Y.; Wang, X.; Zhou, D.; Kang, F.; Li, B.; et al. Rational Electrolyte Design toward Cyclability Remedy for Room-Temperature Sodium-Sulfur Batteries. *Angew. Chem., Int. Ed.* **2022**, *61*, No. e202205416.

(687) Zheng, J.; Chen, S.; Zhao, W.; Song, J.; Engelhard, M. H.; Zhang, J.-G. Extremely Stable Sodium Metal Batteries Enabled by Localized High-Concentration Electrolytes. *ACS Energy Lett.* **2018**, *3*, 315–321.

(688) Jin, Y.; Xu, Y.; Le, P. M. L.; Vo, T. D.; Zhou, Q.; Qi, X.; Engelhard, M. H.; Matthews, B. E.; Jia, H.; Nie, Z.; et al. Highly Reversible Sodium Ion Batteries Enabled by Stable Electrolyte-Electrode Interphases. *ACS Energy Lett.* **2020**, *5*, 3212–3220.

(689) Barnes, P.; Smith, K.; Parrish, R.; Jones, C.; Skinner, P.; Storch, E.; White, Q.; Deng, C.; Karsann, D.; Lau, M. L.; et al. A Non-aqueous Sodium Hexafluorophosphate-Based Electrolyte Degradation Study: Formation and Mitigation of Hydrofluoric Acid. *J. Power Sources* **2020**, *447*, 227363.

(690) Terborg, L.; Nowak, S.; Passerini, S.; Winter, M.; Karst, U.; Haddad, P. R.; Nesterenko, P. N. Ion Chromatographic Determination of Hydrolysis Products of Hexafluorophosphate Salts in Aqueous Solution. *Anal. Chim. Acta* **2012**, *714*, 121–126.

(691) Ould, D. M. C.; Menkin, S.; Smith, H. E.; Riesgo-Gonzalez, V.; Jonsson, E.; O'keefe, C. A.; Coowar, F.; Barker, J.; Bond, A. D.; Grey, C. P.; et al. Sodium Borates: Expanding the Electrolyte Selection for Sodium-Ion Batteries. *Angew. Chem., Int. Ed.* **2022**, *61*, No. e202202133.

(692) Xu, X.; Zhou, D.; Qin, X.; Lin, K.; Kang, F.; Li, B.; Shanmukaraj, D.; Rojo, T.; Armand, M.; Wang, G. A Room-Temperature Sodium-Sulfur Battery with High Capacity and Stable Cycling Performance. *Nat. Commun.* **2018**, *9*, 3870.

(693) Yang, C.; Feng, J.; Lv, F.; Zhou, J.; Lin, C.; Wang, K.; Zhang, Y.; Yang, Y.; Wang, W.; Li, J.; et al. Metallic Graphene-Like  $\text{VSe}_2$  Ultrathin Nanosheets: Superior Potassium-Ion Storage and Their Working Mechanism. *Adv. Mater.* **2018**, *30*, No. e1800036.

(694) Fan, L.; Hu, Y.; Rao, A. M.; Zhou, J.; Hou, Z.; Wang, C.; Lu, B. Prospects of Electrode Materials and Electrolytes for Practical Potassium-Based Batteries. *Small Methods* **2021**, *5*, No. e2101131.

(695) Chihara, K.; Katogi, A.; Kubota, K.; Komaba, S.  $\text{KVPO}_4\text{F}$  and  $\text{KVPO}_4$  Toward 4 V-Class Potassium-Ion Batteries. *Chem. Commun.* **2017**, *53*, 5208–5211.

(696) Tan, H.; Du, X.; Huang, J. Q.; Zhang, B.  $\text{KVPO}_4\text{F}$  as a Novel Insertion-Type Anode for Potassium Ion Batteries. *Chem. Commun.* **2019**, *55*, 11311–11314.

(697) Liao, J.; Hu, Q.; He, X.; Mu, J.; Wang, J.; Chen, C. A long lifespan potassium-ion full battery based on  $\text{KVPO}_4\text{F}$  cathode and  $\text{VPO}_4$  anode. *J. Power Sources* **2020**, *451*, 227739.

(698) Fedotov, S. S.; Luchinin, N. D.; Aksyonov, D. A.; Morozov, A. V.; Ryazantsev, S. V.; Gaboardi, M.; Plaisier, J. R.; Stevenson, K. J.; Abakumov, A. M.; Antipov, E. V. Titanium-Based Potassium-Ion Battery Positive Electrode with Extraordinarily High Redox Potential. *Nat. Commun.* **2020**, *11*, 1484.

(699) Kim, H.; Seo, D. H.; Bianchini, M.; Clément, R. J.; Kim, H.; Kim, J. C.; Tian, Y.; Shi, T.; Yoon, W. S.; Ceder, G. A New Strategy for High-Voltage Cathodes for K-Ion Batteries: Stoichiometric  $\text{KVPO}_4\text{F}$ . *Adv. Energy Mater.* **2018**, *8*, 1801591.

(700) Dong, J.; Liao, J.; He, X.; Hu, Q.; Yu, Y.; Chen, C. Graphene Encircled  $\text{KFeSO}_4\text{F}$  Cathode Composite for High Energy Density Potassium-Ion Batteries. *Chem. Commun.* **2020**, *56*, 10050–10053.

(701) Recham, N.; Rousse, G.; Sougrati, M. T.; Chotard, J.-N.; Frayret, C.; Mariyappan, S.; Melot, B. C.; Jumas, J.-C.; Tarascon, J.-M. Preparation and Characterization of a Stable  $\text{FeSO}_4\text{F}$ -Based Framework for Alkali Ion Insertion Electrodes. *Chem. Mater.* **2012**, *24*, 4363–4370.

(702) Ling, C.; Mizuno, F. Mechanistic Study of the Electrochemical Extraction of  $\text{K}^+$  from  $\text{KFeSO}_4\text{F}$ . *J. Mater. Chem. A* **2013**, *1*, 8000.

(703) Jian, Z.; Luo, W.; Ji, X. Carbon Electrodes for K-Ion Batteries. *J. Am. Chem. Soc.* **2015**, *137*, 11566–11569.

(704) Zhou, M.; Bai, P.; Ji, X.; Yang, J.; Wang, C.; Xu, Y. Electrolytes and Interphases in Potassium Ion Batteries. *Adv. Mater.* **2021**, *33*, No. e2003741.

(705) Xu, Y.; Ding, T.; Sun, D.; Ji, X.; Zhou, X. Recent Advances in Electrolytes for Potassium-Ion Batteries. *Adv. Funct. Mater.* **2023**, *33*, 2211290.

(706) Xiao, N.; McCulloch, W. D.; Wu, Y. Reversible Dendrite-Free Potassium Plating and Stripping Electrochemistry for Potassium Secondary Batteries. *J. Am. Chem. Soc.* **2017**, *139*, 9475–9478.

(707) Zhang, W.; Wu, Z.; Zhang, J.; Liu, G.; Yang, N.-H.; Liu, R.-S.; Pang, W. K.; Li, W.; Guo, Z. Unraveling the Effect of Salt Chemistry on Long-Durability High-Phosphorus-Concentration Anode for Potassium Ion Batteries. *Nano Energy* **2018**, *53*, 967–974.

(708) Zhang, W.; Pang, W. K.; Sencadas, V.; Guo, Z. Understanding High-Energy-Density  $\text{Sn}_4\text{P}_3$  Anodes for Potassium-Ion Batteries. *Joule* **2018**, *2*, 1534–1547.

(709) Xie, J.; Li, X.; Lai, H.; Zhao, Z.; Li, J.; Zhang, W.; Xie, W.; Liu, Y.; Mai, W. A Robust Solid Electrolyte Interphase Layer Augments the Ion Storage Capacity of Bimetallic-Sulfide-Containing Potassium-Ion Batteries. *Angew. Chem., Int. Ed.* **2019**, *58*, 14740–14747.

(710) Zhang, Q.; Mao, J.; Pang, W. K.; Zheng, T.; Sencadas, V.; Chen, Y.; Liu, Y.; Guo, Z. Boosting the Potassium Storage Performance of Alloy-Based Anode Materials via Electrolyte Salt Chemistry. *Adv. Energy Mater.* **2018**, *8*, 1703288.

(711) Wang, H.; Wang, H.; Chen, S.; Zhang, B.; Yang, G.; Gao, P.; Liu, J.; Fan, X.; Huang, Y.; Lin, J.; et al. A Depth-Profiling Study on the Solid Electrolyte Interface: Bis(fluorosulfonyl)imide Anion toward Improved  $\text{K}^+$  Storage. *ACS Appl. Energy Mater.* **2019**, *2*, 7942–7951.

(712) Deng, L.; Zhang, Y.; Wang, R.; Feng, M.; Niu, X.; Tan, L.; Zhu, Y. Influence of  $\text{KPF}_6$  and  $\text{KFSI}$  on the Performance of Anode Materials for Potassium-Ion Batteries: A Case Study of  $\text{MoS}_2$ . *ACS Appl. Mater. Interfaces* **2019**, *11*, 22449–22456.

(713) Wang, H.; Yu, D.; Wang, X.; Niu, Z.; Chen, M.; Cheng, L.; Zhou, W.; Guo, L. Electrolyte Chemistry Enables Simultaneous Stabilization of Potassium Metal and Alloying Anode for Potassium-Ion Batteries. *Angew. Chem., Int. Ed.* **2019**, *58*, 16451–16455.

(714) Liu, S.; Mao, J.; Zhang, Q.; Wang, Z.; Pang, W. K.; Zhang, L.; Du, A.; Sencadas, V.; Zhang, W.; Guo, Z. An Intrinsically Non-flammable Electrolyte for High-Performance Potassium Batteries. *Angew. Chem., Int. Ed.* **2020**, *59*, 3638–3644.

(715) Nie, P.; Liu, M.; Qu, W.; Hou, M.; Chang, L.; Wu, Z.; Wang, H.; Jiang, J. Unravelling the Solvation Structure and Interfacial Mechanism of Fluorinated Localized High Concentration Electrolytes in K-ion Batteries. *Adv. Funct. Mater.* **2023**, *33*, 2302235.

(716) Yang, H.; Chen, C. Y.; Hwang, J.; Kubota, K.; Matsumoto, K.; Hagiwara, R. Potassium Difluorophosphate as an Electrolyte Additive for Potassium-Ion Batteries. *ACS Appl. Mater. Interfaces* **2020**, *12*, 36168–36176.

(717) Qin, L.; Xiao, N.; Zheng, J.; Lei, Y.; Zhai, D.; Wu, Y. Localized High-Concentration Electrolytes Boost Potassium Storage in High-Loading Graphite. *Adv. Energy Mater.* **2019**, *9*, 1902618.

(718) Jiang, X.; Zhang, T.; Yang, L.; Li, G.; Lee, J. Y. A Fe/Mn-Based Prussian Blue Analogue as a K-Rich Cathode Material for Potassium-Ion Batteries. *ChemElectroChem* **2017**, *4*, 2237–2242.

(719) Bie, X.; Kubota, K.; Hosaka, T.; Chihara, K.; Komaba, S. A Novel K-ion Battery: Hexacyanoferrate(ii)/Graphite Cell. *J. Mater. Chem. A* **2017**, *5*, 4325–4330.

(720) Yuan, F.; Li, Z.; Zhang, D.; Wang, Q.; Wang, H.; Sun, H.; Yu, Q.; Wang, W.; Wang, B. Fundamental Understanding and Research



Progress on the Interfacial Behaviors for Potassium-Ion Battery Anode. *Adv. Sci.* **2022**, 9, No. e2200683.

(721) Xu, C.; Li, B.; Du, H.; Kang, F. Energetic Zinc Ion Chemistry: The Rechargeable Zinc Ion Battery. *Angew. Chem., Int. Ed.* **2012**, 51, 933–935.

(722) Yang, Y.; Liu, C.; Lv, Z.; Yang, H.; Zhang, Y.; Ye, M.; Chen, L.; Zhao, J.; Li, C. C. Synergistic Manipulation of  $\text{Zn}^{2+}$  Ion Flux and Desolvation Effect Enabled by Anodic Growth of a 3D  $\text{ZnF}_2$  Matrix for Long-Lifespan and Dendrite-Free Zn Metal Anodes. *Adv. Mater.* **2021**, 33, No. e2007388.

(723) Cao, L.; Li, D.; Pollard, T.; Deng, T.; Zhang, B.; Yang, C.; Chen, L.; Vatamanu, J.; Hu, E.; Hourwitz, M. J.; et al. Fluorinated Interphase Enables Reversible Aqueous Zinc Battery Chemistries. *Nat. Nanotechnol.* **2021**, 16, 902–910.

(724) Li, D.; Cao, L.; Deng, T.; Liu, S.; Wang, C. Design of a Solid Electrolyte Interphase for Aqueous Zn Batteries. *Angew. Chem., Int. Ed.* **2021**, 60, 13035–13041.

(725) Sun, W.; Wang, F.; Zhang, B.; Zhang, M.; Kupers, V.; Ji, X.; Theile, C.; Bieker, P.; Xu, K.; Wang, C.; et al. A Rechargeable Zinc-Air Battery Based on Zinc Peroxide Chemistry. *Science* **2021**, 371, 46–51.

(726) Rubio, S.; Liang, Z.; Liu, X.; Lavela, P.; Tirado, J. L.; Stoyanova, R.; Zhecheva, E.; Liu, R.; Zuo, W.; Yang, Y.; et al. Reversible Multi-Electron Storage Enabled by  $\text{Na}_3\text{V}(\text{PO}_4)_2\text{F}_2$  for Rechargeable Magnesium Batteries. *Energy Storage Mater.* **2021**, 38, 462–472.

(727) Tang, X.; Zhou, D.; Zhang, B.; Wang, S.; Li, P.; Liu, H.; Guo, X.; Jaumaux, P.; Gao, X.; Fu, Y.; et al. A Universal Strategy towards High-Energy Aqueous Multivalent-Ion Batteries. *Nat. Commun.* **2021**, 12, 2857.

(728) Zhao-Karger, Z.; Liu, R.; Dai, W.; Li, Z.; Diemant, T.; Vinayan, B. P.; Bonatto Minella, C.; Yu, X.; Manthiram, A.; Behm, R. J.; et al. Toward Highly Reversible Magnesium-Sulfur Batteries with Efficient and Practical  $\text{Mg}[\text{B}(\text{hfp})_4]_2$  Electrolyte. *ACS Energy Lett.* **2018**, 3, 2005–2013.

(729) Sun, Y.; Zou, Q.; Wang, W.; Lu, Y.-C. Non-passivating Anion Adsorption Enables Reversible Magnesium Redox in Simple Non-nucleophilic Electrolytes. *ACS Energy Lett.* **2021**, 6, 3607–3613.

(730) Hou, S.; Ji, X.; Gaskell, K.; Wang, P. F.; Wang, L.; Xu, J.; Sun, R.; Borodin, O.; Wang, C. Solvation Sheath Reorganization Enables Divalent Metal Batteries with Fast Interfacial Charge Transfer Kinetics. *Science* **2021**, 374, 172–178.

(731) Li, Z.; Fuhr, O.; Fichtner, M.; Zhao-Karger, Z. Towards Stable and Efficient Electrolytes for Room-Temperature Rechargeable Calcium Batteries. *Energy Environ. Sci.* **2019**, 12, 3496–3501.

(732) Song, H.; Su, J.; Wang, C. Hybrid Solid Electrolyte Interphases Enabled Ultralong Life Ca-Metal Batteries Working at Room Temperature. *Adv. Mater.* **2021**, 33, No. e2006141.

(733) Kotobuki, M.; Lu, L.; Savilov, S. V.; Aldoshin, S. M. Poly(vinylidene fluoride)-Based Al Ion Conductive Solid Polymer Electrolyte for Al Battery. *J. Electrochem. Soc.* **2017**, 164, A3868–A3875.

(734) Xu, Z. L.; Park, J.; Wang, J.; Moon, H.; Yoon, G.; Lim, J.; Ko, Y. J.; Cho, S. P.; Lee, S. Y.; Kang, K. A New High-Voltage Calcium Intercalation Host for Ultra-Stable and High-Power Calcium Rechargeable Batteries. *Nat. Commun.* **2021**, 12, 3369.

(735) Fan, J.; Zhang, Z.; Liu, Y.; Wang, A.; Li, L.; Yuan, W. An Excellent Rechargeable  $\text{PP}_{14}\text{TFSI}$  Ionic Liquid Dual-Ion Battery. *Chem. Commun.* **2017**, 53, 6891–6894.

(736) Zhang, L.; Li, J.; Huang, Y.; Zhu, D.; Wang, H. Synergistic Effect of Ethyl Methyl Carbonate and Trimethyl Phosphate on  $\text{BF}_4^-$  Intercalation into a Graphite Electrode. *Langmuir* **2019**, 35, 3972–3979.

(737) Özmen-Monkul, B.; Lerner, M. M. The First Graphite Intercalation Compounds Containing Tris(pentafluoroethyl)-trifluorophosphate. *Carbon* **2010**, 48, 3205–3210.

(738) Xiang, L.; Ou, X.; Wang, X.; Zhou, Z.; Li, X.; Tang, Y. Highly Concentrated Electrolyte towards Enhanced Energy Density and Cycling Life of Dual-Ion Battery. *Angew. Chem., Int. Ed.* **2020**, 59, 17924–17930.

(739) Wang, M.; Jiang, C.; Zhang, S.; Song, X.; Tang, Y.; Cheng, H. M. Reversible Calcium Alloying Enables a Practical Room-Temperature Rechargeable Calcium-Ion Battery with a High Discharge Voltage. *Nat. Chem.* **2018**, 10, 667–672.

(740) Yu, D.; Zhu, Q.; Cheng, L.; Dong, S.; Zhang, X.; Wang, H.; Yang, N. Anion Solvation Regulation Enables Long Cycle Stability of Graphite Cathodes. *ACS Energy Lett.* **2021**, 6, 949–958.

(741) Sun, Z.; Zhu, K.; Liu, P.; Chen, X.; Li, H.; Jiao, L. Fluorination Treatment of Conjugated Protonated Polyanilines for High-Performance Sodium Dual-Ion Batteries. *Angew. Chem., Int. Ed.* **2022**, 61, No. e202211866.

(742) Read, J. A.; Cresce, A. V.; Ervin, M. H.; Xu, K. Dual-Graphite Chemistry Enabled by a High-Voltage Electrolyte. *Energy Environ. Sci.* **2014**, 7, 617–620.

(743) Wang, Y.; Zhang, Y.; Wang, S.; Dong, S.; Dang, C.; Hu, W.; Yu, D. Y. W. Ultrafast Charging and Stable Cycling Dual-Ion Batteries Enabled via an Artificial Cathode-Electrolyte Interface. *Adv. Funct. Mater.* **2021**, 31, 2102360.

(744) Wang, Y.; Zhang, Y.; Dong, S.; Zhou, W.; Lee, P. K.; Peng, Z.; Dang, C.; Sit, P. H. L.; Guo, J.; Yu, D. Y. W. An All-Fluorinated Electrolyte Toward High Voltage and Long Cycle Performance Dual-Ion Batteries. *Adv. Energy Mater.* **2022**, 12, 2103360.

(745) Zhu, J.; Xu, Y.; Fu, Y.; Xiao, D.; Li, Y.; Liu, L.; Wang, Y.; Zhang, Q.; Li, J.; Yan, X. Hybrid Aqueous/Nonaqueous Water-in-Bisalt Electrolyte Enables Safe Dual Ion Batteries. *Small* **2020**, 16, No. e1905838.

(746) Wrogemann, J. M.; Künne, S.; Heckmann, A.; Rodríguez-Pérez, I. A.; Siozios, V.; Yan, B.; Li, J.; Winter, M.; Beltrop, K.; Placke, T. Development of Safe and Sustainable Dual-Ion Batteries Through Hybrid Aqueous/Nonaqueous Electrolytes. *Adv. Energy Mater.* **2020**, 10, 1902709.

(747) Rodríguez-Pérez, I. A.; Zhang, L.; Wrogemann, J. M.; Driscoll, D. M.; Sushko, M. L.; Han, K. S.; Fulton, J. L.; Engelhard, M. H.; Balasubramanian, M.; Viswanathan, V. V.; et al. Enabling Natural Graphite in High-Voltage Aqueous Graphite || Zn Metal Dual-Ion Batteries. *Adv. Energy Mater.* **2020**, 10, 2001256.

(748) Zhang, Z.; Hu, X.; Zhou, Y.; Wang, S.; Yao, L.; Pan, H.; Su, C.-Y.; Chen, F.; Hou, X. Aqueous Rechargeable Dual-Ion Battery Based on Fluoride Ion and Sodium Ion Electrochemistry. *J. Mater. Chem. A* **2018**, 6, 8244–8250.

(749) Yang, C.; Chen, J.; Ji, X.; Pollard, T. P.; Lu, X.; Sun, C. J.; Hou, S.; Liu, Q.; Liu, C.; Qing, T.; et al. Aqueous Li-Ion Battery Enabled by Halogen Conversion-Intercalation Chemistry in Graphite. *Nature* **2019**, 569, 245–250.

(750) Wang, H.; Sun, Y.; Li, M.; Li, G.; Xue, K.; Chen, Z.; Yu, D. Y. W. Engineering Solvation Complex-Membrane Interaction to Suppress Cation Crossover in 3 V Cu-Al Battery. *Small* **2020**, 16, No. e2003438.

(751) Yu, M.; Sui, Y.; Sandstrom, S. K.; Wu, C. Y.; Yang, H.; Stickle, W.; Luo, W.; Ji, X. Reversible Copper Cathode for Nonaqueous Dual-Ion Batteries. *Angew. Chem., Int. Ed.* **2022**, 61, No. e202212191.

# Ultrafast Charging and Stable Cycling Dual-Ion Batteries Enabled via an Artificial Cathode–Electrolyte Interface

Yao Wang, Yanjun Zhang, Shuo Wang, Shuyu Dong, Chaoqun Dang, Weichen Hu, and Denis Y. W. Yu\*

Low-cost and environment-friendly dual-ion batteries (DIBs) with fast-charging characteristics facilitate the development of high-power energy storage devices. However, the incompatibility between the cathode and electrolyte at high voltage results in low Coulombic efficiency (CE) and short lifespan. Here, the addition of  $\approx 0.5$  wt% lithium difluoro(oxalate) borate salt into the electrolyte forms a robust and durable cathode–electrolyte interface (CEI) in situ on the graphite surface, which enables remarkable cycling of the graphite||Li battery with 87.5% capacity retention after 4000 cycles at 5 C and ultrafast rate capability with 88.8% capacity retention under 40 C ( $4 \text{ A g}^{-1}$ ), delivering high-power of  $0.4\text{--}18.8 \text{ kW kg}^{-1}$  at energy densities of  $422.7\text{--}318.8 \text{ Wh kg}^{-1}$ . Taking advantage of this robust CEI, a graphite||graphite full battery demonstrates high reversible capacities of 97.6, 92.8, 88.7, and  $85.4 \text{ mAh (g cathode)}^{-1}$  at current rates of 10, 20, 30, and 40 C, respectively. The full battery also shows a long cycling life of over 6500 cycles with 92.4% capacity retention and an average CE of  $\approx 99.4\%$  at  $1 \text{ A g}^{-1}$ , which is superior to other dual-graphite (carbon) batteries in the literature. This work offers an effective interface-stabilizing strategy on protecting graphite cathodes and a promising approach for developing DIBs with high-power capability.

## 1. Introduction

Electric energy storage technologies such as lithium-ion batteries (LIBs) are becoming indispensable in various fields to reduce the reliance on fossil fuels and to promote the efficient utilization of alternative energy sources (e.g., solar, wind, and tidal energy).<sup>[1]</sup> Despite the appreciable advantages of high energy density and long lifetime, the grid/utility applications of LIBs are limited due to low power density, safety, cost, and

eco-friendliness concerns.<sup>[1c]</sup> Considering the demands for sustainability, low cost, high-power characteristics, and fast charging capability, various types of battery systems have been developed, among which dual-ion battery (DIB) is undoubtedly a highly interesting candidate and is attracting increasing attention. In contrast to the rocking-chair type cells such as LIB where the cations (i.e.,  $\text{Li}^+$ ) are transported between the two electrodes upon charging/discharging, DIB exhibits a different working mechanism which involves simultaneous intercalation of anions into the cathode and cations into the anode during charge, and simultaneous extraction of both ions during discharge.<sup>[2]</sup> Compared to conventional LIBs, the higher working voltage of above 4.5 V for the graphite cathode is favorable for improving the energy density of DIBs, but it also leads to continuous side reactions such as undesirable electrolyte decomposition and structural deterioration of the

graphite material.<sup>[3]</sup> Even though a few research works have demonstrated that cell performances of DIBs (e.g., reversible capacity, energy density, rate performance, and the cell voltage) are highly dependent on the type of electrolyte, more efforts are still needed to understand the underlying mechanism.<sup>[1a,2d,3a,4]</sup>


The reversible anion de-/intercalation behavior at high cut-off voltage could be compromised by the incompatibility between electrolyte and the cathode–electrolyte interface (CEI) on graphite, resulting in inevitable electrolyte decomposition, fast capacity decay, and low Coulombic efficiency (CE).<sup>[5]</sup> Therefore, searching for more convenient, economical, and effective methods to ameliorate the interfacial stability of cathode is undoubtedly one of the most influential research undertakings for enhancing the long-term cycle stability of DIBs. Recently, modification of the solid electrolyte interphase (SEI) via electrolyte additives has been reported as an effective strategy to facilitate cation (such as  $\text{Li}^+$  or  $\text{K}^+$ ) insertion/extraction into/from graphite anode,<sup>[6]</sup> so one can also strengthen the CEI to reduce side reactions. Nevertheless, the role of electrolyte additive in manipulating the CEI layer on graphite cathode and the effect of the CEI layer on  $\text{PF}_6^-$  anion de-/intercalation performances in DIBs are still elusive, requiring further systematic investigations.

Here, we introduce a promising lithium salt-type additive, lithium difluoro(oxalate) borate ( $\text{LiDFOB}$ ) to the bulk electrolyte

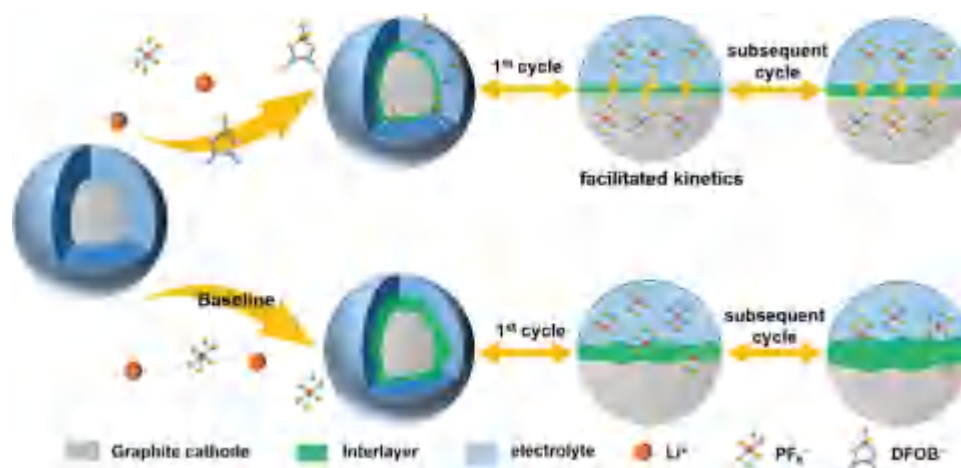
Y. Wang, Dr. Y. Zhang, Dr. S. Wang, S. Dong, W. Hu, Dr. D. Y. W. Yu  
School of Energy and Environment  
City University of Hong Kong  
Hong Kong SAR 999077, China  
E-mail: denisyu@cityu.edu.hk

Dr. C. Dang  
Department of Mechanical Engineering  
City University of Hong Kong  
Hong Kong SAR 999077, China

Dr. D. Y. W. Yu  
Center of Super-Diamond and Advanced Films (COSDAF)  
City University of Hong Kong  
Hong Kong SAR 999077, China

 The ORCID identification number(s) for the author(s) of this article can be found under <https://doi.org/10.1002/adfm.202102360>.

DOI: 10.1002/adfm.202102360



**Scheme 1.** Illustration of the CEI evolution during cycling in electrolyte with and without LiDFOB additive.

in DIBs and demonstrate that the charging capability and long cyclability are significantly enhanced. With an optimal additive amount (0.5 wt%), a robust and conductive CEI layer is formed in situ on the graphite cathode, facilitating the anion storage reaction, suppressing side reactions, and stabilizing the graphite structure (**Scheme 1**). At a low current rate (1 C, 1 C = 100 mA g<sup>-1</sup>), the achievable energy density is as high as 422.7 Wh kg<sup>-1</sup>. The LiDFOB-modified CEI layer significantly improves the capacity retention of the DIB to 87.5% even after 4000 cycles at 500 mA g<sup>-1</sup> (5 C). Besides, the reduced activation energy and promoted diffusion kinetics for anion intercalation process enable an ultrafast charging capability of 88.8% at 40 C, achieving high power density up to 18.8 kW kg<sup>-1</sup> with corresponding energy densities of 318.8 Wh kg<sup>-1</sup> with respect to the mass of the graphite cathode. The characteristics of the protective CEI on the cathode are elucidated and are further correlated with the PF<sub>6</sub><sup>-</sup> de-/intercalation performance in DIBs. As a proof of concept, a dual graphite (graphite||graphite) battery delivers high discharge capacities of 976, 92.8, 88.7, and 85.4 mAh g<sup>-1</sup> at current rates of 10, 20, 30, and 40 C, respectively. The prototype demonstrates attractive energy density of up to 179.8 Wh kg<sup>-1</sup> and power density up to 7.8 kW kg<sup>-1</sup>, calculated with respect to the total mass of both graphite anode and cathode, along with a long lifetime of 6500 cycles with 92.4% capacity retention with a high average CE of 99.4% at 1 A g<sup>-1</sup>.

## 2. Results and Discussion

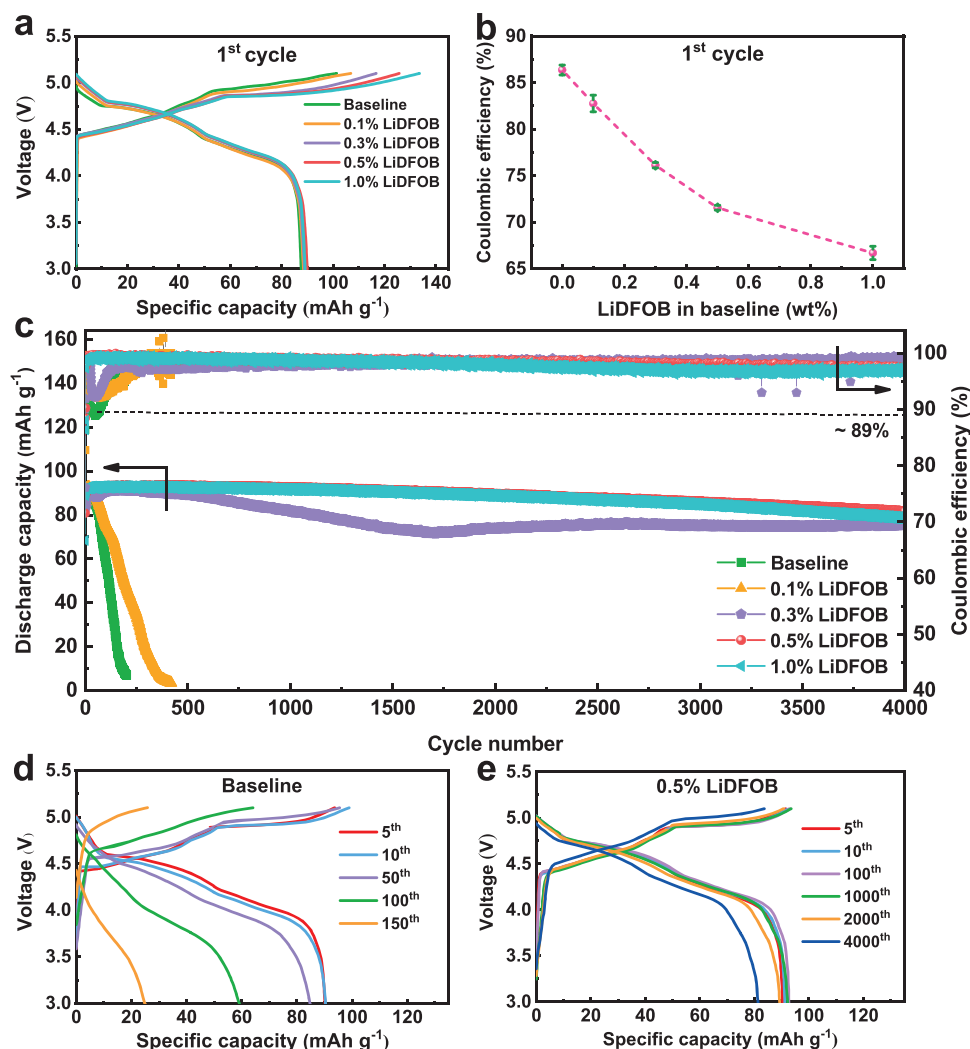
The graphite||Li cells were pre-cycled in 3M LiPF<sub>6</sub> in ethyl methyl carbonate (EMC) electrolyte without (baseline) and with different amounts of LiDFOB at a constant current of 20 mA g<sup>-1</sup> for three cycles to form the CEI. Thereafter, the cells were galvanostatically cycled at 5 C rate. The first charge/discharge voltage curves and cycle efficiency of the cells are compared in **Figure 1a,b**, respectively. The 1st cycle charge capacity increases with a higher LiDFOB amount, while the discharge capacity remains the same. The decrease in the initial CE is seen obviously with the addition of a small amount (≤1.0 wt%) of LiDFOB into the baseline electrolyte, resulting from

the additional irreversible charge capacity. This can be attributed to the preferential decomposition of the LiDFOB additive which has a higher HOMO energy level than that of the EMC solvent, as reported before.<sup>[7]</sup> Another noteworthy feature is that the electrode polarization (the difference between the average charge and discharge plateaus) decreases due to the addition of LiDFOB. This is indicative of a less-resistive surface film derived from LiDFOB oxidation compared with that formed in the baseline electrolyte, allowing facile PF<sub>6</sub><sup>-</sup> de-/intercalation from/into the graphite cathode.

The comparison of cycle stabilities and CEs of graphite||Li cells with various contents of LiDFOB are shown in **Figure 1c**. CE of the graphite cathodes with the baseline electrolyte decreases to ≈90% within the first 30 cycles and remains between 89–90% in the following 50 cycles, indicating that side reactions occur continuously to form new interface layer. As a result, cells with baseline electrolyte experience rapid capacity fading to 25 mAh g<sup>-1</sup> (24.3% capacity retention) after 150 cycles. In comparison, the introduction of LiDFOB additive improves cycle performance of graphite cells and the cycle stability increases with LiDFOB concentration. The addition of 0.3 wt% LiDFOB is however insufficient to suppress the side reactions during the initial 60 cycles, resulting in a continuous capacity fading during 1700 cycles even though the capacity maintains stability afterward. Our results indicate that 0.5 wt% LiDFOB is necessary to enhance CE and cycle stability, with a corresponding capacity retention of 87.5% after 4000 cycles with an average CE of 98.4%. However, when the LiDFOB content is further increased to 1.0 wt%, the cells show comparable capacity retention and average CE to that with LiDFOB amount of 0.5 wt% without additional benefits, suggesting that the cycle stability is saturated with ≈0.5 wt% LiDFOB-containing electrolyte. Thus, the electrolyte with 0.5 wt% LiDFOB additive was selected here for further analysis.

The evolution of charge/discharge voltage profiles of graphite||Li cells in electrolytes with 0%, 0.1%, 0.3%, 0.5%, and 1.0% (wt%) LiDFOB additives are presented in **Figure 1d,e** and **Figure S1**, Supporting Information. The characteristic charge–discharge plateaus corresponding to PF<sub>6</sub><sup>-</sup> de-/intercalation from/into graphite can be seen for cells with various electrolytes.





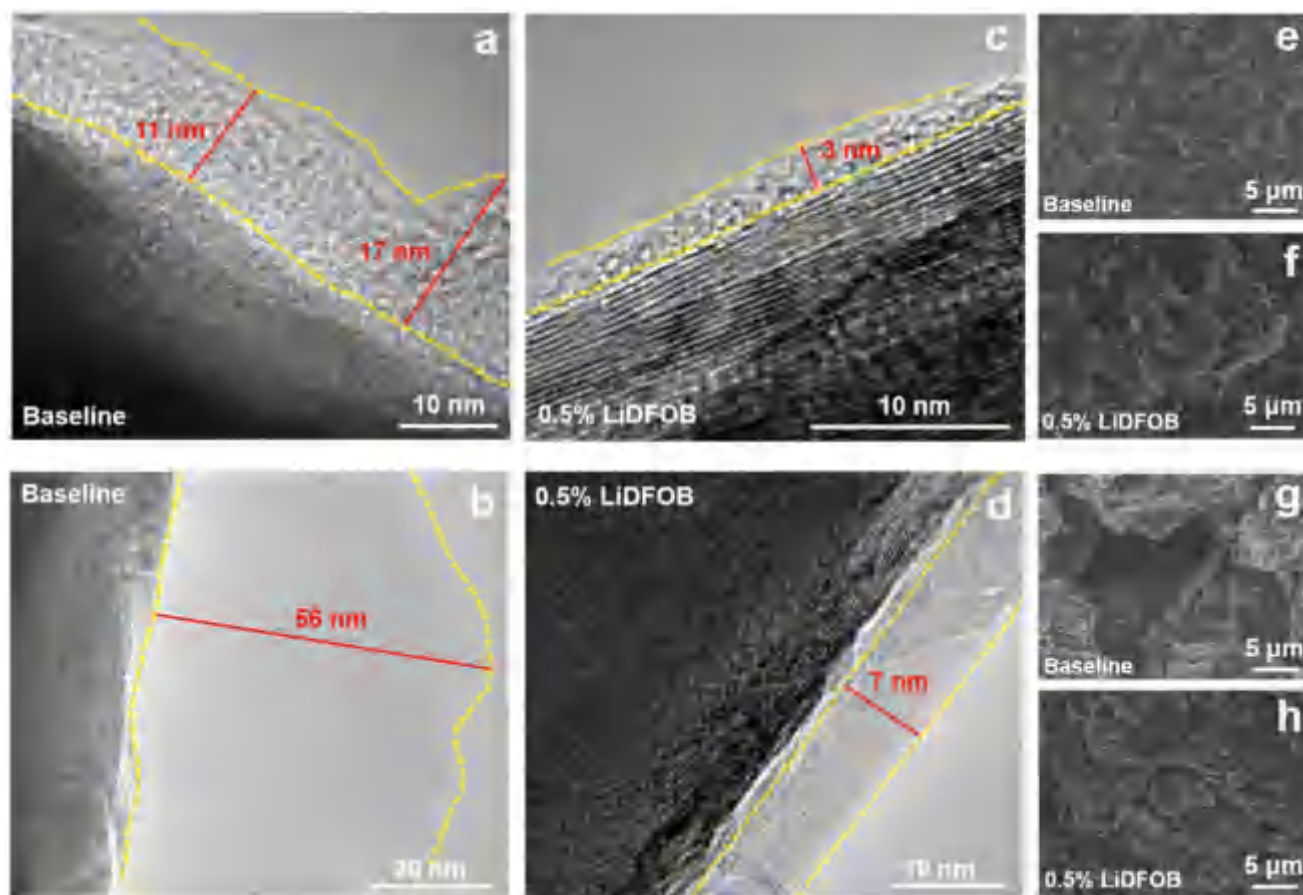
**Figure 1.** a) The 1st cycle voltage profiles and b) the 1st cycle Coulombic efficiency, c) cycle performance and CE of graphite||Li cells with 0% (baseline), 0.1%, 0.3%, 0.5%, and 1.0% (wt%) LiDFOB-containing electrolytes. Charge–discharge curves of graphite||Li cells in electrolytes d) without and e) with 0.5 wt% LiDFOB. Upper cutoff voltage: 5.1 V, current density: 500 mA g<sup>-1</sup>.

During the 5th cycle, smaller cell polarization of  $\approx 0.32$  V is observed with 0.5 wt% LiDFOB-containing electrolyte compared with that of  $\approx 0.47$  V for cell cycled without LiDFOB (baseline). This is indicative of the reduced cell impedance by introducing LiDFOB additive. As illustrated in Figure 1d, the decrease in discharge capacity with cycling in the absence of LiDFOB is due to a drastic increase in cell polarization with the vanishing of the voltage plateaus corresponding to the  $\text{PF}_6^-$  de-/intercalation process within 150 cycles. The addition of LiDFOB into the electrolyte improves the capacity retention of graphite||Li cells by suppressing the increase in polarization with cycling. In particular, for cells with 0.5 wt% LiDFOB-containing electrolyte, a well-overlapped voltage curve is maintained even after charging/discharging for 2000 cycles. In subsequent characterizations, graphite electrode cycled in baseline electrode and that in 0.5 wt% LiDFOB electrolyte is compared.

To explore the underlying reason for the performance enhancement with LiDFOB additive, the morphological evolution of the cathodes at fully-charged state was studied by

transmission electron microscopy (TEM) and scanning electron microscopy (SEM). **Figure 2** presents the SEM and TEM images of the graphite electrodes after the 2nd and 150th cycles for the cell with baseline and with 0.5 wt% LiDFOB-containing electrolytes. For the graphite electrode cycled in the baseline electrolyte, a thick and uneven CEI film is observed on the material surface after the 2nd cycle (Figure 2a). The CEI thickness further increases to  $\approx 56$  nm after 150 cycles (Figure 2b). This result is consistent with the poor cycle performance of the electrode material, where continuous side reactions between the electrolyte and the surface of graphite, as suggested by the low CE, leads to a thickening of the CEI layer, resulting in large interfacial resistance and impedes the transport of  $\text{PF}_6^-$  anions into graphite cathodes. In addition, damages on the surface of the materials, which are evidence of graphite exfoliation, are discovered after 150 cycles (Figure 2g).

In contrast, for the graphite electrode cycled in electrolyte with 0.5 wt% LiDFOB, a thin CEI of  $\approx 3$  nm in thickness is observed on the graphite surface at both charged and



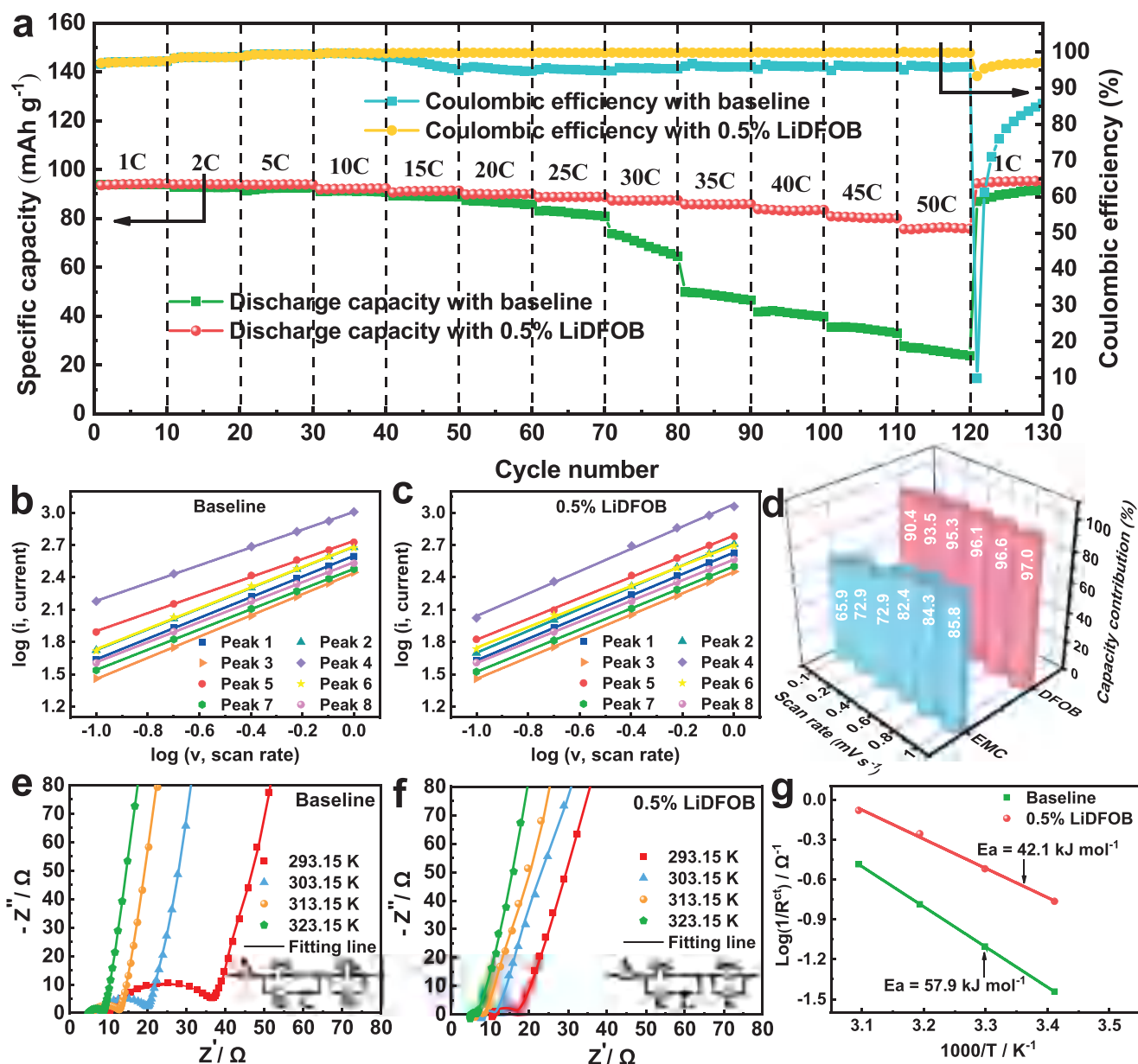
**Figure 2.** Morphological characterizations of graphite electrodes: TEM and SEM images after a,e) the 2nd and b,g) the 150th cycle using baseline electrolyte, after c,f) the 2nd and d,h) the 150th cycle in 0.5 wt% LiDFOB-containing electrolyte.

discharged states after the 2nd cycle (Figure 2c and Figure S2a, Supporting Information). The CEI remains around 7 nm after 150 cycles (Figure 2d), suggesting an enhanced interfacial stability of the CEI layer modified by LiDFOB additive. In addition, no CEI layer is observed on the graphite electrode with LiDFOB-containing electrolyte before charge/discharge (Figure S2b, Supporting Information), suggesting that the CEI is formed by electrochemical reactions between the graphite cathode and the electrolyte. The overall morphology of the graphite maintains intact after cycling in LiDFOB-containing electrolyte (Figure 2h), similar to the appearance of the pristine material (Figure S2c, Supporting Information). Thus, the stable CEI formed in situ with LiDFOB additive significantly reduces parasitic reactions and improves the cycle stability.

In addition to the cathode, LiDFOB could also influence the anode side.<sup>[7]</sup> To evaluate the effect of LiDFOB on the Li electrode in graphite||Li battery, the Li plating/stripping behaviors were investigated via Li||Li symmetrical cells that were cycled with a current density of 0.05 and 1.15 mA cm<sup>-2</sup> (corresponding to a current of 20 and 500 mA g<sup>-1</sup> in the graphite||Li cells). Compared with the Li||Li cells cycled at 0.05 mA cm<sup>-2</sup>, the voltage gap between charge and discharge increases noticeably under a high current density of 1.15 mA cm<sup>-2</sup> (see Figure S3, Supporting Information), indicating a large

overpotential. It is noted that the Li||Li symmetrical cell cycled in LiDFOB-containing electrolyte experiences a larger polarization compared with that in baseline electrolyte. Thus, it can be concluded that LiDFOB additive has no significant effect on the Li stripping/plating behavior and therefore, the improvement in electrochemical performance of the graphite||Li batteries is mainly attributed to the LiDFOB-induced CEI on the graphite cathode.<sup>[7,8]</sup>

To elucidate the effect of LiDFOB-induced CEI on the rate capability of graphite cathodes, graphite||Li cells were charged and discharged at current rates ranging from 1 to 50 C (Figure 3a and Figure S4, Supporting Information). Clearly, when charging/discharging at increasing C rates, the graphite cathode cycled in electrolyte with LiDFOB additive shows a smaller increase in cell polarization up to 50 C (see Figure S4, Supporting Information), further confirming this uniform thin CEI is highly conductive for anions.<sup>[9]</sup> As a result, high reversible capacities of 83.7 and 76.3 mAh g<sup>-1</sup> are achieved for graphite||Li cells even when they are charged at 40 and 50 C, corresponding to capacity retentions of 88.8% and 80.9%, respectively. Based on the measured capacity of the cathode material and the average discharge voltage, the graphite||Li cell can be cycled between a high power of 0.4–18.8 kW kg<sup>-1</sup> with respect to the mass of the cathode while



**Figure 3.** a) Rate capability of graphite||Li cells with baseline and 0.5 wt% LiDFOB-containing electrolytes. log *i* versus log *v* to determine *b* values for graphite cathodes with b) baseline and c) 0.5 wt% LiDFOB-containing electrolytes. d) The capacitive contribution towards PF<sub>6</sub><sup>-</sup> storage at different scan rates. Nyquist plots of the cycled graphite||Li cells with e) baseline and f) 0.5 wt% LiDFOB-containing electrolytes. Inset shows the equivalent circuit model for EIS analysis. g) Arrhenius plots of log(1/*R*<sub>ct</sub>) versus 1000/*T* calculated from the EIS results.

maintaining a corresponding energy density in the range of 422.7–318.8 Wh kg<sup>-1</sup> (Table S1 and Note S1, Supporting Information), which is much superior to the activated carbon cathode for supercapacitors (Figure S5, Supporting Information). The cell cycled in baseline electrolyte, in sharp contrast, suffers from large polarization at high current rate, resulting in a largely reduced capacity of ≈25 mAh g<sup>-1</sup> at 50 C. In addition, the CE of the cell with baseline electrolyte is reduced when it is cycled above 10 C, and is also significantly reduced after the high-rate test. This indicates that the surface structure of the graphite material is damaged due to the high current rate, leading to the exposure of fresh graphite surface to the

electrolyte with higher reactivity and lower CE, as seen from the SEM and TEM analysis (Figure S6, Supporting Information). These results demonstrate that LiDFOB additive plays a dominant role in generating a protective and low-resistive CEI layer, contributing to the highly improved interfacial dynamics.

In order to explore the origins for this fast chargeability of cells with LiDFOB-containing electrolyte, cyclic voltammetry (CV) and electrochemical impedance spectroscopy (EIS) were systematically conducted. Specifically, CV measurements of graphite electrodes in baseline and 0.5 wt% LiDFOB-containing electrolytes at various sweep rates from 0.1 to 1.0 mV s<sup>-1</sup> were evaluated to investigate the kinetics for anion storage of



graphite cathodes, as displayed in Figure S7, Supporting Information. The relationship between the redox peak currents ( $i$ ) and the scan rates ( $v$ ) follows the power law:

$$i = av^b \quad (1)$$

The electrochemical reaction is distinguished between semi-infinite diffusion dominated ( $b = 0.5$ ) and surface controlled ( $b = 1$ ) by the value of  $b$ .<sup>[10]</sup> Correspondingly, the measured current can be divided into surface-controlled ( $k_1v$ ) and diffusion-controlled ( $k_2v^{1/2}$ ) parts by the equation:<sup>[5a,11]</sup>

$$i = k_1v + k_2v^{1/2} \quad (2)$$

The  $b$  values of the graphite electrode with baseline electrolyte are determined to be 0.96 (peak 1), 0.96 (peak 2), 0.98 (peak 3), 0.82 (peak 4), 0.83 (peak 5), 0.95 (peak 6), 0.93 (peak 7), and 0.92 (peak 8), respectively (Figure 3b). By integrating the CV profiles, we can find that the percentage of surface capacitive contribution to the capacity increases with higher scan rate (Figure 3d). These results imply that capacitive reactions occurring near the surface region of graphite cathodes account for a considerable proportion of the  $\text{PF}_6^-$  anion storage capacity.<sup>[1b,5a]</sup> After LiDFOB addition, it is found that  $b$  values of all redox peaks increase (from peak 1 to peak 8: 1.00, 0.99, 0.99, 0.99, 0.97, 0.95, 0.98, and 0.96), along with higher contribution from capacitive behavior (Figure 3d). These results confirm that the CEI layer generated from LiDFOB-containing electrolyte improves the kinetics of the graphite surface especially at high voltage (above 4.8 V).

In order to further explore the kinetics of the charge transfer process, EIS of the graphite cathodes was conducted at different temperatures (see Figure 3e,f). It is found that all the impedance curves exhibit a depressed semicircle in the high-frequency region. The Nyquist plots were quantitatively analyzed using the equivalent circuit in the inset (Figure 3e,f), where  $R_s$  and  $R_{ct}$  are attributed to the resistance of electrolyte and charge-transfer, respectively;  $\text{CPE}_1$  and  $\text{CPE}_2$  represent the capacitance of the double layer and the active material, while  $Z_w$  is the Warburg impedance associated with the  $\text{PF}_6^-$  ion diffusion in the active material.<sup>[1b,12]</sup>  $R_{ct}$  is a significant parameter indicating the kinetics of the Faradic reactions and accordingly, the apparent activation energy ( $E_a$ ) can be calculated based on the following Arrhenius equation:<sup>[13]</sup>

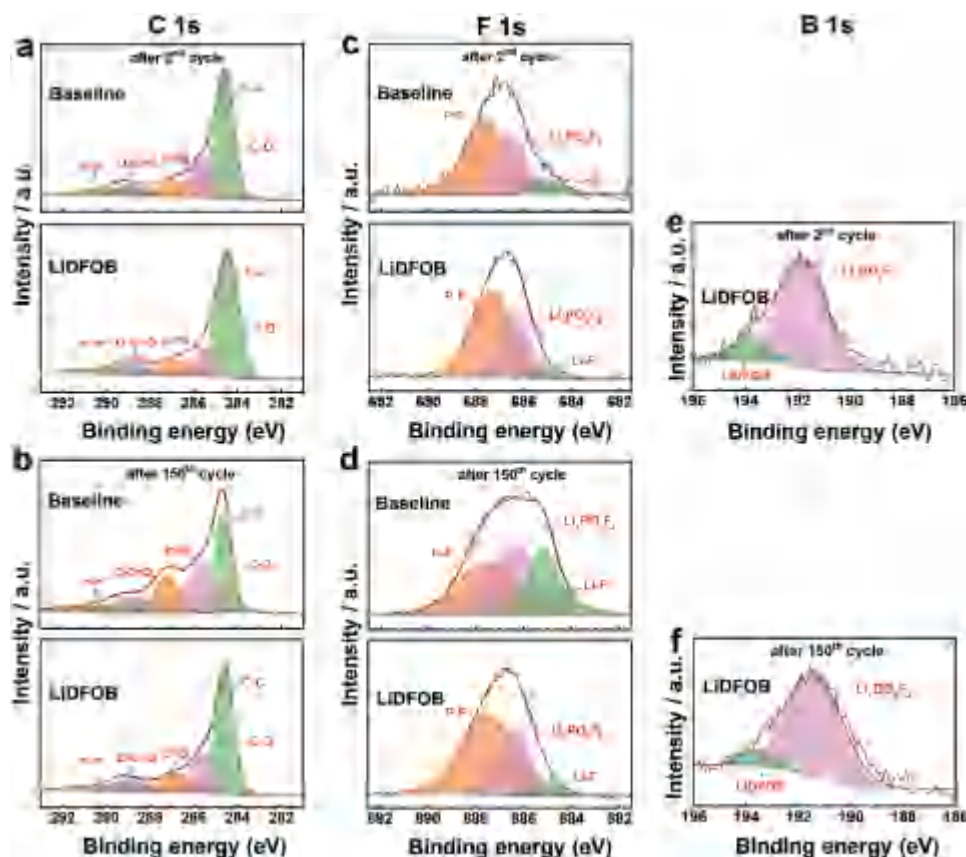
$$\log\left(\frac{1}{R_{ct}}\right) = -\frac{E_a}{2.303RT} + A \quad (3)$$

where  $T$  is the absolute temperature (in K),  $R$  and  $A$  are the gas constant, and Arrhenius constant, respectively. As the test temperature rises, cells cycled in the baseline electrolyte exhibit a drastic decrease in  $R_{ct}$ , indicating that the anion intercalation process is facilitated. It is noted that the dependence of  $R_{ct}$  on temperature is weakened with LiDFOB-containing electrolyte. Accordingly, the activation energy obtained from the fitting line in Figure 3d,e is 42.1 and 579 kJ mol<sup>-1</sup> for graphite cells in electrolyte with and without LiDFOB, respectively (Figure 3g). The

lower activation energy of the cell using LiDFOB-containing electrolyte suggests that it is easier for  $\text{PF}_6^-$  to transport through the LiDFOB-induced CEI, leading to the significant enhancement of rate capability and reduction of electrode polarization over the additive-free cell.

These results indicate the CEI layer formed in LiDFOB-containing electrolyte is robust and is capable of providing a stabilized interface for graphite cathodes. The characteristics of the formed CEI are known to be closely associated with its chemical compositions, which is further analyzed by X-ray photoelectron spectroscopy (XPS). The C 1s, F 1s, and B 1s spectra of pristine and cycled graphite cathodes in the baseline and LiDFOB-containing electrolytes are compared in Figure 4 and Figure S8, Supporting Information. After the 2nd cycle, similar oxygenated organic groups, including C–O (285.6 eV), C = O (287.0 eV), and O–C = O (288.9 eV) species, are observed for graphite electrodes in both electrolytes (Figure 4a). However, these peaks become stronger and the relative content of oxygenated organic groups increases largely on the graphite surface after 150 cycles in the baseline electrolyte, which is due to the accumulation of surface deposits from electrolyte decomposition and the oxidation of graphite surface.<sup>[14]</sup> In contrast, the amount of these oxygenated organic species remains almost the same in 0.5 wt% LiDFOB-containing electrolyte, suggesting that LiDFOB is able to suppress undesirable surface reactions. The results are consistent with the morphological changes on the surface of the materials from TEM observations and confirm the excellent capability of LiDFOB additive to enhance the interfacial stability of graphite cathodes. In the core level F 1s spectra, new peaks corresponding to LiF and  $\text{Li}_x\text{PO}_y\text{F}_z$  species appear after cycling due to the decomposition of  $\text{LiPF}_6$  salt.<sup>[15]</sup> After 150 cycles, the content of LiF increases for the cell tested in the baseline electrolyte. In comparison, the graphite surface shows smaller amount of LiF and  $\text{Li}_x\text{PO}_y\text{F}_z$  fractions in the presence of LiDFOB additive even after 150 cycles (Figure 4c,d). Owing to the reduced amount of electronically-insulating LiF, the CEI formed with LiDFOB-containing electrolyte is less resistive, contributing to the highly improved rate capability and low electrode resistance after long-term cycling. The B 1s spectrum of cycled graphite cathodes with LiDFOB-containing electrolyte contains two peaks, one occurring at 191.4 eV which is attributed to  $\text{Li}_x\text{BO}_y\text{F}_z$  while another strong peak at around 193.5 eV which is characteristic of LiDFOB.<sup>[16]</sup> This suggests the compound decomposed from LiDFOB participates in generating a stable and uniform CEI film. Further, the considerably larger  $\text{Li}_x\text{BO}_y\text{F}_z$  fraction compared with the amount of LiDFOB confirms the reaction of LiDFOB in the electrolyte, which is well consistent with the result in Figure 1a. The uniform distribution of B, P, and F elements further illustrate the homogeneity of the CEI layer that is formed in situ (Figure S9, Supporting Information). These results demonstrate  $\text{Li}_x\text{BO}_y\text{F}_z$  is a critical and effective component in providing a stable interface for  $\text{PF}_6^-$  transport and enhancing cycle performance.

The evolution of graphitic structure after cycling is investigated by X-ray diffractometry (XRD), as presented in Figure 5a. The average interlayer spacing between two graphene sheets ( $d(002)$ ) is associated with the graphitic structure order and



**Figure 4.** XPS spectra of graphite cathodes with baseline and 0.5 wt% LiDFOB-containing electrolytes after 2nd and 150th cycles at the upper cutoff voltage of 5.1 V: a,b) C 1s, c,d) F 1s, e,f) B 1s.

accordingly, the degree of graphitization (DG) of the graphite can be determined by the following equation:<sup>[4c,17]</sup>

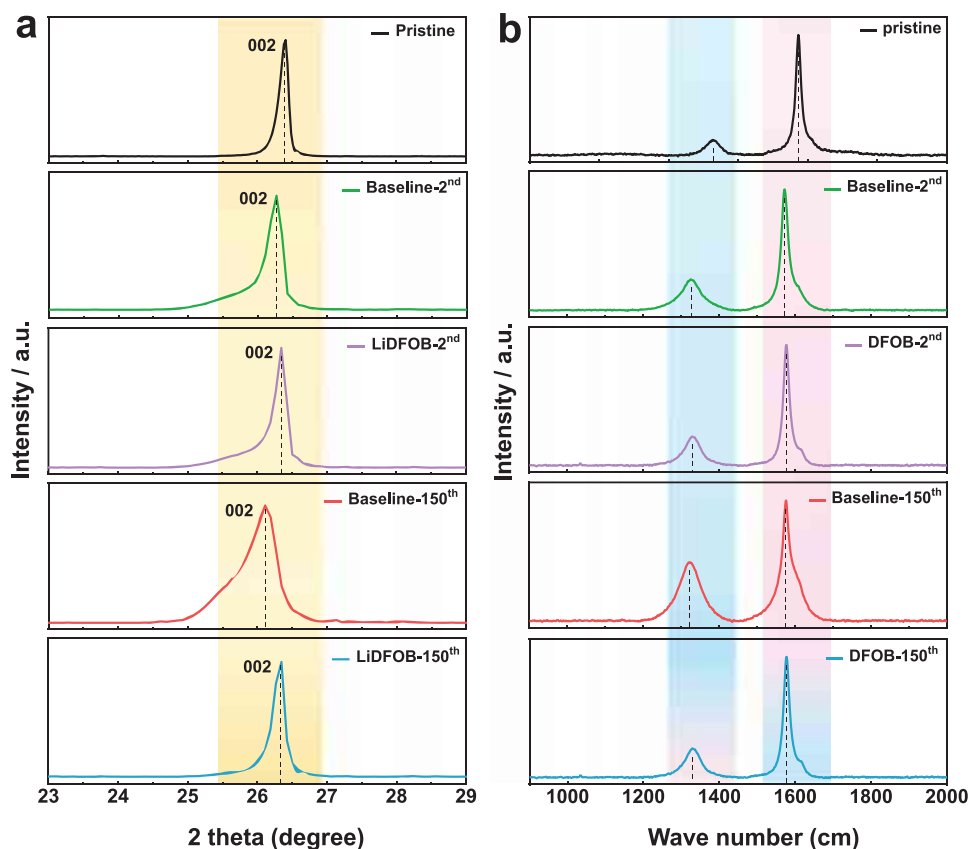
$$\text{DG}(\%) = \frac{0.3440 - d(002)}{0.3440 - 0.3354} \times 100\% \quad (4)$$

where 0.3440 and 0.3354 nm represent the  $d(002)$  values of the fully non-graphitic carbon and the perfect graphite crystallite. The graphite electrode in baseline electrolyte exhibits a significantly decreased DG from 77.9% of the fresh electrode to 55.8% and 34.9% after the 2nd and 150th cycle, respectively (Table S2, Supporting Information). Besides, a broader peak of graphite can be noticed after 150 cycles in baseline electrolyte, which implies a randomly arranged crystal phase (002) and in stark contrast to the high crystallization structure of the pristine graphite electrode with a sharp (002) peak. With LiDFOB addition, the graphite electrode displays a DG of 69.8% and 65.1% after the 2nd and 150th cycle, respectively. These results confirm the capability of LiDFOB-induced CEI on maintaining an orderly and highly-integrated graphitic structure of the graphite cathode, largely improving the cycle stability of  $\text{PF}_6^-$  de-/intercalation process.

The protection of the graphite structure by the LiDFOB-induced CEI is further confirmed by Raman spectroscopy, as shown in Figure 5b. Two sharp peaks at  $1580\text{ cm}^{-1}$  (G band) and  $1350\text{ cm}^{-1}$  (D band) are noted for the pristine graphite,

corresponding to the crystalline lattice and the disordered structure of graphite (such as defects), respectively.<sup>[4c,18]</sup> The level of defectiveness in graphite can be estimated by the intensity ratio of the D band and G band ( $I_D/I_G$ ). The  $I_D/I_G$  of the graphite electrode increases from 0.13 for the pristine material to 0.25 and 0.48 after the 2nd and 150th cycle (discharged state) with the baseline electrolyte (see Table S3, Supporting Information), respectively, indicating significant structural deterioration and decreasing graphitization degree after repeated anion de-/intercalation. The structural change of graphite after charging/discharging with LiDFOB-containing electrolyte for 150 cycles is similar to that after one cycle, revealing that the protective CEI induced by LiDFOB can suppress the detrimental structural collapse of graphite cathodes during cycling. In addition, with LiDFOB-containing electrolyte, the resistance of the graphite cathode decreases gradually during cycling and then remains nearly unchanged after 20 cycles, in contrast to the continuous growth of the cell resistance using baseline electrolyte (Figure S10, Supporting Information). These results further confirm the protective effect of the LiDFOB-induced CEI layer on maintaining an integrated graphitic structure of the graphite cathode upon repeated cycling.

To demonstrate the possibility of DIB with LiDFOB additive for practical applications, a graphite||graphite battery with 0.5 wt% LiDFOB additive was constructed as a proof of concept without the use of lithium metal—the cell consists of



**Figure 5.** a) XRD patterns and b) Raman spectra of the pristine and cycled graphite cathodes in baseline and 0.5 wt% LiDFOB-containing electrolytes.

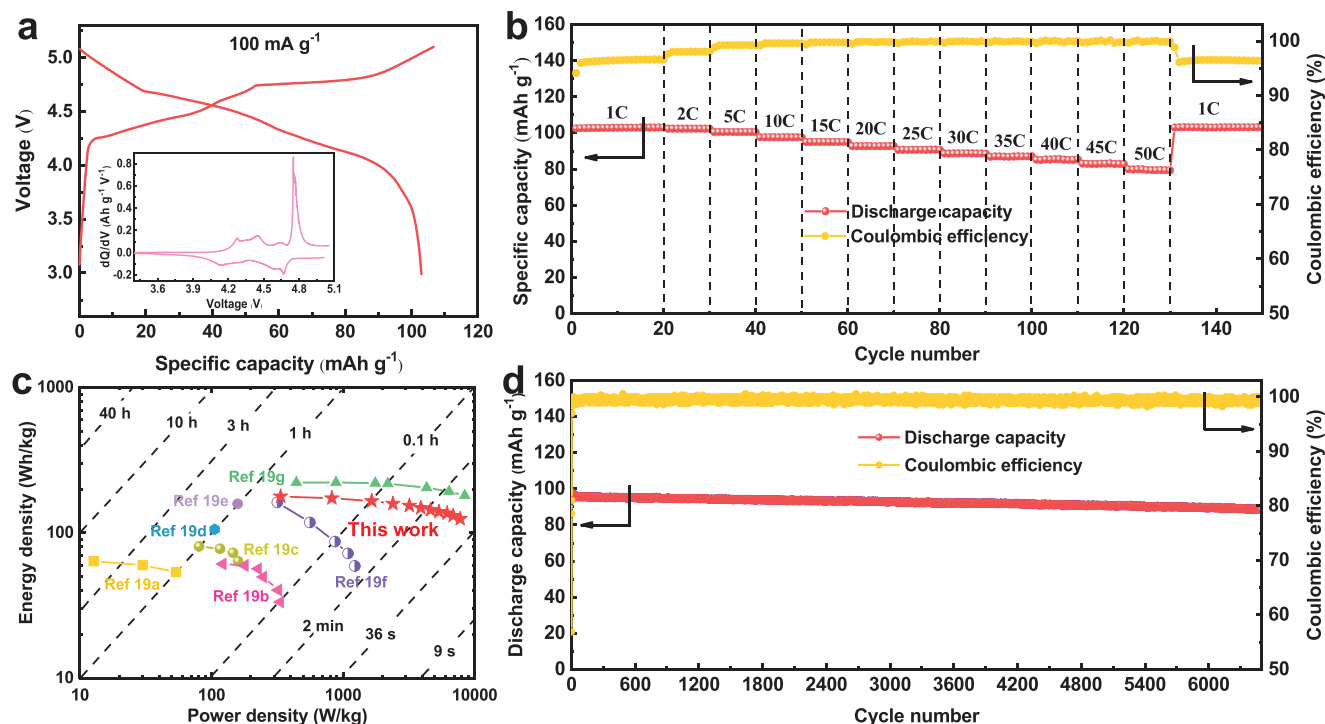
a graphite cathode and pre-lithiated graphite anode (Figure S11, Supporting Information). The graphite||graphite full cell shows similar redox peaks to graphite||Li half cell (Figure 6a and Figure 1e), delivering a discharge capacity of  $103.0 \text{ mAh g}^{-1}$  at a current density of  $100 \text{ mA g}^{-1}$  (with respect to the mass of the cathode). Excellent rate performance is achieved with reversible capacities of 100.5, 97.6, 92.8, 88.7, and  $85.4 \text{ mAh g}^{-1}$  at current rates of 5, 10, 20, 30, and 40 C, corresponding to capacity retention of 97.6%, 94.8%, 90.1%, 86.1%, and 82.9% (Figure 6b and Figure S12a, Supporting Information), respectively, which indicates a superior cell reaction kinetics. The increase in cell polarization is small with the increase in current rate. A Ragone plot of the graphite||graphite battery in our work is shown in comparison with reported dual-graphite (carbon) batteries (Figure 6c), where the energy density and power density are calculated based on the total mass of graphite in both electrodes with the pre-lithiated lithium (Table S4 and Note S2, Supporting Information, gives the details of the calculation). The cell demonstrates superior power density of  $0.17\text{--}78 \text{ kW kg}^{-1}$  while maintaining energy densities of  $179.8\text{--}124.6 \text{ Wh kg}^{-1}$ , which is among the best performance of reported dual-graphite (carbon) batteries (see Table S5, Supporting Information). Under the current rate of 10 C ( $1000 \text{ mA g}^{-1}$ ), the graphite||graphite cell with LiDFOB exhibits excellent stability, maintaining 92.4% of the discharge capacity over 6500 cycles with a high CE of 99.4% (Figure 6d). Besides, as shown in Figure S12b, Supporting Information, the corresponding charge-discharge curves are

well maintained during cycling with obvious  $\text{PF}_6^-$  de-/intercalation plateaus. A small drop in discharge voltage with cycling is probably due to some loss in active Li in the cell, which can be overcome with better optimization of the full cell. To the best of our knowledge, this long-term cycle capability is the most outstanding result thus far reported for a dual-carbon (graphite) battery (summarized in Table S5, Supporting Information).<sup>[19]</sup>

### 3. Conclusion

In this work, we have demonstrated that by designing an in situ CEI layer on the graphite cathode, the corresponding DIB can undergo long-term cycling with a high-power capability under high voltage. The thin but robust CEI formed with LiDFOB addition not only inhibits undesirable side reactions between electrolyte and cathode, but stabilizes the graphite cathode against structural deterioration or exfoliation, thus contributing to the excellent cycle performance. In addition, the reduced interfacial resistance with the LiDFOB-induced CEI facilitates fast electrode reaction kinetics and enables an ultra-fast charging capability up to 50 C (i.e., charge time of less than 2 min). When coupling the graphite cathode with a pre-lithiated graphite anode, the full battery achieves superior power density up to  $78 \text{ kW kg}^{-1}$  with energy density up to  $179.8 \text{ Wh kg}^{-1}$ , which is among the best performance reported for dual-graphite (carbon) batteries. Besides, this is the first report that





**Figure 6.** a) Charge–discharge curve of graphite||graphite cells using 0.5 wt% LiDFOB-containing electrolyte. Inset is the corresponding  $dQ/dV$  curve. b) Rate capability of graphite||graphite using 0.5 wt% LiDFOB-containing electrolyte. c) Ragone plot of the graphite||graphite DIB in comparison with reported dual-graphite (carbon) batteries.<sup>[19]</sup> d) Cycle performance and CE of graphite||graphite batteries with 0.5 wt% LiDFOB-containing electrolyte under a current rate of 10 C. Upper cutoff voltage: 5.1 V, 1 C = 100 mA g<sup>-1</sup>.

a dual-graphite battery can be cycled for more than 6500 cycles and still keeps superb cycle stability of 92.4% capacity retention with a high average CE of 99.4%. Overall, this work sheds light on the strategy of regulating CEI on graphite cathode to enhance DIB performance. However, the understanding of the CEI layer for anion transport is still at its infant stage, more research work should be conducted in the future. Besides, further works such as the adjustment of cathode–anode capacity ratio, optimization of electrolyte formulation, etc. are needed to facilitate the practical application of dual-graphite batteries with enhanced energy/power density.

## 4. Experimental Section

**Electrolytes Preparation and Cell Assembly:** The baseline electrolyte was 3 M LiPF<sub>6</sub> (DoDoChem, purity ≥ 99.9%) in EMC (Sigma Aldrich). The LiDFOB-containing electrolyte was prepared by dissolving 0.1%, 0.3%, 0.5%, and 1.0% (wt%) LiDFOB (Sigma Aldrich) to the baseline electrolyte.

The electrode slurry for the cathode in the dual-ion cells was composed of 85 wt% graphite (MTI SAG-R) as the active material, 10 wt% conducting agent (carbon black AB – acetylene black, Alfa Aesar), and 5 wt% binder (polyacrylic acid (PAA, Sigma Aldrich MW 450 000) dissolved in *N*-methyl-2-pyrrolidone). The anode slurry was prepared by mixing graphite (RGS, from Dongguan Shanshan Battery Materials Co., Ltd), acetylene black and PAA binder in a ratio of 85:5:10. The slurry was coated onto an aluminum foil and copper foil, respectively, with a doctor blade and dried at 80 °C. The dried electrode was punched into circular discs (16 mm in diameter) and then pressed with a roll press. The average mass loading of active material

on each cathode and anode was  $2 \pm 0.2$  mg cm<sup>-2</sup> and  $3 \pm 0.2$  mg cm<sup>-2</sup>, respectively. The weight of the electrodes was measured using a balance by AND (GR-202, 0.01 mg precision). Electrodes were further dried at 150 °C overnight under vacuum prior to cell assembly. CR2032-type coin cells with the cathode and lithium metal (purchased from China Energy Lithium Co., Ltd., diameter × thickness:  $\phi 16 \times 0.6$  mm) were fabricated in an Ar-filled glove box with both O<sub>2</sub> and H<sub>2</sub>O content being less than 0.1 ppm. A PVdF membrane (Merck Millipore Ltd., pore size: 0.2  $\mu$ m) wetted with approximately 120  $\mu$ L electrolyte was used as the separator for graphite||Li and graphite||graphite cells. For the dual graphite battery, it was constructed with a cell balancing of 1:1.5 (graphite in cathode: graphite in anode) by weight as a proof of concept. Before the full cell assembly, the graphite anode was pre-lithiated with lithium metal as the counter electrode to form an SEI layer by discharging/charging at a current rate of 0.05 C (1 C = 372 mAh g<sup>-1</sup>) for 2 cycles, then discharging at 0.1 C to 200 mAh g<sup>-1</sup>. The pre-lithiation process reduces the initial irreversible capacity and improves the stability of the dual graphite battery. The reported capacity for the full cell was with respect to the weight of the cathode.

**Electrochemical Tests:** Galvanostatic charge–discharge tests were conducted using a Neware battery tester at room temperature (22 °C). The cells were pre-cycled at a current density of 20 mA g<sup>-1</sup> for three formation cycles. Then cells were typically cycled with a constant current of 500 mA g<sup>-1</sup> (5 C) for graphite||Li cells and 1 A g<sup>-1</sup> (10 C) as for dual-graphite batteries, in a voltage range of 3.0–5.1 V (versus Li/Li<sup>+</sup>). Rate performance tests were carried out within the current rates of 1 to 50 C. CV measurements were performed with a Bio-Logic potentiostat (VMP3) at various scan rates from 0.1 to 1.0 mV s<sup>-1</sup>. Impedance measurements were performed also using the Bio-Logic potentiostat (VMP3) by applying a 10 mV AC potential amplitude within the frequency range from 100 kHz to 5 mHz.

**Sample Characterizations:** In order to investigate the surface chemistry and morphological changes of the graphite cathodes, the cycled cells were disassembled in the glove box. The graphite electrodes were rinsed with

dimethyl carbonate solvent several times to remove the salt residuals, followed by drying in the antechamber of the glove box under vacuum. The morphological evolutions of the cathode material were studied using a field-emission SEM (FE-SEM, Zeiss SUPRA-55 microscope) and a TEM (JEOL 2100F). XRD (X'Pert3 Powder X-ray Diffractometer, PANalytical) and Raman spectroscopy (Renishaw Invia Raman) were performed to investigate the crystal structure of the cycled electrodes. XPS (ESCALAB 250X from Thermo Fisher) measurements were conducted to examine the chemical compositions of graphite surface.

## Supporting Information

Supporting Information is available from the Wiley Online Library or from the author.

## Acknowledgements

This work was supported by the Strategic Research Grant (Project #7005285) from City University of Hong Kong.

## Conflict of Interest

The authors declare no conflict of interest.

## Data Availability Statement

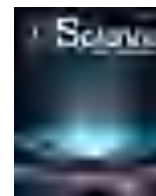
Data available on request from the authors.

## Keywords

cathode–electrolyte interface, dual-ion battery, graphite cathode, LiDFOB, PF<sub>6</sub><sup>−</sup> intercalation

Received: April 5, 2021  
Published online: May 3, 2021

- [1] a) X. Jiang, L. Luo, F. Zhong, X. Feng, W. Chen, X. Ai, H. Yang, Y. Cao, *ChemElectroChem* **2019**, 6, 2615; b) G. Wang, M. Yu, J. Wang, D. Li, D. Tan, M. Löffler, X. Zhuang, K. Müllen, X. Feng, *Adv. Mater.* **2018**, 30, 1800533; c) K. V. Kravchyk, P. Bhauriyal, L. Piveteau, C. P. Guntlin, B. Pathak, M. V. Kovalenko, *Nat. Commun.* **2018**, 9, 4469; d) Y. Shuai, X. He, Z. Zhang, K. Chen, J. Lou, Y. Wang, N. Li, *Energy Technol.* **2019**, 7, 1800729; e) H. Ding, J. Zhou, A. M. Rao, B. Lu, *Natl. Sci. Rev.* **2020**, 0, nwaa 276; f) T. Wang, D. Shen, H. Liu, H. Chen, Q. Liu, B. Lu, *ACS Appl. Mater. Interfaces* **2020**, 12, 57907; g) Q. Zhang, X. Cheng, C. Wang, A. M. Rao, B. Lu, *Energy Environ. Sci.* **2021**, 14, 965; h) J. Hao, K. Xiong, J. Zhou, A. M. Rao, X. Wang, H. Liu, B. Lu, *Energy Environ. Mater.* **2020**, 0, 1.
- [2] a) T. Placke, A. Heckmann, R. Schmich, P. Meister, K. Beltrop, M. Winter, *Joule* **2018**, 2, 2528; b) I. A. Rodríguez-Pérez, X. Ji, *ACS Energy Lett.* **2017**, 2, 1762; c) Y. Wang, S. Wang, Y. Zhang, P. K. Lee, D. Y. W. Yu, *ACS Appl. Energy Mater.* **2019**, 2, 7512; d) B. Heidrich, A. Heckmann, K. Beltrop, M. Winter, T. Placke, *Energy Storage Mater.* **2019**, 21, 414; e) C. Jiang, L. Xiang, S. Miao, L. Shi, D. Xie, J. Yan, Z. Zheng, X. Zhang, Y. Tang, *Adv. Mater.* **2020**, 32, 1908470.
- [3] a) Y. Sui, C. Liu, R. C. Masse, Z. G. Neale, M. Atif, M. AlSalhi, G. Cao, *Energy Storage Mater.* **2020**, 25, 1; b) X. Han, G. Xu, Z. Zhang, X. Du, P. Han, X. Zhou, G. Cui, L. Chen, *Adv. Energy Mater.* **2019**, 9, 1804022; c) J. A. Read, *J. Phys. Chem. C* **2015**, 119, 8438; d) J. Gao, M. Yoshio, L. Qi, H. Wang, *J. Power Sources* **2015**, 278, 452.
- [4] a) X. Jiang, X. Liu, Z. Zeng, L. Xiao, X. Ai, H. Yang, Y. Cao, *Adv. Energy Mater.* **2018**, 8, 1802176; b) Y. Wang, Y. Zhang, Q. Duan, P.-K. Lee, S. Wang, D. Y. W. Yu, *J. Power Sources* **2020**, 471, 228466; c) T. Liu, X. Han, Z. Zhang, Z. Chen, P. Wang, P. Han, N. Ding, G. Cui, *J. Power Sources* **2019**, 437, 226942.
- [5] a) W.-H. Li, H.-J. Liang, X.-K. Hou, Z.-Y. Gu, X.-X. Zhao, J.-Z. Guo, X. Yang, X.-L. Wu, *J. Energy Chem.* **2020**, 50, 416; b) X. Han, G. Xu, Z. Zhang, X. Du, P. Han, X. Zhou, G. Cui, L. Chen, *Adv. Energy Mater.* **2019**, 9, 1804022.
- [6] a) Q. Liu, A. M. Rao, X. Han, B. Lu, *Adv. Sci.* **2021**, 2003639; b) T. Yim, Y. K. Han, *ACS Appl. Mater. Interfaces* **2017**, 9, 32851; c) M. Nie, J. Demeaux, B. T. Young, D. R. Heskett, Y. Chen, A. Bose, J. C. Woicik, B. L. Lucht, *J. Electrochem. Soc.* **2015**, 162, A7008; d) V. A. Agubra, J. W. Fergus, *J. Power Sources* **2014**, 268, 153; e) H. Ota, Y. Sakata, A. Inoue, S. Yamaguchi, *J. Electrochem. Soc.* **2004**, 151, A1659; f) H. Lee, S. Choi, S. Choi, H.-J. Kim, Y. Choi, S. Yoon, J.-J. Cho, *Electrochem. Commun.* **2007**, 9, 801; g) M. Xu, W. Li, X. Zuo, J. Liu, X. Xu, *J. Power Sources* **2007**, 174, 705.
- [7] Q. Dong, F. Guo, Z. Cheng, Y. Mao, R. Huang, F. Li, H. Dong, Q. Zhang, W. Li, H. Chen, Z. Luo, Y. Shen, X. Wu, L. Chen, *ACS Appl. Energy Mater.* **2019**, 3, 695.
- [8] L. Zhang, Y. Ma, X. Cheng, P. Zuo, Y. Cui, T. Guan, C. Du, Y. Gao, G. Yin, *Solid State Ionics* **2014**, 263, 146.
- [9] J. Zheng, M. H. Engelhard, D. Mei, S. Jiao, B. J. Polzin, J.-G. Zhang, W. Xu, *Nat. Energy* **2017**, 2, 1.
- [10] a) Q. Guo, Y. Ma, T. Chen, Q. Xia, M. Yang, H. Xia, Y. Yu, *ACS Nano* **2017**, 11, 12658; b) J. Besenhard, M. Winter, J. Yang, W. Biberacher, *J. Power Sources* **1995**, 54, 228.
- [11] J. Wang, J. Polleux, J. Lim, B. Dunn, *J. Phys. Chem. C* **2007**, 111, 14925.
- [12] W. H. Li, Q. L. Ning, X. T. Xi, B. H. Hou, J. Z. Guo, Y. Yang, B. Chen, X. L. Wu, *Adv. Mater.* **2019**, 31, 1804766.
- [13] a) L. Liao, P. Zuo, Y. Ma, X. Chen, Y. An, Y. Gao, G. Yin, *Electrochim. Acta* **2012**, 60, 269; b) J. Xu, S. L. Chou, Q. F. Gu, H. K. Liu, S. X. Dou, *J. Power Sources* **2013**, 225, 172; c) P. Suresh, A. Shukla, N. Munichandraiah, *J. Appl. Electrochem.* **2002**, 32, 267.
- [14] a) M. Phaner-Goutorbe, A. Sartre, L. Porte, *Microsc., Microanal., Microstruct.* **1994**, 5, 283; b) L. Shen, L. Zhang, K. Wang, L. Miao, Q. Lan, K. Jiang, H. Lu, M. Li, Y. Li, B. Shen, *RSC Adv.* **2018**, 8, 17209.
- [15] a) J. Cha, J.-G. Han, J. Hwang, J. Cho, N.-S. Choi, *J. Power Sources* **2017**, 357, 97; b) N.-S. Choi, J.-G. Han, S.-Y. Ha, I. Park, C.-K. Back, *RSC Adv.* **2015**, 5, 2732; c) Y.-M. Song, C.-K. Kim, K.-E. Kim, S. Y. Hong, N.-S. Choi, *J. Power Sources* **2016**, 302, 22.
- [16] J. Y. Liang, X. D. Zhang, X. X. Zeng, M. Yan, Y. X. Yin, S. Xin, W. P. Wang, X. W. Wu, J. L. Shi, L. J. Wan, *Angew. Chem., Int. Ed.* **2020**, 132, 6647.
- [17] a) J. O. Besenhard, H. P. Fritz, *Angew. Chem., Int. Ed.* **1983**, 22, 950; b) A. Heckmann, O. Fromm, U. Rodehorst, P. Münster, M. Winter, T. Placke, *Carbon* **2018**, 131, 201.
- [18] a) K. V. Kravchyk, M. V. Kovalenko, *Adv. Energy Mater.* **2019**, 9, 1901749; b) A. C. Ferrari, *Solid State Commun.* **2007**, 143, 47; c) V. A. Sethuraman, L. J. Hardwick, V. Srinivasan, R. Kostecki, *J. Power Sources* **2010**, 195, 3655.
- [19] a) S. Wang, S. Jiao, W.-L. Song, H.-S. Chen, J. Tu, D. Tian, H. Jiao, C. Fu, D.-N. Fang, *Energy Storage Mater.* **2018**, 12, 119; b) Z. Li, J. Liu, B. Niu, J. Li, F. Kang, *Small* **2018**, 14, 1800745; c) L. Fan, Q. Liu, S. Chen, K. Lin, Z. Xu, B. Lu, *Small* **2017**, 13, 1701011; d) K. Beltrop, S. Beuker, A. Heckmann, M. Winter, T. Placke, *Energy Environ. Sci.* **2017**, 10, 2090; e) J. Zhu, Y. Li, B. Yang, L. Liu, J. Li, X. Yan, D. He, *Small* **2018**, 14, 1801836; f) L. Fan, Q. Liu, S. Chen, Z. Xu, B. Lu, *Adv. Energy Mater.* **2017**, 7, 1602778; g) G. Wang, F. Wang, P. Zhang, J. Zhang, T. Zhang, K. Müllen, X. Feng, *Adv. Mater.* **2018**, 30, 1802949.



## Review

## Electrolyte design for rechargeable anion shuttle batteries

Yao Wang<sup>a</sup>, Xu Yang<sup>b</sup>, Zhijia Zhang<sup>b</sup>, Xia Hu<sup>a</sup>, Yuefeng Meng<sup>a</sup>, Xia Wang<sup>c</sup>, Dong Zhou<sup>a,\*</sup>, Hao Liu<sup>b</sup>, Baohua Li<sup>a,\*</sup>, Guoxiu Wang<sup>b,\*</sup>

<sup>a</sup> Tsinghua Shenzhen International Graduate School, Tsinghua University, Shenzhen 518055, China

<sup>b</sup> Centre for Clean Energy Technology, School of Mathematical and Physical Sciences, Faculty of Science, University of Technology Sydney, Sydney, NSW 2007, Australia

<sup>c</sup> Max-Planck-Institute for Chemical Physics of Solids, Topological Catalysis Group, Nöthnitzer Straße 40, 01187 Dresden, Germany



## HIGHLIGHTS

- The working mechanisms, achievements, and challenges in developing anion shuttle battery (ASBs) electrolytes are reviewed.
- The unique properties and basic principles for designing ASB electrolytes are described and illustrated.
- Future perspectives on strategies to design electrolytes for ASBs are presented to facilitate grid-scale applications.

## GRAPHICAL ABSTRACT



## ARTICLE INFO

## Keywords:

Anion shuttle batteries  
Electrolytes  
Electrochemical stability  
Interfacial compatibility  
Grid-scale energy storage

## ABSTRACT

As an emerging new type of battery chemistry, the anion shuttle battery (ASB), based on the shuttling and storage of anions, is considered a sustainable alternative to gigawatt-scale energy storage due to the associated resource abundance, low cost, high safety, and high energy density. Although significant progress has been achieved, practical applications of ASBs are still hindered by tough challenges, such as short lifetime, limited reversible capacity, and low Coulombic efficiency. Therefore, it is very necessary to design and explore new electrolyte systems with high electrochemical/chemical stability, sufficient compatibility towards electrodes, and excellent kinetics/reversibility for anion electrochemical reactions. Here, we review the recent achievements and main challenges in developing electrolytes for ASBs, which include solid, non-aqueous, and aqueous electrolytes. We mainly focus on the unique properties and basic principles of designing these electrolytes, and their various performance parameters. Perspectives on design strategies for ASB electrolytes are also presented, which could facilitate the development of advanced ASBs for grid-scale energy storage.

## 1. Introduction

The current worldwide energy economy still relies heavily on fossil fuels, which causes severe air pollution and global warming. Motivated by the ever-increasing demands for renewable energy and its extensive applications, from portable electronics to grid storage, it is of vital

significance to develop highly efficient energy storage and conversion technologies, such as rechargeable batteries [1,2]. Owing to their high energy density and long lifespan, lithium-ion batteries (LIBs) have come to dominate the battery markets, from portable electronics to electric vehicles [3,4]. However, the high cost and limited reserves of lithium and transition metals (e.g., Co, Ni) strongly hinder their applications for stationary energy

\* Corresponding authors.

E-mail addresses: [zhou.d@sz.tsinghua.edu.cn](mailto:zhou.d@sz.tsinghua.edu.cn) (D. Zhou), [libh@sz.tsinghua.edu.cn](mailto:libh@sz.tsinghua.edu.cn) (B. Li), [Guoxiu.Wang@uts.edu.au](mailto:Guoxiu.Wang@uts.edu.au) (G. Wang).

<https://doi.org/10.1016/j.esci.2022.10.003>

Received 25 July 2022; Received in revised form 6 October 2022; Accepted 17 October 2022

Available online 21 October 2022

2667-1417/© 2022 The Authors. Published by Elsevier B.V. on behalf of Nankai University. This is an open access article under the CC BY-NC-ND license (<http://creativecommons.org/licenses/by-nc-nd/4.0/>).



storage [5]. Alternative rechargeable metal-ion batteries based on other univalent or multivalent cations as charge carriers (e.g.,  $\text{Na}^+$ ,  $\text{Ca}^{2+}$ ,  $\text{Mg}^{2+}$ ,  $\text{Zn}^{2+}$ ,  $\text{Al}^{3+}$ ) have been developed [6,7]. However, their large ionic radii mean they suffer from limited energy density and/or significant challenges when it comes to ion transport and reversible cycling, which makes them less competitive for widespread applications.

Recently, a new type of battery chemistry based on the shuttling and storage of anions (e.g.,  $\text{Cl}^-$ ,  $\text{F}^-$ ,  $\text{NO}_3^-$ ,  $\text{PF}_6^-$ ,  $\text{TFSI}^-$ ,  $\text{FSI}^-$ ) has attracted increasing attention due to low cost, resource abundance, safety, and high energy/power density. In contrast to cation rocking-chair batteries (CRBs, e.g., LIB), where the cations are transported between cathode and anode upon charging/discharging, anion shuttle batteries (ASBs) utilize anions as the principal charge carriers for electrochemical reactions [8,9].

ASBs can be divided into three configurations: (i) anion rocking-chair batteries (ARBs), e.g., chloride-ion batteries (CIBs) and fluoride-ion batteries (FIBs), which rely on the shuttling of anions between the two electrodes for charge storage; specifically, anions are released from the cathode and transfer to the anode upon discharging, while the process occurs in reverse during the charge process [8–10]; (ii) dual-ion batteries (DIBs), which exhibit a different operating mechanism involving the simultaneous incorporation of anions and cations into the cathode and the anode, respectively, during charging, and the simultaneous release of the charge carriers into the electrolyte during discharging (Fig. 1c) [11,12]; (iii) analogous to DIBs, reverse dual-ion batteries (RDIBs) utilize both cations and anions for the energy storage process, with anions being incorporated into the anode and cations

into the cathode upon discharging, while in the subsequent charge process, both ions return to the electrolyte simultaneously [13].

Generally, the unique features of anions as charge carriers give ASBs key advantages, such as high energy density (theoretical energy density of  $2500 \text{ Wh L}^{-1}$  for CIBs and  $5000 \text{ Wh L}^{-1}$  for FIBs, respectively) and/or high power capability (with DIBs) [14–16]. In addition, ASBs utilize earth-abundant anions in place of  $\text{Li}^+$  as the principal charge carrier, and their inexpensive electrode materials are effective for reducing manufacturing cost [10]. These merits facilitate the development of ASBs, which offer great potential for low-cost grid-scale energy storage. Thus far, however, our understanding of the relationship between anionic charge carriers and their electrochemical performance remains limited.

It is essential that ASB electrolytes comply with the same key requirements as LIBs: (i) high ionic conductivity to enable fast anion transport, and negligible electronic conductivity to suppress battery self-discharge; (ii) excellent chemical stability and inertness towards the cathode and anode materials, as well as the separator, current collector, and other cell packing components to mitigate side reactions; (iii) a wide electrochemical stability window (ESW), i.e., a large energy gap between the lowest unoccupied molecular orbital (LUMO) and the highest occupied molecular orbital (HOMO), to achieve high energy density and to prevent electrolyte side reactions within the cell operating voltage; (iv) low interfacial resistance to ensure good contact, and a low energy barrier for ionic conduction between the electrode and the electrolyte. These electrolyte properties play a decisive role in the kinetics/reversibility of

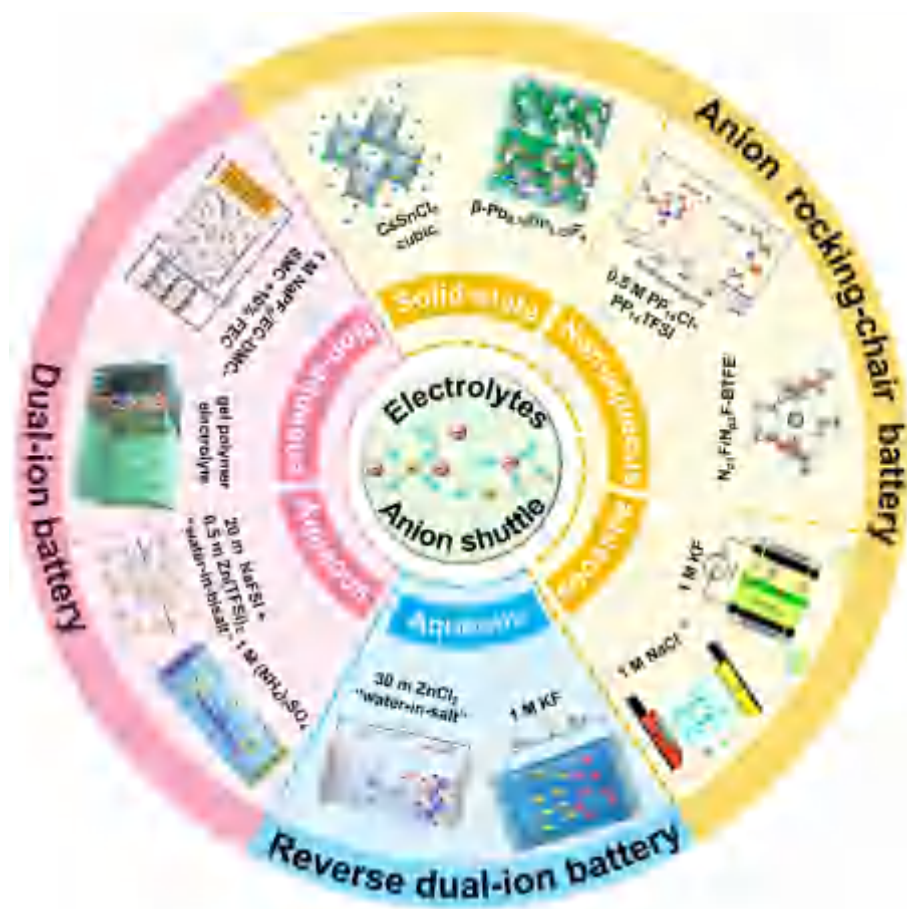


Fig. 1. Overview of electrolyte progress for anion rocking-chair batteries, dual-ion batteries, and reverse dual-ion batteries, including aqueous, non-aqueous, and solid-state electrolytes. Reproduced with permission [13,17]. Copyright 2019, American Chemical Society. Reproduced with permission [18,19]. Copyright 2021, Wiley-VCH. Reproduced with permission [20]. Copyright 2017, American Chemical Society. Reproduced with permission [21]. Copyright 2020, American Chemical Society. Reproduced with permission [22,23]. Copyright 2021, American Chemical Society. Reproduced with permission [24]. Copyright 2020, Elsevier. Reproduced with permission [25]. Copyright 2019, Royal Society of Chemistry. Reproduced with permission [26]. Copyright 2018, American Association for the Advancement of Science. Reproduced with permission [27]. Copyright 2019, The Electrochemical Society.

electrochemical reactions and the lifespan of ASBs. However, compared with the extensive studies on electrode materials (cathode and anode), research work and reviews on electrolyte development for ASBs are lacking [8–10,12,28–31].

Notably, the migrated anions in ARBs are initially stored in the cathode materials, and the electrolyte only serves as the charge carrier to transport anions, hence the ion concentration remains unchanged during the charge/discharge process. In contrast, for DIBs and RDIBs, since both the cations and the anions for charge transfer are supplied by the electrolyte, the ions in the electrolyte should be considered the active material. Consequently, in DIBs and/or RDIBs, the concentrations of both cations and anions, and the corresponding physical qualities of the electrolyte, such as ionic conductivity and viscosity, are highly dependent on the state of charge (SOC). Remarkably, the reversible capacity, energy/power density, and cell voltage of DIBs and/or RDIBs depend largely on the electrolyte formulation (e.g., the type of solvent, the salt type and content, the additive amount) [32].

In this review, we focus on discussing the recent achievements and main challenges in developing electrolytes — including solid, non-aqueous, and aqueous (Fig. 1) — for ARBs, DIBs, and RDIBs. The unique properties of each type of electrolyte (ESW, ionic transport, electrode/electrolyte compatibility, etc.) are summarized, and perspectives on future design strategies for ASB electrolytes are proposed.

## 2. Electrolytes for ARBs

ARBs function based on anion shuttling across cathodes and anodes for electrochemical reactions during charging/discharging, two representative examples being CIBs and FIBs. In general, these batteries utilize a metal as the anode and a metal halide or metal halide-containing material as the cathode. As mentioned in the introduction, the rich abundance of halide materials makes far less expensive redox pairs in ARBs than in LIBs. More interestingly, the wide range of possible redox pairs and/or multiple-electron transfer reactions can potentially yield extremely high energy densities for ARBs. However, several major obstacles remain, one crucial factor being the need for a suitable electrolyte design that achieves high ionic conductivity, superb interfacial stability, as well as stable/reversible charge storage reactions. This will be comprehensively discussed in the following section.

### 2.1. Chloride-ion batteries (CIBs)

The first proof-of-concept CIB based on  $\text{Cl}^-$  shuttling through a  $\text{Cl}^-$ -containing electrolyte was proposed by Fichtner et al., in 2014, and since then, the CIB has attracted intensive attention owing to its high theoretical volumetric energy density, low cost, dendrite-free operation, and other features [33–35]. In particular, the massive abundance of  $\text{Cl}^-$ -containing materials allows a wide array of potential redox pairs, giving CIBs a theoretical energy density comparable to that of lithium–sulfur batteries ( $\sim 2800 \text{ Wh L}^{-1}$ ) [35]. As the charge carrier across the cathode and anode, the electrolyte plays a critical role in CIB performance, such as cyclability. Two of the biggest challenges for developing CIB electrolytes lie in providing fast  $\text{Cl}^-$  anion conduction and superior electrode compatibility at room temperature (RT). The key progress and main challenges for state-of-the-art CIB electrolytes will be discussed in detail below.

#### 2.1.1. Solid electrolytes

Solid electrolytes have been demonstrated to be effective in solving issues associated with electrode dissolution and/or undesirable side reactions between electrode materials and liquid electrolytes, and they are garnering increasing interest in the field of LIB systems. Nevertheless, only a few studies have been reported on chloride-ion-conducting solid electrolytes for CIBs [21,36,37]. Zhao et al. developed the first all-solid-state rechargeable CIB by employing a ternary solid electrolyte, which consisted of a poly(ethylene oxide) (PEO) matrix, a quaternary ammonium

chloride salt (TBMACl), and a succinonitrile (SN) solid plasticizer. The  $\text{PEO}_1\text{-TBMACl}_1\text{-SN}_3$  solid electrolyte exhibited a high anti-oxidation stability of more than 4.2 V vs.  $\text{Li/Li}^+$  and a conductivity of  $10^{-5}\text{--}10^{-4} \text{ S cm}^{-1}$  within the temperature range of 198–343 K. Consequently, a  $\text{FeOCl}$  (cathode)|| $\text{Li}$  (anode) battery using this electrolyte displayed reversible redox reactions during charging/discharging (Figs. 2a–c) [36].

Inorganic compounds such as  $\text{BaCl}_2$ ,  $\text{SrCl}_2$ , and  $\text{LaOCl}$  can also be utilized as chloride-ion conductors. However, the ionic conductivity ( $\sim 10^{-6} \text{ S cm}^{-1}$ ) of these polycrystalline materials can only be achieved at an operating temperature above 500 K [38,39]. Some metal chlorides, such as  $\text{SnCl}_2$ - and  $\text{PbCl}_2$ -based materials, have exhibited enhanced ionic conductivities ( $\sim 10^{-6} \text{ S cm}^{-1}$ ) at RT, but they suffered from reduced electrochemical reduction stability [40,41]. Zhao et al. reported a room-temperature-stable inorganic halide perovskite of  $\text{CsSnCl}_3$  prepared by mechanical milling and subsequent mild heat treatment, which demonstrated highly enhanced structural stability against phase transformation of the cubic structure (Fig. 2d), thus enabling a high ionic conductivity of  $3.6 \times 10^{-4} \text{ S cm}^{-1}$  at RT together with a wide electrochemical window of  $\sim 6.1 \text{ V}$  (Fig. 2e) [21]. Although remarkable progress has been made, extensive efforts are still needed to enhance the  $\text{Cl}^-$  ion conductivity and/or interfacial properties of solid electrolytes, such as by structurally engineering inorganic chloride ion conductors (e.g., doping), to achieve solid CIBs that operate at room temperature.

#### 2.1.2. Non-aqueous liquid electrolytes

Compared with solid electrolytes, the high ionic conductivities of non-aqueous liquid electrolytes enable the operation of rechargeable CIBs at RT. Since their first development in 2014, the majority of rechargeable CIBs have been explored based on non-aqueous electrolytes (Table 1) comprising mixtures of ionic liquids (IL) and/or carbonates as solvents.

A binary IL electrolyte was designed by mixing 1-methyl-3-octylimidazolium chloride ([OMIM][Cl]), possessing low melting point but high viscosity, with 1-butyl-3-methylimidazolium tetrafluoroborate ([BMIM][BF<sub>4</sub>]) in a 1:3 volume ratio, which accelerated the movement of  $\text{Cl}^-$  ions. Owing to the combined merits of the two ILs, reversible  $\text{Cl}^-$  transfer was achieved at RT, contributing to a high discharge capacity of  $142.9 \text{ mAh g}^{-1}$  for a  $\text{BiCl}_3$ || $\text{Li}$  cell based on the mass of  $\text{BiCl}_3$  [33]. To further improve the  $\text{Cl}^-$  ionic conductivity/mobility, carbonates have been introduced into IL electrolytes as co-solvents. By dissolving 0.5 M 1-butyl-1-methylpiperidinium chloride (PP<sub>14</sub>Cl) in propylene carbonate (PC) solvent, Fichtner and co-workers reported a novel electrolyte that demonstrated both a high ionic conductivity of  $4.4 \text{ mS cm}^{-1}$  and a wide electrochemical window of 3.2 V versus  $\text{Li/Li}^+$ . Coupling this electrolyte with a  $\text{VOCl}$  cathode and a  $\text{Li}$  anode, an initial discharge capacity of  $189 \text{ mAh g}^{-1}$  at 2 C based on the active material of the cathode was achieved for the CIB, which retained a high discharge capacity ( $113 \text{ mAh g}^{-1}$ ) even after 100 cycles (Figs. 3a and b) [43]. Han et al. developed a highly reversible CIB comprising  $\text{Ni}_2\text{V}_{0.9}\text{Al}_{0.1}\text{-Cl}$  layered double hydroxides (LDH) as the cathode and  $\text{Li}$  as the anode, and employing 1 M 1-butyl-1-methylpyrrolidinium chloride (BpyCl) in PC and 1-butyl-1-methylpiperidinium bis(trifluoromethylsulfonyl) imide (PP<sub>14</sub>TFSI) as the electrolyte. Electrode dissolution was mitigated, contributing to a high capacity of  $312.2 \text{ mAh g}^{-1}$  and an ultralong lifetime of 1000 cycles, with a stable capacity of  $113.8 \text{ mAh g}^{-1}$  based on the mass of the cathode material [45].

Although these IL-based electrolytes have been regarded as a possible choice for CIB applications due to the high  $\text{Cl}^-$  ionic conductivity and wide ESW, they generally suffer from serious interfacial side reactions (e.g., electrode dissolution into the electrolytes) and carry high risks of leakage, volatility, and flammability. To resolve these issues, gel polymer electrolytes were developed as potential candidates for rechargeable CIBs. Gschwind et al. reported three types of  $\text{Cl}^-$ -conducting polymer electrolytes that combined the polymer with chloride salts containing large cations — tetraethyl ammonium chloride with gelatin, tetrabutyl ammonium chloride (TBACl) with polyvinylidene fluoride-hexafluoropolymer (PVDF-HF),

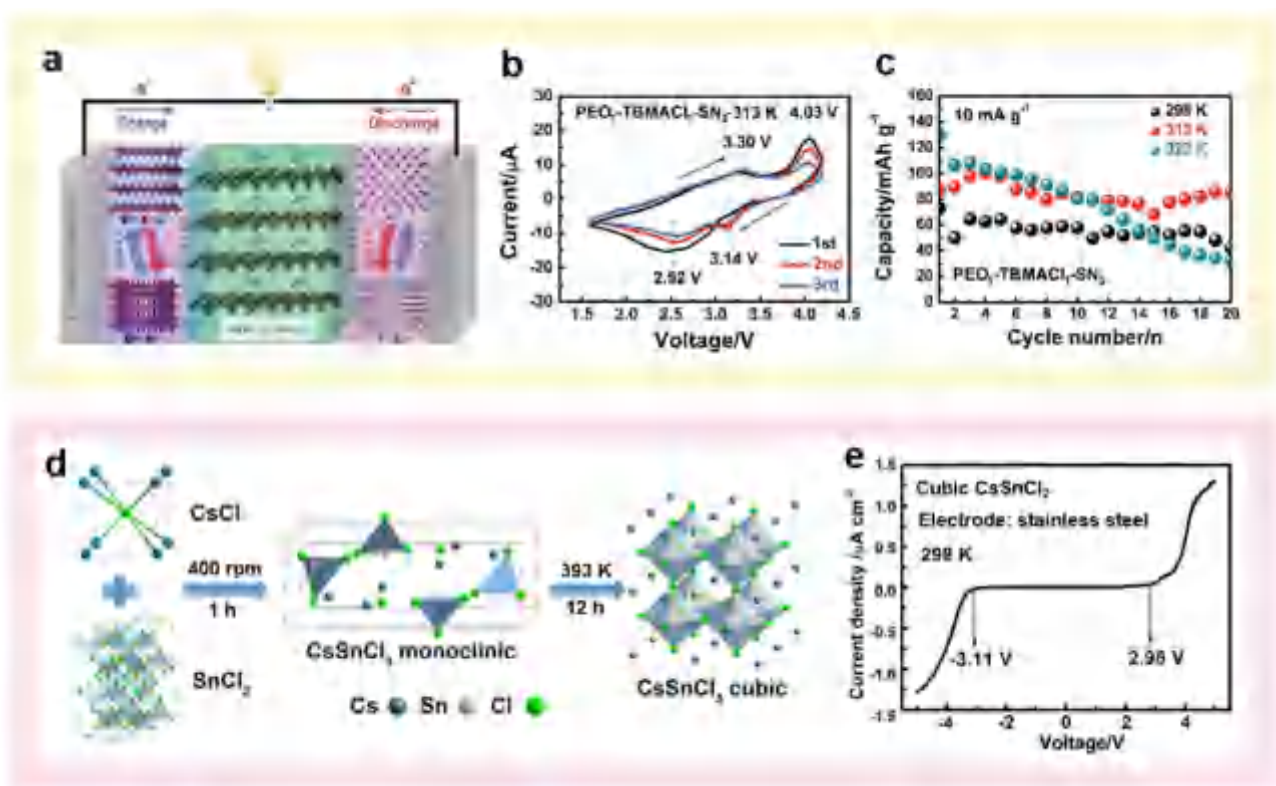


Fig. 2. Solid electrolytes for CIBs. (a) Schematic diagram, (b) cyclic voltammetry (CVs,  $50 \mu\text{V s}^{-1}$ ), and (c) cycle performance ( $10 \text{ mA g}^{-1}$ ) of a  $\text{FeOCl}|\text{PEO}_1\text{-TBMACl-SN}_3|\text{Li}$  cell. Reproduced with permission [36]. Copyright 2019 Wiley-VCH. (d) Schematic of the preparation of  $\text{CsSnCl}_3$  perovskite solid-state electrolyte. (e) Linear sweep voltammetry (LSV) of the cubic  $\text{CsSnCl}_3$  electrolyte at 298 K with a scan rate of  $5 \text{ mV s}^{-1}$ , demonstrating an electrochemical stability window of  $\sim 6.1 \text{ V}$ . Reproduced with permission [21]. Copyright 2020, American Chemical Society.

and octyltrimethyl ammonium chloride (TOACl) with polyvinylchloride (PVC), respectively [49]. The PVC-based electrolyte displayed the lowest ionic conductivity of  $10^{-7} \text{ S cm}^{-1}$ , whereas the other two electrolytes showed higher conductivity ( $10^{-4} \text{ S cm}^{-1}$ ). However, the  $\text{Cl}^-$  conductivities of these polymer electrolytes were lower compared to IL-based electrolytes, and electrochemical processes only occurred at the electrode/electrolyte interface. In addition, although these electrolytes were combined with a Zn anode and a  $\text{CuCl}_2$ ,  $\text{BiCl}_3$ , or polyaniline (PANI) cathode, respectively, as prototype batteries, only discharge performance was reported, while their reversibility was doubtful. Further studies of the stability/reversibility of the electrochemical reactions upon charging/discharging with improved battery setups are therefore urgently required.

Immobilization of Cl-containing ILs within polymer matrices can be another effective approach, forming IL-based polymer electrolytes that have high ionic conductivity as well as enhanced thermal and electrochemical stability. Such IL-based polymer electrolytes exhibit rather better electrode compatibility compared with solid electrolytes. Recently, a  $\text{Cl}^-$ -conducting IL-based polymer electrolyte based on cross-linked poly(methyl methacrylate) (PMMA)-0.5 M  $\text{PP}_{14}\text{Cl-PP}_{14}\text{TFSI}$  was demonstrated, where the IL acted as both plasticizer and  $\text{Cl}^-$  supplier. When containing 80 wt% ILs, the IL-based polymer electrolyte exhibited a high ionic conductivity of  $0.90 \times 10^{-4} \text{ S cm}^{-1}$  and a high anodic stability limit of 5.0 V (using stainless steel as the counter electrode) at RT. An as-assembled  $\text{FeOCl}|\text{PMMA-0.5 M PP}_{14}\text{Cl-PP}_{14}\text{TFSI}|\text{Li}$  cell yielded a high discharge capacity of  $122 \text{ mAh g}^{-1}$  based on the mass of  $\text{FeOCl}$  after 7 cycles at  $10 \text{ mA g}^{-1}$ , demonstrating the application feasibility of  $\text{Cl}^-$ -conducting IL-based polymer electrolytes for high-performance CIBs [47].

### 2.1.3. Aqueous electrolytes

In addition to non-aqueous electrolytes containing ILs or organic solvents, aqueous electrolytes have also been explored in rechargeable CIBs, displaying obvious advantages that include nonflammability,

eco-friendliness, safety, and low cost due to the facile fabrication process [8,9,14]. However, most electrode materials for CIBs suffer from significant dissolution or stability issues in aqueous electrolytes. In addition, the narrow stability window of the electrolyte solvent, i.e. water, restricts the battery energy density. By pairing a silver cathode with a  $\text{BiOCl}$  anode, Yang et al. demonstrated the first aqueous CIB by using 1 M NaCl as an electrolyte [14]. This aqueous CIB exhibited obvious redox peaks representing  $\text{Cl}^-$  insertion and extraction between the two electrodes, leading to a stable discharge capacity of  $92.1 \text{ mAh g}^{-1}$  (based on the mass of the  $\text{BiOCl}$  anode) that was maintained for 45 cycles at a current density of  $400 \text{ mA g}^{-1}$  (Fig. 3c) [14]. After that, Sun et al. replaced the anode material with  $\text{Sb}_4\text{O}_5\text{Cl}_2$ , and the resulting  $\text{Ag}|\text{Sb}_4\text{O}_5\text{Cl}_2$  full battery (Fig. 3d) using 1 M NaCl electrolyte demonstrated a discharge capacity of  $34.6 \text{ mAh g}^{-1}$  (based on the mass of  $\text{Sb}_4\text{O}_5\text{Cl}_2$ ) after 50 cycles at  $600 \text{ mA g}^{-1}$  [17]. In another effort to address the poor stability and volume expansion/contraction for the conversion reaction between Bi and  $\text{BiOCl}$  during the electrochemical process, a Bi-nanoparticle@carbon-film composite electrode was employed as an anode. When this anode was coupled with a  $\text{AgCl}$  cathode and NaCl electrolyte, a high capacity of  $87.9 \text{ mAh g}^{-1}$  based on the Bi weight was achieved after 200 cycles at  $400 \text{ mA g}^{-1}$  [48]. Nevertheless, the aqueous CIBs reported thus far have relied on NaCl as the chloride salt. Other chloride salts and/or highly concentrated electrolytes (HCEs) should be explored to enhance the electrolyte electrochemical window and further improve the compatibility/stability of the electrode materials towards aqueous electrolytes.

### 2.2. Fluoride-ion batteries (FIBs)

Similar to CIBs, the rechargeable FIB operated by a  $\text{F}^-$  shuttle has emerged as a competitive battery technology that is attracting increasing attention. Owing to the high electronegativity of F, the  $\text{F}^-$  anion exhibits superb anti-oxidation stability, which enables the utilization of high-



Table 1

Comparison of the electrochemical performance of non-aqueous and aqueous electrolytes for CIBs.

Electrolyte	Cathode  Anode	Output voltage (V)	Specific capacity (mAh g <sup>-1</sup> )	Retained capacity (mAh g <sup>-1</sup> )/cycles	Ref.
0.5 M PP <sub>14</sub> Cl-PP <sub>14</sub> TFSI	FeOCl  Li	1.6–3.5	158 at 10 mA g <sup>-1</sup>	60/30	[35]
0.5 M N <sub>116(14)</sub> Cl-N <sub>114</sub> TFSI	BiOCl  Li	1.6–3.0	60 at 5 mA g <sup>-1</sup>	60/6	[35]
0.5 M PP <sub>14</sub> Cl-PP <sub>14</sub> TFSI	FeOCl/CMK-3  Li	1.6–3.5	202 at 10 mA g <sup>-1</sup>	162/30	[42]
0.5 M PP <sub>14</sub> Cl-PP <sub>14</sub> TFSI	PPyCl@CNTs   Li	1.0–4.0	118 at 500 mA g <sup>-1</sup>	~90/40	[20]
[OMIM][Cl]-[BMIM][BF <sub>4</sub> ] (1:3)	VCl <sub>3</sub>   Li	1.6–3.5	111.8 at 3 mA g <sup>-1</sup>	–	[33]
[OMIM][Cl]-[BMIM][BF <sub>4</sub> ] (1:3)	BiCl <sub>3</sub>   Li	1.6–3.5	142.9 at 3 mA g <sup>-1</sup>	~80/3	[33]
0.5 M PP <sub>14</sub> Cl-PC	VOCl  Li	1.0–2.8	151 at 522 mA g <sup>-1</sup>	113/100	[43]
0.5 M BpyCl-PC/PP <sub>14</sub> TFSI	CoFe-Cl LDH  Li	1.2–3.0	239.3 at 100 mA g <sup>-1</sup>	160/100	[44]
0.5 M BpyCl-PC/PP <sub>14</sub> TFSI	Ni <sub>2</sub> V <sub>0.9</sub> Al <sub>0.1</sub> -Cl LDH  Li	1.2–3.0	312 at 200 mA g <sup>-1</sup>	113.8/1000	[45]
0.5 M Bpy <sub>14</sub> Cl-PC	NiFe-Cl LDH  Li	1.2–3.0	350.6 at 100 mA g <sup>-1</sup>	101.1/800	[46]
PMMA-0.5 M PP <sub>14</sub> Cl-PP <sub>14</sub> TFSI	FeOCl  Li	1.6–3.5	~122 at 10 mA g <sup>-1</sup>	122/7	[47]
1 M NaCl	Ag  BiOCl	0–1.5	153 at 400 mA g <sup>-1</sup>	92.1/45	[14]
1 M NaCl	Ag  Sb <sub>2</sub> O <sub>3</sub> Cl <sub>2</sub>	0–1.5	41 at 600 mA g <sup>-1</sup>	34.6/50	[17]
1 M NaCl	AgCl  Bi@carbon-texture	0–1.2	94.2 at 400 mA g <sup>-1</sup>	87.9/200	[48]

Note: Benzyltrimethyltetradecylammonium chloride (N<sub>116(14)</sub>Cl); Butyltrimethylammonium bis(trifluoromethyl-sulfonyl)imide (N<sub>114</sub>TFSI).

voltage redox couples [9,10,50]. In addition, the multiple-electron electrochemical reactions for F<sup>-</sup> storage are promising for achieving high theoretical energy density [50]. Compared to the use of Cl<sup>-</sup> as the charge carrier in CIBs, the smaller size and lower weight of the F<sup>-</sup> anion enables faster ionic transport and higher energy density for FIBs [10,51]. Although research into rechargeable FIBs is in the fledgling stage, electrolyte design and related mechanism studies have been a significant research area, especially in recent years [52–57]. In the following section, we will provide an overview of the current F<sup>-</sup>-transporting solid and liquid electrolytes suitable for the efficient functioning of FIBs.

### 2.2.1. Solid electrolytes

The first proof-of-principle rechargeable FIB was demonstrated by Fichtner et al., in 2011 and employed La<sub>0.9</sub>Ba<sub>0.1</sub>F<sub>2.9</sub> as a F<sup>-</sup> ion-conducting solid electrolyte, achieving a high ionic conductivity of  $\sim 2.0 \times 10^{-4}$  S cm<sup>-1</sup> at 150 °C [50]. When combined with a BiF<sub>3</sub>/Ce redox couple, a discharge capacity of 190 mAh g<sup>-1</sup> based on the mass of BiF<sub>3</sub> was delivered for the initial cycle. However, due to the large volume change in electrode materials and the consequent loss of electrode-electrolyte contact upon repeated charging/discharging, the cell suffered from poor cycling stability. Following this pioneering work, numerous reports exploring solid electrolytes for FIBs have appeared [52,

55,56,58–62]. In solid electrolytes, ionic transport is mainly achieved via Schottky and anti-Frenkel point defects (i.e., the vacancy mechanism, interstitial mechanism, and interstitial-substitutional exchange mechanism). Therefore, creating more defects in the solid structure can enhance ionic conductivity [31]. Typically, F<sup>-</sup>-ion transporting solid electrolytes are categorized into two types: alkaline-earth fluorides with a fluorite-type structure (MF<sub>2</sub>, M = Ba, Ca, Sr) and rare-earth fluorides with a tysonite-type structure (MF<sub>3</sub>, M = La, Ce, Pr, Nd) [63,64]. However, some of these solid electrolytes can achieve high ionic conductivity without a high concentration of defects.

Owing to the lone pair of electrons on the Sn<sup>2+</sup> atom, SnF<sub>2</sub>-containing compounds (e.g., MSnF<sub>4</sub>, M = Pb, Ba, Ca, etc.) have been reported to possess high ionic conductivity. The polarizable lone pair can reorient while moving, and the mobile F<sup>-</sup> between Sn–Sn and Sn–Ba layers thus can participate in the conduction process, leading to an enhanced ionic conductivity from  $2 \times 10^{-10}$  S cm<sup>-1</sup> at 160 °C for BaF<sub>2</sub> to above  $1 \times 10^{-4}$  S cm<sup>-1</sup> at RT for BaSnF<sub>4</sub> solid electrolytes [31,53]. Unfortunately, the low electrochemical stability of Sn<sup>2+</sup> has largely restricted the application of highly reductive electrode materials. On the other side, the widely studied tysonite-type La<sub>0.9</sub>Ba<sub>0.1</sub>F<sub>2.9</sub> displayed low ionic conductivity ( $4 \times 10^{-7}$  S cm<sup>-1</sup> at RT), while it was compatible towards metal anodes like Ce and La. To combine advantages from both electrolytes, Mohammad et al. pressed together a thick BaSnF<sub>4</sub> layer with a thin La<sub>0.9</sub>Ba<sub>0.1</sub>F<sub>2.9</sub> layer. The resulting interlayer electrolyte achieved a much higher ionic conductivity ( $8.9 \times 10^{-6}$  S cm<sup>-1</sup>) than La<sub>0.9</sub>Ba<sub>0.1</sub>F<sub>2.9</sub> electrolyte on its own ( $4.0 \times 10^{-7}$  S cm<sup>-1</sup>) while also preventing physical contact between the less stable BaSnF<sub>4</sub> and the anode. This interlayer electrolyte enabled a BiF<sub>3</sub>/Ce battery to be charged/discharged at RT, though the first discharge capacity (only 27 mAh g<sup>-1</sup>) decayed rapidly [54].

To further demonstrate that lone pairs could improve electrolyte ionic conductivity, Reddy et al. substituted trivalent Sb<sup>3+</sup> for divalent Ba<sup>2+</sup>, revealing that the fluorite-type structured Ba<sub>1-x</sub>Sb<sub>x</sub>F<sub>2+x</sub> ( $0.1 \leq x \leq 0.4$ ) solid conductors displayed enhanced ionic conductivities (Figs. 4a and b) [64]. The migration of fluoride vacancies along the grain boundaries accounts for the ionic conductivity of Ba<sub>1-x</sub>Sb<sub>x</sub>F<sub>2+x</sub> compounds, wherein the lone pair of electrons on Sb<sup>3+</sup> appear to facilitate the F<sup>-</sup> mobility. Though the highest ionic conductivity ( $4.4 \times 10^{-4}$  S cm<sup>-1</sup> at 160 °C) was obtained with Ba<sub>0.7</sub>Sb<sub>0.3</sub>F<sub>2.3</sub> solid electrolyte, insufficient evidence was provided to determine the role of lone pairs in improving the ionic conductivity.

In the case of tysonite-type fluorides (R<sub>1-x</sub>M<sub>x</sub>F<sub>3-x</sub>, where R is the rare-earth element and M is the divalent element), a F<sup>-</sup> interstitial site cannot be formed because it is much smaller (0.84 Å) than the F<sup>-</sup> radius (1.19 Å). The ionic conductivity of tysonite-type fluorides can be improved via creating F<sup>-</sup> vacancies in RF<sub>3</sub> [65]. Fichtner et al. investigated the conduction mechanism of a La<sub>1-y</sub>Ba<sub>y</sub>F<sub>3-y</sub> ( $0 \leq y \leq 0.15$ ) solid compound synthesized by mechanical milling, revealing that the mechanism of conductivity was rather different from that of fluorite-type structured compounds (Figs. 4c and d) [61]. In contrast to the dominant role played by the migration of vacancies along the grain boundaries in the ionic conductivity of fluorite-type compounds (Ba<sub>1-x</sub>La<sub>x</sub>F<sub>2+x</sub>), the grain boundaries had detrimental impacts on ionic conduction for tysonite-type compounds (La<sub>1-y</sub>Ba<sub>y</sub>F<sub>3-y</sub>). Sintering of the La<sub>0.9</sub>Ba<sub>0.1</sub>F<sub>2.9</sub> compound led to grain growth and a reduction in grain boundaries, causing enhancement of the F<sup>-</sup> ionic conductivity. This confirmed that the grain boundaries acted as a barrier to conduction; however, the exact contribution of grain boundaries to ion conduction remains uncertain.

Reducing the thickness of electrolyte films has been recognized as another strategy to improve the ionic conductivity of solid electrolytes. A thick solid electrolyte layer (700–800 μm) typically results in high resistance for the ionic conductor and poor contact between the solid electrolyte and the electrodes, which can be mitigated by employing a thin-film mode (Fig. 4e). Preparing thin-film electrolytes of La<sub>1-x</sub>Ba<sub>x</sub>F<sub>3-x</sub> ( $0 \leq x \leq 0.15$ ) by a sol-gel spin-coating method, Fichtner et al. achieved an ionic conductivity of  $8.8 \times 10^{-5}$  S cm<sup>-1</sup> at 170 °C (La<sub>0.9</sub>Ba<sub>0.1</sub>F<sub>2.9</sub>) [60]. In spite of the conductivity being lower than with bulk solid electrolytes

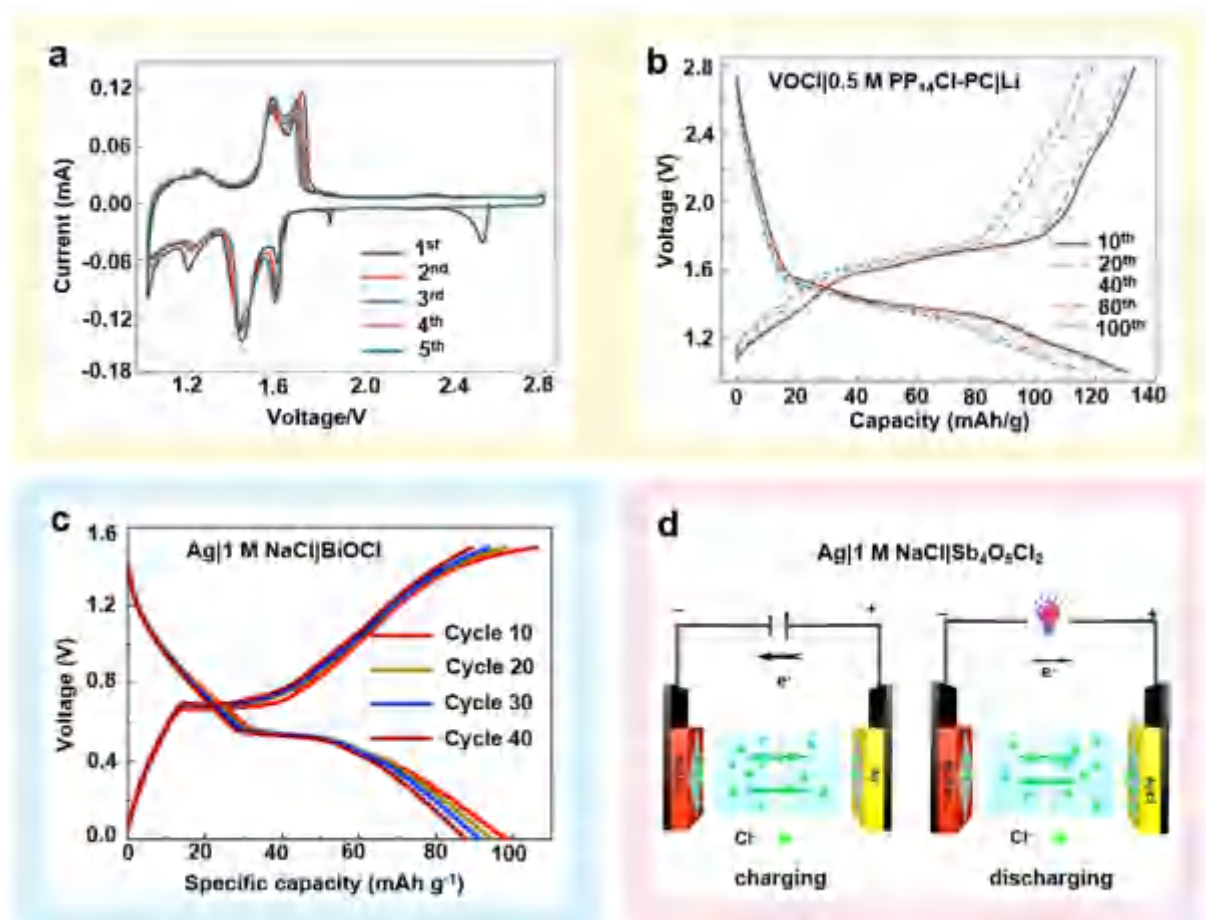


Fig. 3. Non-aqueous and aqueous electrolytes for CIBs. A non-aqueous VOCl|0.5 M PP<sub>14</sub>Cl-PC|Li CIB with (a) CV measurements at a scan rate of 0.1 mV s<sup>-1</sup> and (b) cycling performance at 2 C (1 C = 261 mA g<sup>-1</sup>). Reproduced with permission [43]. Copyright 2016, Wiley-VCH. (c) Charge and discharge curves for an aqueous Ag|1 M NaCl|BiOCl CIB at a current density of 400 mA g<sup>-1</sup>. Reproduced with permission [14]. Copyright 2017, Elsevier. (d) Schematic illustration of the working mechanism for an aqueous Ag|1 M NaCl|Sb<sub>4</sub>O<sub>5</sub>Cl<sub>2</sub> CIB. Reproduced with permission [17]. Copyright 2019, American Chemical Society.

synthesized by ball milling, the thin-film strategy reduced the overall resistance of the FIBs. Soon after, using La<sub>0.9</sub>Ba<sub>0.1</sub>F<sub>2.9</sub> as a thin-film electrolyte, Fichtner et al. achieved initial discharge capacities of 66 and 76 mAh g<sup>-1</sup> based on the weight of the active material in the cathode at 160 °C for Bi||MgF<sub>2</sub> and Cu||MgF<sub>2</sub> FIBs, respectively. Nevertheless, the capacity for both cells faded sharply during subsequent cycles [66]. Very recently, a tetragonal β-Pb<sub>0.78</sub>Sn<sub>1.22</sub>F<sub>4</sub> thin film synthesized by pulsed laser deposition (PLD) was employed as a solid electrolyte for FIBs [22]. The ionic conductivity of the thin-film electrolyte was enhanced due to the regulation of preferential growth under various annealing atmospheres. The rate-determining factor of the interfacial reaction kinetics for solid-state FIBs was investigated (Fig. 4f), revealing that mass transfer (F<sup>-</sup> conduction in electrolyte) should be the limiting process at the interface between an electrode and the thin-film electrolyte.

Solid electrolytes bring FIBs several obvious advantages, such as safety, high chemical stability, and a wide ESW. However, their high operating temperature (> 140 °C), low ionic conductivity, poor interfacial contact, and incompatibility with most conversion-type electrode materials are still tough challenges for the practical application of rechargeable solid FIBs.

#### 2.2.2. Non-aqueous liquid electrolytes

Non-aqueous liquid electrolytes generally possess higher ionic conductivities than those of solid electrolytes. Unfortunately, due to the existence of lone pairs within the ionic radius, “naked” F<sup>-</sup> ions are highly reactive with nucleophilicity and basicity. As a result, organic cations

possessing β-hydrogens easily undergo Hoffman elimination and salt decomposition, posing a great challenge for designing stable liquid electrolytes in FIBs at RT [10]. Pioneering reports demonstrate that designing electrolytes that are resistive to nucleophilic F<sup>-</sup> attack and solvating F<sup>-</sup> with Lewis acidic agents to reduce its basicity are effective strategies for developing liquid fluoride electrolytes [51,67–69].

In 2017, dissolving 1 M organic fluoride (1-methyl-1-propylpiperidinium fluoride: MPPF) in ILs (N,N,N-trimethyl-N-propylammonium bis(trifluoromethanesulfonyl)-amide: TMPA/TFSI) as the F<sup>-</sup>-transporting electrolyte, Okazaki et al. produced a 0.35 M MPPF-TMPA/TFSI electrolyte with a high ionic conductivity of 2.5 mS cm<sup>-1</sup> [70]. By combining this electrolyte with a Bi cathode and a PbF<sub>2</sub>|Pb anode, a charge capacity of 1.2 mAh cm<sup>-2</sup> was achieved with a Coulombic efficiency of ~56%. Nevertheless, organic cations with β-hydrogens in ILs were considered to potentially generate bifluoride ions, attributed to Hofmann elimination [9,65]. Despite such drawbacks, these reports were still pioneering in designing liquid electrolytes for room-temperature FIBs.

A significant advance in designing stable room-temperature F<sup>-</sup>-conducting electrolytes was achieved by Jones et al., in 2018 [51]. The electrolytes were prepared by dissolving tetraalkylammonium fluoride salts (i.e., neopentyl (Np)-substituted alkylammonium fluorides) in ethers. The solubility of the organic fluoride salt could be improved due to the branched Np chain, while the decomposition of F<sup>-</sup> to HF<sub>2</sub><sup>-</sup> could be suppressed in the absence of β-hydrogens. Bis(2,2,2-trifluoroethyl) ether (BTFE) was found to be the only organic solvent able to dissolve

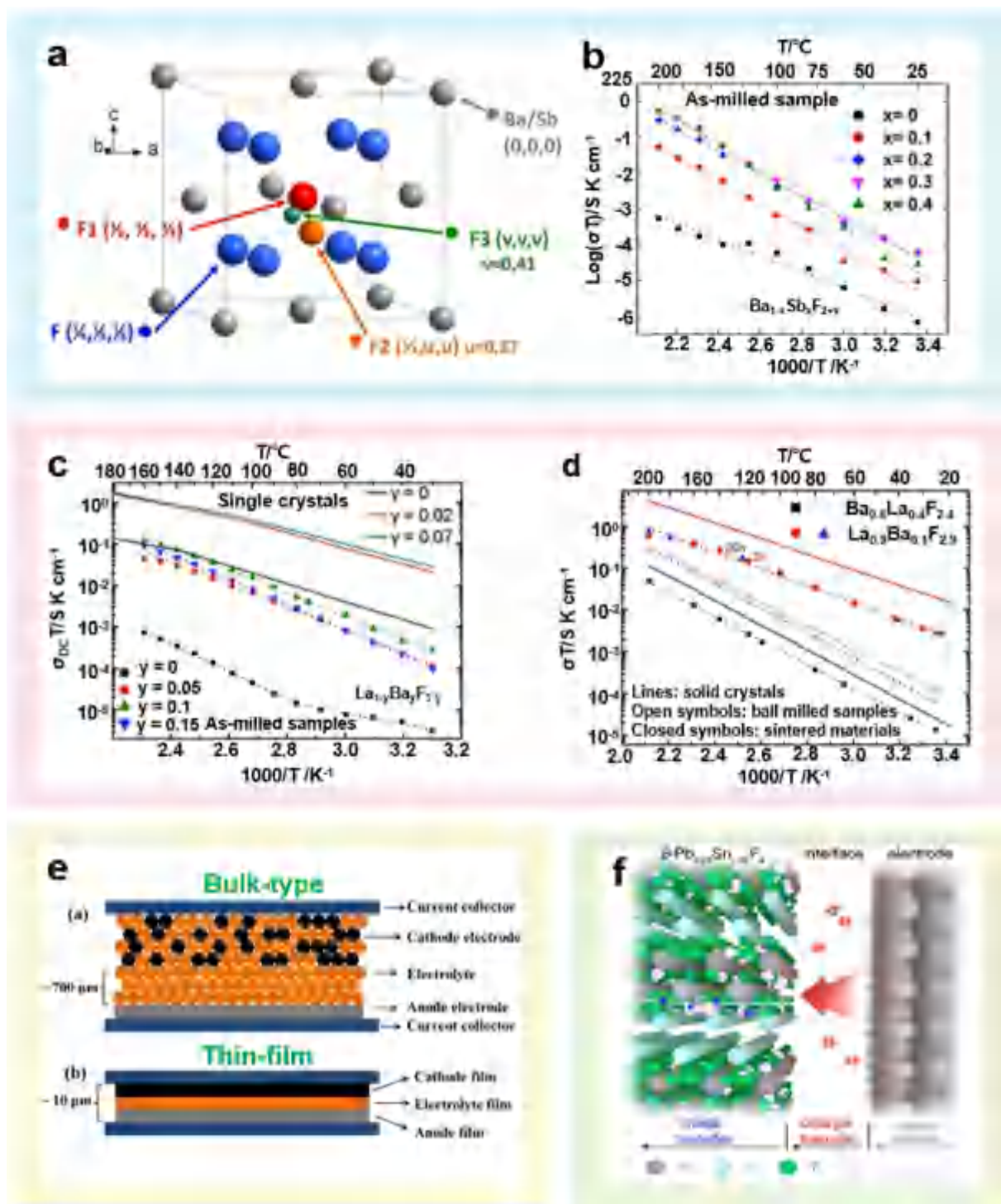


Fig. 4. Solid electrolytes for FIBs. (a) Representative structure of  $\text{Ba}_{1-x}\text{Sb}_x\text{F}_{2+x}$  (doped fluorite). (b) Arrhenius plots of ionic conductivity of ball-milled  $\text{Ba}_{1-x}\text{Sb}_x\text{F}_{2+x}$  ( $0 \leq x \leq 0.4$ ) compounds. Conductivities were measured from impedance measurements, while the dotted lines represent the linear fitted results. Reproduced with permission [64]. Copyright 2018, American Chemical Society. (c) Arrhenius plot of the conductivity for  $\text{La}_{1-y}\text{Ba}_y\text{F}_{3-y}$  electrolyte prepared by ball milling. (d) Arrhenius plots of the conductivities for ball-milled and sintered samples of tysonite-type  $\text{La}_{0.9}\text{Ba}_{0.1}\text{F}_{2.9}$  and fluorite-type  $\text{Ba}_{0.6}\text{La}_{0.4}\text{F}_{2.4}$ . Reproduced with permission [61]. Copyright 2014, American Chemical Society. (e) Schematic illustrations of a bulk-type solid battery and a thin-film electrolyte-based battery. Reproduced with permission [60]. Copyright 2014, Elsevier. (f) Schematic illustration of mass/charge-transfer processes at an electrode/electrolyte (thin-film) interface. Reproduced with permission [22]. Copyright 2021, American Chemical Society.

$\text{NpF}$  salt at high concentrations ( $> 2.2 \text{ M}$ ) without reacting with  $\text{F}^-$  (Fig. 5a). Electrolytes composed of N,N,N-trimethyl-N-neopentylammonium fluoride ( $\text{Np}_1\text{F}$ ) and N,N,N-dimethyl-N,N-dineopentylammonium fluoride ( $\text{Np}_2\text{F}$ ) in BTFE solvent were designed, respectively, demonstrating high ionic conductivity comparable with values obtained in

traditional LIB electrolytes ( $10^{-3}$  to  $10^{-2} \text{ S cm}^{-1}$ ; Fig. 5b). By pairing 1 M  $\text{Np}_1\text{F}$ -BTFE electrolyte with a  $\text{Cu@LaF}_3$  composite cathode, reversible fluorination and defluorination reactions in a FIB were achieved at RT. However, poor cycling stability was displayed, attributed to the insufficient ESW of this liquid electrolyte. Following this groundbreaking work,



the authors continued exploring liquid FIB electrolytes by studying ion-solvent properties. They demonstrated that various organic solvents were capable of dissolving  $\text{Np}_1\text{F}$  salt that can stabilize  $\text{F}^-$  in solution, including propionitrile (PN), 2,6-difluoropyridine (2,6-DFP), and BTFE, among which 2,6-DFP solvent enabled the highest  $\text{F}^-$  ion mobility (Fig. 5c), while BTFE solubilized a larger amount of  $\text{Np}_1\text{F}$ . In addition, the electrolyte ionic conductivity was improved via mixing amide into BTFE as a co-solvent (Fig. 5d), which was attributed to the ability of BTFE/co-solvent mixtures to promote ion dissociation between  $\text{Np}_1^+$  cations and  $\text{F}^-$  anions [57].

To mitigate  $\beta$ -hydrogen elimination and/or other nucleophilic fluoride attacks towards atoms like  $\alpha\text{-H}$ ,  $\text{C}=\text{O}$ ,  $\text{CHN}$ ,  $\text{P}$ ,  $\text{Si}$ , etc. under acidic conditions, Lewis acidic solvating agents (i.e., anion acceptors: AAs) such as organic compounds containing electropositive elements (e.g.,  $\text{B}$ ,  $\text{Si}$ ,  $\text{P}$ , etc.) can be employed to enhance the solvation of  $\text{F}^-$  [10,71]. Ogumi et al. demonstrated that a variety of boron-containing compounds, such as fluorobis(2,4,6-trimethylphenyl) borane (FBTMPb), triphenylboroxine (TPhBX), and triphenylborane (TPhB) could be employed as AAs in FIB electrolytes. With the aid of 0.5 M FBTMPb as an AA, a stable electrolyte consisting of 0.45 M CsF in tetraglyme solvent was formed, achieving a high anti-oxidative voltage of  $\sim 3.6$  V vs.  $\text{Li}/\text{Li}^+$ . Unfortunately, the authors found this AA also contributed to the dissolution

of the active material upon charging, which caused capacity fading during subsequent cycles [72]. Afterwards, the authors demonstrated that both the type of AA and the salt concentration of CsF in the electrolytes had significant effects on the electrochemical performance of  $\text{PbF}_2$  electrodes.

To solve the above issues of active materials' dissolution in these electrolytes, the extensively studied lithium bis(oxalato)borate (LiBOB), which is effective in suppressing cathode material dissolution in LIBs, has been considered a promising candidate for FIBs. For the first time, using tetraglyme (G4) electrolytes containing CsF and different amounts of LiBOB, Kucuk et al. investigated the effects of LiBOB on the solubility of fluorine-based salts and found the optimum  $\text{BOB}^-$  concentration and formulation to be  $\text{LiBOB}_{0.25}/\text{CsF}/\text{G4}$  [73]. Following this effort, they found the addition of  $\text{BOB}^-$  not only suppressed cathode material dissolution [73–78] but also enhanced the electrochemical stability of the LiBOB-containing electrolytes compared with AA/G4 systems (e.g., via the interactions between  $\text{BOB}^-$  and  $\text{Cs}^+$ , and between fluoride and the  $\text{CH}_2$  groups of G4) [74,76]. This design enabled the successful operation of FIBs. In this pursuit, exploring and regulating liquid electrolytes with the appropriate AA type and fluoride salt/AA ratio should be done to achieve high-performance FIBs. When designing an F-containing electrolyte, one should keep in mind that ultimately, the

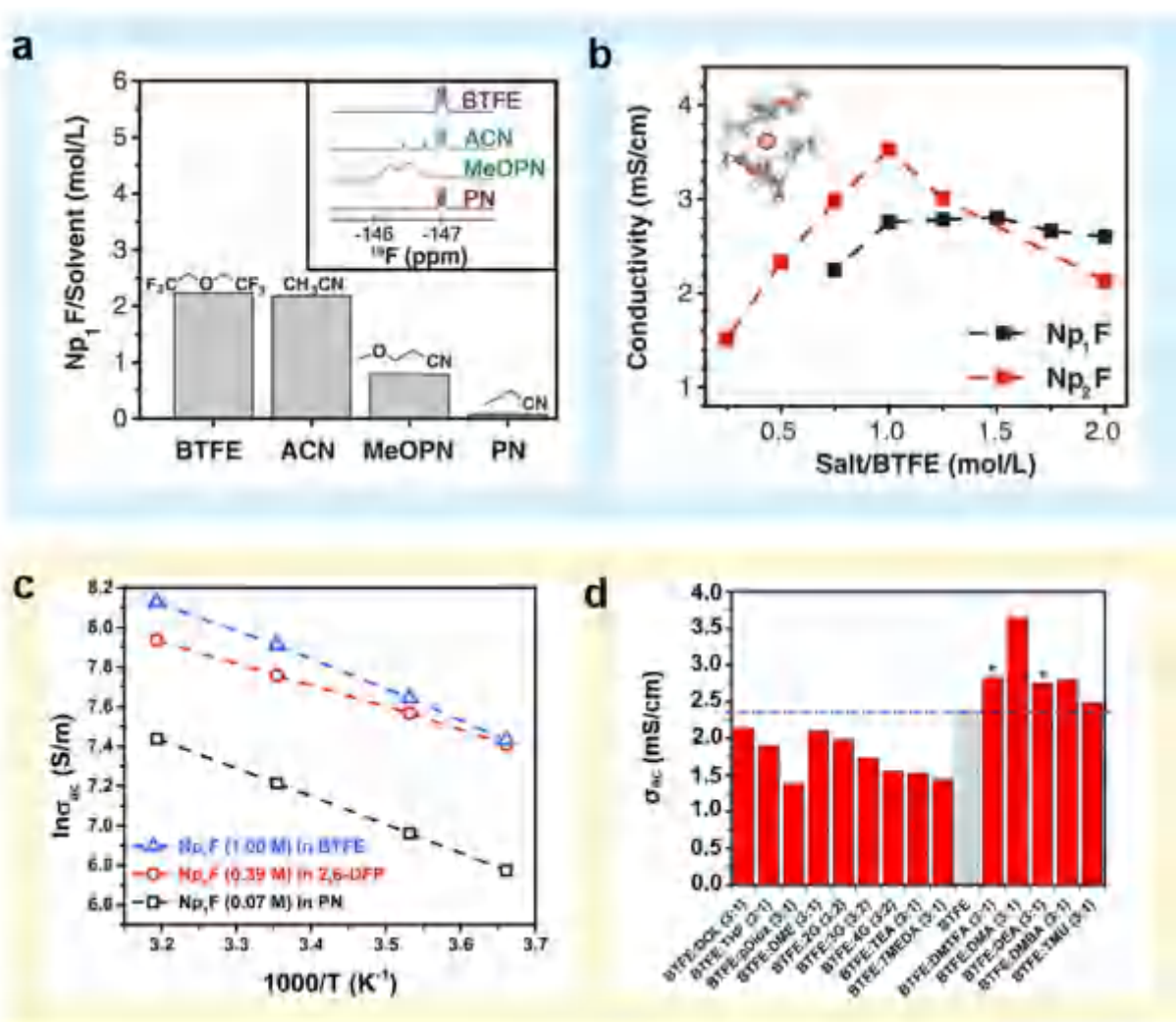


Fig. 5. Non-aqueous electrolyte for FIBs. (a)  $\text{Np}_1\text{F}$  solubility in BTFE, acetonitrile (can), 3-methoxypropionitrile (MeOPN), and PN. Inset shows  $^{19}\text{F}$  NMR spectra in the bifluoride region for  $\text{Np}_1\text{F}$  dissolved in each solvent. (b) Ionic conductivity of  $\text{Np}_1\text{F}$  and  $\text{Np}_2\text{F}$  in liquid BTFE solutions as a function of concentration. Inset shows the simulated solvation shell of BTFE molecules surrounding  $\text{F}^-$  (pink sphere). Reproduced with permission [26]. Copyright 2018, American Association for the Advancement of Science. (c) Ionic conductivity of  $\text{Np}_1\text{F}$  in PN, 2,6-DFP, and BTFE solvents. (d) Ionic conductivity of  $\text{Np}_1\text{F}$  (0.75 M) in BTFE:co-solvent mixtures. Reproduced with permission [57]. Copyright 2019, Royal Society of Chemistry.

conduction and reactivity of  $F^-$  will be suppressed when  $F^-$  ion solvation is enhanced [10].

### 2.2.3. Aqueous electrolytes

Aqueous solutions have also been considered for designing liquid electrolytes for rechargeable FIBs. Recently, an aqueous NaF salt solution acting as the electrolyte for FIBs was proposed by Chen et al., where 4-hydroxy-2,2,6,6-tetramethyl-piperidinoxy (TEMPO) and  $BiF_3$  were used as the cathode and anode, respectively [27]. To ensure only  $F^-$  were transported upon cell cycling, an anion exchange membrane was employed to prevent side effects due to insoluble compounds from both electrodes. After 85 cycles, the cell displayed a reversible and stable discharge capacity of  $89.5 \text{ mAh g}^{-1}$  based on the  $BiF_3$  weight at a current density of  $1000 \text{ mA g}^{-1}$ . However, the voltage hysteresis was relatively large ( $\sim 1.0 \text{ V}$ ), especially when compared with those obtained with traditional LIBs. Moreover, the formation of HF or bifluoride in the aqueous electrolyte was not discussed. For the implementation of FIBs with high capacity and environmental friendliness, other salts besides NaF need to be developed, and electrode materials compatible with aqueous electrolytes should be explored.

Above all, it should be noted that the safety issue is probably the greatest concern facing liquid  $F^-$ -conducting electrolytes. These electrolytes are generally corrosive and toxic towards cell components due to the highly reactive  $F^-$ . They are also potentially more flammable than solid electrolytes, which require tuning of the electrolyte chemistry to allow practical FIBs with high safety [10]. For further detailed and specific discussion on developments in FIB electrode materials and electrolytes, readers are strongly encouraged to see Nowroozi et al.'s and Yu et al.'s excellent reviews [31,53].

## 3. Electrolytes for DIBs and RDIBs

By involving anions and cations simultaneously for charge transfer, unique operating mechanism for DIBs and RDIBs are achieved. Serving as a reservoir for active ions (both cations and anions), the electrolyte plays a decisive role in the cell performance of DIBs and RDIBs — e.g., the voltage of DIBs and RDIBs relies heavily on the active ions, solvent, and electrolyte concentration — while the voltage of ARBs is determined by the Gibbs free energy [79,80]. Obviously, the electrolyte design principles and related research directions for these kinds of batteries are distinctly different from those of CRBs (e.g., LIBs). This section will systematically discuss various types of electrolyte systems utilized, and their impacts on the electrochemical properties of DIBs and RDIBs.

### 3.1. Dual-ion batteries (DIBs)

Typically, the anion insertion/extraction at the cathode endows DIBs with a high working voltage, which is beneficial for enhancing energy/power characteristics. However, the oxidation stability of conventional organic electrolytes cannot meet the high voltage requirements for anion reaction, resulting in low Coulombic efficiency and short lifetimes for DIBs. The following section will review recent progress in electrolytes for DIBs and RDIBs, including non-aqueous (e.g., conventional organic electrolytes, fluorinated electrolytes, HCEs, ILs, and gel polymer electrolytes) and aqueous electrolytes, focusing on their ESWs and compatibility with the anion intercalation process.

#### 3.1.1. Non-aqueous liquid electrolytes

The solvent is a vital component in an electrolyte and affects the anion insertion behaviors at the cathode. Owing to their low cost, high ionic conductivity, high dielectric constant, low viscosity, and suitable ESW, carbonates — including EC, PC, ethyl methyl carbonate (EMC), DMC, and dimethyl carbonate (DEC) — are the most extensively used organic solvents in DIBs [15,81–83]. Wang et al. revealed that the kinetics for the  $PF_6^-$  intercalation reaction was promoted with EMC solvent more than with PC, EC, or sulfone (SL) solvent, which can be

ascribed to EMC's stronger affinity for  $PF_6^-$  (presumably, EMC forms stronger  $H \cdots F$  hydrogen bonds, where H comes from the solvent and  $F^-$  is provided by  $PF_6^-$ ) [84–86]. Nevertheless, such promotion of the anion insertion process by EMC solvent was not obtained when  $PF_6^-$  was replaced with other anions. The authors further revealed that the  $Li^+ \cdots BF_4^-$  ionic bonding was too tight to be split by EMC, which possessed low permittivity (dielectric constant:  $\sim 2.96$ ), kinetically retarding the insertion process of  $BF_4^-$  into graphite cathodes. To liberate  $BF_4^-$  from  $Li^+$ , a co-solvent with high permittivity (e.g., PC, SL) to bond with  $Li^+$ , or another salt containing a larger cation, such as tetrafluoroborate ( $TBABF_4$ ; the van der Waals radius of  $TBA^+$  is  $4.15 \text{ \AA}$ , compared with  $0.76 \text{ \AA}$  for  $Li^+$ ) were employed, achieving a much higher anion intercalation capacity [87,88].

Unfortunately, the high voltage required for the anion intercalation process exceeds the oxidation stability voltage of conventional carbonates, hindering the development of high-voltage electrolyte systems. Ascribed to the decreased HOMO energy level, solvent molecules containing the sulfonyl group ( $-S(=O)_2-$ ) were demonstrated to enhance the electrolyte oxidation stability to  $\sim 6 \text{ V}$  (vs.  $Li/Li^+$ ) [89]. An electrolyte composed of 2 M  $LiPF_6$  salt in ethyl methyl sulfone (EMS) solvent allowed a graphite||Li DIB to work within 3.5–5.45 V with a high capacity of  $95 \text{ mAh g}^{-1}$  [90]. Phosphates have also proven effective in achieving high-voltage electrolytes, owing to their ability to form protective CEI films and their nonflammability [91]. As a strong electron-donating solvent, trimethyl phosphate (TMP) was used by Cui et al. to reconfigure the anion solvation structure, yielding a 1.5 M  $Zn(TFSI)_2$ -EMC/TMP (1:3 by volume) electrolyte. Thereby, the TFSI $^-$  anions were confined in the solvation regime of TMP, liberating the EMC solvent from the EMC-TFSI $^-$  complex into a free state (Figs. 6a and b), which elevated the oxidation voltage of carbonate electrolytes to 3 V vs.  $Zn/Zn^{2+}$ . The resulting graphite||Zn DIB achieved a capacity retention of 92% over 1000 cycles [92]. By introducing electron-withdrawing fluorine, fluorinated solvents with lower HOMO energy contributed to enhanced anti-oxidation stability.

Fluorinated solvents have also proven effective in forming a stable SEI layer on the anode and/or CEI layer on the cathode [93]. The first fluorinated electrolyte employed in DIBs was reported by Read et al., consisting of 1.7 M  $LiPF_6$  in fluoroethylene carbonate (FEC)/EMC with 5 mM tris(hexafluoro-isopropyl) phosphate (HFIP) as an additive. This electrolyte was demonstrated to support the reversible charging/discharging process of a 5.2 V graphite||graphite battery with a lifetime of 50 cycles [94]. Recently, Yang et al. proposed that FEC co-solvent participated in the solvation structures of  $Na^+$  cations and  $PF_6^-$  anions via replacing the original EMC solvent, constructing both a fluorinated CEI film on graphite cathodes and a NaF-rich SEI layer on Na metal anodes. Based on a modified 1 M  $NaPF_6$ -EC/DMC/EMC (1:1:1 by volume) electrolyte containing 10 wt% FEC additive, graphite cathodes with long cyclability and high reversibility were achieved [23]. Notably, owing to their high anti-oxidation ability (stable over 6 V vs.  $Li/Li^+$ ), nitriles have been considered as potential high-voltage electrolytes in LIBs [95], yet no related work with DIBs has been reported.

Owing to their broad ESW, excellent thermal stability, nonflammability, and low volatility, ILs — specifically room-temperature-molten salts-based electrolytes — have emerged as a strategy to enable outstanding stability/reversibility in high-voltage DIBs [98,99]. However, the major challenge facing these IL-based electrolytes is their inability to form an effective SEI film on anode materials (e.g., graphite anode), leading to the co-intercalation of large IL cations (e.g., 1-butyl-1-methylpyrrolidinium cations;  $Py_{14}^+$ ) along with  $Li^+$  insertion ( $Py_{14}TFSI$ - $LiTFSI$  electrolyte system) [100]. Additives such as vinylene carbonate and vinyl ethylene carbonate have been reported to suppress solvent co-intercalation by forming effective SEI layers [101,102]. In another effort, pure IL ( $PP_{14}TFSI$ ) was employed to supply ionic charge carriers, where TFSI $^-$  and  $PP_{14}^+$  were successfully intercalated into a graphite cathode and graphite anode simultaneously upon charging. Within the voltage range of 1.0–5.0 V, a discharge capacity of  $82 \text{ mAh g}^{-1}$  was obtained without obvious capacity decay over 600 cycles. In addition, the

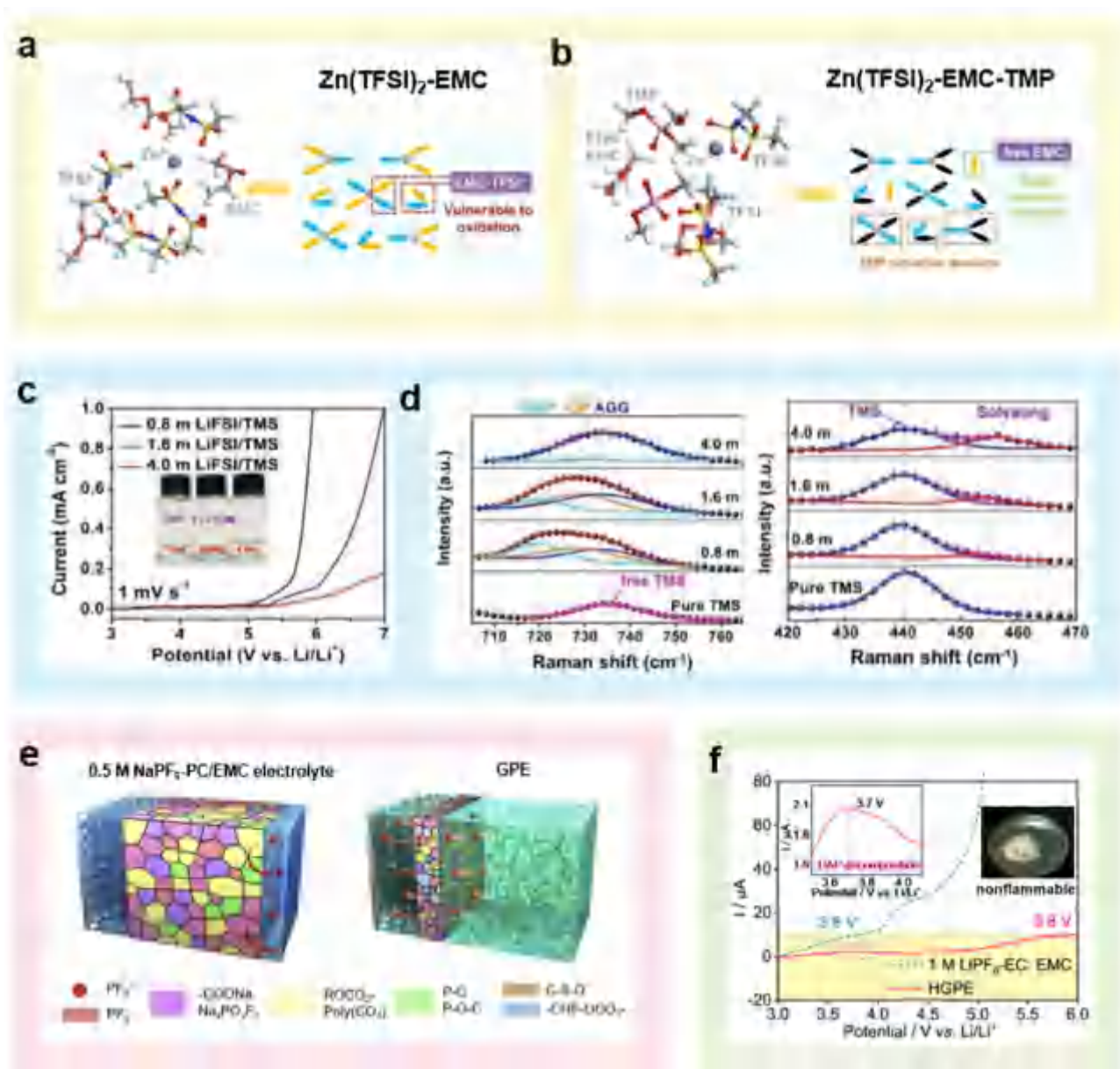


Fig. 6. Non-aqueous electrolytes for DIBs. Representative solvation structures for (a) 1.5 M  $\text{Zn}(\text{TFSI})_2$ -EMC and (b) 1.5 M  $\text{Zn}(\text{TFSI})_2$ -EMC/TMP electrolyte for graphite||Zn DIB. Reproduced with permission [92]. Copyright 2020, Wiley-VCH. (c) LSV results under different electrolyte concentrations. (d) Raman results for  $\text{LiFSI}/\text{TMS}$  electrolytes. Reproduced with permission [96]. Copyright 2021, Wiley-VCH. (e) Schematic illustrations of the CEI compositions on graphite cathodes using  $0.5 \text{ M NaPF}_6\text{-PC/EMC}$  electrolyte and GPE, respectively. Reproduced with permission [24]. Copyright 2020, Elsevier. (f) LSV curves of  $1 \text{ M LiPF}_6\text{-EC/EMC}$  electrolyte and GPE at a scan rate of  $5 \text{ mV s}^{-1}$  (inset shows the nonflammability of the GPE). Reproduced with permission [97]. Copyright 2020, Springer.

appropriate viscosity and conductivity of the  $\text{PP}_{14}\text{TFSI}$  electrolyte enabled a reduced self-discharge rate compared with other pure ILS [103]. Overall, current IL systems require further exploration to enhance the compatibility of both the cathode and the anode, as well as reduce the viscosity and improve the ionic conductivity.

In recent years, HCEs have been recognized as a new electrolyte design strategy to reinforce the interactions between cations and anions/solvent molecules and also reduce the fraction of free solvent molecules [104]. HCEs display peculiar physicochemical and electrochemical properties in comparison to conventional dilute electrolytes: with fewer free solvents, HCEs are expected to achieve higher oxidation stability; in addition, enhanced solvent-cation interaction can decrease solvent volatility, thus endowing the battery with a high level of safety [104]. Since active ions are supplied solely by the electrolyte salts, employing HCEs is beneficial to decrease the usage of electrolyte solvent, thus

enhancing the energy density of DIBs. Kravchik et al. presented a graphite||K DIB that utilized an HCE of 5 M potassium bis(fluorosulfonyl) imide (KFSI)-EC/DMC, achieving an energy density of up to  $207 \text{ Wh kg}^{-1}$  (calculated based on the mass of electrolyte and the active materials of both electrodes) with an average discharge voltage of  $4.7 \text{ V}$  [105]. Recently, Tang et al. developed an HCE consisting of 4 M lithium bis(fluorosulfonyl)imide (LiFSI) in tetramethylene sulfone (TMS). Owing to the disappearance of free TMS solvent in this HCE, excellent anti-oxidative stability of up to  $\sim 6.0 \text{ V vs. Li/Li}^+$  was achieved (Figs. 6c and d), contributing to significantly suppressed detrimental gas formation and thus a reversible de-/insertion process for  $\text{FSI}^-$  at the graphite cathode under a high working voltage. The resulting graphite||Li DIB delivered a reversible capacity of  $113.3 \text{ mAh g}^{-1}$  with a medium voltage of  $\sim 4.6 \text{ V}$ , based on the active mass of the cathode, along with 94.7% retention after 1000 cycles [96]. Although their wide ESWs can satisfy



the high working voltage required for anion insertion, HCEs still face major challenges, such as high viscosity, high cost, and poor wettability towards both the separator and the electrodes.

In light of their high safety (e.g., avoiding liquid leakage), high ionic conductivity, excellent electrochemical stability, and good flexibility, gel polymer electrolytes (GPEs) have also been explored in DIBs. In 2018, Tang et al. developed the first GPE based on the poly(vinylidene fluoride-hexafluoro propylene) (PVDF-HFP) polymer, which was co-doped with PEO and graphene oxide (GO) via weak bond interactions. The GO was favorable for improving the mechanical property and thermal stability, while the PEO optimized the pore configuration of the GPE. After soaking in a liquid electrolyte (4 M LiPF<sub>6</sub>-EMC with 2% vinylene carbonate (VC) additive), this modified GPE with a 3D porous network greatly increased the ionic conductivity to 2.1 mS cm<sup>-1</sup>, contributing to excellent rate capability and cycling stability (92% capacity retention after 2000 cycles) at 5 C for graphite||Al DIBs [106]. Later in 2020, Tang and coworkers further demonstrated that a GPE consisting of PVDF-HFP crosslinked by Al<sub>2</sub>O<sub>3</sub> nanoparticles via Lewis acid–base intermolecular bonding is also promising for realizing high-performance flexible DIBs [107].

Multifunctional GPEs prepared by in situ thermal-induced polymerization were previously reported by our group [24]. In one work, ethoxylated pentaerythritol tetraacrylate (EPTA) monomer was polymerized in situ in an optimized electrolyte of 0.5 M NaPF<sub>6</sub>-PC/EMC/FEC (1:1:1 by volume) with 1,3-propanesultone (PS) as an additive to obtain a GPE [24]. The FEC co-solvent and PS additive significantly enhanced the anti-oxidative stability of the electrolyte (up to 5.5 V vs. Na/Na<sup>+</sup>), constructed stable CEI/SEI layers on both electrodes, and enabled highly efficient intercalation/plating of anions and cations. The as-designed GPE also displayed a high ionic conductivity (5.33 mS cm<sup>-1</sup>) and high safety. As a result, a graphite||Na DIB (Fig. 6e) achieved an energy density of up to 484 Wh kg<sup>-1</sup> at a working voltage of 4.4 V based on the graphite mass, as well as superior long-term cycling stability. Following this work, our group developed a new GPE prepared from in situ copolymerization of diethyl allyl phosphate (DAP) monomer and pentaerythritol tetraacrylate (PETEA) crosslinker in an all-fluorinated electrolyte. This GPE demonstrated similar advantages (Fig. 6f), such as high safety (i.e., nonflammability and non-leakage), high ionic conductivity, and a high anti-oxidative voltage of up to 5.5 V vs. Li/Li<sup>+</sup>. It is very interesting to note that residual DAP after polymerization acted as a CEI-forming additive to suppress solvent co-intercalation and other side reactions between the GPE and the graphite cathode. Consequently, a highly reversible de-/intercalation process of PF<sub>6</sub><sup>-</sup> anions from/into graphite cathodes was enabled [97]. These reports demonstrate the great potential of GPEs for realizing high-performance DIBs, and more interesting work can be expected in the future.

### 3.1.2. Aqueous electrolytes

Organic liquids may give rise to concerns about cost, eco-friendliness, and safety, severely restricting the large-scale applications of DIBs. To tackle these issues, aqueous or hybrid aqueous/nonaqueous electrolytes (Table 2) have emerged as highly interesting candidates for developing novel DIBs [25,108–110]. Employing a simple aqueous NH<sub>4</sub>NO<sub>3</sub> electrolyte (1 M), Ji et al. demonstrated reversible intercalation/de-intercalation into/from Mn<sub>3</sub>O<sub>4</sub> cathode for the first aqueous DIBs. Electrochemical quartz crystal microbalance (EQCM) tests revealed that around two H<sub>2</sub>O molecules were co-intercalated into Mn<sub>3</sub>O<sub>4</sub>, accompanied by one NO<sub>3</sub><sup>-</sup> insertion. The as-prepared Mn<sub>3</sub>O<sub>4</sub>||activated carbon (AC) DIB delivered a discharge capacity as high as 183 mAh g<sup>-1</sup> at 0.1 A g<sup>-1</sup>, based on the active mass of the cathode, which is one of the highest reversible capacities achieved by state-of-the-art graphite cathode-based DIBs. This cell also demonstrated fast reaction kinetics for NO<sub>3</sub><sup>-</sup> in the Mn<sub>3</sub>O<sub>4</sub> structure [110]. Later on, another work based on 1 M (NH<sub>4</sub>)<sub>2</sub>SO<sub>4</sub> aqueous electrolyte was reported by Zhang and co-workers, who presented a novel DIB consisting of an n-type polyimide (PI) anode for the NH<sub>4</sub><sup>+</sup> reaction and a p-type radical polymer cathode (PTMA) for the SO<sub>4</sub><sup>2-</sup> reaction

during battery operation. This as-assembled battery enabled a high working voltage of 1.9 V and an excellent cycle life of 10,000 cycles with 86.4% capacity retention at 5 A g<sup>-1</sup>, as well as a maximum energy density of 51.3 Wh kg<sup>-1</sup> and a maximum power density of 15.8 kW kg<sup>-1</sup> (based on the total weight of the cathode and anode materials) [25]. These reports provide new insights into designing novel aqueous DIBs; nevertheless, the narrow stability window limits the working voltage and energy output of aqueous DIBs.

Recently, a new class of “water-in-salt” (WiS) electrolytes formulated with superconcentrated lithium salts (> 21 m, mol kg<sup>-1</sup>) has been developed by Xu and co-workers, significantly enlarging the stability window of aqueous electrolytes from 1.23 to ~4.9 V [108,122]. With regard to relatively dilute electrolytes (≤ 5 m), hydrated Li<sup>+</sup> remains in its primary solvation sheath in the presence of free H<sub>2</sub>O molecules, whereas the activity of H<sub>2</sub>O molecules is significantly suppressed in a WiS electrolyte, as nearly all H<sub>2</sub>O molecules participate in forming the ion solvation shells (Fig. 7a). A WiS electrolyte of 20 m NaFSI + 0.5 m Zn(TFSI)<sub>2</sub> was explored in a graphite||Zn DIB by Placke et al., where Zn<sup>2+</sup> and TFSI<sup>-</sup> functioned as the predominant intercalants, while a 20 m NaFSI concentration effectively reduced the free water amount in the WiS electrolyte (Fig. 7b) [19]. The WiS electrolyte provided enhanced anodic stability, from ~1.4 V for the dilute electrolyte (1 m NaFSI + 0.5 m Zn(TFSI)<sub>2</sub>) to ~1.8 V vs. Ag|AgCl, enabling anion storage during the electrochemical oxidation of the graphite cathode (Fig. 7c). As a consequence, the as-assembled graphite||Zn DIB displayed a reversible capacity of ~110 mAh g<sup>-1</sup> at 200 mA g<sup>-1</sup>, which retained > 80% capacity over 200 cycles. Benefiting from the high average discharge voltage of ~2.25 V, an energy density of ~200 Wh kg<sup>-1</sup> was achieved based on the active material of the cathode.

More interestingly, WiS electrolytes also promote highly efficient halogen conversion–intercalation chemistry at graphite cathodes. According to the work by Wang et al., the sequential intercalation of Br<sup>-</sup> and Cl<sup>-</sup> (Figs. 7b and c) was realized by developing a composite cathode consisting of (LiBr)<sub>0.5</sub>(LiCl)<sub>0.5</sub>C<sub>-3.7</sub> (LBC-G). A hydrated LiBr/LiCl layer (LiBr·0.34H<sub>2</sub>O–LiCl·0.34H<sub>2</sub>O) was formed via extracting water from a WiS electrolyte (21 m LiTFSI + 7 m lithium trifluoromethanesulfonate (LiOTf) in water), separating the LBC-G surface from the electrolyte, and regulating the dynamic water equilibrium. During charging, Br<sup>-</sup> within the hydration layer was oxidized to Br<sup>0</sup> first, then intercalated into graphite via one-electron transfer. When the charging continued, the oxidation and intercalation of Cl<sup>-</sup> occurred (one-electron transfer), forming a mixed intercalation compound (Figs. 7d and e). The Cl<sup>0</sup> and Br<sup>0</sup> were extracted from the graphite material to form solid LiCl/LiBr upon discharging. It was demonstrated that a stage-1 graphite intercalation compound (GIC) was formed, contributing to a high reversible capacity of 243 mAh g<sup>-1</sup> based on the total weight of the electrode. When paired with a highly fluorinated ether (HFE)/PEO-protected graphite anode, a 4 V-class full cell enabled full reversibility with ~100% CE, along with a high energy density of 460 Wh kg<sup>-1</sup>, based on the total mass of the cathode and anode [111]. Inspired by this work, Ji et al. demonstrated reversible storage of I–Cl interhalogen ([ICl<sub>2</sub>]<sup>-</sup>) at a graphite cathode by employing an aqueous deep eutectic solvent (DES) gel electrolyte of 120 m choline chloride (ChCl) + 30 m ZnCl<sub>2</sub> + 5 m KI. As a consequence, the graphite cathode delivered a high reversible capacity of 291 mAh g<sup>-1</sup> at 30 mA g<sup>-1</sup>, based on the mass of the cathode material, with stable cycling performance [118]. Overall, these findings reveal that the WiS strategy not only widens the ESWs of aqueous electrolytes but also facilitates the intercalation/de-intercalation process of anions into/from cathode materials.

Hybrid aqueous/nonaqueous electrolytes have also been explored to achieve both high safety from nonflammable aqueous WiS electrolytes and broad ESWs via non-aqueous solvents. Combining 21 M LiTFSI–H<sub>2</sub>O with 9.25 M LiTFSI–DMC in a mass ratio of 1:1, Placke et al. demonstrated a stage-2 GIC of the TFSI<sup>-</sup> intercalation reaction with a graphite cathode. When coupled with lithium titanium phosphate (LiTi<sub>2</sub>(PO<sub>4</sub>)<sub>3</sub>; LTP) material as the anode, the full battery exhibited a reversible capacity of ~42 mAh g<sup>-1</sup>, based on the active mass of the cathode, as well as 71% capacity

Table 2

Electrochemical performance of typical aqueous electrolytes for DIBs and RDIBs.

Electrolyte	Cathode  Anode	Output voltage (V)	Specific capacity (mAh g <sup>-1</sup> )	Retained capacity (mAh g <sup>-1</sup> )/cycles	Ref.
1 M NH <sub>4</sub> NO <sub>3</sub>	Mn <sub>3</sub> O <sub>4</sub>   AC	0.0–1.0 (vs. Ag AgCl)	~150 at 1 A g <sup>-1</sup>	50/3500	[110]
1 M (NH <sub>4</sub> ) <sub>2</sub> SO <sub>4</sub>	PTMA  PI	0.0–1.9	~100 at 5 A g <sup>-1</sup>	~86.4/10,000	[25]
20 m NaFSI + 0.5 m Zn(TFSI) <sub>2</sub>	Graphite  Zn	0.2–2.7	110 at 80 mA g <sup>-1</sup>	~88/200	[19]
21 m LiTFSI + 7 m LiOTf	LBC-G  Graphite	3.4–4.5	127 at 3 mA g <sup>-1</sup>	94/150	[111]
8 m Zn(ClO <sub>4</sub> ) <sub>2</sub>	Graphite  Zn	0.5–2.5	45 at 100 mA g <sup>-1</sup>	~23.5/500	[112]
21 M KFSI	PTPAn  PTCDI	0.0–1.6	47 at 500 mA g <sup>-1</sup>	~25/900	[113]
2 M NaClO <sub>4</sub>	NNH  NTP@C	0.2–1.5	~76 at 1.33 A g <sup>-1</sup> (-20 °C)	~64.6/10,000	[114]
1 m Zn(OTf) <sub>2</sub> + 19 m LiTFSI	BDB  Zn	0.4–2.1	112 at 390 mA g <sup>-1</sup>	~91.8/500	[115]
30 m ZnCl <sub>2</sub>	NFG  Zn	0.8–1.95	134 at 100 mA g <sup>-1</sup>	82/800	[116]
33.3 m LiFSI + 3.7 m LiTFSI	Graphite  AC	0.0–3.2	72 at 100 mA g <sup>-1</sup>	~70/100	[117]
120 m choline chloride + 30 m ZnCl <sub>2</sub> + 5 m KI	Graphite  Zn	-0.2–1.4 (vs. Ag AgCl)	291 at 30 mA g <sup>-1</sup>	260/40	[118]
30 m ZnCl <sub>2</sub>	Polypyrrene  Zn	0.6–1.8	180 at 50 mA g <sup>-1</sup>	175.3/800	[119]
5 m MgCl <sub>2</sub> + 5 m TBMACl	Graphite  PTCDI	0.0–2.18	41 at 50 mA g <sup>-1</sup>	33/200	[120]
1 M KF	Prussian blue  BFO	0.0–2.0	153.7 at 1 A g <sup>-1</sup>	~61.5/1000	[18]
0.8 M NaF	Na <sub>0.44</sub> MnO <sub>2</sub>   BiF <sub>3</sub>	0.0–1.5	123 at 100 mA g <sup>-1</sup>	47.28/40	[121]
30 m ZnCl <sub>2</sub>	Zn <sub>3</sub> [Fe(CN) <sub>6</sub> ] <sub>2</sub>   ferrocene/AC	0.0–1.6	25 at 150 mA g <sup>-1</sup>	14.5/1000	[13]

Note: (PTMA); (PI); activated carbon (AC); (LiBr)<sub>0.5</sub>(LiCl)<sub>0.5</sub>C<sub>3.7</sub> (LBC-G); polytriphenylamine (PTPAn); 3,4,9,10-perylenetetracarboxylic diimide (PTCDI); nano/microstructured Ni(OH)<sub>2</sub> (NNH); carbon-coated NaTi<sub>2</sub>(PO<sub>4</sub>)<sub>3</sub> (NTP@C); 1,4 bis(diphenylamino)-benzene (BDB); nitrogen-doped few-layered graphene (NFG); tributylmethylammonium chloride (TBMACl); BiF<sub>3</sub>@BiF<sub>11</sub>O<sub>5</sub>@reduced graphene oxide (BFO).

retention after 500 cycles at 200 mA g<sup>-1</sup>. The low average discharge voltage of 1.5 V was unsatisfactory but could be further enhanced to 2.5 V by substituting the LTP with a LTO anode [109]. Following this work, Yan et al. designed another hybrid electrolyte by mixing a WiS electrolyte (7 m LiOTf and 21 m LiTFSI dissolved in water) with a non-aqueous electrolyte of 9.25 m LiTFSI in DMC. Despite the high salt concentration, the hybrid electrolyte achieved an ionic conductivity of 0.65 mS cm<sup>-1</sup> at 25 °C, providing good wettability towards the cathode and anode materials. A full DIB based on the hybrid electrolyte was constructed, with graphite as cathode and niobium pentoxide (Nb<sub>2</sub>O<sub>5</sub>) as anode, delivering a reversible capacity of 47.6 mAh g<sup>-1</sup> at a current density of 200 mA g<sup>-1</sup>, based on the cathode material, a medium voltage of up to ~2.2 V, and a high CE of 93.9% [108].

### 3.2. Reverse dual-ion batteries (RDIBs)

RDIBs follow a similar operating mechanism as DIBs, but the sequence of the anion- and cation-storage chemistries is flipped. In addition, the incorporation of both types of ions into the electrodes occurs during the discharging process, which is opposite to what occurs upon charging in DIBs.

Up till now, only aqueous electrolytes have been reported to support RDIB chemistries. The concept of the RDIB was defined by Ji et al. for the first time, employing a 30 m ZnCl<sub>2</sub> WiS electrolyte that supplied ZnCl<sub>4</sub><sup>2-</sup> anions and Zn<sup>2+</sup> cations for charge storage. Combined with a Zn-insertion Prussian blue (Zn<sub>3</sub>[Fe(CN)<sub>6</sub>]<sub>2</sub>) cathode and a ferrocene/activated carbon nanocomposite (Fc/C) anode, this electrolyte enabled the RDIB to proceed by an initial discharge process via the insertion of ZnCl<sub>4</sub><sup>2-</sup> and Zn<sup>2+</sup> into the anode and cathode, respectively. During charging, both cations and anions were released back to the electrolyte (Fig. 8a). Notably, the electrolyte also served as the sole reservoir of ionic charge carriers (anions and cations) for energy storage, thus being regarded as the active material in RDIBs [13]. Benefiting from the unique nature of a WiS electrolyte with few free water molecules, the dissolution issue of the ferrocene material was mitigated. Furthermore, the voltage for cation insertion was raised while the voltage related to anion insertion was reduced, thereby enlarging the Zn<sub>3</sub>[Fe(CN)<sub>6</sub>]<sub>2</sub>||Fc/C battery voltage by 0.35 V compared with one using a dilute electrolyte containing 5 m ZnCl<sub>2</sub> (Fig. 8b). Consequently, a reversible capacity of ~30 mAh g<sup>-1</sup> was achieved, based on the active masses of both electrodes [13].

In 2018, a rechargeable RDIB based on F<sup>-</sup> anion and Na<sup>+</sup> cation electrochemistry was proposed by Hou and co-workers, comprising 0.8 M

NaF aqueous electrolyte, Na<sub>0.44</sub>MnO<sub>2</sub> cathode, and BiF<sub>3</sub> anode. During the initial charging process, F<sup>-</sup> and Na<sup>+</sup> were released from the anode and cathode materials, respectively, to the electrolyte, while the two types of ions were captured by the corresponding electrodes in the following discharge period. This battery exhibited a high discharge capacity of ~123 mAh g<sup>-1</sup> at 100 mA g<sup>-1</sup>, based on the mass of the BiF<sub>3</sub> material, but the capacity decayed rapidly to 47.28 mAh g<sup>-1</sup> within 40 cycles [121]. Very recently, utilizing KF aqueous solution as the electrolyte, Li et al. constructed a fluorine/potassium RDIB based on Prussian blue (PB) as the cathode material and BiF<sub>3</sub>@BiF<sub>11</sub>O<sub>5</sub>@reduced graphene oxide (BFO) as the anode material. It was revealed that although the capacity decreased with lower electrolyte concentration (1–12 M), the cycling stability was improved due to less dissolution of BiF<sub>3</sub> and fewer undesirable surface deposits. In addition, the rational design of the anode with added BiF<sub>11</sub>O<sub>5</sub> and a graphene coating contributed to reduced volume change, enhanced electronic conductivity, and suppressed pulverization. Therefore, with 1 M KF electrolyte, a high discharge capacity of 218 mAh g<sup>-1</sup> at 1 A g<sup>-1</sup>, based on the mass of the anode material, and excellent rate performance with 47% retention maintained at 5 A g<sup>-1</sup> were achieved (Figs. 8c and d) [18].

### 4. Conclusions and perspective

As an emerging new type of battery chemistry, ASBs (i.e., ARBs, DIBs, and RDIBs) utilizing anions as charge carriers for storage reactions have received growing interest and exhibited great potential for grid-scale energy storage. As an essential and indispensable component, ASB electrolytes should comply with the same key requirements as LIBs, including high ionic conductivity, good chemical stability/inertness, wide ESW, low interfacial resistance, etc., thus enhancing the kinetics/reversibility of electrochemical reactions in ASBs. In this review, we have summarized the research progress and recent achievements in electrolytes for ARBs, DIBs, and RDIBs, including solid electrolytes, non-aqueous liquid electrolytes, and aqueous electrolytes. We have mainly focused on discussing the unique properties and basic principles for designing each type of electrolyte, as well as various performance parameters, such as working voltage, lifetime, energy/power density, safety, cost, etc. The properties of different types of electrolytes in ARBs and DIBs/RDIBs were compared in terms of the six aspects depicted in Fig. 9. It is clear that except for high ionic conductivity, these aspects are far from satisfactory in aqueous electrolytes for ARB applications. In addition, although solid electrolytes display high resistance for ionic

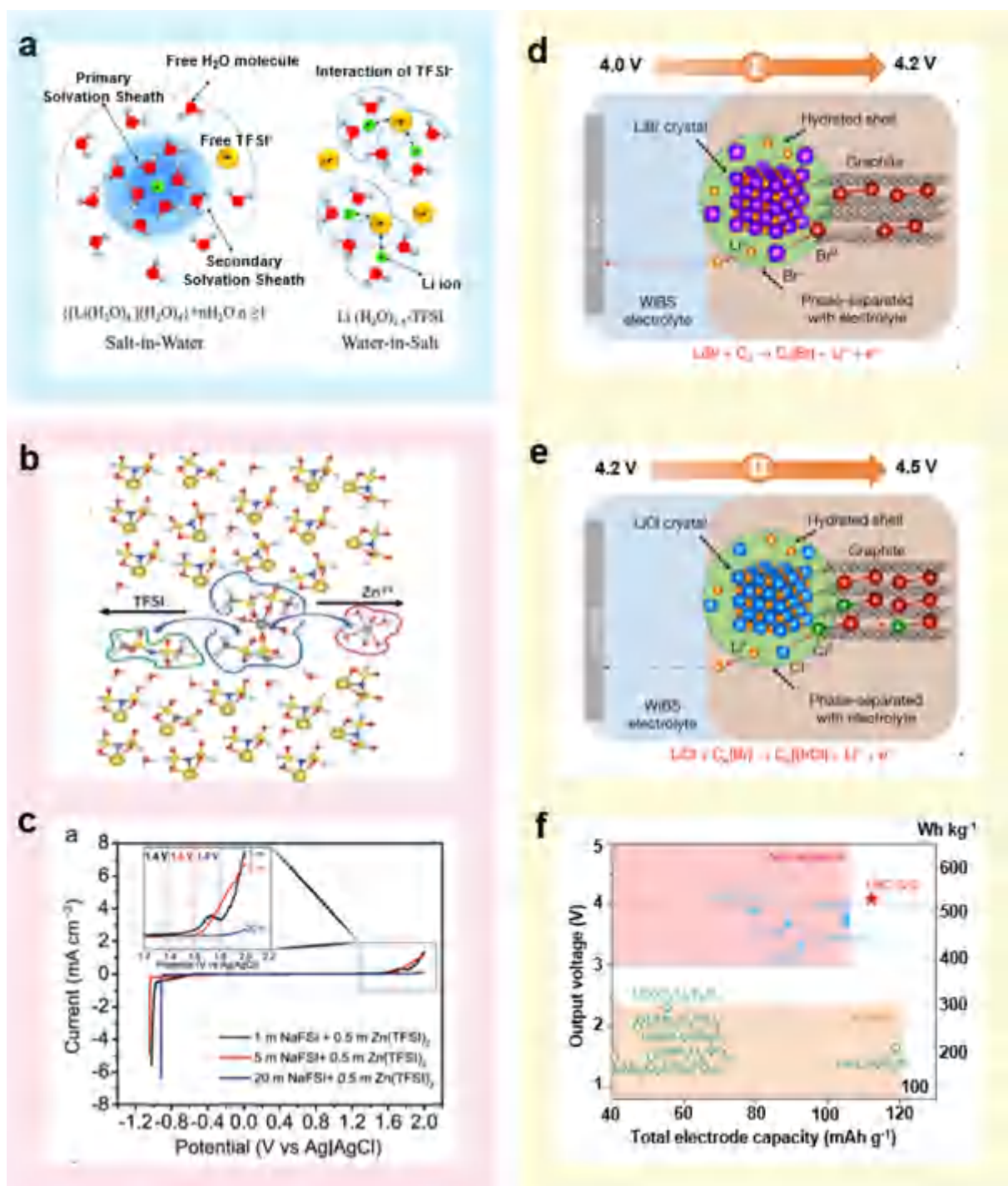


Fig. 7. Aqueous electrolytes in DIBs. (a) Illustration of the  $\text{Li}^+$  primary solvation sheath in dilute and WiS electrolytes. Reproduced with permission [122]. Copyright 2015, American Association for the Advancement of Science. (b) Simulated cation solvation structure in 20 m NaFSI + 0.5 m Zn(TFSI)<sub>2</sub> WiS electrolyte (based on optimized first solvation shells of  $\text{Na}^+$  and  $\text{Zn}^{2+}$ ). (c) ESWs of electrolytes measured at a scan rate of 1 mV s<sup>-1</sup> in an AC||Ti cell with an Ag|AgCl reference electrode. Reproduced with permission [19]. Copyright 2020, Wiley-VCH. Schematic of the two-stage reaction for the LBC-G composite cathode in WiS aqueous-gel electrolyte during the charging process: (d) oxidation and intercalation of  $\text{Br}^-$ , (e) oxidation and intercalation of  $\text{Cl}^-$ , (f) energy density (red star) of the LBC-G||graphite full cells in comparison with state-of-the-art commercial and reported  $\text{Li}^+$  chemistries using non-aqueous (blue color) and aqueous (green color) electrolytes. The energy densities were calculated based on the total weight of the cathode and anode. Reproduced with permission [111]. Copyright 2019, Springer.

conduction, they surpass liquid electrolytes in mechanical properties and thermal stability. With respect to electrolytes developed in DIBs/RDIBs, the electrochemical stability of aqueous electrolytes requires further improvement to broaden their applications.

Different types of ASBs have unique electrolyte requirements. With respect to DIBs and/or RDIBs, where the electrolyte serves as the

reservoir supplying both cations and anions for charge transfer, the salt concentration and the corresponding physical nature of the electrolyte depend highly on the SOC in DIBs and/or RDIBs, compared with the unchanged ion concentration during charging/discharging for ARBs, where the electrolyte only acts as the charge carrier to transport anions. Thus, besides physical properties, the electrolyte formulation (e.g., the



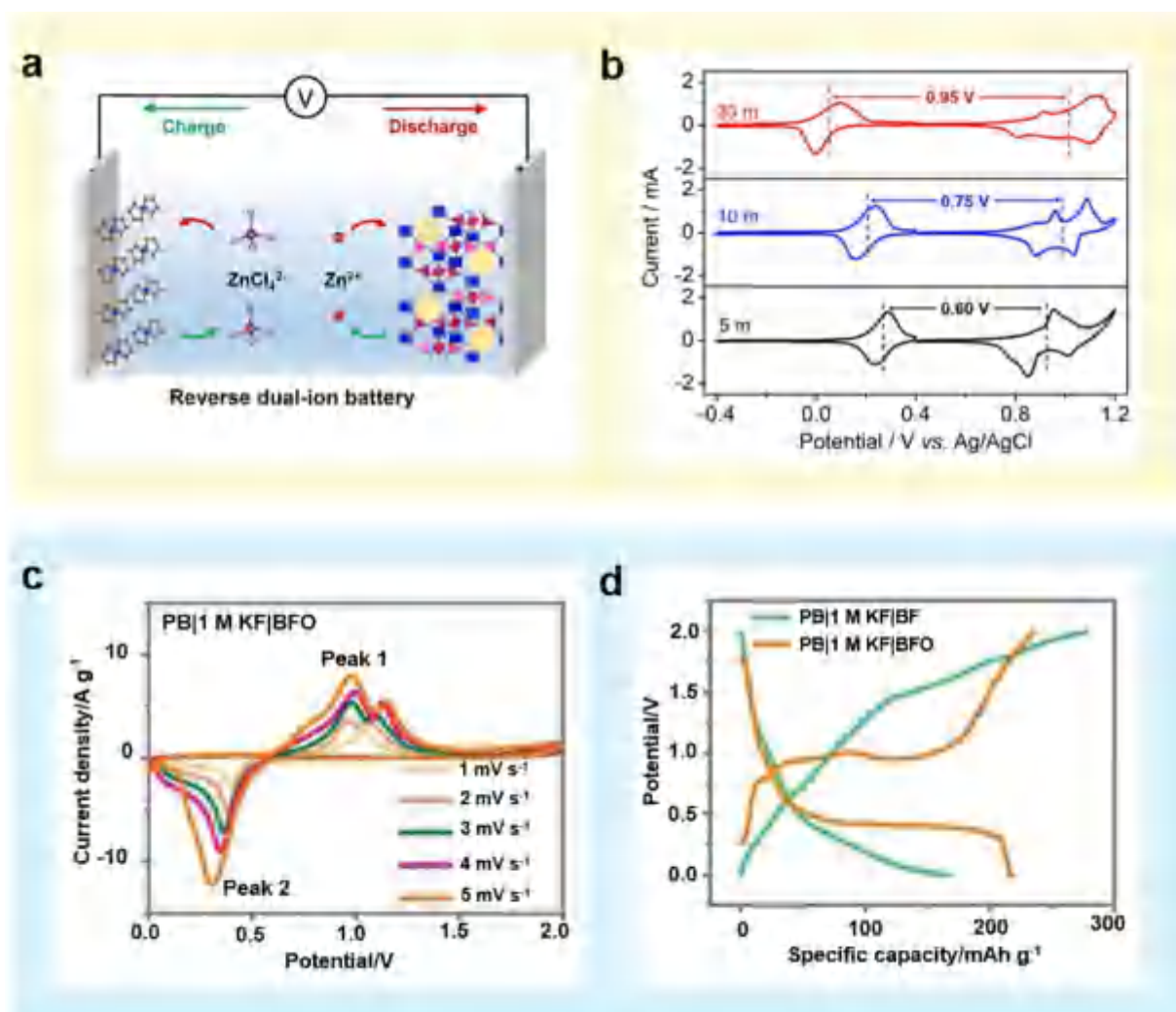


Fig. 8. Aqueous electrolytes in RDIBs. (a) Schematic of the working mechanism of a  $\text{Zn}_3[\text{Fe}(\text{CN})_6]_2||\text{Fc}/\text{C}$  RDIB. (b) CV curves of the Fc/C anode and  $\text{Zn}_3[\text{Fe}(\text{CN})_6]_2$  cathode in  $\text{ZnCl}_2$  electrolyte. Reproduced with permission [13], Copyright 2019, American Chemical Society. (c) CV curves at various scan rates and (d) charge/discharge profiles of 1 A g<sup>-1</sup> of PB||BFO cell with 1 M KF electrolyte. Reproduced with permission [18], Copyright 2021, Wiley-VCH.

solvent type, salt and salt content, and additive amount) will also affect the reversible capacity, cell voltage, energy/power density, etc. of DIBs and/or RDIBs. In addition, electrolyte–electrode compatibility plays a significant role in reversible/stable storage reactions in ARBs. Generally, most CIBs/FIBs suffer from severe electrode dissolution and/or irreversible side reactions between electrode materials and liquid electrolytes, leading to fast capacity decay and short lifetime, and poor interfacial contact remains a tough challenge for CIBs/FIBs to improve the cycling stability. With regard to DIBs, especially with graphite cathodes, reversible anion de-/intercalation at high voltage can be compromised by incompatibility between the electrolyte and graphite, resulting in inevitable electrolyte decomposition, solvent co-intercalation, and low Coulombic efficiency. Although encouraging progress has been achieved in recent years, limitations and challenges remain for electrolyte development. Therefore, great efforts in electrolyte design should continue in the following directions:

#### (1) ARBs

With regard to CIBs, solid, non-aqueous liquid, and aqueous electrolytes can be developed for  $\text{Cl}^-$  conduction. The employment of solid electrolytes is a promising strategy to resolve issues related to electrode dissolution and/or side reactions between the electrolyte and the

electrode. Through structural engineering, exploring inorganic chloride ion conductors (like halide perovskites) and multifunctional polymer-based solids can achieve high ionic conductivity and high structural stability at RT. In addition, synergistic effects can be obtained via immobilizing  $\text{Cl}^-$ -containing ILs within polymer matrices, where the ILs act as both plasticizer and  $\text{Cl}^-$  supplier, which can be a promising solution to achieve high ionic conductivity as well as thermal and electrochemical stability [47]. With regard to aqueous electrolytes, employing other chloride salts beyond NaCl, and applying WiS or DES strategies are expected to widen the electrolyte electrochemical window and improve the compatibility/stability of electrode materials towards aqueous electrolytes. It should be noted that the onset potential for  $\text{Cl}_2$  gas formation is 1.36 V vs. SHE, which ought to be considered when designing aqueous electrolyte systems.

Compared to the use of  $\text{Cl}^-$  as the charge carrier in CIBs, the smaller size and higher electronegativity of  $\text{F}^-$  enables faster ionic transport and higher anti-oxidation stability for FIBs. Although significant progress has been made in recent years regarding fluorite-type and tysonite-type structured solids, high operating temperature (> 140 °C), low ionic conductivity, poor interfacial contact, etc. are still tough challenges, requiring further exploration and optimization of  $\text{F}^-$  solid conductors (e.g., creating more defects, utilizing the effect of lone pairs, optimizing synthesis strategies). Further, considering liquid electrolytes can achieve

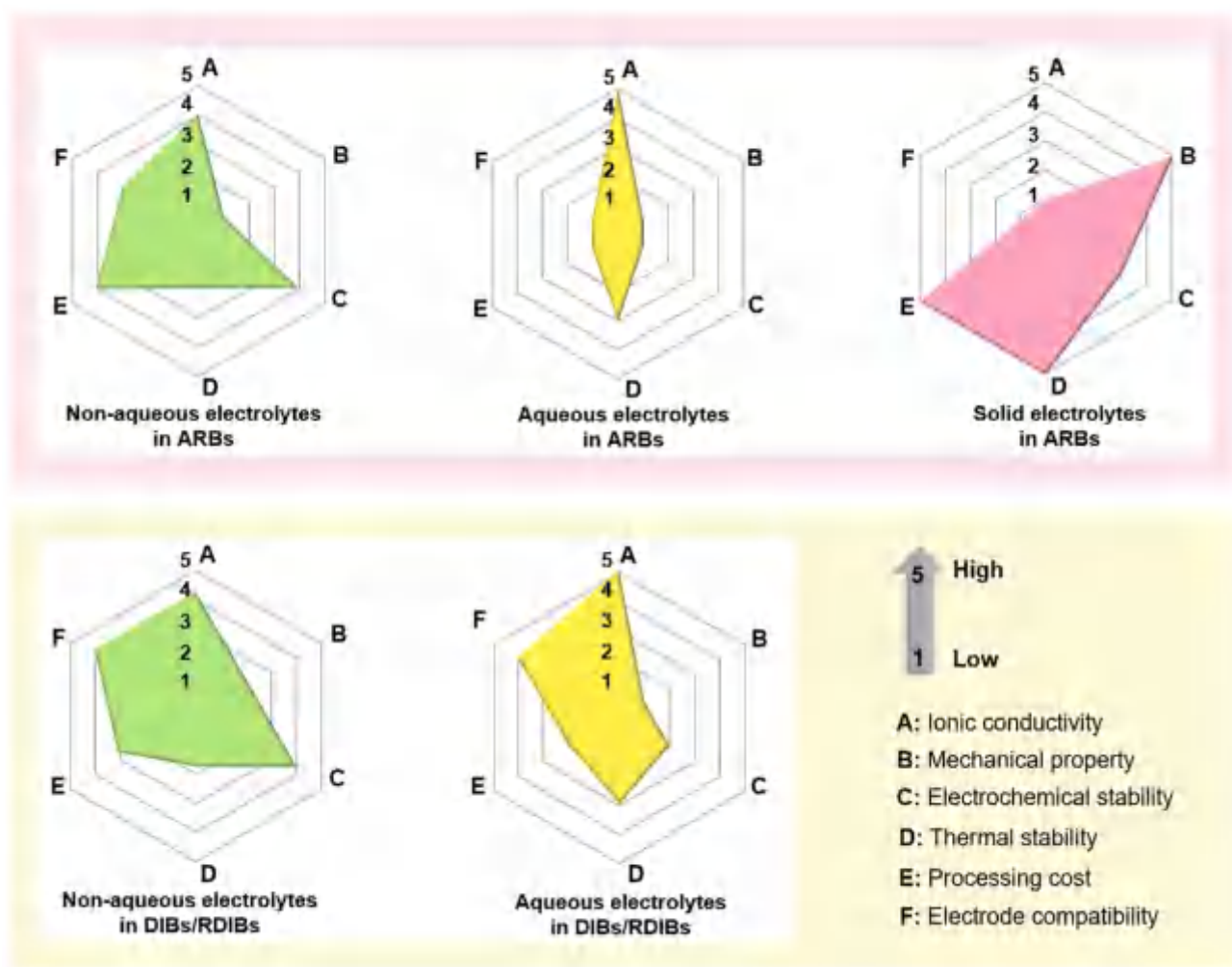


Fig. 9. Radar plots of properties for non-aqueous, aqueous, and solid electrolytes in ARBs (top), and DIBs or RDIBs (bottom).

ambient battery operation, developing stable liquid electrolytes to enable efficient FIB functioning is of vital significance, pointing toward the exploration of suitable solvents and/or fluoride salts to suppress nucleophilic  $F^-$  attack (e.g.,  $\beta$ -hydrogen elimination) or solvating  $F^-$  by Lewis acidic agents to reduce its basicity. The safety issue is probably the greatest concern facing liquid  $F^-$ -conducting electrolytes, which are potentially corrosive and toxic towards cell components due to the chemically reactive  $F^-$  ions. These electrolytes are generally flammable, requiring updating of the electrolyte chemistry to promote practical FIBs with high safety.

## (2) DIBs

The anion intercalation process in DIBs requires a high working voltage, which relies heavily on the active ions, solvents, and electrolyte concentration. Ideally, one would design high-voltage electrolyte systems based on anti-oxidative solvents like sulfoxes, phosphates, fluorinated carbonates, nitriles, etc. Developing concentrated non-aqueous electrolytes, and aqueous or hybrid aqueous/nonaqueous-based WiS electrolytes are also effective strategies to facilitate the anion intercalation/de-intercalation process and enhance the energy density of DIBs. In addition, functional additives that can promote the formation of multifunctional surface layers (i.e., CEIs) on the graphite cathode should be explored further, to potentially suppress solvent co-intercalation and side reactions between the electrolyte and the cathode at high voltage. Furthermore, multivalent anions with more charge numbers and/or single

halide ions (e.g.,  $F^-$ ,  $Cl^-$ ) with smaller anionic charge carriers should be explored to potentially provide high theoretical specific capacity and energy density. To achieve high safety, high ionic conductivity, excellent electrochemical stability, and good flexibility, developing a multifunctional GPE via in situ polymerization (e.g., thermal-induced) is regarded as a feasible path for promoting high-performance DIBs.

## (3) RDIBs

Up till now, only aqueous electrolytes have been reported for achieving RDIB chemistries, providing vast opportunities for electrolyte exploration. In addition to single halide ions (e.g.,  $F^-$ ,  $Cl^-$ ), metal-based superhalides (e.g., based on  $Zn-Cl$  or  $Mg-Cl$ ) formed in WiS- or DESs-based electrolytes may also serve as promising charge carriers [9]. As more new electrolyte systems are designed, the output voltage and the corresponding energy density of RDIBs will be expected to improve.

## (4) Microscopic mechanisms for anions as the charge carriers

Compared with the extensive investigations of cation solvation in CRBs (e.g., LIBs), the solvation/de-solvation behavior of anions and their impacts on CEI/SEI features (e.g., chemical composition, atomic-level microstructure, mechanical property, structural evolution, interfacial resistance, ionic transport, etc.) and anion storage performance remain unclear. Therefore, theoretical calculations in combination with advanced characterization technologies (e.g., cryo-electron microscopy,

in situ transmission electron microscopy (TEM), in situ X-ray photoelectron spectroscopy (XPS), and time-of-flight secondary ion mass spectrometry (TOF-SIMS)) should be conducted to investigate the microscopic mechanisms of anions as charge carriers and further manipulate the anion storage process.

Overall, the ASB technology employing anions as charge carriers for storage reactions is currently at a rather early stage, offering vast opportunities for further improvements in both fundamental and technical aspects. Significant efforts to address the above challenges and pursue these new directions will greatly enhance progress in ASB electrolyte systems, thus endowing ASBs with highly competitive features compared with state-of-the-art LIBs or other rechargeable metal-ion batteries. It is expected that with ongoing developments and enhancements in cycling stability and energy density, ASB technology will be a highly promising candidate for grid-scale energy storage at low cost.

#### Declaration of competing interest

The authors declare that they have no known competing financial interests or personal relationships that could have appeared to influence the work reported in this paper.

#### Acknowledgments

B.H. Li would like to thank the support provided by National Nature Science Foundation of China (No. 51872157 and No. 52072208) and Local Innovative and Research Teams Project of Guangdong Pearl River Talents Program (2017BT01N111).

#### References

- [1] M.S. Whittingham, Lithium batteries and cathode materials, *Chem. Rev.* 104 (2004) 4271–4302.
- [2] B. Dunn, H. Kamath, J.-M. Tarascon, Electrical energy storage for the grid: a battery of choices, *Science* 334 (2011) 928–935.
- [3] R. Schmich, R. Wagner, G. Hörpel, T. Placke, M. Winter, Performance and cost of materials for lithium-based rechargeable automotive batteries, *Nat. Energy* 3 (2018) 267–278.
- [4] G.E. Blomgren, The development and future of lithium ion batteries, *J. Electrochem. Soc.* 164 (2016) A5019–A5025.
- [5] P.K. Nayak, L. Yang, W. Brehm, P. Adelhelm, From lithium-ion to sodium-ion batteries: advantages, challenges, and surprises, *Angew. Chem. Int. Ed.* 57 (2018) 102–120.
- [6] Y. Liang, H. Dong, D. Aurbach, Y. Yao, Current status and future directions of multivalent metal-ion batteries, *Nat. Energy* 5 (2020) 646–656.
- [7] C. Vaalma, D. Buchholz, M. Weil, S. Passerini, A cost and resource analysis of sodium-ion batteries, *Nat. Rev. Mater.* 3 (2018) 1–11.
- [8] Q. Liu, Y. Wang, X. Yang, D. Zhou, X. Wang, P. Jaumaux, F. Kang, B. Li, X. Ji, G. Wang, Rechargeable anion-shuttle batteries for low-cost energy storage, *Chem* 7 (2021) 1993–2021.
- [9] S.K. Sandstrom, X. Chen, X. Ji, A review of halide charge carriers for rocking-chair and dual-ion batteries, *Carbon Energy* 3 (2021) 627–653.
- [10] A.W. Xiao, G. Galatolo, M. Pasta, The case for fluoride-ion batteries, *Joule* 5 (2021) 2823–2844.
- [11] L. Zhang, H. Wang, X. Zhang, Y. Tang, A review of emerging dual-ion batteries: fundamentals and recent advances, *Adv. Funct. Mater.* 31 (2021) 2010958.
- [12] X. Ou, D. Gong, C. Han, Z. Liu, Y. Tang, Advances and prospects of dual-ion batteries, *Adv. Energy Mater.* 11 (2021) 2102498.
- [13] X. Wu, Y. Xu, C. Zhang, D.P. Leonard, A. Markir, J. Lu, X. Ji, Reverse dual-ion battery via a ZnCl<sub>2</sub> water-in-salt electrolyte, *J. Am. Chem. Soc.* 141 (2019) 6338–6344.
- [14] F. Chen, Z.Y. Leong, H.Y. Yang, An aqueous rechargeable chloride ion battery, *Energy Stor. Mater.* 7 (2017) 189–194.
- [15] Y. Wang, Y. Zhang, S. Wang, S. Dong, C. Dang, W. Hu, D.Y. Yu, Ultrafast charging and stable cycling dual-ion batteries enabled via an artificial cathode–electrolyte interface, *Adv. Funct. Mater.* (2021) 2102360.
- [16] Y. Wang, Y. Zhang, Q. Duan, P.-K. Lee, S. Wang, Y. Denis, Engineering cathode–electrolyte interface of graphite to enable ultra long-cycle and high-power dual-ion batteries, *J. Power Sources* 471 (2019) 9144–9148.
- [17] X. Hu, F. Chen, S. Wang, Q. Ru, B. Chu, C. Wei, Y. Shi, Z. Ye, Y. Chu, X. Hou, Electrochemical performance of Sb<sub>4</sub>O<sub>5</sub>Cl<sub>2</sub> as a new anode material in aqueous chloride-ion battery, *ACS Appl. Mater. Interfaces* 11 (2019) 9144–9148.
- [18] X. Li, Y. Tang, J. Zhu, H. Lv, Y. Xu, W. Wang, C. Zhi, H. Li, Initiating a room-temperature rechargeable aqueous fluoride-ion battery with long lifespan through a rational buffering phase design, *Adv. Energy Mater.* 11 (2021) 2003714.
- [19] I.A. Rodríguez-Pérez, L. Zhang, J.M. Wrogoemann, D.M. Driscoll, M.L. Sushko, K.S. Han, J.L. Fulton, M.H. Engelhard, M. Balasubramanian, V.V. Viswanathan, V. Murugesan, X. Li, D. Reed, V. Sprenkle, M. Winter, T. Placke, Enabling natural graphite in high-voltage aqueous graphite||Zn metal dual-ion batteries, *Adv. Energy Mater.* 10 (2020) 2001256.
- [20] X. Zhao, Z. Zhao, M. Yang, H. Xia, T. Yu, X. Shen, Developing polymer cathode material for the chloride ion battery, *ACS Appl. Mater. Interfaces* 9 (2017) 2535–2540.
- [21] T. Xia, Y. Li, L. Huang, W. Ji, M. Yang, X. Zhao, Room-temperature stable inorganic halide perovskite as potential solid electrolyte for chloride ion batteries, *ACS Appl. Mater. Interfaces* 12 (2020) 18634–18641.
- [22] D. Zhang, H. Nakano, K. Yamamoto, K. Tanaka, T. Yahara, K. Imai, T. Mori, H. Miki, S. Nakanishi, H. Iba, T. Watanabe, T. Uchiyama, K. Amezawa, Y. Uchimoto, Rate-determining process at electrode/electrolyte interfaces for all-solid-state fluoride-ion Batteries, *ACS Appl. Mater. Interfaces* 13 (2021) 30198–30204.
- [23] D. Yu, Q. Zhu, L. Cheng, S. Dong, X. Zhang, H. Wang, N. Yang, Anion solvation regulation enables long cycle stability of graphite cathodes, *ACS Energy Lett.* 6 (2021) 949–958.
- [24] X. Xu, K. Lin, D. Zhou, Q. Liu, X. Qin, S. Wang, S. He, F. Kang, B. Li, G. Wang, Quasi-solid-state dual-ion sodium metal batteries for low-cost energy storage, *Chem* 6 (2020) 902–918.
- [25] Y. Zhang, Y. An, B. Yin, J. Jiang, S. Dong, H. Dou, X. Zhang, A novel aqueous ammonium dual-ion battery based on organic polymers, *J. Mater. Chem. A* 7 (2019) 11314–11320.
- [26] V.K. Davis, C.M. Bates, K. Omichi, B.M. Savoie, N. Momčilović, Q. Xu, W.J. Wolf, M.A. Webb, K.J. Billings, N.H. Chou, Room-temperature cycling of metal fluoride electrodes: liquid electrolytes for high-energy fluoride ion cells, *Science* 362 (2018) 1144–1148.
- [27] X. Hou, Z. Zhang, K. Shen, S. Cheng, Q. He, Y. Shi, D.Y.W. Yu, C.-Y. Su, L.-J. Li, F. Chen, An aqueous rechargeable fluoride ion battery with dual fluoride electrodes, *J. Electrochem. Soc.* 166 (2019) A2419–A2424.
- [28] T. Placke, A. Heckmann, R. Schmich, P. Meister, K. Beltrop, M. Winter, Perspective on performance, cost, and technical challenges for practical dual-ion batteries, *Joule* 2 (2018) 2528–2550.
- [29] Y. Sui, C. Liu, R.C. Masse, Z.G. Neale, M. Atif, M. AlSalhi, G. Cao, Dual-ion batteries: the emerging alternative rechargeable batteries, *Energy Stor. Mater.* 25 (2020) 1–32.
- [30] K.V. Kravchik, M.V. Kovalenko, Rechargeable dual-ion batteries with graphite as a cathode: key challenges and opportunities, *Adv. Energy Mater.* 9 (2019) 1901749.
- [31] M.A. Nowroozi, I. Mohammad, P. Molaiyan, K. Wissel, A.R. Munnangi, O. Clemens, Fluoride ion batteries – past, present, and future, *J. Mater. Chem. A* 9 (2021) 5980–6012.
- [32] P. Meister, V. Sizios, J. Reiter, S. Klamor, S. Rothermel, O. Fromm, H.-W. Meyer, M. Winter, T. Placke, Dual-ion cells based on the electrochemical intercalation of asymmetric fluorosulfonyl-(trifluoromethanesulfonyl) imide anions into graphite, *Electrochim. Acta* 130 (2014) 625–633.
- [33] X. Zhao, S. Ren, M. Bruns, M. Fichtner, Chloride ion battery: a new member in the rechargeable battery family, *J. Power Sources* 245 (2014) 706–711.
- [34] F. Gschwind, H. Euchner, G. Rodriguez-Garcia, Chloride ion battery review: theoretical calculations, state of the art, safety, toxicity, and an outlook towards future developments, *Eur. J. Inorg. Chem.* 2017 (2017) 2784–2799.
- [35] X. Zhao, Z. Zhao-Karger, D. Wang, M. Fichtner, Metal oxychlorides as cathode materials for chloride ion batteries, *Angew. Chem. Int. Ed.* 125 (2013) 13866–13869.
- [36] C. Chen, T. Yu, M. Yang, X. Zhao, X. Shen, An all-solid-state rechargeable chloride ion battery, *Adv. Sci.* 6 (2019) 1802130.
- [37] X. Zhao, Z. Zhao-Karger, M. Fichtner, X. Shen, Halide-based materials and chemistry for rechargeable batteries, *Angew. Chem. Int. Ed.* 59 (2020) 5902–5949.
- [38] C. Derrington, A. Lindner, M. O'keeffe, Ionic conductivity of some alkaline earth halides, *J. Solid State Chem.* 15 (1975) 171–174.
- [39] N. Imanaka, K. Okamoto, G.y. Adachi, Water-insoluble lanthanum oxychloride-based solid electrolytes with ultra-high chloride ion conductivity, *Angew. Chem. Int. Ed.* 41 (2002) 3890–3892.
- [40] H. Matsumoto, T. Miyake, H. Iwahara, Chloride ion conduction in PbCl<sub>2</sub>-PbO system, *Mater. Res. Bull.* 36 (2001) 1177–1184.
- [41] I. Murin, O. Glumov, N. Mel'Nikova, Solid electrolytes with predominant chloride conductivity, *Russ. J. Electrochem.* 45 (2009) 411–416.
- [42] T. Yu, Q. Li, X. Zhao, H. Xia, L. Ma, J. Wang, Y.S. Meng, X. Shen, Nanoconfined iron oxychloride material as a high-performance cathode for rechargeable chloride ion batteries, *ACS Energy Lett.* 2 (2017) 2341–2348.
- [43] P. Gao, M.A. Reddy, X. Mu, T. Diemant, L. Zhang, Z. Zhao-Karger, V.S. Chakravadhanula, O. Clemens, R.J. Behm, M. Fichtner, VOCl as a cathode for rechargeable chloride ion batteries, *Angew. Chem. Int. Ed.* 55 (2016) 4285–4290.
- [44] Q. Yin, D. Rao, G. Zhang, Y. Zhao, J. Han, K. Lin, L. Zheng, J. Zhang, J. Zhou, M. Wei, CoFe-Cl layered double hydroxide: a new cathode material for high-performance chloride ion batteries, *Adv. Funct. Mater.* 29 (2019) 1900983.
- [45] Q. Yin, J. Luo, J. Zhang, S. Zhang, J. Han, Y. Lin, J. Zhou, L. Zheng, M. Wei, Ultralong-life chloride ion batteries achieved by the synergistic contribution of intralayer metals in layered double hydroxides, *Adv. Funct. Mater.* 30 (2019) 1907448.
- [46] Q. Yin, J. Luo, J. Zhang, L. Zheng, G. Cui, J. Han, D. O'Hare, High-performance, long lifetime chloride ion battery using a NiFe-Cl layered double hydroxide cathode, *J. Mater. Chem. A* 8 (2020) 12548–12555.



- [47] L. Wu, Chloride ion conducting polymer electrolytes based on cross-linked PMMA-PP<sub>14</sub>Cl-PP<sub>14</sub>TFSI ion gels for chloride ion batteries, *Int. J. Electrochem. Sci.* (2019) 2414–2421.
- [48] Z. Zhang, K. Shen, Y. Zhou, X. Hou, Q. Ru, Q. He, C.-y. Su, L. Sun, S.H. Aung, F. Chen, The composite electrode of Bi@carbon-texture derived from metal-organic frameworks for aqueous chloride ion battery, *Ionics* 26 (2019) 2395–2403.
- [49] F. Gschwind, D. Steinle, D. Sandbeck, C. Schmidt, E. von Hauff, Facile preparation of chloride-conducting membranes: first step towards a room-temperature solid-state chloride-ion battery, *ChemistryOpen* 5 (2016) 525–530.
- [50] M. Anji Reddy, M. Fichtner, Batteries based on fluoride shuttle, *J. Mater. Chem. A* 21 (2011) 17059–17062.
- [51] V.K. Davis, C.M. Bates, K. Omichi, B.M. Savoie, N. Momcilovic, Q. Xu, W.J. Wolf, M.A. Webb, K.J. Billings, N.H. Chou, S. Alayoglu, R.K. McKenney, I.M. Darolles, N.G. Nair, A. Hightower, D. Rosenberg, M. Ahmed, C.J. Brooks, T.F. Miller III, R.H. Grubbs, S.C. Jones, Room-temperature cycling of metal fluoride electrodes: liquid electrolytes for high-energy fluoride ion cells, *Science* 362 (2018) 1144–1148.
- [52] L. Liu, L. Yang, M. Liu, X. Wang, X. Li, D. Shao, K. Luo, Z. Luo, G. Chen, A flexible tysonite-type La<sub>0.95</sub>Ba<sub>0.05</sub>F<sub>2.95</sub>@ PEO-based composite electrolyte for the application of advanced fluoride ion battery, *J. Energy Storage* 25 (2019) 100886.
- [53] Y. Yifan, G. Yuping, L. Chilin, Progress on fluoride ion shuttle batteries, *Energy Storage Sci. Technol.* 9 (2020) 217.
- [54] I. Mohammad, R. Witter, M. Fichtner, M.A. Reddy, Introducing interlayer electrolytes: toward room-temperature high-potential solid-state rechargeable fluoride ion batteries, *ACS Appl. Energy Mater.* 2 (2019) 1553–1562.
- [55] T. Yoshinari, D. Zhang, K. Yamamoto, Y. Kitaguchi, A. Ochi, K. Nakanishi, H. Miki, S. Nakanishi, H. Iba, T. Uchiyama, T. Watanabe, T. Matsunaga, K. Amezawa, Y. Uchimoto, Kinetic analysis and alloy designs for metal/metal fluorides toward high rate capability for all-solid-state fluoride-ion batteries, *J. Mater. Chem. A* 9 (2021) 7018–7024.
- [56] L. Liu, L. Yang, M. Liu, X. Li, D. Shao, K. Luo, X. Wang, Z. Luo, SnF<sub>2</sub>-based fluoride ion electrolytes MSnF<sub>4</sub> (M = Ba, Pb) for the application of room-temperature solid-state fluoride ion batteries, *J. Alloys Compd.* 819 (2020) 152983.
- [57] V.K. Davis, S. Munoz, J. Kim, C.M. Bates, N. Momcilovic, K.J. Billings, T.F. Miller, R.H. Grubbs, S.C. Jones, Fluoride-ion solvation in non-aqueous electrolyte solutions, *Mater. Chem. Front.* 3 (2019) 2721–2727.
- [58] I. Mohammad, R. Witter, M. Fichtner, M. Anji Reddy, Room-temperature, rechargeable solid-state fluoride-ion batteries, *ACS Appl. Energy Mater.* 1 (2018) 4766–4775.
- [59] H. Bhatia, D.T. Thieu, A.H. Pohl, V.S.K. Chakravadhanula, M.H. Fawey, C. Kubel, M. Fichtner, Conductivity optimization of tysonite-type La<sub>1-x</sub>Ba<sub>x</sub>F<sub>3-x</sub> solid electrolytes for advanced fluoride ion battery, *ACS Appl. Mater. Interfaces* 9 (2017) 23707–23715.
- [60] L. Zhang, M. Anji Reddy, M. Fichtner, Development of tysonite-type fluoride conducting thin film electrolytes for fluoride ion batteries, *Solid State Ionics* 272 (2015) 39–44.
- [61] C. Rongeat, M.A. Reddy, R. Witter, M. Fichtner, Solid electrolytes for fluoride ion batteries: ionic conductivity in polycrystalline tysonite-type fluorides, *ACS Appl. Mater. Interfaces* 6 (2014) 2103–2110.
- [62] J. Wang, J. Hao, C. Duan, X. Wang, K. Wang, C. Ma, A Fluoride-ion-conducting solid electrolyte with both high conductivity and excellent electrochemical stability, *Small* 18 (2022) 2104508.
- [63] J. Chable, B. Dieudonné, M. Body, C. Leguin, M.-P. Crosnier-Lopez, C. Galven, F. Mauvy, E. Durand, S. Fourcade, D. Sheptyakov, Fluoride solid electrolytes: investigation of the tysonite-type solid solutions La<sub>1-x</sub>Ba<sub>x</sub>F<sub>3-x</sub> (x < 0.15), *Dalton Trans.* 44 (2015) 19625–19635.
- [64] I. Mohammad, J. Chable, R. Witter, M. Fichtner, M.A. Reddy, Synthesis of fast fluoride-ion-conductive fluorite-type Ba<sub>1-x</sub>Sb<sub>x</sub>F<sub>2+x</sub> (0.1 < x < 0.4): a potential solid electrolyte for fluoride-ion batteries, *ACS Appl. Mater. Interfaces* 10 (2018) 17249–17256.
- [65] G. Karkera, M.A. Reddy, M. Fichtner, Recent developments and future perspectives of anionic batteries, *J. Power Sources* 481 (2021) 228877.
- [66] L. Zhang, M.A. Reddy, P. Gao, T. Diemant, R. Jürgen Behm, M. Fichtner, Study of all solid-state rechargeable fluoride ion batteries based on thin-film electrolyte, *J. Solid State Electrochem.* 21 (2016) 1243–1251.
- [67] H. Konishi, T. Minato, T. Abe, Z. Ogumi, Electrochemical performance of a lead fluoride electrode mixed with carbon in an electrolyte containing triphenylboroxine as an anion acceptor for fluoride shuttle batteries, *Mater. Chem. Phys.* 226 (2019) 1–5.
- [68] H. Konishi, T. Minato, T. Abe, Z. Ogumi, Influence of electrolyte composition on the electrochemical reaction mechanism of bismuth fluoride electrode in fluoride shuttle battery, *J. Phys. Chem. C* 123 (2019) 10246–10252.
- [69] H. Konishi, T. Minato, T. Abe, Z. Ogumi, Reactivity of the anion acceptor in electrolyte: an important factor in achieving high electrochemical performance of a lead (II) fluoride electrode in a fluoride shuttle battery, *J. Electroanal. Chem.* 871 (2020) 114103.
- [70] K.-i. Okazaki, Y. Uchimoto, T. Abe, Z. Ogumi, Charge-discharge behavior of bismuth in a liquid electrolyte for rechargeable batteries based on a fluoride shuttle, *ACS Energy Lett.* 2 (2017) 1460–1464.
- [71] J.H. Clark, Fluoride ion as a base in organic synthesis, *Chem. Rev.* 80 (1980) 429–452.
- [72] H. Konishi, T. Minato, T. Abe, Z. Ogumi, Improvement of cycling performance in bismuth fluoride electrodes by controlling electrolyte composition in fluoride shuttle batteries, *J. Appl. Electrochem.* 48 (2018) 1205–1211.
- [73] A.C. Kucuk, T. Minato, T. Yamanaka, T. Abe, Effects of LiBOB on salt solubility and BiF<sub>3</sub> electrode electrochemical properties in fluoride shuttle batteries, *J. Mater. Chem. A* 7 (2019) 8559–8567.
- [74] A.C. Kucuk, T. Yamanaka, T. Minato, T. Abe, Influence of LiBOB as an electrolyte additive on the performance of BiF<sub>3</sub>/C for fluoride shuttle batteries, *J. Electrochem. Soc.* 167 (2020) 120508.
- [75] T. Yamanaka, A.C. Kucuk, Z. Ogumi, T. Abe, Evolution of fluoride shuttle battery reactions of BiF<sub>3</sub> microparticles in a CsF/LiBOB/tetraglyme electrolyte: dependence on structure, size, and shape, *ACS Appl. Energy Mater.* 3 (2020) 9390–9400.
- [76] A.C. Kucuk, T. Yamanaka, T. Abe, Fluoride shuttle batteries: on the performance of the BiF<sub>3</sub> electrode in organic liquid electrolytes containing a mixture of lithium bis (oxalato) borate and triphenylboroxine, *Solid State Ionics* 357 (2020) 115499.
- [77] A.C. Kucuk, T. Abe, Electrochemical behavior of CuF<sub>2</sub> as reversible cathode in an organic liquid electrolyte for room-temperature fluoride-shuttle batteries, *J. Power Sources* 496 (2021) 229828.
- [78] A.C. Kucuk, T. Abe, Influence of conductive additives on the electrochemical compatibility of copper fluoride cathode for FSB, *J. Electroanal. Chem.* 900 (2021) 115744.
- [79] X. Jiang, L. Luo, F. Zhong, X. Feng, W. Chen, X. Ai, H. Yang, Y. Cao, Electrolytes for dual-carbon batteries, *ChemElectroChem* 6 (2019) 2615–2629.
- [80] M. Wang, Y. Tang, A Review on the features and progress of dual-ion batteries, *Adv. Energy Mater.* 8 (2018) 1703320.
- [81] A. Heckmann, J. Thienekamp, K. Beltrop, M. Winter, G. Brunklaus, T. Placke, Towards high-performance dual-graphite batteries using highly concentrated organic electrolytes, *Electrochim. Acta* 260 (2018) 514–525.
- [82] L. Xiang, X. Ou, X. Wang, Z. Zhou, X. Li, Y. Tang, Highly concentrated electrolyte towards enhanced energy density and cycling life of dual-ion battery, *Angew. Chem. Int. Ed.* 59 (2020) 17924–17930.
- [83] Y. Wang, S. Wang, Y. Zhang, P.-K. Lee, D.Y. Yu, Unlocking the true capability of graphite-based dual-ion batteries with ethyl methyl carbonate electrolyte, *ACS Appl. Energy Mater.* 2 (2019) 7512–7517.
- [84] H. Fan, L. Qi, M. Yoshio, H. Wang, Hexafluorophosphate intercalation into graphite electrode from ethylene carbonate/ethylmethyl carbonate, *Solid State Ionics* 304 (2017) 107–112.
- [85] H. Fan, L. Qi, H. Wang, Intercalation behavior of hexafluorophosphate into graphite electrode from propylene/ethylmethyl carbonates, *J. Electrochem. Soc.* 164 (2017) A2262.
- [86] H. Fan, J. Gao, L. Qi, H. Wang, Hexafluorophosphate anion intercalation into graphite electrode from sulfolane/ethylmethyl carbonate solutions, *Electrochim. Acta* 189 (2016) 9–15.
- [87] L. Zhang, J. Li, Y. Huang, D. Zhu, H. Wang, Synergetic effect of ethyl methyl carbonate and trimethyl phosphate on BF<sub>4</sub><sup>-</sup> intercalation into a graphite electrode, *Langmuir* 35 (2019) 3972–3979.
- [88] Y. Wang, J. Li, Y. Huang, H. Wang, Anion storage behavior of graphite electrodes in LiBF<sub>4</sub>/sulfone/ethyl methyl carbonate solutions, *Langmuir* 35 (2019) 14804–14811.
- [89] W. Wu, Y. Bai, X. Wang, C. Wu, Sulfone-based high-voltage electrolytes for high energy density rechargeable lithium batteries: progress and perspective, *Chin. Chem. Lett.* 32 (2021) 1309–1315.
- [90] J. Seel, J. Dahn, Electrochemical intercalation of PF<sub>6</sub> into graphite, *J. Electrochem. Soc.* 147 (2000) 892.
- [91] W. Zhao, B. Zheng, H. Liu, F. Ren, J. Zhu, G. Zheng, S. Chen, R. Liu, X. Yang, Y. Yang, Toward a durable solid electrolyte film on the electrodes for Li-ion batteries with high performance, *Nano Energy* 63 (2019) 103815.
- [92] Z. Chen, Y. Tang, X. Du, B. Chen, G. Lu, X. Han, Y. Zhang, W. Yang, P. Han, J. Zhao, G. Cui, Anion solvation reconfiguration enables high-voltage carbonate electrolytes for stable Zn/graphite cells, *Angew. Chem. Int. Ed.* 59 (2020) 21769–21777.
- [93] Y. Wang, Y. Zhang, S. Dong, W. Zhou, P.K. Lee, Z. Peng, C. Dang, P.H.L. Sit, J. Guo, D.Y. Yu, An all-fluorinated electrolyte toward high voltage and long cycle performance dual-ion batteries, *Adv. Energy Mater.* (2022) 2103360.
- [94] J.A. Read, A.V. Cresce, M.H. Ervin, K. Xu, Dual-graphite chemistry enabled by a high voltage electrolyte, *Energy Environ. Sci.* 7 (2014) 617–620.
- [95] Y. Abu-Lebdeh, I. Davidson, High-voltage electrolytes based on adiponitrile for Li-ion batteries, *J. Electrochem. Soc.* 156 (2009) A60–A65.
- [96] X. Tong, X. Ou, N. Wu, H. Wang, J. Li, Y. Tang, High oxidation potential ≈6.0 V of concentrated electrolyte toward high-performance dual-ion battery, *Adv. Energy Mater.* 11 (2021) 2100151.
- [97] J. Wu, X. Wang, Q. Liu, S. Wang, D. Zhou, F. Kang, D. Shanmukaraj, M. Armand, T. Rojo, B. Li, G. Wang, A synergistic exploitation to produce high-voltage quasi-solid-state lithium metal batteries, *Nat. Commun.* 12 (2021) 5746.
- [98] S. Rothermel, P. Meister, G. Schmuelling, O. Fromm, H.-W. Meyer, S. Nowak, M. Winter, T. Placke, Dual-graphite cells based on the reversible intercalation of bis(trifluoromethanesulfonyl)imide anions from an ionic liquid electrolyte, *Energy Environ. Sci.* 7 (2014) 3412–3423.
- [99] G.A. Elia, U. Ulissi, S. Jeong, S. Passerini, J. Hassoun, Exceptional long-life performance of lithium-ion batteries using ionic liquid-based electrolytes, *Energy Environ. Sci.* 9 (2016) 3210–3220.
- [100] M. Nádherná, J. Reiter, J. Moskon, R. Dominko, Lithium bis (fluorosulfonyl) imide-PYR<sub>14</sub>TFSI ionic liquid electrolyte compatible with graphite, *J. Power Sources* 196 (2011) 7700–7706.
- [101] A. Lewandowski, A. Świdarska-Mocek, Properties of the lithium and graphite-lithium anodes in N-methyl-N-propylpyrrolidinium bis (trifluoromethanesulfonyl) imide, *J. Power Sources* 194 (2009) 502–507.

- [102] Y. Fu, C. Chen, C. Qiu, X. Ma, Vinyl ethylene carbonate as an additive to ionic liquid electrolyte for lithium ion batteries, *J. Appl. Electrochem.* 39 (2009) 2597–2603.
- [103] J. Fan, Z. Zhang, Y. Liu, A. Wang, L. Li, W. Yuan, An excellent rechargeable  $\text{PP}_{14}\text{TFSI}$  ionic liquid dual-ion battery, *Chem. Commun.* 53 (2017) 6891–6894.
- [104] Y. Yamada, J. Wang, S. Ko, E. Watanabe, A. Yamada, Advances and issues in developing salt-concentrated battery electrolytes, *Nat. Energy* 4 (2019) 269–280.
- [105] K.V. Kravchik, P. Bhauriyal, L. Piveteau, C.P. Guntlin, B. Pathak, M.V. Kovalenko, High-energy-density dual-ion battery for stationary storage of electricity using concentrated potassium fluorosulfonylimide, *Nat. Commun.* 9 (2018) 4469.
- [106] G. Chen, F. Zhang, Z. Zhou, J. Li, Y. Tang, A flexible dual-ion battery based on PVDF-HFP-modified gel polymer electrolyte with excellent cycling performance and superior rate capability, *Adv. Energy Mater.* 8 (2018) 1801219.
- [107] D. Xie, M. Zhang, Y. Wu, L. Xiang, Y. Tang, A flexible dual-ion battery based on sodium-ion quasi-solid-state electrolyte with long cycling life, *Adv. Funct. Mater.* 30 (2020) 1906770.
- [108] J. Zhu, Y. Xu, Y. Fu, D. Xiao, Y. Li, L. Liu, Y. Wang, Q. Zhang, J. Li, X. Yan, Hybrid aqueous/nonaqueous water-in-bisalt electrolyte enables safe dual ion batteries, *Small* 16 (2020) e1905838.
- [109] J.M. Wrogemann, S. Künne, A. Heckmann, I.A. Rodríguez-Pérez, V. Stozios, B. Yan, J. Li, M. Winter, K. Beltrop, T. Placke, Development of safe and sustainable dual-ion batteries through hybrid aqueous/nonaqueous electrolytes, *Adv. Energy Mater.* 10 (2020) 1902709.
- [110] H. Jiang, Z. Wei, L. Ma, Y. Yuan, J.J. Hong, X. Wu, D.P. Leonard, J. Holoubek, J.J. Razink, W.F. Stickle, F. Du, T. Wu, J. Lu, X. Ji, An aqueous dual-ion battery cathode of  $\text{Mn}_3\text{O}_4$  via reversible insertion of nitrate, *Angew. Chem. Int. Ed.* 58 (2019) 5286–5291.
- [111] C. Yang, J. Chen, X. Ji, T.P. Pollard, X. Lü, C.-J. Sun, S. Hou, Q. Liu, C. Liu, T. Qing, Y. Wang, O. Borodin, Y. Ren, K. Xu, C. Wang, Aqueous Li-ion battery enabled by halogen conversion–intercalation chemistry in graphite, *Nature* 569 (2019) 245–250.
- [112] Z.A. Zafar, G. Abbas, K. Knizek, M. Silhavi, P. Kumar, P. Jiricek, J. Houdková, O. Frank, J. Cervenka, Chaotropic anion based “water-in-salt” electrolyte realizes a high voltage Zn–graphite dual-ion battery, *J. Mater. Chem.* 10 (2022) 2064–2074.
- [113] J. Ge, X. Yi, L. Fan, B. Lu, An all-organic aqueous potassium dual-ion battery, *J. Energy Chem.* 57 (2021) 28–33.
- [114] Q. Nian, S. Liu, J. Liu, Q. Zhang, J. Shi, C. Liu, R. Wang, Z. Tao, J. Chen, All-climate aqueous dual-ion hybrid battery with ultrahigh rate and ultralong life performance, *ACS Appl. Energy Mater.* 2 (2019) 4370–4378.
- [115] H. Glatz, E. Lizundia, F. Pacifico, D. Kundu, An organic cathode based dual-ion aqueous zinc battery enabled by a cellulose membrane, *ACS Appl. Energy Mater.* 2 (2019) 1288–1294.
- [116] Q. Guo, K.-i. Kim, H. Jiang, L. Zhang, C. Zhang, D. Yu, Q. Ni, X. Chang, T. Chen, H. Xia, X. Ji, A High-potential anion-insertion carbon cathode for aqueous zinc dual-ion battery, *Adv. Funct. Mater.* 30 (2020) 2002825.
- [117] H. Li, T. Kurihara, D. Yang, M. Watanabe, T. Ishihara, A novel aqueous dual-ion battery using concentrated bisalt electrolyte, *Energy Stor. Mater.* 38 (2021) 454–461.
- [118] Q. Guo, K.-I. Kim, S. Li, A.M. Scida, P. Yu, S.K. Sandstrom, L. Zhang, S. Sun, H. Jiang, Q. Ni, Reversible insertion of I–Cl interhalogen in a graphite cathode for aqueous dual-ion batteries, *ACS Energy Lett.* 6 (2021) 459–467.
- [119] C. Zhang, W. Ma, C. Han, L.-W. Luo, A. Daniyar, S. Xiang, X. Wu, X. Ji, J.-X. Jiang, Tailoring the linking patterns of polypyrrene cathodes for high-performance aqueous Zn dual-ion batteries, *Energy Environ. Sci.* 14 (2021) 462–472.
- [120] K.i. Kim, L. Tang, J.M. Muratli, C. Fang, X. Ji, A graphite||PTCDI aqueous dual-ion battery, *ChemSusChem* 15 (2022) e202102394.
- [121] Z. Zhang, X. Hu, Y. Zhou, S. Wang, L. Yao, H. Pan, C.-Y. Su, F. Chen, X. Hou, Aqueous rechargeable dual-ion battery based on fluoride ion and sodium ion electrochemistry, *J. Mater. Chem. A* 6 (2018) 8244–8250.
- [122] L. Suo, O. Borodin, T. Gao, M. Olguin, J. Ho, X. Fan, C. Luo, C. Wang, K. Xu, “Water-in-salt” electrolyte enables high-voltage aqueous lithium-ion chemistries, *Science* 350 (2015) 938–943.



# Engineering cathode-electrolyte interface of graphite to enable ultra long-cycle and high-power dual-ion batteries

Yao Wang<sup>a</sup>, Yanjun Zhang<sup>b</sup>, Qiaohui Duan<sup>a</sup>, Pui-Kit Lee<sup>a</sup>, Shuo Wang<sup>a</sup>, Denis Y.W. Yu<sup>a,c,\*</sup>

<sup>a</sup> School of Energy and Environment, City University of Hong Kong, 999077, Hong Kong, China

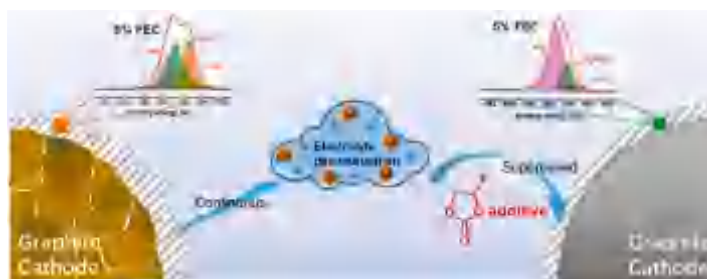
<sup>b</sup> School of Advanced Materials, Peking University Shenzhen Graduate School, Shenzhen, 518055, China

<sup>c</sup> Center of Super-Diamond and Advanced Films (COSDAF), City University of Hong Kong, 999077, Hong Kong, China

## HIGHLIGHTS

- A protective cathode electrolyte interface is constructed on the graphite cathode.
- The graphite surface is effectively stabilized for  $\text{PF}_6^-$  de-/intercalation process.
- The cathode electrolyte interface significantly suppresses electrolyte decomposition.
- The graphite-based dual-ion batteries with FEC additive exhibits low self-discharge.
- Highly reversible/stable cycling and ultrahigh power capability are achieved.

## GRAPHICAL ABSTRACT



## ARTICLE INFO

### Keywords:

Dual-ion battery  
FEC  
Graphite cathode  
 $\text{PF}_6^-$  intercalation  
Cathode electrolyte interface

## ABSTRACT

Dual-ion battery (DIB) can potentially provide higher power, lower cost and faster charging capability than traditional lithium-ion batteries. Even though graphite can effectively accommodate anions as a cathode for DIB, the high working voltage of around 5 V vs.  $\text{Li}/\text{Li}^+$  leads to continuous side reactions, yielding to low Coulombic efficiency ( $\text{CE} < 90\%$ ) and poor cycle life. Here, we demonstrate that fluoroethylene carbonate (FEC) additive can induce a protective cathode electrolyte interface (CEI) on the graphite cathode, effectively suppressing electrolyte decomposition and stabilizing the graphite surface. This CEI enables a high CE ( $\sim 99.0\%$ ) and an excellent cycle stability of 5000 cycles with capacity retention of 85.1% at the cutoff voltage of 5.1 V. The CEI layer can also reduce the self-discharge of the battery. Furthermore, the DIB exhibits a high-rate capability with 93.3% utilization at 30C ( $3000 \text{ mA g}^{-1}$ ), enabling an ultrafast charging time within two minutes. This work sheds light on the features of CEI on graphite cathodes and provides a facile and economically effective strategy to achieve highly reversible/stable cycling of DIBs with high power capability.

## 1. Introduction

While lithium-ion battery (LIB) has become the state-of-the-art energy storage technology which dominates the electronics and electric

vehicle markets, its limited cycle life, safety issues, high cost and environmental concerns make it less competitive for gigawatt-scale applications [1–3]. In the search for alternative low-cost sustainable battery technologies with high energy density and fast charging capability,

\* Corresponding author. G5702, Academic 1, Tat Chee Ave, Kowloon, 999077, Hong Kong, China.

E-mail address: [denisyu@cityu.edu.hk](mailto:denisyu@cityu.edu.hk) (D.Y.W. Yu).

<https://doi.org/10.1016/j.jpowsour.2020.228466>

Received 6 April 2020; Received in revised form 23 May 2020; Accepted 31 May 2020

Available online 17 June 2020

0378-7753/© 2020 Elsevier B.V. All rights reserved.



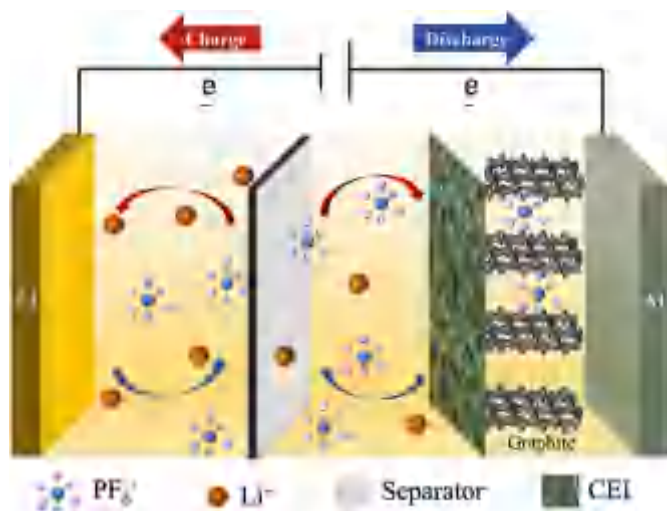


Fig. 1. Illustration of the charge-discharge mechanisms of graphite (+)/Li (-) DIBs.

dual-ion battery (DIB) (see Fig. 1) emerges as a potential candidate [4–12]. Significantly different from the typical “rocking chair” storage mechanism of LIBs where the cations (i.e.  $\text{Li}^+$ ) are transported between the two electrodes for charging/discharging, in DIBs, both cations and anions supplied by the electrolyte are involved in the de-/intercalation process [6,13–15]. Specifically, graphite has been demonstrated as a promising cathode material for DIB which can accommodate anions such as  $\text{AlCl}_4^-$ ,  $\text{ClO}_4^-$ ,  $\text{PF}_6^-$ ,  $\text{TFSI}^-$ ,  $\text{FSI}^-$ , etc. [16–25], reaching an operating potential of around 5 V versus  $\text{Li}/\text{Li}^+$ . Since the cations and anions for charge transfer are supplied by the electrolyte, developing electrolytes that have good stability and compatibility with the electrode is urgently needed for DIB development [25–28]. However, the high working voltage of up to 5 V vs.  $\text{Li}/\text{Li}^+$  on the cathode leads to continuous side reactions such as electrolyte decomposition and electrode exfoliation, yielding to low Coulombic efficiency (CE, <90%) and poor cycle life of DIBs [29–34].

While it has rarely been reported in DIB systems, modifying the cathode-electrolyte interface (CEI) is a feasible strategy to promote cycle stability [31,35–38]. Li et al. pre-formed an anodic solid electrolyte interface (SEI) layer on the graphite electrode and then used it as a cathode in DIB, achieving a capacity retention of 96% after 500 cycles at  $200 \text{ mA g}^{-1}$  [35]. Han et al. introduced a  $\text{Li}_4\text{Ti}_5\text{O}_{12}$  (LTO) layer on the graphite surface by chemical coating and showed a capacity retention of 85.1% after 2000 cycles at 5C rate [31]. Therefore, it is of great significance to construct a robust and stable CEI layer on the cathode with more economical and effective ways, such as the use of electrolyte additives to further impede electrolyte decomposition and minimize capacity loss.

Read et al. employed a fluorinated additive in DIBs for the first time and reported that graphite cells can be sustained for 200 cycles using 1.7 M  $\text{LiPF}_6$  in fluoroethylene carbonate/ethyl methyl carbonate (FEC/EMC) = 4:6 + 5 mM tris(hexafluoro-isopropyl)phosphate (HFIP) [4]. Nevertheless, the role of fluorinated carbonates in improving cycle capability, in particular their effects on the anion de-/intercalation process and on the surface film of graphite cathodes, are still unclear. In this study, we introduce FEC additive in a graphite-based DIBs for  $\text{PF}_6^-$  intercalation and reveal that a stable CEI layer with superior protection capability is constructed on the graphite cathode, which enables DIBs to maintain 85.1% of the maximum capacity even after 5000 cycles. In addition, an ultrafast charge transport is achieved at the interface between the electrolyte and electrode with significant reduction of cell resistance. Through physical characterizations such as X-ray diffraction (XRD), X-ray photoelectron spectroscopy (XPS) and transmission

electron microscopy (TEM), the characteristics of CEI layer on the surface of graphite cathodes are elucidated and their correlations with electrochemical performances of DIBs are explored.

## 2. Experimental section

### 2.1. Cell assembly

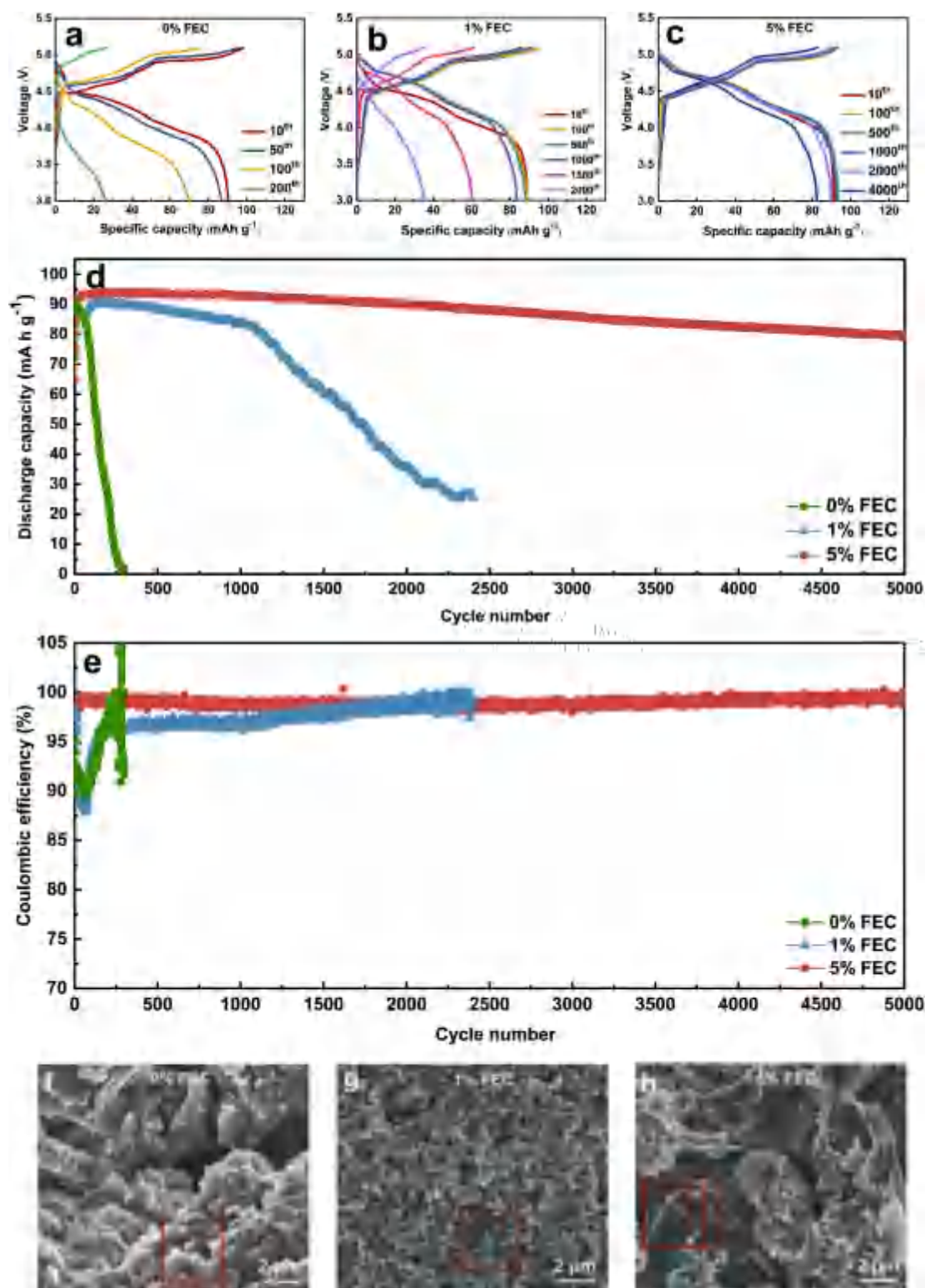
The cathode slurry was prepared by mixing a 85:5:10 mass ratio of graphite (MTI SAG-R) as the active material, carbon black (AB - acetylene black, Alfa Aesar) as the conducting agent and polyacrylic acid (PAA (Sigma Aldrich MW 450,000) in NMP) as the binder. The obtained slurry was coated onto an Al current collector with a doctor blade. The electrodes were dried at  $80^\circ\text{C}$ , cut into 16 mm diameter circular discs and then roll-pressed. The average active mass loading of the electrodes was  $2.5 \text{ mg cm}^{-2}$  with an electrode density of  $1.2 \text{ g cm}^{-3}$  after pressing. Electrodes were further dried at  $150^\circ\text{C}$  for 12 h in vacuum and transferred into an Ar-filled glove box with both  $\text{O}_2$  and  $\text{H}_2\text{O}$  content being less than 1 ppm. The electrodes were assembled into 2032-type coin cells with lithium metal (purchased from China Energy Lithium Co., Ltd., diameter  $\times$  thickness:  $\phi 16 \times 0.6 \text{ mm}$ ) as both counter and reference electrodes. The electrolyte solution was 3 M  $\text{LiPF}_6$  (DoDoChem, purity  $\geq 999\%$ ) dissolved in FEC/EMC (EMC (purity 98%) was purchased from Sigma Aldrich and FEC (purity 99.9%) was from DoDoChem) with FEC fractions of 0%, 1%, 5%, 20% and 40% by volume. The electrolytes were prepared and stirred overnight in the glove box before use. A 19 mm diameter PVdF separator (Merck Millipore Ltd., pore size:  $0.2 \mu\text{m}$ ) wetted with approximately  $200 \mu\text{L}$  electrolyte was used to prevent the cell from short circuit. After assembly, the cells were rested for 8 h to ensure sufficient wetting of the electrodes by the corresponding electrolyte before conducting electrochemical measurements.

### 2.2. Electrochemical tests

Galvanostatic charge-discharge cycling tests were performed using a Neware battery tester in a voltage window from 3.0 to 5.1 V vs.  $\text{Li}/\text{Li}^+$ . Cyclic voltammetry (CV) measurements were performed on a Bio-Logic potentiostat (VMP3) at various scan rate of  $0.1 \text{ mV s}^{-1}$ ,  $0.2 \text{ mV s}^{-1}$ ,  $0.4 \text{ mV s}^{-1}$ ,  $0.6 \text{ mV s}^{-1}$ ,  $0.8 \text{ mV s}^{-1}$  and  $1 \text{ mV s}^{-1}$ . Electrochemical impedance spectroscopy (EIS) of cells at a fully-discharged state after cycling were conducted using the Bio-Logic potentiostat (VMP3) with an AC potential amplitude of 10 mV in the frequency range of 100 kHz to 0.1 Hz. The cells were rested for 8 h to attain a steady state before EIS tests. All electrochemical tests were conducted at room temperature ( $22^\circ\text{C}$ ).

### 2.3. Sample characterizations

In order to investigate the changes on the surface of graphite, the cells were disassembled in the glove box after charge-discharge and the graphite electrodes were washed with dimethyl carbonate (DMC) for several times to remove the salt residuals, followed by drying in the antechamber of the glove box under vacuum. XPS investigations of graphite electrodes at fully charged state were performed on an X-ray photoelectron spectrophotometer (ESCALAB 250X from Thermo Fisher). The transmission electron microscopy (TEM) images of fully charged electrodes after cycling were collected using the JEM-3200FS (from JEOL). The morphology evolutions of the cathode material were studied through field-emission scanning electron microscopy (FE-SEM) analysis on a Zeiss SUPRA-55 microscope. The crystal structure of fully discharged electrodes after cycling was investigated by Raman spectroscopy (Renishaw Invia Raman, 633 nm laser) and XRD (X'Pert3 Powder X-ray Diffractometer, PANalytical). For the XRD tests, the electrodes at fully-discharged state were covered with a Kapton film to protect them from ambient environment, and the data were collected between  $15$  and  $60^\circ$  with an acquisition rate of  $0.1^\circ$  per second with  $\text{Cu K}\alpha_1$  radiation ( $\lambda$



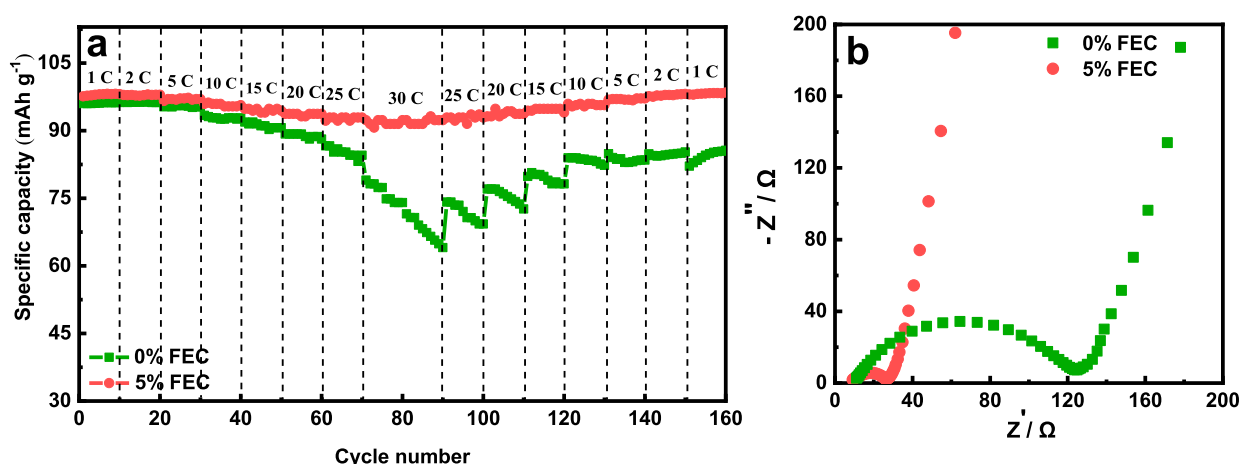
**Fig. 2.** Charge-discharge curves of graphite//Li cells with electrolytes containing (a) 0%, (b) 1% and (c) 5% FEC. (d) Cycling performances and (e) Coulombic efficiency of graphite//Li cells. Cutoff voltage: 3.0–5.1 V, current density: 500 mA g<sup>-1</sup>. SEM images of graphite electrodes after cycling in (f) 0%, (g) 1% and (h) 5% FEC electrolytes for 200 cycles at a charged state of 5.1 V.

= 1.540598 Å) as the X-ray source.

### 3. Results and discussion

In order to investigate the effectiveness of FEC on the de-/intercalation behavior of PF<sub>6</sub><sup>-</sup> from/into the cathode, graphite (+)//Li (-) cells

in 3 M LiPF<sub>6</sub>/EMC electrolytes with various amount of FEC additive were fabricated. These cells were cycled at a constant current of 500 mA g<sup>-1</sup> (5C) and the corresponding charge-discharge curves are displayed in Fig. 2a–c and Fig. S1. The reversible capacity increases during the initial 10 cycles with a decrease in electrode polarization, which is attributed to the gradual activation of graphite that facilitates PF<sub>6</sub><sup>-</sup> transportation



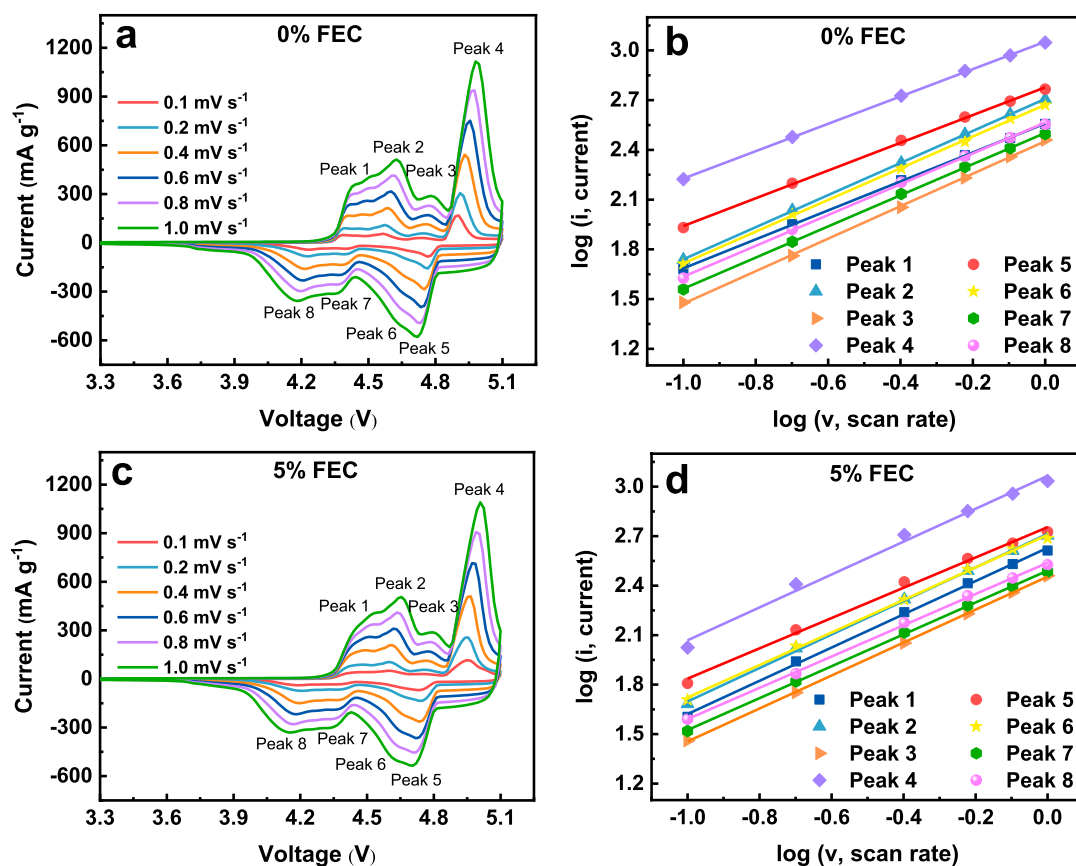
**Fig. 3.** (a) Rate capability of graphite//Li cells in electrolyte with 0% and 5% FEC (charge/discharge current rates: 1C–30C where 1C is taken as 100 mA g<sup>-1</sup>). (b) Nyquist plots of the graphite cathodes at a discharged state after 20 cycles with 0% and 5% FEC-containing electrolytes.

[35]. Here, the of polarization is determined by taking the difference in the average voltages between the charge and discharge processes. After activation (10 cycles), the electrode polarization with 5% FEC electrolyte is  $\sim 0.34$  V compared with that of  $\sim 0.61$  V in FEC-free (0%) electrolyte (Fig. S1), suggesting that FEC addition reduces the charge transfer resistance.

Fig. 1d and e show the cycle performance and Coulombic efficiency (CE) of the graphite electrodes at a current rate of 5C. It is apparent that the capacity decreases rapidly from  $\sim 90$  mAh g<sup>-1</sup> to 26.2 mAh g<sup>-1</sup> after 200 cycles for cells with 0% FEC electrolyte. Charge and discharge

curves (Fig. 2a) display a notable increase in polarization with the vanishing of voltage plateaus corresponding to anion de-/intercalation process within 200 cycles, which is attributed to side reactions such as electrolyte decomposition, as the CE is low particularly during the initial 60 cycles [39]. Apparently, SEM image of the electrode cycled for 200 times without FEC (Fig. 1f) shows a roughened surface compared to that of a pristine graphite electrode (Fig. S2), indicating the occurrence of side reactions on the graphite surface.

Addition of FEC into the electrolyte improves cycle performance and reduces the increase in electrode polarization. With 1% FEC, the cells



**Fig. 4.** CV curves of graphite cathodes in (a) 0% and (c) 5% FEC electrolytes at various scan rates; corresponding log  $i$  versus log  $v$  plots to determine  $b$  value of each peak for cathodes with (b) 0% FEC and (d) 5% FEC electrolytes.



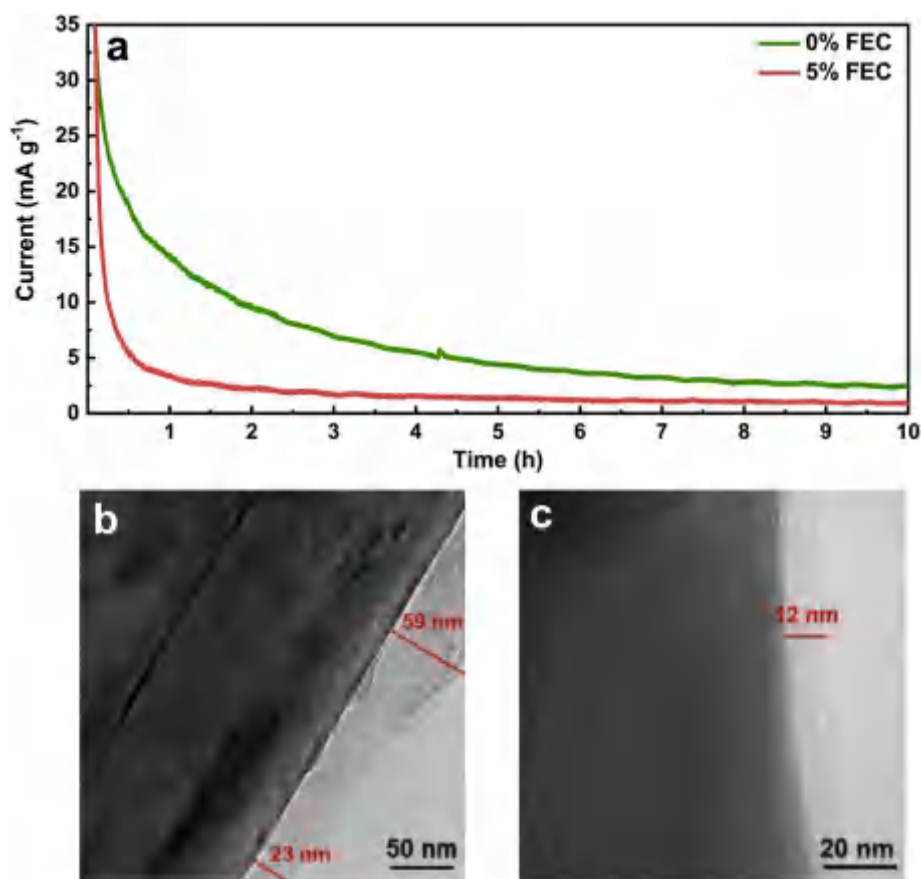


Fig. 5. (a) Potentiostatic profiles of graphite//Li cells at constant voltage of 5.1 V after 5 cycles between 3.0 and 5.1 V. TEM images of graphite electrodes at the fully charged state after 200 cycles in electrolyte with (b) 0% FEC and (c) 5% FEC.

can survive 1000 cycles with a capacity retention of 92.5% ( $83.7 \text{ mAh g}^{-1}$ ), but the capacity decays to only  $25.5 \text{ mAh g}^{-1}$  after 2400 cycles. Ledges are observed on the surface of the graphite particles (highlighted area in Fig. 2g) which are not present in the pristine graphite. These results indicate that 1% dosage is insufficient to suppress irreversible side reactions which can be seen from the low CE during the initial 60 cycles. In sharp contrast, cycle performance is significantly improved with 5% FEC, with a capacity retention as high as 85.1% even after 5000 cycles with an average CE of  $\sim 99.0\%$  throughout the entire period. To the best of our knowledge, this long-term cycling capability is one of the most outstanding results of graphite-based DIBs for  $\text{PF}_6^-$  intercalation (summarized in Table S1). The CE is significantly enhanced particularly during the first 60 cycles and the morphology of the pristine graphite particle is still preserved for the graphite cathode in 5% FEC electrolyte after 200 cycles (Fig. 2h). In addition, well-overlapped voltage profiles are clearly seen with small changes in polarization even after charging/discharging for 4000 cycles, implying a highly reversible  $\text{PF}_6^-$  extraction/insertion process (Fig. 2c) [35]. Similar cycle performance and CE are observed for graphite in electrolytes containing 20% and 40% FEC (see Fig. S3), so 5% FEC electrolyte was selected for further analysis since it has lower viscosity and lower freezing point than those with higher FEC content. It should be noted that FEC additive can also protect the Li metal anode upon cycling, which have been reported previously [40–42].

Besides the excellent long-term cycling performance, the graphite cathodes with 5% FEC also exhibits superb rate capability, as illustrated in Fig. 3a. Even when the current density is raised from  $100 \text{ mA g}^{-1}$  (1C) to  $3 \text{ A g}^{-1}$  (30C), 93.3% of the initial capacity is still obtainable from the graphite cathode in electrolyte with 5% FEC, corresponding to a charge/discharge time within 2 min. In contrast, the electrode cycled in 0% FEC

electrolyte exhibits only  $\sim 74.8\%$  utilization at  $3 \text{ A g}^{-1}$ . Corresponding charge-discharge curves of the two cells at various current rates are shown in Fig. S4. It is clear that the graphite cathodes with FEC electrolyte exhibit smaller increase in polarization with higher current rate, even up to 30C. The extremely high rate capability suggests that FEC additive can improve interfacial dynamics significantly to allow anions de-/intercalate from/into graphite with small resistance.

To gain further insight into the high-power origin of the graphite cathodes, EIS measurements of the graphite electrodes in 0% and 5% FEC electrolytes after 20 cycles were conducted to verify the effect of FEC addition (see Fig. 3b). The result shows that the charge transfer resistance of the graphite electrode cycled in 5% FEC is smaller than that with 0% FEC, indicating FEC addition can remarkably reduce the cell impedance. This is consistent with the smaller electrode polarization with FEC-containing electrolyte in Fig. 2c.

To investigate the charge storage kinetics of graphite cathodes, the representative CV profiles of graphite electrodes in 0% and 5% FEC-containing electrolytes at various sweep rates from  $0.1$  to  $1.0 \text{ mV s}^{-1}$  were displayed in Fig. 4. The relationship between the peak currents ( $i$ ) and the scan rates ( $v$ ) follows the power law:

$$i = av^b \quad (1)$$

where  $b$  can be obtained from the slope of the fitted line. In general, the electrochemical reaction is dominated by semi-infinite diffusion when  $b = 0.5$ , while the reaction is pseudocapacitive when  $b = 1$  [43,44]. From our data, the  $b$  values of the CV peaks for graphite electrode with FEC-free electrolyte are calculated to be 0.87 (peak 1), 0.96 (peak 2), 0.94 (peak 3), 0.82 (peak 4), 0.82 (peak 5), 0.95 (peak 6), 0.93 (peak 7) and 0.92 (peak 8). The  $b$  values are less than 1, indicating the kinetics of charge-discharge of  $\text{PF}_6^-$  anions into the graphite cathodes is partially

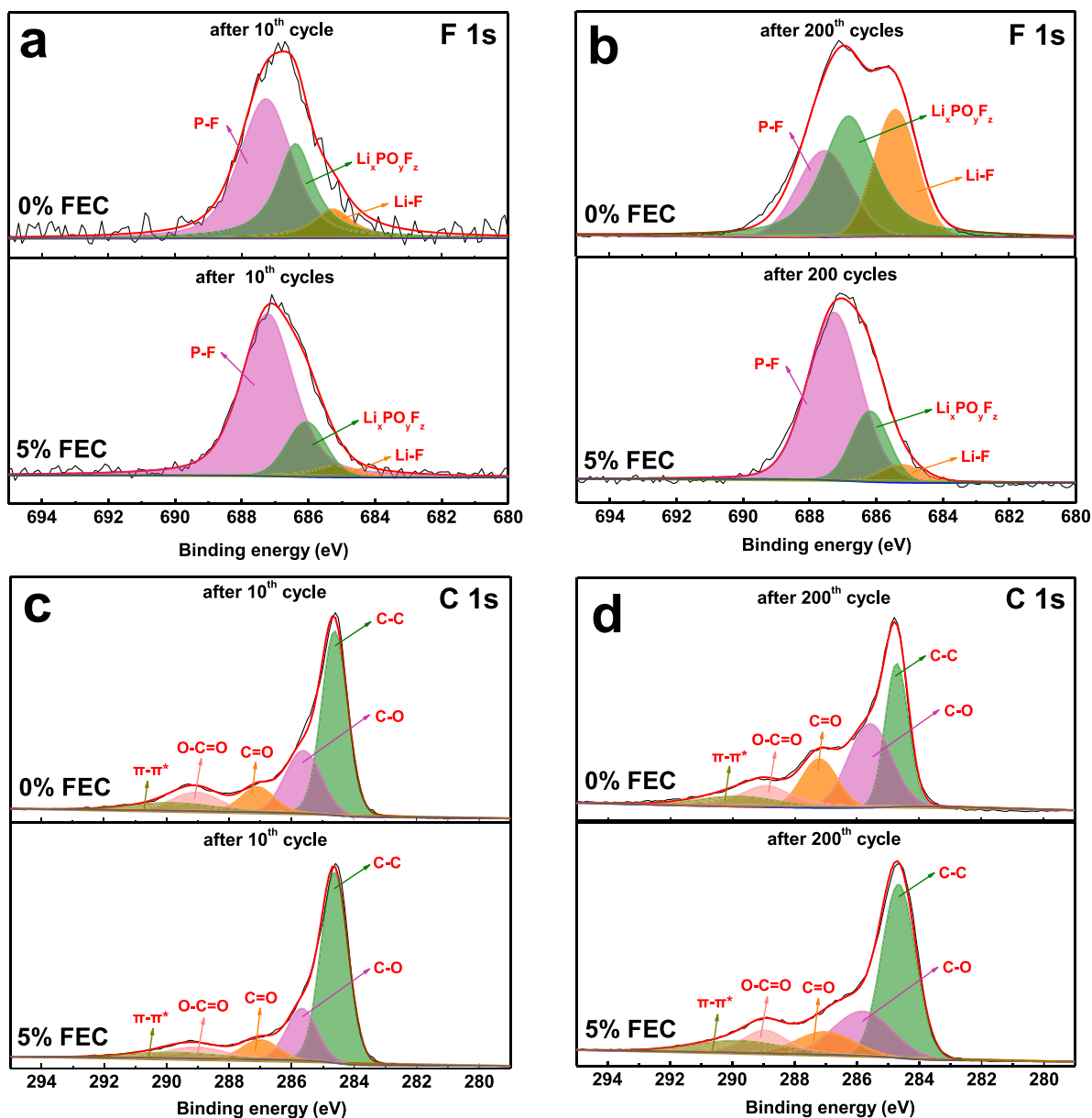


Fig. 6. XPS spectra (F1s and C1s) of graphite cathodes at 5.1 V tested in 0% and 5% FEC-containing electrolytes: (a and c) after 10th cycle; (b and d) after 200th cycle, respectively.

diffusion-limited [45,46]. It is interesting to note that with FEC addition,  $b$  values of the peaks become 1.03 (peak 1), 1.03 (peak 2), 1.01 (peak 3), 1.04 (peak 4), 0.93 (peak 5), 1.00 (peak 6), 0.97 (peak 7) and 0.96 (peak 8). All  $b$  values are close to 1, suggesting that FEC-containing electrolyte changes the kinetics of the graphite surface to allow fast and reversible anion de-/intercalation.

The addition of FEC also reduces the parasitic reactions on the graphite surface. This is illustrated by potentiostatic tests where the graphite cells in electrolytes with 0% and 5% FEC were first charged and discharged for 5 cycles, and then held at a constant voltage of 5.1 V (see Fig. 5a). During the 5.1 V-holding period, an extra capacity of about  $63.8 \text{ mAh g}^{-1}$  and  $19.5 \text{ mAh g}^{-1}$  are observed for the graphite in 0% and 5% FEC electrolyte, respectively, as calculated from the area underneath the curves of Fig. 5a. The capacity is attributed to irreversible side reaction at high voltage, which can be significantly suppressed by FEC additive. Both the impedance and potentiostatic test results suggest that there is a CEI layer on the surface of the graphite material which is induced with FEC addition.

To visualize the CEI layer on the surface of the active materials, TEM images of the cycled graphite cathodes were conducted, as presented in Fig. 5b and c. It is clear that the graphite surface after cycling in FEC-free electrolyte is covered with a non-uniform and thick CEI layer with a thickness ranging from 23 nm to 59 nm. In comparison, 5% FEC electrolyte enables a more homogeneous and thinner CEI layer with a thickness of  $\sim 12 \text{ nm}$  on the surface of the graphite cathode. The thinner CEI is consistent with the smaller impedance of the electrode cycled with FEC additive.

The change in chemical compositions of the CEI layer on graphite cathodes with cycling (after 10th and 200th cycles) were investigated by XPS characterizations to understand the effects of FEC additive on the surface chemistries (Fig. 6 and Fig. S5). After 10th cycle, we can see a difference in the chemical composition of the CEI layer on the surface of the graphite electrodes from the F 1s spectra with or without FEC additive (Fig. 6a) - the relative fractions of LiF and  $\text{Li}_x\text{PO}_y\text{F}_z$  species are significantly reduced in the presence of FEC additive compared with those without FEC. This is attributed to less decomposition of  $\text{LiPF}_6$  salt

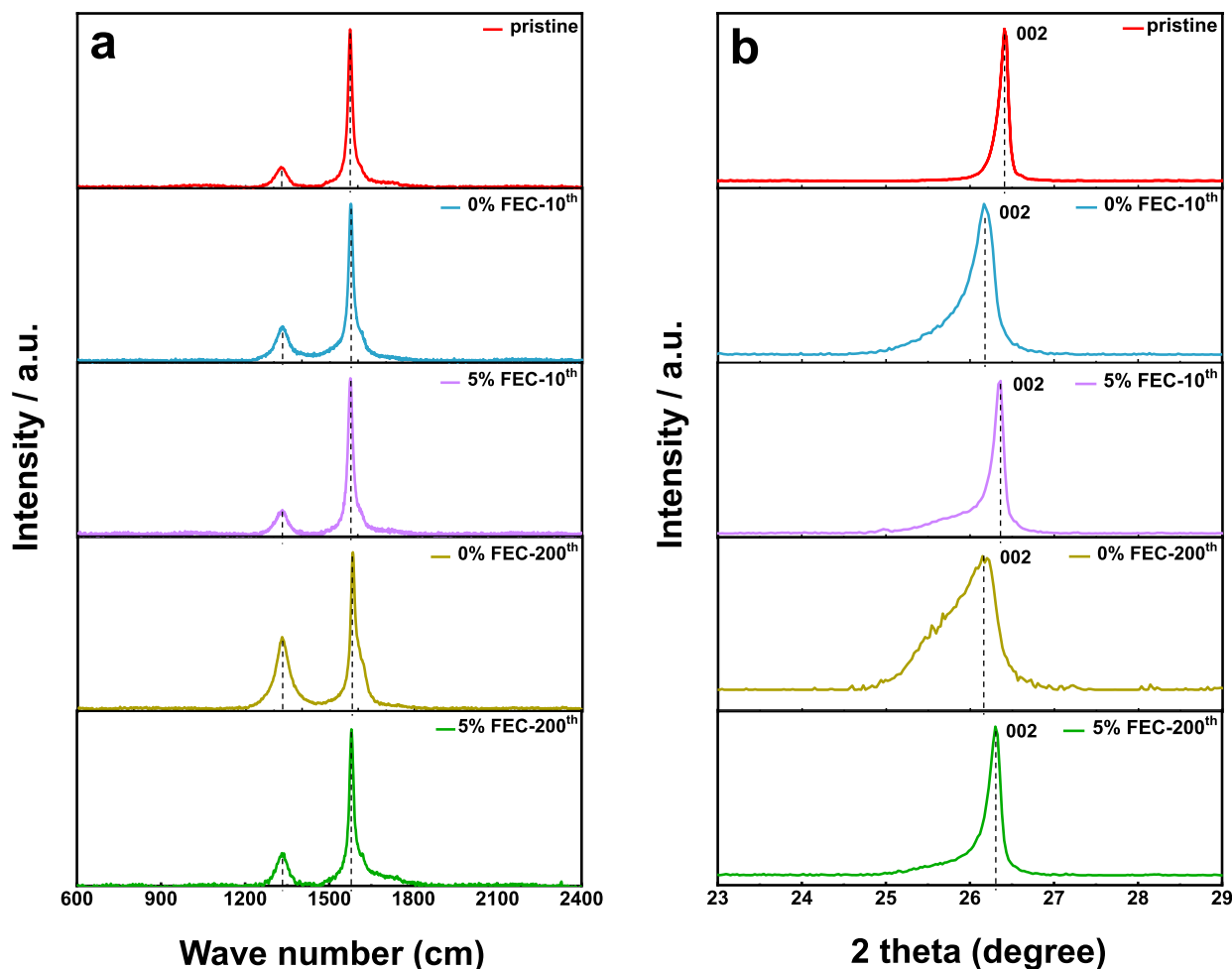


Fig. 7. (a) Raman spectra and (b) XRD patterns of the pristine and cycled graphite cathodes (after 10th or 200th cycles) with 0% and 5% FEC electrolytes.

( $\text{LiPF}_6 \rightleftharpoons \text{LiF} + \text{PF}_5$  and  $\text{PF}_5 + 2\text{xLi}^+ + 2\text{xe}^- \rightarrow \text{Li}_x\text{PF}_{5-x} + \text{xLiF}$ ) on the graphite surface with FEC additive [47–49]. The reduced amount of electronically-insulating LiF probably leads to a less-resistive CEI layer, contributing to the observed reduction in electrode resistance and excellent rate capability of graphite cathodes in 5% FEC electrolyte. In addition, the CEI formed with 5% FEC is robust. Even after 200 cycles, no apparent increase in LiF and  $\text{Li}_x\text{PO}_y\text{F}_z$  contents is observed on graphite cathodes with FEC electrolyte, as opposed to that for the electrode tested in 0% FEC electrolyte (Fig. 6b).

For the C 1s XPS spectra, similar chemical compositions corresponding to C–O (285.6 eV), C=O (287.0 eV) and O–C=O (288.9 eV) bonds are observed on the graphite cathodes with or without FEC after 10th cycle (Fig. 6c and Fig. S5b). However, after 200 cycles, an obvious increase in the relative content of oxygenated organic groups is observed on the graphite tested in the FEC-free electrolyte (Fig. 6d), which is attributed to further electrolyte decomposition and oxidation of the graphite surface [50,51]. In contrast, the changes in XPS peak areas are much smaller with 5% FEC, indicating that side reactions are suppressed. The XPS results confirm that FEC additive is crucial in generating a stable CEI, mitigating the undesirable reactions between the active material and electrolyte and enhancing the interfacial stability for cycling.

Previous reports revealed that the crystallinity of the graphite affects the cycle stability of DIB [52]. As presented in Fig. 7a, Raman results show two sharp peaks at  $1580\text{ cm}^{-1}$  (G band) and  $1350\text{ cm}^{-1}$  (D band), representing the crystalline lattice and the disordered structure of graphite (such as defects), respectively [8,53–55]. The level of

defectiveness in graphite can be estimated by the intensity ratio of the D band and G band ( $I_D/I_G$ ). The  $I_D/I_G$  of the graphite electrodes increase from 0.13 of the pristine graphite to 0.23 and 0.46 after cycling in the FEC-free electrolyte for 10 and 200 cycles (see Table S2), respectively, suggesting a gradual change in structure after repeated  $\text{PF}_6^-$  de-/intercalation. In comparison, slight increase in  $I_D/I_G$  of graphite cycled in 5% FEC electrolyte reveals that FEC-derived CEI can suppress the detrimental structural collapse of graphite cathodes.

The protection of graphite structure by this stable CEI can also be verified by studying the changes in the degree of graphitization (DG) of the graphite with cycling. The DG can be defined by the following equation [53,56]:

$$DG(\%) = \frac{0.3440 - d(002)}{0.3440 - 0.3354} \times 100\% \quad (2)$$

where  $d(002)$  is the interlayer spacing of the graphite, and 0.3440 nm and 0.3354 nm are the  $d(002)$  of the fully non-graphitized carbon and the ideal graphite crystallite, respectively. XRD patterns of the pristine and cycled graphite electrode are shown in Fig. 7b. While the pristine graphite has a  $d(002)$  spacing of 0.3373 nm and DG of 77.9%, the graphite electrode in electrolyte without FEC shows  $d(002)$  spacing of 0.3403 and 0.3412 nm after 10th and 200th cycle, respectively, corresponding to DG of 43.0% and 32.5%. It is notable that compared to the highly crystallization structure of graphite electrode which exhibits a sharp (002) peak, the broader peak of graphite after 200th cycle in FEC-free electrolyte indicates a randomly arranged crystal phase (002). In sharp contrast, graphite electrodes in 5% FEC-containing electrolyte



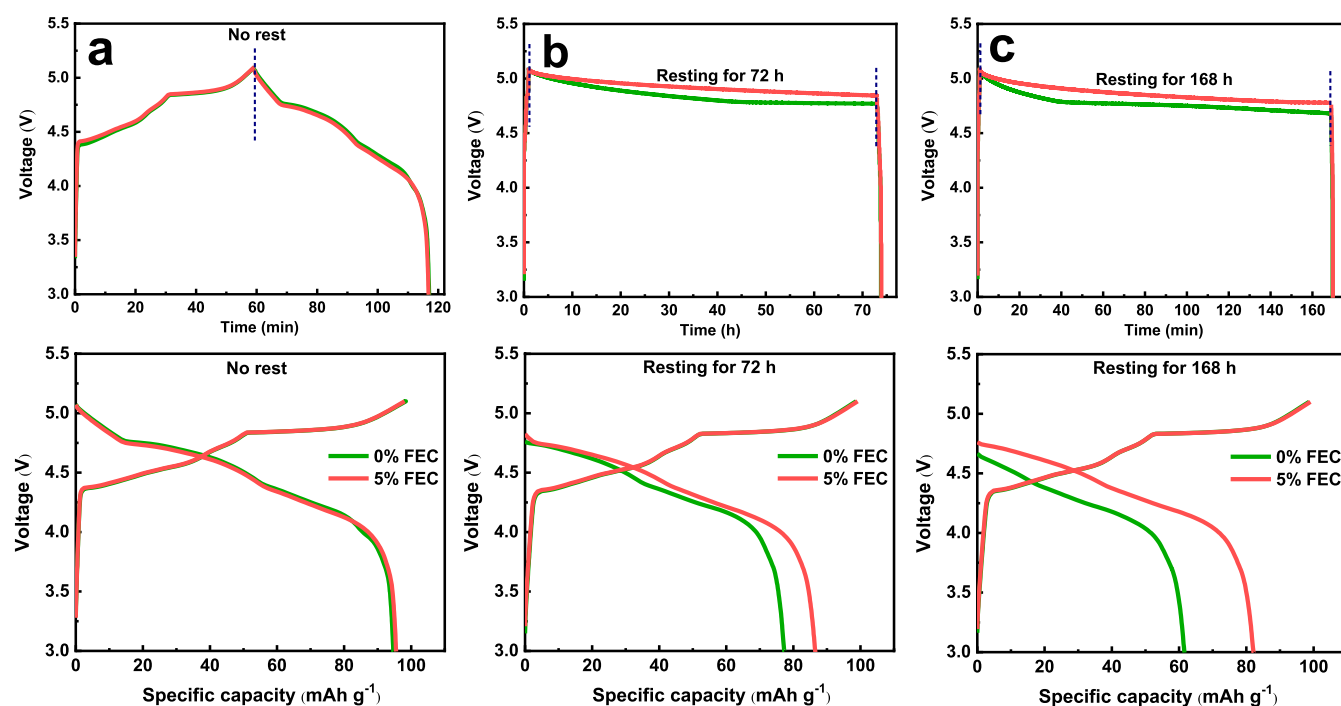


Fig. 8. The voltage-time and the charge/discharge curves after charging to 5.1 V and then resting for (a) 0, (b) 72 and (c) 168 h before discharging.

display DG of 72.1% and 65.1% after 10th and 200th cycle, respectively, suggesting the graphite cathode can maintain a more orderly and highly-integrated graphitic structure after cycling in FEC-containing electrolyte, largely improving the cycle stability of  $\text{PF}_6^-$  de-/intercalation.

The self-discharge is a critical challenge in DIBs for large-scale applications which has largely been neglected. Therefore, the self-discharge behavior was investigated by charging the cells to the upper cut-off voltage of 5.1 V and stored for 0, 72 or 168 h, followed by discharging to 3 V, as illustrated in Fig. 8. It is remarkable to find that the cell with 0% FEC electrolyte experiences a faster voltage drop and a larger capacity loss in contrast to the cell with FEC-containing electrolyte - specifically, the electrode tested in FEC-free electrolyte shows a rapid voltage drop to 4.68 V after 168 h rest, and the available capacity is reduced to  $61.5 \text{ mAh g}^{-1}$ ; in comparison, the electrode tested in 5% FEC electrolyte shows a smaller voltage drop to 4.78 V after 168 h with  $82.2 \text{ mAh g}^{-1}$  available upon discharge. Thus, FEC additive is able to reduce self-discharge. We attribute it to the reduced amount of electrolyte oxidation under high voltage. A possible mechanism is proposed to account for part of the self-discharge phenomenon (Fig. S6). However, the same electrochemical curves as that of the pristine cell can be observed for subsequent recharging of the cells (Fig. S7), indicating that self-discharge is mostly a reversible process. Future work should be conducted to further reduce the self-discharge of DIB and to reveal the involved fundamental mechanism.

#### 4. Conclusion

In summary, DIB with excellent cyclability, low self-discharge and high power is enabled by forming an effective CEI layer on the graphite cathode with FEC additive. This protective CEI with less LiF can reduce undesirable electrolyte decomposition on the graphite surface and prevent the graphite from structure deterioration, stabilizing the highly reversible  $\text{PF}_6^-$  anion de-/intercalation process. As a result, the graphite cathode displays high average CE of 99.0% and an extremely long cycle life of 5000 cycles with 85.1% capacity retention at  $500 \text{ mA g}^{-1}$ . Impressively, an ultrafast charging time within two minutes (93.3% capacity utilization at 30C) is achieved with the LiF-less CEI. In addition,

self-discharge is significantly reduced with FEC, although the mechanism of self-discharge needs to be further studied. Overall, this work offers insights into the characteristics of the CEI on the graphite cathode and provides a feasible approach to develop DIBs with superior cycle stability and high power capability.

#### Declaration of competing interest

The authors declare that they have no known competing financial interests or personal relationships that could have appeared to influence the work reported in this paper.

#### CRediT authorship contribution statement

**Yao Wang:** Conceptualization, Methodology, Investigation, Formal analysis, Writing - original draft. **YanJun Zhang:** Investigation, Formal analysis. **Qiaohui Duan:** Resources, Investigation. **Pui-Kit Lee:** Validation, Formal analysis. **Shuo Wang:** Investigation, Data curation. **Denis Y.W. Yu:** Supervision, Writing - review & editing.

#### Acknowledgements

This work was supported by the Strategic Research Grant (Project #7005285) from City University of Hong Kong.

#### Appendix A. Supplementary data

Supplementary data to this article can be found online at <https://doi.org/10.1016/j.jpowsour.2020.228466>.

#### References

- [1] S. Hy, H. Liu, M. Zhang, D. Qian, B.-J. Hwang, Y.S. Meng, Performance and design considerations for lithium excess layered oxide positive electrode materials for lithium ion batteries, *Energy Environ. Sci.* 9 (2016) 1931–1954, <https://doi.org/10.1039/C5EE03573B>.
- [2] K.V. Kravchik, P. Bhauriyal, L. Piveteau, C.P. Guntlin, B. Pathak, M.V. Kovalenko, High-energy-density dual-ion battery for stationary storage of electricity using




- concentrated potassium fluorosulfonylimide, *Nat. Commun.* 9 (2018) 4469, <https://doi.org/10.1038/s41467-018-06923-6>.
- [3] R. Schmich, R. Wagner, G. Hörpel, T. Placke, M. Winter, Performance and cost of materials for lithium-based rechargeable automotive batteries, *Nat. Energy* 3 (2018) 267–278, <https://doi.org/10.1038/s41560-018-0107-2>.
  - [4] J.A. Read, A.V. Cresce, M.H. Ervin, K. Xu, Dual-graphite chemistry enabled by a high voltage electrolyte, *Energy Environ. Sci.* 7 (2014) 617–620, <https://doi.org/10.1039/C3EE43333A>.
  - [5] M. Zhang, X. Song, X. Ou, Y. Tang, Rechargeable batteries based on anion intercalation graphite cathodes, *Energy Storage Mater.* 16 (2019) 65–84, <https://doi.org/10.1016/j.ensm.2018.04.023>.
  - [6] B. Heidrich, A. Heckmann, K. Beltrop, M. Winter, T. Placke, Unravelling charge/discharge and capacity fading mechanisms in dual-graphite battery cells using an electron inventory model, *Energy Storage Mater.* 21 (2019) 414–426, <https://doi.org/10.1016/j.ensm.2019.05.031>.
  - [7] T. Placke, A. Heckmann, R. Schmich, P. Meister, K. Beltrop, M. Winter, Perspective on performance, cost, and technical challenges for practical dual-ion batteries, *Joule* 2 (2018) 2528–2550, <https://doi.org/10.1016/j.joule.2018.09.003>.
  - [8] K.V. Kravchyk, M.V. Kovalenko, Rechargeable dual-ion batteries with graphite as a cathode: key challenges and opportunities, *Adv. Energy Mater.* 9 (2019) 1901749, <https://doi.org/10.1002/aenm.201901749>.
  - [9] X. Zhou, Q. Liu, C. Jiang, B. Ji, X. Ji, Y. Tang, H.M. Cheng, Strategies towards low-cost dual-ion batteries with high performance, *Angew. Chem. Int. Ed.* 59 (2020) 3802–3832, <https://doi.org/10.1002/anie.201814294>.
  - [10] Y. Sui, C. Liu, R.C. Masse, Z.G. Neale, M. Atif, M. Alsalhi, G. Cao, Dual-Ion Batteries: the emerging alternative rechargeable batteries, *Energy Storage Mater.* 25 (2020) 1–32, <https://doi.org/10.1016/j.ensm.2019.11.003>.
  - [11] D. Yu, L. Cheng, M. Chen, J. Wang, W. Zhou, W. Wei, H. Wang, High-performance phosphorus-graphite dual-ion battery, *ACS Appl. Mater. Interfaces* 11 (2019) 45755–45762, <https://doi.org/10.1021/acsami.9b16819>.
  - [12] E. Zhang, W. Cao, B. Wang, X. Yu, L. Wang, Z. Xu, B. Lu, A novel aluminum dual-ion battery, *Energy Storage Mater.* 11 (2018) 91–99, <https://doi.org/10.1016/j.ensm.2017.10.001>.
  - [13] M. Winter, B. Barnett, K. Xu, Before Li ion batteries, *Chem. Rev.* 118 (2018) 11433–11456, <https://doi.org/10.1021/acs.chemrev.8b00422>.
  - [14] I.A. Rodríguez-Pérez, X. Ji, Anion hosting cathodes in dual-ion batteries, *ACS Energy Lett.* 2 (2017) 1762–1770, <https://doi.org/10.1021/acseenergylett.7b00321>.
  - [15] R.J. Dubey, J. Nussli, K. V. Kravchyk, M.D. Rossell, M. Campanini, R. Erni, M.V. Kovalenko, N.P. Stadie, Zeolite-templated carbon as the cathode for a high energy density dual-ion battery, *ACS Appl. Mater. Interfaces* 11 (2019) 17686–17696, <https://doi.org/10.1021/acsami.9b03886>.
  - [16] H. Fan, L. Qi, M. Yoshio, H. Wang, Hexafluorophosphate intercalation into graphite electrode from ethylene carbonate/ethylmethyl carbonate, *Solid State Ionics* 304 (2017) 107–112, <https://doi.org/10.1016/j.ssi.2017.04.001>.
  - [17] J. Gao, S. Tian, L. Qi, H. Wang, Intercalation manners of perchlorate anion into graphite electrode from organic solutions, *Electrochim. Acta* 176 (2015) 22–27, <https://doi.org/10.1016/j.electacta.2015.06.152>.
  - [18] M.C. Lin, M. Gong, B. Lu, Y. Wu, D.Y. Wang, M. Guan, M. Angell, C. Chen, J. Yang, B.J. Hwang, H. Dai, An ultrafast rechargeable aluminium-ion battery, *Nature* 520 (2015) 325–328, <https://doi.org/10.1038/nature14340>.
  - [19] S. Rothermel, P. Meister, G. Schmuelling, O. Fromm, H.-W. Meyer, S. Nowak, M. Winter, T. Placke, Dual-graphite cells based on the reversible intercalation of bis(trifluoromethanesulfonyl)imide anions from an ionic liquid electrolyte, *Energy Environ. Sci.* 7 (2014) 3412–3423, <https://doi.org/10.1039/C4EE01873G>.
  - [20] S. Aladinli, F. Bordet, K. Ahlbrecht, J. Tübke, M. Holzapfel, Anion intercalation into a graphite cathode from various sodium-based electrolyte mixtures for dual-ion battery applications, *Electrochim. Acta* 231 (2017) 468–478, <https://doi.org/10.1016/j.electacta.2017.02.041>.
  - [21] S. Miyoshi, T. Akbay, T. Kurihara, T. Fukuda, A.T. Staykov, S. Ida, T. Ishihara, Fast diffusivity of PF<sub>6</sub><sup>-</sup> anions in graphitic carbon for a dual-carbon rechargeable battery with superior rate property, *J. Phys. Chem. C* 120 (2016) 22887–22894, <https://doi.org/10.1021/acs.jpcc.6b07957>.
  - [22] T. Placke, S. Rothermel, O. Fromm, P. Meister, S.F. Lux, J. Huesker, H.-W. Meyer, M. Winter, Influence of graphite characteristics on the electrochemical intercalation of bis(trifluoromethanesulfonyl) imide anions into a graphite-based cathode, *J. Electrochem. Soc.* 160 (2013) A1979–A1991, <https://doi.org/10.1149/2.027311jes>.
  - [23] K. Beltrop, P. Meister, S. Klein, A. Heckmann, M. Grünebaum, H.-D. Wiemhöfer, M. Winter, T. Placke, Does size really matter? New insights into the intercalation behavior of anions into a graphite-based positive electrode for dual-ion batteries, *Electrochim. Acta* 209 (2016) 44–55, <https://doi.org/10.1016/j.electacta.2016.05.012>.
  - [24] K. Beltrop, S. Beuker, A. Heckmann, M. Winter, T. Placke, Alternative electrochemical energy storage: potassium-based dual-graphite batteries, *Energy Environ. Sci.* 10 (2017) 2090–2094, <https://doi.org/10.1039/C7EE01535F>.
  - [25] C.Y. Chan, P.-K. Lee, Z. Xu, D.Y.W. Yu, Designing high-power graphite-based dual-ion batteries, *Electrochim. Acta* 263 (2018) 34–39, <https://doi.org/10.1016/j.electacta.2018.01.036>.
  - [26] J. Seel, J. Dahn, Electrochemical intercalation of PF<sub>6</sub><sup>-</sup> into graphite, *J. Electrochem. Soc.* 147 (2000) 892, <https://doi.org/10.1149/1.1393288>.
  - [27] M. Wang, Y. Tang, A review on the features and progress of dual-ion batteries, *Adv. Energy Mater.* 8 (2018) 1703320, <https://doi.org/10.1002/aenm.201703320>.
  - [28] Y. Wang, S. Wang, Y. Zhang, P.-K. Lee, D.Y.W. Yu, Unlocking the true capability of graphite-based dual-ion batteries with ethyl methyl carbonate electrolyte, *ACS Appl. Energy Mater.* 2 (2019) 7512–7517, <https://doi.org/10.1021/acs.aem.9b01499>.
  - [29] P. Qin, M. Wang, N. Li, H. Zhu, X. Ding, Y. Tang, Bubble-sheet-like interface design with an ultrastable solid electrolyte layer for high-performance dual-ion batteries, *Adv. Mater.* 29 (2017) 1606805, <https://doi.org/10.1002/adma.201606805>.
  - [30] G. Wang, M. Yu, J. Wang, D. Li, D. Tan, M. Löffler, X. Zhuang, K. Müllen, X. Feng, Self-activating, capacitive anion intercalation enables high-power graphite cathodes, *Adv. Mater.* 30 (2018) 1800533, <https://doi.org/10.1002/adma.201800533>.
  - [31] X. Han, G. Xu, Z. Zhang, X. Du, P. Han, X. Zhou, G. Cui, L. Chen, An in situ interface reinforcement strategy achieving long cycle performance of dual-ion batteries, *Adv. Energy Mater.* 9 (2019) 1804022, <https://doi.org/10.1002/aenm.201804022>.
  - [32] J.A. Read, In-situ studies on the electrochemical intercalation of hexafluorophosphate anion in graphite with selective cointercalation of solvent, *J. Phys. Chem. C* 119 (2015) 8438–8446, <https://doi.org/10.1021/jp5115465>.
  - [33] A. Zhou, Q. Liu, Y. Wang, W. Wang, X. Yao, W. Hu, L. Zhang, X. Yu, J. Li, H. Li, Al<sub>2</sub>O<sub>3</sub> surface coating on LiCoO<sub>2</sub> through a facile and scalable wet-chemical method towards high-energy cathode materials withstanding high cutoff voltages, *J. Mater. Chem. A* 5 (2017) 24361–24370, <https://doi.org/10.1039/C7TA07312G>.
  - [34] J. Gao, M. Yoshio, L. Qi, H. Wang, Solvation effect on intercalation behaviour of tetrafluoroborate into graphite electrode, *J. Power Sources* 278 (2015) 452–457, <https://doi.org/10.1016/j.jpowsour.2014.12.107>.
  - [35] W.H. Li, Q.L. Ning, X.T. Xi, B.H. Hou, J.Z. Guo, Y. Yang, B. Chen, X.-L. Wu, Highly improved cycling stability of anion de-/intercalation in the graphite cathode for dual-ion batteries, *Adv. Mater.* 31 (2019) 1804766, <https://doi.org/10.1002/adma.201804766>.
  - [36] K.W. Hathcock, J.C. Brumfield, C.A. Goss, E.A. Irene, R.W. Murray, Incipient electrochemical oxidation of highly oriented pyrolytic graphite: correlation between surface blistering and electrolyte anion intercalation, *Anal. Chem.* 67 (1995) 2201–2206, <https://doi.org/10.1021/ac00109a045>.
  - [37] G. Bussetti, R. Yivlialin, D. Allia, A. Li Bassi, C. Castiglioni, M. Tommasini, C. S. Casari, M. Passoni, P. Biagioni, F. Ciccacci, L. Duò, Disclosing the early stages of electrochemical anion intercalation in graphite by a combined atomic force microscopy/scanning tunneling microscopy approach, *J. Phys. Chem. C* 120 (2016) 6088–6093, <https://doi.org/10.1021/acs.jpcc.6b00407>.
  - [38] X. Qi, B. Bliznac, A. DuPasquier, P. Meister, T. Placke, M. Oljaca, J. Li, M. Winter, Investigation of PF<sub>6</sub><sup>-</sup> and TFSI<sup>-</sup> anion intercalation into graphitized carbon blacks and its influence on high voltage lithium ion batteries, *Phys. Chem. Chem. Phys.* 16 (2014) 25306–25313, <https://doi.org/10.1039/c4cp04113e>.
  - [39] E.J. Park, Y.-G. Kwon, S. Yoon, K.Y. Cho, Synergistic high-voltage lithium ion battery performance by dual anode and cathode stabilizer additives, *J. Power Sources* 441 (2019) 126668, <https://doi.org/10.1016/j.jpowsour.2019.05.074>.
  - [40] R. Mogi, M. Inaba, S.-K. Jeong, Y. Iriyama, T. Abe, Z. Ogumi, Effects of some organic additives on lithium deposition in propylene carbonate, *J. Electrochem. Soc.* 149 (2002) A1578–A1583, <https://doi.org/10.1149/1.1516770>.
  - [41] X.Q. Zhang, X.B. Cheng, X. Chen, C. Yan, Q. Zhang, Fluoroethylene carbonate additives to render uniform Li deposits in lithium metal batteries, *Adv. Funct. Mater.* 27 (2017) 1605989, <https://doi.org/10.1002/adfm.201605989>.
  - [42] X.Q. Zhang, X.B. Cheng, Q. Zhang, Advances in interfaces between Li metal anode and electrolyte, *Adv. Mater. Interfaces* 5 (2018) 1701097, <https://doi.org/10.1002/admi.201701097>.
  - [43] Q. Guo, Y. Ma, T. Chen, Q. Xia, M. Yang, H. Xia, Y. Yu, Cobalt sulfide quantum dot embedded N/S-doped carbon nanosheets with superior reversibility and rate capability for sodium-ion batteries, *ACS Nano* 11 (2017) 12658–12667, <https://doi.org/10.1021/acsnano.7b07132>.
  - [44] J. Besenhard, M. Winter, J. Yang, W. Biberacher, Filming mechanism of lithium-carbon anodes in organic and inorganic electrolytes, *J. Power Sources* 54 (1995) 228–231, [https://doi.org/10.1016/0378-7753\(94\)02073-C](https://doi.org/10.1016/0378-7753(94)02073-C).
  - [45] W.H. Li, H.J. Liang, X.K. Hou, Z.Y. Gu, X.X. Zhao, J.Z. Guo, X. Yang, X.L. Wu, Feasible engineering of cathode electrolyte interphase enables the profoundly improved electrochemical properties in dual-ion battery, *J. Energy Chem.* 50 (2020) 416–423, <https://doi.org/10.1016/j.ijechem.2020.03.043>.
  - [46] G. Wang, M. Yu, J. Wang, D. Li, D. Tan, M. Löffler, X. Zhuang, K. Müllen, X. Feng, Self-activating, capacitive anion intercalation enables high-power graphite cathodes, *Adv. Mater.* 30 (2018) 1800533, <https://doi.org/10.1002/adma.201800533>.
  - [47] J. Cha, J.-G. Han, J. Hwang, J. Cho, N.-S. Choi, Mechanisms for electrochemical performance enhancement by the salt-type electrolyte additive, lithium difluoro (oxalato) borate, in high-voltage lithium-ion batteries, *J. Power Sources* 357 (2017) 97–106, <https://doi.org/10.1016/j.jpowsour.2017.04.094>.
  - [48] N.-S. Choi, J.-G. Han, S.-Y. Ha, I. Park, C.-K. Back, Recent advances in the electrolytes for interfacial stability of high-voltage cathodes in lithium-ion batteries, *RSC Adv.* 5 (2015) 2732–2748, <https://doi.org/10.1039/c4ra11575a>.
  - [49] Y.-M. Song, C.-K. Kim, K.-E. Kim, S.Y. Hong, N.-S. Choi, Exploiting chemically and electrochemically reactive phosphite derivatives for high-voltage spinel LiNi<sub>0.5</sub>Mn<sub>1.5</sub>O<sub>4</sub> cathodes, *J. Power Sources* 302 (2016) 22–30, <https://doi.org/10.1016/j.jpowsour.2015.10.043>.
  - [50] M. Phaner-Goutorbe, A. Sartre, L. Porte, Soft oxidation of graphite studied by XPS and STM, *Microsc. Microanal. Microsc.* 5 (1994) 283–290, <https://doi.org/10.1051/mm:0199400504-6028300>.
  - [51] L. Shen, L. Zhang, K. Wang, L. Miao, Q. Lan, K. Jiang, H. Lu, M. Li, Y. Li, B. Shen, Analysis of oxidation degree of graphite oxide and chemical structure of corresponding reduced graphite oxide by selecting different-sized original graphite, *RSC Adv.* 8 (2018) 17209–17217, <https://doi.org/10.1039/c8ra01486h>.

- [52] W. Märkle, N. Tran, D. Goers, M.E. Spahr, P. Novák, The influence of electrolyte and graphite type on the  $\text{PF}_6$  intercalation behaviour at high potentials, *Carbon* 47 (2009) 2727–2732, <https://doi.org/10.1016/j.carbon.2009.05.029>.
- [53] T. Liu, X. Han, Z. Zhang, Z. Chen, P. Wang, P. Han, N. Ding, G. Cui, A high concentration electrolyte enables superior cycleability and rate capability for high voltage dual graphite battery, *J. Power Sources* 437 (2019) 226942, <https://doi.org/10.1016/j.jpowsour.2019.226942>.
- [54] A.C. Ferrari, Raman spectroscopy of graphene and graphite: disorder, electron–phonon coupling, doping and nonadiabatic effects, *Solid State Commun.* 143 (2007) 47–57, <https://doi.org/10.1016/j.ssc.2007.03.052>.
- [55] V.A. Sethuraman, L.J. Hardwick, V. Srinivasan, R. Kostecki, Surface structural disordering in graphite upon lithium intercalation/deintercalation, *J. Power Sources* 195 (2010) 3655–3660, <https://doi.org/10.1016/j.jpowsour.2009.12.034>.
- [56] J.O. Besenhard, H.P. Fritz, The electrochemistry of black carbons, *Angew. Chem. Int. Ed.* 22 (1983) 950–975, <https://doi.org/10.1002/anie.198309501>.

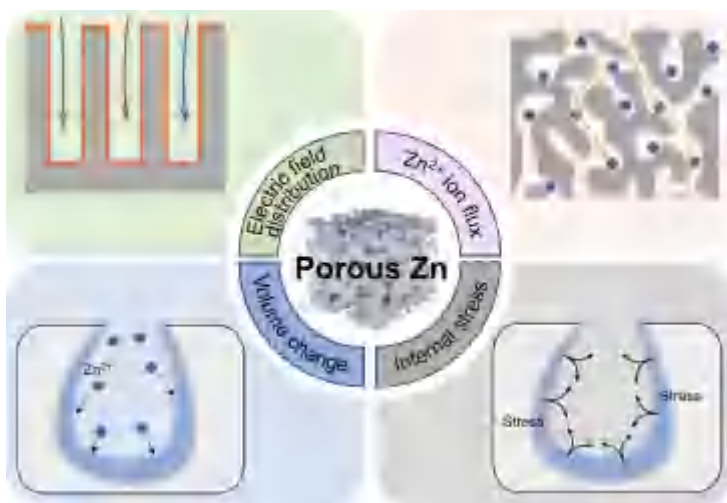


## Review

# Porous zinc metal anodes for aqueous zinc-ion batteries: Advances and perspectives

Yichen Ding, Bingyue Ling, Xin Zhao, Xu Yang, Yao Wang , Dong Zhou , and Guoxiu Wang 

## Graphical Abstract



The failure of Zn metal anodes in aqueous zinc-ion batteries is highly related to excessive dendrite growth. The implementation of porous Zn anodes has been demonstrated to be an effective strategy to regulate the deposition/stripping behavior of  $\text{Zn}^{2+}$  ions, thereby inhibiting the growth of Zn dendrites. This review provides a comprehensive overview of the recent advancements in the engineering of porous Zn metal anodes, emphasizing the structural orderliness and summarizing the merits of porous Zn anodes.

 Address correspondence to  
Yao Wang,  
[ywang99@sz.tsinghua.edu.cn](mailto:ywang99@sz.tsinghua.edu.cn);  
Dong Zhou,  
[zhou.d@sz.tsinghua.edu.cn](mailto:zhou.d@sz.tsinghua.edu.cn);  
Guoxiu Wang,  
[Guoxiu.Wang@uts.edu.au](mailto:Guoxiu.Wang@uts.edu.au)

Received: May 6, 2024  
Revised: May 23, 2024  
Accepted: May 26, 2024

 Read Online

 Submit Online

**Citation:** Ding Y., Ling B., Zhao X., et al. Porous zinc metal anodes for aqueous zinc-ion batteries: Advances and perspectives. *Energy Mater. Devices*, 2024, 2(3), 9370040. <https://doi.org/10.26599/EMD.2024.9370040>

## Review

<https://doi.org/10.26599/EMD.2024.9370040>

# Porous zinc metal anodes for aqueous zinc-ion batteries: Advances and prospectives

Yichen Ding<sup>1,†</sup>, Bingyue Ling<sup>1,†</sup>, Xin Zhao<sup>1</sup>, Xu Yang<sup>2</sup>, Yao Wang<sup>1</sup> ✉, Dong Zhou<sup>1</sup> ✉, and Guoxiu Wang<sup>2</sup> ✉

<sup>1</sup> Tsinghua Shenzhen International Graduate School, Tsinghua University, Shenzhen 518055, China

<sup>2</sup> Center for Clean Energy Technology, School of Mathematical and Physical Sciences, Faculty of Science, University of Technology Sydney, Sydney 2007, Australia

<sup>†</sup> Yichen Ding and Bingyue Ling contributed equally to this work.

Received: May 6, 2024 / Revised: May 23, 2024 / Accepted: May 26, 2024

## ABSTRACT

The intensifying challenges posed by climate change and the depletion of fossil fuels have spurred concerted global efforts to develop alternative energy storage solutions. Aqueous zinc-ion batteries (AZIBs) have emerged as promising candidates for large-scale electrochemical energy storage systems because of their intrinsic safety, cost-effectiveness, and environmental sustainability. However, Zn dendrite growth consistently poses a remarkable challenge to the performance improvement and commercial viability of AZIBs. The use of three-dimensional porous Zn anodes instead of planar Zn plates has been demonstrated as an effective strategy to regulate the deposition/stripping behavior of Zn<sup>2+</sup> ions, thereby inhibiting the dendrite growth. Here, the merits of porous Zn anodes were summarized, and a comprehensive overview of the recent advancements in the engineering of porous Zn metal anodes was provided, with a particular emphasis on the structural orderliness and critical role of porous structure modulation in enhancing battery performance. Furthermore, strategic insights into the design of porous Zn anodes were presented to facilitate the practical implementation of AZIBs for grid-scale energy storage applications.

## KEYWORDS

aqueous zinc-ion battery, porous zinc metal anode, dendrite, structural orderliness, grid-scale energy storage.

## 1 Introduction

The depletion of fossil energy sources can no longer satisfy the growing energy demands of humanity, which exacerbates numerous irremediable environmental issues<sup>[1]</sup>. In mitigating these challenges, renewable energy sources (e.g., wind, solar, and tidal) have received considerable attention because of their abundance and environmental friendliness. However, the integration of these energy sources into the electrical grid, constrained by indirectness and geographic limitations, can disrupt the stability of electrical energy storage systems, highlighting the demand for the development of efficient and sustainable energy storage technologies<sup>[2–4]</sup>. Electrochemical

batteries, which are renowned for their inherent reliability and high energy conversion efficiency, stand out as an optimal solution for electrical energy conversion and storage<sup>[5]</sup>. Therefore, the demand for secondary battery systems that are cost-effective, safe, and eco-friendly is increasing. Lithium-ion batteries (LIBs) are widely used in electric vehicles and consumer electronics because of their high energy density and long cycle life. However, the increasing costs associated with limited lithium mineral resources, in addition to persistent safety concerns, have hindered their widespread adoption in stationary grid energy storage systems<sup>[6]</sup>. In this context, aqueous zinc-ion batteries (AZIBs) with Zn metal

✉ Address correspondence to Yao Wang, [ywang99@sz.tsinghua.edu.cn](mailto:ywang99@sz.tsinghua.edu.cn); Dong Zhou, [zhou.d@sz.tsinghua.edu.cn](mailto:zhou.d@sz.tsinghua.edu.cn); Guoxiu Wang, [Guoxiu.Wang@uts.edu.au](mailto:Guoxiu.Wang@uts.edu.au)

© The Author(s) 2024. Published by Tsinghua University Press. The articles published in this open access journal are distributed under the terms of the Creative Commons Attribution 4.0 International License (<http://creativecommons.org/licenses/by/4.0/>), which permits use, distribution and reproduction in any medium, provided the original work is properly cited.

anodes, which were first proposed by Kang et al. in 2012<sup>[7]</sup>, have attracted increasingly interests in recent years because of their relatively high theoretical capacity (820 mAh g<sup>-1</sup> and 5,855 mAh cm<sup>-3</sup>), relatively low redox potential (−0.762 V vs. standard hydrogen electrode), and low cost of Zn metal<sup>[8]</sup>. Moreover, compared with their organic counterparts, aqueous electrolytes provide inherent safety, superior ionic conductivity, and cost-effectiveness, thereby indicating their great potential for large-scale energy storage applications.

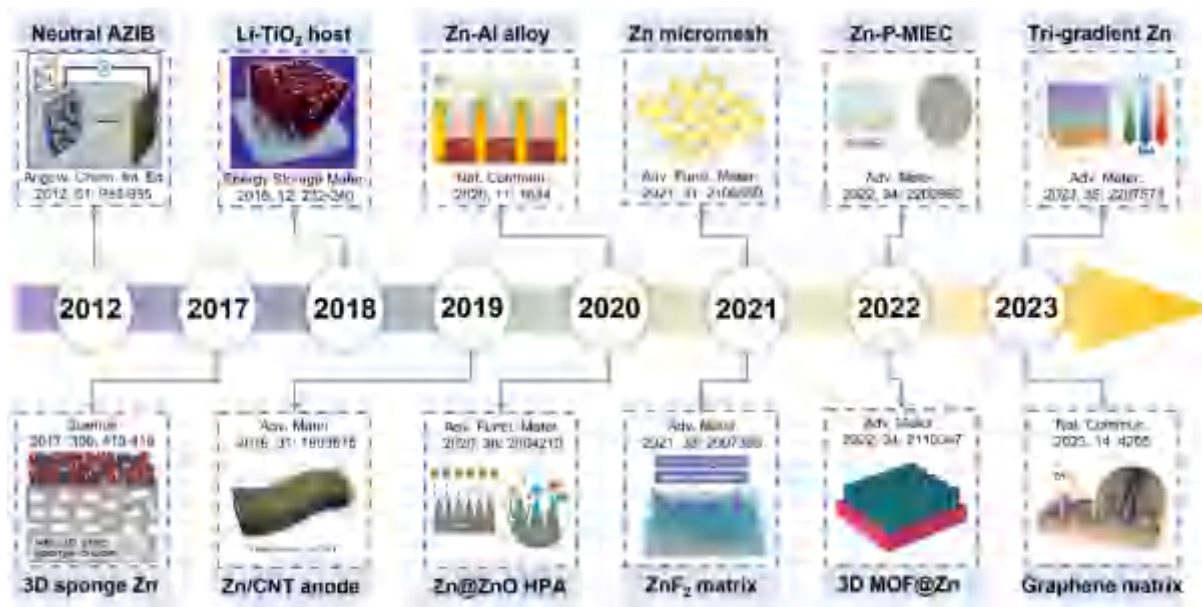
Despite their potential, AZIBs remain in an early stage of development, with challenges such as dendrite growth and side reactions (e.g., corrosion, passivation, and hydrogen precipitation reactions), thereby hindering their commercialization<sup>[9]</sup>. Notably, the formation of Zn dendrites poses a critical risk because of their propensity to penetrate the separator, leading to direct contact between the cathode and anode, which triggers internal short circuits and cell failure<sup>[10,11]</sup>. Numerous strategies have been used to inhibit the dendrite growth, including electrolyte and additive design<sup>[12–14]</sup>, anode surface modification<sup>[15]</sup>, and anode structural engineering. Among these, the development of porous structures has emerged as an effective approach to regulate the stripping/plating behavior of Zn metal and prevent dendrite growth, leveraging their capability of

homogenizing the electric field distribution and ion flux, mitigating volume expansion, and releasing the internal stresses associated with Zn deposition<sup>[10]</sup>. Various porous fabrication techniques have been applied, including etching<sup>[16]</sup>, self-assembly<sup>[17]</sup>, laser lithography<sup>[18]</sup>, electrochemical methods<sup>[19]</sup>, rolling<sup>[20]</sup>, freeze drying<sup>[21]</sup>, and three-dimensional (3D) printing<sup>[22]</sup>. Although extensive research has been conducted on porous Zn electrodes to enhance battery performance, spanning from Zn sponges to gradient electrodes (Fig. 1), systematic analysis from the perspective of the structural orderliness of the porous architecture remains lacking.

Herein, a comprehensive summary of the research advances in porous Zn anode design for AZIBs was provided, elucidating the role of porous structures in the overall battery performance, particularly the precise regulation of the pore structure. In addition, Zn powder-based anodes, which have been largely overlooked in previous reviews, were comprehensively overviewed. This review aims to provide novel insights and strategic guidance for the development of high-performance AZIBs through the optimization of porous Zn anodes.

## 2 Merits of porous Zn anodes

Although commercial planar Zn foils can serve as anodes for AZIBs, the uneven distribution of charge



**Figure 1** Timeline of the development of porous Zn anodes in AZIBs. Reproduced from Ref. [7] with permission ©2012, Wiley-VCH Verlag GmbH & Co. KGaA, Weinheim. Reproduced from Ref. [23] with permission ©2017, American Association for the Advancement of Science. Reproduced from Ref. [24] with permission ©2018, Elsevier B.V. Reproduced from Ref. [25] with permission ©2019, Wiley-VCH Verlag GmbH & Co. KGaA, Weinheim. Reproduced from Ref. [26] under the CC BY 4.0 license ©2020, The Authors. Reproduced from Ref. [27] with permission ©2020, Wiley-VCH Verlag GmbH & Co. KGaA, Weinheim. Reproduced from Ref. [28] with permission ©2021, Wiley-VCH GmbH. Reproduced from Ref. [29] with permission ©2021, Wiley-VCH GmbH. Reproduced from Ref. [30] with permission ©2022, Wiley-VCH GmbH. Reproduced from Ref. [21] with permission ©2022, Wiley-VCH GmbH. Reproduced from Ref. [31] with permission ©2023, Wiley-VCH GmbH. Reproduced from Ref. [32] under the CC BY 4.0 license ©2023, The Authors.



density and cation concentration disrupts Zn deposition and stripping, leading to dendrite growth and impeding the practical application of AZIBs. By contrast, 3D porous anodes provide numerous nucleation sites and reduce nuclear energy barriers because of their enlarged electrochemically active area. This enhancement greatly mitigates the localized charge accumulation, facilitates the uniform electric field distribution and mass transport, suppresses the dendrite growth, and ensures a longer battery lifespan. Moreover, the substantial internal volume in 3D porous anodes can accommodate volume changes and deposition stress caused by deposition/stripping. In particular, 3D porous anodes exhibit four main merits (Fig. 2).

### 2.1 Uniform electric field distribution

Electric field distribution plays a pivotal role in affecting the deposition behavior of Zn ions. According to the space charge theory proposed by Chazalviel et al., anion depletion is induced when the mass flux surpasses a threshold, compelling anions to migrate away from the anode<sup>[33]</sup>. Sand's temporal model provides an approximation of the time ( $\tau_s$ ) required for anion depletion, which leads to the formation of a space charge region caused by the disruption of localized electroneutrality. This phenomenon results in a large electric field-driven electroconvection on the metal surface, thereby exacerbating dendrite growth<sup>[34]</sup>. In general, this model is grounded on a high mass-transport-limited current density<sup>[33,35]</sup>. However, experimental results reveal that the duration of dendrite growth at low current densities is consistent with the predictions of the Sand's model, indicating a strong correlation between dendrite formation and the ion concentration gradient on the electrode surface<sup>[35]</sup>. On planar Zn foils, the restricted ion transport exacerbates the concentration of electric field distribution, resulting in local-

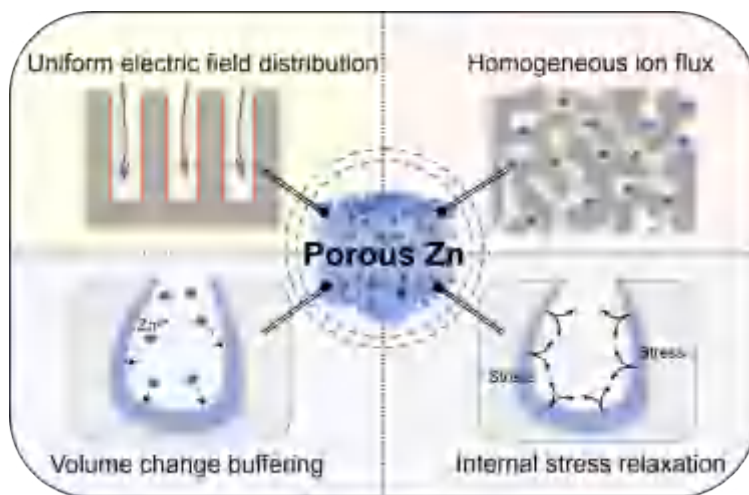
ized high current densities that aggravate side reactions and accelerate AZIB degradation. By contrast, 3D porous electrodes provide an increased number of electrochemically active surfaces and abundant nucleation sites that contribute to a more uniform electric field distribution, thereby extending  $\tau_s$  associated with the formation of space charge layers<sup>[10]</sup>.

### 2.2 Homogeneous ion flux

The transport of  $\text{Zn}^{2+}$  ions remarkably affects the electrochemical deposition behavior and morphology of the electrode surface<sup>[36]</sup>. However, the uneven and rough surface of planar Zn foils results in the accumulation of negative charges at the bumps, resulting in a "tip effect" that induces the preferential deposition of Zn ions and fosters dendrite growth. The ionic electrochemical kinetics at the anode surface includes the migration of metal ions across the concentration gradient in the electrolyte and the charge transfer at the electrode-electrolyte interface<sup>[37]</sup>. Herein, ion diffusion resistance plays a key role, which follows the Nernst-Planck equation<sup>[38]</sup>:

$$J_i = -D_i \frac{dC_i}{dx} - u_i z_i F \frac{dV}{dx} \quad (1)$$

where  $J$  denotes the ion flux,  $D$  is the diffusion coefficient,  $C$  represents the ion concentration,  $u$  is the ion mobility,  $z$  signifies the number of electrons,  $F$  is the Faraday constant, and  $V$  is the voltage. The first term of the Nernst-Planck equation describes ion diffusion, whereas the second term corresponds to ion mobility under an electric field. At high current densities, ion diffusion dominates because of substantial concentration gradients in Zn ion. In 3D porous electrodes, the electrolyte penetrates deeply into the electrode, and an increased electrochemically active area effectively reduces the local current density and mitigates the concentration polarization



**Figure 2** Advantages of porous structured Zn metal anodes, including uniform electric field distribution, homogeneous ion flux, buffering volume change, and internal stress relaxation.

of the electrolyte, thereby reducing the ion diffusion resistance and facilitating a homogeneous ion flux. Moreover, the abundance of nucleation sites effectively lowers the nucleation energy barrier and increases the deposition overpotential, thereby enabling rapid and uniform deposition<sup>[39]</sup>.

### 2.3 Volume change buffering

The hostless feature of Zn metal leads to vigorous volume swelling and shrinking during repeated plating/stripping<sup>[20]</sup>. The nonuniform distribution of charge and ion flux on planar Zn metal surfaces induces uneven Zn deposition. Hence, Zn metal is prone to being deposited in dendritic, mossy, and rod-like forms, which lead to substantial volume changes that exacerbate dendritic growth. In addition, the increased specific surface area and decreased lattice match caused by volume expansion can lead to the disordered deposition of Zn, thereby reducing the lifetime of AZIBs<sup>[40]</sup>. The substantial volume changes in planar Zn foil anode systems lead to the formation of “dead Zn” and the puncture of separator by dendrites<sup>[41]</sup>. The construction of porous Zn metal anodes can provide a sufficient internal space to effectively accommodate the volume change of Zn metal and inhibit dendrite growth. A well-designed porous anode can induce Zn to achieve bottom-up deposition behavior and maintain a flat electrode sheet morphology<sup>[26]</sup>.

### 2.4 Internal stress relaxation

Internal stresses arise during Zn deposition, which could affect the deposition behavior<sup>[42]</sup>. Under nonequilibrium growth conditions, the migration of Zn metal atoms across grain boundaries is a decisive factor influencing the accumulation of internal stresses<sup>[10]</sup>. In planar electrodes, these stresses are not effectively released, leading to the chaotic deposition behavior of Zn atoms along the grain boundaries, which drives the growth of a disordered dendritic metal structure. By contrast, porous structures can effectively alleviate the internal stress induced by metal deposition, thereby facilitating an orderly deposition process for Zn.

## 3 Porous Zn anodes with a disordered structure

Prior to the burgeoning interest in mild AZIBs, monolithic porous Zn anodes had been investigated in alkaline Zn batteries, which focused on Zn sponge and Zn foam structures. In 2017, Parker et al. designed porous Zn sponge electrodes to improve Zn utilization and charging capacity<sup>[23]</sup>. This design effectively modulated the local current density to retard dendrite formation. Zn foam, which plays a similar role to Zn sponge, has been used as an anode to

enhance battery performance by modulating the electric field<sup>[43]</sup>. In another work, a hyper-dendritic nanoporous Zn foam was developed via *in situ* electrochemical synthesis<sup>[44]</sup>. This Zn foam achieved an impressive anode material utilization of ~100% at 100% depth of discharge (DOD) in an alkaline medium. However, the structures of Zn sponge and Zn foam are susceptible to structural collapse after long-term high-rate cycling, and their fabrication generally requires great energy expenditure, which hinders their practical applications. In the study of neutral AZIBs, random porous Zn anodes have been developed to enhance the anode-to-cathode reversible capacity ratio (N/P ratio), specific capacity, cycle life, and rate performance. At present, the realization of porous Zn anodes is achieved through three main methods, that is, the *in situ* creation of pores on commercial Zn foils, the deposition of Zn on 3D zincophilic substrates, and the construction of porous structures utilizing the plasticity of Zn powders.

### 3.1 Zn foil anodes with a disordered structure

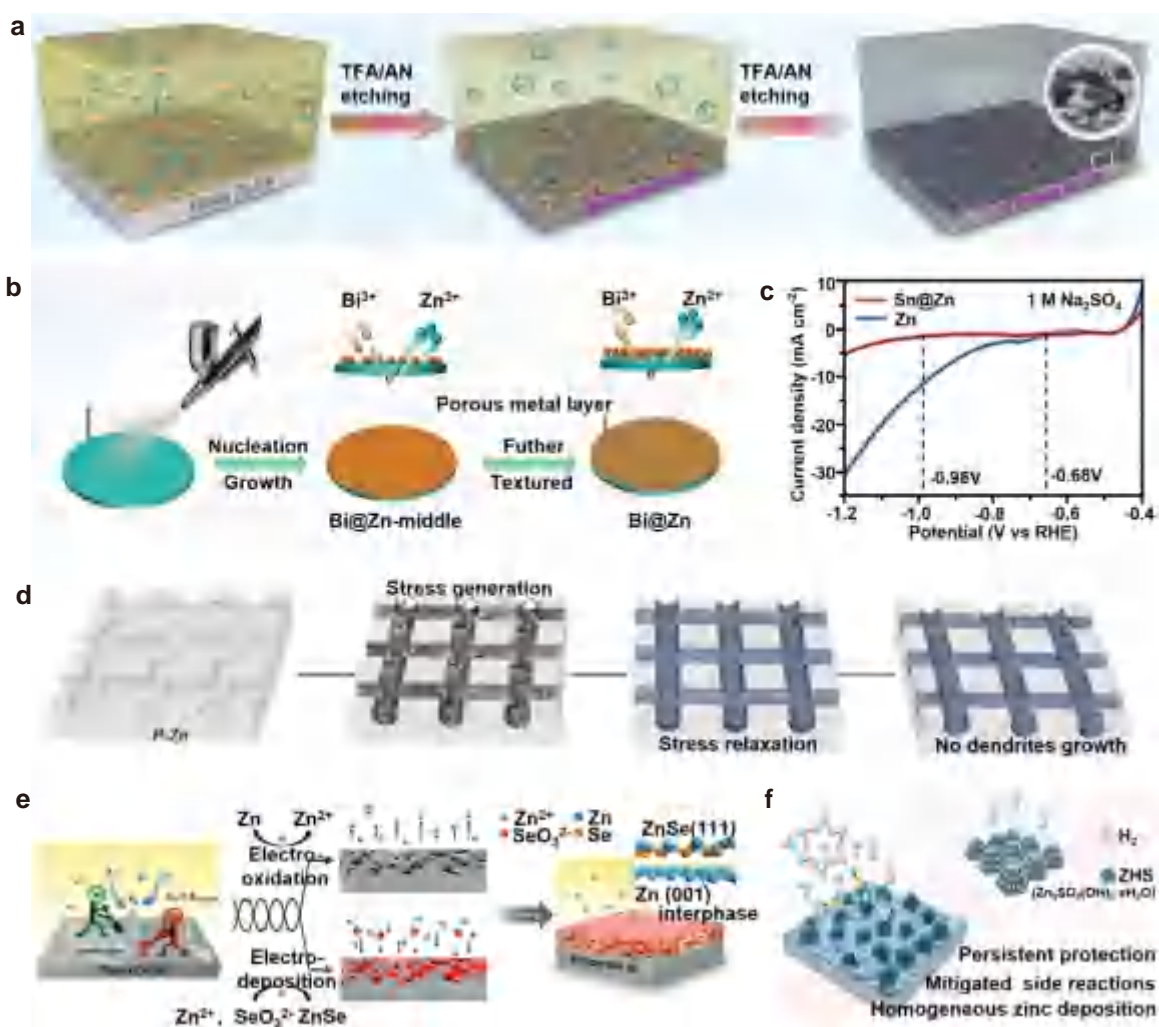
The surface of commercial Zn foils is rough, and it lacks planarity, which can induce the accelerated formation of Zn dendrites. The *in situ* construction of a porous layer on the surface of Zn foils reduces the local current density, homogenizing the ion flux and inhibiting the dendrite growth. Compared with alternative methods for fabricating 3D anodes, direct etching of commercial Zn foils using simple processes such as immersion and ultrasonic waves shows great application potential. This etching process not only eliminates the original passivation layer on the surface of Zn foils, but also establishes a 3D structure. Meanwhile, under specific conditions, Zn compounds can be generated *in situ* on the surface of Zn foils, self-assembling into an interfacial layer to protect the Zn anode. Notably, the structural morphology and etching dynamics of Zn foils vary with the etchant and etching parameters used. Given the formation of a porous structure, further enhancements can be achieved by manipulating the crystal orientation<sup>[40,45–47]</sup> and by forming protective layers composed of Zn compounds or inert metals on the surface.

Acid solutions serve as effective etching agents for Zn foils, facilitating the redox reaction where Zn atoms react with hydrogen ions (ionized by the acid), to form the corresponding Zn salts and hydrogen. In addition, if the acid's anion can coordinate, then it can bind with Zn<sup>2+</sup> to regulate the flux, and the resulting coordination compounds generated *in situ* can serve as a protective layer to reduce corrosion. As demonstrated by Sun et al., hydrochloric acid was utilized to selectively etch the crystal surface of Zn foils, forming a 3D ridge-like structure<sup>[48]</sup>. This engi-

neered surface of the Zn electrode facilitated the uniform plating and stripping of metal Zn, which increased the infiltration surface area of the electrolyte and reduced the local current density, thereby improving the cycling stability of the Zn anode. Organic acids, which are less aggressive than their inorganic counterparts, provide a gradual and controllable etching process for Zn foils. Different organic acids, including phytic acid<sup>[49]</sup>, humic acid<sup>[50]</sup>, amino acid<sup>[51]</sup>, and cysteine<sup>[16,52]</sup>, have been used to fabricate porous Zn anodes. A 3D Zn foil with a hierarchical porous structure was developed by Alshaarief et al. using an organic mixed solution of trifluoromethanesulfonic acid (TFA) and acetonitrile<sup>[53]</sup>. TFA with a relatively slow and controllable chemical corrosion of Zn effectively removed the surface passi-

vation layer (Fig. 3a), resulting in a multitude of porous structures with diameters ranging from nanoscale to microscale on the Zn surface. This solution improved the electrolyte accessibility and nucleation site density. Organic acids, with their reactive groups, provide abundant adsorption sites for metal ions, forming exceptionally stable complexes with Zn ions<sup>[58]</sup>. Consequently, the etched Zn foil surface can generate organic Zn compounds *in situ* as a protective interface layer, reducing the electrolyte–Zn anode contact and effectively preventing the corrosion of the Zn foil surface by O<sub>2</sub> or water.

Zn foil etching using metal salt solutions as etchants is also a feasible strategy, where the metal salt solution facilitates the formation of a porous inert protective film on the surface of Zn foils



**Figure 3** Zn foil anodes with a disordered structure. (a) Schematic diagram showing the fabrication of a 3D porous Zn foil in an organic mixture of trifluoromethanesulfonic acid (TFA) and acetonitrile (AN). Reproduced from Ref. [53] with permission ©2022, Wiley-VCH GmbH. (b) Schematic depiction of the fabrication and formation of Zn anodes with a metallic interface. Reproduced from Ref. [54] with permission ©2023, Wiley-VCH GmbH. (c) Line sweep voltammetry curves of pristine Zn and Sn@Zn electrodes at 1 mV s<sup>-1</sup> (using 1 mol/L NaSO<sub>4</sub>). Reproduced from Ref. [55] with permission ©2023, Wiley-VCH GmbH. (d) Schematic illustration of the stress induced by Zn plating and its effect on the plating/stripping behavior of Zn on P-Zn. Reproduced from Ref. [56] with permission ©2022, Elsevier Ltd. (e) Schematic illustration of the preparation of the 3D-Zn@ZnSe anode under constant potentials. Reproduced from Ref. [57] with permission ©2022, Wiley-VCH GmbH. (f) Schematic diagram of Zn deposits on a ZnCo alloy surface. Reproduced from Ref. [19] with permission ©2023, Wiley-VCH GmbH.



through a simple redox reaction between metal ions and Zn. By introducing zincophilic metals with high hydrogen evolution potentials, the Zn anode demonstrated improved deposition behavior of  $\text{Zn}^{2+}$  for drastically increased cycling stability<sup>[59]</sup>.

Notably, studies have shown that the inert metal deposited on the Zn foil surface during cycling can be electrochemically converted into Zn alloys, which exhibit superior oxidation resistance and load-bearing capacity compared with pure metal Zn. Chao et al. optimized zincophilic sites from thermodynamic inertia and kinetic zincophilicity indices by using  $\text{BiCl}_3$  and ethylene glycol solvent to form *in situ* nanoporous  $\text{Bi@Zn}$  nanosheets on Zn foils (Fig. 3b)<sup>[54]</sup>. The  $\text{Bi@Zn}$  interface greatly suppressed the side reactions. The *in situ* formed Zn–Bi alloy solid solution interfaces spatially promoted the homogeneous growth of Zn and effectively accelerated the Zn deposition kinetics. Given the high thermodynamic inertia and rapid electrochemical kinetic zincophilicity, the  $\text{Bi@Zn}$  heterometallic interface enabled a long cycle lifespan of more than 4,700 cycles with a low overpotential of around 55 mV, even at a high current density of  $10 \text{ mA cm}^{-2}$ . In addition, Wu et al. reported a versatile and economical strategy for constructing artificial metal interfaces on Zn anodes within only 10 s<sup>[55]</sup>. The kinetic process of replacement reaction was regulated by the complexation of thiourea molecules with metal ions, and the metal deposition was gradually adjusted, achieving superfilling on the surface of common commercial Zn flakes. As shown in Fig. 3c, the hydrogen evolution reaction (HER) onset potential of  $\text{Sn@Zn}$  ( $-0.98 \text{ V}$  vs. reversible hydrogen electrode) was lower than that of Zn ( $-0.68 \text{ V}$ ), indicating the sluggish HER response of  $\text{Sn@Zn}$  with regard to current density. Considering the evaluated parameters such as surface morphology, interfacial resistance, corrosion current, and nucleation overpotential, Sun et al. selected  $\text{MoCl}_5$ /ethanol etchant from high-valent metal chlorides for the *in situ* construction of porous Zn surfaces<sup>[60]</sup>. Electrochemical analyses and theoretical calculations showed that an increased exposure of the Zn(002) crystal plane enhanced the corrosion resistance of the anode.

The corrosion mechanism of Zn foils exposed to metallic salt solutions can be summarized in three key aspects: (1) The selective adsorption of different anions to the Zn metal crystal surface induces the oriented deposition of  $\text{Zn}^{2+}$  ions<sup>[61]</sup>. (2) Once an inert metal or compound is *in situ* substituted on the surface of the Zn foil, it functions as a protective barrier to isolate the Zn anode from the electrolyte and improves the corrosion resistance of the Zn anode because of its chemical inertness<sup>[62,63]</sup>. (3) Under certain conditions, the deposited inert metal on the surface can spontaneously alloy with

Zn, thereby improving the corrosion resistance and ensuring the structural stability of the battery during cycling<sup>[54]</sup>. Notably, the concentration and duration of the metal salt solution remarkably influence the particle size and thickness of the deposited metal layer<sup>[64]</sup>.

The growth of Zn dendrites is closely related to the accumulation of internal stresses during the electroplating process. Thus, Zn metal anodes with a patterned micro-groove structure have been demonstrated to effectively release the stress induced by galvanization, thereby inhibiting dendrite growth. Zhao et al. adopted micro-zone stress relaxation to introduce ordered grooves ( $\sim 30 \text{ }\mu\text{m}$  wide and  $\sim 25 \text{ }\mu\text{m}$  deep) to the surface of Zn metal foils (P–Zn) by metal mesh-assisted rolling, which inhibited Zn dendrite growth (Fig. 3d)<sup>[56]</sup>. The post-patterned recesses provided a sufficient buffer space to effectively reduce stress accumulation from plating, enabling dendrite-free Zn metal plating even at a high capacity of  $10 \text{ mAh cm}^{-2}$ . Apart from physical imprinting and chemical etching, some electrochemical methods are available to fabricate intricate porous structures on the surface of Zn foils. The uneven deposition of Zn can be attributed to various factors<sup>[65]</sup>, including surface roughness, passivation, the “tip effect”, as well as inhomogeneous ion fluxes in the electrolyte. Zhi et al. successfully obtained a 3D porous Zn skeleton with a ZnSe overlayer ( $3\text{D-Zn@ZnSe}$ ) through one-step electrochemical scanning, accurately repairing intrinsic defects on the surface of Zn foils and remodeling the electrolyte–anode interface<sup>[57]</sup>. Under a certain electric field, the preferential reaction at protrusions caused by a higher surface current density facilitated the simultaneous electrooxidation of Zn and the electrodeposition of ZnSe in a  $\text{SeO}_2$  powder-rich electrolyte (Fig. 3e). The anode–electrolyte interface was reconfigured, effectively homogenizing the charge distribution and Zn ion flux; thus, the  $3\text{D-Zn@ZnSe}||\text{V}_2\text{O}_5$  cells exhibited 90.63% capacity retention after 8,500 cycles at  $5 \text{ A g}^{-1}$ , which maintained a high specific capacity of  $107.3 \text{ mAh g}^{-1}$ . Zhou et al. designed a novel approach to fabricate spiral-grown 3D ZnCo overlayers on one side of commercial Zn foils using constant current electrodeposition. The ZnCo crystalline plane, which is predominantly exposed to the side of the 3D spiral structure, had enhanced zincophilicity compared with the Zn crystalline plane<sup>[19]</sup>. During electroplating, the Zn metal surface with a ZnCo cladding layer was gradually smoothed because of the restricted diffusion behavior of  $\text{Zn}^{2+}$ . Meanwhile, the superior corrosion resistance of ZnCo alloy effectively inhibited the corrosion reaction on the anode surface (Fig. 3f).

Overall, the fabrication of random porous structures on the surface of commercial Zn foils through

physical, chemical, or electrochemical methods represents a feasible yet effective strategy to improve the performance of AZIBs. These porous structures can effectively optimize ion flux, inhibit side reactions, and regulate Zn nucleation growth. However, the efficacy of the modification approach is highly contingent on the reaction conditions because of the inherent variability in the size and arrangement of pore structures. Thus, a more in-depth investigation into the impact of the characteristics of a porous structure on the Zn deposition/stripping kinetics is warranted to optimize the performance of AZIBs.

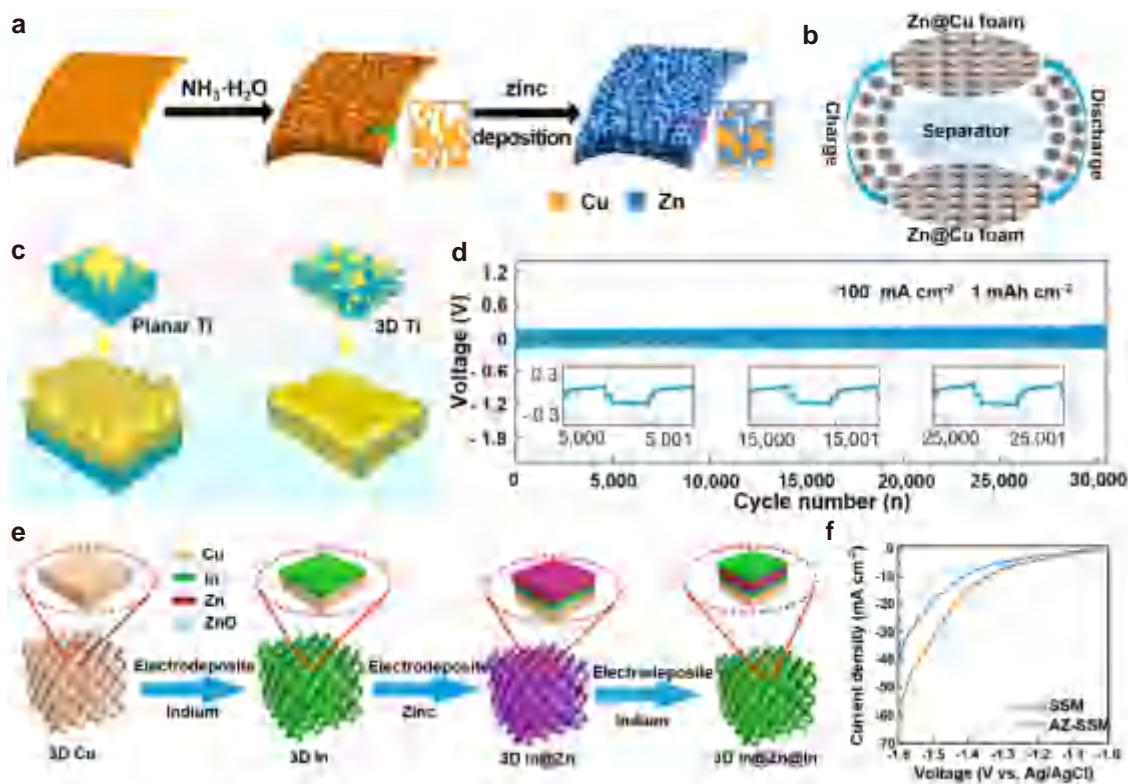
### 3.2 Current collectors with a disordered structure

#### 3.2.1 Metallic current collectors with a disordered structure

Metal materials, which are known for their high electrical conductivity, thermal conductivity, and good ductility, are considered optimal candidates for battery current collectors. In addition, metal

substrates typically exhibit zincophilic properties, which facilitates the deposition of  $\text{Zn}^{2+}$  ions onto them.

Among numerous metals, copper stands out because of its relatively low cost, excellent conductivity, and low Zn nucleation overpotential. Huang et al. scrutinized the nucleation behavior of Zn on different metal substrates (e.g., Cu, Ag, Ti, or Sn), revealing that Zn tends to deposit on the surface of Cu in the absence of nucleation barriers<sup>[66]</sup>. Therefore, copper is a favorable material for Zn anode current collectors. 3D Cu used for Zn anode current collectors has two types, namely, modified commercial copper foil and direct porous copper, such as copper mesh and copper foam<sup>[67]</sup>. Kang et al. prepared 3D porous Cu from a flat Cu foil via chemical etching (Fig. 4a), providing a substrate for the uniform electrodeposition of Zn<sup>[68]</sup>. In addition, foam Cu can be used directly to obtain porous structures, as demonstrated by Shi et al.<sup>[69]</sup>. The 3D porous foam Cu exhibited a low Zn nucleation overpotential of 65.2 mV and superior plating/stripping reversibility, leading to enhanced cycling performance in the assembled



**Figure 4** Metallic current collectors with a disordered structure. (a) Schematic illustration of the fabrication of a 3D Zn anode. Reproduced from Ref. [68] with permission ©2019, American Chemical Society. (b) Schematic illustration of Zn@Cu collector symmetric cells. Reproduced from Ref. [69] with permission ©2019, American Chemical Society. (c) Zn deposition diagram representing planar Ti and 3D Ti current collectors. Reproduced from Ref. [70] with permission ©2021, American Chemical Society. (d) Long-term stripping/plating behavior of Zn@CuNWs||Zn@CuNWs symmetric cells at a current density of  $100.0 \text{ mA cm}^{-2}$  with an areal capacity of  $1.0 \text{ mAh cm}^{-2}$ . Reproduced from Ref. [71] with permission ©2022, Wiley-VCH GmbH. (e) Scheme of the synthesis of a 3D porous sandwich-structured In@Zn@In (3D In@Zn@In) electrode. Reproduced from Ref. [72] with permission ©2022, Elsevier B.V. (f) Linear polarization curves of symmetric SSM and AZ-SSM electrodes in a 2 mol/L aqueous  $\text{Na}_2\text{SO}_4$  electrolyte. Reproduced from Ref. [73] with permission ©2022, Science Press and Dalian Institute of Chemical Physics, Chinese Academy of Sciences.

full cell (Fig. 4b). Apart from Cu, other metals are also viable as anode current collector hosts. For example, An et al. developed 3D porous Ti derived from commercial Ti foil as a host for the anode<sup>[70]</sup>. The 3D Ti/Zn metal anode suppressed dendrite growth because of its uniform current distribution (Fig. 4c), homogeneous nucleation, and volume change accommodation, enabling stable Zn plating/stripping for up to 2,000 h with low polarization. The full cell with Zn@3D Ti-TiO<sub>2</sub> as the anode and S@MXene/MnO<sub>2</sub> as the cathode was assembled to evaluate the practical electrochemical performance. The cyclic voltammetry (CV) curves after the initial cycle displayed consistent redox peaks, indicating the reversibility of the electrochemical process.

Certain metals with unique structures have been utilized as anode current collectors. For example, Yi et al. have successfully used a fivefold twin-crystal Cu nanowire as a substrate for Zn anodes<sup>[71]</sup>. The regular Cu(111) crystal facets exposed at the ridges of these nanowires could regulate the growth of Zn dendrites because of their low lattice mismatch between Cu(111) and Zn(002). This heteroepitaxial growth method allowed Zn to be deposited along the Zn(002) orientation, in alignment with Cu(111), guiding uniform Zn nucleation and growth, and remarkably reducing the overpotential. Consequently, the Zn@CuNW anode exhibited unprecedented stability under ultra-high current density, as evidenced by symmetric cell operations exceeding 30,000 cycles at the rate of 100.0 mA cm<sup>-2</sup> (Fig. 4d). A sandwich-like architecture has also been adopted for metallic anode current collectors. Fan et al. reported a distinctive In@Zn@In tri-layer structure deposited on the 3D porous Cu framework (referred to as 3D In@Zn@In), which effectively suppressed dendrite growth and side reactions (Fig. 4e)<sup>[72]</sup>. The sandwich configuration not only facilitated an even electric field distribution but also served as protective shield for the active material, thereby preventing the formation of “dead Zn”. Besides, Yu et al. introduced a stainless-steel mesh (SSM) coated with a rapid ion-diffusing Ag-Zn alloy layer as an anode collector (AZ-SSM@Zn)<sup>[73]</sup>. This alloy layer accelerated Zn<sup>2+</sup> ion diffusion, regulated flux uniformity, and suppressed HER (Fig. 4f). The AZ-SSM@Zn anode, when matched with commercial activated carbon, exhibited superior rapid charge and discharge capabilities. Even under a high current density of 5 A g<sup>-1</sup> for 4,000 cycles, the capacity retention rate remained close to 100%.

Overall, metal current collectors are endowed with excellent conductivity and mechanical properties, which are pivotal for enhancing the battery cycling performance. The intrinsic zincophilic nature of these metal substrates promotes the uniform deposition of Zn, a critical factor in mitigating dendrite

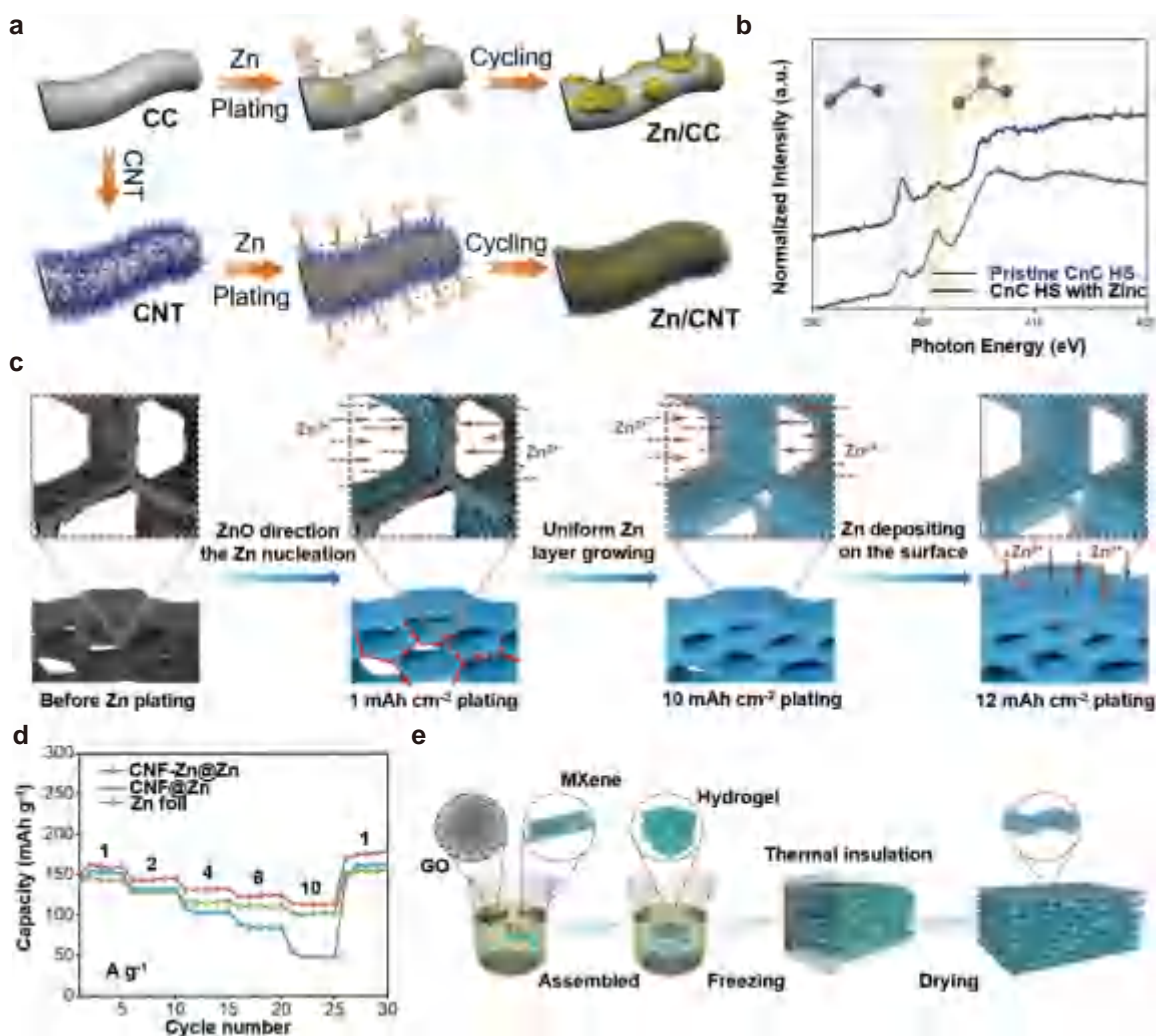
growth and ensuring stable operation. The strategic deployment of single or composite metals, along with the incorporation of alloys, to fabricate 3D anode current collectors is a burgeoning research avenue aimed at stabilizing Zn anodes and augmenting the performance of AZIBs.

### 3.2.2 Carbon-based current collectors with a disordered structure

In general, carbon materials have high conductivity, large specific surface areas, and porous structures, which provide abundant nucleation sites for Zn deposition and optimize surface electric field distribution. These attributes are consistent with the design criteria for 3D Zn anode current collectors<sup>[74–76]</sup>. Notably, certain unique structures in carbon materials can affect Zn precipitation. For example, graphene, with its atomic arrangements similar to the Zn(002) crystal planes, can be strategically utilized to induce Zn deposition along the (002) plane, thereby promoting uniform deposition and inhibiting dendrite growth<sup>[77]</sup>. Here, the application of carbon materials in the disordered Zn anode collector as the host was discussed. Carbon nanotubes (CNTs) are lightweight and stable one-dimensional materials, which can be used as a conductive scaffold for Zn anode current collectors, achieving dendrite-free Zn plating/stripping. Zeng et al. demonstrated the importance of a flexible CNT framework as the conductive host for Zn anode current collectors<sup>[25]</sup>. They adopted chemical vapor deposition to grow CNTs on a carbon cloth (CC), thereby effectively reducing Zn nucleation overpotential and improving the homogeneous electric field distribution (Fig. 5a). The as-fabricated Zn/CNT anode exhibited highly reversible Zn deposition/stripping behavior with a high coulombic efficiency (CE). In a parallel approach, Cao et al. have grown 3D nitrogen-doped vertical graphene nanosheets directly on a CC (N-VG@CC) as a current collector to achieve dendrite-free Zn anodes<sup>[81]</sup>. This nitrogen-containing group in N-VG remarkably enhanced the Zn affinity of carbon-based current collectors, thereby promoting uniform Zn deposition. In elucidating the underlying mechanism of this Zn affinity, Xie et al. used carbon hollow spheres (referred to as CnCHS), derived from resorcinol formaldehyde, as model current collector<sup>[78]</sup>. As shown in Fig. 5b, the pyridinic nitrogen sites were attached by Zn<sup>2+</sup> ions after Zn deposition, leading to the formation of the Zn–N bonds. The establishment of these Zn–N bonds not only altered the chemical state of the initial pyridinic, aligning it with that of graphitic nitrogen, but also promoted Zn nucleation and inhibited Zn dendrite formation.

Constructing 3D carbon nanomaterials doped with heteroatoms is a promising strategy for the development of Zn anode current collectors, as these





**Figure 5** Carbon-based current collectors with a disordered structure. (a) Schematic illustrations of Zn deposition on CC and CNT electrodes. Reproduced from Ref. [25] with permission ©2019, Wiley-VCH Verlag GmbH & Co. KGaA, Weinheim. (b) Nitrogen 1s near-edge X-ray absorption fine structure spectra of pristine CnC HS and CnC HS after Zn deposition. Reproduced from Ref. [78] with permission ©2021, Wiley-VCH GmbH. (c) Schematic illustration of Zn plating on the 3D-ZGC host under various electrochemical conditions. Reproduced from Ref. [21] with permission ©2022, Wiley-VCH GmbH. (d) Rate capabilities of full batteries using the NVO cathode and different anode hosts. Reproduced from Ref. [79] with permission ©2023, American Chemical Society. (e) Schematic illustration of the fabrication process for the MGA material. Reproduced from Ref. [80] with permission ©2021, Wiley-VCH GmbH.

heteroatoms enhance the affinity for Zn deposition. Metal-organic frameworks (MOFs), which are known for their periodic nanoporous structures and exceptional specific surface areas<sup>[82,83]</sup>, yield carbon-derived materials that can function as anode current collectors, effectively suppressing dendrite formation and HER<sup>[84]</sup>. Xue et al. designed a 3D framework by combining CNTs and graphene into a hierarchical porous structure (3D-ZGC), onto which they introduced MOF-derived ZnO/C nanoparticles<sup>[21]</sup>. The 3D porous frameworks, in conjunction with ZnO particles that exhibit Zn affinity, induce uniform Zn deposition (Fig. 5c). The symmetric battery using 3D-ZGC as the electrode current collector cycled 1,500 times at a high current density of 20 mA cm<sup>-2</sup> with a low overpotential of less than 65 mV. Carbon nanofibers (CNF) are also considered viable candi-

dates for Zn anode current collectors. Wang et al. used an eco-friendly strategy to fabricate a flexible 3D CNF architecture with uniformly distributed Zn seeds (CNF-Zn) derived from bacterial cellulose<sup>[79]</sup>. The CNF-Zn@Zn||NaV<sub>3</sub>O<sub>8</sub>·1.5H<sub>2</sub>O (NVO) AZIBs exhibited a remarkably improved rate capability and cycling stability (Fig. 5d). Yu et al. designed a 3D macroporous fiber network current collector, featuring carbon cages decorated with hierarchical lotus root-like Zn/N-doped carbon hollow nanofibers (LRZCF@CC)<sup>[85]</sup>. The layered 3D hollow network of LRZCF@CC fibers provided additional space to accommodate metallic Zn, effectively addressing volume expansion during cycling.

Apart from the modulation of zincophilic properties, the design of current collectors plays a pivotal role in the formation of the solid electrolyte inter-

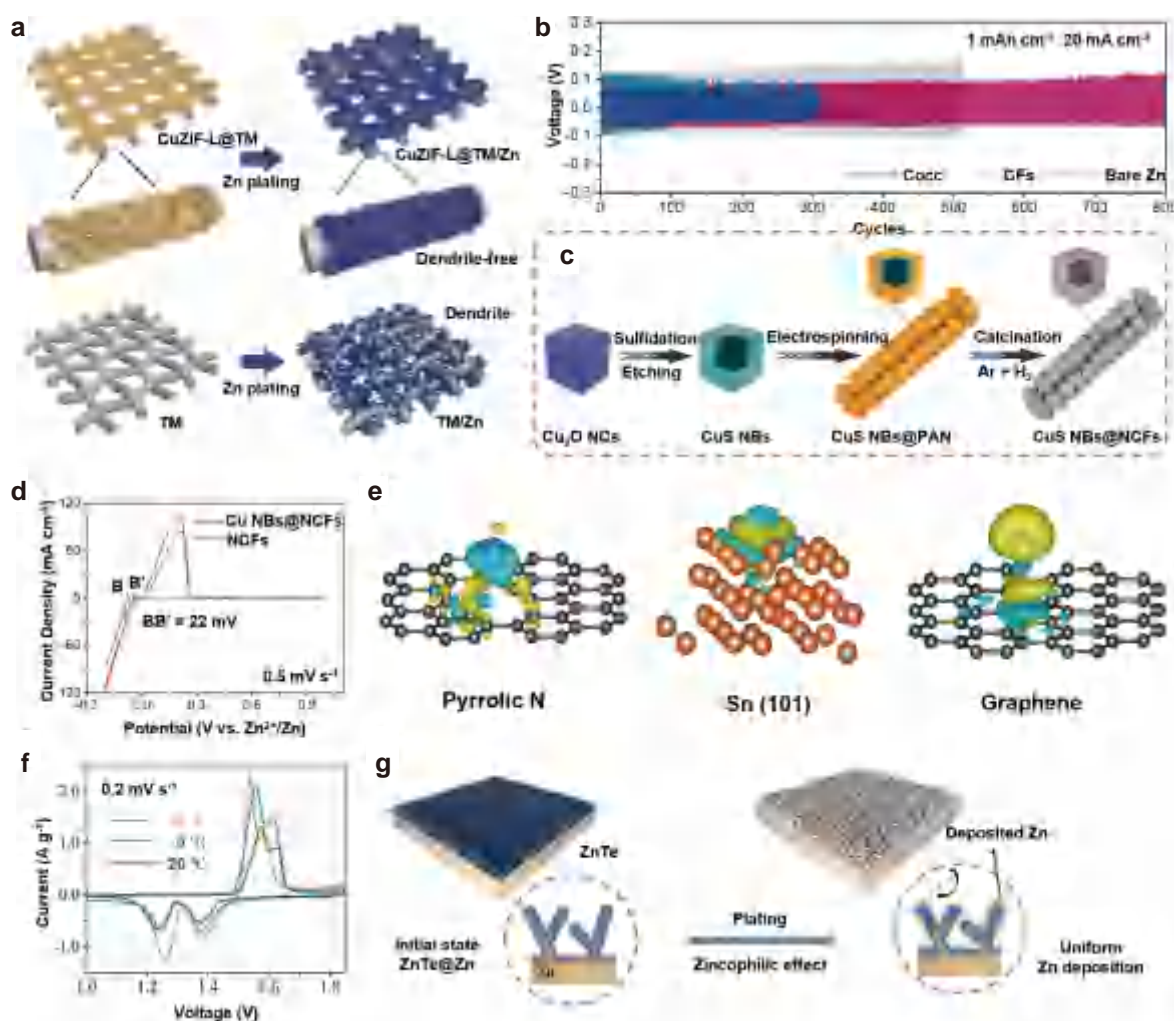
phase (SEI) layer. Zhou et al. have constructed an anode collector by integrating MXene sheets onto a flexible reduced graphene oxide framework, utilizing an oriented freezing technique to fabricate an MXene/graphene aerogel structure (Fig. 5e)<sup>[80]</sup>. The inherent fluorine-terminated surface of MXene contributed to the *in situ* formation of an SEI enriched with Zn fluoride during cycling, which effectively suppressed dendritic growth.

The majority of 3D Zn anode current collectors, which are characterized by their disordered structure and constructed on carbon substrates, have achieved CE exceeding 95%<sup>[86]</sup>. Heteroatom doping remarkably affects the overall performance. Composite bases, in contrast to single-carbon materials, often

exhibit superior performance.

### 3.2.3 Other disordered current collectors

Apart from the abovementioned materials, researchers have also explored alternative materials for the construction of disordered anode collectors. For example, metal/carbon composite materials have been used as composite-based current collectors. Tao et al. reported a leaf-like Zn-coordinated zeolitic imidazolate framework (ZIF-L) nanoflake with atomically dispersed Cu, which is grown onto a Ti mesh (CuZIF-L@TM), serving as the collector (Fig. 6a)<sup>[87]</sup>. The 3D conductive framework connected by ZIF-L effectively reduced the local current density and homogenized electric field distribution, thereby



**Figure 6** Other disordered current collectors. (a) Schematic illustrations of Zn depositions on CuZIF-L@TM host and TM host. Reproduced from Ref. [87] with permission ©2022, Wiley-VCH GmbH. (b) Long-term cycling performance of symmetric cells under a current density of 20 mA cm<sup>-2</sup> with a capacity of 1.0 mAh cm<sup>-2</sup>. Reproduced from Ref. [88] with permission ©2022, American Chemical Society. (c) Schematic illustration of the synthetic procedure for Cu NBs@NCFs. (d) CV curves of the asymmetric cells employing Cu NBs@NCFs and NCF electrodes at a scan rate of 0.5 mV s<sup>-1</sup>. Reproduced from Ref. [89] with permission ©2022, Wiley-VCH GmbH. (e) Interfacial charge density models for pyrrolic N, Sn(101), and graphene. Reproduced from Ref. [90] under the CC BY-NC 4.0 license ©2022, The Authors. (f) CV curves of wood-based flexible antifreezing AZIBs at various temperatures. Reproduced from Ref. [91] with permission ©2022, Elsevier B.V. (g) Illustrations depicting the Zn plating behavior on the ZnTe@Zn electrode. Reproduced from Ref. [92] with permission ©2022, Wiley-VCH GmbH.

lowering concentration polarization. Meanwhile, Li et al. designed a carbon fiber-based collector host scaffold with zincophilic porous Co-embedded carbon cages (denoted as CoCC)<sup>[88]</sup>. They implemented a “hierarchical confinement strategy” that maximized the benefits of zinc-binding affinity sites while improving kinetics and stability. This strategy enabled dendrite-free Zn plating/stripping behavior, exhibiting exceptional stability over 800 cycles at a high current density of 20 mA cm<sup>-2</sup> and a low overpotential of 65 mV (Fig. 6b). In addition, Zeng et al. developed a 3D carbon nanostructure with metal-based zincophilic sites<sup>[89]</sup>. This 3D multifunctional collector, which is composed of zincophilic Cu nano boxes and N-doped carbon fibers (Cu NBs@NCFs), is illustrated schematically in Fig. 6c. This hierarchical Cu NBs@NCFs host was conducive to Zn deposition along the Zn(002) plane, facilitating smooth Zn plating. Compared with pristine NCFs current collector, Cu NBs@NCFs exhibited superior Zn plating/stripping performance, with reduced polarization and improved reaction kinetics (Fig. 6d). In another study, Yu et al. reported a 3D hybrid fiber directly embedded with N-doped Sn nanoparticles (Sn@NHCF)<sup>[90]</sup>. The strong Sn–Zn affinity, which is supported by density functional theory simulation results (Fig. 6e), reduced Zn aggregation on the surface and prevented dendrite formation. This robust Zn affinity on the Sn@NHCF substrate during deposition could alleviate Zn aggregation, thereby preventing the formation of Zn dendrites.

Furthermore, various materials have been explored as Zn anode current collectors, such as semiconductor<sup>[92]</sup> and wood<sup>[91]</sup>. Wood-based collector was fabricated by ultraviolet light irradiation-assisted delignification of wood veneer, with conductivity derived from nickel and Zn-plated layers. This wooden current collector effectively limited the two-dimensional (2D) diffusion of Zn<sup>2+</sup> ions, thereby facilitating desolvation, which in turn enhanced Zn deposition kinetics and led to a more homogeneous deposition. As shown in Fig. 6f, the wood-based AZIB with wood@Ni@Zn as the anode and wood@Ni coated with  $\alpha$ -MnO<sub>2</sub> as the cathode achieved stable performance even at low temperatures. The resilience of wooden current collectors to deformation and their adaptability to low-temperature conditions indicate their great potential for diverse flexible energy storage applications. For example, the ZnTe semiconductor collector exhibited zincophilic properties that induced Zn deposition along the (002) plane, whereas its excellent mechanical properties withstand the anode volume changes during cycling (Fig. 6g). The architecture of this current collector prevented the formation of Zn dendrites, whereas its high chemical stability mitigated metal corrosion and HER. Thus, semiconductor materials can be incorpo-

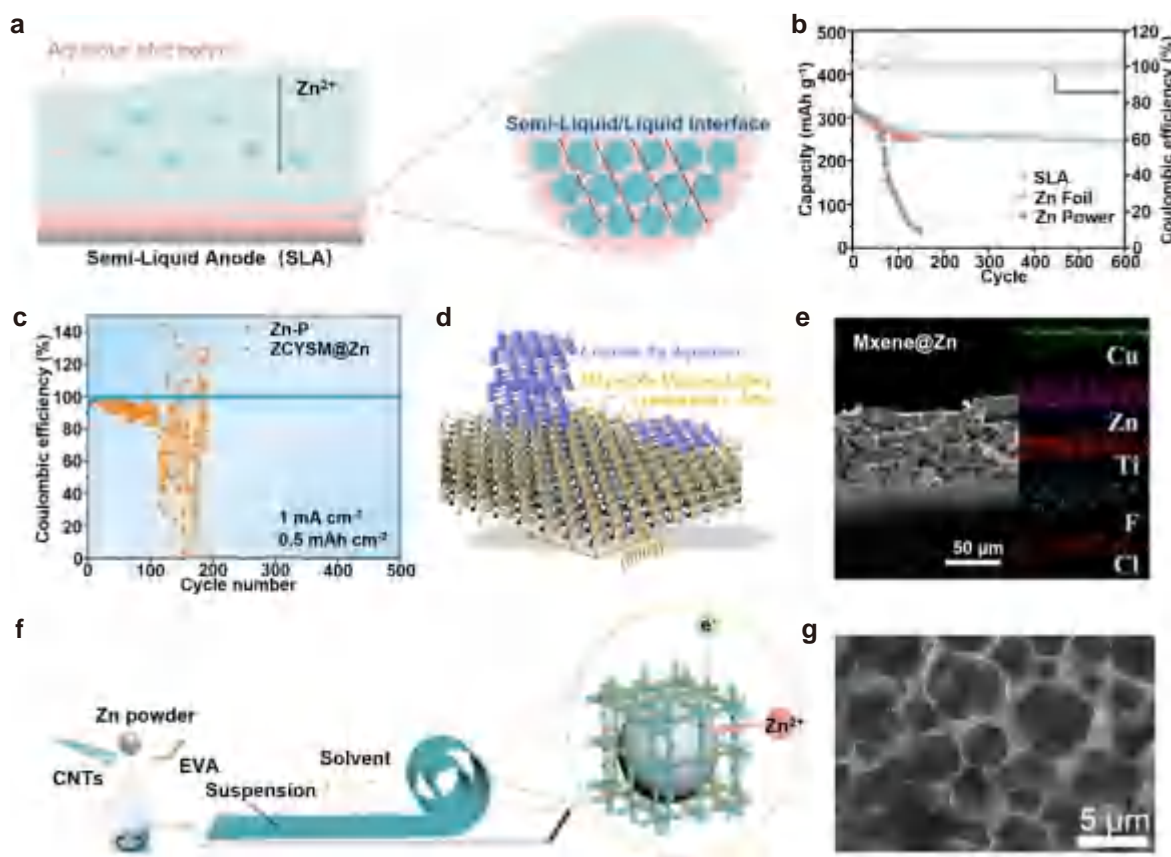
rated into the design of an anode current collector in AZIB, thereby suppressing the dendritic structure growth.

### 3.3 Zn powder anodes with a disordered structure

Despite the low cost, controllable particle size, and N/P ratio of Zn powder anodes compared with a Zn foil anode, their practical application has been hindered by inherent limitations. The Zn powder anode is susceptible to corrosion, leading to the formation of surface voids and cracking during static and cycling processes in aqueous electrolytes. This degradation affects the structural integrity of the anode<sup>[93]</sup>. In addition, Zn electrodes undergo volume changes during charge/discharge cycles. The structural instability of the Zn powder anode exceeds the elasticity limit of the binder, initiating binder failure that propagates from the interior of the material<sup>[17]</sup>. Although Zn powder anode electrodes exhibit high electrochemical activity, they lack macroscopic electrical conductivity. The stripping of Zn powder leads to volume reduction, thereby causing the loss of physical contact among adjacent Zn powder particles. This loss of electrical contact sharply increases polarization voltage, thereby leading to the rapid failure of the Zn powder anode over a short operational lifespan.

Semi-liquid electrodes provide a solution to the stress concentration issues associated with the rigid structure of conventional solid Zn powder electrodes. Semi-liquid materials are non-Newtonian fluids, which consist of a direct mixture of two-phase substances with specific contents, such as metal particles and liquids<sup>[94]</sup>. This homogeneous colloidal dispersion exhibits fluidity and liquid-like rheological (shear thinning) properties when subjected to vibration. Under external forces, the semi-liquid material loses its strength to release deposition stress. Therefore, semi-liquid anodes provide dendrite-free plating behavior similar to the function of liquid metals. Zhang et al. designed a semi-liquid anode (SLA) by mixing Zn powder with a dual conductive (ionically and electronically) poly(ethylene glycol) (PEG)-Zn<sup>2+</sup>/carbon composite matrix (Fig. 7a)<sup>[95]</sup>. This unique anode utilized its rheological properties to effectively release stresses caused by Zn plating, especially at high current densities. The dual conductive network within the SLA ensured a homogeneous Zn<sup>2+</sup> flux and facilitated stripping/plating throughout the bulk of the electrode. As shown in Fig. 7b, the SLA endowed the full battery with impressive long-term cycle performance, achieving over 600 cycles with a capacity of 250 mAh g<sup>-1</sup>. In addition, Sn powder was incorporated as a zincophilic additive within polyacrylamide elastic rheological networks, where Zn was uniformly deposited on dispersed Sn





**Figure 7** Zn powder anodes with a disordered structure. (a) Schematic illustrations of the morphological evolution of SLA/Zn powder anodes. (b) Cyclic performance of the  $\text{Zn}||\text{Cu}_x\text{V}_2\text{O}_5 \cdot n\text{H}_2\text{O}$  full cell at  $1 \text{ A g}^{-1}$ . Reproduced from Ref. [95] with permission ©2023, Wiley-VCH GmbH. (c) CE of Zn plating/stripping for the ZCYSM@Zn electrode at  $2 \text{ mA cm}^{-2}$  with a capacity of  $1 \text{ mAh cm}^{-2}$ . Reproduced from Ref. [96] with permission ©2023, Wiley-VCH GmbH. (d) Atomic-level illustration of the heterointerface and uniform Zn depositions. (e) Cross-sectional SEM image of the MXene@Zn anode on a Cu substrate, with energy dispersive spectroscopy (EDS) elemental mapping of Cu, Zn, Ti, Cl, and F. Reproduced from Ref. [17] with permission ©2021, American Chemical Society. (f) Schematic illustration of the synthesis procedure for the fabrication of Zn-P-MIEC. Reproduced from Ref. [30] with permission ©2022, Wiley-VCH GmbH. (g) SEM image of the carbon network after Zn etching for the bulk Zn@C composite anode. Reproduced from Ref. [97] with permission ©2024, Wiley-VCH GmbH.

particles, thereby preventing the agglomeration of Zn deposition and mitigating volume changes during repeated Zn stripping/plating cycles<sup>[98]</sup>. In another report, Li et al. proposed a high-performance soft-solid-phase viscoelastic Zn powder composite anode, utilizing an oligomer gluing strategy. Given its viscoelasticity, the soft-solid Zn powder composite (ss-ZnP) anode remarkably enhanced the charge transfer, weakened the volume effect, and homogenized the interfacial electric field. This phenomenon resulted in fast plating/stripping kinetics and a dendrite-free deposition morphology<sup>[99]</sup>. Given the low viscosity of the substrate in rheological soft-solid electrodes, conductive fillers were allowed to respond to stresses induced by volume changes, reconstructing conductive paths by diffusion or induced dipole interactions. This reaction effectively mitigated the electrical contact failure in rigid porous structures, effectively extending the cycling life of Zn powder anodes.

The conventional doctor-blade coated Zn powder anode cannot alleviate Zn powder corrosion and electrode delamination during long cycling process. Thus, researchers have endeavored to address these challenges by refining the porous structure of Zn powder electrodes<sup>[100–102]</sup>. Liu et al. developed porous Zn@C solid hollow yolk-shell microsphere membranes as Zn anode antifluctuation agents. The yolk-shell microsphere (ZCYSM) films exhibited good buffering properties, effectively confining Zn deposition within their structure and inhibiting volume expansion during plating/stripping cycles. Consequently, the ZCYSM@Zn electrode demonstrated a stable and reversible voltage profile for over 4,000 h. The ZCYSM@Zn||Ti cell delivered an ultra-long cycle life of 500 cycles with an average CE of 99.52% (Fig. 7c).

Recently, Niu et al. anchored zincophilic Bi metal nanosheets onto the surface of Zn powder anodes, where zincophilic metals served as preferential Zn

nucleation sites and as charge-aggregated protrusions. The resulting gradient-free  $\text{Zn}^{2+}$  ion distribution across the powder electrode contributed to an unprecedented life exceeding 5,600 h at a current density of  $1 \text{ mA cm}^{-2}$ . Furthermore, this innovative approach achieved an exceptionally high Zn utilization of 60% (with  $40 \text{ mA cm}^{-2}$  and  $10 \text{ mAh cm}^{-2}$ )<sup>[103]</sup>.

The inherent volume expansion associated with Zn powder electrodes poses challenges when paired with planar collectors such as Cu foils, necessitating the development of self-supporting porous structures to enhance 3D ionic and electronic conductivity, thereby homogenizing ion flux. Wu et al. designed a binder-free anode using the spontaneous reaction of commercial Zn powder and graphene oxide<sup>[104]</sup>. The remaining functional groups on the graphene sheets endowed the electrodes with intact and robust mechanistic properties. A stable, highly reversible, and dendrite-free Zn powder anode was constructed using 2D flexible conducting  $\text{Ti}_3\text{C}_2\text{T}_x$  MXene flakes with a hexagonally and closely spaced lattice as a redistributor of electrons and ions<sup>[17]</sup>. The low lattice mismatch ( $\sim 10\%$ ) led to the formation of a coherent, non-uniform interface between the (0002) side of deposited Zn and the (0002) side of  $\text{Ti}_3\text{C}_2\text{T}_x$  MXene (Fig. 7d). This interface induced rapid homogeneous nucleation of  $\text{Zn}^{2+}$  and sustained reversible stripping/plating with minimal energy barriers through internally bridged shuttle channels. The MXene@Zn anodes were coated on a Cu substrate (Fig. 7e), revealing densely stacked MXene@Zn composite spheres that formed a flat yet rough surface.

Apart from optimizing conductive additives, polymers could also serve as versatile scaffolds for Zn powder electrodes. Liang et al. used ethylene-vinyl acetate (EVA) copolymers as scaffolds, introducing a mixed ionic–electronic conducting scaffold into Zn-P (donated as Zn-P-MIEC) to fabricate flexible and dendrite-free Zn anodes via a scalable tape-casting strategy (Fig. 7f). The high ductility of EVA allowed for easy curling without cracking, and the electrodes maintained their integrity even after repeated folding, demonstrating their excellent flexibility. Recently, Han et al. developed a 3D continuous carbon network-reinforced Zn-powder-based composite anode (Zn@C) by utilizing glucose as a carbon precursor to *in situ* form a carbonaceous layer on the surface of the Zn powder. Subsequently, they used spark plasma sintering to remelt and reconnect the carbon layer into a continuous conductive network (Fig. 7g)<sup>[97]</sup>. The Zn@C electrode achieved favorable results in suppressing side reactions and improving electrical conductivity, providing valuable insights into industrial-scale fabrication. Similarly, a Zn composite anode was developed by compacting Zn powder with zincophilic site-enriched

nanosheets. This anode design effectively fastened ion diffusion and charge transfer kinetics, thereby boosting the fast-cycling performance of AZIBs. The symmetric cell exhibited excellent durability, sustaining for over 13,000 cycles at  $50 \text{ mA cm}^{-2}$  with  $1 \text{ mAh cm}^{-2}$ <sup>[105]</sup>.

In general, research on Zn powder electrodes remains in its early stages because of the complex electrochemistry of Zn powder. Further studies should focus on understanding the mass transport and charge transport mechanisms of Zn powder electrodes. Ensuring the structural integrity and electrochemical performance of the porous structure during extensive cycling remains a critical area for future investigation.

## 4 Porous Zn anodes with an ordered structure

In general, porous Zn electrodes exhibit macroscopic isotropy, incorporating active materials, conductive additives, binders, and an interconnected network of pores. However, the tortuous nature of ion migration within these pores, coupled with the anisotropic electric field during battery operation, leads to non-uniform mass transport along the direction of the electrode depth<sup>[106]</sup>. This phenomenon results in a concentration gradient that causes disparate reaction kinetics at varying depths, with not all active materials being accessed and activated simultaneously<sup>[107,108]</sup>. The difference in charge transport kinetics and reaction kinetics results in the polarization and insufficient utilization of active materials, especially at high current rates. Under certain magnification conditions, the reaction polarization increases with the electrode thickness because of the prolongation of the diffusion path<sup>[109]</sup>. The preferential deposition of  $\text{Zn}^{2+}$  ions at regions of higher ion flux, such as the separator–anode interface, can induce “top growth” and Zn dendrite formation. Therefore, designing electrodes with tailored structures is important to regulate charge transfer. In particular, the development of electrodes with gradient microstructures or compositions along the depth direction can reduce the resistance of the process during charge transfer, thereby compensating for the reactive polarization. By controlling the surface zincophilicity or conductivity of the electrode framework, the diffusion and deposition dynamics of  $\text{Zn}^{2+}$  ions can be regulated, thereby improving the rate performance and power density of AZIBs.

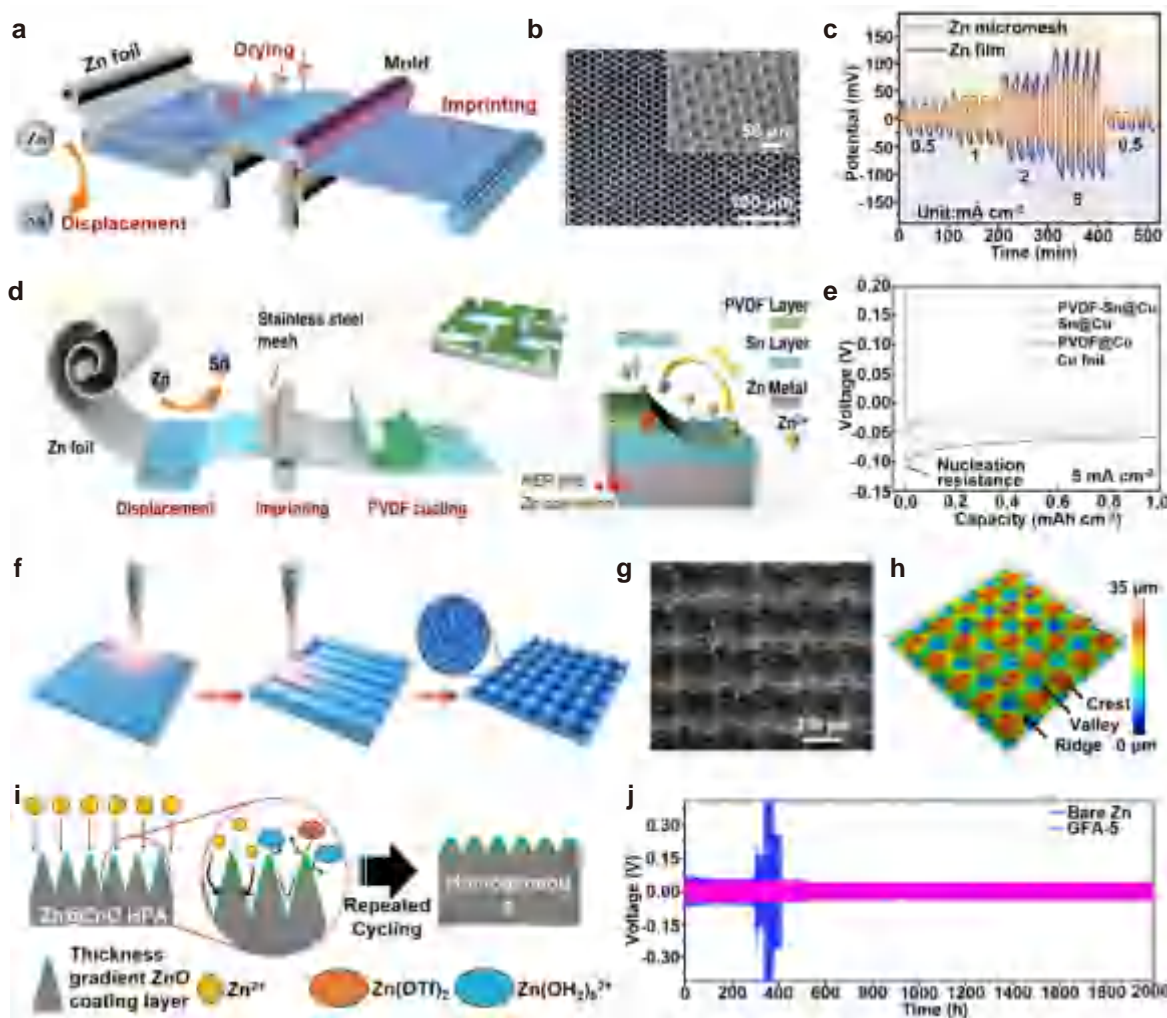
### 4.1 Zn foil anodes with an ordered structure

In general, most of the porous structures constructed on the surface of Zn foils are created using etching agents. However, the deployment of these agents necessitates meticulous control over their concentra-

tion and the duration of etching to ensure a uniform array of pores or stripes. Precision is critical to prevent over-etching, which can lead to side reactions at the enlarged active sites. Furthermore, the impact of the resultant disordered pore structure on the transport path of  $\text{Zn}^{2+}$  ions and the associated charge transfer resistance has not been extensively investigated. Therefore, designing an ordered structure along the electrode thickness direction is necessary to optimize pore morphology, electrical conductivity, and zincophilicity.

The imprint-induced microchannels, which

exhibit enhanced  $\text{Zn}^{2+}$  affinity, effectively regulate the concentration distribution of  $\text{Zn}^{2+}$  ion and prevent the risk of short circuits caused by vertical dendrite growth<sup>[110]</sup>. Utilizing zincophilic Zn foils as the anode (obtained by an *in situ* substitution reaction with Sn salts) improved the deposition behavior at the top of conventionally imprinted electrodes (Fig. 8a). Notably, the microchannel portion of the imprinted electrode displayed a higher concentration of  $\text{Zn}^{2+}$  ions, directing the preferential migration of  $\text{Zn}^{2+}$  ions to the inner wall of the microchannel. This redistribution of  $\text{Zn}^{2+}$  concentration promoted the nucle-



**Figure 8** Zn foil anodes with an ordered structure. (a) Schematic illustration of the scalable imprinting technique used for the fabrication of porous Zn anodes. Reproduced from Ref. [110] with permission ©2022, Wiley-VCH GmbH. (b) Microscopic photo of a Zn micromesh, with an inset showing a SEM image of the Zn micromesh. (c) Rate performance of the symmetric cells based on Zn micromesh and Zn film anodes at current densities ranging from 0.5 to 5 mA cm<sup>-2</sup>. Reproduced from Ref. [28] with permission ©2021, Wiley-VCH GmbH. (d) Schematic illustration of the fabrication of a PVDF-Sn@Zn gradient electrode and the subsequently induced Zn deposition. (e) Voltage–time curves for Zn deposition at a constant current density of 5 mA cm<sup>-2</sup> on different electrodes. Reproduced from Ref. [20] under the CC BY 4.0 license ©2023, The Authors. (f) Schematic depiction of the top-down fabrication of the geometrically periodic concave-convex laser lithography-patterned Zn foils (LLP@ZF) by nanosecond laser lithography. Low-magnification SEM image (g) and confocal light microscope map (h) for the surface morphology of LLP@ZF. Reproduced from Ref. [111] with permission ©2022, Elsevier B.V. (i) Schematic illustration of the deposition behavior of Zn ions on the Zn@ZnO HPA anode in an aqueous electrolyte. Reproduced from Ref. [27] with permission ©2020, Wiley-VCH Verlag GmbH & Co. KGaA, Weinheim. (j) Voltage profiles of the modified Zn anode at a current density of 1 mA cm<sup>-2</sup> and a capacity of 1 mAh cm<sup>-2</sup>. Reproduced from Ref. [112] with permission ©2022, The Royal Society of Chemistry.



ation and deposition of  $\text{Zn}^{2+}$  ions at the inner wall of the microchannel, thereby preventing uneven deposition and dendrite growth<sup>[113]</sup>. The majority of reported structurally engineered Zn anodes have not achieved precise control over the actual dimensions of the 3D network and efficient regulation of the micro/nanostructure, thereby failing to utilize the full potential of the porous design<sup>[114]</sup>. In particular, cross-scale variations and the disordered nature of micro/nanopores decreased the charge transport rate<sup>[115]</sup>. By contrast, electrodes with regularly arranged structures show superior performance over their disordered counterparts by achieving highly organized charge transfer pathways and adjustable internal voids. Zhang et al. synthesized flexible, ultrathin, and ultralight Zn micromesh (with a thickness of 8  $\mu\text{m}$  and an areal density of 4.9  $\text{mg cm}^{-2}$ ) through a synergistic approach combining photolithography and electrochemical processing, resulting in the regular arrangement of micropores<sup>[28]</sup>. The engineered microporous Zn micromesh exhibited excellent flexibility, enhanced mechanical strength, and improved wettability (Fig. 8b). The voltage hysteresis of Zn micromesh symmetric cells was consistently lower than that of cells assembled with Zn films across all tested current densities. This difference became more pronounced with the increase of current density (Fig. 8c). Guan et al. reported an imprinted gradient Zn anode (PVDF-Sn@Zn) that integrated conductive and hydrophilic gradients<sup>[20]</sup>. The top layer, which is composed of hydrophobic and insulating PVDF, and the bottom layer, which consisted of hydrophilic and conductive Sn, worked synergistically to enhance the corrosion resistance of the Zn anode and inhibited the HER (Fig. 8d). This bottom-up deposition behavior of Zn metal could effectively avoid the issue of top dendrite growth. As shown in Fig. 8e, the PVDF-Sn@Cu gradient electrode demonstrated the lowest nucleation overpotential (18.9 mV), indicating that the optimized gradient structure facilitated Zn nucleation and deposition. The well-designed regular pore structure fully exploited the ability of micropores to induce a favorable ion concentration and current distribution, a phenomenon that can be rationalized through computational simulations.

Laser-based techniques can precisely control the arrangement and size of micropores on the surface layer of Zn foils, thereby modulating Zn deposition and enhancing electrochemical performance. Yang et al. applied laser processing to create a periodic concave-convex pattern on commercial Zn foils (Fig. 8f)<sup>[111]</sup>, resulting in hydrophilic properties caused by enhanced wettability. This uniform secondary roughness, combining microscale and nanoscale features, was attributed to localized Zn melting and evaporation during laser processing. The periodic patterned egg crate-shaped concave-convex surface is shown in Fig. 8g.

The confocal light microscope map confirmed well-defined crests (red), ridges (green), and valleys (blue), with consistent intervals and height differences (Fig. 8h). Laser processing also enabled vertical gradient conductivity in Zn electrodes, as demonstrated by Huang et al. who developed a gradient Zn anode with an insulating hydrophobic passivation layer at the top and a conductive hydrophilic fresh Zn layer at the bottom<sup>[18]</sup>. This design effectively reduced corrosion and guided Zn deposition to prevent dendrite growth.

The construction of gradient porous structures on the surface of Zn foils often requires novel fabrication processes and sophisticated designs. As illustrated in Fig. 8i, Lee et al. engineered a novel Zn metal electrode with a compositionally and morphologically controllable surface through periodic anodic oxidation, resulting in a ZnO layer with a gradient thickness coated on a Zn hexagonal pyramidal array (Zn@ZnO HPA)<sup>[27]</sup>. The ZnO islands, formed through homogeneous dissolution and selective deposition, exhibited a thickness gradient that diminished from the top to the bottom (Fig. 8i). The ZnO coated on hexagonal pyramidal structures induced  $\text{Zn}^{2+}$  ion plating at the sides and bottom because of their relatively low interfacial resistance and served as passivation layers against aqueous electrolytes. Zhi et al. have introduced a simple *in situ* constructed porous framework coating that not only eliminated Zn dendrites but also suppressed HER<sup>[112]</sup>. This coating consisted of spatially gradient fluorinated alloy (GFA) nanoparticles, with  $\text{ZnF}_2$  in the outermost layer and CuZn alloy in the inner layer. The lateral growth within the GFA coating was induced by the formation of CuZn alloys within the particles, which stored the plated Zn and filled the interparticle voids, thereby adapting to a dendrite-free morphology. Consequently, the symmetric cell demonstrated excellent long-term cycling stability over 2,000 h (1,000 cycles) with stable voltage profiles at 1  $\text{mA cm}^{-2}$  and 1  $\text{mAh cm}^{-2}$  (Fig. 8j). Despite these advancements, a cohesive theoretical framework elucidating the impact of pore structures on the electrochemical kinetics of Zn anodes in AZIBs remains unknown, which requires further investigation and development.

## 4.2 Current collectors with an ordered structure

Designing 3D porous current collectors is a prevalent approach to address the challenges associated with Zn electrodes. The enhanced specific surface area of these current collectors reduces the localized current density at the 3D Zn electrode, thereby decreasing the overpotential and moderating Zn deposition. Carbon-based materials, which are known for their high electrical conductivity, light

weight, and facile fabrication, are commonly used as conductive substrates for Zn anodes.

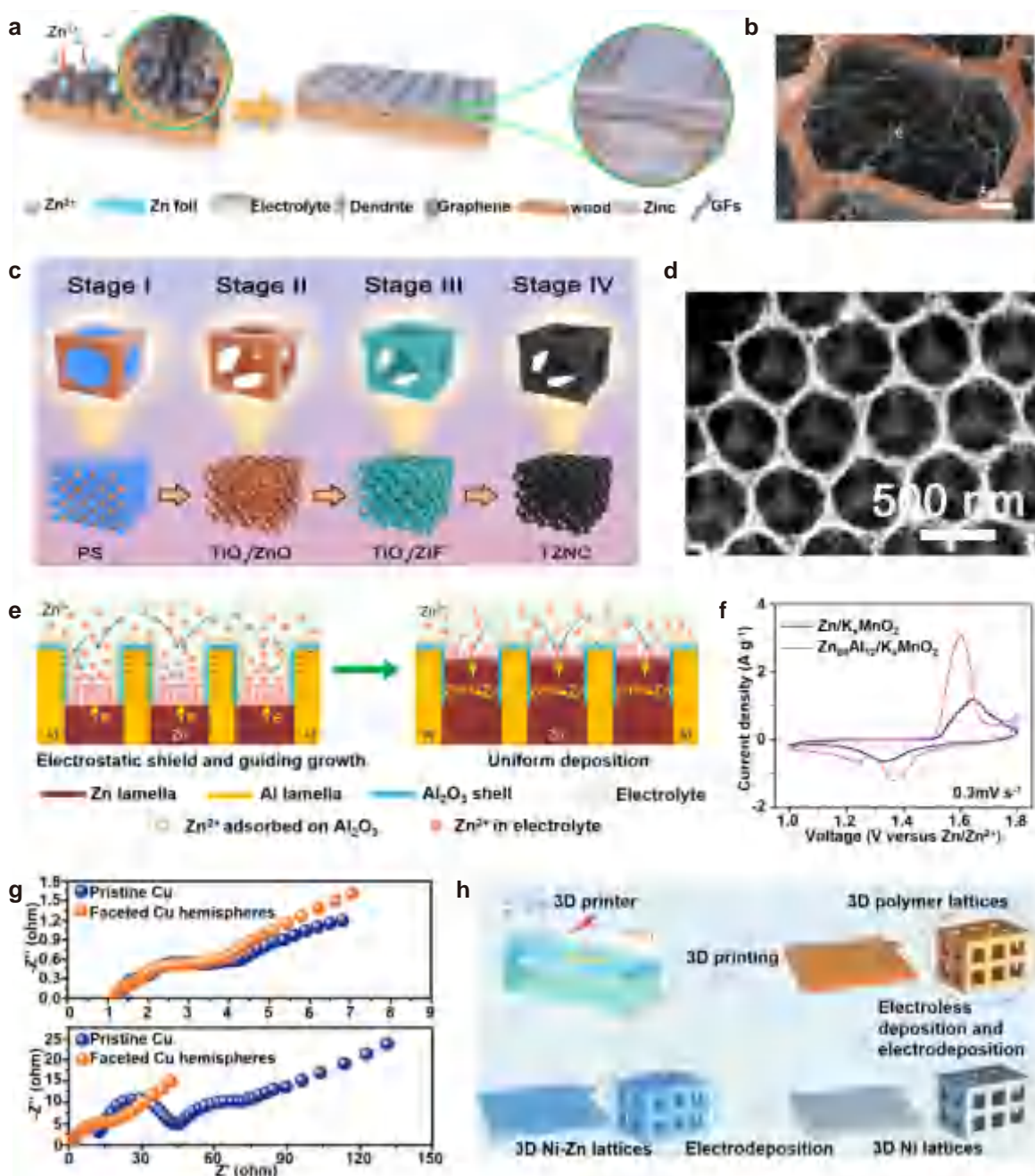
However, the uneven ion flux distribution at high current densities leads to Zn deposition on the upper surfaces of the porous structures, resulting in the inefficient utilization of 3D space and potentially causing short-circuit issues due to dendrite growth. Therefore, strategically manipulating the electric field distribution and ion concentration by rationally designing a spatial structure of the carbon-based current collectors is of great importance. Zhao et al. developed two 3D hierarchical graphene matrices consisting of nitrogen-doped graphene nanofiber clusters (GFs) anchored on vertical graphene arrays (VGs) of modified multichannel carbon (Fig. 9a)<sup>[32]</sup>. The Zn metal was deposited along the longitudinal direction (3D-LFGC) and radial direction (3D-RFGC) of the 3D multichannel carbon matrices. The modified carbon matrix exhibited channels with sizes ranging from 10 to 30  $\mu\text{m}$  (with a typical size of 20  $\mu\text{m}$ ). In particular, GFs with a diameter of 250 nm and VGs were firmly embedded within the channels, creating a 3D interconnected and versatile framework (Fig. 9b). Compared with 3D-LFGC, 3D-RFGC showed reduced plateau overpotentials at different current densities, indicating lower local current densities and more homogeneous  $\text{Zn}^{2+}$  ion distributions. This finding was attributed to the effective electrolyte infiltration into the substrate and the robust interaction between Zn and VGs and GFs, which promoted homogeneous Zn ion flux distribution and dense Zn deposition. Apart from modifying ordered graphene arrays, constructing highly organized carbon frameworks to homogenize the ion flux is also a viable approach. Lou et al. developed a highly ordered  $\text{TiO}_2/\text{Zn}/\text{N}$ -doped carbon inverse opal (denoted as TZNC IO) to spatially stabilize Zn anodes<sup>[116]</sup>. The fabrication of TZNC IO involved evaporation-induced self-assembly, impregnation, and calcination (Figs. 9c and 9d). The 3D macroporous framework with a periodic structure allowed precise electric field control, minimizing the local current and inducing uniform Zn deposition. In addition, the interconnected pores provide ample void space to regulate  $\text{Zn}^{2+}$  ion flux and alleviate volume expansion.

Given the inherent lack of a host for Zn,  $\text{Zn}^{2+}$  ions nucleate preferentially at defect sites such as dislocations, leading to the formation of dendrite protrusions. To modulate the deposition/stripping behavior of Zn, the design of metal-based current collectors is meticulously optimized to enhance crystal surface orientation, local conductivity, and atomic binding energy, while also engineering orderly pore architectures. The  $\text{Zn}_{88}\text{Al}_{12}$  alloy formed by casting, featured symbiotic Zn and Al lamellas<sup>[26]</sup>, exhibited improved oxidation resistance in air and aqueous

electrolytes compared with monometallic Zn because of the formation of a stable and passive  $\text{Al}_2\text{O}_3$  surface layer that prevented further oxidation (Fig. 9e). The insulating  $\text{Al}_2\text{O}_3$  shell, which substantially blocked the electron transfer from Al to  $\text{Zn}^{2+}$ , facilitated uniform Zn deposition at the interlayer spacing along the Zn precursor sites. Compared with the  $\text{Zn}||\text{K}_x\text{MnO}_2$  cell, the  $\text{Zn}_{88}\text{Al}_{12}||\text{K}_x\text{MnO}_2$  cell demonstrated a marked increase in current density, with  $\text{Zn}_{88}\text{Al}_{12}$  showing more reversible deposition/stripping behavior than pure Zn (Fig. 9f). In addition, commercial Cu foams generally suffer from irrational pore distribution and poor utilization of internal space. Jiang et al. developed Cu current collectors with periodically arranged 3D hemispherical pits through a synergistic approach involving photolithography and wet chemistry<sup>[117]</sup>. The battery based on faceted Cu hemispherical electrodes exhibited a lower charge transfer resistance (18  $\Omega$ ) than that of pristine Cu electrodes (30  $\Omega$ ) because of the improved electrolyte wettability (Fig. 9g). The integration of a controllable spatial arrangement with a zincophilic design in porous metal current collectors is emerging as a research trend for dendrite-free AZIBs. However, the complexity and high cost of such batteries hinder their widespread applications.

The application of 3D printing technology as a high-precision additive manufacturing method for energy storage devices has received considerable attention<sup>[118,119]</sup>. This advanced technique diverges from conventional porous collectors (e.g., Cu foam and CC) by enabling the precise engineering of pore architectures that facilitate controlled ion flux and electric field distribution. Duan et al. innovated a strategy that combined 3D printing with chemical deposition to fabricate conductive 3D nickel lattice current collectors<sup>[115]</sup>. The process involved the sequential application of chemical and electrochemical deposition to coat a pre-printed 3D polymer framework with a metallic Ni layer, which exhibited strong binding affinity to Zn atoms. Subsequently, the formed conductive metal network was electrodeposited with Zn to yield the final electrodes (Fig. 9h). The multichannel lattice structure of the 3D porous Ni-Zn anode optimized the electric field distribution across the electrode, thereby promoting uniform Zn deposition and enhancing the electrochemical performance of AZIBs. The 3D printing paradigm provides a versatile and customizable platform, with demonstrated efficacy in incorporating advanced materials such as graphene<sup>[120]</sup> and N-doped inter-faces<sup>[121]</sup> into the fabrication of Zn anodes.

Ion diffusion within the porous electrode plays a key role in the charge transport kinetics; thus, the modulation of the pore structure of electrodes is a strategic approach to regulate ion flux and alleviate polarization. Researchers have used porous carbon



**Figure 9** Current collectors with an ordered structure. (a) Schematic depiction of the engineered 3D hierarchical graphene matrix architecture that is designed to stabilize Zn anodes. (b) SEM images of the 3D hierarchical graphene matrix. Reproduced from Ref. [32] under the CC BY 4.0 license ©2023, The Authors. (c) Schematic illustration of the synthesis process for the  $\text{TiO}_2/\text{Zn}/\text{N}$ -doped carbon inverse opal (TZNC IO) anode. (d) Field-emission scanning electron microscopic images of TZNC IO. Reproduced from Ref. [116] with permission ©2021, Wiley-VCH GmbH. (e) Schematic illustration of the eutectic strategy utilizing Zn/Al lamellar eutectic structures for suppressing dendrite growth and crack formation. (f) Typical CV curves of  $\text{Zn}_{88}\text{Al}_{12}||\text{K}_x\text{MnO}_2$  and  $\text{Zn}||\text{K}_x\text{MnO}_2$  full cells using eutectic  $\text{Zn}_{88}\text{Al}_{12}$  alloy ( $\lambda \approx 450 \text{ nm}$ ) or the monometallic Zn as the anode. Reproduced from Ref. [26] under the CC BY 4.0 license ©2020, The Authors. (g) Nyquist plots before and after galvanostatic discharge and charge processes. Reproduced from Ref. [117] with permission ©2023, Wiley-VCH GmbH. (h) Schematic illustration of the fabrication procedure for 3D Ni-Zn lattice structures. Reproduced from Ref. [115] with permission ©2021, Wiley-VCH GmbH.

skeletons or metal structures as the host framework to build 3D structures that facilitate extensive ion diffusion. Despite these efforts, the concentration gradient within the porous Zn anode still induces nonhomogeneous transport of  $\text{Zn}^{2+}$  ions, which is particularly pronounced in thick electrodes subjected

to fast charging and discharging cycles.  $\text{Zn}^{2+}$  ions are preferentially deposited at the electrolyte–electrode interface, where the ion flux is elevated, rather than within the electrode. This behavior leads to the inefficient utilization of the internal electrode space and the formation of dendrites, which compromises



battery safety and longevity<sup>[122,123]</sup>. Therefore, designing electrode structures with a pore structure gradient that promotes ion flow toward the interior of the electrode is instrumental in promoting favorable reaction kinetics. Studies have demonstrated that optimizing the electrode porosity through model-based simulations effectively reduces ohmic resistance and increases LIB capacity<sup>[124,125]</sup>. Given these findings, researchers have implemented gradient porosity in porous Zn anodes for AZIBs, thereby enhancing the overall battery performance<sup>[31,126]</sup>.

Considering that Zn deposition occurs where Zn ions encounter electrons, the electric field distribution plays an important role in regulating Zn deposition. Therefore, constructing a gradient framework that enhances the electronic conductivity from the separator side to the cell shell side is recommended. This design facilitates the directional deposition of Zn from the bottom and grows upward. Several studies have demonstrated the successful implementation of gradient conductivity in porous Zn anodes. By constructing an electronically insulating layer such as  $\text{Al}_2\text{O}_3$ <sup>[26]</sup>,  $\text{NiO}$ <sup>[31,127]</sup>, or PVDF<sup>[110]</sup>, on top of the electrode structure, a vertical variation in localized conductivity has been achieved. This strategy has been instrumental in achieving dendrite-free AZIBs.

A zincophilic gradient could be constructed in the opposite direction of the Zn ion concentration gradient to regulate Zn ion fluxes within the pore structure. This strategy can be accomplished by incorporating zincophilic metal layers or nanoparticles at the bottom of the electrode, which reduces the nucleation overpotential of Zn ions and increases the ion flux. By meticulously adjusting the thickness, particle concentration, or composition of these zincophilic modifications, a gradient in zincophilicity can be engineered, thereby facilitating a more controlled and efficient Zn deposition<sup>[128]</sup>.

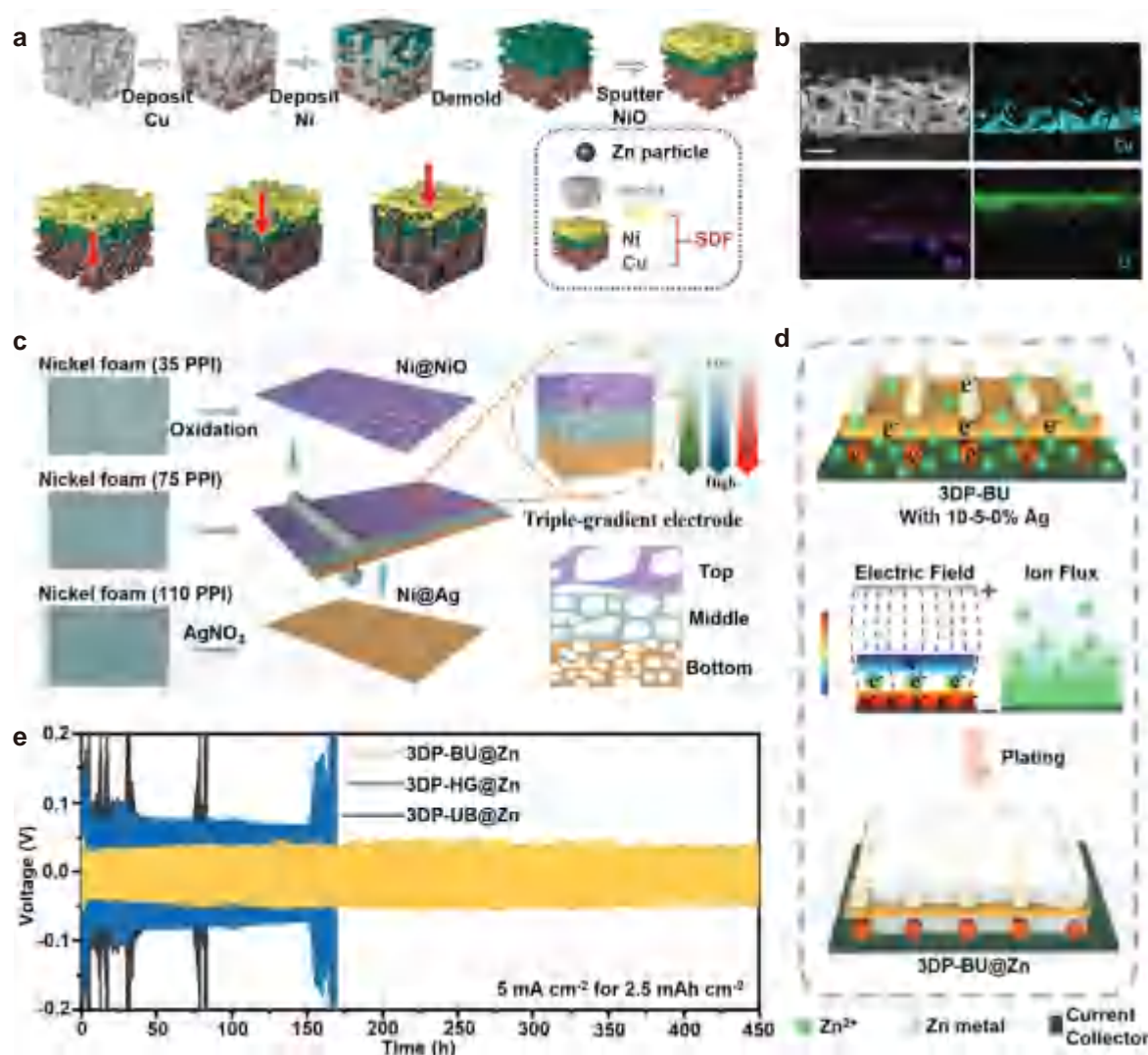
In enhancing the electrochemical performance of AZIBs, studies have explored the integration of zincophilic and conductive gradients into a dual-gradient framework to improve the reaction kinetics by synergistically modulating the ion and electron transport kinetics. In addressing “top growth” associated with commercial Cu foam, Hong et al. fabricated porous foam electrodes with a gradient in conductivity and zincophilicity<sup>[127]</sup>. As shown in Fig. 10a, a hydrophilic yet electrically insulating NiO layer was formed on the separator side of the electrode by using a novel bilateral template method, complemented by a conductive Cu foam on the cell shell side (Fig. 10b), which exhibited a high binding energy to Zn. This layered deposition strategy achieved a “bottom-to-up” deposition mode, thereby enhancing the capacity and rate performance of the battery. Similarly, a GFA electrode, featuring a conductive bottom layer and an insulating top layer, demonstrated highly reversible Zn plating/stripping

behavior for 700 h at  $3 \text{ mA cm}^{-2}$ <sup>[112]</sup>. Guan et al. designed a tri-gradient dendrite-free electrode that integrated gradients in conductivity, zincophilicity, and porosity<sup>[31]</sup>. This tri-gradient design introduced an enhanced  $\text{Zn}^{2+}$  ion flux and optimized local charge transport kinetics at the bottom of the electrode, facilitating the downward migration of  $\text{Zn}^{2+}$  ions and promoting the bottom-up deposition of Zn metal (Fig. 10c). Recently, a novel electron/ion flux dual-gradient 3D porous Zn anode has been engineered by using a layer-by-layer bottom-up approach with attenuating Ag nanoparticles (3DP-BU@Zn). This established hierarchical porous architecture facilitated a preferential bottom-up Zn deposition, thereby enhancing the overall anode performance (Fig. 10d)<sup>[41]</sup>. At a high current density of  $5 \text{ mA cm}^{-2}$  and a capacity of  $2.5 \text{ mAh cm}^{-2}$ , 3DP-BU@Zn exhibited low-voltage hysteresis of 41.9 mV within 450 h, surpassing the performance of electrodes without dual-gradient and inverse-gradient designs (Fig. 10e).

### 4.3 Zn powder anodes with an ordered structure

Given its malleability, Zn powder can be used to fabricate regular porous electrodes through 3D printing<sup>[22]</sup>. However, the inherent drawbacks of Zn powder anodes, such as susceptibility to corrosion and uncontrolled dendrite growth, have limited their broader applications. Studies have shown that encapsulating the Zn-P surface with 2D conductive materials, such as MXenes, could mitigate volume expansion and dendrite growth. Xu et al. utilized an innovative 3D cold-trap environment printing (3DCEP) technique, which combined laminar flow and ice crystal sensing, to achieve an orderly arrangement of MXene nanosheets during 3D printing<sup>[129]</sup>. The high lattice matching between MXene and Zn, along with spatial constraints at the MXene interface, inhibited the dendrite growth (Fig. 11a). To solve the issue of uneven MXene encapsulation on Zn powder, which is common in traditional ink direct writing, Pang et al. introduced a novel microfluidic-assisted 3D printing strategy<sup>[130]</sup>. This strategy used a magneto-thermal flow microfluidic technique that modified the raw materials within the microfluidic channel by external conditions during the ink flow process, inducing the aggregation of MOF and MXene on the surface of Zn powder. The MXene in this context was endowed with a functional layer of Cu-tetrahydroxy-1,4-benzoquinone (Cu-THBQ)-conductive MOF, which provided stable adsorption and diffusion coefficients for  $\text{Zn}^{2+}$ , facilitating uniform Zn deposition.

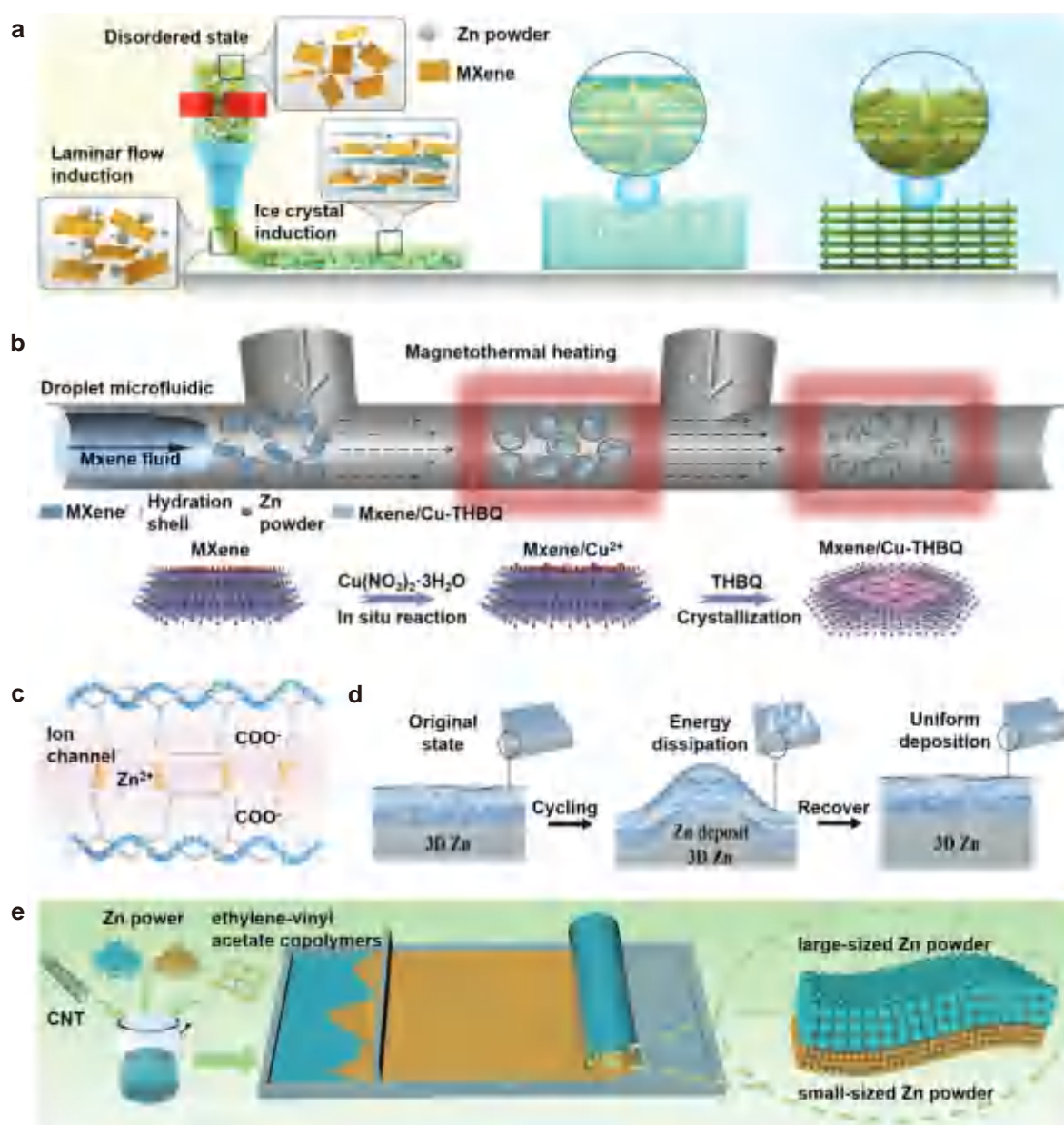
Achieving a balance between the design of 3D structures and corrosion mitigation is challenging, as the increased contact area between the electrode and electrolyte exacerbates electrode corrosion<sup>[64,132,133]</sup>. Consequently, designing appropriate coatings on



**Figure 10** Gradient design of porous current collectors. (a) The prepared procedures of the innovative tri-layers frame collector (SDF) structure. (b) Cross-sectional SEM images of vacant SDF structure with EDS images of Cu, Ni, and O. Reproduced from Ref. [127] with permission ©2021, Wiley-VCH GmbH. (c) Schematic diagram of the triple-gradient electrode fabrication utilizing a mechanical rolling technique. Reproduced from Ref. [31] with permission ©2023, Wiley-VCH GmbH. (d) Schematic diagrams of electron/ion flux dual-gradient scaffolds illustrating the Zn deposition behavior under various electron/ion flux conditions. (e) Cycling performances of different symmetrical cells under a current density of  $5 \text{ mA cm}^{-2}$  and an areal capacity of  $2.5 \text{ mAh cm}^{-2}$ . Reproduced from Ref. [41] under the CC BY-NC 4.0 license ©2023, The Authors.

porous Zn anode surfaces is a promising strategy<sup>[134,135]</sup>. Guan et al. coated a 3D-printed Zn scaffold with a layer of ion-conducting conformal hydrogel composed of sodium alginate and polyacrylamide, demonstrating impressive cycling stability of 4,700 h at  $5 \text{ mA cm}^{-2}$  and  $5 \text{ mAh cm}^{-2}$  for the symmetric cell<sup>[131]</sup>. As illustrated in Fig. 11c, the diffusion behavior of  $\text{Zn}^{2+}$  during Zn stripping/deposition was modulated by aryl and carboxylate salts within the hydrogel chains, providing specific ion diffusion channels and accelerating  $\text{Zn}^{2+}$  desolvation, thereby preventing unwanted dendrite growth. Dynamic adaptive hydrogel coatings alleviated stress accumulation from dendrite growth during cycling, maintaining long-term cycling stability of the anode (Fig. 11d).

Furthermore, the same group has pioneered the gradient design strategy for Zn powder anodes, which effectively regulated the Zn deposition behavior<sup>[126]</sup>. The particle size of the Zn powder and the porosity of the electrodes decreased in the depth direction, generating a bottom-up gradient of ion fluxes along the pore depth (Fig. 11e), which prevented the notorious “top growth” and relieved the stress concentration. Despite these advantages, Zn powder electrodes remain in the nascent stages of exploration, with cycling performance and thick electrode performance yet to meet expectations. The challenge lies in reconciling severe corrosion and structural collapse with the uniform ion fluxes caused by the expanded specific surface area of the porous structure of Zn powder.



**Figure 11** (a) Schematic illustration of 3D cold-trap environment printing for fabricating and aligning MXene/Zn-P aerogel. Reproduced from Ref. [129] with permission ©2023, Wiley-VCH GmbH. (b) Illustration of the microfluidic synthesis of MXene/Cu-tetrahydroxy-1,4-benzoquinone (THBQ)/Zn-P printable mixed ink and the synthetic mechanism underlying the formation of hetero-structured MXene/Cu-THBQ. Reproduced from Ref. [130] with permission ©2023, Wiley-VCH GmbH. (c) Schematic illustration of the ionic diffusion of  $\text{Zn}^{2+}$  in the hydrogel coating layer. (d) Schematic depiction of the interface coating and protective mechanism provided by a hydrogel layer on porous Zn anodes. Reproduced from Ref. [131] with permission ©2023, Wiley-VCH GmbH. (e) Schematic illustration of the fabrication of the gradient electrode. Reproduced from Ref. [126] with permission ©2023, Wiley-VCH GmbH.

Overall, the meticulously engineered porous architecture (characterized by optimized pore size, orderly pore arrangement, and gradient design), confers remarkable advancements to Zn anodes with regard to electric field distribution, ion flux dynamics, and nucleation overpotential. However, the introduction of a large number of inert materials could reduce the overall energy density of the battery, and the structural stability of these configurations under external stresses must be further investigated.

## 5 Summary and outlook

AZIBs are emerging as potential energy storage devices because of their inherent safety, low cost, and environmental benignity. However, their commercialization is hindered by challenges, such as persistent side reactions, low CE, and limited DOD for Zn anodes. The adoption of porous structures is a strategic solution to these issues. In this review, the research advancements in the design strategies of porous structures for Zn metal anodes were summa-



alized. Categorizing into disordered and ordered porous anode structures, the relationship between the fabrication method and the pore morphology has been elucidated. We focus on zincophilic modifications and gradient design in porous structure engineering and provide a comprehensive overview of the research on Zn powder anodes. Although remarkable progress has been achieved in recent years, scientific and engineering challenges remain to be addressed for the advancement of porous Zn metal anodes. Therefore, carrying out the following research directions is necessary to design and optimize porous Zn anodes:

**1. Material synthesis and structural optimization.** The use of porous structures has been instrumental in facilitating uniform Zn nucleation and growth, but it does not inherently prevent the side reactions that arise from the increased surface area. In addition, the fabrication of thick electrodes with low tortuosity provides unique advantages with regard to transport kinetics, a feature that has not been extensively reported in AZIBs. The precise control of low tortuosity electrode structures and the interplay between microstructural characteristics and performances warrant meticulous investigation to promote practical applications of AZIBs. Furthermore, the optimization of preparation methods, the exploration of new template materials, and the improvement of electrochemical corrosion methods are urgently necessary to achieve higher porosity and better structural control in the preparation of porous Zn metal anodes. For example, the use of nanoscale porous structures can enhance reactivity and reduce stress caused by electrode volume changes. The development of porous electrodes with gradient conductivity and zincophilicity is conducive to improving charge transfer kinetics.

Moreover, novel Zn alloy materials should be developed to improve the durability of porous Zn anodes by adjusting the alloy composition and the proportion of different metal elements. Optimizing the grain size and orientation of the alloy anode can further improve ion diffusion and electron conduction. By introducing interface modification layers or coatings, the compatibility and stability between the electrodes and the electrolyte can be enhanced, thereby suppressing electrolyte evaporation and solvent decomposition.

**2. Theoretical computation and advanced characterization.** Although the development of AZIBs has been of interest in recent years, the theoretical study of the electrochemical kinetics of AZIBs, particularly porous Zn anodes, has remained largely overlooked. Moreover, the applicability of formulas derived from LIBs to AZIBs is yet to be established. Theoretical computations complement experimental findings by exploring physical processes such as reac-

tion kinetics, charge transport kinetics, and structural evolution that extend beyond the limitations of experimental results. The integration of cutting-edge theoretical advancements with precise experimental data modeling is crucial for elucidating the intricacies of reaction kinetics and reversibility of porous Zn anodes.

Meanwhile, a profound understanding of microstructural evolution and its impact on battery performance is pivotal for optimizing porous Zn anodes. By using *in situ* atomic-scale characterization techniques, such as *in situ* electrochemical fluorescence microscopy, *in situ* electrochemical Raman spectroscopy, atomic force microscopy, and transmission electron microscopy, the electrochemical reaction process related to porous Zn anodes can be observed real time. In addition, the transport mechanism of  $\text{Zn}^{2+}$  ions between the electrodes and the electrolyte can be elucidated, providing key information for optimizing the material design and battery performance. Through surface and interface analysis (e.g., X-ray photoelectron spectroscopy, electrochemical impedance spectroscopy, and neutron diffraction), the surface composition, chemical state, and morphology of porous Zn anodes can be obtained, enabling a comprehensive understanding of the surface electrochemical properties and interfacial reaction characteristics of AZIBs. Moreover, differential scanning calorimetry and thermal gravimetric analysis can be used to study the thermal stability, phase behavior, and thermal decomposition characteristics of porous Zn anodes, which provides valuable insights into battery safety assessment and material design.

**3. System integration and practical evaluation.** The system integration design of AZIBs is an important direction for their future development, requiring the optimization of electrolyte formulation, battery components, and module design to achieve higher energy density, longer cycle life, and improved safety features. The majority of previous research work in the field of Zn anodes has emphasized cycling life as a key performance indicator. Although this indicator can be remarkably improved by incorporating excess Zn, standardized test parameters for battery cycling evaluation are lacking, such as current density, N/P ratio, and DOD. In particular, the areal capacity of cathodes is generally constrained to less than  $0.5 \text{ mAh cm}^{-2}$  to achieve high-multiplicity performance, resulting in low Zn utilization and a reduced mass energy density of the AZIBs.

Furthermore, the current production of porous Zn anodes typically involves complex manufacturing steps, thereby increasing production cost. Most of the meticulously considered designs, especially those involving gradient porous anodes, are not yet amenable to large-scale production. Consequently,

developing cost-effective and scalable methods for fabricating porous Zn anodes is crucial. In addition, assessing the battery performance under practical conditions is necessary to promote the practical applications of AZIBs.

Despite the need for further improvement with regard to battery cycle life, porous Zn anodes present distinct advantages, including the alleviation of local current density, uniformization of ion flux, and mitigation of volume expansion. The integration of advanced scientific investigations with engineering optimization strategies can facilitate the practical implementation of porous Zn anodes for high-performance AZIBs (Fig. 12).

### Acknowledgements

Yao Wang would like to acknowledge the support from National Natural Science Foundation of China (Grant No. 22309102) and China Postdoctoral Science Foundation (Grant No. 2022M711788). Dong Zhou would like to acknowledge the support from National Key Research and Development Program of China (Grant No. 2022YFB2404500) and Fundamental Research Project of Shenzhen (Grant No. JCYJ20230807111702005). Guoxiu Wang would like to acknowledge the support from the Australian

Research Council (ARC) through the ARC Discovery Project (Grant No. DP230101579) and ARC Linkage Project (Grant No. LP200200926).

### Author contribution statement

Yichen Ding and Bingyue Ling are responsible for writing the original drafts. Xin Zhao, Xu Yang and Yao Wang contributed greatly to the review and revision of the article. Dong Zhou and Guoxiu Wang took the oversight and leadership responsibility for the whole process. All the authors have approved the final manuscript.

### Data availability

Not applicable.

### Declaration of competing interest

All the contributing authors report no conflict of interests in this work.

### Funding

This work is granted by National Natural Science Foundation of China (Grant No. 22309102), China Postdoctoral Science Foundation (Grant No.



**Figure 12** Future research directions associated with the development of advanced porous Zn metal anodes for high-performance AZIBs.

2022M711788), National Key Research and Development Program of China (Grant No. 2022YFB2404500), Fundamental Research Project of Shenzhen (Grant No. JCYJ20230807111702005), the Australian Research Council through the ARC Discovery Project (Grant No. DP230101579) and ACR Linkage Project (Grant No. LP200200926).

## Use of AI statement

None.

## References

- [1] Yan, J. P., Ang, E. H., Yang, Y., Zhang, Y. F., Ye, M. H., Du, W. C., Li, C. C. (2021). High-voltage zinc-ion batteries: Design strategies and challenges. *Adv. Funct. Mater.* 31, 2010213.
- [2] Dunn, B., Kamath, H., Tarascon, J. M. (2011). Electrical energy storage for the grid: a battery of choices. *Science* 334, 928–935.
- [3] Zhu, Z. X., Jiang, T. L., Ali, M., Meng, Y. H., Jin, Y., Cui, Y., Chen, W. (2022). Rechargeable batteries for grid scale energy storage. *Chem. Rev.* 122, 16610–16751.
- [4] Ni, Q., Kim, B., Wu, C., Kang, K. (2022). Non-electrode components for rechargeable aqueous zinc batteries: Electrolytes, solid-electrolyte-interphase, current collectors, binders, and separators. *Adv. Mater.* 34, 2108206.
- [5] Li, Y., Wu, F., Li, Y., Liu, M. Q., Feng, X., Bai, Y., Wu, C. (2022). Ether-based electrolytes for sodium ion batteries. *Chem. Soc. Rev.* 51, 4484–4536.
- [6] Li, H. F., Ma, L. T., Han, C. P., Wang, Z. F., Liu, Z. X., Tang, Z. J., Zhi, C. Y. (2019). Advanced rechargeable zinc-based batteries: Recent progress and future perspectives. *Nano Energy* 62, 550–587.
- [7] Xu, C. J., Li, B. H., Du, H. D., Kang, F. Y. (2012). Energetic zinc ion chemistry: The rechargeable zinc ion battery. *Angew. Chem. Int. Ed.* 51, 933–935.
- [8] Gourley, S. W. D., Brown, R., Adams, B. D., Higgins, D. (2023). Zinc-ion batteries for stationary energy storage. *Joule* 7, 1415–1436.
- [9] Yu, X. H., Li, Z. G., Wu, X. H., Zhang, H. T., Zhao, Q. G., Liang, H. F., Wang, H., Chao, D. L., Wang, F., Qiao, Y., et al. (2023). Ten concerns of Zn metal anode for rechargeable aqueous zinc batteries. *Joule* 7, 1145–1175.
- [10] Chen, J. Y., Wang, Y. Z., Tian, Z. N., Zhao, J., Ma, Y. W., Alshareef, H. N. (2024). Recent developments in three-dimensional Zn metal anodes for battery applications. *InfoMat* 6, e12485.
- [11] Guo, N., Huo, W. J., Dong, X. Y., Sun, Z. F., Lu, Y. T., Wu, X. W., Dai, L., Wang, L., Lin, H. C., Liu, H. D., et al. (2022). A review on 3D zinc anodes for zinc ion batteries. *Small Methods* 6, 2200597.
- [12] Tian, H., Yang, J. L., Deng, Y. R., Tang, W. H., Liu, R. P., Xu, C. Y., Han, P., Fan, H. J. (2023). Steel anti-corrosion strategy enables long-cycle Zn anode. *Adv. Energy Mater.* 13, 2202603.
- [13] Wang, Y., Wang, T. R., Bu, S. Y., Zhu, J. X., Wang, Y. B., Zhang, R., Hong, H., Zhang, W. J., Fan, J., Zhi, C. Y. (2023). Sulfolane-containing aqueous electrolyte solutions for producing efficient ampere-hour-level zinc metal battery pouch cells. *Nat. Commun.* 14, 1828.
- [14] Feng, D. D., Jiao, Y. C., Wu, P. Y. (2023). Guiding Zn uniform deposition with polymer additives for long-lasting and highly utilized Zn metal anodes. *Angew. Chem., Int. Ed.* 62, e202314456.
- [15] Xie, X. S., Liang, S. Q., Gao, J. W., Guo, S., Guo, J. B., Wang, C., Xu, G. Y., Wu, X. W., Chen, G., Zhou, J. (2020). Manipulating the ion-transfer kinetics and interface stability for high-performance zinc metal anodes. *Energy Environ. Sci.* 13, 503–510.
- [16] Sun, G. Q., Zhou, M. Q., Dong, X. Y., Zang, S. Q., Qu, L. T. (2022). An efficient and versatile biopolishing strategy to construct high performance zinc anode. *Nano Res.* 15, 5081–5088.
- [17] Li, X. L., Li, Q., Hou, Y., Yang, Q., Chen, Z., Huang, Z. D., Liang, G. J., Zhao, Y. W., Ma, L. T., Li, M., et al. (2021). Toward a practical Zn powder anode:  $\text{Ti}_3\text{C}_2\text{T}_x$  MXene as a lattice-match electrons/ions redistributor. *ACS Nano* 15, 14631–14642.
- [18] Na, Z., Qi, H. K., Li, S. H., Wu, Y. B., Wang, Q. S., Huang, G. (2023). Stable zinc metal anode by nanosecond pulsed laser enabled gradient design. *ACS Energy Lett.* 8, 3297–3306.
- [19] Wang, T. Q., Tang, Y., Yu, M. X., Lu, B. G., Zhang, X. T., Zhou, J. (2023). Spirally grown zinc-cobalt alloy layer enables highly reversible zinc metal anodes. *Adv. Funct. Mater.* 33, 2306101.
- [20] Cao, Q. H., Gao, Y., Pu, J., Zhao, X., Wang, Y. X., Chen, J. P., Guan, C. (2023). Gradient design of imprinted anode for stable Zn-ion batteries. *Nat. Commun.* 14, 641.
- [21] Xue, P., Guo, C., Li, L., Li, H. P., Luo, D., Tan, L. C., Chen, Z. W. (2022). A MOF-derivative decorated hierarchical porous host enabling ultrahigh rates and superior long-term cycling of dendrite-free Zn metal anodes. *Adv. Mater.* 34, 2110047.
- [22] Zeng, L., He, J., Yang, C. Y., Luo, D., Yu, H. B., He, H. N., Zhang, C. H. (2023). Direct 3D printing of stress-released Zn powder anodes toward flexible dendrite-free Zn batteries. *Energy Storage Mater.* 54, 469–477.
- [23] Parker, J. F., Chervin, C. N., Pala, I. R., Machler, M., Burz, M. F., Long, J. W., Rolison, D. R. (2017). Rechargeable nickel-3D zinc batteries: An energy-dense, safer alternative to lithium-ion. *Science* 356, 415–418.
- [24] Li, P. P., Jin, Z. Y., Xiao, D. (2018). Three-dimensional nanotube-array anode enables a flexible Ni/Zn fibrous battery to ultrafast charge and discharge in seconds. *Energy Storage Mater.* 12, 232–240.
- [25] Zeng, Y. X., Zhang, X. Y., Qin, R. F., Liu, X. Q., Fang, P. P., Zheng, D. Z., Tong, Y. X., Lu, X. H. (2019). Dendrite-free zinc deposition induced by multifunctional CNT frameworks for stable flexible Zn-ion batteries. *Adv. Mater.* 31, 1903675.
- [26] Wang, S. B., Ran, Q., Yao, R. Q., Shi, H., Wen, Z., Zhao, M., Lang, X. Y., Jiang, Q. (2020). Lamella-nanostruc-



- tured eutectic zinc–aluminum alloys as reversible and dendrite-free anodes for aqueous rechargeable batteries. *Nat. Commun.* 11, 1634.
- [27] Kim, J. Y., Liu, G. C., Shim, G. Y., Kim, H., Lee, J. K. (2020). Functionalized Zn@ZnO hexagonal pyramid array for dendrite-free and ultrastable zinc metal anodes. *Adv. Funct. Mater.* 30, 2004210.
- [28] Liu, H. Z., Li, J. H., Zhang, X. N., Liu, X. X., Yan, Y., Chen, F. J., Zhang, G. H., Duan, H. G. (2021). Ultrathin and ultralight Zn micromesh-induced spatial-selection deposition for flexible high-specific-energy Zn-ion batteries. *Adv. Funct. Mater.* 31, 2106550.
- [29] Yang, Y., Liu, C. Y., Lv, Z. H., Yang, H., Zhang, Y. F., Ye, M. H., Chen, L. B., Zhao, J. B., Li, C. C. (2021). Synergistic manipulation of Zn<sup>2+</sup> ion flux and desolvation effect enabled by anodic growth of a 3D ZnF<sub>2</sub> matrix for long-lifespan and dendrite-free Zn metal anodes. *Adv. Mater.* 33, 2007388.
- [30] Zhang, M., Yu, P. F., Xiong, K. R., Wang, Y. Y., Liu, Y. L., Liang, Y. R. (2022). Construction of mixed ionic-electronic conducting scaffolds in Zn powder: A scalable route to dendrite-free and flexible Zn anodes. *Adv. Mater.* 34, 2200860.
- [31] Gao, Y., Cao, Q. H., Pu, J., Zhao, X., Fu, G. W., Chen, J. P., Wang, Y. X., Guan, C. (2023). Stable Zn anodes with triple gradients. *Adv. Mater.* 35, 2207573.
- [32] Mu, Y. B., Li, Z., Wu, B. K., Huang, H. D., Wu, F. H., Chu, Y. Q., Zou, L. F., Yang, M., He, J. F., Ye, L., et al. (2023). 3D hierarchical graphene matrices enable stable Zn anodes for aqueous Zn batteries. *Nat. Commun.* 14, 4205.
- [33] Chazalviel, J. N. (1990). Electrochemical aspects of the generation of ramified metallic electrodeposits. *Phys. Rev. A* 42, 7355–7367.
- [34] Hou, Z., Gao, Y., Zhou, R., Zhang, B. (2022). Unraveling the rate-dependent stability of metal anodes and its implication in designing cycling protocol. *Adv. Funct. Mater.* 32, 2107584.
- [35] Zheng, X. Y., Huang, L. Q., Ye, X. L., Zhang, J. X., Min, F. Y., Luo, W., Huang, Y. H. (2021). Critical effects of electrolyte recipes for Li and Na metal batteries. *Chem* 7, 2312–2346.
- [36] Li, B., Liu, S. D., Geng, Y. F., Mao, C. W., Dai, L., Wang, L., Jun, S. C., Lu, B. G., He, Z. X., Zhou, J. (2024). Achieving stable zinc metal anode via polyaniline interface regulation of Zn ion flux and desolvation. *Adv. Funct. Mater.* 34, 2214033.
- [37] Du, Z. J., Wood, D. L., Daniel, C., Kalnaus, S., Li, J. L. (2017). Understanding limiting factors in thick electrode performance as applied to high energy density Li-ion batteries. *J. Appl. Electrochem.* 47, 405–415.
- [38] Wu, J. Y., Ju, Z. Y., Zhang, X., Marschlok, A. C., Takeuchi, K. J., Wang, H. L., Takeuchi, E. S., Yu, G. H. (2022). Gradient design for high-energy and high-power batteries. *Adv. Mater.* 34, 2202780.
- [39] Cao, R., Zhu, L. Q., Liu, H. C., Yang, W., Li, W. P. (2015). The effect of silica sols on electrodeposited zinc coatings for sintered ndfeb. *RSC Adv.* 5, 104375–104385.
- [40] Wang, X., Meng, J. P., Lin, X. G., Yang, Y. D., Zhou, S., Wang, Y. P., Pan, A. Q. (2021). Stable zinc metal anodes with textured crystal faces and functional zinc compound coatings. *Adv. Funct. Mater.* 31, 2106114.
- [41] He, H. N., Zeng, L., Luo, D., He, J., Li, X. L., Guo, Z. P., Zhang, C. H. (2023). 3D printing of electron/ion-flux dual-gradient anodes for dendrite-free zinc batteries. *Adv. Mater.* 35, 2211498.
- [42] Wang, X., Zeng, W., Hong, L., Xu, W. W., Yang, H. K., Wang, F., Duan, H. G., Tang, M., Jiang, H. Q. (2018). Stress-driven lithium dendrite growth mechanism and dendrite mitigation by electroplating on soft substrates. *Nat. Energy* 3, 227–235.
- [43] Wang, C. C., Zhu, G. Y., Liu, P., Chen, Q. (2020). Monolithic nanoporous Zn anode for rechargeable alkaline batteries. *ACS Nano* 14, 2404–2411.
- [44] Chamoun, M., Hertzberg, B. J., Gupta, T., Davies, D., Bhadra, S., Van Tassell, B., Erdonmez, C., Steingart, D. A. (2015). Hyper-dendritic nanoporous zinc foam anodes. *NPG Asia Mater.* 7, e178.
- [45] Zhang, Y. R., Han, X. P., Liu, R. Z., Yang, Z. X., Zhang, S. J., Zhang, Y. M., Wang, H. L., Cao, Y., Chen, A., Sun, J. (2022). Manipulating the zinc deposition behavior in hexagonal patterns at the preferential Zn(100) crystal plane to construct surficial dendrite-free zinc metal anode. *Small* 18, 2105978.
- [46] Li, F., Ma, D. T., Ouyang, K. F., Yang, M., Qiu, J. M., Feng, J., Wang, Y. Y., Mi, H. W., Sun, S. C., Sun, L. N., et al. (2023). A theory-driven complementary interface effect for fast-kinetics and ultrastable Zn metal anodes in aqueous/solid electrolytes. *Adv. Energy Mater.* 13, 2204365.
- [47] Xu, D. M., Chen, B. Q., Ren, X. T., Han, C., Chang, Z., Pan, A. Q., Zhou, H. S. (2024). Selectively etching-off the highly reactive (002) Zn facet enables highly efficient aqueous zinc-metal batteries. *Energy Environ. Sci.* 2, 642–654.
- [48] Wang, J. D., Cai, Z., Xiao, R., Ou, Y. T., Zhan, R. M., Yuan, Z., Sun, Y. M. (2020). A chemically polished zinc metal electrode with a ridge-like structure for cycle-stable aqueous batteries. *ACS Appl. Mater. Interfaces* 12, 23028–23034.
- [49] Fu, H., Wen, Q., Li, P. Y., Wang, Z. Y., He, Z. J., Yan, C., Mao, J., Dai, K. H., Zhang, X. H., Zheng, J. C. (2022). In-situ chemical conversion film for stabilizing zinc metal anodes. *J. Energy Chem.* 73, 387–393.
- [50] Deng, C. B., Li, Y., Liu, S. J., Yang, J. L., Huang, B. L., Liu, J. P., Huang, J. Q. (2023). Nature-inspired interfacial engineering for highly stable Zn metal anodes. *Energy Storage Mater.* 58, 279–286.
- [51] Lv, L. L., Wu, X. C., Han, X. S., Li, C. X. (2020). Amino acid modified graphene oxide for assembly of nanoparticles for wastewater treatment. *Appl. Surf. Sci.* 534, 147620.
- [52] Wen, Q., Fu, H., Wang, Z. Y., Huang, Y. D., He, Z. J., Yan, C., Mao, J., Dai, K. H., Zhang, X. H., Zheng, J. C.

- (2022). A hydrophobic layer of amino acid enabling dendrite-free Zn anodes for aqueous zinc-ion batteries. *J. Mater. Chem. A* 10, 17501–17510.
- [53] Wang, W. X., Huang, G., Wang, Y. Z., Cao, Z., Cavallo, L., Hedhili, M. N., Alshareef, H. N. (2022). Organic acid etching strategy for dendrite suppression in aqueous zinc-ion batteries. *Adv. Energy Mater.* 12, 2102797.
- [54] Zhao, R. Z., Dong, X. S., Liang, P., Li, H. P., Zhang, T. S., Zhou, W. H., Wang, B. Y., Yang, Z. D., Wang, X., Wang, L. P., et al. (2023). Prioritizing hetero-metallic interfaces via thermodynamics inertia and kinetics zincophilia metrics for tough Zn-based aqueous batteries. *Adv. Mater.* 35, 2209288.
- [55] Jiao, Q. Y., Zhai, X. W., Sun, Z. X., Wang, W. J., Liu, S. H., Ding, H., Chu, W. S., Zhou, M., Wu, C. Z. (2023). Ultrafast superfilling construction of a metal artificial interface for long-term stable zinc anodes. *Adv. Mater.* 35, 2300850.
- [56] Chen, J. Y., Qiao, X., Han, X. R., Zhang, J. H., Wu, H. B., He, Q., Chen, Z. B., Shi, L., Wang, Y. Z., Xie, Y. N., et al. (2022). Releasing plating-induced stress for highly reversible aqueous Zn metal anodes. *Nano Energy* 103, 107814.
- [57] Bie, Z., Yang, Q., Cai, X. X., Chen, Z., Jiao, Z. Y., Zhu, J. B., Li, Z. F., Liu, J. Z., Song, W. X., Zhi, C. Y. (2022). One-step construction of a polyporous and zincophilic interface for stable zinc metal anodes. *Adv. Energy Mater.* 12, 2202683.
- [58] Nayaka, G. P., Zhang, Y. J., Dong, P., Wang, D., Zhou, Z. R., Duan, J. G., Li, X., Lin, Y., Meng, Q., Pai, K. V., et al. (2019). An environmental friendly attempt to recycle the spent Li-ion battery cathode through organic acid leaching. *J. Environ. Chem. Eng.* 7, 102854.
- [59] Li, J. J., Liu, Z. X., Han, S. H., Zhou, P., Lu, B. G., Zhou, J. D., Zeng, Z. Y., Chen, Z. Z., Zhou, J. (2023). Hetero nucleus growth stabilizing zinc anode for high-biosecurity zinc-ion batteries. *Nano-Micro Lett.* 15, 237.
- [60] Zou, Y. H., Su, Y. W., Qiao, C. P., Li, W. P., Xue, Z. K., Yang, X. Z., Lu, M. Y., Guo, W. Y., Sun, J. Y. (2023). A generic “engraving in aprotic medium” strategy toward stabilized Zn anodes. *Adv. Energy Mater.* 13, 2300932.
- [61] Zhang, X. T., Li, J. X., Liu, Y. F., Lu, B. G., Liang, S. Q., Zhou, J. (2024). Single [0001]-oriented zinc metal anode enables sustainable zinc batteries. *Nat. Commun.* 15, 2735.
- [62] Hong, L., Wang, L. Y., Wang, Y. L., Wu, X. M., Huang, W., Zhou, Y. F., Wang, K. X., Chen, J. S. (2022). Toward hydrogen-free and dendrite-free aqueous zinc batteries: Formation of zincophilic protective layer on Zn anodes. *Adv. Sci. (Weinh.)* 9, 2104866.
- [63] Ouyang, K. F., Ma, D. T., Zhao, N., Wang, Y. Y., Yang, M., Mi, H. W., Sun, L. N., He, C. X., Zhang, P. X. (2022). A new insight into ultrastable Zn metal batteries enabled by in situ built multifunctional metallic interphase. *Adv. Funct. Mater.* 32, 2109749.
- [64] He, P., Huang, J. X. (2022). Chemical passivation stabilizes Zn anode. *Adv. Mater.* 34, 2109872.
- [65] Zhang, L., Zhang, B., Zhang, T., Li, T., Shi, T. F., Li, W., Shen, T., Huang, X. X., Xu, J. J., Zhang, X. G., et al. (2021). Eliminating dendrites and side reactions via a multifunctional ZnSe protective layer toward advanced aqueous Zn metal batteries. *Adv. Funct. Mater.* 31, 2100186.
- [66] Huang, Y. F., Chang, Z. W., Liu, W. B., Huang, W. T., Dong, L. B., Kang, F. Y., Xu, C. J. (2022). Layer-by-layer zinc metal anodes to achieve long-life zinc-ion batteries. *Chem. Eng. J.* 431, 133902.
- [67] Zhang, Q., Luan, J. Y., Fu, L., Wu, S. G., Tang, Y. B., Ji, X., Wang, H. Y. (2019). The three-dimensional dendrite-free zinc anode on a copper mesh with a zinc-oriented polyacrylamide electrolyte additive. *Angew. Chem. Int. Ed.* 58, 15841–15847.
- [68] Shi, X. D., Xu, G. F., Liang, S. Q., Li, C. P., Guo, S., Xie, X. S., Ma, X. M., Zhou, J. (2019). Homogeneous deposition of zinc on three-dimensional porous copper foam as a superior zinc metal anode. *ACS Sustainable Chem. Eng.* 7, 17737–17746.
- [69] Kang, Z., Wu, C. L., Dong, L. B., Liu, W. B., Mou, J., Zhang, J. W., Chang, Z. W., Jiang, B. Z., Wang, G. X., Kang, F. Y., et al. (2019). 3D porous copper skeleton supported zinc anode toward high capacity and long cycle life zinc ion batteries. *ACS Sustainable Chem. Eng.* 7, 3364–3371.
- [70] An, Y. L., Tian, Y., Xiong, S. L., Feng, J. K., Qian, Y. T. (2021). Scalable and controllable synthesis of interface-engineered nanoporous host for dendrite-free and high rate zinc metal batteries. *ACS Nano* 15, 11828–11842.
- [71] Yi, Z. H., Liu, J. X., Tan, S. D., Sang, Z. Y., Mao, J., Yin, L. C., Liu, X. G., Wang, L. Q., Hou, F., Dou, S. X., et al. (2022). An ultrahigh rate and stable zinc anode by facet-matching-induced dendrite regulation. *Adv. Mater.* 34, 2203835.
- [72] Fan, X. Y., Yang, H., Feng, B., Zhu, Y. Q., Wu, Y., Sun, R. B., Gou, L., Xie, J., Li, D. L., Ding, Y. L. (2022). Rationally designed In@Zn@In trilayer structure on 3D porous Cu towards high-performance Zn-ion batteries. *Chem. Eng. J.* 445, 136799.
- [73] Yu, H. M., Li, Q. Y., Liu, W., Wang, H., Ni, X. Y., Zhao, Q. W., Wei, W. F., Ji, X. B., Chen, Y. J., Chen, L. B. (2022). Fast ion diffusion alloy layer facilitating 3D mesh substrate for dendrite-free zinc-ion hybrid capacitors. *J. Energy Chem.* 73, 565–574.
- [74] Douka, A. I., Xu, Y. Y., Yang, H., Zaman, S., Yan, Y., Liu, H. F., Salam, M. A., Xia, B. Y. (2020). A zeolitic-imidazole frameworks-derived interconnected macroporous carbon matrix for efficient oxygen electrocatalysis in rechargeable zinc–air batteries. *Adv. Mater.* 32, 2002170.
- [75] Pan, Y. L., Hu, M., Ma, M. D., Li, Z. H., Gao, Y. F., Xiong, M., Gao, G. Y., Zhao, Z. S., Tian, Y. J., Xu, B., et al. (2017). Multithreaded conductive carbon: 1d conduction in 3D carbon. *Carbon* 115, 584–588.
- [76] Borchardt, L., Zhu, Q. L., Casco, M. E., Berger, R., Zhuang, X. D., Kaskel, S., Feng, X. L., Xu, Q. (2017). Toward a molecular design of porous carbon materials.

- Mater. Today* 20, 592–610.
- [77] Zheng, J. X., Zhao, Q., Tang, T., Yin, J. F., Quilty, C. D., Renderos, G. D., Liu, X. T., Deng, Y., Wang, L., Bock, D. C., et al. (2019). Reversible epitaxial electrodeposition of metals in battery anodes. *Science* 366, 645–648.
- [78] Xie, F. X., Li, H., Wang, X. S., Zhi, X., Chao, D. L., Davey, K., Qiao, S. Z. (2021). Mechanism for zincophilic sites on zinc-metal anode hosts in aqueous batteries. *Adv. Energy Mater.* 11, 2003419.
- [79] Wang, J. H., Chen, L. F., Dong, W. X., Zhang, K. L., Qu, Y. F., Qian, J. W., Yu, S. H. (2023). Three-dimensional zinc-seeded carbon nanofiber architectures as lightweight and flexible hosts for a highly reversible zinc metal anode. *ACS Nano* 17, 19087–19097.
- [80] Zhou, J. H., Xie, M., Wu, F., Mei, Y., Hao, Y. T., Li, L., Chen, R. J. (2022). Encapsulation of metallic Zn in a hybrid MXene/graphene aerogel as a stable Zn anode for foldable Zn-ion batteries. *Adv. Mater.* 34, 2106897.
- [81] Cao, Q. H., Gao, H., Gao, Y., Yang, J., Li, C., Pu, J., Du, J. J., Yang, J. J., Cai, D. M., Pan, Z. H., et al. (2021). Regulating dendrite-free zinc deposition by 3D zincophilic nitrogen-doped vertical graphene for high-performance flexible Zn-ion batteries. *Adv. Funct. Mater.* 31, 2103922.
- [82] Wang, Q., Astruc, D. (2020). State of the art and prospects in metal–organic framework (MOF)-based and MOF-derived nanocatalysis. *Chem. Rev.* 120, 1438–1511.
- [83] Wang, Z., Xu, J., Yang, J. H., Xue, Y. H., Dai, L. M. (2022). Ultraviolet/ozone treatment for boosting oer activity of MOF nanoneedle arrays. *Chem. Eng. J.* 427, 131498.
- [84] Yuksel, R., Buyukcikir, O., Seong, W. K., Ruoff, R. S. (2020). Metal-organic framework integrated anodes for aqueous zinc-ion batteries. *Adv. Energy Mater.* 10, 1904215.
- [85] Yu, H., Yao, H. X., Zheng, Y. Q., Liu, D., Chen, J. S., Guo, Y., Li, N. W., Yu, L. (2024). Formation of hierarchical Zn/N-doped carbon hollow nanofibers towards dendrite-free Zn metal anodes. *Adv. Funct. Mater.* 34, 2311038.
- [86] Gong, Y., Xue, Y. H. (2023). Carbon nanomaterials for stabilizing zinc anodes in zinc-ion batteries. *New Carbon Mater.* 38, 438–454.
- [87] Tao, Y., Zuo, S. W., Xiao, S. H., Sun, P. X., Li, N. W., Chen, J. S., Zhang, H. B., Yu, L. (2022). Atomically dispersed Cu in zeolitic imidazolate framework nanoflake array for dendrite-free Zn metal anode. *Small* 18, 2203231.
- [88] Li, H. P., Guo, C., Zhang, T. S., Xue, P., Zhao, R. Z., Zhou, W. H., Li, W., Elzatahry, A., Zhao, D. Y., Chao, D. L. (2022). Hierarchical confinement effect with zincophilic and spatial traps stabilized Zn-based aqueous battery. *Nano Lett.* 22, 4223–4231.
- [89] Zeng, Y. H., Sun, P. X., Pei, Z. H., Jin, Q., Zhang, X. T., Yu, L., Lou, X. W. D. (2022). Nitrogen-doped carbon fibers embedded with zincophilic Cu nanoboxes for stable Zn-metal anodes. *Adv. Mater.* 34, 2200342.
- [90] Yu, H., Zeng, Y. X., Li, N. W., Luan, D. Y., Yu, L., Lou, X. W. D. (2022). Confining Sn nanoparticles in interconnected N-doped hollow carbon spheres as hierarchical zincophilic fibers for dendrite-free Zn metal anodes. *Sci. Adv.* 8, eabm5766.
- [91] Zhou, W. J., Wu, T., Chen, M. F., Tian, Q. H., Han, X., Xu, X. W., Chen, J. Z. (2022). Wood-based electrodes enabling stable, anti-freezing, and flexible aqueous zinc-ion batteries. *Energy Storage Mater.* 51, 286–293.
- [92] Wang, R., Xin, S., Chao, D. L., Liu, Z. X., Wan, J. D., Xiong, P., Luo, Q. Q., Hua, K., Hao, J. N., Zhang, C. F. (2022). Fast and regulated zinc deposition in a semiconductor substrate toward high-performance aqueous rechargeable batteries. *Adv. Funct. Mater.* 32, 2207751.
- [93] Li, Q., Wang, Y. B., Mo, F. N., Wang, D. H., Liang, G. J., Zhao, Y. W., Yang, Q., Huang, Z. D., Zhi, C. Y. (2021). Calendar life of Zn batteries based on Zn anode with Zn powder/current collector structure. *Adv. Energy Mater.* 11, 2003931.
- [94] Li, S. P., Wang, H., Cuthbert, J., Liu, T., Whitacre, J. F., Matyjaszewski, K. (2019). A semiliquid lithium metal anode. *Joule* 3, 1637–1646.
- [95] Liu, Q., Yu, Z. L., Zhou, R., Zhang, B. (2023). A semi-liquid electrode toward stable Zn powder anode. *Adv. Funct. Mater.* 33, 2210290.
- [96] Hu, Q., Hou, J. M., Liu, Y. B., Li, L., Ran, Q. W., Mao, J. Q., Liu, X. Q., Zhao, J. X., Pang, H. (2023). Modulating zinc metal reversibility by confined antifluator film for durable and dendrite-free zinc ion batteries. *Adv. Mater.* 35, 2303336.
- [97] Wang, J. X., Zhang, H., Yang, L. Z., Zhang, S. Y., Han, X. P., Hu, W. B. (2024). *In situ* implanting 3D carbon network reinforced zinc composite by powder metallurgy for highly reversible Zn-based battery anodes. *Angew. Chem. Int. Ed.* 63, e202318149.
- [98] Yang, Z. F., Zhang, Q., Li, W. B., Xie, C. L., Wu, T. Q., Hu, C., Tang, Y. G., Wang, H. Y. (2023). A semi-solid zinc powder-based slurry anode for advanced aqueous zinc-ion batteries. *Angew. Chem. Int. Ed.* 62, e202215306.
- [99] Cao, C. H., Zhou, K. Q., Du, W. C., Li, C. C., Ye, M. H., Zhang, Y. F., Tang, Y. C., Liu, X. Q. (2023). Designing soft solid-like viscoelastic zinc powder anode toward high-performance aqueous zinc-ion batteries. *Adv. Energy Mater.* 13, 2301835.
- [100] Du, Y. X., Chi, X. W., Huang, J. Q., Qiu, Q. L., Liu, Y. (2020). Long lifespan and high-rate Zn anode boosted by 3D porous structure and conducting network. *J. Power Sources* 479, 228808.
- [101] Du, W. C., Huang, S., Zhang, Y. F., Ye, M. H., Li, C. C. (2022). Enable commercial zinc powders for dendrite-free zinc anode with improved utilization rate by pristine graphene hybridization. *Energy Storage Mater.* 45, 465–473.
- [102] Huan, X. D., Yi, Z. H., Sang, Z. Y., Tan, S. D., Liu, J. X., Chen, R., Si, W. P., Liang, J., Hou, F. (2023). Polyethylene glycol coating on zinc powder surface: Applications in dendrite-free zinc anodes with enhanced utilization rate. *Appl. Surf. Sci.* 614, 156209.



- [103] Chen, H. L., Zhang, W. Y., Yi, S., Su, Z., Zhao, Z. Q., Zhang, Y. Y., Niu, B., Long, D. H. (2024). Zinc iso-plating/stripping: Toward a practical Zn powder anode with ultra-long life over 5600 h. *Energy Environ. Sci.* 17, 3146–3156.
- [104] Lin, Y. H., Hu, Y. Z., Zhang, S., Xu, Z. Q., Feng, T. T., Zhou, H. P., Wu, M. Q. (2022). Binder-free freestanding 3D Zn-graphene anode induced from commercial zinc powders and graphene oxide for zinc ion battery with high utilization rate. *ACS Appl. Energy Mater.* 5, 15222–15232.
- [105] Xu, X. Y., Li, S. M., Cao, Z. J., Yang, S. B., Li, B. (2024). Boosting ion diffusion and charge transfer by zincophilic accordion arrays to achieve ultrafast aqueous zinc metal batteries. *Adv. Energy Mater.* 14, 2303971.
- [106] Rehnlund, D., Wang, Z. H., Nyholm, L. (2022). Lithium-diffusion induced capacity losses in lithium-based batteries. *Adv. Mater.* 34, 2108827.
- [107] Zhang, Y. Y., Malyi, O. I., Tang, Y. X., Wei, J. Q., Zhu, Z. Q., Xia, H. R., Li, W. L., Guo, J., Zhou, X. R., Chen, Z., et al. (2017). Reducing the charge carrier transport barrier in functionally layer-graded electrodes. *Angew. Chem. Int. Ed.* 56, 14847–14852.
- [108] Ju, Z. Y., Zhang, X., Wu, J. Y., Yu, G. H. (2021). Vertically aligned two-dimensional materials-based thick electrodes for scalable energy storage systems. *Nano Res.* 14, 3562–3575.
- [109] Ju, Z. Y., Zhu, Y., Zhang, X., Lutz, D. M., Fang, Z. W., Takeuchi, K. J., Takeuchi, E. S., Marschilok, A. C., Yu, G. H. (2020). Understanding thickness-dependent transport kinetics in nanosheet-based battery electrodes. *Chem. Mater.* 32, 1684–1692.
- [110] Cao, Q. H., Pan, Z. H., Gao, Y., Pu, J., Fu, G. W., Cheng, G. H., Guan, C. (2022). Stable imprinted zincophilic Zn anodes with high capacity. *Adv. Funct. Mater.* 32, 2205771.
- [111] Huang, Z. C., Li, H. Y., Yang, Z., Wang, H. Z., Ding, J. N., Xu, L. Y., Tian, Y. L., Mitlin, D., Ding, J., Hu, W. B. (2022). Nanosecond laser lithography enables concave-convex zinc metal battery anodes with ultrahigh areal capacity. *Energy Storage Mater.* 51, 273–285.
- [112] Liang, G. J., Zhu, J. X., Yan, B. X., Li, Q., Chen, A., Chen, Z., Wang, X. Q., Xiong, B., Fan, J., Xu, J., et al. (2022). Gradient fluorinated alloy to enable highly reversible Zn-metal anode chemistry. *Energy Environ. Sci.* 15, 1086–1096.
- [113] Gao, X. J., Yang, X. F., Adair, K., Li, X. N., Liang, J. W., Sun, Q., Zhao, Y., Li, R. N., Sham, T. K., Sun, X. L. (2020). 3D vertically aligned Li metal anodes with ultrahigh cycling currents and capacities of 10 mA cm<sup>-2</sup> 20 mAh cm<sup>-2</sup> realized by selective nucleation within microchannel walls. *Adv. Energy Mater.* 10, 1903753.
- [114] Li, S. Y., Fu, J., Miao, G. X., Wang, S. P., Zhao, W. Y., Wu, Z. C., Zhang, Y. J., Yang, X. W. (2021). Toward planar and dendrite-free Zn electrodepositions by regulating Sn-crystal textured surface. *Adv. Mater.* 33, 2008424.
- [115] Zhang, G. H., Zhang, X. N., Liu, H. Z., Li, J. H., Chen, Y. Q., Duan, H. (2021). 3D-printed multi-channel metal lattices enabling localized electric-field redistribution for dendrite-free aqueous Zn ion batteries. *Adv. Energy Mater.* 11, 2003927.
- [116] Sun, P. X., Cao, Z. J., Zeng, Y. X., Xie, W. W., Li, N. W., Luan, D. Y., Yang, S. B., Yu, L., Lou, X. W. D. (2022). Formation of super-assembled TiO<sub>x</sub>/Zn/N-doped carbon inverse opal towards dendrite-free Zn anodes. *Angew. Chem. Int. Ed.* 61, e202115649.
- [117] Zeng, W., Wei, P. D., Chen, J. E., Wang, G. Z., Yan, Y., Yu, H. H., Yang, C. Y., Zhang, G. H., Jiang, H. Q. (2023). Ultra-stable zinc metal anodes enabled by uniform Zn deposition on a preferential crystal plane. *Adv. Energy Mater.* 13, 2302205.
- [118] Idrees, M., Batool, S., Din, M. A. U., Javed, M. S., Ahmed, S., Chen, Z. W. (2023). Material-structure-property integrated additive manufacturing of batteries. *Nano Energy* 109, 108247.
- [119] Chang, P., Mei, H., Zhou, S. X., Dassios, K. G., Cheng, L. F. (2019). 3D printed electrochemical energy storage devices. *J. Mater. Chem. A* 7, 4230–4258.
- [120] Wu, B. K., Guo, B. B., Chen, Y. Z., Mu, Y. B., Qu, H. Q., Lin, M., Bai, J. M., Zhao, T. S., Zeng, L. (2023). High zinc utilization aqueous zinc ion batteries enabled by 3D printed graphene arrays. *Energy Storage Mater.* 54, 75–84.
- [121] Zeng, L., He, H. N., Chen, H. Y., Luo, D., He, J., Zhang, C. H. (2022). 3D printing architecting reservoir-integrated anode for dendrite-free, safe, and durable Zn batteries. *Adv. Energy Mater.* 12, 2103708.
- [122] Zhai, P. B., Wang, T. S., Jiang, H. N., Wan, J. Y., Wei, Y., Wang, L., Liu, W., Chen, Q., Yang, W. W., Cui, Y., et al. (2021). 3D artificial solid-electrolyte interphase for lithium metal anodes enabled by insulator-metal-insulator layered heterostructures. *Adv. Mater.* 33, 2006247.
- [123] Cao, Z. J., Li, B., Yang, S. B. (2019). Dendrite-free lithium anodes with ultra-deep stripping and plating properties based on vertically oriented lithium-copper-lithium arrays. *Adv. Mater.* 31, 1901310.
- [124] Qi, Y. B., Jang, T. J., Ramadesigan, V., Schwartz, D. T., Subramanian, V. R. (2017). Is there a benefit in employing graded electrodes for lithium-ion batteries. *J. Electrochem. Soc.* 164, A3196–A3207.
- [125] Ramadesigan, V., Methekar, R. N., Latinwo, F., Braatz, R. D., Subramanian, V. R. (2010). Optimal porosity distribution for minimized ohmic drop across a porous electrode. *J. Electrochem. Soc.* 157, A1328–A1334.
- [126] Zhao, X., Gao, Y., Cao, Q. H., Bu, F., Pu, J., Wang, Y. X., Guan, C. (2023). A high-capacity gradient Zn powder anode for flexible Zn-ion batteries. *Adv. Energy Mater.* 13, 2301741.
- [127] Shen, Z. X., Luo, L., Li, C. W., Pu, J., Xie, J. P., Wang, L. T., Huai, Z., Dai, Z. Y., Yao, Y. G., Hong, G. (2021). Stratified zinc-binding strategy toward prolonged cycling and flexibility of aqueous fibrous zinc metal batteries. *Adv. Energy Mater.* 11, 2100214.
- [128] Li, Y. M., Wang, Z. W., Li, W. H., Zhang, X. Y., Yin, C., Li, K., Guo, W., Zhang, J. P., Wu, X. L. (2023). Trinary

- nanogradients at electrode/electrolyte interface for lean zinc metal batteries. *Energy Storage Mater.* 61, 102873.
- [129] Lu, H. Y., Hu, J. S., Zhang, Y., Zhang, K. Q., Yan, X. Y., Li, H. Q., Li, J. Z., Li, Y. J., Zhao, J. X., Xu, B. G. (2023). 3D cold-trap environment printing for long-cycle aqueous Zn-ion batteries. *Adv. Mater.* 35, 2209886.
- [130] Lu, H. Y., Hu, J. S., Zhang, K. Q., Zhao, J. X., Deng, S. Z., Li, Y. J., Xu, B. G., Pang, H. (2024). Microfluidic-assisted 3D printing zinc powder anode with 2D conductive mof/MXene heterostructures for high-stable zinc-organic battery. *Adv. Mater.* 36, 2309753.
- [131] Yang, J. Y., Xu, X., Gao, Y., Wang, Y. X., Cao, Q. H., Pu, J., Bu, F., Meng, T., Guan, C. (2023). Ultra-stable 3D-printed Zn powder-based anode coated with a conformal ion-conductive layer. *Adv. Energy Mater.* 13, 2301997.
- [132] Tian, H. J., Feng, G. X., Wang, Q., Li, Z., Zhang, W., Lucero, M., Feng, Z. X., Wang, Z. L., Zhang, Y. N., Zhen, C., et al. (2022). Three-dimensional Zn-based alloys for dendrite-free aqueous Zn battery in dual-cation electrolytes. *Nat. Commun.* 13, 7922.
- [133] Li, G. P., Wang, X. L., Lv, S. H., Wang, J. X., Yu, W. S., Dong, X. T., Liu, D. T. (2023). In situ constructing a film-coated 3D porous Zn anode by iodine etching strategy toward horizontally arranged dendrite-free Zn deposition. *Adv. Funct. Mater.* 33, 2208288.
- [134] Zhang, W. Y., Dong, M. Y., Jiang, K. R., Yang, D. L., Tan, X. H., Zhai, S. L., Feng, R. F., Chen, N., King, G., Zhang, H., et al. (2022). Self-repairing interphase reconstructed in each cycle for highly reversible aqueous zinc batteries. *Nat. Commun.* 13, 5348.
- [135] Wang, D. D., Liu, H. X., Lv, D., Wang, C., Yang, J., Qian, Y. T. (2023). Rational screening of artificial solid electrolyte interphases on Zn for ultrahigh-rate and long-life aqueous batteries. *Adv. Mater.* 35, 2207908.



# Vanadium hexacyanoferrate with two redox active sites as cathode material for aqueous Zn-ion batteries

YanJun Zhang<sup>a,1</sup>, Yao Wang<sup>a,1</sup>, Liang Lu<sup>c</sup>, Chunwen Sun<sup>c,\*\*</sup>, Denis Y.W. Yu<sup>a,b,\*</sup>

<sup>a</sup> School of Energy and Environment, City University of Hong Kong, Tat Chee Avenue, Kowloon, Hong Kong, China

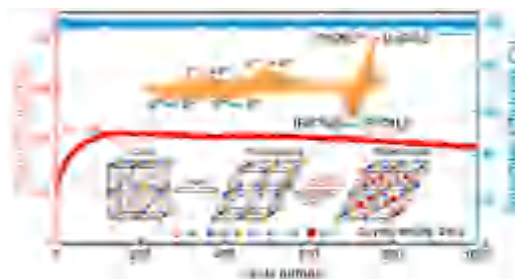
<sup>b</sup> Center of Super-Diamond and Advanced Films (COSDAF), City University of Hong Kong, Tat Chee Avenue, Kowloon, Hong Kong, China

<sup>c</sup> Beijing Institute of Nanoenergy and Nanosystems, Chinese Academy of Sciences, Beijing, 100083, People's Republic of China

## HIGHLIGHTS

- A new kind of Prussian blue, vanadium hexacyanoferrate, is synthesized.
- The vanadium hexacyanoferrate was tested as cathode in aqueous Zn-ion battery.
- Two redox active sites, V and Fe, together contribute to the capacity.
- The material exhibits excellent rate capability and long-term cyclability.
- Structural evolution during the charge-discharge process is investigated.

## GRAPHICAL ABSTRACT



## ARTICLE INFO

### Keywords:

Vanadium hexacyanoferrate  
Cathode material  
Zn-ion battery  
Prussian blue  
Aqueous rechargeable batteries

## ABSTRACT

Aqueous rechargeable Zn-ion batteries (ARZIBs) are attractive due to their low cost, high safety and environmental friendliness. However, the development of ARZIBs still faces many challenges. One of the biggest challenges is to find suitable cathode materials for reversible  $\text{Zn}^{2+}$  ions insertion/extraction. In this work, we synthesize a Prussian blue analogue (PBA) with a new chemical composition, vanadium hexacyanoferrate (VHCF), via a simple co-precipitation method and study its performance as a cathode material for an aqueous rechargeable Zn-ion battery. The VHCF with two electrochemical redox active sites, V and Fe, delivers a three-electron redox reaction with a capacity of  $187 \text{ mA h g}^{-1}$  at current density of  $0.5 \text{ A g}^{-1}$ . Even at a current rate of  $5 \text{ A g}^{-1}$ , VHCF can still deliver a large capacity of  $122 \text{ mA h g}^{-1}$ . The Zn//VHCF battery also exhibits a long cycle life of 1000 cycles with excellent capacity retention of 87.8% and a high Coulombic efficiency close to 100%. During the first charging process, the cubic structure of VHCF changes to a rhombohedral phase, a structure where the  $\text{Zn}^{2+}$  ions can be reversibly inserted into and extracted from in subsequent cycles. The promising performances make VHCF an attractive candidate as cathode material for ARZIBs system.

\* Corresponding author. Center of Super-Diamond and Advanced Films (COSDAF), City University of Hong Kong, Tat Chee Avenue, Kowloon, Hong Kong, China.

\*\* Corresponding author.

E-mail addresses: [sunchunwen@binn.cas.cn](mailto:sunchunwen@binn.cas.cn) (C. Sun), [denisyu@cityu.edu.hk](mailto:denisyu@cityu.edu.hk) (D.Y.W. Yu).

<sup>1</sup> YanJun Zhang and Yao Wang contributed equally to this work.



## 1. Introduction

The search for new battery technologies and systems to meet the ever-increasing demands of high safety, low costs, good reliability and environmental benign power sources, has been a global undertaking over the past few decades [1–3]. Non-aqueous batteries, particularly rechargeable lithium ion batteries (LIBs), have been extensively explored due to their high energy density, cycle stability, and energy efficiency [4]. However, the organic electrolytes used in these batteries carry the intrinsic disadvantages of being flammable, toxic, and highly sensitive to ambient atmosphere, causing safety, cost, and environmental concerns that likely limit their large-scale applications [5]. Aqueous rechargeable batteries using low cost, nonflammable, and environmentally friendly water-based electrolytes are regarded as promising alternatives for grid-scale energy storage systems [6–9].

So far, various types of aqueous rechargeable batteries using mono/multi-valent metal ions (e.g.  $\text{Li}^+$ ,  $\text{Na}^+$ ,  $\text{K}^+$ ,  $\text{Zn}^{2+}$ ,  $\text{Mg}^{2+}$ , and  $\text{Al}^{3+}$ ) and/or mixed metal ions as charge carriers have been proposed [10–12]. Among them, aqueous rechargeable Zn-ion batteries (ARZIBs) are particularly promising because Zn features several attractive attributes including high theoretical gravimetric capacity ( $820 \text{ mA h g}^{-1}$ ) and volumetric capacity ( $5854 \text{ mA h cm}^3$ ), abundance, low cost, non-toxic, easy processability, and a more suitable redox potential ( $-0.76 \text{ V}$  vs. standard hydrogen electrode) in aqueous electrolyte [13]. Generally, a ARZIB is composed of zinc metal anode, mild acidic or neutral electrolyte, and a zinc-ion storage material as cathode [14]. To date, many significant works regarding ARZIBs have been reported. However, the development of ARZIBs systems is still in the incipient stage. One of the greatest challenges is to find suitable cathode materials for reversible  $\text{Zn}^{2+}$  ions insertion/extraction [15].

Till now, various materials have been explored as cathodes for ARZIBs, such as manganese-based oxides [16–19], vanadium-based oxides [20–25], Prussian blue analogues (PBAs) [26–30], olivine-based phosphates [31], quinone [32], *p*-chloranil [33],  $\text{Mo}_6\text{S}_8$  [34], Co(III) rich- $\text{Co}_3\text{O}_4$  [35], etc. Among them, PBAs have been highlighted as a promising candidate of cathode materials for ARZIBs due to their unique crystallographic structure and desirable electrochemical characteristics. The generic chemical formula of a PBA can be roughly represented as  $\text{A}_x\text{M}_{1y}[\text{M}_2(\text{CN})_6]_z \cdot n\text{H}_2\text{O}$ , where  $\text{M}_1$  and  $\text{M}_2$  are usually transition-metal (Mn, Fe, Co, Ni, Cu, or Zn, etc.) ions and A is usually an alkali (Li, Na, or K, etc.) ion [36]. PBAs typically have 3D open framework structures with sufficiently large three-dimensional diffusion channels and large lattice parameters greater than  $10 \text{ \AA}$ , as well as weak interaction with the guest ions, which is beneficial for facile diffusion of electroactive mobile ions and possesses high structural stability against repeated ion insertion/extraction [37]. In addition, the activation energy required to transfer the guest ions is effectively relieved by the weakened bond strength between the frameworks and the ions [38]. However, the specific capacity of most PBAs obtained with aqueous electrolytes is limited to less than  $70 \text{ mA h g}^{-1}$  because only a single type of transition metal ions was believed to be electrochemically activate under aqueous electrolyte systems, resulting in the one-electron redox process [26–30]. The electrochemical performance of PBAs is mostly governed by the electrochemical process of the metal ions upon insertion/extraction of guest ions. Theoretically, PBAs with two different metals ( $\text{M}_1$  and  $\text{M}_2$ ) ions should be capable of undergoing a multi-electron redox reaction [36]. Therefore, it is practicable to improve the electrochemical performance, including specific capacity, rate capability and operating potential, by optimizing the combination of metal ions in the PBAs [39].

Vanadium, a transition metal, exhibits various valence states ranging from +2 to +5. The electrochemical redox of vanadium ions is available within the potential window of aqueous electrolyte [40]. Therefore, vanadium ions can be employed as a redox active site in the PBAs. In this work, vanadium and iron ions are combined together to form a PBA, vanadium hexacyanoferrate (VHCF), with a new chemical composition.

The VHCF nanoparticles were synthesized using a simple co-precipitation method, and their electrochemical performance as well as related mechanisms of  $\text{Zn}^{2+}$  ions insertion/extraction were investigated using aqueous electrolyte. To the best of our knowledge, this is the first report to investigate VHCF nanoparticles as cathode material for ARZIBs. Both V and Fe ions are found to effectively contribute to the multiple-electron electrochemical process, resulting in higher specific capacity than other reported PBAs cathodes for ARZIBs. In addition, VHCF nanoparticles exhibit long cycle life and good rate capability, making it an attractive candidate as cathode material for ARZIBs.

## 2. Experimental

### 2.1. Material synthesis

$\text{VOPO}_4 \cdot 2\text{H}_2\text{O}$  precursor was first synthesized using a simple hydrothermal method. In a typical synthesis process,  $2.5 \text{ g V}_2\text{O}_5$  was added to a mixture solvent containing  $60 \text{ mL DI water}$  and  $15 \text{ mL H}_3\text{PO}_4$  under constant stirring. The mixture was vigorously stirred for  $2 \text{ h}$  and then transferred to a  $100 \text{ mL Teflon autoclave}$ , and then, the autoclave was sealed and heated to  $110^\circ \text{C}$  in an electric oven for  $20 \text{ h}$ . Afterward, the precipitate was collected by centrifugation and washed with acetone for several times. After washing, the precipitate was dried in air at  $60^\circ \text{C}$  overnight. The morphology and structure of the synthesized  $\text{VOPO}_4 \cdot 2\text{H}_2\text{O}$  are shown in Fig. S1. To prepare the VHCF nanoparticles,  $6 \text{ mmol}$  of the obtained  $\text{VOPO}_4 \cdot 2\text{H}_2\text{O}$  precursor was dissolved in  $150 \text{ mL DI water}$  and  $4 \text{ mmol}$  of sodium ferrocyanide decahydrate ( $\text{Na}_4\text{Fe}(\text{CN})_6 \cdot 10\text{H}_2\text{O}$ ) was dissolved in  $50 \text{ mL DI water}$ . Then the former solution was added to the latter solution under gentle stirring. The resulting solution was heated to  $80^\circ \text{C}$  under constant gentle stirring for  $4 \text{ h}$ . Finally, the precipitate was collected by centrifugation, washed with ethanol for several times, and then dried at  $60^\circ \text{C}$  overnight.

### 2.2. Material characterization

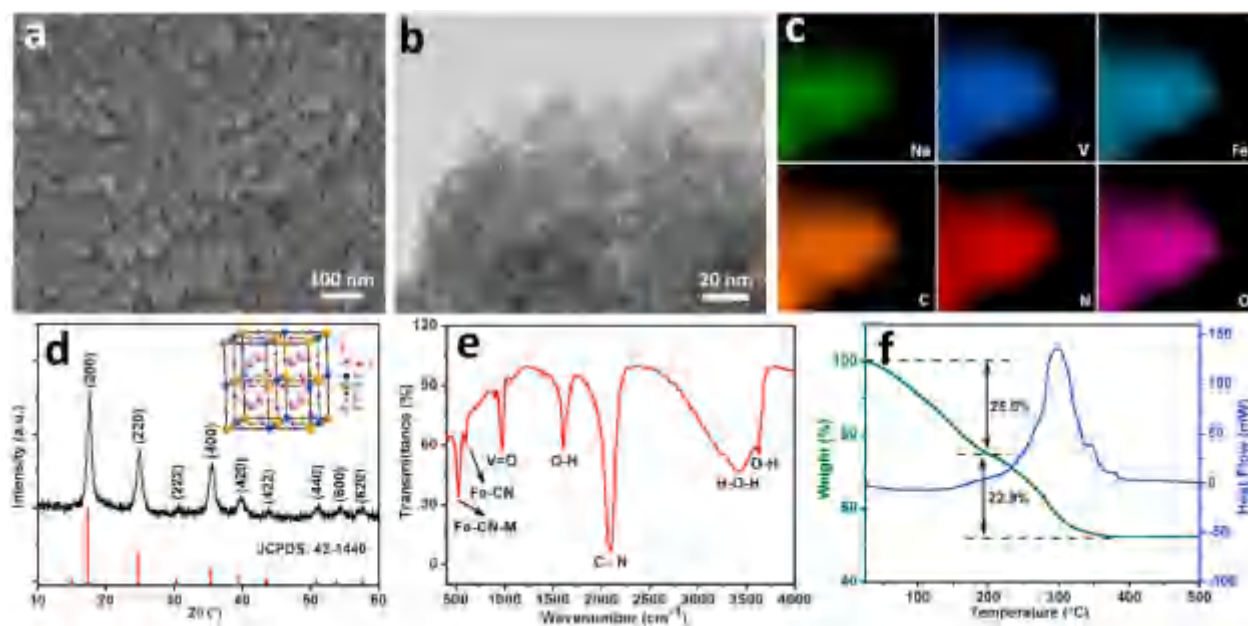
The X-ray diffraction (XRD) patterns of the samples were recorded on a Rigaku D/max-2500 diffractometer with  $\text{Cu K}\alpha$  radiation ( $\lambda = 0.1542 \text{ nm}$ ) at  $40 \text{ kV}$  and  $30 \text{ mA}$  at a step of  $0.02^\circ$ . Data were recorded ranging from  $10^\circ$  to  $60^\circ$ . Scanning electron microscopy (SEM) was performed on a JEOL 6701 F scanning electron microscope with an accelerating voltage of  $10 \text{ kV}$ . Transmission electron microscopy (TEM) observations and energy dispersive spectrometer (EDS) analysis were carried out on FEI Tecnai F20 microscope at  $200 \text{ kV}$ . Dynamic Light Scattering (DLS) was conducted using Zetasizer Nano (Malvern). Thermogravimetric analysis (TGA) was carried out on a TA-Q50 instrument. Fourier transform infrared (FT-IR) spectrum investigation was performed on an IR Rrestige-21 FTIR spectrometer. X-ray photoelectron spectroscopy (XPS) were recorded by a Thermo Electron Corporation ESCALAB 250 XPS spectrometer.

### 2.3. Electrochemical measurements

Electrochemical measurements were performed using 2032 coin-type cells assembled in air. To prepare working electrodes, a mixture of the VHCF nanoparticles, acetylene black (AB) and polyvinylidene fluoride (PVDF) with a weight ratio of  $60:30:10$  in *N*-methylpyrrolidone (NMP) solvent was coated on stainless steel foils. Zinc foil was used as the anode, and glass fiber (GF/D) was used as a separator. The electrolyte was  $4 \text{ M Zn}(\text{CF}_3\text{SO}_3)_2$  aqueous solution. Galvanostatic cycling of the assembled cells was carried out using a Neware battery test system. The cyclic voltammetry (CV) measurements were conducted by Bio-Logic potentiostat (VMP3).

## 3. Results and discussion

VHCF sample was synthesized via a simple co-precipitation method



**Fig. 1.** (a) SEM image, (b) TEM image, (c) EDS elemental mapping images, (d) XRD pattern, (e) FT-IR spectrum, and (f) TG-DTA curves of the as-synthesized VHCF sample.

using homemade  $\text{VOPO}_4 \cdot 2\text{H}_2\text{O}$  (Fig. S1) and purchased  $\text{Na}_4\text{Fe}(\text{CN})_6 \cdot 10\text{H}_2\text{O}$  as reactants (see Experimental Methods). Scanning electron microscopy (SEM) and transmission electron microscopy (TEM) were employed to characterize the morphology of as-synthesized VHCF sample, as shown in Fig. 1a and b. It can be clearly seen that the as-synthesized VHCF sample is composed of well-dispersed nanoparticles. The particle size distribution was analyzed by dynamic light scattering (DLS), as shown in Fig. S2. The average size of the VHCF nanoparticles is 23.6 nm. Such nanosized morphology is structurally favorable for electron and ions transportation during the electrochemical redox reactions. The atomic composition and the distribution of the constituent elements in the as-synthesized VHCF nanoparticles were investigated by energy-dispersive X-ray spectrometry (EDS). Fig. 1c presents the EDS elemental mapping images with selected elements of Na, V, Fe, C, N, and O present in the as-synthesized VHCF nanoparticles. These images confirm that the atomic composition is highly uniform in the as-synthesized VHCF nanoparticles.

Fig. 1d shows the X-ray diffraction (XRD) pattern of the as-synthesized VHCF nanoparticles. All the diffraction peaks were indexed with the cubic phase of the  $\text{V}_3[\text{Fe}(\text{CN})_6]_2$  (JCPDS file No. 42-1440), thus the as-synthesized VHCF nanoparticles are expected to have the same cubic crystal structure. Although there is a lack of accurate crystal structure information on VHCF in the existing crystallographic database, it can be seen that the two patterns are almost identical to each other. By the analogy between the obtained compound and the similar Prussian blue (PB) and MFe-PB compounds, we can speculate that our sample contains the structure of PB, in which both the 3D cyanide-bridged framework and the 3D porous channel exist with  $\text{Na}^+$  in the center of the subunits.

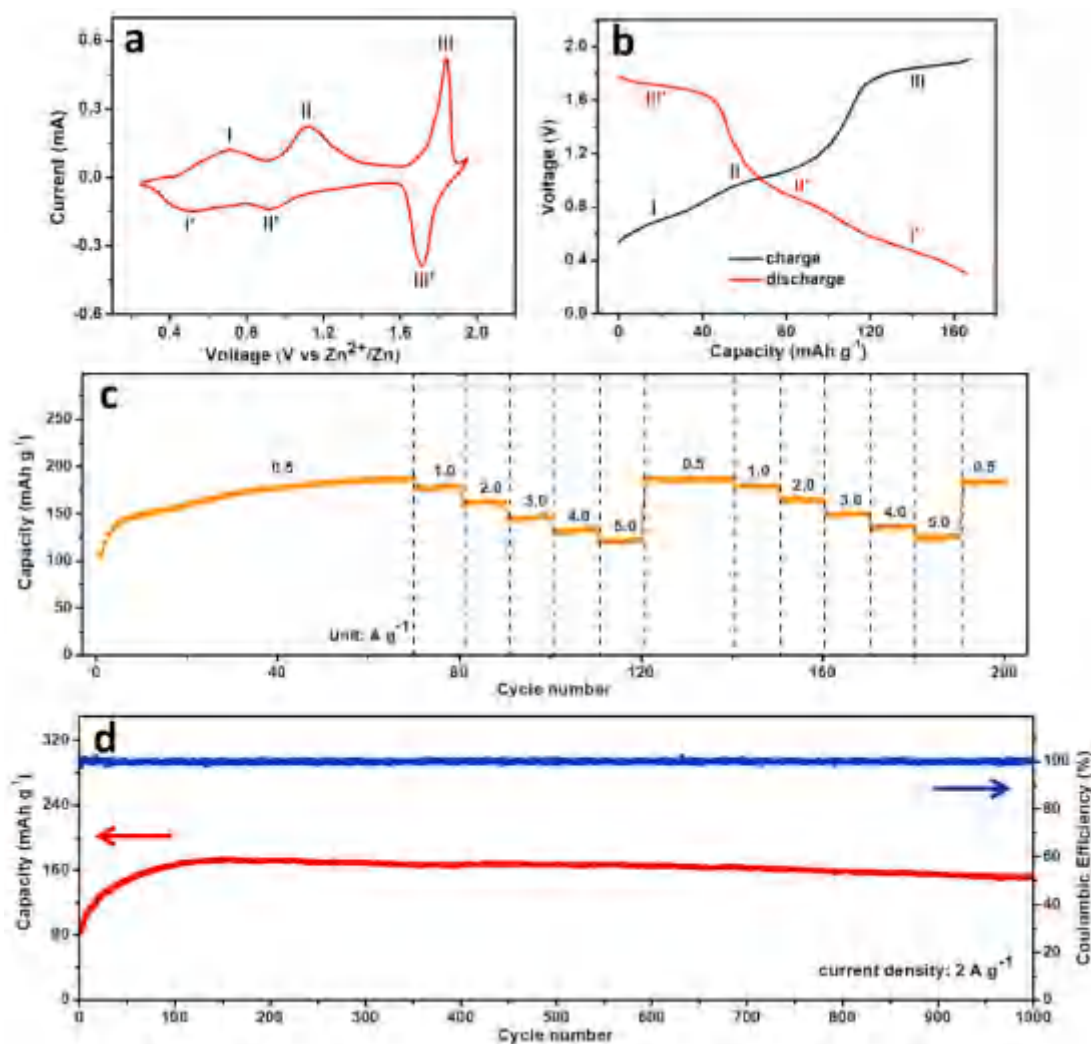
The chemical characteristics of the as-synthesized VHCF sample were investigated by Fourier transform infrared (FT-IR) spectroscopy, as shown in Fig. 1e. The strongest peak located at  $2095\text{ cm}^{-1}$  is the characteristic of the  $\text{C}\equiv\text{N}$  stretching [41]. The peaks appear at 525 and  $597\text{ cm}^{-1}$  are ascribed to the Fe-CN-M bending and Fe-CN vibration, respectively [42]. The peak located at  $978\text{ cm}^{-1}$  corresponds to the stretching mode of  $\text{V}=\text{O}$  [43]. In addition, the peaks observed at 1610 and  $3416\text{ cm}^{-1}$  are attributed to the O-H stretching and H-O-H bending, respectively, indicating the existence of the zeolitic and coordinating water molecules in the structure of the VHCF nanoparticles

[44]. The characteristics of the FT-IR spectrum confirm the Prussian blue structure of the VHCF nanoparticles.

X-ray photoelectron spectroscopy (XPS) was employed to analyze the chemical composition and surface electronic state of the as-synthesized VHCF nanoparticles. As shown in Fig. S3, the peaks arising from Na 1s, V 2p, Fe 2p, C 1s, N 1s and O 1s can be assigned in the survey XPS spectrum of the as-synthesized VHCF nanoparticles. The high-resolution XPS spectra of the Fe 2p orbital exhibit two peaks at 708.6 and 721.5 eV with a spin energy separation of 12.9 eV, which can be assigned to  $\text{Fe}^{\text{II}}$  2p<sub>3/2</sub> and  $\text{Fe}^{\text{II}}$  2p<sub>1/2</sub>, respectively, confirming that  $\text{Fe}^{\text{II}}$  is the main component in the as-synthesized VHCF nanoparticles [45]. For the V 2p spectrum, the binding energies for V 2p<sub>1/2</sub> and V 2p<sub>3/2</sub> are located at 516.8 and 524.5 eV, respectively. The V 2p<sub>3/2</sub> peak can be divided into two different peaks located at 516.6 and 517.5 eV, which correspond to  $\text{V}^{4+}$  2p<sub>3/2</sub> and  $\text{V}^{5+}$  2p<sub>3/2</sub>, respectively, indicating a mixed-valence of V [46]. Based on the peak area ratio of  $\text{V}^{4+}$  to  $\text{V}^{5+}$  (1:1.34), the average valence of V can be determined to be +4.6. From the EDS result (Fig. S4), the atomic ratios of V/Fe and Na/Fe are 1.3 and 0.63, respectively.

Thermal stability and the interstitial water content of the as-synthesized VHCF sample was estimated by thermogravimetric and differential thermal analysis (TG-DTA). As shown in Fig. 1f, weight loss was observed in two steps. From room temperature to 200 °C, the first 25.0% weight loss is attributed to the evaporation of the interstitial water accommodated in the open framework of the as-synthesized VHCF nanoparticles [47]. The second 22.9% weight loss from 200 to 370 °C originates from the thermal decomposition of the as-synthesized VHCF nanoparticles. Based on the XRD, FT-IR, XPS and TG-DTA results, the chemical formula of the as-synthesized VHCF sample can be determined to be  $\text{Na}_{0.63}(\text{VO})_{1.3}[\text{Fe}(\text{CN})_6]_2 \cdot 5.8\text{H}_2\text{O}$ . Because of the presence of vanadyl (VO) ion and non-stoichiometry of  $\text{Na}^+$  ion in the as-synthesized VHCF sample, structural vacancies filled with coordinating water molecules exist in the crystal framework. Nevertheless, the as-synthesized VHCF sample still maintains a cubic crystal structure as confirmed by the XRD result.

The electrochemical performance of the as-synthesized VHCF nanoparticles was characterized by typical coin-type cells assembled in ambient air, employing the VHCF nanoparticles cathode, Zn foil anode, 4 M  $\text{Zn}(\text{CF}_3\text{SO}_3)_2$  aqueous electrolyte, and glass fiber separator. Fig. 2a displays the cyclic voltammetry (CV) curve of VHCF nanoparticles



**Fig. 2.** (a) CV curve of VHCF electrode at  $0.2 \text{ mV s}^{-1}$ . (b) Typical galvanostatic charge-discharge curve at  $2 \text{ A g}^{-1}$  between 0.3 and 1.9 V. (c) Rate performance of the battery tested with the charge-discharge current densities varying from 0.5 to  $5.0 \text{ A g}^{-1}$ . (d) Cycling performance and the corresponding Coulombic efficiency at the current density of  $2 \text{ A g}^{-1}$ .

electrode at a scan rate of  $0.2 \text{ mV s}^{-1}$ . Three pairs of redox peaks located at 0.71/0.51 V (I/I'), 1.12/0.92 V (II/II') and 1.85/1.71 V (III/III') can be observed in the CV curve, suggesting the multistep insertion/extraction processes of  $\text{Zn}^{2+}$  ions through the VHCF lattice framework. Fig. 2b shows the typical charge/discharge profiles at current density of  $0.5 \text{ A g}^{-1}$ . It is obvious that there are three charge plateaus (I, II, and III) with the corresponding discharge plateaus (I', II', and III'), which are in consistent with the three pairs of redox peaks in CV.

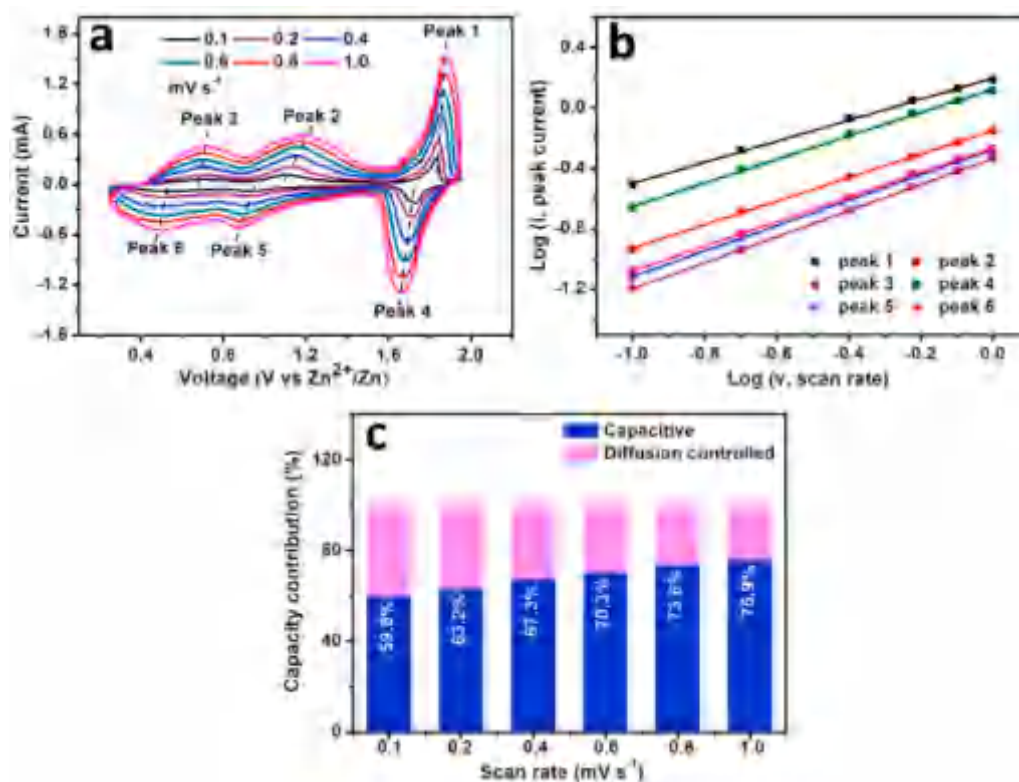
To clarify the electrochemical redox mechanism of V and Fe ions during the  $\text{Zn}^{2+}$  ions insertion/extraction into/from the VHCF lattice framework, ex-situ XPS measurements were conducted. Fig. S5 displays the comparison of high-resolution V  $2p_{3/2}$  and Fe  $2p_{3/2}$  at different states. At the 5th charged state, the intensity of  $\text{V}^{4+}$  peak weakens and the  $\text{V}^{5+}$  peak strengthens in comparison with that of the original state, reflecting the oxidation of  $\text{V}^{4+}$  to  $\text{V}^{5+}$  along with extraction of  $\text{Zn}^{2+}$  ion. After the 5th discharged to 0.3 V, the  $\text{V}^{3+}$  ( $2p_{3/2}$ : 515.6 eV) signals appear, indicating the partial reduction of  $\text{V}^{5+}$  to  $\text{V}^{4+}$ , further to  $\text{V}^{3+}$ , during the insertion of  $\text{Zn}^{2+}$  ions. It is necessary to point out that the V signals shift to higher binding energies, which may be caused by the insertion of  $\text{Zn}^{2+}$  ions and concomitant bonding rearrangements [48]. In addition, the  $\text{Fe}^{3+}$  ( $2p_{3/2}$ : 710.5 eV) signal appears during charging and disappears when discharging, indicating the reversible oxidation/reduction of  $[\text{Fe}(\text{CN})_6]^{4-}/[\text{Fe}(\text{CN})_6]^{3-}$  during the charge/discharge

processes [49]. The XPS results demonstrate that both V and Fe take part in the electrochemical reaction and together contribute to the capacity. According to the ex-situ XPS results, the three pairs of redox peaks and the corresponding three couples of charge/discharge plateaus can be attributed to  $\text{V}^{3+}/\text{V}^{4+}$  (I/I'),  $\text{V}^{4+}/\text{V}^{5+}$  (II/II'), and  $[\text{Fe}(\text{CN})_6]^{4-}/[\text{Fe}(\text{CN})_6]^{3-}$  (III/III') reversible redox processes, respectively. Therefore, the insertion/extraction of  $\text{Zn}^{2+}$  ions into/from VHCF lattice framework corresponds to a three-electron transfer process.

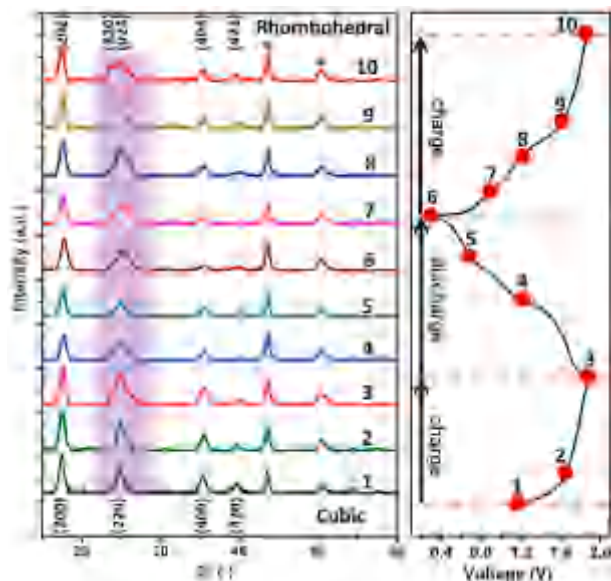
To clarify the electrochemical mechanism of the  $\text{Zn}^{2+}$  ions insertion/extraction into/from the VHCF lattice framework, ex-situ XPS measurements were conducted. As shown in Fig. S6a, no signal of Zn can be detected in the XPS spectrum of VHCF nanoparticles. When discharged to 0.3 V, the  $\text{Zn}^{2+}$  ions can be successfully inserted into VHCF lattice framework as demonstrated by the obvious Zn  $2p_{3/2-1/2}$  spin-orbit doublet. After recharging, smaller peaks corresponding to Zn  $2p$  are also observed that may be due to the irreversible insertion of  $\text{Zn}^{2+}$  ions in the electrode and residue electrolyte on the surface. The intensity of Na 1s core level spectrum after 5 cycles obviously weakens compared with the original state, suggesting that Na is extracted from the lattice (Fig. S6b). No Na 1s signal can be detected after 10 cycles, suggesting that  $\text{Na}^+$  ions are not involved in the insertion process after the initial extraction.

As shown in Fig. 2c, the capacity gradually increased during the





**Fig. 3.** (a) CV curves of the as-synthesized VHCF nanoparticles at different scan rates. (b)  $\log(i)$  versus  $\log(\nu)$  curves of cathodic and anodic peaks. (c) surface-controlled and diffusion-controlled contributions to capacity.



**Fig. 4.** Ex-situ XRD patterns of VHCF nanoparticles electrodes at various charged and discharged states (the diffraction peaks of steel foil current collector are marked with \* symbol).

initial 60 cycles, which is ascribed to the activation process of the VHCF electrode. The charge-discharge curves during the activation process are shown in Fig. S7. It can be seen that there is no significant increase in the capacity of III/III' redox processes, while the capacity of I/I' and II/II' redox processes increased obviously. Therefore, the activation process might be attributed to the incremental utilization of V redox active sites, possibly due to the gradual removal of Na and/or interstitial water from

the lattice during charge-discharge. After the activation cycles, the battery demonstrates a reversible discharge capacity of 187 mA h g<sup>-1</sup> at the current density of 0.5 A g<sup>-1</sup>. The rate capability is an important indicator for evaluating the available power from a battery system. The rate performance of Zn//VHCF battery system was then tested at different current densities from 0.5 to 5.0 A g<sup>-1</sup>. When the current densities is increased to 1.0, 2.0, 3.0, 4.0 and 5.0 A g<sup>-1</sup>, the battery can deliver reversible capacities of 179, 162, 146, 132 and 122 mA h g<sup>-1</sup>, respectively, corresponding to 95.7%, 86.6%, 78.1%, 70.6% and 65.2% capacity retentions of that achieved at 0.5 A g<sup>-1</sup>. When the battery is cycled again at 0.5 A g<sup>-1</sup>, the reversible capacity returns to 186 mA h g<sup>-1</sup>, which is 99.5% of the initial value. These results demonstrate the high reversibility of the redox reactions and the good stability of the crystal structure. The corresponding charge and discharge curves at various current densities are shown in Fig. S8. A comparison of the rate performance of VHCF with other PBAs-based materials (Fig. S9) reveals that VHCF can deliver higher specific capacity, which is attributed to the two redox reaction sites of V and Fe in VHCF.

The long-term cyclability of this aqueous rechargeable Zn-ion battery was evaluated at a current density of 2.0 A g<sup>-1</sup>. As shown in Fig. 2d, the VHCF nanoparticles cathode delivers the highest achievable capacity of 172 mA h g<sup>-1</sup> after the initial activation cycles. An impressive 96.5% of the highest achievable capacity is available after 500 cycles and 87.8% retention is obtained after 1000 cycles. Besides, the high Coulombic efficiency (close to 100%) indicates the reversibility of the charge-discharge reactions.

To further evaluate the electrochemical kinetics of the intercalation behaviors of Zn<sup>2+</sup> in the as-synthesized VHCF nanoparticles, cyclic voltammetry (CV) tests at different scan rates (0.1–1.0 mV s<sup>-1</sup>) were carried out, as shown in Fig. 3a. It can be observed that as the scan rate increases, the curves basically maintain similar shapes and the reduction peaks and oxidation peaks shift to lower and higher voltages, respectively. In principle, the peak current ( $i$ ) from the CV profiles obeys a power-law formula with the scan rate ( $\nu$ ) according to Equation (1) [50]:

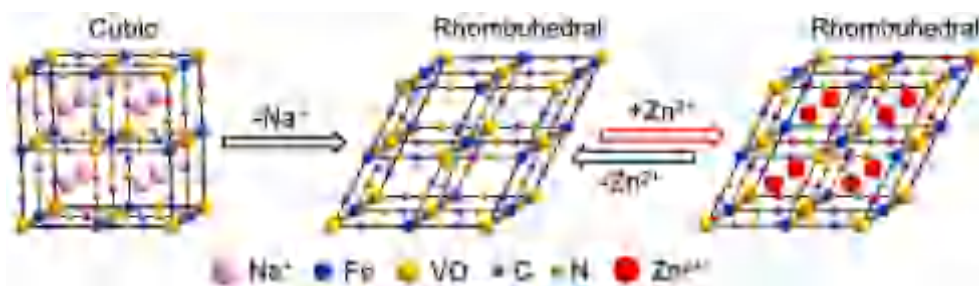


Fig. 5. Schematic illustration of the structural evolution of the VHCF during charge-discharge process.

$$i = a\nu^b \quad (1)$$

Where  $a$  and  $b$  are adjustable parameters. For analytical purposes, we rearrange Equation (1) slightly to

$$\log(i) = b \times \log(\nu) + \log a \quad (2)$$

The  $b$ -values for both cathode and anode peaks can be calculated from the curves of  $\log(i)$  versus  $\log(\nu)$ . Generally,  $b = 0.5$  indicates a totally diffusion-controlled process, while  $b = 1$  reveals a surface-controlled process. As shown in Fig. 3b, the  $b$  values of the six peaks were calculated to be 0.84, 0.81, 0.70, 0.78, 0.86, 0.77, indicating that the charge storage process is synergistically controlled by the capacitive and diffusion behaviors. This leads to a fast  $\text{Zn}^{2+}$  diffusion kinetics, enabling the high-rate capability. Furthermore, the capacity can be divided into surface-controlled ( $k_1\nu$ ) and diffusion-controlled ( $k_2\nu^{1/2}$ ) parts by the following Equation [51]:

$$i(\nu) = k_1\nu + k_2\nu^{1/2} \quad (3)$$

Fig. 3c displays the surface-controlled and diffusion-controlled contributions to capacity ranging from 0.1 to 1.0  $\text{mV s}^{-1}$ . With the incremental scan rate, the contribution ratio of surface-controlled capacity gradually increases from 59.8% to 75.9%, demonstrating that the surface-controlled contribution dominates the electrochemical reaction.

To investigate the structural evolution of VHCF during the charge-discharge process, ex-situ XRD measurements were conducted at different charge and discharge states during the first charge, the first discharge and the second charge processes at a current density of 100  $\text{mA g}^{-1}$ . As shown in Fig. 4, the structure transformation can be detected from the change of XRD pattern with the peak at  $24.8^\circ$ . During the first charge process (from state 1 to 3), with the  $\text{Na}^+$  ions extracted from the lattice framework of the VHCF, a single peak at  $24.8^\circ$  splits into doublets, indicating the crystal structure of VHCF changes from cubic phase to rhombohedral phase [52,53]. During the first discharging process (from state 3 to 6), with the insertion of  $\text{Zn}^{2+}$  ions into the lattice framework, the structure maintains the rhombohedral phase rather than recover to cubic phase. While for the second charge process (from state 6 to 10), the characteristics of the rhombohedral phase are more obvious than that after first charge process. Fig. S10 shows the XRD patterns of the electrodes after the third charged and the third discharged, comparing with the original state. It can be concluded that the crystal structure of the VHCF changes from cubic phase to rhombohedral phase after the first charge process, and then the ions insertion/extraction processes are carried out reversibly in the rhombohedral phase. The structure evolution and the ions insertion/extraction processes are schematically shown in Fig. 5.

#### 4. Conclusions

In summary, a new PBAs,  $\text{Na}_{0.63}(\text{VO})_{1.3}[\text{Fe}(\text{CN})_6] \cdot 5.8\text{H}_2\text{O}$  (vanadium hexacyanoferrate, VHCF), was synthesized via a simple coprecipitation method. The obtained VHCF sample was investigated as

the cathode material for an aqueous rechargeable Zn-ion battery. With the typical nanoparticle morphology and 3D lattice framework structure, the VHCF exhibits an excellent rate capability and a promising long-term cyclability. It is demonstrated that both V and Fe act as electrochemical redox active sites, together contributing to the capacity. The insertion/extraction of  $\text{Zn}^{2+}$  ions into/from VHCF lattice framework undergoes three steps through a three-electron transfer process. The crystal structure of the VHCF changes from cubic phase to rhombohedral phase after the first charge process, and then the  $\text{Zn}^{2+}$  ions are inserted and extracted reversibly in the stable rhombohedral phase. Low cost, simple synthesis, and the good electrochemical performances make VHCF an attractive candidate as cathode material for aqueous rechargeable Zn-ion battery system.

#### CRediT authorship contribution statement

**YanJun Zhang:** Conceptualization, Methodology, Validation, Formal analysis, Investigation, Data curation, Writing - original draft, Writing - review & editing. **Yao Wang:** Conceptualization, Methodology, Validation, Formal analysis, Investigation, Data curation, Writing - review & editing. **Liang Lu:** Formal analysis, Investigation, Resources. **Chunwen Sun:** Funding acquisition, Investigation, Writing - review & editing. **Denis Y.W. Yu:** Supervision, Funding acquisition, Investigation, Writing - review & editing.

#### Declaration of competing interest

The authors declare that they have no known competing financial interests or personal relationships that could have appeared to influence the work reported in this paper.

#### Acknowledgements

This work was financial supported by the National Natural Science Foundation of China (Nos. 51672029 and 51372271), the National Key R & D Project from Ministry of Science and Technology, China (2016YFA0202702) and the Strategic Research Grant from City University of Hong Kong (PJ7005285).

#### Appendix A. Supplementary data

Supplementary data to this article can be found online at <https://doi.org/10.1016/j.jpowsour.2020.229263>.

#### References

- [1] M. Armand, J.-M. Tarascon, *Nature* 451 (2008) 652–657.
- [2] Z. Yang, J. Zhang, M.C.W. Kintner-Meyer, X. Lu, D. Choi, J.P. Lemmon, J. Liu, *Chem. Rev.* 111 (2011) 3577–3613.
- [3] B. Dunn, H. Kamath, J.-M. Tarascon, *Science* 334 (2011) 928–935.
- [4] B. Scrosati, J. Garche, *J. Power Sources* 195 (2010) 2419–2430.
- [5] D. Bin, Y. Wen, Y. Wang, Y. Xia, *J. Energy Chem.* 27 (2018) 1521–1535.
- [6] D. Chao, W. Zhou, F. Xie, C. Ye, H. Li, M. Jaroniec, S.Z. Qiao, *Sci. Adv.* 6 (2020), eaba4098.

- [7] Z. Liu, Y. Huang, Y. Huang, Q. Yang, X. Li, Z. Huang, C. Zhi, *Chem. Soc. Rev.* 49 (2020) 180–232.
- [8] R. Demir-Cakan, M.R. Palacin, L. Croguennec, *J. Mater. Chem.* 7 (2019) 20519–20539.
- [9] F. Beck, P. Ruetschi, *Electrochim. Acta* 45 (2000) 2467–2482.
- [10] J. Huang, Z. Guo, Y. Ma, D. Bin, Y. Wang, Y. Xia, *Small Methods* 3 (2019) 1800272.
- [11] J. Liu, C. Xu, Z. Chen, S. Ni, Z.X. Shen, *Green Energy Environ* 3 (2018) 20–41.
- [12] T. Liu, X. Cheng, H. Yu, H. Zhu, N. Peng, R. Zhang, J. Zhang, M. Shuai, Y. Cui, J. Shu, *Energy Storage Mater* 18 (2019) 68–91.
- [13] B. Tang, L. Shan, S. Liang, J. Zhou, *Energy Environ. Sci.* 12 (2019) 3288–3304.
- [14] M. Song, H. Tan, D. Chao, H.J. Fan, *Adv. Funct. Mater.* 28 (2018) 1802564.
- [15] C.G. Li, X.D. Zhang, W. He, G.G. Xu, R. Sun, *J. Power Sources* 449 (2020) 227596.
- [16] C. Xu, B. Li, H. Du, F. Kang, *Angew. Chem. Int. Ed.* 51 (2012) 933–935.
- [17] N. Zhang, F. Cheng, Y. Liu, Q. Zhao, K. Lei, C. Chen, X. Liu, J. Chen, *J. Am. Chem. Soc.* 138 (2016) 12894–12901.
- [18] H. Pan, Y. Shao, P. Yan, Y. Cheng, K.S. Han, Z. Nie, C. Wang, J. Yang, X. Li, P. Bhattacharya, K.T. Mueller, J. Liu, *Nat. Energy* 1 (2016) 16039.
- [19] B. Wu, G. Zhang, M. Yan, T. Xiong, P. He, L. He, X. Xu, L. Mai, *Small* 14 (2018), e1703850.
- [20] Z. Li, Y. Huang, J. Zhang, S. Jin, S. Zhang, H. Zhou, *Nanoscale* 12 (2020) 4150–4158.
- [21] F. Wan, Z. Niu, *Angew. Chem. Int. Ed.* 58 (2019) 16358–16367.
- [22] C. Liu, Z. Neale, J. Zheng, X. Jia, J. Huang, M. Yan, M. Tian, M. Wang, J. Yang, G. Cao, *Energy Environ. Sci.* 12 (2019) 2273–2285.
- [23] D. Kundu, B.D. Adams, V. Duffort, S.H. Vajargah, L.F. Nazar, *Nat. Energy* 1 (2016) 16119.
- [24] B. Yin, S. Zhang, K. Ke, T. Xiong, Y. Wang, B.K.D. Lim, W.S.V. Lee, Z. Wang, J. Xue, *Nanoscale* 11 (2019) 19723–19728.
- [25] B. Tang, J. Zhou, G. Fang, F. Liu, C. Zhu, C. Wang, A. Pan, S. Liang, *J. Mater. Chem.* 7 (2019) 940–945.
- [26] L. Zhang, L. Chen, X. Zhou, Z. Liu, *Adv. Energy Mater.* 5 (2015) 1400930.
- [27] R. Trócoli, G. Kasiri, F. La Mantia, *J. Power Sources* 400 (2018) 167–171.
- [28] Z. Jia, B. Wang, Y. Wang, *Mater. Chem. Phys.* 149–150 (2015) 601–606.
- [29] K. Lu, B. Song, Y. Zhang, H. Ma, J. Zhang, *J. Mater. Chem.* 5 (2017) 23628–23633.
- [30] Z. Liu, G. Pulletikurthi, F. Endres, *ACS Appl. Mater. Interfaces* 8 (2016) 12158–12164.
- [31] G. Li, Z. Yang, Y. Jiang, C. Jin, W. Huang, X. Ding, Y. Huang, *Nanomater. Energy* 25 (2016) 211–217.
- [32] Q. Zhao, W. Huang, Z. Luo, L. Liu, Y. Lu, Y. Li, L. Li, J. Hu, H. Ma, J. Chen, *Sci. Adv.* 4 (2018), eaao1761.
- [33] D. Kundu, P. Oberholzer, C. Glaros, A. Bouzid, E. Tervoort, A. Pasquarello, M. Niederberger, *Chem. Mater.* 30 (2018) 3874–3881.
- [34] Y. Cheng, L. Luo, L. Zhong, J. Chen, B. Li, W. Wang, S.X. Mao, C. Wang, V. L. Sprenkle, G. Li, J. Liu, *ACS Appl. Mater. Interfaces* 8 (2016) 13673–13677.
- [35] L. Ma, S. Chen, H. Li, Z. Ruan, Z. Tang, Z. Liu, Z. Wang, Y. Huang, Z. Pei, J. A. Zapien, C. Zhi, *Energy Environ. Sci.* 11 (2018) 2521–2530.
- [36] B. Wang, Y. Han, X. Wang, N. Bahlawane, H. Pan, M. Yan, Y. Jiang, *iScience* 3 (2018) 110–133.
- [37] J. Qian, C. Wu, Y. Cao, Z. Ma, Y. Huang, X. Ai, H. Yang, *Adv. Energy Mater.* 8 (2018) 1702619.
- [38] J.-H. Lee, G. Ali, D.H. Kim, K.Y. Chung, *Adv. Energy Mater.* 7 (2017) 1601491.
- [39] L. Ma, S. Chen, C. Long, X. Li, Y. Zhao, Z. Liu, Z. Huang, B. Dong, J.A. Zapien, C. Zhi, *Adv. Energy Mater.* 9 (2019) 1902446.
- [40] S. Liu, L. Kang, J.M. Kim, Y.T. Chun, J. Zhang, S.C. Jun, *Adv. Energy Mater.* (2020) 2000477.
- [41] F.A. Miller, C.H. Wilkins, *Anal. Chem.* 24 (1952) 1253–1294.
- [42] D. Ellis, M. Eckhoff, V.D. Neff, *J. Phys. Chem.* 85 (1981) 1225–1231.
- [43] C.G. Tsiafoulis, P.N. Trikalitis, M.I. Prodromidis, *Electrochem. Commun.* 7 (2005) 1398–1404.
- [44] J. Peng, J. Wang, H. Yi, W. Hu, Y. Yu, J. Yin, Y. Shen, Y. Liu, J. Luo, Y. Xu, P. Wei, Y. Li, Y. Jin, Y. Ding, L. Miao, J. Jiang, J. Han, Y. Huang, *Adv. Energy Mater.* 8 (2018) 1702856.
- [45] C. Zhang, Y. Xu, M. Zhu, L. Liang, H. Dong, M. Wu, Y. Yang, Y. Lei, *Adv. Funct. Mater.* 27 (2017) 1604307.
- [46] X. Guo, G. Fang, W. Zhang, J. Zhou, L. Shan, L. Wang, C. Wang, T. Lin, Y. Tang, S. Liang, *Adv. Energy Mater.* 8 (2018) 1801819.
- [47] X. Bie, K. Kubota, T. Hosaka, K. Chihara, S. Komaba, *J. Power Sources* 378 (2018) 322–330.
- [48] Z. Peng, Q. Wei, S. Tan, P. He, W. Luo, Q. An, L. Mai, *Chem. Commun.* 54 (2018) 4041–4044.
- [49] L. Shen, Z. Wang, L. Chen, *Chem. Eur J.* 20 (2014) 12559–12562.
- [50] V. Augustyn, J. Come, M.A. Lowe, J.W. Kim, P.L. Taberna, S.H. Tolbert, H. D. Abruna, P. Simon, B. Dunn, *Nat. Mater.* 12 (2013) 518–522.
- [51] J. Wang, J. Polleux, J. Lim, B. Dunn, *J. Phys. Chem. C* 111 (2007) 14925–14931.
- [52] L. Wang, Y.H. Lu, J. Liu, M.W. Xu, J.G. Cheng, D.W. Zhang, J.B. Goodenough, *Angew. Chem. Int. Ed.* 52 (2013) 1964–1967.
- [53] Y. You, X.L. Wu, Y.X. Yin, Y.G. Guo, *Energy Environ. Sci.* 7 (2014) 1643–1647.



# Unlocking the True Capability of Graphite-Based Dual-Ion Batteries with Ethyl Methyl Carbonate Electrolyte

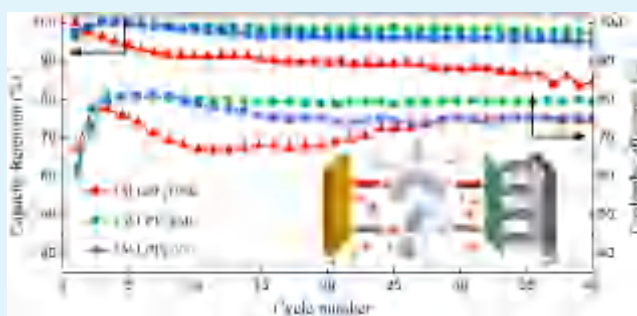
Yao Wang,<sup>†</sup> Shuo Wang,<sup>†</sup> Yanjun Zhang,<sup>†</sup> Pui-Kit Lee,<sup>†</sup> and Denis Y. W. Yu<sup>\*,†,‡</sup>

<sup>†</sup>School of Energy and Environment and <sup>‡</sup>Center of Super-Diamond and Advanced Films, City University of Hong Kong, Tat Chee Avenue, Kowloon, Hong Kong, SAR, China

\* Supporting Information

**ABSTRACT:** Graphite-based dual-ion batteries (DIBs), which involve the intercalation of anions into the carbon layers, are promising for high-power applications. Many researchers inevitably choose ethyl methyl carbonate (EMC) as the electrolyte, as they observe superior electrochemical performances compared to other solvents. Here, we clarify the underlying reason why EMC is better. Specifically, EMC forms a thinner layer of cathode electrolyte interface on the graphite surface with fewer Li–F and ROCO<sub>2</sub>Li species than that with dimethyl carbonate and diethyl carbonate. EMC electrolyte reduces charge-transfer resistance, polarization, and self-discharge of graphite electrodes. It also enhances Coulombic efficiency, cycle, and rate performances. 90% of the available capacity can be obtained even at 12 C (1200 mA g<sup>−1</sup>). Our work also emphasizes the importance of electrolyte and electrolyte interface on future developments of DIBs.

**KEYWORDS:** dual-ion battery, electrolyte, ethyl methyl carbonate, PF<sub>6</sub><sup>−</sup> intercalation, cathode electrolyte interface



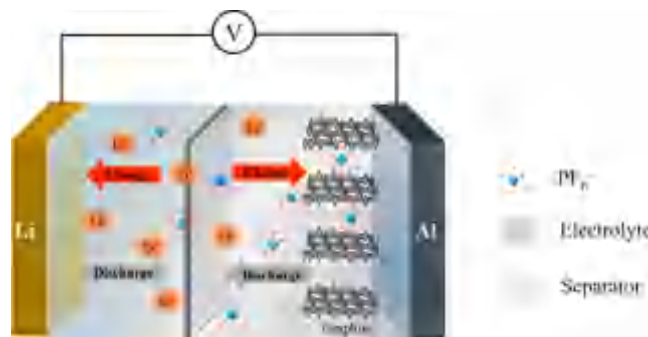
## INTRODUCTION

Because of growing energy demand, electrical energy storage devices are attracting increasing attention. Lithium ion batteries (LIBs) have been widely used in portable electronics and electric vehicles.<sup>1,2</sup> However, the low power densities of LIBs and high cost of the currently used Co- and Ni-based cathode materials hinder its use for large-scale energy storage.<sup>3–5</sup> Therefore, there is an urgent need to search for next-generation energy storage systems with electrode materials from abundant resources with faster kinetics.

Dual-ion battery (DIB) is a possible choice because of its advantages of low cost, high working voltage, and high power.<sup>6–15</sup> Significantly different from traditional LIBs, where only the cation (i.e., Li<sup>+</sup>) is used as the charge carrier, DIBs use both cations and anions in the electrolyte for charge transfer,<sup>12,16</sup> as illustrated in Scheme 1. This allows DIBs to be charged and discharged much faster. On the one hand, since the negative electrode (anode) of DIBs involves redox reaction of cations, common LIB materials such as graphite and lithium titanate can be used. On the other hand, a material that can accommodate anions is needed at the positive electrode (cathode). Currently, graphite is a promising cathode for DIBs, as anions such as AlCl<sub>4</sub><sup>−</sup>, ClO<sub>4</sub><sup>−</sup>, PF<sub>6</sub><sup>−</sup>, TFSI<sup>−</sup>, FSI<sup>−</sup>, etc. can be inserted into the graphene layers.<sup>8,17–25</sup>

In DIBs, electrolyte plays an utmost role, as it supplies the anions and cations for electrochemical reactions. The specific energy density of a DIB cell will be significantly affected by the mass and volume of the electrolyte.<sup>9,26</sup> Moreover, the electrochemical performances of graphite were found to be

Scheme 1. Illustration of the Charge–Discharge Mechanisms of DIB with Graphite Cathode and Li Anode



highly dependent on the type of electrolyte. As early as 2000, Seel and Dahn found that ethylene carbonate (EC)-based electrolytes decompose significantly at ~5.2 V versus Li/Li<sup>+</sup>, while ethyl methyl sulfone (EMS) is stable up to 5.5 V.<sup>26</sup> Wang et al. revealed using X-ray diffraction (XRD), Raman spectroscopy, and electrochemical tests that anions can be intercalated easily into graphite with ethyl methyl carbonate (EMC) and methyl propionate (MP), but not in sulfolane (SL),  $\gamma$ -butyrolactone (GBL), and EC.<sup>20,27–30</sup>

Received: July 31, 2019

Accepted: September 16, 2019

Published: September 16, 2019



Table 1. Parameters of Different Electrolytes

3 M LiPF <sub>6</sub>	solvent density (g mL <sup>-3</sup> )	MW(g mol <sup>-1</sup> )	solvent viscosity <sup>18</sup> [ $\eta$ (cP)]	dielectric constant	molar ratio	conductivity (mS cm <sup>-1</sup> )
DMC	1.069	90.08	0.585	3.1	1:4.0	8.8
EMC	1.006	104.10	0.66	2.9	1:3.2	4.7
DEC	0.975	118.13	0.75	2.8	1:2.8	2.7

Recently, many researchers have chosen to use EMC-based electrolyte for their works on DIBs. It is not a coincidence, but mainly because they can get superior electrochemical performances with EMC as compared to other electrolytes.<sup>16,31–36</sup> Yet, the fundamental reason making EMC better than others is not explained. In this study, we systematically compared graphite electrodes tested with dimethyl carbonate (DMC), EMC, and diethyl carbonate (DEC). We found that EMC enables the largest reversible capacity, best cycle stability, highest cycle Coulombic efficiency, lowest onset potential, smallest polarization, lowest self-discharge rate, and best rate performance from graphite compared to DMC and DEC. We observed that the electrochemical performances are correlated with the cathode electrolyte interface on the graphite surface.

## RESULTS AND DISCUSSION

We chose to study these three linear carbonates as electrolytes, because they have similar dielectric constants, so more insights into what parameters govern the electrochemical performances of PF<sub>6</sub><sup>-</sup> intercalation into graphite can be obtained. Electrolytes with single solvent instead of mixed solvents were used to avoid the complication of solvent interactions. To start out, Table 1 shows the physical parameters of the solvents. While the solvent molecular weight (MW) increases with the number of carbon atoms in the molecule, its density has the opposite trend. Among the three solvents, DMC has the lowest viscosity, followed by EMC and DEC. Ionic conductivity of the electrolytes with 3 M LiPF<sub>6</sub> salt dissolved in them is in the order of 3 M LiPF<sub>6</sub>/DMC > 3 M LiPF<sub>6</sub>/EMC > 3 M LiPF<sub>6</sub>/DEC. The oxidative stability of the electrolytes was tested with a linear sweep voltammetry (LSV) on C-coated aluminum foil without graphite active material (Figure S1a). Within the voltage range (from 3 to 5.1 V) of our tests, no significant electrolyte decomposition was observed.<sup>37,38</sup>

Graphite (KS6, Timcal) was used as the active material in our tests. They were made into electrodes with carbon black and binder on Al foils. Coin cells with KS6 cathodes and Li metal anode in different electrolytes (3 M LiPF<sub>6</sub> in DMC, EMC, or DEC) were made, and their reaction potentials, capacities, cycle stabilities, self-discharge rates, and rate performances were tested with cyclic voltammetry (CV) and galvanostatic charge and discharge.

CV profiles (fourth cycle) of the cells are displayed in Figure 1. Multiple oxidation peaks (intercalation of PF<sub>6</sub><sup>-</sup> into graphite) followed by corresponding reduction peaks (deintercalation), indicating a staging mechanism, are observed.<sup>26,39</sup> However, the number of reaction peaks and their corresponding voltages are different for cells with different solvents. For example, one more pair of redox peaks is observed with DMC at ~5.0 V, while no such peaks are observed for DEC and EMC (Figure S1b–1d). This indicates that the electrolyte solvent influences the energy corresponding to PF<sub>6</sub><sup>-</sup> insertion and extraction. Specifically, we notice that the onset potential during charging is smallest for EMC, followed by DEC and DMC (inset of Figure 1). We suspect that the asymmetric nature of EMC solvent leads to lower interaction between

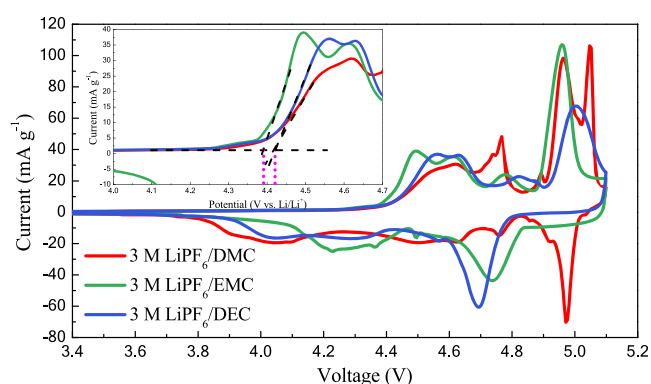


Figure 1. CV profiles of KS6 half cells with Li metal as counter electrode in 3 M LiPF<sub>6</sub>/DMC, LiPF<sub>6</sub>/EMC, and LiPF<sub>6</sub>/DEC electrolytes (scan rate: 0.06 mV s<sup>-1</sup>, the fourth cycle, dashed lines in the inset are linear fits before and after the onset of oxidation peak).

solvent and PF<sub>6</sub><sup>-</sup>. This is a surprising result and suggests that the kinetics of the reaction is not governed by solvent properties such as dielectric constant, ionic conductivity, and viscosity (Table 1).

Differences in electrochemical behaviors with different electrolytes are also confirmed by charge–discharge tests. The first and fourth cycle charge–discharge curves of the cells are shown in Figure 2a,b, respectively. During initial cycle, all electrodes give a charge capacity of more than 120 mAh g<sup>-1</sup> with a discharge capacity between 80 and 95 mAh g<sup>-1</sup>. First cycle efficiency of the three electrodes are ~60–70%, indicating some irreversible reactions on the surface of the graphite. The fourth cycle charge–discharge curves are consistent with the CV profiles in Figure 1. We see that EMC electrolyte is superior over DMC and DEC, as the capacity is highest among the three electrolytes. It also shows the smallest polarization (the difference between the average voltage of the charge and discharge curves) of ~0.26 V compare to that of 0.34–0.38 V for DMC and DEC based on the fourth cycle curves. Therefore, the corresponding voltage efficiency (VE) is highest with EMC electrolyte at ~94%, which is comparable to previously reported EMC-based electrolytes.<sup>37</sup> With respect to the energy efficiency (EE), which is decided by VE and Coulombic efficiency, EMC- and DEC-based electrolytes show higher EE of ~76% compared to ~70% with DMC electrolytes.

Moreover, electrode tested in EMC electrolyte gives the best cycle performance (Figure 2c). Discharge capacity retention is as high as 97.4 ± 0.4% after 40 cycles compared to third cycle discharge capacity with EMC, and the charge–discharge curves do not change upon cycling (Figure S2b). In contrast, large capacity fading is observed for cell with DMC, which is manifested in a gradual increase in polarization upon cycling (Figure S2a).

Coulombic efficiency (CE) during cycling can also give important information about side reactions that are taking place with different electrolytes—CE is highest for electrode tested in EMC, followed by DEC and DMC (Figure 2c). Part

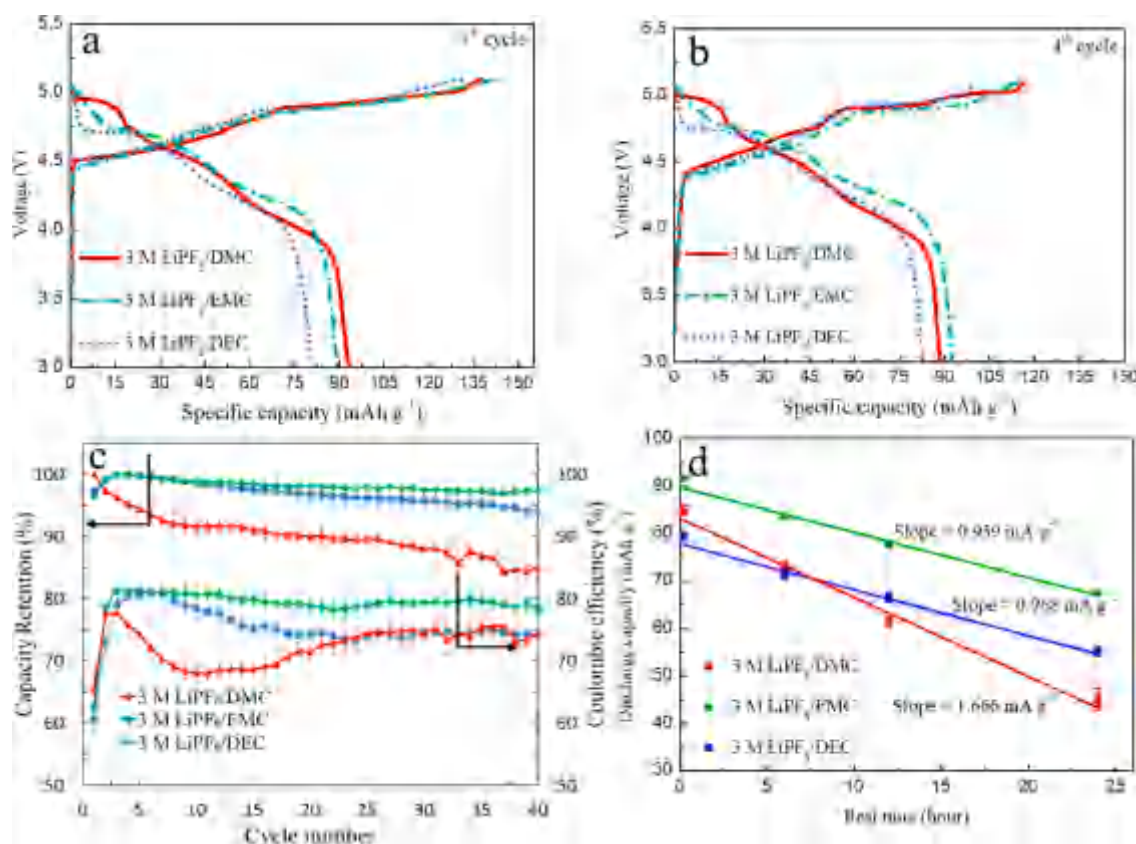


Figure 2. (a) The initial and (b) the fourth charge–discharge curves and (c) cycling stability of KS6/Li half cells using different electrolytes. Cutoff voltage: 3–5.1 V, current density: 10 mA g<sup>-1</sup>. (d) Self-discharge test results with different electrolytes.

of the low CE observed at 10 mA g<sup>-1</sup> is due to a self-discharge process, which is constantly occurring during the 10 h charging period. This is the critical factor causing the low EE obtained with the three electrolytes at low current rate. In particular, the lowest EE with DMC is consistent with the largest polarization and lowest CE. By increasing the current rate to 100 mA g<sup>-1</sup>, CE is significantly increased (Figure S3) with the shortening of charging time to ~1 h. To quantify the self-discharge rate, the electrodes were fully charged to 5.1 V, rested for different amounts of time, and then discharged to record the remaining capacity. The charge–discharge curves with different rest times are shown in Figure S4. The available discharge capacities are summarized in Figure 2d. We note that the discharge capacity decreases linearly with rest time, suggesting that self-discharge is a continuous process. In LIBs, self-discharge is proposed to be due to the shuttling of lithium ions between the two electrodes.<sup>40–43</sup> In DIBs, a similar shuttling mechanism involving oxidized/reduced species in the electrolyte probably plays a role. Among the three electrolytes, EMC again is superior with the lowest self-discharge rate of 0.939 mA g<sup>-1</sup>, followed by DEC (0.968 mA g<sup>-1</sup>) and DMC (1.666 mA g<sup>-1</sup>).

We notice that, even after accounting for self-discharge, Coulombic efficiency and cycle stability during charge–discharge is highest for EMC, followed by DEC and DMC (Figure S2d). Previous reports revealed that the electrolyte decomposition and the structural collapse of the graphite cathode can be inhibited by constructing a robust and favorable surface layer, which optimizes the channels for PF<sub>6</sub><sup>-</sup> intercalation and enhances cyclability.<sup>44–46</sup> This leads us to think that the source of the difference in electrochemical performances may be due to the difference in cathode

electrolyte interface (CEI) layer on the graphite from reactions with the electrolytes. To verify this, X-ray photoelectron spectroscopy (XPS) measurements were conducted on cycled KS6 cathodes to study the chemical composition of the CEI (Figure 3). Specifically, three cells with different electrolytes were charged and discharged at 10 mA g<sup>-1</sup> for one cycle; then, the graphite electrodes were taken out at the fully charged states and washed with DMC for XPS tests. The C 1s profile can be deconvoluted into characteristic peaks corresponding to graphitic carbon C–C, C–OH, carbonate species including ROCO<sub>2</sub>Li, C=O, and C–O bonds,<sup>44</sup> whereas the F 1s profile can be used to determine F-containing species formed upon charge and discharge. While the pristine KS6 electrode shows only XPS peaks corresponding to C–C, C–O, and C–OH bonds with no peaks in F 1s (Figure S5a,b), one can see a definite change in surface chemistry upon cycling due to reactions with the electrolyte (Figure 3). In particular, graphite electrodes tested with DMC and DEC show higher amounts of Li–F and ROCO<sub>2</sub>Li than that tested with EMC, suggesting less reaction between EMC and graphite. This is consistent with the higher CE of electrode tested with EMC.

The existence of the CEI on graphite is further demonstrated by transmission electron microscopy (TEM) (see Figure 3), where we see a thin layer of material on the graphite surface, and the thickness differs with different electrolytes. In particular, CEI is the thinnest for electrode tested in EMC, while it is thickest for DMC. This is consistent with the lower Coulombic efficiency of electrode tested in DMC. With cycling, gradual accumulation of reaction products between DMC and graphite probably accounts for the observed capacity fading.<sup>16</sup> In contrast, EMC forms a thinner



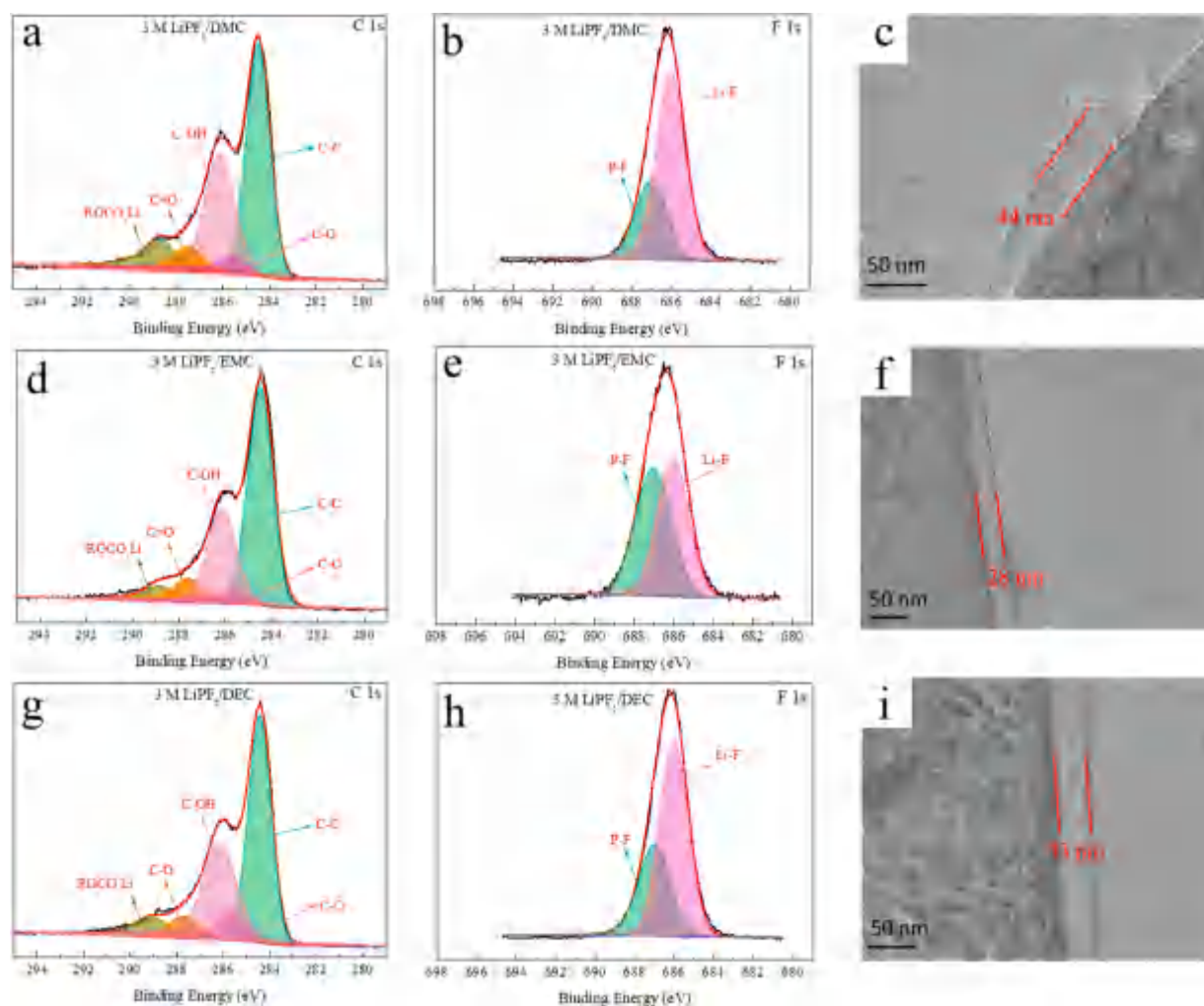


Figure 3. XPS curve fittings for the C 1s, F 1s peaks of cycled KS6 electrodes with (a, b) DMC, (d, e) EMC, and (g, h) DEC electrolytes. TEM images of the electrodes after cycling at the upper cutoff voltage of 5.1 V with (c) DMC, (f) EMC, and (i) DEC electrolytes.

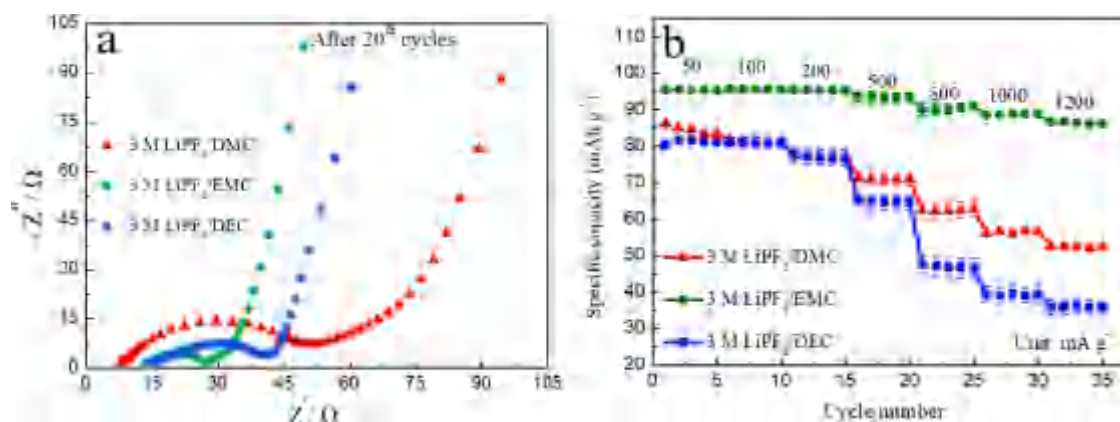


Figure 4. (a) Nyquist plots of the KS6/Li metal half-cells after 20 cycles using different electrolytes. (b) Rate capability of the cells using 3 M LiPF<sub>6</sub>-based electrolytes (current density: 50, 100, 200, 500, 800, 1000, and 1200 mA g<sup>-1</sup>).

and more stable CEI on the graphite surface, leading to better cycling stability and more reversible PF<sub>6</sub><sup>-</sup> de/intercalation. These results are similar to those demonstrated by Han et al. A thinner CEI was found on the lithium titanate (LTO)-modified graphite surface, which reduces electrolyte decomposition.<sup>44</sup>

To further investigate the effect of CEI, impedance and rate performance of the electrode were measured. Figure 4a shows the electrochemical impedance spectroscopy (EIS) profiles of electrodes tested after 20 cycles. Charge transfer resistance ( $R_{ct}$ ) is much smaller with 3 M LiPF<sub>6</sub>/EMC (11 Ω), in comparison with the larger  $R_{ct}$  observed in DEC and DMC (18 and 36 Ω, respectively). The result is consistent with the

thickness of the CEI and the lower polarization of the graphite with EMC in Figure 2b.

Rate performances of the electrodes subjected to different current rates are shown in Figure 4b. EMC gives superior rate performance compared with DMC and DEC, with an impressive 90% capacity retention even at a current rate of 1200 mA g<sup>-1</sup> (charge–discharge rate of ~12 C). A much smaller polarization is observed at higher current for EMC from the charge–discharge profiles in Figure S6, indicating that the kinetics of PF<sub>6</sub><sup>-</sup> uptake/release process in 3 M LiPF<sub>6</sub>/EMC is extremely fast.<sup>35</sup> Even though the CEI layer with DEC is thinner than that with DMC, rate performance is worse for DEC. We ascribe it to the higher viscosity and lower ionic conductivity of the DEC electrolyte, which leads to smaller amount of PF<sub>6</sub><sup>-</sup> intake (smaller capacity) up to 5.1 V during high-rate charging. Rate performance is most likely a compromise between CEI thickness, viscosity, and ionic conductivity in the electrolyte.

## CONCLUSION

In this work, we have demonstrated that the kinetics of PF<sub>6</sub><sup>-</sup> intercalation/deintercalation into graphite electrode is highly affected by the type of electrolyte. In particular, the true capability of graphite is only revealed with the use of EMC-based electrolyte. This is due to the thinner and more stable CEI on the surface of graphite, as observed by XPS and TEM. Our work highlights the importance of EMC as an electrolyte for graphite-based DIBs. In addition, it emphasizes the necessity to conduct more research work to understand the interaction between the solvents and active material surface.

## EXPERIMENTAL METHODS

**Electrolyte and Electrode Preparation.** LiPF<sub>6</sub> was purchased from DoDoChem (purity ≥99.9%), while DMC (≥99%), EMC (98%), and DEC (≥99%) were purchased from Sigma-Aldrich. Three molar LiPF<sub>6</sub>-based electrolytes were made in an Ar-filled glovebox with both O<sub>2</sub> and H<sub>2</sub>O content less than 0.1 ppm. All electrolytes were dried with molecular sieves before use. Ionic conductivity of electrolytes was measured by a conductivity meter (S230 from Mettler-Toledo) in the glovebox.

Electrodes were prepared by mixing 85:5:10 weight ratio of KS6 graphite (Timcal) as the active material, carbon black (AB—acetylene black, Alfa Aesar) as the conducting agent and sodium carboxymethyl cellulose (Na-CMC in deionized water, Sigma-Aldrich) as the binder. The obtained slurry was coated onto an Al current collector with a doctor blade. The electrodes were dried at 80 °C, cut into 16 mm diameter circular discs, and then roll-pressed. The average active mass loading of the electrodes was 4.0 mg cm<sup>-2</sup> with a density of 1.2 g cm<sup>-3</sup> after pressing. Before transferring into an Ar-filled glovebox, electrodes were further dried at 110 °C for 4 h in vacuum.

**Cell Assembly.** The dried electrodes were assembled into 2032-type coin cells with lithium metal as the counter electrode. A 19 mm diameter glass fiber separator (Advantec Toyo GD-120; thickness ~0.5 mm) wetted with ~200 μL electrolyte was used to prevent the cell from short circuit. After assembly, the cells were rested for 5 h to ensure sufficient wetting of the electrodes by the electrolyte before conducting the electrochemical measurements.

**Electrochemical Tests.** Galvanostatic charge–discharge tests of the cells were typically performed at a current density of 10 mA g<sup>-1</sup> within the voltage range of 3.0–5.1 V. For the self-discharge tests, each cell was initially cycled at 10 mA g<sup>-1</sup> for one cycle and then charged to 5.1 V at 100 mA g<sup>-1</sup>, followed by a rest for 6, 12, and 24 h, respectively, at the fully charged state and then discharged to 3.0 V at 100 mA g<sup>-1</sup>. All the galvanostatic charge/discharge tests were performed using a Neware battery tester.

CV measurements were performed in the voltage window of 3.0–5.1 V, respectively. The scan rate was 0.06 mV s<sup>-1</sup>, and five cycles were recorded. Electrochemical impedance spectroscopy (EIS) tests of fully discharged cells after 20 cycles were conducted with an alternating current (AC) amplitude of 10 mV from 100 kHz to 0.1 Hz. The two measurements were tested using the Bio-Logic potentiostat (VMP3). All electrochemical tests were conducted at room temperature (22 °C).

**Post-Mortem Analyses.** The cells were disassembled in the glovebox after charge–discharge, and the graphite electrodes were washed with DMC several times to remove the salt residuals, followed by drying in the antechamber of the glovebox under vacuum. XPS investigations were performed on X-ray photoelectron spectrophotometer (ESCALAB 2201-XL). The surface evolutions of the KS6 cathode were investigated through TEM.

## ASSOCIATED CONTENT

\* Supporting Information

The Supporting Information is available free of charge on the ACS Publications website at DOI: 10.1021/acsaeam.9b01499.

LSV and CV results with different upper cutoff voltage, cycle performance of graphite electrodes, self-discharge results, XPS characterization, rate performance results (PDF)

## AUTHOR INFORMATION

Corresponding Author

\*E-mail: denisyu@cityu.edu.hk.

ORCID

Denis Y. W. Yu: 0000-0002-5883-7087

Notes

The authors declare no competing financial interest.

## ACKNOWLEDGMENTS

This work was supported by the Strategic Research Grant (Project No. 7004688) and Applied Research Grant (Project No. 9667157) from City Univ. of Hong Kong and by the Innovation and Technology Fund (ITS/131/17) of the Hong Kong Special Administrative Region, China.

## REFERENCES

- (1) Zeng, X.; Li, M.; Abd El Hady, D.; Alshitari, W.; Al Bogami, A. S.; Lu, J.; Amine, K. Commercialization of Lithium Battery Technologies for Electric Vehicles. *Adv. Energy Mater.* 2019, 9, 1900161.
- (2) Schmich, R.; Wagner, R.; Höppl, G.; Placke, T.; Winter, M. Performance and Cost of Materials for Lithium-Based Rechargeable Automotive Batteries. *Nat. Energy* 2018, 3, 267–278.
- (3) Hy, S.; Liu, H.; Zhang, M.; Qian, D.; Hwang, B.-J.; Meng, Y. S. Performance and Design Considerations for Lithium Excess Layered Oxide Positive Electrode Materials for Lithium Ion Batteries. *Energy Environ. Sci.* 2016, 9, 1931–1954.
- (4) Kravchik, K. V.; Bhauriyal, P.; Piveteau, L.; Guntlin, C. P.; Pathak, B.; Kovalenko, M. V. High-Energy-Density Dual-Ion Battery for Stationary Storage of Electricity Using Concentrated Potassium Fluorosulfonylimide. *Nat. Commun.* 2018, 9, 4469.
- (5) Olivetti, E. A.; Ceder, G.; Gaustad, G. G.; Fu, X. Lithium-Ion Battery Supply Chain Considerations: Analysis of Potential Bottlenecks in Critical Metals. *Joule* 2017, 1, 229–243.
- (6) Fan, L.; Liu, Q.; Chen, S.; Xu, Z.; Lu, B. Soft Carbon as Anode for High-Performance Sodium-Based Dual Ion Full Battery. *Adv. Energy Mater.* 2017, 7, 1602778.
- (7) Read, J. A.; Cresce, A. V.; Ervin, M. H.; Xu, K. Dual-Graphite Chemistry Enabled by a High Voltage Electrolyte. *Energy Environ. Sci.* 2014, 7, 617–620.

- (8) Chan, C. Y.; Lee, P.-K.; Xu, Z.; Yu, D. Y. W. Designing High-Power Graphite-Based Dual-Ion Batteries. *Electrochim. Acta* 2018, 263, 34–39.
- (9) Placke, T.; Heckmann, A.; Schmuck, R.; Meister, P.; Beltrop, K.; Winter, M. Perspective on Performance, Cost, and Technical Challenges for Practical Dual-Ion Batteries. *Joule* 2018, 2, 2528–2550.
- (10) Rodríguez-Pérez, I. A.; Ji, X. Anion Hosting Cathodes in Dual-Ion Batteries. *ACS Energy Lett.* 2017, 2, 1762–1770.
- (11) Wang, M.; Tang, Y. A Review on the Features and Progress of Dual-Ion Batteries. *Adv. Energy Mater.* 2018, 8, 1703320.
- (12) Zhang, M.; Song, X.; Ou, X.; Tang, Y. Rechargeable Batteries Based on Anion Intercalation Graphite Cathodes. *Energy Storage Mater.* 2019, 16, 65–84.
- (13) Kravchik, K. V.; Kovalenko, M. V. Rechargeable Dual Ion Batteries with Graphite as a Cathode: Key Challenges and Opportunities. *Adv. Energy Mater.* 2019, 1901749.
- (14) Zhang, G.; Ou, X.; Cui, C.; Ma, J.; Yang, J.; Tang, Y. High-Performance Cathode Based on Self-Templated 3D Porous Microcrystalline Carbon with Improved Anion Adsorption and Intercalation. *Adv. Funct. Mater.* 2019, 29, 1806722.
- (15) Wu, N.; Yao, W.; Song, X.; Zhang, G.; Chen, B.; Yang, J.; Tang, Y. A Calcium Ion Hybrid Energy Storage Device with High Capacity and Long Cycling Life under Room Temperature. *Adv. Energy Mater.* 2019, 9, 1803865.
- (16) Li, W.-H.; Ning, Q.-L.; Xi, X.-T.; Hou, B.-H.; Guo, J.-Z.; Yang, Y.; Chen, B.; Wu, X.-L. Highly Improved Cycling Stability of Anion De-/Intercalation in the Graphite Cathode for Dual-Ion Batteries. *Adv. Mater.* 2019, 31, 1804766.
- (17) Gao, J.; Tian, S.; Qi, L.; Wang, H. Intercalation Manners of Perchlorate Anion into Graphite Electrode from Organic Solutions. *Electrochim. Acta* 2015, 176, 22–27.
- (18) Lin, M. C.; Gong, M.; Lu, B.; Wu, Y.; Wang, D. Y.; Guan, M.; Angell, M.; Chen, C.; Yang, J.; Hwang, B. J.; Dai, H. An Ultrafast Rechargeable Aluminium-Ion Battery. *Nature* 2015, 520, 325–328.
- (19) Rothermel, S.; Meister, P.; Schmuelling, G.; Fromm, O.; Meyer, H.-W.; Nowak, S.; Winter, M.; Placke, T. Dual-Graphite Cells Based on the Reversible Intercalation of Bis(trifluoromethanesulfonyl)imide Anions from an Ionic Liquid Electrolyte. *Energy Environ. Sci.* 2014, 7, 3412–3423.
- (20) Fan, H.; Qi, L.; Yoshio, M.; Wang, H. Hexafluorophosphate Intercalation into Graphite Electrode from Ethylene Carbonate/Ethylmethyl Carbonate. *Solid State Ionics* 2017, 304, 107–112.
- (21) Aladinli, S.; Bordet, F.; Ahlbrecht, K.; Tübke, J.; Holzapfel, M. Anion Intercalation into a Graphite Cathode from Various Sodium-Based Electrolyte Mixtures for Dual-Ion Battery Applications. *Electrochim. Acta* 2017, 231, 468–478.
- (22) Miyoshi, S.; Akbay, T.; Kurihara, T.; Fukuda, T.; Staykov, A. T.; Ida, S.; Ishihara, T. Fast Diffusivity of  $\text{PF}_6^-$  Anions in Graphitic Carbon for a Dual-Carbon Rechargeable Battery with Superior Rate Property. *J. Phys. Chem. C* 2016, 120, 22887–22894.
- (23) Beltrop, K.; Beuker, S.; Heckmann, A.; Winter, M.; Placke, T. Alternative Electrochemical Energy Storage: Potassium-Based Dual-Graphite Batteries. *Energy Environ. Sci.* 2017, 10, 2090–2094.
- (24) Placke, T.; Rothermel, S.; Fromm, O.; Meister, P.; Lux, S. F.; Huesker, J.; Meyer, H.-W.; Winter, M. Influence of Graphite Characteristics on the Electrochemical Intercalation of Bis(trifluoromethanesulfonyl) imide Anions into a Graphite-Based Cathode. *J. Electrochem. Soc.* 2013, 160, A1979–A1991.
- (25) Beltrop, K.; Meister, P.; Klein, S.; Heckmann, A.; Grünebaum, M.; Wiemhöfer, H.-D.; Winter, M.; Placke, T. Does Size Really Matter? New Insights into the Intercalation Behavior of Anions into a Graphite-Based Positive Electrode for Dual-Ion Batteries. *Electrochim. Acta* 2016, 209, 44–55.
- (26) Seel, J. A.; Dahn, J. R. Electrochemical Intercalation of  $\text{PF}_6^-$  into Graphite. *J. Electrochem. Soc.* 2000, 147, 892–898.
- (27) Gao, J.; Tian, S.; Qi, L.; Yoshio, M.; Wang, H. Hexafluorophosphate Intercalation into Graphite Electrode from Gamma-Butyrolactone Solutions in Activated Carbon/Graphite Capacitors. *J. Power Sources* 2015, 297, 121–126.
- (28) Fan, H.; Qi, L.; Wang, H. Intercalation Behavior of Hexafluorophosphate into Graphite Electrode from Propylene/Ethylmethyl Carbonates. *J. Electrochem. Soc.* 2017, 164, A2262–A2267.
- (29) Fan, H.; Qi, L.; Wang, H. Hexafluorophosphate Anion Intercalation into Graphite Electrode from Methyl Propionate. *Solid State Ionics* 2017, 300, 169–174.
- (30) Fan, H.; Gao, J.; Qi, L.; Wang, H. Hexafluorophosphate Anion Intercalation into Graphite Electrode from Sulfolane/Ethylmethyl Carbonate Solutions. *Electrochim. Acta* 2016, 189, 9–15.
- (31) Zhang, L.; Huang, Y.; Fan, H.; Wang, H. Flame-Retardant Electrolyte Solution for Dual-Ion Batteries. *ACS Appl. Energy Mater.* 2019, 2, 1363–1370.
- (32) Zhang, L.; Zhu, D.; Wang, H. How Ethyl Methyl Carbonate Assists Ethylene Carbonate in Co-Intercalating into Graphite Electrode with  $\text{PF}_6^-$ . *J. Electrochem. Soc.* 2019, 166, A2654–A2659.
- (33) Wu, L. N.; Peng, J.; Sun, Y. K.; Han, F. M.; Wen, Y. F.; Shi, C. G.; Fan, J. J.; Huang, L.; Li, J. T.; Sun, S. G. High-Energy Density Li metal Dual-Ion Battery with a Lithium Nitrate-Modified Carbonate-Based Electrolyte. *ACS Appl. Mater. Interfaces* 2019, 11, 18504–18510.
- (34) Xi, X.-T.; Li, W.-H.; Hou, B.-H.; Yang, Y.; Gu, Z.-Y.; Wu, X.-L. Dendrite-Free Lithium Anode Enables the Lithium//Graphite Dual-Ion Battery with Much Improved Cyclic Stability. *ACS Appl. Energy Mater.* 2019, 2, 201–206.
- (35) Wang, G.; Yu, M.; Wang, J.; Li, D.; Tan, D.; Löffler, M.; Zhuang, X.; Müllen, K.; Feng, X. Self-Activating, Capacitive Anion Intercalation Enables High-Power Graphite Cathodes. *Adv. Mater.* 2018, 30, 1800533.
- (36) Hu, Z.; Liu, Q.; Zhang, K.; Zhou, L.; Li, L.; Chen, M.; Tao, Z.; Kang, Y. M.; Mai, L.; Chen, J.; Chou, S.; Dou, S. X. All Carbon Dual Ion Batteries. *ACS Appl. Mater. Interfaces* 2018, 10, 35978–35983.
- (37) Heckmann, A.; Thienenkamp, J.; Beltrop, K.; Winter, M.; Brunklaus, G.; Placke, T. Towards High-Performance Dual-Graphite Batteries Using Highly Concentrated Organic Electrolytes. *Electrochim. Acta* 2018, 260, 514–525.
- (38) Miyoshi, S.; Nagano, H.; Fukuda, T.; Kurihara, T.; Watanabe, M.; Ida, S.; Ishihara, T. Dual-Carbon Battery Using High Concentration  $\text{LiPF}_6$  in Dimethyl Carbonate (DMC) Electrolyte. *J. Electrochem. Soc.* 2016, 163, A1206–A1213.
- (39) Placke, T.; Schmuelling, G.; Kloepsch, R.; Meister, P.; Fromm, O.; Hilbig, P.; Meyer, H.; Winter, M. In situ X-ray Diffraction Studies of Cation and Anion Intercalation into Graphitic Carbons for Electrochemical Energy Storage Applications. *Z. Anorg. Allg. Chem.* 2014, 640, 1996–2006.
- (40) Tarnopolskiy, V.; Kalhoff, J.; Nádherná, M.; Bresser, D.; Picard, L.; Fabre, F.; Rey, M.; Passerini, S. Beneficial Influence of Succinic Anhydride as Electrolyte Additive on the Self-discharge of 5V  $\text{LiNi}_{0.4}\text{Mn}_{1.6}\text{O}_4$  Cathodes. *J. Power Sources* 2013, 236, 39–46.
- (41) Guyomard, D.; Tarascon, J. M. The Carbon/ $\text{Li}_{1-x}\text{Mn}_2\text{O}_4$  System. *Solid State Ionics* 1994, 69, 222–237.
- (42) Pistoia, G.; Antonini, A.; Rosati, R.; Zane, D. Storage Characteristics of Cathodes for Li-Ion Batteries. *Electrochim. Acta* 1996, 41, 2683–2689.
- (43) Yazami, R.; Ozawa, Y. A Kinetics Study of Self-discharge of Spinel Electrodes in  $\text{Li}/\text{Li}_x\text{Mn}_2\text{O}_4$  Cells. *J. Power Sources* 2006, 153, 251–257.
- (44) Han, X.; Xu, G.; Zhang, Z.; Du, X.; Han, P.; Zhou, X.; Cui, G.; Chen, L. An In Situ Interface Reinforcement Strategy Achieving Long Cycle Performance of Dual-Ion Batteries. *Adv. Energy Mater.* 2019, 9, 1804022.
- (45) Wang, G.; Wang, F.; Zhang, P.; Zhang, J.; Zhang, T.; Müllen, K.; Feng, X. Polarity-Switchable Symmetric Graphite Batteries with High Energy and High Power Densities. *Adv. Mater.* 2018, 30, No. e1802949.
- (46) Li, W. H.; Ning, Q. L.; Xi, X. T.; Hou, B. H.; Guo, J. Z.; Yang, Y.; Chen, B.; Wu, X. L. Highly Improved Cycling Stability of Anion De-/Intercalation in the Graphite Cathode for Dual-Ion Batteries. *Adv. Mater.* 2019, 31, 1804766.



# Corrosion of polypyrrole: Kinetics of chemical and electrochemical processes in NaOH solutions

Yao Wang<sup>a</sup>, Yubing Qiu<sup>a,c,\*</sup>, Zhenyu Chen<sup>a,b</sup>, Xingpeng Guo<sup>a,b</sup>

<sup>a</sup> School of Chemistry and Chemical Engineering, Huazhong University of Science and Technology, Wuhan 430074, PR China

<sup>b</sup> Key laboratory of Material Chemistry for Energy Conversion and Storage (Huazhong University of Science and Technology), Ministry of Education, PR China

<sup>c</sup> Hubei Key Laboratory of Materials Chemistry and Service Failure, Wuhan 430074, PR China

## ARTICLE INFO

### Article history:

Received 18 November 2016

Received in revised form 23 January 2017

Accepted 26 January 2017

Available online 29 January 2017

### Keywords:

A. Polymer

B. Cyclic voltammetry

B. SEM

B. XPS

C. Kinetic parameters

## ABSTRACT

The corrosion kinetics of PPy/SO<sub>4</sub> in aerated and de-aerated NaOH solutions (0.02–0.5 M) were investigated and the interaction between chemical and electrochemical corrosion processes was verified. The corrosion of PPy is mainly caused by the chemical attack of OH<sup>−</sup> in de-aerated NaOH, but is accelerated largely in aerated NaOH for the occurrence of the electrochemical processes. These two processes are mutually promoted in aerated NaOH. At a constant NaOH concentration ( $C_{\text{NaOH}}$ ), two corrosion stages are proved to follow first-order kinetics. In each corrosion stage, the chemical and electrochemical processes have different kinetic behavior and  $C_{\text{NaOH}}$  has important influence on them.

© 2017 Elsevier Ltd. All rights reserved.

## 1. Introduction

Polypyrrole (PPy) has become one of the most promising and attractive conducting polymers owing to its favorable physical and chemical properties [1–4] and widely application in electrode materials [5–7], sensors [8,9], artificial muscles [10,11], catalysts [12,13] and anticorrosion coatings for metals [14–19], etc. With regard to these applications, the corrosion of PPy which results in the irreversible degradation and the loss of electrochemical activity of PPy [20–23], is still a big problem, particularly in aggressive aqueous media. However, the corrosion mechanism of PPy is not clearly understood.

Various processes can lead to the corrosion of PPy, including over-oxidation [24–27], deprotonation [28], and deactivation by reducing solvents [29–31]. The changes in structure and chemical composition of PPy during corrosion processes have been studied using various analysis methods [32–36]. It's generally believed that nucleophilic attack from H<sub>2</sub>O, OH<sup>−</sup>, CH<sub>3</sub>OH and NH<sub>3</sub> etc. produce carbonyl and hydroxyl groups in PPy chains so as to destroy its conjugated structure and therefore, causing the loss of the elec-

trochemical activity of PPy [37–40]. This kind of corrosion of PPy results from the chemical attack of aggressive media, so it can be considered as pure chemical process and be denoted as a chemical corrosion.

Because PPy is electronic conductive and electrochemical processes can proceed on its surface especially in electrolyte solutions, it also suffers the corrosion due to the electrochemical processes on its surface. According to our previous work [41,42], the corrosion of PPy in NaCl solutions is inhibited to some extent at negative potentials (vs. open circuit potential,  $E_{\text{OCP}}$ ), and promoted with increase in anodic polarisation potentials (vs.  $E_{\text{OCP}}$ ) and polarisation time [41]. Different corrosion cells can be formed and sustained on PPy surface and the oxygen concentration difference cell has great influence on the corrosion of PPy, in which dissolved oxygen (DO) in media is reduced on PPy surface (as cathode) to generate OH<sup>−</sup> ions, while the PPy surface with lower DO is oxidized as anode [42]. This kind of corrosion of PPy is closely related to the electrochemical processes on its surface and can be denoted as an electrochemical corrosion.

In the previous research, we usually focus on the chemical corrosion process of PPy and neglect its electrochemical corrosion, or vice versa. When there are electrochemical processes on PPy surface (e.g. anodic polarisation or formation of corrosion cells) in electrolyte solutions with strong nucleophilic ions (e.g. alkali media), PPy should suffer strong chemical and electrochemical corrosion

\* Corresponding author at: School of Chemistry and Chemical Engineering, Huazhong University of Science and Technology, Wuhan 430074, PR China.  
E-mail address: [qiuyubin@mail.hust.edu.cn](mailto:qiuyubin@mail.hust.edu.cn) (Y. Qiu).

at the same time. Under these conditions, there may be interaction between the two corrosion processes and it is necessary to investigate their kinetic behavior to identify the role of each process in the corrosion of PPy. However, few studies have focused on this.

In fact, little attention has been paid to the study on the corrosion kinetics of conductive polymers in aqueous electrolyte presently. Beck et al. [26] reported that the corrosion reactions of PPy and polythiophene in aqueous buffers (pH 1–13) proceeded in two steps, i.e. an initial rapid electrochemical process and a rather slow second chemical process caused by nucleophilic attack, both following a pseudo-first-order mechanism. Park et al. monitored the absorbance of the degradation products of PPy in aqueous sulfuric acid solutions and found that the increase in the absorbance recorded as a function of time followed the first-order kinetics [43,44]. Mazeikiene et al. [45] investigated kinetics of the electrochemical degradation of PPy in aqueous solutions containing  $\text{HNO}_3$  or  $\text{NaNO}_3$ . They found that the first-order degradation rate constant ( $k$ ) is strongly dependent on the electrode potential and solution pH value. In addition, some kinetic studies on the electrochemical degradation of polyaniline (PANI) [46,47] and poly(N-benzylaniline) [48] were conducted using in situ UV–vis spectroscopic [46,48] and electrochemical tests [47], and their results also showed the first-order degradation rate constants. The above research implies that there is still no generally accepted method for the study on the corrosion kinetics of conductive polymers. Moreover, their corrosion kinetics is still not well understood.

In this paper, the PPy/ $\text{SO}_4$  films were corroded in aerated or de-aerated NaOH solutions with different concentrations for different time, and then their corrosion states were evaluated using cyclic voltammetry (CV), electrochemical impedance spectroscopy (EIS), X-ray photoelectron spectroscopy (XPS) and scanning electron microscope (SEM) analysis. Based on these results, the chemical and electrochemical corrosion kinetics of PPy in NaOH solutions and the interaction between the two corrosion processes were investigated. Furthermore, the role of each process in the corrosion of PPy was identified and the mechanism involved was discussed. The results of this work will be helpful to understand the integrated corrosion mechanism of PPy in aqueous electrolyte from the perspective of chemistry and electrochemistry.

## 2. Experimental

Pyrrole (Py, CP, 98 +%) for the electrochemical synthesis of PPy was distilled and kept refrigerated in the dark before use. Other used reagents and chemicals were analytical grade and all solutions were prepared with deionized water. The electro-polymerization of PPy films and electrochemical tests in this paper were performed with a Gamry (Interface 1000) electrochemical workstation. All experiments were carried out at  $25 \pm 0.5^\circ\text{C}$  controlled with a water bath.

### 2.1. Electro-polymerization of PPy

The PPy films were prepared using a three-electrode system in a glass cell, in which a large Pt foil ( $1.50\text{ cm}^2$ ), a Pt plate ( $0.36\text{ cm}^2$ ) and a saturated calomel electrode (SCE) were used as the counter electrode, working electrode and reference electrode, respectively. The working electrode was sealed by epoxy resins, ground with a diamond polishing paste (the grain diameter is  $0.5\text{ }\mu\text{m}$ ) and rinsed in ethanol and distilled water. The electro-polymerization of PPy films was performed with a constant current density of  $1\text{ mA cm}^{-2}$  for 1600 s in 0.1 M pyrrole aqueous solutions containing 0.1 M  $\text{Na}_2\text{SO}_4$  supporting electrolyte and which had been de-aerated by bubbling pure  $\text{N}_2$  gas for 25 min before synthesis. The polymerization charge density was  $1.6\text{ C cm}^{-2}$ . This freshly prepared PPy/ $\text{SO}_4$  film with the

**Table 1**

Details of the corrosion conditions for the PPy/ $\text{SO}_4$  films.

T ( $^\circ\text{C}$ )	Corrosion media	Aeration status	Corrosion time (h)							
25	0.02 M NaOH	Aerated	3	6	8	12	16	20	24	
25	0.02 M NaOH	Deaerated	8	12	16	20	24	30	36	
25	0.05 M NaOH	Aerated	1	3	6	8	10	12	14	
25	0.05 M NaOH	Deaerated	2.5	6	8	10	12	16		
25	0.1 M NaOH	Aerated	1	2	3	4	6	8	12	14
25	0.1 M NaOH	Deaerated	1	3	4	6	8	12	15	
25	0.3 M NaOH	Aerated	1	2	3	5	6	8	12	
25	0.3 M NaOH	Deaerated	1	2	4	5	8	12		
25	0.5 M NaOH	Aerated	0.5	1	2	3	6	8		
25	0.5 M NaOH	Deaerated	0.5	1	2	3	6	12		

Pt substrate was rinsed in distilled water and then used for other tests.

### 2.2. Corrosion of PPy films in different test media

The freshly prepared PPy/ $\text{SO}_4$  films (with Pt substrates) were corroded in different aqueous solutions for different time, and then taken out and rinsed with distilled water. These PPy/ $\text{SO}_4$  films corroded under different conditions were further used for other tests. Under each corrosion condition, 3–5 or more parallel tests were performed to ensure the reliability of the results. Table 1 lists the detailed corrosion conditions for the PPy/ $\text{SO}_4$  films.

### 2.3. Electrochemical tests

All the electrochemical tests were performed in the same three-electrode system. Freshly prepared and corroded PPy/ $\text{SO}_4$  films were placed in de-aerated 0.1 M  $\text{KNO}_3$  for cyclic voltammetry (CV) and electrochemical impedance spectroscopy (EIS) measurements. The CV measurements were performed within the potential range from  $-0.8\text{ V}$  to  $0.4\text{ V}$  (vs. SCE), starting from  $E_{\text{OCP}}$  towards negative direction. The scan rate was  $20\text{ mV/s}$  and seven cycles were recorded. The EIS measurements were performed at  $0.2\text{ V}$  (vs. SCE) in order to keep the PPy/ $\text{SO}_4$  films in the same oxidized state. The amplitude of the AC perturbation was  $5\text{ mV}$  and the frequency range was  $100\text{ kHz}$ – $0.01\text{ Hz}$ . All the EIS results were fitted using Zview2.0 software.

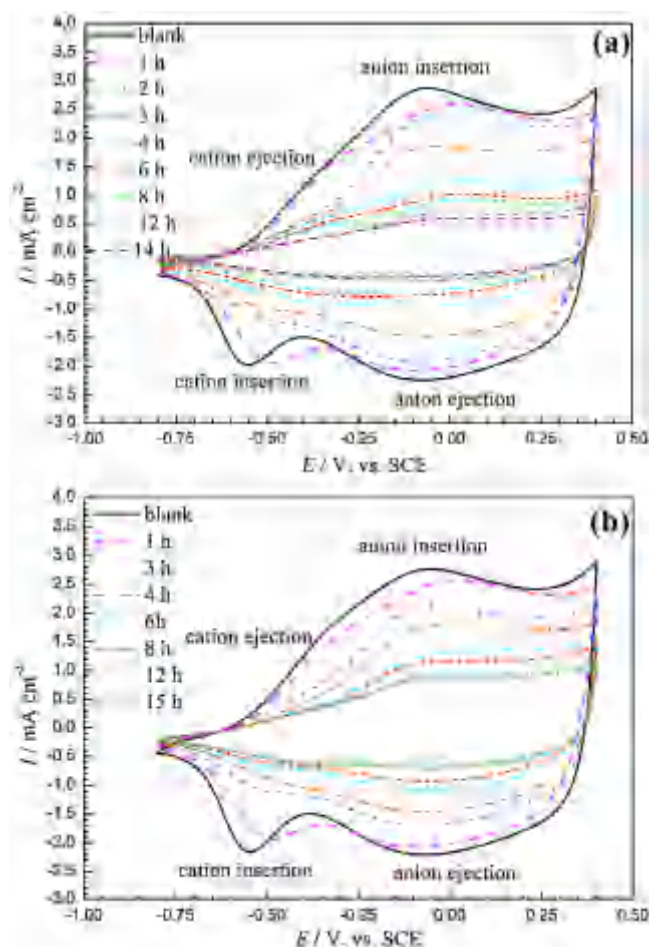
### 2.4. SEM and XPS analysis

Freshly prepared and some corroded PPy/ $\text{SO}_4$  films were cleaned in distilled water and dried in a vacuum-desiccator for more than 12 h at room temperature, and then they were used for microscopic analyses. The surface morphology of these samples was examined using a Phillips Quanta 200 SEM system. XPS measurements were performed with a commercial VG Multilab 2000 system, which was aimed at finding changes in the chemical structure and the composition of PPy films as the corrosion process proceeds. The spectra were measured using Al Ka ( $1486.6\text{ eV}$ ) radiation, and the overall energy resolution was  $0.45\text{ eV}$ . The surface charging effect during measurements was compensated by referencing the binding energy to the C 1s line of residual carbon at  $284.6\text{ eV}$ . The N 1s level spectral decomposition was analyzed using background subtraction and a least-squares fitting program.

## 3. Results

### 3.1. CVs of corroded PPy films and their corrosion kinetics

Fig. 1 shows the typical CVs in de-aerated 0.1 M  $\text{KNO}_3$  for the PPy/ $\text{SO}_4$  films freshly prepared and corroded in aerated and de-aerated 0.1 M NaOH for different time. The CVs of the PPy/ $\text{SO}_4$  films



**Fig. 1.** CVs in de-aerated 0.1 M KNO<sub>3</sub> for the PPy/SO<sub>4</sub> films freshly prepared and corroded in (a) aerated and (b) de-aerated 0.1 M NaOH for different time (scan rate 20 mV/s, starting from the  $E_{ocp}$  towards negative direction, the fifth cycle of seven cycles).

corroded for less than 1 h are nearly overlapped with that of the freshly prepared films, so they are not plotted in Fig. 1. The CV diagram for the freshly prepared film in Fig. 1 shows four ion exchange processes, i.e. cation ejection, anion insertion, anion ejection, and cation insertion, which are associated with anodic current peaks and cathodic current peaks, respectively, and can be clearly distinguished [49]. With an increase in the corrosion time, the corroded PPy films gradually lose their ion exchange capacity owing to the irreversible PPy structural degradation in NaOH [33–37,39,50]. In general, the electrochemical activity of a PPy film can be described by its CV current capacity ( $Q$ ) and the corrosion of PPy can be observed as a loss in its electrochemical activity [50–52]. Thus, the corrosion of PPy is associated to the loss of its electroactivity and the corrosion extent of PPy can be evaluated by the percentage loss of its CV current capacity after corrosion [40,50,52], i.e.  $(Q_0 - Q_R)/Q_0$ , where  $Q_0$  is the CV current capacity of the freshly prepared PPy film and  $Q_R$  is the CV current capacity of the corroded PPy film. According to this definition, the corrosion rate of PPy ( $v_{corr}$ ) can be expressed as Eq. (1):

$$v_{corr} = \frac{\Delta \left( \frac{Q_R}{Q_0} \right)}{\Delta t} = k \left( \frac{Q_R}{Q_0} \right)^i \quad (1)$$

where  $i$  represents the order of the corrosion reaction and  $k$  is the corrosion rate constant.

Fig. 2(a) presents the change of the CV current capacity percentage ( $Q_R/Q_0$ ) as a function of time for the PPy/SO<sub>4</sub> films corroded in

aerated and de-aerated 0.1 M NaOH, which were calculated from the results in Fig. 1. The change of the corrosion rate ( $v_{corr}$ ) under the same condition is shown in Fig. 2(b), which was obtained by the differentiation of the  $Q_R/Q_0$ - $t$  curves in Fig. 2(a). As shown in Fig. 2(a), the decrease of  $Q_R/Q_0$  starts from 1 h and accelerates quickly in the initial 1–6 h. After 6 h, the  $Q_R/Q_0$  values decrease slowly. The  $Q_R/Q_0$  value in aerated 0.1 M NaOH decreases much faster than that in de-aerated 0.1 M NaOH. The results in Fig. 2(b) further show that the  $v_{corr}$  in aerated 0.1 M NaOH ( $v_{corr,ae}$ ) is much larger than that in de-aerated 0.1 M NaOH ( $v_{corr,de}$ ) in the initial 3 h, but after that  $v_{corr,ae}$  approaches  $v_{corr,de}$ . Similarly, both  $v_{corr,ae}$  and  $v_{corr,de}$  decrease quickly in the initial 6 h and gradually tend to stable after 6 h. The above results generally suggest that there may be two stages in the corrosion of PPy/SO<sub>4</sub> in 0.1 M NaOH, i.e. the fast corrosion stage in the initial period of 1–6 h and the slow corrosion stage after 6 h. The kinetic behavior in the two corrosion stages may be different.

Fig. 3 gives the  $\ln(Q_R/Q_0)$ - $t$  curves for the PPy/SO<sub>4</sub> films corroded in aerated and de-aerated 0.1 M NaOH. The results from Fig. 2(a) and from some parallel experiments were used, so the error bar plot is used in Fig. 3 to display the fluctuation of data. The  $\ln(Q_R/Q_0)$ - $t$  curves in Fig. 3 apparently display two different stages and at each stage they all have very good linear relationship, indicating that the corrosion rate at each stage follows the first-order kinetic relationship, i.e.  $i = 1$  in Eq. (1). Therefore, the corrosion rate constant ( $k$ ) can be calculated by the following Eq. (2) [43,45–47]:

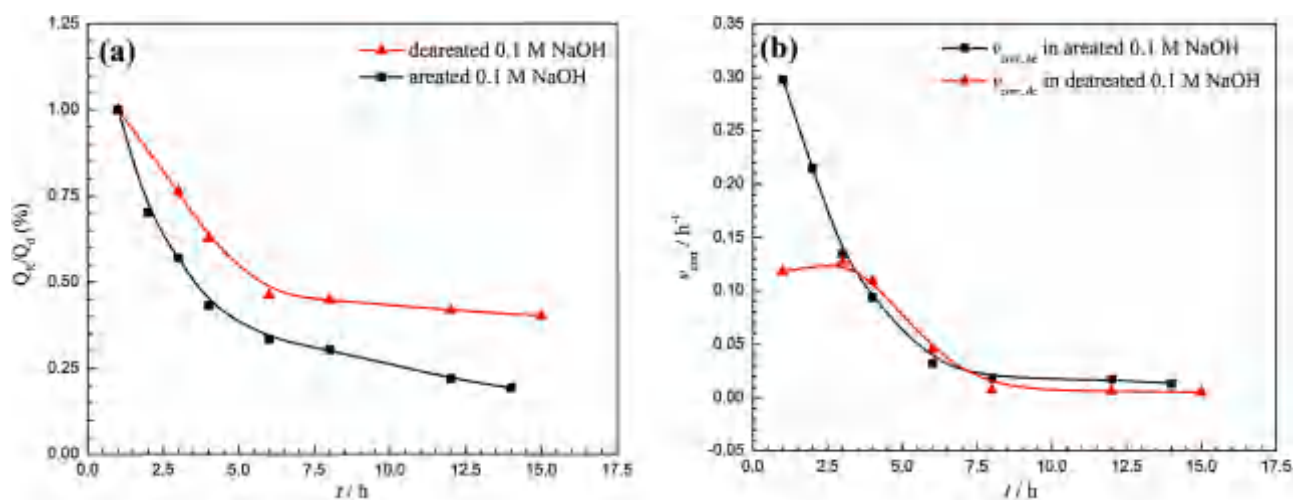
$$k = - \frac{\Delta \ln \left( \frac{Q_R}{Q_0} \right)}{\Delta t} \quad (2)$$

According to Eq. (2), the  $k$  values in  $s^{-1}$  of each stage are calculated by the linear regression of the  $\ln(Q_R/Q_0)$ - $t$  curves and displayed in Fig. 3. In aerated 0.1 M NaOH the two corrosion rate constants are denoted as  $k_{1,ae}$  and  $k_{2,ae}$ , while in de-aerated 0.1 M NaOH, as  $k_{1,de}$  and  $k_{2,de}$ . The results in Fig. 3 indicate that the  $k_1$  values ( $k_{1,ae}$  and  $k_{1,de}$ ) are much larger than the  $k_2$  values ( $k_{2,ae}$  and  $k_{2,de}$ ) and the  $k$  values in aerated 0.1 M NaOH are much larger than those in the de-aerated 0.1 M NaOH ( $k_{1,ae} > k_{1,de}$  and  $k_{2,ae} > k_{2,de}$ ). Apparently, DO in NaOH has obvious effect on the corrosion kinetics of the PPy/SO<sub>4</sub> film.

In order to further verify the above kinetic behavior, the PPy/SO<sub>4</sub> films were corroded in aerated and de-aerated NaOH with different  $C_{NaOH}$  (0.02, 0.05, 0.3, 0.5 M) for different time, as shown in Table 1, and then their CVs were measured in de-aerated 0.1 M KNO<sub>3</sub>. Fig. 4 shows the typical CVs results for these PPy/SO<sub>4</sub> films. Compared with Fig. 1, the CVs in Fig. 4 show similar features and the  $Q_R$  decreases more slowly at low  $C_{NaOH}$  (0.02 M, 0.05 M) while it decreases more quickly at higher  $C_{NaOH}$  (0.3 M and 0.5 M). Apparently,  $C_{NaOH}$  has significant influence on the corrosion of PPy [37,50,53,54]. Fig. 5 presents the  $\ln(Q_R/Q_0)$ - $t$  curves for the PPy/SO<sub>4</sub> films corroded in aerated and de-aerated NaOH solutions (0.02–0.5 M), which were obtained using the same method in Fig. 3. For comparison, the  $\ln(Q_R/Q_0)$ - $t$  curves in Fig. 3 are also plotted in Fig. 5 and the beginning time of each corrosion stage ( $t_0^1$  or  $t_0^2$ ) is displayed on the  $\ln(Q_R/Q_0)$ - $t$  curves. From Fig. 5, it is clearly seen that all the corrosion processes in aerated and de-aerated NaOH solutions (0.02–0.5 M) display two stages and each corrosion stage follows the first-order kinetic relationship. According to Eq. (2), the  $k$  values of each stage in Fig. 5 are calculated by the linear regression of the  $\ln(Q_R/Q_0)$ - $t$  curves and listed in Table 2.

The results in Fig. 5 and Table 2 indicate that in aerated and de-aerated 0.02 M–0.5 M NaOH solutions, there are  $k_1$  ( $k_{1,ae}$  and  $k_{1,de}$ )  $\gg$   $k_2$  ( $k_{2,ae}$  and  $k_{2,de}$ ) and all the  $k$  values ( $k_{1,ae}$ ,  $k_{1,de}$ ,  $k_{2,ae}$  and  $k_{2,de}$ ) increase with an increase in  $C_{NaOH}$ , while the  $t_0^1$  and  $t_0^2$  decrease with an increase in  $C_{NaOH}$ . These results indicate that the corrosion of PPy in the first corrosion stage is always much



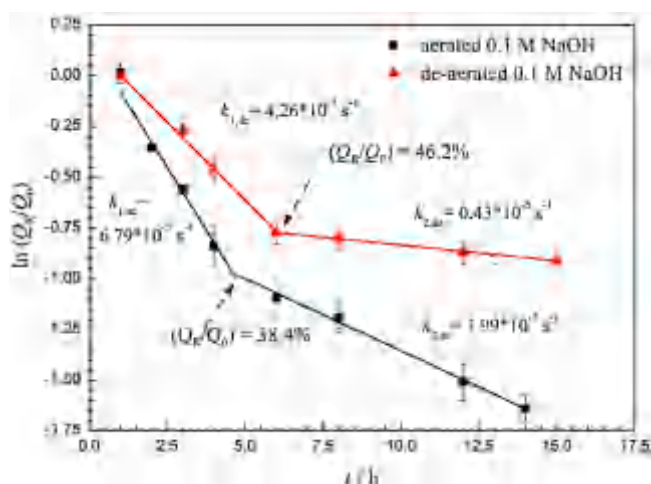


**Fig. 2.** Changes of (a) CV current capacity percentage ( $Q_R/Q_0$ ) and (b) corrosion rate ( $v_{corr}$ ) as a function of time for the PPY/SO<sub>4</sub> films corroded in aerated and de-aerated 0.1 M NaOH.

**Table 2**

Corrosion rate constants ( $k$ ) for the PPY/SO<sub>4</sub> films corroded in the aerated and de-aerated NaOH solutions with different concentrations.

$k$ ( $\text{s}^{-1} \times 10^{-5}$ )		$C_{\text{NaOH}}$ (M)				
Aerated	$k_{1,ae}$	0.02	0.05	0.1	0.3	0.5
	$k_{2,ae}$	3.28	5.58	6.79	9.78	15.71
Deaerated	$k_{1,de}$	0.61	1.15	1.99	2.64	3.14
	$k_{2,de}$	1.01	3.14	4.26	5.86	7.95
		0.05	0.16	0.43	0.6	0.66



**Fig. 3.** Changes of  $\ln(Q_R/Q_0)$  as a function of time for the PPY/SO<sub>4</sub> films corroded in aerated and de-aerated 0.1 M NaOH.

faster than that in the second corrosion stage and the corrosion processes in both corrosion stages are accelerated in NaOH solutions with higher concentration. The  $k$  values in the aerated NaOH are much larger than those in the de-aerated NaOH ( $k_{1,ae} > k_{1,de}$  and  $k_{2,ae} > k_{2,de}$ ), while the  $t_0^1$  and  $t_0^2$  show the opposite change ( $t_{0,ae}^1 \leq t_{0,de}^1$  and  $t_{0,ae}^2 < t_{0,de}^2$ ). Apparently, all the two corrosion stages in aerated NaOH are faster than those in de-aerated NaOH.

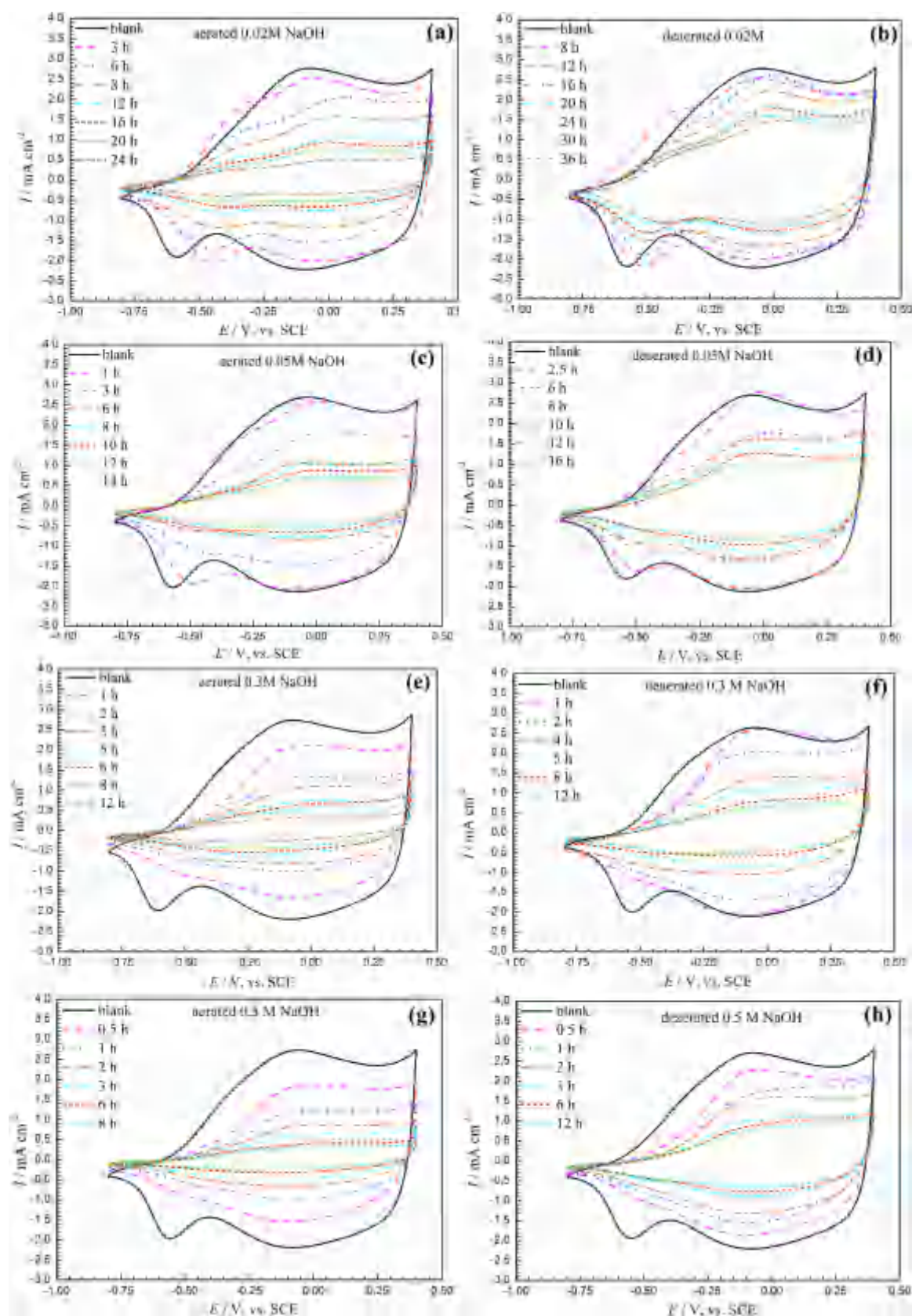
It should be noted that there may be an incubation period for the corrosion of PPY before the  $t_0^1$  of the first corrosion stage, in which the corrosion rate is very slow and  $Q_R/Q_0 \approx 1$ . The results in Fig. 5 clearly show that the incubation period increases significantly with the decrease in  $C_{\text{NaOH}}$  and DO.

### 3.2. EIS of PPY/SO<sub>4</sub> films corroded in NaOH for different time

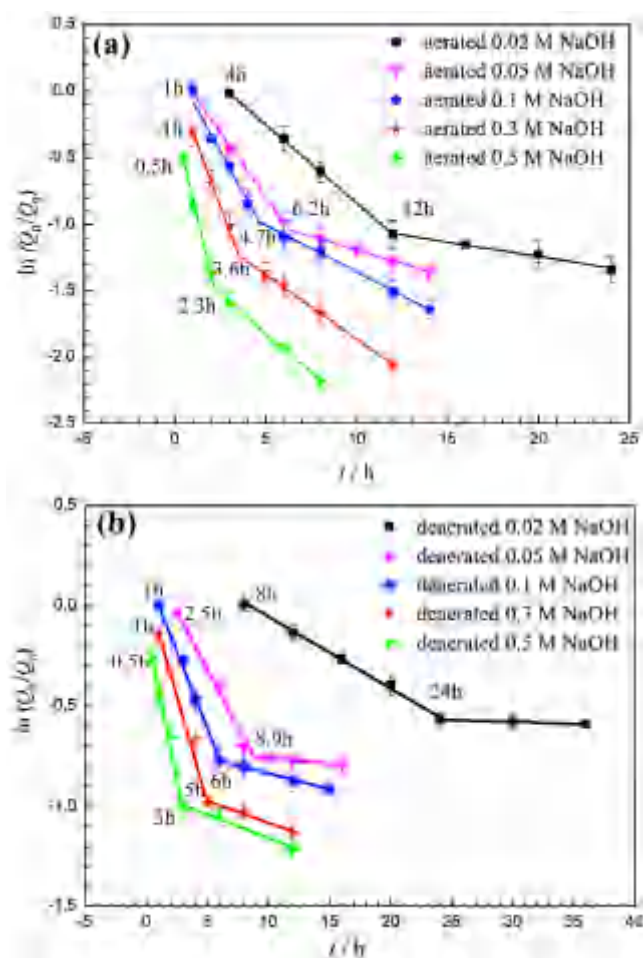
Fig. 6 shows the typical EIS results that were obtained at 0.2 V (vs. SCE) for the PPY/SO<sub>4</sub> films freshly prepared and corroded in aerated and de-aerated 0.1 M and 0.3 M NaOH solutions for different time. In Fig. 6(a), (b) and (d), the Nyquist plots for the PPY/SO<sub>4</sub> films exhibit similar features generally observed in the EIS results of PPY films [55,56], which has been discussed in detail in our previous paper [41].

With an increase in corrosion time and  $C_{\text{NaOH}}$ , there is no change in the above general characteristics, but the total system impedance increases and the low-frequency pseudocapacitance decreases due to the degradation of PPY films in corrosion media [56,57]. Similarly, an equivalent circuit (EC) presented in Fig. 7(a) was constructed to simulate the PPY/solution interface on the PPY/SO<sub>4</sub> films [19,41,55], where  $R_s$  is the solution resistance;  $CPE_{dl}$  and  $CPE_f$  is the constant phase element for the electric double layer and the PPY film, respectively;  $R_{ct}$  is the charge transfer resistance;  $W_s$  is the generalized finite Warburg (GFW) impedance for ion diffusion in PPY film. In Fig. 6(c), the Nyquist plots from 1–6 h display the same features as those in Fig. 6(a), (b) and (d) and can be analyzed with the EC in Fig. 7(a). However, the Nyquist plots in 8–12 h show different features similar to those of overoxidised PPY films [41] and the total system impedance increases apparently. Fig. 6(e) and (f) present the corresponding Bode plots to exhibit the change in impedance characteristics of the corroded PPY/SO<sub>4</sub> films. It is clearly seen that the PPY/SO<sub>4</sub> film gradually transforms to an insulated film [41], which shows typical features of double capacitance loops. Actually, the data in Fig. 5(a) indicates that the  $Q_R/Q_0$  value for the PPY films corroded in aerated 0.3 M NaOH for 8–12 h is less than 0.18, proving that the PPY film in this state loses most of its redox activity and behaves like an insulated film. In this case, Fig. 7(b) was employed to fit these EIS data, where  $R_f$  is the resistance of the redox reactions for the PPY film and other parameters are the same as those in Fig. 7(a) [41,57].

The fitted results are presented in Fig. 6 and the fitting parameters are listed in Tables 3–6. With an increase in corrosion time,  $R_{ct}$  and diffusion resistance ( $W_s$ -R) gradually increase while the electric double layer capacitance ( $C_{dl}$ ) and pseudocapacitance ( $C_f$ ) of PPY film both gradually decrease. Only in aerated 0.3 M NaOH, as shown in Table 5,  $C_{dl}$  and  $C_f$  decrease obviously while  $R_{ct}$  and  $R_f$  increase largely in the period of 8–12 h, displaying a quite different corrosion state. The increase in  $R_{ct}$  and  $W_s$ -R and the decrease in  $C_{dl}$  and  $C_f$  are all directly related to the degradation of PPY films



**Fig. 4.** CVs in de-aerated 0.1 M  $\text{KNO}_3$  for PPY/ $\text{SO}_4$  films freshly prepared and corroded in aerated and de-aerated NaOH solutions for different time: (a) aerated 0.02 M, (b) de-aerated 0.02 M, (c) aerated 0.05 M, (d) de-aerated 0.05 M, (e) aerated 0.3 M, (f) de-aerated 0.3 M, (g) aerated 0.5 M, (h) de-aerated 0.5 M (scan rate 20 mV/s, starting from the  $E_{\text{ocp}}$  towards negative direction, the fifth cycle of seven cycles).



**Fig. 5.** Changes of  $\ln(Q_R/Q_0)$  as a function of time for the PPy/SO<sub>4</sub> films corroded in (a) aerated and (b) de-aerated 0.02–0.5 M NaOH.

in corrosion media [58,59]. Thus, the changes of these parameters with corrosion time can be related to the corrosion extent of PPy films. However, they generally do not display the obvious different corrosion stages like those showing in Fig. 5.

Comparing the parameters in aerated and de-aerated NaOH solutions, it can be seen that at the same  $C_{\text{NaOH}}$ , the  $R_{\text{ct}}$  values in aerated NaOH are larger and increase more rapidly than those in de-aerated NaOH, indicating that DO accelerates the corrosion of PPy, which is consistent with the results in Table 2. In addition, only in aerated NaOH solutions,  $C_{\text{NaOH}}$  shows the obvious influence on the corrosion of PPy. These results suggest that the corrosion processes in aerated NaOH may be quite different from those in de-aerated NaOH.

### 3.3. SEM and XPS analysis

Fig. 8 presents the SEM morphologies of the PPy/SO<sub>4</sub> films freshly prepared and corroded in aerated 0.1 M NaOH for different time. The freshly prepared PPy/SO<sub>4</sub> film generally gives a cauliflower morphology [21], as shown in Fig. 8(a), exhibiting non-uniform structure formed by “knots” of different sizes. Corroded in aerated 0.1 M NaOH for 3 h, the PPy/SO<sub>4</sub> film in Fig. 8(b) displays some damaged “knots” and pitholes certainly due to the breakage of PPy conjugated backbone [51], but generally maintains its compact structure. These pictures show the PPY images in the first corrosion stage according to the results in Fig. 5(a). When the corrosion time increases to 5 h and 10 h, which is in the second corrosion stage, a large number of pinholes occur and grow with corrosion time,

while the PPy “knots” gradually become flat as shown in Figs. 8(c) and (d) [51,58], indicating that the damage degree of the PPY film in this corrosion stage is much heavier than that in the first corrosion stage. Some small white precipitates occur on the PPY film in Fig. 8(c), which should result from the crystallization of the residual NaOH in the PPY film because they are difficult to be completely removed during the rinse process. The SEM morphologies of the PPy/SO<sub>4</sub> films corroded in de-aerated 0.1 M NaOH display the similar change with increase in corrosion time, and the difference is that the period of the first corrosion stage prolongs to more than 6 h which is consistent with the results in Fig. 5(b).

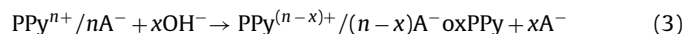
XPS analysis has been shown to be useful in differentiating between the different N species in PPy and to quantify the extent of doping and deprotonation in the polymers. Fig. 9 presents the XPS high resolution spectra of N 1s for PPy/SO<sub>4</sub> films freshly prepared and corroded in aerated 0.1 M NaOH for different time and their survey spectrum. The XPS N 1s spectra can be deconvoluted into three components [35,36,41,42,50,53,60]: a  $\text{N}^{\delta+}$  (BE = 401.1 eV) due to polarons or bipolarons, a  $-\text{NH}-$  (BE = 399.5 eV) that is the characteristic of pyrrolinium nitrogen, and a  $=\text{N}-$  (BE = 398.2 eV) resulting from deprotonation during corrosion. Thus, the ratio of each component's content to the total N content ( $N_{\text{Total}}$ ) can be calculated from the N 1s spectra, which are displayed in Fig. 9. The doping ratio of a PPy/SO<sub>4</sub> film can be represented by  $S/N_{\text{Total}}$  [35,36,50,53].

Table 7 gives the values of  $\text{N}^{\delta+}/N_{\text{Total}}$ ,  $=\text{N}/N_{\text{Total}}$  and  $S/N_{\text{Total}}$  for the PPy/SO<sub>4</sub> films freshly prepared and corroded in aerated 0.1 M NaOH for different time, which imply the changes of PPy in chemical composition and structure. It is seen that with an increase in corrosion time the  $S/N_{\text{Total}}$  and  $\text{N}^{\delta+}/N_{\text{Total}}$  values decrease while the  $=\text{N}/N_{\text{Total}}$  ratio increases, indicating that the loss of counterions, the decrease in polarons or bipolarons and the increase in the deprotonation on the PPY chains are promoted as the corrosion proceeds [36]. However, it should be noted that these ratios change quickly in the period of 0–5 h, but change slightly in the period of 5–9.5 h, implying that there are two different corrosion stages and  $t_0^2$  is around 5 h. This result is consistent with the result in Fig. 5 and further proves that there are two different corrosion stages in aerated 0.1 M NaOH for PPy/SO<sub>4</sub> films.

## 4. Discussion

### 4.1. Chemical and electrochemical processes on PPY/SO<sub>4</sub>

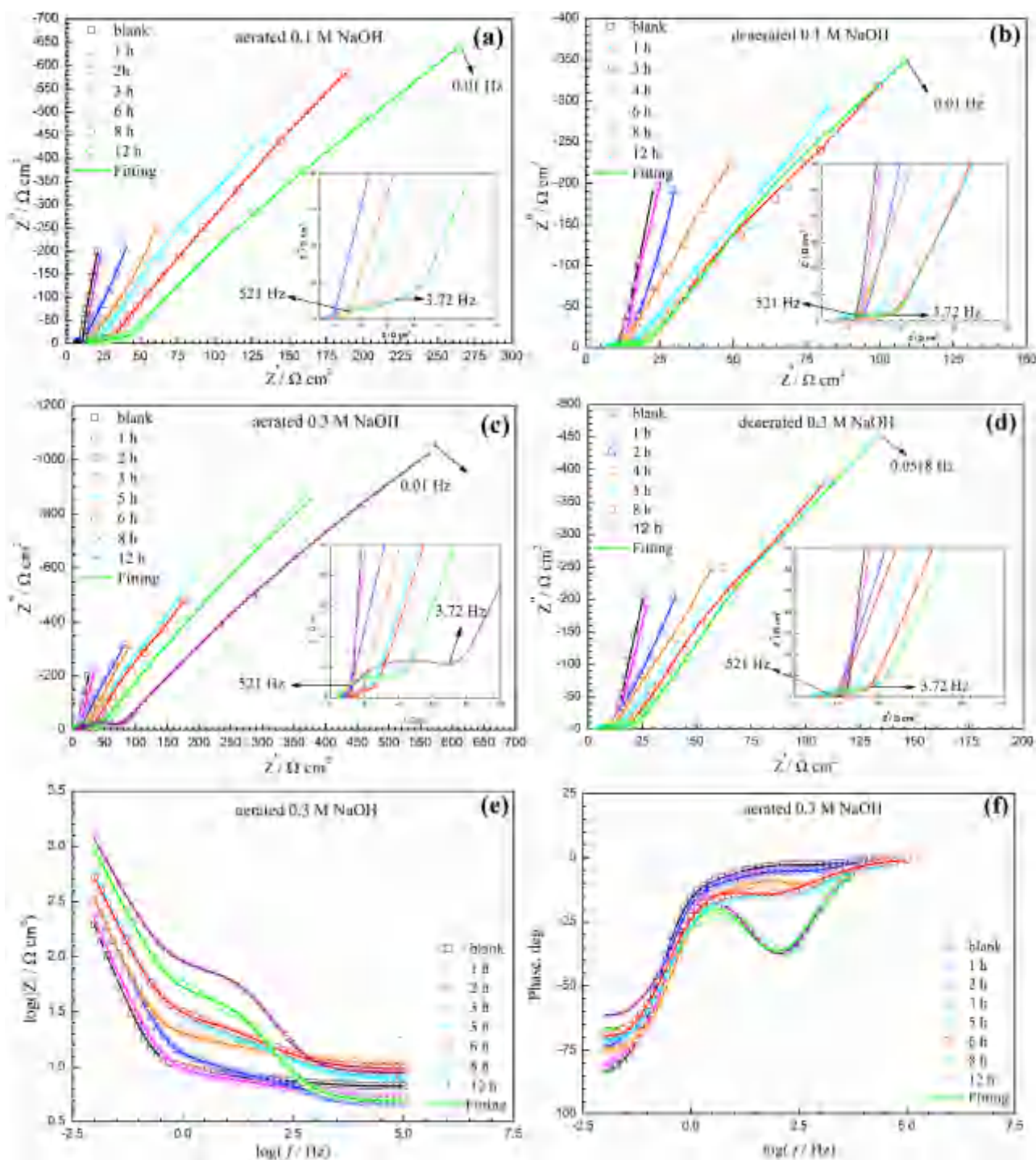
In NaOH solutions, the chemical process on PPy/SO<sub>4</sub> film should result from the chemical attack of  $\text{OH}^-$ ,  $\text{H}_2\text{O}$ ,  $\text{O}_2$  and other intermediate nucleophilic products, among which the strong nucleophilic  $\text{OH}^-$  plays a major role [24,37–39,50]. It is generally considered that  $\text{OH}^-$  can attack PPY films in two ways [37,50,54,61]: (1)  $\text{OH}^-$  exchanges with doping anions first and then the PPy/ $\text{OH}^-$  is over-oxidized to a pyrrole ring with carbonyl groups; (2)  $\text{OH}^-$  attack the  $\beta$ -C of pyrrole ring directly to form carbonyl groups. In this case, the corroded PPy/SO<sub>4</sub> film will lose its conjugated double-bond structure and electrochemical activity. The chemical reaction can be generally described as Reaction (3):



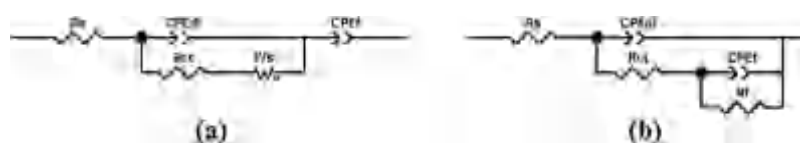
where  $\text{PPy}^{n+}/n\text{A}^-$  is the PPY in doped oxidation state with a certain number of polarons or bipolarons ( $\text{PPy}^{n+}$ ),  $\text{A}^-$  is the doped ions and oxPPy is the PPY in overoxidation state after corrosion.

The electrochemical processes should result from various galvanic cells formed on PPy/SO<sub>4</sub> films in NaOH solutions according to our previous work [42], such as PPY redox state difference cells, oxygen concentration difference cells,  $\text{H}^+$  ion (or  $\text{OH}^-$ ) concentration difference cells and electrolyte (NaOH) concentration difference





**Fig. 6.** Nyquist plots measured at 0.2 V (vs. SCE) in de-aerated 0.1 M  $\text{KNO}_3$  for the PPY/ $\text{SO}_4$  films freshly prepared and corroded in aerated and de-aerated NaOH solutions for different time: (a) aerated 0.1 M, (b) de-aerated 0.1 M, (c) aerated 0.3 M, (d) de-aerated 0.3 M; (e) and (f): Bode plots for the PPY/ $\text{SO}_4$  films freshly prepared and corroded in aerated 0.3 M NaOH for different time (insets are impedance spectrum at high frequencies).



**Fig. 7.** Equivalent circuits to simulate the PPY/solution interface on the freshly prepared and corroded PPY/ $\text{SO}_4$  films.

**Table 3**Fitting parameters of the EIS results in Fig. 6 (a) for the PPY/SO<sub>4</sub> films corroded in aerated 0.1 M NaOH for different time.

Time (h)	$R_s \Omega \text{ cm}^2$	$\text{CPE}_{\text{dl-T}} \text{ mFcm}^{-2} \text{ Hz}^{1-n_1}$	$\text{CPE}_{\text{dl-P}} / n_1$	$R_{\text{ct}} \Omega \text{ cm}^2$	$W_s\text{-R} \Omega \text{ cm}^2$	$\text{CPE}_{\text{r-T}} \text{ mFcm}^{-2} \text{ Hz}^{1-n_2}$	$\text{CPE}_{\text{r-P}} / n_2$
1	21.77	8.20	0.414	6.83	7.89	25.15	0.957
2	22.42	6.72	0.435	13.44	41.54	21.36	0.920
3	22.51	3.25	0.437	22.12	76.33	16.96	0.892
6	21.73	2.49	0.488	39.90	84.61	9.69	0.877
8	19.30	0.89	0.612	60.49	150.91	9.21	0.871
12	24.60	0.75	0.687	78.90	275.8	8.11	0.859

**Table 4**Fitting parameters of the EIS results in Fig. 6(b) for the PPY/SO<sub>4</sub> films corroded in aerated 0.1 M NaOH for different time.

Time (h)	$R_s \Omega \text{ cm}^2$	$\text{CPE}_{\text{dl-T}} \text{ mFcm}^{-2} \text{ Hz}^{1-n_1}$	$\text{CPE}_{\text{dl-P}} / n_1$	$R_{\text{ct}} \Omega \text{ cm}^2$	$W_s\text{-R} \Omega \text{ cm}^2$	$\text{CPE}_{\text{r-T}} \text{ mFcm}^{-2} \text{ Hz}^{1-n_2}$	$\text{CPE}_{\text{r-P}} / n_2$
1	23.75	9.55	0.382	3.15	5.84	27.13	0.975
3	19.33	6.91	0.388	13.51	20.89	24.01	0.946
4	20.03	5.47	0.394	15.59	23.77	20.71	0.925
6	21.73	2.84	0.455	23.84	50.64	16.02	0.918
8	15.27	2.07	0.510	25.26	66.71	13.68	0.899
12	25.53	1.11	0.552	37.30	97.02	11.55	0.859

**Table 5**Fitting parameters of the EIS results in Fig. 6(c) for the PPY/SO<sub>4</sub> films corroded in aerated 0.3 M NaOH for different time.

Time (h)	$R_s \Omega \text{ cm}^2$	$\text{CPE}_{\text{dl-T}} \text{ mFcm}^{-2} \text{ Hz}^{1-n_1}$	$\text{CPE}_{\text{dl-P}} / n_1$	$R_{\text{ct}} \Omega \text{ cm}^2$	$W_s\text{-R} \Omega \text{ cm}^2$	$\text{CPE}_{\text{r-T}} \text{ mFcm}^{-2} \text{ Hz}^{1-n_2}$	$\text{CPE}_{\text{r-P}} / n_2$	$R_f \Omega \text{ cm}^2$
1	19.33	5.58	0.472	14.91	30.89	22.48	0.936	–
2	16.68	4.71	0.426	19.94	38.41	17.54	0.900	–
3	18.38	5.25	0.582	27.97	49.45	11.54	0.875	–
5	25.95	2.90	0.585	50.51	114	7.89	0.846	–
6	19.39	1.91	0.679	62.51	275.6	5.55	0.835	–
8	20.67	0.25	0.725	117.52	–	3.32	0.814	33980
12	24.61	0.11	0.758	196.23	–	2.49	0.776	88382

**Table 6**Fitting parameters of the EIS results in Fig. 6(d) for the PPY/SO<sub>4</sub> films corroded in aerated 0.3 M NaOH for different time.

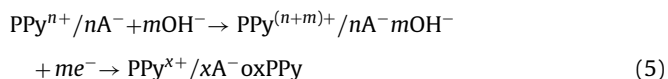
Time(h)	$R_s \Omega \text{ cm}^2$	$\text{CPE}_{\text{dl-T}} \text{ mFcm}^{-2} \text{ Hz}^{1-n_1}$	$\text{CPE}_{\text{dl-P}} / n_1$	$R_{\text{ct}} \Omega \text{ cm}^2$	$W_s\text{-R} \Omega \text{ cm}^2$	$\text{CPE}_{\text{r-T}} \text{ mFcm}^{-2} \text{ Hz}^{1-n_2}$	$\text{CPE}_{\text{r-P}} / n_2$
1	20.63	7.29	0.416	3.21	8.83	26.25	0.962
2	17.08	7.12	0.429	10.45	17.65	22.61	0.923
4	20.32	3.07	0.469	15.82	20.82	16.32	0.890
5	14.24	2.87	0.483	27.80	77.28	13.92	0.892
8	19.61	2.03	0.506	30.73	100.91	10.24	0.876
12	25.53	1.23	0.600	44.25	106.01	9.21	0.873

cells. Among these galvanic cells, only oxygen concentration difference cells have obvious effect on the corrosion of PPY [42], in which electrochemical reactions can be expressed as:

Cathodic reaction:



Anodic reaction:



where  $\text{PPy}^{m+}$  is the new formed polarons or bipolarons under anodic polarisation and  $x < n$ . The  $\text{OH}^-$  created from Reaction (4) and its intermediate products, i.e.  $\text{HO}_2^-$  or adsorbed oxygen atom O, can attack PPY chains and destroy their conjugated structure. At the same time, the anodic polarisation of PPY will increase positive sites in PPY chains ( $\text{PPy}^{m+}$ ) for  $\text{OH}^-$  attacking and let more  $\text{OH}^-$  enter the PPY film so as to accelerate its corrosion [41]. Apparently, the chemical process, i.e. Reaction (3), will also be promoted.

Based on the above discussion, the corrosion of the PPY/SO<sub>4</sub> films in de-aerated NaOH should mainly include the chemical process, i.e. Reaction (3), because the electrochemical processes are so weak that can be ignored [42]. In aerated NaOH solutions, the oxygen concentration difference cells can be formed and sustained on PPY/SO<sub>4</sub> films [42] and therefore, the corrosion of PPY will include chemi-

cal and electrochemical processes, i.e. Reactions (3)–(5), resulting in much faster and severer corrosion than those corroded in de-aerated NaOH, as shown in Fig. 3.

It should be noted that there is an incubation period for the corrosion of PPY in NaOH solutions, as shown in Fig. 5. This may be due to the compact structure of the PPY/SO<sub>4</sub> film, as shown in Fig. 8 (a), which makes the Reactions (3)–(5) hard to occur on the inner layer of the PPY film. In this case, the corrosion of PPY in this period is very slight and  $Q_R/Q_0 \approx 1$ . When the surface of PPY film is damaged and the corrosion processes enter the inner layer of PPY, the corrosion of PPY begins to be displayed. Apparently, the stronger the corrosion medium is, the shorter the incubation period will be. The results in Fig. 5 prove this deduction. Because there is  $Q_R/Q_0 \approx 1$  in this period, the corrosion of PPY in the incubation period is not considered.

#### 4.2. Kinetics of chemical and electrochemical processes on PPY/SO<sub>4</sub>

For Reaction (3), the reaction rate ( $v_c$ ) at a constant  $C_{\text{NaOH}}$  can be described as:

$$v_c = k'_c [\text{PPy}^{n+}]^p C_{\text{NaOH}}^q \quad (6)$$

where  $k'_c$  is the rate constant of Reaction (3),  $[\text{PPy}^{n+}]$  is the concentration of  $\text{PPy}^{n+}$ ,  $p$  is the reaction order of PPY and  $q$  is the reaction

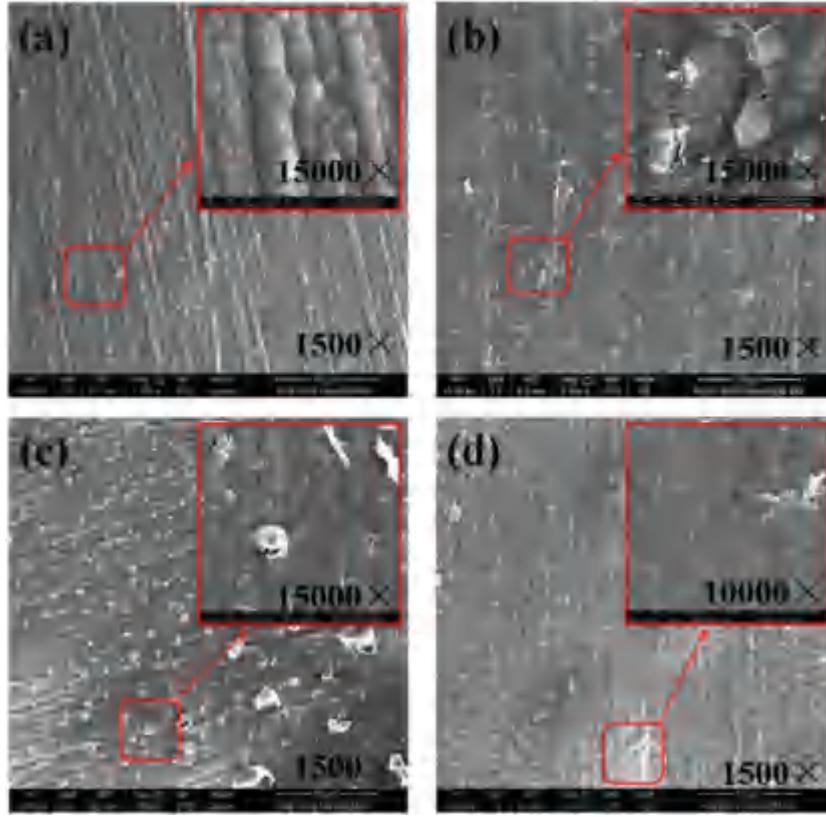


Fig. 8. SEM morphologies of the PPy/SO<sub>4</sub> films (a) freshly prepared and corroded in aerated 0.1 M NaOH for (b) 3 h, (c) 5 h and (d) 10 h.

Table 7

Ratios of  $S/N_{\text{Total}}$ ,  $N^{\delta+}/N_{\text{Total}}$  and  $=N-/N_{\text{Total}}$  obtained by quantitative analysis of XPS spectra for the PPy/SO<sub>4</sub> films freshly prepared and corroded in aerated 0.1 M NaOH for different time.

Ratios	Corrosion time (h)				
	0	2	4	5	9.5
$S/N_{\text{Total}}$	0.220	0.089	0.064	0.044	0.032
$N^{\delta+}/N_{\text{Total}}$	0.221	0.107	0.068	0.050	0.047
$=N-/N_{\text{Total}}$	0	0.133	0.173	0.220	0.229

order of NaOH. Because  $C_{\text{NaOH}}$  is a constant,  $C_{\text{NaOH}}^q$  can be combined into  $k'_c$  by setting  $k'_c = k'_c C_{\text{NaOH}}^q$ .

Thus, in de-aerated NaOH solutions, there is

$$v_{\text{corr,de}} = v_c = k'_c [\text{PPy}^{n+}]^p \quad (7)$$

According to the results in Fig. 5(b) and Eq. (1) ( $i = 1$ ),

$$v_{\text{corr,de}} = v_c = k_{\text{de}} \left( \frac{Q_R}{Q_0} \right) \quad (8)$$

Comparing Eq. (7) with Eq. (8), there is  $Q_R/Q_0 \propto [\text{PPy}^{n+}]$  and  $p = 1$ , thus

$$v_{\text{corr,de}} = v_c = k_c \left( \frac{Q_R}{Q_0} \right) = k_{\text{de}} \left( \frac{Q_R}{Q_0} \right) \quad (9)$$

where  $k_c$  is the apparent rate constant of Reaction (3) that is proportional to  $k'_c$  and  $k_c = k_{\text{de}}$ .

The electrochemical processes on PPy include cathodic Reaction (4), anodic Reaction (5) and the current flow between cathodic and anodic areas on PPy which is related to the conductivity of corrosion medium. The  $R_s$  values in Tables 3–6 are not so large ( $\sim 20 \Omega \text{ cm}^2$ ) and there is no obvious decrease in  $R_s$  with an increase in  $C_{\text{NaOH}}$  from 0.1 to 0.3 M. So, the medium conductivity is not a controlling factor. Cathodic Reaction (4) is generally controlled by the O<sub>2</sub>

diffusion process in NaOH [42,50] and its rate is determined by DO concentration. If Reaction (4) is the controlling process, the effect of the electrochemical processes will be nearly constant because DO in aerated NaOH solutions (0.02–0.5 M) changes slightly. Actually, the effect of the electrochemical processes on the corrosion of PPy increases obviously with  $C_{\text{NaOH}}$ , as shown in Table 2. In this case, anodic Reaction (5) should be the controlling process and its rate ( $v_e$ ) is applied to describe the corrosion rate.

Similarly,  $v_e$  can be obtained assuming that the reaction order of PPy is 1.

$$v_e = k'_e [\text{PPy}^{n+}] C_{\text{NaOH}}^j = k'_e [\text{PPy}^{n+}] = k_E \left( \frac{Q_R}{Q_0} \right) \quad (10)$$

where  $k'_e$  is the rate constant of Reaction (5),  $j$  is the reaction order of NaOH,  $k'_e = k'_e C_{\text{NaOH}}^j$  and  $k_E$  is its apparent rate constant that is proportional to  $k'_e$ .

Thus, if  $k_c$  in aerated NaOH is considered to be the same as those in de-aerated NaOH at a constant  $C_{\text{NaOH}}$ , the corrosion rate of PPy in aerated NaOH solutions ( $v_{\text{corr,ae}}$ ) is

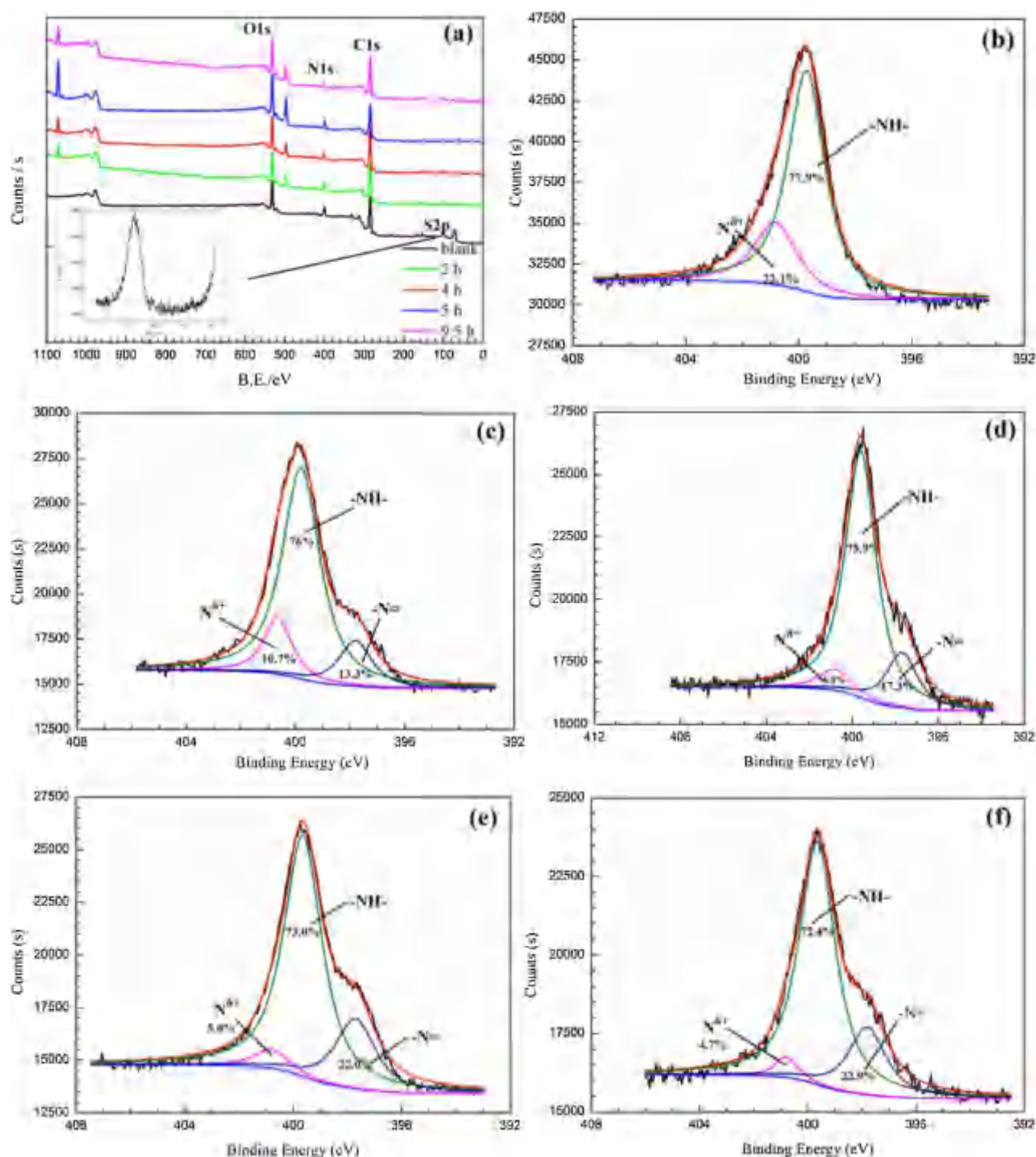
$$v_{\text{corr,ae}} = v_e + v_c = (k_E + k_c) \left( \frac{Q_R}{Q_0} \right) = k_{\text{ae}} \left( \frac{Q_R}{Q_0} \right) \quad (11)$$

$$k_{\text{ae}} = (k_E + k_c) \quad (12)$$

In this case, the corrosion of PPy in aerated NaOH solutions also displays the first-order kinetic relationship, which is proven by the results in Fig. 5(a).

In aerated and de-aerated NaOH solutions, the corrosion of PPy/SO<sub>4</sub> shows two corrosion stages. However, there is no change for the chemical and electrochemical processes in the two corrosion stages, i.e. Reaction (3)–(5), so they all exhibit the first-order kinetic behavior, as shown in Fig. 5. The difference is that their corrosion rates and apparent rate constants are different. In the first corrosion stage, the PPy/SO<sub>4</sub> film just has slight damage (see Fig. 8)





**Fig. 9.** XPS survey spectrum (a) and high resolution spectra of N 1s for the PPY/SO<sub>4</sub> films (b) freshly prepared and corroded in aerated 0.1 M NaOH for (c) 2 h, (d) 4 h, (e) 5 h and (f) 9.5 h.

and smaller  $R_{ct}$  and  $W_s$ -R values (see Tables 3–6), suggesting that the corrosion of PPY mainly occurs on the outer layer of PPY and the reaction resistance is lower. Furthermore, the  $[PPy^{n+}]$  of the PPY/SO<sub>4</sub> film in the first corrosion stage is higher and decreases quickly with an increase in corrosion time, as shown in Table 7. These factors result in larger corrosion rates and  $k_1$  values ( $k_{1,ae}$  and  $k_{1,de}$ ) in the first corrosion stage. When the corrosion of PPY enters the second corrosion stage, a large number of pinholes occur in the PPY film and gradually grow with corrosion time (see Fig. 8), while  $R_{ct}$  and  $W_s$ -R values increase obviously (see Tables 3–6), indicating

that the corrosion of PPY gradually develops into the inner layer of the PPY film and the reaction resistance increases obviously. In addition, the  $[PPy^{n+}]$  of the PPY/SO<sub>4</sub> film in the second corrosion stage becomes very small and decreases very slowly, as shown in Table 7. In this case, the corrosion of PPY in the second stage shows lower corrosion rates and much smaller  $k_2$  values ( $k_{2,ae}$  and  $k_{2,de}$ ).

Based on Eqs. (9), (11) and (12), there is

$$k_{1,de} = k_{1,c} \quad (13)$$

$$k_{2,de} = k_{2,c} \quad (14)$$

**Table 8**

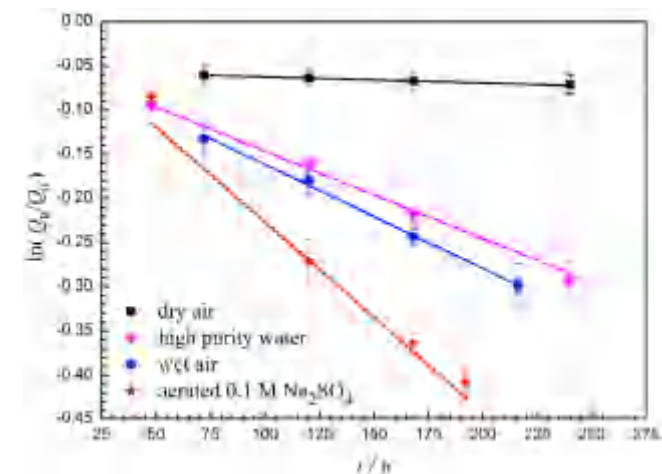
Apparent rate constants of the electrochemical processes ( $k_E$ ) in the two corrosion stages for the PPy/SO<sub>4</sub> films corroded in aerated NaOH solutions.

$k_E$ ( $s^{-1}$ , $\times 10^{-5}$ )	$C_{NaOH}$ (M)				
	0.02	0.05	0.1	0.3	0.5
$k_{1,E}$	2.27	2.44	2.53	3.92	7.76
$k_{2,E}$	0.56	0.99	1.56	2.04	2.48

**Table 9**

Corrosion rate constants ( $k$ ) for the PPy/SO<sub>4</sub> films corroded in dry air, wet air, HPW and aerated 0.1 M Na<sub>2</sub>SO<sub>4</sub>.

Rate constant	Corrosion media			
( $s^{-1}$ , $\times 10^{-6}$ )	Dry air	Wet air	HPW	aerated 0.1 M Na <sub>2</sub> SO <sub>4</sub>
$k$	0.019	0.328	0.275	0.597



**Fig. 10.** Changes of  $\ln(Q_R/Q_0)$  as a function of time for the PPy/SO<sub>4</sub> films corroded in dry air, wet air (with saturated humidity), high purity water, and aerated 0.1 M Na<sub>2</sub>SO<sub>4</sub>.

$$k_{1,ae} = k_{1,C} + k_{1,E} \quad (15)$$

$$k_{2,ae} = k_{2,C} + k_{2,E} \quad (16)$$

where  $k_{1,C}$ ,  $k_{2,C}$ ,  $k_{1,E}$ , and  $k_{2,E}$  are the  $k_C$  and  $k_E$  in the first and second corrosion stage, respectively. Thus,

$$k_{1,E} = k_{1,ae} - k_{1,C} = k_{1,ae} - k_{1,de} \quad (17)$$

$$k_{2,E} = k_{2,ae} - k_{2,C} = k_{2,ae} - k_{2,de} \quad (18)$$

Table 8 presents the  $k_E$  values calculated from Eqs. (17) and (18) using the results in Table 2. It is clearly seen that the  $k_E$  values increase with  $C_{NaOH}$  and there is  $k_{1,E} > k_{2,E}$ , which is consistent with the change of  $k_C$  (i.e.  $k_{de}$ ) as shown in Table 2.

The above discussion ignores the chemical attack of O<sub>2</sub> and H<sub>2</sub>O and do not identify the interaction between the chemical and electrochemical processes. In order to determine these effects quantitatively, the similar corrosion tests as those in NaOH solutions were performed in dry air, wet air (with saturated humidity), aerated high purity water (HPW), and aerated 0.1 M Na<sub>2</sub>SO<sub>4</sub> (pH = 7). In dry air, there is only the chemical attack of O<sub>2</sub>, so its chemical effect on the corrosion of PPy can be verified. In wet air, a thin water layer will cover on PPy surface and dissolve some ions from the PPy film and air to form a thin electrolyte layer (TEL). Thus, the corrosion of PPy in aerated 0.1 M Na<sub>2</sub>SO<sub>4</sub>, wet air and aerated HPW should contain the chemical action of H<sub>2</sub>O, O<sub>2</sub> and the electrochemical processes, i.e. Reactions (4) and (5). In aerated HPW, the electrochemical processes on PPy are expected to be suppressed largely for its very lower conductivity ( $\sigma_{HPW} = 0.056 \mu S/cm$ ), then the chemical effect of H<sub>2</sub>O may be displayed. Based on these results, the effect of the electrochemical processes on the corrosion of PPy may also be identified.

Fig. 10 presents the  $\ln(Q_R/Q_0)$ - $t$  curves for the PPy/SO<sub>4</sub> films corroded in dry air, wet air, aerated HPW, and aerated 0.1 M Na<sub>2</sub>SO<sub>4</sub>. The  $\ln(Q_R/Q_0)$ - $t$  curves in Fig. 10 all have good linearity and just show one corrosion stage, demonstrating that the corrosion of the PPy/SO<sub>4</sub> films in these four corrosion media is in the first corrosion

stage and also follows the first-order kinetic relationship during the test periods. In addition, the incubation periods in these four corrosion media are much longer than those in the NaOH solutions, suggesting that these four corrosion media are much weaker than the NaOH solutions.

Table 9 lists the  $k$  values for the PPy/SO<sub>4</sub> films corroded in dry air ( $k_{dryair}$ ), wet air ( $k_{wetair}$ ), aerated HPW ( $k_{HPW}$ ) and aerated 0.1 M Na<sub>2</sub>SO<sub>4</sub> ( $k_{Na_2SO_4}$ ), obtained from the results in Fig. 10. The four  $k$  values are lower by 1 ~ 2 orders of magnitude compared to those  $k_1$  values ( $k_{1,de}$  and  $k_{1,ae}$ ) in the NaOH solutions, as shown in Table 2, indicating that the corrosion of PPy in these four media is very weak. Apparently, it is appropriate to neglect the chemical effect of O<sub>2</sub> and H<sub>2</sub>O in the NaOH solutions. Among the four  $k$  values,  $k_{dryair}$  is one order smaller than the other three  $k$  values, so the chemical effect of O<sub>2</sub> on the corrosion of PPy can be generally ignored.  $k_{HPW}$  is one order higher than  $k_{dryair}$  and just slightly smaller than  $k_{wetair}$  and  $k_{Na_2SO_4}$  ( $k_{Na_2SO_4} > k_{wetair} > k_{HPW}$ ), suggesting that the electrochemical processes on PPy in aerated HPW may not be inhibited obviously. This may be attributed to the dissolution of ions from the PPy film and the OH<sup>-</sup> produced from Reaction (4), which increases the conductivity in local area so as to accelerate the electrochemical processes on PPy. In addition, these three  $k$  values ( $k_{Na_2SO_4}$ ,  $k_{wetair}$  and  $k_{HPW}$ ) increase with an increase in their conductivities. This result further demonstrates that the electrochemical processes still play a major role in these three corrosion media. So,  $k_{Na_2SO_4}$ ,  $k_{wetair}$  and  $k_{HPW}$  mainly reflect the kinetics of the electrochemical processes. Because  $k_{HPW}$  is relatively small, the chemical effect of H<sub>2</sub>O on the corrosion of PPy should be generally ignored too, even though it is not distinguished from  $k_{HPW}$ .

It should be noted that the conductivity of aerated 0.1 M Na<sub>2</sub>SO<sub>4</sub> ( $\sigma_{Na_2SO_4} = 14.4 mS/cm$ ) is close to that of aerated 0.1 M NaOH ( $\sigma_{NaOH} = 18.9 mS/cm$ ) and their DO concentrations are similar, but  $k_{Na_2SO_4}$  ( $0.597 \times 10^{-6} s^{-1}$ ) is much less than  $k_{1,E}$  in 0.1 M NaOH ( $2.53 \times 10^{-5} s^{-1}$ ). Apparently, the electrochemical processes on PPy has been promoted significantly in 0.1 M NaOH. This result can be attributed to two reasons: one is that the chemical attack of OH<sup>-</sup> make it enter the PPy film and exchange with doped SO<sub>4</sub><sup>2-</sup> easily and therefore, Reaction (5) is accelerated; another is that the potential of PPy ( $E_{PPy}$ ) decreases with an increase in  $C_{NaOH}$  [20,42,62–64] so as to increase the potential difference between the anodic and cathodic areas in the oxygen concentration difference cells and then Reaction (5) is accelerated as well. So in aerated NaOH solutions, there is mutual promotion between the chemical action of OH<sup>-</sup> and the electrochemical processes on PPy. However, interactions between the two processes can hardly be distinguished, so they are not considered during the derivation of  $k_E$  and  $k_C$ .

#### 4.3. Effect of NaOH concentration on the kinetics of PPy corrosion

Fig. 11 presents the changes of the apparent rate constants ( $k_{1,E}$ ,  $k_{2,E}$ ,  $k_{1,C}$ ,  $k_{2,C}$ ) as a function of  $C_{NaOH}$ , which is plotted based on the results in Table 2 and Table 8. In Fig. 11, all the apparent rate constants increase with an increase in  $C_{NaOH}$ , while each  $k$ - $C_{NaOH}$  curve does not have a good linearity and shows different change rules. In the discussion above,  $C_{NaOH}$  is considered as a constant and included in  $k'_C (= k_C C_{NaOH}^q)$  and  $k'_E (= k_E C_{NaOH}^j)$ , as shown in Eqs.

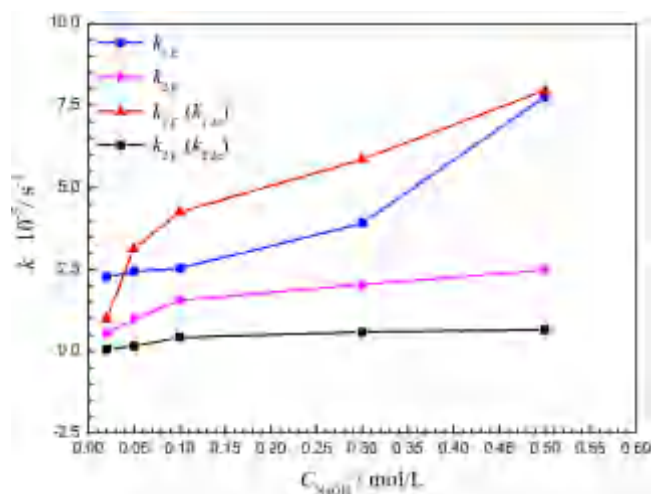


Fig. 11. Changes of the apparent rate constants ( $k_{1,C}$ ,  $k_{2,C}$ ,  $k_{1,E}$  and  $k_{2,E}$ ) as a function of  $C_{\text{NaOH}}$ .

(6) and (10). Certainly,  $k_E$  and  $k_C$  increase with  $C_{\text{NaOH}}$ , because they are proportional to  $k'_C$  and  $k'_E$ , respectively.

In addition, it also can be deduced that  $q \neq j \neq 1$  and their values may be different in different corrosion stages, suggesting that the chemical and electrochemical processes have different kinetic behavior in different corrosion stages. In Fig. 11, there is always  $k_{1,C} \gg k_{2,C}$  and  $k_{1,E} \gg k_{2,E}$ , while the increase extents of  $k_{1,C}$  and  $k_{1,E}$  are much larger than those of  $k_{2,C}$  and  $k_{2,E}$ , demonstrating that in the first corrosion stage, the chemical and electrochemical processes are much faster and the effect of  $C_{\text{NaOH}}$  on  $k_C$  and  $k_E$  is much stronger. These results should be attributed to the higher  $[\text{PPy}^{n+}]$  and lower reaction resistance in the out layer of PPy film in the first corrosion stage.

In the first corrosion stage, the effect of  $C_{\text{NaOH}}$  on the chemical process is also different from that on the electrochemical processes. When  $C_{\text{NaOH}}$  is lower, such as 0.02 M, there is  $k_{1,E} > k_{1,C}$ , indicating that the chemical effect of  $\text{OH}^-$  is weak and the electrochemical processes dominate the corrosion of PPy. But it should be noted that  $k_{1,E}$  in 0.02 M NaOH ( $2.27 \times 10^{-5} \text{ s}^{-1}$ ) is still much larger than  $k_{\text{Na}_2\text{SO}_4}$  ( $0.597 \times 10^{-6} \text{ s}^{-1}$ ), implying that Reaction (5) is still largely promoted by the weak chemical attack at this lower  $C_{\text{NaOH}}$ . When  $C_{\text{NaOH}}$  increases to a medium range, such as 0.05 – 0.3 M, there is  $k_{1,C} \gg k_{1,E}$  and  $k_{1,C}$  increases more largely than  $k_{1,E}$ . Within this  $C_{\text{NaOH}}$  range, the chemical attack of  $\text{OH}^-$  is much faster than the electrochemical processes and  $[\text{PPy}^{n+}]$  is preferentially consumed by  $\text{OH}^-$ , thus the chemical process, Reaction (3), dominates the corrosion of PPy. At a higher  $C_{\text{NaOH}}$ , such as 0.5 M,  $k_{1,E}$  increases largely to approximate  $k_{1,C}$ , indicating that both chemical and electrochemical processes control the corrosion of PPy. At this higher  $C_{\text{NaOH}}$ , the electrochemical processes are accelerated obviously, which may be attributed to the large increase in the driving force of the oxygen concentration difference cells, as discussed above, and the increase in the medium conductivity.

In the second corrosion stage, there is always  $k_{2,E} > k_{2,C}$  and the effect of  $C_{\text{NaOH}}$  on the electrochemical processes is much larger than that on the chemical process. Apparently, the electrochemical processes are much faster than the chemical process and dominate the corrosion of PPy in the second corrosion stage. These results may be due to the following reasons: (1) anodic Reaction (5) can increase  $[\text{PPy}^{n+}]$  to some extent; (2)  $E_{\text{PPy}}$  [20,42,62–64] decreases with an increase in  $C_{\text{NaOH}}$  so as to increase the driving force of the oxygen concentration difference cells; (3) the medium conductivity increases with an increase in  $C_{\text{NaOH}}$  to lower the solution resistance.

## 5. Conclusions

The chemical and electrochemical corrosion kinetics of PPy/ $\text{SO}_4$  in aerated and de-aerated NaOH solutions (0.02–0.5 M) was investigated using various electrochemical methods and spectroscopic analyses. The interaction between the chemical and electrochemical processes was verified. The following conclusions are drawn from the results of experiments:

- (1) The corrosion of PPy/ $\text{SO}_4$  in aerated and de-aerated NaOH at a constant  $C_{\text{NaOH}}$  includes two corrosion stages and at each stage the corrosion rate follows the first-order kinetics. The rate constants in aerated NaOH ( $k_{\text{ae}}$ ) are much larger than those in de-aerated NaOH ( $k_{\text{de}}$ ), and the rate constants in the first corrosion stage are always much larger than those in the second corrosion stage, i.e.  $k_{1,\text{ae}} \gg k_{2,\text{ae}}$  and  $k_{1,\text{de}} \gg k_{2,\text{de}}$ .
- (2) In de-aerated NaOH, the chemical attack of  $\text{OH}^-$  dominates the corrosion of PPy/ $\text{SO}_4$ . The chemical attack of  $\text{O}_2$  and  $\text{H}_2\text{O}$  on PPy can be generally ignored. In aerated NaOH, apart from the chemical attack of  $\text{OH}^-$ , the corrosion of PPy also includes electrochemical processes mainly resulting from the formation of the oxygen concentration difference cells, which causes much faster and severer corrosion of PPy than that in de-aerated NaOH. It is proved that the apparent rate constants of the chemical and electrochemical processes ( $k_C$  and  $k_E$ ) have the relationships with  $k_{\text{ae}}$  and  $k_{\text{de}}$  as:  $k_{\text{de}} = k_C$  and  $k_{\text{ae}} = k_C + k_E$ .
- (3)  $C_{\text{NaOH}}$  plays a key role in the corrosion kinetics of PPy/ $\text{SO}_4$  in NaOH solutions. All  $k_C$  and  $k_E$  in the two corrosion stages ( $k_{1,E}$ ,  $k_{2,E}$ ,  $k_{1,C}$ ,  $k_{2,C}$ ) increase with an increase in  $C_{\text{NaOH}}$  and there is always  $k_{1,C} \gg k_{2,C}$  and  $k_{1,E} \gg k_{2,E}$ . In aerated NaOH, the detailed effect of  $C_{\text{NaOH}}$  on  $k_C$  and  $k_E$  is also different in the two corrosion stages. In the first corrosion stage, when  $C_{\text{NaOH}} = 0.02 \text{ M}$ , there is  $k_{1,E} > k_{1,C}$  and the electrochemical processes are dominant; When  $0.05 \text{ M} \leq C_{\text{NaOH}} \leq 0.3 \text{ M}$ , there is  $k_{1,C} \gg k_{1,E}$  and the chemical process dominates the corrosion of PPy; When  $C_{\text{NaOH}}$  reaches to a higher value, such as 0.5 M, there is  $k_{1,E} \approx k_{1,C}$  and both chemical and electrochemical processes control the corrosion of PPy. In the second corrosion stage, there is always  $k_{2,E} \gg k_{2,C}$  and the electrochemical processes control the corrosion of PPy.
- (4) In aerated NaOH solutions, there is obvious mutual promotion between the chemical action of  $\text{OH}^-$  and the electrochemical processes on PPy/ $\text{SO}_4$ . However, these interactions between the two processes can hardly be distinguished.

## Acknowledgements

This work was supported by the National Natural Science Foundation of China (51371088). We appreciate the analysis supported of State Key Laboratory of Material Processing and Die & Mould Technology and Center of Forecasting and Analysis, Huazhong University of Science and Technology.

## References

- [1] Z. Shi, H. Gao, J. Feng, B. Ding, X. Cao, S. Kuga, Y. Wang, L. Zhang, J. Cai, In situ synthesis of robust conductive cellulose/polypyrrole composite aerogels and their potential application in nerve regeneration, *Angew. Chem. Int. Edit.* 53 (2014) 5380–5384.
- [2] C. Zhao, K. Shu, C. Wang, S. Gambhir, G.G. Wallace, Reduced graphene oxide and polypyrrole/reduced graphene oxide composite coated stretchable fabric electrodes for supercapacitor application, *Electrochim. Acta* 172 (2015) 12–19.
- [3] X. Zhou, J. Tang, J. Yang, J. Xie, B. Huang, Seaweed-like porous carbon from the decomposition of polypyrrole nanowires for application in lithium ion batteries, *J. Mater. Chem. A* 1 (2013) 5037–5044.
- [4] B. Doğru Mert, Corrosion protection of aluminum by electrochemically synthesized composite organic coating, *Corros. Sci.* 103 (2016) 88–94.



- [5] A. Bahloul, B. Nessark, E. Briot, H. Groult, A. Mauger, K. Zaghib, C. Julien, Polypyrrole-covered MnO<sub>2</sub> as electrode material for supercapacitor, *J. Power Sources* 240 (2013) 267–272.
- [6] Y. Shi, L. Pan, B. Liu, Y. Wang, Y. Cui, Z. Bao, G. Yu, Nanostructured conductive polypyrrole hydrogels as high-performance, flexible supercapacitor electrodes, *J. Mater. Chem. A* 2 (2014) 6086–6091.
- [7] W. Sun, X. Chen, Preparation and characterization of polypyrrole films for three-dimensional micro supercapacitor, *J. Power Sources* 193 (2009) 924–929.
- [8] A. Joshi, S. Gangal, S. Gupta, Ammonia sensing properties of polypyrrole thin films at room temperature, *Sens. Actuators B* 156 (2011) 938–942.
- [9] S.S. Jeon, H.H. An, C.S. Yoon, S.S. Im, Synthesis of ultra-thin polypyrrole nanosheets for chemical sensor applications, *Polymer* 52 (2011) 652–657.
- [10] L. Valero, J. Arias-Pardilla, J. Cauch-Rodríguez, M. Smit, T. Otero, Characterization of the movement of polypyrrole –dodecylbenzenesulfonate –perchlorate/tape artificial muscles. Faradaic control of reactive artificial molecular motors and muscles, *Electrochim. Acta* 56 (2011) 3721–3726.
- [11] K.K. Lee, N.R. Munce, T. Shoa, L.G. Charron, G.A. Wright, J.D. Madden, V.X. Yang, Fabrication and characterization of laser-micromachined polypyrrole-based artificial muscle actuated catheters, *Sens. Actuators B* 153 (2009) 230–236.
- [12] M. Sevilla, L. Yu, T.P. Fellinger, A.B. Fuentes, M.-M. Titirici, Polypyrrole-derived mesoporous nitrogen-doped carbons with intrinsic catalytic activity in the oxygen reduction reaction, *RSC Adv.* 3 (2013) 9904–9910.
- [13] S. Fujii, S. Matsuzawa, H. Hamasaki, Y. Nakamura, A. Bouleghlimat, N.J. Buurma, Polypyrrole–palladium nanocomposite coating of micrometer-sized polymer particles toward a recyclable catalyst, *Langmuir* 28 (2012) 2436–2447.
- [14] V. Annibaldi, A. Rooney, C. Breslin, Corrosion protection of copper using polypyrrole electrosynthesised from a salicylate solution, *Corros. Sci.* 59 (2012) 179–185.
- [15] M. Yan, C.A. Vetter, V.J. Gelling, Corrosion inhibition performance of polypyrrole Al flake composite coatings for Al alloys, *Corros. Sci.* 70 (2013) 47–45.
- [16] M.B. González, S.B. Saidman, Electrodeposition of polypyrrole on 316L stainless steel for corrosion prevention, *Corros. Sci.* 53 (2011) 276–282.
- [17] H. Ryu, N. Sheng, T. Ohtsuka, S. Fujita, H. Kajiyama, Polypyrrole film on 55% Al–Zn-coated steel for corrosion prevention, *Corros. Sci.* 56 (2012) 67–77.
- [18] D.O. Flaminio, S.B. Saidman, Electrodeposition of polypyrrole onto NiTi and the corrosion behaviour of the coated alloy, *Corros. Sci.* 52 (2010) 229–234.
- [19] Y. Lei, N. Sheng, A. Hyono, M. Ueda, T. Ohtsuka, Electrochemical synthesis of polypyrrole films on copper from phytic solution for corrosion protection, *Corros. Sci.* 76 (2013) 302–309.
- [20] A. Alumaa, A. Hallik, V. Sammelselg, J. Tamm, On the improvement of stability of polypyrrole films in aqueous solutions, *Synth. Met.* 157 (2007) 485–491.
- [21] Y. Tian, F. Yang, W. Yang, Redox behavior and stability of polypyrrole film in sulfuric acid, *Synth. Met.* 156 (2006) 1052–1056.
- [22] N. Billingham, P. Calvert, P. Foot, F. Mohammad, Stability and degradation of some electrically conducting polymers, *Polym. Degrad. Stab.* 19 (1987) 323–341.
- [23] C. Debiemme-Chouvy, T.T.M. Tran, An insight into the overoxidation of polypyrrole materials, *Electrochem. Commun.* 10 (2008) 947–950.
- [24] F. Beck, P. Braun, M. Oberst, Organic electrochemistry in the solid State: Overoxidation of polypyrrole, *Phys. Chem.* 91 (1987) 967–974.
- [25] A. Pud, Stability and degradation of conducting polymers in electrochemical systems, *Synth. Met.* 66 (1994) 1–18.
- [26] F. Beck, U. Barsch, R. Michaelis, Corrosion of conducting polymers in aqueous media, *J. Electroanal. Chem.* 351 (1993) 169–184.
- [27] I. Fernández, M. Trueba, C. Nunez, J. Rieumont, Some features of the overoxidation of polypyrrole synthesized on austenitic stainless steel electrodes in aqueous nitrate solutions, *Surf. Coat. Technol.* 191 (2005) 134–139.
- [28] Q. Pei, R. Qian, Protonation and deprotonation of polypyrrole chain in aqueous solutions, *Synth. Met.* 45 (1991) 35–48.
- [29] D. Blackwood, M. Josowicz, Work function and spectroscopic studies of interactions between conducting polymers and organic vapors, *J. Phys. Chem.* 95 (1991) 493–502.
- [30] L. Ruangchuay, A. Sirivat, J. Schwank, Electrical conductivity response of polypyrrole to acetone vapor: effect of dopant anions and interaction mechanisms, *Synth. Met.* 140 (2004) 15–21.
- [31] P.N. Bartlett, S.K. Ling-Chung, Conducting polymer gas sensors Part III: Results for four different polymers and five different vapours, *Sens. Actuators* 20 (1989) 287–292.
- [32] M.M. Chehimi, E. Abdeljalil, A study of the degradation and stability of polypyrrole by inverse gas chromatography X-ray photoelectron spectroscopy, and conductivity measurements, *Synth. Met.* 145 (2004) 15–22.
- [33] J.G. Ibanez, A. Alatorre-Ordaz, S. Gutiérrez-Granados, N. Batina, Nanoscale degradation of polypyrrole films under oxidative stress: an atomic force microscopy study and review, *Polym. Degrad. Stab.* 93 (2008) 827–837.
- [34] S. Ghosh, G.A. Bowmaker, R.P. Cooney, J.M. Seakins, Infrared and Raman spectroscopic studies of the electrochemical oxidative degradation of polypyrrole, *Synth. Met.* 95 (1998) 63–67.
- [35] K. Neoh, K. Lau, V. Wong, E. Kang, K. Tan, Structure and degradation behavior of polypyrrole doped with sulfonate anions of different sizes subjected to undoping-redoping cycles, *Chem. Mat.* 8 (1996) 167–172.
- [36] K. Neoh, T. Young, E. Kang, K. Tan, Structural and mechanical degradation of polypyrrole films due to aqueous media and heat treatment and the subsequent redoping characteristics, *J. Appl. Polym. Sci.* 64 (1997) 519–526.
- [37] Y. Li, R. Qian, Electrochemical overoxidation of conducting polypyrrole nitrate film in aqueous solutions, *Electrochim. Acta* 45 (2000) 1727–1731.
- [38] J. Mostany, B.R. Scharifker, Direct microcalorimetric measurement of doping and overoxidation processes in polypyrrole, *Electrochim. Acta* 42 (1997) 291–301.
- [39] H. Xie, M. Yan, Z. Jiang, Transition of polypyrrole from electroactive to electroinactive state investigated by use of in situ FTIR spectroscopy, *Electrochim. Acta* 42 (1997) 2361–2367.
- [40] T.F. Otero, M. Marquez, I.J. Suarez, Polypyrrole: diffusion coefficients and degradation by overoxidation, *J. Phys. Chem. B* 108 (2004) 15429–15433.
- [41] K. Qi, Y. Qiu, Z. Chen, X. Guo, Corrosion of conductive polypyrrole: effects of continuous cathodic and anodic polarisation, *Corros. Sci.* 69 (2013) 376–388.
- [42] K. Qi, Y. Qiu, Z. Chen, X. Guo, Corrosion of conductive polypyrrole: effects of possibly formed galvanic cells, *Corros. Sci.* 80 (2014) 318–330.
- [43] D.S. Park, Y.B. Shim, S.M. Park, Degradation kinetics of polypyrrole films, *J. Electrochem. Soc.* 140 (1993) 2749–2752.
- [44] D.S. Park, Y.B. Shim, S.M. Park, Degradation of electrochemically prepared polypyrrole in aqueous sulfuric acid, *J. Electrochem. Soc.* 140 (1993) 609–614.
- [45] R. Mazeikiene, A. Malinauskas, Kinetics of the electrochemical degradation of polypyrrole, *Polym. Degrad. Stab.* 75 (2002) 255–258.
- [46] A. Malinauskas, R. Holze, In situ UV–vis spectroelectrochemical study of polyaniline degradation, *J. Appl. Polym. Sci.* 73 (1999) 287–294.
- [47] R. Mazeikiene, A. Malinauskas, Kinetic study of the electrochemical degradation of polyaniline, *Synth. Met.* 123 (2001) 349–354.
- [48] A. Malinauskas, R. Holze, A UV–visible spectroelectrochemical study of the electropolymerisation of N-benzylaniline, *J. Solid State Chem.* 3 (1999) 429–436.
- [49] Sheng Li, Yubing Qiu, Xingpeng Guo, Influence of doping anions on the ion exchange behavior of polypyrrole, *J. Appl. Polym. Sci.* 114 (2009) 2307–2314.
- [50] K. Qi, Y. Qiu, Z. Chen, X. Guo, Corrosion of conductive polypyrrole: effects of environmental factors, electrochemical stimulation, and doping anions, *Corros. Sci.* 60 (2012) 50–58.
- [51] A. Kumar, R.K. Singh, K. Agarwal, H.K. Singh, P. Srivastava, R. Singh, Effect of p(toluenesulfonate) on inhibition of overoxidation of polypyrrole, *J. Appl. Polym. Sci.* 130 (2013) 434–442.
- [52] T. Otero, I. Boyano, Characterization of polypyrrole degradation by the conformational relaxation model, *Electrochim. Acta* 51 (2006) 6238–6242.
- [53] J. Molina, J. Fernández, A. Del Rio, R. Lapuente, J. Bonastre, F. Cases, Stability of conducting polyester/polypyrrole fabrics in different pH solutions. Chemical and electrochemical characterization, *Polym. Degrad. Stab.* 95 (2010) 2574–2583.
- [54] L. Yongfang, Q. Renyuan, On the nature of redox processes in the cyclic voltammetry of polypyrrole nitrate in aqueous solutions, *J. Electroanal. Chem.* 362 (1993) 267–272.
- [55] C. Ho, I. Raistrick, R. Huggins, Application of AOC techniques to the study of lithium diffusion in tungsten trioxide thin films, *J. Electrochem. Soc.* 127 (1980) 343–350.
- [56] J. Mostany, B.R. Scharifker, Impedance spectroscopy of undoped, doped and overoxidized polypyrrole films, *Synth. Met.* 87 (1997) 179–185.
- [57] A. Hallik, A. Alumaa, J. Tamm, V. Sammelselg, M. Väärtnõu, A. Jänes, E. Lust, Analysis of electrochemical impedance of polypyrrole|sulfate and polypyrrole|perchlorate films, *Synth. Met.* 156 (2006) 488–494.
- [58] L. Marchesi, F. Simoes, L. Pocrifka, E. Pereira, Investigation of polypyrrole degradation using electrochemical impedance spectroscopy, *J. Phys. Chem. B* 115 (2011) 9570–9575.
- [59] G. Garcia-Belmonte, J. Bisquert, Impedance analysis of galvanostatically synthesized polypyrrole films. Correlation of ionic diffusion and capacitance parameters with the electrode morphology, *Electrochim. Acta* 47 (2002) 4263–4272.
- [60] R. Rajagopalan, J.O. Iroh, Characterization of polyaniline–polypyrrole composite coatings on low carbon steel: a XPS and infrared spectroscopy study, *Appl. Surf. Sci.* 218 (2003) 58–69.
- [61] Y. Li, R. Qian, Stability of conducting polymers from the electrochemical point of view, *Synth. Met.* 53 (1993) 149–154.
- [62] K. Doblhofer, The non-metallic character of solvated conducting polymers, *J. Electroanal. Chem.* 331 (1992) 1015–1027.
- [63] J. Dumańska, K. Maksymiuk, Studies on spontaneous charging/discharging processes of polypyrrole in aqueous electrolyte solutions, *Electroanal.* 13 (2001) 567–573.
- [64] A. Lewenstam, J. Bobacka, A. Ivaska, Mechanism of ionic and redox sensitivity of p-type conducting polymers, *J. Electroanal. Chem.* 368 (1994) 23–31.

报告编号: 2025-0119

# 论文收录引用

## 检索证明报告



中华人民共和国教育部科技查新站 (SH01)

论文作者：王瑶

委托单位：中国石油大学（北京）

论文发表年限：2017-2025 年

检索数据库：

SCI-EXPANDED	2001- present	网络版
--------------	---------------	-----

检索结果：（作者提供文章）

1) SCI-E 收录：有 9 篇被收录

（详细结果见附件）

特此证明！

检索报告人：

王瑶





# 附件 1 SCI-E 收录情况

## 第 1 条, 共 9 条

标题: Difluoroester solvents toward fast-rate anion-intercalation lithium metal batteries under extreme conditions

作者: Wang, Y (Wang, Yao); Dong, SY (Dong, Shuyu); Gao, YF (Gao, Yifu); Lee, PK (Lee, Pui-Kit); Tian, Y (Tian, Yao); Meng, YF (Meng, Yuefeng); Hu, X (Hu, Xia); Zhao, X (Zhao, Xin); Li, BH (Li, Baohua); Zhou, D (Zhou, Dong); Kang, FY (Kang, Feiyu)

来源出版物: NATURE COMMUNICATIONS 卷: 15 期: 1 文献号: 5408 DOI: 10.1038/s41467-024-49795-9 Published Date: 2024 JUN 26

Web of Science 核心合集中的 "被引频次": 6

被引频次合计: 7

入藏号: WOS:001256234400036

文献类型: Article

地址: [Wang, Yao; Gao, Yifu; Tian, Yao; Meng, Yuefeng; Hu, Xia; Zhao, Xin; Li, Baohua; Zhou, Dong; Kang, Feiyu] Tsinghua Univ, Tsinghua Shenzhen Int Grad Sch, Shenzhen 518055, Peoples R China.

[Dong, Shuyu; Lee, Pui-Kit] City Univ Hong Kong, Sch Energy & Environm, Hong Kong 999077, Peoples R China.

通讯作者地址: Zhou, D; Kang, FY (通讯作者), Tsinghua Univ, Tsinghua Shenzhen Int Grad Sch, Shenzhen 518055, Peoples R China.

电子邮件地址: zhou.d@sz.tsinghua.edu.cn; fykang@tsinghua.edu.cn

eISSN: 2041-1723

2023 年期刊的影响因子: 14.7

2023 年期刊的中科院分区 (升级版): 大类 综合性期刊 | TOP

## 第 2 条, 共 9 条

标题: Fluorine Chemistry in Rechargeable Batteries: Challenges, Progress, and Perspectives

作者: Wang, Y (Wang, Yao); Yang, X (Yang, Xu); Meng, YF (Meng, Yuefeng); Wen, ZX (Wen, Zuxin); Han, R (Han, Ran); Hu, X (Hu, Xia); Sun, B (Sun, Bing); Kang, FY (Kang, Feiyu); Li, BH (Li, Baohua); Zhou, D (Zhou, Dong); Wang, CS (Wang, Chunsheng); Wang, GX (Wang, Guoxiu)

来源出版物: CHEMICAL REVIEWS 卷: 124 期: 5 页: 3494-3589 DOI: 10.1021/acs.chemrev.3c00826 Early Access Date: MAR 2024 Published Date: 2024 MAR 13

Web of Science 核心合集中的 "被引频次": 48

被引频次合计: 48

入藏号: WOS:001184909400001

文献类型: Review

地址: [Wang, Yao; Meng, Yuefeng; Wen, Zuxin; Han, Ran; Hu, Xia; Kang, Feiyu; Li, Baohua; Zhou, Dong] Tsinghua Univ, Tsinghua Shenzhen Int Grad Sch, Shenzhen 518055, Peoples R China.

[Yang, Xu; Sun, Bing; Wang, Guoxiu] Univ Technol Sydney, Fac Sci, Ctr Clean Energy Technol, Sch Math & Phys Sci, Sydney, NSW 2007, Australia.

[Wang, Chunsheng] Univ Maryland, Dept Chem & Biomol Engn, College Pk, MD 20742 USA.

通讯作者地址: Li, BH; Zhou, D (通讯作者), Tsinghua Univ, Tsinghua Shenzhen Int Grad Sch, Shenzhen 518055, Peoples R China.

Wang, GX (通讯作者), Univ Technol Sydney, Fac Sci, Ctr Clean Energy Technol, Sch Math & Phys Sci,

Sydney, NSW 2007, Australia.

Wang, CS (通讯作者), Univ Maryland, Dept Chem & Biomol Engh, College Pk, MD 20742 USA.

电子邮件地址: libh@sz.tsinghua.edu.cn; zhou.d@sz.tsinghua.edu.cn; cswang@umd.edu;  
Guoxiu.Wang@uts.edu.au

ISSN: 0009-2665

2023 年期刊的影响因子: 51.5

2023 年期刊的中科院分区 (升级版): 大类 化学 | TOP

### 第 3 条, 共 9 条

标题: Electrolyte design for rechargeable anion shuttle batteries

作者: Wang, Y (Wang, Yao); Yang, X (Yang, Xu); Zhang, ZJ (Zhang, Zhijia); Hu, X (Hu, Xia); Meng, YF (Meng, Yuefeng); Wang, X (Wang, Xia); Zhou, D (Zhou, Dong); Liu, H (Liu, Hao); Li, BH (Li, Baohua); Wang, GX (Wang, Guoxiu)

来源出版物: ESCIENCE 卷: 2 期: 6 页: 573-590 DOI: 10.1016/j.escl.2022.10.003 Published Date: 2022 NOV

Web of Science 核心合集中的 "被引频次": 31

被引频次合计: 30

入藏号: WOS:001078544300001

文献类型: Review

地址: [Wang, Yao; Hu, Xia; Meng, Yuefeng; Zhou, Dong; Li, Baohua] Tsinghua Univ, Tsinghua Shenzhen Int Grad Sch, Shenzhen 518055, Peoples R China.

[Yang, Xu; Zhang, Zhijia; Liu, Hao; Wang, Guoxiu] Univ Technol Sydney, Fac Sci, Ctr Clean Energy Technol, Sch Math & Phys Sci, Sydney, NSW 2007, Australia.

[Wang, Xia] Max Planck Inst Chem Phys Solids, Topol Catalysis Grp, Nothnitzer Str 40, D-01187 Dresden, Germany.

通讯作者地址: Zhou, D; Li, BH (通讯作者), Tsinghua Univ, Tsinghua Shenzhen Int Grad Sch, Shenzhen 518055, Peoples R China.

Wang, GX (通讯作者), Univ Technol Sydney, Fac Sci, Ctr Clean Energy Technol, Sch Math & Phys Sci, Sydney, NSW 2007, Australia.

电子邮件地址: zhou.d@sz.tsinghua.edu.cn; libh@sz.tsinghua.edu.cn; Guoxiu.Wang@uts.edu.au

eISSN: 2667-1417

2023 年期刊的影响因子: 42.9

2023 年期刊的 JCR 分区: ELECTROCHEMISTRY 其中 ESCI 版本 1/45 Q1

MATERIALS SCIENCE, MULTIDISCIPLINARY 其中 ESCI 版本 3/439 Q1

### 第 4 条, 共 9 条

标题: An All-Fluorinated Electrolyte Toward High Voltage and Long Cycle Performance Dual-Ion Batteries

作者: Wang, Y (Wang, Yao); Zhang, YJ (Zhang, Yanjun); Dong, SY (Dong, Shuyu); Zhou, WC (Zhou, Wenchong); Lee, PK (Lee, Pui-Kit); Peng, ZH (Peng, Zehua); Dang, CQ (Dang, Chaoqun); Sit, PHL (Sit, Patrick H-L); Guo, JP (Guo, Junpo); Yu, DYW (Yu, Denis Y. W.)

来源出版物: ADVANCED ENERGY MATERIALS 卷: 12 期: 19 文献号: 2103360 DOI: 10.1002/aenm.202103360 Early Access Date: FEB 2022 Published Date: 2022 MAY

Web of Science 核心合集中的 "被引频次": 49

被引频次合计: 52

入藏号: WOS:000752947400001

文献类型: Article

地址: [Wang, Yao; Zhang, Yanjun; Dong, Shuyu; Zhou, Wenchong; Lee, Pui-Kit; Peng, Zehua; Sit, Patrick H-L; Yu, Denis Y. W.] City Univ Hong Kong, Sch Energy & Environm, Hong Kong, Peoples R China.

[Dang, Chaoqun] City Univ Hong Kong, Dept Mech Engrn, Hong Kong, Peoples R China.

[Guo, Junpo] Univ Macau, Inst Appl Phys & Mat Engrn, Macau 999078, Peoples R China.

[Yu, Denis Y. W.] City Univ Hong Kong, Ctr Super Diamond & Adv Films COSDAF, Hong Kong 999077, Peoples R China.

通讯作者地址: Yu, DYW (通讯作者), City Univ Hong Kong, Sch Energy & Environm, Hong Kong, Peoples R China.

Yu, DYW (通讯作者), City Univ Hong Kong, Ctr Super Diamond & Adv Films COSDAF, Hong Kong 999077, Peoples R China.

电子邮件地址: denisyu@cityu.edu.hk

ISSN: 1614-6832

2023 年期刊的影响因子: 24.4

2023 年期刊的中科院分区 (升级版): 大类 材料科学 1 TOP

#### 第 5 条, 共 9 条

标题: Ultrafast Charging and Stable Cycling Dual-Ion Batteries Enabled via an Artificial Cathode-Electrolyte Interface

作者: Wang, Y (Wang, Yao); Zhang, YJ (Zhang, Yanjun); Wang, S (Wang, Shuo); Dong, SY (Dong, Shuyu); Dang, CQ (Dang, Chaoqun); Hu, WC (Hu, Weichen); Yu, DYW (Yu, Denis Y. W.)

来源出版物: ADVANCED FUNCTIONAL MATERIALS 卷: 31 期: 29 文献号: 2102360 DOI: 10.1002/adfm.202102360 Early Access Date: MAY 2021 Published Date: 2021 JUL

Web of Science 核心合集中的 "被引频次": 61

被引频次合计: 64

入藏号: WOS:000646201700001

文献类型: Article

地址: [Wang, Yao; Zhang, Yanjun; Wang, Shuo; Dong, Shuyu; Hu, Weichen; Yu, Denis Y. W.] City Univ Hong Kong, Sch Energy & Environm, Hong Kong 999077, Peoples R China.

[Dang, Chaoqun] City Univ Hong Kong, Dept Mech Engrn, Hong Kong 999077, Peoples R China.

[Yu, Denis Y. W.] City Univ Hong Kong, Ctr Super Diamond & Adv Films COSDAF, Hong Kong 999077, Peoples R China.

通讯作者地址: Yu, DYW (通讯作者), City Univ Hong Kong, Sch Energy & Environm, Hong Kong 999077, Peoples R China.

Yu, DYW (通讯作者), City Univ Hong Kong, Ctr Super Diamond & Adv Films COSDAF, Hong Kong 999077, Peoples R China.

电子邮件地址: denisyu@cityu.edu.hk

ISSN: 1616-301X

2023 年期刊的影响因子: 18.5

2023 年期刊的中科院分区 (升级版): 大类 材料科学 1 TOP

#### 第 6 条, 共 9 条

标题: Vanadium hexacyanoferrate with two redox active sites as cathode material for aqueous Zn-ion batteries

作者: Zhang, YJ (Zhang, Yanjun); Wang, Y (Wang, Yao); Lu, L (Lu, Liang); Sun, CW (Sun, Chunwen); Yu, DYW (Yu, Denis Y. W.)



来源出版物: JOURNAL OF POWER SOURCES 卷: 484 文献号: 229263 DOI: 10.1016/j.jpowsour.2020.229263 Published Date: 2021 FEB 1

Web of Science 核心合集中的“被引频次”: 54

被引频次合计: 55

入藏号: WOS:000605008600006

文献类型: Article

地址: [Zhang, Yanjun; Wang, Yao; Yu, Denis Y. W.] City Univ Hong Kong, Sch Energy & Environm, Kowloon, Tat Chee Ave, Hong Kong, Peoples R China.

[Yu, Denis Y. W.] City Univ Hong Kong, Ctr Super Diamond & Adv Films COSDAF, Kowloon, Tat Chee Ave, Hong Kong, Peoples R China.

[Lu, Liang; Sun, Chunwen] Chinese Acad Sci, Beijing Inst Nanoenergy & Nanosyst, Beijing 100083, Peoples R China.

通讯作者地址: Yu, DYW (通讯作者), City Univ Hong Kong, Ctr Super Diamond & Adv Films COSDAF, Kowloon, Tat Chee Ave, Hong Kong, Peoples R China.

Sun, CW (通讯作者), Chinese Acad Sci, Beijing Inst Nanoenergy & Nanosyst, Beijing 100083, Peoples R China.

电子邮件地址: sunchunwen@binn.cas.cn; denisyu@cityu.edu.hk

ISSN: 0378-7753

2023 年期刊的影响因子: 8.1

2023 年期刊的中科院分区 (升级版): 大类 工程技术 2 TOP

#### 第 7 条, 共 9 条

标题: Engineering cathode-electrolyte interface of graphite to enable ultra long-cycle and high-power dual-ion batteries

作者: Wang, Y (Wang, Yao); Zhang, YJ (Zhang, Yanjun); Duan, QH (Duan, Qiaohui); Lee, PK (Lee, Pui-Kit); Wang, S (Wang, Shuo); Yu, DYW (Yu, Denis Y. W.)

来源出版物: JOURNAL OF POWER SOURCES 卷: 471 文献号: 228466 DOI: 10.1016/j.jpowsour.2020.228466 Published Date: 2020 SEP 30

Web of Science 核心合集中的“被引频次”: 70

被引频次合计: 71

入藏号: WOS:000551511800001

文献类型: Article

地址: [Wang, Yao; Duan, Qiaohui; Lee, Pui-Kit; Wang, Shuo; Yu, Denis Y. W.] City Univ Hong Kong, Sch Energy & Environm, Hong Kong 999077, Peoples R China.

[Zhang, Yanjun] Peking Univ, Sch Adv Mat, Shenzhen Grad Sch, Shenzhen 518055, Peoples R China.

[Yu, Denis Y. W.] City Univ Hong Kong, Ctr Super Diamond & Adv Films COSDAF, Hong Kong 999077, Peoples R China.

通讯作者地址: Yu, DYW (通讯作者), G5702, Acad 1, Tat Chee Ave, Hong Kong 999077, Peoples R China.

电子邮件地址: denisyu@cityu.edu.hk

ISSN: 0378-7753

2023 年期刊的影响因子: 8.1

2023 年期刊的中科院分区 (升级版): 大类 工程技术 2 TOP

#### 第 8 条, 共 9 条

标题: Unlocking the True Capability of Graphite-Based Dual-Ion Batteries with Ethyl Methyl Carbonate

Electrolyte

作者: Wang, Y (Wang, Yao); Wang, S (Wang, Shuo); Zhang, YJ (Zhang, Yanjun); Lee, PK (Lee, Pui-Kit); Yu, DYW (Yu, Denis Y. W.)

来源出版物: ACS APPLIED ENERGY MATERIALS 卷: 2 期: 10 页: 7512-7517 DOI: 10.1021/acsami.9b01499 Published Date: 2019 OCT

Web of Science 核心合集中的 "被引频次": 14

被引频次合计: 36

入藏号: WOS:000502688800062

文献类型: Article

地址: [Wang, Yao; Wang, Shuo; Zhang, Yanjun; Lee, Pui-Kit; Yu, Denis Y. W.] City Univ Hong Kong, Sch Energy & Environm, Kowloon, Tat Chee Ave, Hong Kong, Peoples R China.

[Yu, Denis Y. W.] City Univ Hong Kong, Ctr Super Diamond & Adv Films, Kowloon, Tat Chee Ave, Hong Kong, Peoples R China.

通讯作者地址: Yu, DYW (通讯作者), City Univ Hong Kong, Sch Energy & Environm, Kowloon, Tat Chee Ave, Hong Kong, Peoples R China.

Yu, DYW (通讯作者), City Univ Hong Kong, Ctr Super Diamond & Adv Films, Kowloon, Tat Chee Ave, Hong Kong, Peoples R China.

电子邮件地址: denisyu@cityu.edu.hk

ISSN: 2574-0962

2023 年期刊的影响因子: 5.5

2023 年期刊的中科院分区 (升级版): 大类 材料科学 3

第 9 条, 共 9 条

标题: Corrosion of polypyrrole: Kinetics of chemical and electrochemical processes in NaOH solutions

作者: Wang, Y (Wang, Yao); Qiu, YB (Qiu, Yubing); Chen, ZY (Chen, Zhenyu); Guo, XP (Guo, Xingpeng)

来源出版物: CORROSION SCIENCE 卷: 118 页: 96-108 DOI: 10.1016/j.corsci.2017.01.023 Published Date: 2017 APR

Web of Science 核心合集中的 "被引频次": 32

被引频次合计: 33

入藏号: WOS:000396969800009

文献类型: Article

地址: [Wang, Yao; Qiu, Yubing; Chen, Zhenyu; Guo, Xingpeng] Huazhong Univ Sci & Technol, Sch Chem & Chem Engrt, Wuhan 430074, Peoples R China.

[Chen, Zhenyu; Guo, Xingpeng] Huazhong Univ Sci & Technol, Minist Educ, Key Lab Mat Chem Energy Convers & Storage, Wuhan, Peoples R China.

[Qiu, Yubing] Hubei Key Lab Mat Chem & Serv Failure, Wuhan 430074, Peoples R China.

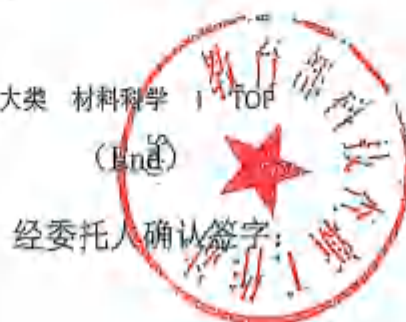
通讯作者地址: Qiu, YB (通讯作者), Huazhong Univ Sci & Technol, Sch Chem & Chem Engrt, Wuhan 430074, Peoples R China.

电子邮件地址: qiuyubin@mail.hust.edu.cn

ISSN: 0010-938X

2023 年期刊的影响因子: 7.4

2023 年期刊的中科院分区 (升级版): 大类 材料科学 1



论文作者： 王瑶

委托单位： 中国石油大学（北京）

论文发表年限： 2017-2025 年

检索数据库：

SCI-EXPANDED	2001- present	网络版
--------------	---------------	-----

检索结果：（作者提供文章）

1) SCI-E 收录：有 9 篇被收录

（详细结果见附件）

特此证明！

检索报告人：王瑶





# 国家自然科学基金资助项目批准通知

## (包干制项目)

王瑶 先生/女士:

根据《国家自然科学基金条例》、相关项目管理办法规定和专家评审意见,国家自然科学基金委员会(以下简称自然科学基金委)决定资助您申请的项目。项目批准号: 22309102, 项目名称: 高功率、宽温域双离子电池用羧酸酯基电解液设计及界面特性研究, 资助经费: 30.00万元, 项目起止年月: 2024年01月至 2026年12月, 有关项目的评审意见及修改意见附后。

请您尽快登录科学基金网络信息系统(<https://grants.nsfc.gov.cn>), **认真阅读《国家自然科学基金资助项目计划书填报说明》并按要求填写《国家自然科学基金资助项目计划书》(以下简称计划书)**。对于有修改意见的项目,请您按修改意见及时调整计划书相关内容;如您对修改意见有异议,须在电子版计划书报送截止日期前向相关科学处提出。

请您将电子版计划书通过科学基金网络信息系统(<https://grants.nsfc.gov.cn>)提交,由依托单位审核后提交至自然科学基金委。自然科学基金委审核未通过者,将退回的电子版计划书修改后再行提交;审核通过者,打印纸质版计划书(一式两份,双面打印)并在项目负责人承诺栏签字,由依托单位在承诺栏加盖依托单位公章,且将申请书纸质签字盖章页订在其中一份计划书之后,一并报送至自然科学基金委项目材料接收工作组。纸质版计划书应当保证与审核通过的电子版计划书内容一致。**自然科学基金委将对申请书纸质签字盖章页进行审核,对存在问题的,允许依托单位进行一次修改或补齐。**

向自然科学基金委提交电子版计划书、报送纸质版计划书并补交申请书纸质签字盖章页截止时间节点如下:

1. **2023年9月7日16点:** 提交电子版计划书的截止时间;
2. **2023年9月14日16点:** 提交修改后电子版计划书的截止时间;
3. **2023年9月21日:** 报送纸质版计划书(一式两份,其中一份包含申请书纸质签字盖章页)的截止时间。
4. **2023年10月7日:** 报送修改后的申请书纸质签字盖章页的截止时间。

请按照以上规定及时提交电子版计划书，并报送纸质版计划书和申请书纸质签字盖章页，逾期不报计划书或申请书纸质签字盖章页且未说明理由的，视为自动放弃资助；未按要求修改或逾期提交申请书纸质签字盖章页者，将视情况给予暂缓拨付经费等处理。

附件：项目评审意见及修改意见表

国家自然科学基金委员会

2023年8月24日





二、请评述申请项目所关注问题的科学价值以及对相关前沿领域的潜在贡献。

双离子电池具有工作电压高、成本低等优点，具有重要的研究与应用价值。其中，电解液是影响电池性能的重要因素。项目聚焦宽液程、高电导的羧酸酯基电解液进行改性研究，将溶剂分子结构设计及动力学调控作为拟解决的关键科学问题。所关注的问题具有较强的科学价值，研究结果有望为双离子电池电解液设计提供有价值的借鉴与参考。

三、请评述申请人的创新潜力与研究方案的可行性。

申请人近年来围绕双离子电池电解液开展了系列工作，发表了多篇高水平研究论文，具有较扎实的研究基础。此外，项目研究思路清晰，方案可行，研究工作有相应的平台支撑，项目申请人有能力、条件按计划推进研究工作，有望取得一定成果。

四、其他建议

建议重点针对电解液某方面的明显不足，加强针对性论述并细化研究方案；同时建议项目申请书中不对项目本身进行主观评价。

修改意见：

化学科学部

2023年8月24日



# 资助证书

清华大学

王瑶

(博士后编号: 307755 )

入选 2022年度博士后国(境)外交流项目

引进项目

。 资助编号: YJ20220134 。

特颁此证。

This certificate hereby certifies that its holder has been awarded an International  
Postdoctoral Exchange Program Fellowship .

中国博士后科学基金会

2024年 11 月 04日





# 资助证书

清华大学 王瑶 (全国博管会编号:307755) 获得中国博士后科学基金  
第71批面上资助二等。 资助编号: 2022M711788

特颁此证。

The certificate certifies its holder is awarded the fellowship of China Postdoctoral  
Science Foundation .

中国博士后科学基金会

2022 年 06 月 30 日





基本科研业务费优秀青年学者项目追加预算审批表

项目名称	宽温域适配型锂基二次电池电解液设计及界面反应机理研究		
项目负责人	王瑶	所在单位	理学院
项目执行期	顺延至2028年12月31日	项目编号	ZX20250051
追加经费	40万元	经费卡号	01JB20250041
总项目经费	60万元		

1、预算表

序号	科目名称	金额 (万元)	备注（此列不可修改）
1	设备费	40.4	不可购买大型设备及家具、通用办公设备。
2	材料费	4	用于购买实验试剂、耗材、元器件、办公耗材（不超过总经费的5%）等。
3	测试化验加工费	4	不可校内测试转账；超过3万元需签订合同，按外协项目管理流程执行。
4	会议、差旅费	5	按照财务标准编写，不得支出餐费、汽油费。北京市内交通不超过总经费的10%。
5	国际合作与交流费	3	结合考核指标必须列支，邀请专家来访不得支出餐费、劳务费。
6	出版/文献/信息传播/知识产权事务费	0	不得购买通用性操作系统、办公软件等，不得列支电话通讯费。
7	劳务费	3.6	可用于支付给无工资性收入的在校研究生，不超过总经费的30%。
合计		60万元	

2、预算计算依据及说明

(1) 设备费					
序号	名称	单价/万元	数量	小计/万元	备注说明
1	高低温试验箱	3.3	1	3.3	合肥巨阙电子，温度范围-60~150℃
2	分析天平	1	1	1	欧莱博MF1035C
3	电动扣式电池封口机	1.6	1	1.6	合肥科晶MSK-E110

请打印一式三份，签章齐全。项目负责人、学院、科技处各留存一份。

4	新威电池测试仪	3.4	1	3.4	新威Neware,112个扣电通道
5	法国 Bio-logic 多通道电化学工作站	30.4	1	30.4	SP-200高精度多通道电化学工作站, 购买设备必要性: 多通道可以同时原位测试不同电池的电化学行为, EIS测试更精准, 频率测试范围: 10uHZ-7MHz; 电流分辨率很高: <0.004%, 这些高分辨率仪器可以满足本项目宽温域电池电解液在不同温度下离子传输、离子扩散系数、可逆性等测试的精密要求
6	打印一体机	0.2	1	0.2	联想CS1831
7	台式电脑	0.5	1	0.5	华硕 RTX4060+i5 14600KF
合计				40.4万元	

## (2) 材料费

材料名称	单价/万元	数量	小计(万元)
电池壳	0.11/1000套	6	0.66
PAA高分子量粘结剂	0.3	1	0.3
锂盐	0.2	4	0.8
碳酸乙烯酯等溶剂	0.08	8	0.64
氟化定制试剂	0.16	10	1.6
合计	4万元		

## (3) 测试化验加工费

电池材料高精度、多维度(原位)表征测试, 比如TOF-SIMS、XPS、HR-TEM、原位Raman、原位XRD等, 每篇文章花费约1.3-1.4万元左右, 共计4万元。

测试表征名称	单价/万元	次数	小计(万元)
TOF-SIMS	0.3	4	1.2

请打印一式三份, 签章齐全。项目负责人、学院、科技处各留存一份。

XPS	0.2	4	0.8
HR-TEM	0.2	4	0.8
原位Raman	0.2	3	0.6
原位XRD	0.2	3	0.6
合计	4万元		

#### (4) 会议、差旅费

去清华大学深圳国际研究生院, 1人·次, 每次7天, (住宿费320元+补助180元) × 7天=0.35万元, 往返路费飞机 (北京到深圳, 1500元×2=0.3万元, 共0.65万元), 出差4-5次, 共计3万元。

北京市内交通费: 2万元。

会议、差旅费合计: 3万+2万=5万元。

#### (5) 国际合作与交流费

去美国/加拿大参加境外国际会议, 往返飞机票: 1.5万元, (住宿费150美元+补助包干100美元) × 8天×汇率7.3≈1.5万元, 共3万元。

#### (6) 出版/文献/信息传播/知识产权事务费

0万元。

#### (7) 劳务费

两个硕士生, 每个月劳务费 500 元/人, 3 年共: ((500 元/月×12 个月)/人×2 人)/年×3 年=3.6 万元

### 3、考核指标

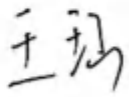

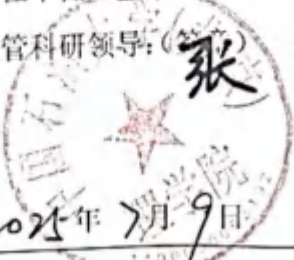

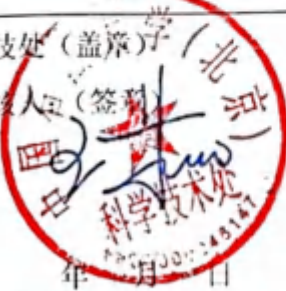
考核内容	数量	备注说明
论文发表	3	Angew. Chem. Int. Ed., Adv. Energy Mater., Adv. Funct. Mater., Energy Environ. Sci., Electrochimica Acta, J. Power Sources, Chemical Engineering Journal 等
专利		
国际合作交流	1	ECS (Electrochemical Society) 国际会议, MRS

请打印一式三份, 签章齐全。项目负责人、学院、科技处各留存一份。



		(Materials Research Society) 秋季会议, International Meeting on Lithium Batteries (IMLB) 国际锂电池会议, 能源材料前沿国际学术研 讨会 (新加坡会场)
高级别项目		国家自然科学基金面上基金
个人成长与获奖		
其他		

#### 4、签字盖章

负责人: (签字)    2025 年 7 月 9 日	所在单位 (盖章) 主管科研领导: (签字)   2025 年 7 月 9 日	科技处 (盖章) 审核人: (签字)   年 月 日
--	---	--

请打印一式三份, 签章齐全。项目负责人、学院、科技处各留存一份。